AD-A110 109   ARMY RESEARCH OFFICE RESEARCH TRIANGLE PARK NC   F/G 12/1
                TRANSACTIONS OF THE TWENTY-SEVENTH CONFERENCE OF ARMY MATHEMATI--ETC(U)
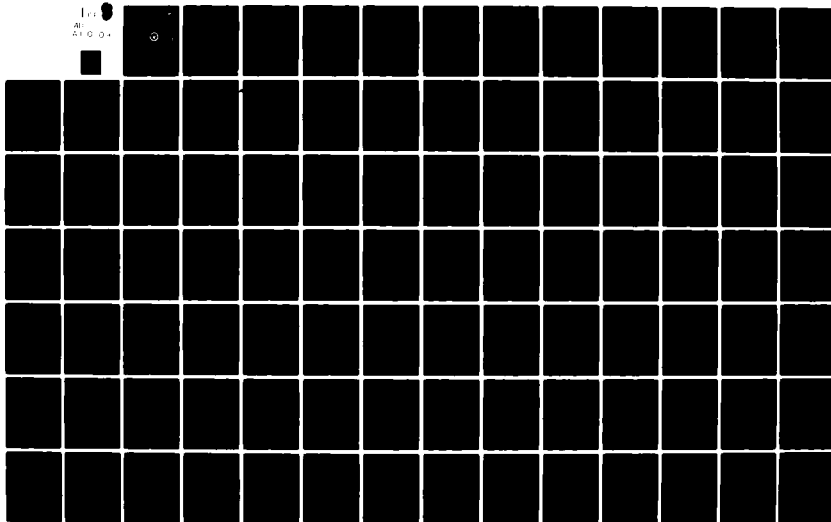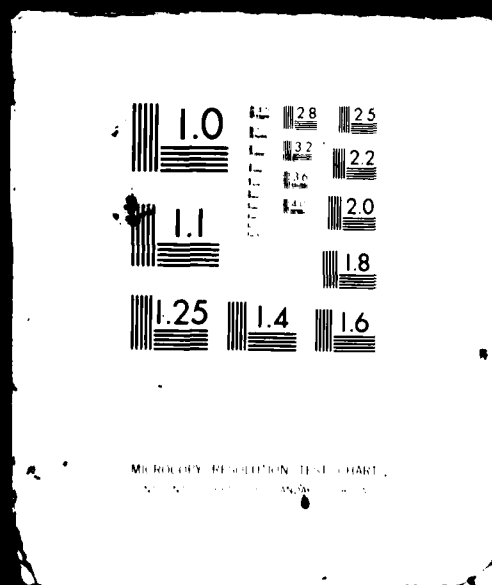   JAN 82
UNCLASSIFIED   ARO-82-1   NL

AD-
A110109

1.0
1.1
1.25 1.4 1.6
2.8 2.5
3.2 2.2
3.6
2.0
1.8

MICROCOPY RESOLUTION TEST CHART

ARO Report 82-1

LEVEL

TRANSACTIONS OF THE TWENTY - SEVENTH

CONFERENCE OF ARMY MATHEMATICIANS

AD A110109

DTIC FILE COPY

DTIC JAN 25 1982 H

0125 82030

U. S. ARMY RESEARCH OFFICE

Report No. 82-1

January 1982

TRANSACTIONS OF THE TWENTY-SEVENTH CONFERENCE

OF ARMY MATHEMATICIANS

Sponsored by the Army Mathematics Steering Committee

Host

United States Military Academy

West Point, New York

10-12 June 1981

FOREWORD

The Transactions of the Twenty-Seventh Conference of Army Mathematicians are being issued in order to preserve in print some of the scientific developments presented in the invited addresses and in the contributed papers. These conferences are sponsored by the Army Mathematics Steering Committee (AMSC) on behalf of the Chief of Research, Development and Acquisition. Members of this committee request that the guest lecturers be internationally known researchers who are presently active in scientific fields that are of current interest. They feel that the addresses by the invited speakers as well as the contributed papers by Army personnel will help fulfill the main purpose for holding these conferences, namely to stimulate the interchange of scientific information among the scientists attending said meetings.

Colonel Harvey H. Perritt, Jr., Chief of Staff/Deputy Post Commander, in a letter under date of 2 October 1980 to Dr. Jagdish Chandra, Chairman of the AMSC, issued the formal invitation to hold the 27th Conference of Army Mathematicians at the U. S. Military Academy. His letter stated that his Command would be pleased to host this meeting on the dates 10-12 June 1981. He assigned Colonel Jack M. Pollin to act as Chairperson for local arrangements. Captain Gordon Dietrick and Bard Mansager were assigned Project Officers to coordinate administrative details. Those in attendance at this conference would like to thank these gentlemen for all their efforts to make this an enjoyable and smooth running conference, and for providing excellent physical facilities for the conduction of this meeting.

The theme of this meeting was "Combustion and Explosive Dynamics". This is currently a very active area of research, which is also of great importance to the Army. This year the planned program of the conference consisted of three parts, namely: (a) Four one-hour invited addresses; (b) Ten thirty minute solicited addresses. These solicited papers represented an amplification of the theme set by the guest lecturers; and (c) Contributed papers by Army and other scientific personnel. The names of the invited speakers are noted below:

Speaker and Institution	Title
Professor David Kassoy University of Colorado	Gas Dynamics Aspects of Thermal Explosions
Professor Andrew Majda University of Cal-Berkeley	A Theory for the Formation of Mach Stems in Reacting Shock Fronts
Professor Martin Sichel University of Michigan	Modeling of Gaseous and Heterogeneous Detonation Phenomena
Professor F. A. Williams University of Cal-San Diego	Use of Activation-Energy Asymptotics for Reacting Flows

We are sorry to say that Professor Andrew Majda was unable to attend this meeting.

iii

The success of the conference was due to many individuals, the active and enthusiastic members of the audience, the chairpersons, and the many speakers. The members of the AMSC were pleased with the fact that most of the speakers were able to find time to prepare papers for these Transactions. These research articles will enable many persons that were not able to attend the symposium to profit by these contributions to the scientific literature.

TABLE OF CONTENTS*

*This Table of Contents contains only the papers that are published in this technical manual. For a list of all papers presented at the Twenty-Seventh Conference of Army Mathematicians, see the Program of the meeting.

27th CONFERENCE OF ARMY MATHEMATICIANS

Tuesday
9 June 1981

1800-2000   Registration   Hotel Thayer

Wednesday
10 June 1981

0815-0845   Registration   Room 220, Bartlett Hall

0845-0900   Opening Remarks   Room 220, Bartlett Hall

0900-1000   <u>GENERAL SESSION I</u>   Room 220, Bartlett Hall

    CHAIRPERSON - Dr. Edward W. Ross, U.S. Army Natick
                Research and Development Command, Natick, Massachusetts

    SPEAKER   - Professor F.A. Williams, University of
               California-San Diego, La Jolla, California

    TITLE   - USE OF ACTIVATION-ENERGY ASYMPTOTICS FOR REACTING FLOWS

1000-1015   Break

1015-1215   <u>SPECIAL SESSION A</u>   Room 220, Bartlett Hall

    CHAIRPERSON - Dr. Douglas E. Kooker, Ballistic Research Laboratory,
               Aberdeen Proving Ground, Maryland

MULTISCALE METHOD AND ACTIVATION ENERGY ASYMPTOTICS FOR PREMIXED
TURBULENT FLAME

Professor Paul Clavin, Universite de Provence, France

ELEMENTARY CHEMISTRY IN THE MODELING OF ONE DIMENSIONAL COMBUSTION
SYSTEMS

Drs. J.M. Heimerl and T.P. Coffee, Ballistic Research Laboratory,
Aberdeen Proving Ground, Maryland

PULSATING FLAMES

Professor Bernard J. Matkowsky, Northwestern University, Evanston,
Illinois

COMPUTATIONAL NEEDS IN THE PHYSICS AND CHEMISTRY OF REACTIVE FLOWS

Drs. Gentner, Norman Slagg, and Barry Fishburn, US Army Armament Research
and Develment Command, Dover, New Jersey

1215-1330   LUNCH

1330-1530 TECHNICAL SESSION I Room 217, Bartlett Hall

CHAIRPERSON - Dr. S.L. Pu, Benet Weapons Laboratory, Watervliet
Arsenal, Watervliet, New York

STRESS INTENSITY FACTORS FOR AN INFINITE ARRAY OF COLLINEAR
RIVET-LOADED CRACKS

Drs. A.P. Parker and J. Mason, Army Materials and Mechanics Research
Center, Watertown, Massachusetts

THE WEIGHT FUNCTION FOR VARIOUS BOUNDARY CONDITION PROBLEMS

Drs. A.P. Parker and O.L. Bowie, Army Materials and Mechanics
Research Center, Watertown, Massachusetts

CYCLIC PLASTICITY AHEAD OF A BLUNT CRACK

Drs. Dennis M. Tracey and Colin E. Freese, Army Materials and
Mechanics Research Center, Watertown, Massachusetts

AN INCREMENTAL APPROACH TO NONISOTHERMAL ELASTIC-PLASTIC DEFORMATION

Dr. Shih C. Chu, US Army Armament Research and Development
Command, Dover, New Jersey

THERMO-ELASTIC-PLASTIC STRESSES IN MULTI-LAYERED CYLINDERS

Dr. John D. Vasilakis, Benet Weapons Laboratory, Watervliet
Arsenal, Watervliet, New York

ELASTIC-PLASTIC THICK-WALLED TUBES SUBJECTED TO INTERNAL PRESSURE
AND TEMPERATURE GRADIENT

Dr. P.C.T. Chen, Benet Weapons Laboratory, Watervliet Arsenal,
Watervliet, New York

1330-1530 TECHNICAL SESSION II Room 218, Bartlett Hall

CHAIRPERSON - Dr. M.A. Hussain, Benet Weapons Laboratory,
Watervliet Arsenal, Watervliet, New York

A SEMI-INFINITE BOUNDARY-VALUE PROBLEM FROM THE THEORY OF
CHAMBERED DIFFUSION FLAMES

Prof Roger Alexander, Department of Mathematical Sciences,
Rensselaer Polytechnic Institute, Troy, New York

SECONDARY COMBUSTION IN GUN EXHAUST FLOWS

Dr. E.M. Schmidt, Ballistic Research Laboratory, Aberdeen Proving
Ground, Maryland

IRREGULAR MACH REFLECTION FROM THREE-DIMENSIONAL STUDIES

Drs. Ralph E. Reisler and John H. Keefer, Ballistic Research
Laboratory, Aberdeen Proving Ground, Maryland

MACH STEM FORMATION FROM MULTIPLE DETONATIONS

Drs. John H. Keefer and Noel H. Ethridge, Ballistic Research
Laboratory, Aberdeen Proving Ground, Maryland

BLOW-OFF OF A FLAME LOCATED IN A REAR STAGNATION POINT FLOW

Profs D. Mikolaitis and J. Buckmaster, University of Illinois
at Champaign-Urbana, Champaign, Illinois

THE EQUATION GOVERNING THE PROPAGATION OF FAST DEFLAGRATION
WAVES FOR SMALL HEAT RELEASE

Profs D.S. Stewart and G.S.S. Ludford, Cornell University,
Ithaca, New York

1530-1545   Break

1545-1645   <u>GENERAL SESSION II</u>   Room 220, Bartlett Hall

CHAIRPERSON - Dr. Norman Slagg, U.S. Army Armament Research and
                Development Command, Dover, New Jersey

SPEAKER - Professor Martin Sichel, The University of Michigan,
            Ann Arbor, Michigan

TITLE   - MODELING OF GASEOUS AND HETEROGENEOUS DETONATION PHENOMENA

1900-2100   Hudson River Boat Trip

<div align="center">

Thursday
<u>11 June 1981</u>
</div>

0830-1030   <u>TECHNICAL SESSION III</u>   Room 217, Bartlett Hall

CHAIRPERSON - COL Jack M. Pollin, Department of Mathematics, United
                States Military Academy, West Point, New York

A POWER SERIES TECHNIQUE FOR MULTIPLE INTEGRATION

Dr. Gerald S. Garfinkel, U.S. Army White Sands Missile Range,
White Sands, New Mexico

ON THE NUMERICAL SOLUTION OF SINGULAR EQUATIONS USING GAUSS-JACOBI
QUADRATIVE

Prof Ram Srivastav, State University of New York-Stony Brook,
Stony Brook, New York

METHOD OF SOLUTION FOR VARIATIONAL PRINCIPLE USING BICUBIC
HERMITE POLYNOMIAL

Dr. C.N. Shen, Benet Weapons Laboratory, Watervliet Arsenal,
Watervliet, New York

SMOOTHEST LOCAL INTERPOLATION FORMULAS FOR EQUALLY SPACED DATA

Drs. T.N.E. Greville and Hubert Vaughan (deceased), Mathematics
Research Center, University of Wisconsin-Madison, Madison,
Wisconsin

INTERVAL ANALYSIS: A NEW TOOL FOR APPLIED MATHEMATICS

Prof L.B. Rall, Mathematics Research Center, University of Wisconsin-Madison, Madison, Wisconsin

ON POLYNOMIAL INTERPOLATION IN THE POINTS OF A GEOMETRIC PROGRESSION, STIRLING, SCHELLBACH, RUNGE AND ROMBERS

Prof I.J. Schoenberg, Mathematics Research Center, University of Wisconsin-Madison, Madison, Wisconsin

0830-1030   TECHNICAL SESSION IV   Room 218, Bartlett Hall

CHAIRPERSON - Dr. Raymond Sedney, Ballistic Research Laboratory, Aberdeen, Maryland

DYNAMIC RESPONSE OF A HEMISPHERICAL ENCLOSURE SUBJECTED TO EXPLOSIVE BLAST LOADING

Drs. Aaron Gupta and Henry L. Wisniewski, Ballistic Research Laboratory, Aberdeen Proving Ground, Maryland

EXPLICIT DIFFERENCE SCHEMES FOR WAVE PROPAGATION AND IMPACT PROBLEMS

Prof Joseph E. Flaherty, Department of Mathematical Sciences, Rensselaer Polytechnic Institute, Troy, New York

NUMERICAL SIMULATION OF THE GAS DYNAMIC CYCLE OF COMPLEX, LARGE-SCALE SHOCK TUBES

Dr. Andrew Mark, Ballistic Research Laboratory, Aberdeen Proving Ground, Maryland

INITIAL AND BOUNDARY-VALUE PROBLEMS FOR MODEL EQUATIONS FOR WATER WAVES

Prof Jerry Bona, Mathematics Research Center, University of Wisconsin-Madison, Madison, Wisconsin and Prof Ragnar Winther, Ostfold Diskriktshogskole, Halden, Norway.

EVALUATION OF A MODEL EQUATION FOR WATER WAVES

Profs J.L. Bona, W.G. Pritchard, and L.R. Scott, Mathematics Research Center, University of Wisconsin-Madison, Madison, Wisconsin

FREE-SURFACE FLOWS AT SMALL REYNOLDS NUMBERS

Prof W.G. Pritchard, Mathematics Research Center, University of Wisconsin-Madison, Madison, Wisconsin

1030-1045   Break

1045-1145   SPECIAL SESSION B   Room 220, Bartlett Hall

CHAIRPERSON - Dr. Robert Genter, U.S. Army Armament Research and Development Command, Dover, New Jersey

A THEORY OF DEFLAGRATION WAVES IN A COMBUSTIBLE GAS MEDIUM

Prof S.S. Lin, Mathematics Research Center, University of Wisconsin-Madison, Madison, Wisconsin

NUMERICAL STUDY OF A CONFINED PREMIXED LAMINAR FLAME

Dr. Douglas E. Kooker, Ballistic Research Laboratory, Aberdeen
Proving Ground, Maryland

1145-1300   Lunch

1300-1530   TECHNICAL SESSION V   Room 217, Bartlett Hall

CHAIRPERSON - Dr. James Thompson, U.S. Army Tank-Automotive
                Research and Development Command, Warren, Michigan

EFFECT OF SUPPORT CONDITIONS ON BEAM VIBRATIONS SUBJECTED TO
MOVING LOADS

Dr. Julian J. Wu, Benet Weapons Laboratory, Watervliet Arsenal
Watervliet, New York

FINITE ELEMENTS FOR INITIAL VALUE PROBLEMS IN DYNAMICS

Dr. T.E. Simkins, Benet Weapons Laboratory, Watervliet Arsenal,
Watervliet, New York

MATHEMATICAL MODELING OF COMPRESSIBLE FLUID RECOIL MECHANISM

Dr. R. Yalamanchili, U.S. Army Armament Research and Development
Command, Dover, New Jersey

NUMERICAL ANALYSIS OF IMPACT STRESSES IN AN ELASTO-VISCOPLASTIC BAR

Dr. Julian L. Davis, U.S. Army Armament Research and Development
Command, Dover, New Jersey and Prof Yu Chen, Department of
Mechanics Science, Rutgers, the State University, New Brunswick,
New Jersey

ON THE DYNAMICS AND STRESS ANALYSIS OF INTERMITTENT-MOTION
MECHANISMS

Profs Ting W. Lee, A.C. Wang, and G.R. Niederoest, Department of
Mechanical and Aerospace Engineering, Rutger, the State University,
New Brunswick, New Jersey

A NONLINEAR VOLTERRA EQUATION IN VISCOELASTICITY

Prof John A. Nohel, Mathematics Research Center, University of
Wisconsin-Madison, Madison, Wisconsin

1300-1530   TECHNICAL SESSION VI   Room 218, Bartlett Hall

CHAIRPERSON - Dr. B.Z. Jenkins, U.S. Army Missile Command,
                Redstone Arsenal, Alabama

ADAPTIVE GRIDDING SCHEMES FOR FINITE ELEMENT METHODS

Dr. Stephen Davis, Ballistic Research Laboratory, Aberdeen
Proving Ground, Maryland

ANALYSIS OF IMPLICIT SCHEMES FOR COMPUTATIONAL FLUID DYNAMICS

Dr. James Schmitt, Ballistic Research Laboratory, Aberdeen
Proving Ground, Maryland

THE DEVELOPMENT OF MASS DETONATION IN STORES TREATED AS A
STOCHASTIC PROCESS

Drs. A.R. Kiwan and P.M. Howe, Ballistic Research Laboratory,
Aberdeen Proving Ground, Maryland

TERRAIN MICROROUGHNESS AND THE DYNAMIC RESPONSE OF VEHICLES

Dr. Richard A. Weiss, U.S. Army Waterways Experiment Station, Vicksburg, Mississippi

TITLE TO BE ANNOUNCED LATER

Dr. Raymond Sedney, Ballistic Research Laboratory, Aberdeen Proving Ground, Maryland

MERGING AND SCATTERING OF ISOLATED VORTEX STATES OF THE EULER EQUATIONS

Profs Normal Zabusky and E.A. Overman, University of Pittsburgh, Pittsburgh, Pennsylvania

1530-1545	Break

1545-1645   GENERAL SESSION III   Room 220, Bartlett Hall

CHAIRPERSON - Dr. Donald Drew, U.S. Army Research Office, Research Triangle Park, North Carolina

SPEAKER   - Professor David Kassoy, University of Colorado, Boulder, Colorado

TITLE   - GAS DYNAMICS ASPECTS OF THERMAL EXPLOSIONS

1700-1800   BUS TOUR OF WEST POINT

Friday
12 June 1981

0830-1030   SPECIAL SESSION C   Room 220, Bartlett Hall

CHAIRPERSON - Dr. J.M. Heimerl, Ballistic Research Laboratory, Aberdeen Proving Ground, Maryland

AN ASYMPTOTIC THEORY OF DEFLAGRATIONS AND DETONATIONS

Prof Ashwani Kapila, Rensselaer Polytechnic Institute, Troy, New York

DEFLAGRATION TO DETONATION TRANSITION

Prof Geoffrey S. S. Ludford, Cornell University, Ithaca, New York

A COMPARISON TECHNIQUE FOR SOME COMBUSTION MODELS

Dr. Jagdish Chandra, US Army Research Office, Research Triangle Park, North Carolina and Dr. Paul Davis, Worcester Polytechnic Institute, Worcester, Massachusetts

TITLE TO BE ANNOUNCED LATER

Prof John F. Clarke, Cranfield Institute of Technology, England

1030-1045   Break

1045-1145   <u>GENERAL SESSION IV</u>   Room 220, Bartlett Hall

CHAIRPERSON - Dr. Jagdish Chandra, US Army Research Office,
                   Research Triangle Park, North Carolina

SPEAKER   - Prof Andrew Majda, University of California-Berkeley,
                   Berkeley, California

TITLE   - A THEORY FOR THE FORMATION OF MACH STEMS IN REACTING
                   SHOCK FRONTS

1200   ADJOURN

USE OF ACTIVATION-ENERGY ASYMPTOTICS FOR REACTING FLOWS

F. A. Williams

Department of Mechanical and Aerospace Engineering
Princeton University
Princeton, New Jersey

ABSTRACT.   Attention is focused on asymptotic analyses in which the ratio of the overall energy of activation for reaction to the thermal energy of the reacting medium is a large parameter.   Advances achieved in theories of ignition, extinction and flame propagation are reviewed with emphasis on physical implications.

1. INTRODUCTION.   The subject of activation-energy asymptotics (AEA) is now sufficiently mature to have been expounded in a book [1].   This attests to its widespread utility in describing reacting systems and to the fact that it has now been applied to many problems.   It will not be possible here to give a thorough review of applications of the technique.   Instead, attention will be focused on physical aspects of its basis and on some of the physical implications of results obtained by exercising the method.

1.1 Definition.   AEA constitutes a particular brand of asymptotic expansions that differs in detail from other applications of such techniques by fluid mechanicians and applied mathematicians.   Nonlinearity in a source term is essential to the method.   The general form of the problems addressed may be illustrated by the equation

$$L \{T\} = F(T) e^{-E/(RT)} , \tag{1}$$

where L is a differential operator, possibly linear, F is a regular function and E/R is a constant.   The dependent variable T represents temperature, E is an activation energy and R the universal gas constant.   The operator L and the function F are independent of E/R, as are the boundary and/or initial conditions

1

applied to equation (1). The factor $e^{-E/(RT)}$ is an Arrhenius reaction-rate factor.

In AEA there is a fixed reference temperature T_r such that the source term is important for T near T_r. The nondimensional grouping $E/(RT_r)$ then becomes a parameter of the problem. AEA is concerned with developing an asymptotic expansion of the solution for the limit $E/(RT_r) \to \infty$. Systematic approaches to AEA generally involve scaling the independent variables, space and/or time, appearing in L and also scaling T, in fashions suitable for generation of nontrivial asymptotic expansions. Usually scalings are different for different ranges of independent variables, there being a narrow reaction stage or reaction zone in which the source term is significant. These reaction regions separate broader regions in which the source term is comparatively negligible in the limit. The techniques of matched asymptotic expansions then come into play, exhibiting nuances peculiar to AEA.

1.2 Generalizations. The ideas of AEA are readily applied to equations more general than (1). Usually a system of equations is considered -- the conservation equations for reacting flows. There may be a number of source terms, more than one of which may have large values of parameters like $E/(RT_r)$. The Arrhenius factor may occur in boundary conditions when heterogeneous reactions or phase changes are considered. Autocatalytic reactions in isothermal systems may be addressed in an analogous manner. The Arrhenius form is inessential; the key attribute is the occurrence, in a source term, of a dependent variable that tends to increase as the reaction proceeds, accompanied by a parameter, an increase in which strengthens without limit the sensitivity of the source to this dependent variable.

1.3 History. It may be considered that the seeds of AEA were sown more than forty years ago, before the growth of matched asymptotic expansion, when Zeldovich and Frank-Kamentskii proposed approximate solutions to the problems of laminar flame propagation [2] and of thermal ignition [3,4]. Their approaches were physically motivated yet produced results coinciding with the lowest approximation obtained by formal application of AEA. Formalisms of AEA are just slightly more than ten years old. Bush and Fendell [5] published the first systematic analysis amenable to development to higher orders, again in connection with laminar flame propagation. Reviews have been prepared covering early [6] and some of the more recent [7] work. The numerous papers using AEA now in the literature span a variety of different avenues to suitable formalisms.

2. PHYSICAL BASIS OF EXPANSION. Results obtained through AEA often have been viewed with suspicion by researchers interested in experimental aspects of reacting flows. This skepticism stems at least partially from questions concerning validity of the approximations underlying the analyses. All good chemists know that in the vast majority of reacting flows numerous reactions contribute to chemical source terms. Most AEA analyses employ just one source term with a single parameter E representing an overall energy of activation for heat release. Justifications for introduction of this one-step approximation generally are absent from AEA papers.

Applied mathematicians often are content with results that mimic experimental behavior and usually do not seek numerical comparison with experiment, reasoning that the approximations are insufficiently accurate to warrant such comparisons. In this view, justifications for AEA with one-step chemistry need be little more than analogy. A consequence of this stand is that experimentalists can utilize the AEA results only for intuitive guidance, and they turn to numerical solutions of partial differential equations for detailed comparisons.

3

It appears that physical bases for AEA approaches can be given that are better than analogy and that motivate numerical comparisons of AEA results with experiment. It has long been known empirically that a one-step, Arrhenius representation of chemistry is useful for many purposes, over a sufficiently narrow range of conditions, despite the complexity of the true kinetics. If such a representation applies to a specific experimental process analyzed by AEA, then it is possible to compare theoretical predictions with experiment. Moreover, in such cases $E/(RT_r)$ generally is sufficiently large to make AEA appropriate, since the inequalities $T_r \leq 2,500°K$ and $E/R \geq 10,000 °K$ usually are obeyed; values of $E/(RT_r)$ in the range of 10 to nearly 100 are typical, depending on the problem. Therefore the comparisons can be quite successful if completed properly.

2.1 Basis of One-Step Approximation. The physical reason for the empirical success of the one-step, Arrhenius approximation with $E/(RT_r)$ large can be quite complex. Paradoxically, the three-body recombination steps responsible for the major heat release in most combustion processes have essentially zero energy of activation. However, these steps proceed at rates proportional to concentrations of active radicals, and the radicals are formed in largely endothermic steps that generally have appreciable activation energies. Therefore the effective rate of the overall process, obtained through a combination of all steps, has an overall activation energy E such that $E/(RT_r)$ is large. While individual E's for many steps are zero in reactive flows, seldom will an overall E occur such that $E/(RT_r)$ is not large; otherwise the system likely would be either too reactive to be contained at room temperature or negligibly reactive at all temperatures attainable.

2.2 Limitations on One-Step Approximation. Limitations on the overall
Arrhenius description, especially the limited range of conditions over which the
overall E remains constant, should be kept clearly in mind when comparisons
with experiment are made. A given fuel-oxidizer pair does not have one fixed E
but instead exhibits a variety of different E's that pertain to different situa-
tions. For exampl , an E for thermal ignition will differ from an E for flame
propagation; the reason is that the chemical kinetic mechansims of thermal igni-
tion differ substantially from those for flame propagation. Even when attention
is restricted to a particular type of flow, variations in E should be anticipated.
For example, in premixed flame propagation it is well established from chemical
kinetics that the overall E for fuel-rich conditions differs from that for fuel-
lean conditions; conclusions concerning variation of behavior with mixture ra-
tion cannot be drawn completely without taking the E variation into account.
In diffusion flames there is an automatic adjustment causing most of the exo-
thermic chemistry to occur near stoichiometric conditions; success has been
achieved in applying AEA [8] to diffusion-flame extinction, finding from extinc-
tion experiments overall values of E for conditions of combustion near extinction
[9]. However, this success does not occur if chemical species are added that
modify the chemical kinetic mechanisms [9]. Thus, ideas concerning kinetic
mechanisms responsible for an overall E are of importance in evaluating limita-
tions on comparisons with experiment.

2.3 Consideration of Multi-Step Kinetics. The time seems ripe for exten-
sion of AEA methods to the consideration of full kinetic mechanisms. Some work
along these lines has been initiated [10]. Information on rates of individual
steps, accumulated over the years, has achieved enough detail and accuracy to
enable thorough kinetic investigations to be undertaken for many real systems.
In some cases detailed kinetic studies may justify approximations, such as a
steady-state approximation for reaction intermediaries, that lead to a one-step

5

description of the heat-release process with overall E; in such cases comparison of the overall E obtained from the detailed mechanism, with that found by use of AEA in conjunction with experiment, would provide improved knowledge of the relevant chemistry. In many cases studies of detailed kinetics, using AEA, can identify significant simplifications of the chemical description that nevertheless are more complex than a one-step approximation. These descriptions could increase greatly our understanding of influences of chemistry in reacting flows. They could afford possibilities of comparing AEA predictions with fine-tuned experimental results currently emerging, such as observations of occurrences of particular species in regions away from major heat-release zones. They could indicate specific effects of chemistry on fluid dynamics of combustion processes. In general, introduction of real chemistry into AEA approaches appears to offer numerous avenues for future advances. So little work has been done along these lines that none of it is considered in the following discussion, which is restricted to one-step approximations.

3. IGNITION THEORY. The theory of thermal ignition of materials capable of reacting exothermically has been one of the major arenas of success of AEA. Experimentally, ignition is a sudden event. Reactive materials often exhibit induction periods, during which slow chemical changes occur, followed by a rapid heat release with an associated abrupt increase of temperature. Chemical kinetics of chain reactions can describe this kind of behavior, the induction period being a time during which reactive radicals are produced slowly. However, the one-step approximation with $E/(RT_r)$ large also is consistent with such behavior. It can be difficult to distinguish ignition events in which multi-step kinetics play an essential role from those properly describable by AEA with one-step chemistry.

6

Questions asked in ignition theory are first whether ignition will occur for a given material subject to given conditions (i.e., specification of criticality conditions) and second what the time delay prior to the ignition event will be (the ignition time) for conditions under which ignition occurs. The AEA methods are well suited to addressing both of these questions since they describe nearly discontinuous phenomena quite naturally. Numerous ignition problems have now been solved by AEA. Ad hoc approaches to theories of thermal ignition are now largely obsolete because of AEA.

3.1 Representative Formulation. We shall not consider the spatially homogeneous system characteristic of explosion theory, although appreciable progress in describing behaviors of such systems has been made by AEA [11]. Instead, a one-dimensional, time-dependent problem of ignition of a combustible material by an external energy source will be considered on the basis of a two-equation description. Introduce a one-reactant approximation with 1-Y denoting the ratio of the reactant concentration to its initial value, so that Y may be viewed as a reaction progress variable that goes from zero initially to unity at completion of the reaction. The equations for energy and reactant conservation then become

$$\rho c \frac{\partial T}{\partial t} + \rho v c \frac{\partial T}{\partial x} - \frac{\partial}{\partial x} (\lambda \frac{\partial T}{\partial x}) = \rho q \nu (1-Y)^a e^{-E/RT} \qquad (2)$$

and

$$\rho \frac{\partial Y}{\partial t} + \rho v \frac{\partial Y}{\partial x} - \frac{\partial}{\partial x} (\frac{\lambda}{cLe} \frac{\partial Y}{\partial x}) = \rho \nu (1-Y)^a e^{-E/RT} \quad . \qquad (3)$$

Here T denotes temperature, c the specific heat and ρ the density of the material; t is time and x distance, with v representing the velocity in the x-direction. The thermal conductivity of the material is λ, and the Lewis number Le denotes the ratio of heat to mass diffusivities, the thermal conductivity divided by the product of c with the coefficient of diffusion for the reactant, Fick's law having been adopted for diffusion. The overall order of the reaction

7

is $\underline{a}$, and the heat released in the reaction per unit mass of material consumed is q. The pre-exponential factor in the reaction rate has been denoted by ν, which involves the initial reactant concentration as well. Overall conservation of mass relates ν to ρ. The four terms in (2) and (3) represent accumulation, convection, diffusion and reaction, respectively; the first three of these correspond to the operator $L\{T\}$ in (1).

Initial conditions are $T = T_i$ and $Y = 0$ at $t = 0$. Boundary conditions depend on the problem considered. Although conditions may be applied at two boundaries, it is simpler to consider a semi-infinite problem, with the combustible material occupying the region $x > 0$ and to apply boundary conditions only at $x = 0$, requiring T to approach T_i and Y zero as x approaches infinity. This restricts attention to times short enough for reaction to produce negligible changes in T and Y at temperature T_i. The material must be heated to begin to react appreciably, and this heating is achieved through the boundary conditions at $x = 0$. Such a formulation is useful only if $E/(RT_i)$ is large.

One problem of interest is ignition by a step in surface temperature [12,13]. Here $T = T_s = $ const. is imposed at $x = 0$ for $t > 0$, with $T_s > T_i$. This problem turns out to be more complicated than many other ignition problems, in that the rate of the reaction cannot be neglected near $x = 0$ even for very small t. A simpler problem is that of radiant or convective ignition, by a constant energy flux $\dot{q}$, in which $\dot{q} = -\lambda \partial T/\partial x$ is imposed at $x = 0$ [14]. Various boundary conditions on Y at $x = 0$ also are of interest [13].

3.2 Character of Results. For the simpler problem identified above it is found by AEA that there is an initial stage of inert heat conduction, during which reaction is negligible. Following the inert stage is a stage of rapid transition to an ignited state. The appropriate large parameter of expansion is $ET_i/(RT_c^2)$, where T_c is the inert temperature at $x = 0$ at the time of onset of the stage of

8

transition to ignition; thus, $T_r = T_c^2/T_i$. In this problem it is found that eventually ignition always occurs. The time t_c required for ignition to occur, if Le = ∞ and if cT_i/q is of order unity or less, is found to be given by

$$t_c = \frac{\pi\rho\lambda c T_i^2}{4\dot{q}^2}\left[\frac{E}{RT_i\ell n(1/D)} - 1\right]^2 , \qquad (4)$$

in which

$$D = \frac{0.65\dot{q}^2}{q\rho\lambda\nu T_i}\sqrt{\frac{RT_c^2}{T_i E}}\left(\frac{\pi\dot{q}^2 t_c}{\rho\lambda c T_i^2}\right)^{\frac{1}{4}}\left[1 + 0\left(\frac{RT_c^2}{T_i E}\right)\right] , \qquad (5)$$

where

$$T_c = T_i\left[1 + \sqrt{\frac{4\dot{q}^2 t_c}{\pi\rho\lambda c T_i^2}}\right] . \qquad (6)$$

The main functional dependence of t_c may be obtained from (4) by putting $D = \dot{q}^2/(q\rho\lambda\nu T_i)$ and yields in a rough approximation $t_c \sim \rho\lambda c E^2/(R^2\dot{q}^2)$.

The results in (4), (5) and (6) are obtained through a detailed analysis of the stage of transition to ignition. Since temperature-time histories are continuous, precise definition of t_c necessitates adoption of a specific definition of ignition. AEA methods provide a very convenient way to do this since they introduce a divergence in the transition-stage solution, a "thermal runaway", arising essentially from a type of linearization of $1/T$ within the exponential in the Arrhenius factor. The ignition time is identified with the time of divergence. Other definitions of ignition time give slightly different results that converge to those given here as $E/(RT_r) \to \infty$. The accuracy of (4) through (6) has been verified by numerical integrations of the original partial differential equations; these integrations in fact had been performed before the asymptotic analysis was developed.

9

3 3 Types of Problems Solved. These AEA methods have now been employed to solve a wide variety of ignition problems. The constant energy flux applied to the surface, in the problem considered above, is equivalent to a constant radiant flux if the absorptivity of the combustible material for the radiation is infinite. Finite absorptivity leads to in-depth absorption and introduces an additional parameter, the characteristic absorption length for the radiation. Inert-stage histories and ignition-time formulas and graphs have been developed for this problem, parametrically in the absorption length [15]. With radiant energy application surface cooling may occur by convection or conduction. For transient, one-dimensional conductive loss, an additional parameter enters Γ, the ratio of the thermal responsivity $(c\rho\lambda)$ of the inert medium to that of the reactive medium [16]. The AEA analyses for ignition time have been completed for small Γ [16] as well as for Γ of order unity or large [17], thereby producing a sequence of ignition-time curves with Γ and a non-dimensional absorption length as parameters [17]. Results with conductive loss may be applied approximately for convective loss through the identification $\Gamma = hT_i/\dot{q}$, where h denotes the heat-transfer coefficient. However, proper AEA analyses for influences of specific types of convective losses have not been pursued and could improve accuracies of predictions for such losses.

Results of the AEA analyses can be presented in such a way that they are applicable to general flux-time histories [15], subject to exclusion of the limiting case involving a delta function, in which at time zero the surface temperature is raised to a specified value and maintained constant thereafter. This more difficult problem has been solved by AEA [12], including effects of reactant consumption for both Le = ∞ and Le of order unity. Extension has been made to allow for surface catalysis, an additional parameter being the rate of catalysis [13], but reactive bodies of finite sizes, e.g. small spheres, have not

yet been treated by AEA. Another problem solved by AEA is the endothermic gasification of a solid by a constant energy flux, for an Arrhenius surface process [18], for a distributed condensed-phase Arrhenius process [18] and for surface equilibrium [19]. In this case, instead of thermal runaway there is a sudden leveling of the surface temperature at onset of endothermic gasification, and the surface temperature remains nearly constant thereafter.

The three classical theories for ignition of solids are condensed-phase, heterogeneous and gas-phase ignition theories, the qualifiers here designating the site of the principal exothermic process. Condensed-phase ignition theory has mainly been considered above. Heterogeneous ignition theory is simpler in that the rate is only in the boundary condition; this has been treated by AEA [20]. Gas phase-phase ignition theory is the most complex since it involves at least two steps, first gasification and then distributed exothermic reaction in the gas. This ignition problem has been solved by AEA for a constant radiant energy flux applied to the surface of the solid [21], as well as for radiant ignition with in-depth absorption of radiation [22], for Arrhenius kinetics [22] and for surface equilibrium [19]. A richer variety of parametric ignition-time curves arises from these gas-phase ignition theories because of the greater number of parameters [22].

There are many ignition problems for which further work remains to be done in application of AEA. One aspect requiring further study is the development of the combustion processes following the ignition event, including possible occurrences of pressure-wave generation. Some work on problems of this type has been completed by AEA [23,24]. Another outstanding area involves problems in which reactive gas motions occur that are not one-dimensional.

4. LAME PROPAGATION. Steady propagation of laminar flames may be described by (2) and (3) with the time derivative deleted and the boundary condi-

11

tions revised. Since the work of Bush and Fendell [5], much has been accomplished in analyzing such flames by AEA. In addition to one-reactant flames with Le $\neq$ 1, two-reactant flames with two Lewis numbers have also been considered. One source of more recent references is the note by Mitani [25], in which AEA predictions by various authors are compared.

With AEA, premixed flames are found to be composed of two regions. There is an upstream convective-diffusive zone in which reaction is negligible, followed by a thinner reactive-diffusive zone in which convection is negligible in the first approximation. The appropriate large parameter of expansion is $E(T_b-T_u)/(RT_b^2)$, where T_u is the temperature of the fresh mixture and T_b that of the reaction products; thus $T_r = T_b^2/(T_b-T_u)$. It is seen that for the expansion parameter to be large, the heat release, $c(T_b-T_u)$, cannot be too small. The laminar flame propagates at a definite velocity, the laminar flame speed S_L. The AEA analyses provide formulas for S_L through the matching conditions *between the two zones and show that $\rho_u S_L$ is proportional to $\sqrt{\nu\lambda/c}\ e^{-E/(2RT_b)}$.*

Practitioners of computer routines with full chemistry usually question AEA results for S_L. The computer calculations typically show many species with reactions occurring in what should be the convective-diffusive zone. Unfortunately sensitivity studies of the importance of such reactions and of the extent to which their effects can be approximated by AEA have not been pursued. Therefore additional studies remain to be done on AEA in steady laminar flames.

4.1 Flame Instabilities. A major area of success of AEA in laminar flame theory has been to provide a convenient means for investigating flame instabilities. The reaction-zone analysis provides jump conditions that can be used in studying essentially linear equations that apply in the broader zones on either side of the reaction zone. This enables attention to be focused more easily on instability mechanisms. Occurrences of cellular flames and of pulsating flames have been identified in this manner.

12

Jump conditions across the reaction zone are best derived by formal asymptotic analysis rather than by intuitive appeal to reaction-rate delta functions. Jump conditions are available in the literature [e.g., 26,27].

Pulsating flames are found to occur if Le is sufficiently large [28]. Such phenomena are relevant to the combustion of solids but seldom are expected for gases. The pulsating instability cannot be understood on the basis of static stability arguments because of their essentially dynamic character. With attenton restricted to Le = ∞, one may imagine a reaction sheet to be rapidly displaced a small distance toward reactants. With insufficient time for conduction to remove the heat generated, the displacement may increase the local temperature at the sheet. According to the flame-speed formula, this increases S_L and therefore tends to produce a further displacement, thus providing a mechanism for instability.

Cellular instabilities are more common than pulsations for gases and have also been predicted successfully by use of AEA. These instabilities occur for Le less than a cricical value less than unity and can be understood physically on the basis of qualitative reasoning concerning static stability. Assume that a small bulge develops in the reaction sheet, protruding toward the reactant side. Since the reaction sheet is a sink for reactant and a source for heat, this protrusion has a character somewhat like a point source or sink. For Le < 1, the higher diffusivity of reactant, in comparison with that of heat, allows proportionally more reactant to diffuse to the bulge, in comparison with the heat that is allowed to escape. The reactant releases energy by combustion at the reaction sheet, and the consequent imbalance between heat release and heat conducted forward must result in an increased temperature at the bulge. This increased temperature increases S_L locally and thereby causes the bulge to tend to be extended even farther into the reactant. Thus, there is an instability mechanism for development of nonplanar shapes of reaction sheets if Le < 1. The cellular

13

flames that result from this instability have shapes fairly rounded toward the fresh mixture and pointed toward the burnt gas.

A number of AEA studies of cellular instabilities may now be found in the literature [e.g., 27, 29-34]. These studies address a variety of influences on cellular structure, such as effects of heat loss, effects of an acceleration field, nonlinear behavior and effects of interdiffusion of two reactants. Concerning this last effect, it seems clear physically that if a reactant mixture is deficient in a readily diffusing reactant, then preferential diffusion of this reactant to a bulge may cause the mixture to be locally more nearly stoichiometric there and hence to have a higher flame speed at the bulge, again promoting cellular instability. This is indeed what is predicted [34] and also observed experimentally [35].

4.2 Behaviors of Stretched and Curved Flames. Additional phenomena of flame propagation can be understood on the basis of the same reasoning employed to describe cellular instabilities. For example, a reaction sheet situated normal to a decelerating flow experiences stretch, in that flow streamlines tend to diverge as they approach the sheet. This divergence tends to shorten distances over which gradients occur and therefore enhances driving forces for diffusive processes. More easily diffusing species therefore enter the stretched reaction sheet relatively more rapidly. For one-reactant systems with $Le < 1$, this causes the flame temperature and therefore the flame speed to increase. For $Le > 1$, stretch causes the flame speed to decrease and may eventually produce flame extinction even under adiabatic conditions. There is a similar behavior concerning curved flames; flames convex toward the fresh mixture have reduced flame speeds for $Le > 1$.

14

These physical results have been clarified well by AEA analyses [e.g., 36]. It is helpful for many purposes to derive general partial differential equations for the evolution of a reaction sheet. This has been done by a number of investigators using AEA ideas [e.g., 37,38]. Further study of evolution equations offers promise of clarifying dynamics of flame propagation.

5. EXTINCTION THEORY. The ability of AEA to describe extinction phenomena has proven to be one of its most useful attributes. Extinction of premixed flames has been mentioned above. Extinction phenomena also can be observed readily in nonpremixed systems. For example, fuel and oxidizing gaseous jets can be directed towards each other and ignited. A steady, flat, diffusion flame then may exist where the jets meet. By increasing the velocities of the jets, a situation eventually may be reached at which the diffusion flame is suddenly extinguished. A detailed analysis of this type of extinction by AEA methods has been given [39]. This analysis has provided a basis for comparisons with experiment.

Other nonpremixed extinctions that have been treated by AEA include those in droplet burning and in the combustion of surface-burning particles such as carbon. Objectives have been to ascertain whether extinction is gradual or abrupt and to identify critical conditions for abrupt extinction. Steady-state equations may be employed to investigate these questions, the large parameter usually being $QE/(cRT_{af}^2)$, where T_{af} is the adiabatic flame temperature and Q a heat release per unit mass in the reaction. It is found that there is a thin reactive-diffusive zone usually having thicker convective-diffusive zones on both sides. Extinction conditions are those beyond which the reactive-diffusive zone can no longer exist. Such extinctions occur if the strain rate or diffusion rate becomes too large in comparison with the rate of the chemical heat release. Radiant energy loss has been shown by AEA to enhance extinction [40].

The principal outstanding question in analyzing extinction by AEA concerns influences of multi-step chemistry. This question can be addressed by AEA methods.

6. CONCLUDING COMMENT. This paper has only touched upon a selected few of the many accomplishments of AEA. The reference list could be doubled in length and still not contain all of the important contributions made in the past decade. Moreover, the topic shows no sign of a decrease in growth rate. There are many outstanding problems to be tackled. The subject is in a stage of Arrhenius-like growth and has not yet encountered appreciable "reactant depletion". It has not yet reached steady propagation and certainly is far from extinction.

REFERENCES.

1. J. Buckmaster and G.S.S. Ludford, Theory of Laminar Flames, Cambridge University Press, Cambridge (1981).

2. Y. B. Zeldovich and D. A. Frank-Kamenetskii, Zh. Fiz. Khim. 12, 100 (1938).

3. Y. B. Zeldovich, Zh. Eksperim. i. Teor. Fiz. 9, 12 (1939).

4. D. A. Frank-Kamenetskii, Zh. Fiz. Khim. 13, 738 (1939).

5. W. B. Bush and F. E. Fendell, Combust. Sci. Tech. 6, 421 (1970).

6. F. A. Williams, Annual Rev. Fluid Mechanics 3, 171 (1971).

7. F. A. Williams, "Current Problems in Combustion Research," in Dynamics and Modelling of Reactive Systems, W. E. Stewart, W. H. Ray and C. C. Conley, editors, Academic Press, New York (1980), p. 293.

8. L. Krishnamurthy, F. A. Williams and K. Seshadri, Combustion and Flame 26, 363 (1976).

9. F. A. Williams, Fire Safety Journal 3, 163 (1981).

10. A. Liñán, unpublished works (1980).

11. D. R. Kassoy and A. Liñán, Quart. J. Mech. Appl. Math. 31, 99 (1978).

12. A. Liñán and F. A. Williams, SIAM J. Appl. Math. 36, 587 (1979).

13. A. Liñán and F. A. Williams, SIAM J. Appl. Math. 40, 261 (1981).

14. A. Liñán and F. A. Williams, Combust. Sci. Tech. 3, 91 (1971).

15. A. Liñán and F. A. Williams, Combustion and Flame, 18, 85 (1972).

16. W. B. Bush and F. A. Williams, Acta Astronautica 2, 445 (1975).

17. W. B. Bush and F. A. Williams, Combustion and Flame 27, 321 (1976).

18. M. Kindelan and F. A. Williams, Combust. Sci. Tech. 10, 1 (1975).

19. T. Niioka and F. A. Williams, Seventeenth Symposium (International) on Combustion, The Combustion Institute, Pittsburgh, PA (1979), p. 1168.

20. A. Liñán and A. Crespo, Combust. Sci. Tech. 6, 223 (1972).

21. M. Kindelan and F. A. Williams, Acta Astronautica 2, 955 (1975).

22. M. Kindelan and F. A. Williams, Combust. Sci. Tech. 16, 47 (1977).

23. A. K. Kapila, SIAM J. Appl. Math. 39, 21 (1980).

24. D. R. Kassoy and J. Poland, SIAM J. Appl. Math 39, 412 (1980).

25. T. Mitani, Combust. Sci. Tech. 21, 175 (1980).

26. G. Joulin and P. Clavin, Acta Astronautica 3, 233 (1976).

27. G. Joulin and P. Clavin, Combustion and Flame 35, 139 (1979).

28. B. J. Mathewsky and G. I. Sivashinsky, SIAM J. Appl. Math. 35, 465 (1978).

29. G. I. Sivashinsky, Combust. Sci. Tech. 15, 137 (1977).

30. B. J. Matkowsky and G. I. Sivashinsky, SIAM J. Appl. Math. 37, 669 (1979).

31. T. Mitani, Combust. Sci. Tech. 23, 93 (1980).

32. B. J. Matkowsky, L. J. Putnick and G. I. Sivashinsky, SIAM J. Appl. Math. 38, 489 (1980).

33. G. I. Sivashinsky and B. J. Matkowsky, SIAM J. Appl. Math. 40, 255 (1981).

34. G. Joulin and T. Mitani, Combustion and Flame, 40, 235 (1981).

35. T. Mitani and F. A. Williams, Combustion and Flame 39, 169 (1980).

36. G. I. Sivashinsky, Acta Astronautica 3, 889 (1976).

37. G. I. Sivashinsky, Acta Astronautica 4, 1177 (1977).

38. G. I. Sivashinsky, SIAM J. Appl. Math. 39, 67 (1980).

39. A. Liñán, Acta Astronautica 1, 1007 (1974).

40. S. H. Sohrab, A. Liñán and F. A. Williams, Combust. Sci. Tech., to appear (1981).

MULTISCALE METHOD AND ACTIVATION ENERGY ASYMPTOTICS FOR THE STUDY OF THE DYNAMICAL PROPERTIES OF PREMIXED FLAME FRONTS

Paul CLAVIN and Pierre PELCE

Laboratoire de Dynamique et Thermophysique des Fluides (LA 72)

Université de Provence

Centre St Jérôme, rue H. Poincaré, 13397 Marseille cedex 13, France

ABSTRACT

In a recent publication /8/, one of us (P.C.) in collaboration with F.A. WILLIAMS, has derived the local relation between the dynamical properties of the premixed flames front and the local characteristics of the flow field in the fresh mixture just ahead of the front. This has been done including the thermal expansion effect of the gases using a multiscale method and assuming that the flame thickness is small compared to the wave length of the wrinkles.

But, due to the fluid mechanics, the characteristics of this umpstream flow on the flame front are functionnals of the front position.

In this work, we solve the fluid mechanical problem in the presence of gravity in order to derive the dispersion relation controlling the stability properties of the planar front.

Two main results are obtained. First, the viscosity effects in the gases do not affect the stability properties. Second, for slow flames (velocity <15cm/s), the gravitational acceleration associated with a realistic positive value of the "Markstein constant" can make the planar front stable for all the wave lengths even in the presence of the strongly destabilizing hydrodynamical mechanism of "Darrieus and Landau".

I - INTRODUCTION -

New interest was shown recently in the
dynamical properties of flame fronts which are expected to
control the efficiency of the turbulent combustion. There are several
reasons for this renewal of interest. The first one, which is
of fundamental nature, is related to the occurence, beyond the
stability threshold, of cellular structures on the front which
can produce chaotic movements in premixed combustion even for
laminar upstream flows. This phenomena which is related to the
general problem in physics of the transition mechanism to the
chaos was experimentally shown, for the first time in premixed
flame, by the pioneering works of MARKSTEIN /1/ and verified re-
cently in our laboratory /2/ for carefully controlled flow condi-
tions. The second reason is the developpement in our laboratory
of a new optical technic perfected by L. BOYER /3/ which provides
us with quantitative experimental data concerning these dynamical
behaviors of premixed flame fronts /2//4/. The last one is the
developpement of power_full mathematical technics which opened
the field of theoretical investigations of these phenomena in
combustion. One decisive step in this direction was the use of
an asymptotic expansion in large values of the reduced activation
energy to describe the inner structure of both the premixed /5/,
/6/ and diffusion /7/ flames.   Another step was accomplished
recently by P. CLAVIN and F.A. WILLIAMS /8/ by coupling this asym-
totic expansion with a multiscale method which allowed them to take
into account completely, for the first time, the effect of the gas expan-
sion on the structure of a tilted front and thus on the dynamics
of wrinkled fronts.

The purpose of the present paper is to inves-
tigate theoretically by these methods the stability properties of the
premixed flame front including a complete description of the
thermal expansion effect.

As the early works of DARRIEUS /9/ and
LANDAU /10//11/ showed, this effect is expected to produce a
strong instability mechanism. In fact, the flame front is consi-
dered in these works as a surface of discontinuity with a normal
velocity kept constant relatively to the gas flow. This surface is
the frontieer between the fresh cold mixture and the hot burnt
gases which can be both considered for the slow flow velocities
involved in the combustion, as incompressible flows. Thus, the cou-
pling of the hydrodynamics of the incompressible gas flow with
the deflection of the velocity due to the thermal expansion
through the tilted front produces an increase (lowering) of the
gas velocity near the concave part A (convex part B) of the front
as it is shown on figure 1. The resulting effect is to push the
part A downstream toward the burnt gas and the part B upstream.
This produces a strong instability of the front which is descri-
bed by the following dispersion relation /10//11/

$$(2-\gamma)\sigma^2 + 2k\sigma - k^2(\gamma/1-\gamma) = 0 \qquad (1)$$

Where σ is the growing rate of the instability, and, k the corres-
ponding wave number of the wrinkled front, $e^{\sigma t} e^{iky}$. γ is the
expansion ratio defined by $\gamma = (\rho_f - \rho_b)/\rho_f$ which is equal in the
isobaric approximation to $(T_b - T_f)/T_b$ where ρ and T denote the
density and the temperature respectively. The subscripts f and b
identify the fresh and burned mixture respectively, $0<\gamma<1$.
For usual premixed flame γ varies between 0.75 and 0.95. The equa-
tion (1) shows that there is a strong unstable branch given by :

$$\sigma = [\frac{-2 + \sqrt{4 + (2-\gamma)/(1-\gamma)}}{2(2-\gamma)}] k \qquad (2)$$

and that such a flame is always unstable. These last result does
not agree with experimental observations on laboratory burners
where flat fronts of planar premixed flame of 10cm of diameter are stabilized
in an upstream uniform gas flow /2/.

The weakness of the Darrius-Landau model is to comple-
tely neglect the inner structure of the flame front which must be modified
by the local curvature of the front in such a way that the normal velocity

21

of the front cannot be considered as constant. Such modifications
were first introduced in a phenomenological manner by W. ECKHAUS
/12/ and G.H. MARKSTEIN /1/ in the Darrieus-Landau model. Before
to recall the effects of such modifications on the stability pro-
perties, let us briefly present the diffusive thermal model first
proposed by G.I. BARENBLAIT, Y.B. ZEL'DOVICH and A.G. ISTRATOV /13/
which can be now analytically solved by an asymptotic expansion
/6//14/ to provide these curvature effects in a systematic way.

DIFFUSIVE-THERMAL MODEL

This model is exactely the opposite of Darrieus
Landau'sone. By completely neglecting the expansion of gases through
the flame thickness it uncouples the flow velocity field from
the equations of species and energy conservation which then govern
alone, the dynamics of the wrinkled front. Contrarily to the
Darrieus-Landau model, this last model considers the inner struc-
ture of the front but without the effects of the flow velocity
deflections mechanisms through the flame thickness. The heat and
species diffusion and the constant convection in the longitudinal
direction are the only transport mechanisms which are retained,
the transverse convection is completely neglected because the
constant density approximation makes the flow completely insen-
sitive to flame wrinkling. When only one species is supposed to
control the reaction rate, the problem is reduced to solving two
coupled equations concerning the normalized reactant concentration
ψ and the reduced temperature variable $\theta = (T-T_f)/(T_b-T_f)$. Because
the flame velocity is very small compared to the sound velocity,
the energy conservation can be written with the assumption that
the Mach number is negligible in such a way that the two equations
for ψ and θ only differ by the values of the thermal and molecular
diffusivities D_{th} and D. In gases the Lewis number, defined by
$L = D_{th}/D$, is close to unity and constant. These two equations
are coupled by the chemical production of heat $F(\theta, \psi)$ which is
also the chemical consumption of the reactive species. This term
is well known to be highly sensitive to the temperature and its
temperature dependence is usually well represented by an Arrhenius

factor exp $-E/kT$ where the reduced value of the activation energy $\beta = \frac{E}{kT_b} \left(\frac{T_b - T_f}{T_b}\right)$ is assumed to be very large, $\beta \gg 1$.
A direct consequence is that the velocity of a planar and adiabatic flame is also a strongly increasing function of the burning temperature T_b. As it is shown on Fig.2, the key fact for this model to be analiticaly solvable by an asymptotic expansion in large value of β is that, in the limit $\beta \to \infty$, the nonlinear production term $F(\Theta, \Psi)$, becomes negligible except in a very thin reactive zone of d/β thickness located at the end of a large convective-diffusive zone of thickness $d = \rho D_{th}/\rho_f U_f$, d is called the flame thickness, U_f being the flame velocity relative to the fresh mixture. For usual deflagration waves the order of magnitude are the following : $d \approx 5 \; 10^{-1}$mm, $U_f \approx 10$cm/s and $\beta \approx 10$. The second step in understanding the front dynamics is to introduce the local modification of the flame temperature by the curvature of the front. Because the temperature and species concentrations vary through the flame thickness, a curvature of the front induces a transverse diffusive flux of heat and mass which produces a local modification of the temperature of the thin reactive zone. As it is shown in the figure 2, whenever the diffusion of heat is more efficient than the diffusion of the species limiting the reaction, the net effect of the wrinkling is to produce a lowering of the combustion temperature and thus of the local flame velocity in B(and the contrary at A). It turns out, that the flame front is stable in this case and that it can become unstable when the diffusion of heat is less efficient than the diffusion of mass. Thus, a critical value of the Lewis number L:: is expected to separate a stable region L> L:: from an unstable one L<L::. In fact, when β is large the sensitivity to the temperature is so high that a very small departure of the Lewis number from one produces a strong effect and a detailed analysis /6//14/ shows that the precise bifurcation parameter is $\ell = \beta(L_e - 1)$ whith a critical value ℓ:: $= -2$. Close to this critical value, the dispersion relation takes the following form :

$$\sigma = - \frac{(\ell+2)}{2} k^2 - 4k^4 \tag{3}$$

Where d and $t = d/U_f$ are the unit of length and time respectively.

The k^2 term illustrates the transverse diffu-
sive nature of the response mechanism. The
sign of the coefficient of k^2 controls the bifurcation. The always
stabilizing 4th order term k^4 comes from the heat diffusion rela-
xation of the perturbation of the combustion temperature which is
seen to be itself of order k^2. As it is shown on the figure 3.b,
a small range of wave numbers around $k=0$ becomes unstable at the
bifurcation. However, the general dispersion relation given by
a detailed analysis for different values of ℓ is more complicated
than (3) :

$$-\Gamma^2(1-\Gamma) = \frac{\ell}{2}(1-\Gamma+2\omega) \text{ with } \Gamma = \sqrt{1+4(\sigma+k^2)} \qquad (4)$$

Equation (4) shows that   another instability appears for a
moderatly high value of $\ell(\ell_t \sim 32/3)$ for which an Hopf bifurcation
($\text{Im}\sigma \neq 0$) occurs /6/. This result has been used recently to explain
spinning deflagration waves /15/ and travelling combustion waves
/2/ observed in premixed combustion in solid and gaseous phases
respectively. As is indicated by a simple developpement of (4) in
small k and large ℓ with $k\ell$ of order one, $\sigma = -\frac{\ell}{2}(k^2 - \frac{\sigma^2}{4})$, the res-
ponse mechanism is so strong that the effects of acceleration
cannot be neglected and can produce   another mechanism of ins-
tability.

The results given by this diffusive thermal
model are very attractive for gas combustion because they involve
critical values of Lewis number sufficiently close to unity to be
relevant in gases. In fact the upper limit correponding to Lewis
number around 2 seems to be a little too high to be easily attai-
ned. But the lower limit corresponding to Lewis number slighly
smaller than one can be more frequently observed and has been
extensively used /6//14//16/, these last five years, to explain
the cellular structure which appears on premixed flame front
when the limiting component is sufficiently light (rich mixture
of hydrocarbons). The result of the analysis presented in the
following shows that this conclusion is doubtfull and we propose
another interpretation.

A TENTATIVE MODEL OF COUPLING

In fact, the weakness of the diffusive ther-
mal model is to ignore the strong unstability mechanism of Darrieus
and Landau presented at the beginning of this section. A realistic
theory of flame stability must couple the reactive diffusive phe-
nomena with the advective involved in the hydrodynamics.
Up to now, the theoretical description of this complete coupling
was considered as a formidable challenge. It will be shown in the
following that this can be systematically accomplished by associa-
ting a multiscale method to the asymptotics analysis. One of the
recent tentatives of coupling hydrodynamics effects and the dif-
fusive ones in flame was done by G.I. SIVASHINSKY /17/ who used
a tricky approximation. In the preheated zone (diffusive non
reactive), the density ρ was considered as constant and equal to
its upstream value ρ_f but, in the burned gas, the value of the
density was taken to be equal to its actual value ρ_b, $\gamma = (\rho_f - \rho_b)/\rho_f$.
This approximation consists simply in adding the two kind of me-
chanisms without a real coupling. Thus the corresponding dispersion
relation near $\ell = \ell^*$ is a combination of (2) and (3) which, when γ
is small enough, reduces simply to :

$$\sigma = \frac{\gamma}{2} k - \frac{(\ell+2)}{2} k^2 - 4k^4 \tag{5}$$

As it is shown on figure (3.C) this model predicts that contrarely
to experimental observations, the flame front is always unstable
for wave lengths larger than a critical value which is of order
of the flame thickness d. It is clear that this qualitative result,
obtained by this simple analysis, cannot be modified without addi-
tion of a new stabilizing phenomena.

GRAVITY EFFECTS

The direct observations of the difference between a downward and an upward flame propagation /18/, has lead to think, some thirty years ago /1/, that the gravity must play an important role in the stability properties of premixed flames.

It is worthwhile noticing the following property. When the simple coupling model is used in presence of the gravity, the dispersion relation is similar to the one corresponding to a burning liquid layer which was obtained by L. LANDAU /11/ with the pure hydrodynamical model of a reactive interface under gravity but provided with an interfacial tension. The adimensional coefficient of proportionality between the curvature and the pressure jump produced by the surface tension has simply to be replaced by the adimensional response time, $1/(\ell/2+1)$ appearing in the diffusive thermal dispersion relation (3). This clearly indicates that, as it is shown by a comparison of the Markstein result with the Landau's one, these two distincts mechanisms act in a similar manner on the stability properties. Thus, the corresponding dispersion relation is given by (cf./11/) :

$$\sigma^2(2-\gamma)+\sigma(2k)+k(\gamma b-k\frac{\gamma}{1-\gamma} + k^2(\ell+2))= 0 \qquad (5)$$

where $b=gD_{th}/U_f^3$ is an adimensional measure of the effects of the gravity acceleration g. It must be kept in mind that this adimensional parameter varies from $5\ 10^{-1}$ for the slowest flame $(U_f \approx 10cm/s)$ $4\ 10^{-3}$ for flames of usual hydrocarbon-air mixtures $(U_f \approx 40cm/s)$ propagating downward and, thus, must be considered as a small positive quantity. When the flame propagates in the upward direction the gravity has a destabilizing effect $(b<0)$. As it is shown on figure 3.d, it turns out that the flame front of a premixed flame propagating downward could be stable for every wave numbers if the values of ℓ would be larger than the critical value $\ell_c= -2 + \frac{\gamma}{4(1-\gamma)^2 b}$. At this critical value ℓ_c, an unstable wave number appears with the critical value $k_c= 2b(1-\gamma)$. Contrarely to the case of the pure thermal diffusive model, for which the

Lewis number is less than one at the bifurcation, the presence
of the hydrodynamical instability mechanisms, even with a sta-
bilizing gravity effect, requires at the bifurcation a very stron-
gly stabilizing diffusive mechanism characterized by a value of
the Lewis number larger than one (L>1). But in both the cases
the stability limit is a lower bound (L>L_c or $\ddot{L}$ characterizing
in both the cases the domain of stability). In fact, even for the
slowest flame (corresponding to the smallest accessible values
of γ, γ~0.75), the critical value ℓ_c of ℓ has a too high value
(ℓ_c >10) to be   accessible in the actual gases mixtures.
Furthermore, it is readily seen that, for a realistic small value
ϵ of b, k_c and ℓ_c are of order ϵ and ϵ^{-1} respectively, in such
a way that the product $k_c \ell_c$ being of order unity, the upper dif-
fuse thermal limit of stability, ℓ_t=32/3 corresponding to the
Hopf bifurcation mentionned earlier, is surely exceeded, ℓ_c>ℓ_t.
Then this model predicts clearly that there is always a range
of small wave numbers for which usual premixed flames are unstable
By using the troubling approximation, γ→0 with b(1-γ) kept equal
of order unity, B.J. MATKOWSKY and G.I. SIVASHINSKY /19/ derived
a model which leads to conclusions different of those presented
just above. But it is clear by looking at the order of magnitude
that this approximation cannot be relevant for usual flames for
which γ~0.8 and b≤10^{-1}.

DETAILED ANALYSIS OF THE COUPLING BETWEEN THE DIFFUSION PROCESSES AND THE HYDRODYNAMICS OF THE GAS FLOW

For usual flames whose the thickness is
less than one millimeter, the wave lengths involved in the cellu-
lar structures observed experimentally are of an magnitude order
of one centimer /2/. Thus, the hydrodynamics phenomena are seen
to occur on a larger length scale than the diffusion processes
and it is natural to look for describing their coupling by a
multiscale method where the small parameter ϵ is the ratio of
the flame thickness d by the wave length λ, ϵ=d/λ. Such a method
was developped recently by P. CLAVIN and F.A. WILLIAMS /8/ to

describe the modifications of the local flame structure induced
by the deflection mechanism of the stream lines through the flame
thickness. A further investigation shows that these mechanisms
produce a pressure jump accross the flame thickness which acts
at the lowest order in k expansion like a surface tension of a
dynamical nature. In /8/ the flow velocity $\underline{u}_{-\infty}$ at the upstream
boundary of the preheated zone was considered as a given quantity.

In the present work, these quantities have to be com-
puted, like in the Darrieus-Landau approach, by solving the hydro-
dynamical problem occuring on the λ scale. One of the main result
of /8/ is to obtain the evolution equation of the flame front
position $\alpha(y,t)$ in terms of $\underline{u}_{-\infty}$. Its linearized version is sim-
ply given by /8/ :

$$\frac{\partial}{\partial T} \alpha(Y,T) = u_{-\infty} - D_0(\gamma,\ell) \left(u_{-\infty X} - \nabla^2_{YY}\alpha \right) \tag{6}$$

with
$$D_0(\gamma,\ell) = \frac{1}{\gamma} \ln\left(\frac{1}{1-\gamma}\right) + \frac{\ell}{2} \left(\frac{1-\gamma}{\gamma}\right) D_1(\gamma)$$

$$\tag{7}$$

. and
$$D_1(\gamma) = \int_0^{\gamma/1-\gamma} dx \; x^{-1} \; \ell n(1+x)$$

Formula (6) indicates that the main effect on the front dynamics
produced by the flow deflection through the flame thickness is to
replace the coefficient $\frac{\ell}{2}$ +1 appearing in the pure diffusive ther-
mal model (cf.formula (3)) by $D_0(\lim_{\gamma\to 0} D_0 = 1 + \frac{\ell}{2})$.

Formula (6) shows also that, not only the longitudinal component
of the velocity $u_{-\infty}$ of the approaching flow immediately upstream
from the preheated zone affects the front dynamics, but also its
longitudinal gradient $u_{-\infty X}$. In the traditionnal litterature on Combus-
tion/18/20/ the effect of the gradient of the flow velocity is
called the KARLOWITZ-effect. As it was anticipated by W. ECKHAUS
/12/ in his pioneering analytical work, this effect
appears in (6) to be simply, in its linearized version and at the
lowest order in ϵ, a correction of the front curvature in order
to make efficient only the relative curvature of the front compa-
red to the "curvature of the flow".

The result of the work presented in the next section points out that the main effect of the complete coupling in the limit of small k, is that the "dynamical surface tension" and "the Karlowitz effect" stabilize enough the flame to make the critical Lewis number L_c close to one, in such a manner that the bifurcation can be experimentally reached in usual reactive gas mixtures. The critical wave number k_c being roughly unmodified. Thus, even with the Darrieus-Landau instability mechanism, the present theory predicts in agreements with the experiments, that a range of Lewis number must exist for which the planar flame front is stable (at least for slow flame). Furthermore, the bifurcation mechanism is seen to be quite different than the one predicted by the diffusive thermal model.

. . . .\. . .

II - ANALYSIS -
========

        Except for slight modifications introduced by the gravity, the formulation of the problem parallels the works of CLAVIN and WILLIAMS /8/ and the reader is referred to this publication. The conservation equations to be written in the moving coordinates are those for mass, momentum, energy and reactant. Except, for the equations (3), the equations (1) to (9) of the reference /8/ are similar. Only the term $\gamma r.b$ is added to (3). According with the arguments presented in the introduction, b is considered as small parameter $b=\epsilon B$ where $\epsilon<<1$ and $B=O(1)$. As (5) shows, the order of magnitude of the relevant wave numbers ($_{-}k_c$) and of the frequency is expected to be of the same order ϵ. Furthermore, as it is shown by the results of Darrieus and Landau /9//11/, the amplitude of the flow velocity involved in the stability analysis is of the same order ϵ than the wave number. Thus, the scaling presented in /8/ can be used for the present analysis. In the spirit of the multiscale method /21/, the space coordinates appropriate to describe the upstream incompressible flow and the preheated zone are ($X=\epsilon x$, $Y=\epsilon y$, $Z=\epsilon z$) and $\xi = x-\alpha$ respectively where $x=\alpha(Y,Z,T)$ is the equation of the reactive surface /8/. Thus, the expansion introduced in the formula (11) of /8/ can be used with a slight modification for the pressure due to the gravity :

$$p = p_0(\xi)-\epsilon B\xi-\epsilon B\alpha(Y,Z,T)+\epsilon\ P_{-\infty}(X,Y,Z,T)$$
$$+ \epsilon\hat{p}_1(\Xi,\xi,Y,Z,T)+\ldots\ldots \qquad (8)$$

$$U = u_0(\xi)+\epsilon\hat{u}_{-\infty}(X,Y,Z,T)+\epsilon\bar{u}_1(\Xi,\xi,Y,Z,T)+\ldots$$
$$(9)$$
$$V = \epsilon\hat{V}_{-\infty}(X,Y,Z,T)+\epsilon\ \hat{V}_1(\Xi,\xi,Y,Z,T)+\ldots$$

where Ξ is defined by $\Xi=\epsilon\xi$. In fact $p_0(\xi)-\epsilon B\xi$ and $u_0(\xi)$ correspond to the planar steady solution and $p= -\epsilon B\alpha+\epsilon P_{-\infty}$ with $u_-= \epsilon\hat{u}_{-\infty}$ and $v_-= \epsilon\hat{V}_{-\infty}$ are the modifications by the front

wrinkling of the pressure and of the velocity field in the ups-
tream incompressible flow. The multiscale analysis associated
with the asymptotic expansion in β allows to compute order by
order in ϵ the pressure and the velocity jump accross the flame
thickness $\delta p = p_+(X=0)-p_-(X=0)$ $\delta u = u_+(X=0)-u_-(X=0)$ ... where
$p_+(X,Y,Z,T)$ $u_+(X,Y,Z,T)$, V_+ and W_+ are the fields[*] in the
burnt gases. It must be noticed that, for the present stability
analysis, *only the version of /8/, linearized in the amplitudes*
and limited to the ϵ^2 terms, is required. It turns out, from the
multiscale analysis, that u_+, v_+, p_+ and u_-, v_-, p_- verifie the
linearized equations of the incompressible fluid dynamics which
are simply[**] :

$$\frac{\partial}{\partial X} u_- + \frac{\partial}{\partial Y} v_- = 0 \quad , \quad \frac{\partial}{\partial X} u_+ + \frac{\partial}{\partial Y} v_+ = 0 \quad ,$$

(10)

$$\frac{\partial}{\partial T} u_- + \frac{\partial}{\partial X} u_- = - \frac{\partial}{\partial X} p_- \quad , \quad \frac{\partial}{\partial T} u_+ + \frac{1}{1-\gamma} \frac{\partial}{\partial X} u_+ = - \frac{1}{1-\gamma} \frac{\partial}{\partial X} p_+ \quad ,$$

$$\frac{\partial}{\partial T} v_- + \frac{\partial}{\partial X} v_- = - \frac{\partial}{\partial Y} p_- - \alpha_\gamma b \quad , \quad \frac{\partial}{\partial T} v_+ + \frac{1}{1-\gamma} \frac{\partial}{\partial X} v_+ = - \frac{1}{1-\gamma} \frac{\partial}{\partial Y} p_+ - \alpha_\gamma b \quad .$$

Using the normal-modes decomposition of Fourier $\alpha = C\, e^{ikY}\, e^{\sigma T}$,
$u = U(X) e^{ikY+\sigma T}$, $v = V(X) e^{ikY+\sigma T}$, $p_- = -\alpha b + P_-(X) e^{ikY+\sigma T}$,

$$p_+ = -(1-\gamma)\alpha b + P_+(X) e^{ikY+\sigma T}$$

(11)

and assuming bounded values everywhere in the space, the solution
can be written in the following form :

$$P_-(X) = P_-(0) e^{kX} \quad , \quad P_+(X) = P_+(0) e^{-kX}$$

$$U_-(X) = - \frac{k}{k+\sigma} P_-(0) e^{kX} \quad , \quad U_+(X) = A e^{-(1-\gamma)\sigma X} + \frac{k}{(1-\gamma)\sigma - k} P_+(0) e^{-kX} \quad ,$$

$$V_-(X) = i U_+(X) \quad , \quad V_+(X) = \frac{i}{k} \frac{\partial}{\partial X} U_+(X) \quad .$$

(12)

[**] In order to save the notations only one transverse component
of the velocity V will be used.

Notice that, in the linear analysis, the variable Ξ can be replace by X

with the following boundaries conditions on the flame front $X=0$ which are valid up to the ϵ^2 order :

$$\delta P = \begin{cases} \partial_T u_- \ln \frac{1}{(1-\gamma)} - \ell(\partial_x u_{-\infty} - \nabla^2_{yy}\alpha)D_1 + \frac{\gamma}{1-\gamma}(1-P-P')\nabla^2_{yy}\alpha \\[2mm] +(P+P')(\partial_x u_+ - \partial_x u_-) - \gamma\alpha b , \end{cases} \qquad (13)$$

$$\delta u = \frac{\ell}{2}(\partial_x u_- - \nabla^2_{yy}\alpha)D_1 ,$$

$$\delta v = (\partial_T v_- + \partial_T \alpha_y)\ln\frac{1}{1-\gamma} + P(\partial_x v_+ - \partial_x v_-) - \alpha_y\left(\frac{\gamma}{1-\gamma} + b\ln\frac{1}{1-\gamma}\right) .$$

Where P and P' are the Prandtl numbers associated to the shear and bulk viscosity. It is worthwhile to notice that the pressure jump contains a term proportional to $\nabla^2_{yy}\alpha$ which can be interpreted at this ϵ^2 order, as a surface tension. Its origin lies in a second order mechanism of the deflection of the flow velocity through the tilted front.

In order to obtain a non trivial solution for $P_+(0)$ $P_-(0)$, A and C of the system (12) verifying the conditions (13) and (6), the following 4-4 determinant must be zero

	P_-	P_+	A	C
δp	$-\sigma k \ln\frac{1}{1-\gamma}$ $+\ell D_1 k^2$ $+(P+P')k^2$ $+k+\sigma$	$-(P+P')k^2$ $-\left[(1-\gamma)\sigma-k\right]$	$-(P+P')(1-\gamma)\sigma$	$-\gamma b$ $-\frac{1}{1-\gamma}(1-P-P')k^2$ $-\ell D_1 k^2$
δu	$-k$ $-k^2 \frac{\ell}{2} D_1$	$-k$	-1	$\frac{\ell}{2} D_1 k^2$
δv	$-k$ $-k\sigma \ln\frac{1}{1-\gamma}$ $+Pk^2$	k $+Pk^2$	$(1-\gamma)\sigma/k$ $P(1-\gamma)^2\sigma^2/k$	$-k\gamma/1-\gamma$ $+kb\sigma\ln\frac{1}{1-\gamma}$ $kb\ln\frac{1}{1-\gamma}$
$\frac{\partial}{\partial T}\alpha$	$-k(1-kD_0)$	0	0	$-\sigma-k^2 D_0$

32

This relation provides us with the dispersion relation which after factorizing the term $(1-\gamma)\sigma-k$ takes the form :

$$0 = \left[\begin{array}{l} (2-\gamma)\sigma^2+\sigma\{2k+k^2[\log \frac{1}{1-\gamma} + \frac{\ell}{2} D_1(3-\gamma)+(2-\gamma)D_0] \}\\[2mm] +k\{\gamma b-k(\gamma/1-\gamma)+k^2[\frac{\gamma}{1-\gamma} + D_0 (2 + \frac{\gamma}{1-\gamma}) + \ell D_1] \} \end{array} \right. \tag{15}$$

Dynamical   Diffusive   Karlowitz δp
superficial response   +
tension   mechanism velocity deflection

Except a non important difference in the coefficient of σ, this dispersion relation is similar to (5) but with an important modification in the order of magnitude of the coefficient of the last term.

III - DISCUSSIONS OF THE RESULTS -

Except negligible terms which are omitted, the
relation (15) corresponds to the first three terms of the
developpement in power of ϵ of the general dispersion relation
which is supposed to be an analytical function of ϵ. This deve-
loppement is a developpement in the amplitude of the gradient
and (15) corresponds in fact to the following order of the
Darrieus-Landau's result concerning the purely hydrodynamical
model /9//11/. As it is clearly seen on the structure of the
determinant (14) the ϵ^3 order in (15) corresponds to a ϵ^2 order
in the developpement of p, u, v and $\frac{\partial}{\partial T} \alpha$.

The first remark is that the viscosity does not
appear in the dispersion relation at this ϵ^3 order and thus,
can be considered as a negligible effect on the flame stability.
This result is not trivial because the ϵ^3 order of the disper-
sion relation is high enough in principle to contain the vis-
cosity effects which are seen to cancel exactely at this order.

The critical values k_c and ℓ_c are obtained by equa-
ling to zero simultaneously the last term of (15) and its k
derivative to obtain :

$$\cdot \quad = 2b(1-\gamma) \tag{16}$$

$$\frac{\gamma}{1-\gamma} + D_0(\gamma,\ell_c)(2+\frac{\gamma}{1-\gamma})+\ell_c D_1(\gamma) = \gamma/4(1-\gamma)^2 b \tag{17}$$

One verifies directely on (16) the consistency of the choosen
scaling, $b=0(\epsilon)$ with $\epsilon=d/\lambda$. Thus the right hand side of (17) is
seen to be of a large order of magnitude $=1/(1-\gamma)^2 b$. But, as
it is shown by a simple inspection of the order of magnitude
for $\gamma=0.8$ and $b=0.15$, the equation (17) can be satisfied by a
not too high value of $\ell_c=5$ and a small enough value of $k_c=6.10^{-2}$
to preclude the dangerous limit $k_c\ell_c = 0(1)$(cf.Introduction).
This result is due to the fact that each of the four terms of
the left hand side of (17) have the same positive sign (for $\ell>0$)
and are large enough for a realistic value of γ. The physical
reasons are that every k^2 terms, like the thermal diffusive

34

response of the front given by (6), the "dynamical surface tension" and the coupling of the Karlowitz effect with the velocity deflection identified in (15), are all, stabilizing phenomena.

Furthermore a detailed investigation of the structure of the determinant (14) shows that, contrarely to the k^2 terms, the k^3 ones which are neglected in (13) and (6) can produce only negligible effects on the dispersion relation (15) which is thus seen to contain the dominant physical phenomena necessary to make the premixed flame front stable.

But, as the adimensional gravity coefficient b varies like the inverse of the cubic power of the flame velocity, (17) shows that for fast enough deflagration $U_f \geq 20$ cm/s the ℓ_c becomes too high enough to be experimentally accessible.

Thus, the present analysis shows that for slow enough flame, the planar front can be stable even when the hydrodynamics destabilizing effect of Darrieus and Landau is taken into account. One possible experimental test, of these theoretical results could be provided by measuring the cell sizes at the bifurcation (thereshold of the cell apparition) in order to verify whether the following predicted relation corresponding to (16) is true or not :

"the cells size varies like the second power of the flame velocity $U_f^2/(1-\gamma)g$".

Another possibility is to use the laser tomographic method /3/ for measuring, as in /4/, the flame response coefficient D_o of a premixed flame in a weakly upstream turbulent flow to check whether or not D_o goes systematically to zero at the bifurcation. The purely diffusive theory /16//14/ predicts a zero value but not the present theory.

FIGURE 1

INCOMPRESSIBLE FLOW FIELD IN THE DARRIEUS-LANDAU MODEL

— — — Stream lines

——— wrinkled flame front

$U_b/U_f = \rho_f/\rho_b = T_b/T_f > 0$

36

reaction rate $F(\Psi,\theta)$

Reactive species limiting the chemical reaction Ψ

Temperature profile θ

Ψ

1

d

d/ß

A

U_f

U_b

$T = T_f$, $\theta = 0$
$\Psi = 1$

Fresh Mixture

Burnt Gases

$T = T_b$, $\theta = 1$
$\Psi = 0$

U_f

U_b

B

U_f

U_b

Thin reactive zone

Diffusive non-reactive zone
preheated zone
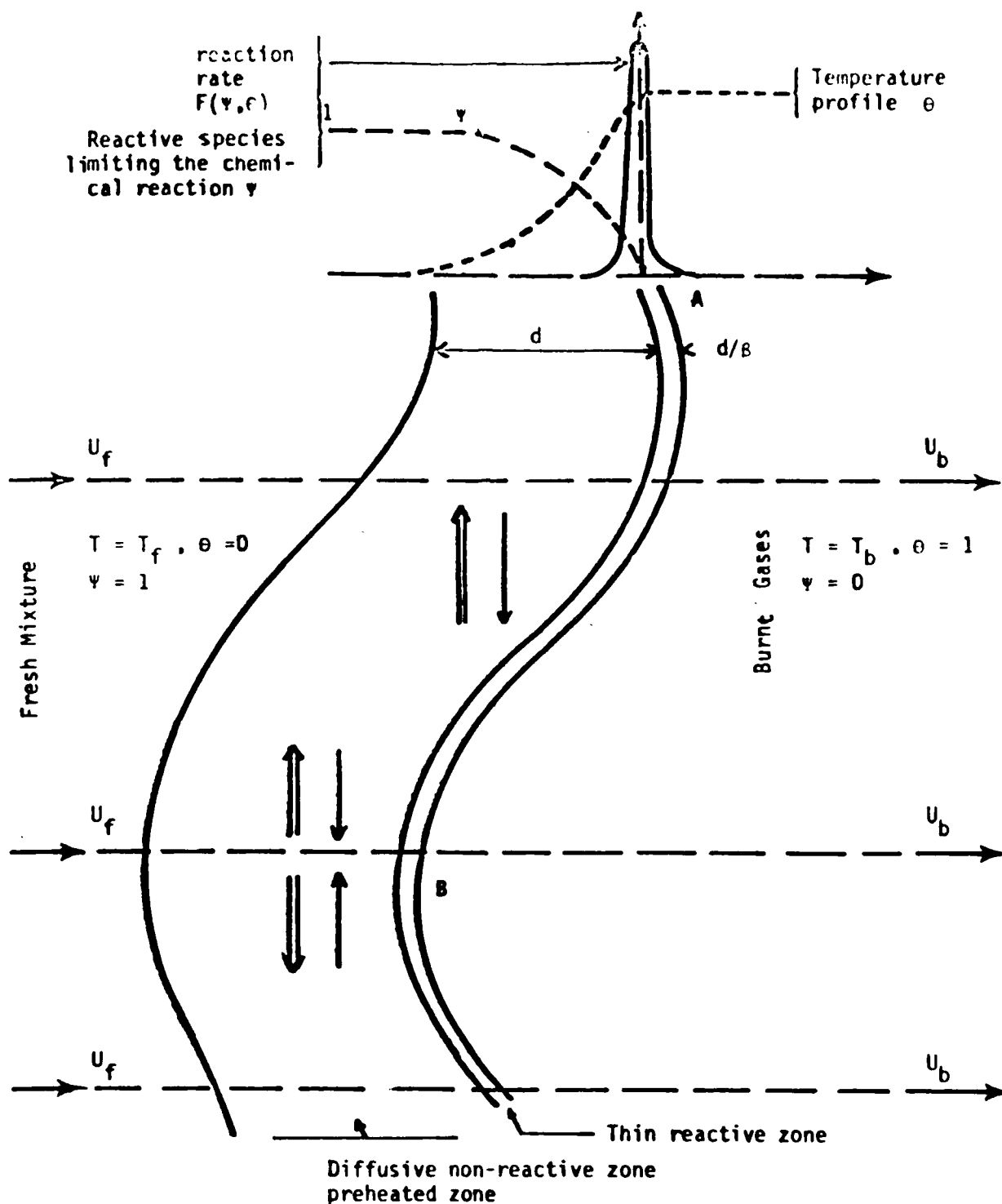
FIGURE 2

FLAME STRUCTURE IN THE DIFFUSIVE-THERMAL MODEL

⟹ Transverse diffusive flux of heat

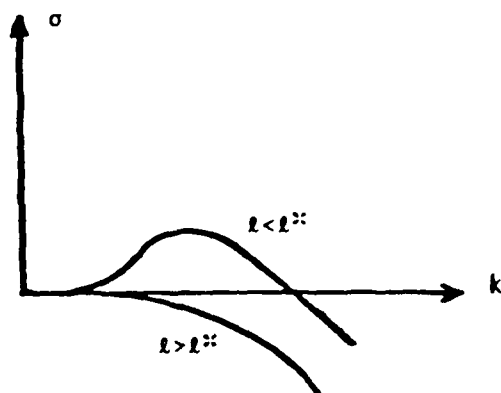→ Transverse diffusive flux of mass

FIG. 3b

DISPERSION RELATION FOR THE DIFFU-
SIVE THERMAL MODEL NEAR $\ell=\ell^{*}$
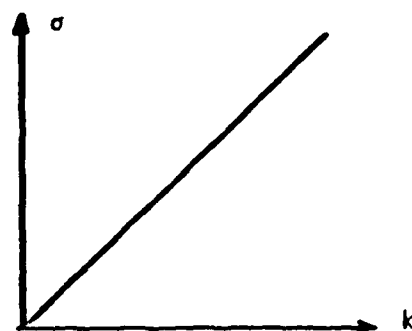

FIG. 3a
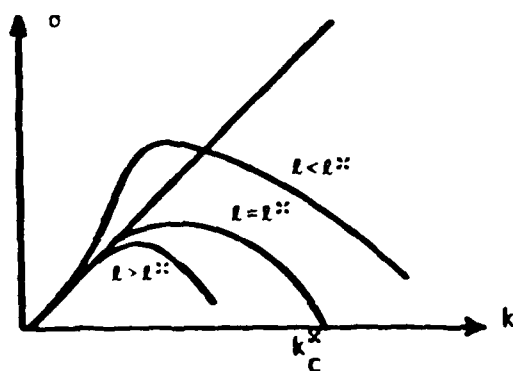
DISPERSION RELATION FOR THE
LANDAU-DARRIEUS MODEL

FIG. 3c

$k_{c}^{*} = 0.5/d$ for $\gamma \_ 0.8$
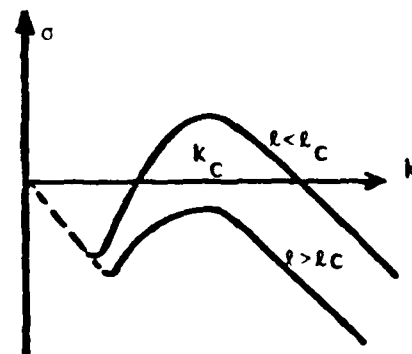$\lambda_{c}^{*} = \Pi d$

FIG. 3d

DISPERSION RELATION WITH A
STABILIZING EFFECT OF THE
GRAVITY.

FIGURES 3

REFERENCES

/1/ G.H. MARKSTEIN. "Nonsteady flame propagation" Pergamon Press (1964)

/2/ F. SABATHIER, L. BOYER and P. CLAVIN. "Experimental study of weak turbulent premixed flame" Proceedings of the Seventh International Colloquium on Gasdynamics of Explosions and Reactive Systems - To appear in AIAA Series Progress in Aeronautics and Astronautics (1981)

/3/ L. BOYER. "Laser Tomographic method for flame front movement studies" Combustion and Flame, 39, 321 (1980)

/4/ L. BOYER, P. CLAVIN and F. SABATHIER. "Dynamical behavior of the front of a premixed turbulent flame". Proceedings of the Eighteenth Symposium (International) on Combustion. The Combustion Institute Pittsburg p.1041-1049 (1981)

/5/ W.B. BUSH and F.E. FENDELL. "Asymptotic analysis of laminar flame propagation for general Lewis number" Combustion Science and Technology, 1, 421 (1970)

/6/ G. JOULIN and P. CLAVIN. "Linear stability analysis of nonadiabatic flames Thermal-Diffusive model" Combustion and Flame, 35, 139 (1979)

/7/ A. LINAN. "The asymptotic structure of counter-flow diffusion flames for large activation energies" Acta Astronautica, 1, 1007 (1974)

/8/ P. CLAVIN and F.A. WILLIAMS. "Effects of molecular diffusion and of thermal expansion on the structure and dynamics of premixed flames in turbulent flows of large scale and low intensity" Accepted in Journal of Fluid. Mech. (1981)

/9/ G. DARRIEUS. Propagation d'un front de flamme : Essai de théorie des vitesses anormales de déflagration par développement spontané de la turbulence. Conférence-faite à la Technique Moderne en 1938 et Congrès de Mécanique Appliquée 194

/10/ L. LANDAU. "Theory of slow combustion" Acta Physico Chim.(URSS) 19, 77 (1944)

/11/ L. LANDAU et E. LIFCHITZ. "Mécanique des Fluides" ed. MIR, Moscou (1971)p.596-597

/12/ W. ECKHAUS. "Theory of flame front stability" J. Fluid. Mech. 10, 80 (1961)

/13/ G.I. BARENBLATT, Y.B. ZEL'DOVICH and A.G. ISTRATOV. "On diffusional thermal stability of laminar flame" Prikl. Mekh. Tekh. Fiz. 2, 21 (1962)

/14/ G.I. SIVASHINSKY. "Diffusional thermal theory of cellular flame", Combustion Science and Technology, 15, 137 (1977)

/15/ G.I. SIVASHINSKY."On Spinning Propagation of Combustion Waves". To be published in SIAM Journal (1981)

/16/ J. BUCKMASTER and G.S.S. LUDFORD. "Theory of Laminar Flames, Cambridge Univ. Press, Cambridge, to appear in 1981 .

/17/ G.I. SIVASHINSKY. "Non Linear Analysis of hydrodynamic instability in laminar flames – I". Acta Astronautica, 4, 1177-1206 (1977)

/18/ LEWIS and Von ELBE,"Combustion Flames and Explosions of Gases, Academic Press (1961)

/19/ B.J. MATKOWSKY and G.I. SIVASHINSKY. "An asymptotic derivation of two models in flame theory associated with the constant density approximation" "Acceleration effects on the stability of flame propagation" SIAM Journal, 37, 669 (1979)

/20/ F.A. WILLIAMS. "Combustion theory", Addison Wesley, Reading Mass (1965)

/21/ A. NAYFEH. "Perturbation methods", Pure & Applied Mathematics (1973)

ELEMENTARY CHEMISTRY IN THE MODELLING
OF ONE DIMENSIONAL COMBUSTION SYSTEMS

Joseph M. Heimerl and Terence P. Coffee
USA Ballistic Research Laboratory, ARRADCOM
Aberdeen Proving Ground, MD   21005

ABSTRACT.   In order to obtain validated kinetic reaction networks we have assembled a code that models the one dimensional, premixed, laminar, steady-state flame.   Our objective is to check model predictions in detail with experimental measurements.   Herein we discuss (1) the results for our test case, ozone and (2) the effects of employing different mixing algorithms for the well characterized multispecies flame $H_2-O_2-N_2$.

The ozone results show explicity that burning velocity comparisons are necessary but not sufficient to define the chemistry; and that profile measurements are in fact necessary.

The five different mixing algorithms used predict essentially the same flame speeds and species profiles for a wide range of $H_2-O_2-N_2$ concentrations. This does not indicate that transport phenomena are unimportant, but rather that the selection of the input values for the species transport properties is more important than the selection of the method used to approximate multispecies transport.

I.   INTRODUCTION.   The overall objective of these studies is to delineate and validate the elementary gas phase kinetic mechanisms involved in the combustion of HMX/RDX propellants.   The modeling of premixed, laminar, steady state flames is the approach taken; first because the governing equations are simple relative to other combustion processes and so one can focus upon the kinetics; and second because laser-based diagnostics enable species and temperature profiles to be experimentally probed and so the model can be validated. Detailed comparison of predicted and measured profiles of species and of temperature serve either to validate the model if agreement is attained or to indicate refinements in the model's kinetic mechanism and/or in the model's input coefficients, if agreement is not attained.   In the later situation the validation process is iterated until agreement is reached.   A sequence of flame studies is underway; from the test case, ozone, through the recognized intermediates, formaldehyde/oxides of nitrogen, to the gas phase elementary network that describes the HMX/RDX flames.   This paper deals with two aspects of this sequence.   The first is a discussion of model results for the ozone flame.   The second examines the effects of using different methods of approximating multispecies transport phenomena.

II.   RESULTS FOR OZONE.   The ozone chemistry itself is simple and relatively well known.   It is thus of potential importance in the testing and checking of new codes that simulate rather complex combustion phenomena and employ elementary chemical reactions (A complete description of the background, motivation and other details can be found elsewhere (1))

The governing equations that describe a one dimensional, premixed, laminar, unbounded flame for a multicomponent ideal gas mixture are [2-4]:

$$(\rho)_t + (\rho u)_x = 0 \tag{1}$$

$$\rho(Y_k)_t + \rho u(Y_k)_x = - (\rho Y_k V_k)_x + R_k M_k, \quad (k = 1,\ldots,N), \text{ and} \tag{2}$$
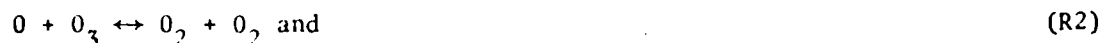
$$\rho(T)_t + \rho u(T)_x = c_p^{-1} \{-q_x + \sum_{i=1}^{N} h_k [(\rho Y_k V_k)_x - R_k M_k]\} \tag{3}$$

where for the ozone case we have taken $q = -\lambda T_x$. For the kth species Y_k and X_k are the mass and mole fractions, respectively, R_k is the net rate of production due to chemistry and M_k is the molecular weight. In addition the diffusion velocity V_k is given by the Stefan-Maxwell relation

$$(X_k)_x = \sum_{j=1}^{N} X_k X_j (V_j - V_k) D_{kj}^{-1} ; \tag{4}$$

and the other symbols have their usual meaning. The pressure through the flame is one atmosphere and constant [4,5]. We neglect effects of viscosity, thermal diffusion, body forces and radiation. The boundary conditions are those of an unbounded flame namely: $T(-\infty) = T_u$, $Y_k(-\infty) = Y_{iu} (i=1,\ldots,N)$; and $(T)_x = (Y_i)_x = 0 (i=1,\ldots N)$ at $x = +\infty$. We employ a relaxation technique and use a modification of the PDECOL package [6] to obtain a solution. PDECOL is based on a finite element collocation method employing B-splines. For computing efficiency we have developed a method of concentrating our breakpoints in the steep flame front where accuracy is necessary [7].

Kinetic, transport and thermodynamic coefficients are required as input to the model. The kinetic mechanism is:

$$O_3 + M \leftrightarrow O + O_2 + M \tag{R1}$$

$$O + O_3 \leftrightarrow O_2 + O_2 \text{ and} \tag{R2}$$

$$O + O + M \leftrightarrow O_2 + M \tag{R3}$$

and expressions for the rate coefficients are taken from the literature [8-10] and are shown in Table 1. Expressions for the transport coefficients [1,11-13] are shown in Table 2 while the specific enthalpy, h_k, and specific heat capacity, c_{pk}, are taken from Gordon and McBride [14]. Each expression for the input coefficients is based on separate, independent measurements and the methodology for obtaining them has been discussed [1].

The viscosity expressions are not explicitly used in the model presented herein, but they have been used implicitly in the derivation of some of. the other transport coefficients [1].

III. RESULTS AND DISCUSSION. Figure 1 shows the O, O_2, O_3 and temperature profiles computed for an initial ozone mole fraction of unity. No experimental profiles are known for comparison; however, we can compare burning velocities. As can be seen in Figure 2 our computed burning velocities compare favorably with both the experimental results of Streng and Grosse [15] and the modeling results of Warnatz [16] (Warnatz has developed a finite difference model that also requires species dependent input coefficients). The solid line in the figure is Streng and Grosse's fit to their data. Over the range of 0.25 to 1.0 initial ozone mole fractions our results are no more than 30% greater than Streng and Grosse's. Over the entire range shown our results agree with Warnatz' with ± 12%. However, this agreement does not imply that the sets of input coefficients used in the respective models are equivalent.

Figure 3 shows the ratio of the values of Warnatz' input coefficients to our corresponding values. This figure shows that at the higher temperatures (i.e., at the larger initial ozone mole fractions), the values for k_1 and k_2 change in opposite directions (see Figure 3). This suggests that the individual effects of k_1 and k_2 on the burning velocity offset each other. This hypothesis is checked by substituting Warnatz' expressions for k_1 and k_2 into our code (This is done in such a way that the equilibrium constants remain unchanged). For the case of the initial ozone fraction of unity, we obtain a burning velocity of 459 cm/s. This value is to be compared to Warnatz' computed value of 445 cm/s. As an added bonus, the difference in these two values provides a measure of the collective effects of differing transport coefficients and different numerical techniques.

In comparing profiles, there are sensible differences in some model results. As an example consider the atomic oxygen profile for an initial ozone mole fraction of unity, Figures 4. (For ease in viewing, the curves have been arbitrarily displaced from each other along the distance axis.) Following the method of comparison discussed above, we substitute Warnatz' expressions for k_1 and k_2 into our code and find the dashed-line profile. Thus, we find that difference in the model profiles are due mainly to the different expressions for k_1 and k_2.

We have recently and critically evaluated the available high temperature experimental data for the ozone decomposition reaction [8], Reaction 1. The expression used here and shown in Table 1 is consistent with all the direct experimental data known to us and is valid over a decade range in temperature.

The expression for k_2 is another story. Figure 5 shows plots of the values of k_2 against reciprocal temperature. Warnatz [17] has developed and used his own expression for k_2 and we have employed Hampson's [9]. To use them in our codes, we both have assumed that the respective expressions are valid for temperatures greater than 1000K, the stated upper limit of applicability of each.

In order to distinguish which expression for k_2, if either, is correct high temperature measurements and/or *ab initio* calculations of the rate coefficient for reaction (2) are required. Alternately, the computed differences in the values for atomic oxygen in the burned region at an initial ozone mole fraction of unity appears to be large enough that profile measurements above such a flame may be sufficient to distinguish between the two expressions.

43

In summary we have shown that this model and its input parameters predict burning velocities that are in reasonable agreement both with the measurements of Streng and Grosse and with the computations of Warnatz. We have also demonstrated that agreement with burning velocities, even over a wide range of initial ozone mole fractions is a necessary but not sufficient condition to ensure that the input coefficients are realistic; for this reason profile measurements are vital to test a model's kinetic input coefficients; and by a comparison of computed profiles, we have indicated the need to measure or to calculate high temperature values for k_2, say in the range 1500-2000K.

IV. TRANSPORT ALGORITHMS. As outlined above our model requires as input not only the kinetics information (of our immediate interest), but also thermodynamic and transport data. Fortunately for the types of chemical species we are interested in, the thermodynamics input is by and large well defined [14,18]. In addition, while some transport coefficients are only well defined through low temperature (< 1000 K) measurements [19], the theory is sufficiently developed to allow reasonable estimates to be made at higher temperatures [2]. A theory has been developed for multicomponent mixtures [2,20-23], but it is computationally cumbersome. To circumvent this, previous workers have generally employed some level of simplification [16,24-33].

This section of the paper addresses the question: which of the mathematical approximations to the multicomponent transport properties provides a desirable trade-off between precision and computational effort. Another way of phrasing this question is to ask what loss in precision of predicted flame speeds and profiles occurs as the mathematical approximations to the multicomponent, polyatomic transport expressions are made cruder.

We have approached this problem by actually computing the properties of the H_2-O_2-N_2* which has a set of well characterized input parameters. We fix these input parameters and vary the transport algorithms. The computed flame speeds and profiles are then compared. The numerical method is discussed in [34,35], and the details of the input parameters and transport algorithms are discussed elsewhere [30,36]. It shall suffice here to simply enumerate the approximations used and briefly discuss the results.

We shall now outline five approximations to the multicomponent, polyatomic formalism, based on the theory of Wang, Chang, and Uhlenbeck [2,20-23]. We start with the most accurate and progressively consider cruder approximations.

Method I

We can write for the heat flux

$$q = \sum_{i=1}^{N} \rho Y_i V_i h_i - \lambda_o T_x - \sum_{i=1}^{N} \frac{RTD_i^T}{M_i X_i} (X_i)_x \tag{5}$$

---

*The ozone flame discussed above is essentially a binary mixture as far as the transport coefficients are concerned and so will not suffice as a test case.

and for the diffusion velocity, which enters into the mass flux, $\rho_i Y_i V_i$, we have

$$V_i = \frac{1}{X_i} \sum_{j=1}^{N} \frac{Y_j}{X_j} D_{ij} (X_j)_x - \frac{D_i^T}{\rho Y_i} (\ln T)_x. \tag{6}$$

Expressions for D_{i_j}, D_k^T and λ_o are computed by a formal expansion.

Method I is the three term Sonine approximation to the formalism expressed in equation (5) and (6), [37] gives a discussion of this approximation. The three term expansion requires the solutions of two matrix equations each involving a matrix of dimension 3NX3N, where N is the number of species. The elements of this matrix are complicated functions of the pressure, temperature, mole fractions, viscosities, binary diffusion coefficients, specific heats, collision numbers and collision integrals. For further details see [36] or [37].

Method II

The above formalism is quite complicated to work with, and so further simplifications are almost invariable made. We can simplify by taking only one term in the Sonine polynomial expansions. For diffusion this simplification can be rearranged [2] to give the Stefan-Maxwell equations, equation (4). This set of equations is not independent, and the constraint

$$\sum_{i=1}^{N} Y_i V_i = 0 \tag{7}$$

must be used in place of one of the equations in (4). Then the diffusion velocities can be found by solving a set of N equations in N unknowns.

Thermal conductivity is also simplified in this manner. But the resulting expression, λ_{mix}^{mon}, is valid only for a mixture of monatomic gases.

To define the heat conductivity for a mixture of polyatomic gases, we adopt Hirshfelder's Eucken-type relation [19,38],

$$\lambda_{mix}^{poly} = \lambda_{mix}^{mon} + \sum_{i=1}^{N} \frac{\lambda i - \lambda i^{mon}}{1 + \sum_{j \neq i} \frac{\mathcal{D}_{ii}}{\mathcal{D}_{ij}} \frac{X_j}{X_i}} \tag{8}$$

Method III

By making additional assumptions, the Stefan-Maxwell equations (4) can be further simplified. A common assumption is that all but the ith species move with the same velocity V. Then we find that

$$(X_i)_x = X_i (V - V_i) \sum_{j \neq i} \frac{X_j}{\mathcal{D}_{ij}} . \tag{9}$$

Employing (7) we find

$$V = \frac{-Y_i V_i}{1 - Y_i} \tag{10}$$

which when substituted into (9) yields the formula recommended by Hirshfelder and Curtiss [39]

$$V_i = - \frac{(1 - Y_i)}{X_i \sum\limits_{j \neq i} \frac{X_j}{\mathcal{D}_{ij}}} (X_i)_x . \tag{11}$$

Unfortunately, the expression in (11) does not in general satisfy equation (7). One technique to satisfy this constraint is due to Boris and Oran [40]. They note that if a set of diffusion velocities V_i satisfy the Stefan-Maxwell equations (4), then so does the set $(V_i + V_c)$, where V_c is some constant. The value of V_c is chosen such that the constraint (7) is satisfied.

The heat conductivity formula employed at this level of approximation is taken from Mason and Saxena's [19,41] simplification of (8), specifically

$$\lambda_o = \sum_{i=1}^{N} \frac{\lambda_i}{1 + \sum\limits_{j \neq 1} \phi_{ij} (X_j / X_i)} \tag{12}$$

where

$$\phi_{ij} = \frac{1.065}{8^{1/2}} \left(1 + \frac{M_i}{M_j}\right)^{-1/2} \left[1 + \left(\frac{n_i M_j}{n_j M_i}\right)^{1/2} \left(\frac{M_i}{M_j}\right)^{1/4}\right]^2 . \tag{13}$$

Here n_i and M_i are the viscosity and molecular weight of the ith species.

Method IV

Equation (11) or some analogous form has often been used to compute diffusion. However, the usual procedure has been to use (11) only to compute $V_1, \ldots, V_{N-1}$. Then V_N is computed from (7). This is less accurate than the Boris and Oran procedure, expecially for V_N.

Also, an empirical formula for the thermal conductivity,

$$\lambda_0 = 0.5 \; [\; \sum_{i=1}^{N} X_i \lambda_i \; + \; \{\; \sum_{i=1}^{N} X_i/\lambda_i \}^{-1}] \; , \tag{14}$$

is often used [19,42].

Method IV is comprised of these common approximations.

Method V

In the case of binary mixture the Stefan-Maxwell equations (4) reduce to Fick's law. Specifically we have,

$$Y_1 V_1 = -\mathcal{D}_{12} \; (Y_1)_x \quad . \tag{15}$$

A generalization of (15) can be made [3], and yields

$$Y_i V_i = -D_{im}(Y_i)_x \; , \tag{16}$$

where

$$D_{im} = \frac{1 - X_1}{\sum_{\substack{j \neq i}} \dfrac{X_j}{\mathcal{D}_{ij}}} \quad . \tag{17}$$

Additional assumptions that $\rho^2 D_{im}$, $\rho\lambda$ and $(c_p)_{mix}$ are each independent of temperature are made and the procedure that permits an *a priori* selection of these quantities has been discussed [36].

Table 3 shows a summary of the five methods of computing the transport properties used in this paper. Five H_2-O_2-N_2 flames were selected and their initial conditions listed in Table 4. The total pressure is fixed at one atmosphere for all flames. The computed flame speed for each flame as a function of transport method is tabulated in Table 5 (The flame speeds for .flame A are not corrected to 291 K, as has been done [24]. If this were done, the value AI for example would be 12.2 cm/s instead of 14.1 cm/s). The values of the flame speeds span a large range and for a given flame are essentially independent of the transport method. The largest difference between Method I, the most complete formulation of the transport, and any other method is 16% (Compare Methods I and III, flame D).

Note that even our *a priori* method of selecting constant transport coefficients, Method V, gives results that are quite close to the much more complex Method I.

As we have seen in the ozone flame, reproduction of flame speeds is a necessary but not sufficient condition to judge the relative effectiveness of the transport methods. We must also examine the species and temperature profiles of these flames. As examples we consider two sets of profiles that exhibit differences among the five methods that are as large as any observed. Figures 6 and 7 show the OH profiles for flame D. Figures 8 and 9 show the H_2 profiles for flame C. As can be seen these profiles are very similar. The other species profiles and the temperature profiles show at least this degree of similarity among the five profiles as in the example given.

V. DISCUSSION. The numerical results shown in Table 5 demonstrate that reliable results can be obtained for the H_2-O_2-N_2 system even for the case of our *a priori* determined constant transport method. Note that we cannot infer that transport is unimportant! The computed profiles and flame speeds can be sensitive to the choice of transport parameters selected. For the relative tests of the transport methods here, we have employed the same set of species viscosities, thermal conductivities and binary diffusion coefficients in all cases. We have demonstrated that the method used to generate the multicomponent, polyatomic transport coefficients is not critical for the H_2-O_2-N_2 flame. And since this flame is reasonably complex we infer that this result has a high probability of being valid for other flames.

Indeed, we conclude that gross errors detected in comparing the results of different models are more likely to be traceable to differences in input data rather than to the method of approximating multicomponent polyatomic transport properties.

In summary we find that the choice of a multicomponent transport algorithm is not critical.

Note added in proof: In practice the solution to equation *(1)-(3)* is facilitated through the introduction of the transformation $(\psi)_x = \rho$. See [1] for details.

Table 1. Kinetic Coefficients

COEFFICIENT	EXPRESSION*	REFERENCES	REMARKS
k_1	$4.31 \times 10^{14} \exp(-11{,}161/T)$	Heimerl & Coffee, 8	$300K \leq T \leq 3000K$, $M=O_3$
k_{-1}	$1.2 \times 10^{13} \exp(+976/T)$		Derived from equilibrium const.
k_2	$1.14 \times 10^{13} \exp(-2300/T)$	Hampson, 9	$200K \leq T \leq 1000K$
k_{-2}	$1.19 \times 10^{13} \exp(-50600/T)$		Derived from equilibrium const.
k_3	$1.38 \times 10^{18} T^{-1} \exp(-171/T)$	Johnston, 10	$1000K \leq T \leq 8000K$, $M=O_2$
k_{-3}	$2.75 \times 10^{19} T^{-1} \exp(-59732/T)$	Johnston, 10	$1000K \leq T \leq 800K$, $M=O_2$

*centimeter-mole-second units

Table 2. Transport Coefficients

TRANSPORT COEFFICIENT	EXPRESSION	REFERENCES
λ_1[a]	$1.60 \times 10^{-6} \, T^{0.71}$	Dalgarno and Smith, 11
λ_2	$5.74 \times 10^{-7} \, T^{0.827}$	Hanley and Ely, 12
λ_3	$3.90 \times 10^{-7} \, T^{0.842}$	Heimerl and Coffee, 1
pD_{12}[b]	$1.32 \times 10^{-5} \, T^{1.774}$	Marrero and Mason, 13
pD_{13}	$1.66 \times 10^{-5} \, T^{1.665}$	Heimerl and Coffee, 1
pD_{23}	$1.18 \times 10^{-5} \, T^{1.665}$	Heimerl and Coffee, 1
η_1[c]	$3.34 \times 10^{-6} \, T^{0.71}$	Dalgarno and Smith, 11
η_2	$4.16 \times 10^{-6} \, T^{0.689}$	Hanley and Ely, 12
η_3	$4.24 \times 10^{-6} \, T^{0.65}$	Heimerl and Coffee, 1

[a] Heat conductivity in units of $cal-cm^{-1}-s^{-1}-K^{-1}$. Subscripts 1, 2, 3 refer to O, O_2 and O_3, respectively.

[b] Pressure multiplied by binary diffusion coefficient in units of $atmos-cm^2-s^{-1}$.

[c] Viscosity in units of $gm-cm^{-1}-s^{-1}$.

TABLE 3. SUMMARY OF TRANSPORT METHODS

Method	Remarks
I	3 terms of Sonine polynomial expansion (3 N by 3 N matrix); only method that has non-zero thermal diffusion.
II	For diffusion, 1 term of Sonine polynomial expansion (N by N matrix), Eq. (4) and (7). For thermal conductivity, Hirshfelder-Eucken method (N by N matrix), Eq. (8).
III	Diffusion velocities computed from simplified Stefan-Maxwell relation, Eq. (11). Each is adjusted by a common factor, V_c, so as to satisfy $\sum_{i=1}^{N} Y_i V_i = 0$. Thermal conductivity from Mason and Saxena, Eq. (12) and (13).
IV	Diffusion velocities computed from the simplified Stefan-Maxwell relation, Eq. (11), for N-1 species. V_n is computed from Eq. (7). Empirical thermal conductivity formula, Eq. (14).
V	Diffusion velocities from generalized Fick's law, Eq (16) and (17). Empirical thermal conductivity formula, Eq (14). In addition $\rho^2 D_{im} = constant$; $\rho\lambda = constant$; $c_p = constant$; constants are determined *a priori*.

TABLE 4. INITIAL TEMPERATURE AND MOLE FRACTIONS
FOR THE FIVE FLAMES STUDIED

Flame	X_{H2}	X_{O2}	X_{N2}	T_u
A	.1883	.0460	.7657	336
B	.2000	.1680	.6320	298
C	.5000	.1050	.3950	298
D	.9000	.1000	0	298
E	.6000	.4000	0	298

TABLE 5. FLAME SPEEDS CALCULATED USING
THE FIVE TRANSPORT MODELS

Flame	I	II	III	IV	V
A	14.1	14.6	14.9	14.9	16.0
B	98	101	102	103	96
C	292	300	310	308	291
D	378	379	438	402	348
E	892	922	971	969	847
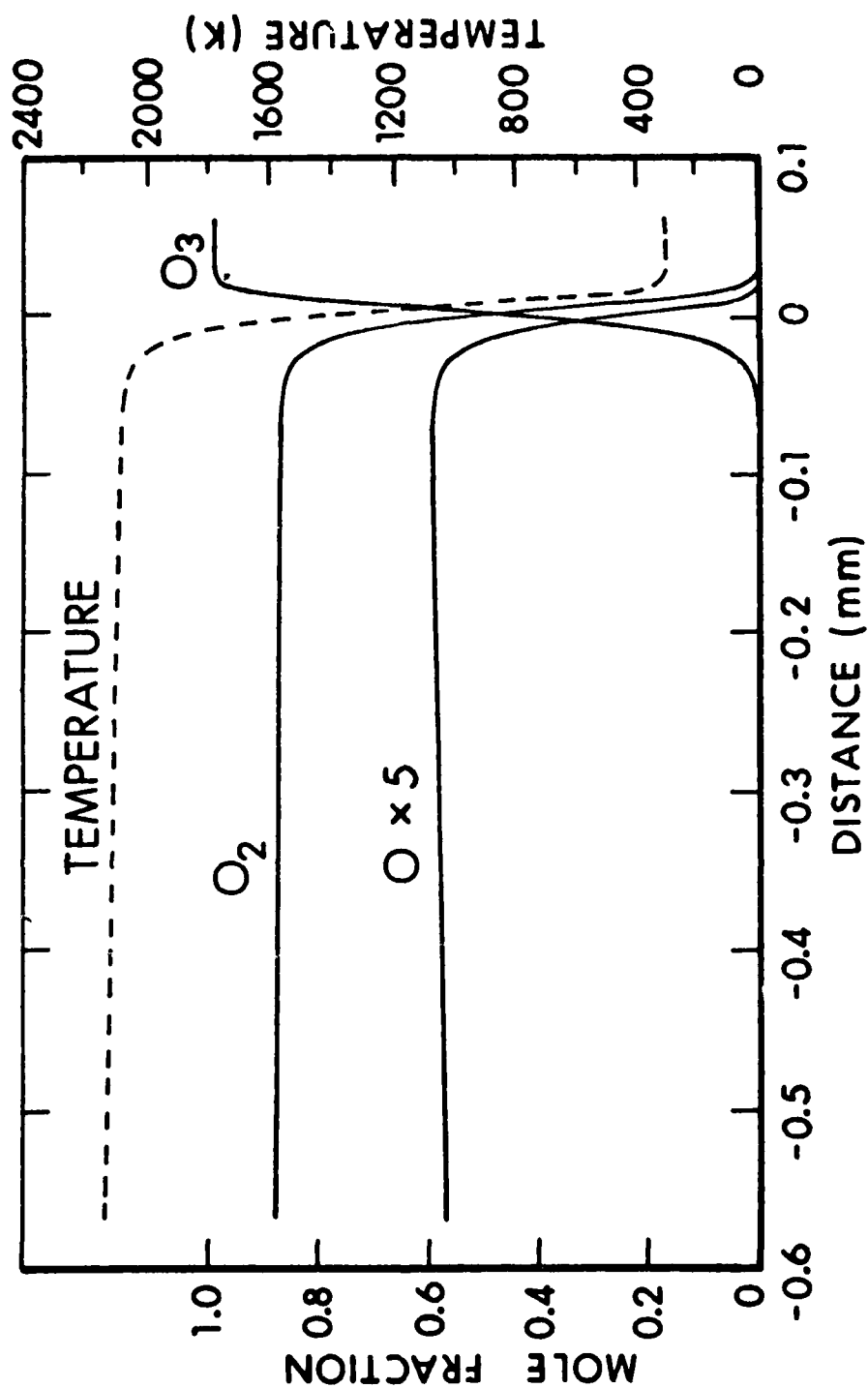
Figure 1. Computed profiles for unity initial ozone mole fraction.

53
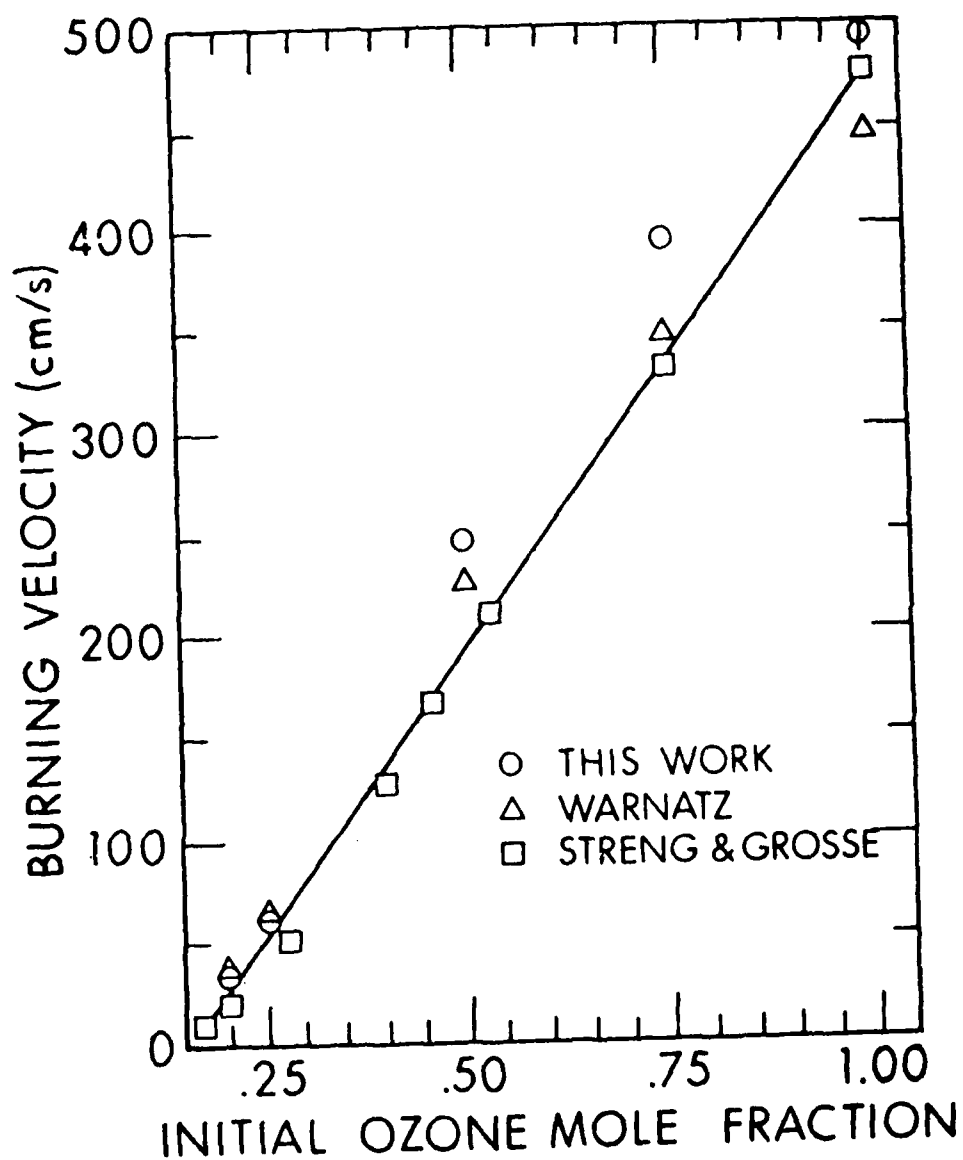
Figure 2. Comparison of experimental (Streng and Grosse) and computed burning velocities over a wide range of initial ozone mole fractions.
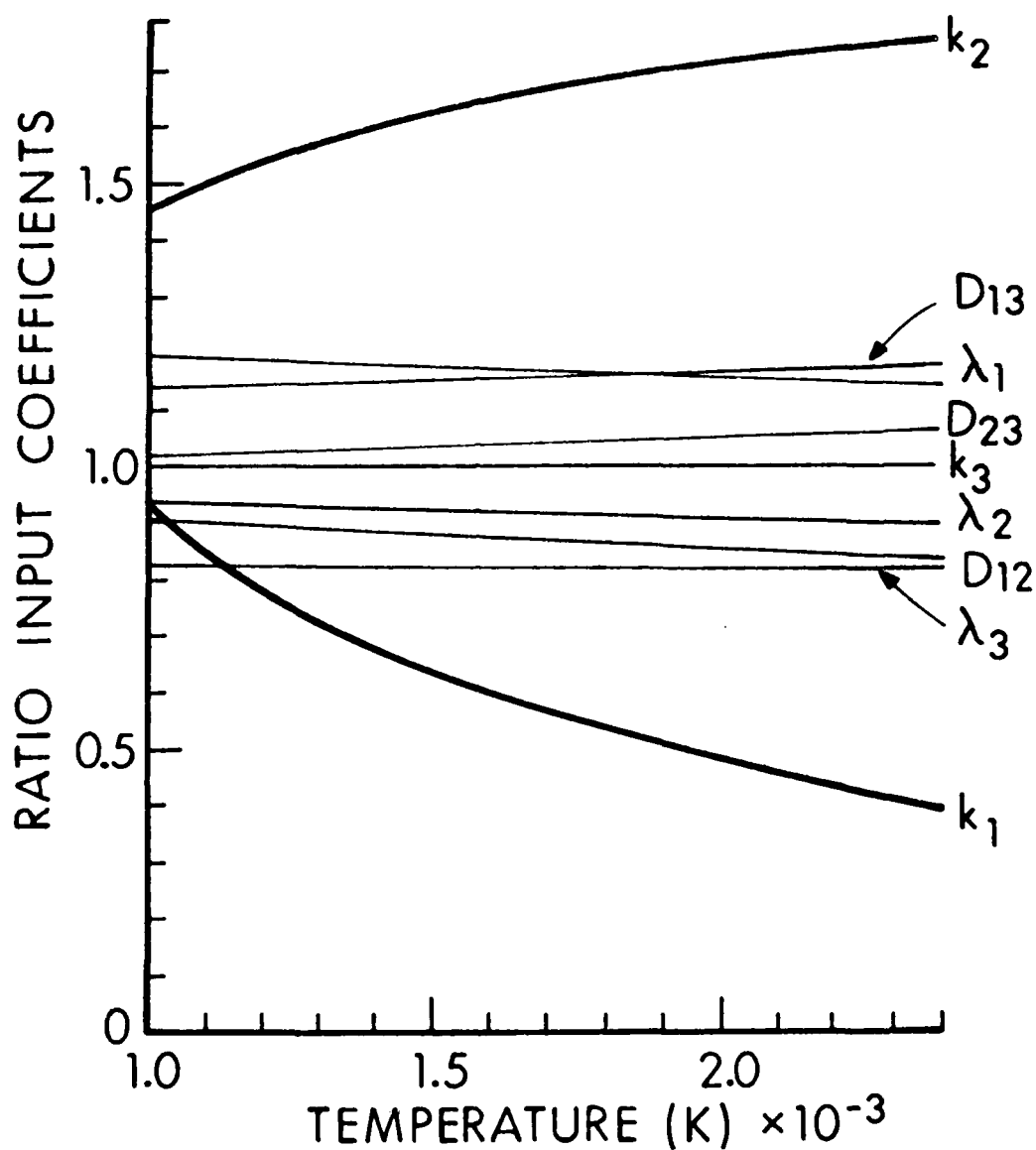
Figure 3. Ratio of the values of Warnatz' and our input coefficients; for example, the ratio $k_{1,Warnatz}/k_{1,this\ paper}$ is given by the curve identified by k_1. Subscripts on the rate coefficients refer to reactions. Subscripts 1, 2 and 3 on the transport coefficients refer to O, O_2 and O_3, respectively.
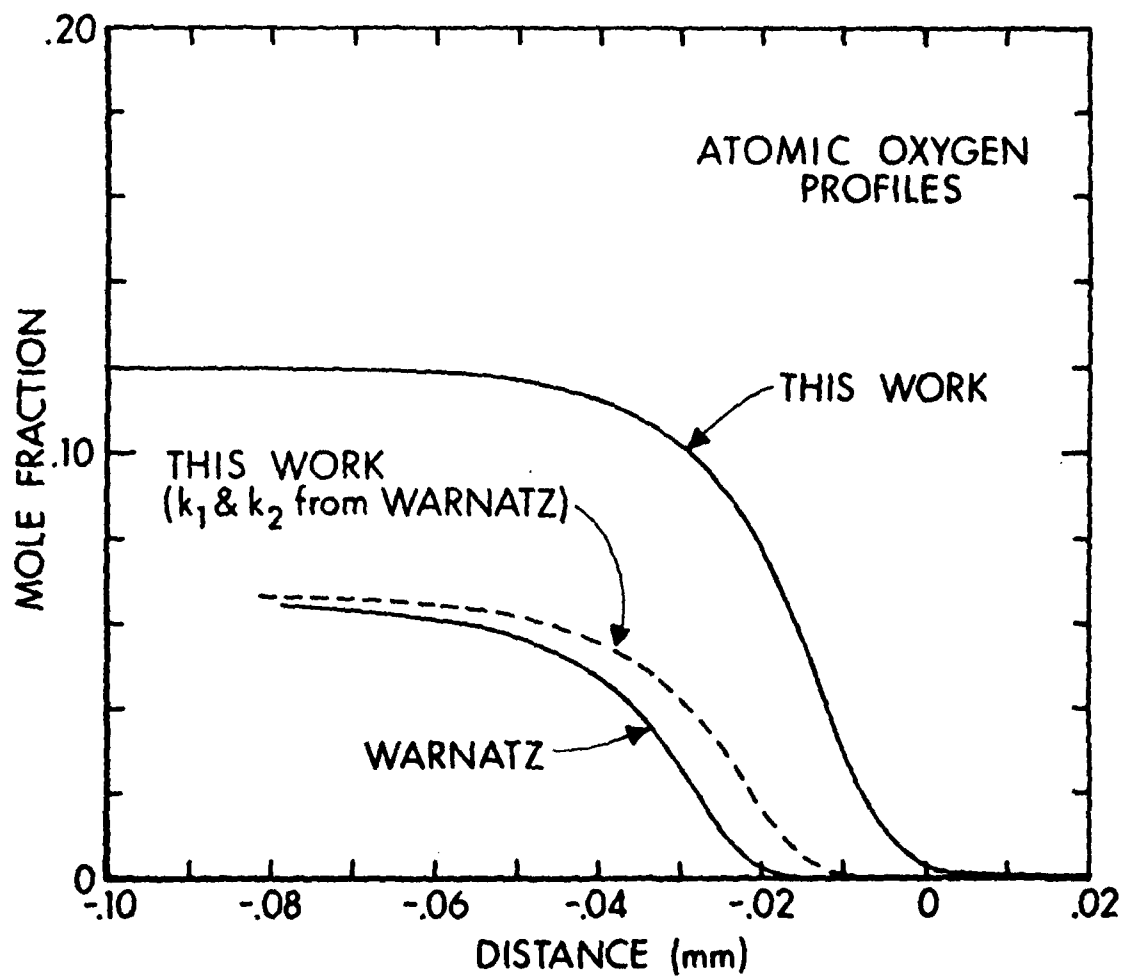
Figure 4. Calculated atomic oxygen profiles for unity initial ozone mole fraction. The dashed profile is the result of substituting Warnatz' expression for k_1 and k_2 into our model.
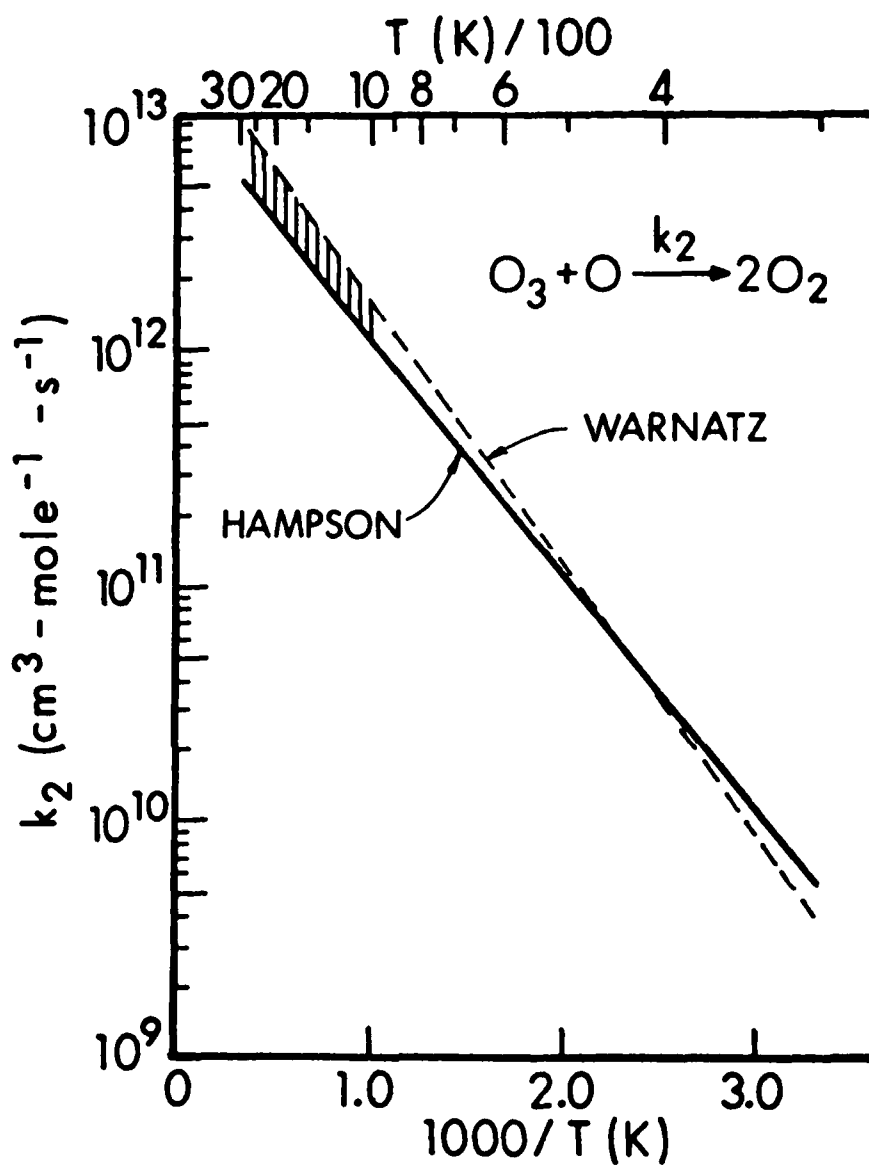
Figure 5. Expression for the rate coefficient for reaction 2. The filled-in area denotes the region of temperature over which both expressions have been assumed to be valid.
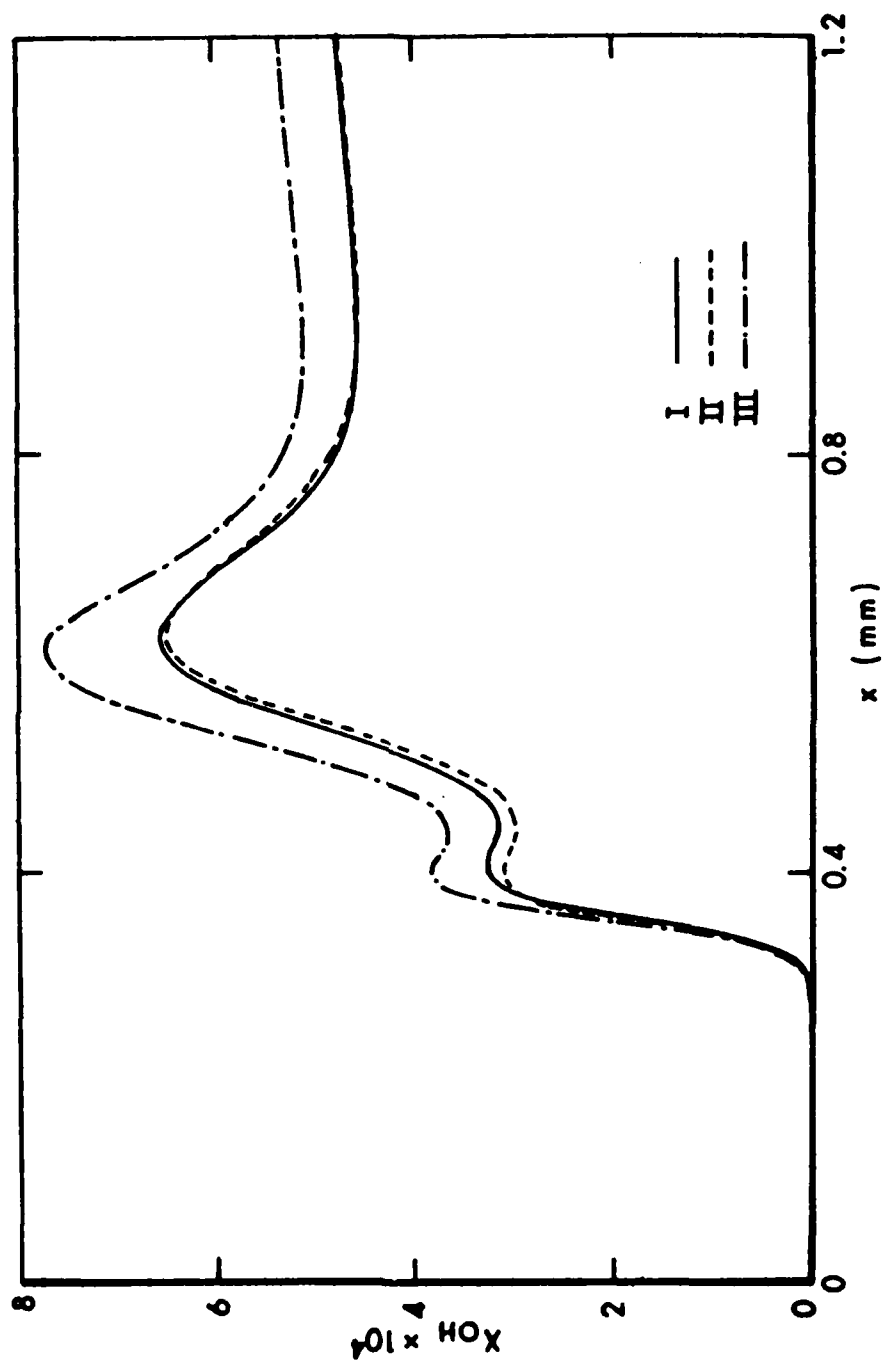
Figure 6. The OH Profile for Flame D.

58
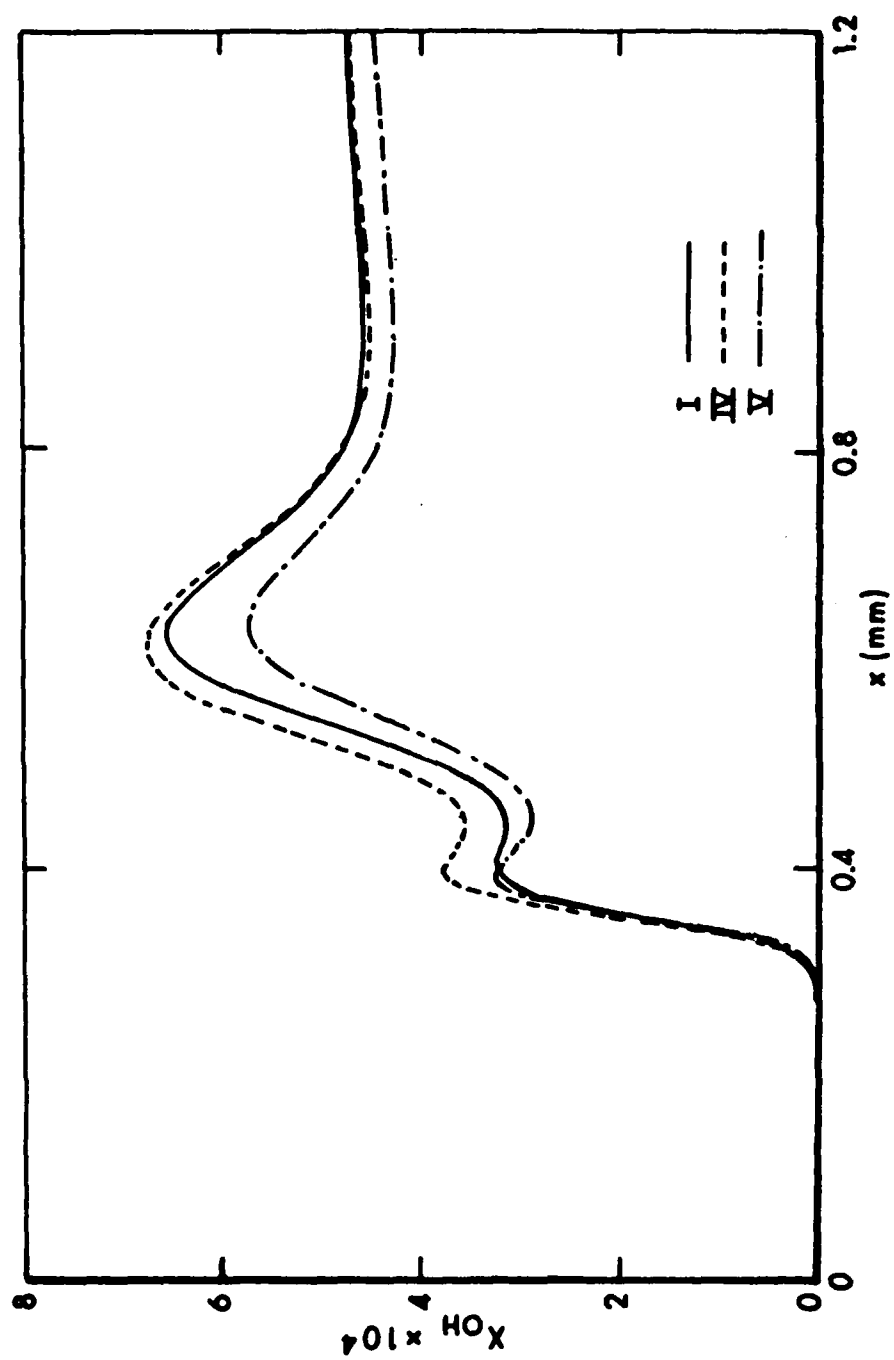
Figure 7. The OH Profile for Flame D.
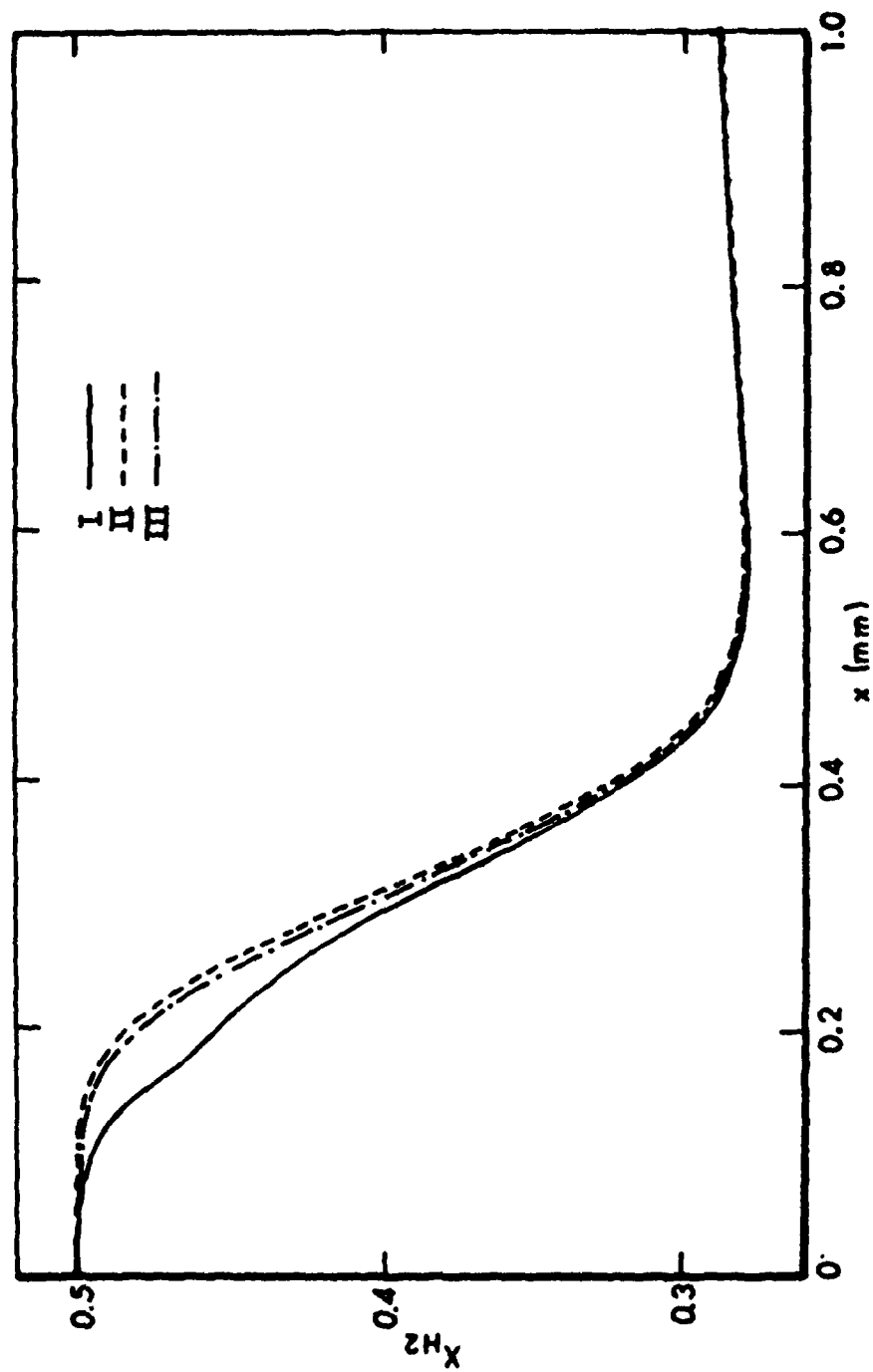
Figure 8. The H_2 Profile for Flame C.

Figure 9. The H_2 Profile for Flame C

61

REFERENCES

1. J.M. Heimerl and T.P. Coffee, Combust. Flame, 39, 301-315 (1980).

2. J.O. Hirschfelder, C.F. Curtis and R.B. Bird, "Molecular Theory of Gases and Liquids," 2nd printing, corrected, with noted, John Wiley and Sons, NY, 1960.

3. R.B. Bird, W.S. Stewart and E.N. Lightfoot, ".ransport Phenomena," John Wiley and Sons, NY, 1960.

4. F.A. Williams, "Combustion Theory," Addison-Wesley, Reading, MA, 1965.

5. R.M. Fristrom and A.A. Westenberg, "Flame Structure", McGraw-Hill, NY, 1965, p. 319.
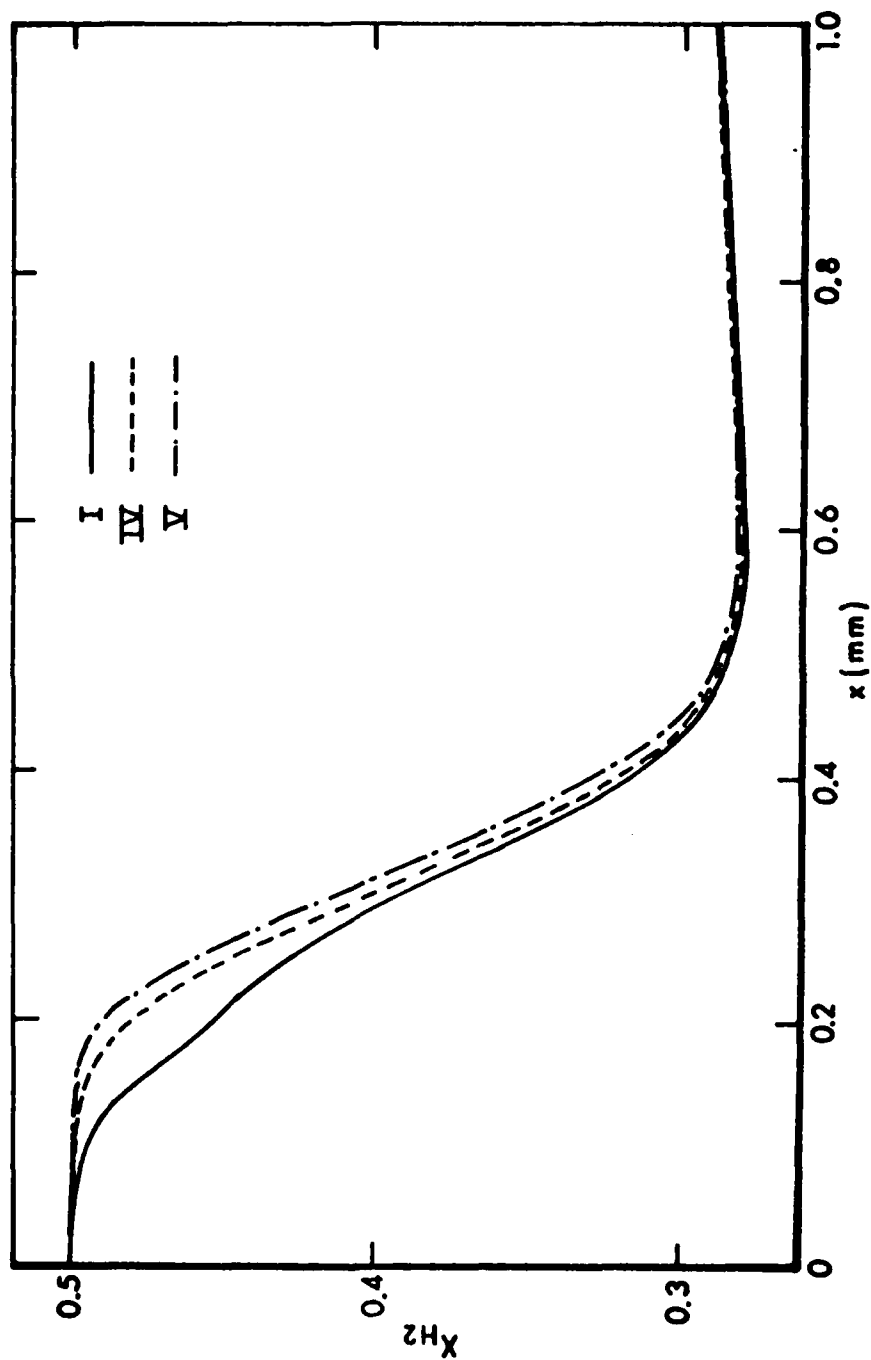
6. B.K. Madsen and R.F. Sincovec, Preprint UCRL-78263 (Rev 1), Lawrence Livermore Laboratory, 1977, PDECOL: General Collocation Software for Partial Differential Equations.

7. T.P. Coffee and J.M. Heimerl, BRL Technical Report ARBRL-TR-02212, January 1980 (AD-E430 386), A Method for Computing the Flame Speed for a Laminar, Premixed, One Dimensional Flame.

8. J.M. Heimerl and T.P. Coffee, Combust. Flame, 1979, 35, 117-123, The Unimolecular Ozone Decomposition Reaction.

9. R.F. Hampson, (ed), J. Phys. Chem. Ref. Data, 1973, 2, 267-312, Survey of Photochemical and Rate Data for Twenty-Eight Reactions of Interest in Atmospheric Chemistry.

10. H.S. Johnston, NSRDS-NBS-20, September 1968, Gas Phase Reaction Kinetics of Neutral Oxygen Species.

11. A. Dalgarno and F.J. Smith, Planet Spac. Sci, 1962, 9, 1-2, The Thermal Conductivity and Viscosity of Atomic Oxygen.

12. H.J.M. Hanley and J.F. Ely, J. Phys. Chem. Ref. Data, 1973, 2, 735-755, The Viscosity and Thermal Conductivity Coefficients of Dilute Nitrogen and Oxygen.

13. T.R. Marrero and E.A. Mason, J. Phys. Chem. Ref. Data, 1972, 1, 3-118, Gaseous Diffusion Coefficients.

14. G.S. Gordon and B.J. McBride, NASA-SP-273, 1971, Computer Program for Calculation of Complex Chemical Equilibrium Compositions, Rocket Performance, Incident and Reflected Shocks, and Chapman-Jouquet Detonations, (1976 program version).

15. A.G. Streng and A.V. Grosse, "The Ozone to Oxygen Flame, Sixth Symposium (International) on Combustion," Reinhold Publishing Company, 1957, pp. 264-273.

16. Warnatz, J., Ber. Bunsenges Phys. Chem., 1978, 82, 193-200, Calculation of the Structure of Laminar Flat Flames I: Flame Velocity of Freely Propagating Ozone Decomposition Flames.

17. J. Warnatz, Berechnung der Flammengeschwindigheit und der Struktur von Laminaren Flashen, Habilitationsschrift, Darmstadt, 1977.

18. D.R. Stull and H. Prophet, JANAF Thermochemical Tables, 2nd Edition, NSRDS-NBS-37, June 1971.

19. Y.S. Touloukian, P.E. Liley and S.C. Saxena, Thermophysical Properties of Matter, Vol. 3, Thermal Conductivity (Nonmetallic Liquids and Gases), IFI/Plenum, NY-Washington, (1970).

20. C.S. Wang Chang, G.E. Uhlenbeck and J. deBoer, Studies in Statistical Mechanics, Vol. 2, JOhn Wiley and Sons, NY, (1964).

21. L. Monchick, K.S. Yun and E.A. Mason, "Formal Kinetic Theory of Transport Phenomena in Polyatomic Gas Mixtures," J. Chem. Phys., 39, 654-669 (1963).

22. L. Monchick, A.N.G. Pereira and E.A. Mason, "Heat Conductivity in Polyatomic and Polar Gases and Gas Mixtures," J. Chem. Phys., 42, 3241-3256 (1965).

23. L. Monchick, R.J. Munn and E.A. Mason, "Thermal Diffusion in Polyatomic Gases: A Generalized Stefan-Maxwell Diffusion Equation," J. Chem. Phys., 45, 3051-3058 (1966).

24. G. Dixon-Lewis, et al., "Flame Structure and Flame Reaction Kinetics," Proc. R. Soc., London A 317, 235-263 (1970); A 330, 199-218 (1972); A 331, 571-584 (1973); and A 346, 261-278 (1975).

25. G. Dixon-Lewis, "Kinetic Mechanism, Structure and Properties of Premixed Flames in Hydrogen-Oxygen-Nitrogen Mixtures," Phil. Trans. R. Soc., London, 292, 45-99 (1979).

26. G. Tsatsaronis, "Prediction of Propagating Laminar Flames in Methane, Oxygen, Nitrogen Mixtures," Combust. and Flame, 33, 217-239 (1978).

27. D.B. Spalding and P.L. Stephenson, "Laminar Flame Propagation in Hydrogen + Bromine Mixtures," Proc. R. Soc. London A, 324, 315-337 (1971).

28. P.L. Stephenson and R.G. Taylor, "Laminar Flame Propagation in Hydrogen, Oxygen, Nitrogen Mixtures," Combust. and Flame 20, 231-244 (1973).

29. L.D. Smoot, W.C. Hecker and G.A. Williams, "Prediction of Propagating Methane-Air Flames," Combust. and Flame 26, 323-342 (1976).

30. J. Warnatz, "Calculation of the Structure of Laminar Flat Flames II; Flame Velocity and Structure of Freely Propagating Hydrogen-Oxygen and Hydrogen-Air Flames," Ber. Bursenges Phys. Chem., 82, 643-649 (1978).

31. D.B. Spalding, P.L. Stephenson and R.G. Taylor, "A Calculation Procedure for the Prediction of Laminar Flame Speeds," Combust. and Flame 17, 55-64 (1971).

32. L. Bledjian, "Computation of Time-Dependent Laminar Flame Structure," Combust. and Flame, 20, 5-17 (1973).

33. E. Cramarossa and G. Dixon-Lewis, "Ozone Decomposition in Relation to the Problem of the Existance of Steady-State Flames," Combust. and Flame 16, 243-251 (1971).

34. T.P. Coffee and J.M. Heimerl, "A Method for Computing the Flame Speed for a Laminar, Premixed, One Dimensional Flame," BRL Technical Report, ARBRL-TR-02212, Jan 80.

35. T.P. Coffee, "A Computer Code for the Solution of the Equations Governing a Laminar, Premixed, One Dimensional Flame," BRL Memorandum Report, to be published.

36. T.P. Coffee and J.M. Heimerl, "Transport Algorithms for Premixed Laminar Steady-State Flames," BRL Technical Report, ARBRL-TR-02302, March 1981. Also Combust. and Flame to be published.

37. G. Dixon-Lewis, "Flame Structure and Flame Reaction Kinetics II. Transport Phenomena in Multicomponent Systems," Proc. Roy. Soc. A 307, 111-135 (1968).

38. J.O. Hirshfelder, "Heat Conductivity in Polyatomic, Electronically Excited, or Chemical Reacting Mixtures III," Sixth International Combustion Symposium, Reinhold Publishing Corporation, NY, 351-366 (1957).

39. J.O. Hirshfelder and C.F. Curtiss, "Theory of Propagation of Flames Part I: General Equations," Third International Combustion Symposium, Williams and Wilkins Co., Baltimore, 121-127 (1949).

40. E.S. Oran and J.P. Boris, "Detailed Modeling of Combustion Systems," Proj. Energy Combust. Sci. 7, 1-72 (1981).

41. E.A. Mason and S.C. Saxena, "Approximate Formula for the Thermal Conductivity of Gas Mixtures," Phys. Fluids, 1, 361-369 (1958).

42. J.H. Burgoyne and F. Weinberg, "A Method of Analysis of a Plane Combustion Wave," Fourth Symposium on Combustion, Williams and Wilkins Co., Baltimore, 294-302 (1953).

PULSATING COMBUSTION

Bernard J. Matkowsky
Department of Engineering Sciences and Applied Mathematics
The Technological Institute
Northwestern University
Evanston, Illinois 60201

Pulsating combustion, in which the velocity of propagation exhibits periodic oscillations about some mean value, has been observed in a variety of contexts in the combustion of both solid and gaseous fuels.

In this paper we will review some of our work on pulsating combustion in the gasless combustion of solid fuels, as well as in the combustion of gases.

1. Pulsations in the Gasless Combustion of Solid Fuels

In an interesting paper, Merzhanov, Filonenko and Borovinskaya [1] reported on their experimental findings in the gasless combustion of condensed systems. This type of combustion occurs without formation of a gas, so that the solid sample itself burns and is tranformed directly into solid products. The authors reported the phenomena of autooscillatory combustion and of spin combustion. In experiments with a cylindrical sample consisting of a mixture of niobium and boron, the observed autooscillatory combustion consisted of a propagating planar reaction front whose velocity pulsated periodically. The burned samples retained their cylindrical shape and exhibited a layered structure; the number of layers was equal to the number of pulsations. The authors described the phenomenon of spin combustion, which was observed in cylindrical samples of hafnium in a nitrogen/argon

mixture, as follows. Upon ignition of the specimen, a small luminous spot appeared and moved in a helical motion along the surface of the unburned specimen. The spot was observed to rotate in both clockwise and counter-clockwise directions, and sometimes several spots were observed rotating either in the same or in opposite directions. Spin effects were also observed in the combustion of zirconium and titanium in a nitrogen/argon mixture.

Further observations of spin combustion of gasless systems were reported in [2]. These systems involved compressed titanium/ferrocarbon, and titanium/aluminum mixtures in helium or argon, under low pressure. In contrast to the experiments in [1], where the burning occurred only on and near the lateral surface of the cylinder, these experiments exhibited spiral propagation throughout the interior of the cylindrical sample, as well as on its surface.

In a theoretical study, Matkowsky and Sivashinsky [3] described how the phenomenon of autooscillatory combustion in condensed systems originated from an instability of a uniformly propagating plane front. Employing a nonlinear reaction diffusion model for the temperature and the concentration of the chemical species which limits the reaction, they showed that a plane front solution which propagates with constant velocity from the high temperature combustion products to the low temperature unburned fuel, existed for all values of the parameters. As a parameter α increased beyond a critical value α_c, the uniform front became unstable and a new solution corresponding to a pulsating propagating front bifurcated from the uniformly propagating solution. The parameter α was proportional to a nondimensional activation energy, and to the difference between the nondimensional temperature in the burned and unburned regions. In the model, diffusion of the reactant was

neglected, since the unburned fuel and the combustion products were both solid. Employing numerical methods on a similar model, Shkadinsky, Khaikin and Merzhanov [4] observed the existence of pulsating plane combustion fronts.

Recently, Ivleva, Merzhanov and Shkadinsky [5] employed a simplified model of combustion in a cylindrical shell, to numerically describe spinning combustion as a surface phenomenon. That is, they describe the situation in which the burning occurred only on the surface of the cylindrical sample. In order to describe spinning combustion in which the burning occurs throughout the cylindrical sample, Sivashinsky [6] considered the model of Matkowsky and Sivashinsky [3] in a cylindrical geometry. He presented a linear stability analysis of the uniformly propagating plane front and showed that, as a parameter increases beyond a critical value, the plane front is unstable to perturbations which correspond to spinning modes of propagation. Of course, to show that the model actually describes spinning propagation, it is necessary to derive spinning solutions of the full nonlinear problem, and to show that these solutions are stable. Therefore Kaper, Leaf and Matkowsky [7], presented a nonlinear analysis to show that various types of solutions bifurcate supercritically from the uniformly propagating plane front solution. One type corresponds to a propagating pulsating reaction with waves travelling in both clockwise and counter-clockwise directions along its front, another corresponds to a pulsating reaction with standing waves along its front. The former type of solution corresponds to spinning propagation. The travelling wave solutions describing spinning propagation were then shown to be stable, whereas the standing wave solutions were unstable. In addition, other combinations of axial, radial and tangential modes of propagation were observed to bifurcate and their stability was studied.

2. Pulsations in Gaseous Combustion

In the model employed in the analysis of gasless combustion, diffusion of the reactant was neglected, since the unburned fuel as well as the combustion products were both solid. Mathematically, this corresponds to an infinite Lewis number, defined as the ratio of thermal diffusivity to diffusivity of the reactant which limits the reaction. Some authors have attributed the appearance of the pulsating solutions to the fact that the Lewis number was infinite. However, it has been shown that such pulsations can occur at finite Lewis numbers L, exceeding a critical L, thus describing combustion in gases. Employing a simplified model for flame propagation in gases, derived by Matkowsky and Sivashinsky [8], Matkowsky and Olagunju presented nonlinear analyses of the problem for gases in one [9], and two [10] dimensions respectively. They showed in [9] that for $L > L_c$, a plane pulsating front arises as a stable supercritical bifurcation from the uniformly propagating plane front, while in [10] they showed that for $L > L_c$, a stable pulsating solution with travelling waves along its front bifurcated supercritically. In [15], Matkowsky and Olagunju showed how pulsations arise in burner stabilized flat flames, thus explaining the experimental results involving ammonia-oxygen mixtures, referred to in [11]. Pulsating plane fronts have been observed experimentally in gases [cf. 11], as have fronts with travelling waves along their surfaces [12,13,14]. In [16], Matkowsky and Olagunju consider the problem in a cylindrical domain, and allow three dimensional perturbations. A nonlinear analysis is presented to show that for $L > L_c$, various types of solutions, including spinning waves, bifurcate from the uniformly propagating plane front. The amplitude and frequency of the bifurcated solutions are calculated, and it is shown that their

average speeds are less than the speed of the uniformly propagating solution. Finally the stability of the bifurcated solutions is discussed. Numerical studies by Margolis [11], who considered hydrogen-oxygen flames, and by Golovichev, Grishin, Agranat and Bertsun [17] who considered hydrogen-bromine flames, also exhibited pulsating flame fronts.

REFERENCES

1. A. G. Merzhanov, A. K. Filonenko and I. P. Borovinskaya, "New phenomena in combustion of condensed systems," Proc. Acad. Sci. U.S.S.R., Phys. Chem. Soc., Vol. 208 (1973), pp. 122-215.

2. Y. M. Maksimov, A. T. Pak, G. B. Lavrenchuk, Y. S. Naiborodenko and A. G. Merzhanov, "Spin combustion of gasless systems," Combustion, Explosion and Shock Waves, Vol. 15, No. 4 (1979), pp. 415-418.

3. B. J. Matkowsky and G. I. Sivashinsky, "Propagation of a pulsating reaction front in solid fuel combustion," SIAM Journal on Applied Mathematics, Vol. 35 (1978), pp. 465-478.

4. K. G. Shkadinsky, B. I. Khaiken and A. G. Merzhanov, "Propagation of a pulsating exothermic reaction front in the condensed phase, Combustion, Explosion and Shock Waves, Vol. 1 (1971), pp. 15-22.

5. T. P. Ivleva, A. G. Merzhanov and K. G. Shkadinsky, "Math'l model of spin combustion, Soviet Physics Doklady, Vol. 239 (1978), pp. 255-256.

6. G. I. Sivashinsky, "On spinning propagation of combustion waves," SIAM Journal on Applied Mathematics, Vol. 40 (1981), pp. 432-438.

7. H. G. Kaper, G. K. Leaf and B. J. Matkowsky, "Spinning waves in gasless combustion," to appear.

8. B. J. Matkowsky and G. I. Sivashinsky, "An asymptotic derivation of two models in flame theory associated with the constant density approximation," SIAM Journal on Applied Mathematics, Vol. 37 (1979), pp. 686-699.

9. B. J. Matkowsky and D. O. Olagunju, "Propagation of a pulsating flame front in a gaseous combustible mixture," Vol. 39, No. 2 (1980), pp. 290-300.

10. B. J. Matkowsky and D. O. Olagunju, "Travelling waves along the front of a pulsating flame, accepted for publication.

11. S. B. Margolis, "Bifurcation Phenomena in burner-stabilized premixed flames," Combustion Science and Technology, Vol. 22 (1980), pp. 143-169.

12. G. H. Markstein, Nonsteady flame propagation, Pergamon Press (1964).

13. C. R. Ferguson and J. C. Keck, "Stand-off distances on a flat flame burner,"Combustion and Flame, Vol. 34 (1979), pp. 85-98.

14. F. Sabathier, L. Boyer and P. Clavin, "Experimental study of weak turbulent premixed flames," Proc. Seventh Int'l Colloq. on Gasdynamics of Explosions and Reactive Systems, to appear in AIAA Series Progress in Aeronautics and Astronautics.

15. B. J. Matkowsky and D. O. Olagunju, "Pulsations in a burner-stabilized plane flame," SIAM Journal on Applied Mathematics, Vol. 40 (1981),pp. 551-562.

16. B. J. Matkowsky and D. O. Olagunju, "Spinning waves in gaseous combustion," to appear.

17. V.I. Golovichev, A. M. Grishin, V. M. Agranat and V. I. Bertsun, "Thermokinetic oscillations in distributed homogeneous mixtures," Sovier Physics Doklady, Vol. 241 (1978), pp. 477-479.

STRESS INTENSITY FACTORS FOR AN INFINITE ARRAY OF

COLLINEAR CRACKS SUBJECTED TO VARYING PRESSURE

A. P. Parker
Department of Civil Engineering
Royal Military College of Science
Shrivenham, Swindon, Wilts, England
(On attachment to Army Materials and Mechanics Research Center
Watertown, Massachusetts 02172, USA)

J. C. Mason
Department of Mathematics & Ballistics
Royal Military College of Science
Shrivenham, Swindon, Wilts, England

ABSTRACT. In this paper a weight function, obtained from an existing stress intensity factor solution and associated crack shape, is used to determine the class of analytic solutions corresponding to a more general loading for the same geometry. By this technique, the stress intensity factor for an infinite array of collinear cracks, whose surfaces are subjected to a variable pressure distribution, is expressed in the form of an integral. This integral is solved explicitly for the case of a band of constant pressure acting over a portion of the crack surfaces. A possible use of this solution in the construction of a Dugdale model is discussed, and an application to the case of an array of rivet-loaded cracks is demonstrated.

INTRODUCTION. Consider a two dimensional, linearly elastic body, under conditions of plane strain, containing an infinite array of straight cracks (Fig. 1). Suppose that each crack is of length $2a$, and that distances between centers of adjacent cracks are each equal to $2b$.

Stress intensity factors are sought for the case in which the same pressure distribution is applied to the upper and lower surfaces of each crack. The pressure distribution $p(x)$, where x is measured from one of the crack centers, is then periodic of period $2b$ in x. Defining direct stress, shear stress and vertical displacement as σ, τ and v, respectively, the boundary conditions for the solution are

$$\sigma_y(x, 0) = -p(x) \quad , \quad |x - 2nb| \le a \quad , \tag{1}$$

$$\tau_{xy}(x, 0) = 0 \quad , \quad -\infty < x < \infty \quad , \tag{2}$$

$$v(x, o) = 0 \quad , \quad a \le |x - 2nb| \le 2b - a \quad . \tag{3}$$

Sneddon & Srivastav [1] have obtained a plane strain solution to this problem for the special case $p(x) = p_o$, in which the pressure on the crack faces is constant. The crack tip stress intensity factor is then given by

$$K = p_o \ (2b \ \tan \frac{\pi a}{2b})^{1/2} \tag{4}$$

and the associated crack shape is

$$v(x, a) = (\frac{2b}{\pi a}) \ \epsilon^\omega \quad \ell n(\cos \frac{\pi x}{2b} + [\cos^2 \frac{\pi x}{2b} - \cos^2 \frac{\pi a}{2b}]^{1/2}) - \ell n \cos \frac{\pi a}{2b} \quad , \tag{5}$$

where

$$\omega = \frac{2(1 - v^2) \ p_o \ a}{1} \quad . \tag{6}$$

Here E and v denote Young's Modulus and Poisson's ratio, respectively.

THE WEIGHT FUNCTION. One approach which may be used to obtain new stress intensity factor solutions is the weight function method of Bueckner [2] and Rice [3]. (See also [4], [5], [6].) The weight function, which is unique to a given cracked geometry, may be derived from one known stress intensity factor solution and associated crack shape. It may then be used to obtain other K solutions for the same geometry, under a different set of applied loads. The additional information required to determine the second solution is simply the stress distribution along the line of the crack, in the equivalent uncracked geometry.

72

In general the weight function for plane strain is defined as

$$m(x, a) = \frac{E}{(1 - \nu^2)} \cdot \frac{1}{2K} \cdot \frac{\partial v(x, a)}{\partial a} \ . \tag{7}$$

The new stress intensity factor K_{new} for the same geometry under a given crack-face loading $p(x)$ is then given by:

$$K_{new} = \int_{-a}^{a} p(x) \cdot m(x, a) \ dx \ , \tag{8}$$

provided that $p(x)$ has the same symmetries as the original solution (see [2] for details).

For the geometry under consideration, differentiation of equation (5) yields

$$\frac{\partial v(x, a)}{\partial a} = \frac{4b(1 - \nu^2)}{\pi E} P_0 \left\{ \frac{\frac{\pi}{2b} \cos \frac{\pi a}{2b} \sin \frac{\pi a}{2b} \ [\cos^2 \frac{\pi x}{2b} - \cos^2 \frac{\pi a}{2b}]^{-1/2}}{\cos \frac{\pi x}{2b} + [\cos^2 \frac{\pi x}{2b} - \cos^2 \frac{\pi a}{2b}]^{1/2}} + \frac{\pi}{2b} \tan \frac{\pi a}{2b} \right\}$$

Rewriting $\cos^2 \frac{\pi x}{2b} - \cos^2 \frac{\pi a}{2b}$ as $\sin^2 \frac{\pi a}{2b} - \sin^2 \frac{\pi x}{2b}$ and making simplifications, we obtain

$$\frac{\partial v(x, a)}{\partial a} = \frac{2(1 - \nu^2)}{E} P_0 \tan \frac{\pi a}{2b} \cdot \frac{\cos \frac{\pi x}{2b}}{[\sin^2 \frac{\pi a}{2b} - \sin^2 \frac{\pi x}{2b}]^{1/2}} \ . \tag{10}$$

Substituting for K and $\frac{\partial v(x, a)}{\partial a}$ from (4) and (10) into (7), we obtain the weight function

$$m(x, a) = (2b \tan \frac{\pi a}{2b})^{1/2} \frac{1}{2b} \frac{\cos \frac{\pi x}{2b}}{[\sin^2 \frac{\pi a}{2b} - \sin^2 \frac{\pi x}{2b}]^{1/2}} \ . \tag{11}$$

STRESS INTENSITY FACTOR SOLUTIONS. Substituting equation (11) into (8), we obtain the stress intensity factor

$$K_{new} = (2b \tan \frac{\pi a}{2b})^{1/2} \; \frac{1}{2b} \int_{-a}^{a} p(x) \; \frac{\cos \frac{\pi x}{2b}}{[\sin^2 \frac{\pi a}{2b} - \sin^2 \frac{\pi x}{2b}]^{1/2}} \; dx \; . \qquad (12)$$

To test this solution as the crack spacing increases, we note that

$$\operatorname*{lt}_{b \to \infty} K_{new} = (\frac{a}{\pi})^{1/2} \int_{-a}^{a} \frac{p(x)}{[a^2 - x^2]^{1/2}} \; dx, \qquad (13)$$

which conforms with the solution due to Sih et al [7] for a single, symmetrically-loaded crack in an infinite sheet.

For the case of a band of constant pressure, p, acting over upper and lower crack faces from -d to d, for any d between 0 and a (Fig. 2), equation (12) becomes

$$K_{new} = p(2b \tan \frac{\pi a}{2b})^{1/2} \cdot \frac{1}{2b} \int_{-d}^{d} \frac{\cos \frac{\pi x}{2b}}{[\sin^2 \frac{\pi a}{2b} - \sin^2 \frac{\pi x}{2b}]^{1/2}} \; dx \; . \qquad (14)$$

By making the substitution

$$z = \frac{\sin \frac{\pi x}{2b}}{\sin \frac{\pi a}{2b}} \; , \quad dz = \frac{\pi}{2b} \; \frac{\cos \frac{\pi x}{2b}}{\sin \frac{\pi a}{2b}} \qquad (15)$$

equation (14) can be integrated immediately to give

$$K_{new} = p \; [2b \tan \frac{\pi a}{2b}]^{1/2} \; \frac{2}{\pi} \; \arcsin \left[\frac{\sin \frac{\pi d}{2b}}{\sin \frac{\pi a}{2b}} \right] . \qquad (16)$$

Two special cases of equation (16) are as follows:

(a) d = a, i.e. constant pressure over the whole of both crack faces for an infinite array of cracks. In this case (16) reduces to:

$$K_{new} = p \; [2b \tan \frac{\pi a}{2b}]^{1/2}$$

which is precisely the value of K given by (4).

(b) d → 0, i.e. central point loading for an infinite array of cracks. In this case (16) gives

$$\underset{d \to 0}{Lt} \quad \frac{K_{new}}{2pd} = [b \sin \frac{\pi a}{b}]^{-1/2}$$

which conforms with the solution due to Tada [8], obtained by the use of Westergaard stress functions.

A MODEL TO TAKE ACCOUNT OF CRACK-TIP PLASTICITY. By employing the superposition illustrated in Figure 3, it is a simple procedure to obtain K for a narrow band of constant, negative pressure along the parts of the crack faces nearest to the tips. This may be used as a Dugdale model [9] in order to take account of crack tip plasticity in the infinite array. In this case the magnitude of the pressure and the necessary modification to crack length are dictated by the yield strength of the material.

GRAPHICAL PRESENTATION OF RESULTS.

(a) Band of Pressure

Figure 4 shows a plot, based on equation (16), of dimensionless stress intensity factor versus $\frac{d}{a}$ for various $\frac{b}{a}$ ratios. Note that the solution is non-dimensionalized with respect to K for a fully pressurized crack carrying an identical force over the crack faces.

(b) Application to Riveted Configurations

A simple model to represent an array of cracked, rivet-loaded holes is illustrated in Figure 5a. The opening-mode stress intensity factor, K_I, for this configuration may be obtained by the superposition technique illustrated in Figure 5. Figure 6 shows a plot of the superposed, dimensionless K_I solution for various $\frac{b}{d}$ ratios. This presentation keeps the ratio of pressure band dimension to crack spacing constant, in order to model a riveted configuration.

CONCLUSIONS. Weight functions, which are unique to a geometry containing an array of cracks may be calculated from existing stress intensity and crack shape solutions. These weight functions may be integrated to obtain new stress intensity solutions for a different loading applied to the same geometry. A simple superposition allows the extension of such solutions to the case of an array of cracked, rivet-loaded holes in an infinite sheet.

REFERENCES

1. I. N. Sneddon and R. P. Srivastav, The Stress in the Vicinity of an Infinite Row of Collinear Cracks. P.R.S.E. LXVII, A, Part I, 39-49 (1963-64).

2. H. F. Bueckner, A Novel Principle for the Computation of Stress Intensity Factors. ZAMM 50, 9, 529-546 (1970).

3. J. R. Rice, Some Remarks on Elastic Crack-tip Stress Fields, Int. J. Solids Structures, 8, 751-758 (1972).

4. A. F. Grandt, Stress Intensity Factors for Some Through-cracked Fastener Holes. Int. J. of Fracture, 11, 2, 283-294 (1975).

5. A. F. Grandt, Two Dimensional Stress Intensity Factor Solutions for Radially Cracked Rings. Technical Report AFML-TR-75-121, Wright Patterson AFB (1975).

6. L. F. Impellizzeri and D. L. Rich. Spectrum Fatigue Crack Growth in Lugs. ASTM STP 595, 320-336 (1976).

7. G. C. Sih, P. C. Paris, F. Erologan, Crack Tip Stress Intensity Factors for Plane Extension and Plate Bending Problems. Trans ASME, J. Appl. Mech., 306-312 (1962).

8. H. Tada, Westergaard Stress Functions for Several Periodic Crack Problems. Engng. Fracture Mech., 2, 177-180 (1970).

9. D. S. Dugdale, Yielding of Steel Sheets Containing Slits. J. Mech. Phys. Sol., 8, 100-108 (1960).
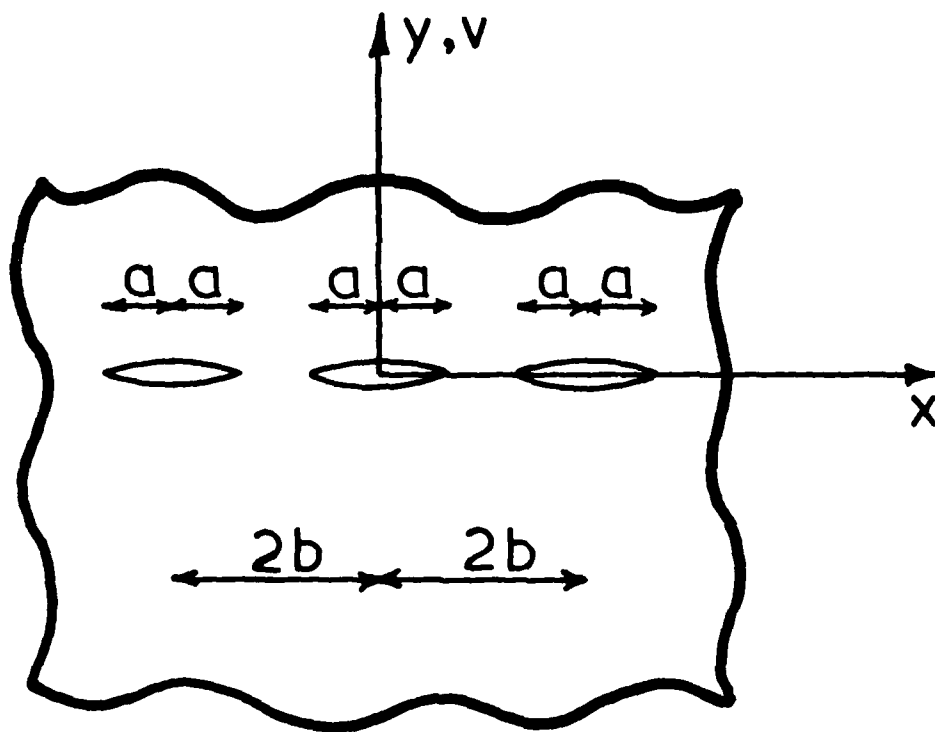
Figure 1 : Infinite Array Configuration.
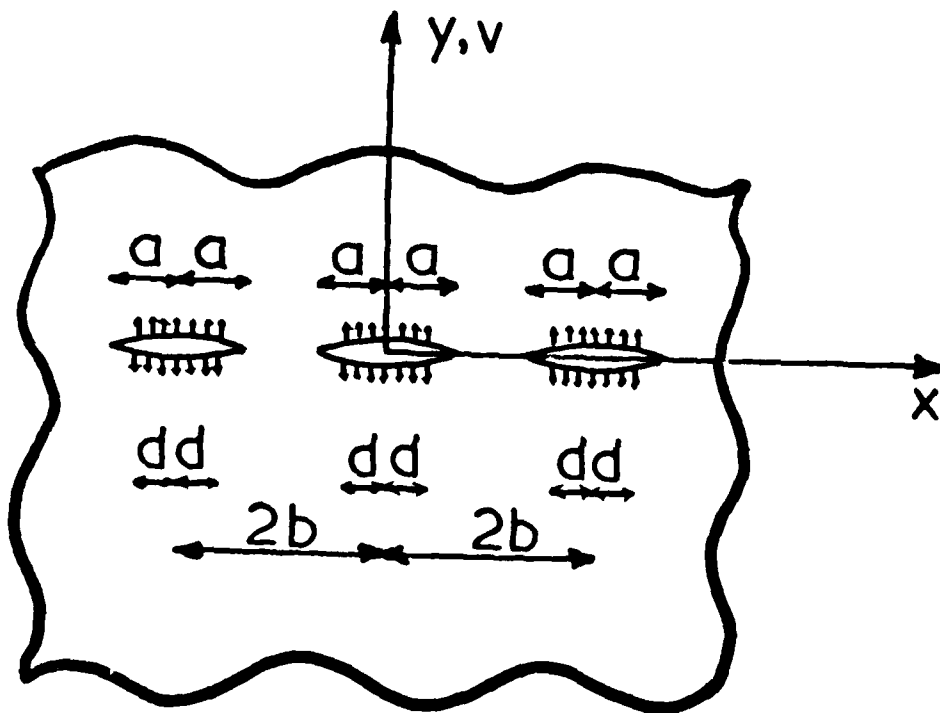
Figure 2 : Infinite Array with Band of Pressure on Crack Faces.
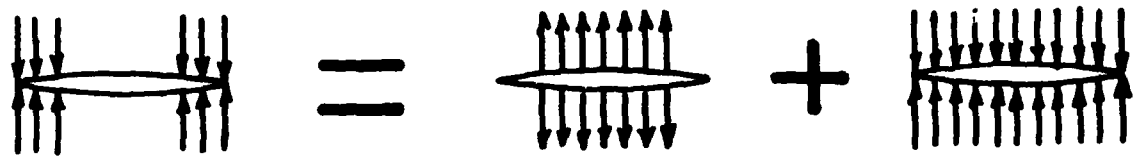
Figure 3 : Superposition Technique to Obtain Dugdale Model.

$$K_o = P\frac{d}{a}\left[2b \tan\frac{\pi a}{2b}\right]^{1/2}$$
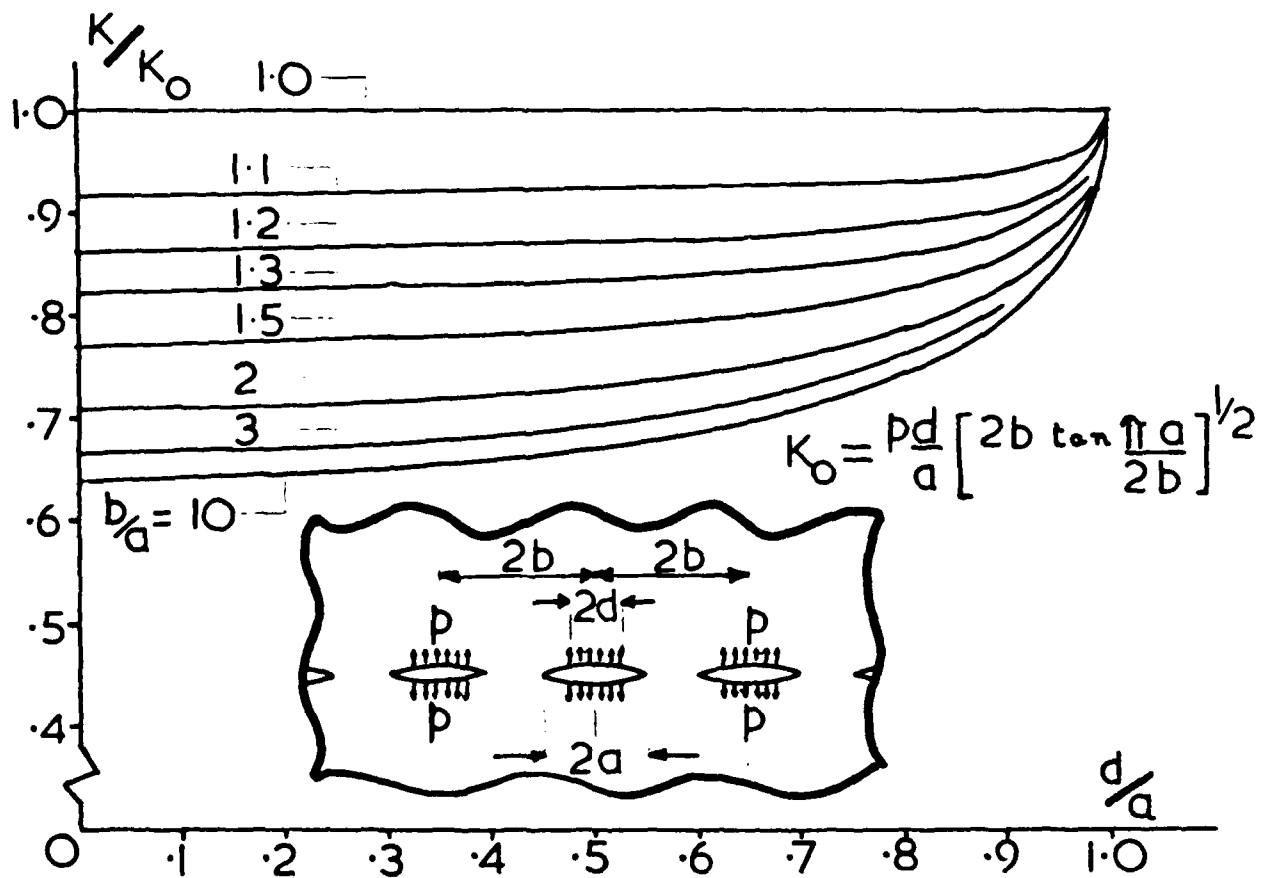
Figure 4 : Stress Intensity Factors for an Array of Cracks
Loaded by a Band of Pressure on Crack Faces.

$$(K_I + K_{II}) + (K_I - K_{II}) = 2K_I = K_{Ip} + K_{I\sigma}$$

(a)   (b)   (c)   (d)
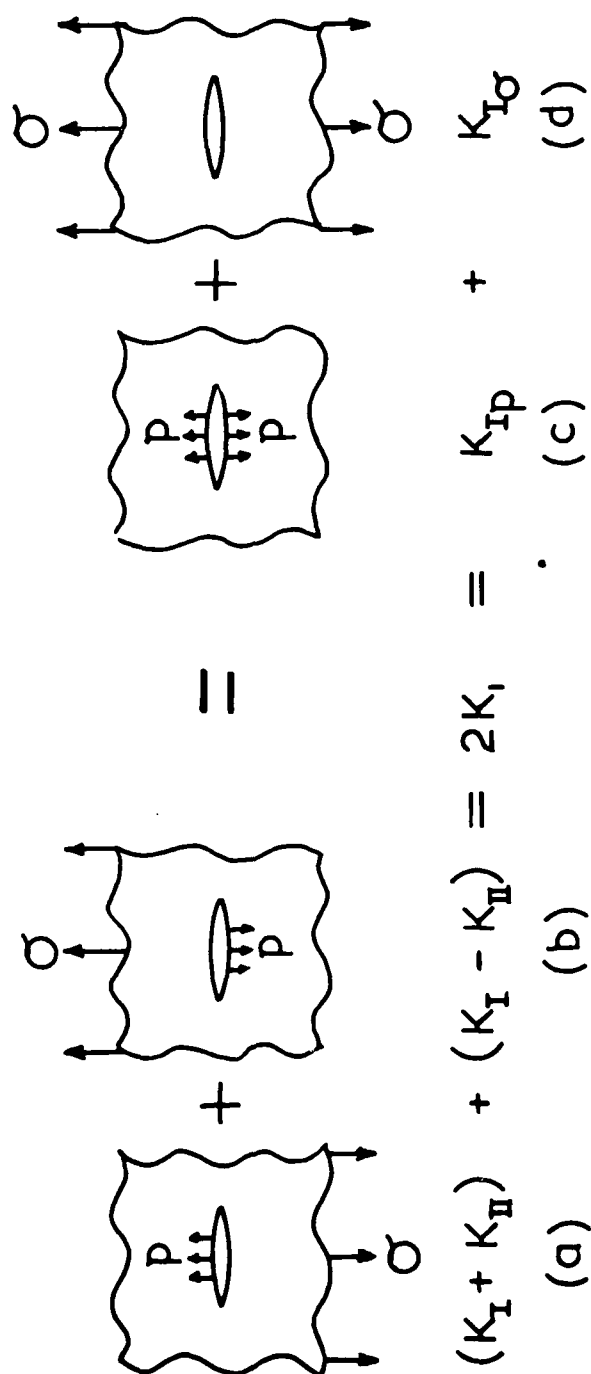
Figure 5 : Superposition Technique to Model Rivet Loading.

$$K_0 = \sigma \left[2b \tan \frac{\pi a}{2b} \right]^{\frac{1}{2}}$$
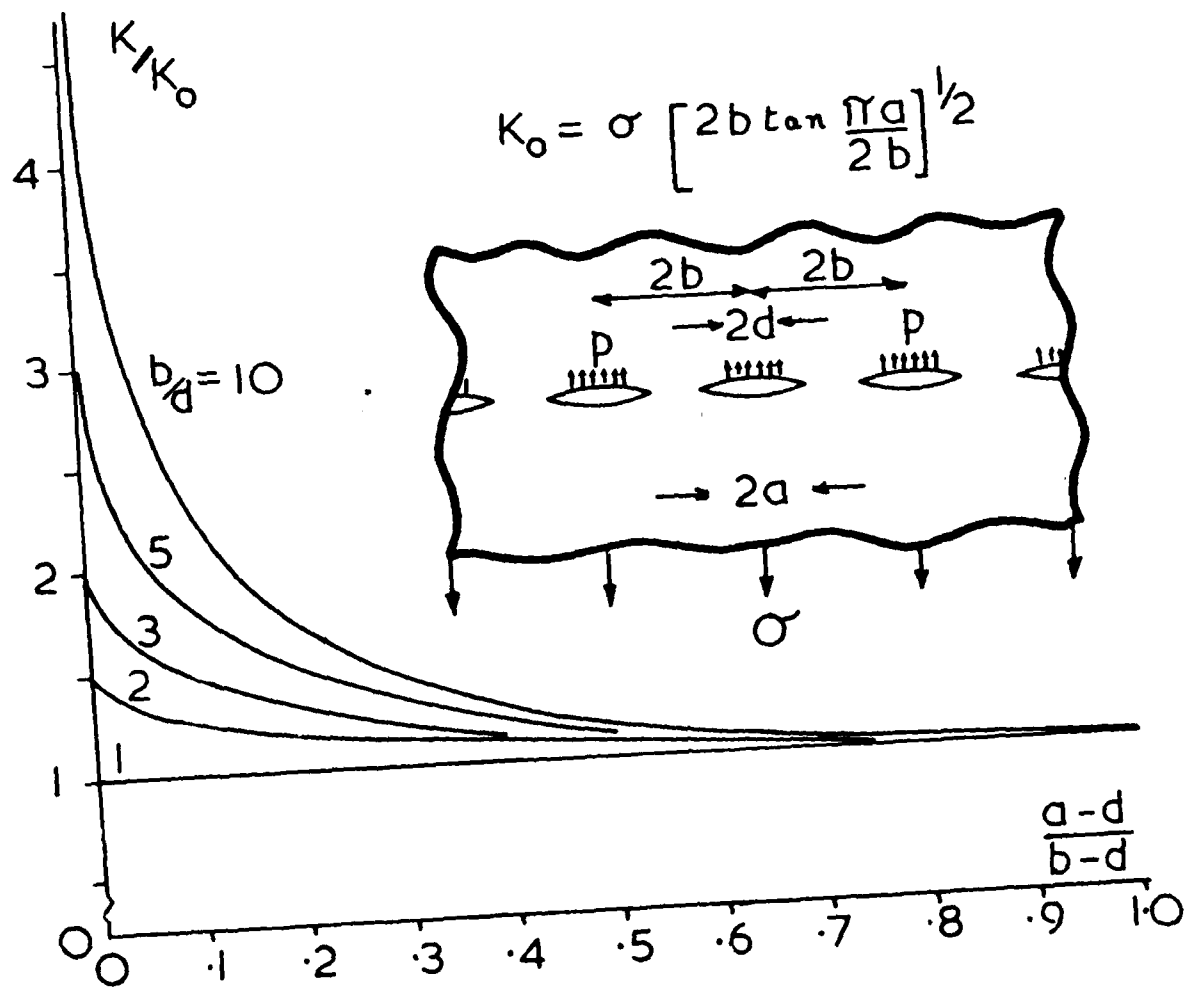
Figure 6 : Stress Intensity Factors for an Array of Loaded Cracks Balanced by Remote Stress.

THE WEIGHT FUNCTION FOR VARIOUS BOUNDARY CONDITION PROBLEMS

A. P. Parker
Department of Civil Engineering
Royal Military College of Science
Shrivenham, Swindon, Wilts, England
(On attachment to Army Materials and Mechanics Research Center
Watertown, Massachusetts 02172, USA)

O. L. Bowie
Army Materials and Mechanics Research Center
Watertown, Massachusetts 02172

ABSTRACT. In this paper it is shown that the weight function 'm' due to Bueckner [1] and Rice [2] may be generalized to include the effects of boundaries on which displacement conditions are imposed, giving rise to an additional weight function 'm*'.

Superposition arguments are employed extensively to demonstrate in a straightforward manner that it is possible to use either crack-line loading or boundary loading, or a combination of the two, in the derivation of stress intensity factors provided the correct weight function is selected. Furthermore, all of the components of the weight function may be derived concurrently by careful selection of the applied loading. After calculating stress intensity, it is possible to recover displacements for the new loading (via 'm') and stresses (via 'm*'). The body force term associated with 'm' is equivalent to a "distributed strain" term associated with 'm*'.

Finally, some possible practical applications of the generalized weight function are noted, in particular residual stress and thermal stress problems, bonded sheet and stiffener problems, contact problems, and special elements for numerical applications.

INTRODUCTION. Bueckner [1] and Rice [2] have demonstrated that a particular function, normally termed the weight function, is a property of a cracked geometry and is independent of the loading. The weight function may be employed in the derivation of additional stress intensity factor solutions provided details of boundary loading (or the equivalent crack-line loading) are available.

FORMULATION. Consider the cracked configuration illustrated in Fig. 1, having displacement boundary conditions over Γ_U and traction conditions on the remainder of the boundary, Γ_T. Bowie and Freese [3] have modified the formulation due to Rice [2] to allow the applied tractions to be functions of both position and crack length, demonstrating that:

$$K^{(1)}K^{(2)} = \frac{H}{2} \int_{\Gamma_T + \Gamma_U} \left\{ T^{(2)} \frac{\partial U^{(1)}}{\partial a} - U^{(2)} \frac{\partial T^{(1)}}{\partial a} \right\} d\Gamma \qquad (1)$$

and $H = E$ (plane stress), $H = E/(1 - \nu^2)$ (plane strain), where E is the modulus of elasticity, ν is Poisson's ratio and $K^{(i)}$ (i = 1,2) is the crack tip stress intensity factor for a loading system (i) which consists of stresses $T^{(i)}$ applied over Γ_T, and displacements $U^{(i)}$ applied over Γ_U. In general $K^{(i)} = K^{(i)}(a)$, $T^{(i)} = T^{(i)}(x,y)$ and $U^{(i)} = U^{(i)}(x,y)$.

Consider now two particular loading systems applied to the geometry under consideration:

First Loading System

In the event that $\partial T^{(1)}/\partial a = 0$ over Γ_T (representing traction boundary conditions alone) and $U^{(2)} = 0$ over Γ_0 (representing so-called 'fixed grip' conditions) from Equation (1) we obtain:

1.0	2.8	2.5
1.1	3.2	2.2
	3.6	
	4.0	2.0
		1.8
1.25	1.4	1.6
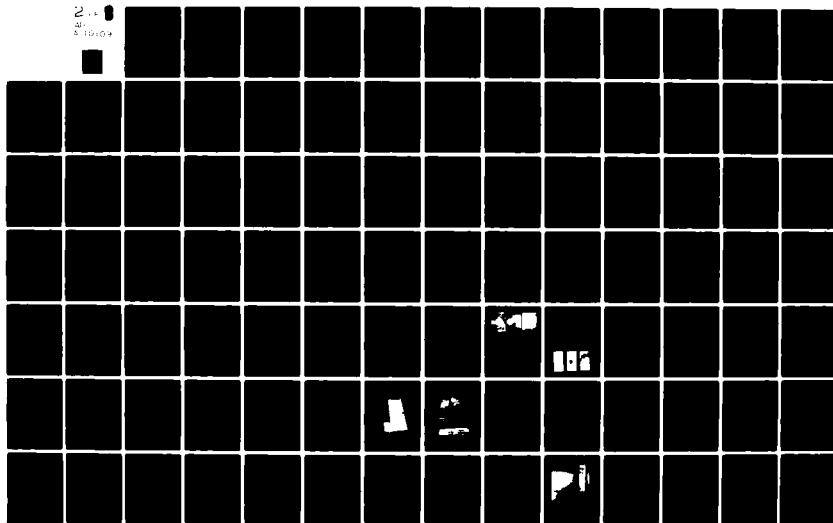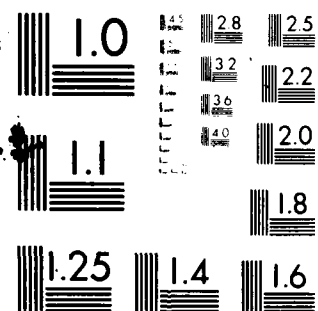
MICROCOPY RESOLUTION TEST CHART

$$K^{(2)} = \int_{\Gamma_T} T^{(2)} \, m(x,y,a) \, d\Gamma, \tag{2}$$

where:

$$m(x,y,a) = \frac{H}{2K^{(1)}} \frac{\partial U^{(1)}}{\partial a}, \tag{3}$$

and $m(x,y,a)$ is the familiar weight function of Bueckner [1] and Rice [2].

Second Loading System

In this case $\partial U^{(1)}/\partial a = 0$ over Γ_U (representing displacement boundary conditions) and $T^{(2)} = 0$ over Γ_T (traction-free boundary). From Equation (1) we obtain:

$$K^{(2)} = \int_{\Gamma_U} U^{(2)} \, m^*(x,y,a) \, d\Gamma, \tag{4}$$

where:

$$m^*(x,y,a) = \frac{-H}{2K^{(1)}} \frac{\partial T^{(1)}}{\partial a}. \tag{5}$$

The implications of Equations (2) to (5) are that it is possible to obtain a conventional weight function $m(x,y,a)$ with $U = 0$ along Γ_U and arbitrary tractions applied to Γ_T. Furthermore, one may obtain an additional function $m^*(x,y,a)$ with $T = 0$ along Γ_T for arbitrary displacements along Γ_U.

SUPERPOSITION OF RESULTS. In order to solve the mixed boundary condition problem, loading system 'A' in Fig. 2, consisting of tractions $\widetilde{T}(x,y)$ over Γ_T and displacements $\widetilde{U}(x,y)$ over Γ_U, we invoke the linear superposition illustrated in Fig. 2(b) and (c) wherein system B has

83

displacements set to zero over Γ_U and system C has tractions set to zero over Γ_T. Denoting the stress intensity factors for systems A, B, and C as K_A, K_B, and K_C, respectively, we see:

$$K_A = K_B + K_C \tag{6}$$

clearly, K_B may be obtained from Equation (2) as:

$$K_B = \int_{\Gamma_T} \widetilde{T}(x,y) \ m(x,y,a) \ d\Gamma \tag{7}$$

whilst K_C is given by Equation (4) as:

$$K_C = \int_{\Gamma_U} \widetilde{U}(x,y) \ m^*(x,y,a) \ d\Gamma. \tag{8}$$

This approach requires a knowledge of 'm' for the evaluation of K_B and 'm^*' for the evaluation of K_C. As an alternative, system C may be solved by the additional superposition $K_{C1} + K_{C2}$, illustrated in Fig. 2, which requires 'm', and a knowledge of the crack-line loading in the unflawed structure caused by the displacement boundary conditions applied alone.

Finally, an alternative approach to the solution of system B is the superposition $K_{B1} + K_{B2}$, which again requires 'm', and a knowledge of the crack-line loading in the unflawed structure arising from traction boundary conditions alone. In the event that the crack-line loading due to nondisplacement boundary conditions is caused by residual stresses or body forces, the latter superposition may be the most straightforward solution method.

DETERMINATION OF 'm' AND 'm*'. Consider the configuration illustrated in Fig. 3(a), where $U = \widetilde{U}$ over Γ_U and $T = 0$ over Γ_T. In order to determine m* a solution is sought for $\partial \widetilde{T}/\partial a$ and $\widetilde{K}$. Employing the superposition of Fig. 3(b) and (c) we note that not only does $\widetilde{K} = \widetilde{\widetilde{K}}$, but $\partial \widetilde{T}/\partial a = \partial \widetilde{\widetilde{T}}/\partial a$, indicating that m* may be obtained from $\widetilde{\widetilde{K}}$ and $\partial \widetilde{\widetilde{T}}/\partial a$.

The implications of this result are that not only may $\partial U/\partial a$, and hence 'm', be obtained with arbitrary loading applied to the crack line, but so may $\partial T/\partial a$, and hence 'm*'. Thus, m and m* may be derived simultaneously with an arbitrary crack-line loading, provided displacements or tractions are set to zero over appropriate portions of the remainder of the boundary.

RECOVERING DISPLACEMENTS AND STRESSES. Knowing K_B and K_C it is possible to rearrange Equation (3) to give:

$$U_B = \frac{2}{H} \int K_B \; m(x,y,a) \; da , \qquad (9)$$

and hence reconstruct the complete displacement field with appropriate boundary conditions to evaluate the constant of integration. The displacements for system A may be obtained from the superposition illustrated in Fig. 4 wherein system D is the equivalent uncracked geometry, loaded by the same tractions and displacements as system A. The term $\sigma(x)$ is the crack-line loading for system D, and system E has U and T set to zero over Γ_U and Γ_T, respectively, the crack being loaded by $-\sigma(x)$. If only crack-line displacements are required (which will frequently be the case), for cracks oriented along the x-axis:

$$U_A(x) = U_E(x). \qquad (10)$$

Equation (9) is essentially equivalent to the method proposed by Paris [4], and employed in the derivation of crack-opening data in [5]. However, it is important to note the functional dependence of K_B on a, and the need to include this dependency when evaluating the integral. It appears that some displacements quoted in [5] may be in error, since this dependency is ignored in calculating certain displacements.

In similar vein, rearranging Equation (5), the stresses for system C, T_C are given by:

$$T_C = \frac{2}{H} \int K_C \, m^*(x,y,a) \, da \qquad (11)$$

with appropriate boundary conditions. Once again, stresses for system A may be obtained from the superposition of Fig. 4.

BODY FORCE AND DISTRIBUTED STRAINS. Equation (2) is generalized by *Rice [2] to account for body forces, giving:*

$$K = \int_{\Gamma_T} T \, m(x,y,a) \, d\Gamma + \int_{A_T} F \, m(x,y,a) \, dA, \qquad (12)$$

where $F = F(x,y)$ is the body force, and A_T is the area over which body forces are distributed. In similar fashion it is possible to generalize Equation (4) giving:

$$K = \int_{\Gamma_U} U \, m^*(x,y,a) \, d\Gamma + \int_{A_U} D \, m^*(x,y,a) \, dA, \qquad (13)$$

where D represents a distributed strain field, and A_U is the area over which it acts.

POSSIBLE APPLICATIONS

(a) Residual Stress and Thermal Stress Problems

Consider the case of a complex thermal stress field applied to a clamped plate which is initially stress free, and clamped along the horizontal faces, Fig. 5(a). Provided the profile of the plate without crack and clamping $U(x, \pm h)$ is known it will be possible to apply equal and opposite displacements which straighten the horizontal faces as in Fig. 5(c), this will require an 'm*' type weight function. It will also be necessary to apply a crack-line loading with zero-end displacements, Fig.5(d) to eliminate any thermal residual stresses $\sigma_t(x)$, this will require an 'm' type weight function. As an alternative, the superposition outlined in section (3) may be employed in the solution of Fig. 5(c), via an 'm' type weight function.

(b) Bonded Sheets and Stiffeners

Configurations in which sheets are bonded or glued to stiffeners or to other sheets (including the case of 'patch' repairs of cracked structures) are becoming more common. Tradionally these problems are solved by ensuring compatibility and equilibrium at a number of discrete points, the number of points being increased until the solution converges. By employing the 'distributed strain' term in Equation (13) it may be possible to match distributed displacements in a cracked sheet with those in a bonded sheet, stiffener or repair patch.

(c) Contact Problems

Contact problems (particularly nonlinear problems) present significant difficulties in their solution. The presence of cracks and defects

can make such problems even less attractive, since the crack may serve to increase the nonlinearity of the problem. Employing weight function methods a direct (in the linear case) or iterative (nonlinear case) approach could produce accurate, economical solutions in a short time with modest computing effort.

For example, the problem of cracked, pin and rivet loaded holes is commonplace in aeronautical and civil engineering. A single, accurate weight function will permit the subsequent recovery of stress intensity factors and displacement fields for various combinations of pin-fit, material properties, frictional effects, and residual stress (mandrel enlargement), including testing for (and correcting) physically unacceptable 'overlapping' of crack surfaces [6].

(d) Special Elements

Various techniques are currently employed in the determination of accurate stress intensity factors via finite element analyses, for example, collapsed isoparametric elements, and classical solution and polynomial-based functions. Some disadvantages of the latter formulation are the large number of boundary points required, the complexity of the functions employed, the problems of accuracy at short crack lengths (particularly important if K solutions are to be used to predict component lifetime under fatigue loading), and representation of residual stress effects as a loading along the crack line.

It is already clear that weight function data may be 'packaged' with minimal loss of accuracy [7]. In principle therefore, it would be possible to obtain weight functions for a limited number of appropriate geometries, using methods of high accuracy (collocation, modified mapping collocation),

and to subsequently fit the data in convenient form as the basis of a special element capable of high accuracy.

CONCLUSIONS. The familiar weight function 'm' of Bueckner and Rice which is unique to a given cracked geometry may be employed in the determination of stress intensity factors with stress boundary conditions applied to the geometry. There also exists an additional weight function 'm*', also unique to a given cracked geometry, which may be employed in the derivation of stress intensity factors with displacement boundary conditions applied to portions of the geometry. Weight functions 'm' and 'm*' may be derived simultaneously with an arbitrary crack-line loading.

The weight function 'm' permits the recovery of displacements for a new set of stress boundary conditions, whilst 'm*' permits the recovery of stresses for a new set of displacement boundary conditions. In using 'm' and 'm*' to recover additional information, it is important to recognize the functional dependency of stress intensity on crack length.

Whilst the weight function 'm' may be employed in the determination of stress intensity in the presence of a distributed body force, in like manner 'm*' may be employed in the determination of stress intensity in the presence of a distributed strain field. The combination of weight functions 'm' and 'm*' may have application to residual and thermal stress problems, bonded sheets and stiffeners, nonlinear contact problems, and special elements for numerical applications.

REFERENCES

1. H. F. Bueckner, A Novel Principle for the Computation of Stress Intensity Factors. ZAMM, 50, 529-546 (1970).

2. J. R. Rice, Some Remarks on Elastic Crack-Tip Stress Fields. Int. J. Solids Structures, 8, 751-758 (1972).

3. O. L. Bowie and C. E. Freese, Cracked Rectangular Sheet with Linearly Varying End Displacements. Engng. Frac. Mech., 14, 519-526 (1981).

4. P. C. Paris, The Mechanics of Fracture Propagation and Solutions to Fracture Arrester Problems. Document D2-2195, The Boeing Company (1957).

5. H. Tada, P. C. Paris, and G. R. Irwin, The Stress Analysis of Cracks Handbook. Del Research Corp., Hellertown, Penn. (1973).

6. O. L. Bowie and C. E. Freese, On the 'Overlapping' Problem in Crack Analysis. Engng. Frac. Mech., 8, 373-379 (1976).

7. C. P. Andrasic and A. P. Parker, Weight Functions for Cracked, Curved Beams. Second Int. Conf. on Numerical Methods in Frac. Mech., Swansea, 67-82 (1980).
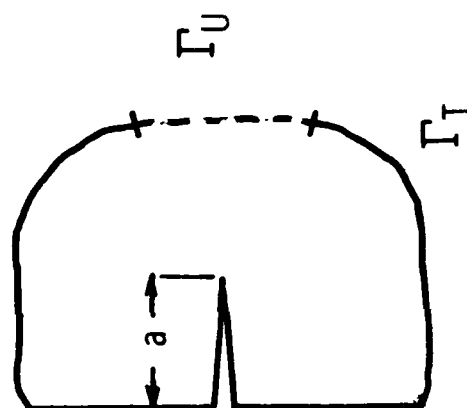
Fig. 1: CRACKED CONFIGURATION EMPLOYED IN FORMULATION
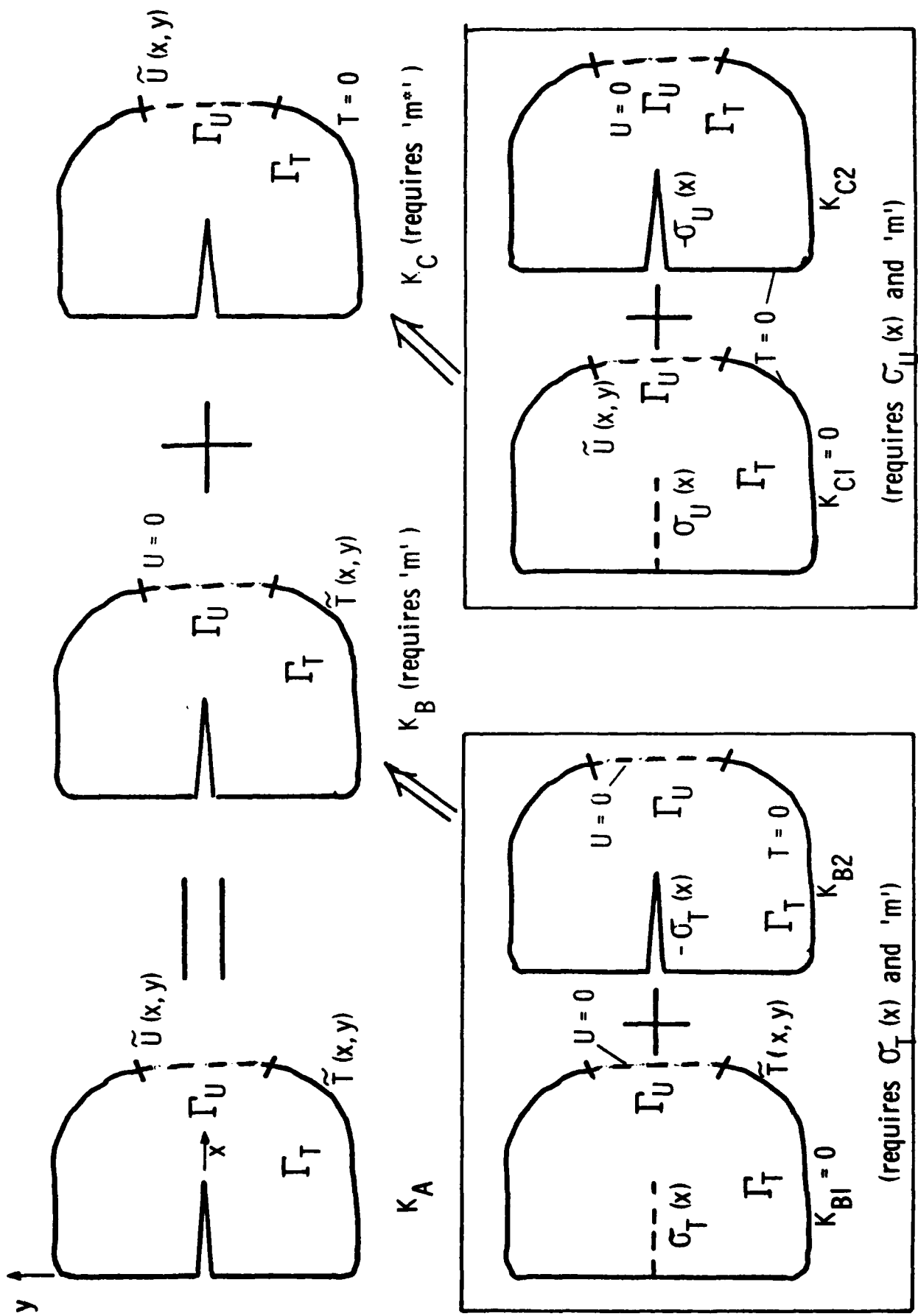
Fig. 2 : SUPERPOSITION OPTICNS IN SOLVING MIXED BOUNDARY CONDITICN PROBLEM.
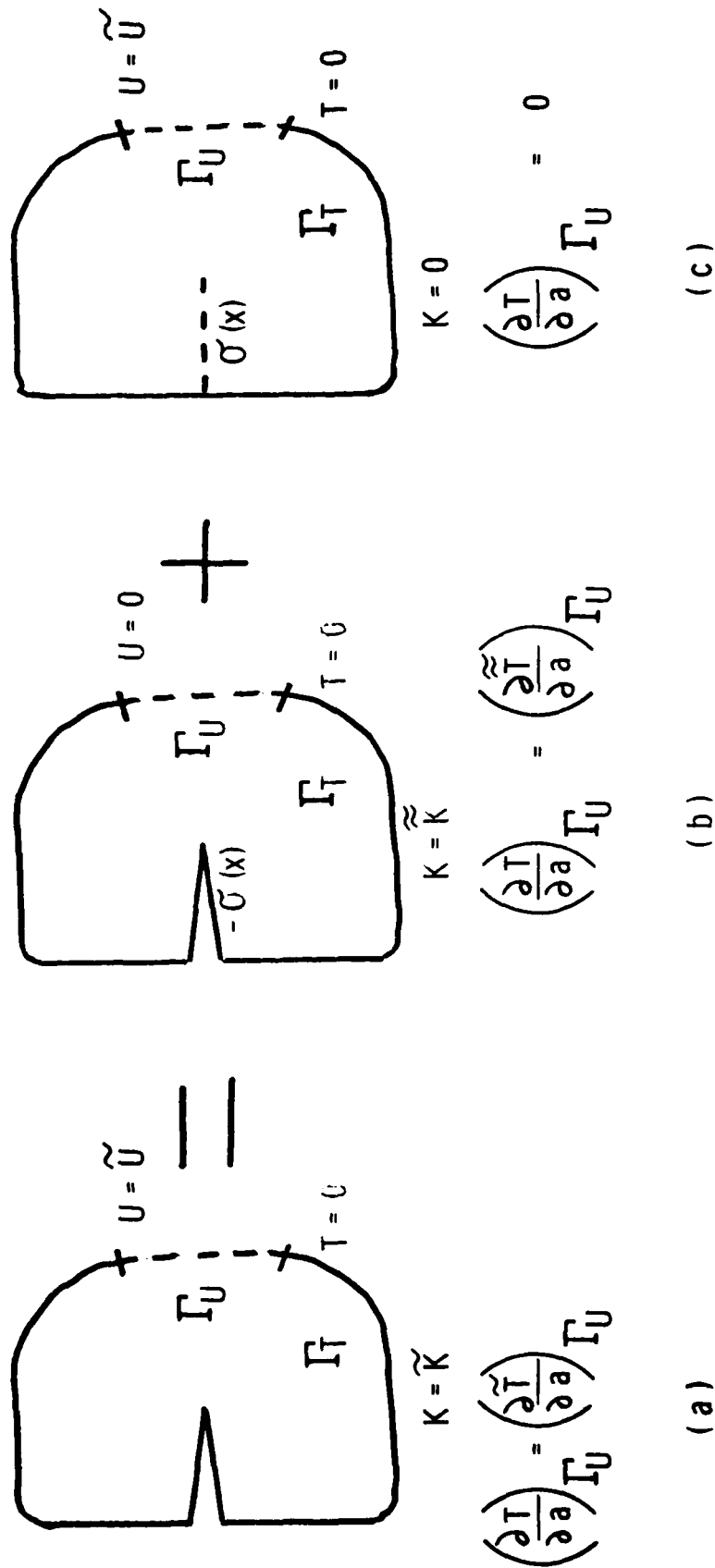
Fig. 3 : SUPERPOSITION FOR DETERMINATION OF m* USING ARBITRARY CRACK-LINE LOADING

System E
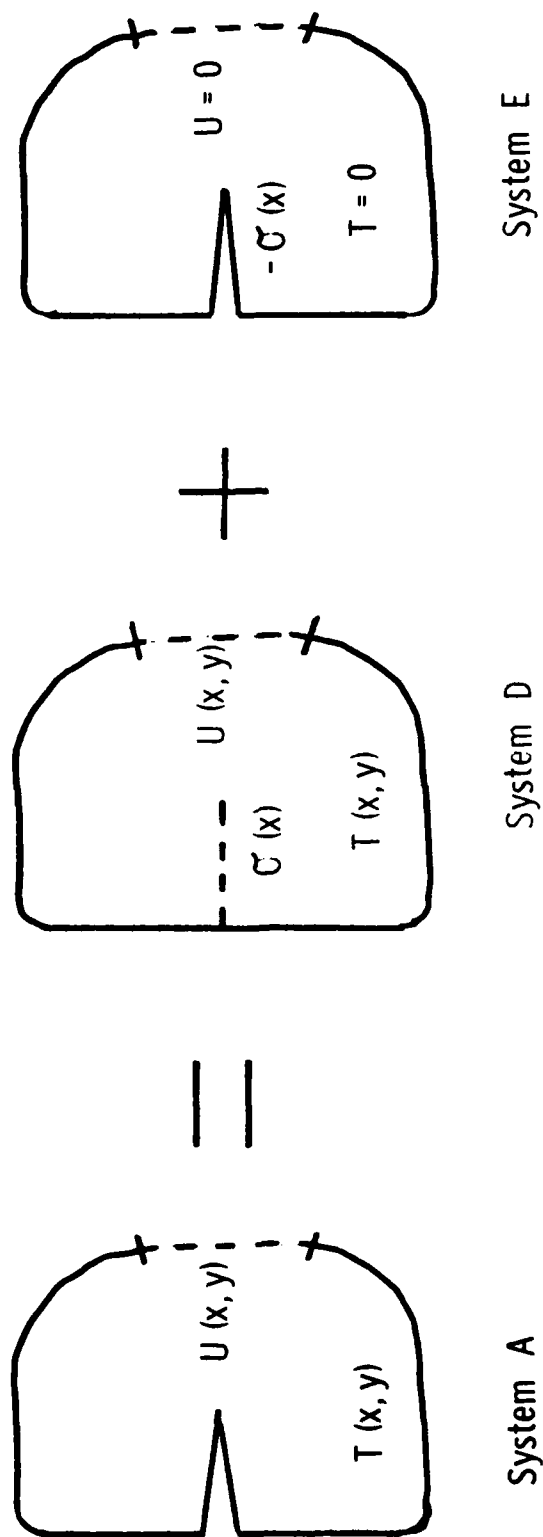
System D

System A

Fig. 4 : SUPERPOSITION TO DETERMINE DISPLACEMENTS FOR SYSTEM A

94
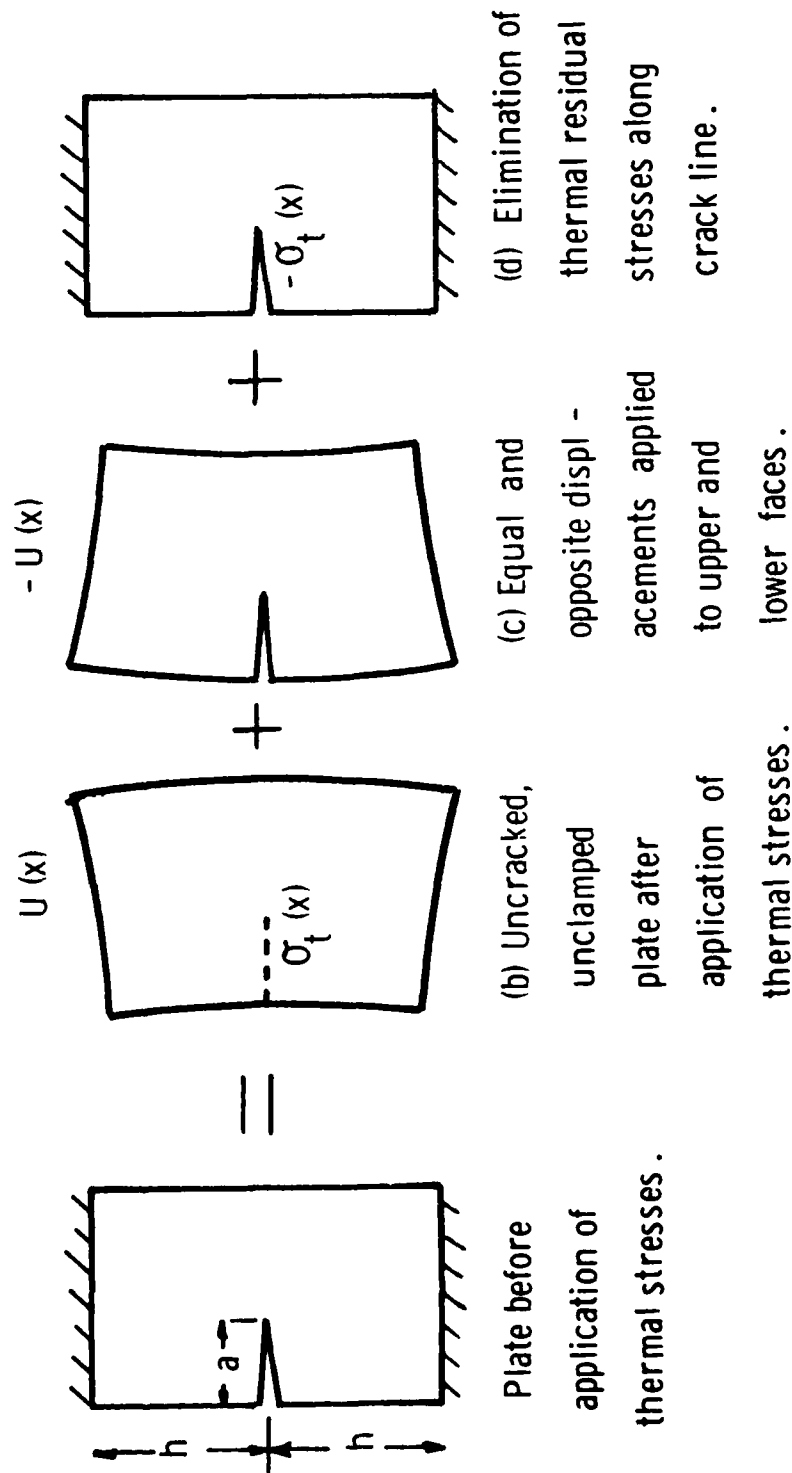
Fig. 5 : THERMALLY STRESSED, CLAMPED PLATE.

(b) Uncracked, unclamped plate after application of thermal stresses.

(c) Equal and opposite displacements applied to upper and lower faces.

(d) Elimination of thermal residual stresses along crack line.

Plate before application of thermal stresses.

$U(x)$

$-U(x)$

$\sigma_t(x)$

$-\sigma_t(x)$

AN INCREMENTAL APPROACH TO NONISOTHERMAL ELASTIC-PLASTIC DEFORMATION

SHIH C. CHU

TECHNOLOGY BRANCH, ARMAMENT DIVISION
FIRE CONTROL & SMALL CALIBER WEAPON SYSTEMS LABORATORY
U.S. ARMY ARMAMENT RESEARCH AND DEVELOPMENT COMMAND, DOVER, NJ 07801

ABSTRACT

On the basis of Drucker's flow rule and Ziegler's kinematic rule, a general nonisothermal incremental constitutive law for elastoplastic, work-hardening solids has been developed. The derived incremental constitutive relative contains an unspecified loading function of stress, stress history and temperature. Several special explicit constitutive relations have derived on the basis of von Mises' yield criterion with temperature-dependent yield strength of materials. Since Ziegler's kinematic hardening rule is included in the analysis, the derived nonisothermal elastoplastic theory is particularly suitable for analyzing the inelastic behavior of work-hardening solids subjected to both cyclic mechanical loading and cyclic thermal loading.

I. INTRODUCTION

The isothermal constitutive rules for work-hardening solids have been discussed in great detail in literature [1-9][2]. However, very little work has been done on the theory of plasticity under nonisothermal condition. Prager [10] presents a nonisothermal plastic deformation theory in which he considered a special case that the nonisothermal stress tensor is equal to the product of the isothermal stress tensor and a temperature-dependent parameter. Moreover, since elastic strain and thermal strain were neglected, Prager's nonisothermal theory can be applied only to rigid, work-hardening solids. No general nonisothermal theory is available for elastoplastic problems of work-hardening solids subjected to both cyclic mechanical and cyclic thermal loading. On the basis of Drucker's flow rule and Ziegler's kinematic hardening rule, a general nonisothermal incremental constitutive law will be derived in this paper for analyzing elastoplastic deformation of work-hardening solids in which the elastic, the plastic, and the thermal deformation are taken into account.

II. DEVELOPMENT OF CONSTITUTIVE LAW

In this investigation, small deformations are assumed to be valid. Hence, the strain tensor ϵ_{ij} is given by

$$\epsilon_{ij} = 1/2 \ (u_{i,j} + u_{i,j}) \tag{1}$$

where u_i are the displacement components referring to rectangular cartesian coordinates x_i, $i=1,2$, and 3. Differentiation with respect to a coordinate is indicated by a comma followed by the approximate subscript ($u_{i,j} = \partial u_i / \partial x_j$).

---

[2]Numbers in brackets designate references at end of paper.

The total incremental strain tensor $d\epsilon_{ij}$ is assumed to be the sum of elastic part $d\epsilon_{ij}^e$, plastic part $d\epsilon_{ij}^P$, and the part of thermal strain $d\epsilon_{ij}^\theta$, i.e.,

$$d\epsilon_{ij} = d\epsilon_{ij}^e + d\epsilon_{ij}^P + d\epsilon_{ij}^\theta \tag{2}$$

As indicated Ziegler [5], the inelastic behavior of a material can be described by the following:

(1) An initial yield condition by which the elastic limit of a material is defined.

(2) A flow rule by which the plastic-strain increments are related to stresses and strain increments.

(3) A hardening rule by which conditions are established for subsequent yield from a plastic state.

Therefore, to study inelastic behavior of a material requires, first, a functional representation constituting a generalization of the yield point associated with uniaxial stress. In the case of initial yielding, the function is termed the yield function and the equation constitutes the yield surface. In the case of subsequent yielding from plastic state, the surface used to define the elastic limit is referred to the subsequent yield surface, or the loading function, and can be represented as

$$f\left(\sigma_{ij} - \alpha_{ij}, \theta\right) = 0 \tag{3}$$

where α_{ij} is a tensor representing the total translation of the center of the initial yield surface, and θ is temperature.

On the basis of Drucker's postulate [11], the work done by an external agency during a complete cycle of loading and unloading must be nonnegative, the yield loading surfaces must be convex with respect to the origin in the stress space.

The state of stress at any material point can be specified by the function f accordingly as

(i) Plastic loading, if $f = 0$ and $\frac{\partial f}{\partial \sigma_{ij}} d\sigma_{ij} + \frac{\partial f}{\partial \theta} d\theta > 0$ (4)

(ii) Neutral loading, if $f = 0$ and $\frac{\partial f}{\partial \sigma_{ij}} d\sigma_{ij} + \frac{\partial f}{\partial \theta} d\theta = 0$ (5)

(iii) Unloading $d\epsilon_{ij} = 0$, if $f < 0$ or $\frac{\partial f}{\partial \sigma_{ij}} d\sigma_{ij} + \frac{\partial f}{\partial \theta} d\theta < 0$ (6)

In addition to the yield and loading condition, a constitutive relation between plastic strain increments, stress, and stress increments is required to describe the inelastic behavior of a material. The constitutive relation (flow rule) used in this investigation is based on Drucker's postulate for work-hardening materials [11]. The flow rule is given as

$$de_{ij}^{p} = d\lambda \frac{\partial f}{\partial \sigma_{ij}}$$ (7)

where $d\lambda$ is a positive scalar quantity. On the basis of Drucker's statement, this plastic strain increment tensor must lie on the outward normal to the loading surface at the instantaneous stress state.

After yield condition and flow rule have been determined, a hardening rule must be chosen to complete the description of the inelastic behavior of a material. With the use of the kinematic hardening rule proposed by Prager [2,7], the increment of the translation of the center of the loading surface in a nine-dimensional stress space in the direction of the external normal to the surface at the instantaneous stress state can be predicted, i.e.,

$$d\alpha_{ij} = Cde_{ij}^{p}$$ (8)

where C is a parameter characterizing the hardening behavior of the material and can be determined from a uniaxial stress-strain test

$$C(\theta) = \frac{2}{3} \frac{d\sigma_{11}}{d\epsilon_{11}^P} \bigg|_\theta \tag{9}$$

in which $d\sigma_{11}$ is the uniaxial stress increment and $d\epsilon_{11}^P$ is the corresponding plastic strain increment at specified temperature θ.

Inconsistencies have been found when Prager's hardening rule is applied to various subspaces of stress [4]. To avoid the difficulty associated with the implementation of Prager's hardening rule, Ziegler [5] has proposed a modification by which the increment of translation of the center of the loading surface is assumed to be directed along the radius vector connecting the center of the loading surface to the instantaneous stress state, i.e.,

$$d\alpha_{ij} = (\sigma_{ij} - \alpha_{ij}) \, d\mu, \quad d\mu > 0 \tag{10}$$

where $d\mu$ can be determined provided the stress point remains on the translated yield surface during plastic flow, i.e.,

$$d\mu = \frac{\frac{\partial f}{\partial \sigma_{k1}} d\sigma_{k1} + \frac{\partial f}{\partial \theta} d\theta}{(\sigma_{mn} - \alpha_{mn}) \frac{\partial f}{\partial \sigma_{mn}}} \tag{11}$$

A comparison of Prager's hardening rule and Ziegler's modification was shown in Figure 1 (a).

An expression for $d\lambda$, associated with the flow rule equation (7), can be determined if the vector $C d\epsilon_{ij}^P$, as shown in Figure 1 (b) is considered as the projection of $d\sigma_{ij}$ (and thus of $d\alpha_{ij}$) on the exterior normal to the loading surface at the instantaneous stress state. Hence, for small incremental of stress and strain, one can readily find that

$$d\lambda = \frac{1}{C} \frac{\frac{\partial f}{\partial \sigma_{ij}} d\sigma_{ij} + \frac{\partial f}{\partial \theta} d\theta}{(\frac{\partial f}{\partial \sigma_{mn}}) (\frac{\partial f}{\partial \sigma_{mn}})} \tag{12}$$

101

Therefore, the flow rule becomes

$$d\epsilon_{ij}^{P} = \frac{\frac{\partial f}{\partial \sigma_{ij}}}{C \left(\frac{\partial f}{\partial \sigma_{mn}}\right)\left(\frac{\partial f}{\partial \sigma_{mn}}\right)} \left[\frac{\partial f}{\partial \sigma_{kl}} d\sigma_{kl} + \frac{\partial f}{\partial \theta} d\theta\right] \tag{13}$$

The sum of incremental elastic strain and thermal strain can be determined by use of the Duhamel-Neumann law, i.e.,

$$d\epsilon_{ij}^{e} + d\epsilon_{ij}^{\theta} = \frac{1+\nu}{E}d\sigma_{ij} - \left(\frac{\nu}{E} d\sigma_{kk} - \beta d\theta\right) \delta_{ij} \tag{14}$$

in which E is Young's modulus, ν is Poisson's ratio, $d\theta$ is the change of temperature, β is the thermal expansion coefficient which may be a function of temperature, and δ_{ij} is the Kroneker delta.

Substituting equations (13) and (14) into equation (2), one obtains

$$d\epsilon_{ij} = \frac{(1+\nu)}{E}d\sigma_{ij} - \left(\frac{\nu}{E} d\sigma_{kk} - \beta d\theta\right) \delta_{ij} + \frac{\frac{\partial f}{\partial \sigma_{ij}}}{C \left(\frac{\partial f}{\partial \sigma_{mn}}\right)\left(\frac{\partial f}{\partial \sigma_{mn}}\right)} \left[\frac{\partial f}{\partial \sigma_{kl}} d\sigma_{kl} + \frac{\partial f}{\partial \theta} d\theta\right] \tag{15}$$

Hence, the general formulation of a nonisothermal incremental theory of elastoplastic, work-hardening solids has been completed.

III. SPECIAL CASES

The incremental stress-strain-temperature relation given in equation (15) is very general which satisfies any given loading function f and all states of stress, strain, and temperature. On the basis of the von Mises' yield criterion with temperature-dependent yield strength of a material, several explicit expressions of equation (15) will be derived in this section.

102

A. Six-Space. If the symmetry of stress and strain tensors is assumed, a general nine-space problem is reduced to a six-space problem. For convenience here and for the subsequent specializations, the physical coordinates are denoted by x, y, z; the stresses, by σ_x, σ_y, σ_z, τ_{xy}, τ_{yz}, τ_{zx}; the strains, by ϵ_x, ϵ_y, ϵ_z, ϵ_{xy}, ϵ_{yz}, ϵ_{zx}; and the translation of the center of yield surface, by α_x, α_y, α_z, α_{xy}, α_{yz}, α_{zx}.

If the material is assumed to be von Mises' material, then the temperature-dependent loading function, equation (3), may be written

$$f = \frac{1}{2}\{[(\sigma_x-\alpha_x)-(\sigma_y-\alpha_y)]^2 + [(\sigma_y-\alpha_y)-(\sigma_z-\alpha_z)]^2 + [(\sigma_z-\alpha_z)-(\sigma_x-\alpha_x)]^2$$

$$+ 6[(\tau_{xy}-\alpha_{xy})^2 + (\tau_{yz}-\alpha_{yz})^2 + (\tau_{zx}-\alpha_{zx})^2]\} - \sigma_\theta^2 = 0 \qquad (16)$$

where $\sigma_\theta = \sigma_\theta(\theta)$ is the temperature-dependent yield strength of the material in tension.

Substituting equation (16) into equation (7), one obtains the incremental plastic-strain components:

$$d\epsilon_x^P = \bar{S}_x d\lambda, \quad d\epsilon_y^P = \bar{S}_y d\lambda, \quad d\epsilon_z^P = \bar{S}_z d\lambda, \quad d\epsilon_{xy}^P = \bar{S}_{xy} d\lambda, \quad d\epsilon_{yz}^P = \bar{S}_{yz} d\lambda,$$

$$\text{and } d\epsilon_{zx}^P = \bar{S}_{zx} d\lambda \qquad (17)$$

in which

$$\bar{S}_x = \frac{\partial f}{\partial \sigma_x} = 2(\sigma_x-\alpha_x) - (\sigma_y-\alpha_y) - (\sigma_z-\alpha_z)$$

$$\bar{S}_y = \frac{\partial f}{\partial \sigma_y} = 2(\sigma_y-\alpha_y) - (\sigma_z-\alpha_z) - (\sigma_x-\alpha_x)$$

$$\bar{S}_z = \frac{\partial f}{\partial \sigma_z} = 2(\sigma_z-\alpha_z) - (\sigma_x-\alpha_x) - (\sigma_y-\alpha_y)$$

$$\bar{S}_{xy} = \frac{\partial f}{\partial \tau_{xy}} = 6(\tau_{xy}-\alpha_{xy})$$

$$\bar{S}_{yz} = \frac{\partial f}{\partial \tau_{yz}} = 6(\tau_{yz}-\alpha_{yz})$$

$$\bar{S}_{zx} = \frac{\partial f}{\partial \tau_{zx}} = 6(\tau_{zx}-\alpha_{zx}) \qquad (18)$$

Substituting equation (16) into equation (12), one obtains:

$$d\lambda = \frac{1}{C\bar{S}^2} [\bar{S}_x d\sigma_x + \bar{S}_y d\sigma_y + \bar{S}_z d\sigma_z + \bar{S}_{xy} d\tau_{xy} + \bar{S}_{yz} d\tau_{yz} + \bar{S}_{zx} d\tau_{zx}$$

$$+ 2\sigma_\theta \frac{\partial \sigma_\theta}{\partial \theta} d\theta] \tag{19}$$

in which

$$\bar{S}^2 = \bar{S}_x{}^2 + \bar{S}_y{}^2 + \bar{S}_z{}^2 + \bar{S}_{xy}{}^2 + \bar{S}_{yz}{}^2 + \bar{S}_{zx}{}^2 \tag{20}$$

Ziegler's hardening parameter, $d\mu$, can be determined by substitution of equation (16) into equation (11), i.e.,

$$d\mu = \frac{\bar{S}_x d\sigma_x + \bar{S}_y d\sigma_y + \bar{S}_z d\sigma_z + \bar{S}_{xy}\tau_{xy} + \bar{S}_{yz}\tau_{yz} + \bar{S}_{zx}\tau_{zx} + 2\sigma\frac{\partial\sigma}{\partial\theta}d\theta}{(\sigma_x-\alpha_x)\bar{S}_x + (\sigma_y-\alpha_y)\bar{S}_y + (\sigma_z-\alpha_z)\bar{S}_z + (\tau_{xy}-\alpha_{xy})\bar{S}_{xy} + (\tau_{yz}-\alpha_{yz})\bar{S}_{yz} + (\tau_{zx}-\alpha_{zx})\bar{S}_{zx}} \tag{21}$$

Hence, the incremental translation of the center of loading surface can be determined

$$d\alpha_x = (\sigma_x-\alpha_x)d\mu, \quad d\alpha_y = (\sigma_y-\alpha_y)d\mu, \quad d\alpha_z = (\sigma_z-\alpha_z)d\mu$$

$$d\alpha_{xy} = (\tau_{xy}-\alpha_{xy})d\mu, \quad d\alpha_{yz} = (\tau_{yz}-\alpha_{yz})d\mu, \quad \text{and} \quad d\alpha_{zx} = (\tau_{zx}-\alpha_{zx})d\mu \tag{22}$$

The incremental stress-strain-temperature relation, equation (15), can now be written in the following simple matrix form:

$$\{d\epsilon\} = [K_1 \vdots K_2] \{\frac{d\sigma}{d\theta}\} \tag{23}$$

in which $\qquad \{d\epsilon\}^T = <d\epsilon_x, d\epsilon_y, d\epsilon_z, d\epsilon_{xy}, d\epsilon_{yz}, d\epsilon_{zx}> \tag{24}$

$$\{\frac{d\sigma}{d\theta}\}^T = <d\sigma_x, d\sigma_y, d\sigma_z, d\tau_{xy}, d\tau_{yz}, d\tau_{zx} \vdots d\theta> \tag{25}$$

and

$$[K] = [K_1 \vdots K_2] = \begin{bmatrix} k_{11} & k_{12} & k_{13} & k_{14} & k_{15} & k_{16} & \vdots & k_{17} \\ k_{21} & k_{22} & k_{23} & k_{24} & k_{25} & k_{26} & \vdots & k_{27} \\ k_{31} & k_{32} & k_{33} & k_{34} & k_{35} & k_{36} & \vdots & k_{37} \\ k_{41} & k_{42} & k_{43} & k_{44} & k_{45} & k_{46} & \vdots & k_{47} \\ k_{51} & k_{52} & k_{53} & k_{54} & k_{55} & k_{56} & \vdots & k_{57} \\ k_{61} & k_{62} & k_{63} & k_{64} & k_{65} & k_{66} & \vdots & k_{67} \end{bmatrix} \tag{26}$$

where

$$k_{11} = \frac{\overline{S}_x^2}{C\overline{S}^2} + \frac{1}{E} \qquad\qquad k_{12} = k_{21} = \frac{\overline{S}_x \overline{S}_y}{C\overline{S}^2} - \frac{\nu}{E}$$

$$k_{13} = k_{31} = \frac{\overline{S}_x \overline{S}_z}{C\overline{S}^2} - \frac{\nu}{E} \qquad\qquad k_{14} = k_{41} = \frac{\overline{S}_x \overline{S}_{xy}}{C\overline{S}^2}$$

$$k_{15} = k_{51} = \frac{\overline{S}_x \overline{S}_{yz}}{C\overline{S}^2} \qquad\qquad k_{16} = k_{61} = \frac{\overline{S}_x \overline{S}_{yz}}{C\overline{S}^2}$$

$$k_{22} = \frac{\overline{S}_y^2}{C\overline{S}^2} + \frac{1}{E} \qquad\qquad k_{23} = k_{32} = \frac{\overline{S}_y \overline{S}_z}{C\overline{S}^2} - \frac{\nu}{E}$$

$$k_{24} = k_{42} = \frac{\overline{S}_y \overline{S}_{xy}}{C\overline{S}^2} \qquad\qquad k_{25} = k_{52} = \frac{\overline{S}_y \overline{S}_{yz}}{C\overline{S}^2}$$

$$k_{26} = k_{62} = \frac{\overline{S}_y \overline{S}_{zx}}{C\overline{S}^2} \qquad\qquad k_{33} = \frac{\overline{S}_z^2}{C\overline{S}^2} + \frac{1}{E}$$

$$k_{34} = k_{43} = \frac{\overline{S}_z \overline{S}_{xy}}{C\overline{S}^2} \qquad\qquad k_{35} = k_{53} = \frac{\overline{S}_z \overline{S}_{yz}}{C\overline{S}^2}$$

$$k_{36} = k_{63} = \frac{\overline{S}_z \overline{S}_{zx}}{C\overline{S}^2}$$

$$k_{44} = \frac{\overline{S}_{xy}^2}{C\overline{S}^2} + \frac{1+\nu}{E}$$

$$k_{45} = k_{54} = \frac{\overline{S}_{xy} \overline{S}_{yz}}{C\overline{S}^2}$$

$$k_{46} = k_{64} = \frac{\overline{S}_{xy} \overline{S}_{zx}}{C\overline{S}^2}$$

$$k_{55} = \frac{\overline{S}_{yz}^2}{C\overline{S}^2} + \frac{1+\nu}{E}$$

$$k_{56} = k_{65} = \frac{\overline{S}_{yz} \overline{S}_{zx}}{C\overline{S}^2}$$

$$k_{66} = \frac{\overline{S}_{zx}^2}{C\overline{S}^2} + \frac{1+\nu}{E}$$

$$k_{17} = \frac{2\overline{S}_x \sigma_\theta}{C\overline{S}^2} \frac{\partial\sigma_\theta}{\partial\theta} + \beta$$

$$k_{27} = \frac{2\overline{S}_y \sigma_\theta}{C\overline{S}^2} \frac{\partial\sigma_\theta}{\partial\theta} + \beta$$

$$k_{37} = \frac{2\overline{S}_z \sigma_\theta}{C\overline{S}^2} \frac{\partial\sigma_\theta}{\partial\theta} + \beta$$

$$k_{47} = \frac{2\overline{S}_{xy} \sigma_\theta}{C\overline{S}^2} \frac{\partial\sigma_\theta}{\partial\theta}$$

$$k_{57} = \frac{2\overline{S}_{yz} \sigma_\theta}{C\overline{S}^2} \frac{\partial\sigma_\theta}{\partial\theta}$$

$$k_{67} = \frac{2\overline{S}_{zx} \sigma_\theta}{C\overline{S}^2} \frac{\partial\sigma_\theta}{\partial\theta} \tag{27}$$

From the definitions given above of k_{ij}, one can conclude that K_1 is a symmetric partition of matrix $[K]$.

B. Plane-Strain. On the basis of plane-strain assumption, the nonvanish incremental strain components are $d\epsilon_x$, $d\epsilon_y$, $d\epsilon_{xy}$, and the nonvanish incremental stress components are $d\sigma_x$, $d\sigma_y$, $d\sigma_z$, $d\tau_{xy}$.

Since $d\varepsilon_z = 0$, one can readily find

$$d\sigma_z = -\frac{1}{k_{33}}[k_{31}d\sigma_x + k_{32}d\sigma_y + k_{34}d\tau_{xy} + k_{37}d\theta] \tag{28}$$

Hence, the axial stress component can be eliminated by use of the equation given above. The resulting incremental stress-strain temperature relation is given in the following form:

$$\{d\varepsilon\} = [L_1 \vdots L_2] \{\tfrac{d\sigma}{d\theta}\} \tag{29}$$

where

$$\{d\varepsilon\}^T = \langle d\varepsilon_x, d\varepsilon_y, d\varepsilon_{xy}\rangle \tag{30}$$

$$\{\tfrac{d\sigma}{d\theta}\}^T = \langle d\sigma_x, d\sigma_y, d\tau_{xy} \vdots d\theta\rangle \tag{31}$$

and

$$[L] = [L_1 \vdots L_2] = \begin{bmatrix} (k_{11} - \dfrac{k_{13}k_{31}}{k_{33}}) & (k_{12} - \dfrac{k_{13}k_{32}}{k_{33}}) & (k_{14} - \dfrac{k_{13}k_{34}}{k_{33}}) & \vdots & (k_{17} - \dfrac{k_{13}k_{37}}{k_{33}}) \\[2mm] (k_{21} - \dfrac{k_{23}k_{31}}{k_{33}}) & (k_{22} - \dfrac{k_{23}k_{32}}{k_{33}}) & (k_{24} - \dfrac{k_{23}k_{34}}{k_{33}}) & \vdots & (k_{27} - \dfrac{k_{23}k_{37}}{k_{33}}) \\[2mm] (k_{41} - \dfrac{k_{43}k_{31}}{k_{33}}) & (k_{42} - \dfrac{k_{43}k_{32}}{k_{33}}) & (k_{44} - \dfrac{k_{34}k_{43}}{k_{33}}) & \vdots & (k_{47} - \dfrac{k_{43}k_{37}}{k_{33}}) \end{bmatrix} \tag{32}$$

in which k_{ij} are defined in equation (27). Since $k_{ij} = k_{ji}$, $(i,j=1,\cdots,6)$, one can readily see that L_1 is a symmetric partition of matrix $[L]$.

C. Plane-Stress. On the basis of plane-stress condition, the nonvanish incremental stress components are $d\sigma_x$, $d\sigma_y$, and $d\tau_{xy}$; and the nonvanish incremental strain components are $d\varepsilon_x$, $d\varepsilon_y$, $d\varepsilon_z$, and $d\varepsilon_{xy}$. By definition,

$$\sigma_z = \tau_{yz} = \tau_{zx} = 0 \tag{33}$$

Following Ziegler's argument [5], one has

$$\alpha_z = \alpha_{yz} = \alpha_{zx} = 0 \qquad (34)$$

Then the explicit expression of equation (15) can readily be written in the following simple matrix form:

$$\{d\epsilon\} = [M_1 \vdots M_2] \{\frac{d\sigma}{d\theta}\} \qquad (35)$$

in which

$$\{d\epsilon\}^T = <d\epsilon_x, \ d\epsilon_y, \ d\epsilon_z, \ d\epsilon_{xy}> \qquad (36)$$

$$\{\frac{d\sigma}{d\theta}\}^T = <d\sigma_x, \ d\sigma_y, \ d\tau_{xy} \vdots d\theta> \qquad (37)$$

and

$$[M] = [M_1 \vdots M_2] = \begin{bmatrix} m_{11} & m_{12} & m_{13} & m_{14} \\ m_{21} & m_{22} & m_{23} & m_{24} \\ m_{31} & m_{32} & m_{33} & m_{34} \\ m_{41} & m_{42} & m_{43} & m_{44} \end{bmatrix} \qquad (38)$$

where

$$m_{11} = \frac{1}{Cd^2} [2(\sigma_x - \alpha_x) - (\sigma_y - \alpha_y)] + \frac{1}{E}$$

$$m_{12} = m_{21} = \frac{1}{Cd^2} [2(\sigma_x - \alpha_x) - (\sigma_y - \alpha_y)][2(\sigma_y - \alpha_y) - (\sigma_x - \alpha_x)]$$

$$m_{13} = m_{41} = \frac{6}{Cd^2} [2(\sigma_x - \alpha_x) - (\sigma_y - \alpha_y)](\tau_{xy} - \alpha_{xy})$$

$$m_{22} = \frac{1}{Cd^2} [2(\sigma_y - \alpha_y) - (\sigma_x - \alpha_x)] + \frac{1}{E}$$

$$m_{23} = m_{42} = \frac{6}{Cd^2} [2(\sigma_y - \alpha_y) - (\sigma_x - \alpha_x)](\tau_{xy} - \alpha_{xy})$$

$$m_{31} = \frac{-1}{Cd^2} [2(\sigma_x - \alpha_x) - (\sigma_y - \alpha_y)][(\sigma_x - \alpha_x) + (\sigma_y - \alpha_y)]$$

$$m_{32} = \frac{-1}{Cd^2} [2(\sigma_y - \alpha_y) - (\sigma_x - \alpha_x)][(\sigma_x - \alpha_x) + (\sigma_y - \alpha_y)]$$

$$(39)$$

108

$$m_{33} = \frac{-6}{Cd^2} \left[\sigma_x - \alpha_x \right) + (\sigma_y - \alpha_y)](\tau_{xy} - \sigma_{xy})$$

$$m_{43} = \frac{36}{Cd^2} (\tau_{xy} - \sigma_{xy})^2 + \frac{1+\nu}{E}$$

$$m_{14} = \frac{2}{Cd^2} \left[2(\sigma_x - \alpha_x) - (\sigma_y - \alpha_y) \right] \sigma_\theta \frac{\partial \sigma_\theta}{\partial \theta} + \beta$$

$$m_{24} = \frac{2}{Cd^2} \left[2(\sigma_y - \alpha_y) - (\sigma_x - \alpha_x) \right] \sigma_\theta \frac{\partial \sigma_\theta}{\partial \theta} + \beta$$

$$m_{34} = \frac{2}{Cd^2} \left[(\sigma_x - \alpha_x) + (\sigma_y - \alpha_y) \right] \sigma_\theta \frac{\partial \sigma_\theta}{\partial \theta} + \beta$$

$$m_{44} = \frac{12}{Cd^2} (\tau_{xy} - \alpha_{xy}) \sigma_\theta \frac{\partial \sigma_\theta}{\partial \theta}$$

and

$$d^2 = 6 \left[(\sigma_x - \alpha_x)^2 - (\sigma_x - \alpha_x)(\sigma_y - \alpha_y) + (\sigma_y - \alpha_y)^2 + 6(\tau_{xy} - \alpha_{xy})^2 \right] \quad (40)$$
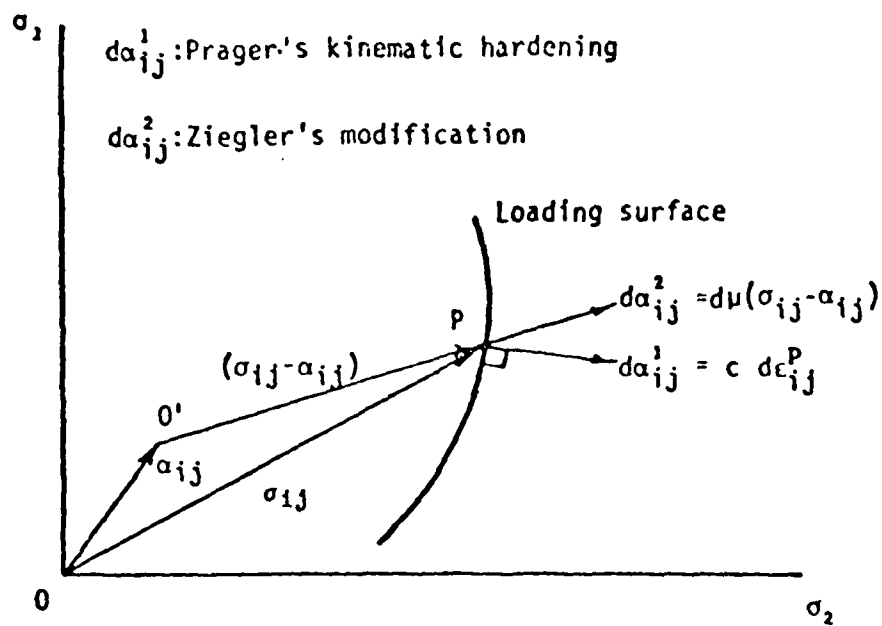
REMARK

One implicit assumption made so far is that the temperature-dependent yield strength $\sigma_\theta(\theta)$ of the material is differentiable. The actual relationship of yield strength of the material vs temperature must be determined by experiment. Fortunately, this relationship can usually be approximated by a polynomial; hence, it is differentiable. The test data of yield strength vs temperature for chrominum-molybdenum-vanadium (Cr-Mo-V) steel are shown in Figure 2 by open circles. A fourth-degree polynomial approximation for test data, as shown in Figure 2 by solid curve, is

$$\sigma_\theta = 131,000 - 10.89047\theta + 0.06483536\theta^2$$
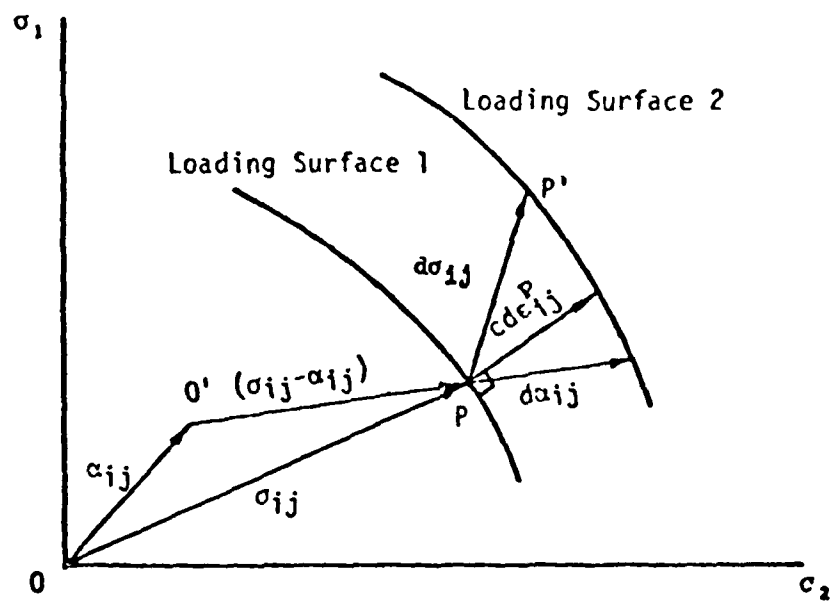
$$- 0.0001666979\theta^3 + 0.0000000598456\theta^4$$

One can see that this relation exhibits a very good approximation of test data.

REFERENCES

1. D. C. Drucker, "Some Implication of Work-Hardening and Ideal Plasticity," Quarterly Appl. Math. Vol. 7, 1950.

2. W. Prager, "A New Method of Analyzing Stresses and Strains in Work-Hardening Plastic Solids," Journal Appl. Mech. Vol. 23, 1956.

3. W. Prager, "Recent Development in Mathematical Theory of Plasticity," Journal Appl. Phys. 20, 1949.

4. R. T. Shield, and H. Ziegler, "On Prager's Hardening Rule," Zutschrift fur Angewondte Matheratel und Physics, Vol. IXa, 1958.

5. H. Ziegler, "A Modification of Prager's Hardening Rule," Quarterly of Appl. Math. Vol. 17, 1959.

6. R. Hill, "On The Problem of Uniqueness in the Theory of a Rigid-Plastic Solid," Journal Mech. Phys. Solid, Vol. 4, 1956.

7. W. Prager, "The Theory of Plasticity: A Survey of Recent Achievements," Proc. Inst. Mech. Eng. Vol. 169, 1955.

8. P. G. Hodge, Jr., "Numerical Applications of Minimum Principles in Plasticity," Proc. Conf. on Eng. Plasticity, Cambridge, England, 1968.

9. G. Maier, "Complementary Plastic Work Theories in Piecewise-Linear Elastoplasticity," Int. J. Solids and Structures," Vol. 5, 1969.

10. W. Prager, "Non-Isothermal Plastic Deformation," K. Mederl. Ak. Wetensch., Proc. Vol. 61, 1958.

11. D. C. Drucker, "A More Fundamental Approach to Plastic Stress-Strain Relations," Proc. 1st U. S. National Congress Applied Mechanics, New York, 1952.

da^1_{ij}:Prager's kinematic hardening

da^2_{ij}:Ziegler's modification

Loading surface

$da^2_{ij} = d\mu(\sigma_{ij} - \alpha_{ij})$

$da^1_{ij} = c\ d\varepsilon^P_{ij}$

$(\sigma_{ij} - \alpha_{ij})$

α_{ij}

σ_{ij}

(a) Comparison of Prager's kinematic hardening rule with Ziegler's Modification

Loading Surface 2

Loading Surface 1

$d\sigma_{ij}$

$cd\varepsilon^P_{ij}$

$(\sigma_{ij} - \alpha_{ij})$

$d\alpha_{ij}$

α_{ij}

σ_{ij}

(b) Hardening rule and Definition of Plastic Strain Increment for strain-hardening material

Fig. 1 Kinematic Hardening Rules

111

$$\sigma_\theta(\theta) = 131,000 - 10.89047\theta + 0.06483536\theta^2$$
$$- 0.0001666979\theta^3 + 0.00000005984565\theta^4$$

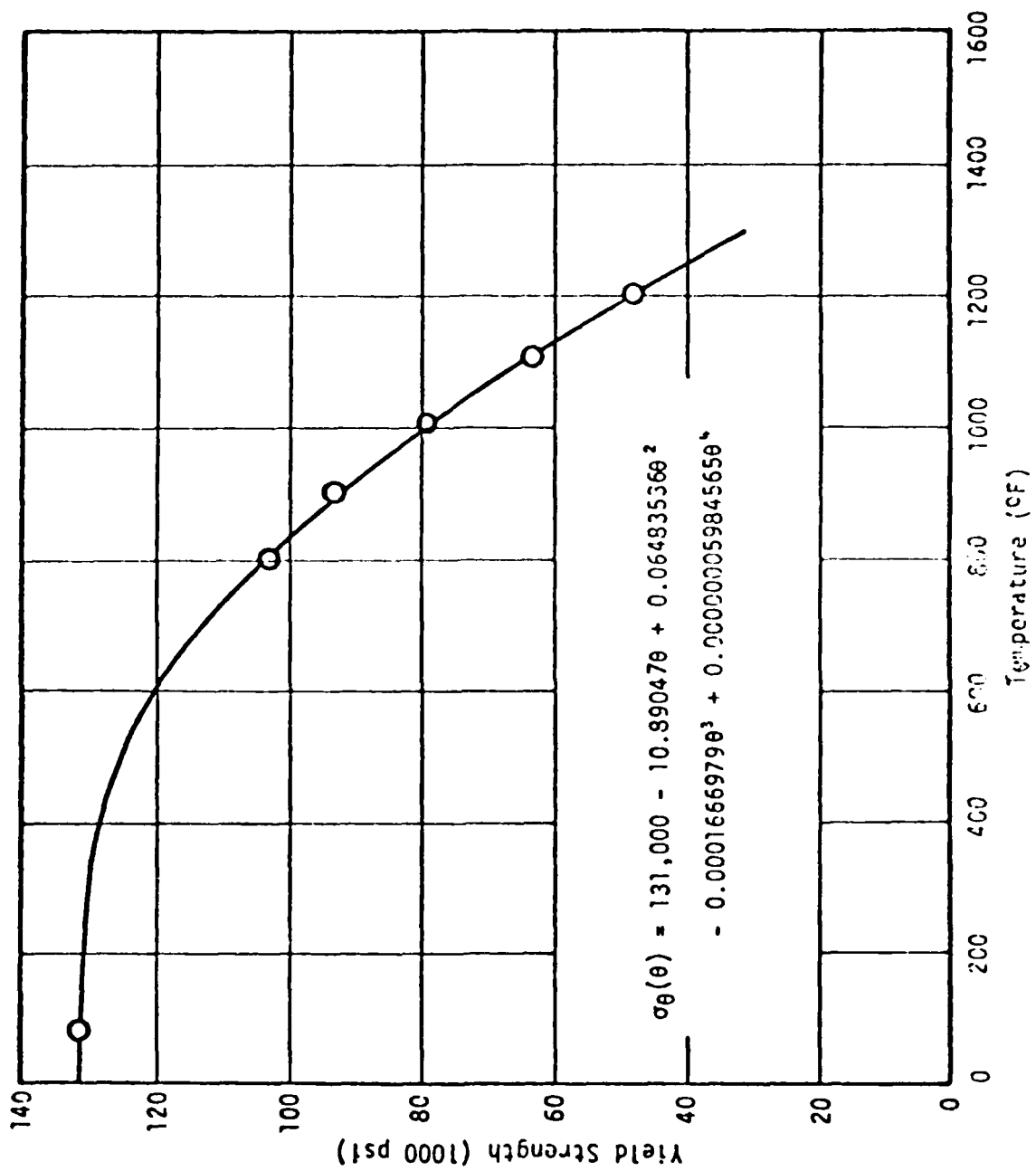Yield Strength (1000 psi)

Temperature (°F)

Fig. 2 Yield strength at elevated temperature for chromium molybdenum vanadium steel

112

ELASTIC-PLASTIC THICK-WALLED TUBES SUBJECTED TO INTERNAL PRESSURE

AND TEMPERATURE GRADIENT

P. C. T. Chen
U.S. Army Armament Research and Development Command
Large Caliber Weapon Systems Laboratory
Benet Weapons Laboratory
Watervliet, NY 12189

ABSTRACT. Using von Mises' criterion and the Prandtl-Reuss flow theory, numerical solutions are obtained for the stresses, strains, and displacements in an elastic-plastic thick-walled tube subjected to internal pressure and temperature gradient. The material is ideally-plastic or obeys the isotropic hardening rule. The formulation is based on the incremental finite-difference method in conjunction with a scaled loading approach. All incremental quantities are determined in the program and no iteration is needed. The approach is simpler than others yet quite general and accurate.

I. INTRODUCTION. The elastic-plastic problems of thick-walled tubes subjected to mechanical loadings have been solved by many investigators based on different theories or methods [1-4]. Very little work has been done on the elastoplastic solutions for thick-walled tubes subjected to thermal loadings [5-7]. Recently, a new finite-difference approach was developed for solving the plane-strain problems of elastic-plastic thick-walled tubes subjected to mechanical loadings [3] or thermal loadings [7]. The approach has been extended to solve the generalized plane-strain problem subjected to mechanical loadings [4].

In the present paper, the generalized plane-strain problems of elastic-plastic thick-walled tubes subjected to mechanical as well as thermal loadings will be considered. The formulation includes internal pressure, external pressure, axial force, steady or transient thermal loadings. The numerical result will be reported for a closed-end tube subjected to internal pressure and to temperature gradient. The formulation is based on the incremental finite-difference method using von Mises' criterion, the Prandtl-Reuss flow theory and the isotropic hardening rule. All incremental quantities are determined in the program and no iteration is needed. In order to improve the efficiency of the program, a scaled loading approach has been implemented. The numerical results have been compared with those of Bland [5] and additional results due to large temperature gradient are to be reported.

II. BASIC EQUATIONS. Assuming small strain and no body forces in the axisymmetric state of generalized plane strain, the radial and tangential stresses, σ_r and σ_θ, must satisfy the equilibrium equation,

$$r(\partial \sigma_r/\partial r) = \sigma_\theta - \sigma_r \; ; \tag{1}$$

and the corresponding strains, ε_r and ε_θ, are given in terms of the radial displacement, u, by

$$\varepsilon_r = \partial u/\partial r \quad , \quad \varepsilon_\theta = u/r \quad . \tag{2}$$

It follows that the strains must satisfy the equation of compatibility

$$r(\partial \varepsilon_\theta/\partial r) = \varepsilon_r - \varepsilon_\theta \quad . \tag{3}$$

Whereas the differential equations (1), (2), and (3) hold throughout the tube regardless of the material properties, the constitution equations assume various forms according to the adopted form of yield function, hardening rule, total or incremental theory of plasticity. In the present paper, the material is assumed to be elastic-plastic, obeying the Mises' yielding criterion, the Prandtl-Reuss flow theory and the isotropic hardening law. The complete stress-strain relations are:

$$\Delta\varepsilon_i' = \Delta\sigma_i'/2G + (3/2)\sigma_i'\Delta\sigma/(\sigma H') \tag{4}$$

$$\Delta\sigma \geq 0 \quad \text{for} \quad i = r,\theta,z$$

$$\Delta\varepsilon_m = E^{-1}(1-2\nu)\Delta\sigma_m + \alpha\Delta T \tag{5}$$

where E, ν, α are Young's modulus, Poisson's ratio, coefficient of thermal expansion, respectively, ΔT is the temperature increment,

$$2G = E/(1+\nu) \quad ,$$

$$\varepsilon_m = (\varepsilon_r+\varepsilon_\theta+\varepsilon_z)/3 \quad , \quad \varepsilon_i' = \varepsilon_i - \varepsilon_m \quad ,$$

$$\sigma_m = (\sigma_r+\sigma_\theta+\sigma_z)/3 \quad , \quad \sigma_i' = \sigma_i - \sigma_m \quad ,$$

$$\sigma = (1/\sqrt{2})[(\sigma_r-\sigma_\theta)^2 + (\sigma_\theta-\sigma_z)^2 + (\sigma_z-\sigma_r)^2]^{1/2} \geq \sigma_0 \quad , \tag{6}$$

and σ_0 is the yield stress in simple tension or compression. For a strain-hardening material, H' is the slope of the effective stress/plastic strain curve

$$\sigma = H(\int d\varepsilon^p) \quad . \tag{7}$$

For an ideally-plastic material ($H' = 0$), the quantity $(3/2)d\sigma(\sigma H')$ is replaced by $d\lambda$, a positive factor of proportionality. When $\sigma < \sigma_0$ or $d\sigma < 0$, the state of stress is elastic and the second term in equation (4) disappears. Following Yamada et al [8], equations (4) and (5) can be rewritten in an incremental form

$$\Delta\sigma_i = d_{ij}\Delta\varepsilon_j - E\alpha\Delta T/(1-2\nu) \quad \text{for} \quad i,j = r,\theta,z$$

and

$$d_{ij}/2G = \nu/(1-2\nu) + \delta_{ij} - \sigma_i'_j'/S \quad , \tag{8}$$

where

$$S = \frac{2}{3} (1 + \frac{1}{3} H'/G)\sigma^2 \quad , \quad H'/E = \omega/(1-\omega) \quad , \tag{9}$$

ωE is the slope of the effective stress-strain curve, and δ_{ij} is the Kronecker delta.

Consider an open-end or closed-end thick-walled tube of inner radius a and external radius b. The tube is subjected to inner pressure p, external pressure q, and force f, inner temperature T_a and external temperature T_b. The boundary conditions for the problem are

$$\sigma_r(a,t) = -p \quad , \quad \sigma_r(b,t) = -q \quad ,$$

$$2\pi \int_a^b r\sigma_z dr = \mu\pi a^2 p + f \tag{10}$$

where μ is 0 for open-end tubes and 1 for closed-end tubes.

When the temperature T is not varying with respect to time, the steady state distribution is given by

$$T = T_a + N \log (r/a)$$

and

$$N = (T_b - T_a)/\log (b/a) \tag{11}$$

The stress solution in the elastic range is well-known. The quantities p^*, q^*, f^*, T_a^* or T_b^* required to cause initial yielding can be determined by using the Mises' yield criterion.

III. FINITE-DIFFERENCE FORMULATION. For loading beyond the elastic limit, an incremental approach of the finite-difference formulation is used. The cross section of the tube is divided into n rings with $r_1=a, r_2, \ldots, r_k=\rho$, $\ldots, r_{n+1}=b$, where ρ is the radius of the elastic-plastic interface. At the beginning of each increment of loading, the distribution of temperature, displacements, strains, and stresses is assumed to be known and we want to determine Δu, $\Delta\epsilon_r$, $\Delta\epsilon_\theta$, $\Delta\epsilon_z$, $\Delta\sigma_r$, $\Delta\sigma_\theta$, $\Delta\sigma_z$ at all grid points for the applied incremental loading, Δp, Δq, Δf, ΔT_i (i = 1 to n+1). Since the incremental stresses are related to the incremental strains by the incremental form (Eq. (8)) and $\Delta u = r\Delta\epsilon_\theta$, there exists only three unknowns at each station that have to be determined for each increment of loading. Accounting for the fact that the axial strain ϵ_z is independent of r, the unknown variables in the present formulation are $(\Delta\epsilon_\theta)_i$, $(\Delta\epsilon_r)_i$, for i = 1,2,...n,n+1, and $\Delta\epsilon_z$.

The equation of equilibrium (1) and the equation of compatibility (3) are valid for both the elastic and the plastic regions of a thick-walled tube. The finite-difference forms of these two equations at i = 1,...,n are given by

$$(r_{i+1}-2r_i)(\Delta\sigma_r)_i - (r_{i+1}-r_i)(\Delta\sigma_\theta)_i + r_i(\Delta\sigma_r)_{i+1}$$

$$= (r_{i+1}-r_i)(\sigma_\theta-\sigma_r)_i - r_i[(\sigma_r)_{i+1} - (\sigma_r)_i] \tag{12}$$

for the equation of equilibrium, and

$$(r_{i+1}-2r_i)(\Delta\epsilon_\theta)_i - (r_{i+1}-r_i)(\Delta\epsilon_r)_i + r_i(\Delta\epsilon_\theta)_{i+1}$$

$$= (r_{i+1}-r_i)(\epsilon_r-\epsilon_\theta)_i - r_i[(\epsilon_\theta)_{i+1} - (\epsilon_\theta)_i] \tag{13}$$

for the equation of compatibility. With the aid of the incremental stress-strain relations (Eq. (8)), equation (12) can be rewritten as

$$[(r_{i+1}-2r_i)(d_{12})_i + (-r_{i+1}+r_i)(d_{22})_i](\Delta\epsilon_\theta)_i$$

$$+ [(r_{i+1}-2r_i)(d_{11})_i + (-r_{i+1}+r_i)(d_{21})_i](\Delta\epsilon_r)_i$$

$$+ r_i(d_{12})_{i+1}(\Delta\epsilon_\theta)_{i+1} + r_i(d_{11})_{i+1}(\Delta\epsilon_r)_{i+1}$$

$$+ [(r_{i+1}-2r_i)(d_{13})_i + (-r_{i+1}+r_i)(d_{23})_i + r_i(d_{13})_{i+1}]\Delta\epsilon_z$$

$$= (r_{i+1}-r_i)(\sigma_\theta-\sigma_r)_i - r_i[(\sigma_r)_{i+1} - (\sigma_r)_i]$$

$$+ r_i\, E\alpha(1-2\nu)^{-1}(\Delta T_{i+1}-\Delta T_i) \quad . \tag{14}$$

The boundary conditions for the problem are

$$\Delta\sigma_r(a,t) = -\Delta p \quad , \quad \Delta\sigma_r(b,t) = -\Delta q \quad ,$$

$$\pi \sum_{i=1}^{n} [r_i(\Delta\sigma_z)_i + r_{i+1}(\Delta\sigma_z)_{i+1}](r_{i+1}-r_i) = \mu\pi a^2\Delta p + \Delta f \quad , \tag{15}$$

where μ is 0 for open-end tubes and 1 for closed-end tubes. Using the incremental relations (Eq. (8)), we rewrite equation (15) as

$$(d_{12})_1(\Delta\epsilon_\theta)_1 + (d_{11})_1(\Delta\epsilon_r)_1 + (d_{13})_1\Delta\epsilon_z = -\Delta p + E\alpha(1-2\nu)^{-1}\Delta T_1 \tag{16}$$

$$(d_{12})_{n+1}(\Delta\epsilon_\theta)_{n+1} + (d_{11})_{n+1}(\Delta\epsilon_r)_{n+1} + (d_{13})_{n+1}\Delta\epsilon_z = -\Delta q + E\alpha(1-\nu)^{-1}\Delta T_{n+1}$$

$$\tag{17}$$

and

$$\sum_{i=1}^{n} (r_{i+1}-r_i)\{r_i[(d_{23})_i(\Delta\epsilon_\theta)_i + (d_{13})_i(\Delta\epsilon_r)_i] + r_{i+1}[(d_{23})_{i+1}(\Delta\epsilon_\theta)_{i+1}$$

$$+ (d_{13})_{i+1}(\Delta\epsilon_r)_{i+1}]\} + \sum_{i=1}^{n} (r_{i+1}-r_i)[r_i(d_{33})_i + r_{i+1}(d_{33})_{i+1}]\Delta\epsilon_z$$

$$= \mu a^2\Delta p + \Delta f/\pi + \sum_{i=1}^{n} (r_{i+1}-r_i)[r_i\Delta T_i + r_{i+1}\Delta T_{i+1}]E\alpha/(1-2\nu) \tag{18}$$

116

Now we can form a system of $2n+3$ equations for solving $2n+3$ unknowns, $(\Delta\epsilon_\theta)_i$, $(\Delta\epsilon_r)_i$, at $i = 1,2,\ldots,n,n+1$ and $\Delta\epsilon_z$. Equations (16), (17), and (18) are taken as the first and last two equations, respectively, and the other $2n$ equations are set up at $i = 1,2,\ldots,n$ using (13) and (14). The final system is an unsymmetric matrix of arrow type with the nonzero terms appearing in the last row and column and others clustered about the main diagonal, two below and one above.

IV. INCREMENTAL LOADING - FIXED VS. SCALED. When the total applied pressure p or temperature $T_i(i=1$ to $n+1)$ are given, it is natural to divide the loading path into m equal fixed increments such as $\Delta p = (p-p*)/m$, $\Delta T_i = (T_i-T_i*)/m$. These fixed increments need not be equal for all steps and any sequence of m increments can be supplied by the user. A sequence of decreasing load increments is a better choice than that of equal increments.

In order to increase the efficiency of the program, an adaptive algorithm based on a scaled incremental-loading approach [8] has been implemented. In each step, a dummy load-increment such as Δp is applied and the incremental results $\Delta\sigma_i$ for $i = r,\theta,z$ at all grids are determined. For all grid points at which $\sigma = ||\sigma_i|| < \sigma_0$, we compute the scaler α's by the formula

$$\alpha = \frac{1}{2} \{\Gamma + [\Gamma^2 + 4||\Delta\sigma_i||^2(\sigma_0^2-||\sigma_i||^2)]^{1/2}\}/||\Delta\sigma_i||^2 \quad , \qquad (19)$$

where

$$\Gamma = ||\sigma_i||^2 + ||\Delta\sigma_i||^2 - ||\sigma_i + \Delta\sigma_i||^2 \quad , \qquad (20)$$

and $||\sigma_i||$, $||\Delta\sigma_i||$, $||\sigma_i + \Delta\sigma_i||^2$ are computed by

$$||\sigma_i||^2 = \frac{1}{2} [(\sigma_r-\sigma_\theta)^2 + (\sigma_\theta-\sigma_z)^2 + (\sigma_z-\sigma_r)^2] \quad . \qquad (21)$$

Let λ be the minimum of the α's. Then λ is the load-increment factor just sufficient to yield one additional point. A sequence of $\lambda^{(j)}$ can be determined for all steps $j = 1,2,\ldots,m$ and the updated results are

$$p^{(j)} = p^{(j-1)} + \lambda^{(j)}\Delta p^{(j)}$$

$$\sigma_i^{(j)} = \sigma_i^{(j-1)} + \lambda^{(j)}\Delta\sigma_i^{(j)} \quad , \quad \text{etc.} \qquad (22)$$

V. NUMERICAL RESULTS AND DISCUSSIONS. Consider a closed-end tube subjected to internal pressure p, inner and outer temperature T_a and T_b. The numerical results were based on the following parameters: $b = 2"$, $a = 1"$, $n = 100$, $\nu = 0.3$, $E = 30\times10^6$ psi, $\sigma_0 = 30\times10^3$ psi, $\omega = 0$, $\alpha = 7.75\times10^{-6}$ in/in°F.

According to Bland [5], let us define

$$\theta = E\alpha N/[2(1-\nu)\sigma_0/\sqrt{3}]$$

as a measure of the effect of the temperature differences in the stress system. The mean temperature

$$T_m = 2(b^2-a^2)^{-1} \int_a^b Trdr$$

is taken as zero in the calculation of u/r. Three values of the temperature stress factor θ are chosen: $\theta = -1/2$, 0, and 1/2, i.e., $T_b-T_a = -72.3°F$, $0°F$, and $72.3°F$. The thermal stresses are in the elastic range. In the presence of these temperature gradients, internal pressure p is applied incrementally until fully plastic state is reached. The internal pressure p and inside displacement U_a are obtained as functions of elastic-plastic interface ρ as shown in Figure 1. The effect of temperature gradient on these relations is clearly shown in the figure. In order to compare the results by Bland [5], the state of stress is evaluated at $\rho/a = 1.73$. The dimensionless stresses $(\sigma_r,\sigma_\theta,\sigma_z)/\sigma_0$ are expressed as functions of r/a as shown in Figures 2 through 4 for three cases of $\theta = 0$, -1/2, 1/2, respectively. After removing the temperature gradients and internal pressure, the residual stresses have been obtained for all three cases. The states of residual stresses for the first two cases are still elastic but reverse yielding occurs when unloading the last case. Five scaled-incremental-loading steps and one applied-incremental-loading step are needed to unload completely. The residual stresses for the last case are shown in Figure 5. The results in Figures 1 through 5 are roughly the same as those of Bland [5] except σ_z. This difference is reasonable because Tresca's yield criterion is used in [5].

As a last example let us consider a closed-end tube subjected to inner temperature T_a only. When the temperature gradient is of sufficient magnitude, yielding will first expand from the inside. When T_a is larger than a certain limit (238.4°F), plastic zone will expand from both the inside and outside surface toward the interior. The relation between the inside temperature and elastic-plastic interface is shown in Figure 6. The stresses in a closed-end tube subjected to temperature gradient ($T_a = 299°F$, $T_b = 0$) is shown in Figure 7. The dotted lines are elastic-plastic interfaces.

REFERENCES

1. S. C. Chu, "A More Rational Approach to the Problem of an Elastoplastic Thick-Walled Cylinder," J. of the Franklin Institute, Vol. 294, 1972, pp. 57-62.

2. P. C. T. Chen, "The Finite Element Analysis of Elastic-Plastic Thick-Walled Tubes," Proceedings of Army Symposium on Solid Mechanics, 1972, pp. 243-253.

3. P. C. T. Chen, "A Finite Difference Approach to Axisymmetric Plane-Strain Problem Beyond the Finite Elastic Limit," Transactions of the Twenty-Fifth Conference of Army Mathematicians, pp. 455-465, January 1980.

4. P. C. T. Chen, "Generalized Plane-Strain Problems in an Elastic-Plastic Thick-Walled Cylinders," Transactions of the Twenty-Sixth Conference of Army Mathematicians, pp. 265-275, January 1981.

5. D. R. Bland, "Elastoplastic Thick-Walled Tubes of Work-Hardening Material Subject to Internal and External Pressures and to Temperature Gradients," Journal of the Mechanics and Physics of Solids, 1956, Vol. 4, pp. 209-229.

6. S. C. Chu, "A Numerical Thermo-Elastic-Plastic Solution of a Thick-Walled Tube," AIAA Journal, Vol. 12, No. 3, February 1974, pp. 176-179.

7. J. D. Vasilakis and P. C. T. Chen, "Thermo-Elastic-Plastic Stresses in Hollow Cylinders Due to Quenching," Transactions of the Twenty-Fifth Conference of Army Mathematicians, pp. 661-674, January 1980.

8. Y. Yamada, N. Yoshimura, and T. Sakuri, "Plastic Stress-Strain Matrix and Its Application For the Solution of Elastic-Plastic Problems by the Finite Element," International Journal of Mechanical Sciences, 1968, Vol. 10, pp. 343-354.
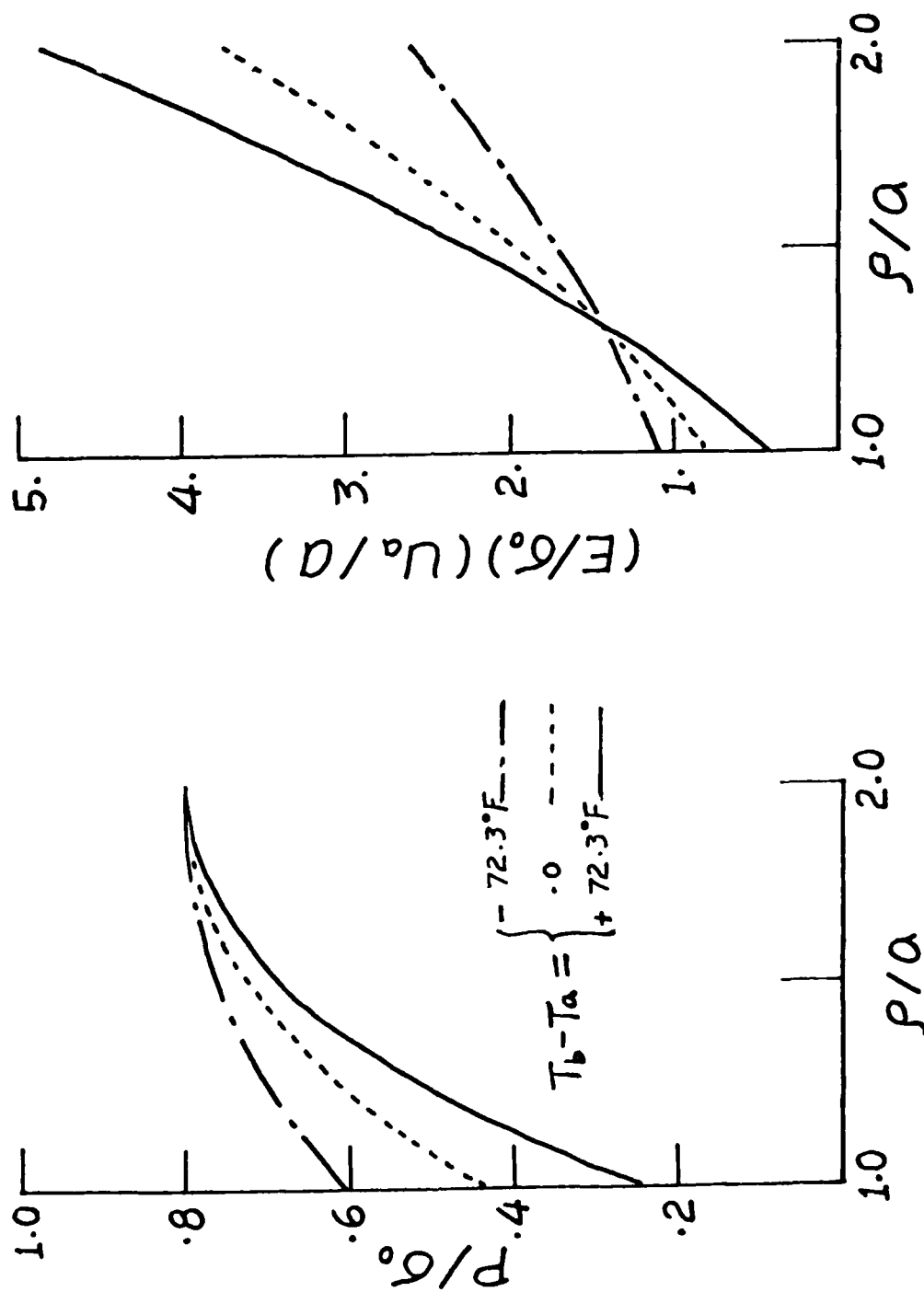
Figure 1. Internal pressure and displacement as functions of elastic-plastic interface in a closed end tube. (a) Internal pressure; (b) Internal displacement.
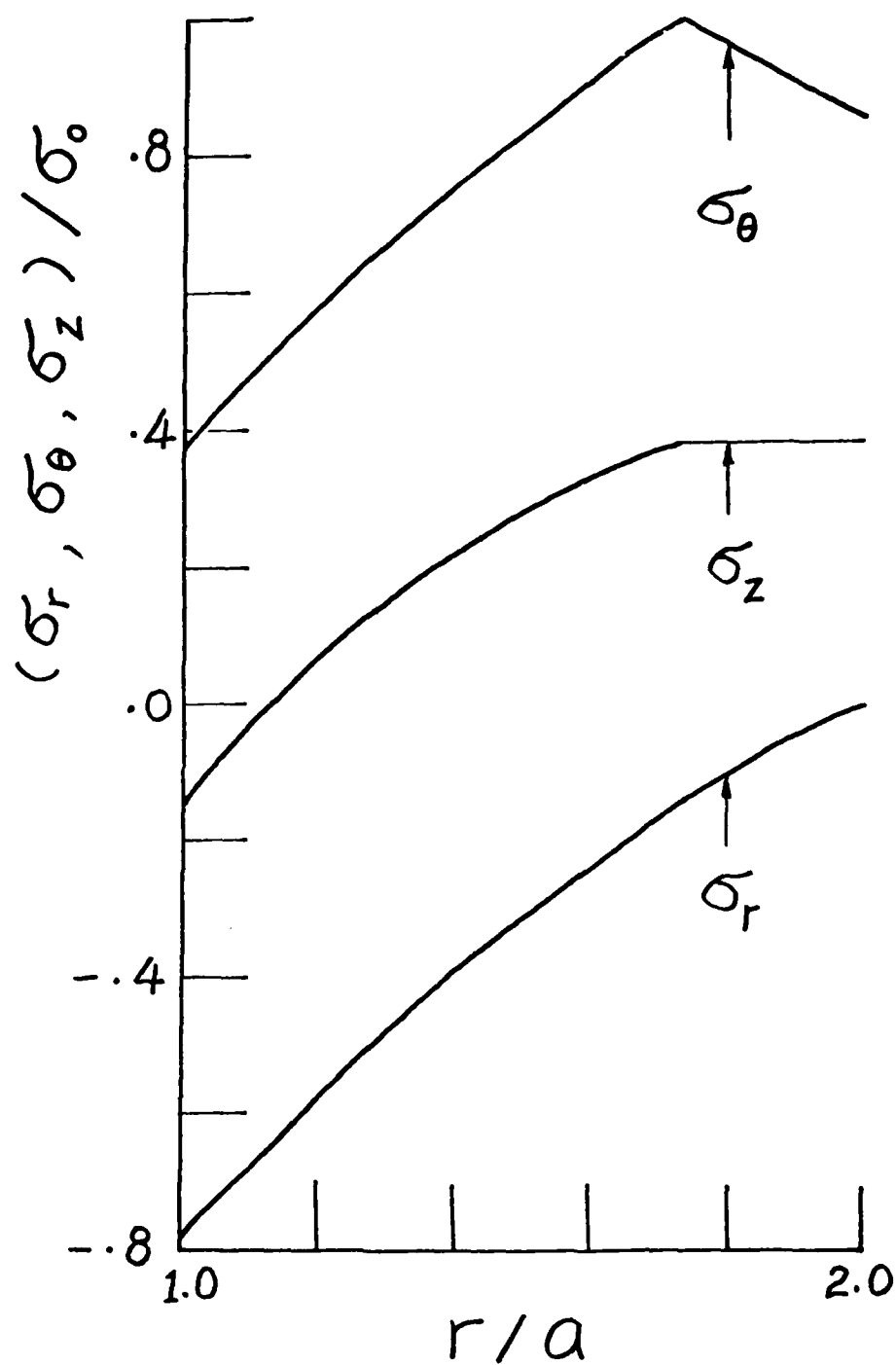
120

Figure 2.   Stresses in a closed-end tube subjected to internal pressure (ρ/a = 1.73; θ = 0).
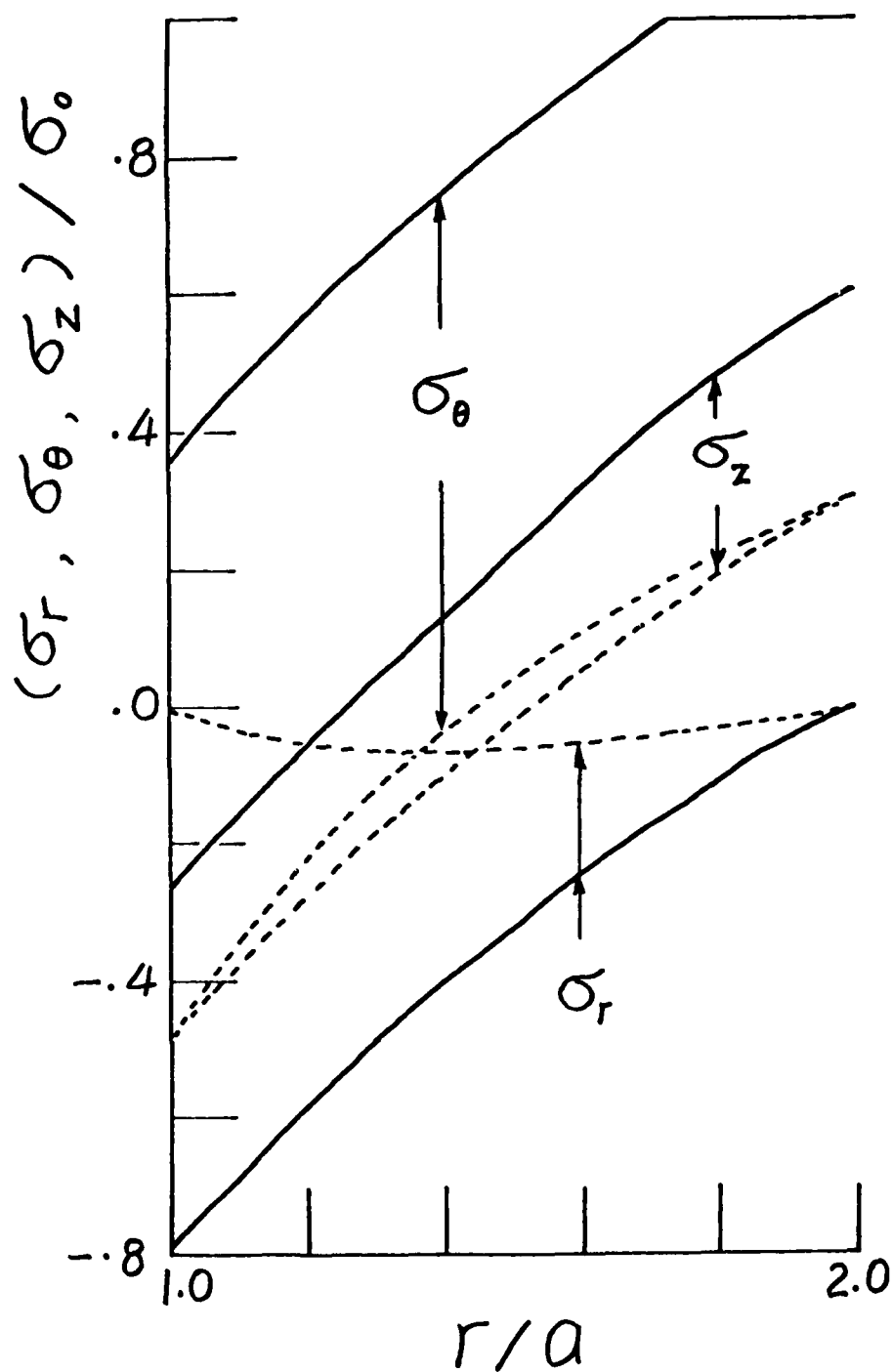
Figure 3. Stresses in a closed end tube subjected to internal pressure and temperature gradient ($\rho/a = 1.73$; $\theta = -1/2$).
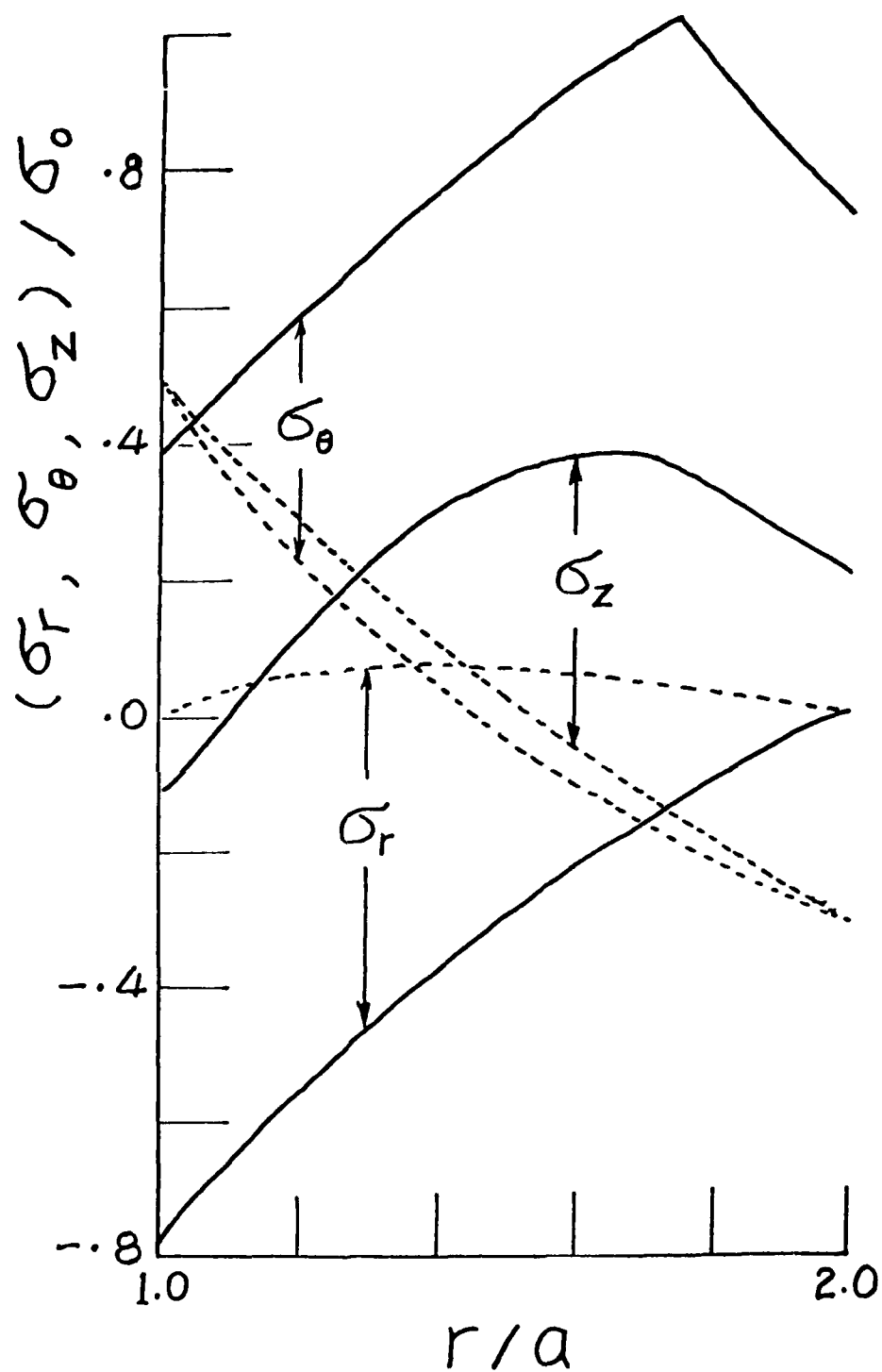
122

Figure 4. Stresses in a closed-end tube subjected to internal pressure and temperature gradient ($\rho/a = 1.73$; $\theta = 1/2$).
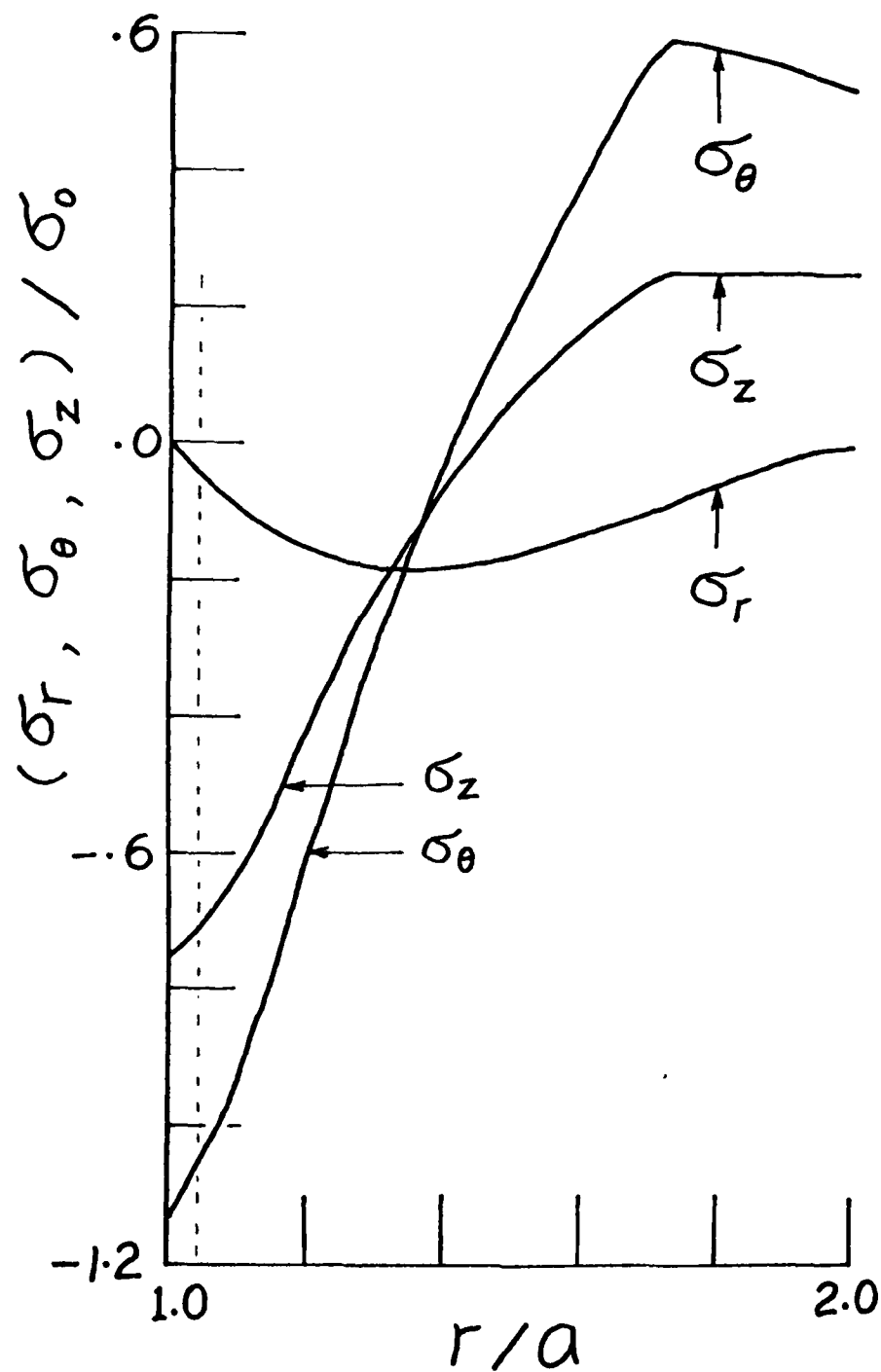
Figure 5. Residual stresses in a closed end tube, unloading from Figure 4, $1.04 < \rho/a < 1.05$.
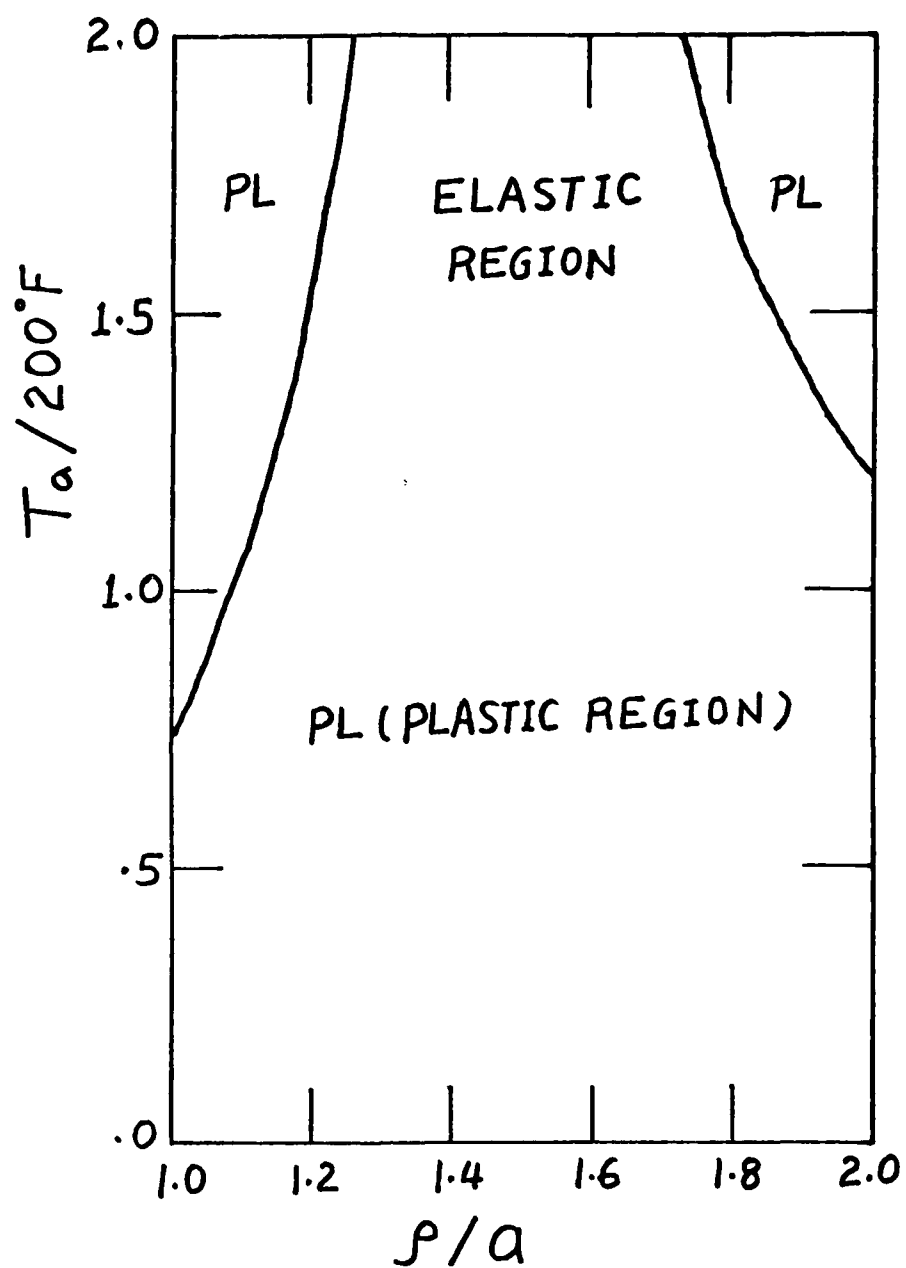
Figure 6. The relation between internal temperature and elastic-plastic interface, Tb = 0.
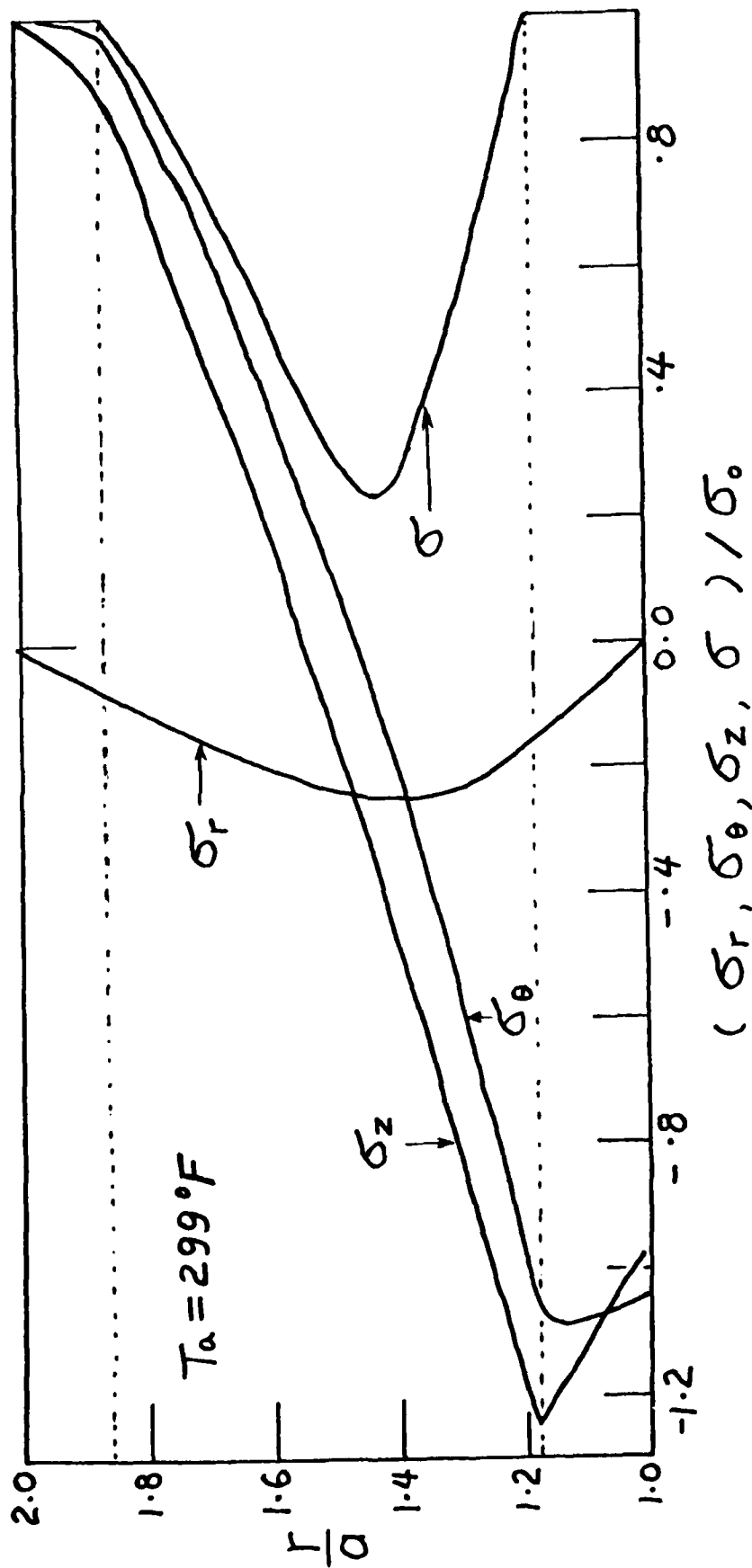
125

Figure 7. Stresses in a closed end tube subjected to temperature gradient, Tb = 0.

126

FLAME PROPAGATION WITH MULTIPLE FUELS

Stephen B. Margolis
Applied Mathematics Division
Sandia National Laboratories, Livermore, CA 94550

Bernard J. Matkowsky
Department of Engineering Sciences and Applied Mathematics
Northwestern University, Evanston, IL 60201

ABSTRACT

The steady propagation of a flame through a premixed combustible mixture is studied for the case in which the mixture consists of two distinct fuels. The overall chemical reaction mechanism is represented by $A + \nu_A O \rightarrow \mu_A P$, $B + \nu_B O \rightarrow \mu_B Q$, where A and B denote the fuels, O is the oxidizer, P and Q are the corresponding products, and $\nu_A, \mu_A, \nu_B, \mu_B$ are stoichiometric coefficients. We employ the method of matched asymptotic expansions to derive a solution for large activation energies, in which case both chemical reactions are confined to a thin layer. The (small) separation distance H between the points where the two reactions go to completion and the propagation velocity U are determined as functions of such quantities as Lewis numbers, activation energies, Damköhler numbers, and heat release fractions. The formula for H represents a relative measure of the flame thickness in terms of standard parameters, while that for U determines the role of each reaction in the overall flame speed.

1. Introduction

In analytical work on combustion, it is now commonplace to approximate the complicated chemical reaction mechanisms that occur by a global one-step reaction in which fuel and oxidizer react to form a product. By exploiting the fact that the activation energy of the reaction is large, a whole theory of asymptotics, peculiar to combustion problems with Arrhenius reaction rates, has been developed. They range from steady-state studies of one dimensional flames[3-5], to stability and bifurcation analyses in various geometries.[7,11,12,14-18] However, there are many chemical reaction mechanisms for which a global one-step reaction might not be a suitable approximation. Examples include systems with multiple fuels (the case considered here), inhibitors, catalysts, and branched chains. For such problems, it is often desired to obtain profiles of intermediate, catalytic or additional reactant species, as well as to study their effects on flame thickness, propagation velocity, and stability.

There have been only a few asymptotic analyses of flames consisting of more than one reaction. Berman and Riazentsev[1,2] considered a sequential mechanism of the form $A \rightarrow B \rightarrow C$ and a semi-parallel mechanism of the type $B \leftarrow A \rightarrow C$. By assuming that the Damköhler numbers (i.e., reaction rates) of the two reactions were of the same order of magnitude, they obtained asymptotic expressions for the steady-state propagation velocity of an adiabatic one-dimensional flame. Their analysis dealt with those

cases for which the corresponding flame separation distance was either identically zero or O(1). Generalizations of the A → B → C flame to account for widely disparate Damkohler numbers have been pursued by several authors.[6,8,9,10]

The present work considers steady one-dimensional flame propagation governed by a global parallel reaction mechanism of the form

$$A + \nu_A O \to \mu_A P \quad , \quad B + \nu_B O \to \mu_B Q \ , \tag{1a,b}$$
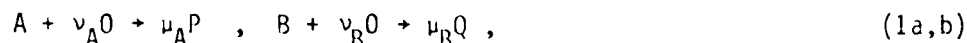
where A and B denote distinct fuels, O is the oxidizer, and P,Q are products. The quantities $\nu_A, \nu_B, \mu_A, \mu_B$ are stoichiometric coefficients which need not be integers for these types of global mechanisms. Reactions (1a,b) are coupled by a common dependence on temperature and are useful for modelling systems with multiple fuels. In our analysis, we employ reasonable assumptions on the large activation energies and the diffusion-weighted reaction rates (consumption rates). These approximations result in a merged flame to leading order and permit the derivation of explicit analytical expressions for both the propagation velocity U and the (small) separation distance H between the points where the two reactions go to completion. In what follows, we only present a summary of the analysis and emphasize the physical results. A more comprehensive analytical presentation is contained in another publication.[13]

2. Governing Equations

In a density-weighted coordinate system whose origin is attached to the flame zone, a set of nondimensional equations governing a freely propagating flame with the mechanism (1a,b) is[13]

$$\alpha \frac{dY}{d\psi} = L^{-1} \frac{d^2 Y}{d\psi^2} - \Lambda Y \exp \left[\frac{N(1-\sigma)(\theta-1)}{\sigma+(1-\sigma)\theta} \right] \tag{2}$$

$$\alpha \frac{dZ}{d\psi} = K^{-1} \frac{d^2 Z}{d\psi^2} - \frac{k}{\ell} \Lambda Z \exp \left[\frac{M(1-\sigma)(\theta-1)}{\sigma+(1-\sigma)\theta} \right] \tag{3}$$

$$\alpha \frac{d\theta}{d\psi} = \frac{d^2 \theta}{d\psi^2} + \beta \Lambda Y \exp \left[\frac{N(1-\sigma)(\theta-1)}{\sigma+(1-\sigma)\theta} \right] + (1-\beta) \frac{k}{\ell} \Lambda Z \exp \left[\frac{M(1-\sigma)(\theta-1)}{\sigma+(1-\sigma)\theta} \right] \tag{4}$$

$$Y = Z = 1, \quad \theta = 0 \quad \text{at} \quad \psi = -\infty; \quad Y = Z = 0, \quad \theta = 1 \quad \text{at} \quad \psi = +\infty . \tag{5a,b}$$

Here, Y and Z are the mass fractions of species A and B divided by their unburned values at $\psi = -\infty$, and θ is a normalized temperature variable. The nondimensional parameters appearing in Eqs. (2)–(4) are the Lewis numbers L and K, activation energies N and M, modified Damkohler numbers (reaction rates) ℓ and k, unburned temperature σ, expansion parameter α, and heat release fractions $\beta, (1-\beta)$ due to reactions (1a,b). Λ is the flame speed eigenvalue, proportional to U^{-2}, where U is the nondimensional adiabatic flame speed.

Equations (2)–(6) are solved by exploiting the fact that the activation energies N and M are large. We assume that

$$\frac{M}{N} = 1 + \frac{\gamma}{\Delta} \ , \quad \frac{K \cdot k}{L \cdot \ell} = 1 + \frac{\nu}{\Delta} \ , \quad \Delta \equiv N(1-\sigma) \ , \tag{6a,b,c}$$

where $\gamma, \nu \sim O(1)$ and $\Delta \gg 1$ is introduced as our large expansion parameter. We refer to the diffusion-weighted Damkohler numbers $K \cdot k, L \cdot \ell$ as consumption rates.

3. Outer Solution

In the limit of large activation energies, the reaction rate terms become negligible except in a thin $O(\Delta^{-1})$ zone where Θ is close to unity, just as in the case of a single reaction mechanism. The reaction zone is considered as a chemical boundary layer and the regions within and outside the layer are treated by the method of matched asymptotic expansions. In the outer region, each reaction term is replaced by a δ-function distribution, whereas in the inner region all quantities are expanded in inverse powers of Δ. To all algebraic orders, the outer solution satisfies

$$\alpha Y_0' = L^{-1} Y_0'' - P\delta(\psi), \qquad \alpha Z_0' = K^{-1} Z_0'' - Q\delta(\psi - H) \qquad (7a,b)$$

$$\alpha\Theta_0' = \Theta_0'' + \beta P\delta(\psi) + (1-\beta)Q\delta(\psi - H) , \qquad (8)$$

subject to the boundary conditions (5a,b). This has the solution $P=Q=\alpha$,

$$Y_0(\psi) = \begin{vmatrix} 1 - \exp(\alpha L \psi), & \psi < 0 \\ 0, & \psi > 0 \end{vmatrix} , \quad Z_0(\psi) = \begin{vmatrix} 1 - \exp[\alpha K(\psi - H)], & \psi < H \\ 0, & \psi > H \end{vmatrix} , (9,10)$$

$$\Theta_0(\psi) = \begin{cases} \beta \exp(\alpha\psi) + (1-\beta) \exp[\alpha(\psi - H)], & \psi < \min(0,H) \\ \beta + (1-\beta) \exp[\alpha(\psi - H)], & 0 < \psi < H, \ H > 0 \\ 1-\beta + \beta \exp(\alpha\psi), & H < \psi < 0, \ H < 0 \\ 1, & \psi > \max(0,H) \end{cases} , \quad (11)$$

and is sketched in Fig. 1 for typical parameter values.
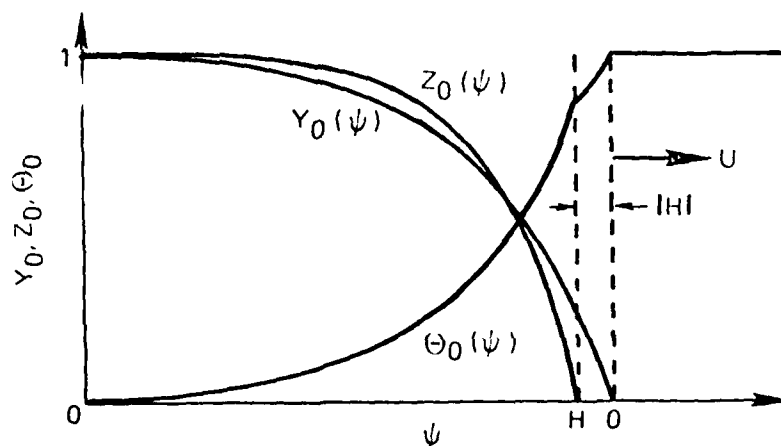
Figure 1. Outer Solution Profiles for Typical Parameter Values

The flame separation distance H, like Λ, plays the role of an eigenvalue, since both quantities are determined in the course of the analysis. The fact that neither reaction can occur until $\Theta \approx 1$ (a consequence of Eq. (6)), implies that H is small. Consequently, H might also be interpreted as a relative measure of flame thickness. Both H and Λ are determined as functions of the various flame parameters by a boundary layer analysis in the reaction zone.

4. Reaction Zone Analysis

In the thin reaction zone, the independent variable ψ is stretched according to $\psi = \eta/\Delta$ and the remaining unknown quantities are expanded as follows:

$$Y = \sum_{i=1}^{\infty} y_i \Delta^{-i} , \quad Z = \sum_{i=1}^{\infty} z_i \Delta^{-i} , \quad \Theta = 1 + \sum_{i=1}^{\infty} \Theta_i \Delta^{-i} , \quad \Lambda = \sum_{i=1}^{\infty} \lambda_i \Delta^{3-i} , \quad H = \sum_{i=1}^{\infty} h_i \Delta^{-i} . \quad (12a,b,c,d,e)$$

Substituting these expansions into Eqs. (2)-(4), equating the coefficient of each power of Δ separately to zero, and matching with the outer solution (9)-(11) yields a sequence of problems, the first two of which are considered in detail.

The solution to the first order problem is[13]

$$\lambda_1 = \frac{1}{2} L^{-1} \alpha^2 , \quad h_1 = 0 , \quad y_1 = -L\Theta_1 , \quad z_1 = -K\Theta_1 \quad (13a,b,c,d)$$

$$\eta = \frac{1}{2} \int_a^{\Theta_1} \left[1 + (\overline{\Theta}_1 - 1) e^{\overline{\Theta}_1} \right]^{-1/2} d\overline{\Theta}_1 , \quad a \approx -.935 . \quad (14)$$

This solution is essentially equivalent to that obtained for the single-step flame problem.[3,19] To this order of analysis the multi-fuel flame behaves as if it were governed by a single reaction, since both reactions occur at the same spatial location. In order to determine the effects of the parallel reaction mechanism on the flame speed and the flame thickness, it is necessary to calculate λ_2 and h_2, the second order correction to these quantities.

Since our main purpose in considering the second order problem is to determine h_2 and μ as functions of the flame parameters, we do not attempt to completely solve the second order problem. Rather, we derive a coupled pair of solvability conditions for these two unknowns based on an analysis of the adjoint problem. The result is[13]

$$h_2 = \frac{1}{\alpha} (2\gamma I_2 + \nu I_1) \quad (15)$$

$$\lambda_2 = \alpha^2 L^{-1} \{ 3(1-\sigma) + \frac{1}{2} (1-\beta)(2\gamma-\nu) - \frac{1}{2} I_2 + \frac{1}{2} [\beta L + (1-\beta)K](2I_1 + I_2) \} \quad (16)$$

$$I_1 = \int_0^{-\infty} [1 - p(\tau)^{1/2}] d\tau = -1.344, \quad I_2 = \int_0^{-\infty} \tau [1 - p(\tau)^{1/2}] d\tau = +1.731 . \quad (17a,b)$$

5. Results

The final dimensional form of the second-order accurate asymptotic expressions for the flame thickness $\tilde{\Pi}$ and the adiabatic flame speed $\tilde{U}$ are

$$\tilde{\Pi} = \left(\frac{\tilde{\lambda}_a}{\tilde{U} \tilde{c}_p} \right) \left(\frac{\tilde{E}_A}{\tilde{R} \tilde{T}_a} \right)^{-1} \left(1 - \frac{\tilde{T}_u}{\tilde{T}_a} \right)^{-2} \left(\frac{\tilde{\rho}_u}{\tilde{\rho}_a} \right)^{-1} \left\{ 2I_2 \left[\frac{\tilde{T}_B}{\tilde{T}_A} - 1 \right] \right.$$

$$\left. + I_1 \left[\frac{(\tilde{k}_B / \tilde{D}_B^a) \exp(-\tilde{E}_B / \tilde{R} \tilde{T}_a)}{(\tilde{k}_A / \tilde{D}_A^a) \exp(-\tilde{E}_A / \tilde{R} \tilde{T}_a)} - 1 \right] \right\} \quad (18)$$

130

$$\tilde{U}^2 = \frac{2\tilde{k}_A \tilde{\lambda}_a^2}{\tilde{\rho}_a^2 \tilde{D}_A^a \tilde{c}_p} \left(\frac{\tilde{E}_A}{\tilde{R}\tilde{T}_a}\right)^{-2} \left(1 - \frac{\tilde{T}_u}{\tilde{T}_a}\right)^{-2} \left(\frac{\tilde{\rho}_u}{\tilde{\rho}_a}\right)^{-2} \exp\left(-\frac{\tilde{E}_A}{\tilde{R}\tilde{T}_a}\right)$$

$$\times \left\{ 1 + (1-\beta)\left[1 + \frac{(\tilde{k}_B/\tilde{D}_B^a)\exp(-\tilde{E}_B/\tilde{R}\tilde{T}_a)}{(\tilde{k}_A/\tilde{D}_A^a)\exp(-\tilde{E}_A/\tilde{R}\tilde{T}_a)} - 2\frac{\tilde{E}_B}{\tilde{E}_A} \right] \right. \tag{19}$$

$$\left. - 6\left(\frac{\tilde{E}_A}{\tilde{R}\tilde{T}_a}\right)^{-1} + \left(\frac{\tilde{E}_A}{\tilde{R}\tilde{T}_a}\right)^{-1}\left(1 - \frac{\tilde{T}_u}{\tilde{T}_a}\right)^{-1}\left[I_2 - \frac{\tilde{\lambda}_a}{\tilde{\rho}_a \tilde{c}_p}\left(\frac{\beta}{\tilde{D}_A^a} + \frac{1-\beta}{\tilde{D}_B^a}\right)(2I_1 + I_2) \right] \right\} \quad .$$

In these formulas, $\tilde{k}_A$ and $\tilde{k}_B$ are the rate constants for reactions (1a,b), $\tilde{E}_A$ and $\tilde{E}_B$ are the activation energies, $\tilde{D}_A^a$ and $\tilde{D}_B^a$ are the values of the multicomponent diffusion coefficients evaluated at the adiabatic burned state, $\tilde{T}_u$, $\tilde{T}_a$, $\tilde{\rho}_u$, $\tilde{\rho}_a$ are the unburned and burned values of temperature and density, despectively, and $\tilde{\lambda}_a$, $\tilde{c}_p$ are the adiabatic values of thermal conductivity and heat capacity. The combination $(\tilde{K}/\tilde{D}^a)\exp(-\tilde{E}/\tilde{R}\tilde{T}_a)$ is a consumption rate. Note that $\tilde{U}$ appears in the formula for $\tilde{H}$, which has the units of mass x length^{-2}. The flame thickness $\tilde{D}$ in units of length is

$$\tilde{D} = \int_0^{\tilde{H}} \frac{1}{\tilde{\rho}(\tilde{\psi})} d\tilde{\psi} \quad . \tag{20}$$

By studying the above formulas for $\tilde{H}$ and $\tilde{U}^2$, it is easy to see quantitatively how parameters such as Lewis numbers, activation energies, and consumption rates affect the thickness of the flame and its propagation velocity. The sign of $\tilde{H}$ is determined by the ratios of activation energies and consumption rates. If the activation energies of the two reactions are equal (M=N), but the second reaction has a larger (smaller) consumption rate than the first reaction [i.e., K·k >(<) L·ℓ], then species B is depleted upstream (downstream) from species A [i.e., H <(>) 0]. Conversely, if the consumpion rates are equal but the activation energy of the second reaction is larger (smaller) than the first [i.e., M >(<) N], then species B is depleted downstream (upstream) from species A [i.e., H <(>) 0]. In fact, we see from Eq. (18) that the ratios of activation energies and consumption rates have opposite effects (since $I_1 < 0$ and $I_2 > 0$) and thus H may be positive; negative, or zero depending on the relative values of these parameters. Similar statements can be made for the effects of consumption rates and activation energies on the flame speed. In particular, larger (smaller) consumption rates and smaller (larger) activation energies produce larger (smaller) values for the flame speed $\tilde{U}$.

The effects of selective diffusion on $\tilde{H}$ and $\tilde{U}$ are contained in the term involving the quantity $(2I_1 + I_2) < 0$ in Eq. (19). Assuming fixed consumption rates and activation energies, a value of $\tilde{D}_B^a >(<) \tilde{D}_A^a$, $\tilde{D}_A^a$ fixed, [i.e., K<(>) L, L fixed], results in a decrease (increase) in the flame speed from that for the case of equal diffusion of both species. Although the sign of H depends only on consumption rates and activation energies and is thus fixed in this argument, the magnitude of $\tilde{H}$ is inversely proportional to $\tilde{U}$. Thus, the decrease (increase) in the flame speed is accompanied by an increase (decrease) in $\tilde{H}$. Although one might think that an increase in the diffusion of species B would tend to result in a larger flame speed, we now see that the increased spatial separation of the two reactions hinders the flame propagation and produces the opposite conclusion.

131

Finally, we emphasize that it is the consumption rates $(k \cdot K, \ell \cdot L)$, and not merely the reaction rate coefficients, which are important in determining the flame speed and thickness. The fact that smaller diffusion coefficients are associated with higher consumption rates, and therefore higher flame speeds, can be qualitatively understood by recognizing that smaller diffusion coefficients (higher Lewis numbers) intensify the chemical reactions. This occurs through a greater concentration of the reacting species in the reaction zone. Thus, the consumption rates are a measure of the rate of depletion of the reactants, taking into account both the temperature and concentration dependence of the reaction rate terms.

6. Conclusion

Thus, in summary, we have considered a steadily propagating planar flame governed by a global parallel reaction mechanism of the form (1a,b). Employing the method of matched asymptotic expansions, we have obtained explicit analytical formulas for the propagation velocity $\tilde{U}$ and the relative flame thickness, or separation distance, $\tilde{H}$ in terms of various flame parameters. Our approach extends to other types of reaction mechanisms, and future papers will deal with flames governed by sequential, reversible, chain branching, and catalytic chemical reactions.

References

1. V. S. Berman and Iu. S. Riazantsev, J. Appl. Math. Mech. (PMM), 37 (1973), pp. 995-1004.
2. V. S. Berman and Iu. S. Riazantsev, J. Appl. Math. Mech. (PMM), 39 (1975), pp. 286-296.
3. W. B. Bush and F. E. Fendell, Combust. Sci. Technol., 1 (1970), pp. 421-428.
4. W. B. Bush, Combust. Sci. Technol., 23 (1980), pp. 263-266.
5. G. F. Carrier, F. E. Fendell, and W. B. Bush, Combust. Sci. Technol., 18 (1978), pp. 33-46.
6. G. Joulin and P. Clavin, Combust. Flame, 25 (1975), pp. 389-392.
7. G. Joulin and P. Clavin, Combust. Flame, 35 (1979), pp. 139-153.
8. A. K. Kapila and G. S. S. Ludford, Combust. Flame, 29 (1977), pp. 167-176.
9. A. Linan, unpublished tech. report (1971).
10. S. B. Margolis, Q. Appl. Math., 38 (1980a), pp. 61-89.
11. S. B. Margolis, Combust. Sci. Technol., 22 (1980b), pp. 143-169.
12. S. B. Margolis, Eighteenth International Symposium on Combustion (1980c), to appear.
13. S. B. Margolis and B. J. Matkowsky, to appear in SIAM J. Appl. Math.
14. B. J. Matkowsky and G. I. Sivashinsky, SIAM J. Appl. Math., 37 (1979), pp. 669-685.
15. B. J. Matkowsky, L. J. Putnick, and G. I. Sivashinsky, SIAM J. Appl. Math., 38 (1980), pp. 489-504.
16. B. J. Matkowsky and D. O. Olagunju, SIAM J. Appl. Math., 39 (1980), pp. 290-300.
17. G. I. Sivashinsky, Combust. Sci. Technol. 15 (1977), pp. 137-146.
18. G. I. Sivashinsky, SIAM J. Appl. Math., 39 (1980), pp. 67-82.
19. F. A. Williams, AGARD Conference Proc., No. 164 (1975), pp. III.1-25.

SECONDARY COMBUSTION IN GUN EXHAUST FLOWS

Edward M. Schmidt
Fluid Physics Branch
Launch and Flight Division
Ballistic Research Laboratory, USAARRADCOM
Aberdeen Proving Ground, MD 21005

ABSTRACT. The muzzle flash from cannon is analyzed using a simple description of the gun exhaust plume flow structure coupled to an empirical ignition criteria. The effect of muzzle devices such as recoil brakes is estimated through an approximate description of their internal flow. The influence of the transient nature of the weapon exhaust plume is examined by using a one-dimensional, unsteady numerical model to develop the flow properties along the axis of symmetry. These properties are input into the ignition model and the possibility of the occurrence of secondary combustion is determined as a function of time during gun tube emptying.

INTRODUCTION. Excessive blast overpressure in the crew area of artillery pieces is restricting the operation of certain current systems. One reason for the emergence of the problem with newer cannon is the requirement to increase weapon performance, generally through the use of highly energetic propellants. These produce high pressure and temperature in the gases exhausting from the weapon muzzle following shot ejection. As a result the blast overpressure due to the expanding gases increases. Additionally, the propensity of the exhaust plume to ignite into secondary combustion of the unoxidized propellant gas species increases. Secondary combustion results in excessive flash signature of the weapon improving probability of detection and reducing night vision of the artillery crew. Another, equally serious effect of this combustion is the generation of strong pressure disturbances which can reinforce the initial blast pulse and lead to excessive overpressure in the vicinity of the crew member. In the present paper, muzzle flash is described and an attempt to analyze some of the features of the phenomena using relatively simple methodology is presented.

The development of the flow from the muzzle of a gun has been extensively investigated for the bare muzzle configuration (1-4). The structure (Fig. 1) consists of two impulsive jets. The first, or precursor, develops as the air in the gun tube is forced out ahead of the projectile. The second, propellant gas, jet develops when these high pressure gases are released by projectile separation. The muzzle pressure level of the precursor jet is typically an order of magnitude lower than that in the propellant gases. As such, this initial flow is rapidly engulfed in the expanding propellant gas jet and associated air blast. The propellant gas plume growth is influenced by the precursor flow, the projectile, and the ambient conditions. However, the gross nature of the plume development is highly directional[3]. The Mach disc moves continuously away from the muzzle leaving behind a lateral shock structure which is essentially invariant once established. This is contrary to the decay of the plume wherein the total jet structure shrinks toward the muzzle.

The behavior of the Mach disc is of particular importance since the shock heating of the propellant gases strongly influences the occurrence of secondary

combustion. From optical measurements it is observed that at early times, the Mach disc dominates the flow. Almost all of the exhausting gases are processed through it. At later times when the plume has grown to its maximum dimensions, the Mach disc attains its greatest strength but only processes a small fraction of the exhaust flow (10-15%). During this period of rapid changes in the flow structure, the muzzle exit conditions are continuously decaying. Thus, the properties of the exhaust gases which mix with the surrounding air in the lateral viscous layers, impulsive vortex, and turbulent jet are spatially and temporally non-uniform.

Cannon flash is related to the development of these jet flowfields (Fig. 2). As the projectile accelerates down the gun tube, high pressure propellant gases leak around it and mix with the tube gas. If this gas was largely air, the ejected mixture could be burning upon exit; or, if the tube gas was mainly the propellant gases remaining from a previously fired round, then mixture with the atmosphere could cause ignition. In any case, the flash which can occur prior to the round breaking the muzzle is known as *preflash*. With uncorking of the projectile, the propellant gases are released. At the muzzle, the propellant gases are at a high temperature and particulates in the flow incandesce. This bright orange glow is known as *primary flash*. As the gases move away from the muzzle, the strong expansion within the supersonic core of the jet quenches this incandescence. When the gases pass the Mach disc, the temperature rises toward the stagnation value (in excess of the muzzle temperature) and strong luminosity may once more be observed. This region is termed *intermediate flash*. By far the most severe flash phenomena is *secondary flash* resulting from the combustion of the propellant gas/air mixture at the boundary to the impulsive jet. The propellant gases mix with air in the turbulent shear layer on the lateral jet boundary and in the vortex ring which entrains flow which passes the Mach disc. Since the propellant gases are not fully oxidized, mixture with air can develop a combustible mixture requiring only a suitable source of ignition. Some possible sources of ignition include; preflash, burning powder particles, hot muzzle for burst fire, tracer rounds, or, more likely, ignition due to elevated temperatures in the gases behind the Mach disc and in the lateral shear layers.

The presence of muzzle devices can alter the flash characteristics of a particular weapon. Flash suppressors consist of conical or slotted nozzles which are placed on the muzzle of guns. These devices alter the shock structure in the exhaust plume preventing the formation of a strong normal shock in the plume and thereby reducing the temperature in the propellant gases. On the other hand, muzzle brakes can act as flash inducers. These devices consist of a series of baffles placed in the exhaust gases in order to deflect the flow and recover momentum for the attenuation of the recoil impulse. However, shock formation on baffle surfaces can cause severe heating of the exhaust gases. This is illustrated by examining the flash from a 30mm cannon (Fig. 3). With no muzzle attachments, only minor luminosity is recorded on the photograph (color Polaroid film, ASA 75, f2.5). With a single baffle muzzle brake installed, the luminosity increases in the form of intermediate flash. With a double baffle muzzle brake installed, secondary flash completely envelops the exhaust field.

The energy released by secondary combustion of the propellant gases in the exhaust plume of guns can result in the generation of blast waves which

may be as strong as or stronger than the primary blast due to initial free expansion of the jet. Additionally, the secondary combustion induced blast may interact with the primary blast in a manner that significantly raises the overpressure level at a given position. For example, consider the blast field about a 155mm, M109 self-propelled howitzer firing a Zone 7 charge. From high speed photography, it was determined that in one of the firings, the weapon flashed; while in the second case no flash was observed. The pressure transducers were located along a 90° radial at a distance of 30 feet from the weapon (Fig. 4).

For the round where no flash was observed, the peak overpressure was 0.15 atmospheres and corresponds to the arrival of the ground reflection at the gage station. For the round with flash, the peak overpressure is 0.24 atmospheres and corresponds to the arrival of a strong secondary pulse roughly coincidental with the ground reflection. In both cases, the free field blast due to the expansion of the muzzle gases has an identical level of 0.14 atmospheres. Similar alterations of the blast pulse due to the occurrence of muzzle flash have been observed in a number of other weapons. For the 81mm mortar, the problem was quite critical in that flash related overpressures two to three times greater than the expansion driven blast were recorded. In order to be capable of anticipating such problems, a means of predicting the probability of a particular weapon/projectile/propellant combination to produce secondary flash is desirable.

FLASH PREDICTION TECHNIQUE. Previous Approximations. The approach taken is to adapt existing techniques to approximate the gasdynamic processes occurring during transient mixing of the exhausting propellant gases with the ambient. A significant amount of research has been dedicated to modeling the steady exhaust plume from rockets and has led to the development of standardized models of the flow, combustion, and radiation processes in these plumes[5,6]. However, these models are formulated to treat steady, axisymmetric flows from nozzles having relatively low exit pressure ratios. The exhaust from large caliber artillery firing high zone charges can leave the muzzle with pressures of 500 atmospheres or more. Additionally, the flow is transient and often three-dimensional. Attempts to estimate the ignition and combustion in such a flow requires the application of significant simplifying assumptions.

Carfagno[7,8] conducted extensive experimental investigations into the occurrence of and radiation from gun muzzle flash. He developed a set of ignition temperature limits for various mixtures of air and propellant gas at atmospheric pressure. The limits were established in shock tube tests. Combustion gas composition was determined from equilibrium calculations of the chemistry. Five propellants were simulated. Each had combustion products containing between 40 and 70 percent of combustible CO and H_2. Muzzle gas

mixtures were simulated from commercial bottled gas and then mixed with air and water vapor. The mixture was placed in a shock tube and subject to the incident and reflected waves in order to achieve the required pressure (atmospheric) and temperature. Ignition was determined from luminosity measurements.

From these tests, the ignition temperatures shown in Fig. 5 were established. Carfagno found that there was relatively little variation with propellant composition; although, the addition of flash suppressants such as K_2SO_4 did raise the ignition temperatures measurably. After concentrations of 3% suppressant, little additional benefit was achieved.

Using these ignition temperature limits, Carfagno[8] examined the structure of the muzzle flow field. Through one-dimensional mixing and gasdynamic models, he attempted to characterize the flow processes that led to ignition. His recommended model (Fig. 6) assumed that the propellant gas expanded isentropically to atmospheric pressure, mixed with the ambient, passed through a normal shock, re-expanded to atmospheric pressure, and finally was ignited if the mixture temperature exceeded the specified limits (Fig. 5).

May and Einstein[9] point out that the flow model recommended by Carfagno is not in good agreement with experiment. Only the propellant gas passes through the normal shock (Mach disc) in the exhaust plume (Fig. 1). They recommend an alternative approach (Fig. 7). The propellant gas expands isentropically to atmospheric pressure, pass through a normal shock and re-expand to atmospheric pressure where mixing with air occurs followed by possible ignition. May and Einstein also use an improved interior ballistic model[10] to arrive at the weapon exit conditions.

While the models of Carfagno and May and Einstein agree qualitatively with experiment, the approximations of the basic propellant plume flowfield are not satisfactory. Yousefian[11] uses a more realistic model of the supersonic jet as input to a finite difference computation of two-dimensional plume mixing and chemistry (Fig. 8). He uses empirical correlations[12,13] to locate the downrange position and lateral extent of the Mach disc:

$$X_{m.d.}/D = 0.69 \left(\gamma p^*/p_\infty \right)^{\frac{1}{2}} , \tag{1}$$

$$d_{m.d.}/D = 0.49 \left(\gamma p^*/p_\infty \right)^{\frac{1}{2}} . \tag{2}$$

From computations of the supersonic core flow[12], Yousefian develops an expression which may be used to interpolate for the Mach number upstream of the Mach disc:

$$\left(X_{m.d.}/D \right)^2 = 0.49 \; \gamma \left[2+(\gamma-1)M^2 \right]^{\gamma/\gamma-1} \left[\gamma+1 \right]^{-\frac{1}{\gamma-1}} \left[2\gamma M^2 - (\gamma-1) \right] \tag{3}$$

Yousefian assumes that the only shock heating of importance occurs in the gas passing the Mach disc. Lateral shocks are taken to be sufficiently weak that isentropic expansion from muzzle conditions may be assumed. The fraction of propellant gas passing the Mach disc is given as

$$a = 0.52 \left(X_{m.d.}/D \right)^2 M \left[(\gamma+1)/(2+(\gamma-1)M^2) \right]^{(\gamma+1)/2(\gamma-1)} \tag{4}$$

The two propellant gas streams are assumed to undergo instantaneous, one-dimensional mixing and form the input to a steady, two-dimensional finite difference computation of mixing and chemistry between the propellant gas and air.

While providing the most realistic model of muzzle flash to date, Yousefian fails to examine the influence of the basic unsteady nature of gun exhaust flow and does not treat the effect of muzzle devices common to large caliber gun systems. To examine these factors, a flash model is suggested which combines many of the features of the above approximations.

Present Model. The present model is illustrated schematically in Fig. 9. To determine weapon exit conditions, the Baer and Frankle[10] interior ballistic model is applied. The expansion to sonic conditions is computed if the initial exit properties are subsonic. The jet plume is approximated as a steady plume[12] with the shock structure and mixing of the propellant gas streams processed through the lateral shocks and Mach disc according to Yousefian[11]. The mixing of the propellant gas and air occurs in an instantaneous, one-dimensional fashion using the approach of May and Einstein[9]. Finally, the Carfagno[8] ignition temperature criteria is applied.

To account for the unsteady development of the flow, the decay of the muzzle properties is computed in an approximate manner and coupled with both experimental[3] and numerical[1] descriptions of the growth and decay of the propellant gas plume and associated air blast. However, the basic application will assume quasi-steady conditions with muzzle exit conditions at the initial sonic value. A step-wise procedure is summarized below:

1. Compute weapon exit properties using a suitable interior ballistic analysis: (u_e, a_e, p_e)

2. Compute sonic conditions following projectile separation:

$$u^*/a_e = \frac{2}{\gamma+1} + \frac{\gamma-1}{\gamma+1} \frac{u_e}{a_e} \tag{5}$$

$$p^*/p_e = \left[\frac{u^*}{a_e}\right]^{2\gamma/(\gamma-1)} \tag{6}$$

$$T^* = u^{*2}/\gamma R \tag{7}$$

$$T_s^* = \frac{\gamma+1}{2} T^* \tag{8}$$

3. Isentropic expansion through lateral shocks to atmospheric pressure:

$$T_i = T^* \, (p_\infty/p^*)^{(\gamma-1)/\gamma} \tag{9}$$

$$u_i = [(T_s^* - T_i)/2 \, c_{p_e}] \tag{10}$$

4. Flow properties following transit of Mach disc may be estimated once Mach disc is located, Eq. (1), and the Mach number of the flow entering the Mach disc, M_1, is determined, Eq. (3). The properties of interest are:

$$p_2/p_\infty = [(2\gamma M_1^2 - (\gamma-1))/(\gamma+1)] \, [(\gamma+1)/(2 + (\gamma-1)M_1^2)]^{\gamma/(\gamma-1)} \, (p^*/p_\infty) \tag{11}$$

$$M_2 = [((\gamma-1)M_1^2 + 2)/(2\gamma M_1^2 - (\gamma-1))]^{\frac{1}{2}} \tag{12}$$

$$T_2 = T_s^*/(1 + \frac{\gamma-1}{2} M_2^2) \tag{13}$$

In general, the steady state location of the Mach disc should be such that $p_2/p_\infty \doteq 1.0$; however, if this is not the case, the flow will be assumed to undergo isentropic expansion to ambient conditions:

$$T_\delta = T_2 \, (p_\infty/p_2)^{(\gamma-1)/\gamma} \tag{14}$$

$$u_\delta = [(T_s^* - T_\delta)/2c_{p_e}] \tag{15}$$

5. The ratio of propellant gases passing the Mach disc is given by*:

$$\alpha = 0.96 \, (X_{m.d.}/D)^2 \, M_1 [(\gamma+1)/(2+(\gamma-1)M^2)]^{(\gamma+1)/2(\gamma-1)} \tag{16}$$

6. Compute mixing of propellant gas streams:

$$\overline{u} = (1-\alpha) \, u_i + \alpha u_\delta$$

$$\overline{T}_s = T_s^*$$

7. Compute mixing of propellant gas with air:

$$\overline{\overline{c}}_p = rc_{p_\infty} + (1-r) \, c_{p_e}$$

$$\overline{\overline{u}} = (1-r) \, \overline{u}$$

$$\overline{\overline{T}}_s = [rc_{p_\infty} T_{s_\infty} + (1-r) \, c_{p_e} \overline{T}_s]/\overline{\overline{c}}_p$$

---

*As described in following section, the coefficient is increased from that given by Yousefian to account for measured shock structure of actual muzzle flow.

$$\bar{\bar{T}} = \bar{\bar{T}}_s - \bar{\bar{u}}^2/2 \ \bar{\bar{c}}_p$$

8. Compute the variation of the final temperature, $\bar{\bar{T}}$, versus mixture ratio and compare with the ignition limits specified by Carfagno (Fig. 5).

155MM HOWITZER FLASH. The 155mm, M109A1, self-propelled howitzer is used to examine the capabilities of the proposed flash prediction methodology. The weapon is equipped with a high efficiency muzzle brake (Fig. 10). Firings of a 46kg, M483 projectile were conducted for Zones 3-8S. These data are supplemented by firings at Zone 8S with no muzzle brake attached to the tube. The latter firings were conducted by the Interior Ballistics Division, BRL, on a test stand.

Both blast field pressure measurements and high speed cinematography were taken for each firing event. The high speed cinematography was accomplished with 16mm Fastax cameras framing at 2000 frames/s. Occurrence of secondary flash was quite evident in these photographs.

Launch properties were computed by Keller[13] and are summarized below (Table 1). The Zone 8S firings are of particular interest since this is the "super charge" configuration for the system. The thermodynamic properties for the M30A1 propellant which makes up this charge are:

$$\gamma = 1.24$$

$$T_a = 3012 \ °k$$

$$c_p = 1849 \ m^2/S^2 \ °k$$

$$R = 357.9 \ m^2/S^2 \ °k$$

As previously mentioned, the M109A1 is equipped with a double-baffle muzzle brake. The presence of a baffle has been shown[14] to generate strong shock waves in the flow. To approximate the heating associated with the shocks standing off the baffle surfaces, the gasdynamic model shown in Fig. 11 is employed. An axisymmetric plume expands from the muzzle and passes a normal shock at the first baffle. The shocked gas exits laterally as a plate jet and axially through the projectile hole. The gas passing the projectile hole reaches sonic velocity and forms a second plume which impinges upon the next baffle. After repeating the shock/expansion process on the second baffle, the flow expands as a free jet through the exit hole of the brake. This final exit flow is analyzed using the techniques described in the previous section.

For a Zone 8S firing, the mixture temperature is computed at various air/fuel ratios for both the bare muzzle and muzzle brake cases (Fig. 12). The difference between the two temperature profiles is dramatic. With a bare muzzle, ignition is not predicted to occur; however, with the muzzle brake in place, mixture temperatures reach quite high values and ignition would be expected. Experiment shows that for Zone 8S with the muzzle brake in place, secondary combustion occurs in each of 20 observations. For the bare muzzle firings, the picture is not as clear. When the Zone 8S firings were conducted with the

standard charge, secondary flash was not observed (one round); however, when
0.23kg of propellant was removed, secondary flash was observed (five rounds).
Additionally, when the amount of flash suppressant was reduced to 1%, flash
was observed (five rounds). In order to resolve this disagreement and to
expand the bare muzzle data base, more firings are required.

The prediction procedure was used for the remainder of the M109A1 tests
conducted with the muzzle brake in place, Fig. 13. The results are summarized
in Table 2.

Table 1 155mm, M109A1 Launch Properties

Zone	Propellant (kg/type)	%Suppressant	V_e (m/s)	T_e (°k)	a_e (m/s)	pe/p_∞	u^* (m/s)	p^*/p_∞	T_s^* (°k)
3	1.50/M1(SP)	2.0	250	1418	793	68	735	31.4	1319
5	3.21/M1(7P)	2.0	379	1425	795	148	749	82.6	1376
7	6.07/M1(7P)	1.5	542	1353	775	273	749	196.9	1376
8	9.59/M6(MP)	3.6	649	1490	813	486	795	393.1	1549
8S	12.24/M30(MP)	4.7	790	1756	883	703	872	629.5	1865

Table 2 155, M109A1 Secondary Flash

Zone	Measured Secondary Flash	Predicted Secondary Flash
3	No	No
5	No	No
7	Yes	Yes
8	Yes	(?)
8S	Yes	Yes

The firings at Zone 7 showed two types of flash behavior. In some instances,
secondary flash was observed only in the gas exiting through the projectile
hole but not that passing out of the lateral vents. On other occasions,
secondary combustion completely enveloped the field.

For the Zone 8 firings, the mixture temperature was predicted to be 70°K
below the ignition limit. The observations showed combustion only in the
gases exiting the projectile hole. With this charge, suppressant is added in
the form of a 0.34kg bag of K_2SO_4 tied to the front of the charge (ammunition

140

for the 155mm is separate loaded). There is some debate as to the nature of suppressant mixing with the propellant gases; thus, if the effective percentage of suppressant is lower, the mixture temperature could exceed the ignition limit.

Since the muzzle exhaust process is basically an unsteady phenomena, it is of interest to examine the sensitivity of muzzle flash predictions to changes in the nature of the flow.

UNSTEADY FLASH ANALYSIS: BARE MUZZLE 155MM HOWITZER. The development of the muzzle flow field is illustrated in Fig. 1. The shock structure within the propellant gas plume grows in a manner which is strongly influenced by the projectile presence and pressure field associated with the expanding air blast. Both medium caliber[14] and small caliber[3] weapons show nearly identical flow field properties at correctly scaled times if the exit conditions are similar in each case. Assuming that the inviscid flow structure for a 155mm howitzer can be scaled from data acquired on a 5.56mm rifle[3] will permit estimation of the influence of muzzle flow field growth and decay.

The technique[10] used by Keller[13] to calculate weapon exit conditions can not define the temporal decay of propellant gas properties during tube emptying. For the 155mm, M109A1 firing the Zone 8S charge, this decay is estimated using data acquired from a 20mm cannon[14]. It is assumed that the property decay from peak values occurs similarly for both weapons if the time scale is

$$\bar{t} = t/\tau$$

where

$$\tau = L/a_o^*$$

$$L = \text{gun tube length}$$

$$a_o^* = \text{initial sonic velocity in propellant gas at muzzle}$$

For the 20mm case, only exit pressure could be measured. Lacking additional data, the remaining gas properties were estimated under the assumption that the emptying process was isentropic. For the 155mm howitzer, these approximations lead to the following:

Table 3   155mm, M109A1 Muzzle Exit Property Variation when
Firing Zone 8S Charge

t (ms)	u* (m/s)	p^*/p_∞	T^*_s (°K)
0	872	630	1918
1.9	835	446	1759
3.7	808	316	1647
5.6	784	234	1551
7.4	762	179	1469
9.3	741	134	1385
11.1	723	106	1319
14.8	692	67	1208
20.4	660	42	1099
26.0	626	25	989
30.0	594	15	890

The flow development was computed using a one-dimensional, unsteady
numerical model developed by Erdos and DelGuidice[1] (Fig. 14). It is inter-
esting to note that by the time the propellant gas plume reaches its maximum
size (t ≐ 6 ms), the muzzle exit conditions have dropped markedly from the
initial levels. Five points were selected as representative of various stages
of development. Two of the conditions were taken during growth of the plume;
the fully developed stage was selected; and two conditions representing plume
decay were examined.

From spark shadowgraph records of small caliber firings[3], the shock
structure internal to the plume at each condition is determined (Fig. 15).
The following properties were determined:

Table 4 Mach Disc Properties During Growth and Decay of Propellant Gas Plume

Stage	t (ms)	$X_{m.d.}/D$	α	$V_{m.d.}$ (m/s)	$M_{l_{rel.}}$
1	1	6.0	.99	698	3.7
2	3	12.3	.28	328	6.2
3	6	15.3	.16	0	7.7
4	9	12.5	.06	-255	8.2
5	15	6.5	.10	- 87	5.8

Using the computed Mach disc velocity, a relative flow Mach number is determined. Using this, the shock jump conditions are evaluated. The flash analysis described previously is then directly applied. For each stage of the flow life cycle, the mixture temperature variations are shown in Fig. 16.

The most interesting feature of this plot is the prediction that the gas processed through the shock early in the development cycle, stage 1, produces very high mixture temperatures with an increased probability of ignition. This stage shows that very high fractions of the exhausting propellant gas are passing the Mach disc. Even though the wave is relatively weak, the mixture temperatures are significantly elevated.

As the growth of the plume continues, the mixture temperatures monotonically decay. Apparently, this portion of the cycle is dominated by the variation in muzzle exit properties and by the diminishing mass flow through the Mach disc.

The results of this analysis could help explain some of the bare muzzle firing data with the 155mm howitzer. Assuming the prediction of high mixture temperature propellant gases exiting at early times is correct, the Zone 8S charge would be borderline for even bare muzzle firings. Additionally, these results are partially supported by experimental results of Klingenberg and Mach[15] who show time-resolved, smear photographs of the muzzle flash from a 7.62mm rifle. Their data indicates combustion initiates behind the Mach disc in the gases which exit early in the tube emptying cycle. Additionally, the high speed cinematography of the 155mm shows a tendency for the propellant gas to ignite early in the venting. This initial secondary combustion may be extinguished as the fuel is consumed only to reignite later in the exhaust cycle.

SUMMARY AND CONCLUSIONS. The muzzle flow field from guns is analyzed to determine features which influence the tendency of the weapon to produce secondary flash. The gun tube exit conditions and plume shock structure are strong factors in the flash process. The presence of muzzle devices also is shown to alter the properties of the exhaust flow. Finally, the basic unsteady nature of the process appears to require serious consideration.

The model used in the analysis is overly simplistic. It does not treat the gasdynamics or chemical kinetics of the process in a satisfactory manner. However, the ignition criteria can be easily coupled to existing inviscid analyses of muzzle flow and used to point out qualitative variations in flash processes.

Additional experimental data is required to define the temporal sequence of muzzle flow ignition and combustion. Improved analytical techniques are needed to address the problem of transient, high pressure exhaust flows.

ACKNOWLEDGMENT. The author wishes to thank Drs. K. Fansler and G. Keller for many useful suggestions and essential inputs.

REFERENCES.

1. J. Erdos and P. DelGuidice, "Calculation of Muzzle Blast Flowfields," AIAA J., Vol. 13, No. 8, August 1975.

2. G. Moretti, "Muzzle Blast Flow and Related Problems," AIAA Fluid and Plasma Dynamics Conference, Seattle, July 1978.

3. E. Schmidt and D. Shear, "Optical Measurements of Muzzle Blast," AIAA J., Vol. 13, No. 8, August 1975.

4. T. Taylor and T. Lin, "A Numerical Model for Muzzle Blast Flow Fields," AIAA J., Vol. 19, No. 3, March 1981.

5. S. M. Dash and H. S. Pergament, "The JANNAF Standard Plume Flowfield Model: Operational Features and Preliminary Assessment," JANNAF 12th Plume Technology Meeting, Colorado Springs, CO, 18-20 November 1980.

6. C. Ludwig, "Standard Infra-Red Radiation Model," JANNAF Plume Flow Field/Radiation Workshop, Redstone Arsenal, AL, 2-3 April 1981.

7. G. Carfagno, Spectral Characteristics of Muzzle Flash, AMC Pamphlet 706-255, Army Materiel Command, Washington, D.C., June 1967.

8. G. Carfagno, Handbook on Gun Flash, The Franklin Institute, 1961.

9. I. May and S. Einstein, "Prediction of Gun Muzzle Flash," JANNAF Combustion Meeting, Lake Taho, NV, 1977.

10. P. G. Baer and J. M. Frankle, "The Simulation of Interior Ballistic Performance of Guns by Digital Computer Program," BRL R 1183, U. S. Army Ballistic Research Laboratory, APG, MD, December 1962. AD 299980.

11. V. Yousefian, "Muzzle Flash Onset," Aerodyne Research, Inc., Bedford, MA, ARI-RR-162.1, May 1979.

12. A. Vick, et al, "Comparison of Free Jet Boundaries with Theoretical Results Obtained with the Method of Characteristics," NASA TN D-2327, June 1964.

13. G. Keller, Private Communication, Ballistic Research Laboratory, APG, MD, July 1980.

14. E. M. Schmidt, E. J. Gion and K. S. Fansler, "Measurement of Muzzle Blast and Its Impingement Upon Surfaces," AIAA Paper No. 79-1550, July 1979.

15. G. Klingenberg and H. Mach, "Investigation of Combustion Phenomena Associated with the Flow of Hot Propellant Gases," Combustion and Flame, Vol. 27, 1976, pp 163-176.

a. t = -26 μs   b. t = 77 μs   c. t = 168 μs

Figure 1.   Spark shadowgraphs of muzzle flow from a 20mm cannon
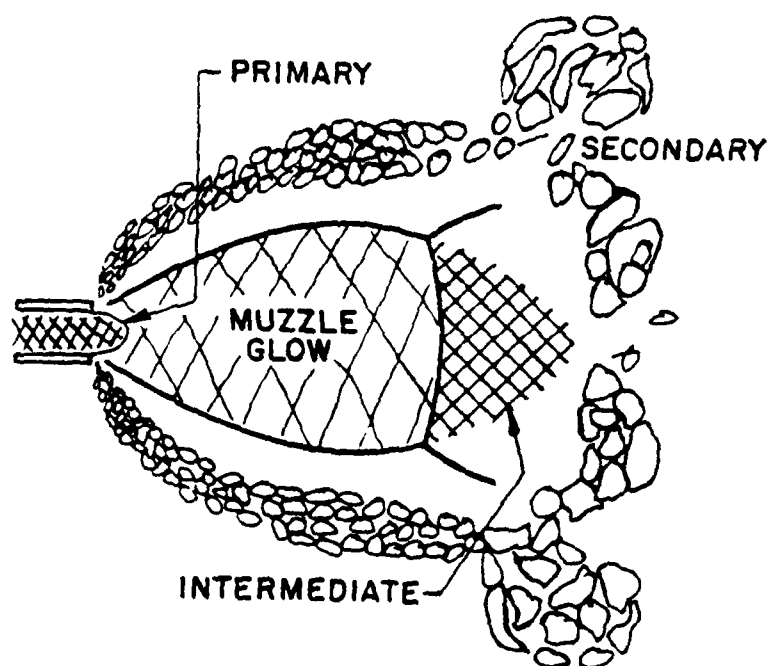
Figure 2.   Schematic of muzzle flash

a. Without Secondary Flash

$(p-p_\infty)/p_\infty$

ground reflection

free air blast

0.1

0

t(ms)

b. With Secondary Flash

$(p-p_\infty)/p_\infty$

secondary flash induced peak

free expansion peak

0.2

0.1

0

t(ms)

Figure 4. Free field blast overpressure from 155mm M109A1 Howitzer, Zone 7

Bare Muzzle

Single Baffle Brake

Double Baffle Brake

Figure 3. Muzzle flash from a 30mm cannon

147
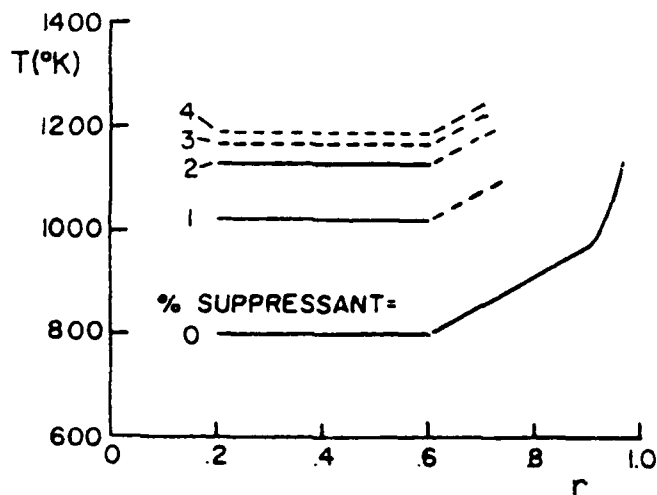
Figure 5. Carfagno ignition limits: r = 0, all propellant gas, and r = 1.0, all air (note: limits include 100°K safety factor of May and Einstein).
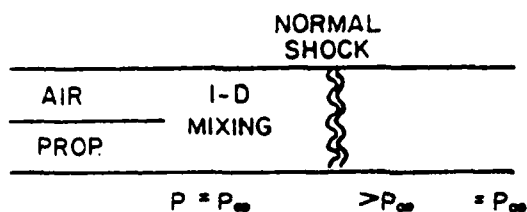
Figure 6. Carfagno flow model
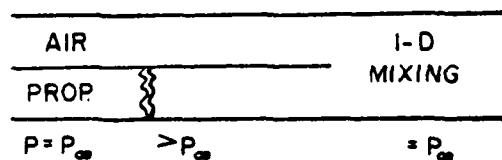
Figure 7. May and Einstein flow model
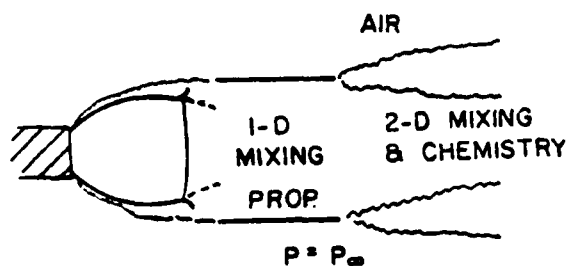
Figure 8. Yousefian flow model
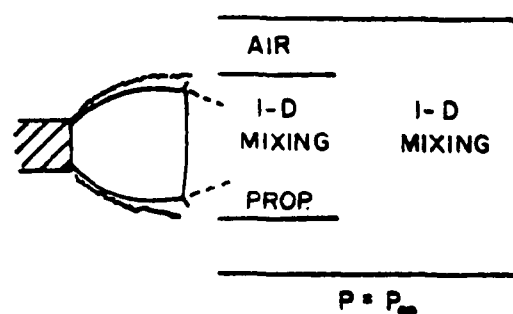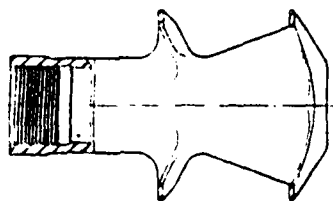

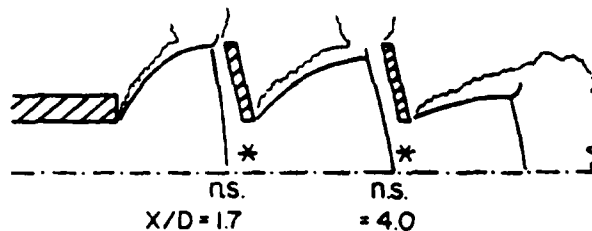Figure 9. Present flow model

Figure 10.   Double baffle brake for 155mm, M109 Howitzer

Figure 11.   Schematic of flow internal to brake
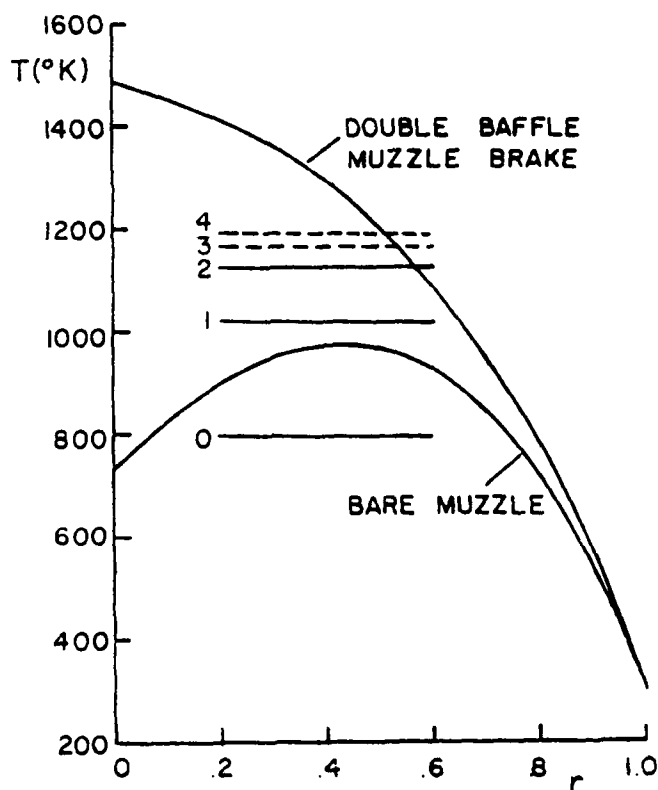

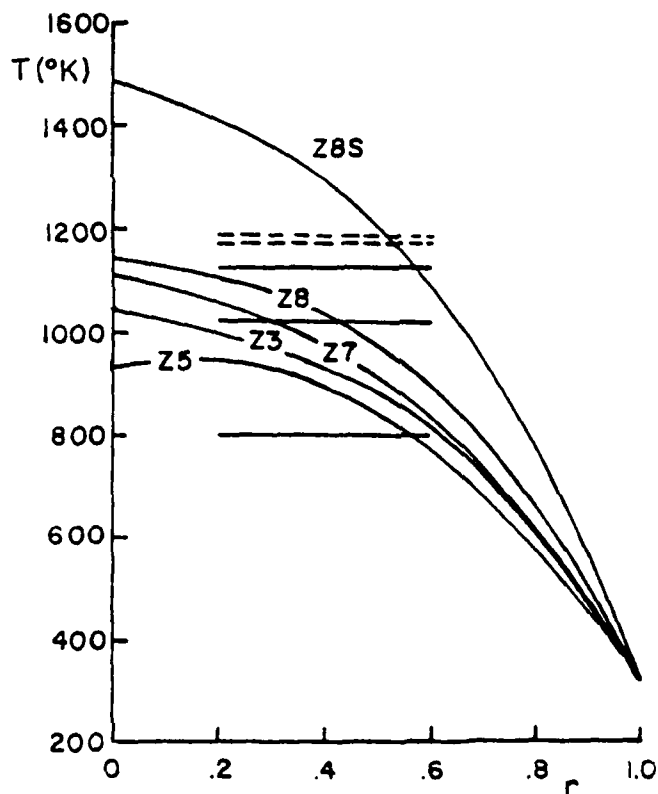Figure 12.   Comparison of mixture temperatures with and without brake

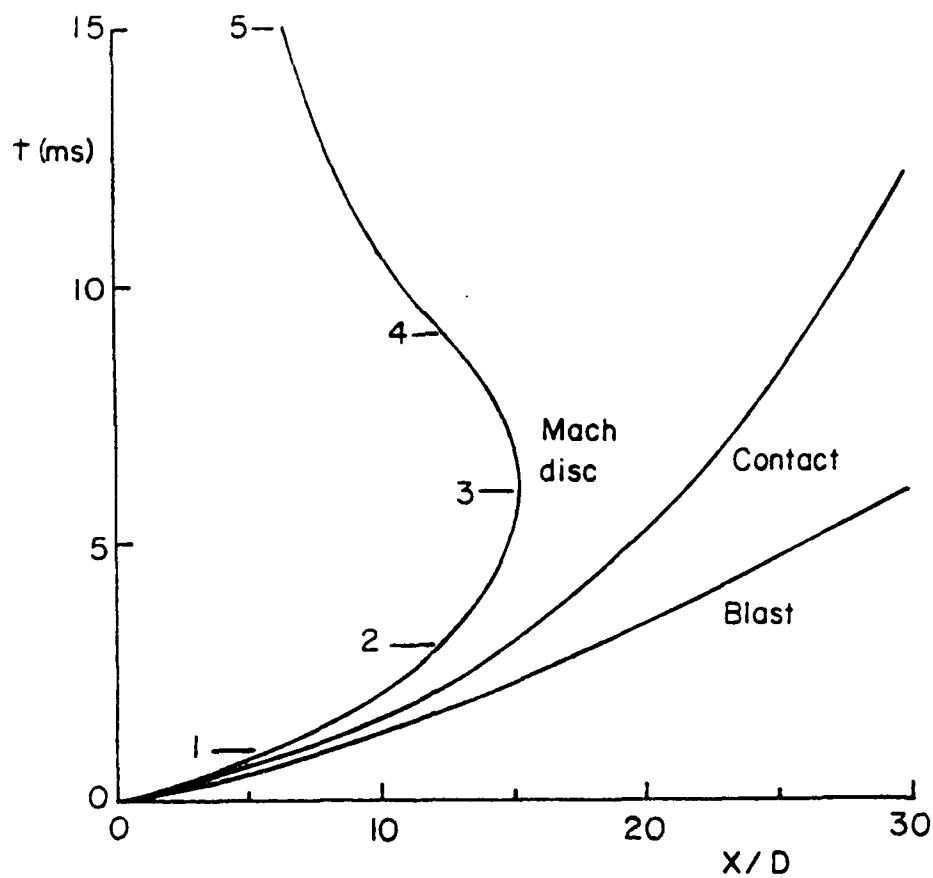Figure 13.   Mixture temperatures for various zones of fire

149

Figure 14. Muzzle discontinuity trajectories for 155mm, M109A1 Howitzer at Zone 8S with bare muzzle
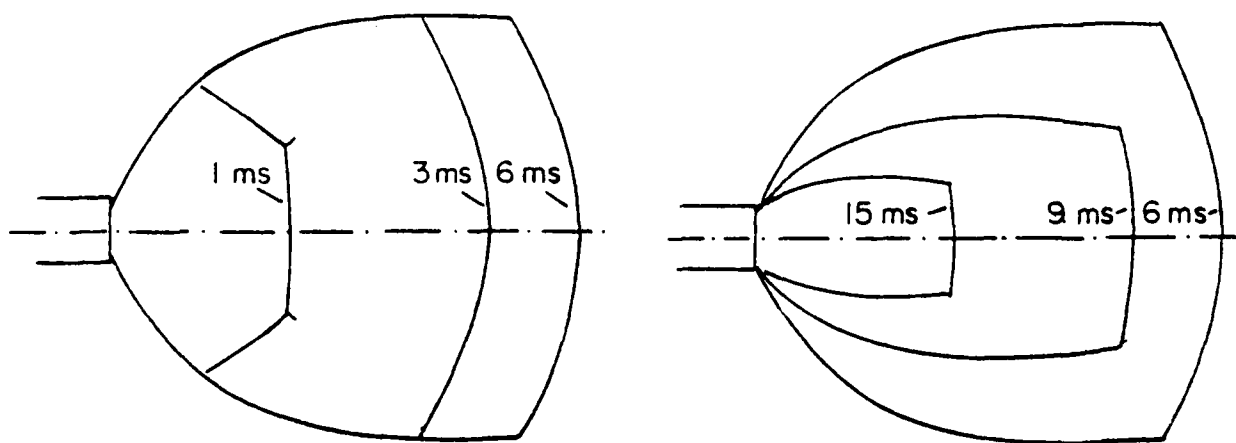

Figure 15. Growth and decay of muzzle flow plume for 155mm, M109A1 Howitzer firing Zone 8S with bare muzzle
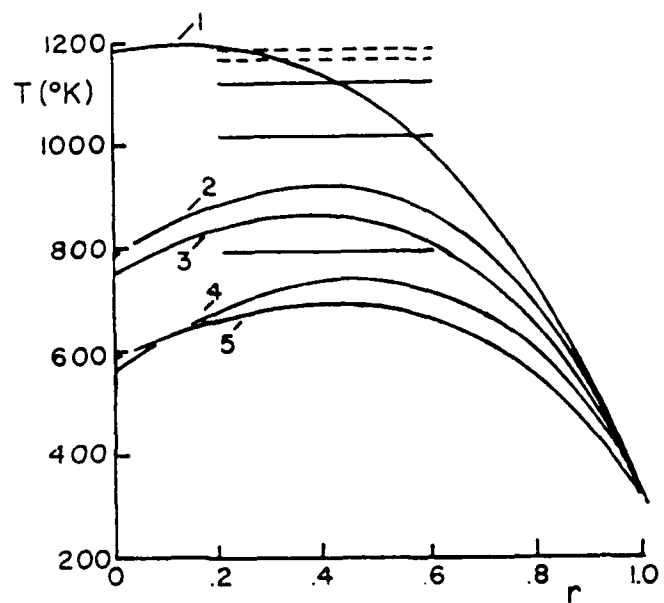
Figure 16. Propellant gas mixture temperatures for different temporal exhaust plume conditions

IRREGULAR MACH REFLECTION EXPERIMENTS WITH
THREE DIMENSIONAL FLOWS

Ralph E. Reisler
John H. Keefer

Ballistic Research Laboratory
U.S. Army Armament Research & Development Command
Aberdeen Proving Ground, Maryland 21005

ABSTRACT

The air blast in the irregular Mach region was investigated in a series of high explosive experiments known as Operation Mighty Mach. These tests used 490 kg, spherical, Pentolite charges detonated at heights of burst of 3.26 to 6.04m over a concrete surface. High response piezoelectric pressure recordings made with wide band FM magnetic tape provided side-on and stagnation overpressure time histories of the flow phenomena at shock strengths of 8000 to 350 kPa. The progression of the air shock through the reflection regions is presented in this paper.

The reflection of shock waves has long been a subject of investigation by numerous researchers using both analytic and experimental techniques. Research activities using shock tubes have examined one-dimensional flows over a range of shock strengths, with some having as high a Mach number as 10. Works of such researchers as Gvozdeva[1], Glass & Ben-Dor[2], Helig[3], Takayama[4], and Bertrand[5] are well known, and established much of the ground work for the various conditions and domains of shock wave reflection in the region of transition from regular to Mach reflection.

As a result of this research work, many people within the U.S. became virtually interested in the transition zone for high shock strengths as it develops from height-of-burst (HOB) explosions. The surface reflection for HOB air blast is illustrated in Figure 1 with the transition region between regular reflection and regular Mach reflection labeled irregular Mach reflection (IMR). The general term of irregular was used to cover both the regions of complex Mach and Double Mach reflection as described by Ben-Dor[6]. The structure of the irregular Mach for three dimensional flows was first observed by Carpenter[7] in 3.6 kg HOB experiments conducted in 1973. The investigation was done over a planar surface instrumented to measure static overpressure above 689 kPa. Subsequent to these experiments, the Defense Nuclear Agency sponsored the Ballistic Research Laboratory in an extensive HOB program to study the flow characteristics of the air blast in IMR. The effort was code named Operation Mighty Mach, and as shown in Table I. was carried out in 1978 and 1979, with a continuation into 1980. The recent work placed the emphasis on models and generic shapes located in the IMR for blast loading.

Table 1. Summary — Operation Mighty Mach

YEAR	OBJECTIVE	NO. SHOTS	AVG CHARGE WT (kg)	EXPLOSIVE (sphere)	HOB (m)
1978	Phenomena Studies	2	500.0	Pentolite	1.56
1979	Phenomena Studies	5 (2)	490.8	Pentolite	4.55
		(3)	487.9	Pentolite	3.05
1980	Model	6 (1)	484.0	Pentolite	6.04
	Loading	(4)	487.0	Pentolite	1.80
	Studies	(1)	485.0	Pentolite	3.26

Operation Mighty Mach was fielded as a joint effort with the Defence Research Establishment, Suffield (DRES), Alberta, Canada, at their south boundary test range. Quartz piezoelectric pressure transducers of commercial manufacture were used in a static and stagnation measurement mode. The transducers have a 500 kHz resonant frequency and were configured for field use as shown in Figure 2. Signals from the transducers were transmitted through line drivers located near the test pad over RG-58 cable 600m in length to wide-band (400 kHz) FM magnetic tape recording systems in a recording trailer.

The pressure gages were mounted in steel wedge-shaped mounts called rakes at elevations near the surface to observe the conditions close to the triple point as it rises with distance. The elevations chosen were 1.27, 3.81, 8.89, 13.90, and 24.13 cm. Although static and stagnation gages were of necessity mounted in different rakes, they were located at equal radial distances from ground zero. Figure 3 shows a photograph of the gage rakes. A reinforced concrete pad was installed to provide an ideal reflecting surface, as shown in Figure 1. Pressure gages were located in the concrete surface at various radial distances from station ground zero directly under the charge to 9.2m. A Scotchlite screen for laser photography is seen on the right side of the photograph, and striped backdrops for late time photogrammetric studies of the triple point path are seen in the background.

Pressure-time records from the surface-mounted gages are presented in Figures 5-7 from a HOB of 4.55m (Mighty Mach II-79, Shot 4). Stations 0.0 through station 12.5.0, Figure 5, indicate the regular reflection region with typical exponential decaying waveforms. Figures 6 and 7 show waveforms of gages in the irregular Mach region. A second peak is first seen at station 11.0, 4.27m, which is 2½ times the magnitude of the initial peak. The secondary peak is a compression wave. It decreases in magnitude and occurs later in time as the wave moves outward. At station 30.0, 9.15m, whose waveform is shown in Figure 7, the secondary peak has disappeared and the transition is complete.

The stagnation (T) and static pressure records were used to calculate the Mach number and dynamic pressure (Q) according to the procedures described in Reference 8. Results from a typical station located in the region of early irregular Mach development are shown in Figures 8-10. The gages were located at elevations of 1.27 (.05), 3.81 (1.5), and 8.89 (3.5) cm at station 16. The time of occurrence of the second peak of the stagnation pressure record is noteworthy as it occurs at the beginning of the rise of the second peak of the static record. At greater distances, such as station 22 (6.71m), whose waveform is shown in Figure 11, for instance, the time of occurrence of the two is the same. A second observation is seen in Figure 9, station 16.15, where the stagnation and Q records show a very decided fall-off in pressure, evidently created by a downward component in the flow. A very turbulent flow is indicated in this region and is supported by the velocity results of the hydro-code HULL computations of Reference 9 discussed below.

Needham and Booen[9] in January 1981 published HULL computations of a 4.57m HOB, 498 kg Pentolite shot equal to that of Mighty Mach II-4. For relative correlation, the pressure gradient of the HULL run for 2.787 ms is shown in Figure 12 with the static pressure record positions superimposed and the time histories associated with those positions shown. The gages are all located within the region of IMR as indicated by the pressure contour and confirmed by the double peak in the waveforms. The triple points together with the shocks, slip streams, and vortex are also shown by the HULL computation. Pressure as a function of time is compared in Figure 13 for static pressure for the experiment and the code for station 16, 4.8m at the three elevations. A very good correlation is evident.

The structure of the IMR as determined from laser photograpy is shown in Figure 14, Part A. It compares well with the density contour of the code. The time occurrence is difference so the height of the Mach stems do not compare.

In summary, the irregular Mach reflection produced by explosions in air has been investigated and the double peak phenomena clearly recorded by high resolution pressure instrumentation. Comparisons made with the hydro-code HULL show good correlation.

155

LIST OF REFERENCES

1. L. G. Gvozdeva, and V. P. Fokeev, "Transition from Mach to Regular Reflection and Domains of Various Mach Reflection Configurations", Institute for High Temperatures, Academy of Sciences, Moscow, U.S.S.R.

2. G. Ben-Dor and I. I. Glass, "Domains and Boundaries of Non-Stationary Oblique Shock Wave Reflexions 1. Diatomic Gas/ 2. Monatomic Gas", Institute for Aerospace Studies, University of Toronto, J. Fluid Mech. (1979).

3. Helig, W. H., "A Result Concerning the Transition from Regular Reflection to Mach Reflection of Strong Shock Waves", Proceedings of the 11th International Shock Tube Symposium, University of Washington, Seattle, Washington (1977).

4. G. Ben-Dor and K. Takayama, "The Transition from Regular to Mach Reflection and from Mach to Regular Reflection in Truly Nonstationary Flows" (to be published).

5. Bertrand, B. P., "Measurement of Pressure in Mach Reflections of Strong Shock Waves in a Shock Tube", Ballistic Research Laboratories Memorandum Report No. 2196 (1972).

6. G. Ben-Dor, "Regions and Transitions of Nonstationary Oblique Shock Wave Diffractions in Perfect and Imperfect Gases", Institute for Aerospace Studies, University of Toronto, Report No. 232 (1978).

7. H. J. Carpenter, and H. L. Brode, "Height of Burst at High Overpressure", Fourth International Symposium on Military Applications of Blast Simulation, held at Southend-on-Sea, England, 9-12 September 1974.

8. R. E. Reisler and L. W. Kennedy, "Air Blast Dynamic Pressures from Simultaneous and Non-Simultaneous Multiburst", ARBRL-TR-02045 (1978).

9. M. W. Booen and C. E. Needham, "Two-Dimensional HULL Code Simulation of Complex and Double Mach Reflections", AFWL Tech 81-001 (1981).
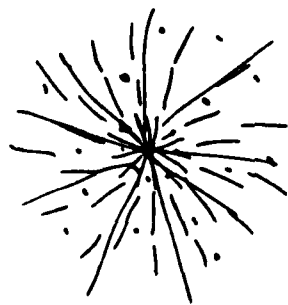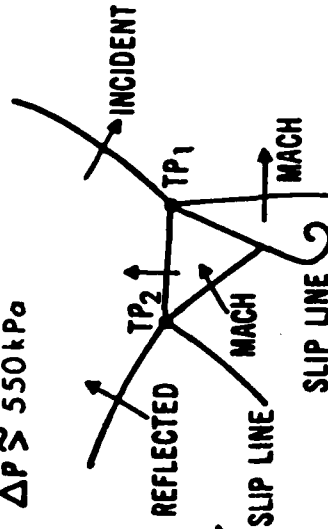
SURFACE REFLECTION FOR HOB AIRBLAST

REGULAR REFLECTION
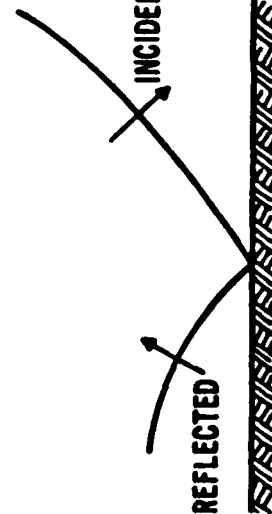
IRREGULAR MACH REFLECTION

$\Delta P \gtrsim 550\,kPa$

REGULAR MACH REFLECTION

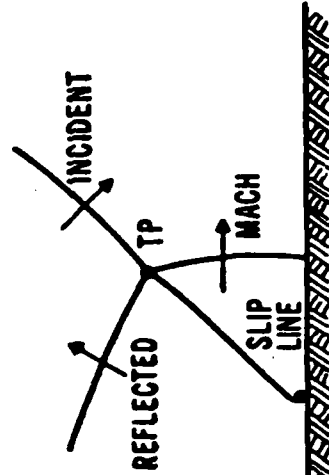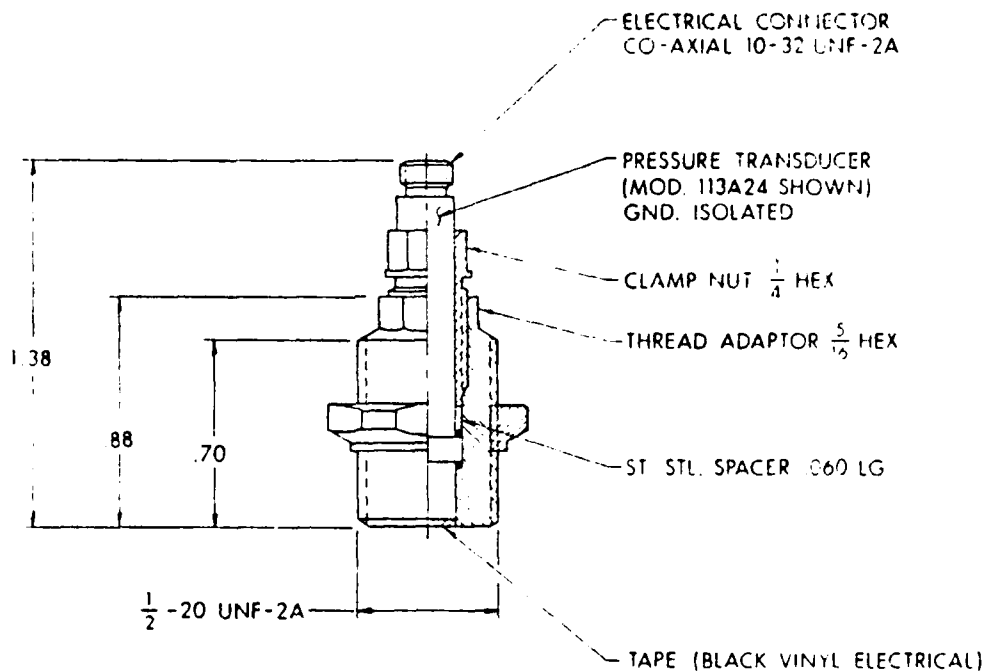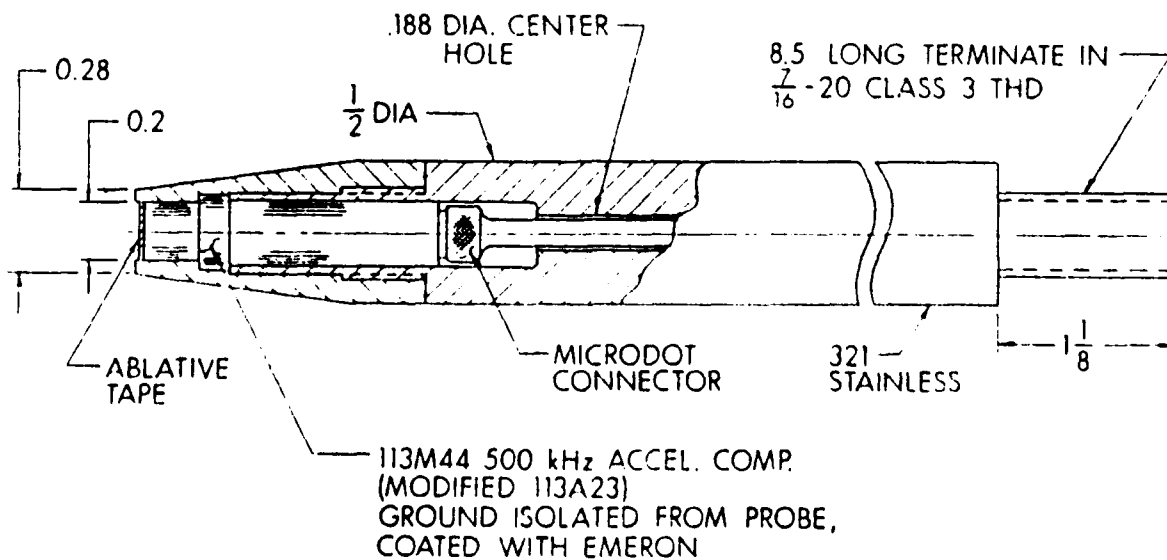Figure 1. Surface Reflection for HOB Air Blast.

STATIC PRESSURE GAGE

ELECTRICAL CONNECTOR
CO-AXIAL 10-32 UNF-2A

PRESSURE TRANSDUCER
(MOD. 113A24 SHOWN)
GND. ISOLATED

CLAMP NUT $\frac{1}{4}$ HEX

THREAD ADAPTOR $\frac{5}{16}$ HEX

ST STL. SPACER .060 LG

TAPE (BLACK VINYL ELECTRICAL)

$\frac{1}{2}$-20 UNF-2A

DIMENSIONS IN INCHES

STAGNATION PRESSURE PROBE

.188 DIA. CENTER HOLE

8.5 LONG TERMINATE IN
$\frac{7}{16}$-20 CLASS 3 THD

0.28

0.2

$\frac{1}{2}$ DIA

ABLATIVE TAPE

MICRODOT CONNECTOR

321 STAINLESS

$1\frac{1}{8}$

113M44 500 kHz ACCEL. COMP.
(MODIFIED 113A23)
GROUND ISOLATED FROM PROBE,
COATED WITH EMERON

DIMENSIONS IN INCHES

Figure 2. Schematic of Static and Stagnation Pressure Gages.

158

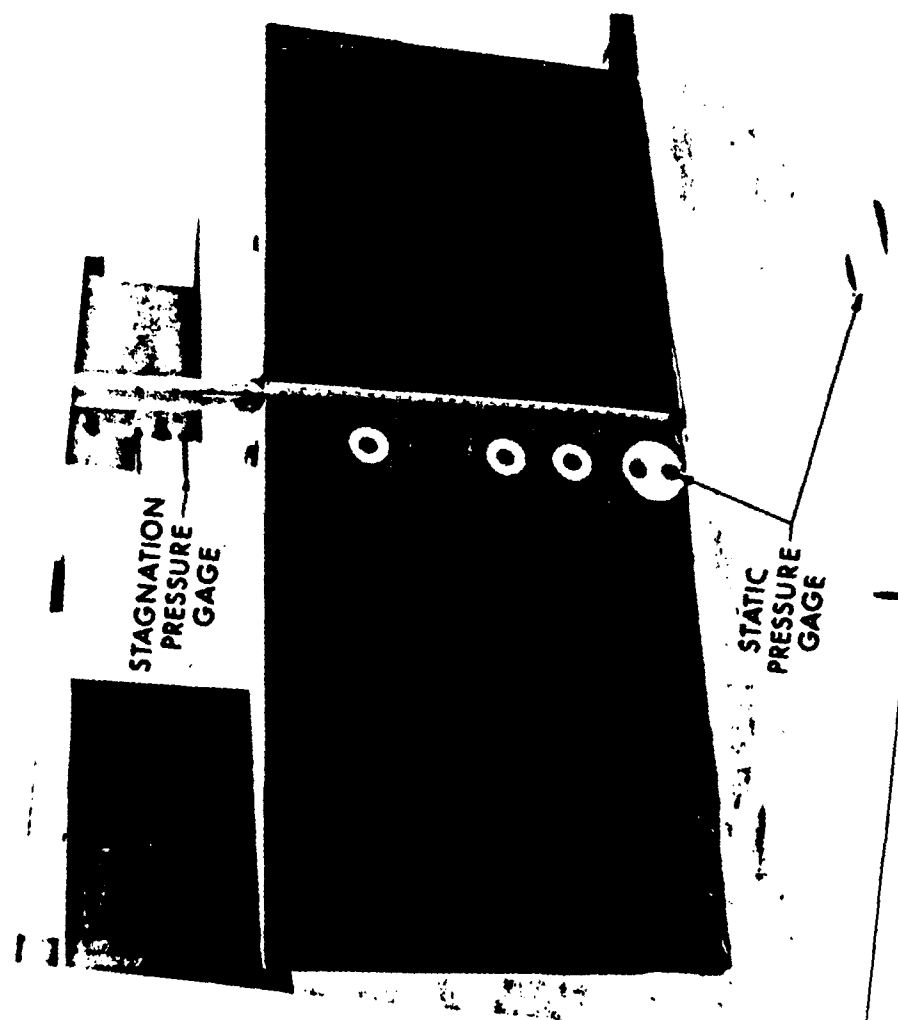STAGNATION PRESSURE GAGE

STATIC PRESSURE GAGE

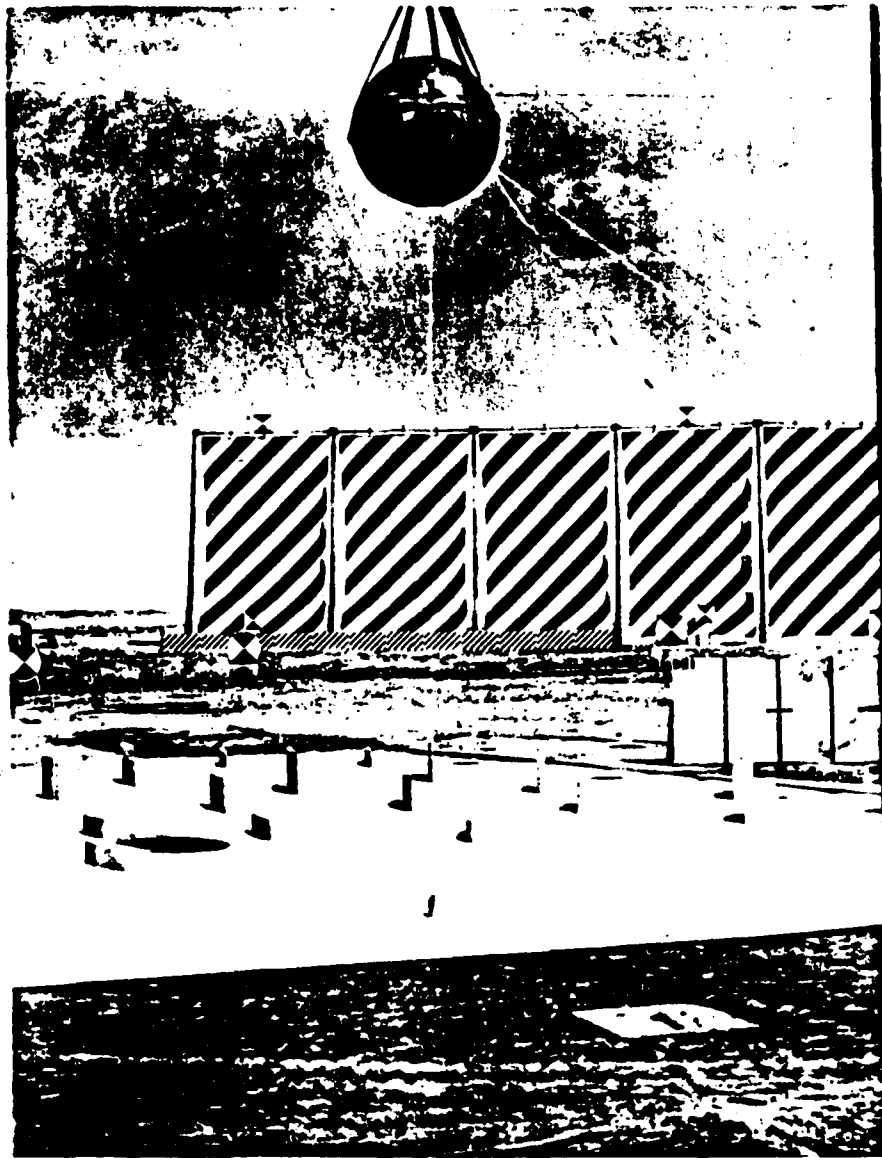Figure 3. Photograph of Gage Rakes.

159

Figure 4. Photograph of Test Bed.
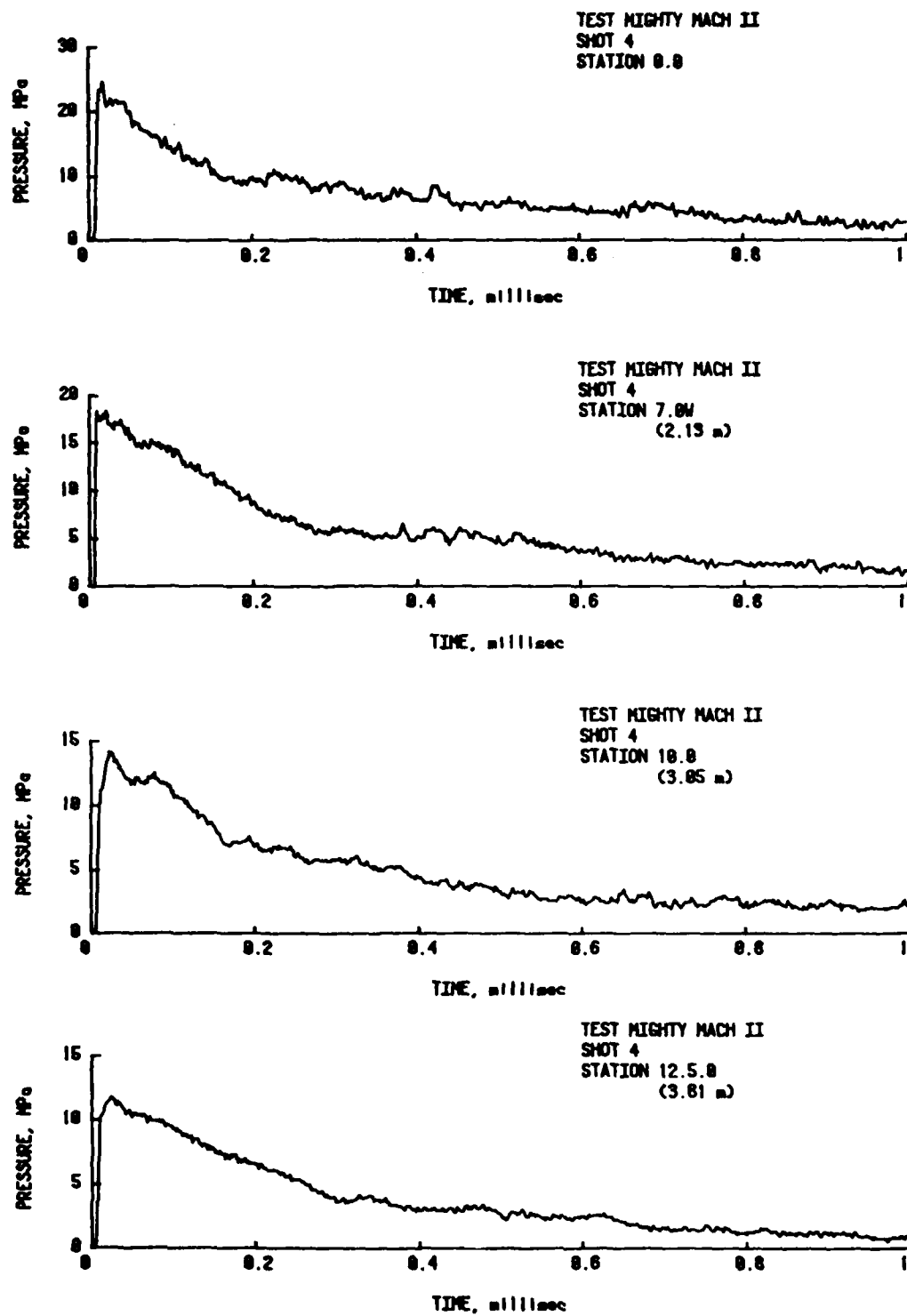
Figure 5. Static Pressure Records, Regular Reflection Region.

161

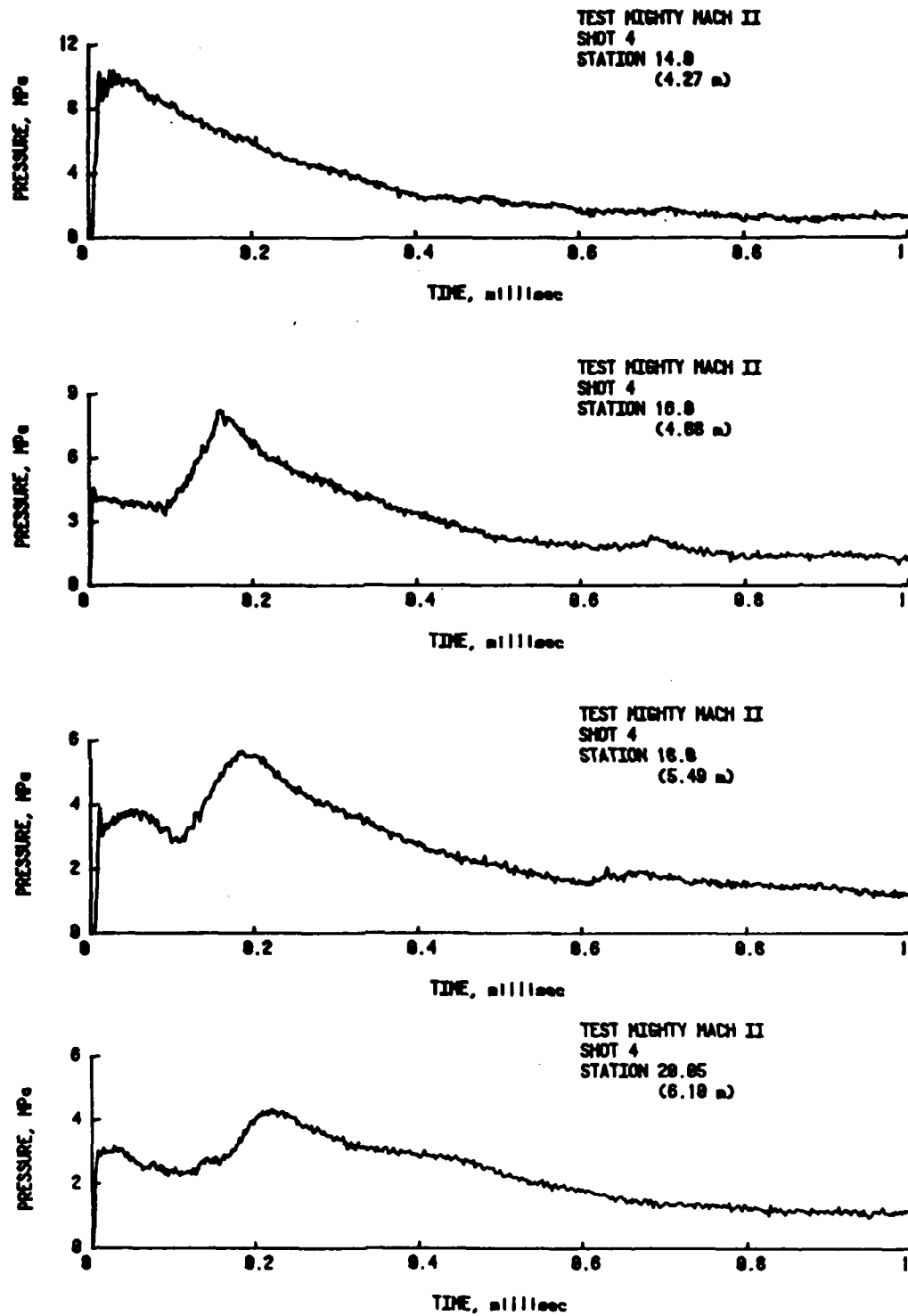Figure 6.   Static Pressure Records, 4.27-6.10m Range, Irregular
Mach Reflection Region.

162
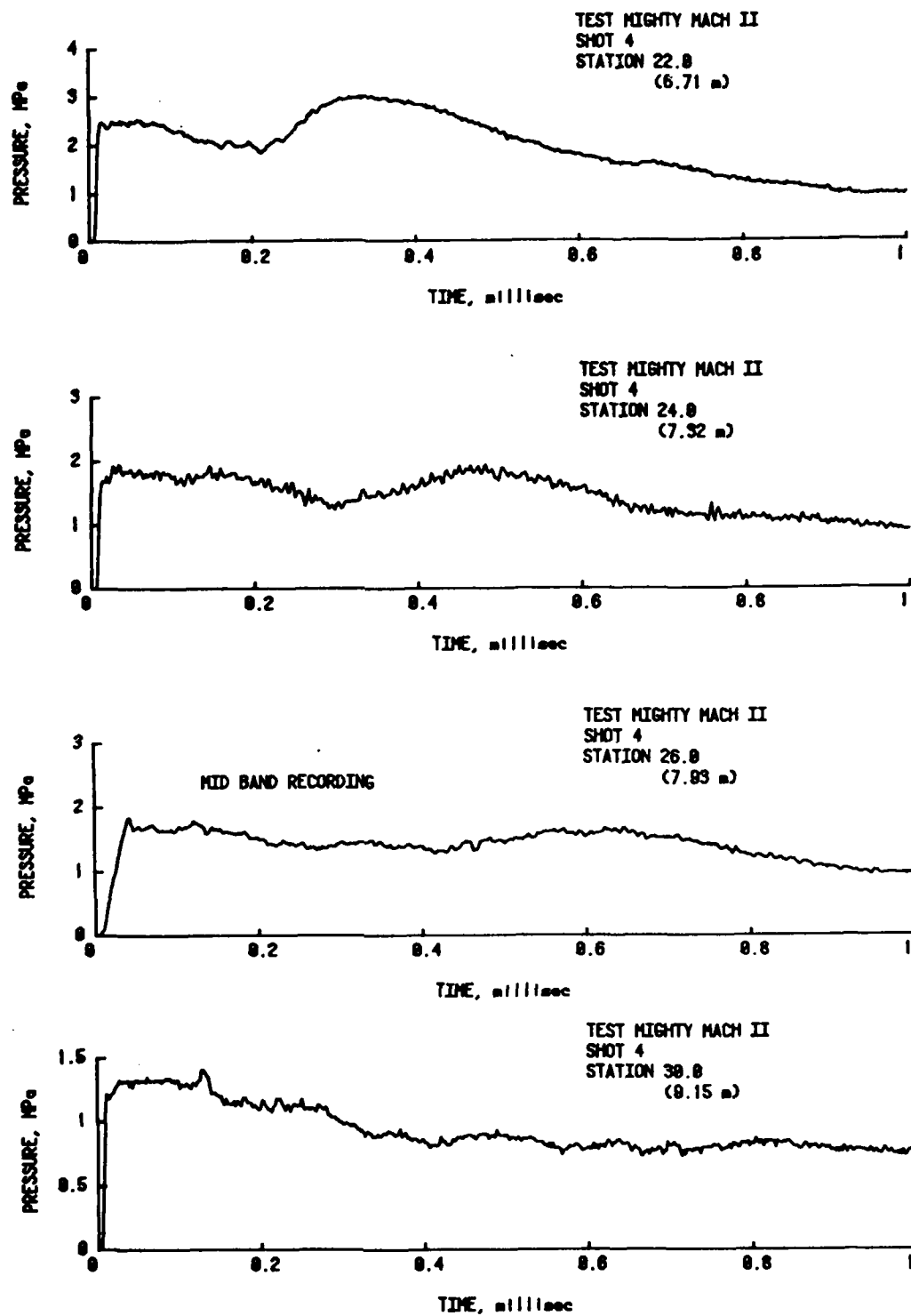
Figure 7. Static Pressure Records, 6.71-9.15m Range, Irregular and Regular Mach Reflection Region.

163

Figure 8.   Dynamic Pressure Data, 4.88m at 1.27 cm Elevation.

164
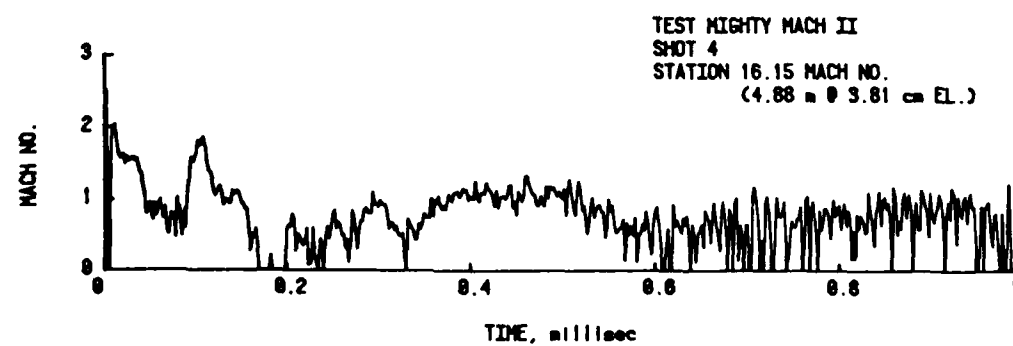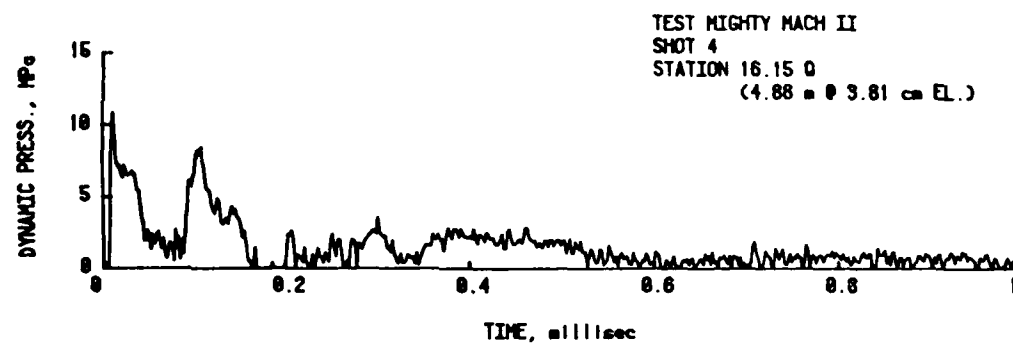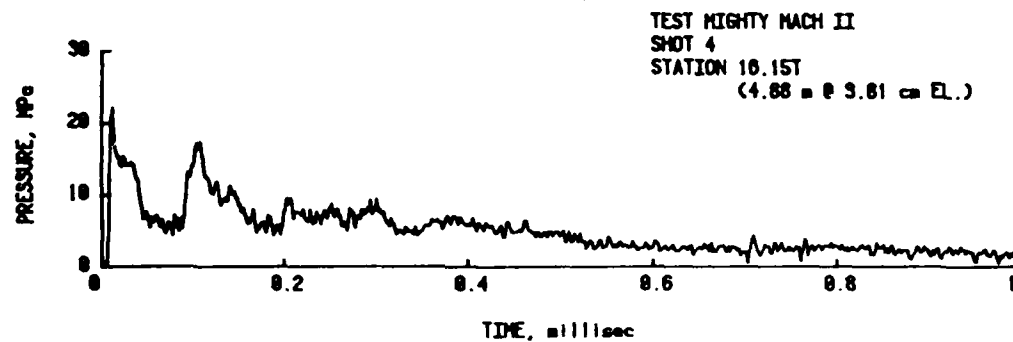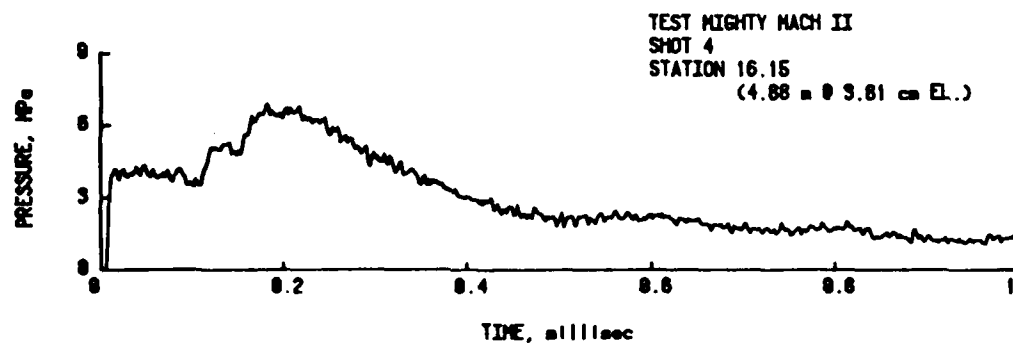
Figure 9.   Dynamic Pressure Data, 4.88 m at 3.81 cm Elevation.
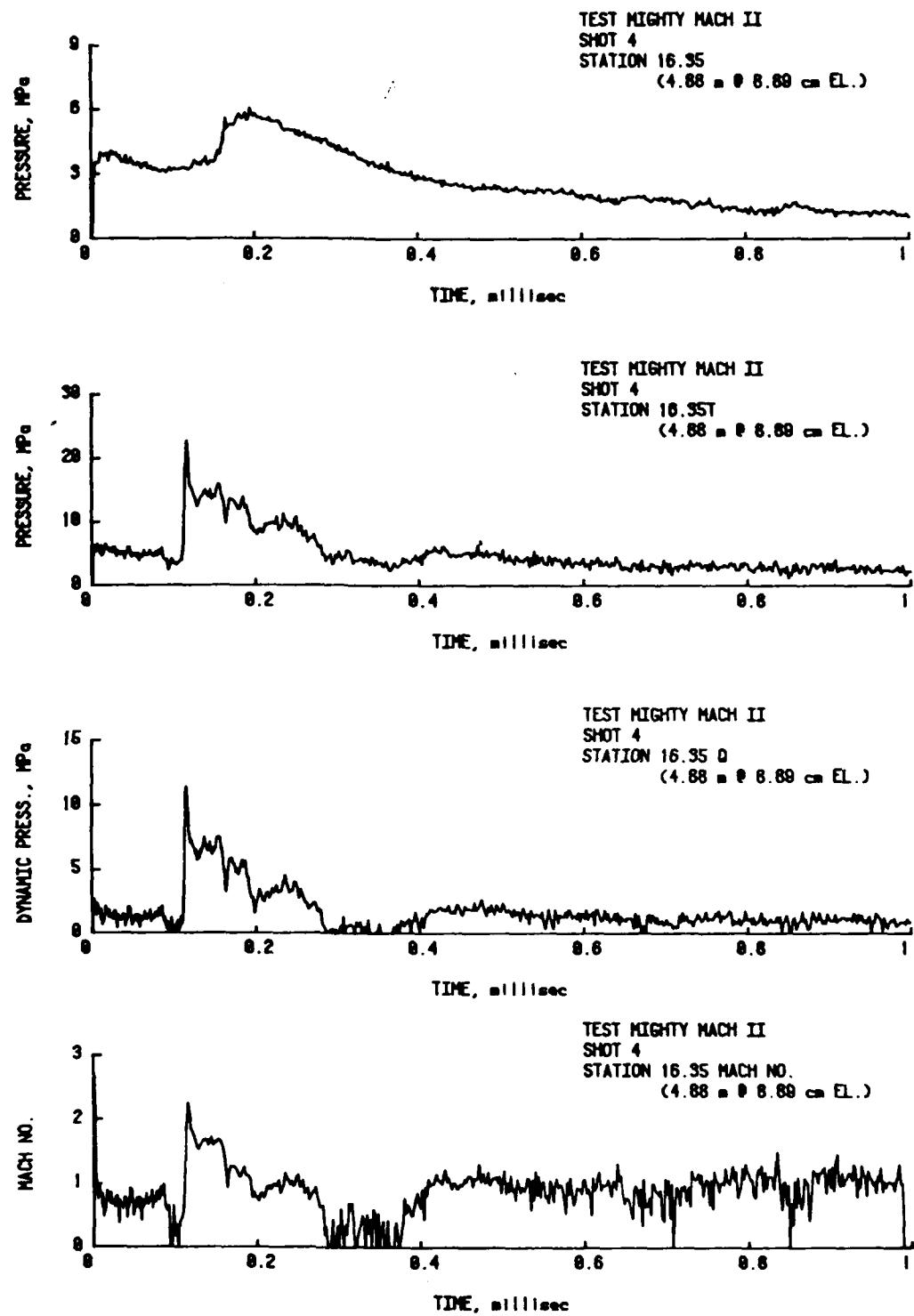
Figure 10.   Dynamic Pressure Data, 4.88 m at 8.89 cm Elevation.

166

TEST MIGHTY MACH II
SHOT 4
STATION 22.85
(6.71 m @ 1.27 cm EL.)

TEST MIGHTY MACH II
SHOT 4
STATION 22.85T
(6.71 m @ 1.27 cm EL.)

TEST MIGHTY MACH II
SHOT 4
STATION 22.85 Q
(6.71 m @ 1.27 cm EL.)

TEST MIGHTY MACH II
SHOT 4
STATION 22.85 MACH NO.
(6.71 m @ 1.27 cm EL.)
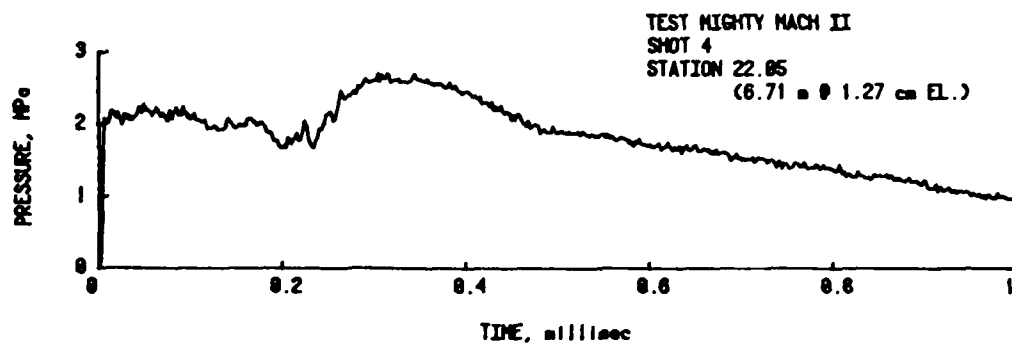
Dynamic Pressure Data, 6.71 m at 1.27 cm Elevation.
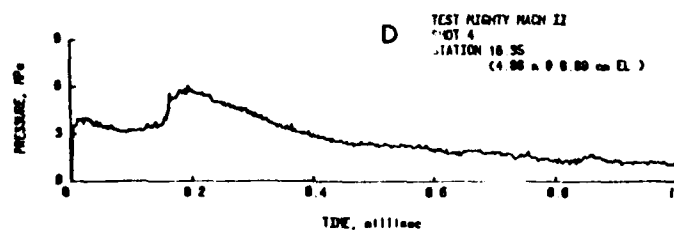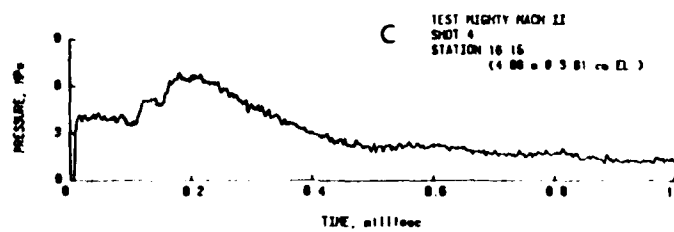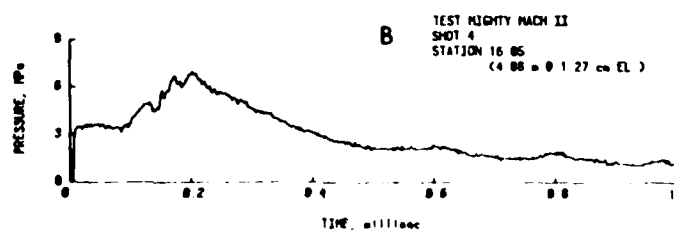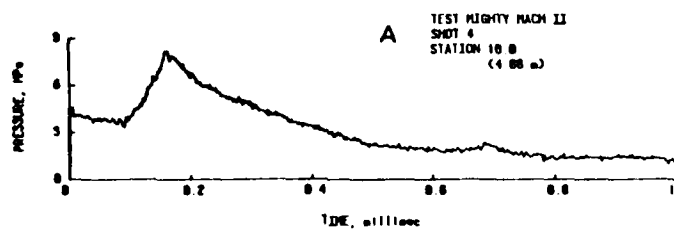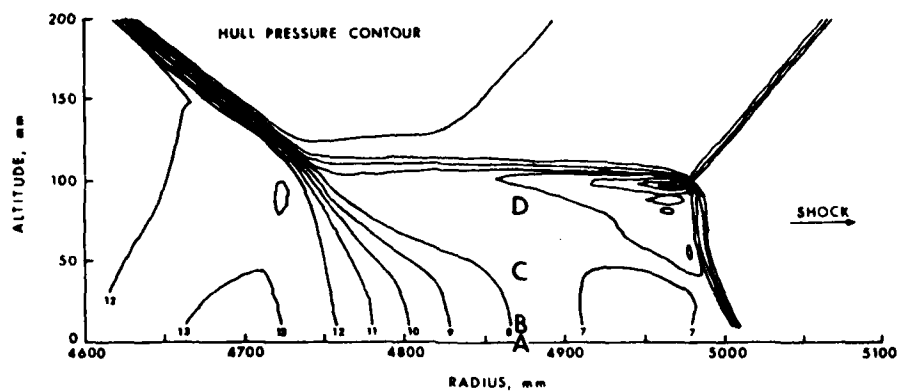
Figure 12.   Relative Comparison of HULL Pressure Contour With
Static Gage Records.

168
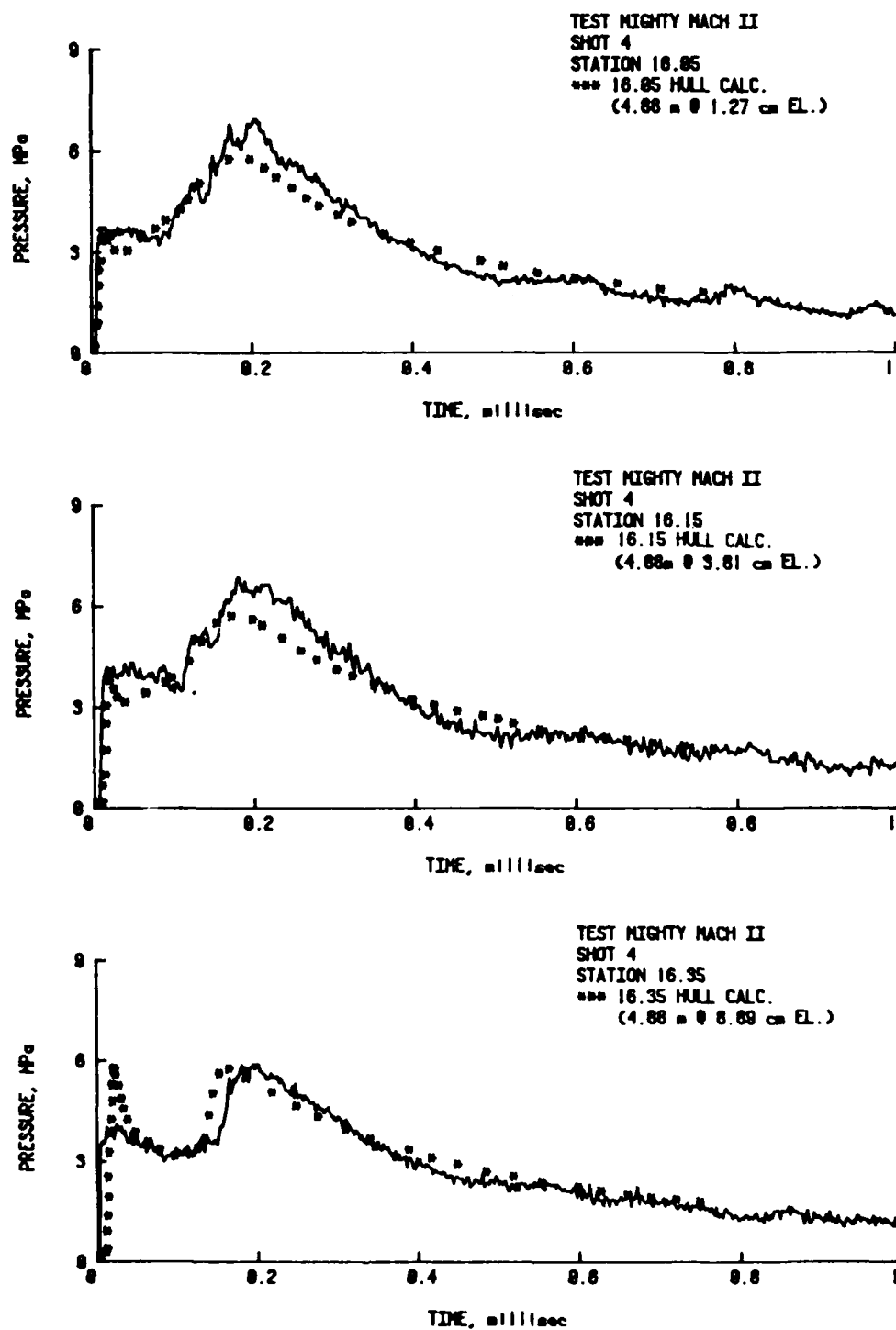
Figure 13. Static Pressure Gage Records Compared with HULL Code.

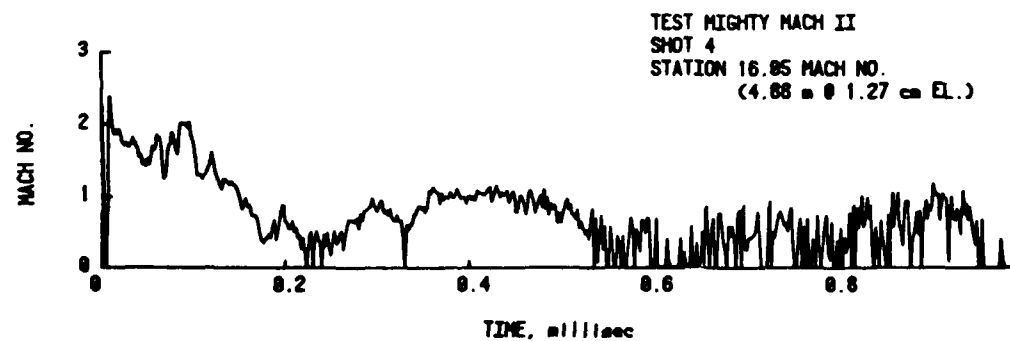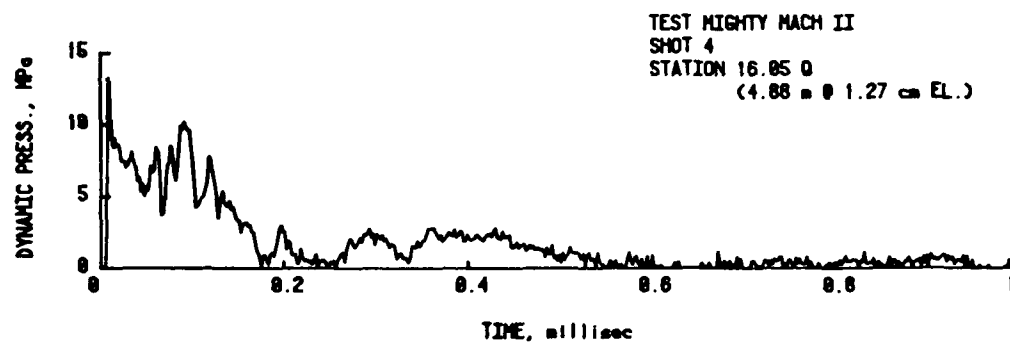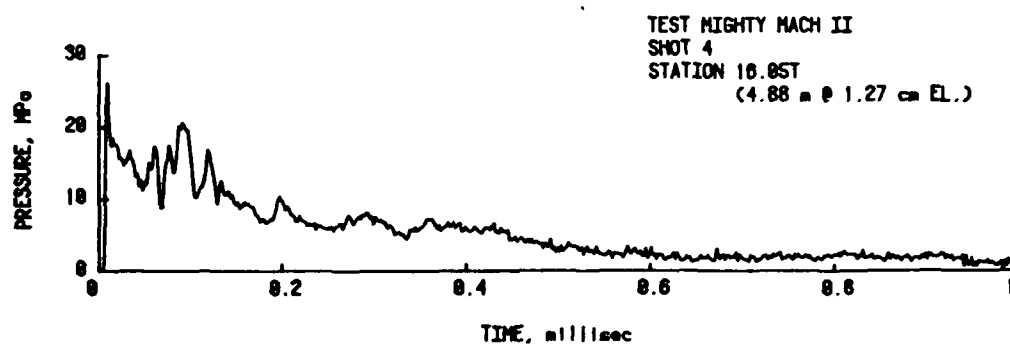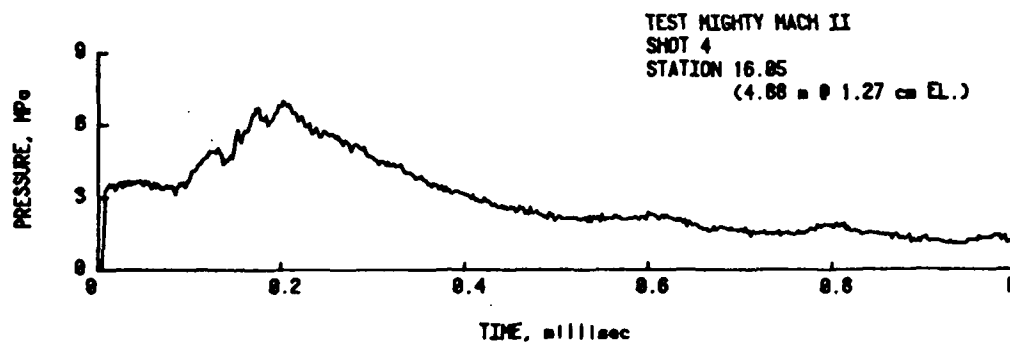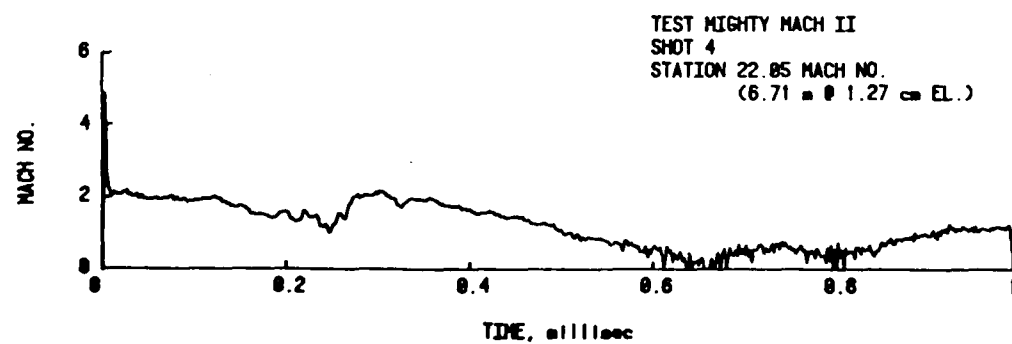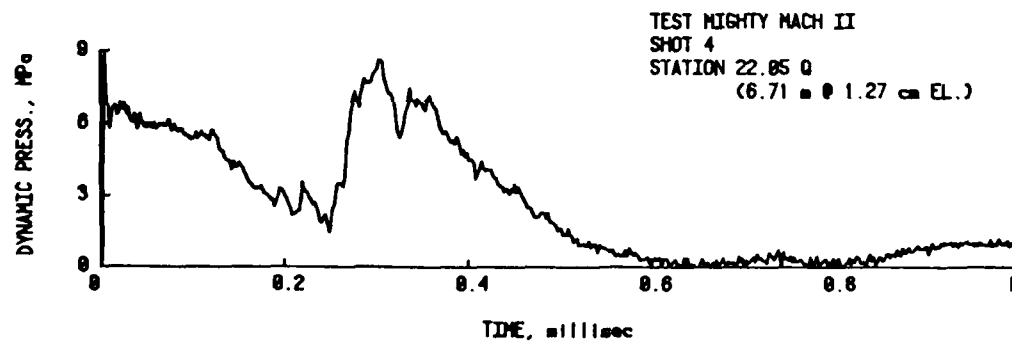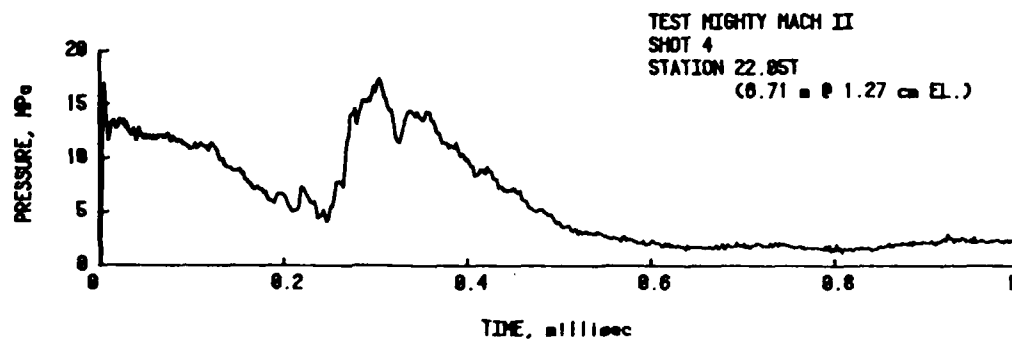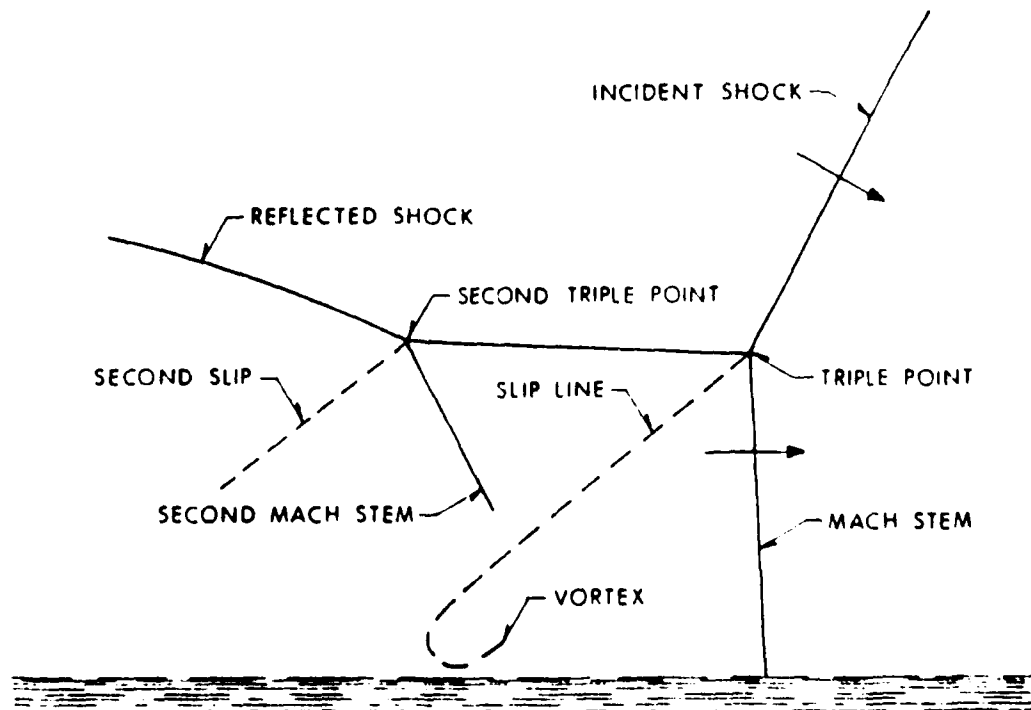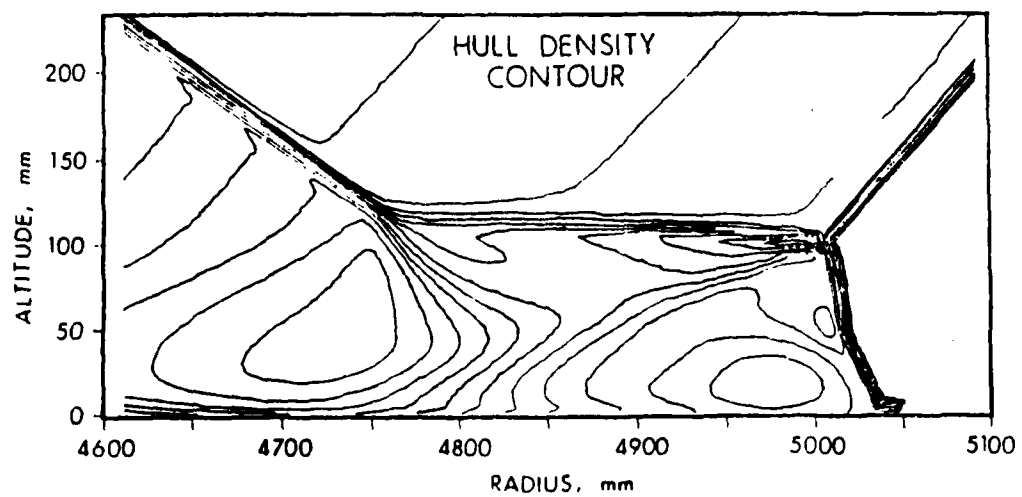Figure 14.   Structure of Irregular Mach Reflection, Experiment and Code.

170

Mach Stem Formation From Multiple Detonations

John H. Keefer
Noel H. Ethridge

Ballistic Research Laboratory
U.S. Army Armament Research & Development Command
Aberdeen Proving Ground, Maryland 21005

ABSTRACT

The shock phenomena from single detonations have been studied and discussed in many technical papers and reports. Far less attention has been given to the interaction of multiple detonations. This paper will review the work that has been done to better understand Mach stem formation with interacting shock fronts.

Analytical prediction techniques will be compared with the actual measurements. In the multiple charge case, the overpressure is enhanced at the expense of the dynamic pressure thus resulting in damage at greater distance than if the total explosive weight had been detonated as a single charge.

When a spherical charge is detonated above the ground surface the resulting spherical blast wave reflects from the ground. At a distance from the point on the ground immediately beneath the charge, approximately equal to the height of the charge above the ground but varying with shock strength, the reflected shock begins to overtake and combine with the primary shock to form a single shock known as the Mach stem. The point at which the primary shock, the reflected shock and the Mach stem meet is called the triple point. As the Mach stem shock moves outwards the height of the triple point continues to grow, as described by several Computer Codes[1], in a hyperbola-like trajectory.

The physical properties of the Mach stem blast wave and the trajectory of the triple point depend upon the energy yield of the charge; the height of burst of the charge above the ground, and on the nature of the ground surface. When the primary shock reflects from the ground, some energy will be absorbed by the ground and will appear as seismic disturbances, including cratering if the explosion is close enough to the ground. As the blast wave continues to move across the ground surface, there will be a continued transfer of energy between the air and the ground, and also a redistribution of energy within the blast wave.

A better understanding of the air blast environment surrounding a two charge multiburst detonation above the ground was gained through an experimental research program known as DIPOLE WEST. This series of 16 experiments was conducted at the Defence Research Establishment, Suffield, Alberta, Canada.

It was postulated by R. Reisler (BRL) that if two identical charges are simultaneously detonated, at a certain distance apart, the two resulting identical spherical blast waves will interact along a plane, and since there will be no energy loss in this interaction it will be possible to observe an ideal spherical shock reflection.

In two of the experiments (DIPOLE WEST, Shots 8 and 11) one of the charges was at 7.6 metres above the ground and the second charge at a further height of 15.2 metres above the first. A photograph of Shot 11 fireballs at 0.05 seconds after detonation is shown in Figure 1. For each charge configuration, one experiment was carried out over smooth ground and another over rough ground. In each experiment photogrammetrical measurements were made of the trajectories of the primary spherical shock from the bottom charge; of the Mach stem shock along the ground surface, and of the Mach stem shock produced along the ideal reflecting plane between the two charges. Comparisons of the shock strengths of the Mach stems along the ground and close to the ideal reflecting plane, indicated an energy loss in the shock front of approximately 10% over the smooth ground and of approximately 57% over the rough ground. The trajectories of the triple points formed by the junction of the primary shocks, reflected shocks and Mach stems, also show a difference for the rough ground compared with the smooth ground, and the smooth ground compared with the ideal reflecting plane[2]. See Figure 2.

In order to consider the effect of surface absorptivity for a given height of burst (HOB) a power function best described the variation in growth (y) of the path of the triple point with range (r) feet

$$y = (a) (r^f)$$

where $f = 1.53 - (\frac{15}{r^2})$

$a = .139 \times e$

and $e = 1.00$ for Ideal Surfaces

$e = .90$ for Hard Surfaces

$e = .63$ for Soft Surfaces

Comparison of maximum overpressure for the 15.2 metre vertical separated events with the Air Force Weapons Laboratory HULL code results are presented in Figure 3. Correlation between the calculated results and the measured data is excellent[3,4].

In a multiple burst of more than two charges, the interaction of the blast waves begins as an interaction between blast wave pairs. The interaction for a pair would develop to a point where a third blast wave becomes involved in the interaction.

Several small scale tests were conducted in 1960 at the Ballistic Research Laboratory (BRL)[5] to establish the enhancement in air blast coverage on the ground that can be obtained from the simultaneous detonations of a cluster of explosive charges as compared to the detonation of a single large charge. In those early studies it was shown, using trios of bare explosive spheres located on the vertices of an equilateral triangle, that efficient use of such simultaneously detonated charges requires an optimization of the separation distance between charges and their height of burst to obtain maximum coverage on the ground with a given overpressure. Particular emphasis had been placed on developing iso-pressure contours for special pressure levels in and about the triad for both ground and air bursts.

Several phenomenological aspects of the blast problems associated with simultaneous detonations remained uncertain at the completion of the small scale studies. Therefore, it was felt by the Air Force Special Weapons Center (AFSWC) and the BRL that a large scale test should be conducted. Consequently a larger scale test was considered with the following air blast objectives: (1) to determine the dynamic pressure field both within and outside a triad of charges, (2) to determine more precise mapping of the peak overpressure field in the region close to the center of the charges and in other regions of reflection enhancement. The test site selected for the program was White Sands Missile Range, New Mexico. The nickname "White Tribe", an acronym derived from White Sands Triple Burst Experiment, was selected. The test conditions were scaled from the previous 454g and 3.6kg charges fired to give the optimum separation of a triangular array, for ground bursts, for the case of maximizing ground coverage with peak pressure exceeding 689.5 kPa[6]. Thus, a nominal separation of 53.6 metres between each of three 4536 kg bare charges of Pentolite was selected. Moreover, these conditions could simulate those predicted for the simultaneous detonation of three 200 KT nuclear weapons at a separation of approximately 1463.0 metres.

The air blast in and about the triad of explosive charges was measured at a large number of stations using several different techniques. A total of 29 piezo-electric gages of BRL design, 27 strain gages and 43 mechanical self-recording pressure transducers were used. Several motion picture and still cameras were used to observe the detonation from both the ground and from the air.

A day or two before the three tests, when all instrumentation was nearly ready, the large explosive charges were prepared at the vertices of the triangle. The explosive was TNT, formed in 3.6 kg blocks, and stacked in an hemispherical shape to yield an air blast equivalent to that from a 4536 kg charge of 50/50 Pentolite at sea level conditions. So the charges weighed 5248 kg in order to compensate for the 1220 metre elevation of the White Sands site[6].

With the exception of several variations in the location of gages, each of the White Tribe firings was conducted in essentially the same manner and yielded similar results. The side-on overpressure contour plot for the first shot is shown in Figure 4. From these results it can be seen that by dividing the charge into three approximately equal portions and then detonating them simultaneously that the area on the ground covered by at least 689.5 kPa is

increased by 55% over the coverage that would have been obtained if the total quantity of explosive had been left in one charge. Mapping of the dynamic overpressure field was not accomplished, although some of the expected dynamic pressure phenomena were observed.

If n-charges are placed in a row and n>3 the resulting shock pattern is shown in Figure 5 for simultaneously detonated charges. If additional rows are added to the multi burst array blast focusing will occur.

LIST OF REFERENCES

1. Needham, C. E. and Wittmer, L.A., "The Air Force Weapons Laboratory Low Altitude Multiple Burst (LAMB) Model", AFWL-DYT-75-2, 1980.

2. Dewey, J. M., et al, "Photogrammetry of the Shock Front Trajectories on Dipole West Shots 8, 9, 10, and 11", DNA 3777F, University of Victoria, B.C., Canada V8W 2Y2, July 1975.

3. Keefer, John H. and Reisler, Ralph E., "Multiburst Environment - Simultaneous Detonations", Project Dipole West, BRL Report No. 1766, March 1975, USA Ballistic Research Laboratory, Aberdeen Proving Ground, MD 21005.

4. Reisler, Ralph E. and Pettit, Burnett A., "Project Dipole West - Multiburst Environment (Non-Simultaneous Detonations)", BRL Report No. 1921, September 1976, USA Ballistic Research Laboratory, Aberdeen Proving Ground, MD 21005.

5. Armendt, B. F., Hippensteel, R. G., Hoffman, A. J., and Kingery, C. N., "The Air Blast from Simultaneously Detonated Explosive Spheres", USA Ballistic Research Laboratories Memorandum Report No. 1294, Aberdeen Proving Ground, MD 21005, August 1960 (Unclassified).

6. Armendt, B. F., Hippensteel, R. G., Hoffman, A. G., and Keefer, J. H., "Project WHITE TRIBE: Air Blast from Simultaneously Detonated Large Scale Explosive Charges", BRL Report No. 1145, USA Ballistic Research Laboratory, Aberdeen Proving Ground, MD 21005, September 1961.
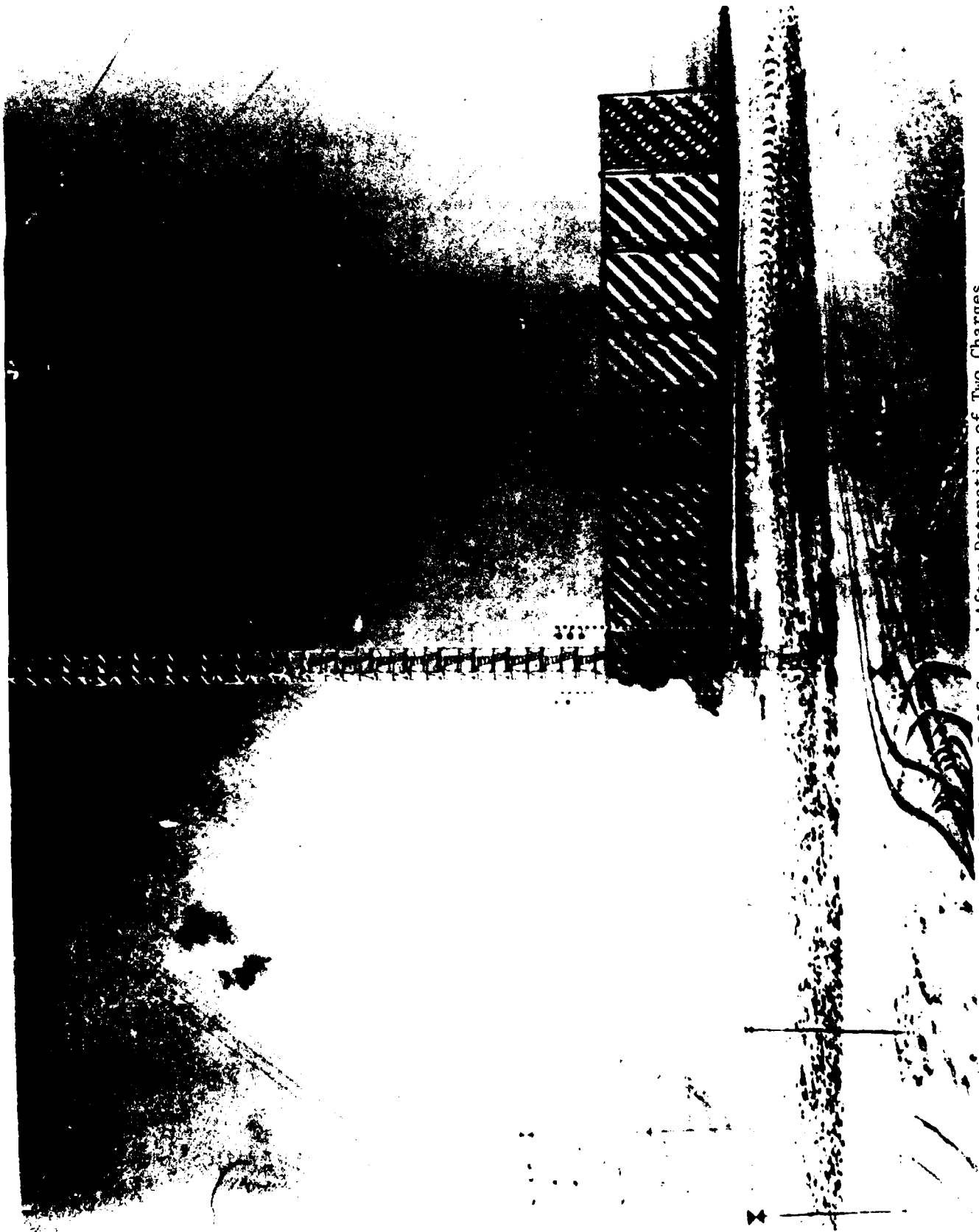
Figure 1. Fireballs at 0.05 Second After Detonation of Two Charges.

176
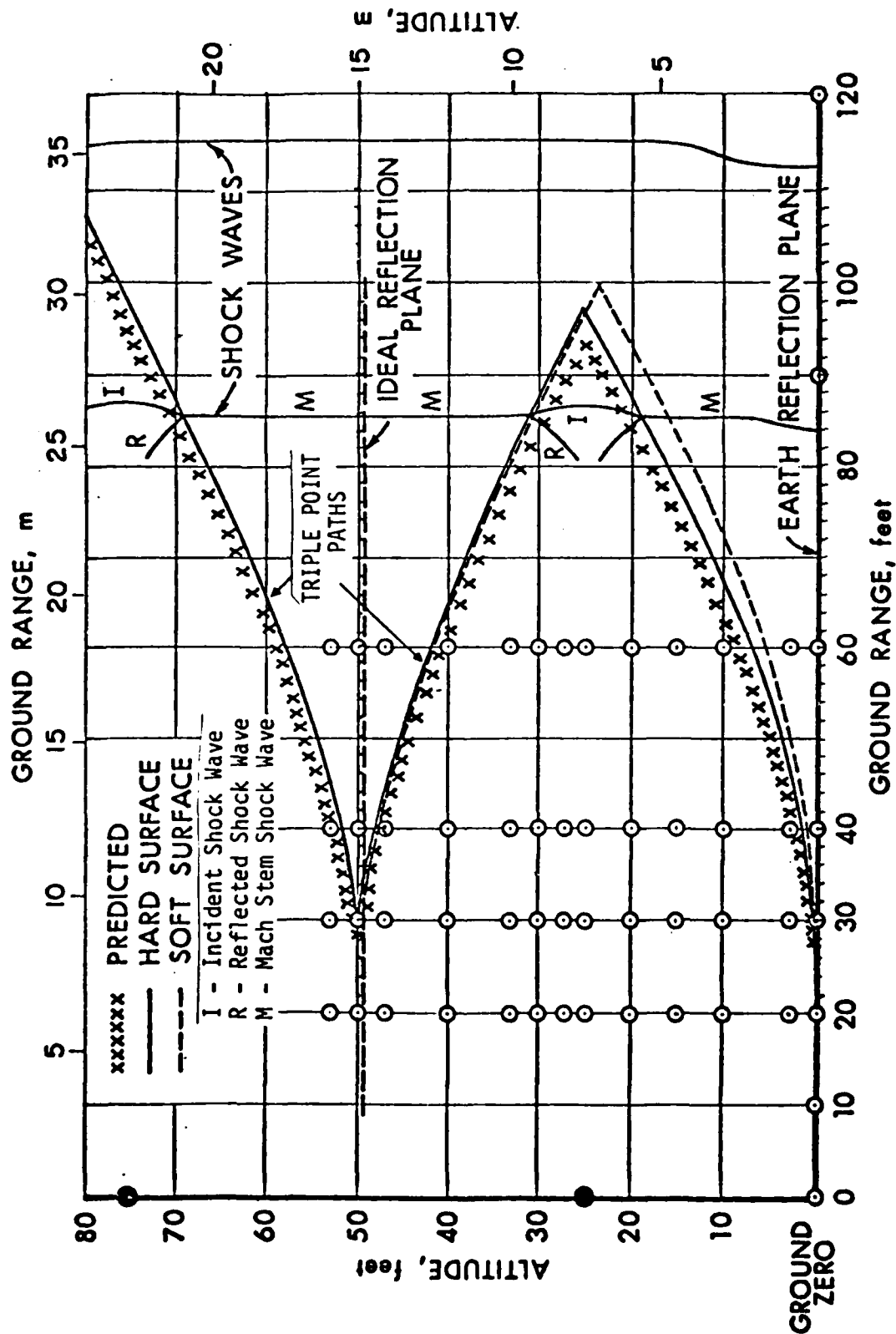
Figure 2. Triple-Point Paths and Shock Systems from Detonation Over Different Types of Surfaces.

(Hard Surface-Shot 8, Soft Surface-Shot 11).
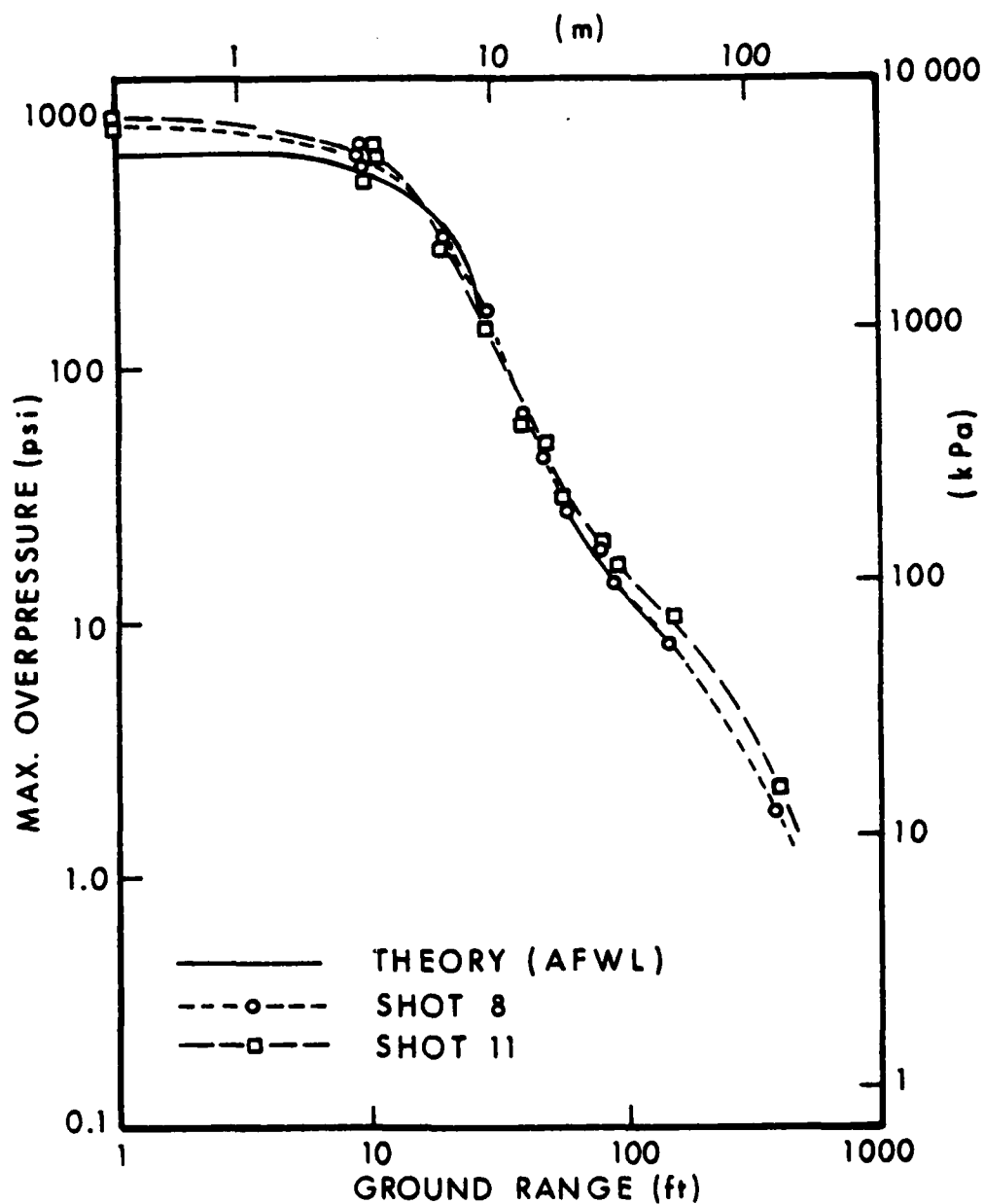
Figure 3.   Comparison of Calculated and Experimental Maximum
Overpressure at Ground Level from Two Charges.

Figure 4. Overpressure Contours for the Three Charge Array.
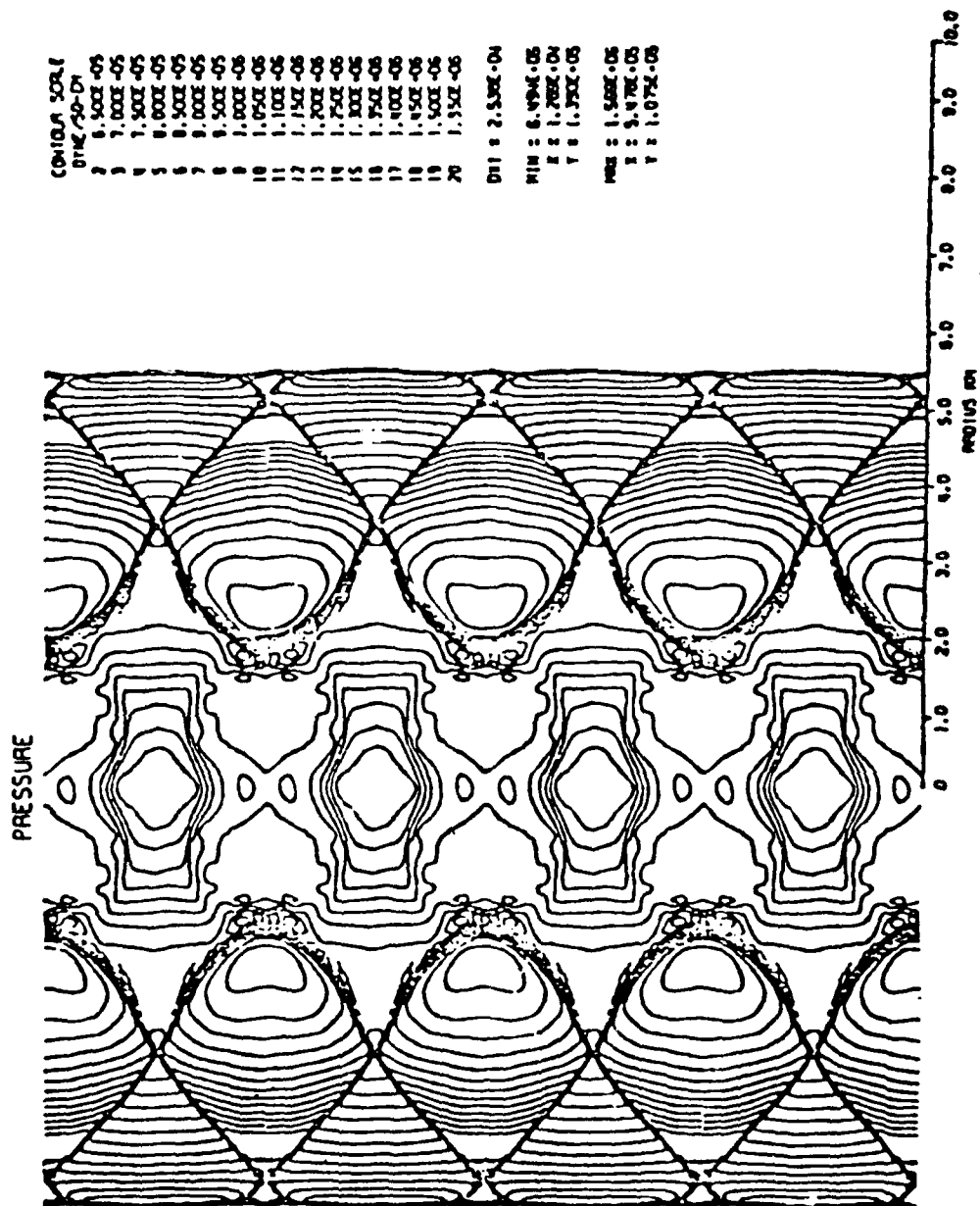
Figure 5. Shock Wave Interaction from a Row of Charges Detonated Simultaneously.

1.0

2.8 2.5

3.2 2.2

3.6

1.1 4.0 2.0

1.8

1.25 1.4 1.6

MICROCOPY RESOLUTION TEST CHART
NATIONAL BUREAU OF STANDARDS 1963 A
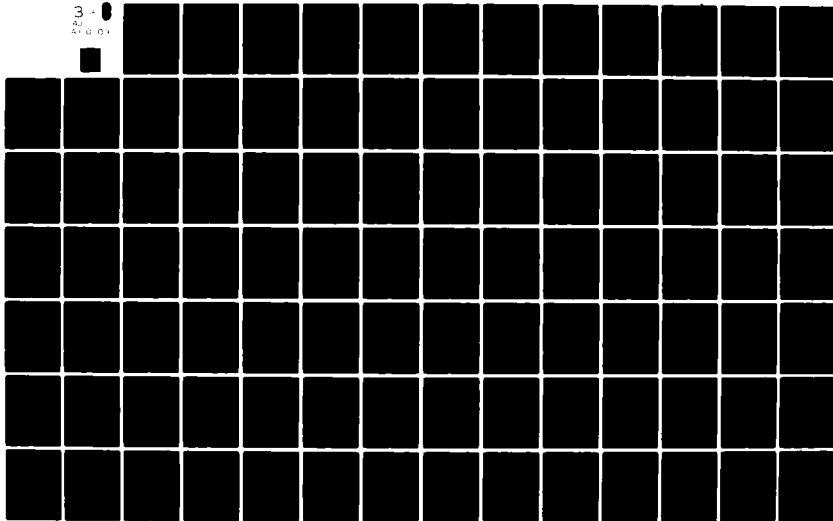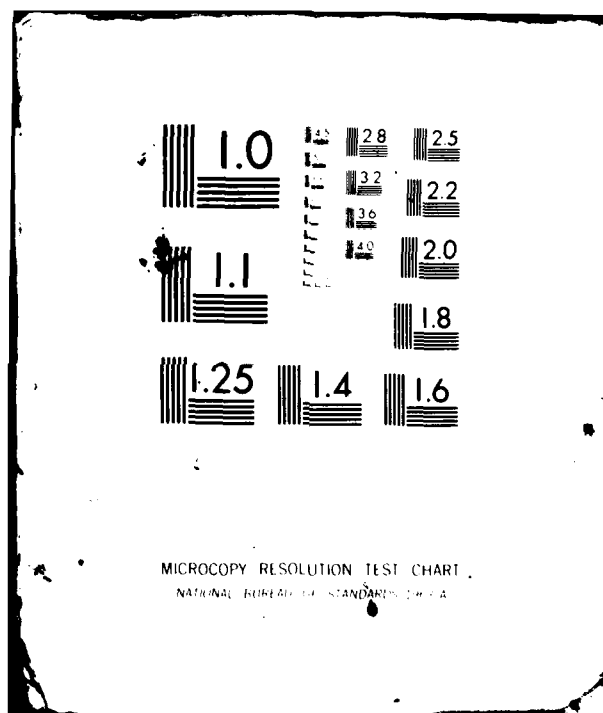
BLOW-OFF OF A FLAME LOCATED IN A REAR STAGNATION POINT FLOW

D. Mikolaitis and J. Buckmaster
University of Illinois, Urbana 61801

Abstract

If a combustible mixture flows past a thin plate, experiment shows that a flame may be stabilized in the wake. At moderate Reynolds Numbers the wake is characterized, near the symmetry axis, by a rear stagnation point flow and this is the fundamental ingredient of a mathematical model of this situation. Analysis shows that static stability is determined by the outcome of a conflict between the destabilizing effects of heat transfer to the rear of the plate, and if the flow is too strong blow-off occurs.

Introduction

Gas flow at modest Reynolds Numbers past the blunt trailing edge of a thin plate is characterized by a closed laminar wake, and it is possible, if the gas is combustible, to stabilize a flame in the rear stagnation point flow immediately downstream of this wake (Kawamura, Asato, Mazaki, Hamaguchi & Kayahara (1979)). At large enough flow rates the flame is blown off, and the aim of our investigation is to understand these phenomena in the context of an elementary combustion model. This model is defined by the following system of equations:

$$(\vec{v}\cdot\vec{\nabla})(T,Y) = \nabla^2(T,\frac{1}{L}Y) + BYe^{-\theta/T} \quad (1,-1) \tag{1}$$

$$\vec{v} = 2\beta(x,-y)$$

$$B = \frac{Y_f^2\theta^2}{2(T_f+Y_f)^4} \exp\left(\frac{\theta}{T_f+Y_f}\right)$$

Here fresh mixture is characterized by a temperature T_f and mass fraction of reactants Y_f, and x is measured downstream from the stagnation point. These equations are solved in the asymptotic limit of infinite activation energy $(\theta \to \infty)$ with the Lewis Number close to 1 $[L - 1 = O(\theta^{-1})]$. Moreover a similarity solution is constructed that is valid only on the axis of symmetry. The stability of the steady solution is examined by adding appropriate time derivatives to the equations and then formulating an eigenvalue problem that is solved numerically using the method of weighted residuals.

Results

The essential results are shown in Fig. 1 which reveals how h ,

181
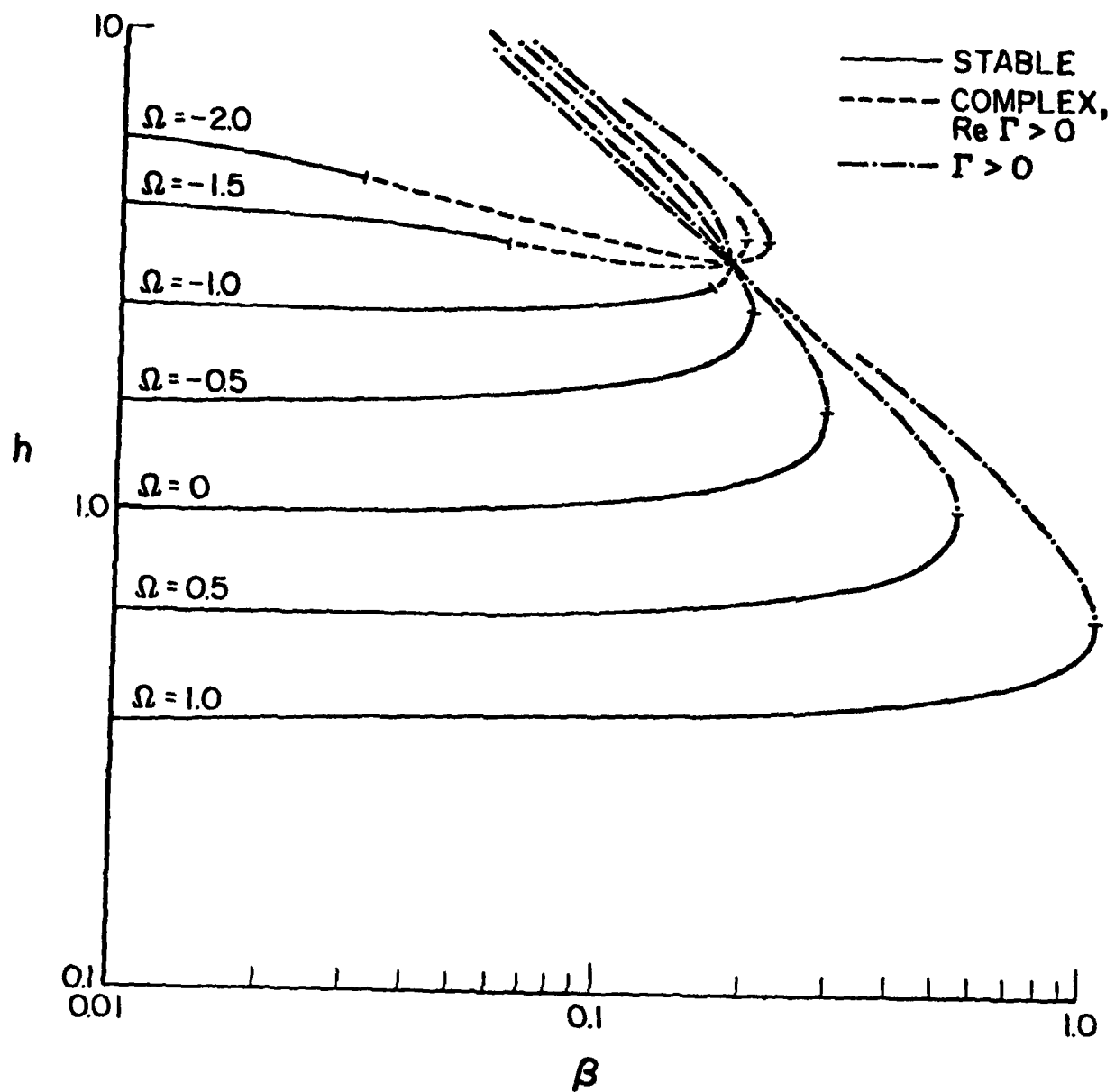
FIGURE 1

the distance between the flame and the stagnation point, varies with the straining rate β . These results are expressed in terms of the single parameter

$$\Omega \equiv - \frac{Y_f \theta (L-1)}{2(T_f + Y_f)^2} \tag{2}$$

Note that there is a maximum straining rate that any flame can tolerate, beyond which it may be inferred that blow-off occurs. Only those portions of the curve that are solid are stable so that for $\Omega \leqslant -.9$ the steady state becomes physically unattainable before β reaches its maximum. It is possible that bifurcation occurs at the transition point but no analysis has been undertaken of this question. It would be an interesting matter to examine experimentally.

Acknowledgement

Reference

Kawamura, T., Asato, K., Mazaki, T., Hamaguchi, T., & Kayahara, H. (1979) 'Explanation of the Blow-Off of Inverted Flames by the Area-Increase Concept" Combustion & Flame 35, 109.

THE EQUATION GOVERNING THE PROPAGATION
OF FAST DEFLAGRATION WAVES FOR SMALL HEAT RELEASE[†]

D.S. Stewart[*] and G.S.S. Ludford
Department of Theoretical and Applied Mechanics
Cornell University, Ithaca, N.Y.   14853

ABSTRACT. The initial-value problem of a plane flame subjected to arbitrary upstream and downstream disturbances is treated using activation energy-asymptotics (AEA) and the limit of small heat-release. The flame is a discontinuity whose locus is found from an appropriate ordinary differential equation. The position of the shock wave formed by the expanding burnt gas can be calculated. The unsteady analysis uses the solution for the fast deflagration developed in a paper by Stewart & Ludford (1981); under suitable circumstances the flame behavior is quasi-steady. This asymptotic solution to the unsteady equations of combustion allows study of the flame acceleration and shock formation incipient to the transition from deflagration to detonation.

I. INTRODUCTION. The question of transition from deflagration to detonation (DDT) has long defied being answered by a simple theory. This is in part due to the inherent nonlinearities of the equations of reacting flow which have precluded analytical solutions. In their recent book on detonation theory, Fickett & Davis (1979) wrote, "Except for a few very special cases, there are no explicit solutions of the equations. They are studied by theoretical analysis of their general properties and by numerical calculation of particular cases". In this paper we give a simple, explicit solution to the unsteady, one-dimensional, reacting flow equations for the initial-value problem of a plane flame subjected to suitably prescribed disturbances.

The present work is preceded by two papers. Recently Lu & Ludford (1981) analyzed steady detonations; the assumptions required in using AEA in their paper are made here as well. Then Stewart & Ludford (1981) discussed steady deflagrations for wave speeds which are appreciable as must be the case in DDT. In their paper they gave an explicit asymptotic solution for deglagrations which this paper uses as a starting point.

The development of the present model proceeds in two distinct steps. First, we treat the reaction term, $\Lambda Y \exp(-\theta/T)$ in the governing equations (system (1) of Section II) by using the limit of large activation energy, $\theta \to \infty$. This limit, with no other assumptions allows us to pose an unsteady, initial-value problem in which the reaction term is eliminated; but the effect of treating the reaction term in this way is to produce a moving discontinuity across which certain asymptotically derived conditions must hold. We will give a brief discussion of how this problem is arrived at in Section III, but the full details of this step are worked out by Stewart (1981). The second step is treated in detail in this paper and involves the solution of the problem posed by $\theta \to \infty$ when the heat released by the chemical reaction, β, is small.

Stewart & Ludford (1981) discussed the steady deflagration wave solutions for system (1), using the limit $\theta \to \infty$, for finite β. This steady wave solution is parametrized by the flame speed, V, which is $O(1)$ instead of being small as is usually assumed in the combustion approximation; they dubbed these solutions, for finite wave speeds, "fast deflagrations". Throughout the steady flame-zone, the density, velocity, temperature and mass fraction vary from quiescent values upstream to downstream equilibrium values. The overall changes, upstream to downstream, which depend on V, can also be found directly from the classic Rankine-Hugoniot relations as well as from integrating the appropriate differential equations. Stewart & Ludford also showed that when β is small, the fast deflagration solutions have a simple, explicit form. The small heat-release version of the Rankine-Hugoniot conditions can be inferred directly from these solutions as well.

If the upstream and downstream disturbances, away from the flame, are "sufficiently" gradual, then these "outer" disturbances are governed by acoustic solutions. The fast deflagration solution for small heat-release can then be used as the appropriate description for the flame-zone which interacts with the upstream and downstream disturbances as a Rankine-Hugoniot discontinuity. Thus, as we well show in Section V, if the heat release is small and if the initial data is sufficiently gradual, the solution to (1) is an acoustic solution modified by the presence of an (quasi-steady) accelerating or decelerating flame; the solution is then completely determined by integrating an appropriate first-order differential equation for the flame location.

At a certain point in the paper we specialize our treatment to consider problems when the flame is initially disturbed only downstream. We show that it is possible to accelerate a flame with a rarefaction disturbance downstream; our results also imply that a flame may be decelerated or even extinguished by a downstream compression wave that passes through the flame. This might seem surprising at first until one considers the ordinary results of a Rankine-Hugoniot diagram which shows that the mass flux through a flame increases with the negative pressure drop across it. We briefly discuss the development of a precursor shock that occurs upstream of an accelerating flame.

II. THE GOVERNING EQUATIONS. The equations used here are the equations of one-dimensional, unsteady combustion. In order to obtain tractable equations, certain simplifying assumptions must be made, the most important being: one step reaction, Arrhenius kinetics, perfect gases, Newtonian fluids, equal specific heats, equal molecular masses and constant material properties. For a discussion of these assumptions and their justification, see Buckmaster & Ludford (1981).

The equations for ρ, v, T and Y, the dimensionless density, fluid velocity, temperature and reduced mass fraction of the deficient reactant, express the usual balances of mass, momentum, energy and species. The dimensional units of ρ and T have been chosen with respect to a quiescent, unreacted state, so that if quiescent, ρ and T are 1. The reduced mass fraction

Y is the mass fraction of the reactant divided by its quiescent value, so that if quiescent $Y = 1$. The velocity unit is chosen to be the quiescent sound speed. x denotes dimensionless distance and the distance unit is $\lambda/c_p M$, where λ and c_p are respectively the thermal conductivity and specific heat of the fluid, and M is the mass flux found by multiplying the quiescent density times the quiescent speed of sound. t represents non-dimensional time and the time unit is formed from the length unit and divided by the velocity unit.

To simplify the present discussion we have set both the Prandtl and Lewis numbers equal to 1; it is a simple matter to generalize the present discussion to include other values. The other parameters that appear in the governing equations are γ, the ratio of specific heats, β a non-dimensional measure of the amount of heat released by the reaction, $\Lambda \equiv DM^{-2}$ where D is the Damköhler number and θ, the dimensionless activation energy. The governing equations are written concisely in a vector form, where $\underset{\sim}{u}$ is the column vector formed by respective components ρ, v, T and Y, as

$$\underset{\sim}{u}_t + \underset{\sim}{C} \cdot \underset{\sim}{u}_x = \underset{\sim}{D} \cdot \underset{\sim}{u}_{xx} + \underset{\sim}{G} + \Lambda Y \exp(-\theta/T) \; \underset{\sim}{H}. \tag{1}$$

Here the subscripts x and t denote partial differentiation and $\underset{\sim}{C}$, $\underset{\sim}{D}$, $\underset{\sim}{G}$, and $\underset{\sim}{H}$ are square matrices and column vectors

$$\underset{\sim}{C} = \begin{bmatrix} v & \rho & 0 & 0 \\ T/(\gamma\rho) & v & 1/\gamma & 0 \\ 0 & (\gamma-1)T & v & 0 \\ 0 & 0 & 0 & v \end{bmatrix} , \quad \underset{\sim}{D} = \begin{bmatrix} 0 & 0 & 0 & 0 \\ 0 & 1/\rho & 0 & 0 \\ 0 & 0 & \gamma/\rho & 0 \\ 0 & 0 & 0 & 1/\rho \end{bmatrix}$$

$$\tag{2}$$

$$\underset{\sim}{G} = \begin{bmatrix} 0 \\ 0 \\ \gamma(\gamma-1)(v_x)^2/\rho \\ 0 \end{bmatrix} , \quad \underset{\sim}{H} = \begin{bmatrix} 0 \\ 0 \\ \beta \\ -1 \end{bmatrix}$$

In general, the task is to solve the system (1) when $\underset{\sim}{u}$ is prescribed initially at $t = 0$. In particular we will focus on the initial value problem of a flame propagating to the left into an initially quiescent mixture upstream, while subjected to an initially prescribed disturbance downstream.

III. ACTIVATION-ENERGY ASYMPTOTICS; FAST DEFLAGRATIONS. Here we present
the results of using the limit of large activation energy, $\theta \to \infty$, in order to
treat the reaction term, $\Lambda Y \exp(-\theta/T)$, in (1). The effect of $\theta \to \infty$ is to
eliminate the reaction term everywhere except in a thin flame sheet (a region
of reactive-diffusive balance). The flame sheet is effectively a discontinuity
which separates unburnt, upstream gases from burnt, downstream gases and re-
quires certain jumps across it. The advantage of this limit is that the flame
speed is precisely defined as the speed of the discontinuity.

A standard flame-sheet analysis requires that we consider the stretched
coordinate

$$z = \theta[x - x^*(t)] , \qquad (3)$$

where $x = x^*(t)$ is the flame location, expansions of the type

$$\underset{\sim}{u} = \underset{\sim}{u}_o(t) + 0(\theta^{-1}) , \qquad (4)$$

and a distinguished limit for the Damköhler number, namely,

$$D = C\theta^2 \exp(\theta/T_*) . \qquad (5)$$

C and T_* are $0(1)$ constants that characterize D. The analysis is
straightforward (See Stewart (1981)) and we are led to the following conditions
across the flame sheet. Denoting a jump across the flame sheet at $x = x^*$ by,
$[\phi] = \phi(x_+^*) - \phi(x_-^*)$, we find

$$[\underset{\sim}{u}_o] = [\rho_{o_x}] = [v_{o_x}] = [T_{o_x} + \beta Y_{o_x}] = 0 , \qquad (6)$$

$$T_o = T_* \quad \text{at} \quad x = x^* \quad \text{and} \quad Y_o = 0 \quad \text{for} \quad x \geq x^* . \qquad (7)$$

Using AEA, the problem of unsteady flame propagation is posed by solving
the reactionless equations (1) subject to the conditions (6) and (7). Initial
disturbances may be arbitrarily prescribed both upstream and downstream with
the requirement that the conditions at the flame sheet are satisfied initially.
This problem is well-posed and we will solve it explicitly for a limited class
of disturbances whenever the heat release β is small, and the initial distur-
bances are sufficiently gradual.

Stewart & Ludford (1981) found the steady wave solutions of the above
problem for deflagrations when V, the flame speed, is $0(1)$. They found
that such "fast" deflagrations are composed of three regions; a convective-
diffusive zone on the x scale, upstream of the flame sheet, the flame sheet,
(now the discontinuity given by (6) and (7)), and a downstream convective-
diffusive zone which adjusts the solution to its final equilibrium state.
Finally, the main result in their paper is that the flame temperature T_*
(a property determined by the mixture) is determined as a function of the
flame speed V.

IV. THE LIMIT OF SMALL HEAT RELEASE. Stewart & Ludford also showed that the steady solution of a fast deflagration takes a simple limiting form when the heat release β is small. Determination of this steady solution is found when $\underset{\sim}{u}_0$ is expanded as

$$\underset{\sim}{u}_0 = \underset{\sim}{u}_c + \beta \underset{\sim}{u}_1 (x - Vt) + \ldots , \quad \text{where } Y_1 = Y/\beta \text{ (say)}. \tag{8}$$

Here $\underset{\sim}{u}_c$ and $\underset{\sim}{u}_1$ are the column vectors $(1,0,1,0)$ and (ρ_1, v_1, T_1, Y_1) respectively. Substitution of (8) into reactionless equation (1) leads to a set of linear equations for the components of $\underset{\sim}{u}_1$ containing the flame speed V as a parameter. The resulting equation for $\underset{\sim}{u}_1$ must be solved subject to the flame sheet conditions (6) and (7) and, in general, matching conditions that $\underset{\sim}{u}_1 \to \underset{\sim}{u}_+$ (say) as $x - x^* \to \pm \infty$.

The upstream, convective, diffusive zone followed by the flame sheet, and the downstream adjustment region has been referred to as the flame-zone. As $x - x^*$ varies between $-\infty$ and $+\infty$, the components of $\underset{\sim}{u}_1$ vary continuously from $\underset{\sim}{u}_-$ to $\underset{\sim}{u}_+$. On a scale larger than x, $\beta x = X$ for example, this flame zone can be viewed as a discontinuity similar to a shock wave. These overall jumps are found in terms of the wave speed V from the solution for $\underset{\sim}{u}_1$, or equivalently from the small heat release version of the Rankine-Hugoniot relations. Denoting the overall jump in a quantity $\phi(x - x^*)$ by $\{\phi\} \equiv \phi(+\infty) - \phi(-\infty)$, these jumps are given by

$$\{v_1\} = -[V/(1 - \gamma V^2)]\{T_1\} = V\{\rho_1\} = [V/(1 - V^2)] \{Y_1\} = -Y_- V/(1 - V^2) \tag{9}$$

The detailed structure of the flame-zone is needed, however, to determine the flame-temperature, flame-speed relationship. The flame temperature, T_*, is assumed to be given as $1 + \beta t_*$, so that setting $T_1 = t_*$ at $x = x^*$ in the solution for $\underset{\sim}{u}_1$, described above, leads to the equation

$$t_* = T_- + Y_-/[1 + (\gamma - 1)V^2] . \tag{10}$$

V. QUASI-STEADY ANALYSIS. The unsteady solution developed in this paper requires that the flame behaves quasi-steadily in the manner described by (9) and (10). Hence, we restrict the disturbances applied to the flame-zone to those that vary sufficiently slowly, spatially and temporally, so as not to destroy the quasi-steady flame response. Therefore it is necessary to assume the outer hydrodynamic disturbances evolve on the slowly varying length and time scales $X = \beta x$ and $T = \beta t$.

Under this change of variable and by expanding $\underset{\sim}{u}_0$ as in (8), $\underset{\sim}{u}_1$ satisfies the linear wave equation

$$\underset{\sim}{u}_{1_T} + \underset{\sim}{C}_c \cdot \underset{\sim}{u}_{1_X} = 0 , \tag{11}$$

where $\underset{\sim}{C}_c = \underset{\sim}{C}(\underset{\sim}{u}_c)$. Equation (11) has a simple solution given by

$$u_1 = \sum_{i=1}^{4} f_i(\xi_i) r_i , \qquad \xi_i = X - \lambda_i T , \tag{12}$$

where λ_i and r_i are the eigenvalues and right eigenvalues satisfying

$$(C_c - \lambda_i I) \cdot r_i = 0 . \tag{13}$$

The eigenvalues are easily found to be $\lambda_1 = 1$, $\lambda_2 = -1$, $\lambda_3 = \lambda_4 = 0$, and the eigenvectors (as column vectors) are $r_1 = (1,1,\gamma-1,0)$, $r_2 = (1,-1,\gamma-1,0)$ $r_3 = (1,0,-1,0)$ and $r_4 = (0,0,0,1)$. From (12) it is easy to write out the components of u_1 in terms of f_i and vice-versa. Note that the solution for u_1 is a superposition of four traveling waves; $f_1(\xi_1)$ and $f_2(\xi_2)$ represent waves that travel at the sound speed to the right and left respectively, and $f_3(\xi_3)$ and $f_4(\xi_4)$ are stationary.

The solution for u_1 is determined by evaluating f_i. Prescribing the initial data u_1 at $T = 0$ is equivalent to specifying $f_i = F_i(X)$, (say), as seen from (12). If there is no flame present, (i.e., we are dealing with purely acoustic disturbances) then $f_i(\xi_i) = F_i(\xi_i)$. Now consider how the existence of a flame modifies this acoustic solution.

Let the flame location on the X scale be $X^*(T)$, where $\dot{X}^*(T) = V$. Note that the jumps in the components of u_1 imply jumps in f_i as well and are given by

$$\{f_1\} = -Vf_{4-}/[2(1-V)], \quad \{f_2\} = Vf_{4-}/[2(1+V)], \quad \{f_3\} = \{f_4\} = -f_{4-} \tag{14}$$

The initial data $F_i(\xi_i)$ is assumed to be arbitrarily given except that initially it must satisfy the flame-zone jumps (14). Construction of the solution for f_i when a flame is present will be illustrated by solving for $f_1(\xi_1)$.

At this point, and for the remainder of the paper, we will make the explicit assumption that the flame is propagating into an initially quiescent mixture. Also, we will assume that the flame is originally at the origin and that the initial flame speed is V_o. Note that for this example it is proper to set $f_{4-} = 1$; f_{4-} would be different from 1 if the mixture ahead was not initially quiescent. Then the initial data required for f_1, consistent with (14), has the form

$$F_1 = 0 \text{ for } X < 0, \; F_1(X) \text{ bounded for } X > 0, \text{ where } F_1(0^+) = -V_o/[2(1-V_o)]. \tag{15}$$

Consider the flame locus $X = X^*(T)$ as a monotonically increasing curve to the left, (say). For points (X,T) such that $X > T$ or $X < X^*(T)$, f_1 is assigned the initial value $F_1(\xi_1)$. However, in the region $T > X > X^*(T)$, the characteristic which passes through the point (X,T) also passes through the flame locus. See Figure 1. f_1 is then given by the value of f_1 on

the downstream side of the flame sheet, i.e., f_{1+}, which is simply calculated using the jump condition (14). Thus, for the region $T > X > X^*(T)$

$$f_1 = F_1(\xi_1) - V/[2(1 - V)] .\tag{16}$$

Thus, we have determined $f_1(\xi_1)$ once we are given the initial data for f_1 and know the location of the flame locus, $X = X^*(T)$. It is a simple matter to verify that similar arguments apply for f_2, f_3 and f_4 as well. The only restriction on the construction of this solution is that the flame locus never have characteristic slope, i.e.,

$$V = \dot{X}^* \neq \pm 1, 0 .\tag{17}$$

To determine the flame locus we note that equation (10) is a first-order ordinary differential equation for $X^*(T)$ which is to be solved subject to the initial condition $X^*(0) = 0$ (say). And for a particular initial-value problem it is necessary to evaluate T_- and Y_- in equation (10). By the definition of u_1 from equation (12) we find

$$Y_- = f_{4-} \quad \text{and} \quad T_- = (\gamma - 1)(f_{1-} + f_{2-}) - f_{3-}\tag{18}$$

and for our present example of initially quiescent upstream conditions

$$f_{1-} = f_{3-} = 0 \quad \text{and} \quad f_{4-} = 1 .\tag{19}$$

The only remaining unknown in (18), f_{2-}, is to be evaluated at $X = X^*(T)$ and is found in terms of V and $f_{2+} = F_2(X^*(T) + T)$ from the jump condition in equation (14). The differential equation for the flame speed becomes

$$t_* = (\gamma - 1)\{F_2(X^* + T) - \dot{X}^*/[2(1 + \dot{X}^*)]\} + 1/[1 + (\gamma - 1)\dot{X}^{*2}] .\tag{20}$$

Note that since initially $\dot{X}^* = V_o$ and $F_2(0_+) = V_o/[2(1 + V_o)]$, t_* and V_o are related by the steady result (10) as expected.

It is important to emphasize that equation (20) and the conclusions drawn from it apply specifically for flame propagation into an initially quiescent atmosphere. However, it is possible to treat many other initial value problems in a similar way by simply reevaluating T_- and Y_- in equation (10).

VI. AN EXAMPLE. In this section we present the results of integrating equation (20) and the subsequent determination of u_1 for a particular initial downstream disturbance. We examine the case where initially far downstream of the flame the burnt gas is motionless, at the quiescent temperature but at a different pressure, i.e.,

$$v_1 = T_1 = Y_1 = o(1) \quad \text{and} \quad p_1 \equiv \rho_1 + T_1 = p_\infty + o(1) \quad \text{as } X \to \infty.\tag{21}$$

For purposes of illustration let the initial downstream disturbance $(X > 0)$ be given by

$$F_1 = - V_o/[2(1 - V_o)] + \{p_\infty/2\gamma + V_o/[2(1 - V_o)]\}\ g(X)\ ,$$

$$F_2 = V_o/[2(1 + V_o)] + \{p_\infty/2\gamma - V_o/[2(1 + V_o)]\}\ g(X)\ ,$$

$$\text{(22)}$$

$$F_3 = - 1 + [p_\infty(\gamma - 1)/\gamma + 1]\ g(X)\ ,\quad F_4 = 0\ ,$$

where $g(X) = 1 - \exp(-X)$.

The result of integrating (20) for $\gamma = 1.4$, $V_o = -.1$ and $p_\infty = -1$ is shown in Figure 2 and the profiles for ρ_1, v_1, T_1, Y_1 and p_1 are evaluated at times $T = 1, 2.5, 5$ and 10 and are shown in Figures 3 through 7 respectively.

The first thing to notice is that a negative pressure gradient downstream causes the flame to accelerate. It is a simple matter to calculate the final speed of the wave $X^*(\infty)$ in terms of $p_\infty = 2\gamma\ F_2(\infty)$ directly from (20); the result is shown in Figure 8. As p_∞ becomes more negative, the flame accelerates towards sonic velocity. This effect can be understood in terms of a Rankine-Hugoniot diagram which clearly shows that as the pressure drop across the flame becomes more negative, the mass flux and, hence, the flame velocity must increase. This conclusion is the direct consequence of the quasi-steady assumption.

VII. SHOCK FORMATION. It is well known that the rapid acceleration of a flame acts as a piston and causes compression of the unburnt gases upstream of the flame. For our example the compression upstream of the flame-zone is clearly shown in Figure 7. Ultimately the piston effect of the flame-zone leads to the development of a precursor shock wave which must be described by taking into account the convective steepening in the hydrodynamic regions outside the flame zone.

The precursor shock wave can be described if we assume that the disturbance evolves on the long time scale $\tau = \beta T$. Assuming a traveling wave solution of the form

$$u_o = u_c + \beta\ f_2(\xi_2, \tau) r_2 + \beta^2\ g(\xi_2, T, \tau) r_2 + \cdots\ ,\tag{23}$$

and the expansions

$$C(u) = C_c(u_c) + \beta\ C_1(f_2) + \cdots\ ,\quad D = D_c(u_c) + \cdots\ ,\tag{24}$$

we find that g must satisfy

$$g_T r_2 = - f_{2\tau} r_2 - C_1 \cdot r_2 f_{2X} + D_c \cdot r_2 f_{2XX} \qquad (25)$$

To obtain a scalar equation for g_T we multiply (24) by ℓ_2, where ℓ_2 satisfies

$$\ell_2 \cdot (C_c + I) = 0 \quad \text{and} \quad \ell_2 \cdot r_2 = 1 . \qquad (26)$$

In order to suppress the secularity that otherwise develops in g we must require that the right hand side of (25) vanishes. That requirement implies that

$$f_{2\tau} - [(\gamma + 1)/2] f_2 f_{2\xi_2} = (\gamma/2) f_{2\xi_2 \xi_2} \qquad (27)$$

which is Burger's equation for the evolution of f_2.

To obtain the initial data for f_2 we examine the region in the X,T plane where the focusing of characteristics caused by the flame takes place, namely, $X < X^*(T)$. This region can be further divided into two regions $X < -T$ and $-T < X < X^*(T)$. In the region $X < -T$, $\xi_2 < 0$ and by choosing any non-characteristic path (starting from the origin) we can evaluate f_2 for $\xi_2 < 0$. A convenient path, of course, is $T = 0$, $X < 0$; the initial data for f_2 when $\xi_2 < 0$ is $F_2(\xi_2)$. Note that for our specific example $F_2(X) = 0$ for $X < 0$. In the region $-T < X < X^*(T)$, $\xi_2 > 0$, and we can similarly choose any non-characateristic path on which to evaluate $f_2(\xi_2)$. The simplest choice is the flame locus $X = X^*(T)$; each point on the flame locus is assigned a value of $\xi_2 = X^*(T) + T$ and f_2 is then given by $f_{2-}(\xi_2)$, a function which has been calculated in the course of solving for u_1 in Section V. This data then forms the initial data for f_2 on $\tau = 0$ in the (ξ_2, τ) plane. Thus equation (27) is to be solved subject to

$$f_2 = F_2(\xi_2) \quad \text{for} \quad \xi_2 < 0 \quad \text{and} \quad f_2 = f_{2-}(\xi_2) \quad \text{for} \quad \xi_2 > 0 . \qquad (28)$$

The result of calculating f_2 according to (28) for the example of Section VI is shown in Figure 9.

In the usual analysis of weak shocks an additional length scale, characteristic of the disturbance at hand, is introduced. Typically, δ^{-1} represents the non-dimensional length that measures the maximum initial fluid velocity of the hydrodynamic disturbance divided by the maximum initial velocity gradient. Letting $\hat{\xi} = \delta \xi_2$, $\hat{\tau} = \delta \tau$ in equation (26) allows us to replace (26) with the nonlinear wave equation

$$f_{\hat{\tau}} - (\gamma + 1)/2 f f_{\hat{\xi}} = 0 . \qquad (29)$$

This equation has a simple characteristic solution (see Whithan (1974)) that shows that the time of breaking, or initial formation of the shock caused by the flame acceleration, is given by

$$\hat{\tau}_B = 2/(\gamma + 1)|F_2'(\hat{\xi}_B)| , \tag{30}$$

where $\hat{\xi}_B$ corresponds to the characteristic where $|F_2'(\hat{\xi}_B)|$ is maximum for the initial data and $F_2'(\hat{\xi}_B) > 0$. For our example $|F_2'(\hat{\xi}_B)|$ is maximum at $\hat{\xi}_B = 0$ and has the value .25. Thus the time of breaking is estimated to be $\tau = .33$. If desired, an entire shock trajectory may be calculated by standard shock fitting.

REFERENCES

1. Buckmaster, J. & Ludford, G.S.S. 1981, _Theory of Laminar Flames_, Cambridge University Press (to appear).

2. Fickett, W. & Davis, W.C. 1979, _Detonation_, University of California Press.

3. Lu, G.C. & Ludford, G.S.S. 1981, Asymptotic analysis of plane steady detonations. _SIAM J. Appl. Math._ (to appear).

4. Stewart, D.S. 1981, _The Transition from Deflagration to Detonation_. Ph.D. Thesis, Cornell University.

5. Stewart, D.S. & Ludford, G.S.S. 1982, Fast deflagration waves (in review).

6. Whitham, G.B. 1974, _Linear and Nonlinear Waves_, Wiley & Sons.
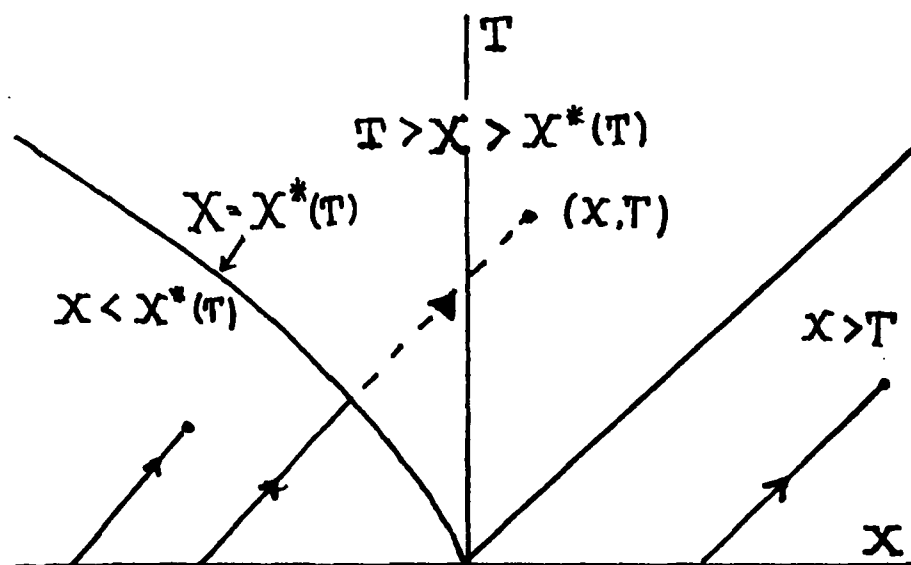
Figure 1. Characteristic plane for the solution of $f_1(\xi_1)$. Solid lines represent characteristics that carry f_1 with initial values. Dotted lines require evaluation of f_1 at the flame locus.
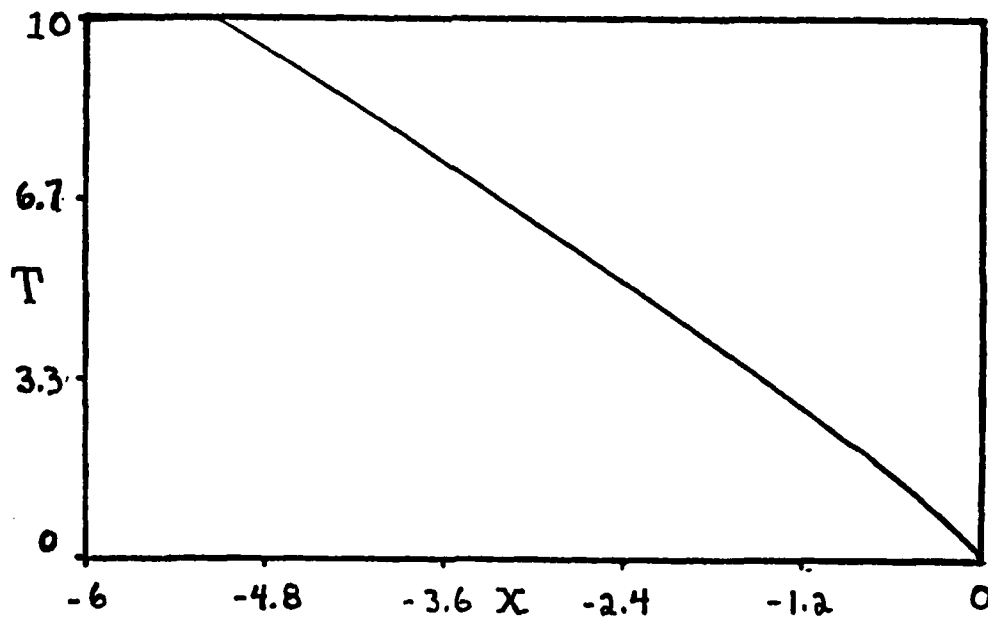
Figure 2. Result of integrating (20) for the example in Section VI.
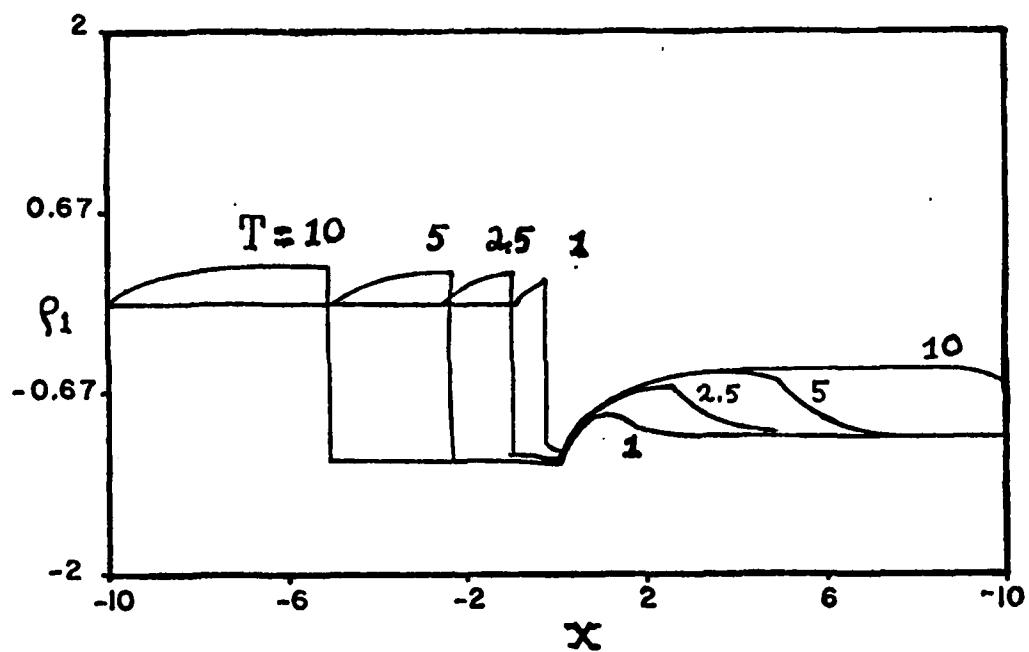
Figure 3. Density profile ρ_1 for times $T = 1, 2.5, 5$ and 10, for the example in Section VI.
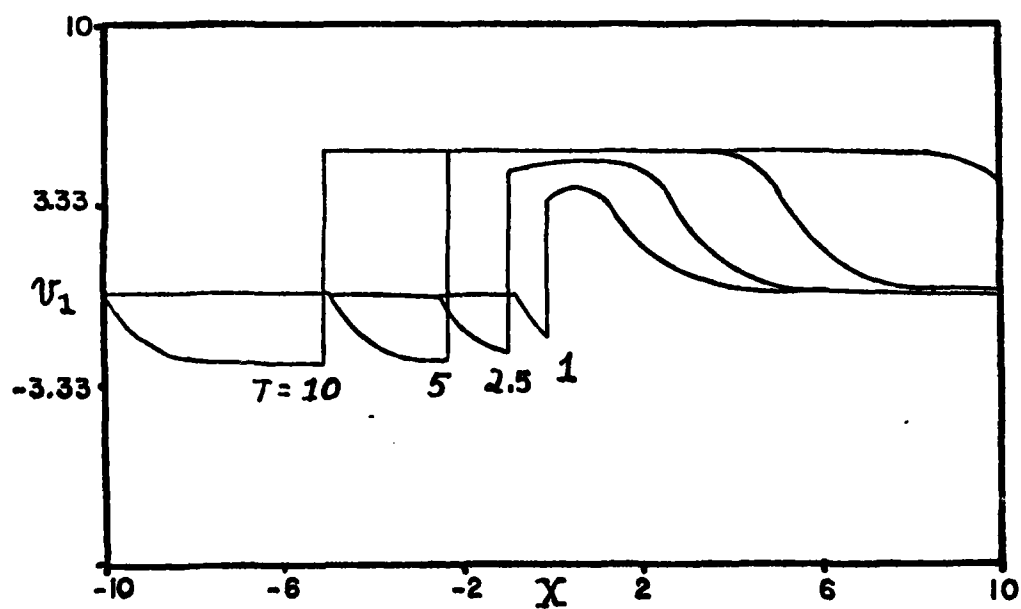
Figure 4. Velocity profile v_1 for times $T = 1, 2.5, 5$ and 10, for the example in Section VI.
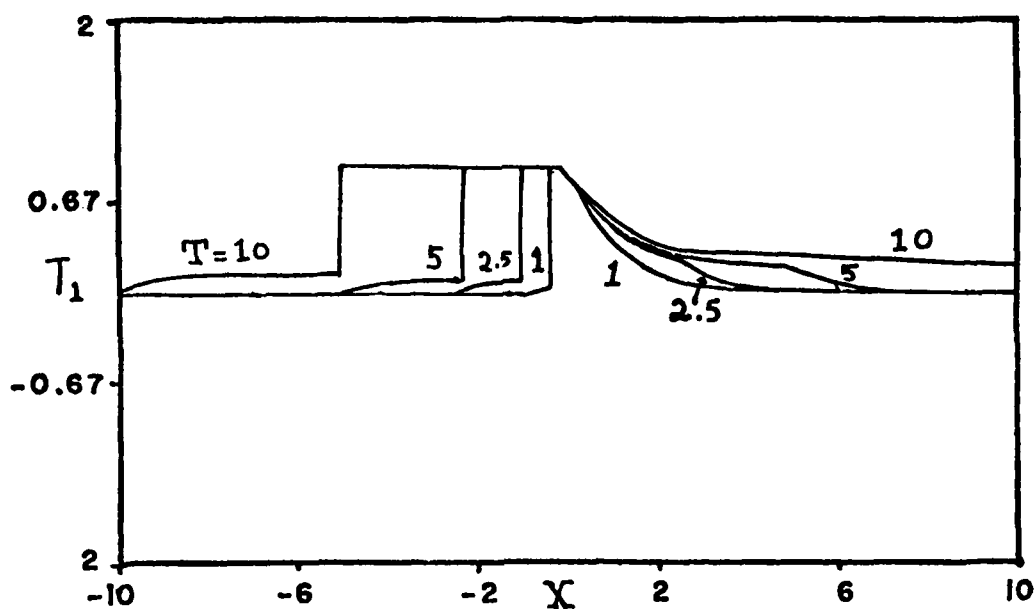
Figure 5. Temperature profile T_1 for times $T = 1, 2.5, 5$ and 10, for the example in Section VI.
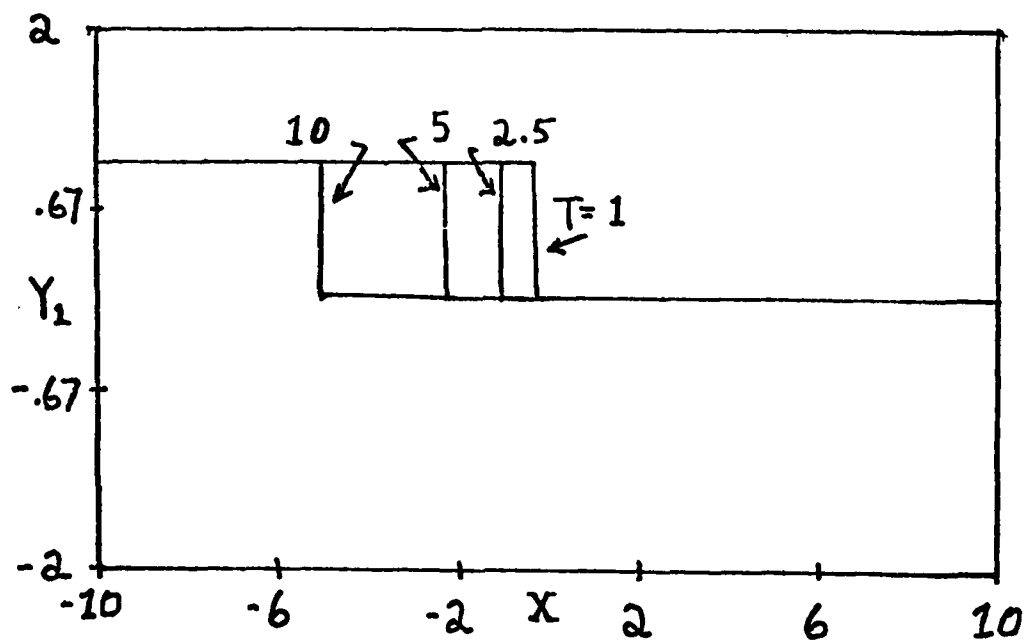
Figure 6. Fuel fraction profile Y_1 for times $T = 1, 2.5, 5$ and 10, for the example in Section VI.
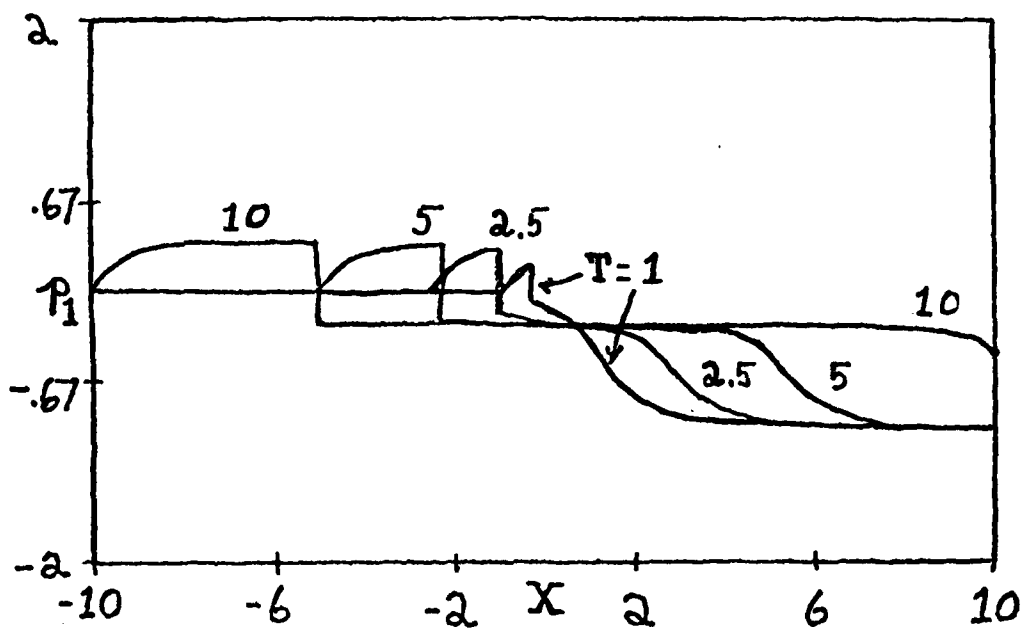
Figure 7. Pressure profile p_1 for times $T = 1, 2.5, 5$ and 10, for the example of Section VI.
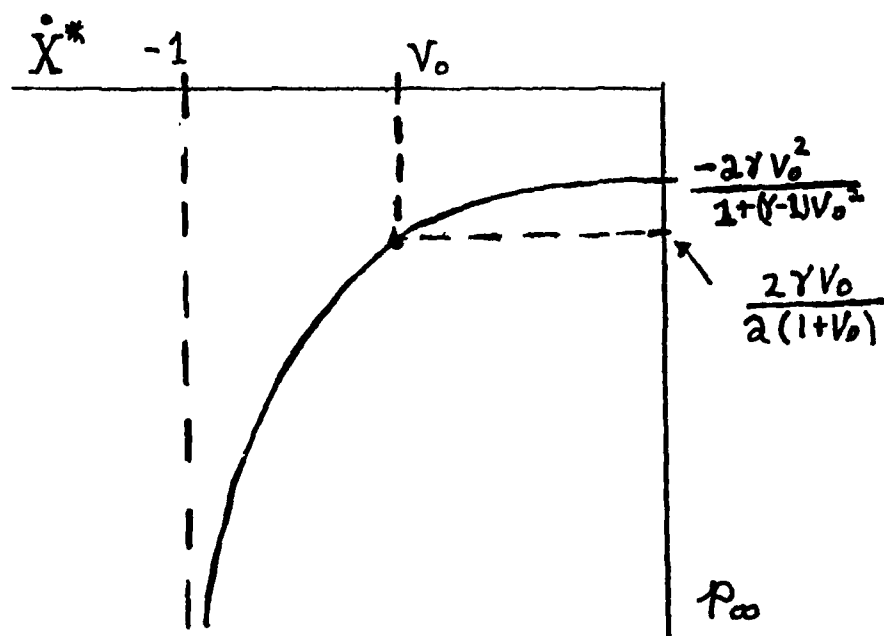
Figure 8. Sketch of p_∞ versus $\dot{X}^*$ derived from equation (20).
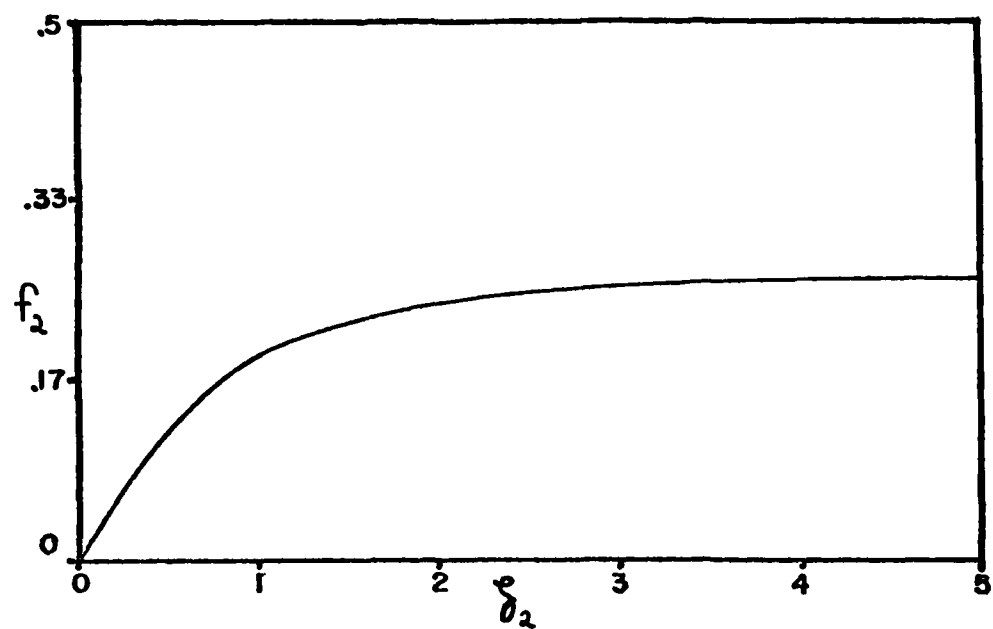
Figure 9. The initial data (28) for the example of Section VI. Note $f_2 = 0$ for $\xi_2 < 0$.

CYCLIC PLASTICITY AHEAD OF A BLUNT CRACK

Dennis M. Tracey and Colin E. Freese

Mechanics and Engineering Laboratory
Army Materials and Mechanics Research Center
Watertown, Massachusetts

ABSTRACT. Results are given for the elastic-plastic stress and strain states which develop ahead of a cracklike elliptical flaw isolated within an unbounded plane strain tension field. A finite element-boundary collocation formulation was employed to obtain the numerical results. Comparisons are made with elastic and fully plastic stress predictions and these provide guidelines to the range of applicability of these theories. Plastic zone growth is discussed and also the stress variation which occurs during load cycling. The sensitivity of solution to element capability to accommodate near-incompressible deformation was tested and, by comparison with slipline results, the four-triangle quadrilateral was found to provide highly accurate results.

INTRODUCTION. We are concerned with the details of stress and deformation in the material immediately ahead of a blunt-tipped, cracklike flaw. In our analysis, we have employed the non-hardening *Prandtl-Reuss constitutive theory and* have considered problems of plane strain. An elliptical shaped flaw was considered as buried in an infinite domain, with a uniform remote stress T directed perpendicular to the flaw's major axis. For general applicability, results are given in dimensionless form. The stress data is normalized by the yield stress Y, strain data is normalized by the simple tension yield strain Y/E and distance scales are normalized by either the flaw half length, a, or the flaw root radius, ρ.

The elastic-plastic results have been generated for the elliptical flaw with a/ρ ratio of 1000 (major to minor axis ratio of 31.6). Fully plastic results have been obtained for a set of large aspect ratio cracklike elliptical flaws. The elastic solution to these problems is available in analytical form. We have compared the elastic, elastic-plastic and fully plastic results with the goal of establishing when, in the load history, the slipline result holds near the flaw surface and when, away from the surface, the elastic results become unrepresentative.

We have described the elastic-plastic numerical formulation in a previous report, Ref. (1), along with preliminary results for the cracklike ellipse problem. Finite elements are used to model the nonlinear behavior and beyond the finite element mesh the solution is represented by elastic stress functions. The finite element mesh surrounds the flaw root, Fig. 1, and extends a distance of 8ρ ahead of the root in the analysis that was performed. In the computations, symmetry conditions were invoked so that only the upper part of the mesh illustrated in Fig. 1 was used. Results over a smaller finite element region extending 4ρ ahead of the root were discussed in Ref. (1). Since elastic stress functions are used to represent the solution beyond Γ, load incrementation in the elastic-plastic analysis must be terminated when the plastic zone reaches Γ. This occurred at a load level of $T = 0.12\ Y$ for the problem of Fig. 1.

Complex variable techniques involving conformal mapping and analytic continuation were employed in establishing the elasticity equations governing beyond Γ, following the work of Bowie and Freese, Ref. (2). The elliptical flaw in the physical plane is mapped onto the unit circle $|\zeta| \leq 1$ in an auxiliary ζ-plane. The simple circular shape allows conditions to be formulated which implicitly satisfy the traction free condition on the flaw surface $|\zeta| = 1$. A single analytic stress function ϕ then governs over the entire ζ-plane and it was chosen to have the following approximate form:

$$\phi = \Delta T\ [(a+b)\zeta - (3a+b)/\zeta]/8 + \sum_{n=1}^{15} \alpha_n\ \zeta/(\zeta^2-1)^n$$

The first term is the exact elastic solution corresponding to a remote load increment ΔT, for a flaw with semi-axes a and b. This elastic solution is expected to be adequate far from the plastic zones. As the plastic zone is approached, the elastic solution will become less and less meaningful, hence the choice of a negative power series expanded about the flaw ends $\zeta = \pm 1$ to complete the approximate representation of the unknown function ϕ. With real coefficients α_n, the remote stress condition and the symmetry conditions are satisfied by this stress function.

The conventional collocation approach employs truncated power series approximations for the governing stress function(s) and establishes the undetermined coefficients from known data at distinct boundary locations. Here the coefficients

are determined in conjunction with the finite element unknowns. The two sets of unknowns are coupled by conditions of equilibrium and compatibility at the nodal locations on the boundary Γ. Force increments acting on the Γ nodes, which represent the load transfer across Γ, are expressed in terms of ΔT, α_n and likewise displacement increments of these nodes are expressed in terms of ΔT, α_n. By eliminating the interior nodal degrees of freedom from the finite element stiffness equation, a system of equations in α_n is established. As is characteristic in collocation analysis, the system is overdetermined and solution is by least squares. Whereas 15 coefficients appear in the stress function, there are 53 nodal degrees of freedom along Γ. Overall, there are 608 finite element degrees of freedom. With α_n determined, the nodal displacement increments and then strain and stress increments are determined throughout the finite element mesh. The value of ΔT at each step in the incrementation is adaptively established to accurately trace the spread of plasticity and flow rule changes in the finite element region, Ref. (3).

An important consideration in the finite element formulation is the ability of the network of elements to accommodate the near-incompressible deformation that will develop in the highly strained root region. Nagtegaal et. al., Ref. (4), have demonstrated that a mesh of four node quadrilaterals each of which is subdivided by its diagonals into four constant strain triangles can represent a non-homogeneous pure incompressible deformation field, while the four node bi-linear isoparametric quad cannot. For a given problem, it is not possible to a priori establish when in the loading history the near-incompressible state will be achieved and thus predict when this modeling facet will become significant. To establish when the effect is important for our problem, we obtained two separate solutions. In one analysis, the quads of the mesh shown in Fig. 1 were considered to be four node isoparametric elements. In the other, the quads of the mesh were subdivided into triangles. We found significant differences at the load levels reached and were able to quantify errors by comparing against slipline stress predictions. Before discussing the elastic-plastic results we will first describe the numerical procedure used to establish the slipline solution to our problem.

SLIPLINE ANALYSIS OF ELLIPTICAL FLAWS

Slipline analysis provides the stress state which is asymptotically approached as the deformation becomes predominantly plastic during load increase. Although the slipline solution gives the limiting stress state, elastic-plastic analysis is necessary to establish when the slipline result is effectively achieved. When the elastic strain is neglected as in slipline theory, the equilibrium equations and yield condition constitute a set of hyperbolic equations governing the variation of the stress components σ_{xx}, σ_{xy}, σ_{yy}. Hill (5) classifies our problem of developing the stress field ahead of the flaw from the known fully plastic stress state along the flaw surface (tangential stress equals $2Y/\sqrt{3}$) as a Cauchy problem. Solutions are obtained by utilizing the relationships which hold along the sliplines (maximum shear directions), the characteristics of the problem.

In our analysis, we employed the Hencky equations which govern the slipline stress variations. The equations involve the mean normal stress σ_m and the angle ψ which the α-slipline makes with the x-axis (CCW positive). Of course, both σ_m and ψ are functions of position, and knowledge of these variables is sufficient to determine the stress components at a point. The convention used to distinguish the α and β-sliplines has the α-line clockwise 45 degrees from the maximum principal stress direction. The Hencky stress conditions holding along the α and β-lines are given in terms of the constants C_1 and C_2 as follows:

$$\sqrt{3}\ \sigma_m - 2\ Y\ \psi = C_1 \text{ along an } \alpha\text{-line}$$

$$\sqrt{3}\ \sigma_m + 2\ Y\ \psi = C_2 \text{ along a } \beta\text{-line}$$

Both stress parameters are known on the flaw surface: σ_m equals $Y/\sqrt{3}$ and ψ follows from the fact that sliplines intersect free surfaces at 45 degrees. The numerical algorithm for developing the slipline field ahead of the flaw starts with selecting a finite number of stations on the flaw surface and computing C_1 and C_2 at each. Using C_1 and C_2 from adjacent stations, the Hencky equations are simultaneously solved for σ_m, ψ which gives the stress solution at the location in the domain where the C_1 α-line and the C_2 β-line intersect. An approximate slipline network is constructed by following this procedure in a step-by-step fashion, progressing deeper into the domain at each step. A final aspect of the computation is to establish the (x,y) location of the slipline

intersections making up the network. This is done by computing the intersection of chordal approximations to the slipline arcs by using the average slopes from the previously determined nodal ψ values. Symonds (6) suggested this method of slipline construction in 1949 and, coincidently, he used elliptical cutouts as demonstration problems. Graphical tools were required then to make the construction manageable, as the number of arithmetic operations are too great for manual calculation. By necessity, he limited his analysis to small aspect ratio ellipses. We computerized his algorithm and obtained results for a set of cracklike elliptical flaws.

The slipline stress distribution for the various flaws considered are plotted in Fig. 2. Considering crack length fixed, the figure demonstrates the effect of flaw root acuity on the stress magnitude at locations out to a distance of 0.01a ahead of the flaw. Excepting the sharp crack case, $a/\rho = \infty$, the value of σ_{yy} at the root is always equal to 1.15 times the yield stress and, as can be seen, the stress gradient increases with acuity ratio a/ρ. The sharp crack has the root value of 2.97 $Y = (2+\pi)Y/\sqrt{3}$ and this value remains fixed ahead of the crack, corresponding to the constant state region of the Prandtl slipline field. The blunt tipped flaws have distributions which approach the Prandtl value over the size scale plotted. For elliptical flaws this value is achieved only when plasticity has progressed to encompass the entire crack. For the 1000/1 flaw, the Prandtl value would be realized very far from the root, at x = 2.06a. If distance is normalized by the root radius, the stress distribution for all cracklike ellipses blend into one over the 8ρ range used in our finite element analysis. We have generated results which show this to be true for a/ρ greater than 100. This single representative distribution is given in Fig. 4. The manner in which the root region stress field evolves into the limiting slipline prediction will be considered after the following discussion of the plastic zone growth.

ELASTIC PLASTIC RESULTS

Growth of Plastic Zone

The nature of our elastic-plastic formulation is such that incrementation of the remote tension must be terminated when the plastic zone spreads to the modeling interface Γ, Fig. 1. The zone had spread to within one finite element of Γ at a T value of 0.12 Y. The elastic-plastic boundary at this peak load and at 0.045 Y and 0.09 Y are illustrated in Fig. 3. In the very early stages of loading, the boundary tends to parallel the flaw surface and the dimension of the plastic zone along the surface exceeds the maximum depth into the material. Sharp crack solutions suggest that the zone will eventually take a "butterfly" shape, with the maximum distance of the elastic-plastic boundary from the crack tip at an angle of roughly 70 degrees from the symmetry axis. The boundaries shown in the Figure suggest that the zone is indeed approaching this crack zone shape.

It is useful to contrast these results with the crack solutions of Rice and Tracey (7) and Larsson and Carlsson (8). The former is a general small scale yielding solution following from an analysis which set remote boundary conditions according to the leading term of the elastic singular solution. The latter is a specific small scale yielding solution for a center cracked tension plate (with crack length one-half the plate width). Results for both solutions are given in terms of the length parameter $(K/Y)^2$, which equals $\pi a (T/Y)^2$ for an isolated tension crack, $a/\rho = \infty$. For the load T = 0.12 Y, the angle of maximum plastic zone extent is very close to the 65 degree angle found by Larsson and Carlsson for their problem. It would be of interest to determine how the angle changes with further loading. The Rice and Tracey asymptotic solution has the maximum extent at 71 degrees from the x-axis. At T = 0.12 Y, this maximum distance (r_p^{max}) from the root tip (x=a) to the elastic-plastic boundary is equal to 7.6ρ or 0.0076 a. There is substantial difference in the sharp crack predictions. At our peak load level, the two solutions bound the result for the cracklike ellipse:

$$r_p^{max} = .15 \ (K/Y)^2 = .0065 \ a \qquad \text{Ref. (7)}$$

$$r_p^{max} = .23 \ (K/Y)^2 = .010 \ a \qquad \text{Ref. (8)}$$

The differences in the crack solutions have been attributed to the constant valued non-singular term in the crack tip expansion for the stress component σ_{xx}. This term was not included in the asymptotic analysis reported in Ref. (7). Both crack plastic zone results have the maximum extent far exceeding the extent along the x-axis. This result is anticipated for our problem once the plastic zone dimensions become large compared to root radius, at which point the flaw shape does not significantly influence the solution at the elastic-plastic boundary.

Stress Ahead of Flaw

We have discussed the slipline solution to our problem and have noted that while slipline theory provides the limiting stress state in monotonic loading, elastic-plastic analysis is required to establish how stress varies with load prior to attaining its fully plastic value. Here of course we are considering the solution at points within the plastic zone. Another consideration is the solution in the unyielded region. It is of interest to establish how the elastic-plastic results for this region deviate from the predictions of elastic analysis at different load levels.

Comparisons have been made and are plotted at T values of 0.06, 0.09 and 0.12 Y in Fig. 4. The data show that as load increases the slipline state is achieved over an expanding region, corresponding to the growth of the plastic zone. From a numerical accuracy viewpoint, the agreement of the elastic-plastic results with the slipline result is exceptionally good. It is worth noting that at any particular load level the slipline result holds only over a portion of the plastic zone, the portion which has plastic strain levels far in excess of elastic strain. The elastic-plastic results are seen to rapidly approach the elasticity solutions. Deviations drop to within 10% at distances roughly three times the x-axis plastic zone dimension.

In our previous report, Ref. (1), we discussed the near root stress solution for a cyclic variation of load. We found that the method of plastic super-position, Ref. (9), provides very accurate estimates of the solution after load reversal. With the method, all that is required is the monotonic solution. We have used the method to generate the residual stress state after unloading from the load value of 0.12 Y. This residual state is plotted in Fig. 5 along with

the distributions for the intermediate load level 0.06 Y and peak load. The residual state is simply computed as the state at peak load minus twice the state at intermediate load. Another result verified in the previous work is that the cyclic plastic zone is essentially the same as the yielded region at the intermediate load level in monotonic loading.

Solution Sensitivity to Element Interpolation

The results discussed above were obtained with the four-triangle quadrilateral finite element mesh. At the stress level T = 0.12 Y, the significant differences between that solution and the one following from the bilinear quads occurred within a distance of one root radius from the flaw root, a distance approximately one-third the x-axis plastic zone extent. It was in this region that plastic strain far exceeded elastic strain magnitudes. Of course, as the elastic-plastic boundary is approached, the magnitudes become comparable and differences caused by near-incompressible deformation are not expected. The solution differences were greatest at the flaw surface and comparisons of results for the first quadrilateral element bordering the x-axis are shown in Figs. 6 and 7.

The numerical results for the variation of σ_{yy} at this near root location during load increase is displayed in Fig. 6 along with the slipline result. The element spans the region $0 \le (x-a) \le 0.187\rho$, so the slipline result $(\sigma_{yy} = 1.258$ Y) chosen for comparison corresponds to the solution at $(x-a,y) = (.0935\rho, 0)$. The data for the constant state triangle with base along the x-axis represents one solution, while the average stress data for the two Gauss stations nearest the x-axis represents the other. The bilinear quad solution is seen to rise above the slipline result very early in the loading and the deviation grows with load at an increasing rate. In contrast, the four-triangle quad solution quickly levels off to a value 1.251 Y and remains there; step to step changes are in the fifth significant figure. It would be of interest to establish how this result might change with further loading.

The excellent agreement found with slipline theory, displayed in Fig. 6 and earlier in Fig. 4, is ample justification for claiming high accuracy for our solution using the four-triangle quads. Certainly, the data show that the ability to model near-incompressible deformation is essential to our problem at

very low load levels, and thus the isoparametric element should not be used for problems in this class. The differences in the solution for the equivalent plastic strain using the data from the first element ahead of the root are shown in Fig. 7. The strain levels using the triangles exceed those using the bilinear element over the entire loading history. At peak load there is an 18 percent difference in the solutions and the trend suggests that the differences will be more pronounced with further loading.

Data displaying the spatial gradient of equivalent plastic strain over a one root radius distance ahead of the flaw is given in Fig. 8. Results are given for T/Y levels of 0.06, 0.09, and 0.12. The plastic strain at T = .06 Y is seen to fall to a value below the yield strain at x-a = ρ, corresponding to the fact that the elastic-plastic boundary is then at x-a = 1.2ρ. The accelerated strain intensification during load elevation that is displayed in Fig. 7 is also evidence in Fig. 8. At the load levels represented, extrapolation gives surface plastic strain values of 6.2, 13.6, and 26.7 times the yield strain. These results suggest local to global strain concentration factors of 103, 151, and 223 for the respective load levels, in contrast to the concentration factor of 64 suggested by the elastic solution to our problem.

REFERENCES

1. D. M. Tracey and C. E. Freese, "Cyclic Stress-Strain Behavior Near A Narrow Elliptical Flaw," in Proc. 26th Conf. Army Mathematicians, ARO Report 81-1, 1981.

2. O. L. Bowie and C. E. Freese, "Analysis of Notches Using Conformal Mapping," in Mechanics of Fracture, Vol. 5, Stress Analysis of Notch Problems, ed. G. C. Sih, Noordhoff, 1978.

3. D. M. Tracey and C. E. Freese, "Adaptive Load Incrementation in Elastic-Plastic Finite Element Analysis," Computers and Structures, Vol. 13, 45-53, 1981.

4. J. C. Nagtegaal, D. M. Parks, and J. R. Rice, "On Numerically Accurate Finite Element Solutions in the Fully Plastic Range," Comp. Meths. Appl. Mech. Engrg., Vol. 4, 153-177, 1974.

5. R. Hill, The Mathematical Theory of Plasticity, Oxford Univ. Press, London, 1950.

6. P. S. Symonds, "The Determination of Stresses in Plastic Regions in Problems of Plastic Flow," Jour. App. Phys., Vol. 20, 107-112, 1949.

7. J. R. Rice and D. M. Tracey, "Computational Fracture Mechanics," in Num. and Computer Methods in Struc. Mechs., eds. S. J. Fenves et. al., 585-623, Academic Press, N.Y., 1973.

8. S. G. Larsson and A. J. Carlsson, "Influence of Non-Singular Stress Terms on Small Scale Yielding at Crack Tips in Elastic-Plastic Materials," Jour. Mechs. Phys. Solids, Vol. 21, 263-277, 1973.

9. J. R. Rice, "Mechanics of Crack Tip Deformation and Extension by Fatigue," in Fatigue Crack Propagation, ASTM STP 415, 1967.
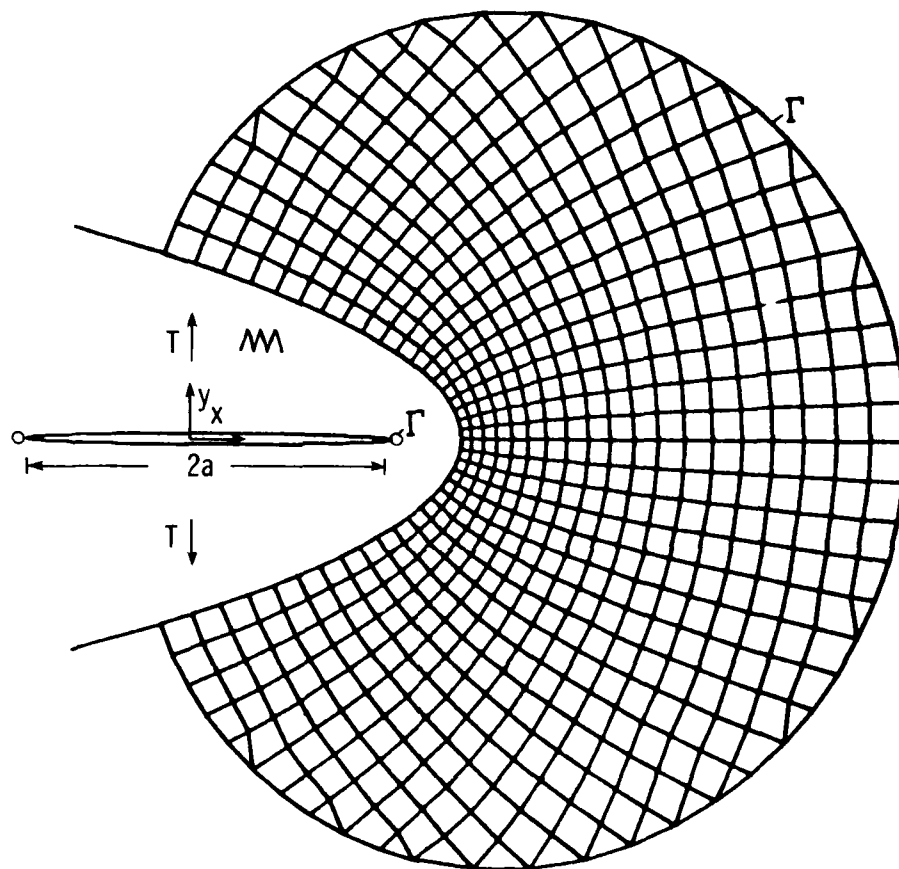
Figure 1.   Cracklike Elliptical Flaw and Enlarged Root Region
with Finite Element Mesh.
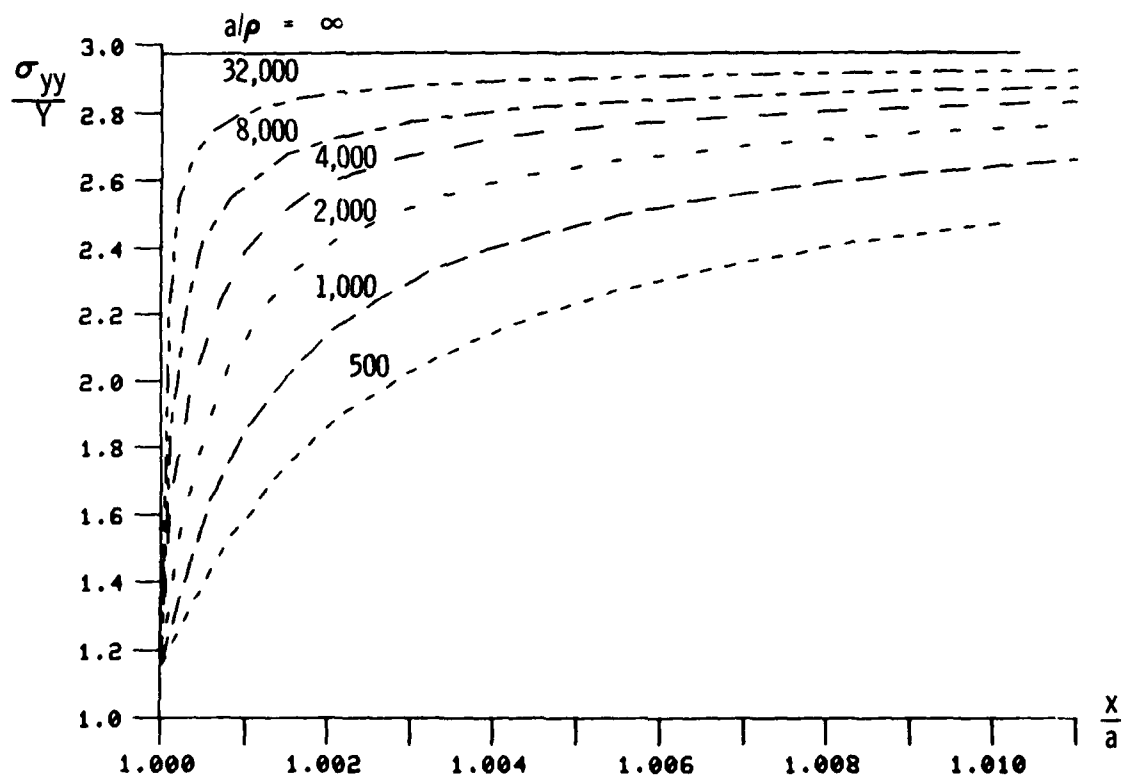
Figure 2. Near Tip Slipline Stress Distribution for Set of Cracklike Elliptical Flaws.
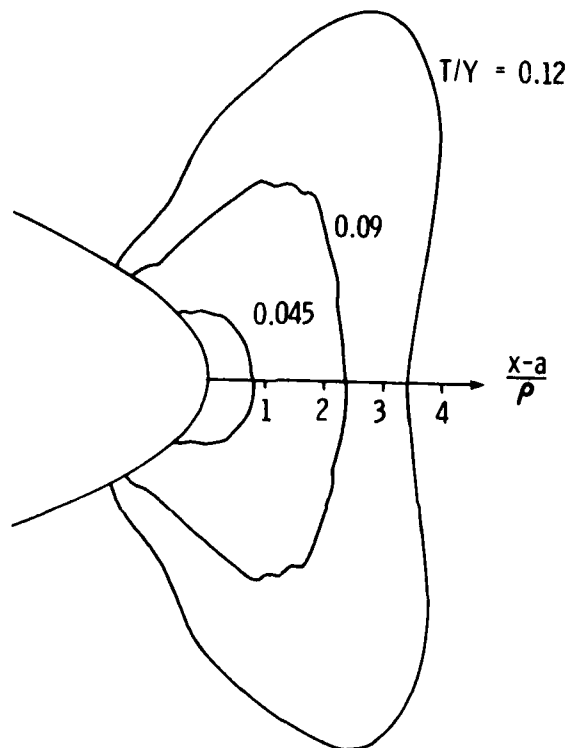
Figure 3. Elastic-Plastic Boundaries at
Three Load Levels in Monotonic Loading.
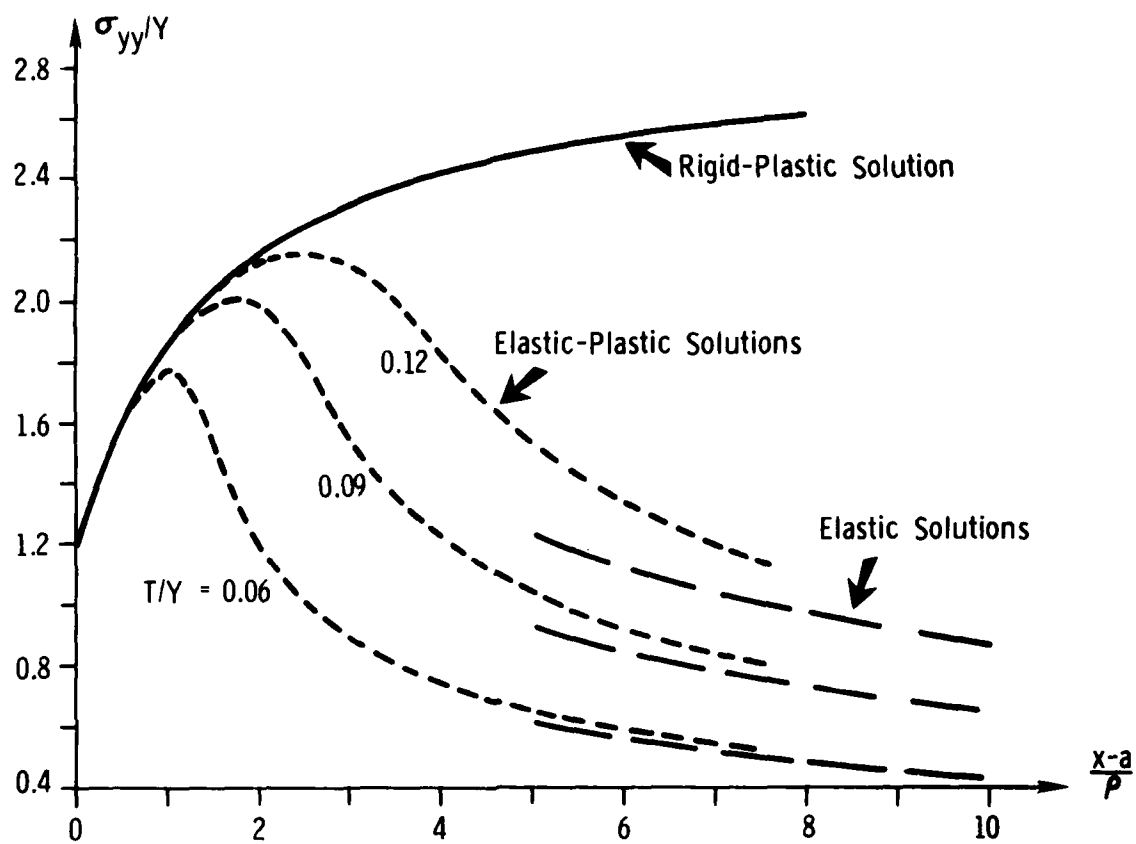
Figure 4. Elastic-Plastic, Rigid-Plastic and Elastic Near Tip Stress Solutions.
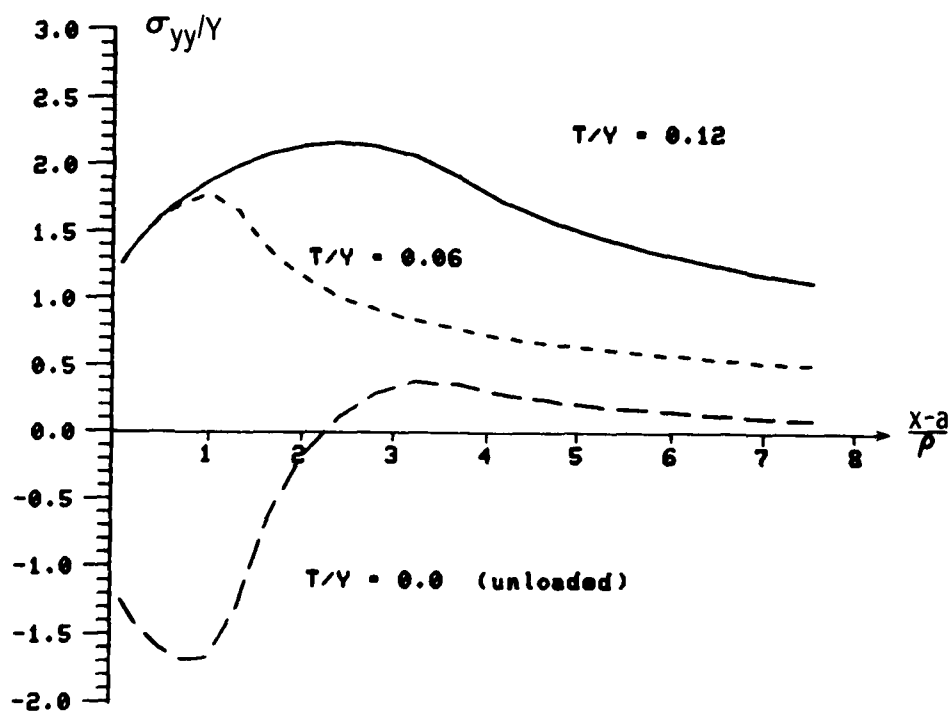
Figure 5. Near Tip Stress Variation at $T_{max}/2$, T_{max} and $T = 0$, Using Plastic Superposition.
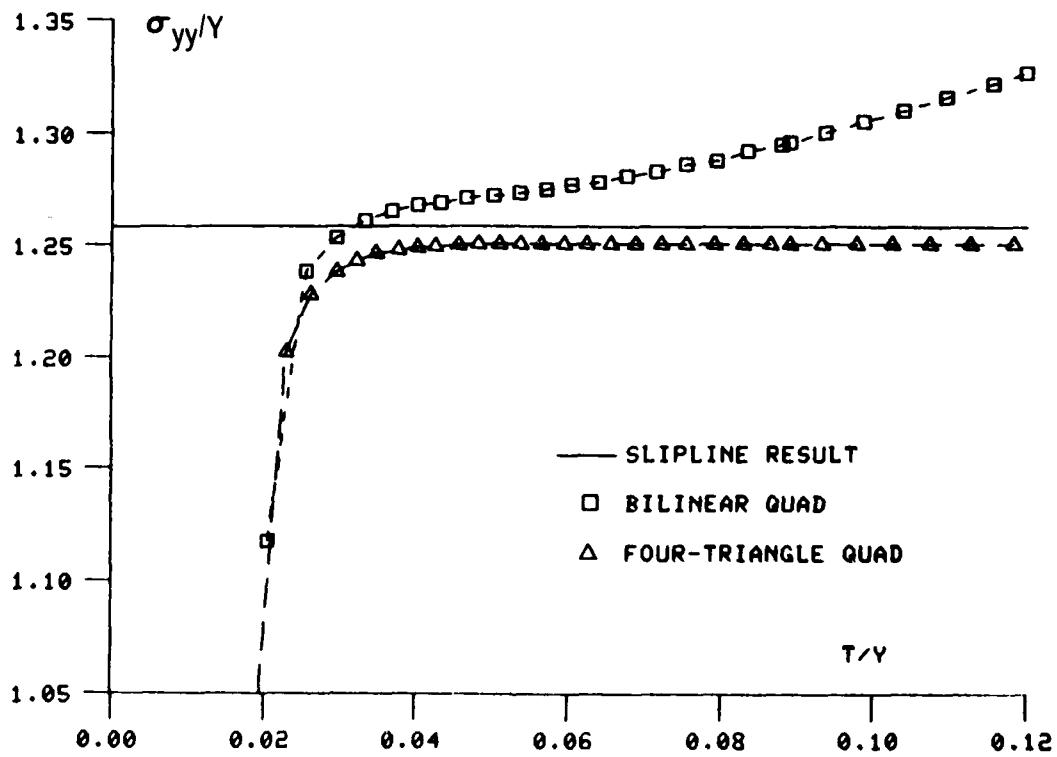
Figure 6. Stress History at a Location with a Near-Incompressible Deformation History.
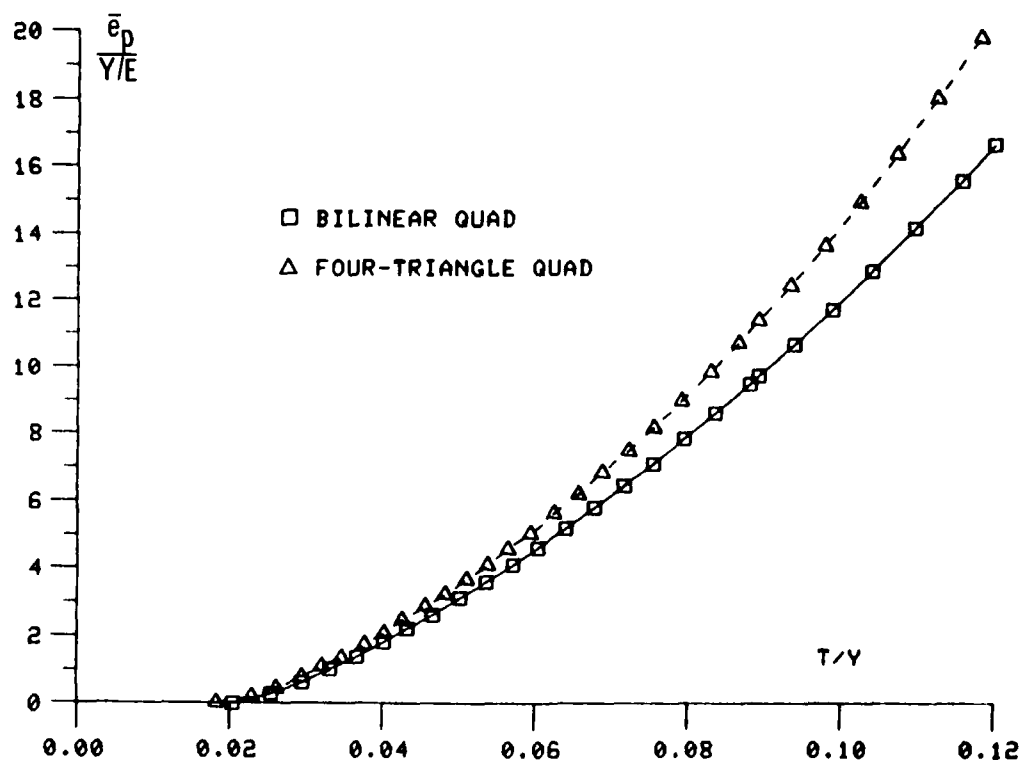
Figure 7. Data Showing Dependency on Element Type of Plastic Strain at a Near Tip Location.
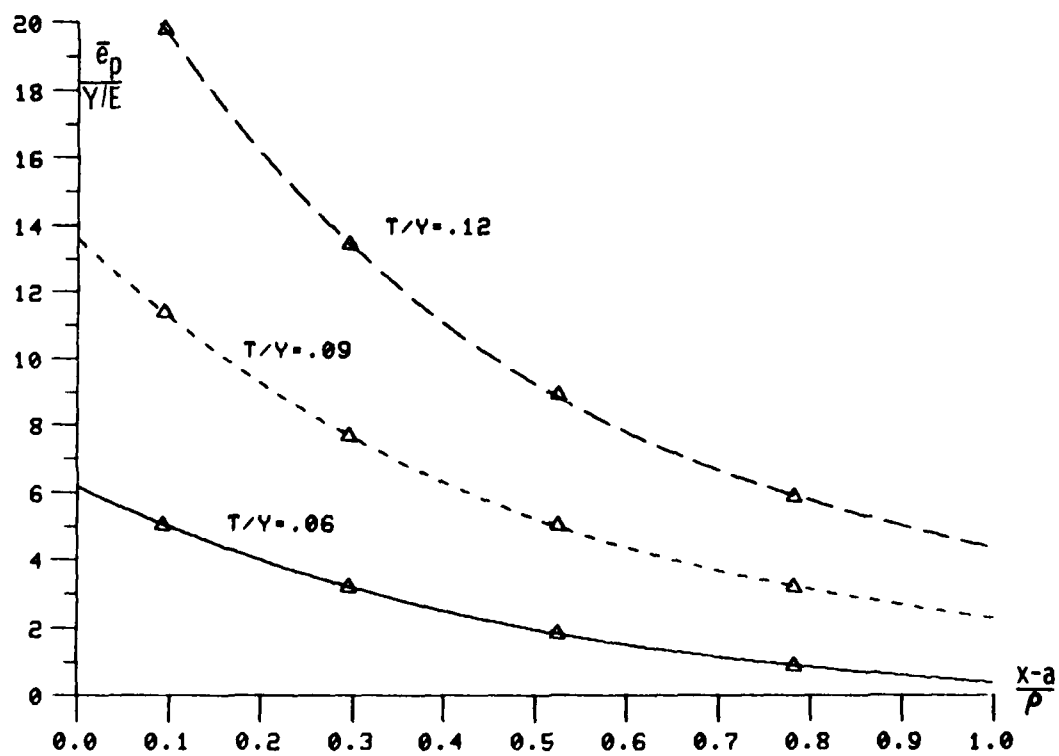
Figure 8. Plastic Strain Distribution Ahead of Flaw at Three Load Levels.

THERMO-ELASTIC-PLASTIC STRESSES IN MULTI-LAYERED CYLINDERS

John D. Vasilakis
U.S. Army Armament Research and Development Command
Large Caliber Weapon Systems Laboratory
Benet Weapons Laboratory
Watervliet, NY 12189

ABSTRACT. One of the many efforts undertaken to increase the life of gun tubes and/or increase their resistance to erosion involves the use of liners fabricated from different materials. A finite difference computer code for investigating the thermo-elastic-plastic response of gun tubes has been expanded to include multi-layered cylinder response to time dependent boundary conditions. Considered are both cyclic heat input and cyclic stress input. Response curves from inputs representative of repeated firing cycles will be presented. The emphasis in this report is on the transient temperature response and on the thermo-elastic stresses and mechanical stresses in the layers.

I. INTRODUCTION. One of the many efforts undertaken to increase the life of gun tubes and/or increase their erosion resistance involves the use of liners fabricated from materials differing from the base material of the gun tube. Typical properties sought in these materials, many of which are refractory materials or alloys of them, are high melting points for protection against erosion due to the high flame temperatures, different elastic moduli to effect transmission of loads to the base gun tube, etc. Currently most designs are of the two-layer system or liner-jacket type and with a variation that the liner may be coated or not. This paper does not consider coatings for reasons to be mentioned later.

In this paper, the response of monobloc and multi-layered large caliber gun tubes due to a typical firing schedule will be calculated. This response is found using a finite difference computer code reported in [1,2] for transient temperatures and thermo-elastic-plastic stresses. The program was updated to accept time dependent boundary conditions and to apply to multiple layers. A consistent set of data for a firing pulse was found in [3] for a specific weapon and this configuration was chosen for this study.

The computer program is a two part program. Knowing gas temperatures and heat transfer coefficients as a function of time during the firing cycle allows the computation of the transient temperatures in the gun tube. This is accomplished in the first part of the program. These temperatures are then used in the second part to calculate the associated thermo-elastic stresses. The program is capable of computing the thermal response of the tube for any desired firing cycle, thus monitoring an average temperature use at the bore. This can be used in cook-off studies, cook-off being the undesirable condition of premature propellant ignition. The temperatures at any time are saved on disk and are used as input to the stress portion of the program. The interest here is in the mechanical and thermal stresses due to the pressure pulse and the thermal pulse respectively. It should be mentioned that the thermal problem and stress problem are treated as uncoupled.

II. DESCRIPTION OF THE PROBLEM. The partial differential equation for determining the temperature in a cylinder is given by

$$\frac{1}{r}\frac{\partial}{\partial r}\left(rk^L(T)\frac{\partial T}{\partial r}\right) = \rho^L(T)c^L(T)\frac{\partial T}{\partial t} \tag{1}$$

where the superscript L refers to the layer number and

T is temperature,
$k^L(T)$ is thermal conductivity in layer L,
$\rho^L(T)$ is density in layer L,
$c^L(T)$ is specific heat in layer L,
r is radial distance

and t is time. The problem is assumed to be axisymmetric and axial effects are ignored. Figure 1 shows a typical geometry. At the interface between layers, the following continuity conditions must apply:

continuity of temperature

$$T^L\Big|_{r_L^-} = T^{L+1}\Big|_{r_L^+} \tag{2}$$

and continuity of heat flux

$$k^L(T)\frac{\partial T}{\partial r}\Big|_{r_L^-} = k^{L+1}(T)\frac{\partial T}{\partial r}\Big|_{r_L^+} \tag{3}$$

where r_L is the radius to the outer surface of the Lth layer. Contact resistance between layers is ignored at this time.

The above quantities are dimensionless, normalized to the properties of the steel layer.* Thus if the thermal conductivity can be written as

$$\bar{k}^L(T) = k^{SL}_{So}k^L(T) \tag{4}$$

where $\bar{k}^L(T)$ is the dimensioned thermal conductivity of the Lth layer and k^{SL}_{So} is the thermal conductivity of the steel layer at some reference temperature, then for L = 1

$$\frac{k^1(T)}{k^{SL}_{So}} = k^1(T) \tag{5}$$

and L > 1,

$$\frac{\bar{k}^L(T)}{k^{SL}_{So}} = \frac{k^L_o}{k^{SL}_{So}}\, kL(T) \tag{6}$$

---

*In the results that follow, one of the layers was steel. Other definitions or material properties can be used so long as one is consistent.
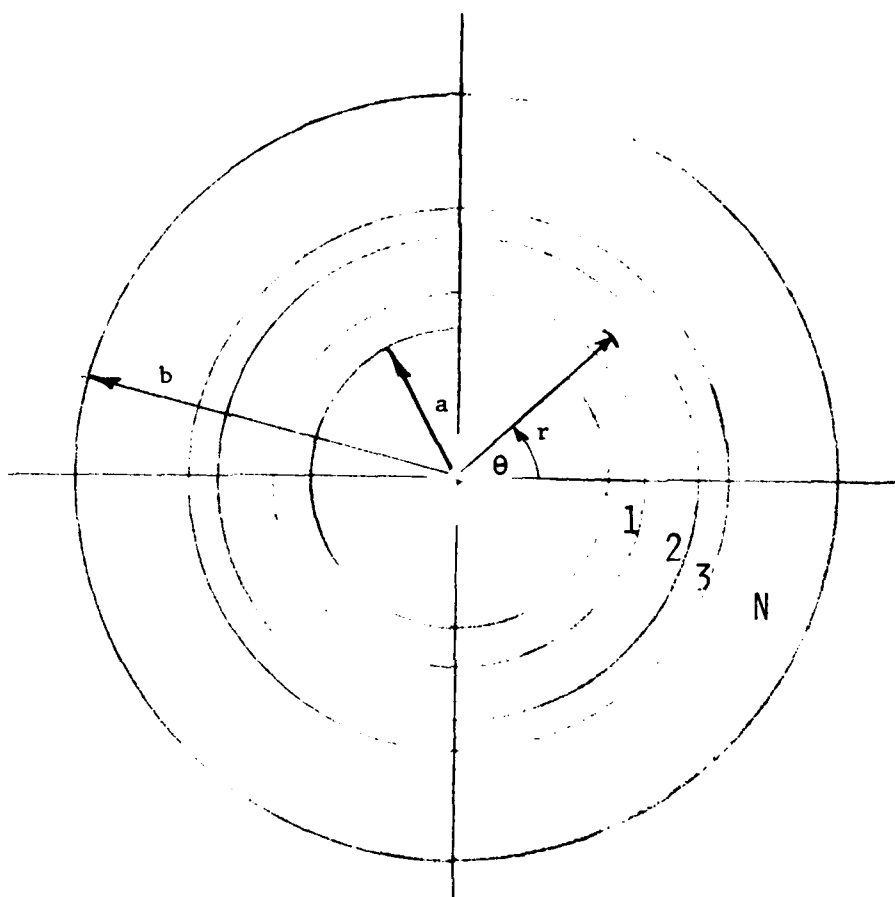
FIGURE 1. TYPICAL MULTI-LAYERED GEOMETRY

The specific heat and density are defined in similar fashion. Also

$$r = \frac{r}{b} \quad , \quad T = \frac{T}{T_{gas}} \tag{7}$$

where T_{gas} is initial gas temperature, and time

$$\tau = \frac{k^{SL}{}_{So}t}{\rho^{SL}{}_{o}c^{SL}{}_{o}b^2} \tag{8}$$

The stresses are computed in the second part of the program. Again, finite differences are used. The equations of compatibility and equilibrium are written at each node,

$$\frac{\partial \sigma_r}{\partial r} + \frac{1}{r}(\sigma^L{}_r - \sigma^L{}_\theta) = 0 \tag{9}$$

$$\frac{\partial \varepsilon_\theta{}^L}{\partial r} + \frac{1}{r}(\varepsilon^L{}_\theta - \varepsilon^L{}_r) = 0 \tag{10}$$

where L identifies the layer. Between layers, the continuity conditions for radial stress and radial displacement must be satisfied. Between the L and L+1 layer, therefore,

$$\sigma^L{}_r = \sigma^{L+1}{}_r \quad \text{and} \quad u^L = u^{L+1} \tag{11}$$

Initial stresses may exist due to fabrication methods used for the multilayered cylinder. the Prandtl-Reuss equations are used to relate the incremental stress and strain. The assumption of plane strain is used. The equations (9) and (10) are written in finite difference form. Expressions relating incremental stress to incremental strain similar to those of Yamada, et al [4] but including the effect of temperature are used to express equation (9) in terms of the incremental strains.

For the computation of the thermal stresses, the new temperature distribution and temperature increments are used at each time step. As the yield criterion is approached, the temperature increments are themselves divided into smaller increments to maintain smaller load steps.

III. BOUNDARY CONDITIONS. It is important when solving for the response due to firing pulses of these geometries to have a set of consistent boundary conditions. For the thermal response, either the temperature versus time on the boundaries or the gas temperature and heat transfer coefficients is required and for the pressure pulse, the bore pressure versus time. Kovacs [3] considered the transient temperature response for several firing cycles, see Figure 2, and did give in his report a complete set of data. The data is based on a program relying on empirical information for heat flux and applied to a large caliber weapon with chrome plating. It was felt that the heat transfer coefficients generated would apply to a steel monobloc tube or to a multi-layered tube where the steel layer was at the bore. Lacking better input, however, the data was used in all cases.

222
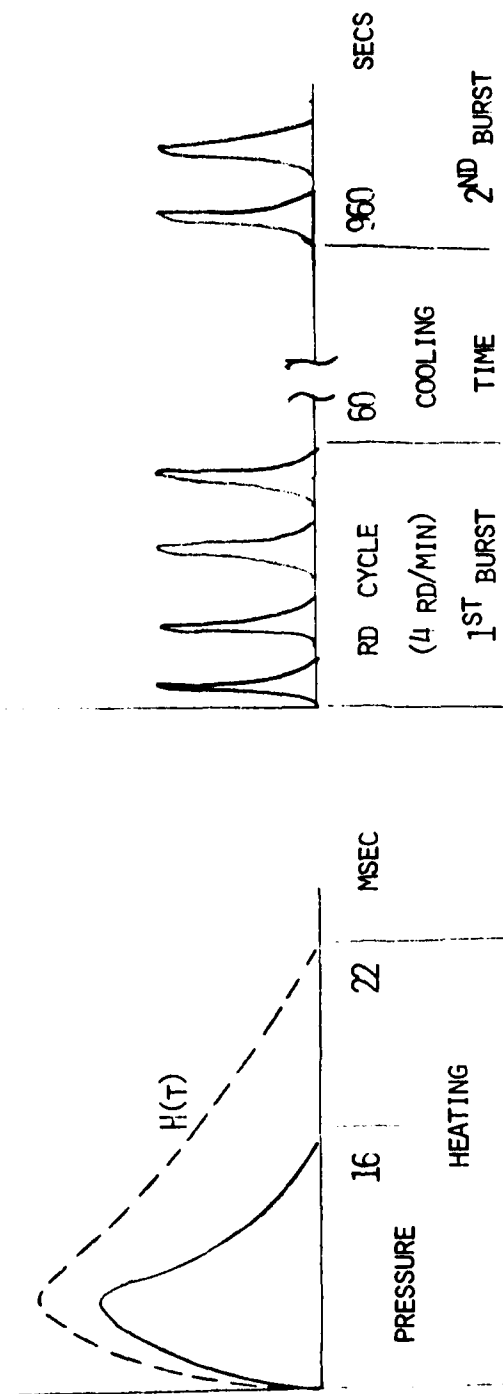
FIGURE 2. HEATING AND PRESSURE PULSES (AFTER REF. (3))

Future plans include the incorporation of an initial program for the purpose of analytically computing the heat transfer coefficients for the designated multilayer properties. The problems encountered in comparing responses of different multi-layered designs would then be alleviated.

IV. RESULTS. Several runs have been made, mainly to show the different problems that can be accommodated by the computer program. Once a geometry has been chosen, either monobloc or multi-layer, and the material properties found, the first part of the program can be run for temperature response versus time. One can look at both the temperature distribution throughout the tube wall and the change in bore temperature in time. If a firing cycle consists of a number of firing pulses and pauses, the bore temperature can be monitored in time. If stresses are required, the temperature distributions at each time step are saved in a file which is subsequently used as input to the second part of the computer program. These temperature distributions are used to compute the thermal stresses. The associated stress pulse can also be applied to the tube, either by itself for a mechanical response or with the thermal loads for a combined response. As mentioned before, however, the thermo-mechanical problem is considered to be uncoupled. If the distortion energy criterion is satisfied, then an incremental thermo-elastic-plastic analysis will be performed. It should be noted that while some examples showing elastic-plastic response are presented, the loading generated from the data of Ref. [3] was not of sufficient magnitude to cause this and the stress pulse was increased to cause the program to perform a plasticity solution. If the problem is more realistically modeled with material properties and yield strength a function of temperature, it may not be necessary to artifically induce this type of solution.

Figure 3 shows the result of the problem of thermal response due to the heat pulse for a monobloc tube. The response to a single pulse is shown for different time increments. An important function of this type of analysis is to be able to predict bore temperatures under various firing cycles and for long firing periods. Being able to use coarser time increments allows the prediction of bore temperatures for longer periods. Figure 4 shows the response of a monobloc tube for about five cycles.

Table I shows the properties for the multi-layered geometry chosen. The liner is a tantalum tungsten alloy (Ta-10W) with a steel jacket. The bore diameter is 3.351 inches, the outside diameter is 5.6 inches, and the interface diameter is 4.1 inches. The properties are assumed constant in temperature but a variation in temperature is allowed. Figures 5 and 6 are equivalent to Figures 3 and 4 for a multi-layered tube. Figures 7 and 8 show the stress response of a monobloc tube to a stress pulse and a thermal pulse, respectively. It should be noted that most of these results show the effect at the bore. During the early stages of the response, there is little effect on the rest of the tube.

Figure 9 shows the stress response of a multi-layered cylinder (Ta-10W/Steel). The material behavior is assumed to be elastic. The change in the tangential stress at the bore with time is shown for the stress pulse (M curve) and for the temperature distributions (T curve). The combined curve shows the computed stresses due to both the thermal and mechanical loading.
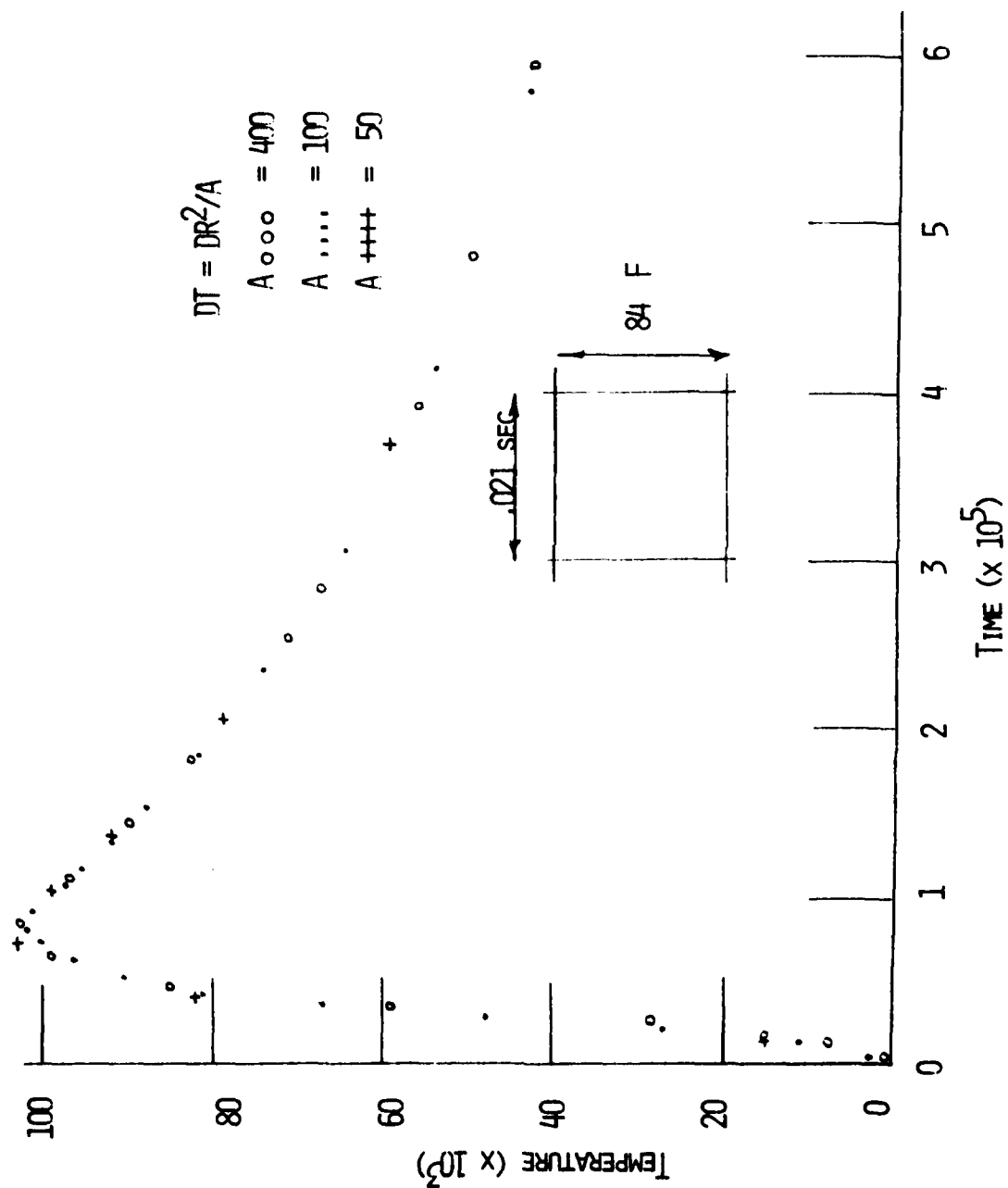
FIGURE 3. EFFECT OF TIME INCREMENT ON PULSE SHAPE, MONOBLOC TUBE.
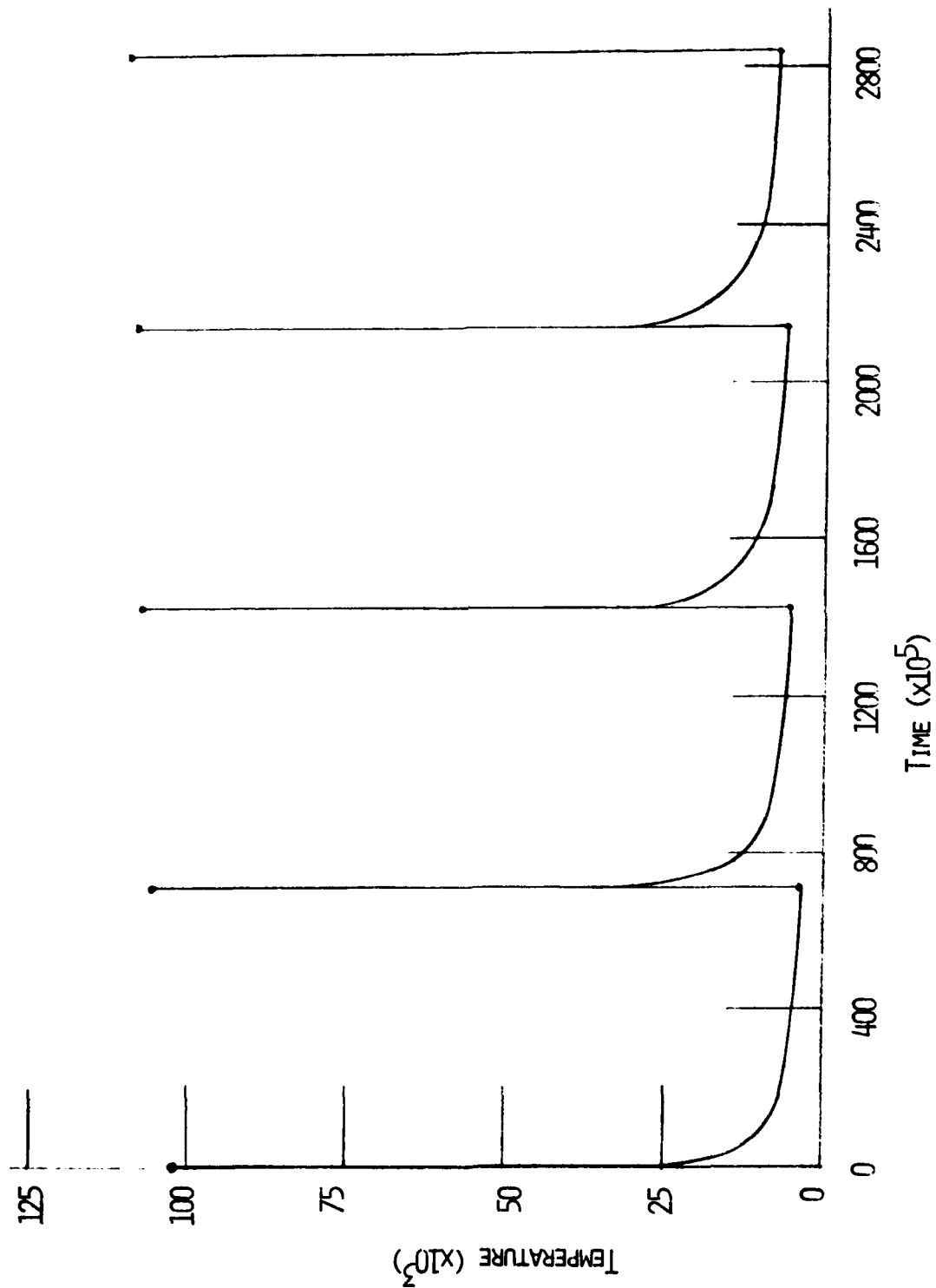
FIGURE 4. BORE TEMPERATURE CHANGE UNDER REPEATED FIRING, MONOBLOC TUBE.

TABLE 1. MATERIAL PROPERTIES OF MULTI-LAYERED CYLINDER

LINER: TA-10W
JACKET: STEEL

Radius				Properties (Room Temp)			
	Inch			Liner		Jacket	
Inside	3.351	.6	K	.0012	2.65	.000453	1	BTU/sec°F in
Interface	4.101	.732	C	.0339	.317	.107	1	BTU/#°F
Outside	5.6	1.0		.607	2.14	.284	1	#/in

FIGURE 5. BORE TEMPERATURE VS TIME
MULTI-LAYERED TUBE
TA-10W / STEEL
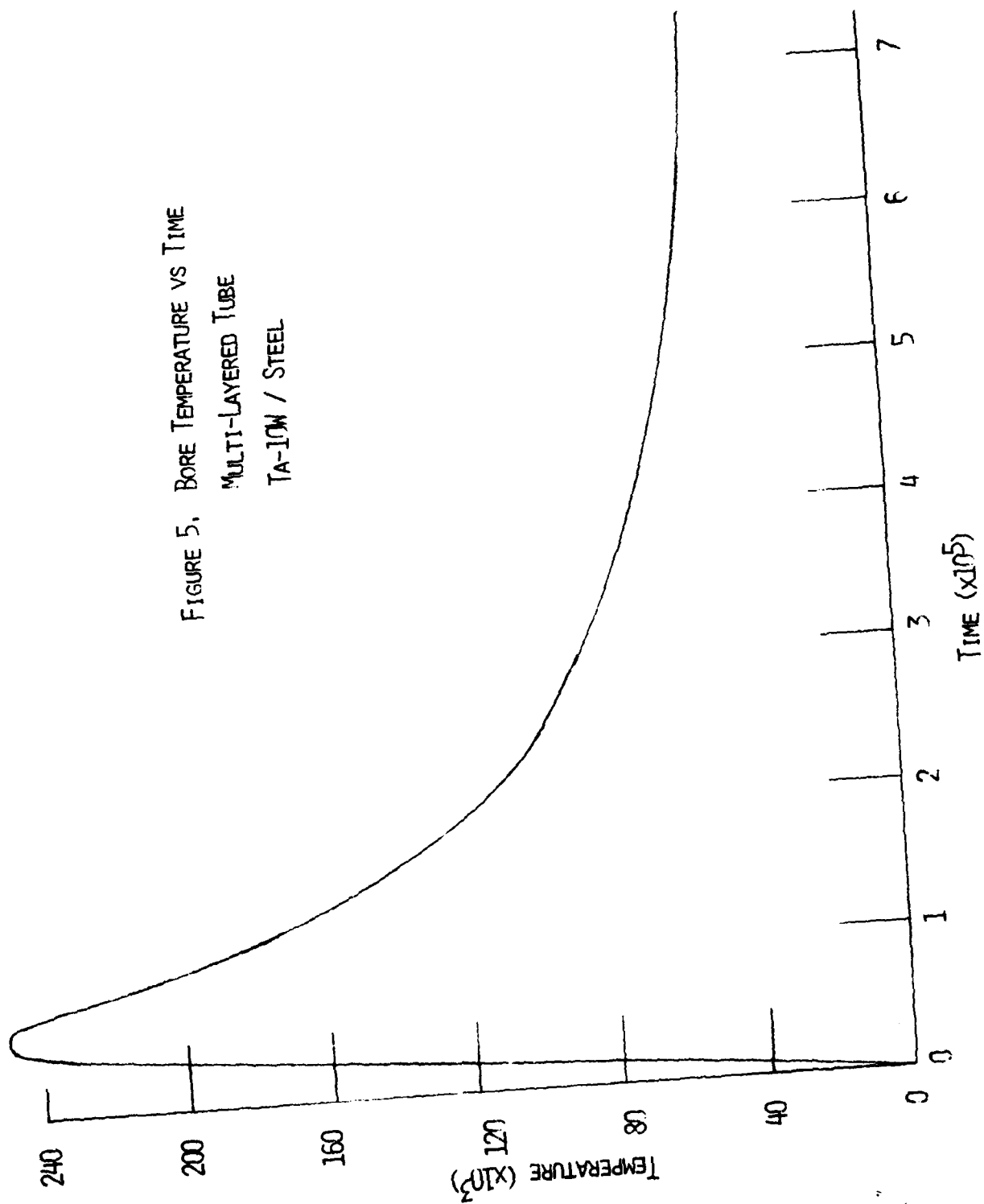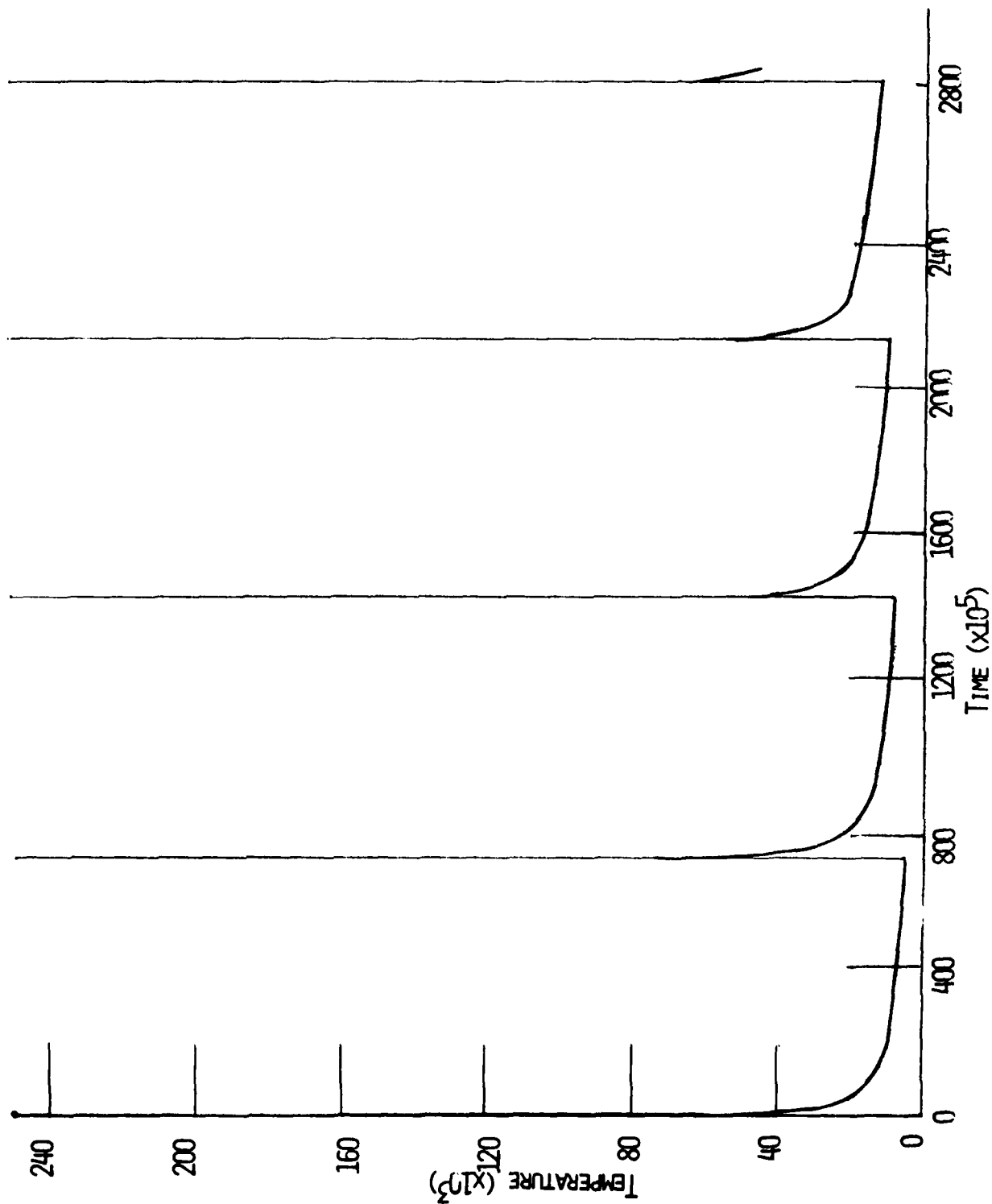
Figure 6. Bore Temperature vs Time (5 cycles), Ta-10W / Steel
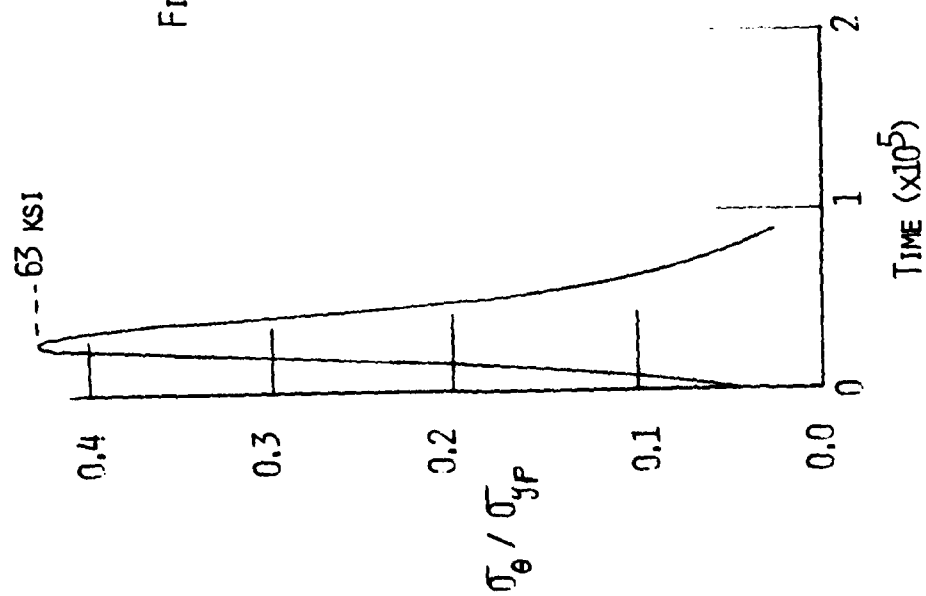
FIGURE 7. RESPONSE OF MONOBLOC TUBE (BORE STRESS) TO A GIVEN STRESS PULSE.
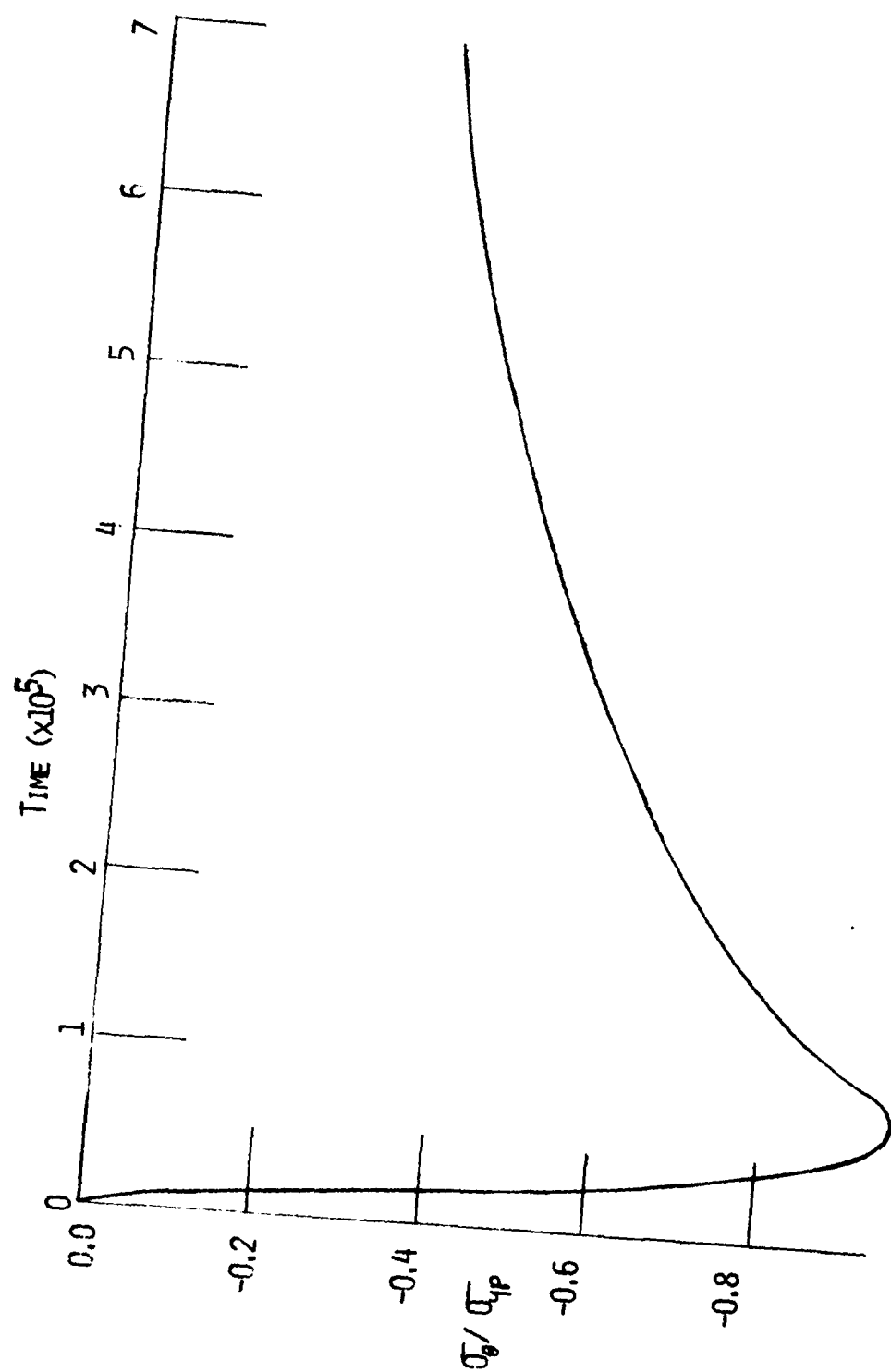
FIGURE 8. THERMAL STRESSES DUE TO SINGLE FIRING PULSE. (MONOBLOC TUBE)
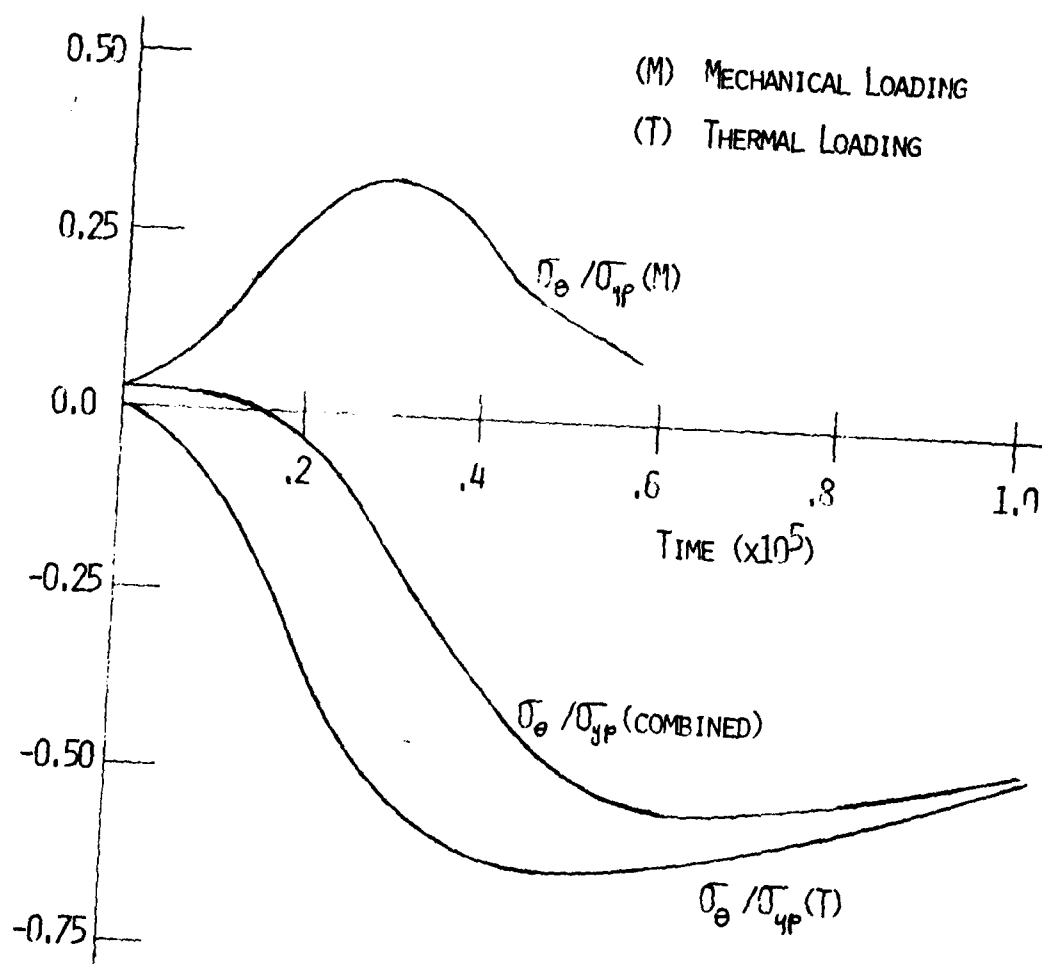
FIGURE 9. BORE STRESS VS TIME.
ELASTIC RESPONSE, MULTILAYERED CYLINDER

Since only elastic behavior occurs, however, the same combined loading curve could be arrived at by assuming the results for the individual loads.

An elastic-plastic response due to the applied pressure pulse is shown in Figure 10. The curve labeled pressure is actually the radial stress at the bore, σ_r, and the pressure should be $|\sigma_r|$. The other three curves are the response of a monobloc steel tube and two multi-layered systems, a Ta-10W liner with a steel jacket and a steel liner with a Ta-10W jacket. The figure shows mainly the effect of the elastic modulus of the materials. The Ta-10W liner, having a modulus approximately one third less than steel, transmits the load towards the interior of the tube better than the other configuration which has a more rigid liner. Figure 11 was included just to show that the stresses throughout the wall thickness are computed. The figure shows the response of a Ta-10W liner/steel jacket cylinder to combined thermo-mechanical loads.

Figure 12 shows the elastic response due to thermo-mechanical loads in a multi-layered cylinder with a steel liner and Ta-10W jacket. Figure 13 shows the thermo-elastic-plastic response for the same configuration. The radial stress and the tangential stress at the bore are shown as the change in time.

V. CONCLUSIONS. The above results are an indication of the type of problems to which the computer program can be applied. Several layers can be handled and for the two layer geometry initial stresses, due to interference fits (for fabrication reasons) can be calculated. In either program part, the properties can be considered as a function of temperature. While the program does not have the full responsibility of a general purpose finite element program, for the allowed geometry, a wide variety of behavior can be examined.

REFERENCES

1. Vasilakis, J. D., "Temperatures and Stresses Due to Quenching of Hollow Cylinders," Transactions of the Twenty-Fourth Conference of Army Mathematicians, ARO Report 79-1.

2. Vasilakis, J. D. and Chen, P. C. T., "Thermo-Elastic-Plastic Stresses in Hollow Cylinders Due To Quenching," Transactions of the Twenty-Fifth Conference of Army Mathematicians, ARO Report 80-1.

3. Kovacs, J. E., "Computer Methodology For Large Caliber Artillery Cannon Heating and Cooling," Technical Report ARSED-TR-80001, December 1980.

4. Yamada, Y., Yoshimura, N., and Sakuri, T., "Plastic Stress-Strain Matrix and Its Application For the Solution of Elastic-Plastic Problems by the Finite Element," International Journal of Mechanical Sciences, 1968, V 10, pp. 343-354.

FIGURE 10. BORE STRESS VS TIME
PRESSURE PULSE
ELASTIC/PLASTIC
PRESSURE ..Z
TA-10W/STEEL ..+
STEEL ..X
STEEL/TA-10W ..Y
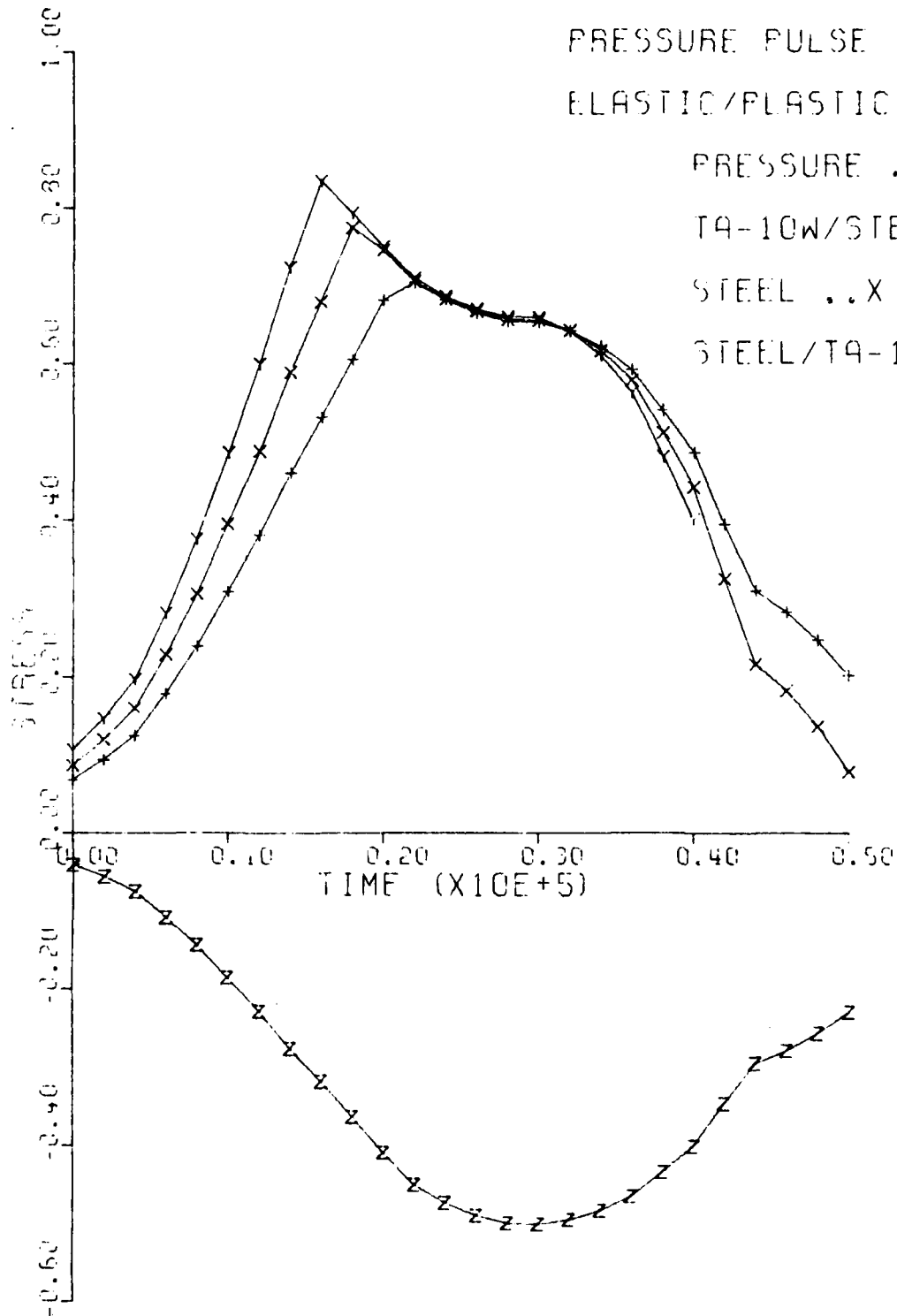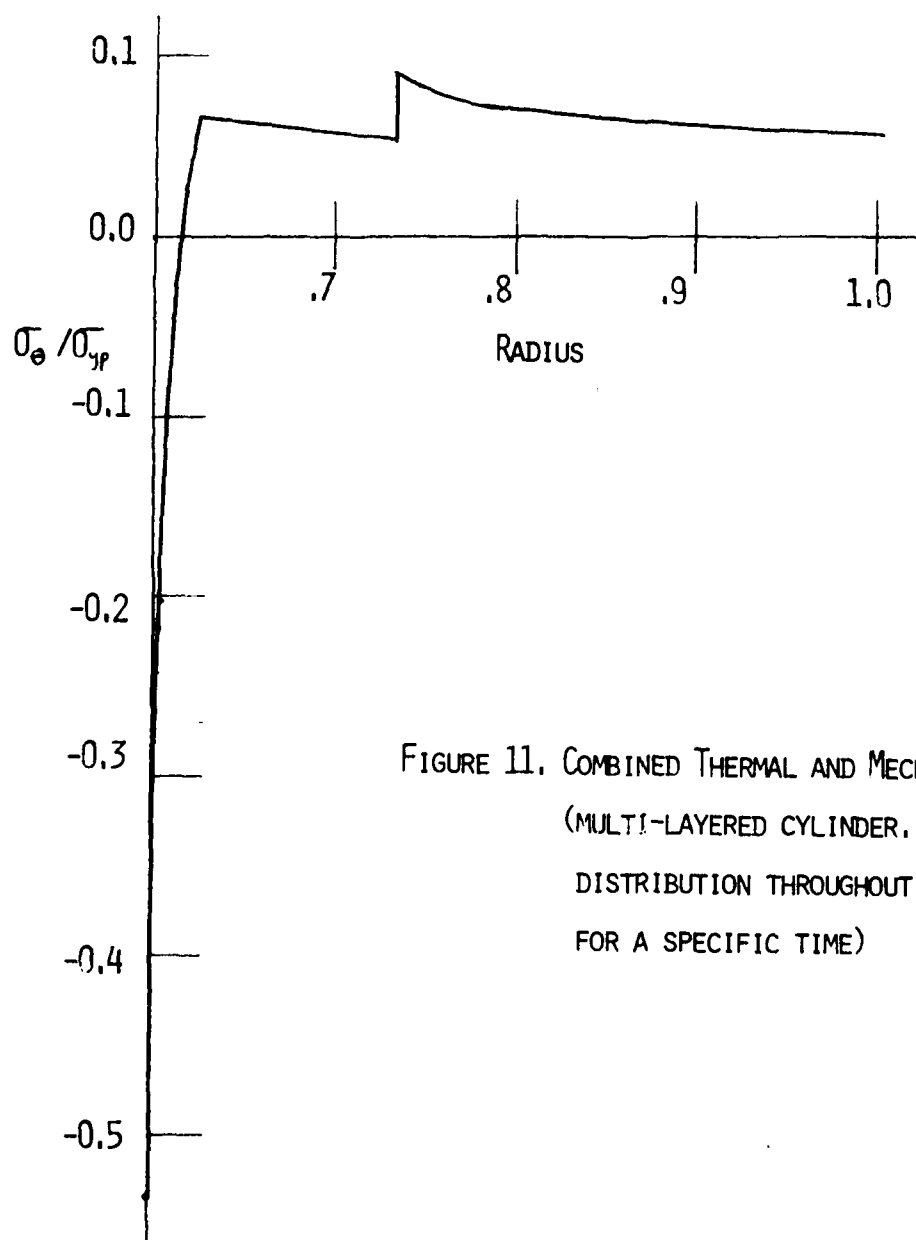
FIGURE 11. COMBINED THERMAL AND MECHANICAL LOADS
(MULTI-LAYERED CYLINDER, STRESS
DISTRIBUTION THROUGHOUT THE WALL
FOR A SPECIFIC TIME)
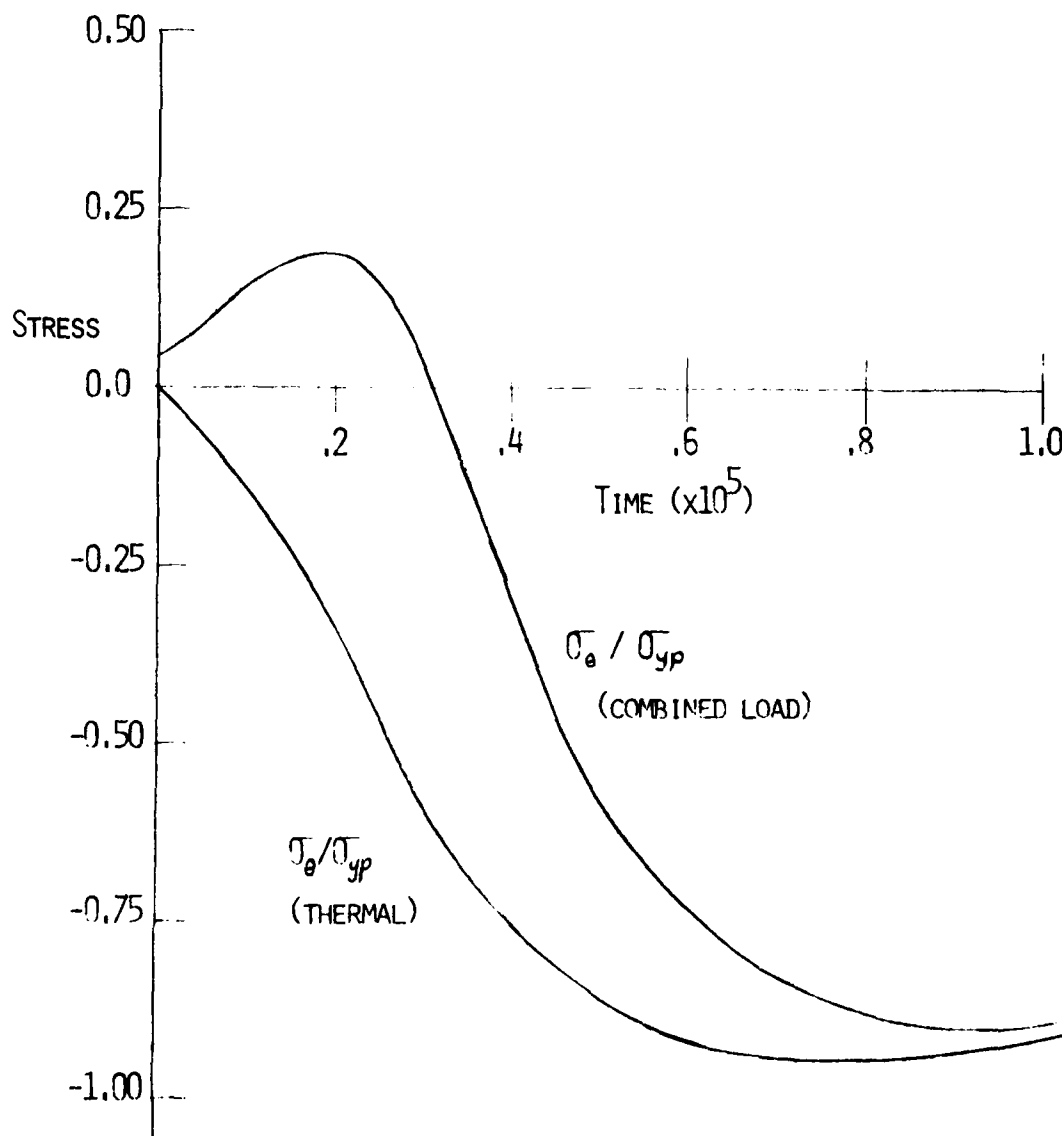
FIGURE 12. BORE STRESS VS TIME. ELASTIC RESPONSE.
COMBINED THERMAL AND MECHANICAL LOADS
MULTI-LAYERED CYLINDER. STEEL/TA-1W

236
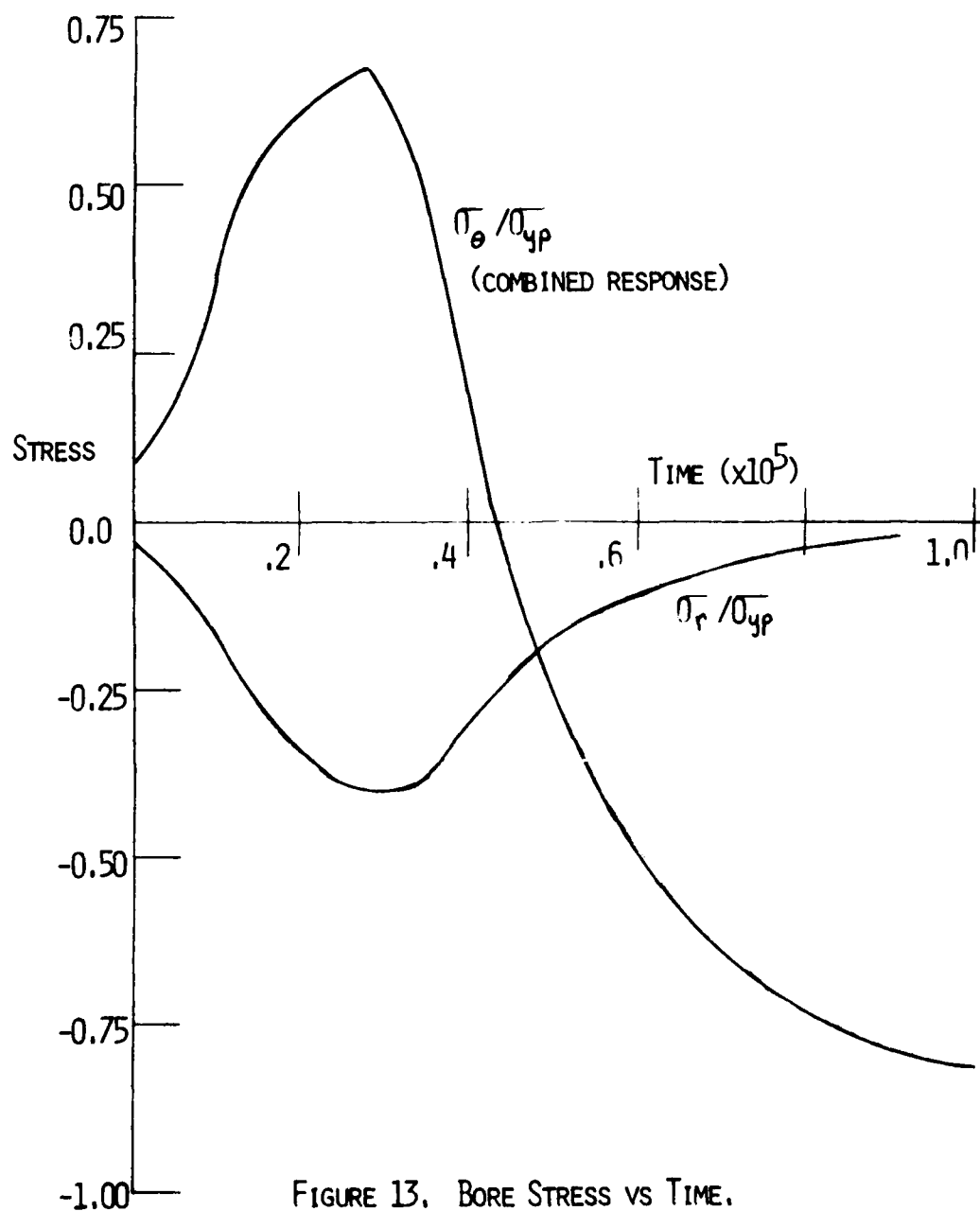
FIGURE 13. BORE STRESS VS TIME.
ELASTIC-PLASTIC RESPONSE. STEEL/TA-10W.
COMBINED THERMAL AND MECHANICAL LOADS.

ON THE NUMERICAL SOLUTION OF SINGULAR
INTEGRAL EQUATIONS USING GAUSS-JACOBI FORMULAE*

R. P. Srivastav
Department of Applied Mathematics and Statistics
State University of New York at Stony Brook
Stony Brook, New York 11794

ABSTRACT: Of concern here is the question of convergence of computed solutions of integral equations with principal value integrals. Using the Jackson Theorem on "best approximation" and an estimate for the norm of the inverse matrix of the discretized system, it is shown that a direct method of solution based on collocation yields convergence.

1. Introduction

In this paper, we consider the question of convergence of interpolatory polynomials interpolating the numerically computed approximate values of the solution of the singular integral equation

$$(1.1) \quad Tg \equiv a\, g(s) + \frac{b}{\pi}\int_{-1}^{1} \frac{g(t)dt}{t-s} + \lambda\int_{-1}^{1} K(s,t)g(t)dt = f(s), \quad -1 < s < 1.$$

Such integral equations arise in the mixed boundary value problems of solid and fluid mechanics, and are solved frequently using direct methods based on quadrature and collocation. Of concern here is a method proposed by Krenk [4], which consists of Gauss-Jacobi quadrature and collocation at zeros of a suitable Jacobi polynomial, after $g(t)$ has been replaced by $w(t)y(t)$, where

$$(1.2) \quad w(t) = (1-t)^{\alpha}(1+t)^{\beta}.$$

The exponents α, β are determined by the index of the equation, which is either 1, 0 or -1. In this paper, we consider only the index 1 for which $\alpha + \beta = -1$, $\alpha = -\sigma$, where σ is given by the equation

$$(1.3) \quad \cot(\sigma \pi) = (a/b), \quad 0 < \sigma < 1.$$

The solution of (1.1) is not unique. Usually, the equation (1.1) is augmented by an additional condition of the form

$$(1.4) \quad \frac{1}{\pi}\int_{-1}^{1} g(t)dt = N.$$

Let w_j and w_j^* respectively, denote the weights of the classical Gaussian quadrature, using the zeros $\{t_j\}$ and $\{s_j\}$ of the polynomials

---

$$P_n^{(-\sigma,\sigma-1)}(x) \qquad \text{and} \qquad P_{n-1}^{(\sigma,1-\sigma)}(x).$$

(The weight corresponding to the zeros $\{x_\nu\}$ of $P_n^{(\alpha,\beta)}(x)$ are given by Szegö ([7], p. 352) as

$$\lambda_\nu = 2^{\alpha+\beta+1} \cdot \frac{\Gamma(n+\alpha+1)\Gamma(n+\beta+1)}{\Gamma(n+1)\Gamma(n+\alpha+\beta+1)} (1-x_\nu^2)^{-1}[P_n^{(\alpha,\beta)'}(x_\nu)]^{-2}$$

for $\alpha > -1$, $\beta > -1$.)

For the approximate solution of (1.1), quadrature and collocation yield the equations

$$(1.5) \qquad b\sum_{j=1}^{n} w_j \frac{y(t_j)}{t_j - s_k} + \lambda\pi\sum_{j=1}^{n} w_j K(s_k, t_j) y(t_j) = f(s_k), \qquad k = 1, 2, \ldots, n-1$$

$$(1.6) \qquad \sum_{j=1}^{n} w_j y(t_j) = N.$$

The method is an extension of the popular Erdogan-Gupta method [1] for dealing with the integral equations of the first kind, i.e. with $a = 0$. In [4], it is argued that if

$$T\varepsilon_n = \delta_n(x)$$

and $\delta_n(x) \to 0$ uniformly, then $\varepsilon_n \to 0$ uniformly. However, Stewart [6] has shown that uniformity is not enough to interchange limiting processes involving singular integrals. We are able to prove convergence for the problems in which $y(t) \in C^3[-1,1]$ and $K(s,t)$ is equally smooth, with λ sufficiently small. For simplicity, we describe only the case $\lambda = 0$.

The paper is organized as follows: In Section 2, we derive an estimate for the norm of the inverse matrix of the system of equations (1.5), (1.6). In Section 3, using Jackson's theorems on "best approximation" and the properties of the Lebesgue constants on Jacobi nodes, we prove the convergence of the sequence of interpolatory polynomials to the solution of the integral equation. Finally, in Section 4 we show that a "natural interpolant" also converges to the solution of the integral equation.

2. Norm of the Inverse Matrix

It has been shown by Gerasoulis and Srivastav [2], that the coefficient matrix

$$(2.1) \qquad A_n = (a_{ij}) = b\, w_j/(t_j - s_i), \qquad i = 1, 2, \ldots, n-1; \ j = 1, 2, \ldots, n$$

$$a_{nj} = w_j, \qquad j = 1, 2, \ldots, n$$

has the inverse

$$(2.2) \quad A_n^{-1} = (b_{ij}) = b \, w_j^* / \{(a^2+b^2)(t_i - s_j)\}, \quad j = 1, 2, \ldots, n-1; \; i = 1, 2, \ldots, n$$

$$b_{in} = 1, \qquad\qquad\qquad i = 1, 2, \ldots, n.$$

Observe that

$$(2.3) \quad A_n^{-1} = D \, A_n^T \Lambda,$$

where D and Λ are diagonal matrices, whose elements $d_j \delta_{jk}$ and $\lambda_j \delta_{jk}$ (δ_{jk} is the Kronecker delta) are given by

$$(2.4) \quad \begin{array}{lll} d_j = 1/w_j, & \lambda_j = w_j^*/(a^2+b^2), & j = 1, 2, \ldots, n-1 \\ d_n = 1/w_n, & \lambda_n = 1. \end{array}$$

Now, let $A_n = QC$ where Q is non-singular and C is non-singular, diagonal. This decomposition is not unique. A routine calculation gives

$$(2.5) \quad Q^{-1} = (CDC^T) Q^T \Lambda.$$

C is now chosen so that (CDC^T) is reduced to the identity matrix.

The elements of C are simply $w_j^{\frac{1}{2}}$. $\|Q^{-1}\|$ is the spectral radius of the matrix

$$(Q^{-1})^T Q^{-1} = \Lambda \, Q \, Q^{-1} = \Lambda.$$

Hence,

$$\|Q^{-1}\| = \max(|w_j^*|^{\frac{1}{2}}_{j=1,2,\ldots,n-1}, 1).$$

From the inequality

$$\|A_n^{-1}\| \leq \|C^{-1}\| \, \|Q^{-1}\|$$

it follows that

$$(2.6) \quad \|A_n^{-1}\| \leq \max_{1 \leq j \leq n} |w_j|^{-\frac{1}{2}} \max(\max_{1 \leq j \leq n-1} |w_j^*|^{\frac{1}{2}}, 1).$$

In a similar way, noting that $A = \Lambda^{-1}(A^{-1})^T D^{-1}$, it can be shown that

$$(2.7) \quad \|A_n\| \leq \max_{1 \leq j \leq n} |w_j|^{\frac{1}{2}} \max(\max_{1 \leq j \leq n-1} |w_j^*|^{-\frac{1}{2}}, 1).$$

In the special case, $\alpha = \beta = -\frac{1}{2}$, which corresponds to $a = 0$, $b = 1$, we have $w_j = 1/n$, $w_j^* = n^{-1} \sin^2(\pi/n)$. Then (2.6) and (2.7) reduce respectively to

$$(2.8) \quad \|A_n^{-1}\| \leq \sqrt{n}$$

$$(2.9) \quad \|A_n\| \leq \operatorname{cosec}(\pi/n).$$

241

It has been shown in [5] that in this case,

$$\|A_n^{-1}\| = \sqrt{n}$$

and

$$\|A_n\| = \operatorname{cosec}(\pi/n).$$

Hence, in the general case, there does not seem to be much room for improvement in the estimates (2.6) and (2.7).

The asymptotic properties of the classical polynomials given by Szegö ([7], p. 238) may be used to derive an upper bound for the right-hand sides of (2.6) and (2.7). By definition,

$$(2.10) \quad w_j^{-1} = \frac{\Gamma(n+1)\Gamma(n)}{\Gamma(n-\sigma+1)\Gamma(n+\sigma)} (1-t_j^2)\{P_n^{(-\sigma,\sigma-1)\prime}(t_j)\}^2.$$

Since $t_j = \cos\{n^{-1}[j\pi + O(1)]\}$, where $O(1)$ represents terms uniformly bounded for all values of $j = 1,2,\ldots,n$, and for positive zeros,

$$(2.11) \quad |P_n^{(-\sigma,\sigma-1)\prime}(t_j)| \le O(1)j^{\sigma-3/2}n^{-\sigma+2},$$

using the Stirling formula for the Gamma functions and the inequality $\sin^2 x \le x^2$, we can show that

$$(2.12) \quad |w_j|^{-1} \le O(1)n^{2-2\sigma} \qquad \text{if } 2\sigma < 1$$

$$(2.13) \quad |w_j|^{-1} \le O(1)n \qquad \text{if } 2\sigma > 1.$$

Similarly, for negative zeros, since these are the positive zeros of $P_n^{(\sigma-1,-\sigma)}(x)$, it can be shown that

$$(2.14) \quad |w_j|^{-1} \le O(1)n^{2\sigma-1} \qquad \text{if } 2\sigma > 1$$

$$(2.15) \quad |w_j|^{-1} \le O(1) \qquad \text{if } 2\sigma < 1.$$

Hence

$$(2.16) \quad \max_{1\le j\le n} |w_j|^{-\frac{1}{2}} \le O(1)n^p, \qquad p = \max(1-\sigma,\tfrac{1}{2}),$$

and consequently (see [7], p. 355 for a bound of w_j^*)

$$(2.17) \quad \|A_n^{-1}\| \le O(1)n^p, \qquad p = \max(1-\sigma,\tfrac{1}{2}).$$

$\|A_n\|$ can be similarly estimated.

3. The Interpolatory Polynomial

The equations (1.5), (1.6) are approximate because the quadrature error has been neglected. Let

$$y = [y(t_1), y(t_2), \ldots, y(t_n)]^T$$

$$y^- = [y^-(t_1), y^-(t_2), \ldots, y^-(t_n)]^T.$$

242

Instead of solving

$$A_n y = f + \epsilon$$

we solve

$$A_n \tilde{y} = f.$$

Hence,

$$\|y - \tilde{y}\| \le \|A_n^{-1}\|_\infty \|\epsilon\|_\infty.$$

Since $\|A_n^{-1}\|_\infty \le \sqrt{n}\, \|A_n^{-1}\|_2$, it follows that

$$(3.1) \qquad \|y - \tilde{y}\|_\infty \le \sqrt{n}\, \|A_n^{-1}\|_2 \|\epsilon\|_\infty \equiv c_n \text{ (say)}.$$

Now, let $y_{n-1}(t)$ and $\tilde{y}_{n-1}(t)$ denote the polynomials interpolating $y(t_j)$ and $\tilde{y}(t_j)$, respectively. Then

$$(3.2) \qquad \|y(t) - \tilde{y}_{n-1}(t)\|_\infty \le \|y(t) - y_{n-1}(t)\|_\infty + \|y_{n-1}(t) - \tilde{y}_{n-1}(t)\|_\infty.$$

For a given f, let $E_{n-1}(f)$ denote the error of "best approximation" by a polynomial of degree $n-1$ and let

$$(3.3) \qquad \lambda_n = \max_{-1 < t < 1} \sum_{j=1}^n |\ell_j(t)|,$$

where $\ell_j(t)$, $j = 1, 2, \ldots, n$ are the Lagrange polynomials for the Jacobi nodes $\{t_j\}$. The first term on the right hand side of (3.2) is the error of interpolation using the true values of $y(t)$, and cannot exceed $E_{n-1}(y)(1 + \lambda_n)$. For the second term, we note that

$$y_{n-1}(t) - \tilde{y}_{n-1}(t) = \sum_{j=1}^n [y(t_j) - \tilde{y}(t_j)] \ell_j(t)$$

and hence its supremum is bounded above by $c_n \lambda_n$ [cf. (3.1)]. The error of Gaussian quadrature is

$$(3.4) \qquad \|\epsilon\|_\infty \le \mu\, E_{n-1}^*(F)(1 + \lambda_n)$$

where

$$(3.5) \qquad \mu = \frac{b}{\pi} \int_{-1}^1 w(x)\, dx$$

and

$$(3.6) \qquad E_{n-1}^*(F) = \max_{1 \le k \le n-1} [E_{n-1} F(x, s_k)]$$

where

$$(3.7) \qquad F(x, s) = \begin{cases} \dfrac{y(x) - y(s)}{x - s}, & x \ne s \\ y'(x), & x = s. \end{cases}$$

Summing up the above results, we get the inequality

$$(3.8) \quad \|y(t) - y_{n-1}^-\|_\infty \le (1+\lambda_n)[E_{n-1}(y) + O(1)E_{n-1}^*(F)n^{p+\frac{1}{2}}]$$

From Jackson's theorem on "best approximation," if $f \in C^{k+1}[-1,1]$, then $E_{n-1}(f) = O(n^{-k-1})$. Moreover, $\lambda_n = O(1)$, $O(\log n)$ or $O(n^{\frac{1}{2}-\sigma})$, respectively for $\sigma > \frac{1}{2}$, $\sigma = \frac{1}{2}$ and $\sigma < \frac{1}{2}$. Hence, it is sufficient for the convergence of the sequence y_{n-1}^- that y belongs to $C^3[-1,1]$.

Remark: The above analysis can be easily extended to deal with $y \in C^2[-1,1]$ and y'' satisfying an appropriate Lipschitz condition using Jackson's theorem in that form.

4. The "Natural" Interpolant

For $\cot \sigma\pi = (a/b)$, $w(t) = (1-t)^{-\sigma}(1+t)^{\sigma-1}$ and $\lambda = 0$, the equation (1.1) may be written in the form

$$(4.1) \quad \frac{b}{\pi} \int_{-1}^{1} w(t) \frac{y(t) - y(s)}{t - s} dt = f(s), \qquad -1 < s < 1.$$

Using the Gaussian integration formula, we obtain the equation

$$(4.2) \quad b\left(\sum_{j=1}^{n} \frac{w_j y^-(t_j)}{t_j - s} - y^*(s) \sum_{j=1}^{n} \frac{w_j}{t_j - s} \right) = f(s), \quad -1 < s < 1.$$

The asterisk indicates that it is an approximation to $y(s)$. Furthermore,

$$(4.3) \quad \sum_{j=1}^{n} \frac{w_j}{x - t_j} = \frac{1}{2} \operatorname{cosec} \pi\sigma \frac{P_{n-1}^{(\sigma, 1-\sigma)}(x)}{P_n^{(-\sigma, \sigma-1)}(x)},$$

and

$$(4.4) \quad y^-(t_i) = A_n^{-1}(f) = N + \frac{b}{a^2+b^2} \sum_{j=1}^{n-1} \frac{w_j^* f(s_j)}{t_i - s_j} .$$

(4.2), (4.3) and (4.4) together yield the equation

$$(4.5) \quad y^*(s) = -\frac{b(\sin^2 \sigma\pi)}{a^2+b^2} \sum_{k=1}^{n-1} \frac{w_k^*[f(s_k) - f(s)]}{s_k - s}$$

$$+ \frac{2b \sin \pi\sigma}{a^2+b^2} P_1^{(-\sigma, \sigma-1)}(s)f(s) + N.$$

Recall that

$$P_1^{(-\sigma, \sigma-1)}(s) = \frac{1}{2} s + \frac{1}{2}(1-2\sigma).$$

Thus, for $\sigma = \frac{1}{2}$, it reduces to the expression for the Gauss-Chebyshev nodes ([3],[5]).

Annalytically,

$$y(s) = N + \frac{a}{a^2+b^2} f(s)(1-s)^{\sigma}(1+s)^{1-\sigma}$$

(4.6)

$$- \frac{b}{\pi(a^2+b^2)} \int_{-1}^{1} \frac{(1-t)^{\sigma}(1+t)^{1-\sigma}f(t)dt}{t-s} .$$

If the integral in (4.6) is replaced by Gauss-Jacobi quadrature, the resulting expression is $y^*(s)$. The convergence of the "natural" interpolant is tantamount to the convergence of the Gauss-Jacobi quadrature. Once again, using the theorems on "best approximation" if $f \in C^1[-1,1]$ and f' satisfies the Lipschitz condition, it can be shown that y^* converges uniformly to y.

The interpolatory polynomial $y_{n-1}(t)$ can be expressed as follows:

(4.7) $\quad y_{n-1}(t) = N + \frac{b}{a^2+b^2} \sum_{j=1}^{n-1} \frac{w_j^* f(s_j)\{P_n^{(-\sigma,\sigma-1)}(t) - P_n^{(-\sigma,\sigma-1)}(s_j)\}}{-P_n^{(-\sigma,\sigma-1)}(s_j)(t-s_j)} .$

After some simplification, we find that

(4.8) $\quad y_{n-1}(t) - y^* = O(1) \cdot \frac{P_n^{(-\sigma,\sigma-1)}(t)}{P_{n-1}^{(\sigma,1-\sigma)}(t)} \theta_n(t)$

where

$$\theta_n(t) = \sum_{j=1}^{n-1} w_j^* \frac{f(t) - f(s_j)}{t-s_j} \cdot \frac{P_{n-1}^{(\sigma,1-\sigma)}(t)}{P_n^{(-\sigma,\sigma-1)}(s_j)}$$

is the error of interpolation to $f(t)$ at the zeros of $P_{n-1}^{(\sigma,1-\sigma)}(t)$. It is quite likely that a careful analysis of (4.8) may give weaker conditions for the uniform convergence of y_{n-1} to y.

Acknowledgment

References

[1] Erdogan, F. and G. D. Gupta: "On the Numerical Solution of Singular Integral Equations," Quart. Appl. Math. 30, 525-534 (1972).

[2] Gerasoulis, A. and R. P. Srivastav: "On the Solvability of Singular Integral Equations via Gauss-Jacobi Quadrature (to be published).

[3] Ioakimidis, N. I.: "On the Natural Interpolation Formula for Cauchy-type Singular Integral Equations of the First Kind," Computing 26, 73-77 (1981).

[4] Krenk, Steen: "On Quadrature Formulas for Singular Integral Equations of the First and the Second Kind," Quart. Appl. Math. 33, 225-232 (1975).

[5] Srivastav, R. P.: "Numerical Solution of Singular Integral Equations Using Gauss-type Formulae - I: Quadrature and Collocation on Chebyshev Nodes," (to be published).

[6] Stewart, Charles E.: "On the Numerical Evaluation of Singular Integrals of Cauchy-type," J. Soc. Indust. Appl. Math. 8, 342-353 (1960).

[7] Szegö, G.: "Orthogonal Polynomials," AMS COLL. PUB., Vol. 23, 4th ed. (1975).

METHOD OF SOLUTION FOR VARIATIONAL PRINCIPLE
USING BICUBIC HERMITE POLYNOMIAL

C. N. Shen
U.S. Army Armament Research and Development Command
Large Caliber Weapon Systems Laboratory
Benet Weapons Laboratory
Watervliet, NY   12189

ABSTRACT. In solving mixed boundary and initial value problems of a
second order partial differential equation using spline functions, the
computation may be simplified considerably if the variable in time can be
truncated into arbitrary sections. Each section may have several node points
for the spline functions in the time domain. This is true because we found
from a previous paper [1] that the initial value problem can be solved in one
direction using variational principle and cubic Hermite Polynomials, without
worrying about the conditions at the other end.

The end conditions of the adjoint system can be adjusted according to the
end conditions of the original system so that the bilinear concomitant is
identically zero. This satisfies the variational principle. A bilinear form
of the original and adjoint variables is employed in determining the
coefficients of the variations of the functions and their first derivatives.
There is no term involving the variations of any higher derivatives. A
bicubic Hermite Polynomial spline function will be used which gives continuity
in the function and first partial derivatives in space or time, together with
the mixed first partial derivative in space and time. Algorithm and procedure
of computation are given.

I. INTRODUCTION. This paper is concerned with the use of variational
principles to solve a mixed boundary and initial value problem. From a
previous paper [1] we understand that the far end conditions are not imposed
for solutions in an initial value problem. This implies that the boundary
value problem can be solved in strips of arbitrarily chosen intervals of time.
The size of the computation can be reduced substantially if the time interval
taken is sufficiently large and number of strips small. This depends, of
course, on the accuracy of the method.

A procedure can be obtained for a recursive relationship in the time
domain, where the final conditions of first strip can be regarded as initial
conditions of the second strip. These recursive solutions can be obtained by
using variational principles with the aid of the bicubic Hermite polynomial
spline functions as finite elements.

II. ESTIMATION. A dynamical system can be modeled by the following
partial differential equation.

$$L(\zeta)\ y_a(\zeta) = -Q(\zeta) \tag{1}$$

with appropriate boundary and initial conditions. In the above equation L is
a linear operator, in both spatial and temporal domain, y_a is the dependent

variable, Q is a forcing function and ζ represents all independent variables, both spatial and temporal.

The inner product $\langle\ \rangle$ of an adjoint forcing function $\bar{Q}$ and the solution $(y_a(\zeta))$ of Eq. (1) can be used for the purpose of estimation. This inner product is

$$G[y_a] = \langle \bar{Q} y_a \rangle \tag{2}$$

The estimate y which differs from the actual solution y_a of Eq. (1) by an increment δy can be written as

$$\delta y = y - y_a \tag{3}$$

Then the estimate y becomes

$$G[y] = G[y_a + \delta y]$$
$$= \langle \bar{Q},\ (y_a + \delta y) \rangle$$
$$= G[y_a] + \langle \bar{Q}, \delta y \rangle \tag{4}$$

which is in error to first order in δy and $\bar{Q}$. This is undesirable because the error depends on the variation δy which is supposed to be arbitrary. Thus the estimate will not be accurate.

III. THE VARIATIONAL PRINCIPLE. A more accurate estimate can be made by constructing a variational principle [2] for Eq. (2). By using the adjoint variable $\bar{y}$ as a Lagrange multiply for Eq. (1) added to G[y] we have

$$J[y,\bar{y}] = G[y] + \langle \bar{y}, (Q + Ly) \rangle$$
$$= \langle \bar{Q}, y \rangle + \langle \bar{y}, Q \rangle + \langle \bar{y}, Ly \rangle \tag{5}$$

In order that J be a variational principle for G the following requirements must be satisfied.

(a) J is stationary about the function y_s which satisfies the relation in Eq. (1).

$$Ly_s = -Q \tag{6}$$

(b) The stationary value of J deduced from Eqs. (2) through (5) is

$$J[\bar{y},y] = G[y_s] + G[y_a] \tag{7}$$

Consider first the stationarity of J by taking the variation of Eq. (5)

$$\delta J = \langle \bar{Q}, \delta y \rangle + \langle \bar{\delta y}, Q \rangle + \langle \bar{\delta y}, Ly \rangle + \langle \bar{y}, L\delta y \rangle$$

$$= \langle \bar{\delta y}, (Ly+Q) \rangle + \langle \delta y, (\overline{Ly+Q}) \rangle$$

$$- \langle \delta y, \overline{Ly} \rangle + \langle \bar{y}, L\delta y \rangle = 0. \tag{8}$$

We will make an effort later to impose certain conditions in order that the following equality holds:

$$\langle \bar{y}, L\delta y \rangle = \langle \delta y, \overline{Ly} \rangle \tag{9}$$

where $\bar{L}$ is the adjoint operator.

By combining Eqs. (8) and (9) one obtains

$$\delta J = \langle \bar{\delta y}, (Ly+Q) \rangle + \langle \delta y, (\overline{Ly+Q}) \rangle = 0 \tag{10}$$

Since the variations δy and $\delta \bar{y}$ are arbitrary it leads to the requirement that the stationary values y_s and $\bar{y}s$ must satisfy

$$Ly_s = -Q \tag{11}$$

$$\overline{Ly_s} = -\bar{Q} \tag{12}$$

Since Eq. (11) is the same as Eq. (6) therefore, J is stationary about the function y_s.

Equation (12) is the adjoint equation in terms of the adjoint operator $\bar{L}$, the adjoint variable $\bar{y}$, and the adjoint forcing function $\bar{Q}$.

It is noted that δJ in Eq. (10) vanishes and is independent of the arbitrary variations δy and $\delta \bar{y}$, in contrast with Eq. (4), where δG is in error to the first order in δy. By using δJ instead of δG one can claim that the estimate is more accurate and free from the arbitrary variations.

Using the relationship in Eq. (11) the stationary value of J from Eq. (5) is

$$J[\bar{y}_s, y_s] = \langle \bar{Q}, y_s \rangle + \langle \bar{y}_s, Q \rangle + \langle \bar{y}_s, Ly_s \rangle = G[y_s] \tag{13}$$

Since J is stationary and $\delta J \rightarrow 0$, then

$$G[y_s] \rightarrow G[y_a] \tag{14}$$

which is the requirement given in Eq. (7).

It is noted that Eq. (10) contains no boundary terms to be satisfied. This bears an important point in the future discussion.

IV. BILINEAR CONCOMITANT. We will find out the conditions for the assumed equality in Eq. (9) to be true. Let us consider the following bilinear concomitant [2]:

$$D = \langle \bar{y}, Ly \rangle - \langle y, \overline{Ly} \rangle \tag{15}$$

The above expression can be integrated in two different ways and can also be written in terms of boundary conditions and initial conditions. It is assumed that these boundary conditions are assigned in such a manner that the above bilinear concomitant is identically zero for all independent variables, i.e.,

$$D \equiv 0 \tag{16}$$

Then the first variations of D also vanish.

$$\delta D = \delta D(\delta \bar{y}) + \delta D(\delta y) = 0 \tag{17}$$

Since $\delta \bar{y}$ and δy are independent of each other, then

$$\delta D(\delta \bar{y}) = \langle \delta \bar{y}, Ly \rangle - \langle y, \overline{L \delta y} \rangle = 0 \tag{18}$$

$$\delta D(\delta y) = \langle \bar{y}, L \delta y \rangle - \langle \delta \bar{y}, \overline{Ly} \rangle = 0 \tag{19}$$

Equation (19) is identical to Eq. (9), which is the assumed equality previously. The implication is that if Eq. (16) is true then Eq. (9) or (19) is automatically true.

Since Eq. (15) can be expressed in terms of some integrals involving boundary conditions, Eq. (16) can be true if these boundary conditions are satisfied. The next section will discuss integral of bilinear expression and its boundary conditions.

V. INTEGRAL OF BILINEAR EXPRESSION. The integral of a bilinear expression for a two dimensional second order problem in space-time can be written as

$$I = \int_{x_0}^{x_b} \int_{t_0}^{t_b} \psi[y(x,t), \bar{y}(x,t)] dt \, dx \tag{20}$$

where $\psi[y,\bar{y}]$ is a given bilinear expression in the form

$$\psi[y,\bar{y}] = \alpha \bar{y}_t y_t + \beta \bar{y}_t y + \gamma \bar{y} y_t + \ell \bar{y}_x y_x + \mu \bar{y}_x y + \nu \bar{y} y_x + \epsilon \bar{y} y \tag{21}$$

The subscripts t and x indicate the partial derivatives of the function y and $\bar{y}$.

Equation (20) can be integrated by parts. Two different forms of integration and end conditions can be obtained. The first form of the integral is

$$I = -\int_{x_o}^{x_b} \int_{t_o}^{t_b} \bar{y}Lydtdx + \int_{x_o}^{x_b} (\alpha y_t + \gamma y)\bar{y}\Big|_{t_o}^{t_b} dx + \int_{t_o}^{t_b} (\ell y_x + \nu y)\bar{y}\Big|_{x_o}^{x_b} dt \qquad (22)$$

which is obtained by integrating by parts on the adjoint variable. On the other hand, we can perform integration on the original variables to give

$$I = -\int_{x_o}^{x_b} \int_{t_o}^{t_b} y\overline{Ly}dtdx + \int_{x_o}^{x_b} (\bar{\alpha}\bar{y}_t + \bar{\beta}\bar{y})y\Big|_{t_o}^{t_b} dx + \int_{t_o}^{t_b} (\bar{\ell}\bar{y}_x + \bar{\mu}\bar{y})y\Big|_{x_o}^{x_b} dt \qquad (23)$$

where

$$Ly = (\alpha y_t)_t - \beta y_t + (\gamma y)_t + (\ell y_x)_x - \mu y_x + (\nu y)_x - \varepsilon y \qquad (24)$$

and

$$\overline{Ly} = (\bar{\alpha}\bar{y}_t)_t + (\bar{\beta}\bar{y})_t - \bar{\gamma}\bar{y}_t + (\bar{\ell}\bar{y}_x)_x + (\bar{\mu}\bar{y})_x - \bar{\nu}\bar{y}_x - \bar{\varepsilon}\bar{y} \qquad (25)$$

For a two dimensional second order system in space-time domain, Eq. (15) becomes

$$D = \int_{x_o}^{x_b} \int_{t_o}^{t_b} \bar{y}Lydtdx - \int_{x_o}^{x_b} \int_{t_o}^{t_b} y\overline{Ly}dtdx \qquad (26)$$

By equating Eqs. (22) and (23) and solving for D in Eq. (26) we are converting the double integral into two simple integrals in terms of the boundary conditions.

We can express the quantity D as the sum of two parts D_1 and D_2 as

$$D = D_1 + D_2$$

The terms in D_1 involve the initial conditions of y and $\bar{y}$ as

$$D_1 = \int_{x_o}^{x_b} \{\alpha_b(y_{tb}\bar{y}_b - \bar{y}_{tb}y_b) - \alpha_o(y_{to}\bar{y}_o - \bar{y}_{to}y_o)$$
$$+ (\gamma_b - \beta_b)\bar{y}_b y_b - (\gamma_o - \beta_o)y_o\bar{y}_o\}dx \qquad (27)$$

The terms in D_2 involve the boundary conditions of y and $\bar{y}$ as

$$D_2 = \int_{t_o}^{t_b} \{\ell_b(y_{xb}\bar{y}_b - \bar{y}_{xb}y_b) - \ell_o(y_{xo}\bar{y}_o - \bar{y}_{xo}y_o)$$
$$+ (\nu_b - \mu_b)\bar{y}_b y_b - (\nu_o - \mu_o)y_o\bar{y}_o\}dt \qquad (28)$$

In order that $D \equiv 0$ in Eq. (16) it requires that

$$D_1 \equiv 0 \tag{29a}$$

and

$$D_2 \equiv 0 \tag{29b}$$

<u>VI. END CONDITIONS FOR THE ADJOINT SYSTEMS</u>. We may take four different cases in discussing the end conditions for the adjoint systems in order to satisfy the requirements in Eqs. (29).

(a). The Wave Equation: In this case Eq. (24) becomes

$$Ly = (\alpha y_t)_t + (\ell y_x)_x = 0 \tag{30}$$

and the coefficients are

$$\gamma_b = \beta_b, \quad \gamma_o = \beta_o, \quad \nu_b = \mu_b, \quad \nu_o = \mu_o$$

$$\alpha_b \neq 0, \quad \alpha_o \neq 0, \quad \ell_b \neq 0, \text{ and } \ell_o \neq 0 \tag{31}$$

Let us assume that the adjoint variables are

$$\bar{y}_b = ky_o, \quad \bar{y}_o = ky_b \tag{32}$$

$$\bar{y}_{tb} = -\alpha_b^{-1}\alpha_o ky_{to}, \quad \bar{y}_{to} = -\alpha_o^{-1}\alpha_b ky_{tb} \tag{33}$$

$$\bar{y}_{xb} = -\ell_b^{-1}\ell_o ky_{xo} \quad \text{and} \quad \bar{y}_{xo} = -\ell_o^{-1}\ell_b ky_{xb} \tag{34}$$

where k is constant.

The above boundary values satisfy the requirement that $D_1 = D_2 = 0$ in Eqs. (27) and (28). Thus it also satisfies Eq. (16) that

$$D \equiv 0$$

(b). Heat Equation: In this case Eq. (24) is

$$Ly = -\beta y_t + (\gamma y)_t + (\ell y_x)_x = 0 \tag{35}$$

and the coefficients are

$$\nu_b = \mu_b, \quad \nu_o = \mu_o, \quad \alpha_b = 0, \quad \alpha_o = 0$$

$$\gamma_b \neq \beta_b, \quad \gamma_o \neq \beta_o, \quad \ell_b \neq 0, \quad \ell_o \neq 0 \tag{36}$$

Let the adjoint variables be

$$\bar{y}_b = (\gamma_o - \beta_o)ky_o, \quad \bar{y}_o = (\gamma_b - \beta_b)ky_b \tag{37}$$

$$\bar{y}_{xb} = -\ell_b^{-1}\ell_o(\gamma_b - \beta_b)ky_{xo}, \quad \bar{y}_{xo} = -\ell_o^{-1}\ell_b(\gamma_o - \beta_o)ky_{xb} \tag{38}$$

We also have $D_1 = D_2 = 0$ and $D \equiv 0$.

(c). First order partials of x in Eq. (24) are missing, i.e.,

$$\nu_b = \mu_b, \quad \nu_o = \mu_o, \quad \gamma_b \neq \beta_b, \quad \gamma_o \neq \beta_o \tag{39}$$

Let

$$\bar{y}_b = (\gamma_o - \beta_o)ky_o, \quad \bar{y}_o = (\gamma_b - \beta_b)ky_o \tag{40}$$

$$\bar{y}_{tb} = -\alpha_b^{-1}\alpha_o(\gamma_b - \beta_b)ky_{to}, \quad \bar{y}_{to} = -\alpha_o^{-1}\alpha_b(\gamma_o - \beta_o)ky_{tb} \tag{41}$$

$$\bar{y}_{xb} = -\ell_b^{-1}\ell_o(\gamma_b - \beta_b)ky_{xo}, \quad \bar{y}_{xo} = -\ell_o^{-1}\ell_b(\gamma_o - \beta_o)ky_{xb} \tag{42}$$

We also have $D_1 = D_2 = 0$ and $D \equiv 0$.

(d). First order partial of t in Eq. (24) are missing.

$$\gamma_b = \beta_b, \quad \gamma_o = \beta_o, \quad \nu_b \neq \mu_b, \quad \nu_o \neq \mu_o$$

$$\alpha_b \neq 0, \quad \alpha_o \neq 0, \quad \ell_b \neq 0, \text{ and } \ell_o \neq 0 \tag{43}$$

Let

$$\bar{y}_b = (\nu_o - \mu_o)ky_o, \quad \bar{y}_o = (\nu_b - \mu_b)ky_b \tag{44}$$

$$\bar{y}_{tb} = -\alpha_b^{-1}\alpha_o(\nu_b - \mu_b)ky_{to}, \quad \bar{y}_{to} = -\alpha_o^{-1}\alpha_b(\nu_o - \mu_o)ky_{tb} \tag{45}$$

$$\bar{y}_{xb} = -\ell_b^{-1}\ell_o(\nu_b - \mu_b)ky_{xo}, \quad \bar{y}_{xo} = -\ell_o^{-1}\ell_b(\nu_o - \mu_o)ky_{xb} \tag{46}$$

We also have $D_1 = D_2 = 0$, and $D \equiv 0$.

From the expression $D \equiv 0$ in Eq. (15) we can conclude that $\delta D = 0$ in Eq. (19) and Eq. (9) hold, which leads to the condition in Eq. (10) that

$$\delta J = 0$$

for all arbitrary variations δy and $\delta \bar{y}$.

VII. FIRST VARIATION. Since the variations δy and $\delta \bar{y}$ are independent to each other, the part of δJ in Eq. (10) with variation $\delta \bar{y}$ can be expressed as

$$\delta J(\delta \bar{y}) = \int_{x_o}^{x_b} \int_{t_o}^{t_b} \delta \bar{y} Ly \, dt \, dx + \int_{x_o}^{x_b} \int_{t_o}^{t_b} \delta \bar{y} Q \, dt \, dx = 0 \tag{47}$$

where Ly is given in Eq. (24) and contains second order partial differentials in y. It is intended to include only first order partial differentials and the function y itself in $\delta J(\delta \bar{y})$. This can be achieved by considering the variation of the bilinear expression I in Eqs. (20) and (21) which gives

$$\delta I = \delta I(\delta \bar{y}) + \delta I(\delta y) \tag{48}$$

where

$$\delta I(\overline{\delta y}) = \int_{x_o}^{x_b} \int_{t_o}^{t_b} [(\alpha y_t + \gamma y)\overline{\delta y_t} + (\beta y_t + \varepsilon y + \mu y_x)\overline{\delta y} + (\ell y_x + \nu y)\overline{\delta y_x}]dt\,dx \quad (49)$$

A different version of the above variation can be obtained from Eq. (22) as

$$\delta I(\overline{\delta y}) = -\int_{x_o}^{x_b} \overline{\delta y} Ly\,dt\,dx + \int_{x_o}^{x_b} \delta y(\alpha y_t + \gamma y)\Big|_{t_o}^{t_b} dx$$
$$+ \int_{t_o}^{t_b} \overline{\delta y}(\ell y_x + \nu y)\Big|_{x_o}^{x_b} dt \quad (50)$$

Equating Eqs. (49) and (50), solving for the term containing integral for $\overline{\delta y}Ly$ and substituting into Eq. (47) we have

$$\delta J(\overline{\delta y}) = \int_{x_o}^{x_b} (\alpha y_t + \gamma y)\overline{\delta y}\Big|_{t_o}^{t_b} dx + \int_{t_o}^{t_b} (\ell y_x + \nu y)\overline{\delta y}\Big|_{x_o}^{x_b} dt$$

$$+ \int_{x_o}^{x_b} \int_{t_o}^{t_b} \overline{\delta y} Q\,dt\,dx$$

$$- \int_{x_o}^{x_b} \int_{t_o}^{t_b} [(\alpha y_t + \gamma y)\overline{\delta y_t} + (\beta y_t + \varepsilon y + \mu y_x)\overline{\delta y} + (\ell y_x + \nu y)\overline{\delta y_x}]dt\,dx = 0 \quad (51)$$

This is the key equation which uses variational principle in solving a mixed initial and boundary value problem. The above equation contains only δy, δy_t, and δy_x and none of the variations of higher derivatives. The dependent variable contains only y, y_t, and y_x and no higher partials.

VIII. TRANSFORMATION OF COORDINATES. The integral signs in Eq. (51) can be converted into summation signs if discrete intervals for integration are used. We may take some scale factors to nondimensionalize the problem by giving

$$t_o = 0, \ t_b = 1 \qquad 0 < t < 1 \quad (52)$$

$$x_o = 0, \ x_b = 1 \qquad 0 < x < 1 \quad (53)$$

Moreover, Eq. (51) can be discretized by letting

$$\xi = Ht - i+1 \qquad 0 < \xi < 1 \qquad i = 1,2,\ldots,H \quad (54)$$

$$\eta = Kx - j+1 \qquad 0 < \eta < 1 \qquad j = 1,2,\ldots,K \quad (55)$$

where H and K are number of intervals for t and x respectively.

Thus the partial derivatives are

$$y_t = \frac{\partial y}{\partial t} = H \frac{\partial y}{\partial \xi} = Hy_\xi \tag{56}$$

$$y_x = \frac{\partial y}{\partial x} = K \frac{\partial y}{\partial \eta} = Ky_\eta \tag{57}$$

Use of Eqs. (52) through Eq. (57) then leads to

$$\delta J(\overline{\delta y}) = \sum_{j=1}^{K} \int_0^1 [\alpha H y_\xi(i,j) + \gamma y(i,j)] \overline{\delta y}(i,j) \Big|_{t_o}^{t_b} \frac{1}{K} d\eta$$

$$+ \sum_{i=1}^{H} \int_0^1 [\ell K y_\eta(i,j) + \nu y(i,j)] \overline{\delta y}(i,j) \Big|_{x_o}^{x_b} \frac{1}{H} d\xi$$

$$+ \sum_{j=1}^{K} \int_0^1 \{ \sum_{i=1}^{H} \int_0^1 \overline{\delta y}(i,j) Q \frac{1}{H} d\xi \} \frac{1}{K} d\eta$$

$$- \sum_{j=1}^{K} \int_0^1 \{ \sum_{i=1}^{H} \int_0^1 [(\alpha H y_\xi(i,j) + \gamma y(i,j)) H \overline{\delta y}_\xi(i,j)$$

$$+ (\beta H y_\xi(i,j) + \epsilon y(i,j) + \mu K y_\eta(i,j)) \overline{\delta y}(i,j)$$

$$+ (\ell K y_\eta(i,j) + \nu y(i,j)) K \overline{\delta y}_\eta(i,j)] \frac{1}{H} d\xi \} \frac{1}{H} d\eta \tag{58}$$

IX. GRID SYSTEMS. The (16x1) vector $Y(i,j)$ has a grid of four (4x1) vectors $Y_1(i,j)$ through $Y_4(i,j)$, thus

$$Y(i,j) = \{[Y_1(i,j)]T \ [Y_2(i,j)]T \ [Y_3(i,j)]T \ [Y_4(i,j)]T \tag{59}$$

Each of the (4x1) vector has four components, consisting of the function, its first partials in both directions, and its mixed partial.

$$
Y_1(i,j) = \begin{bmatrix} y(\xi_i, \eta_j) \\ y_\xi(\xi_i, \eta_j) \\ y_\eta(\xi_i, \eta_j) \\ y_{\xi\eta}(\xi_i, \eta_j) \end{bmatrix}
\qquad
Y_3(i,j) = \begin{bmatrix} y(\xi_i, \eta_{j+1}) \\ y_\xi(\xi_i, \eta_{j+1}) \\ y_\eta(\xi_i, \eta_{j+1}) \\ y_{\xi\eta}(\xi_i, \eta_{j+1}) \end{bmatrix}
$$

$$
Y_2(i,j) = \begin{bmatrix} y(\xi_{i+1}, \eta_j) \\ y_\xi(\xi_{i+1}, \eta_j) \\ y_\eta(\xi_{i+1}, \eta_j) \\ y_{\xi\eta}(\xi_{i+1}, \eta_j) \end{bmatrix}
\qquad
Y_4(i,j) = \begin{bmatrix} y(\xi_{i+1}, \eta_{j+1}) \\ y_\xi(\xi_{i+1}, \eta_{j+1}) \\ y_\eta(\xi_{i+1}, \eta_{j+1}) \\ y_{\xi\eta}(\xi_{i+1}, \eta_{j+1}) \end{bmatrix}
\qquad (60)
$$

If we increase the row index from i to i+1, then the grid point shifts down by one step and the following holds

$$
Y_1(i+1,j) = Y_2(i,j) \qquad Y_3(i+1,j) = Y_4(i,j) \qquad (61)
$$

If we increase the column index from j to j+1 then the grid point shifts to the right by one step and one obtains

$$
Y_1(i,j+1) = Y_3(i,j) \qquad Y_2(i,j+1) = Y_4(i,j) \qquad (62)
$$

The following diagram shows the relationship of the grid system.
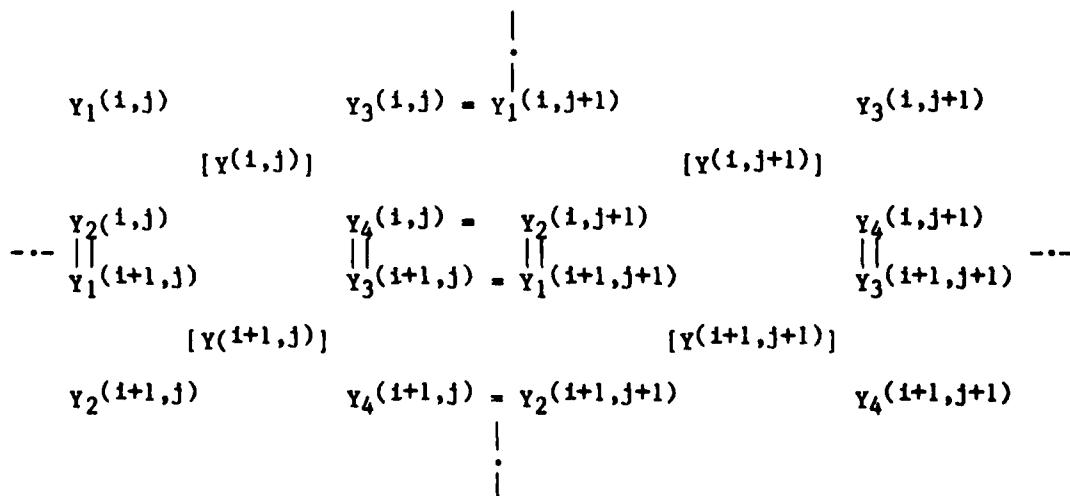
X. SPLINE FUNCTION. We may express the variables $y^{(i,j)}$ and $\delta y^{(i,j)}$ in Eq. (58) in terms of the (1x16) spline function $a^T(\xi,n)$ and the (16x1) node point function $Y^{(i,j)}$ as follows.

$$y^{(i,j)}(\xi,n) = a^T(\xi,n)Y^{(i,j)} \tag{63}$$

where

$$a^T(\xi,n) = \{[a^1(\xi,n)]^T \ [a^2(\xi,n)]^T \ [a^3(\xi,n)]^T \ [a^4(\xi,n)]^T\} \tag{64}$$

and

$$\delta\bar{y}^{(i,j)}(\xi,n) = a^T(\xi,n)\delta\bar{Y}^{(i,j)} \tag{65}$$

A typical term for a product can be written as

$$\delta\bar{y}^{(i,j)}y^{(i,j)} = [\delta\bar{Y}^{(i,j)}]^T a(\xi,n)a^T(\xi,n)Y^{(i,j)} \tag{66}$$

XI. BICUBIC HERMITE POLYNOMIAL SPLINES. With the aid of Eq. (59), Eq. (63) may be expressed as

$$y^{(i,j)}(\xi,n) = [a^1(\xi,n)]^T Y_1^{(i,j)} + [a^2(\xi,n)]^T Y_2^{(i,j)}$$
$$+ [a^3(\xi,n)]^T Y_3^{(i,j)} + [a^4(\xi,n)]^T Y_4^{(i,j)} \tag{67}$$

The bicubic Hermite polynomial spline is continuous in the functional value, its first partials in two directions, and its mixed first partial in both directions. The bicubic Hermite polynomial spline gives

$$a^1(\xi,n) = \begin{bmatrix} \phi(\xi)\ \phi(n) \\ \psi(\xi)\ \phi(n) \\ \phi(\xi)\ \psi(n) \\ \psi(\xi)\ \psi(n) \end{bmatrix}^T \qquad a^3(\xi,n) = \begin{bmatrix} \phi(\xi)\ \rho(n) \\ \psi(\xi)\ \rho(n) \\ \phi(\xi)\ \omega(n) \\ \psi(\xi)\ \omega(n) \end{bmatrix}^T$$

$$a^2(\xi,n) = \begin{bmatrix} \rho(\xi)\ \phi(n) \\ \omega(\xi)\ \phi(n) \\ \rho(\xi)\ \psi(n) \\ \omega(\xi)\ \psi(n) \end{bmatrix}^T \qquad a^4(\xi,n) = \begin{bmatrix} \rho(\xi)\ \rho(n) \\ \omega(\xi)\ \rho(n) \\ \rho(\xi)\ \omega(n) \\ \omega(\xi)\ \omega(n) \end{bmatrix}^T \tag{68}$$

where

$$\phi(\xi) = 1 - 3\xi^2 + 2\xi^3 \qquad\qquad \phi_\xi(\xi) = -6\xi + 6\xi^2$$

$$\psi(\xi) = \xi - 2\xi^2 + \xi^3 \qquad\qquad \psi_\xi(\xi) = 1 - 4\xi + 3\xi^2$$

$$\rho(\xi) = 3\xi^2 - 2\xi^3 \qquad\qquad \rho_\xi(\xi) = 6\xi - 6\xi^2$$

$$\omega(\xi) = -\xi^2 + \xi^3 \qquad\qquad \omega_\xi(\xi) = -2\xi + 3\xi^2 \qquad (69)$$

At grid points (nodes) the value of ξ or η takes the value of 0 or 1. Thus we have

$$
\begin{bmatrix}
\phi(0) = 1 & \psi(0) = 0 & \phi(1) = 0 & \psi(1) = 0 \\
\phi_\xi(0) = 0 & \psi_\xi(0) = 1 & \phi_\xi(1) = 0 & \psi_\xi(1) = 0 \\
\rho(0) = 0 & \omega(0) = 0 & \rho(1) = 1 & \omega(1) = 0 \\
\rho_\xi(0) = 0 & \omega_\xi(0) = 0 & \rho_\xi(1) = 0 & \omega_\xi(1) = 1
\end{bmatrix}
\qquad (70)
$$

It is noted that the diagonal elements of the matrix are unity and the off diagonal terms are zeroes. Similar expression are held for $\phi(\eta)$, etc. in terms of η. For example

$$\phi(\eta) = 1 - 3\eta^2 + 2\eta^3 \text{ , etc.} \qquad (71)$$

XII. CONSISTENCY AT NODES. To show that Eqs. (67) through (69) are consistent at the node points, we will check only the following cases.

(1) For the case $\xi = 0$ and $\eta = 0$, from Eqs. (68) and (70) we have

$$a^2(0,0) = a^3(0,0) = a^4(0,0) = [0\ 0\ 0\ 0]$$

$$a^1(0,0) = [1\ 0\ 0\ 0] \qquad (72)$$

(a)
$$y^{(i,j)}(\xi,\eta)\Big|_{\substack{\xi=0 \\ \eta=0}} = [a^1(\xi,\eta)]^T_{\substack{\xi=0 \\ \eta=0}} Y_1^{(i,j)}$$

$$= [1\ 0\ 0\ 0] Y_1^{(i,j)} = y^{(i,j)}(0,0) \qquad (73)$$

258

(b)
$$y_\xi^{(i,j)}(\xi,\eta)\bigg|_{\substack{\xi=0\\\eta=0}} = [a^1{}_\xi(\xi,\eta)]^T_{\substack{\xi=0\\\eta=0}} Y_1^{(i,j)}$$

$$= \begin{bmatrix} \phi_\xi(\xi)\ \phi(\eta) \\ \psi_\xi(\xi)\ \phi(\eta) \\ \phi_\xi(\xi)\ \psi(\eta) \\ \psi_\xi(\xi)\ \psi(\eta) \end{bmatrix}^T_{\substack{\xi=0\\\eta=0}} \begin{bmatrix} y^{(i,j)}(0,0) \\ y_\xi^{(i,j)}(0,0) \\ y_\eta^{(i,j)}(0,0) \\ y_{\xi\eta}^{(i,j)}(0,0) \end{bmatrix}$$

$$= [0\ 1\ 0\ 0] Y_1^{(i,j)}$$

$$= y_\xi^{(i,j)}(0,0) \tag{74}$$

(c)
$$y_{\xi\eta}^{(i,j)}(\xi,\eta)\bigg|_{\substack{\xi=0\\\eta=0}} = [a^1{}_{\xi\eta}(\xi,\eta)]^T_{\substack{\xi=0\\\eta=0}} Y_1^{(i,j)}$$

$$= \begin{bmatrix} \phi_\xi(\xi)\ \phi_\eta(\eta) \\ \psi_\xi(\xi)\ \phi_\eta(\eta) \\ \phi_\xi(\xi)\ \psi_\eta(\eta) \\ \psi_\xi(\xi)\ \psi_\eta(\eta) \end{bmatrix}^T_{\substack{\xi=0\\\eta=0}} \begin{bmatrix} y^{(i,j)}(0,0) \\ y_\xi^{(i,j)}(0,0) \\ y_\eta^{(i,j)}(0,0) \\ y_{\xi\eta}(i,j)(0,0) \end{bmatrix}$$

$$= [0\ 0\ 0\ 1] Y_1^{(i,j)}$$

$$= y_{\xi\eta}^{(i,j)}(0,0) \tag{75}$$

The above expressions show that the function, its first partial in one direction, and its mixed partial are consistent and continuous at the node point $\xi = 0$ and $\eta = 0$.

(2) For the case $\xi = 1$ and $\eta = 1$, from Eqs. (68) and (70) we have

$$a^1(1,1) = a^2(1,1) = a^3(1,1) = [0\ 0\ 0\ 0]$$

$$a^4(1,1) = [1\ 0\ 0\ 0] \tag{76}$$

(a) Thus

$$y^{(i,j)}(\xi,n)\Big|_{\substack{\xi=1 \\ \eta=1}} = [a^4(\xi,n)]^T_{\substack{\xi=1 \\ \eta=1}} Y_4^{(i,j)}$$

$$= [1\ 0\ 0\ 0]Y_4^{(i,j)} = y^{(i,j)}(1,1) \tag{77}$$

(b)

$$y_\xi^{(i,j)}(\xi,n)\Big|_{\substack{\xi=1 \\ \eta=1}} = [a^4{}_\xi(\xi,n)]^T_{\substack{\xi=1 \\ \eta=1}} Y_4^{(i,j)}$$

$$= \begin{bmatrix} \rho_\xi(\xi)\ \rho(n) \\ \omega_\xi(\xi)\ \rho(n) \\ \rho_\xi(\xi)\ \omega(n) \\ \omega_\xi(\xi)\ \omega(\xi) \end{bmatrix}^T_{\substack{\xi=1 \\ \eta=1}} \begin{bmatrix} y^{(i,j)}(1,1) \\ y_\xi^{(i,j)}(1,1) \\ y_\eta^{(i,j)}(1,1) \\ y_{\xi\eta}^{(i,j)}(1,1) \end{bmatrix}$$

$$= [0\ 1\ 0\ 0]Y_4^{(i,j)} = y_\xi^{(i,j)}(1,1) \tag{78}$$

(c)

$$y_{\xi\eta}^{(i,j)}(\xi,n)\Big|_{\substack{\xi=1 \\ \eta=1}} = [a^4{}_{\xi\eta}(\xi,n)]^T_{\substack{\xi=1 \\ \eta=1}} Y_4^{(i,j)}$$

$$= \begin{bmatrix} \rho_\xi(\xi)\ \rho_\eta(n) \\ \omega_\xi(\xi)\ \rho_\eta(n) \\ \rho_\xi(\xi)\ \omega_\eta(n) \\ \omega_\xi(\xi)\ \omega_\eta(n) \end{bmatrix}^T_{\substack{\xi=1 \\ \eta=1}} \begin{bmatrix} y^{(i,j)}(1,1) \\ y_\xi^{(i,j)}(1,1) \\ y_\eta^{(i,j)}(1,1) \\ y_{\xi\eta}^{(i,j)}(1,1) \end{bmatrix}$$

$$= [0\ 0\ 0\ 1]Y_4^{(i,j)} = y_{\xi\eta}^{(i,j)}(1,1) \tag{79}$$

It can be proved that all the 16 elements at four corners of the grid are consistant. It can also be proved that the function, its two directional first derivatives and its mixed partial are <u>continuous</u> at all grid points.

XIII. WAVE EQUATION. Let us take a special case for further study of the mixed initial and boundary value problems. We choose the wave equation where the parameters in Eq. (24) are

$$\beta = \gamma = \mu = \nu = \epsilon = 0 \tag{80}$$

$$\text{and} \quad \alpha = \text{const} \neq 0 \tag{81}$$

$$\ell = \text{const} \neq 0 \tag{82}$$

Then Eq. (24) becomes

$$Ly = \alpha y_{tt} + \ell y_{xx} = -Q \tag{83}$$

Eq. (58) is simplified to

$$
\begin{aligned}
\delta J(\bar{\delta y}) = & \sum_{j=1}^{K} \frac{\alpha H}{K} \int_{0}^{1} \bar{\delta y}(1,j) y_{\xi}(1,j) d\eta \Big|_{t_o}^{t_b} \\
& + \sum_{i=1}^{H} \frac{\ell K}{H} \int_{0}^{1} \bar{\delta y}(1,j) y_{\eta}(1,j) d\xi \Big|_{x_o}^{x_b} \\
& + \sum_{j=1}^{K} \sum_{i=1}^{H} \frac{1}{HK} \int_{0}^{1} \int_{0}^{1} \bar{\delta y}(1,j) Q d\xi d\eta \\
& + \sum_{j=1}^{K} \sum_{i=1}^{H} \int_{0}^{1} \int_{0}^{1} [\frac{\alpha H}{K} \bar{\delta y}_{\xi}(1,j) y_{\xi}(1,j) \\
& + \frac{\ell K}{H} \bar{\delta y}_{\eta}(1,j) y_{\eta}(1,j)] d\xi d\eta = 0
\end{aligned}
\tag{84}
$$

Differentiating Eqs. (63) and (65), and substituting into Eq. (84) we have

$$\delta J(\delta \bar{y}) = \sum_{j=1}^{K} \frac{\alpha H}{K} [\delta \bar{Y}(i,j)]^T \int_0^1 a(\xi,\eta) a_\xi(\xi,\eta) d\eta \Big|_{t_o}^{t_b} Y(i,j)$$

$$+ \sum_{i=1}^{H} \frac{\ell K}{H} [\delta \bar{Y}(i,j)]^T \int_0^1 a(\xi,\eta) a_\eta(\xi,\eta) d\xi \Big|_{x_o}^{x_b} Y(i,j)$$

$$+ \sum_{j=1}^{K} \sum_{i=1}^{H} \frac{1}{HK} [\delta \bar{Y}(i,j)]^T \int_0^1 \int_0^1 a(\xi,\eta) Q(\xi,\eta) d\xi d\eta$$

$$+ \sum_{j=1}^{K} \sum_{i=1}^{H} \frac{\alpha H}{H} [\delta \bar{Y}(i,j)]^T \int_0^1 \int_0^1 a_\xi(\xi,\eta) a_\xi^T(\xi,\eta) d\xi d\eta \ Y(i,j)$$

$$+ \sum_{j=1}^{K} \sum_{i=1}^{H} \frac{\ell K}{H} [\delta \bar{Y}(i,j)]^T \int_0^1 \int_0^1 a_\eta(\xi,\eta) a_\eta^T(\xi,\eta) d\xi d\eta \ Y(i,j) = 0 \qquad (85)$$

Eq. (85) may be written into a different form as

$$\delta J(\delta \bar{y}) = \sum_{j=1}^{K} [\delta \bar{Y}(t_b,j)]^T P_{0\xi}(t_b) Y(t_b,j)$$

$$- \sum_{j=1}^{K} [\delta \bar{Y}(t_o,j)]^T P_{0\xi}(t_o) Y(t_o,j)$$

$$+ \sum_{i=1}^{H} [\delta \bar{Y}(i,x_b)]^T P_{0\eta}(x_b) Y(i,x_b)$$

$$- \sum_{i=1}^{H} [\delta \bar{Y}(i,x_o)]^T P_{0\eta}(x_o) Y(i,x_o)$$

$$+ \sum_{j=1}^{K} \sum_{i=1}^{H} [\delta \bar{Y}(i,j)]^T q(i,j)$$

$$- \sum_{j=1}^{K} \sum_{i=1}^{H} [\delta \bar{Y}(i,j)]^T p(i,j) Y(i,j) = 0 \qquad (86)$$

It is noted that the first two terms involve initial values, the next two terms involve boundary values, and the last two terms involve interior quantities within the region.

Equation (86) uses the following notations

$$P_{0\xi}(t_b) = \frac{\alpha H}{K} \int_0^1 a(\xi,\eta) a_\xi^T(\xi,\eta) d\eta \Big|_{t=t_b} \tag{87}$$

$$P_{0\xi}(t_o) = \frac{\alpha H}{K} \int_0^1 a(\xi,\eta) a_\xi^T(\xi,\eta) d\eta \Big|_{t=t_o} \tag{88}$$

$$P_{0\eta}(x_b) = \frac{\ell K}{K} \int_0^1 a(\xi,\eta) a_\eta^T(\xi,\eta) d\xi \Big|_{x=x_b} \tag{89}$$

$$P_{0\eta}(x_o) = \frac{\ell K}{K} \int_0^1 a(\xi,\eta) a_\eta^T(\xi,\eta) d\xi \Big|_{x=x_o} \tag{90}$$

$$P = \frac{\alpha H}{K} P_{\xi\xi} + \frac{\ell K}{H} P_{\eta\eta} \tag{91}$$

$$P_{\xi\xi} = \int_0^1 \int_0^1 a_\xi(\xi,\eta) a_\xi^T(\xi,\eta) d\xi d\eta \tag{92}$$

$$P_{\eta\eta} = \int_0^1 \int_0^1 a_\eta(\xi,\eta) a_\eta^T(\xi,\eta) d\xi d\eta \tag{93}$$

and

$$q(i,j) = \frac{1}{HK} \int_0^1 \int_0^1 a(\xi,\eta) Q(\xi,\eta) d\xi d\eta \tag{94}$$

For a given spline function, such as bicubic Hermite polynomials, $a(\xi,\eta)$ is given in Eqs. (64), (68), and (69). For a given grid the number of node points are known, so are H and K. Thus Eqs. (87) through (93) can be determined and stored in advance. For any given forcing function $Q(\xi,\eta)$, Eq. (94) can also be evaluated.

The (16x1) vector $Y(i,j)$ in Eq. (86) was defined in Eq. (59). Its components can be overlapped as given in Eqs. (61) and (62), we have found previously that the first term in Eq. (86) can be dropped because it can automatically satisfy the final conditions for an initial value problem. In the second term the function $Y(t_o,j)$ are known because they are the initial values. Although some of the boundary values $Y(i,x_b)$ amd $Y(i,x_o)$ are given, most of these terms are to be determined. The entire problem is to solve for $Y(i,j)$ by setting to zero the assembly coefficients of the individual elements of $\delta Y(i,j)$.

It is a tedious task to assemble these coefficients. These will be performed in the future as a separate paper.

263

XIV. CONCLUSION. A bilinear form of the original and adjoint variable
is employed in determining the coefficients of the variations of the functions
and their first derivatives. There is no term involving the variations of any
higher derivatives. A bicubic Hermite polynomial is used which gives continu-
ity in the functions and first partial derivatives in space or time, together
with the mixed first derivating in space and time. In solving mixed boundary
and initial value problems of a second order partial differential equation
using spline functions, the computation may be simplified considerably if the
variable in time can be truncated into arbitrary sections. The entire problem
is divided into several strips of distinct time intervals, each strip contain-
ing mostly the boundary value problem.

The variational principle for spatial and temporal problems with boundary
and initial conditions have been investigated. This variational principle is
very general in scope and can be applied to many linear partial differential
equations. The principle is applicable if the bilinear concomitant is
identically zero. This leads to the requirement that a set of end conditions
for the adjoint systems must be found to satisfy this condition. Otherwise
the variational principle as stated may not be applicable.

Both the wave equation and the heat equation (with one dimensional
spatial direction) satisfy these variational principles. For future work the
analytic solution of these equations using finite element method will be
studied. The assembly of the elements of the matrices involved in the
formulation will be demonstrated. The stability problem in numerical
solutions on these equations will also be investigated. This lays the
foundation for the gun dynamics problem to be studied in the future.

REFERENCES

1. Shen, C. N. and J. J. Wu, "A New Variational Method For Initial Value
    Problems Using Piecewise Hermite Polynomial Spline Functions," presented
    at the 1981 Army Numerical Analysis and Computer Conference, Huntsville,
    AL, February 1981.

2. W. M. Stacey, Jr., Variational Methods in Nuclear Reactor Physics,
    Academic Press, 1974.

SMOOTHEST LOCAL INTERPOLATION FORMULAS
*FOR EQUALLY SPACED DATA**

T. N. E. Greville and Hubert Vaughan[1]
Mathematics Research Center
University of Wisconsin-Madison
Madison, WI 53706

ABSTRACT. Let a moving-average interpolation formula for equally spaced data, exact for the degree r, have a basic function $L \in C^{m-1}$ of finite support with $L^{(m)}$ piecewise continuous. Such a formula is called "smoothest" when the integral of the square of $L^{(m)}$ over the support of L is smallest. If m, r, and the support of L are given, either there is no such formula or there is a unique smoothest formula, for which L is a piecewise polynomial of degree at least r and at most $\max(r, 2m - 1)$, uniquely characterized by certain conditions on the location of its knots and the jumps occurring there. A similar result is obtained if consideration is limited to formulas that preserve (i.e., do not smooth) the given data.

1. INTRODUCTION. Schoenberg pointed out in 1946 [7] that a large class of local interpolation formulas for equally spaced data can be expressed in the form

$$v_x = \sum_{\nu=-\infty}^{\infty} L(x - \nu)y_\nu ,\qquad (1.1)$$

where y_ν denotes a given ordinate, v_x is an interpolated value, and $L(x)$ is a given function called by Schoenberg the basic function of the interpolation formula. This class includes the numerous formulas of so-called "osculatory interpolation" published by actuarial writers (for additional references see [3]). For the latter formulas L is typically a piecewise polynomial function of finite support belonging to continuity class C^1 or C^2.

Also included is what may be called moving Newton-Lagrange interpolation, often used, before computers became available, in the preparation of tables of mathematical functions. An example would be the case in which the function f is interpolated in $(\nu h, (\nu + 1)h)$, ν being any integer, by means of the cubic p uniquely determined by the four conditions

---

$$p(x) = f(x) \qquad (x = (\nu + j)h; \qquad j = -1,0,1,2) \ .$$

In this example L is a continuous piecewise cubic with support in $(-2,2)$, whose first derivative is discontinuous at $x = -2,-1,0,1,2$ (see Fig. 1). These discontinuities did not give rise to any problems in interpolating smooth mathematical functions, but are undesirable if one is interpolating empirical data.

Formula (1.1) is called <u>reproducing</u> when L is such that $v_\nu = y_\nu$ for every integer ν, whatever may be the values of the quantities y_ν. It is clear that (1.1) is reproducing if and only if

$$L(\nu) = \delta_{0\nu} \qquad (\nu = \dots,-1,0,1,\dots) \ . \tag{1.2}$$

where $\delta_{0\nu}$ is a Kronecker symbol. In practice an interpolation formula that is not reproducing smoothes as well as interpolates, since each given ordinate y_ν is, in general, replaced by an adjusted value v_ν. (Whether the adjustment does, in fact, actually increase the smoothness of the data depends on a judicious choice of L; see [7].)

Figure 1 shows the graphs of three typical basic functions. Note that Karup's formula and the Newton-Lagrange central third-difference formula are reproducing, while Jenkins' "modified" third-difference formula is not. On the other hand, note that the Newtonian graph has corners, while the others do not.

BASIC FUNCTIONS OF CERTAIN 4-POINT INTERPOLATION FORMULAS

Figure 1

266
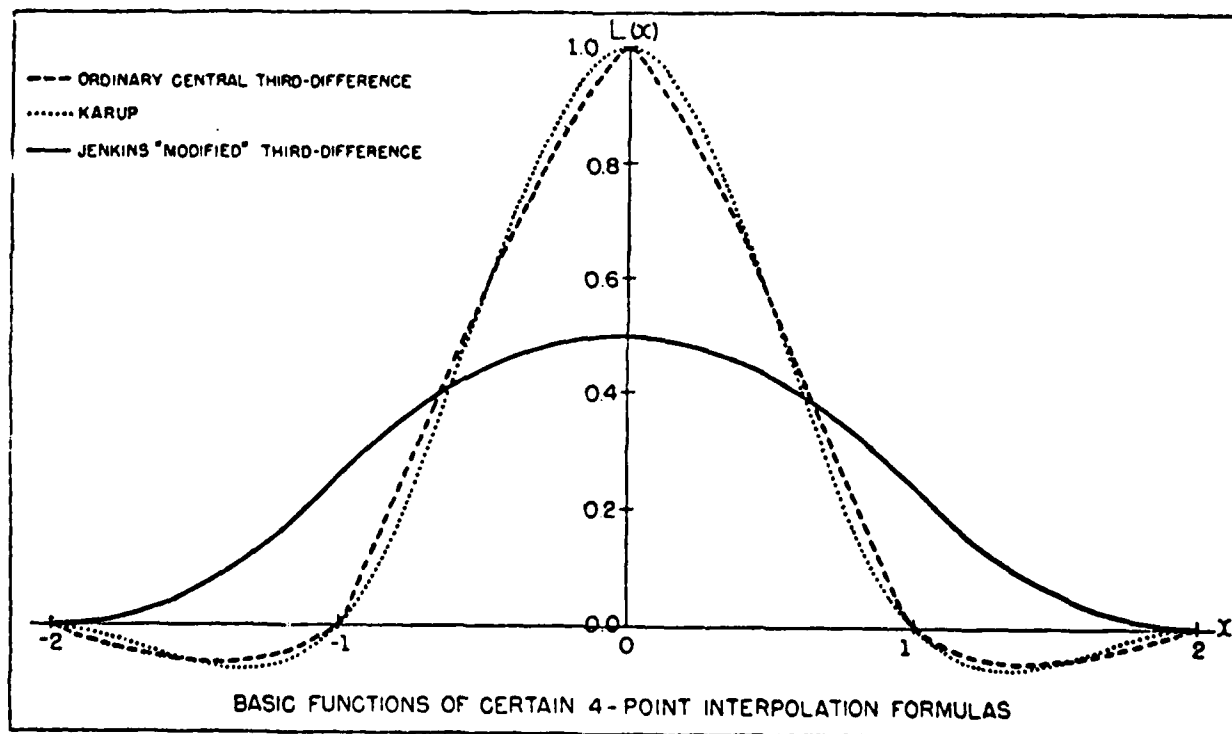
Formula (1.1) is called <u>exact for the degree</u> r when L is such that the formula gives exact values whenever it is used to interpolate a polynomial of degree r or less. In other words, using π_r to denote the class of polynomials of degree r or less, L is such that, for every $p \in \pi_r$, $y_\nu = p(\nu)$ for all integers ν implies $v_x = p(x)$ for all real x.

In the case of moving Newton-Lagrange interpolation, r is merely the degree of the polynomial arcs employed. For the actuarial formulas, r is less than the degree of the piecewise polynomial function L, the "degrees of freedom" thus gained being utilized to increase the order of continuity of L. The latter is, of course, also the order of continuity of the composite interpolating function, for if $L \in C^{m-1}$, then it is clear from (1.1) that $v \in C^{m-1}$.

When L is discontinuous (as occurs, for example, in the case of symmetrical moving Newton-Lagrange interpolation of even degree), the definition of exactness for the degree r requires interpretation. In such a case, it must be assumed that L, though discontinuous, is nevertheless such that, for every $p \in \pi_r$,

$$\phi(x) = \sum_{\nu=-\infty}^{\infty} L(x - \nu)p(\nu)$$

has only removable discontinuities, and they are removed by taking

$$\phi(x) = \phi(x + 0) = \phi(x - 0) \ .$$

2. <u>MINIMIZED-DERIVATIVE FORMULAS</u>. Let $I = (\alpha, \beta)$ be a finite open interval on the real line, and let F_{Irm} denote the set of interpolation formulas of the form (1.1) that are exact for the degree r, and have a basic function $L \in C^{m-1}$ with its support contained in I and with $L^{(m)}$ piecewise continuous. Also let F_{Irm}^{rep} denote the subset of F_{Irm} consisting of reproducing formulas. It follows from (1.2) that F_{Irm}^{rep} is empty unless $0 \in I$. By a piecewise continuous function we mean one having only jump discontinuities and at most a finite set of these.

In each of the classes F_{Irm} or F_{Irm}^{rep} we would like to find that formula which is in some sense smoothest. We shall judge smoothness by the closeness to zero of the mth derivative of the interpolating function v_x. Now, m-fold differentiation of (1.1) gives

$$v_x^{(m)} = \sum_{\nu=-\infty}^{\infty} L^{(m)}(x - \nu)y_\nu \qquad (2.1)$$

almost everywhere. As we have some latitude in the choice of the basic function L, but none as regards the given ordinates y_ν, (2.1) suggests that the values of $v_x^{(m)}$ will be closer to zero than would otherwise be the case, if L is chosen so that the values of $L^{(m)}$ are, in some sense, as close to zero as possible. Accordingly, we shall call a given formula of one of the classes F_{Irm} or F_{Irm}^{rep} a <u>minimized-derivative formula</u> (mdf) of its

class if the quantity

$$J = \int_{-\infty}^{\infty} [L^{(m)}(x)]^2 dx \qquad (2.2)$$

assumes for the given formula its minimum value for the class in question.

The thought leading to the definition of mdf can be made more precise in the following manner. Let a be a given real number. Then, if M denotes the maximum value of $|y_\nu|$ for ν in $(a - \beta, a - \alpha + 1)$, (2.1) gives

$$|v_x^{(m)}| \leq M \sum_{\nu=-\infty}^{\infty} |L^{(m)}(x - \nu)|$$

for every x in $(a, a + 1)$. Consequently,

$$\int_0^1 |v_{a+t}^{(m)}| dt \leq M \int_\alpha^\beta |L^{(m)}(x)| dx . \qquad (2.3)$$

If

$$\mu = \beta - \alpha$$

denotes the width of the interval I, we have, by Schwarz' inequality,

$$\int_\alpha^\beta |L^{(m)}(x)| dx \leq (\mu J)^{1/2} ,$$

where J is given by (2.2). Thus, (2.3) gives

$$\int_0^1 |v_{a+t}^{(m)}| dt \leq M(\mu J)^{1/2} .$$

In other words, we have shown that, for a given M, by minimizing J we minimize a certain upper bound to the integral over a unit interval of the absolute value of $v_x^{(m)}$.

Minimized-derivative interpolation formulas were previously defined by us in [3], and a few examples were given, but no general theory was developed.

In this paper we shall show that the class F_{Irm} is empty for $\mu < r + 1$, is empty or contains a single formula (of moving Newton-Lagrange interpolation) when $\mu = r + 1$, and is infinite when $\mu > r + 1$. In the latter case, we shall show that there is a unique mdf, and shall characterize this formula in a way that leads to an algorithm for its determination in any particular case.

It was previously noted that the class F_{Irm}^{rep} is empty unless the open interval I contains the origin. When this condition is satisfied, we shall

find that F_{Irm}^{rep} is identical to F_{Irm} when the number of integers contained in I does not exceed $r + 1$. This implies, of course, that $r + 1 \leq \mu \leq r + 2$, but the converse is not true.

When the number of integers contained in I exceeds $r + 1$ (and 0 is among them), F_{Irm}^{rep} is a proper subset of F_{Irm}, and the former contains a unique mdf different from that associated with the latter. In this (reproducing) case too, we shall obtain a characterization of the mdf leading to an algorithm for its determination.

In order to arrive at the results just described, it is first necessary to express the requirement that (1.1) be exact for the degree r in manageable form as a set of constraints on the basic function L. A digression for this purpose is the subject of the next section.

3. MAINTENANCE OF DEGREE. Schoenberg noted in [7] that the implications of exactness of formula (1.1) for the degree r become clearer if considered in relation to a certain weaker condition. This weaker condition, in a modified form, was utilized by us in [3] and is used again here. Let H be a given function with its support contained in I, and let a function p and a function ϕ be related by the formula

$$\phi(x) = \sum_{\nu=-\infty}^{\infty} H(x - \nu)p(\nu) . \qquad (3.1)$$

This relation may be regarded as a transformation T_H that transforms p into ϕ, or

$$\phi = T_H p .$$

It is evident that T_H is a linear operator. We shall say that T_H <u>maintains the degree</u> r if it maps the space π_r into itself, or, in other words, if $p \in \pi_r$ implies $\phi \in \pi_r$.

An important special case of maintenance of degree is that in which T_H annihilates π_r: in other words, ϕ is identically zero whenever $p \in \pi_r$.

Schoenberg in [7] defined a transformation T_H that <u>preserves</u> the degree r as one having the property that, for every $p \in \pi_r$, ϕ is a polynomial strictly of the same degree as p with the same leading coefficient. He showed that T_H has this property if its characteristic function (Fourier transform of the basic function H) has the value 1 for the argument 0 and zeros of order $r + 1$ for all nonvanishing integral multiples of 2π.

We showed in [3] that if H has an $(r + 1)$th derivative in the sense of distributions, then T_H maintains the degree r if and only if the convolution of that $(r + 1)$th derivative with every element of π_r vanishes. A more limited result, that can be stated and proved without introducing distributions, will suffice here, and is contained in the next theorem.

If H has a piecewise continuous jth derivative, let $b_{j\xi}$ denote the jump of $H^{(j)}$ at $x = \xi$.

Theorem 3.1. If T_H maintains the degree r and if H is piecewise continuous and has piecewise continuous derivatives of all orders, then, for all real t,

$$\sum_{\nu=-\infty}^{\infty} \nu^i b_{j,t-\nu} = 0 \qquad (i = 0,1,\ldots,r; \; j = 0,1,\ldots) \; . \qquad (3.2)$$

If H is a piecewise polynomial function with finite support and satisfies (3.2), then T_H maintains the degree r.

Proof. If we take $p(\nu) = \nu^i$ in (3.1), the left member of (3.2) is the jump of $\phi^{(j)}(x)$ at $x = t$. But, if T_H maintains the degree r and i is one of the integers $0,1,\ldots,r$, ϕ is a polynomial and this jump vanishes. Thus (3.2) is established.

On the other hand, let H be a piecewise polynomial function of finite support satisfying (3.2), and let $p \in \pi_r$ in (3.1). Then ϕ and all its derivatives are continuous everywhere. But, if d is the maximum degree of the polynomial arcs composing H, then $\phi^{(d+1)}$ vanishes almost everywhere by (3.1). Since $\phi^{(d+1)}$ is continuous everywhere, it is therefore identically zero. It follows that $\phi \in \pi_d$.

If δ denotes the "central-difference" operator defined by

$$\delta f(x) = f(x + \tfrac{1}{2}) - f(x - \tfrac{1}{2}) \; ,$$

we have also from (3.1)

$$\delta^{r+1}\phi(x) = \sum_{\nu=-\infty}^{\infty} p(\nu)\delta^{r+1}H(x - \nu) \; .$$

Expanding $\delta^{r+1}H(x - \nu)$ in terms of $H(x)$ values by the well known binomial formula and rearranging terms gives

$$\delta^{r+1}\phi(x) = \sum_{\nu}' H(x - \nu)\delta^{r+1}p(\nu) \; ,$$

where the summation $\sum_{\nu}'$ is over all the integers when r is odd, and over all the real numbers of the form integer $+ \tfrac{1}{2}$ when r is even. Note that the required rearrangement of terms is permissible because the support of H is finite.

Now, since $p \in \pi_r$, $\delta^{r+1}p(\nu) = 0$ for all ν. Therefore $\delta^{r+1}\phi(x) = 0$ for all real x. But, a polynomial whose $(r + 1)$th derivative vanishes identically belongs to π_r. Therefore T_H maintains the degree r. $\square$

If T_H maintains the degree r, then there is a differential operator of order not exceeding r, which we shall call the <u>signature</u> of T_H and

270

shall denote by S_H, of the form

$$S_H = \sum_{i=0}^{r} a_i D^i ,$$ (3.3)

that is equivalent to T_H over π_r. In other words, $S_H p = T_H p$ whenever $p \in \pi_r$. In (3.3) D denotes differentiation. The following theorem is an immediate consequence of the preceding definitions.

<u>Theorem 3.2</u>. T_H is exact for the degree r if and only if it maintains the degree r and its signature is the identity operator.

We can express S_H in terms of H in various ways. Thus, the coefficients a_i of (3.3) are given by

$$a_i = \frac{(-1)^i}{i!} \sum_{\nu=-\infty}^{\infty} \nu^i H(\nu) \qquad (i = 0,1,\dots,r) .$$ (3.4)

If H is integrable, we have also

$$a_i = \frac{(-1)^i}{i!} \int_{-\infty}^{\infty} x^i H(x) dx \qquad (i = 0,1,\dots,r) .$$

If a basic function L satisfies (1.2), then, by (3.4), the coefficients a_i in the expression (3.3) for S_L are given by

$$a_i = \delta_{0i} \qquad (i = 0,1,\dots,r) .$$

Thus we have established the following corollary, previously noted in [3,7].

<u>Corollary 3.3</u>. The interpolation formula (1.1) is exact for the degree r if it maintains the degree r and is also reproducing.

The existence and properties of the signature S_H were established in [3] (though the term "signature" does not appear there) using the concept of distributions. However, what has been stated here is easily verified by elementary means. A similar remark applies to the following lemma, in which we take

$$\rho = \frac{1}{2}(r + 1) .$$

The lemma can be verified by noting (after some algebraic manipulation) that the function

$$G(x) = \sum_{j=0}^{\infty} \binom{r+j}{j} K(x - \rho - j)$$ (3.5)

has the required properties.

Lemma 3.4. If K is piecewise continuous with its support contained in I and T_K annihilates π_r, then there exists a piecewise continuous function G with support contained in $(\alpha + \rho, \beta - \rho)$, such that

$$\delta^{r+1} G(x) = K(x) \tag{3.6}$$

for all real x such that the left member is defined.

4. CHARACTERIZATION OF GENERAL mdf's. We note that a formula (1.1) that is exact for the degree r must satisfy

$$\sum_{\nu=-\infty}^{\infty} \nu^i L(x - \nu) = x^i \qquad (i = 0,1,\dots,r) . \tag{4.1}$$

If the support of L is contained in I, all but a finite number of the coefficients $L(x - \nu)$ vanish automatically. If $\mu < r + 1$, it follows that there is some interval for x within which each of the $r + 1$ linearly independent functions $1, x, x^2, \dots, x^r$ is expressible as a linear combination of r or less given functions. This is impossible. Therefore F_{Irm} is empty for $\mu < r + 1$.

If $\mu = r + 1$, then for every x such that $x - \alpha$ and $x - \beta$ are nonintegers, (4.1) can be regarded as a system of $r + 1$ linear equations in the $r + 1$ unknown values of $L(x - \nu)$. Moreover, the determinant of the matrix of coefficients of the linear system is a Vandermonde, and therefore nonvanishing. Thus, the system has a unique solution. Now, it is evident that the equations are satisfied by the $r + 1$ fundamental functions of Lagrange interpolation (or extrapolation) for the function value corresponding to the argument x, given those corresponding to the $r + 1$ arguments ν for which $L(x - \nu)$ is undetermined. Moreover, each of these fundamental functions is, indeed, a function of $x - \nu$, as (4.1) requires.

In this case of $\mu = r + 1$, L is discontinuous at those arguments $x \in I$ that differ by an integer from α or β, except in the special case in which α and β are themselves integers and also $0 \in I$. Only in this special case is the formula reproducing and L continuous everywhere.

We conclude from the preceding discussion that the class F_{Irm} is empty for $\mu < r + 1$, and also for $\mu = r + 1$ and $m > 1$, while for $\mu = r + 1$ and $m = 0$ or 1, it is either empty or contains a single formula.

For $\mu > r + 1$, F_{Irm} contains an infinite number of formulas for every nonnegative number m, and among them, as we shall see, a unique mdf. The following theorem is the key to the characterization of this unique mdf.

Theorem 4.1. For any nonnegative integers r and m, and for $\mu > r + 1$, the class F_{Irm} contains a single formula whose basic function L satisfies the following three conditions:

(i) L is a piecewise polynomial function of degree at least r and at most $d = \max(r, 2m - 1)$.

(ii) Each knot of L is an argument that differs by an integer from α
or β (or both).

(iii) The piecewise polynomial function $\delta^{r+1} L$ is given in
$(\alpha + \rho, \beta - \rho)$ by a simple polynomial of degree at most $2m - 1$.

This theorem requires interpretation for $m = 0$. In that case, we
interpret a polynomial of degree -1 (in condition (iii)) to mean one that is
identically zero.

We shall postpone the proof of this theorem, as it will become easier
after we have developed some further paraphernalia. However, without waiting
to prove it, we shall proceed to demonstrate its connection with the existence
of a unique mdf. For this purpose we shall need the following lemma.

Lemma 4.2. Let $K \in C^{m-1}$, with $K^{(m)}$ piecewise continuous, have its
support in I, and let T_K annihilate π_r. Let H be piecewise continuous,
with piecewise continuous derivatives of orders 1 to m, let T_H maintain
the degree r, and let $\delta^{r+1} H$ be given in $(\alpha + \rho, \beta - \rho)$ by a simple
polynomial of degree at most $2m - 1$. Then,

$$\int_{-\infty}^{\infty} H^{(m)}(x) K^{(m)}(x)\, dx = 0 \ . \tag{4.2}$$

Proof. By Lemma 3.4, there exists a function $G \in C^{m-1}$, with support in
$(\alpha + \rho, \beta - \rho)$, such that $G^{(m)}$ is piecewise continuous and (3.6) holds.
Denoting by σ the left member of (4.2), we have

$$\sigma = \int_{-\infty}^{\infty} H^{(m)}(x) \delta^{r+1} G^{(m)}(x)\, dx \ .$$

If $\delta^{r+1} G^{(m)}(x)$ is expanded in terms of $G^{(m)}(x)$ values, the finite support
of $G^{(m)}$ then permits rearrangement of terms, so that

$$\sigma = (-1)^{r+1} \int_{-\infty}^{\infty} G^{(m)}(x) \delta^{r+1} H^{(m)}(x)\, dx \ .$$

Since $G^{(m)}$ vanishes outside of $(\alpha + \rho, \beta - \rho)$, and $\delta^{r+1} H^{(m)}$ is given in
that interval by a polynomial of π_{m-1}, say q, we have

$$\sigma = (-1)^{r+1} \int_{\alpha+\rho}^{\beta-\rho} G^{(m)}(x) q(x)\, dx \ . \tag{4.3}$$

As $G \in C^{m-1}$, m-fold integration by parts now gives $\sigma = 0$, as required. □

Theorem 4.3. The unique interpolation formula determined by Theorem 4.1
is the unique mdf of the class F_{Irm}.

__Proof__. Let L be the basic function of the unique formula determined by Theorem 4.1, and L_1 the basic function of any formula of F_{Irm} . Also let J and J_1 denote the corresponding values of the quantity given by (2.2), and let K_1 be defined by

$$L_1(x) = L(x) + K_1(x) . \qquad (4.4)$$

Then, it is easily verified that K_1 fulfills the conditions required of K in Lemma 4.2. Similarly, L fulfills the requirements for H in that lemma. Therefore, by Lemma 4.2,

$$\int_{-\infty}^{\infty} L^{(m)}(x) K_1^{(m)}(x) dx = 0 . \qquad (4.5)$$

From (4.4) and (4.5) we have

$$J_1 = J + \int_{-\infty}^{\infty} [K_1^{(m)}(x)]^2 dx .$$

It follows that $J \leq J_1$. Moreover, equality holds only if $K_1^{(m)}$ vanishes almost everywhere. Therefore, in this case, $K_1^{(m-1)}$ is a step function. But, since $K_1 \in C^{m-1}$, $K_1^{(m-1)}$ is continuous, and therefore $K_1^{(m)}$ is identically zero. It follows that $K_1 \in \pi_{m-1}$. But a polynomial with finite support is identically zero, and so $L_1 = L$.   []

5. CHARACTERIZATION OF REPRODUCING mdf's. We shall first dispose of the case in which F_{Irm} and F_{Irm}^{rep} are identical. Let t denote the number of integers contained in I .

__Theorem 5.1__. If F_{Irm} is nonempty, it is identical to F_{Irm}^{rep} if and only if $0 \in I$ and $t \leq r + 1$.

__Proof__. We have seen that F_{Irm} is empty for $\mu < r + 1$. Therefore we must have $\mu \geq r + 1$. This implies that $t \geq r$. In fact, t = r occurs only when $\mu = r + 1$ and α and β are integers. By (3.4) and Theorem 3.2, the r + 1 relations

$$\sum_{\nu=-\infty}^{\infty} \nu^i L(\nu) = \delta_{0i} \qquad (i = 0,1,\ldots,r) \qquad (5.1)$$

must be satisfied. These may be regarded as a system of linear equations in the quantities $L(\nu)$ for the t integers ν contained in I . If t = r + 1 , the matrix of coefficients is square. (In the special case of t = r , one of the end values, α or β , may be included.) The matrix is also nonsingular, because its determinant is a Vandermonde and therefore nonvanishing. Thus, the linear system has a unique solution. However, if $0 \in I$, it is evident that the values given by (1.2) are a solution, and therefore the unique solution. Hence the formula is reproducing and F_{Irm} and F_{Irm}^{rep} are identical.

As previously pointed out, there is no reproducing formula if $0 \notin I$. Now, let I be such that $t > r + 1$, and let f_1 be a formula of F_{Irm}. It follows from Theorem 4.1 that such a formula exists. If f_1 is nonreproducing, the theorem is established. Otherwise, let L_1 be the basic function of f_1 and τ the largest integer in I. Then, for some ϵ in $(0,1/2)$, $[\tau - r - 1 - \epsilon, \tau + \epsilon] \subset I$. Now, consider the interpolation formula f_2 under which, for x in $(\lambda - \epsilon, \lambda + \epsilon)$ for every integer λ,

$$v_x = \sum_{\nu = -\infty}^{\infty} L_1(x - \nu)y_\nu + k(x - \lambda + \epsilon)^m (x - \lambda - \epsilon)^m \Delta^{r+1} y_{\lambda - \tau} , \qquad (5.2)$$

k being arbitrary, while, for all other values of x, v_x is given by the summation term only. Here Δ is the usual finite-difference operator. Evidently f_2 belongs to F_{Irm}. However, (5.2) gives

$$v_\lambda = y_\lambda + k(-1)^m \epsilon^{2m} \Delta^{r+1} y_{\lambda - \tau} ,$$

and the formula is clearly nonreproducing for $k \neq 0$. $\qquad \square$

The analogue of Theorem 4.1 for the reproducing case is the following theorem.

Theorem 5.2. For any nonnegative integer r and positive integer m, and any finite interval $I = (\alpha, \beta)$ containing 0 and such that $\mu > r + 1$, the class F_{Irm}^{rep} contains a single formula satisfying the following three conditions:

(i) L is a piecewise polynomial function of degree at least r and at most $d = \max(r, 2m - 1)$.

(ii) Each knot of L is either an integer or an argument that differs by an integer from α or β (or both).

(iii) The piecewise polynomial function $\delta^{r+1}L$ is given in $(\alpha + \rho, \beta - \rho)$ by a spline function of degree $2m - 1$ with simple knots. The knots of $\delta^{r+1}L$ in $(\alpha + \rho, \beta - \rho)$ are at the integers when r is odd, and at the arguments of the form integer $+ 1/2$ when r is even.

As in the case of Theorem 4.1, we shall postpone the proof of this theorem, but we shall now show its relationship to reproducing mdf's, for which the following lemma will be needed.

Lemma 5.3. Let functions K and H satisfy the same hypotheses as in Lemma 4.2 except that (i) K vanishes at the integers, and (ii) $\delta^{r+1}H$ is given in $(\alpha + \rho, \beta - \rho)$ by a spline function of degree $2m - 1$ with knots as specified in condition (iii) of Theorem 5.2. Then (4.2) holds.

Proof. The proof is the same as that of Lemma 4.2 down to equation (4.3) except that q is a spline of degree $m - 1$ with knots as specified in condition (ii), and it follows from the expression (3.5) for G that it vanishes at the knots of q. Thus m-fold integration of (4.3) gives

$$\sigma = (-1)^{m+r+1} \sum_x G(x)[q^{(m-1)}(x + 0) - q^{(m-1)}(x - 0)] ,$$

where the summation is over the knots of q in $(\alpha + \rho, \beta - \rho)$. Since G vanishes at these knots, $\sigma = 0$, as required. □

Theorem 5.4. The unique interpolation formula determined by Theorem 5.2 is the unique mdf of the class F_{Irm}^{rep}.

Proof. The proof is identical to that of Theorem 4.3, except that the role of Lemma 4.2 there is now assumed by Lemma 5.3. □

6. COMPACT EXPRESSION FOR mdf BASIC FUNCTIONS. If there is a formula of F_{Irm} with a basic function that satisfies conditions (i) and (ii) of Theorem 4.1, this basic function can be regarded as a spline function of degree d with multiple knots of multiplicity $d - m + 1$. In general, therefore, it has a unique expression (see [2]) of the form

$$L(x) = \sum_{i=m}^{d} \sum_{j=0}^{n} \left[c_{ij}(x - \alpha - j)_+^i + g_{ij}(x - \beta + j)_+^i \right] , \qquad (6.1)$$

where n denotes the largest integer contained in μ and $y_+^i = \max(y^i, 0)$. The coefficients c_{ij} and g_{ij} are subject to the constraints arising from Theorem 3.1, which can be written as

(a) $\qquad \sum_{j=0}^{n} j^k c_{ij} = 0$

$$(k = 0, 1, \ldots, r; \ i = m, m + 1, \ldots, d) . \qquad (6.2)$$

(b) $\qquad \sum_{j=0}^{n} j^k g_{ij} = 0$

If μ is an integer, the second term of the summand in (6.1) is absent (as are, of course, the constraints (6.2)(b)).

For a formula of F_{Irm}^{rep} that satisfies conditions (i) and (ii) of Theorem 5.2, in general there must be added to the right member of (6.1) the expression

$$\sum_{j \in E} h_j(x - j)_+^{2m-1} , \qquad (6.3)$$

where E denotes the set of integers contained in I, and the constraints

$$\sum_{j \in E} j^k h_j = 0 \qquad (k = 0, 1, \ldots, r) \qquad (6.4)$$

must be satisfied. However, when α or β is an integer, the addition of (6.3) is not required.

276

We shall now show that by taking into account condition (iii) of Theorems 4.1 and 5.2 and by introducing certain special spline functions, we can rewrite (6.1) in a form involving a much smaller number of undetermined coefficients and can also avoid the necessity of considering separately the cases in which μ, α, or β is an integer. For this purpose we shall need the following lemma.

Lemma 6.1. For every nonnegative integer r and every positive integer $n \geq r + 1$, there is a unique polynomial $p_{rn} \in \pi_r$ such that

$$\sum_{j=1}^{n} j^k p_{rn}(j) = \delta_{0k} \qquad (k = 0,1,\ldots,r) \ . \qquad (6.5)$$

Proof. This follows easily from well known properties of orthogonal polynomials, but it is also readily seen as follows. Equations (6.5) may be regarded as a system of $r + 1$ linear equations in the $r + 1$ coefficients of p_{rn}. The latter system has a unique solution if and only if the corresponding homogeneous system has only the trivial solution. But any solution of the homogeneous system gives rise to a polynomial $P \in \pi_r$ such that

$$\sum_{j=1}^{n} P(j)q(j) = 0 \qquad (6.6)$$

for all $q \in \pi_r$. In particular, one may take $q = P$, so that (6.6) becomes a sum of squares, and therefore P vanishes for $j = 1,2,\ldots,n$. Since $n > r$, P is identically zero. $\Box$

We now define the splines of degree r,

$$S_{rn}(x) = x_+^r - \sum_{j=1}^{n} p_{rn}(j)(x - j)_+^r \ ,$$

$$S_{rn}^*(x) = x_+^r - \sum_{j=1}^{n} p_{rn}(j)(x + j)_+^r \ .$$

Parenthetically, we remark that by means of (6.5) and the identity

$$y_+^r = y^r - (-1)^r(-y)_+^r$$

it is easily shown that $S_{rn}^*(x) = (-1)^{r+1} S_{rn}(-x)$. We observe also that S_{rn} has its support in $(0,n)$ and S_{rn}^* in $(-n,0)$.

Note that condition (iii) of Theorem 4.1 or 5.2 implies, in general, that certain knots that the function $\delta^{r+1}L$ would otherwise be expected to have are absent (or reduced in multiplicity in special cases of a reproducing formula). Using the notation of (6.1), this means that

$$\Delta^{r+1} c_{ij} = \Delta^{r+1} g_{ij} = 0 \qquad (j = 1,2,\ldots,N - r - 1; \ i = m,m + 1,\ldots,d) \ ,$$

where the finite differences are taken with respect to j, and N is the largest integer <u>less than</u> μ. (Note that N differs from n when μ is an integer.) This implies the existence, for $i = m, m + 1, \ldots, d$, of a polynomial q_i such that $c_{ij} = q_i(j)$ for $j = 1, 2, \ldots, N$ but not, in general, for $j = 0$. Similar remarks apply to g_{ij}. We conclude from these facts and the constraints (6.2) that

$$\sum_{j=0}^{N} \left[c_{ij}(x - \alpha - j)_+^i + g_{ij}(x - \beta + j)_+^i \right]$$

$$= c_i S_{rN}^{(r-i)}(x - \alpha) + g_i S_{rN}^{*(r-i)}(x - \beta) \tag{6.7}$$

$$(i = m, m + 1, \ldots, d) \ ,$$

where c_i and g_i are obtained by multiplying c_{i0} and g_{i0} by appropriate constants depending only on i and r, and, in case $i > r$, a derivative of negative order denotes that particular integral of corresponding order that vanishes identically for $x < \alpha$. A little reflection will convince the reader that the right member of (6.7) is a valid substitution even when μ is an integer (and $N = \mu - 1$). However, in the case of a reproducing formula, the expression (6.3) now must <u>always</u> be added, *even though* α *or* β (or both) is an integer.

Accordingly, (6.1) can be expressed uniquely in the form

$$L(x) = \sum_{i=m}^{d} \left[c_i S_{rN}^{(r-i)}(x - \alpha) + g_i S_{rN}^{*(r-i)}(x - \beta) \right] . \tag{6.8}$$

A function L satisfying conditions (i)-(iii) of Theorem 4.1 that is the basic function of a formula of F_{Irm} has, therefore, a unique expression of the form (6.8). Similarly, a function L satisfying conditions (i)-(iii) of Theorem 5.2 that is the basic function of a formula of F_{Irm}^{rep} has a unique expression of the form (6.8) with (6.3) added.

The coefficients c_i and g_i (and h_j in the reproducing case) must satisfy certain constraints. These will now be described.

(a) In the reproducing case the $r + 1$ conditions (6.4) must be satisfied. When this is the case, the expression (6.3) vanishes for $x \geq \beta$.

(b) The function given by (6.8) has its support in I when $d = r$. This is also true in the reproducing case if the preceding condition (a) is fulfilled. However, when $d = 2m - 1 > r$, (6.8) gives, for $x \geq \beta$, a polynomial of degree $d - r - 1$. The vanishing of the $d - r$ coefficients of this polynomial involves $d - r$ constraints.

(c) In the *general case, exactness for the degree* r requires that the $r + 1$ conditions (5.1) be satisfied.

(d) In the reproducing case, (c) is replaced by conditions (1.2). This involves t effective constraints.

278

(e) The form of (6.8) ensures that $\delta^{r+1}L$ shall be given in $(\alpha + \rho, \beta - \rho)$ by a polynomial in the general case, and by a polynomial except for discontinuities in the $(2m - 1)$th derivative in the reproducing case. However, in the case when $d = r > 2m - 1$, condition (iii) of Theorem 4.1 or 5.2 involves also a reduction in degree from d to $2m - 1$. This constitutes $d - 2m + 1$ constraints.

7. PROOFS OF THE CHARACTERIZATION THEOREMS. We now have the machinery needed to prove Theorems 4.1 and 5.2.

Proof of Theorem 4.1. If there is a formula of F_{Irm} whose basic function satisfies conditions (i)-(iii) of Theorem 4.1, that function has a unique expression of the form (6.8) with parameters c_i and g_i satisfying conditions (b), (c), and (e) of the preceding section, to the extent these conditions are applicable. On the other hand, if there is an expression of this form with parameters satisfying these conditions, then it is, in fact, the basic function of such a formula.

Now, (6.8) contains $2(d - m + 1)$ undetermined parameters. The numbers of constraints involved in conditions (b), (c) and (e) are, respectively, $d - r$, $r + 1$ and $d - 2m + 1$. (Note that the integers $d - r$ and $d - 2m + 1$ are not both different from zero.) The total number of constraints is $2(d - m + 1)$, the same as the number of parameters. Without spelling out the constraints in detail, it is easily verified that they are linear equations in the parameters. The parameters must therefore satisfy $2(d - m + 1)$ equations in as many unknowns. To prove Theorem 4.1 it is sufficient to show that this linear system is nonsingular.

This is the case if the corresponding homogeneous system has only the trivial solution. In fact, the only one of the constraint equations that has a number other than 0 on its right-hand side is the one obtained by taking $i = 0$ in (5.1). Thus, a function K of the form (6.8) whose parameters satisfy the homogeneous system has the property that T_K annihilates π_r.
This function K therefore fulfills the requirements for both K and H in Lemma 4.2. Consequently, by Lemma 4.2,

$$\int_{-\infty}^{\infty} [K^{(m)}(x)]^2 dx = 0 .$$

By the same reasoning used in the proof of Theorem 4.3, it follows that K is identically zero. Thus, the homogeneous system has only the trivial solution. □

Proof of Theorem 5.2. The perceptive reader may have noticed that the possibility of $m = 0$, though allowed in Theorem 4.1, is excluded in Theorem 5.2. In fact, a reproducing mdf with $m = 0$ is somewhat meaningless, for the following reason. Application to this case of the criteria that we have developed would lead to a solution in which the basic function of the corresponding mdf without the reproducing requirement is modified by arbitrarily assigning at the integers the values given by (1.2), even though these are inconsistent with the values at neighboring arguments. Thus, the resulting basic function would have removable discontinuities at the integers

1.0

2.8   2.5
3.2   2.2
3.6
4.0   2.0

1.1

1.8

1.25   1.4   1.6
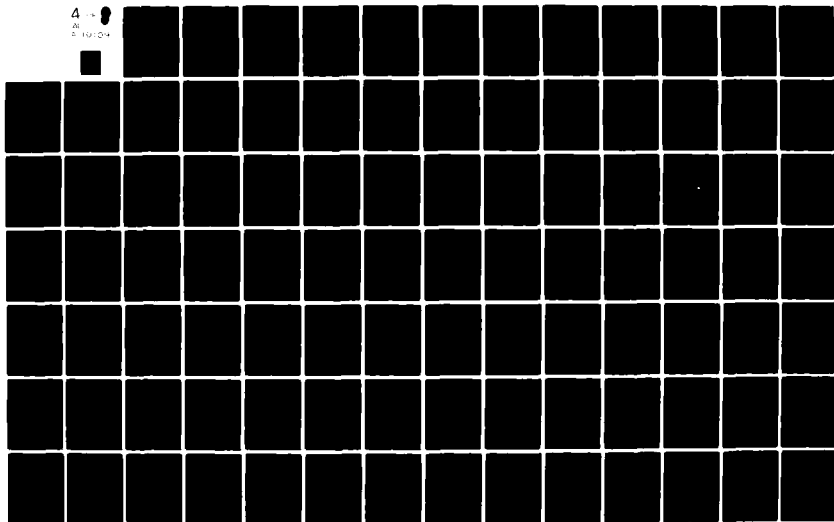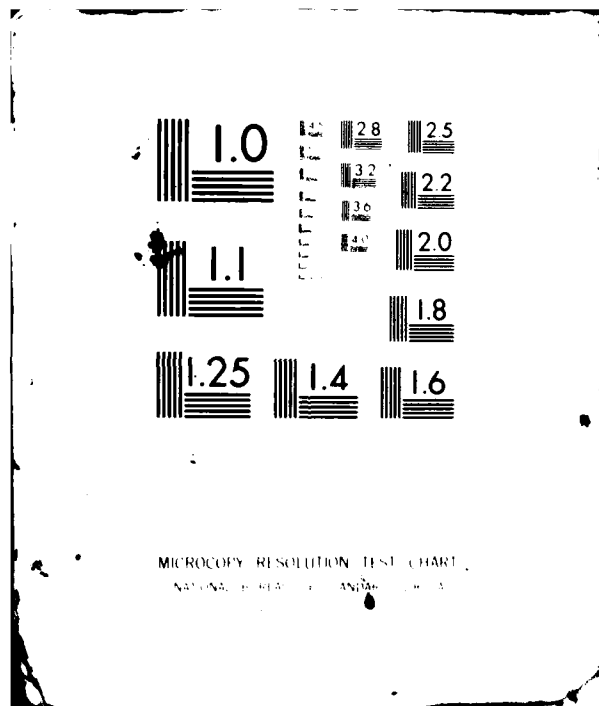
MICROCOPY RESOLUTION TEST CHART
NATIONAL BUREAU OF STANDARDS

in I. Strictly speaking, such a function is not piecewise continuous, and therefore is not the basic function of a formula of the class F_{Ir0}.

If there is a formula of F_{Irm}^{rep} whose basic function satisfies conditions (i)-(iii) of Theorem 5.2, that function has a unique expression of the form (6.8) with (6.3) added, and the parameters c_i, g_i, and h_j satisfy conditions (a), (b), (d), and (e) of the preceding section, to the extent these conditions are applicable. On the other hand, if there is an expression of this form, with parameters satisfying these conditions, then it is, in fact, the basic function of such a formula.

Now (6.8) and (6.3) together contain $2(d - m + 1) + t$ undetermined parameters. The number of constraints involved in conditions (a), (b), (d), and (e) are respectively, $r + 1$, $d - r$, t, and $d - 2m + 1$. The total number of constraints is $2(d - m + 1) + t$, the same as the number of parameters. As in the general case, all the constraints are linear equations in the parameters, and they constitute a linear system having a square coefficient matrix.

The remainder of the proof is the same as for Theorem 4.1, except that Lemma 5.3 now assumes the role played by Lemma 4.2 in the earlier proof.

8. SOME mdf's ARE PREVIOUSLY PUBLISHED FORMULAS. In some instances the minimized-derivative formula of a class turns out to be a previously published formula. Table I lists, for the cases known to us, the class F_{Irm} or F_{Irm}^{rep} involved, the name of the originator, the publication citation, and the year of publication. Two of the papers cited contain a large number of formulas, and in these cases the particular formula is identified. In two instances in which the published formula contains an unspecified parameter, the numerical value of the parameter that yields the mdf is given in a footnote. The entry "Both" in the fourth column means that F_{Irm} and F_{Irm}^{rep} are identical for the case involved.

280

TABLE I. Previously Published Formulas that are mdf's

I	r	m	Rep or Nonrep	Originator and Citation	Publication Year
(-2, 2)	1	2	Nonrep	Jenkins [5]	1927
(-2, 2)	2	2	Both	Karup [6]	1898
(-2, 2)	2	3	Both	Greville [1] (105)	1944
(-5/2, 5/2)	2	2	Nonrep	Greville [1] (67)[2]	1944
(-5/2, 5/2)	3	2	Nonrep	Greville [1] (69)	1944
(-3, 3)	3	2	Nonrep	Greville [1] (73)[3]	1944
(-3, 3)	3	3	Nonrep	Vaughan [10] "C"	1946
(-3, 3)	3	2	Rep	Henderson [4]	1906
(-3, 3)	4	2	Both	Shovelton [8]	1913
(-3, 3)	4	3	Both	Sprague [9]	1880

[2]With a_{13} = 13/80.

[3]With a_{04} = -7/108.

REFERENCES

[1]   T. N. E. Greville, The general theory of osculatory interpolation,
      Trans. Actuar. Soc. Amer., 45 (1944), 202-265.

[2]   T. N. E. Greville, Introduction to spline functions, pp. 1-35 of Theory
      and Applications of Spline Functions (ed. by T. N. E. Greville),
      Academic Press, New York, 1969.

[3]   T. N. E. Greville and H. Vaughan, Polynomial interpolation in terms of
      symbolic operators, Trans. Soc. Actuar., 6 (1954), 413-476.

[4]   R. Henderson, A practical interpolation formula, Trans. Actuar. Soc.
      Amer., 9 (1906), 211-224.

[5]   W. A. Jenkins, Graduation based on a modification of osculatory
      interpolation, Trans. Actuar. Soc. Amer., 28 (1927), 198-215.

[6]   J. Karup. On a new mechanical method of graduation, Trans. 2nd
      Internat. Actuar. Cong., C. & E. Layton, London, 1899, pp. 78-109.

[7]   I. J. Schoenberg, Contributions to the problem of approximation of
      equidistant data by analytic functions. Part A. On the problem of
      smoothing or graduation. A first class of analytic approximation
      formulae, Quart. Appl. Math., 4 (1946), 45-99.

[8]   S. T. Shovelton, On the graduation of mortality tables by
      interpolation, J. Inst. Actuar., 47 (1913), 284-298.

[9]   T. B. Sprague, Explanation ov[4] a new formula for interpolation, J.
      Inst. Actuar., 22 (1880), 270-285.

[10] H. Vaughan, Some notes on interpolation, J. Inst. Actuar., 72 (1946),
      482-497.

---

[4] Sprague was an advocate of simplified spelling and used it in this paper.

INTERVAL ANALYSIS: A NEW TOOL FOR APPLIED MATHEMATICS

L. B. Rall

Mathematics Research Center
University of Wisconsin-Madison
610 Walnut Street
Madison, Wisconsin 53706

ABSTRACT.   Interval arithmetic has been found to be useful in numerical analysis as an automatic means to bound data, truncation, and roundoff errors in computations. Now that the speed of microprogrammed interval arithmetic approaches that of standard floating-point operations, a wider range of application to engineering and other problems has become feasible. Since, in many practical situations, data are only known to lie within intervals and only ranges of values are sought as satisfactory answers, straightforward interval computation can yield the desired results. Examples of this type of application are worst-case analysis of the stability of structures and the performance of electrical circuits. The recently developed theory of integration of interval functions also bears directly on the problems of solution of integral equations and the minimization of functionals defined in terms of integrals. Since certain chaotic phenomena, such as catastrophes and turbulence, are difficult to describe by single-valued functions, the introduction of interval functions and the corresponding analysis may lead to simpler models which will yield results of accuracy satisfactory for practical purposes.

1. **WHAT IS INTERVAL ANALYSIS ?**   This paper is addressed to the questions: What is interval analysis, and what can it do for applied mathematics? Naturally, these are big questions, so only a sketch of the answers can be given here. It is hoped , however, that enough can be conveyed to suggest possible useful applications of the subject, as well as to satisfy curiosity.

First of all, although interval analysis as a discipline is fairly recent (a likely beginning point is the Stanford Ph.D. thesis of R. E. Moore, written in 1962 [16]), it has grown beyond the scope of any single paper. Another survey has been given by Nickel [21], and there are at least three books on the subject [1], [17], [18], and the proceedings of three international conferences [9], [20], [22] are in print. A bibliography published in 1978 [2] lists 757 titles (this bibliography is reproduced in [18], pp. 125-179). Research in interval analysis and its applications is carried on most vigorously at the present time in the Federal Republic of Germany, where an Interval Library is maintained at the Institute for Applied Mathematics, University of Freiburg, under the supervision of Prof. Dr. Karl Nickel.

In spite of the extent of the subject, it is possible to characterize interval analysis by analogy with real analysis. In real analysis, the basic units are real numbers, and one studies transformations f or real numbers x into real numbers y, symbolized by

---

(1.1) $$y = f(x).$$

Properties of these transformations (real functions) are of interest, as well as operations (differentiation, integration, etc.) applied to these transformations.

Similarly, in interval analysis, the basic units are the nonempty closed intervals $X = [a,b]$ on the real line R, where

(1.2) $$X = [a,b] = \{x \mid a \leqslant x \leqslant b,\ x \in R\}.$$

Interval analysis is thus concerned with transformations F of intervals X into intervals Y, that is

(1.3) $$Y = F(X)$$

(see Figure 1).

Real Transformations
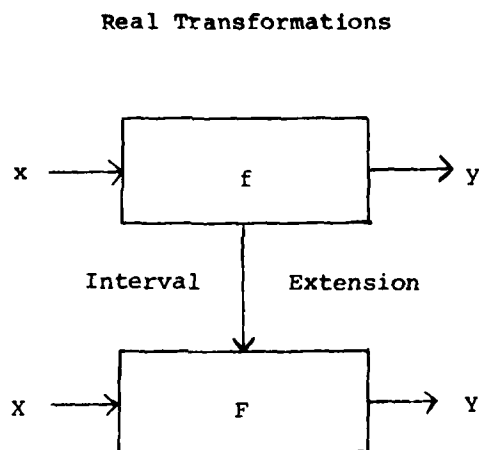
Interval Transformations

Figure 1. Relationship between Real and Interval Analysis

There is an obvious connection between interval analysis on the real line R and real analysis: One can identify each real number x with the corresponding degenerate interval $[x,x]$ having both endpoints equal to x, and write

(1.4) $$x = [x,x].$$

Real and interval transformations are also related through the concept of interval extension, which will be treated in more detail in the next section.

The relationship between real and interval analysis is thus analogous to the relationship between real and complex analysis. The real numbers can also be identified with a subset of the complex numbers, and real transformations can be considered to be a restricted class of complex transformations.

284

However, as everyone knows, complex analysis does not supersede real analysis, but is rather a complementary field of mathematics, with its own theory, techniques, and applications. Interval analysis also complements real analysis in a similar way.

Secondly, the question of the usefulness of interval analysis cannot be answered completely here, since one never knows entirely the capabilities of any mathematical theory or other tool, no matter how long its history. Here, a few examples of interval methods which have proved effective in practice will be given, and some speculation as to other applications will be made in hopes of stimulating further investigations into the uses of interval analysis in the solution of practical problems.

Before going on, it should be noted that just as real analysis extends from numbers R to real vectors in R^n, interval analysis also applies to interval vectors with n components. This simple generalization will be taken for granted below where appropriate. It should also be mentioned that there is a complex version of interval analysis, based on the use of disks or rectangles in the complex plane; attention here, however, will be restricted to real interval analysis.

From a philosophical point of view, it can be observed that measurements of physical phenomena do not yield real numbers and functions in general, but only approximations to these ideal concepts. However, it is usually possible to determine intervals in which the observed data lie, making interval analysis a natural language for the description of processes involving inaccurately know data, or as a way to handle the results of variations in quantities of interest. Some illustrations of these ideas will be given below.

Before going on to a more detailed treatment of the subject, mention will be made of two problems which are solvable by the methods of interval analysis for which no techniques from real analysis are known:

(i) <u>Global optimization</u>: For $f:R^n \to R$, minimize f on R^n (unconstrained optimization), or subject to the constraints

$$(1.5) \qquad\qquad p_i(x) \leqslant 0, \quad i = 1,2,\ldots,m,$$

where f and $p_1,\ldots,p_m$ are at least once differentiable. Algorithms for the solution of these problems have been given respectively by Hansen [10] and Hansen and Sengupta [11].

(ii) <u>Integration</u>: In real analysis, theories of integration of real functions, such as those due to Riemann and Lebesgue [15] define the integral

$$(1.6) \qquad\qquad I = \int_b^a f(x)\,dx$$

for only a subset of the real functions. In the theory of interval integration [6], all real functions (and all interval functions) are integrable. More details will be given in §§6-7 below.

2. <u>INTERVAL EXTENSIONS</u>. Figure 1 indicates another relationship between real and interval analysis, namely, <u>interval extension</u> of a real

transformation. This concept is made precise in the following definition.

Definition 2.1. An interval transformation F is said to be an *interval extension* of a real transformation f if it has the following properties:

(i) *inclusion*,

(2.1)
$$f(X) = \{f(x) \mid x \in x\} \subset F(X);$$

and (ii) *restriction*,

(2.2)
$$F(x) = f(x),$$

where the convention (1.4) has been used to write $F(x) = F([x,x])$.

Of course, there are interval transformations F which are not extensions of real transformations f.

If f is a continuous function of a single variable, then $f(X)$ is an interval by the theorem of Weierstrass, and thus F defined by $F(X) = f(X)$ is an interval extension of f. However, in two or more dimensions, $f(X)$ is not in general an interval of the form $Y = ([c_1,d_1],\ldots,[c_m,d_m])$ for $X = ([a_1,b_1],\ldots,[a_n,b_n])$. For example,

(2.3)
$$f(x,y) = (x \ , \ y\sqrt{1 - x^2})$$

maps $X_0 = ([0,1],[0,1])$ onto the region in the first quadrant bounded by the coordinate axes and a quarter of the unit circle, which is obviously not a rectangle. An interval extension of f given by (2.3) would have the property that $X_0 \subset F(X_0)$, since X_0 is the smallest rectangle X such that $f(X_0) \subset X$.

A fundamental interval extension of real transformations is *interval arithmetic* [17], [18], which extends the real arithmetic operations (considered as functions of two variables, that is, $f(x + y) = x + y$ for addition, etc.). The *rules* of interval arithmetic are as follows:

(i) Addition

(2.4)
$$[a,b] + [c,d] = [a + c \ , \ b + d].$$

(ii) Subtraction

(2.5)
$$[a,b] - [c,d] = [a - d, \ b - c].$$

(iii) Multiplication

(2.6)
$$[a,b] \cdot [c,d] = [\min \Pi, \ \max \Pi],$$

where $\Pi = \{ac,ad,bc,bd\}$.

(iv) Division

(2.7) $[a,b]/[c,d] = [a,b] \cdot [d^{-1},c^{-1}]$ if $cd > 0$,

undefined otherwise.

These interval extensions of the ordinary arithmetic operations have the important property of <u>inclusion monotonicity</u> in the sense of the following definition.

Definition 2.2. An interval transformation F is said to be <u>inclusion monotone</u> if

(2.8) $X \subset Z \Rightarrow F(X) \subset F(Z)$.

Note that since interval analysis deals with set-valued quantities, then set relationships and operations, in certain instances, appear in a natural way.

The importance of interval arithmetic as defined by (2.4)-(2.7) is that it allows the construction of inclusion monotone interval extensions of rational functions <u>automatically</u>, simply by replacing the real variables by intervals and the arithmetic operations by their interval counterparts. For example,

(2.9) $F(X) = \dfrac{3 \cdot X + 1}{2 \cdot X - 1}$

is an inclusion monotone interval extension of the real function

(2.10) $f(x) = \dfrac{3x + 1}{2x - 1}$

on its domain of definition, which is the real line with the point $x = 1/2$ deleted.

Two cautions are in order concerning the straightforward use of interval arithmetic to obtain interval extensions. First of all, intervals do not form a linear space, as illustrated by the simple result,

(2.11) $[0,1] - [0,1] = [-1,1]$,

obtained from (2.5). Without a linear substructure, one cannot expect techniques from real analysis which depend on linearity to work in general in interval analysis. For this reason, interval arithmetic cannot be applied indiscriminately to extend certain methods of linear algebra which are effective in the real case. In fact, the lack of a concept of linearity means that there is no way to distinguish between linear and nonlinear problems in interval analysis without going back to their real restrictions.

Secondly, the rules (2.4)-(2.7) of interval arithmetic are not adequate to produce small interval extensions of even some simple rational functions, for example, the extension

(2.12) $F(X) = X \cdot X$

of

(2.13) $f(x) = x^2$

287

gives

(2.14) $$F([-1,1]) = [-1,1] \cdot [-1,1] = [-1,1],$$

while

(2.15) $$f([-1,1]) = [-1,1]^2 = [0,1]$$

for the extension $f(X)$. Thus,

(v) Squaring

(2.16) $$[a,b]^2 = \begin{cases} [\min\{a^2,b^2\}, \max\{a^2,b^2\}] & \text{if } ab \geqslant 0, \\ [0, \max\{a^2,b^2\}] & \text{if } ab < 0, \end{cases}$$

can be added to the rules for interval arithmetic to obtain improved interval extensions in the appropriate cases, and so on.

One way to improve the accuracy of interval extensions (in the sense of making $F(X)$ as small as possible) is thus to add additional operations to interval arithmetic. Another method is to use alternative expressions for the interval extension, and not just simple substitution of interval values and operations. For example, suppose that f is differentiable and f' has an interval extension F'. Furthermore, let $y = m(X)$ denote the <u>midpoint</u> of x; $m([a,b]) = (a + b)/2$, with a similar expression for vector intervals X. In this case, the <u>mean value form</u> [4]

(2.17) $$F(X) = f(y) + F'(X) \cdot (X - y),$$

defines an inclusion monotone interval extension F of f which is accurate for small intervals X.

Further problems connected with the computation of interval extensions will be considered in the next section.

3. <u>INTERVAL COMPUTATION</u>. In actual practice, it is impossible in general to represent real numbers or evaluate real transformations exactly. This is because one must work with a finite set G of real numbers, called a <u>grid</u> [26] or <u>screen</u> [13]. A typical example of G is the set of fixed and floating-point numbers available on a given computer. The error introduced by having to work with G rather than R presents some thorny problems of numerical analysis in connection with the computation of real transformations. In interval analysis, on the other hand, the transition from R to G does not present any great theoretical difficulty, although one must forego the restriction property (2.2) of interval extensions in general. The construction of what will be called <u>computable interval extensions</u> having properties (2.1) and (2.8) of inclusion and inclusion monotonicity, respectively, will now be described.

It is helpful, but not necessary, to adjoin the extended real numbers $\pm \infty$ to G; otherwise, as in actual practice, the calculation of numbers $x < \underline{g} = \min G$ or $x > \bar{g} = \max G$ is said to <u>overflow</u> the grid G, and will generate an error indication rather than a numerical result. With this in mind, attention will be restricted to the set RG of real numbers x such

that $g \leqslant x \leqslant \bar{g}$.

The set of intervals with endpoints in G will be denoted by IG, that is,

(3.1) $$IG = \{[a,b] \mid a,b \in G, a \leqslant b\}.$$

These are the intervals which are exactly representable using the available set of numbers. Now, the directed rounding operators Δ, ∇ from RG to G, and $\circledast$ from IRG (the set of intervals with endpoints in RG) to IG will be defined.

For $x \in RG$, the <u>upward rounding operator</u> Δ is defined by

(3.2) $$\Delta x = \min\{y \mid y \geqslant x, y \in G\},$$

and the <u>downward rounding operator</u> ∇ by

(3.3) $$\nabla x = \max\{z \mid z \leqslant x, z \in G\}.$$

The <u>directed rounding operator</u> $\circledast$ applied to $[a,b]$, where $a \leqslant b$, $a,b \in RG$ gives

(3.4) $$\circledast[a,b] = [\nabla a, \Delta b],$$

an element of IG. In particular, if $x \in RG$ is a real number, then

(3.5) $$\circledast x = \circledast[x,x] = [\nabla x, \Delta x],$$

using the identification (1.4) of real numbers with degenerate intervals.

For example, if G is the set of four digit decimal numbers, then $\circledast$ applied to the real number $x = 1/3$ gives

(3.6) $$\circledast(1/3) = [.3333, .3334],$$

which is the unique representation of $1/3$ in IG of minimal width (and also of each real number z satisfying $.3333 < z < .3334$).

It follows that $\circledast$ is an inclusion monotone interval operator which maps IRG (and hence IG) into IG. If F is an interval extension of F, then

(3.7) $$\Phi = \circledast F$$

will have properties (2.1) (inclusion) and (2.8) (inclusion monotoncity), and will map IG into IG. Interval operators Φ of this type will be called <u>computable interval extensions</u> of F.

The advantages of working with computable interval extensions Φ of real transformations are obvious: If one starts with an exactly representable interval X (that is, $X \in IG$), then the transformed interval

(3.8) $$Y = \Phi(X)$$

will also be exactly representable; furthermore, one can be sure that if x ∈ X, then y = f(x) ∈ Y. Much of the usefulness of interval computation stems from this latter fact.

On present computers, directed rounding and hence interval computation can be implemented by software [28] or microprogramming [19] with a certain amount of effort. Upward and downward rounding should, of course, be required to be available as a standard feature of future machines so that ordinary and interval arithmetic can be performed rapidly and accurately.

4. <u>APPLICATIONS OF INTERVAL COMPUTATION</u>. Interval computation, which here will mean calculation using computable interval extensions of real functions, has at least two closely related applications. The first, already widely used in numerical analysis, is to <u>error estimation</u>. It is assumed that there are exact data x and that one wishes the result y = f(x) of performing an exact transformation f. However, all that one knows is that x lies in an interval X and that, due to inexact knowledge of coefficients, round-off and truncation error, the best one can compute is an interval transformation F of f. In this case, the interval transformation

$$(4.1) \qquad\qquad Y = F(X)$$

is a precisely defined model of inaccurate computation on inexact data. Here, "the interval contains the answer," since y ∈ Y. Knowing this, it is easy to find an approximate value η of y and a corresponding bound ε for absolute, relative, percentage, or other error of η as an approximation to y [23]. Most of the literature on interval analysis is devoted to applications of this type [2].

A second application of interval computation, possibly equally important, is to give a convenient, automatic way to estimate the effect of variation in input data on output results. For example, most structures, such as buildings, bridges, airframes, offshore drilling platforms, etc., are subject to a range of loadings, not just a single load, and the same is true for electrical power networks, pipelines, communications links, and so on. In these cases, the data X are really intervals, and one wants to examine an interval result Y to determine possible outcomes. In other words, "the interval is the answer" here. In prediction problems, also, the results of financial deals or the outcomes of battles may require estimation of interest rates, costs, military strengths and effectiveness, and so on. Interval analysis thus also provides a natural language for problems of this type, since one may view the results of assuming that the quantities of interest lie in various intervals, and make decisions accordingly.

To be more precise, consider the problem of the stability and safety of an offshore drilling platform attacked by waves having a range of amplitudes A and wavelengths Λ, that is, by an interval wave. In real analysis, suppose that the deflection of the i-th joint (node) of the structure is given by a formula of the form

$$(4.2) \qquad\qquad y_i = f_i(a,\lambda,x_1,\ldots,x_m),$$

i = 1,2,...,n, where the x_j represent loads, strengths of members (not usually known except within intervals), etc. Now, one calculates the interval

values

(4.3)
$$Y_i = F_i(A, \Lambda, X_1, \ldots, X_m),$$

using suitable computable interval extensions. The result is essentially a
"worst-case" analysis, leading to the following conclusions:

     (i) If all the Y_i lie within intervals of deflection considered to be
acceptable, then the structure can be deemed to be safe under the given range
of conditions.

     (ii) On the other hand, if some of the computed intervals Y_i go beyond
acceptable limits, this does not necessarily mean that the structure is
unsafe. However, the nodes in question should be singled out for more exact
investigation and possible reinforcement to insure that the structure will be
stable.

     It can be argued that the use of interval analysis is justified if this
would prevent the failure of a single structure or power or communication
network.

     An interval analysis of linear electric circuits has been carried out by
Skelboe [27] along the above lines. An application in finance, giving
projected returns for rates lying in estimated intervals, has been worked out
by A. S. Moore, and is given in [18], Chap. 9.

     Many significant applications of the above idea are undoubtedly possible;
the crucial point is to produce interval extensions which are realistic and
accurate in the sense that the intervals obtained do not extend far beyond the
limits which would actually be observed.

     Another property of interval computation which is useful in applications
is the intersection property. Suppose that one is trying to compute a point
y, or, more generally, an interval Y, and one knows that

(4.4)
$$Y \subset Y_1$$

on the basis of an interval computation. Another computation gives, say,

(4.5)
$$Y \subset Y_2$$

It follows, since intervals are sets, that

(4.6)
$$Y \subset Y_1 \cap Y_2 = Y_3,$$

and Y_3 may be considerably smaller than Y_1 or Y_2, but never larger.

Thus, additional interval computations can only improve accuracy. This
principle has been used in numerical integration to reduce error bounds, see
[8] for an example.

     Now that interval arithmetic can be microprogrammed to operate at
essentially floating point speeds [19], and is available in the powerful
scientific computing language PASCAL-SC [14], the use of interval computation

in applications is in a position to grow at an explosive rate.

5. __INTERVAL ITERATION__. This section will deal with an application of interval computation to the problem of finding fixed points of real transformations, that is, real numbers, vectors, or functions y which satisfy the equation

$$(5.1) \qquad\qquad y = f(y).$$

Since the formulation here is general enough to include systems of equations in several variables and integral equations [24], many problems in applied mathematics can be reduced to finding solutions of (5.1).

In real analysis, a standard way to obtain approximate solutions of equation (5.1) is by __iteration__. One starts with a point y_0 deemed to be a good approximation to y, and then generates the sequence $\{y_n\}$ by computing

$$(5.2) \qquad\qquad y_{n+1} = f(y_n), \quad n = 0,1,2,\dots .$$

If this sequence converges (and f is continuous, which will be assumed throughout), then

$$(5.3) \qquad\qquad y = \lim_{n \to \infty} y_n$$

satisfies (5.1). In other words, convergence of $\{y_n\}$ implies the existence of a fixed point y for continuous f. This is all very well, but $\{y_n\}$ can diverge, even for y_0 close to y, and thus not yield any useful information (If there is no fixed point y of f, then $\{y_n\}$ must diverge, hence,

nonexistence of y implies divergence of $\{y_n\}$.) Furthermore, since real transformations cannot be performed exactly in general, one does not compute $\{y_n\}$, but rather some approximate sequence $\{z_n\}$. The usefulness of $\{z_n\}$ thus depends on a comparison with $\{y_n\}$ which can be a difficult problem in its own right (although this does provide employment for numerical analysts).

As shown in [26], the situation is quite different in interval analysis. Here, one starts with an interval Y_0 (in IG in actual practice) thought to contain a fixed point y of f, and computes the sequence of intervals $\{Y_n\}$ defined by

$$(5.4) \qquad\qquad Y_{n+1} = Y_n \cap F(Y_n), \quad n = 0,1,2,\dots,$$

where F is a computable interval extension of f. In [26], it is shown that if $y \in Y_0$, then

$$(5.5) \qquad\qquad y \in Y = \bigcap_{n=0}^{\infty} Y_n \neq \emptyset,$$

($\emptyset$ denotes the empty set), so existence of the fixed point y in Y_0 implies

convergence of the interval iteration to a nonempty limit interval Y which also contains y. Furthermore, the endpoints of each Y_n, as well as Y, furnish lower and upper bounds for y. On the other hand, if

$$(5.6) \qquad\qquad Y_N = \emptyset$$

292

for some positive integer N, then Y_0 contains no fixed points of y of f. In this case, the interval iteration (5.4) is said to __diverge__, which implies __nonexistence__ of a fixed point in Y_0.

For computations on a finite grid G, which is the case in actual practice, it has been shown [26] that

(5.7)
$$Y_N = Y_{N+1} = Y \quad \text{or} \quad Y_N = \emptyset$$

for some positive integer N. Thus, interval iteration is a finite process in actual computation. In case $Y \neq \emptyset$, the usefulness of this limit can then be determined by direct inspection.

It should be noted that $Y \neq \emptyset$ __does not__ imply that $y \in Y_0$; it is the

converse which holds. Thus, it may be necessary to apply some existence test to Y. However, in finite dimensions, it is sufficient that

(5.8)
$$F(Y_N) \subset Y_N$$

for some positive integer N to guarantee the existence of a fixed point $y \in Y_0$, and hence the convergence of the interval iteration as a consequence of the Schauder fixed point theorem. Interval iteration can thus be used to find improved bounds for fixed points known to be in Y_0, to obtain regions Y_N possibly smaller than Y_0 to test for existence of fixed points, or to establish nonexistence of fixed points in Y_0 in case (5.6) holds.

6. __INTERVAL FUNCTIONS__. Interval functions are straightforward generalizations of real functions. Given real functions $\underline{y} \leqslant \bar{y}$ (in the sense that $\underline{y}(x) \leqslant \bar{y}(x)$ for each x), the function Y defined for each $x \in X = [a,b]$ by

(6.1)
$$Y(x) = \{y \mid \underline{y}(x) \leqslant y \leqslant \bar{y}(x)\}$$

will be called an __interval function__ on X with __endpoint functions__ $\underline{y}$, $\bar{y}$. Figure 2 illustrates the __graph__

(6.2)
$$Y(X) = \{y \mid \underline{y}(x) \leqslant y \leqslant \bar{y}(x), a \leqslant x \leqslant b\}$$

of a simple interval function.

As a set of functions, the interval function Y can be considered to be the set of __all__ real functions y satisfying $\underline{y} \leqslant y \leqslant \bar{y}$ in the sense cited above. Thus, in order to extend the concept of integration from real to interval functions, one must be prepared to integrate all real functions. The way to do this will be explained in the next section.

An important interval function is the __vertical extent__ ∇Y of an interval function Y. This is defined by

(6.3)
$$\nabla Y(X) = [\inf_{x \in X}\{\underline{y}(x)\}, \sup_{x \in X}\{\bar{y}(x)\}],$$

and is interval-valued. In Figure 2, $\nabla Y(X) = [c,d]$ is indicated on the y-axis. If $\nabla Y(X)$ is a finite interval, as in this case, then Y is said to be a __bounded__ interval function.
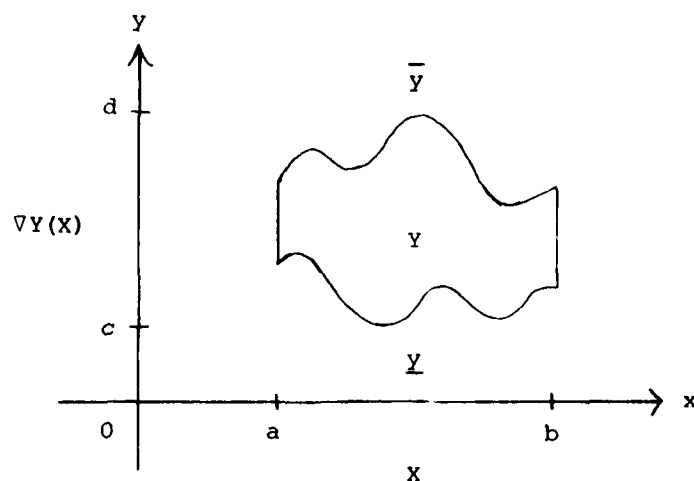
Figure 2. The Graph of an Interval Function.

Given interval functions Y, Z on X, one writes $Y \subseteq Z$ if $Y(X) \subseteq Z(X)$ as point-sets in the plane. Thus, if $Y = [\underline{y}, \overline{y}]$ and $Z = [\underline{z}, \overline{z}]$, then this is equivalent to $\underline{z} \leqslant \underline{y}$ and $\overline{y} \leqslant \overline{z}$ for the endpoint functions of Y and Z. Given an interval function Y, it is possible on this basis to introduce the idea of <u>directed rounding</u> of Y to a larger interval function Z with endpoints belonging to a specified class (step-functions, splines, continuous or Riemann integrable functions, etc.). This idea is useful in the construction of computable extensions of integral operators, etc.

Interval versions of discontinuous real functions can also be constructed to model finite or infinite jumps. For example, consider the real step-function

$$(6.4) \qquad s(x) = \begin{cases} \text{ı}, & x \leqslant 1, \\ 1, & x > 1. \end{cases}$$

The corresponding <u>interval step-function</u> is

$$(6.5) \qquad S(x) = \begin{cases} s(x), & x \neq 1, \\ [-1,1], & x = 1, \end{cases}$$

as illustrated in Figure 3. Thus, interval step-functions include the "risers" as well as the "treads" of real step-functions, considered as mathematical models of staircases.

Note that the graphs of interval versions of discontinuous real functions will be connected sets in the plane. Interval functions of this type may be useful in the description of physical phenomena known as shocks or catastrophes, where rapid changes take place in certain quantities.
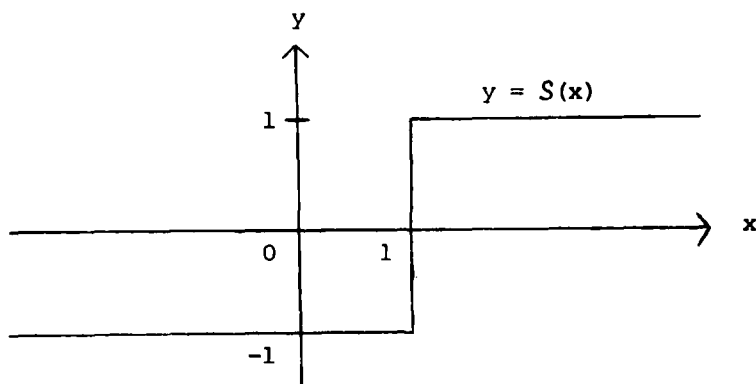
Figure 3. An Interval Step-Function.

7. **INTERVAL INTEGRATION.** A construction of the interval integral and some of its important properties are given in [6]. Briefly, the idea is this: Let y be real function, and suppose $\underline{S}$ and $\bar{S}$ are the sets of step-functions $\underline{s}$, $\bar{s}$ such that
$\underline{s} \leqslant y$ for $\underline{s} \in \underline{S}$, and $y \leqslant \bar{s}$ for $\bar{s} \in \bar{S}$. Since step-functions are integrable in the extended real number system, one can always form the <u>lower</u> and <u>upper Darboux integrals of</u> y [15], denoted respectively by

(7.1) $$\text{(LD)} \int_a^b y(x)\,dx = \sup_{\underline{s} \in \underline{S}} \{\int_a^b \underline{s}(x)\,dx\},$$

and

(7.2) $$\text{(UD)} \int_a^b y(x)\,dx = \inf_{\bar{s} \in \bar{S}} \{\int_a^b \bar{s}(x)\,dx\}.$$

Definition 7.1. The interval

(7.3) $$\int_a^b y(x)\,dx = [\text{(LD)} \int_a^b y(x)\,dx, \ \text{(UD)} \int_a^b y(x)\,dx]$$

is called the <u>interval integral</u> of the real function y over the interval $X = [a,b]$.

The interval integral, thus, always exists in the set of intervals on the extended real line [6], [15]. The interval integral (7.3) of a real function y is degenerate (a real number) if and only if y is Riemann (R) integrable, since

(7.4) $$\text{(R)} \int_a^b y(x)\,dx = \text{(LD)} \int_a^b y(x)\,dx = \text{(UD)} \int_a^b y(x)\,dx$$

by definition of Riemann integration [15].

For Lebesgue (L) integrable functions y,

(7.5) $\qquad$ (L) $\int_a^b y(x)\,dx$ e $\int_a^b y(x)\,dx$

in general [6].

Definition 7.2. The interval

(7.6) $\qquad \int_a^b Y(x)\,dx = [(LD) \int_a^b \underline{y}(x)\,dx, \ (UD) \int_a^b \bar{y}(x)\,dx]$

is called the interval integral of the interval function Y over the interval $X = [a,b]$.

Of course, (7.6) reduces to (7.3) if $Y = [y,y]$ is degenerate (a real function). Interval integrals have many properties similar to those of real integrals, for example, the mean interval value theorem

(7.7) $\qquad \int_a^b Y(x)\,dx = w(X) \cdot \bar{Y}$

holds, where $w(X) = W([a,b]) = b - a$, and $\bar{Y}$ is some interval contained in $\nabla Y(X)$ [6].

Another important property of interval integrals is inclusion monotonicity, that is,

(7.8) $\qquad Y \subset Z \Rightarrow \int_a^b Y(x)\,dx \subset \int_a^b Z(x)\,dx,$

as shown in [6]. Thus, interval integration is an inclusion monotone interval *extension of real integration*, with the restriction property (2.2) holding on the set of Riemann integrable functions by (7.4).

One useful application of interval integration is to construct computable interval extensions of integral transformations, which will be considered in the next section.

For bounded interval functions Y and finite intervals X, it has been shown that for the interval sums

(7.9) $\quad \Sigma_n Y(X) = h \cdot \sum_{i=1}^n \nabla Y([a + (i - 1)h, \ a + ih]), \quad h = \dfrac{b - a}{n}, \quad n = 1,2,\ldots,$

one has

(7.10) $\qquad \int_a^b Y(x)\,dx = \bigcap_{n=1}^{\infty} \Sigma_n Y(X),$

which gives a very simple construction of the interval integral in this case [25].

At the present time, differentiation does not seem to be an appropriate concept for interval functions in general, except by means of interval extensions. Thus, if y is a smooth real function, then one may work with interval extensions Y of y, Y' of y', Y" of y". and so on, to obtain interval versions of results from real analysis. Indefinite interval integrals, however, have a "derivative" equal to their integrands at points of continuity of the latter (that is, points of continuity of both $\underline{y}$ and $\bar{y}$), just as in the case of real integrals [6].

8. APPLICATIONS OF INTERVAL INTEGRATION.

As mentioned in §7, the theory of interval integration can be used to construct computable interval extensions of integral transformations of real functions, such as

$$(8.1) \qquad Gy(x) = \int_a^b g(x,t,y(x),y(t))dt .$$

In real analysis, one assumes Riemann or Lebesgue integrability of the integrand, which is not required in interval analysis. In any case, suppose that it is known that $y \in Y$, an interval function, and that Y is a computable interval extension of g obtained by interval arithmetic or otherwise, in the sense that the endpoint functions $\underline{Y}$, $\overline{Y}$ of Y have computable Riemann integrals. (It may be necessary to use directed rounding to obtain $\underline{Y}$, $\overline{Y}$.) Then, Γ defined by

$$(8.2) \qquad \Gamma Y(x) = \int_a^b Y(x,t,Y(x),Y(t))dt$$

will be a computable interval extension of the integral operator G.

Two applications of this idea will be mentioned: The solution of integral equations and the minimization of functionals. First, consider the fixed point problem for G defined by (8.1) with $X = [0,1]$, that is, the integral equation

$$(8.3) \qquad y(x) = \int_0^1 g(x,t,y(x),y(t))dt .$$

Equation (8.3) is very general. It is of <u>Volterra type</u> if $g(x,t,u,v) \equiv 0$ for $t > x$ (or more generally, for $t > h(x) \nless 1$), in which case the upper limit of integration in (8.3) can be replaced by x (or $h(x)$); otherwise, (8.3) is of <u>Fredholm type</u>. Linear integral equations of first, second, and third kinds correspond to the following integrands:

$$
\begin{aligned}
&\text{1st kind:} \quad g(x,t,y(x),y(t)) = y(x) + f(x) + \lambda K(x,t)y(t), \\
(8.4) \quad &\text{2nd kind:} \quad g(x,t,y(x),y(t)) = f(x) + \lambda K(x,t)y(t), \\
&\text{3rd kind:} \quad g(x,t,y(x),y(t)) = (1 - \phi(x))y(x) + f(x) + \lambda K(x,t)y(t).
\end{aligned}
$$

Among nonlinear integral equations of the form (8.3) which are of special interest are the equations of <u>Hammerstein type</u>,

$$(8.5) \qquad g(x,t,y(x),y(t)) = K(x,t)f(t,y(t)),$$

<u>Urysohn type</u>,

$$(8.6) \qquad g(x,t,y(x),y(t)) = f(x,t,y(t)),$$

the <u>Chandrasekhar H-equation</u> [7],

$$(8.7) \qquad g(x,t,y(x),y(t)) = 1 + \lambda y(x)\frac{t^\Psi(t)}{x + t}y(t),$$

and many others.

An obvious approach to the approximate solution of equation (8.3) is the use of interval iteration,

(8.8) $$Y_{n+1} = \Gamma Y_n \cap Y_n, \quad n = 0,1,2,\ldots,$$

starting with an interval function Y_0 which is presumed to contain a

solution y of the integral equation. The theory of interval iteration [24], [26] applies in this case also: If $y \in Y_0$, then (8.8) will converge to an interval function $Y = [\underline{y}, \bar{y}]$ such that

(8.9) $$\underline{y}(x) \leqslant y(x) \leqslant \bar{y}(x), \quad 0 \leqslant x \leqslant 1,$$

thus giving pointwise bounds for the solution y of the integral equation (8.3). On the other hand, if $Y_N = \emptyset$ for some positive integer N, in the sense that $Y_{N-1}(x) \cap \Gamma Y_{N-1}(x) = \emptyset$ for some x, so that Y_N is not defined

as an interval function, then there is no solution of (8.3) such that

(8.10) $$\underline{y}_0(x) \leqslant y(x) \leqslant \bar{y}_0(x), \quad 0 \leqslant x \leqslant 1,$$

that is, the interval function $Y_0 = [\underline{y}_0, \bar{y}_0]$ does not contain a fixed point y of G [24].

In the case in which the limit of the interval iteration (8.8) is degenerate, the following regularity theorem holds: If the interval iteration (8.8) converges and

(8.11) $$\lim_{n \to \infty} \Gamma Y_n = y,$$

a real function, then y satisfies (8.3) in the sense of Riemann (R) integration [24], that is,

(8.12) $$y(x) = (R) \int_0^1 g(x,t,y(x),y(t))dt.$$

This kind of convergence will occur if the interval operator Γ is what is called an <u>interval contraction</u> [3], [5]. Even if G and hence Γ are not contractive operators, interval iteration can be used to obtain improved lower and upper bounds for y [24].

Another application of interval integration is to the <u>minimization of functionals</u>, to which many problems in applied mathematics reduce. For example, instead of the functional.

(8.13) $$f(y) = \int_a^b \phi(x,y(x),y'(x))dx,$$

one can examine the <u>interval functional</u>

(8.14) $$F(Y) = \int_a^b \phi(x,Y(x),Y'(x))dx,$$

where ϕ, Y, Y' denote computable interval extensions of ϕ, y, y', respectively. It follows that (8.14) provides immediate lower and upper bounds for the values of the functional (8.13) for $y \in Y$, $y' \in Y'$, that is, if $F(Y) = [c,d]$, then $c \leqslant f(y) \leqslant d$ for $y \in Y$, $Y' \in Y'$. An algorithm similar to the one of Hansen and Sengupta [11] could then be applied to locate and obtain lower and upper bounds for

(8.15) $$\min f(y), \ y \in Y, \ y' \in Y'.$$

Since many physical principles, ordinarily formulated as differential equations, have alternative formulations as minima, maxima, or stationary values of functions expressed in integral form, or as integral equations, this is an area in which interval analysis can be extremely useful, particularly if the data are inexactly or imcompletely known. This is a topic for future research; others will be indicated in the next section.

9. <u>DIRECTIONS FOR FUTURE RESEARCH</u>. Research in applied mathematics follows two closely related lines: Application of known mathematical techniques to problems of importance in practice, and the development of new methods when known ones are inadequate or inefficient. The applied mathematician thus functions both as problem-solver and as "toolmaker to the trade". To a certain extent, the emphasis on tool making occurs in academic environments, and on using tools in laboratories. The U. S. Army Mathematics Steering Committee and the U. S. Army Research Office have provided a valuable service for many years by organizing meetings such as the Conferences of Army Mathematicians, which bring together applied mathematicians with both theoretical and practical orientations. To these groups, interval analysis is hereby offered as a new tool. It will work well on some problems, not on others, and will need improvement to be effective in other cases.

The usefulness of interval computation as described in §4 is well-established by now. Given the increased availability of fast interval arithmetic, interval analysis can and will be applied to more computational problems of the type described. This also applies to the solution of systems of equations (§5), integral equations (§8), and finding lower and upper bounds for values of functionals, as described also in §8.

In a more speculative vein, it appears that interval functions might provide a more realistic description of chaotic phenomena, such as turbulent flow, than single-valued real or complex functions. Also, since many physical principles have integral as well as differential formulations, interval integration might be applicable to a whole range of problems now solved approximately by the numerical integration of ordinary or partial differential equations. While interval analysis may or may not work in some of these areas, it has enough potential to at least be investigated, which is what research in applied mathematics is all about.

<div align="center">REFERENCES</div>

[1]   G. Alefeld and J. Herzberger: Einführung in die Intervallrechnung. Bibliographisches Institut, Mannheim, 1974.

[2]   F. Bierbaum and K.-P. Schweirtz: A bibliography on interval-mathematics, J. Comp. Appl. Math. 4(1978), 59-86.

[3]   O. Caprani and K. Madsen: Contraction mappings in interval analysis, BIT 15 (1975), 362-366.

[4]   O. Caprani and K. Madsen: Mean value forms in interval analysis, Computing 25 (1980), 147-154.

[5]   O. Caprani and K. Madsen: Interval contractions for the solution of integral equations, [22], pp. 281-290 (1980).

[6]   O. Caprani, K. Madsen, and L. B . Rall: Integration of interval
        functions, SIAM J. Math. Anal. 12 (1981). Also MRC Tech. Summary Rept.
        No. 2087, University of Wisconsin - Madison, 1980.

[7]   S. Chandrasekhar: Radiative Transfer. Dover, New York, 1960.

[8]   Julia Gray and L. B. Rall: INTE: A UNIVAC 1108/1110 program for
        numerical integration with rigorous error estimation, MRC Tech. Summary
        Rept. No. 1428, University of Wisconsin-Madison, 1975.

[9]   E. Hansen (Ed.): Topics in Interval Analysis. Oxford University
        Press, London, 1969.

[10]   E. Hansen: Global optimization using interval analysis---the multi-
        dimensional case, Numer. Math. 34 (1980), 247-270.

[11]   E. Hansen and S. Sengupta: Global constrained optimization using
        interval analysis, [22], pp. 25-47 (1980).

[12]   D. A. H. Jacobs (Ed.): The State of the Art in Numerical Analysis.
        Academic Press, New York, 1977.

[13]   U. Kulisch and W. Miranker: Computer Arithmetic in Theory and
        Practice. Academic Press, New York, 1981.

[14]   U. Kulisch and H.-W. Wippermann: PASCAL-SC: Pascal for Scientific
        Computation, Institute for Applied Mathematics, University of
        Karlsruhe, Germany, 1980.

[15]   E. J. McShane: Integration. Princeton University Press, Princeton,
        N. J., 1944.

[16]   R. E. Moore: Interval arithmetic and automatic error analysis in
        digital computation, Ph.D. Dissertation, Stanford University, Stanford,
        Calif. , 1962.

[17]   R. E. Moore: Interval Analysis. Prentice-Hall, Engelwood Cliffs,
        N. J., 1966.

[18]   R. E. Moore: Methods and Applications of Interval Analysis. SIAM
        Studies in Applied Mathematics, 2, Soc. for Ind. and Appl. Math.,
        Philadelphia, 1979.

[19]   R. E. Moore: New results on nonlinear systems, [22], pp. 165-180.
        (1980).

[20]   K. Nickel (Ed.): Interval Mathematics. Lecture Notes in Computer
        Science No. 29, Springer-Verlag, Berlin-Heidelberg-New York, 1975.

[21]   K. Nickel: Interval-analysis, [12], pp. 193-225 (1977).

[22]   K. Nickel (Ed.): Interval Mathematics 1980. Academic Press, New York,
        1980.

[23] L. B. Rall: Representations of intervals and optimal error bounds, MRC Tech. Summary Rept. No. 2098, University of Wisconsin-Madison, 1980.

[24] L. B. Rall: Application of interval integration to the solution of integral equations, MRC Tech. Summary Rept. No. 2128, University of Wisconsin-Madison, 1980.

[25] L. B. Rall: Integration of interval functions II. The finite case, MRC Tech Summary Rept. No. 2190, University of Wisconsin-Madison, 1981.

[26] L. B. Rall: A theory of interval iteration, MRC Tech. Summary Rept. No. 2196, University of Wisconsin-Madison, 1981.

[27] S. Skelboe: True worst-case analysis of linear electrical circuits by interval arithmetic, IEEE Trans. on Circuits and Systems, Vol. CAS-26 (1979), 874-879.

[28] J. M. Yohe: Portable software for interval arithmetic, Computing, Suppl. 2 (1980), 211-229.

DYNAMIC RESPONSE OF A HEMISPHERICAL ENCLOSURE SUBJECTED TO EXPLOSIVE BLAST LOADING

Aaron D. Gupta and Henry L. Wisniewski
Terminal Ballistics Division
Ballistic Research Laboratory
U.S. Army Armament Research and Development Command
Aberdeen Proving Ground, Maryland 21005

ABSTRACT. Large deflection elastic-plastic response of a 9 m radius hemispherical shell enclosure structure .0254 m thick clamped to a horizontal rigid foundation and subjected to explosive blast loading due to a 29.03 kg TNT charge at the center was analysed using a finite-difference structural response code i.e. PETROS 3.5.

The peak reflected overpressure was estimated from a scaled distance of the wall from the point of detonation based on a conservative cube-root scaling law. The reflected overpressure decay with time was assumed to obey the modified Friedlander equation. The residual quasi-static overpressure was obtained from an equation developed by Kinney and Sewell based on the ratio of the available vent area and the internal volume.

Only a quarter segment of the structure was modelled using 18 equal width meshes in one layer and four Gaussian integration points through the thickness in each mesh. The 1020 steel was represented by a trilinear curve followed by a perfectly-plastic behavior and elastic-plastic unloading resulting in a polygonal approximation.

The results indicated the initiation of flexural waves at the clamped edge propagating towards the pole and thereby altering the spherically symmetric breathing mode of response of the structure. The peak deflection was predicted by the code to occur at the pole and permanent displacement after releasing the load was found to be quite small. Transient strain components at the inner and outer surfaces near the clamped edge due to mainly elastic oscillations showed significant bending deformation. In conclusion, the protective structure was found to be efficient configuration capable of safe containment of internal explosive blast loading.

I. INTRODUCTION. The Ballistic Research Laboratory is currently in the process of acquiring a target enclosure to facilitate destructive terminal ballistic testing of chemical explosives (CE), armor and kinetic energy (KE) penetrators by safe containment of blast, fragments and resultant harmful combustion products. The present investigation is based on a preliminary concept of the firing range as shown in Figure 1. The target is located inside the hemispherical enclosure at the end of a long concrete pipe-guide. The gun-launched projectile travels through the pipe-guide and enters the enclosure through a .914 m diameter hole. The target interaction with the projectile is monitored photographically with flash X-ray equipment and penetration velocity is
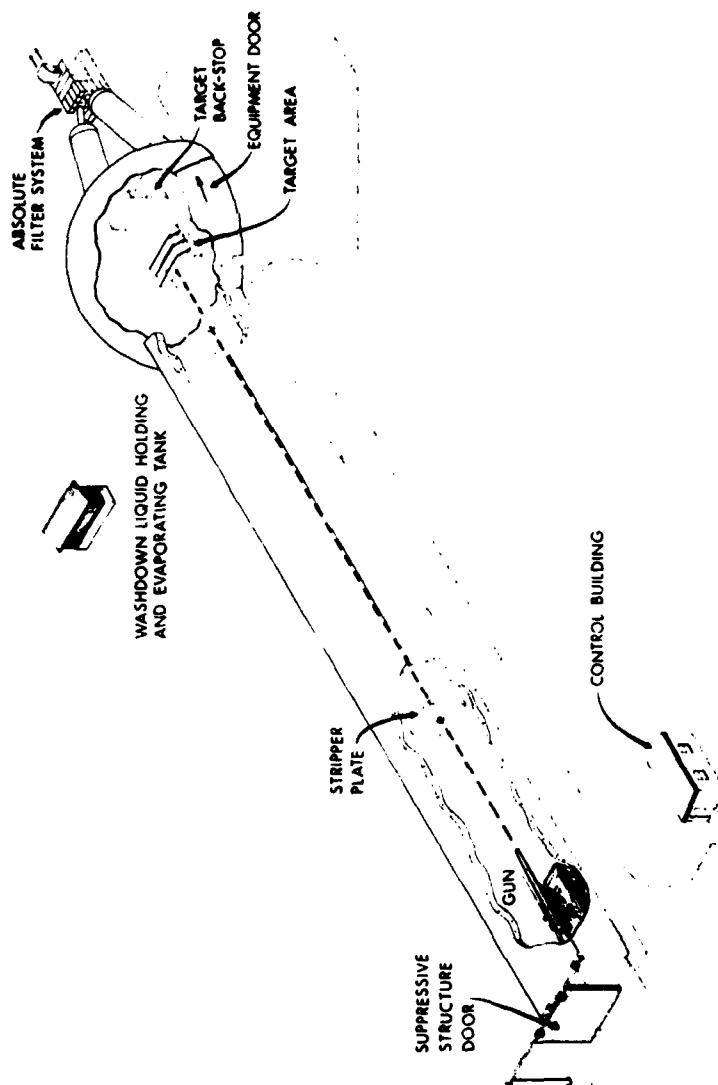
Figure 1. Preliminary concept layout of the AHKELS (Advanced High Kinetic Energy Launch System) range.

obtained using velocity screens and electronic counters. An air exhaust system mounted at the rear of the structure operates during the test and draws back aerosolized material out of the enclosure after a test and traps it in filters in the exhaust ducting. A large sliding door with a configuration to match the curvature of the hemispherical wall allows equipment access inside the enclosure. The door is sealed to the wall with a pressurized hose seal along its perimeter. The entire structure is built to contain blast and fragments, to trap aerosolized materials and to permit photographic observation of the test.

A significant problem associated with the enclosed range tests is the overpressure resulting from shock loading as well as rapid heating of the air within the enclosure as the penetrator and the target are torn apart during their encounter as shown by R. Abrahams et.al [1]. The structure must survive both the reflected and the residual overpressures induced by the interaction until ambient conditions are reached due to venting out to the atmosphere through the exhaust system.

Since the key element of the AHKELS (Advanced High Kinetic Energy Launch System) range is the enclosure structure, The Target Loading and Response Branch was assigned to estimate the overpressure loading on the wall and analyze dynamic response of the preliminary configuration at critical locations and assure structural integrity from a conservative viewpoint. The choice of a hemispherical configuration was influenced by an earlier investigation by N. J. Huffington et.al [2] who demonstrated the effectiveness of such a protective structure.

In the absence of any available experimental data it was decided to obtain a theoretical estimate of the transient and residual overpressure loading due to a centrally located equivalent charge weight at the base. The subsequent objective was to perform an approximate conservative static analysis for an initial estimate of wall thickness. Finally the dynamic, elasto-plastic, large deflection response of the shell configuration clamped to a horizontal rigid foundation was studied to indicate critical locations where peak strains or deflections could occur.

II. ESTIMATION OF TRANSIENT LOADS. The transient loads were estimated under the assumption that the test firing of penetrator rounds would generate overpressures inside the containment chamber similar to those caused by an internal blast due to an equivalent central charge weight of 29.03 Kg at the base as shown in Figure 2. Assuming the walls to be rigid, the symmetry of the charge and the structure about a vertical axis through the center indicates uniform distribution of internal reflected loading upon the structure. For the estimation of peak reflected overpressure, a conservative cube-root scaling law [3] is employed to compute the scaled distance, Z, of the wall from the charge location in the form

$$Z = \frac{R}{W_E^{1/3}} \tag{1}$$

SIDE VIEW —29.03Kg TNT

PLAN VIEW
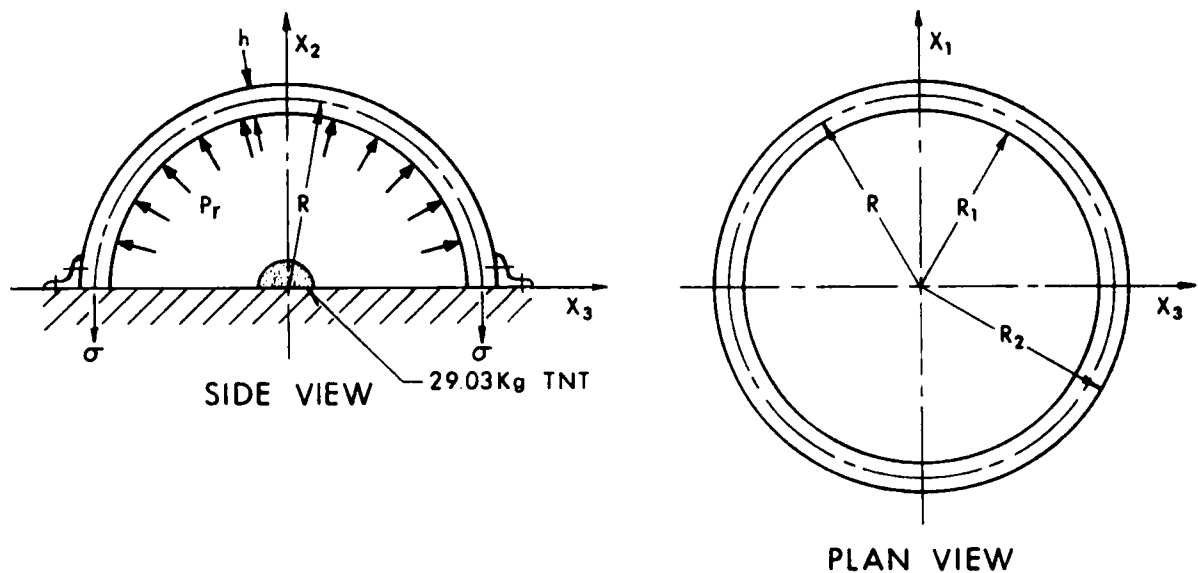
Figure 2. Section through hemispherical containment structure

where W_c is the equivalent charge weight and R is the distance of the wall from the charge location.

Once the scaled distance is known the reflected parameters such as peak overpressure, impulse, time of arrival and duration time of the shock loading could be estimated from compiled airblast tables [4,5]. The decay of the reflected overpressure is assumed to obey the modified Friedlander exponential decay equation which can be written as

$$P_r = P_m[1 - t/t_o]e^{-\alpha t/t_o} \tag{2}$$

where t_o is the positive phase duration of the impulse, P_m is the peak reflected overpressure and t is the elapsed time from impact or detonation. The exponential decay parameter, α, is given as

$$\alpha = .57 \left[\frac{P_m + P_o}{P_o}\right]^{0.65} \tag{3}$$

where P_o is the peak quasi-static overpressure obtained from quasi-steady residual overpressure calculations, the equations for which are given in the following section.

III. ESTIMATION OF QUASI-STATIC LOADS. Quasi-static pressures immediately following the reflected pressure were predicted assuming that the heat of combustion of TNT is used totally to heat the air within the enclosure [6]. A relationship for the resultant increase in pressure is

$$\Delta P = \frac{0.4\ hW_E}{V}\ ,\ kPa,\tag{4}$$

where V = 1513.9 m^3, the internal volume of the enclosure,

W_E = 29.03 kg, weight of the explosive charge, and

h = 13.5 KJ/g, the heat of combustion of TNT.

An internally pressurized structure vents the pressure to the surroundings through openings in its walls causing a slow decay to ambient conditions as shown by Kinney and Sewell [7] and is computed from

$$Ln\ P = Ln\ P_0 - .315\ (A_V/V)\ t_s,\tag{5}$$

where t_s = elapsed time in ms

P = absolute pressure at t_s

A_V = 2.33 m^2, the available vent area.

The long term duration of the decay is essentially due to the relatively small vent area available causing a slow pressure decay to the atmosphere.

The blow-down time, t_g, required to reduce the residual overpressure to ambient conditions developed by Keenan et.al [8], based on the firing of high explosives in chambers with known vent areas and volumes, is given as

$$t_g = 6.28\ (A_V/V)^{-.86}\tag{6}$$

The above equation is valid for $A_V/V^{2/3} < 0.21$. In the current design the ratio, $A_V/V^{2/3}$, equals .018 and the duration time for the quasi-steady pressure is approximately 1600 ms.

The computation involves determination of peak residual overpressure from Eq. (4) which when combined with Eqs. (5) and (6) yields the quasi-steady part of the loading history. The junction between the reflected overpressure history and the quasi-steady loading was smoothed by a curve interpolation scheme in order to avoid a sharp transition. The resulting load profile is shown in Figure 3. This loading is applied uniformly at

307
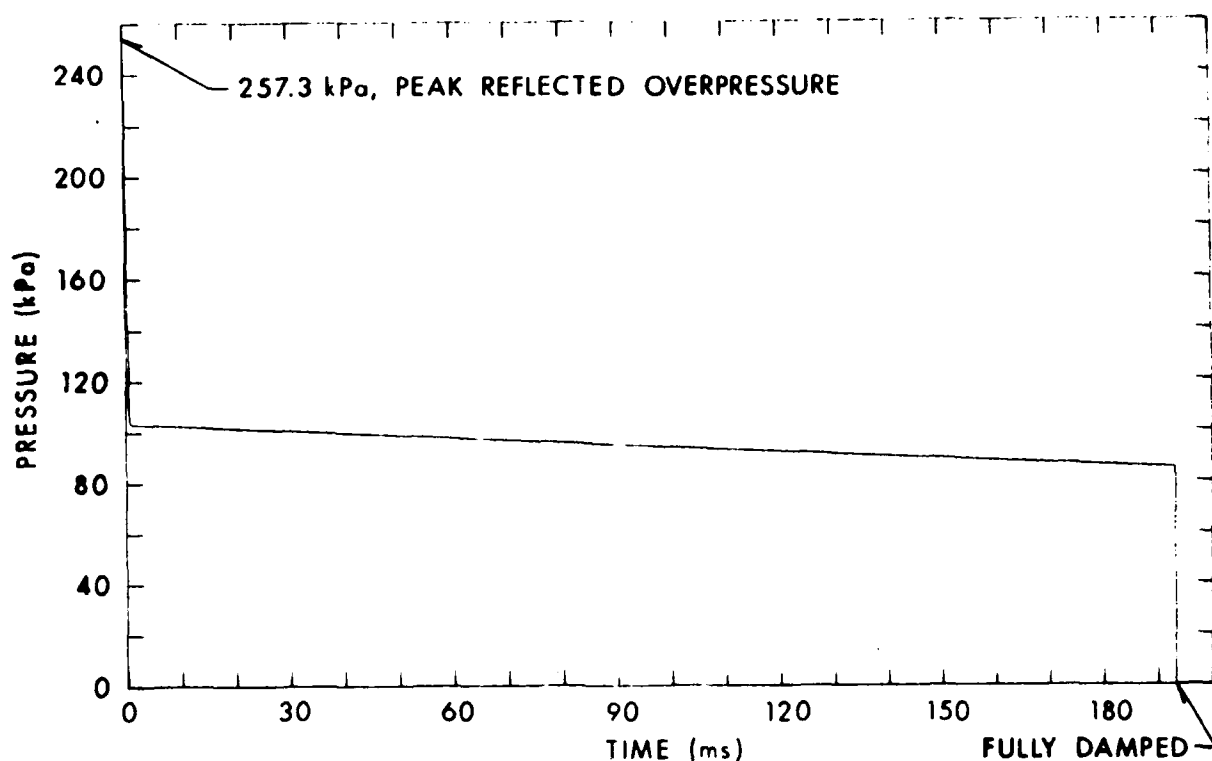
Figure 3. Computed pressure-time history due to internal explosive blast loading of the hemispherical enclosure.

each meshpoint on the inside wall in the radial direction in the finite-difference structural response model in the PETROS 3.5 computer program [9] developed for the BRL. In Figure 3 the load-time history inside the hemispherical enclosure was zeroed out after 180 ms to facilitate damping of small elastic oscillations and to observe any residual deformation of the hemispheric wall. The peak reflected overpressure was found to be 257.3 kPa while the peak residual overpressure was approximately 100 kPa.

IV. STATIC STRESS ANALYSIS. Prior to a detailed dynamic response study, a static stress analysis in the linear-elastic-small deflection regime was conducted to obtain an initial estimate of the enclosure wall thickness. Since the duration of the reflected pressure is less than 1.5 ms compared to 1600 ms for the duration of the quasi-steady over-pressure, an approximate static analysis based on a minimum factor of safety of 2.0, is considered to be satisfactory. For the preliminary investigation, stress-concentration near holes, cutouts and wall openings was neglected. However the effect of ground-plane reflection of the shock

wave was included through a load multiplication factor of k = 2.0, which in effect doubled the applied load.

To contain the initial pressure pulse in an elastic manner only the peak reflected overpressure, P_r, was included in the calculation of stresses and deflections. An equivalent static meridional stress, σ, can be calculated from Figure 2 by equating the resultant upward force due to internal pressurization to the net downward restraining force due to the stress developed at the clamped edge resulting in

$$\sigma = \frac{RkP_r}{2h} \tag{7}$$

where R = 8.987 m, the median radius

k = load multiplication factor

However for an assumed factor of safety of 2.0 $\sigma = \frac{1}{2} \sigma_y$, where σ_y is the static yield stress. Substituting this value of σ in Eq. (7) and rearranging terms results in an expression for the estimated thickness, h, in the form

$$h = \frac{RkP_r}{\sigma_y} \tag{8}$$

The yield stress, σ_y, for the wall material which is 1020 steel is 241.3 MPa. Hence the wall thickness, h, from Eq. (8) is found to be .019 m.

Up to this point no consideration has been given to the possibility that fragment induced damage to a shell might result in catastrophic rupture when the blast loading is applied. One should estimate the material removal produced by the impact of the worst threat fragment and perform a local three dimensional analysis of the stress field to determine whether a crack would be propagated under such loading. This problem in fracture mechanics is difficult to analyze and can be at least partially circumvented by a conservative selection of wall thickness under the assumption that the residual thickness is capable of withstanding the peak quasi-steady pressure even when a 50% depth of penetration has been achieved by a part-through fragment. The final thickness chosen was .0254 m (1 in), a material thickness which is readily available. The .0254 m thickness corresponds to a stress level of 45.5 MPa which when compared to the yield stress results in a final margin of safety of 4.3 which is satisfactory.

The peak radial deflection ΔR at the pole is estimated from reference [10] as

$$\Delta R = -\frac{R \ kP_r(1-\nu)}{2Eh} \tag{9}$$

where E, ν are elastic material properties.

To detect resonance due to coupling of the duration time of the pressure pulse with the natural vibration period, the time period, T, was calculated from reference [10] as

$$T = \pi R \ \frac{2\rho(1-\nu)}{E}, \tag{10}$$

where ρ is the mass density. Further check of interaction of the reflected pressure pulse due to ground plane reflection with the elastic oscillation of the pole did not reveal a significant problem.

The peak radial elastic deflection at the pole from Eq. (9) was .0011 m which is quite small and is consistent with the design objective. The gross weight of the hemispherical enclosure was approximately 96400 kg based on a .0254 m wall thickness. In this study allowance was made for the weight of flanged material at the base but not for extra weight associated with access provisions, welds or foundations.

An optimization study based on equivalent strength showed substantial weight saving for a hemispherical configuration at or below 6 m radius but marginal savings at higher radius up to 9 m due to compensating thickness increase. An equation proposed by R. Karpp et.al [11] for the minimum amount of vessel material, V_m, to contain a specified charge is given as

$$V_m = 4\pi W_E \left(\frac{K}{\varepsilon_y}\right)^{1.0406} \left(\rho_o\right)^{.0406} \left(\frac{R}{h}\right)^{.0406} \tag{11}$$

where ε_y is the yield point strain of the vessel material in biaxial tension, W_E is the charge weight, ρ_o is the density of the vessel material and K is an empirical curve-fit constant found to be 4.08×10^{-6} m^3/kg. Unfortunately the optimum configuration could not be achieved due to constraints of minimum workspace and equipment access requirements.

V. DYNAMIC RESPONSE ANALYSIS. Response of the structure subjected to transient loads from an internal blast shown in Figure 2 was conducted using the BRL version of the PETROS 3.5 computer program [9], which employs the finite-difference method to solve the nonlinear equations governing finite-amplitude elastoplastic response of thin Kirchhoff Shells. The model is valid for large deflections and can be employed to treat the entire structure rather than a small section.

A. **Material Model**. The uniaxial tensile quasi-static stress-strain property for 1020 steel which is used as the primary vessel material is shown by the continuous line in Figure 4. The material is modeled in the code as a combination of three linear segments indicated as the dashed curve in Figure 4 followed by a perfectly plastic behavior and linear elastic-plastic unloading resulting in a polygonal approximation of the experimental data. The strain-hardening part of the stress-strain curve is generated by a sublayer hardening model from a weighted combination of elastic perfectly-plastic curves yielding a piecewise multilinear hardening representation. Strain-rate effects were neglected, which is conservative since these effects increase the structural resistance and thus reduce the total deformation.

Figure 4. Stress-strain property modeling.

B. **Finite-Difference Model**. Since both the responding structure and the applied loads are symmetric with respect to the vertical axis as shown earlier in Figure 3, it is sufficient to model the response of a single pie-shaped segment of the hemispherical enclosure and generate the entire structure by 360° rotation of the structure about the axis of symmetry resulting in quite economical computer runs.

A total of 18 meshes along the surface and a single layer through the thickness were used to represent the pie shaped segment. Four Gaussian integration points through the thickness were used at each mesh for computational purpose. Total number of mesh-points did not exceed 37.

A. Material Model. The uniaxial tensile quasi-static stress-strain property for 1020 steel which is used as the primary vessel material is shown by the continuous line in Figure 4. The material is modeled in the code as a combination of three linear segments indicated as the dashed curve in Figure 4 followed by a perfectly plastic behavior and linear elastic-plastic unloading resulting in a polygonal approximation of the experimental data. The strain-hardening part of the stress-strain curve is generated by a sublayer hardening model from a weighted combination of elastic perfectly-plastic curves yielding a piecewise multilinear hardening representation. Strain-rate effects were neglected, which is conservative since these effects increase the structural resistance and thus reduce the total deformation.

Figure 4. Stress-strain property modeling.

B. Finite-Difference Model. Since both the responding structure and the applied loads are symmetric with respect to the vertical axis as shown earlier in Figure 3, it is sufficient to model the response of a single pie-shaped segment of the hemispherical enclosure and generate the entire structure by 360° rotation of the structure about the axis of symmetry resulting in quite economical computer runs.

A total of 18 meshes along the surface and a single layer through the thickness were used to represent the pie shaped segment. Four Gaussian integration points through the thickness were used at each mesh for computational purpose. Total number of mesh-points did not exceed 37.

Initial configuration of the finite-difference model employed for all subsequent calculations is shown in Figure 5.
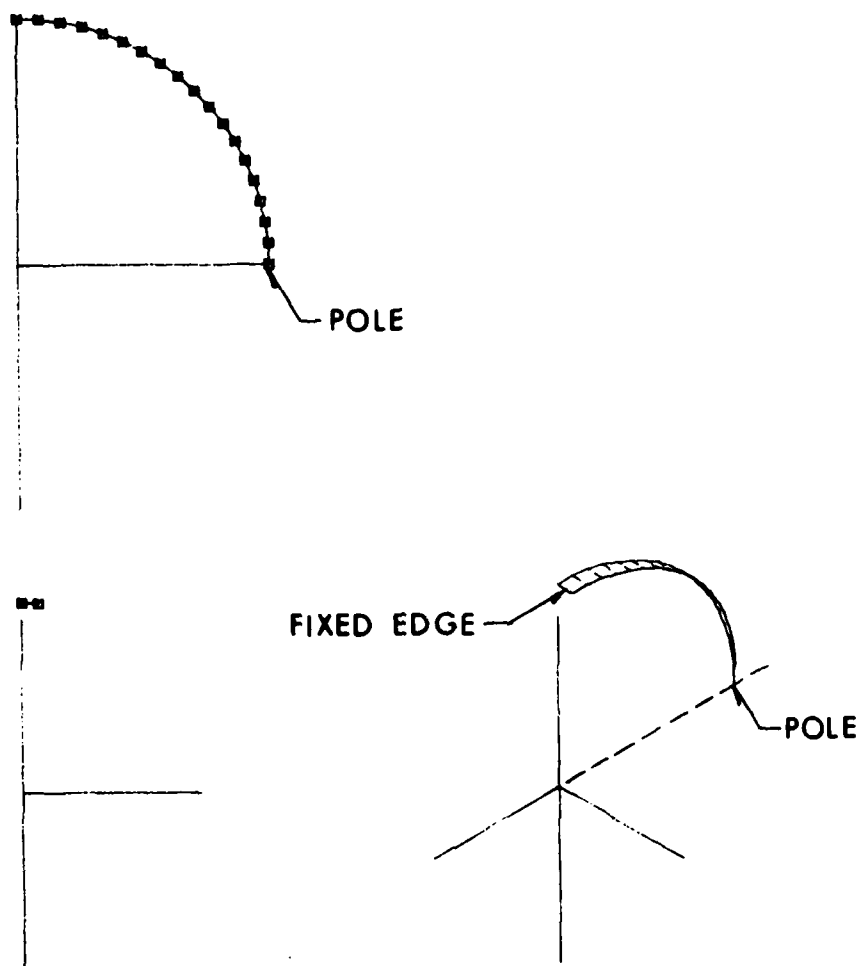
Figure 5. Initial configuration of the finite-difference model.

VI. RESULTS AND DISCUSSION. The deformed cross-section of the hemispherical segment relative to the initial undeformed configuration at 36 ms is shown in Figure 6. At this time the maximum deflection occurs at the pole. The deflections are exaggerated due to a high magnification factor of 1000 and are, in fact, small enough to be in the linear elastic range, in accordance with the design objective.
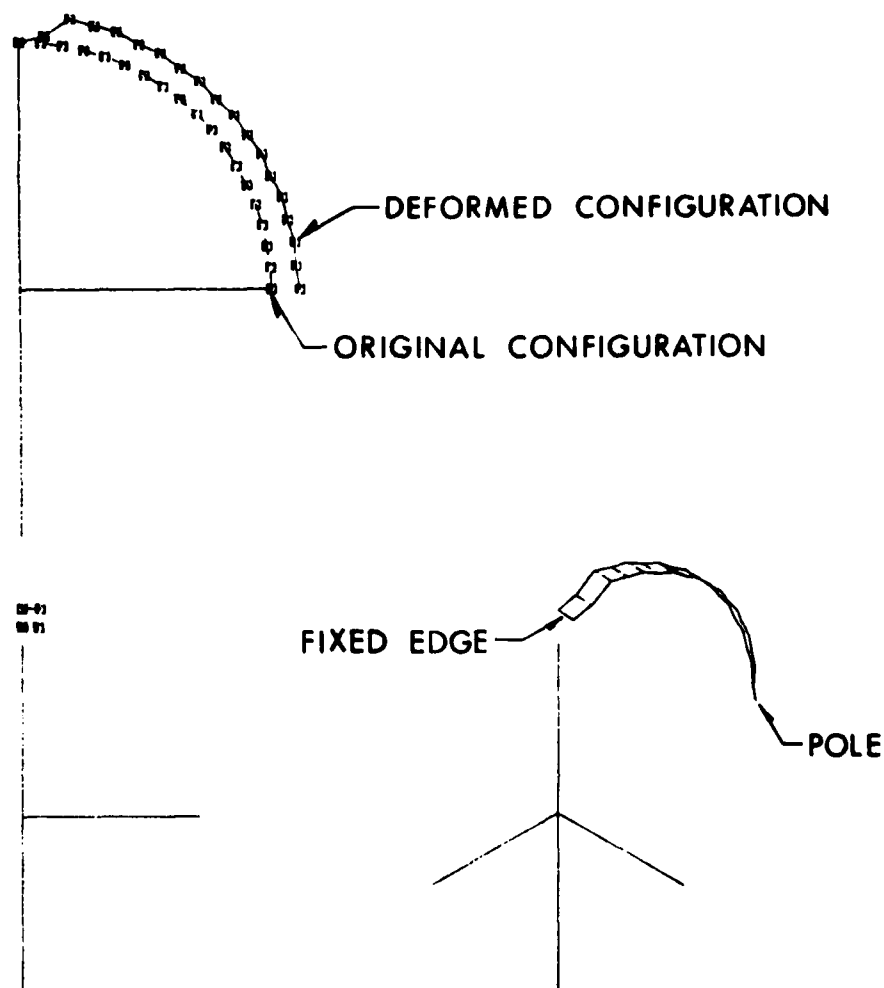
Figure 6. Deformed configuration at 36 ms corresponding to cycle no. 1500.

Figure 7 describes the transient rectangular components of displacement in a meridional plane at point A at 45° from the vertical axis of the hemisphere. The maximum displacement at this point is only .82 mm, essentially radially outward. Displacements at other locations are correspondingly small except in the neighborhood of the pole of the hemisphere where a peak deflection of 1.17 mm is observed at approximately 36 ms as illustrated in Figure 8. However this displacement is less than 4% of the shell thickness so that geometric nonlinearities are insignificant. The peak deflection is of the order of elastic deflection at the pole and any residual deflection, after elastic oscillations are
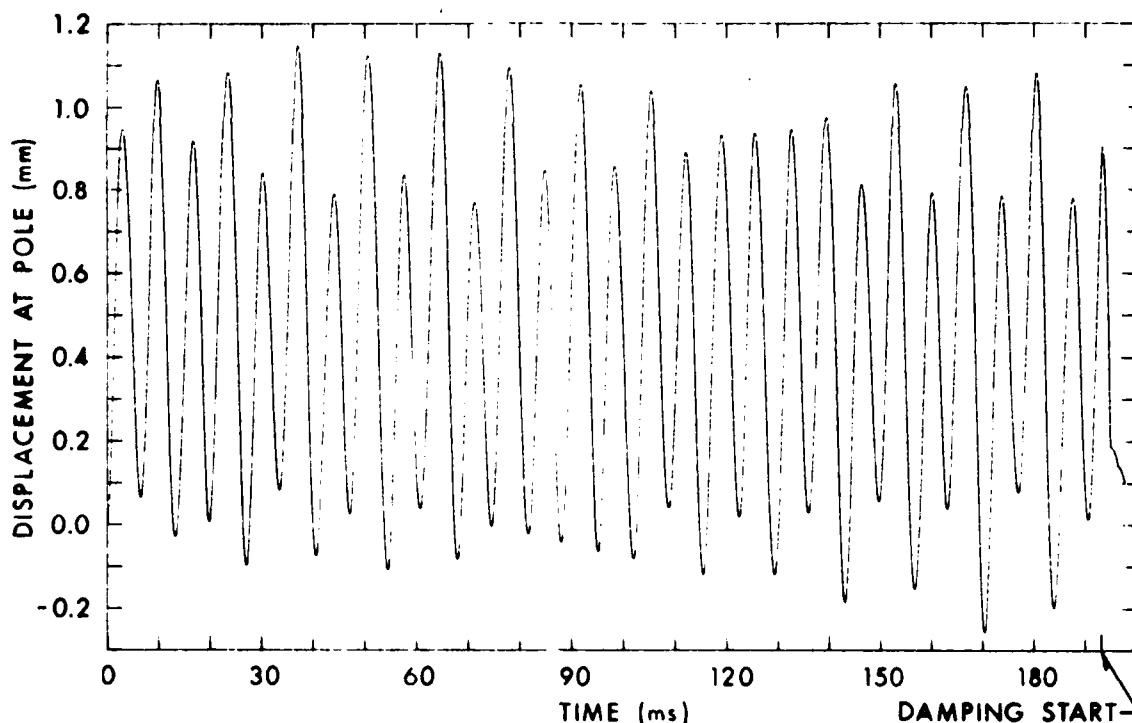
Figure 8. Transient displacement at pole of hemisphere.

Energy balance studies using the code confirmed absence of plastic work and numerical instability. Both total and kinetic energies were bounded. The fluctuations of kinetic energy appeared to have twice the frequency of the work performed by the internal blast pressure.

Transient strain components on the outer and inner surfaces of the hemisphere at a point near the edge are shown in Figures 9a and 9b respectively. The meridional strain components on the inner and outer surfaces are almost in phase initially but become out of phase and un-equal in magnitude with increasing time signaling the build-up of some flexural deformation. The hemisphere moves outward and inward, except at the fixed boundary , in a spherically symmetric breathing mode result-ing in membrane strains upon which the bending strains are subsequently superposed due to propagation of flexural waves from the fixed boundary towards the pole. Significant difference in strains between the outer and the inner walls at the clamped edge could be primarily attributed to domination of the response by the bending strains. The circumferential strains indicated by continuous lines in Figures 9a and 9b are zero as

315
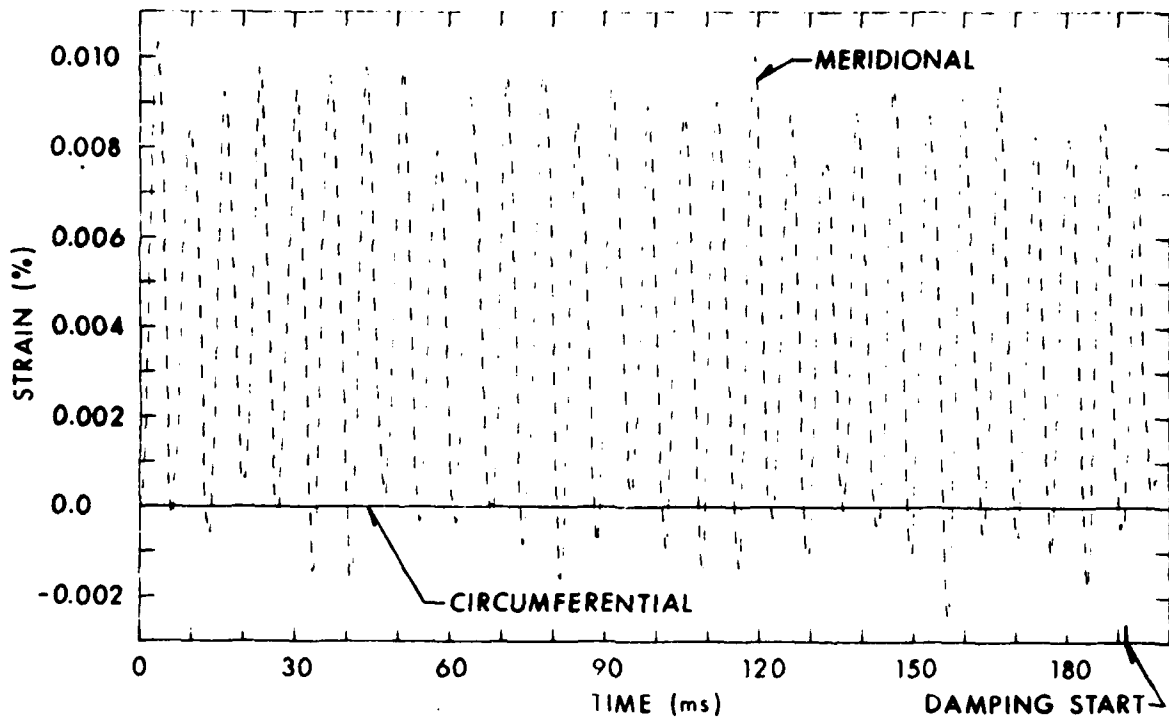
(a) Outer surface strain components
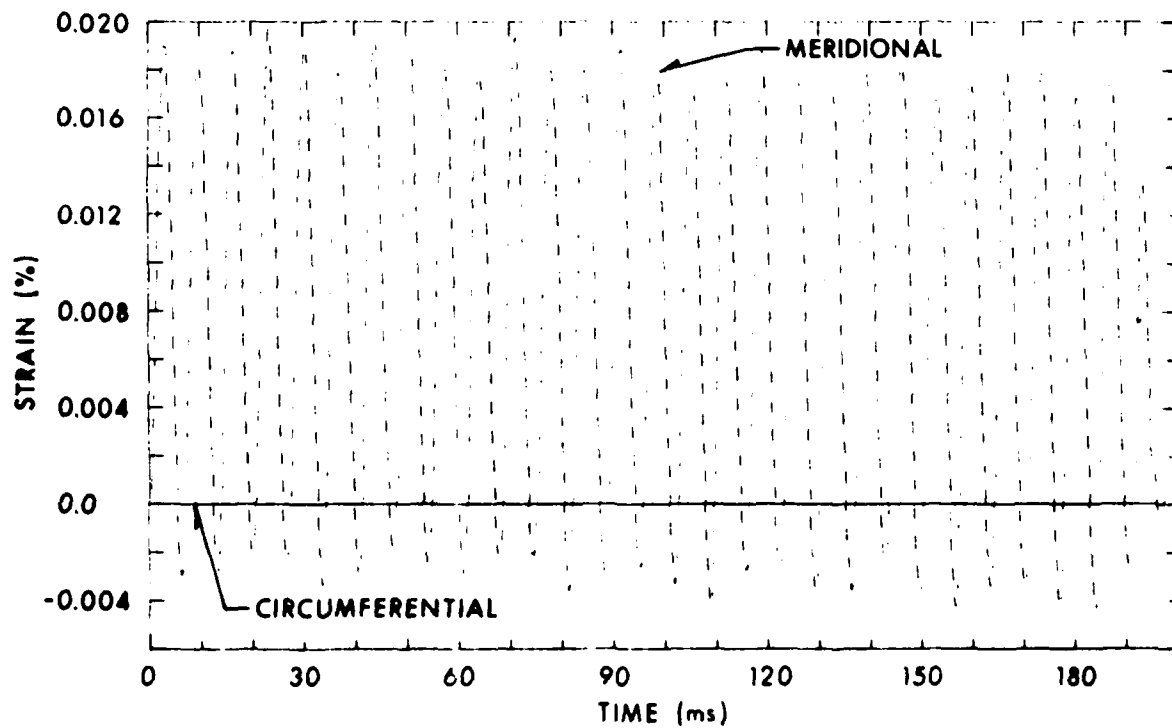
(b) Inner surface strain components

Figure 9. Surface strains at the fixed edge.

expected. Calculations for maximum meridional stress based on peak strain results in a stress level of 48.26 MPa which is equivalent to a safety margin of 4.0. As expected from elastic theory, peak strains occurred at the fixed edge, while maximum deflection occurred at the pole.

The variation of strain at the inner wall with time at a point near the pole is shown in Figure 10. The continuous line depicts the circumferential strain which is in phase and very similar to the meridional strain shown by the intermittent line. The strains at the outer wall near the pole exhibits elastic oscillations of approximately the same magnitude and duration as in Figure 10. This behavior indicates substantial weakening of the flexural wave near the pole and domination of meridional and circumferential strains by the membrane component of strain due to elastic vibration of the wall in the breathing mode. The peak meridional stress at the pole was calculated based on elastic equations and was found to be approximately 25 MPa, which is considerably lower than the maximum stress at the clamped edge. The stress level is equivalent to a safety margin of 8.6 based on the yield stress.
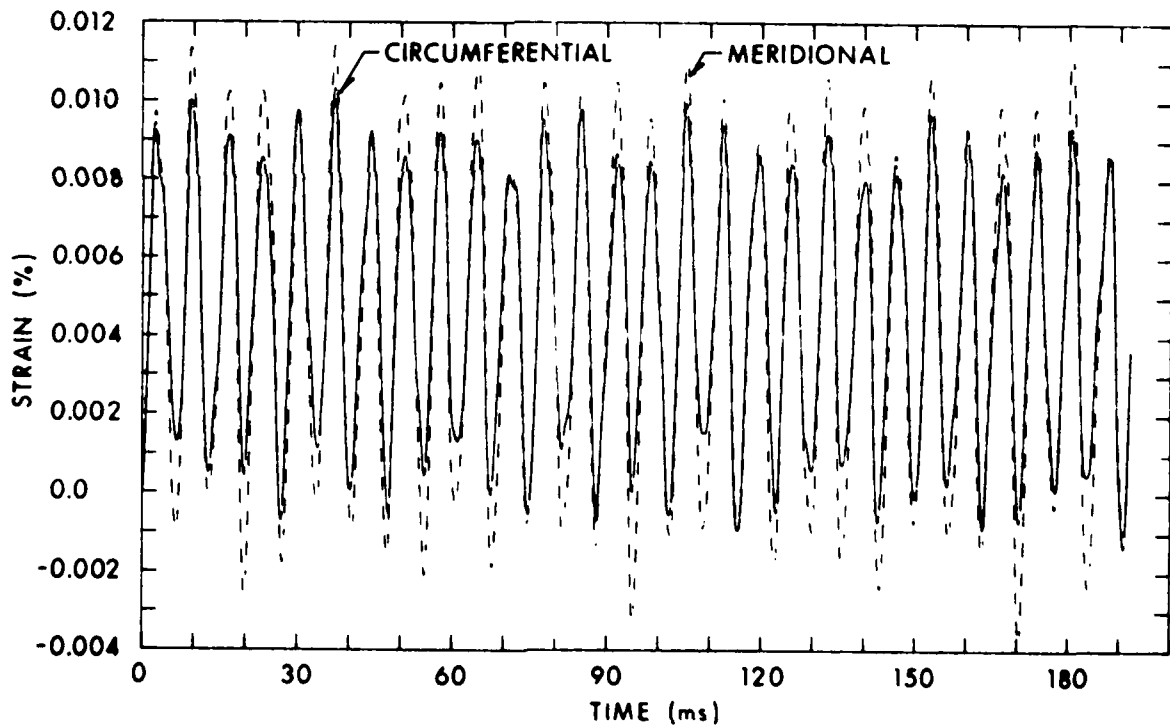
Figure 10. Surface strains at the inner wall near pole.

Both strain components are relieved completely upon damping at approximately 198 ms. An isometric view of the fully damped configuration generated by 360° rotation of the pie-shaped segment about the axis of symmetry is shown in Figure 11. The view through Section A-A in this figure depicts the final configuration upon damping superposed on the initial configuration. The coincidence of the two configurations at a high magnification ratio of 1000 indicates the absence of any plastic deformation and confirms small strains and deformations throughout the structure in accordance with earlier results.
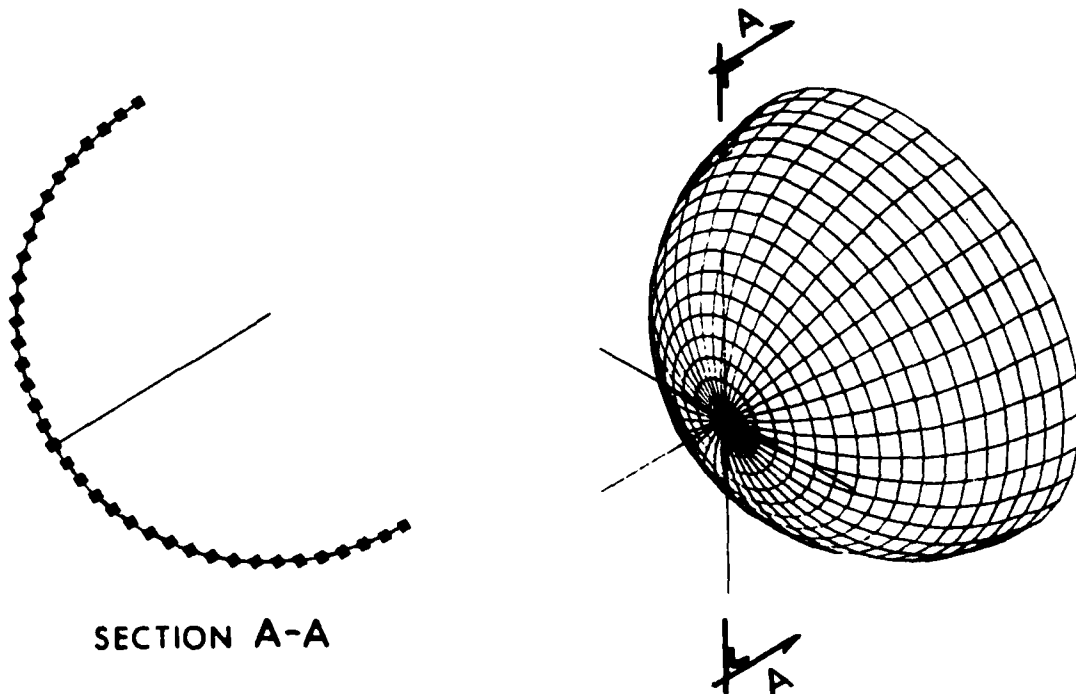
SECTION A-A

Figure 11.   Isometric and sectional view of the fully
damped configuration.

VII.   CONCLUDING REMARKS.   It has been demonstrated, through use of a rigorous nonlinear shell response methodology, that it is possible to design a containment structure with a hemispherical configuration in an efficient and cost effective manner. The methodology could be easily extended to structural optimization studies, resulting in considerable cost savings provided internal volume and access considerations could be met.

In spite of simplifying assumptions and limitations of the PETROS 3.5 version of the shell response analysis code which neglects transverse shear deformation and rotatory inertia, the analysis gives a clear insight into the initial loading mechanism due to structural resistance and interaction of various components of the response. However an examination of the characteristics of the hemispherical structure reveals the following:

1. The 9 m radius, .0254 m thick hemispherical enclosure is an efficient protective structure capable of withstanding internal blast from a 29.03 kg TNT charge with assured structural integrity.

2. The structure is capable of successful containment of combustion products and fragments with sufficient mass and velocity to achieve a 50% depth of penetration with a satisfactory margin of safety.

3. Peak deflection occurs at the pole due to elastic oscillations of the structure in the breathing mode resulting in focusing of vibratory energy at the pole.

4. Peak strain occurs at the clamped edge and exhibits considerable difference in strain magnitude between the inner and outer surfaces due to bending waves originating in this region.

5. The ratio of the vent area to the internal volume is small enough to result in a slow rate of venting and an extended venting time of 1600 ms for the quasi-steady residual overpressure to blow down to the external ambient conditions.

6. Cumulative damage effect due to repeated test firings could conceivably cause low cycle fatigue of the structure and a periodic inspection of the internal surface and joints for cracks in critical regions is recommended.

7. Future work should be directed to modelling of the enclosure structure with wall openings for the equipment and personnel access doors, protective walls for X-ray equipments, detailed analysis of critical joints and stress concentration due to holes and cutouts in corner regions.

REFERENCES.

1. R. Abrahams, R. Peterson, and B. Bertrand, "Measurement of Blast Pressure Produced by Impact of Kinetic Energy Penetrator on a Steel Target," BRL Memorandum Report ARBRL-MR-02983, January 1980, AD# B045141L.

2. N. J. Huffington and S. R. Robertson, "Containment Structures Versus Suppressive Structures," BRL Memorandum Report BRL-MR-2597, February 1976.

3. Engineering Design Handbook, "Explosions in Air, Part One," AMC Pamphlet AMCP 706-181, Headquarters, U.S. Army Material Command, pp. 3-5, July 1974.

4. B. Soroka, "Air Blast Tables for Spherical 30/50 Pentolite Charges at Side-On and Normal Incidence," BRL Memorandum Report ARBRL-MR-0295 (AD# A080537) December 1979.

5. H. Goodman, "Compiled Free Air Blast Data on Bar Spherical Pentolite," BRL Report 1092, February 1960 (AD# 235278).

6. Edward M. Weyer, Editor-in-chief, Annals of the New York Academy of Sciences, Vol. 152, "Prevention of and Protection Against Accidental Explosion of Munitions, Fuels and other Hazardous Mixtures," Published by the Academy, 2 East Sixty-Third Street, New York, NY 10021, p. 317.

7. G. F. Kinney and R. G. S. Sewell, "Venting of Explosives," NWC Technical Memorandum No. 2448, July 1974.

8. W. A. Keenan and J. A. Tamareto, "Blast Environment from Fully and Partially Vented Explosions in Cubicles," U.S. Naval Civil Engineering Laboratory Technical Report No. 51-027, February 1974.

9. S. D. Pirotin, B. A. Berg and E. A. Witmer, "PETROS 3.5: New Developments and Program Manual for the Finite-Difference Calculation of Large Elastic-Plastic Transient Deformations of Multi-Layer Variable-Thickness Shells," U.S. Army Ballistic Research Laboratories Contract Report No. 211, February 1975.

10. R. J. Roark, "Formulas for Stress and Strain," Fifth Edition, McGraw-Hill Book Company, New York, NY pp. 96, 451 (1975).

11. R. R. Karpp, T. A. Duffey and T. R. Neal, "Response of Containment Vessels to Explosive Blast Loading," Report No. LA-8082, UC 38, Los Alamos Scientific Laboratory, Los Alamos, New Mexico, June 1980.

EXPLICIT DIFFERENCE SCHEMES FOR WAVE PROPAGATION AND IMPACT PROBLEMS*

Joseph E. Flaherty
Department of Mathematical Sciences
Rensselaer Polytechnic Institute
Troy, NY 12181

and

U.S. Army Armament Research and Development Command
Large Caliber Weapon Systems Laboratory
Benet Weapons Laboratory
Watervliet, NY 12189

ABSTRACT. Explicit finite difference and finite element schemes are constructed to solve wave propagation, shock, and impact problems. The schemes rely on exponential functions and the solution of linearized Riemann problems in order to reduce the effects of numerical dispersion and diffusion. The relationship of the new schemes to existing explicit schemes is analyzed and numerical results and comparisons are presented for several examples.

I. INTRODUCTION. Exponentially fitted and/or weighted finite difference [9,11], finite element [3,9,10], and collocation [5] schemes have become popular and effective methods of solving steady convection-diffusion problems. They avoid the spurious mesh oscillations that are found near boundary and shock layers when centered schemes are used at high cell Reynolds or Peclet numbers and they reduce the effects of numerical diffusion that are associated with classical upwind difference schemes.

We seek to extend exponential methods to transient problems and as a first step we consider one-dimensional scalar initial value problems of the form

$$u_t + f(u)_x = \varepsilon u_{xx} \quad , \quad t > 0 \quad , \quad |x| < \infty$$

$$u(x,0) = u^0(x) \quad , \quad |x| < \infty \tag{1}$$

where $0 < \varepsilon \ll 1$ is either a real or an artificial viscosity parameter and the x and t subscripts denote partial differentiation.

Our primary motivation for studying exponential schemes is a desire to develop improved numerical methods for elastic-plastic impact problems in solids and blast problems in gases.

In this paper, we confine our attention to explicit difference approximations of (1) having the form

$$U^{n+1}_j = U^n_j - \frac{1}{2}\lambda[(1 + z^n_{j-1/2})(f^n_j - f^n_{j-1}) + (1 - z^n_{j+1/2})(f^n_{j+1} - f^n_j)]$$

$$+ \frac{\varepsilon\lambda}{\Delta x}(U^n_{j-1} - 2U^n_j + U^n_{j+1}) \quad , \quad n > 0 \quad , \quad |j| < \infty$$

$$U^0_j = u^0(j\Delta x) \quad , \quad |j| < \infty \tag{2}$$

where Δx and Δt denote the uniform spatial and temporal grid spacings, respectively, U^n_j is the numerical approximation of $u(j\Delta x, n\Delta t)$,

$$f^n_j := f(U^n_j) \quad , \quad \lambda = \Delta t/\Delta x \tag{3,4}$$

and $z^n_{j+1/2}$ are upwind weighting factors.

Many popular difference schemes have the form of (2) and some of these are discussed and compared in Section II. We also introduce an exponential scheme that is based on determining $z^n_{j\pm1/2}$ so that U^n_j is the exact solution of the linearized steady equation

$$cu_x = \varepsilon u_{xx} \tag{5}$$

when $c = f'(u)$ is a constant. We call this method the linearized steady exponential (LSE) method and it is the simplest extension of the exponentially fitted and weighted schemes [3,9,10,11] to transient problems. The scheme gives improved accuracy for steady shock problems, but offers little improvement over classical upwind differencing for moving shock problems.

In Section III we develop an exponential scheme that is based on the exact solution of a linearized transient equation (1) that is subject to piecewise constant initial data, i.e., a linearized Riemann problem for (1). We call this method the linearized transient exponential (LTE) method and, like other methods based on the solutions of Riemann problems [1,2,4,6,8,13, 15,16], it sharply resolves boundary and shock layers without added diffusion or spurious oscillations. As $\varepsilon \to 0$ the LTE method becomes formally equivalent to Roe's method [15,16] for hyperbolic systems of conservation laws. van Leer [17] has noted that Roe's method treats an expansion fan as a so called "expansion shock" (cf. Figure 6) and, unfortunately, our LTE method also has this disturbing property even when ε is nonzero, but small.

In Section IV we present some preliminary results for vector systems of equations and in Section V we discuss our results and indicate some directions for future work.

II. THE LINEARIZED STEADY EXPONENTIAL (LSE) METHOD.

The LSE method is obtained from (2) by selecting z^n_k, $k = j\pm1/2$, as

$$z^n_k = \coth \rho^n_k/2 - 2/\rho^n_k \tag{6}$$

322

where ρ^n_k is the cell Reynolds number

$$\rho^n_k = \frac{\Delta x}{\varepsilon} \left(\frac{c^n_{k+1/2} + c^n_{k-1/2}}{2} \right) \tag{7}$$

and

$$c^n_j := f'(U^n_j) \tag{8}$$

As previously noted, the LSE method will give a pointwise exact steady state solution of (1) when c^n_j is a constant. This or similar schemes have been used by several investigators [3,9,10,11] for steady singularly-perturbed problems and herein we try to apply it to transient problems.

We first consider a linear stability analysis of the difference scheme (2) by letting $f(u) = cu$ where c is a constant. We also let ρ and z denote the constant values of ρ^n_k and z^n_k, respectively, α denote the Courant number

$$\alpha = c\Delta t/\Delta x \tag{9}$$

and β denote the dissipation parameter

$$\beta = \alpha(z + 2/\rho) \tag{10}$$

In this case, equation (2) can be written as

$$U^{n+1}_j = U^n_j - \frac{1}{2}\alpha(U^n_{j+1} - U^n_{j-1}) + \frac{1}{2}\beta(U^n_{j+1} - 2U^n_j + U^n_{j-1}) \tag{11}$$

Several popular difference schemes have the form of (11) for different values of β (or z) and some of these are listed in Table 1. All of these schemes are first order accurate in time, except the Lax-Wendroff scheme which is second order.

A von Neumann analysis (cf. Richtmyer and Morton [14]) shows that equation (11) is stable in the region $\alpha^2 \leq \beta$, $0 \leq \beta \leq 1$. This region is shown shaded for $\alpha > 0$ in Figure 1. Curves corresponding to the methods in Table 1 are also shown. We see that the LSE method slightly improves upon the stability and accuracy properties of upwind differencing and that centered differencing and the Lax-Friedrichs scheme are outside of the stability region for most values of α and β.

Example 1: We compare the methods in Table 1 on the constant coefficient initial-boundary value problem

$$u_t + u_x = \varepsilon u_{xx} \quad , \quad t > 0 \quad , \quad 0 < x < 1$$

$$u(x,0) = 0 \quad , \quad 0 < x < 1$$

$$u(0,t) = 1 \quad , \quad u(1,t) = 0 \tag{12}$$

The exact solution of this problem features a shock layer that moves from $x = 0$ to $x = 1$ with unit speed and then approaches the steady state solution

$$u(x,t) = \frac{1 - e^{-(1-x)/\epsilon}}{1 - e^{-1/\epsilon}} \qquad (13)$$

as $t \to \infty$.

The maximum error at steady state

$$\max_j |u(j\Delta x, n\Delta t) - U^n_j| \quad , \quad n \to \infty \qquad (14)$$

computed by the Lax-Wendroff, upwind, LSE, and Lax-Friedrichs schemes are shown in Table 2 for $\Delta x = 1/20$, $\rho = 6$, $\alpha = 0.375$, 0.75 and $\Delta x = 1/20$, $\rho = 500$, $\alpha = 0.475$, 0.95*.

The centered difference scheme produced overflows for both $\rho = 6$ and 500, so no results could be listed for it. The Lax-Friedrichs scheme only overflowed for $\rho = 6$. The LSE scheme gives the exact steady state solution for this example and the small errors reported in Table 2 are due to the combined effects of roundoff and our failure to reach the exact steady state.

These results are very encouraging; however, when we examine the LSE solution during the transient phase of the solution the situation is quite different (cf. Figure 2). The LSE solution is overly diffusive and the computed solution is not much better than that obtained by upwind differencing. This observation was also noted by Gresho and Lee [7] about methods that are similar to the LSE method.

III. THE LINEARIZED TRANSIENT EXPONENTIAL (LTE) METHOD. We would like to improve upon the results of the LSE method for transient problems and, thus, we consider developing a method having the form of (2) that gives a pointwise exact solution of (1) when $f(u) = cu$ and c is a constant. Since we are primarily interested in obtaining good resolution near shock and boundary layers we choose to solve (1) subject to Riemann initial data. To be specific, for each j and n we compute U^{n+1}_j as the exact solution of the initial value problem.

$$u_t + cu_x = \epsilon u_{xx} \quad , \quad t > n\Delta t \quad , \quad |x| < \infty \quad ,$$

$$u(x, n\Delta t) = \begin{cases} u_L & , \quad x < (j-1+\delta)\Delta x \\ u_R & , \quad x > (j-1+\delta)\Delta x \end{cases} \qquad (15)$$

where u_L and u_R are constants, δ is a constant on $[0,1)$ to be determined, and we assume that $c > 0$. We shall present results for $c < 0$ later.

The exact solution of (15) at $x = j\Delta x$ and $t = (n+1)\Delta t$ is

$$u(j\Delta x, n\Delta t) = u_R - \frac{1}{2}(u_R - u_L)\,\mathrm{erfc}\,\frac{1}{2}\sqrt{\frac{\rho}{\alpha}}\,(1-\delta-\alpha) \qquad (16)$$

---

*All numerical results were obtained in double precision on an IBM 4341 computer at the Benet Weapons Laboratory.

whereas the solution of equation (2) at this point is

$$U^{n+1}{}_j = u_R - \frac{1}{2} \alpha(1 + z^n{}_{j-1/2} + 2/\rho)(u_R - u_L) \tag{17}$$

The two solutions will be the same provided that

$$z^n{}_{j-1/2} = -1 - \frac{2}{\rho} + \frac{1}{\alpha} \, \text{erfc} \, \frac{1}{2} \sqrt{\frac{\rho}{\alpha}} \, (1-\delta-\alpha) \tag{18}$$

In this paper, we simplify (18) by assuming that $\rho/\alpha \gg 1$ and approximating the complementary error function by $2H(\delta+\alpha-1)$, where H is a Heaviside function. Also, since $z^n{}_{j+1/2}$ is not determined by this procedure, we specify it according to equation (6) with coth $\rho/2$ approximated by unity. Thus, we have

$$z^n{}_{j-1/2} = 1 - \frac{2}{\rho} + 2[\frac{1}{\alpha} H(\delta+\alpha-1) - 1] \quad , \quad z^n{}_{j+1/2} = 1 - \frac{2}{\rho} \tag{19a}$$

When $c < 0$ we choose

$$z^n{}_{j-1/2} = -1 - \frac{2}{\rho} \quad , \quad z^n{}_{j+1/2} = -1 - \frac{2}{\rho} + 2[\frac{1}{\alpha} H(\delta-\alpha-1) + 1] \tag{19b}$$

It remains to specify δ. One possibility is to choose it to be a random variable uniformly distributed on $[0,1)$, in which case equations (2) and (19) would yield a linearized random choice scheme [1,2]. A second possibility is to always select $\delta = 1/2$ which would give a Godunov [6] type scheme. The third possibility is similar to a scheme suggested by Roe [15] and is the one that we have been using. We begin by selecting $\delta = 0$; however, any value of $\delta \epsilon [0,1)$ will do. After each time step we add the magnitude of the Courant number $|\alpha|$ to δ and obtain a new value of δ. We continue this process until δ exceeds unity, in which case we replace δ by $\delta-1$. The procedure has to be modified slightly when α is not a constant and we shall indicate how this is done shortly; however, if α is a rational number of the form p/q and $\varepsilon = 0$ then equations (2) and (19) have the advantage of giving the pointwise exact solution of the linearized Riemann problem every q time steps.

We refer to the scheme consisting of equations (2) and (19) and the above choice of δ as the linearized transient exponential (LTE) method and we begin by applying it to the following linear Riemann problem.

Example 2:

$$u_t + u_x = \varepsilon u_{xx} \quad , \quad t > 0 \quad , \quad |x| < \infty \tag{20}$$

$$u(x,0) = \begin{cases} 1 & , \quad x < 0 \\ 0 & , \quad x > 0 \end{cases}$$

In this example, the initial discontinuity becomes a shock layer which travels with unit speed in the positive x direction while widening as t increases.

We have computed the solution of this problem by the LTE method with $\Delta x = 1/20$, $\rho = 500$, and $\alpha = 0.75$, 0.95. For this value of ρ and for times less than order $1/\varepsilon$, the shock layer is well contained within one mesh subinterval

and we have plotted the locations of the ends of this subinterval along with the exact position of the center of the shock layer in Figures 3 and 4 for $\alpha = 0.75$ and 0.95, respectively. We see that the shock layer is tracked exactly on the average and that we obtain the pointwise exact solution every 4 and 20 time steps when $\alpha = 0.75$ and 0.95, respectively.

For nonlinear scalar problems we still use equations (2) and (19); however, we now use local values of the Courant and Reynolds numbers based on a local shock speed. Thus, on each subinterval we calculate

$$\alpha^n_{j-1/2} = s^n_{j-1/2} \Delta t / \Delta x \quad , \quad \rho^n_{j-1/2} = s^n_{j-1/2} \Delta x / \varepsilon \qquad (21a,b)$$

where $s^n_{j-1/2}$ is a local shock speed which we choose as

$$s^n_{j-1/2} = (f^n_j - f^n_{j-1})/(U^n_j - U^n_{j-1}) \qquad (22)$$

Equations (21) are used in equations (19) to calculate $z^n_{j-1/2}$ and we proceed as in the linear case. After each time step we add

$$(\min_j |\alpha^n_{j-1/2}| + \max_j |\alpha^n_{j-1/2}|)/2$$

to δ and obtain a new value of δ. Once δ exceeds unity we again replace it by $\delta - 1$.

Equation (22) gives the exact shock speed whenever U^n_j and U^n_{j-1} satisfy the Rankine-Hugoniot jump conditions (cf. e.g. Whitham [18] and equation (27)). An alternate definition of $s^n_{j-1/2}$ that is easier to use computationally, but only gives the correct shock speed when f is at most a quadratic function of u is

$$s^n_{j-1/2} = \frac{1}{2} [f'(U^n_j) + f'(U^n_{j-1})] \quad . \qquad (23)$$

<u>Example 3</u>: We consider a Riemann problem for Burgers' equation

$$u_t + \frac{1}{2} (u^2)_x = \varepsilon u_{xx} \quad , \quad t > 0 \quad , \quad |x| < \infty \quad ,$$

$$u(x,0) = \begin{cases} u_L & , \quad x < 0 \\ u_R & , \quad x > 0 \end{cases} \qquad (24)$$

The exact solution of this problem can be obtained by the Hopf-Cole transformation and is given in, e.g., Whitham [18]. Herein, it suffices to give asymptotic formulas which are valid for $t/\varepsilon \gg 1$. Thus, when $u_L > u_R$ we have

$$u(x,t) \sim \frac{1}{2}(u_L + u_R) - \frac{1}{2}(u_L - u_R) \tanh \left(\frac{u_L - u_R}{4\varepsilon}\right)(x - St) \qquad (25a)$$

where

$$S = \frac{1}{2} (u_L + u_R) \qquad (25b)$$

326

and when $u_L < u_R$ we have

$$u(x,t) \sim \begin{cases} u_L & , \quad x/t < u_L \\ x/t & , \quad u_L < x/t < u_R \\ u_R & , \quad u_R < x/t \end{cases} \qquad (26)$$

Equation (25) represents a shock layer moving in the positive x direction with speed S and equation (26) represents an expansion fan.

We calculated solutions with $\varepsilon = 10^{-4}$, $\Delta x = 1/20$, and $\lambda = 0.95$ by the LSE and LTE methods for a shock problem with $u_L = 1$, $u_R = 0$ and an expansion problem with $u_L = -1$, $u_R = -1/2$. In Figure 5 we compare the exact shock position with those calculated by the LSE and LTE methods. We define the shock position for the numerical methods as the point where the solution is $(u_L - u_R)/2$ when linear interpolation is used to compute solution values between mesh points. In Figures 6a and 6b we plot the exact LSE and LTE solutions at $t = 0.95$ for the shock problem and at $t = 0.38$ for the expansion problem, respectively. The LTE method again confines the shock layer to one subinterval and gives the correct shock speed and position on the average. The LSE method is overly diffusive and is giving the correct shock speed, but the position is wrong by about $\Delta x/2$.

The situation is quite different for the expansion fan. The LSE method is still overly diffusive; however, the LTE method is representing the expansion fan as a shock. This phenomenon also occurs with Roe's scheme for hyperbolic systems (cf. Roe [16] and van Leer [17]) and it must be remedied if these schemes are to be useful on expansion problems.

IV. SYSTEMS OF EQUATIONS. In principle the LTE method consisting of equation (2), (19), and (21) may be directly extended to vector systems of the form (1) once we have selected a shock speed $s^n_{j-1/2}$. When $\varepsilon = 0$ the exact shock speed S is determined by the Rankine-Hugoniot condition

$$(u_R - u_L)S = f(u_R) - f(u_L) \qquad (27)$$

where u_R and u_L are the values of $u(x,t)$ on opposite sides of the shock. When ε is nonzero but small we would like the numerical shock speed $s^n_{j-1/2} = S$ whenever the numerical solution U^n_{j-1}, U^n_j satisfies (29).

In a recent paper Harten and Lax [8] suggested selecting

$$s^n_{j-1/2} = \ell(f^n_j - f^n_{j-1})/\ell(U^n_j - U^n_{j-1}) \qquad (28a)$$

where $\ell(w)$ is the linear functional

$$\ell(w) = [V'(U^n_j) - V'(U^n_{j-1})]w \qquad (28b)$$

and $V(u)$ is an entropy function. They show that this choice gives unique physically admissible numerical solutions of their random choice finite difference methods.

Roe [16] suggests an alternate method of calculating $s^n_{j-1/2}$ that is based on the eigenvalue of a matrix approximating the Jacobian $\partial f/\partial u$.

We have not tried either of these alternatives, but instead use the very simple prescription

$$s^n_{j-1/2} = \frac{(\underline{U}^n_j - \underline{U}^n_{j-1})^T(\underline{f}^n_j - \underline{f}^n_{j-1})}{(\underline{U}^n_j - \underline{U}^n_{j-1})^T(\underline{U}^n_j - \underline{U}^n_{j-1})} \qquad (29)$$

Equation (29) gives the exact shock speed whenever U^n_j and U^n_{j-1} satisfy the Rankine–Hugoniot conditions (27), but it may fail to give a physically acceptable solution.

Example 4: We solve the following impact problem for the linear wave equation

$$u_{1t} - u_{2x} = 0 \quad , \quad u_{2t} - u_{1x} = 0 \quad , \quad t > 0 \quad , \quad |x| < \infty$$

$$u_1(x,0) = 0 \quad , \quad u_2(x,0) = \begin{cases} 1 & , \ x < 0 \\ -1 & , \ x > 0 \end{cases} \qquad (30)$$

Here $u_1(x,t)$ and $u_2(x,t)$ represent the strain and velocity in two elastic rods that impact each other with unit speeds at $x = t = 0$.

We calculated the solution of this problem by the LSE and LTE methods and by the EPIC-2 code [12]. The latter is a two-dimensional finite element code for elastic-plastic impact problems. Our results for u_1 at $t = 0.95$ obtained with $\Delta x = 1/10$ and $\lambda = 0.95$ are shown in Figure 7. The LSE and LTE solutions are typical of our results on previous examples. The LTE method again calculates the correct shock position and speed with no diffusion or oscillations. The LSE solution is overly diffusive, although less so than the EPIC-2 solution.

V. DISCUSSION OF RESULTS. The LTE method appears to be a very promising scheme for shock problems. It is simpler to apply than methods based on the exact solution of Riemann problems [1,2] and does not suffer from the effects of artificial diffusion or spurious oscillations. However, our results are very preliminary and there are still many questions to be answered and many problems to be overcome. The performance of the LTE method in regions of expansion must be improved. van Leer [17] has suggested incorporating expansion fans in the approximate Riemann solution of Roe's method [16], and this approach should work for our LTE method as well. Another possibility is to base the difference scheme (2) on the exact solution of (1) when f is a quadratic function of u. The solution of this problem does contain expansion waves; however, extending this method to systems of equations would be considerably more difficult than extending the LTE method.

Both the LSE and LTE methods are first order accurate in time when the solution is smooth. van Leer [17] has developed a two-step procedure that can be used to extend these methods to second order accuracy and we plan to experiment with it shortly.

There is also the possibility of developing implicit exponentially fitted and weighted schemes, which would be desirable when approaching a steady state and which may improve the phase characteristics of the LSE method (cf. Gresho and Lee [7]).

Finally, we note that the LSE and LTE methods can be extended to higher dimensions by using operator splitting techniques. However, this may introduce some numerical diffusion.

REFERENCES

1. A. J. Chorin, "Random Choice Solution of Hyperbolic Systems," *J. Comput. Phys.*, 22, 517-533 (1976).

2. A. J. Chorin, "Random Choice Methods With Applications to Reacting Gas Flow," *J. Comput. Phys.*, 25, 253-272 (1977).

3. I. Christie, D. F. Griffiths, A. R. Mitchell, and O. C. Zienkiewicz, "Finite Element Methods for Second Order Differential Equations With Significant First Derivatives," *Int. J. Num. Meth. Engng.*, 10, 1389-1396 (1976).

4. B. Engquist and S. Osher, "Stable and Entropy Satisfying Approximations for Transonic Flow Calculations," *Math. Comp.*, 34, 45-75 (1980).

5. J. E. Flaherty and W. Mathon, "Collocation With Polynomial and Tension Splines for Singularly Perturbed Boundary Value Problems," *SIAM J. Sci. Stat. Comput.*, 1, 260-289 (1980).

6. S. K. Godunov, "A Finite Difference Method For the Numerical Computation and Discontinuous Solutions of the Equations of Fluid Dynamics," *Mat. Sb.*, 47, 271 (1959).

7. P. Gresho and R. L. Lee, "Don't Suppress the Wiggles - They're Telling You Something," in T. J. R. Hughes, Ed., *Finite Element Methods for Convection Dominated Flows*, AMD - Vol. 34, ASME, New York, 37-62, 1979.

8. A. Harten and P. D. Lax, "A Random Choice Finite Difference Scheme for Hyperbolic Conservation Laws," *SIAM J. Numer. Anal.*, 18, 289-315 (1981).

9. P. W. Hemker, "A Numerical Study of Stiff Two-Point Boundary Problems," Ph.D. dissertation, Mathematisch Centrum, Amsterdam, 1977.

10. T. J. R. Hughes, "A Simple Scheme for Developing Upwind Finite Elements," *Int. J. Num. Meth. Engng.*, 12, 1359-1365 (1978).

11. A. M. Il'in, "Differencing Scheme For A Differential Equation With a Small Parameter Affecting the Highest Derivative," *Math. Notes Acad. Sci.*, USSR, 6, 569-602 (1969).

12. G. R. Johnson, "EPIC-2, A Computer Program For Elastic-Plastic Impact Computations in 2 Dimensions Plus Spin," Rep. AD A058786, U.S. Army Armament Research and Development Command, Ballistic Research Laboratory, Aberdeen Proving Ground, 1977.

13. S. Osher and F. Solomon, "Upwind Difference Schemes for Hyperbolic Systems of Conservation Laws," to appear in Math. Comp., 1981.

14. R. D. Richtmyer and K. W. Morton, Difference Methods For Initial Value Problems, Second Edition, Wiley-Interscience, New York, 1967.

15. P. L. Roe, "The Use of Riemann Problem in Finite-Difference Schemes," Proc. Seventh Int. Conf. on Numer. Meths. in Fluid Dynamics, Springer-Verlag, to appear, 1981.

16. P. L. Roe, "Approximate Riemann Solvers, Parameter Vectors, and Difference Schemes," to appear in J. Comput. Phys., 1981.

17. B. van Leer, "On the Relation Between the Upwind-Differencing Schemes of Godunov, Engquist-Osher and Roe," Rep. 81-11, ICASE, NASA Langley Research Center, Hampton, 1981.

18. G. B. Whitham, Linear and Nonlinear Waves, Wiley-Interscience, New York, 1974.

TABLE 1. VALUES OF z AND β FOR DIFFERENCE METHODS
THAT HAVE THE FORM OF EQUATION (11)

Method	z	$\beta = \alpha(z + 2/\rho)$
Centered	0	$2\alpha/\rho$
Lax-Wendroff	α	$\alpha^2 + 2\alpha/\rho$
Upwind	$\text{sgn}(\rho)$	$\alpha(\text{sgn}(\rho) + 2/\rho)$
Linearized steady exponential (LSE)	$\coth(\rho/2) - 2/\rho$	$\alpha\coth(\rho/2)$
Lax-Friedrichs	$1/\alpha$	$1 + 2\alpha/\rho$

TABLE 2. MAXIMUM ERROR AT STEADY STATE FOR EXAMPLE 1.
AN * INDICATES THAT THE COMPUTED SOLUTION
PRODUCED AN OVERFLOW.

Method	$\rho = 6$		$\rho = 500$	
	$\alpha = 0.375$	0.75	$\alpha = 0.475$	0.95
Lax-Wendroff	2.9 E-1	1.6 E-3	3.5 E-1	2.3 E-2
Upwind	2.0 E-2	2.0 E-2	2.0 E-3	2.0 E-3
Linearized steady exponential (LSE)	2.5 E-14	2.5 E-14	8.5 E-8	2.1 E-12
Lax-Friedrichs	*	*	3.6 E-1	2.8 E-2
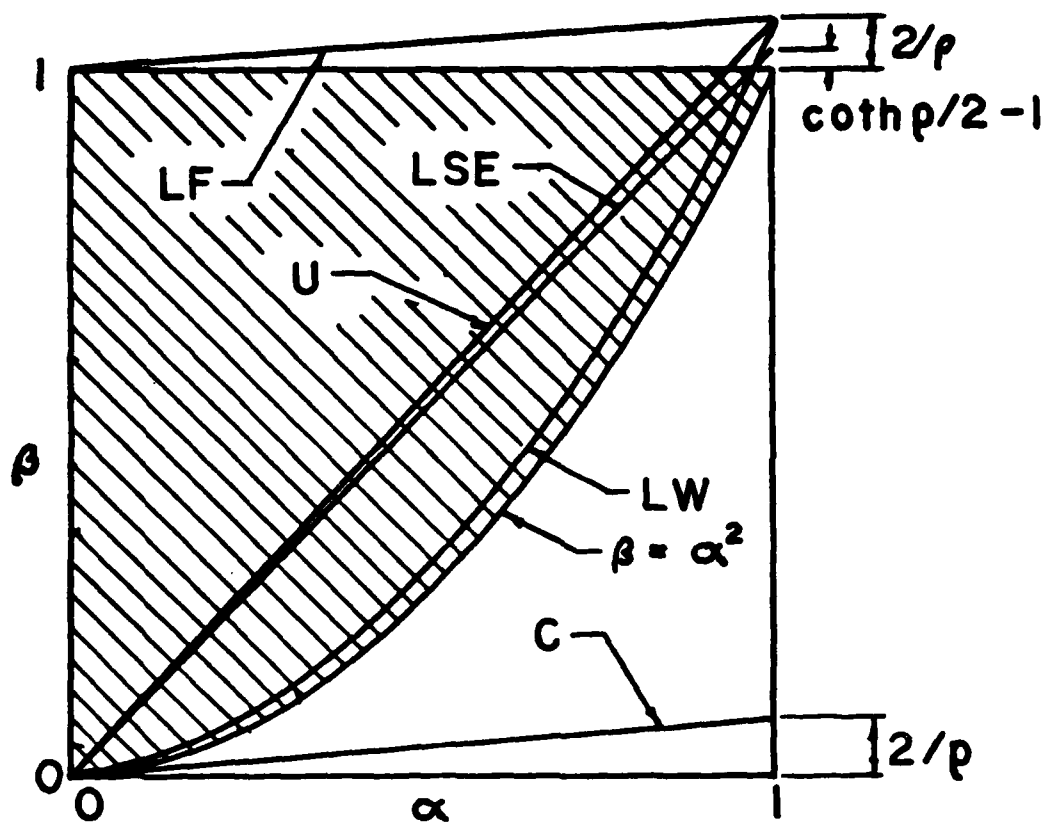
Figure 1. Region of linear stability for equation (11) and curves of β vs. α for the centered difference (C), Lax-Wendroff (LW), upwind difference (U), linearized steady exponential (LSE), and Lax-Friedrichs (LF) methods.
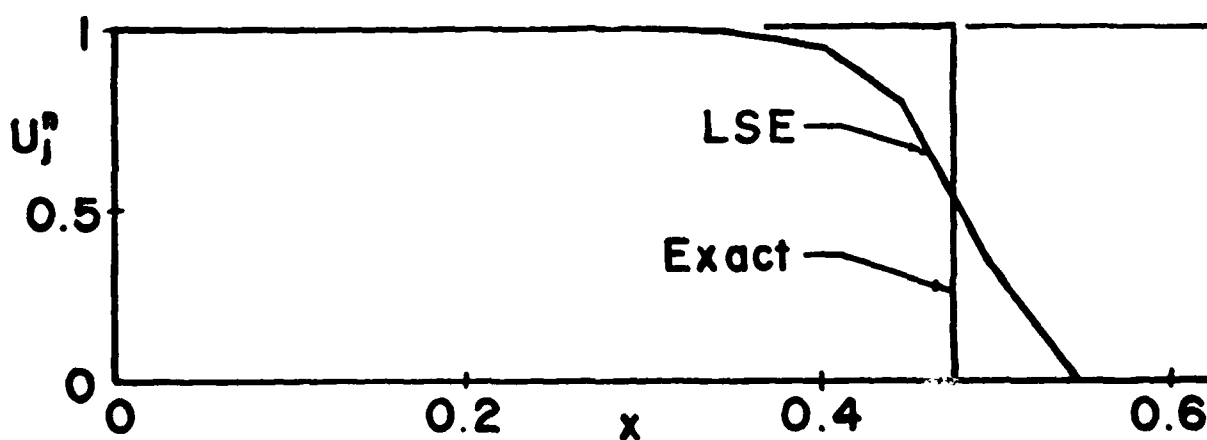
Figure 2. Comparison of exact and LSE solutions of Example 1 at $t = 0.475$. Calculations were performed with $\Delta x = 1/20$, $\alpha = 0.95$, and $\rho = 500$.
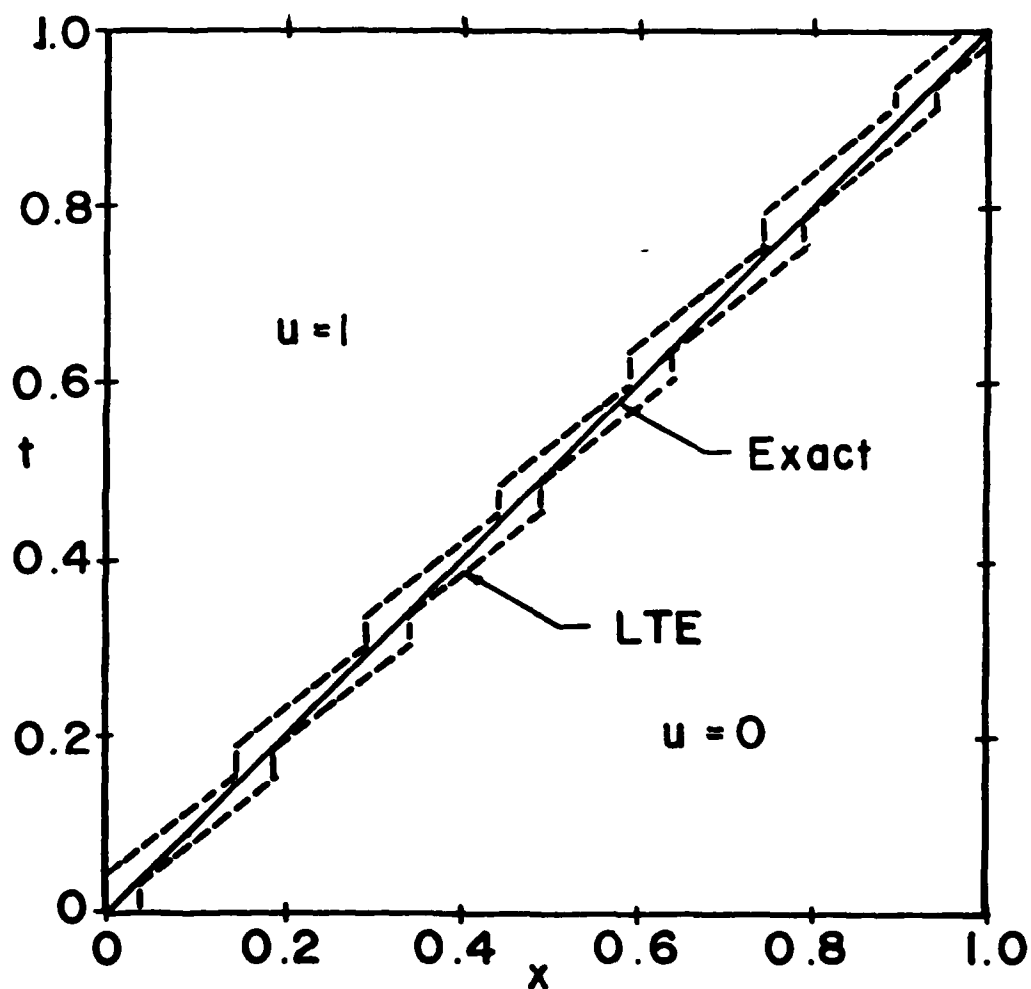
Figure 3. Exact shock layer position and the location of the subinterval
containing the shock layer calculated by the LTE method for Example
2 with $\Delta x = 1/20$, $\alpha = 0.75$, and $\rho = 500$.
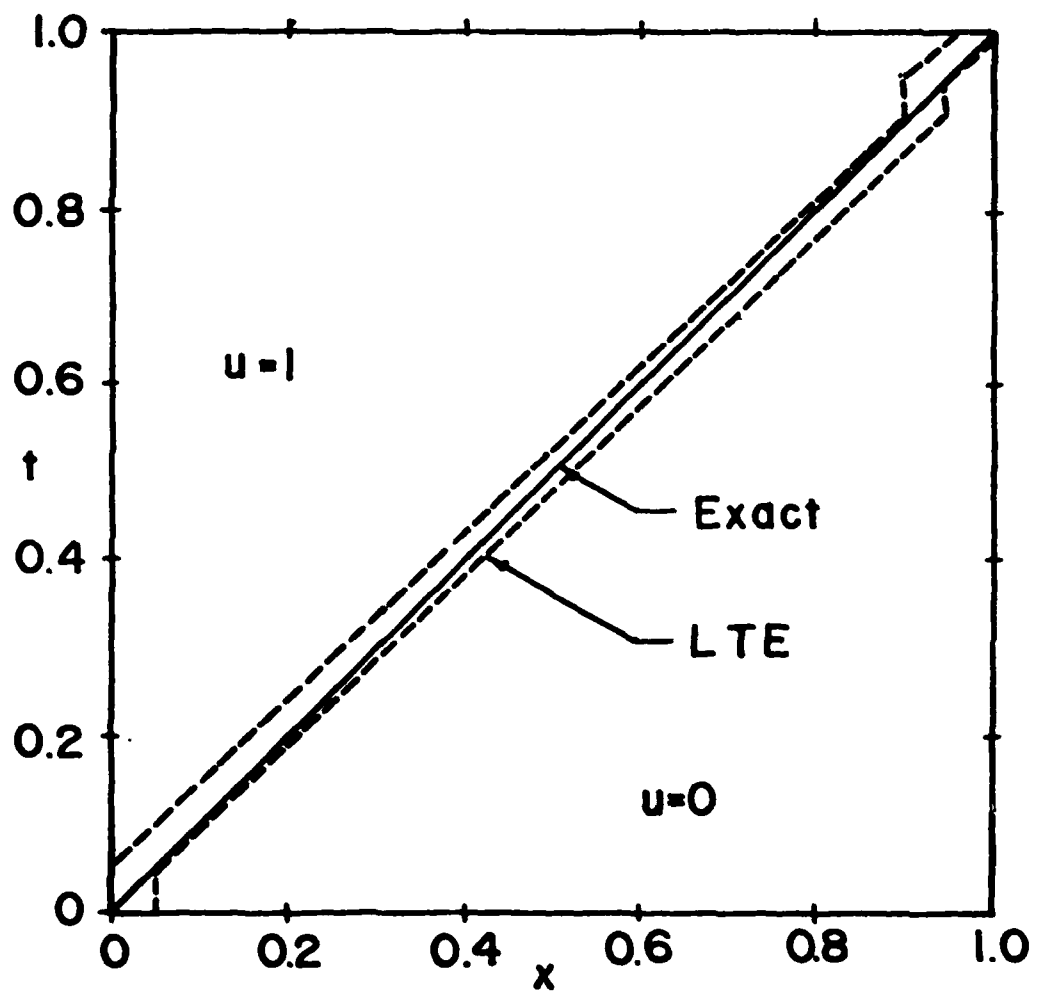
Figure 4. Exact shock layer position and the location of the subinterval containing the shock layer calculated by the LTE method for Example 2 with $\Delta x = 1/20$, $\alpha = 0.95$, and $\rho = 500$.
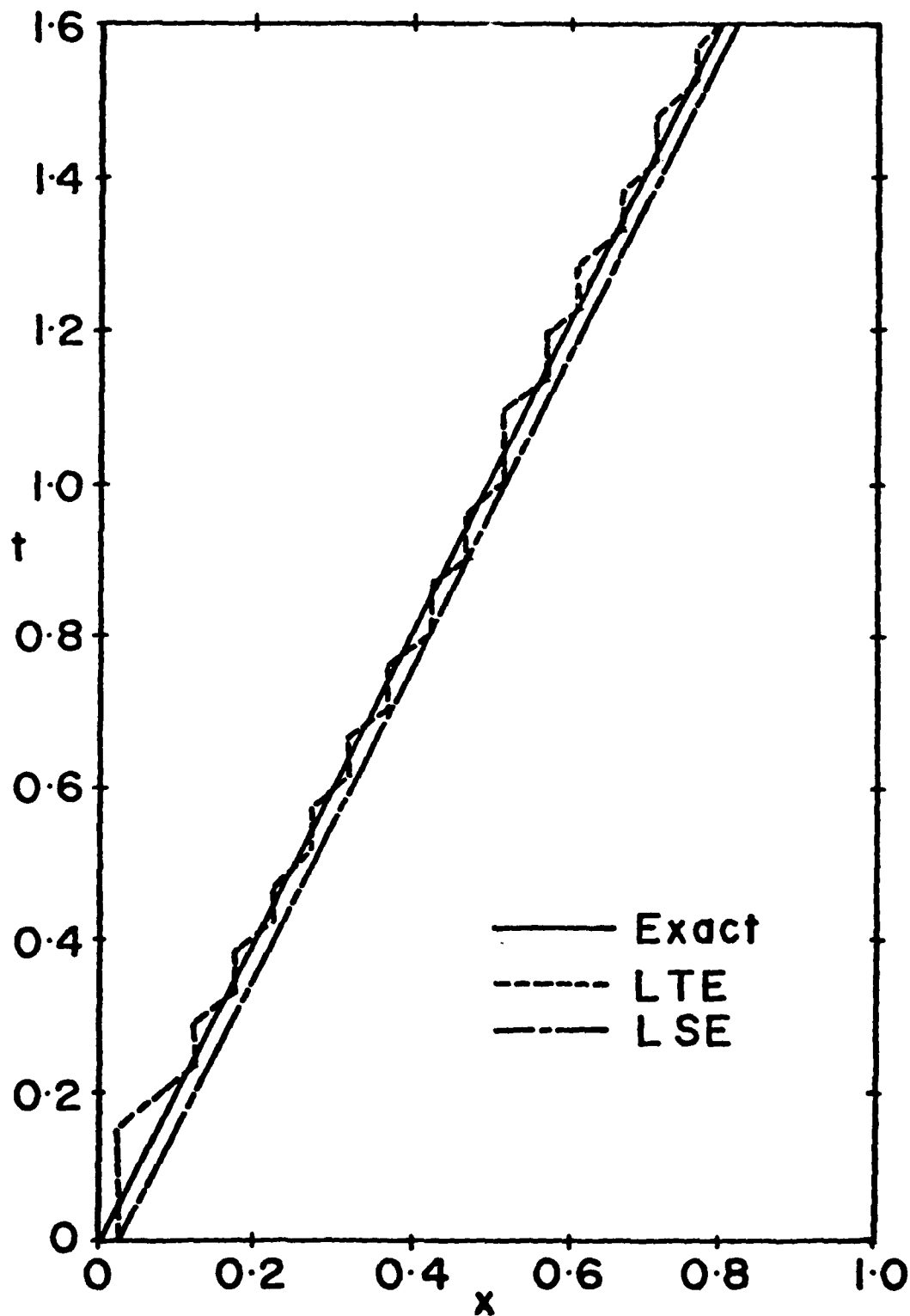
Figure 5. Exact shock layer position and those calculated by the LSE and LTE methods for Example 3 with $\epsilon = 10^{-4}$, $\Delta x = 1/20$, and $\alpha = 0.95$.
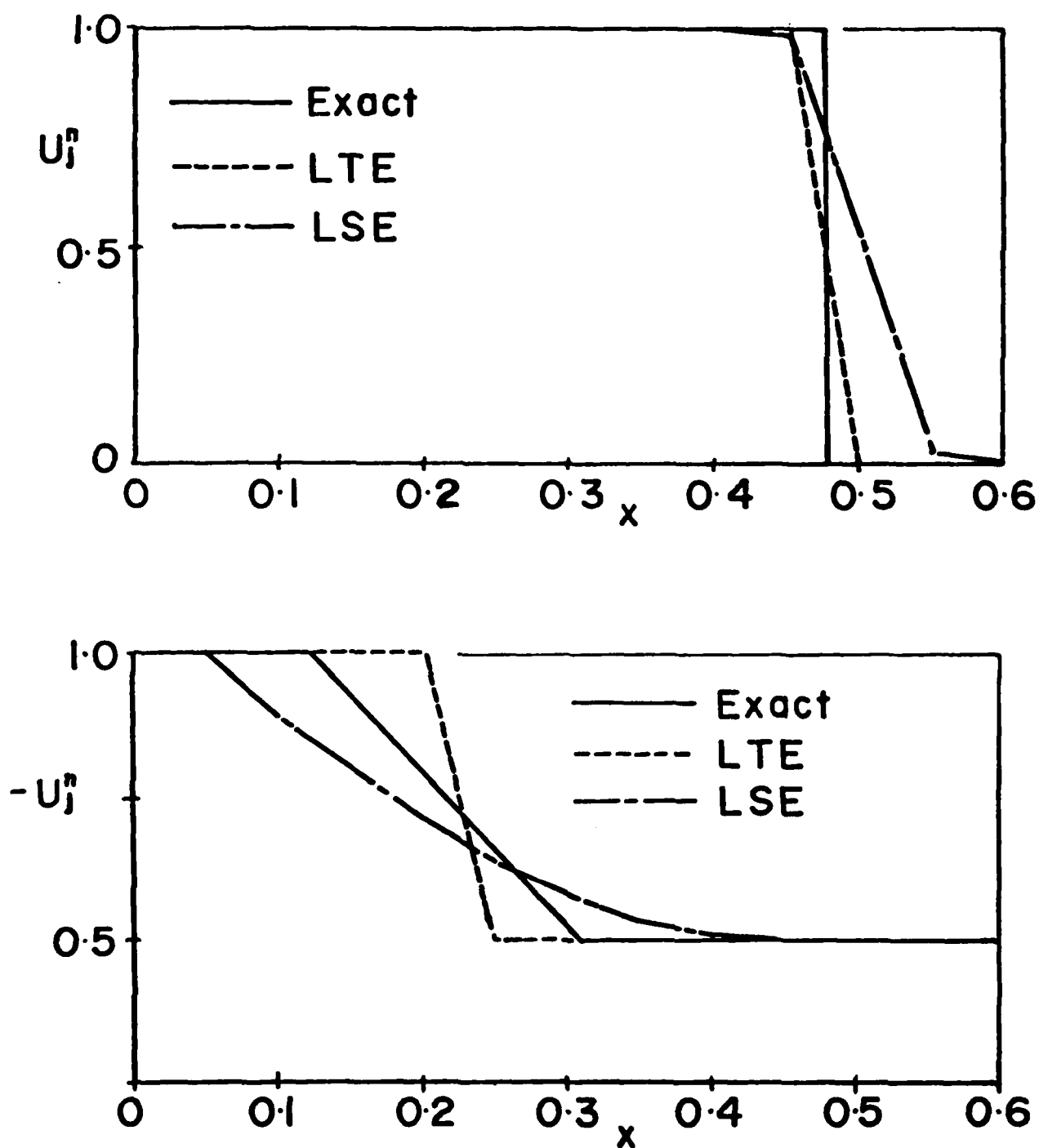
Figure 6. Exact, LSE, and LTE solutions of Example 3 with $\varepsilon = 10^{-4}$, $\Delta x = 1/20$, and $\alpha = 0.95$. In (a) we show the solution at $t = 0.95$ of a shock problem with $u_L = 1$, $u_R = 0$, and in (b) we show the solution at $t = 0.38$ of an expansion problem with $u_L = -1$, $u_R = -1/2$.
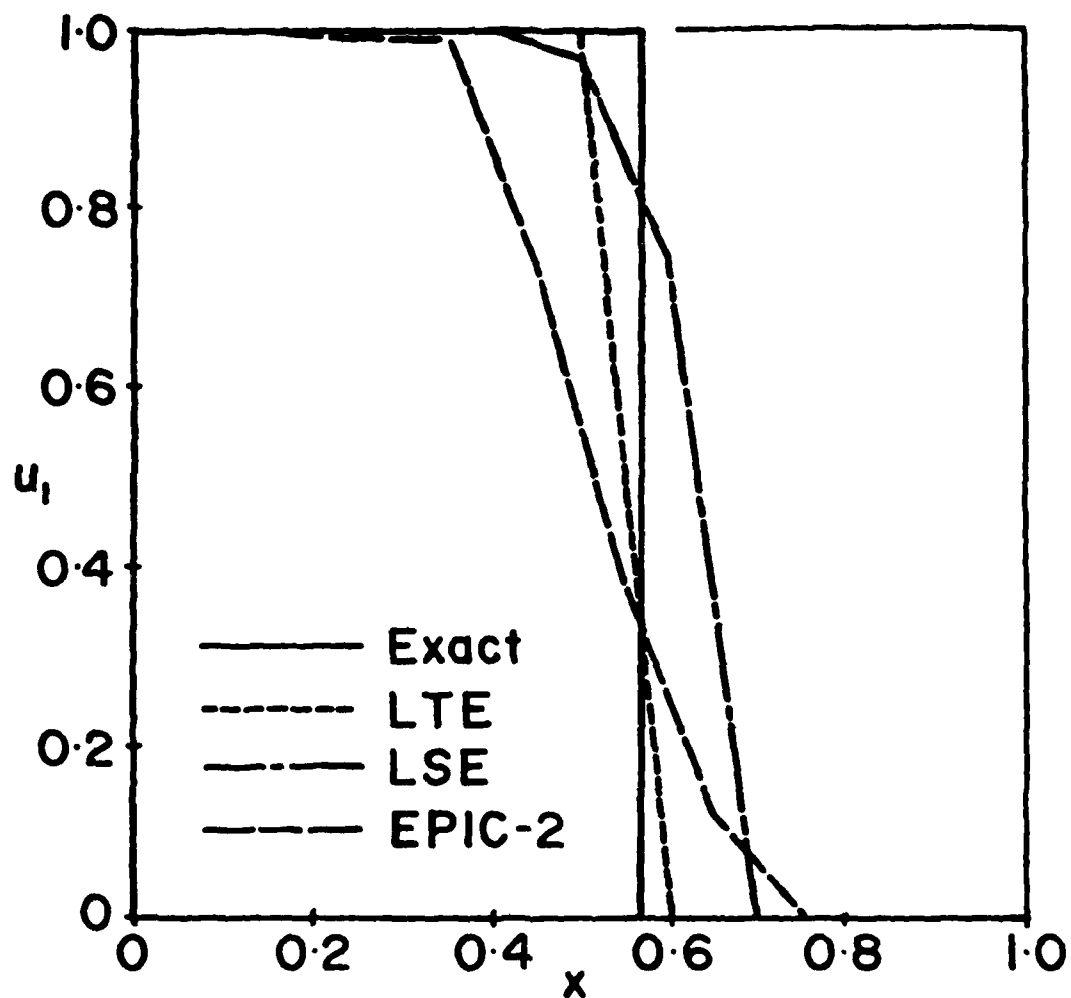
Figure 7. Comparison of exact, LSE, LTE, and EPIC-2 solutions for u_1 of Example 4 at $t = 0.95$ with $\Delta x = 0.1$ and $\Delta t = 0.095$.

NUMERICAL STUDY OF A
CONFINED PREMIXED LAMINAR FLAME:
OSCILLATORY PROPAGATION AND WALL QUENCHING

DOUGLAS E. KOOKER

U.S. Army Ballistic Research Laboratory, ARRADCOM
Aberdeen Proving Ground, Maryland 21005

ABSTRACT - Numerical predictions are shown for constant-volume laminar flame
propagation in ozone/oxygen mixtures. Flame-generated pressure
disturbances lead to pulsating flame velocities. The concept of
burning velocity is discussed; a conservative estimate is shown
to be a factor of two greater than the steady-state value for the
example case considered. Flame quenching at an adiabatic boundary
involves oscillations in internal structure. Quenching at a cold
boundary is dominated by heat loss which suppresses the flame
velocity pulsations and eventually forces the flame to retreat.

The behavior of deflagration waves in premixed gases has been of interest
since the classic work of Mallard and LeChatelier (1). Current numerical
solutions, e.g. Tsatsaronis (2), for one-dimensional, constant-pressure
laminar flame propagation in an infinite medium are limited primarily by un-
known (or uncertain) decomposition mechanisms and chemical rates for the
real gas mixture in question. However, many combustion applications involve
transient processes in complex confinement. The influence of confinement
can be substantial as witnessed by reactive mixtures which exhibit a well-
behaved burner flame, but transit to detonation when suitably confined. In
addition, recent constraints on allowable exhaust emissions and fuel efficiency
of intermittent-burning internal combustion engines have rekindled interest
in theoretical prediction of laminar flame propagation and interaction
with boundaries.

Modeling of one-dimensional flame/end-wall interactions encompasses both
analytical and numerical approaches with assumptions of varying complexity.
Carrier et.al. (3,4) analytically solve a Stefan problem for a unity Lewis
number, isobaric, flame sheet interacting with an adiabatic wall. Sirignano
(5) examines a non-isobaric adiabatic wall case. Kurkov and Mirsky (6)
combine analytical methods with numerical integration to study an isobaric
cold-wall problem. Bush et.al. (7) use numerical integration of an isobaric
Shvab-Zeldovich formulation for an extensive investigation of boundary condi-
tions between cold wall and adiabatic. Carrier et.al. (8) propose a novel
approach to non-isobaric flame problems, but with the pressure field assumed
spatially uniform. Westbrook et.al. (9) carefully examine the influence
of complex decomposition mechanisms for methanol-air and methane-air in cold
wall flame quenching, using a numerical model without restrictions on the
pressure field. However, the computational examples are based on a chamber
whose open end is held at constant pressure.

The present study focuses on constant-volume flame propagation, eliminating
many common assumptions. Flame-generated pressure disturbances which are
trapped by the confining boundaries will be shown to influence flame behavior.

339

With reference to Fig. 1, a time-dependent external heat flux (10) at z=0 ignites the quiescent mixture and is then set to zero. The resulting flame is terminated at the opposing boundary (z=1) which may be held adiabatic or isothermal. No steady-state exists, other than the trivial all-burned condition.

ANALYSIS

The current investigation, based on (10) with modest improvements, looks at one-dimensional transient laminar flame spreading in a real gas mixture of ozone and oxygen whose simple decomposition mechanism and chemical rates are well-established. Reaction rates and transport properties are those of (11), and temperature-dependent specific heats are from (12). No constraints are imposed upon the magnitude or variability of the mixture Lewis or Prandtl numbers. Radiation, gravity, bulk viscosity, the Dufour effect, the Soret effect, and diffusion due to pressure gradients are neglected. Ignition and flame propagation are predicted by numerical solution of the one-dimensional, compressible Navier-Stokes Equations in strong conservation form.

Global Continuity

$$\rho_t + (\rho u)_z = 0 \tag{1}$$

Momentum

$$(\rho u)_t + (\rho u^2 + p)_z = (\mu_R u_z)_z \tag{2}$$

Energy

$$E_t + [(E + p)u]_z = \{k_g T_z + \mu_R u u_z - \rho \sum_{i=1}^{N} Y_i h_i V_i\}_z \tag{3}$$

Species Continuity

$$(\rho_i)_t + [\rho_i(u + V_i)]_z = \omega^i, \quad i=1, \ldots, N-1 \tag{4}$$

State

$$p = \rho R T \quad ; \quad R = R_o \sum_{i=1}^{N} Y_i/M_i \tag{5a}$$

$$h = \sum_{i=1}^{N} Y_i h_i \quad ; \quad h_i = h_i^o + \int_{T^o}^{T} c_{p_i} dT \tag{5b}$$

where $\quad \rho_i = Y_i \rho \, , \, E = \rho h - p + u^2/2$

and $\quad \mu_R = (4/3)\mu/Re$

340

Diffusion velocities, V_i, are functions of the instantaneous mixture composition, local mass fraction gradients, and the binary diffusion coefficients between all pairs of species present. Numerical solution of Eqs. (1-3) is based on a linearized block implicit scheme after solving the Eq. (4) system with a stiff integrator routine (13). Mesh Reynolds numbers are held below two, and no explicit artificial viscosity is added to stabilize the computation. Time steps are constrained by a unity Courant number to preserve small-amplitude wave motion.

RESULTS

Two example cases are based on 25 mole % O_3 in O_2. Initial conditions assume $p \equiv 1$ atm, $u \equiv 0$, $T \equiv 298^\circ K$, chamber length of 0.5 mm and 100 computational cells. Sequential numbers listed on the figures are non-dimensional times from the onset of external heating, which is terminated at $t=12.8$. Figure 2a illustrates the chamber temperature distribution history for an adiabatic wall at $z=1$, and Fig. 2c for a cold wall, $T_w=298$ K. The continuously increasing temperatures downstream of the flame are a result of stagnating the burned gas velocity at $z=o$ and recombination of the radical intermediate, 0, atomic oxygen. A reservoir of O (4 orders of magnitude above equilibrium) is left behind the fast moving flame (Fig. 2b), i.e., flame chemistry is far from equilibrium. Mitchell et.al. (14) discuss exactly this behavior for both premixed and diffusion flames. As the flame advances, compression of the reactants results in an increasing temperature and density field which will accelerate the chemical production rates. As the flame approaches the adiabatic wall (Fig. 2a), the reactants trapped within approximately one-half the flame thickness from the boundary will burn in bulk, reaching a temperature in excess of the local isobaric flame temperature. Since the Lewis number, (thermal/mass diffusion) of the approach flow is greater than 1.2 (based on O_3/O_2 diffusion), this is consistent with the results of (7). As the flame approaches the cold wall (Fig. 2c) heat loss causes it to decelerate and eventually retreat (to be shown) leaving a small pocket of unburned O_3 ("fuel") which will slowly diffuse outward to complete the reaction. Similar behavior is described by Westbrook et.al. (9) and Bush et.al (7).

The velocity of the flame is of considerable interest in a transient problem, but must be preceded by a definition of flame location. No unique definition exists. The present study chose to track a constant value of temperature (850 K) in the high gradient region instead of the maximum reaction rate because of interpolation difficulties in locating the "peak". The resulting flame locus is shown in Fig. 3a. Fitting this data (8000 points) with a third order spline and analytically differentiating produces the flame velocity seen by an _inertial_ observer (Fig. 3b). The result is a pulsating laminar flame, with typical amplitude of 100 cm/sec. This amplitude can be a strong function of heat release in the flame as illustrated by Fig. 4 for a 30 mole % O_3 flame in an otherwise identical calculation. The slowly increasing frequency of the dominant oscillation is within two percent of the fundamental mode predicted by Jost's acoustic analysis (10).

Burning velocity, defined as the linear or fundamental rate of reactant consumption, is a trivial calculation for steady flame propagation into an infinite medium. However, in a transient problem where reactants undergo nonuniform motion, the concept of burning velocity becomes obscure (Here,

flame velocity is that seen by the inertial observer, whereas burning velocity is the fundamental rate). Consider the chamber velocity distributions during one-half cycle of flame oscillation (denoted by arrows in Fig. 4) shown in Fig. 5a, with the temperature distributions superposed (no scale given). A characteristic maximum velocity always appears upstream of the flame, at a location nearly coincident with the "foot" of the temperature distribution. Subtracting this maximum value from the inertial flame velocity provides a conservative estimate for transient burning velocity, i.e., a minimum value. Note that the numerical solution of Eqs. (1-5) is independent of any such definition.

Several observations can be made. The chamber pressure distributions in Fig. 5b during the half-cycle flame oscillation illustrate an obvious point: very small amplitude pressure disturbances can lead to large oscillations in flame velocity. The large initial values of flame velocity in Fig. 3b result from ignition and flame formation within the thermal wave created by the external heat source. The flame then, on average, appears to decelerate. However, the burning velocity (Fig. 3c denoted as velocity difference) shows the anticipated acceleration. These values can be compared to the steady laminar burning velocity (U_{ss}) which would exist at the local values of upstream pressure and temperature. Using identical kinetic rates and transport properties, the steady state analysis (15) predicts the results in Table I which are compared to the transient values (U_{tr}) from Figs. 2 and 3. The transient burning velocity can be a factor of two greater than its steady counterpart. This fact would pose difficulty for the non-isobaric flame propagation analysis of Carrier et.al. (8).

Flame interaction with the adiabatic wall intensifies as the flame approaches within two flame thicknesses of the boundary. The amplitude of oscillation in burning velocity (Fig. 3c) grows significantly. Some insight is possible by tracking the movement of the ozone mass fraction distribution (at 1/2 the initial value) and computing inertial flame speed as before. Figure 6 displays a comparison of two measures of flame velocity, one based on the temperature profile and the other on ozone mass fraction. During most of the travel, the two velocities are coincident. However, as the flame approaches the boundary, the mass fraction profile oscillation grows to a much larger amplitude. Thus, the internal flame structure is changing; the flame does not remain quasi-steady.

Flame tracking results (based on $850^{\circ}K$) for the cold wall case (Fig. 2c) are shown in Fig. 7. Flame speed and burning velocity are nearly the same as in the adiabatic wall case until, again, the flame approaches to within two flame thicknesses of the boundary. Energy losses then suppress the flame pulsations and dramatically decelerate its overall motion. The flame halts before reaching the boundary and actually retreats as indicated by the negative values of both inertial flame velocity and burning velocity. The results indicate a quenching distance of 0.006 mm when the pressure is 5.5 atm. Although the transient process introduces some ambiguity here, the Peclet number is approximately 1.2 which is slightly lower than the values computed by Westbrook et.al. (9) for methane-air and methanol-air flames. As might be anticipated, cold wall quenching of the thin ozone flame involves a very small layer of unburned reactant.

CONCLUDING REMARKS

Confined laminar flames are inherently oscillatory. Momentum conservation through the reaction zone leads to static pressure imbalances which interact with the confining boundaries. Since small amplitude pressure disturbances can cause large velocity fluctuations of premixed flames, modeling assumptions such as a spatially uniform pressure field must be examined carefully for each application. The present numerical prediction for transient burning velocity is a factor of two greater than the steady state burning velocity computed at the local upstream values of pressure and temperature. Flame interactions near an adiabatic boundary can be strong enough to generate internal oscillations of the flame structure. Transient flames may also be far from chemical equilibrium. Present computations would support flame approximations based on the partial chemical equilibrium ideas of Mitchell et.al. (14).

ACKNOWLEDGEMENT

REFERENCES

1. Mallard, E., and LeChatelier H.L. Ann Mines, 4: 379 (1883)

2. Tsatsaronis, G. Combustion and Flame, 33: 217-239 (1978)

3. Carrier, G.F. Fendell, F.E., and Bush, W.B. Combustion Science and Technology, 20: 195-207 (1979)

4. Carrier, G.F., Fendell, F.E. Bush, W.B., and Feldman, P.S. Nonisenthalpic Interaction of a Planar Premixed Flame with a Paralled End Wall, Society of Automotive Engineers Paper 790245 (1979)

5. Sirignano, W.A. Combustion Science and Technology, 7: 99-108 (1973)

6. Kurkov, A.P., and Mirsky, W. Twelfth Symposium (International) on Combustion, The Combustion Institute, pp. 612-624 (1969)

7. Bush, W.B., Fendell, F.E., and Fink, S.F. Combustion Science and Technology, 24: 53-70 (1980)

8. Carrier, G.F., Fendell, F.E., and Feldman, P.S. Dynamics and Modelling of Reactive Systems, Academic Press, New York, pp. 333-352 (1980)

9. Westbrook, C.K., Adamczyk, A.A., and Lavoie, G.A. Combustion and Flame 40: 81-99 (1981)

10. Kooker, D.E. Seventeenth Symposium (International) on Combustion, The Combustion Institute, pp. 1329-1338 (1979)

11. Heimerl, J.M., and Coffee, T.P. Combustion and Flame, 39: 301-315 (1980)

12. Gordon, S., and McBride, B.J. Computer Program for Calculation of Complex Chemical Equilibrium Compositions, Rocket Performance, Incident and Reflected Shocks, and Chapman-Jouget Detonations. NASA/Lewis, NASA-SP-273, 1971. (1976 program version)

13. Hindmarsh, A.C., and Byrne, G.D. EPISODE: An experimental Package for the Integration of Systems of Ordinary Differential Equations. Lawrence Livermore Lab, UCRL-75868, 1975.

14. Mitchell, R.E. Sarofim, A.F., and Clomburg, L.A. Combustion and Flame, 37: 201-206 (1980)

15. Coffee, T.P. (1980). Private Communication, based on model of Heimerl and Coffee (11)

Table 1.

BURNING VELOCITY COMPARISON

25 MOLE % O_3/O_2, ADIABATIC WALL (Z=1)

TIME	UPSTREAM TEMPERATURE (°K)	UPSTREAM PRESSURE (ATM)	U_{ss} (cm/s)*	U_{fr} (cm/s)	RANGE OVER CYCLE
45.87	364	2.2	96.5	198	193-199
65.05	401	3.2	121.2	214	212-220

* STEADY STATE LAMINAR BURNING VELOCITY
COMPUTED BY HEIMERL & COFFEE (REF 11)
FOR THESE CONDITIONS
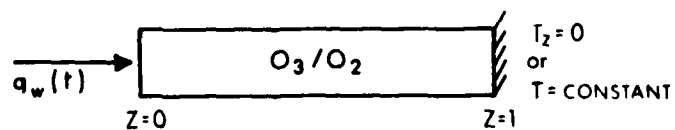
Fig. 1 Problem configuration.
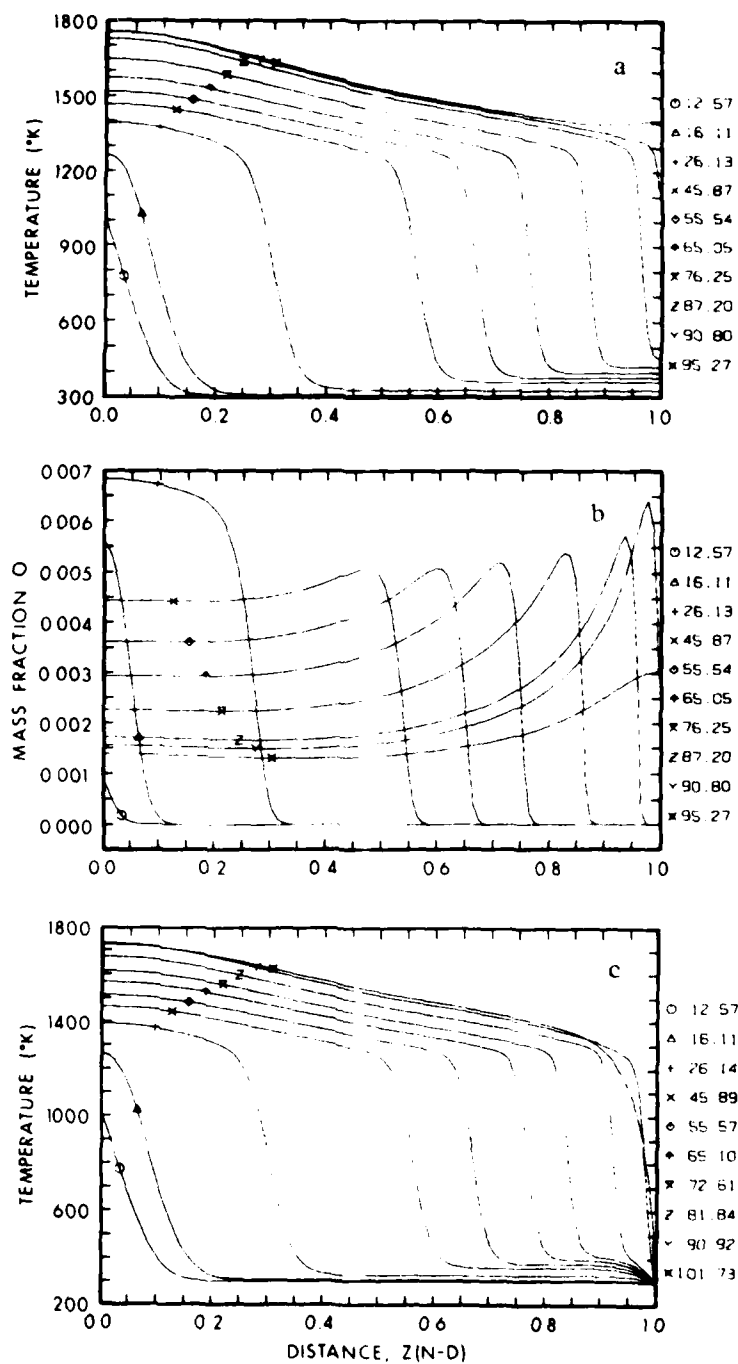
Fig. 2   Mixture 25 mole % O$_3$ in O$_2$.   Chamber distribution
time-history for (a) temperature and (b) atomic
oxygen mass fraction for adiabatic wall; (c)
temperature for cold wall (298°K).
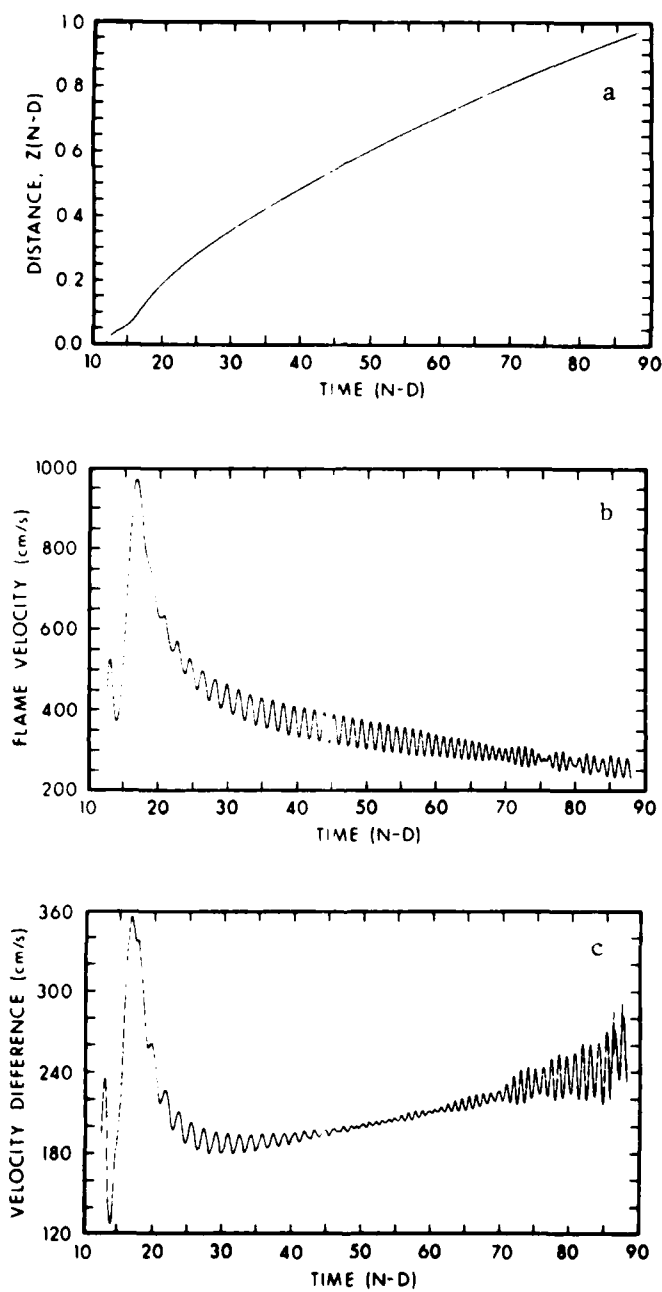
Fig. 3 Mixture 25 mole % O_3 in O_2, adiabatic wall. (a)
Flame locus ($850^{\circ}K$), (b) inertial flame velocity,
and (c) burning velocity, labelled velocity
difference.

347
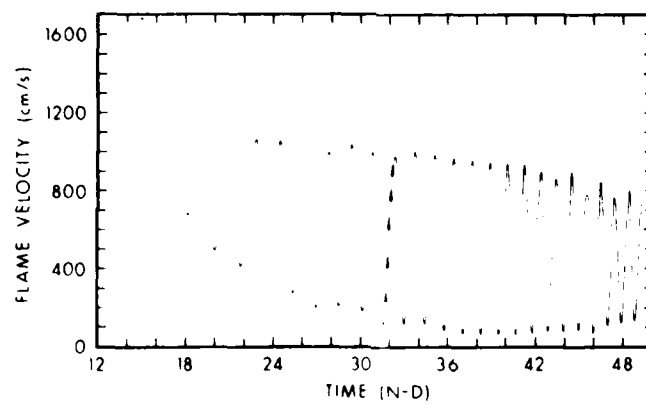
Fig. 4 Mixture 30 mole % O_3 in O_2, adiabatic wall.
Inertial flame velocity.
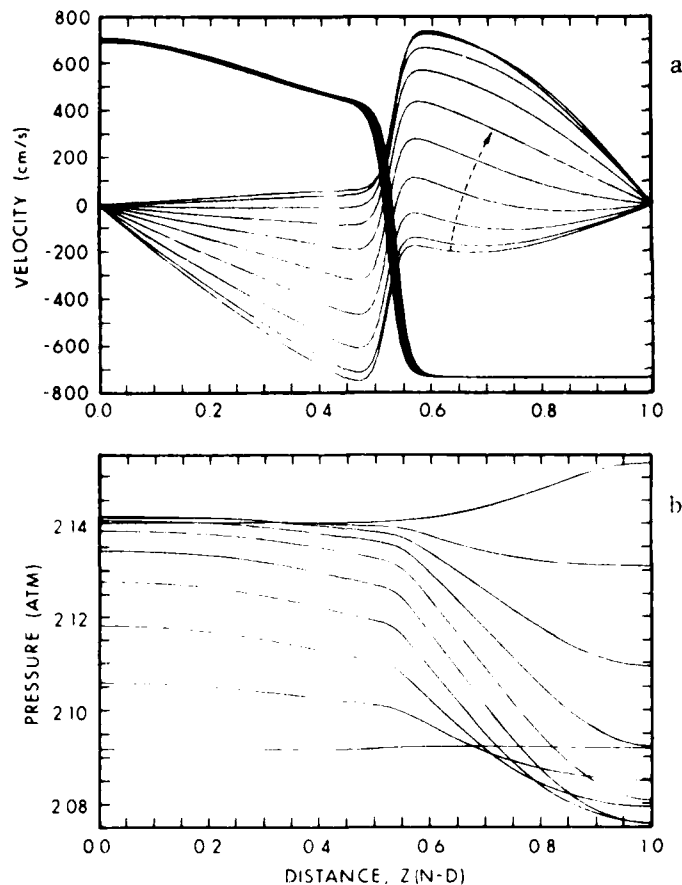
Fig. 5 Mixture 30 mole % O_3 in O_2, adiabatic wall. (a)
Chamber velocity distribution (with temperature
profile superposed) and (b) chamber pressure dis-
tribucion during one-half cycle of flame oscillation
denoted by arrows in Fig. 4.
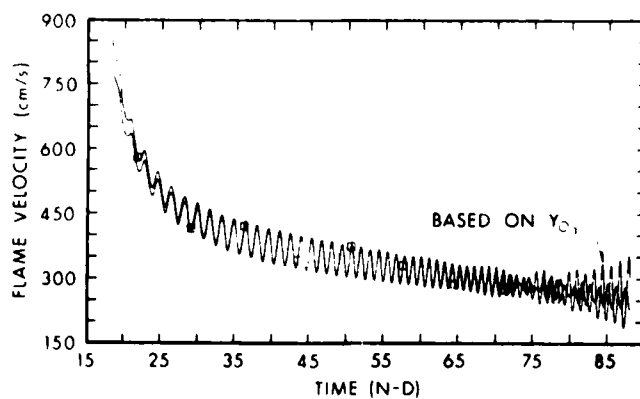
Fig. 6 Mixture 25 mole % O_3 in O_2, adiabatic wall.
Comparison of two measures of inertial flame velo-
city, tracking 850°K and one-half the initial ozone
mass fraction.

349
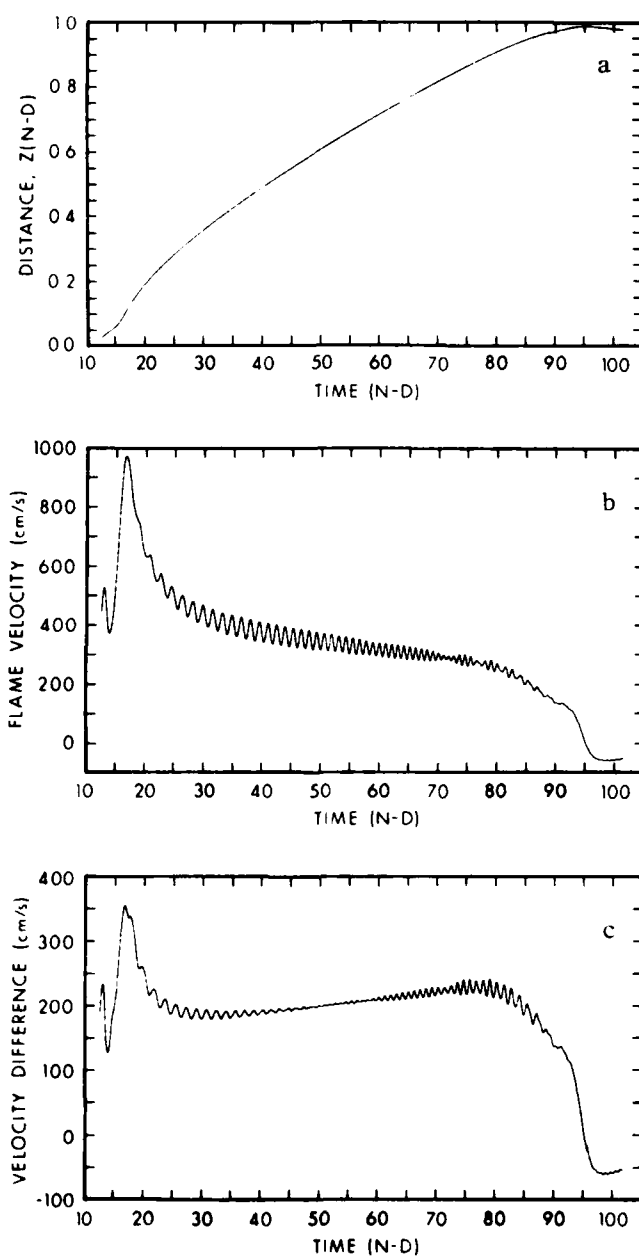
Fig. 7 Mixture 25 mole % O_3 in O_2, cold wall $(298^{\circ}K)$.
(a) Flame locus $(850^{\circ}K)$, (b) inertial flame velo-
city, labelled velocity difference.

EFFECT OF SUPPORT CONDITIONS ON BEAM VIBRATIONS
SUBJECTED TO MOVING LOADS

Julian J. Wu
U.S. Army Armament Research and Development Command
Large Caliber Weapon Systems Laboratory
Benet Weapons Laboratory
Watervliet, NY 12189

ABSTRACT. Solutions of beam vibrations under moving loads are presented
with a variety of support conditions. The purpose is to demonstrat how the
support conditions will effect such beam motions. The solution method and
mathematical background will be reviewed including the introduction of various
support parameters. By slightly modifying an existing computational scheme,
the desired results have been obtained and presented in several tables and
plots showing the effect of support stiffness on beam motions.

I. STATEMENT OF THE PROBLEM. The dynamic equation of Euler-Bernoulli
beam subjected to a moving force can be written as the following

$$EIy'''' + \rho A\ddot{y} = P\delta(x-\bar{x}) \quad , \qquad \begin{array}{l} 0 < x < \ell \\ 0 < t < T \end{array} \tag{1}$$

where $y = y(x,t)$ denotes the beam deflection as a function of the spatial
coordinates x and the time t. The letters E, I, A, ℓ, and ρ denote elastic
modulus, second moment of the cross-sectional area, and the area itself, the
length, and the material density of the beam, respectively. A Dirac delta
function is denoted by δ, $\bar{x} = \bar{x}(t)$ is the location of the force P. T denotes
some finite time of interest. As usual, a prime (') denotes differentiation
with respect to x and a dot (·), differentiation with respect to t.

The boundary conditions are written as

$$EIy'''(0,t) + k_1 y(0,t) = 0$$

$$EIy''(0,t) - k_2 y'(0,t) = 0$$

$$EIy'''(\ell,t) - k_3 y(\ell,t) = 0 \tag{2}$$

$$EIy''(\ell,t) + k_4 y'(\ell,t) = 0$$

where k_i, $i = 1$, 2, 3, and 4 are the spring constant which model the support
characteristics. The initial conditions are

$$y(x,0) = \bar{y}_0(x)$$

$$\dot{y}(x,0) = \bar{y}_1(x) \tag{3}$$

Equations (1) through (3) will be written in dimensionless form for the sake of generality and simplicity. This is accomplished by the introduction of dimensionless parameters. In the following an arrow ($\rightarrow$) will be read as "replaces":

$$y \rightarrow \frac{y}{\ell} \quad , \quad x \rightarrow \frac{x}{\ell} \quad , \quad t \rightarrow \frac{t}{T}$$

$$k_1 \rightarrow \frac{k_1 \ell^3}{EI} \quad , \quad k_2 \rightarrow \frac{k_2 \ell}{EI}$$

$$k_3 \rightarrow \frac{k_3 \ell^3}{EI} \quad , \quad k_4 \rightarrow \frac{k_4 \ell}{EI} \tag{4}$$

$$y_1 \rightarrow T y_1 \quad , \quad P \rightarrow \frac{P \ell^3}{EI}$$

With these new dimensionless parameters, Eqs. (1) through (3) become

$$y'''' + \gamma^2 \ddot{y} = P \delta(x - \bar{x}) \quad , \quad \begin{array}{c} 0 < x < 1 \\ 0 < t < 1 \end{array} \tag{1'}$$

$$y'''(0,t) + k_1 y(0,t) = 0$$

$$y''(0,t) - k_2 y'(0,t) = 0$$

$$\begin{array}{c} 0 < t < 1 \end{array} \tag{2'}$$

$$y'''(1,t) - k_3 y(1,t) = 0$$

$$y''(1,t) + k_4 y(1,t) = 0$$

and

$$y(x,0) = \bar{y}_o(x)$$

$$\dot{y}(x,0) = y_1(x) \qquad 0 < x < 1 \tag{3'}$$

where in Eq. (1'), we have

$$\gamma = \frac{c}{T} \tag{4a}$$

which is dimensionless, with

$$c = \left(\frac{\rho A \ell^4}{EI}\right)^{1/2} \tag{4b}$$

which has the dimension of the physical time.

Hence then, we shall obtain solutions for the problem defined by Eqs. (1') through (3') for various values of k_i, $i = 1, 2, 3,$ and 4.

II. AN EQUIVALENT VARIATIONAL PROBLEM.

The problem of solving the equation (1') through (3') in the previous section will be transformed into a variational problem. Consider

$$\delta I = 0 \tag{5a}$$

with

$$I = \int_0^1 \int_0^1 [y'' y^{*\prime\prime} - \gamma^2 \ddot{y} y^* + Q\bar{\delta}(x-\bar{x}) y^*] dx dt$$

$$+ \int_0^1 dt \{ k_1 y(0,t) y^*(0,t) + k_2 y'(0,t) y^{*\prime}(0,t)$$

$$+ k_3 y(1,t) y^*(1,t) + k_4 y'(1,t) y^{*\prime}(1,t) \}$$

$$+ \gamma^2 \int_0^1 dx \{ k_5 [y(x,0) - \bar{y}_0(x)] y^*(x,1) - \bar{y}_1(x) y^*(x,0) \} \tag{5b}$$

where $y^*(x,t)$ is called the adjoint function of $y(x,t)$. If one takes the first variation of I considering $y(x,t)$ to be fixed and δy^* to be completely arbitrary, it is easy to see that the differential equation (1') and boundary condition (2') will be recovered and the initial condition becomes

$$\dot{y}(x,1) - k_5 [y(x,0) - \bar{y}_0(x)] = 0$$

$$\dot{y}(x,0) - \bar{y}_1(x) = 0 \tag{3''}$$

In Eq. (3''), it is seen that if one let $k_5 \to \infty$ in the limit, the initial condition of (3') will also be recovered. The use of a large parameter such as k_5 is known as the penalty function method or the method of large spring constant [1].

III. OUTLINE OF SOLUTION FORMULATION.

To derive the finite element matrix equations, one begins with Eq. (5a') and write

$$(\delta I)_{\delta y=0} = 0 \tag{6a}$$

$$= \int_0^1 \int_0^1 [y'' \delta y^{*\prime\prime} - \gamma^2 \dot{y} \delta \dot{y}^* + Q\bar{\delta}'(x-\bar{x}) \delta y^*] dx dt$$

$$+ \int_0^1 dt [k_1 y(0,t) \delta y^*(0,t) + k_2 y'(0,t) \delta y^*(0,t)$$

$$+ k_3 y(1,t) \delta y^*(1,t) + k_4 y'(1,t) \delta y^{*\prime}(1,t)]$$

$$+ \gamma^2 \int_0^1 dx \{ k_5 [y(x,0) - \bar{y}_0(x)] \delta y^*(x,1) - \bar{y}_1(x) \delta y^*(x,0) \} \tag{6b}$$

The element local variables are now introduced

$$\xi = \xi^{(i)} = Kx-i+1$$

$$\eta = \eta^{(j)} = Lt-j+1 \tag{7a}$$

or

$$x = \frac{1}{K} (\xi+i-1)$$

$$t = \frac{1}{L} (\eta+j-1) \tag{7b}$$

where K is the number of divisions in x and L, in t. (A typical grid scheme is shown in Figure 6). Equation (6b) can now be written as

$$\sum_{i=1}^{K} \sum_{j=1}^{L} \int_0^1 \int_0^1 [\frac{K^3}{L} y''_{(ij)} \delta y^{*''}_{(ij)} - \frac{\gamma^2 L}{K} y_{(ij)} \delta y^{*}_{(ij)}] d\xi d\eta$$

$$+ \sum_{j=1}^{L} \int_0^1 d\eta \ [\frac{k_1}{L} y_{(ij)}(0,\eta)\delta y^{*}_{(ij)}(0,\eta) + k_2 \frac{K^2}{L} y'_{(ij)}(0,\eta)\delta y^{*'}_{(ij)}(0,\eta)$$

$$+ \sum_{i=1}^{K} \int_0^1 \frac{d\xi}{K} \ [\gamma^2 k_5 (y_{(ij)}(\xi,0)\delta y^{*}_{(ij)}(\xi,1))]$$

$$= - \sum_{i=1}^{K} \sum_{j=1}^{L} \frac{Q}{L} \int_0^1 \int_0^1 \bar{\delta}'(x-\bar{x}) \delta y^{*}_{(ij)}(\xi,\eta) d\xi d\eta$$

$$+ \sum_{i=1}^{K} \frac{\gamma^2 k_5}{K} \int_0^1 d\xi [\bar{y}_{o(i)}(\xi)\delta y^{*}_{(iL)}(\xi,1)]$$

$$+ \sum_{i=1}^{K} \frac{\gamma^2}{K} \int_0^1 d\xi [\bar{y}_{1(i)} \delta y^{*}_{(i1)}(\xi,0) \tag{8}$$

The shape function vector is now introduced. Let

$$y_{(ij)}(\xi,\eta) = \underline{a}^T(\xi,\eta) Y_{(ij)}$$

$$y^{*}_{(ij)}(\xi,\eta) = \underline{a}^T(\xi,\eta) Y^{*}_{(ij)} = Y^{*T}_{(ij)} \underline{a}(\xi,\eta) \tag{9}$$

354

Equation (8) then becomes

$$\sum_{i=1}^{K} \sum_{j=1}^{L} \delta \underset{\sim}{Y}^{*T}(ij) \left\{ \frac{K^3}{L} \underset{\sim}{A} - \frac{\gamma^2 L}{K} \underset{\sim}{B} \right\} \underset{\sim}{Y}(ij)$$

$$+ \sum_{i=1}^{L} \delta \underset{\sim}{Y}^{*T}(ij) \left\{ \frac{k_1}{L} \underset{\sim}{B}_1 + \frac{k_2 K^2}{L} \underset{\sim}{B}_2 \right\} \underset{\sim}{Y}(ij)$$

$$+ \sum_{i=1}^{L} \delta \underset{\sim}{Y}^{*T}(Kj) \left\{ \frac{k_3}{L} \underset{\sim}{B}_3 + \frac{k_4 K^2}{L} \underset{\sim}{B}_4 \right\} \underset{\sim}{Y}(ij)$$

$$+ \sum_{i=1}^{K} \delta \underset{\sim}{Y}^{*T}(iL) \left\{ \frac{\gamma^2 k_5}{K} \underset{\sim}{B}_5 \right\} \underset{\sim}{Y}(iL)$$

$$= \sum_{i=1}^{K} \sum_{j=1}^{L} \delta \underset{\sim}{Y}^{*T}(ij) \frac{P}{L} \underset{\sim}{F}(ij) + \sum_{i=1}^{K} \delta \underset{\sim}{Y}^{*T}(iL) \frac{\gamma^2 k_5}{K} \underset{\sim}{G}(i)$$

$$+ \sum_{i=1}^{K} \delta \underset{\sim}{Y}^{*T}(i1) \frac{\gamma^2}{K} \underset{\sim}{H}(i) \tag{10}$$

where, as it can be seen readily, that

$$\underset{\sim}{A} = \int_0^1 \int_0^1 \underset{\sim}{a}_{,\xi\xi} \, \underset{\sim}{a}^T_{,\xi\xi} \, d\xi d\eta$$

$$\underset{\sim}{B} = \int_0^1 \int_0^1 \underset{\sim}{a}_{,\eta} \, \underset{\sim}{a}^T_{,\eta} \, d\xi d\eta$$

$$\underset{\sim}{B}_1 = \int_0^1 \underset{\sim}{a}(0,\eta) \underset{\sim}{a}^T(0,\eta) d\eta \quad , \quad \underset{\sim}{B}_2 = \int_0^1 \underset{\sim}{a}_{,\xi}(0,\eta) \underset{\sim}{a}^T_{,\xi}(0,\eta) d\eta$$

$$\underset{\sim}{B}_3 = \int_0^1 \underset{\sim}{a}(1,\eta) \underset{\sim}{a}^T(1,\eta) d\eta \quad , \quad \underset{\sim}{B}_4 = \int_0^1 \underset{\sim}{a}_{,\xi}(1,\eta) \underset{\sim}{a}^T_{,\xi}(1,\eta) d\eta$$

$$\underset{\sim}{B}_5 = \int_0^1 \underset{\sim}{a}(\xi,1) \underset{\sim}{a}^T(\xi,0) d\xi$$

$$\underset{\sim}{F}(ij) = \int_0^1 \int_0^1 \underset{\sim}{a}(\xi,\eta) \bar{\delta}(ij)(\xi-\xi) d\xi d\eta \quad , \quad \underset{\sim}{G}(i) = \int_0^1 \underset{\sim}{a}(\xi,1) \bar{y}_{0(i)}(\xi) d\xi$$

and

$$\underset{\sim}{H}_i = \int_0^1 \underset{\sim}{a}(\xi,0) \bar{y}_{1(i)}(\xi) d\xi \tag{11}$$

355

Now Eq. (10) can be assembled in a global matrix equation

$$\delta \underset{\sim}{Y}^{*T} \underset{\sim}{K} \underset{\sim}{Y} = \delta \underset{\sim}{Y}^{*} \underset{\sim}{F} \tag{12}$$

By virtue of the fact that $\delta \underset{\sim}{Y}^{*}$ is not subjected to any constrained conditions, one has

$$\underset{\sim}{K} \underset{\sim}{Y} = \underset{\sim}{F} \tag{13}$$

which can be solved routinely. More details can be found in [1].

IV. RESULTS OF COMPUTATIONS. Appropriate values of physical parameters must be assigned for obtaining numerical results. Let

$$v = \frac{\ell}{T} \tag{14}$$

be the velocity of the travelling force. Only constant velocity will be considered in this paper. Thus T becomes the time required for the force to move from one end of the beam to the other end. As T varies from ∞ to 0, the velocity v varies from 0 to ∞ as ℓ is always finite. Since we have normalized all the parameters in length with respect to ℓ, it is not necessary to specify ℓ in numerical computations. Instead, the beam's length is considered to be unity. The real value in length can be recovered simply by a multiplication of ℓ to the normalized (dimensionless) ones. Then it will be helpful if v in Eq. (14) can be related to some reference velocity associated with the beam's characteristics. We shall select the velocity of the first mode of vibration (standing waves) of a cantilevered beam as this reference velocity and call it v_1. Hence the normalized velocity is defined by

$$\bar{v} = \frac{v}{v_1} \tag{15}$$

Now, we shall relate this $\bar{v}$ with the parameters defined earlier in this paper. It is known in many textbooks on vibrations (for example, see [3]) that for a cantilevered beam, the first mode of vibrations has a circular frequency

$$\omega_1 = (1.875)^2/c = 3.516/c \tag{16}$$

where c is given in (4b). The corresponding frequency and period are then respectively

$$f_1 = \frac{\omega_1}{2\pi} = 0.560/c \quad \text{(in cycles per seconds)}$$

$$T_1 = \frac{1}{f_1} = 1.79 \quad \text{(in seconds)} \tag{16}$$

Hence

$$v_1 = \frac{2\ell}{T_1} = 2\ell f_1 = 1.12 \frac{\ell}{c} \tag{17}$$

356

and

$$\bar{v} = \frac{v}{v_1} = \frac{\ell/T}{1.12 \; \ell/c} = 0.89_{5} \; \frac{c}{T} = 0.895 \; \gamma \qquad (18)$$

where $\gamma = c/T$, as defined in Eq. (5b).

For the results computed in this par.., γ is set to be ten. Hence $\bar{v} = 8.95$ or v is about nine times v_1. At this load velocity, the dynamic effect of the moving force on the beam vibration is quite evident as shown in Figures 1 through 5. This is also approximately a typical speed at which a projectile moves down a cannon tube (see, for example, [4]). Figure 1 shows ... deflection curves for a beam with fixed-fixed supports. Curves numbered I, II, III, and IV are at the moment when P is at 1/4, 2/4, 3/4, and 4/4 of support. Figures 2 through 5 are the same curves for the support conditions of fixed-simply supported, fixed-free, free-free and free-fixed respect vely.

It should be noted that the load P is assumed to move from the left en.' toward the right. The beam motions from fixed-free supports are quite different from those of free-fixed supports as demonstra: 4, for example, by Figures 3 and 5. This dynamic behavior has also been noted by Fryba [3]. In fact, the deflection curves for the case of free-fixed supports resemble more closely to those of free-free supports than the fixed-free ones.

The values of the "spring constants" in Eqs. (2') and (5b) are as follows. For a fixed rigid support the k_1 is taken to be 10^{10}; for no support at all, it is assigned a zero. The value of k_5 in Eq. (5b) is also assigned to be 10^{10}.

Results presented above are based on a grid scheme of 5x8 elements. (A typical grid scheme is shown in Figure 6). Numerical convergence of these data should be fairly good as discussed previously in Reference [1].

REFERENCES

1. J. J. Wu, "Vibrations of a Beam Under Moving Loads by a Finite Element Formulation Consistent in Spatial and Time Coordinates," The 51st Shock and Vibration Bulletin, Part 3; Analytical Methods, Dynamics, and Vehicle Systems, pp. 111-130 (1981).

2. K. N. Tong, Theory of Mechanical Vibration, John Wiley, New York, 1960, p. 256.

3. L. Fryba, Vibration of Solids and Structures Under Moving Loads, Noordhoff International, Groningen, 1971, p. 91.

4. J. J. Wu, "Vibrations of a Beam Under Moving Loads by a Finite Element Formulation Consistent in Spatial and Time Coordinates," The 51st Shock and Vibration Bulletin, Part 3; Analytical Methods, Dynamics, and Vehicle Systems, pp. 126 (1981).

Figure 1. Beam deflections under a moving load for fixed-fixed
supports ($\gamma = 10.0$).

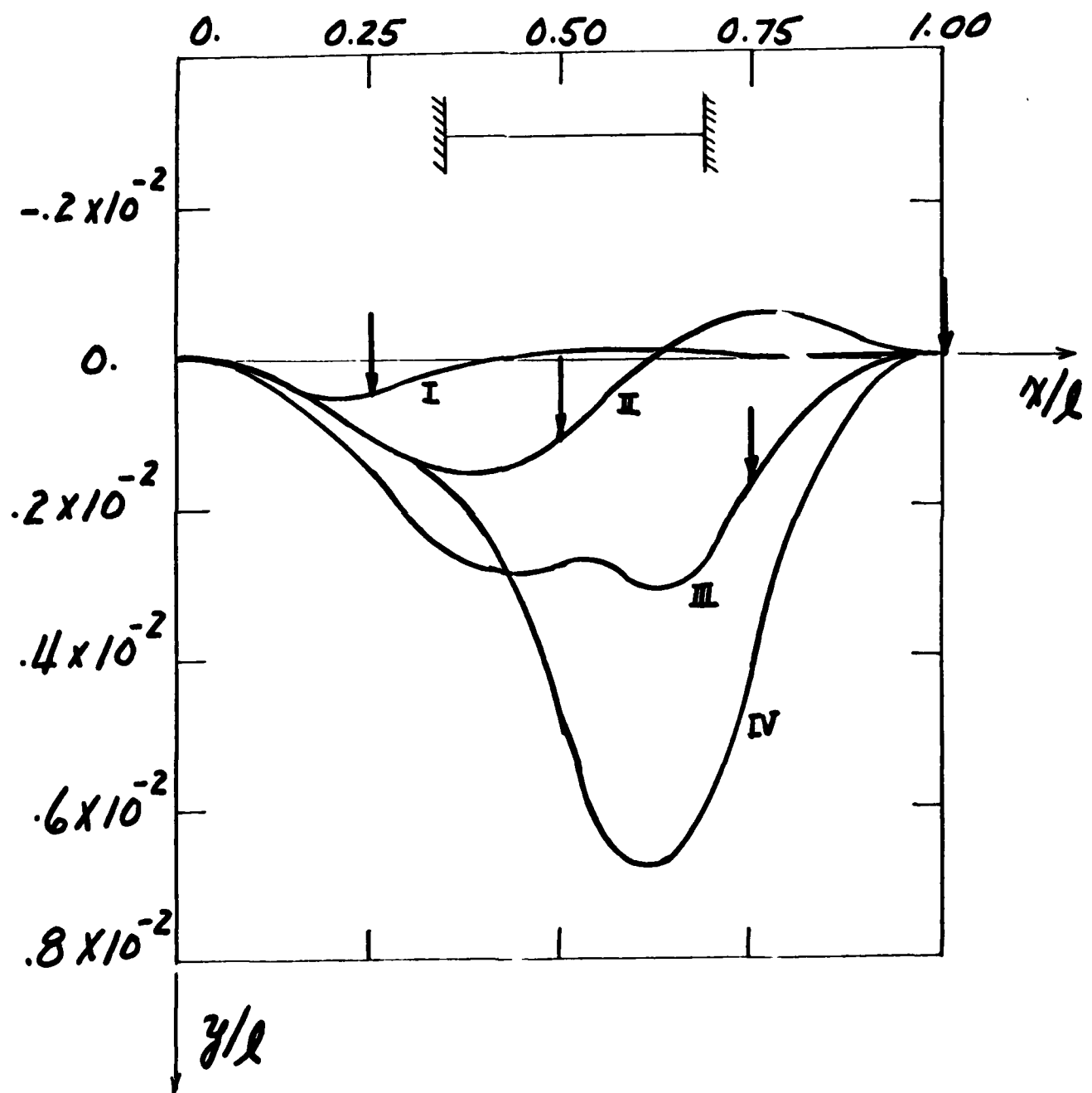Figure 2. Beam deflections under a moving load for fixed-simply supported end conditions (γ = 10.0).

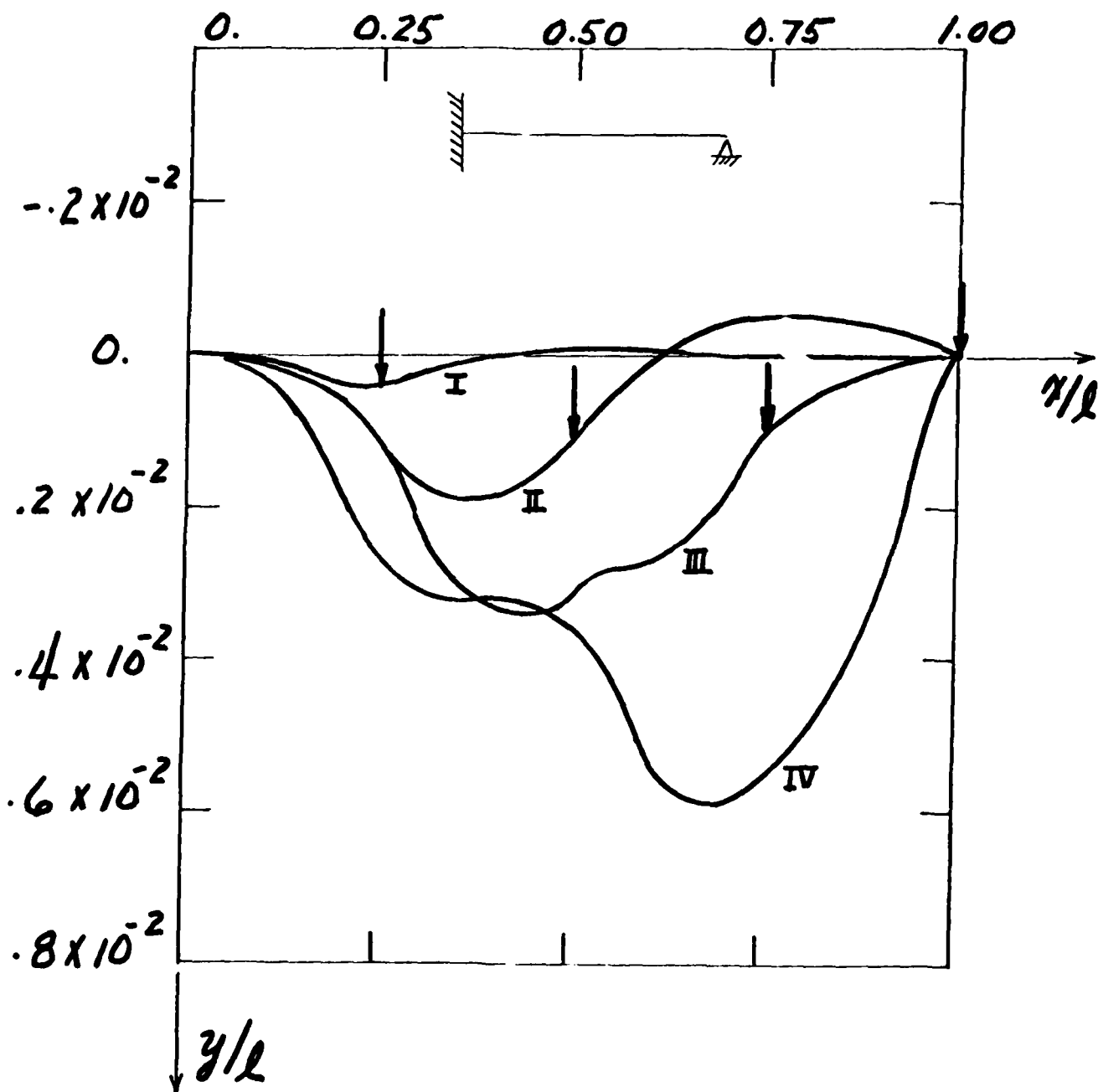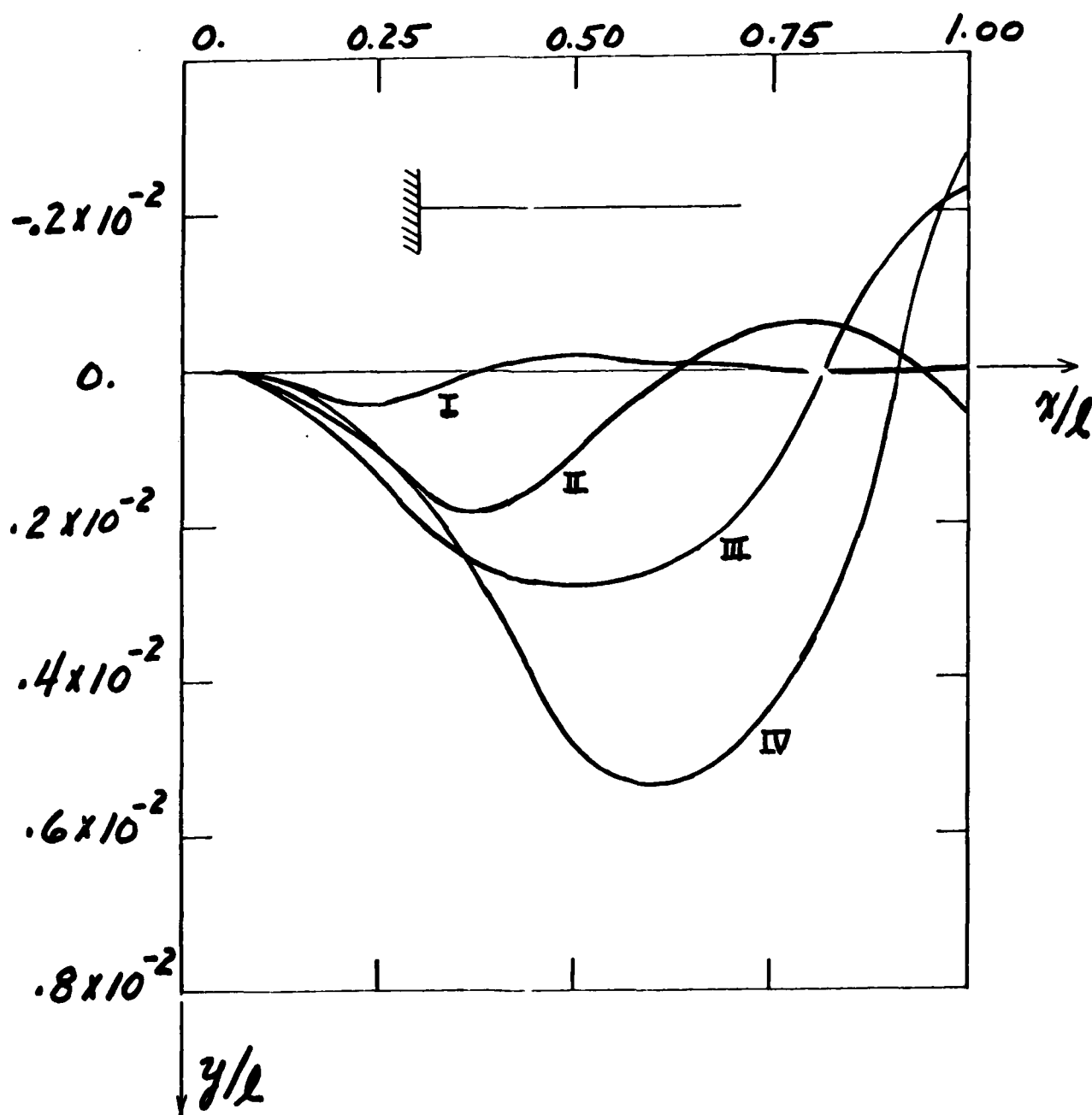Figure 3. Beam deflections under a moving load for fixed-free supports ($\gamma = 10.0$).
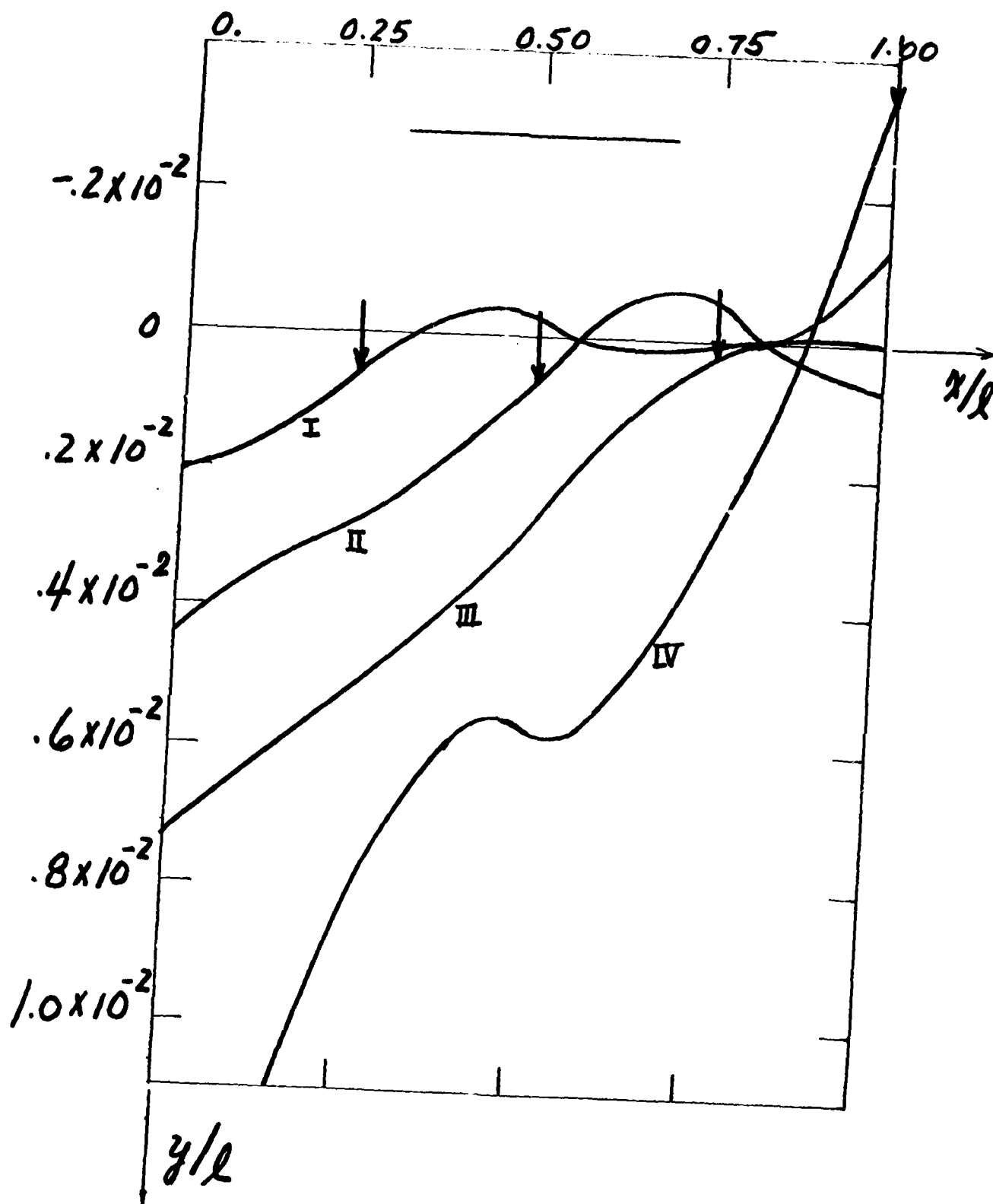
Figure 4. Beam deflections under a moving load for free-free end conditions ($\gamma = 10.0$).
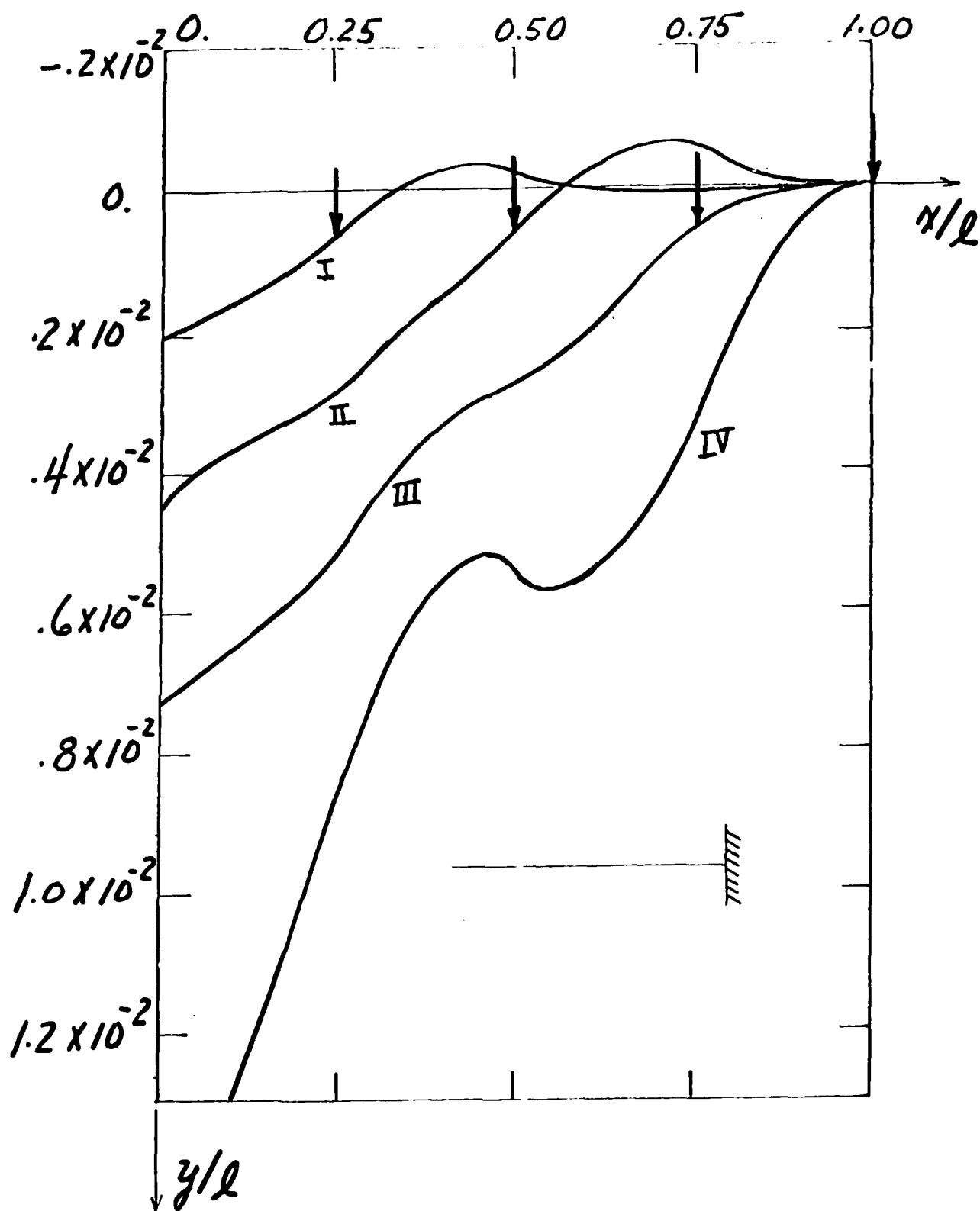
Figure 5. Beam deflections under a moving load for a free-fixed supports ($\gamma = 10.0$).
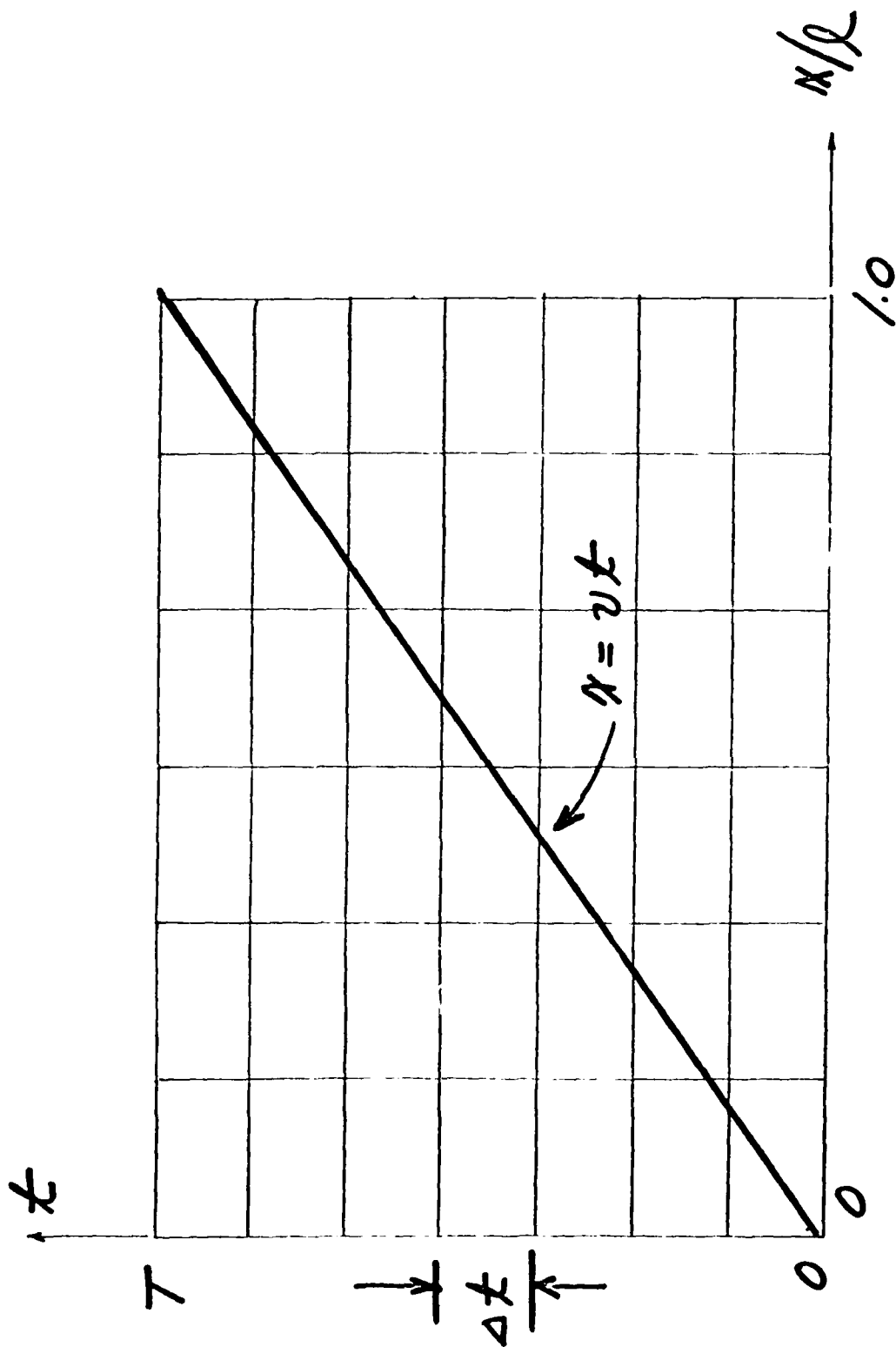
Figure 6. A typical grid of finite elements.

FINITE ELEMENTS FOR INITIAL VALUE PROBLEMS IN DYNAMICS

T. E. Simkins
U.S. Army Armament Research and Development Command
Large Caliber Weapon Systems Laboratory
Benet Weapons Laboratory
Watervliet, NY 12189

ABSTRACT. The work of C. D. Bailey amply demonstrates that a variational principle is not a necessary prerequisite for the formulation of variational approximations to initial value problems in dynamics. While Bailey successfully applies global power series approximations to Hamilton's Law of Varying Action, the work herein shows that a straightforward extension to finite element formulations fails to produce a convergent sequence of solutions. The source of the difficulties and their elimination are discussed in some detail and a workable formulation for initial value problems is obtained. The paper concludes with a few elementary examples showing the utility of finite elements in the time domain.

I. INTRODUCTION. According to Finlayson and Scriven [1] it is not variational notation or even the concept of a varied path which is the key criterion of a true variational 'principle' but rather the existence of a functional which when varied and set to zero, generates the governing equations and constraints for a given class of problems. In this sense, certain fundamental principles of mechanics such as d'Alembert's Principle do not truly qualify as variational principles. That is to say, these mechanical principles or 'laws' cannot be posed as central problems of the calculus of variations. On the other hand there are others, such as Hamilton's principle which do qualify as true variational principles. Yet it is d'Alembert's Principle which forms a basis for all analytical mechanics [2] and it follows, therefore, that the vanishing of the first variation of some functional is not a necessary condition for the scalar formulation of any mechanics problem – however elegant or convenient this may be. Whether a true variational principle or a more fundamental variational statement is used to obtain a numerical solution to a dynamics problem, an important argument is that well established laws such as d'Alembert's Principle or true principles such as Hamilton's, are physically based and avoid the arbitrariness inherent in general weighted residual methods and contrived variational principles. Moreover, only those variational principles which are also maximum or minimum principles appear to offer any special advantage for obtaining approximate solutions – mainly through their ability to provide bounds on the variational integral. Even then the system treated must be positive-definite and the upper and lower bounds are often too far apart to be of practical value. In brief, there seems to be little point in contriving a variational principle in preference to a variational law of mechanics despite the more primitive status of the latter. Indeed the many solutions to initial value dynamics problems obtained by C. Bailey [3] by applying the Ritz method to Hamilton's 'law of varying action' demonstrate the usefulness of variational formulations not based on variational 'principles'. Thus motivated, the work herein explains the difficulties encountered in attempting to generalize Bailey's methods using the method of finite elements.

Zienkiewicz [4] has expressed serious reservations toward the use of finite elements in the time domain. Indeed, when the functions involved are sufficiently smooth, the number of time steps required to integrate a set of ordinary differential equations may not be great and it may require roughly as many finite elements to produce a solution of comparable accuracy. In view of the increased storage required, the use of time-finite elements to solve such systems is questionable. There are many other cases, however, in which conventional algorithms for step-by-step integration may call for a very large number of time steps. This is especially true when dealing with the (hyperbolic) equations of structural dynamics should the excitation and/or material properties change rapidly in time. A physically based variational method, with its inherent stability and physical origin, may lower the computational effort considerably.

The many solutions achieved by C. Bailey were generated by the Ritz method [5] using a power series approximation in which globally defined po..r-nomials are the basis functions. Ultimately the length of interval over whic solutions may be generated as well as the detail to be provided in any subin-terval will be limited by the degree of polynomial used as a basis. The pit-falls of using higher powered polynomials are well documente [6] and partially account for the use of locally (piecewise) defined basis functions (finite elements) to solve problems in many branches of mathematical physics. The extraordinary accuracy and simplicity of procedure attained by Bailey, however, are not to be understated.

Apart from avoiding the problems which can arise when higher powered polynomials are employed as basis functions, finite element formulations have other advantages when used to solve problems in continuum mechanics. Even though the principal motivation for their use has been the need to handle com-plicated boundary shapes (non-existent in the time domain) finite elements are also well suited to handle sudden changes in load functions, extending the in-terval of solution indefinitely without restart, and providing great detail to the solution in any subinterval. Two examples which exploit the advantages afforded by the finite-element discretization of time are given in Section V.

Since 1977, several investigators have publications dealing with the use of finite elements to modify or replace conventional integration methods. Hughes and Liu [7], and Belytschko and Mullen [8] are notable examples. One also notes the work of Serbin, Dougalis, and Gunzberger who have recently begun a computational and theoretical study of finite element methods for hyperbolic equations [9]. Thus despite the reservations expressed by Zienkiewicz, the extension of the finite element method to the solution of transient field problems is well motivated and was first reported by Argyris and Sharpf [10], later by Fried [11], and most recently by Baruch and Riff [12,13]. All of these works attempt to use Hamilton's principle as a starting point for the finite element formulation of initial value problems. As will be pointed out in the following section, this cannot be accomplished without some logical inconsistency when bringing the initial data into the formulation. In the sequel it will be shown that the use of Hamilton's 'law', rather than Hamilton's 'principle', makes possible the logical incorporation of the initial conditions into the variational formulation.

II. HAMILTON'S PRINCIPLE - A CONSTRAINED VARIATIONAL PRINCIPLE. The
following equation is known as the generalized principle of
d'Alembert [14]:

$$\sum_{i=1}^{N} (F_i - \dot{P}_i) \cdot \delta r_i = 0 \quad ; \quad (\dot{\ }) = \partial/\partial t \qquad (1)$$

This equation applies to any system of N-particles, the ith particle having a
position r_i, a momentum P_i, and subject to a resultant applied force F_i.

Under the assumption that the virtual work of the applied forces is
derivable from a scalar V, a time integration of equation (1) leads to
Hamilton's law of varying action [15,16]:

$$\delta \int_{t_1}^{t_2} (T-V)dt - \sum_{i=1}^{N} m_i \dot{r}_i \cdot \delta r_i \Big]_{t_1}^{t_2} = 0 \qquad (2a)$$

T is the kinetic energy of the system

$$T = 1/2 \sum_{i=1}^{N} m_i \dot{r}_i \cdot \dot{r}_i$$

and V is the potential energy of the forces impressed on the N-particles. The
existence of V makes little difference as far as numerical calculations are
concerned. In the event V does not exist, equation (2a) can be written:

$$\int_{t_1}^{t_2} (\delta T + \overline{\delta W})dt - \sum_{i=1}^{N} m_i \dot{r}_i \cdot \delta r_i \Big]_{t_1}^{t_2} = 0 \qquad (2b)$$

The bar signifies that in general the virtual work of the applied forces
cannot be derived from any scalar function of the generalized coordinates.
Either of equations (2) can be used as a basis for a Ritz approximation to a
dynamics problem.

If the r_i are constrained to take on specified values at t_1 and t_2, then
$\delta r_i(t_1)$ and $\delta r_i(t_2)$ vanish in equation (2a) and the result is Hamilton's
principle:

$$\delta \int_{t_1}^{t_2} (T-V)dt = 0 \qquad (3)$$

Since the vanishing of the displacement variations at the end points is
not the only means by which the partial sum in equation (2a) may vanish, equa-
tion (3) may not always represent Hamilton's principle in the strict sense.
Should equation (3) be used as a basis for the numerical solution of a dynam-
ics problem without the requirement that all of the δr_i vanish at t_1 or t_2,
zero momentum conditions will prevail instead as natural boundary conditions
on those displacements whose variations are free. This aspect of variational

principles is covered very clearly in many references (cf. ref. [17]). An observation to be made here is that equation (3) corresponds to a system of boundary value problems - not initial value problems - since the partial sum can only vanish through boundary (end point) constraints either natural or imposed. Thus equation (3) cannot, with complete logic, be used to formulate any system of initial value problems of dynamics. The introduction of initial data has in fact always been the obstacle preventing the use of Hamilton's principle for the variational formulation of initial value problems [18,19].

Since equation (3) is a valid physical statement of mechanics only when the boundary constraints are such that the partial sum vanishes, it is proper to refer to this equation as a 'constrained variational principle' as opposed to equations (2) which are unconstrained variational laws of mechanics, suitable for the application of arbitrary constraint conditions.

III. GLOBAL AND PIECEWISE RITZ APPROXIMATIONS.

Equations (2) and (3) differ only in the presence or absence of boundary terms. For the case of a single particle ($N=1$) having only one degree of freedom $u(t)$, the Ritz procedure when applied to either of equations (2) leads to a scalar relation of the form:

$$\delta U^T[(K-B)U-F] = 0 \qquad (4)$$

whereas for equation (3):

$$\delta U^T[KU-F] = 0 \qquad (5)$$

Equations (4) and (5) are assumed to derive from applying the Ritz procedure whereby the displacement function $u(t)$ is approximated as:

$$u(t) = a^T(t)U \qquad (6)$$

The relation (6) applies to the entire interval of solution when globally defined basis functions are used or to a particular subinterval thereof when piecewise functions (finite elements) are employed. When a global power series approximation is used U is a vector of generalized coordinates, the first two of which are identifiable as $u(t_1)$ and $u(t_2)$. The 'shape function', $a(t)$, in this case is simply:

$$a^T(t) = [1,t,t^2,\ldots,t^n] \quad , \quad t_1 < t < t_2 \qquad (7)$$

If piecewise cubic Hermite polynomials are used instead, the components of U are local values of u and $\dot{u}$ defined at the endpoints of a particular subinterval, and

$$a^T(t) = [2\tau^3-3\tau^2+1, \ h(\tau^3-2\tau^2+\tau), \ 3\tau^2-2\tau^3, \ h(\tau^3-\tau^2)] \qquad (8)$$

where $\tau = t/h$, h being the length of the particular subinterval. Referring first to equation (5), it is noted that K tends to be singular of degeneracy one. For certain simple problems K may compute to be exactly singular. In general, however, K will only become singular in the limit as the number of

basis functions employed in the Ritz approximation becomes infinite. The degeneracy of $\underset{\sim}{K}$ represents the possibility that neither $u(t_1)$ or $u(t_2)$ has been specified. That is, if neither $\delta u(t_1)$ or $\delta u(t_2)$ vanishes, then $m\dot{u}$ must vanish at both endpoints as natural boundary conditions. Under these conditions $u(t)$ may only be determined to within an arbitrary constant. Thus in equation (5) $\underset{\sim}{K}$ may be reduced to a nonsingular matrix by specifying values for $u(t_1)$ and/or $u(t_2)$ so that the variations of one or both of these quantities vanish. The essence of the discussion which follows is not changed if, in the sequel, it is assumed that $u(t_1)$ has been specified. This is known as a 'geometric' or 'imposed' constraint. Because $\delta U_1 \equiv \delta u(t_1) = 0$ multiplies the first row of $\underset{\sim}{K}$ in equation (5), this row is effectively removed from the formulation. Since the remaining variations are arbitrary the final set of equations to be solved is then:

$$\sum_{j=2}^{n} K_{1j}U_j = F_1 - K_{11}U_1 \quad , \quad i = 2,3...n \quad \quad (.)$$

where $U_1 = u(t_1)$ is the specified value and n^2 is the dimension of $\underset{\sim}{K}$. Whether these equations derive from a global power series approximation or from one based on finite elements, one may readily verify that as n is increased their solutions do indeed converge to the exact solution of the corresponding two point time-boundary value problem. Should one wish a solution to an initial value problem, however, equation (4) must be used instead of equation (5). In this case, specifying values for $u(t_1)$ and $u(t_2)$ cause δU_1 and δU_2 to vanish thereby deleting the first two equations of this set. The resulting system of equations to be solved is thus:

$$\sum_{j=3}^{n} (K_{1j} - B_{1j})U_j = F_1 - (K_{11} - B_{11})U_1 - (K_{12} - B_{12})U_2 \quad , \quad i = 3,4,...,n \quad (10)$$

In all cases attempted to date, solutions to equations (10) have been observed to converge to the exact solution if these equations are derived using a global power series approximation but not if they are formulated by finite elements. An example of this anomaly will be given in the next section. As the only difference between equations (4) and (5) is a subtraction of $\underset{\sim}{B}$ in the former, and in as much as convergence is achieved when equation (4) derives from a power series approximation, one suspects that it is the finite element representation of the matrix $\underset{\sim}{B}$ which is somehow at fault. It is therefore of interest to know in more detail just how the subtraction of $\underset{\sim}{B}$ is supposed to affect the coefficient matrix of the system.

In contrast to the matrix $\underset{\sim}{K}$, the matrix $\underset{\sim}{K} - \underset{\sim}{B}$ must tend to be singular of degeneracy two - no constraints having been assumed a priori. Thus when $u(t_1)$ is specified and the first row of $\underset{\sim}{K} - \underset{\sim}{B}$ is deleted, the remaining equations still must possess one degeneracy in the limit as the number of basis functions becomes infinite. Thus the effect of subtracting $\underset{\sim}{B}$ must be to free the natural boundary condition at t_2 (inherent in equation (5)) and to introduce a degeneracy. This remaining degeneracy can only be removed by specifying the value of $u(t)$ at a time other than t_1 or a value for $\dot{u}$, resulting in the deletion of another row of $\underset{\sim}{K} - \underset{\sim}{B}$.

369

IV. ANOMALOUS BEHAVIOR OF FINITE ELEMENT FORMULATIONS.

The degree to which the subtraction of the matrix $\underset{\sim}{B}$ from $\underset{\sim}{K}$ can both free the natural boundary condition at t_2 and introduce a degeneracy differs with the type of approximation employed. When global power series approximations are used the $\underset{\sim}{B}$ matrix is quite full and the subtraction affects many rows of $\underset{\sim}{K}$. When locally defined Hermite polynomials are used, however, $\underset{\sim}{B}$ is very sparse and in fact contains only two non-zero components. Moreover, one of these appears in the first row of $\underset{\sim}{B}$ which is deleted when $u(t_1)$ is specified. In this case freeing the natural boundary condition and introducing a degeneracy depends on the subtraction from a single component of $\underset{\sim}{K}$. Even though both effects may actually be produced in the limit as the number of elements becomes infinite, the degree to which they are approximated for any finite number of elements is evidently insufficient and the solutions do not converge to the correct result. This is exemplified in Figure 1. The problem represented is that of a free oscillator of unit mass and stiffness, subject to the prescribed initial constraints of zero displacement and unit velocity. For this case equation (2a) reads:

$$\int_0^\pi (\dot{u}\delta\dot{u}-\ddot{u}\delta u)dt - \dot{u}\delta u\Big|_0^\pi = 0 \tag{11}$$

or simply,

$$\int_0^\pi (\ddot{u}+u)\delta u\,dt = 0 \quad * \tag{12}$$

The finite element results of Figure 1 were obtained using piecewise cubic Hermite polynomials. (Higher ordered Hermite polynomials yield similar results.) It is observed that the solutions tend to diminish from the exact solution, $\sin(t)$, as the number of elements is increased. Using only two finite elements the finite element matrix formulation (equation (4)) for this problem is as follows:

$$0 = \delta U^T[K-B]U = \{\delta U_1\ \ \delta U_2\ \ \delta U_3\ \ \delta U_4\ \ \delta U_5\ \ \delta U_6\} \ \cdot$$

$$\left\{
\begin{bmatrix}
k_{11} & k_{12} & k_{13} & k_{14} & 0 & 0 \\
k_{21} & k_{22} & k_{23} & k_{24} & 0 & 0 \\
k_{31} & k_{32} & k_{33}+k_{11} & k_{34}+k_{12} & k_{13} & k_{14} \\
k_{41} & k_{42} & k_{43}+k_{21} & k_{44}+k_{22} & k_{23} & k_{24} \\
0 & 0 & k_{31} & k_{32} & k_{33} & k_{34} \\
0 & 0 & k_{41} & k_{42} & k_{43} & k_{44}
\end{bmatrix}
-
\begin{bmatrix}
0 & -1 & 0 & 0 & 0 & 0 \\
0 & 0 & 0 & 0 & 0 & 0 \\
0 & 0 & 0 & 0 & 0 & 0 \\
0 & 0 & 0 & 0 & 0 & 0 \\
0 & 0 & 0 & 0 & 0 & 1 \\
0 & 0 & 0 & 0 & 0 & 0
\end{bmatrix}
\right\}
\cdot
\begin{bmatrix}
U_1 \\ U_2 \\ U_3 \\ U_4 \\ U_5 \\ U_6
\end{bmatrix}
\tag{13}$$

---

*Note that Eq. (12) would also result from application of the Galerkin procedure, implying that the Galerkin method has some physical justification for problems in dynamics.

Using expression (8), the element matrix $\underset{\sim}{k}$ is calculated in terms of the element length h as:

$$\underset{\sim}{k} = \int_0^h (\ddot{\underset{\sim}{a}}\ddot{\underset{\sim}{a}}^T - \underset{\sim}{a}\,\underset{\sim}{a}^T)\,dt = \begin{bmatrix} \dfrac{6}{5h} - \dfrac{13h}{35} & \dfrac{1}{10} - \dfrac{11h^2}{210} & -\dfrac{9h}{70} - \dfrac{6}{5h} & \dfrac{13h^2}{420} + \dfrac{1}{10} \\[2ex] & \dfrac{2h}{15} - \dfrac{h^3}{105} & -\dfrac{13h^2}{420} - \dfrac{1}{10} & \dfrac{h^3}{140} - \dfrac{h}{30} \\[2ex] & \text{- SYMM. -} & \dfrac{6}{5h} - \dfrac{13h}{35} & \dfrac{11h^2}{210} - \dfrac{1}{10} \\[2ex] & & & \dfrac{2h}{15} - \dfrac{h^3}{105} \end{bmatrix}$$

Since U_1 is specified the first row of $\underset{\sim}{K} - \underset{\sim}{B}$ is deleted. As the subtraction of $\underset{\sim}{B}$ only affects one row of the reduced system, the only way in which a degeneracy can be introduced is for the next to last row to join the space defined by the rows remaining. Thus rows two through six in equation (13) ideally would become linearly dependent. This dependency along rows must be quite general as specification of any other of the U_i must remove it.

One suspects that a simple subtraction of unity from K_{56} in equation (13) may not do the best job of introducing a degeneracy or of freeing the natural boundary condition at $t_2 = \pi$. One can gain some idea of how 'close' this subtraction brings the fifth row into the space of rows 2,3,4 and 6 by comparing it with its projection onto this space. Substituting $\pi/2$ for h, the fifth row of equation (13) calculates to be:

[0.0   0.0   -0.96590326   -0.17637194   0.180505097   -0.970755175]

whereas its projection is:

[7.8587183E-3   -8.5978979E-3   -0.974496335

-0.184380835   0.172642875   -0.9617834]

Further calculations show that if the interval of solution remains fixed and the number of finite elements is allowed to increase, closer agreement between the next to last row vector and its projection is observed but this is not accompanied by a convergence of the solution vector toward the exact solution to the problem. While the exact reasons for this instability are not known it is apparent that the rate at which the next to last row tends to become dependent is important. It stands to reason, therefore, that should one invoke the limit condition without actually proceeding to the limit, a convergent sequence may result and indeed this proves to be the case.

Asserting that the row vectors two through six are linearly dependent allows the fifth row (equation) of equations (13) to be replaced by a linear combination of the others. For example, let

$$R_5 = \alpha_2 R_2 + \alpha_3 R_3 + \alpha_4 R_4 + \alpha_6 R_6 \qquad (14)$$

where R_i denotes the ith row of $K - B$. Aftⅇr imposing the second initial constraint, $U_2 = 1$, equations (13) can be wⅰitten:

$$\delta U_3 R_3 \cdot U + \delta U_4 R_4 \cdot U + \delta U_5 (\alpha_2 R_2 + \alpha_3 R_3 + \alpha_4 R_4 + \alpha_6 R_6) \cdot U + \delta U_6 R_6 \cdot U = 0 \qquad (15)$$

Since all variations in equation (15) are arbitrary, there results the following system of equations for solution:

$$0 = R_3 \cdot U = R_2 \cdot U = R_4 \cdot U = R_6 \cdot U \qquad (16)$$

Thus the second equation (row) which was originally deleted through the specⅰ- fication of U_2, is brought back into the formulation in place of the fifth in a logical and consistent manner. Equations (16) are the same set as would result from following the procedure of Argyris and Scharpf. These authors, however, started with Hamilton's prinⅽiple which requires that $\delta U_1 = \delta U_5 = 0$. This would delⅇte the first and fifth equations from the set. Further speci- fication of U_2 should then delete the second equation as weⅼ overspecifying the problem. Argyris and Scharpf [20] allow this equation to remain without justification. Moreover, no explanation is given as to why δU_5 should vanish as U_5 is never specified in an initial value problem. All of these inconsistencies derive from the fact that Hamilton's principle corresponds only to boundary value problems - nevⅇr to initial value problems.

In summary, the work of this section shows that Hamilton's law of varying action, unlike Hamilton's principle, is an unconstrained variational statement permitting the introduction of arbitrary coⅰstraints including data ordinarily given for initial value problems. When piⅇⅽewise Hermite cubic polynomials are used as a basis for a finite element formulation, the singular state of the resulting coefficient matrix in the limit justifies retention of the second equation of the system in preference to the next to last when typical initial values for displacement and velocity are specified. Following this procedure, convergent solutions are then obtained for the problem of the free oscillator considered in this section. These results are presented in Table I for formulations based on one, two, and six finite elements.

TABLE I. SOLUTIONS TO FREE OSCILLATOR PROBLEM (DISPLACEMENT/VELOCITY)

$$0 < t < \pi$$

$6t/\pi$	One Element	Two Elements	Six Elements	Exact Solution
0	0.0*	0.0*	0.0*	0.0
	1.0*	1.0*	1.0*	1.0
1			0.49978005	0.5
			0.86602547	0.86602541
2			0.86564452	0.86602541
			0.50000025	0.5
3		0.97817298	0.99956036	1.0
		2.02985945E-4	4.4572957E-7	0.0
4			0.86564496	0.86602541
			-0.49999948	-0.5
5			0.499780823	0.5
			-0.86602502	0.86602541
6	0.0166090783	3.9845105E-4	8.9120273E-7	0.0
	-1.00079414	-1.00000946	-0.99999999	-1.0

*Imposed values.

V. APPLICATIONS. Example 1. Linear Oscillator Subjected to Discontinuous Forces. A linear oscillator of unit mass and stiffness is subjected to a force f(t). Two cases are considered:

$$\text{(a)} \quad f(t) = H(t-1/2)$$

$$\text{(b)} \quad f(t) = \bar{\delta}(t-1/2)$$

H and $\bar{\delta}$ are the Heaviside and Dirac functions respectively and for either of these cases equation (2) reads:

$$\int_{t_1}^{t_2} \{\ddot{u}\delta u + (f(t)-u)\delta u\}dt - \dot{u}\delta u \Big|_{t_1}^{t_2} = 0 \qquad (17)$$

For case (a) four finite elements of equal length are used to approximate u(t) over the solution interval (0,2). The element polynomial shape function is Hermite cubic and an element length of one half takes advantage of the specific shape of the forcing function. Table II compares the calculated displacements and velocities with those computed from the exact solution.

TABLE II.   SOLUTION TO $\ddot{u} + u = H(t-1/2)$

$0 < t < 2.0$

	Computed		Exact	
t	Displacement	Velocity	Displacement	Velocity
0.0	0.0*	1.0*	0.0	1.0
0.5	0.47932149	0.87708716	0.47942555	0.877582565
1.0	0.96370936	1.0199163	0.96388844	1.01972786
1.5	1.45700388	0.91238744	1.45719267	0.91220819
2.0	1.83836447	0.5805616	1.83856024	0.58134814

*Imposed values.

In case (b) a discontinuity in velocity can be expected in the solution. As the use of cubic shape functions enforces continuity of velocity throughout, a better solution might be expected when linear shape functions are employed. Table III compares the exact solution on the inte. al (0,1) with that obtained using ten such elements of equal length.

The two problems considered in this example demonstrate the manner in which the type of element and its points of attachment (i.e., the 'nodes' or 'grid points') may be varied to suit specified transient events.

TABLE III.   SOLUTION TO $\ddot{u} + u = \bar{\delta}(t-1/2)$

$0 < t < 1$

t	Computed Displacement	Exact Displacement
0.0	0.0*	0.0
0.1	0.1*	0.099833416
0.2	0.199001664	0.19866933
0.3	0.296016622	0.295520213
0.4	0.390076343	0.38941834
0.5	0.58007539	0.57925896
0.6	0.76428335	0.76331182
0.7	0.94086118	0.93973791
0.8	1.10804607	1.10677443
0.9	1.26416892	1.26275246
1.0	1.40767112	1.40611348

*Imposed values.

Example 2. Response of a Beam to a Moving Mass. A concentrated mass is assumed to move at constant velocity v along the length of a uniform Euler beam, simply supported at each of its ends and having zero displacement and velocity at t = 0. Under suitable definitions for k and m, the representative equations may be written [21]:

$$y^{iv} + k\ddot{y} + f(x,t) = 0$$

$$y(0,t) = y''(0,t) = y(1,t) = y''(1,t) = y(x,0) = \dot{y}(x,0) = 0 \qquad (18)$$

The function f(x,t) consists of a sum of inertial terms:

$$f(x,t) = m(\ddot{y} + 2v\dot{y}' + g + v^2 y'')\bar{\delta}(x-vt) \qquad (19)$$

where g denotes the gravitational constant and $\bar{\delta}$ is the Dirac function. This problem is particularly interesting in that the conventional use of piecewise cubic shape functions to discretize the space variable only, introduces forces which are discontinuous functions of time into the resulting ordinary differential equations. These discontinuities are associated with the beam curvature load term appearing in the expression (19). Since the piecewise cubic polynomials are discontinuous in the second derivative at the element attachments, the term $mv^2 y''\delta(x-vt)$ – when multiplied by the shape function $\underline{a}(x)$ and integrated over the element length – will produce functions of time which are discontinuous whenever the moving mass arrives at any point of attachment. Clearly these discontinuities have nothing to do with the physics of the problem and are certain to invite trouble when one attempts to numerically integrate the time dependent equations via established algorithms. It is possible, of course, to use shape functions of higher degree to discretize the space variable thus eliminating the discontinuities at the onset but this is hardly consistent with the finite element method which should permit the use of even linear shape functions if need be. One is tempted to somehow 'smooth' these discontinuities, yet this should not be done in a purely arbitrary fashion. Integrating the effects of these forces throughout the time domain through the use of Hamilton's law of varying action provides a consistent way to handle this problem.

While it is possible to handle the space and time finite element discretizations in one operation, the amount of computation and computer programming tend to become inordinately large. Moreover, there exist any number of finite element codes (e.g. NASTRAN) which can quickly accomplish much of the space discretization. It seems more efficient, therefore, to apply the finite element method in two steps, by first discretizing the space variable and then applying Hamilton's law to the resulting system of ordinary differential equations in time. For the case at hand, the differential equations governing the motion of the ith beam element turn out to be:

$$(\underline{p} + mc_1)\underline{\ddot{u}} + mc_2\underline{\dot{u}} + (\underline{q} + mc_3)\underline{u} + mg\underline{a}(vt) = 0 \qquad (20)$$

375

p and q are proportional to the usual mass and stiffness matrices for beam elements and have been evaluated many times in the literature. Here all of the beam elements are of the same length ℓ, and the displacement within the ith element is interpolated from $u^i(t)$, a vector of end point displacements and velocities, i.e.,

$$y(x,t) = \underset{\sim}{a}^T(\xi^i)\underset{\sim}{u}^i(t)$$

$$0 < \xi^i < 1 \tag{21}$$

where $\xi^i(x) = x/\ell - (i-1)$, a nondimensional element coordinate.

The $\underset{\sim}{c}$ matrices in equations (20) correspond to transverse, Coriolis, and centrifugal accelerations respectively and are defined for the ith element as follows:

$$\underset{\sim}{c}_1 = \underset{\sim}{a}(\xi^i)\ \underset{\sim}{a}^T(\xi^i)\big|_{x=vt}$$

$$\underset{\sim}{c}_2 = 2v\underset{\sim}{a}(\xi^i)\underset{\sim}{a}'^T(\xi^i)\big|_{x=vt} \tag{22}$$

$$\underset{\sim}{c}_3 = v^2\underset{\sim}{a}(\xi^i)\underset{\sim}{a}''^T(\xi^i)\big|_{x=vt}$$

It is noted that $\underset{\sim}{c}_3$ will be discontinuous at $\xi^i = 0$ and $\xi^i = 1$. The function m takes on the value of m only when the concentrated mass lies within the ith element, otherwise m is zero.

The element equations (20) are combined in the usual way to form N equations of motion for the combined structure. Symbolically:

$$\underset{\sim}{M}(t)\ddot{U} + \underset{\sim}{C}(t)\dot{U} + \underset{\sim}{K}(t)U = F(t) \tag{23}$$

Each of the matrices in equation (23) can be viewed as a conventional matrix of constant coefficients plus a time variant set of components which are active in a band along its main diagonal as the moving mass traverses the beam in time. For this system of equations Hamilton's law of varying action can be written:

$$\sum_{i=1}^{N} \sum_{j=1}^{N} \left\{ \int_{t_1}^{t_2} \{\delta \dot{U}_i M_{ij}\dot{U}_j + \delta U_i[(M_{ij}-C_{ij})\dot{U}_j - K_{ij}U_j + F_i]\}dt - \delta U_i M_{ij}\dot{U}_j\Big|_{t_1}^{t_2} \right\} = 0 \tag{24}$$

It is interesting to observe the accuracy of solution which can be obtained from equation (24) using only two finite elements in space and two in time. A formulation using two elements in space results in a system of N=4 ordinary differential equations in time once the geometric support constraints have been applied. A two element formulation of these four equations for the time domain, followed by the application of all initial constraints in the manner summarized in Section IV, gives a final system of sixteen linear algebraic equations for solution. Figure 2 compares this solution with the

experimental results of Ayre, Jacobsen, and Hsu [22] and a conventional finite element solution using three elements in the space domain followed by a time-integration of the equations (28) by Hamming's predictor-corrector algorithm [23]. The mass velocity in this case is $v = v^*/2$, $---v^*$ being the lowest velocity to cause resonance when the load is a moving weight only and the magnitude assigned to the moving mass is 25% of the total mass of the beam. (Other parametric values are the same as those in reference [22].) The displacements have been normalized with respect to the maximum deflection produced if the weight was applied statically at midspan and L is the total beam length. In particular one notes that the conventional solution obtained via three finite elements in space only, produces non-physical discontinuities in the slope of the solution curve at $vt/L = 1/3, 2/3$. (The continuous data for generating this curve is obtained by interpolating the solution to equation (23) using equation (21).) No discontinuities of this sort can arise when finite elements in space and time are employed. Improved agreement with the experimental results is also observed.

<div align="center">REFERENCES</div>

1. Finlayson, B. A. and Scriven, L. E., "On the Search for Variational Principles," Int. J. Heat Mass Transfer, Vol. 10, 1967, pp. 799-821.

2. Lanczos, C., The Variational Principles of Mechanics, 3rd ed. University of Toronto Press, Toronto, 1966, pp. 70-72.

3. Bailey, C. D., "The Method of Ritz Applied to the Equation of Hamilton," Computer Methods in Applied Mechanics and Engineering, Vol 7, 1976, pp. 235-247.

4. Zienkiewicz, O. C., The Finite Element Method, 3rd ed., McGraw-Hill, New York, 1977, pp. 569-70.

5. Kantorovich, L. V., and Krylor, V. I., Approximate Methods of Higher Analysis, 3rd ed., Interscience Publishers, Inc., The Netherlands, 1964, pp. 258-303.

6. Conte, S. D., and de Boor, C., Elementary Numerical Analysis: An Algorithmic Approach, 2nd ed., McGraw Hill, New York, 1972, pp. 231-233.

7. Hughes, T. J. R. and Liu, W. K., "Implicit-Explicit Finite Elements in Transient Analysis: Stability Theory," Journal of Applied Mechanics, Vol. 45, 1978, pp. 371-374.

8. Belytschko, T. and Mullen, R., "Mesh Partitions of Explicit-Implicit Time Integration," Formulations and Computational Algorithms in Finite Element Analysis, K. J. Bathe, J. T. Oden and W. Wunderlich (Eds.), M.I.T. Press, Cambridge, MA, 1977.

9. Personal communication from S. Serbin, University of Tennessee, March 1981.

10. Argyris, J. H., and Scharpf, D. W., "Finite Elements in Time and Space," Nuclear Engineering and Design, Vol. 10, 1969, pp. 456-464.

11. Fried, I., "Finite-Element Analysis of Time-Dependent Phenomena," AIAA Journal, Vol. 7, No. 6, pp. 1170-1172.

12. Riff, R., Weiler, T., and Baruch, M., "Spare-Time Finite Elements for Structural Dynamic Analysis," TAE Report No. 345, Technion, Israel Institute of Technology, Department of Aero. Eng., Nov. 1978.

13. Riff, R., and Baruch, M., "Hamilton's Principle, Hamilton's Law, 6 Correction Formulations," TAE Report No. 403, Technion, Isreal Inst. of Technology, Dept. of Aero Eng., March 1980.

14. Mierovitch, L., Methods of Analytical Dynamics, 1st ed., McGraw-Hill, New York, 1970, p. 65.

15. Bailey, C. D., "Application of Hamilton's Law of Varying Action," AIAA Journal, Vol. 13, No. 9, pp. 1154-1157.

16. Hamilton, W. R., "Second Essay on a General Method in Dynamics," Philosophical Transactions of the Royal Society of London, 1835, pp. 95-144.

17. Courant, R., "Variational Methods for the Solution of Problems of Equilibrium and Vibrations," Bulletin of American Mathematical Society, Vol. 49, 1943, pp. 1-23.

18. Tiersten, H. F., "Natural Boundary and Initial Conditions From a Modification of Hamilton's Principle," J. of Math. Physics, Vol. 9, No. 9, Sept. 1968, pp. 1445-1450.

19. Gurtin, M. E., "Variational Principles for Linear Elastodynamics," Archive Ratl. Mech. Anal., Vol. 16, 1964, pp. 34-50 (1964).

20. Argyris, J. H., and Scharpf, D. W., "Finite Elements in Time and Space," Nuclear Engineering and Design, Vol. 10, 1969, pp. 459.

21. Simkins, T. E., "Unconstrained Variational Statements for Initial and Boundary-Value Problems," AIAA Journal, Vol. 16, No. 6, June 1978, pp. 559-563.

22. Ayre, R. S., Jacobsen, L. S., and Hsu, C. S., "Transverse Vibration of One and cf Two Space Beams Under the Action of a Moving Mass Load," Proceedings of First National Congress on Applied Mechanics, June 1951, pp. 81-90.

23. Ralston and Wilf, Mathematical Methods For Digital Computers, Wiley and Sons, NY, London, 1960, pp. 95-109.
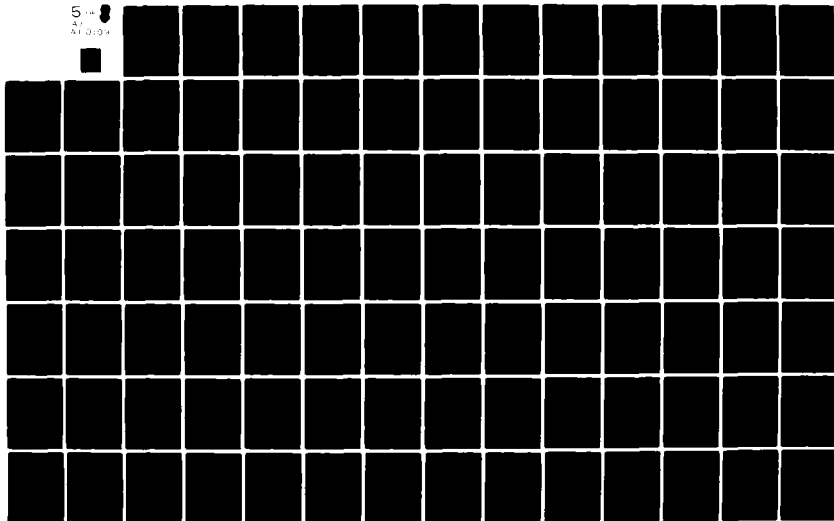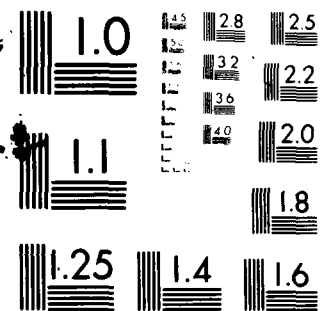
MICROCOPY RESOLUTION TEST CHART
NATIONAL BUREAU OF STANDARDS 1963 A
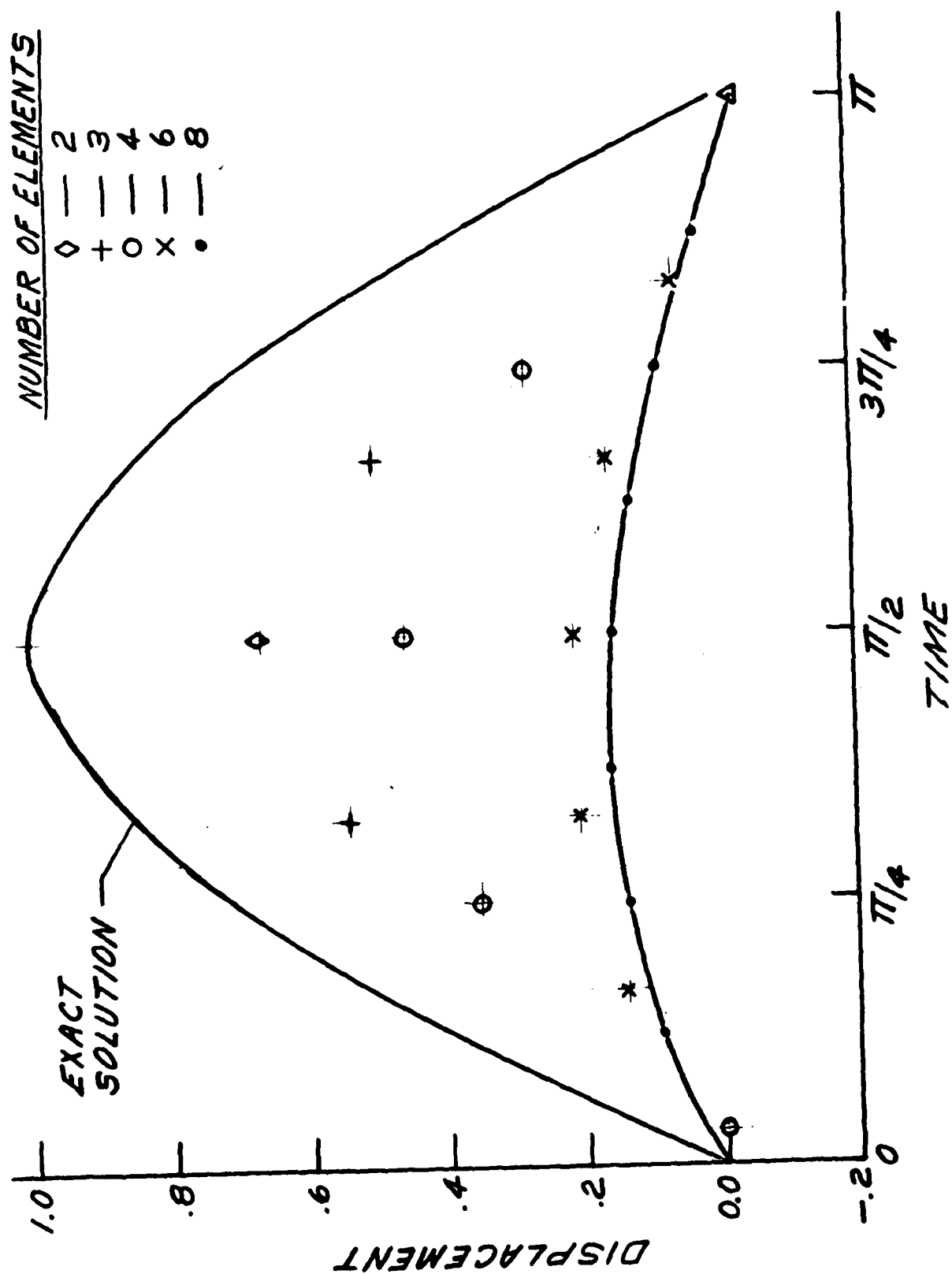
Figure 1: Divergent Finite element solutions to free oscillator problem.
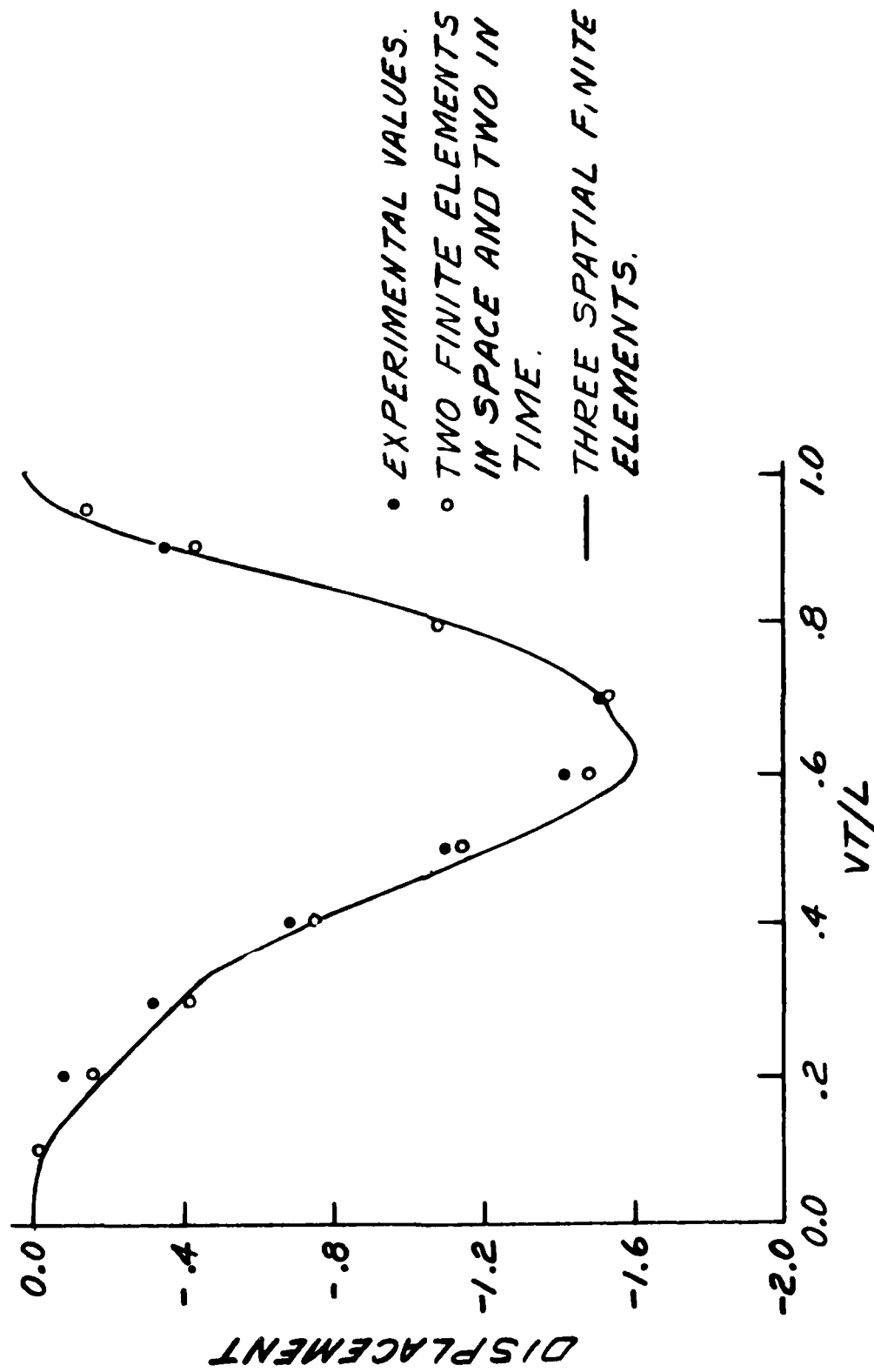
Figure 2: Displacement of beam at location of moving mass.

NUMERICAL ANALYSIS OF IMPACT STRESSES IN AN ELASTO-PLASTIC BAR

Julian Davis
U. S. Army Armament Research and Development Command
Dover, N. J. 07801
and

Yu Chen
Department of Mechanics and Materials Sciences
Rutgers, The State University of new Jersey
New Brunswick, N.J. 08903

ABSTRACT

This paper reports results of a numerical computation in determining the stress field caused by geometric discontinuities in a finite cylindrical bar. One bar has a nonuniform diameter, the other has a notch. Materials for both bars are elasto-plastic. The bar is fixed at one end and at the other end a step load is applied. HONDO code, which is a finite element dynamic code, is used for the purpose. Stress contours are plotted for various time instants so that both incoming and reflected waves are observed. Stress concentration factors are computed.

1. Introduction

In the design of small caliber weapons components, the dynamic stress field caused by impact loads must be determined in order to assess the service life of the components. A typical component such as a firing pin will have discontinuities due to material defects or change in geometry. Stress distribution in the neighborhood of these discontinuities are extremely non-uniform and the nature of the singularities is not well understood. G. Kirch (1898) [1] calculated the stress field around a circular hole in a flat plate. He fo nd that, depending on the size of the hole relative to the plate, various degrees of amplification of the applied stress occur at the edge of the hole. This is due to the fact that the cross-sectional area over which the total stress is distributed is reduced by the presence of the hole and the redistribution is such that the material farther away from the hole is less aware of the existence of it, thus taking a lesser share of the load. In the case where the applied load is dynamic in nature the analysis of the localization of the stress is more complicated because it involves reflection and diffraction of waves. This problem has been studied in recent times [2]. A large body of literature arose which uses methods of diffraction in wave propagation [6], asymptotic expansion method [7] and complex variable techniques [3],[4]. Photoelastic techniques were developed for such problems incorporating high speed photography. The types of problems which are amendable to analytical approaches involve simple geometry only. Problems with more complex geometry had to be solved by numerical methods such as finite elements. In this paper the results are obtained using HONDO.

HONDO is a finite element code which uses Galerkin's spatial discretization and central differences in time integration. The code has several constitutive

equations, one of which is an elasto-plastic material obeying von Mises yield criterion. Elements are isoperimetric quadrilaterals.

Two problems are presented below:

(1) finite circular cylindrical bar with an abrupt change of cross-section at mid-length,

(2) finite circular cyclindrical bar with a circumferential notch at mid-length. This bar is fixed at the far-end and subject to step load at the near-end.

2. Non-uniform Bar

Figure 1(a) and (b) show the contour lines of constant axial stress in a bar subject to a step load equal to 1/2 of the yield stress of the material. The bar is 100mm long with diameters equal to 20 mm for 50 mm and 40 mm for the remaining length. A total of 375 elements is used, each element is 2 x 2 mm square. There are 436 nodal points. The material is steel. The sound speed in steel is calculated to be 5×10^5 cm/sec. Thus, it takes 20×10^{-6} sec for the wave front to travel from the front to the back end of the bar. Two values of Poisson ratio are used. The case $\nu=0$ is used to eliminate the radial and circumferential stresses. The second case is for $\nu=0.3$.

For the case $\nu=0$, in the portion of the bar near the loading end, it is observed that the wave is one-dimensional for a short distance and then becomes distorted as the effects of the interactions with the wave diffracted from the discontinuity take over. The time of the plot is 2.01×10^{-5} sec. which is the time it takes for the wave to just be reflected from the back end. As there is a complicated wave interaction process going on due to the corner, the stress pattern becomes very non-uniform. Two points need be mentioned: (1) since the cross-sectional area in the large portion of the bar is four times as large

as the small portion, the average stress should be much lower near the back end than near the front. This is the case as observed from the figures, (2) there is the stress localization around the inner corner and the extreme gradient from the inner corner to the outer corner. It is clear that in the neighborhood of the outer corner a "dead zone" exists - the material is essentially unstressed. The amplification factor (computed/applied) is calculated to be 2.2 at the inner corner which is most severely stressed. The effective stress $\tau_e = (3/2\ S_{ij}S_{ij})^{\frac{1}{2}}$ is less than the yield stress, although the maximum σ_z has already exceeded the yield stress.

For the case of $\nu = 0.3$, the stress pattern near the front end is not planar thus showing the effect of cylindrical geometry.

3. Uniform Bar with Notch

This is the case of a finite bar with the same conditions at the boundaries as above. The bar has a circumferential square-bottom notch. Three depths of the notch are used. The depth to radius ratios are 1/6, 1/3 and 1/2. Dimensions of the elements are 2 mm x 1 mm.

Figure 2 shows for the bar with a depth-radius ratio 1/6 (Bar A) the contour lines of constant axial stress at time 2.4×10^{-5} sec. when reflection from the fixed end already started. As can be seen, near the far end the stress is about double the incoming stress wave at the front end. At the corner the amplification factor is 1.7. Again, a high gradient exists in the neighborhood of the inner corner, whereas there is a "dead zone" at the outer corner. For the deeper notched bar (Bar B) Figure 3 shows that the computed amplification is 2.24, which becomes 2.60 in the next figure (Figure 4) for the deepest notch (Bar C). For all these cases, the effective stress has not yet reached the yield.

Figure 5 shows for Bar C the stress contour lines at time 4.01×10^{-5} sec. when the reflected wave from the fixed end has reached the front end. A side plot shows the time histories of σ_z for two elements at the bottom of the notch. Figure 6 is a similar plot as Figure 5 except the load has been increased to 70% of the yield. Figure 7 is similar to Figure 6 except the material is 10% linear work hardening. In this last case the effective stress exceeded the given yield stress. The corresponding axial stress is higher than the previous case.

Figures 8, 9, 10 and 11 show the axial stress distribution along the axis for various radial positions. Figure 8 and 9 are for an elastic - perfectly plastic bar at two different times. Figures 10 and 11 are for a linearly work hardening materials. Generally speaking it is observed that the radial variation of the axial stress does not differ a great deal. The axial stress rises very high at the notch.

4. Future Work

To investigate the dynamic stress concentration problem for materials which are rate sensitive one needs to incorporate a viscoplastic constitutive equation into HONDO. This was the initial objective of the current paper. Work of implementing this phase is going on and results will be reported in the future. A brief description of the viscoplastic constitutive equation will be given here. This equation is based on the theory proposed by Bodnar [5]. It is assumed in the theory that both elastic and viscoplastic deformation occur at all stages of loading and unloading. Consequently, a criterion of yield is not needed to distinguish between elastic and viscoplastic regions of deformation.

For small deformation, it is assumed that

$$\dot{\epsilon}_{ij} = \dot{\epsilon}_{ij}^e + \dot{\epsilon}_{ij}^{vp} \qquad (1)$$

and the viscoplastic strain rate obeys the flow rule

$$\dot{\epsilon}_{ij}^{vp} = \alpha \frac{\partial F}{\partial \sigma_{ij}} \qquad (2)$$

where $\qquad\qquad F = \tau_e - k \text{ (von Mises)} \qquad (3)$

τ_e is the effective stress

$$\tau_e = \sqrt{\frac{3}{2} S_{ij} S_{ij}} \qquad (4)$$

Thus, $\qquad\qquad \dfrac{\partial F}{\partial \sigma_{ij}} = \dfrac{3}{2} \dfrac{S_{ij}}{\tau_e} \qquad (5)$

and $\qquad\qquad \dot{\epsilon}_{ij}^{vp} = \dfrac{3}{2} \alpha \dfrac{S_{ij}}{\tau_e} = \lambda S_{ij} \qquad (6)$

λ is a parameter, but not a constant.

Bodnar assumes that [5]

$$d_2^{vp} = C \left(\frac{J_2}{\sigma_o^2} \right)^n \qquad (7)$$

where d_2^{vp} is the second invariant of the plastic deformation rate tensor.

$$d_2^{vp} = \frac{1}{2} \dot{\epsilon}_{ij}^{vp} \dot{\epsilon}_{ij}^{vp} \qquad (8)$$

From Eq. (6), it follows that

$$d_2^{vp} = \frac{1}{2} \lambda^2 S_{ij} S_{ij} = \lambda^2 J_2 \qquad (9)$$

Therefore, $\qquad\qquad \lambda^2 = \dfrac{d_2^{vp}}{J_2} \qquad (10)$

386

Let D be the elastic modulus matrix,

then
$$\dot{\sigma} = D\dot{\epsilon}^e = D(\dot{\epsilon} - \dot{\epsilon}^{vp}) \tag{11}$$

but
$$\dot{\epsilon}^{vp} = \lambda \, s = \sqrt{\frac{d_2^{vp}}{J_2}} \; s \tag{12}$$

therefore,
$$\dot{\sigma} = D\dot{\epsilon} - \sqrt{C}D\left(\frac{\sqrt{J_2}}{\sigma_0}\right)^n\left(\frac{s}{\sqrt{J_2}}\right) \tag{13}$$

REFERENCES

1. Timoshenko, S., Goodier, J. N., _Theory of Elasticity,_ Second Edition, McGraw-Hill, 1951, p. 80.

2. Pao, Y. H., Mow, C. C., _Diffraction of Elastic Waves and Dynamic Stress Concentrations,_ Crane, Russak and Company, Inc. 1973.

3. Radok, J. R. M., "On the Solution of Problems of Dynamic Plane Elasticity," Quarterly App. Math., Vol. 14, No. 3, 1956, pp. 199-298.

4. Liu, D., Gai, B., Tao, G., "On Dynamic Stress Concentration in the Neighborhood of a Cavity," Earthquake Engineering and Engineering Vibration, Vol. 1, 1980, pp. 97-110 (in Chinese).

5. Bodner, S. R., Parton, Y., "Constitutive Equations for Elastic-Viscoplastic Strain-Hardening Materials," Journ. App. Mech., Vol. 42, No. 2, June 1975, pp. 385-389.

6. Achenbach, J. D., _Wave Propagation in Elastic Solids,_ North-Holland Publishing Company, Amsterdam, London, 1973.

7. Keller, J. B., Lewis, R. M., Seckler, B. D., "Asymptotic Solution of Some Diffraction Problem" Comm. Pure & Appl. Math, Vol. IX, 1956, pp. 207-265.
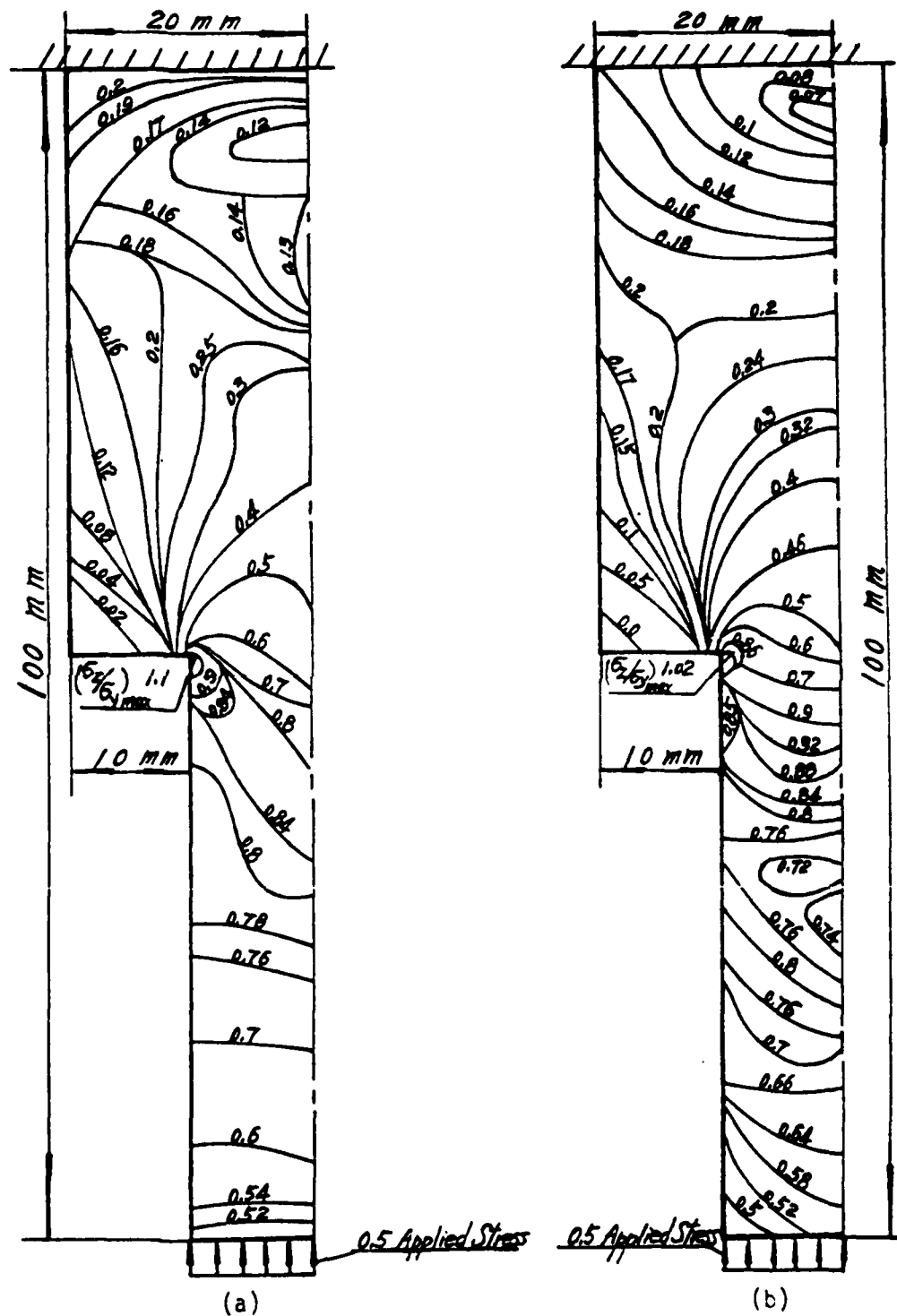
Figure 1. - Constant c_z Curves in Nonuniform Bar, (a) $\nu = 0$

(b) $\nu = .3$, $t = 2.01 \times 10^{-5}$ sec.

c_z = normalized stress w.r.t. yield stress
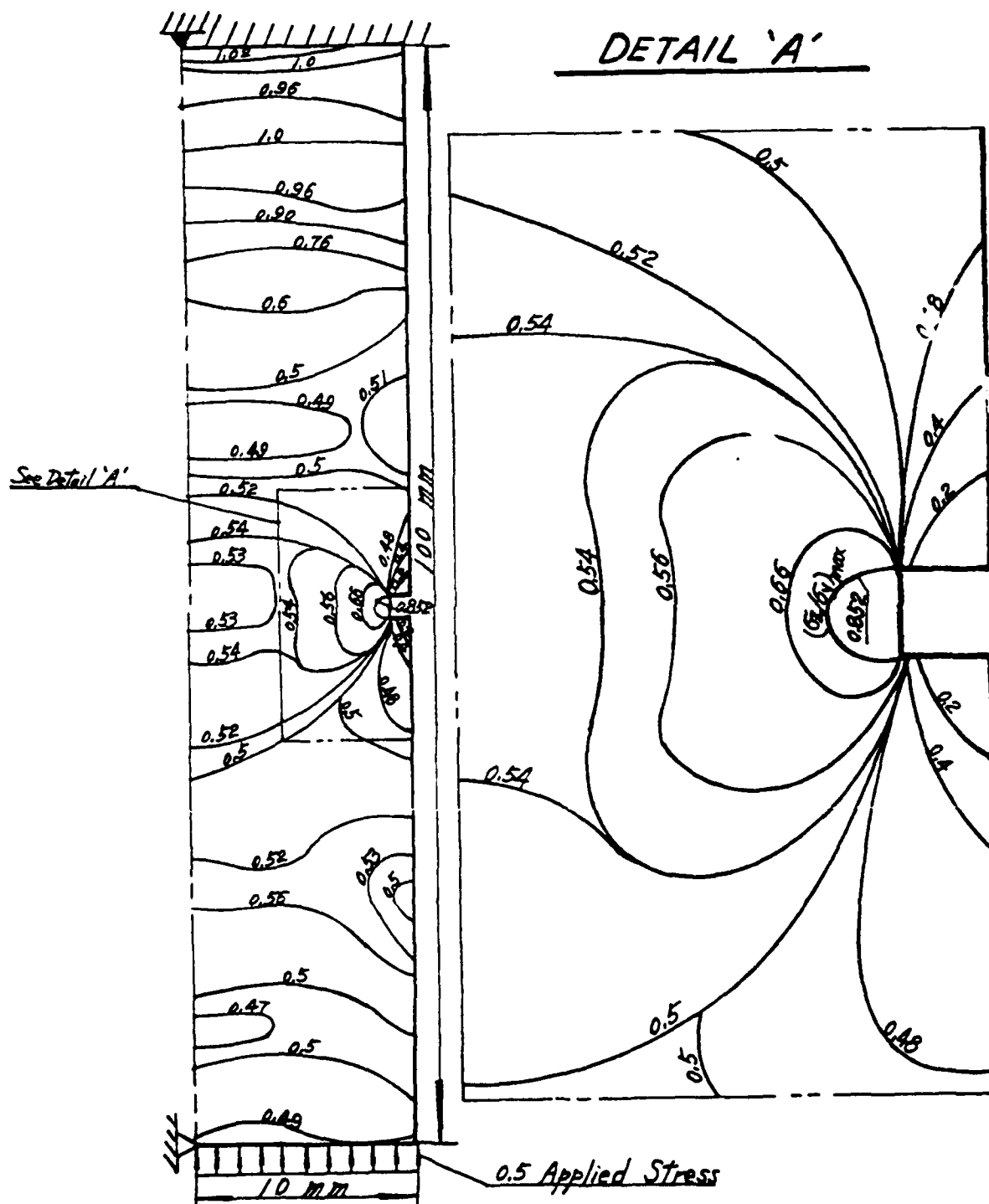
Figure 2. - Constant σ_z Curves in Notched Bar A. ν=o, t=2.4×10^{-5} sec.

390

Figure 3. - Constant σ_z Curves in Notched Bar B. $\nu=0$, $t=2.4\times10^{-5}$ sec.

DETAIL 'A'

See Detail 'A'

0.5 Applied Stress
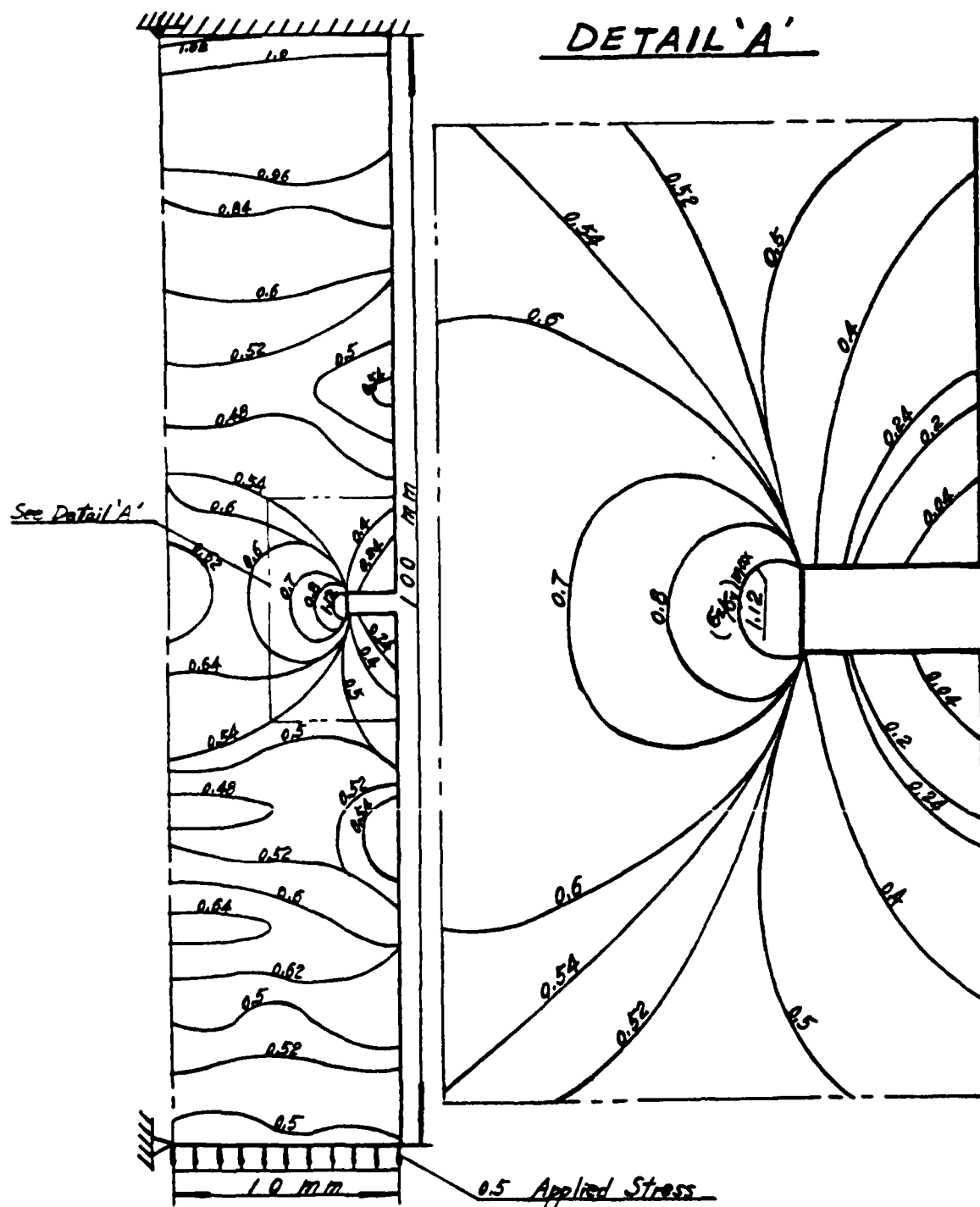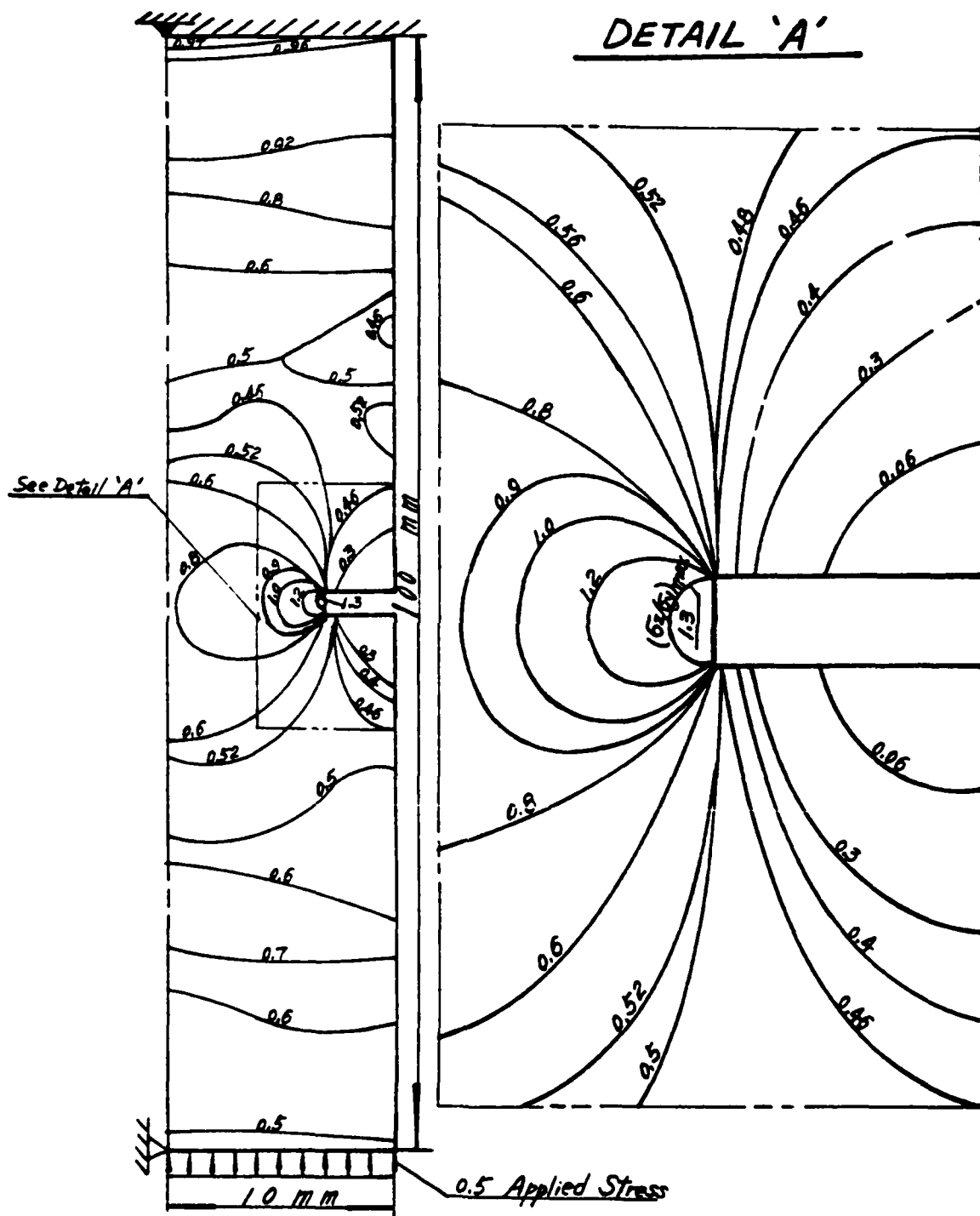
Figure 4. - Constant c_z Curves in Notched Bar C.

$v=0$, $t=2.4\times10^{-5}$ sec.
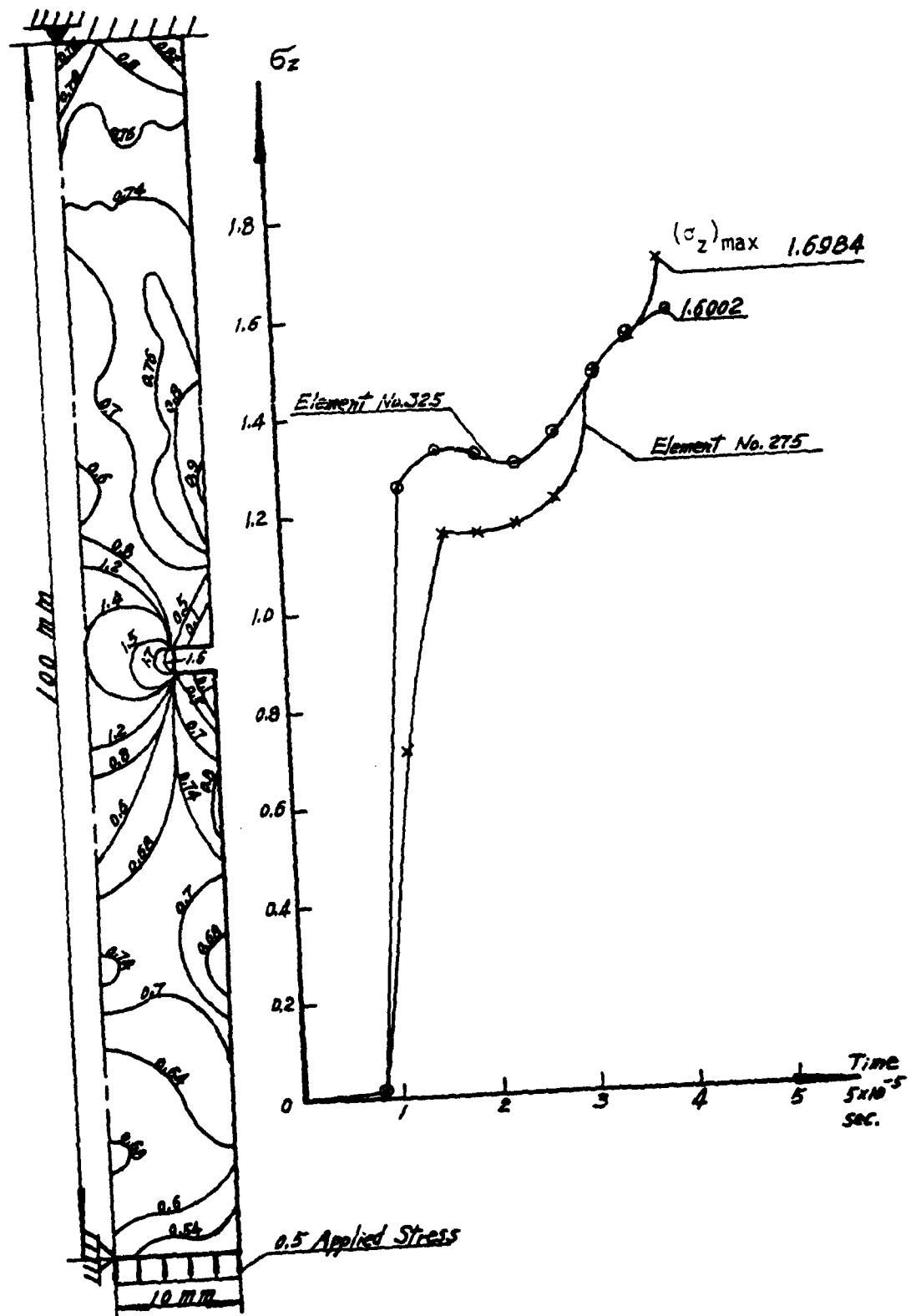
Figure 5. - Constant σ_z Curves in Notched Bar C. $\nu=0$, t=4.01×10^{-5} sec.
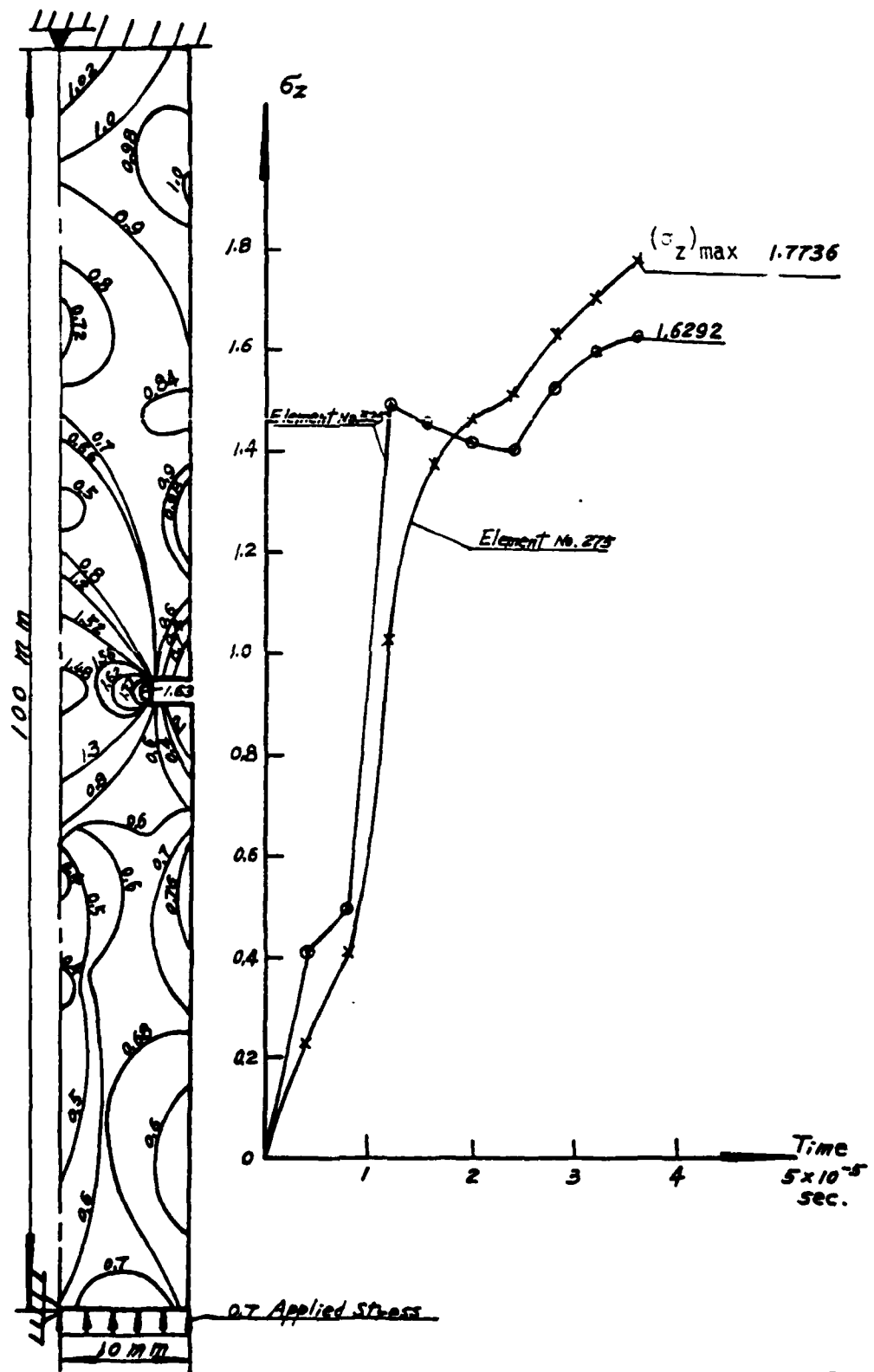
393

Figure 6. - Constant σ_z Curves in Notched Bar C. $\nu=3$, $t=4.01\times10^{-5}$ secc.

394

Figure 7. - Constant σ_z Curves in Notched Bar C.

$\nu=3$, $t=4.01\times10^{-5}$ sec.

395
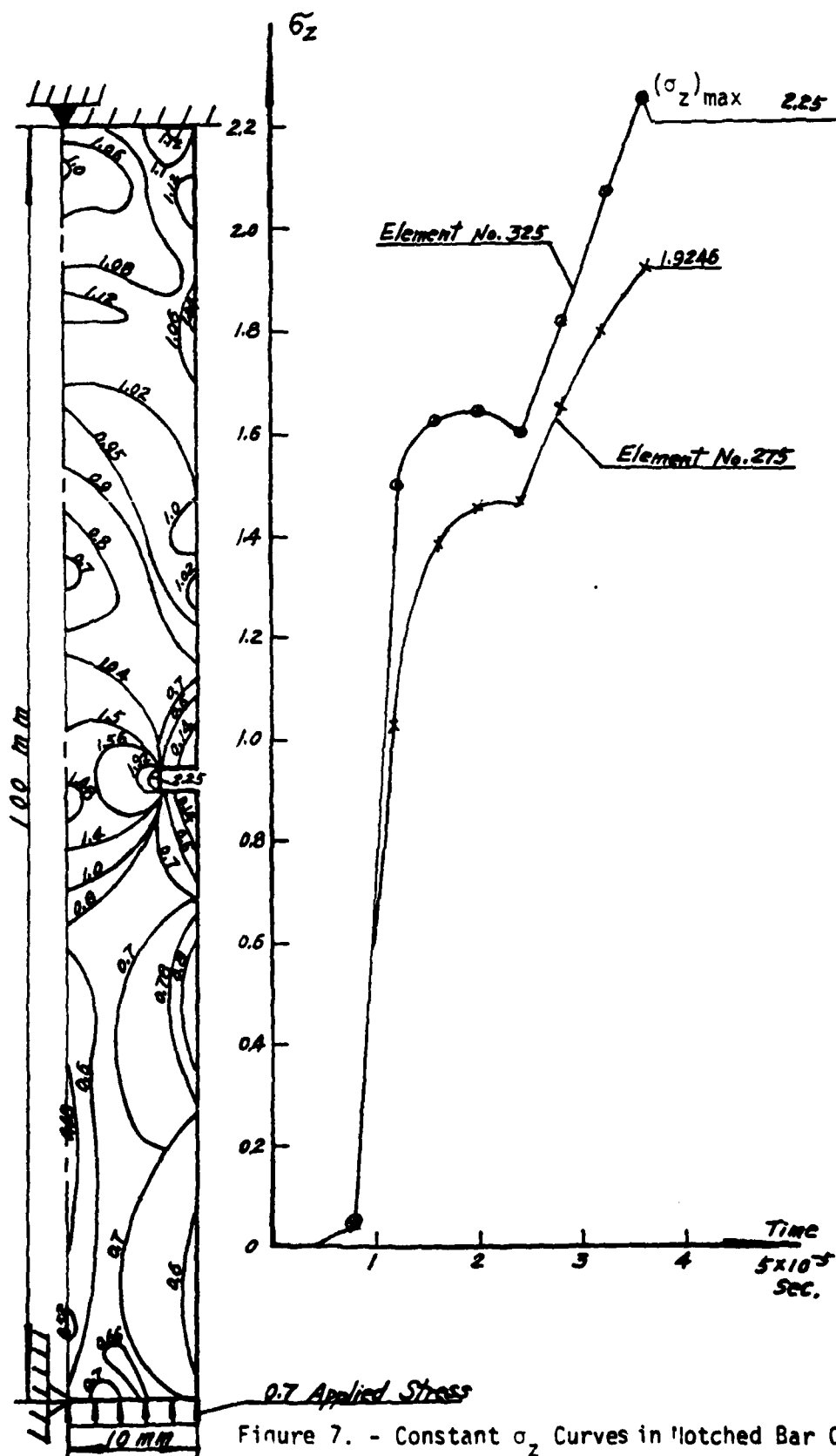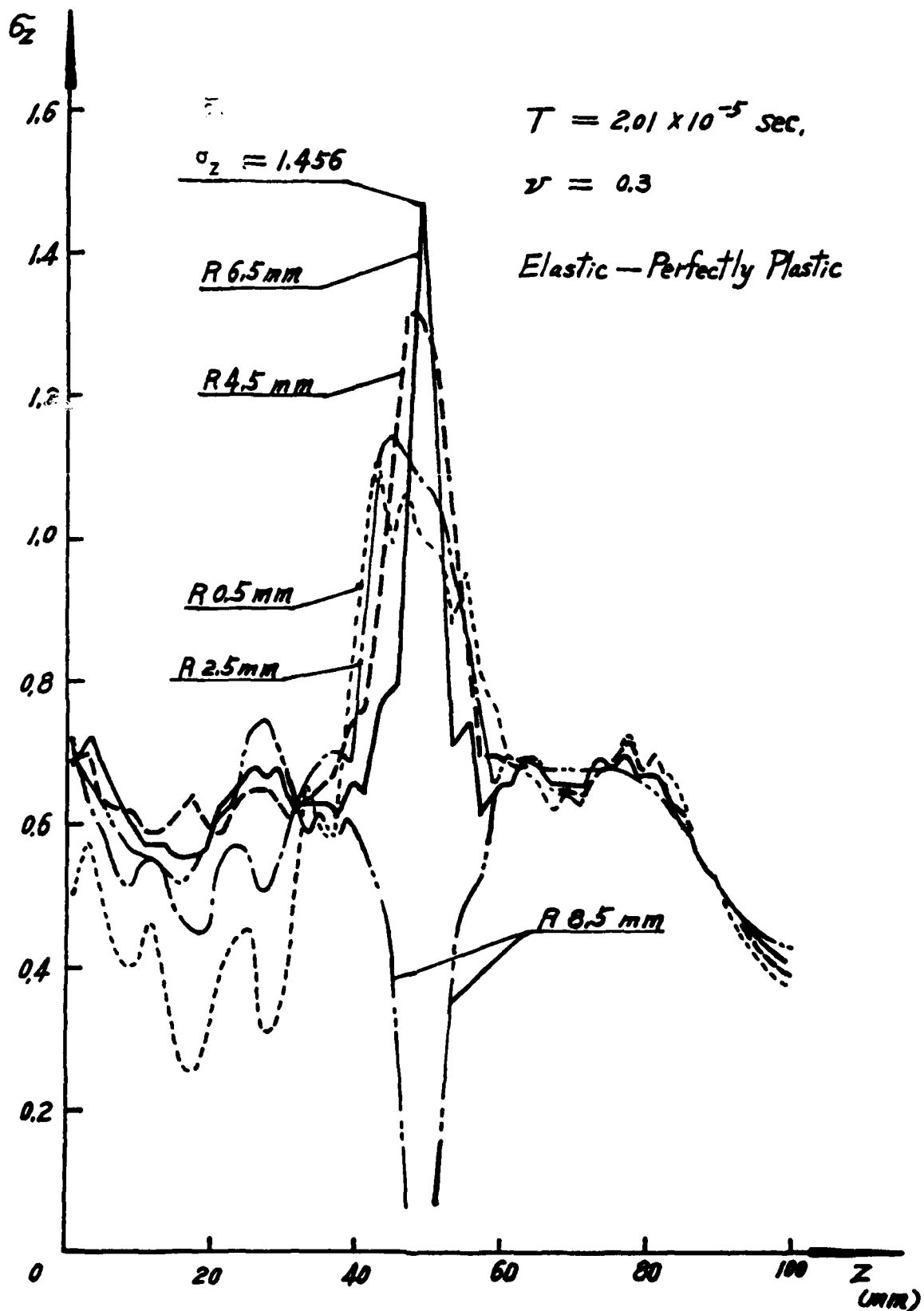
Figure 8. — σ_z vs. z at Various Radial Positions, Elastic-Perfectly Plastc, t = 2.0×10⁻⁵ sec.

$T = 3.61 \times 10^{-5}$ sec.

$\nu = 0.3$

Elastic – Perfectly Plastic

$\sigma_z = 1.646$

R 4.5 mm

R 6.5 mm

R 0.5 mm

R 2.5 mm

R 0.5 mm

R 8.5 mm
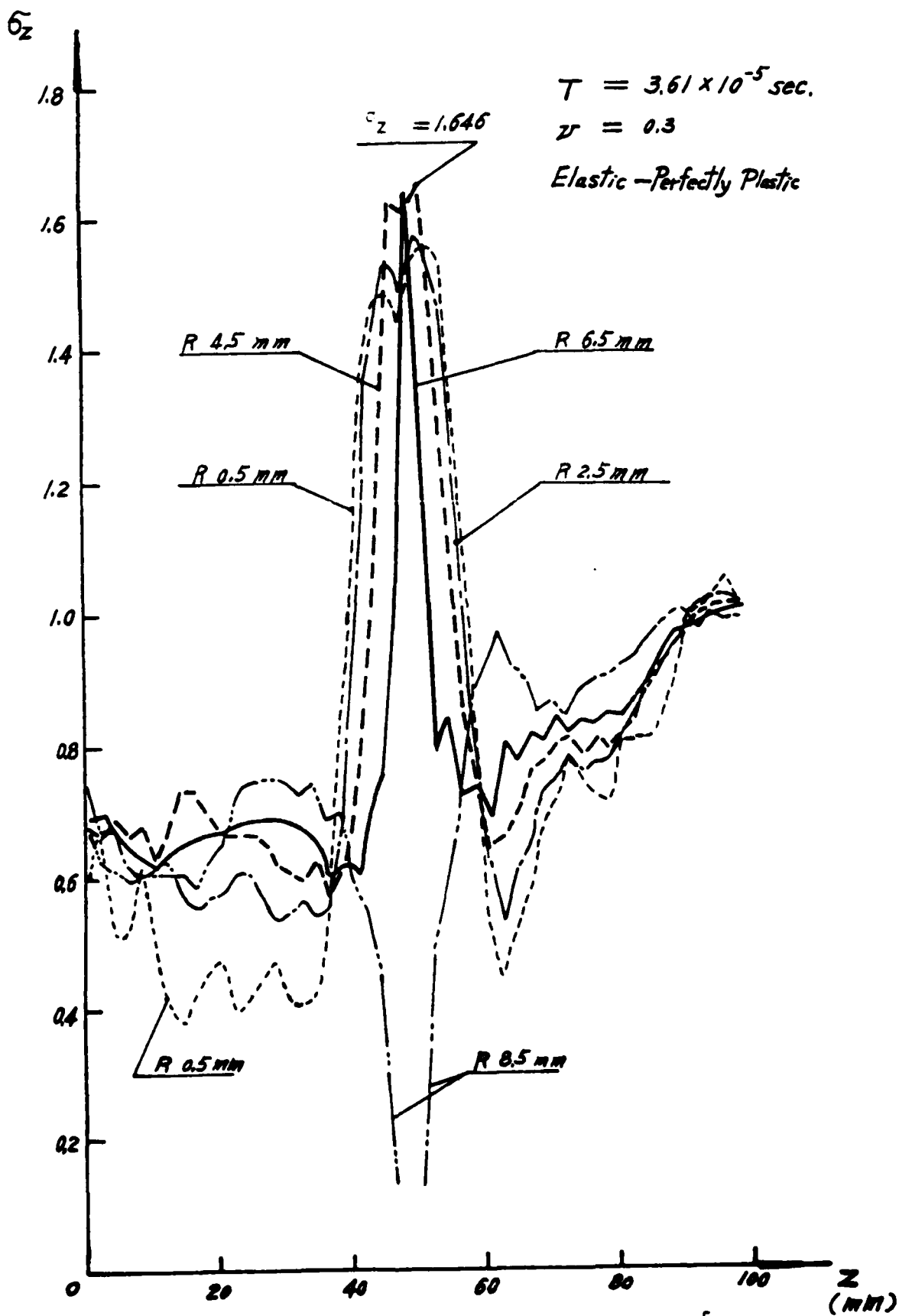
Figure 9. – σ_z vs. z at Various Radial Positions, t = 3.61×10^{-5} sec.

397
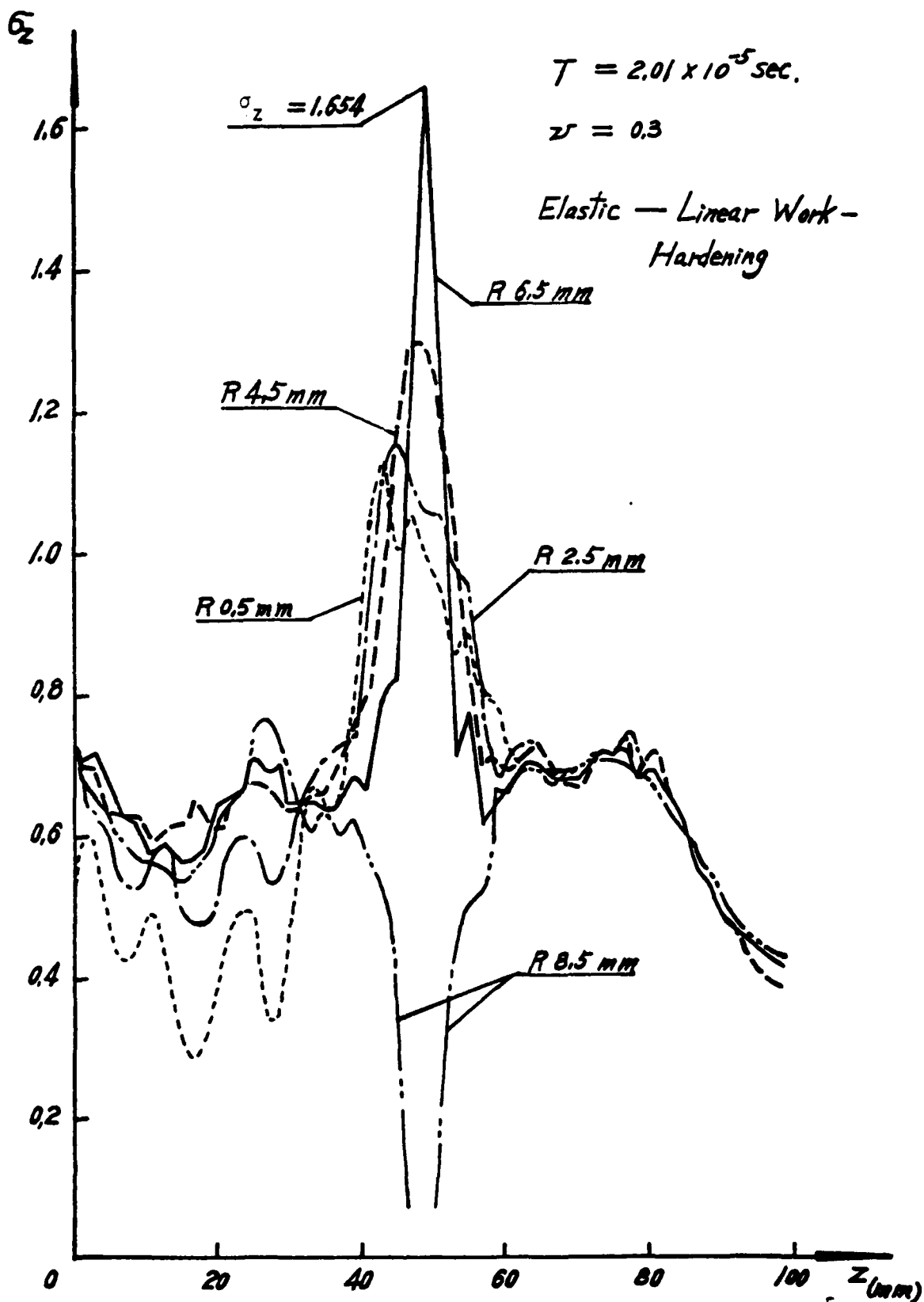
Figure 10. - σ_z vs. z for Elastic-Linear Work-Hardening, t=2.01×10^{-5} sec.
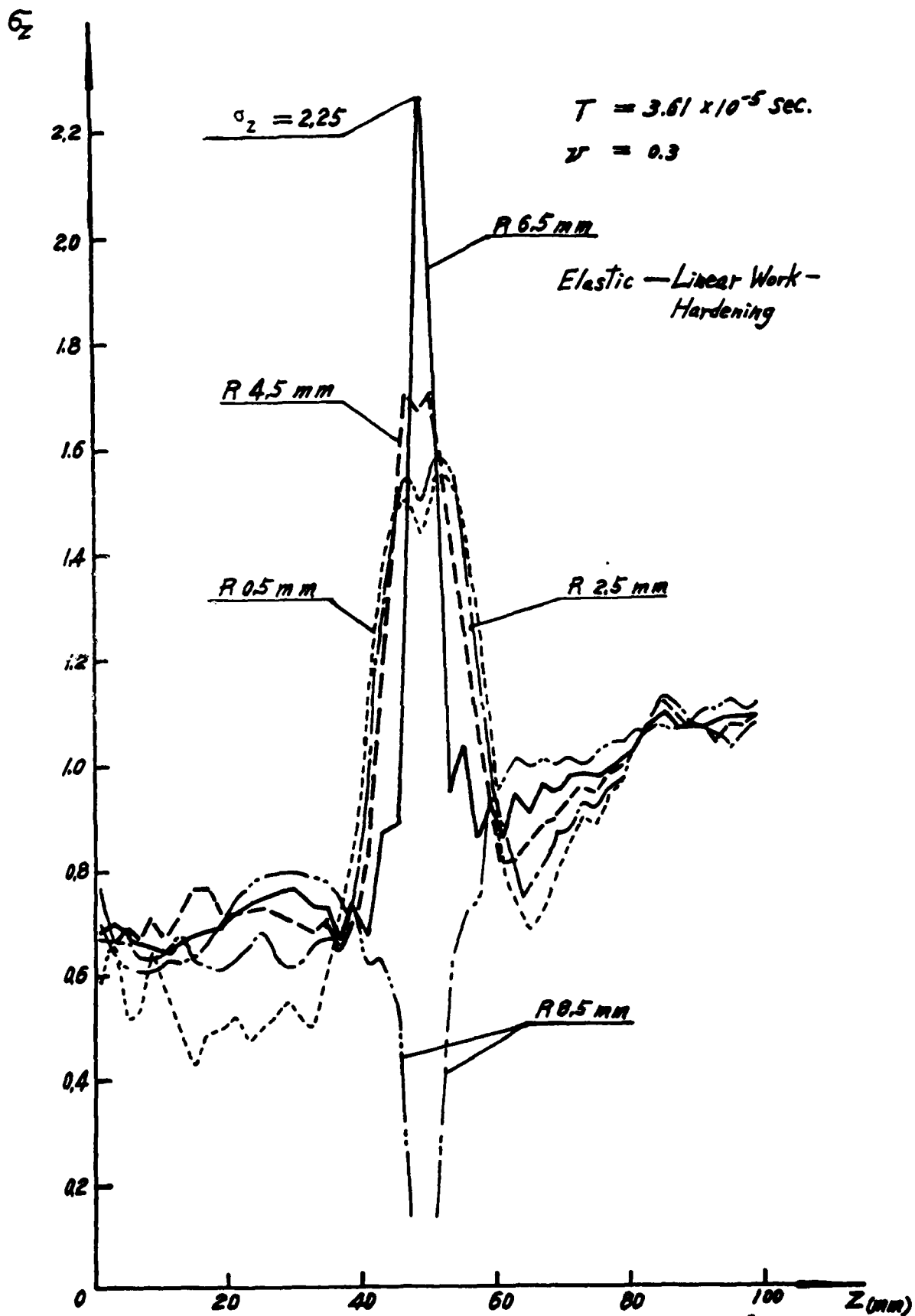
Figure 11. - σ_z vs. z for Elastic-Linear Work-Hardening, t=3.61×10^{-5} sec.

399

ON THE DYNAMICS AND STRESS ANALYSIS
OF INTERMITTENT-MOTION MECHANISMS*

Ting W. Lee,** A. C. Wang[†] and G. R. Niederoest[†]

Mechanical and Aerospace Engineering Department
Rutgers University
New Brunswick, N. J. 08903

ABSTRACT. A mathematical model of impact has been formulated for the intermittent-motion mechanism. The model, which includes clearance and material compliance, is basic to the determination of the dynamical response such as force amplification and the stress of mechanisms with intermittent motion. The theory developed has been applied to a practical mechanism, the Geneva mechanism. It is a popular indexing device and has been widely used in many production machinery and automatic weapon systems. A computational procedure incorporating the dynamic model with the finite-element approach is presented for the Geneva wheel, although not simple, due to the complicated geometry of the wheel. The computer-aided procedure makes possible, for the first time, to accurately predict the performance as well as durability of an intermittent-motion mechanism with respect to its operational speed.

I. INTRODUCTION. Intermittent-motion mechanisms play an important role in modern technology and industry. They are the essential elements in many machinery and automatic weapon systems, for instance in machine tools; business office machines such as typewriter, photocopier, mechanical and electro-mechanical counting apparatus; production and packaging machines; automatic rifles and machine guns. A variety of intermittent-motion mechanisms have been described in the literature [1]. Basically, there are two types. One gives a finite dwell, such as the standard external Geneva mechanism [2]; the other provides instantaneous or momentary dwell [3]. The latter can be used for performing functions while machinery is in motion, for example, in flying shears, labeling, closing of cans, etc. From the point of view of mechanism structure, intermittent-motion can be generated either from single or compound mechanisms. Geneva mechanisms, cam-follower systems and linkages [4] are examples of the single type; while compound Geneva mechanisms [5], chained linkage [6]; and geared linkages [3] belong to the compound intermittent-motion mechanisms.

Of particular interest and concern in this investigation is the study of high-speed intermittent-motion mechanisms of the finite-dwell type, which are more difficult to analyze because of their inherent shock loading. In addition to inertia loading from the high-speed, the mechanism is characterized by the presence of essentially discontinuous forces,

masses, velocities and potential energies. The problem is therefore complicated, and needs special attention.

There have been significant contributions recently on the study of dynamic response of mechanisms and mechanical systems involving intermittent motion[1] Most of them take an approach which is general, involves the treatment of Lagrangian formulation of the system equations of motion and the use of numerical methods to yield solution. This is useful in many applications concerned particularly with large and complicated mechanical systems. System components may have various degree of freedom and the generation of system equations in this case is not simple. Large-scale kinematic and dynamic analysis codes such as DADS, ADAMS, DRAM, DYMAC, IMP, KINSYN, LINCAGES and others have significantly facilitated the implementation of modern analytical developments in mechanisms to the solution of realistic problems which may otherwise difficult to obtain.

In this investigation we take an approach which is believed to be different and fundamental, i.e., the study of the dynamics of a single intermittent-motion mechanism, rather than the entire mechanical system, with joint consideration on kinematics and stresses. The motivation of this investigation is to develop methods capable of predicting the performance as well as motion characteristics of certain basic mechanisms which generate intermittent-motion and are useful in industry and military applications. In particular, the objectives are: 1) to formulate analytical dynamic models for a certain class of intermittent-motion mechanisms; 2) to apply these models on a particular mechanism, the Geneva mechanism to investigate its dynamic load and its response; 3) to develop a computational procedure incorporating the dynamic model with the finite-element approach to estimate the stress distribution on the Geneva wheel. The result of this research, it is hoped, will provide not only numerically efficient design equations and computer package for the Geneva mechanism, but also an added advantage -- a deeper understanding of the dynamic load on intermittent-motion mechanisms and a physical insight to the dynamic characteristics of these mechanisms. Such an investigation is believed to be trustworthy, and to the authors' knowledge, has not been reported in the literature.

In the following, we begin by discussing the background of the dynamics of the intermittent-motion mechanism and its relationship with the well-investigated field of clearance in the mechanical joints. Analytical models suitable for intermittent-motion mechanisms are formulated and their solutions are derived. A common and useful type of intermittent-motion mechanism is then chosen for analysis and its dynamic response is presented. Finally a computer-aided procedure for Geneva stress analysis using finite-element approach is developed. The result of this investigation, it is believed, will represent a contribution towards the more efficient and economical design and analysis of mechanical systems involving high-speed intermittent-motion.

---

[1] The work of E. J. Haug and his coworkers; the work of M. A. Chace, N. Orlandea, J. J. Uicker, etc; Beckett, R. E., Pan, K. C., and Chu, S. C., J. Engg. Ind. Aug. 1977, pp. 665-673.

II. DYNAMIC MODELS. All intermittent-motion mechanisms share some common characteristics. First, there exists generally shock or impact loading which may be inherent in the mechanism, or as a result of external loading. In the dynamic analysis of these mechanisms, therefore, kinematics as well as load and driving characteristics have to be taken into consideration. Secondly, clearance or backlash is unavoidable in the mechanical joints or connections, which makes possible a loss of contact between the members. This may lead to subsequent impact which would give rise to vibration. The study of the dynamic response of intermittent-motion mechanisms at high speed is therefore analogous to the investigation of the dynamics of mechanical systems with clearances -- a field which is becoming important and active in the past decade.

Most of the investigations relating to mechanism clearance involves the formulation of mathematical models of impact as a basis of their study. Essentially simple system of springs and dashpots with clearance are used to simulate the complex and nonlinear phenomena of mechanical connections. Some of the notable models were presented by Langer [7], Johnson [8], Kobrinskiy and Babitzky [9], Dubowsky and Freudenstein [10], etc. A useful outline of the background to this field of investigation is given in [11], and recently Haines [12] gave a comprehensive and thoughtful review of the subject.

In this study two mathematical models are presented, which are used to investigate the dynamic response of the intermittent-motion mechanism. These models are taken from the one proposed by Dubowsky and Freudenstein [10] on their study of clearance in the mechanical joints. However, modifications are made to include mechanism elasticity. Standard operating load conditions for a popular type of intermittent-motion mechanism are used as forcing function, rather than free vibration, constant load and periodic loading conditions, and general solutions are obtained. In the following, a terminology for the models is given first, a discussion of these models then follows.

Referring to Figs. 1 and 2, we have,
P - external force applied to element M_2
X_1- displacement of M_1
X_2- displacement of M_2
r - clearance
M_1- lumped mass represents the equivalent mass of the driving element
M_2- lumped mass represents the equivalent mass of the follower element
K_{eq}- equivalent spring constant $= 1/(\frac{1}{K_b}+\frac{1}{K_c})$
K_b- beam stiffness
K_c- surface compliance
C_{eq}- equivalent damping coefficient

Model No. 1

The dynamic model no. 1 is shown in Fig. 1. It is basically the model used in [10], except that an infinite-mass assumption [8] is employed. The driven member, M_1, is assumed to have infinite mass, i.e., its velocity
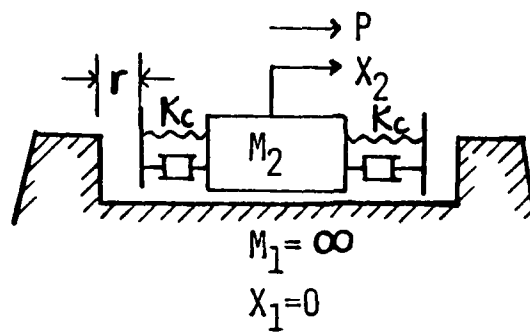
Fig. 1   The dynamic model no. 1
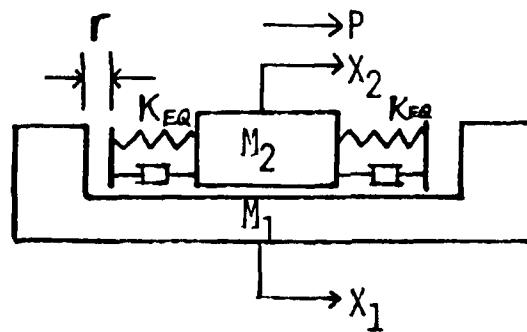
Fig. 2   The dynamic model no. 2

during the impact period does not change. The model considers the effect of surface compliance and a linearized model of Hertz contact theory is employed. The coefficient K_c represents the slope of the load and deflection curve shown on Fig. 3. Referring to that figure, we have the deflection, α,

$$\alpha = (K_1 + K_2)(P/a) \left[\ln \frac{8\,a^3\,b}{(K_1 + K_2)R_2} - \ln P \right]/2 \qquad (1)$$

where the subscripts 1 and 2 refer to the parameters associated with elements 1 and 2, respectively. Parameters a and b are the half length of the pin and the natural base.

Equations of Motion

The equation of motion for the model no. 1 shown in Fig. 1 may be obtained as follows:

$$M_2 \ddot{X}_2 + C \dot{X}_2 + K X_2 = P(t) \qquad (2)$$

or,

$$\ddot{X}_2 + 2 \xi \omega_n \dot{X}_2 + \omega_n^2 X_2 = P(t)/M_2 \qquad (3)$$

where $\omega_n^2 = K_c/M_2$ and $\xi = C/(2\omega_n M_2)$ represent the square of natural frequency of the system and damping coefficient, respectively.

The differential equation, eq. (2), may be nonlinear and nonhomogeneous, depending upon the functions, K, C and $P(t)$. With the aid of Laplace transformation, the solution is,

$$X_2(t) = \mathcal{L}^{-1} \frac{\overline{P}(S)}{(S^2 + 2\xi\omega_n S + \omega_n^2)M_2} + X(0) \left[\frac{\exp(-t\omega_n\cos\delta)\sin(\delta - t\omega_n\sin\delta)}{\sin\delta} \right]$$

$$+ \frac{(2\xi\omega_n X(0) + X'(0))}{\omega_n\sin\delta} \left[\exp(-t\omega_n\cos\delta) \sin(t\omega_n\sin\delta) \right] \qquad (4)$$

where,

$$\cos\delta = \xi \qquad (5)$$

If the forcing function can be expressed in terms of a polynominal of time, say,

$$P(t) = \sum_{i=1}^{n} a_i\, t^i \qquad (5)$$

the solution may then be represented as,

$$X_2(t) = \frac{\sum_i (a_i\, i!)}{M_2\omega_n\sin\delta} \overbrace{\int_0^t \int_0^t \cdots \int_0^t}^{i+1} \exp(-\omega_n t\cos\delta)\, \sin(\omega_n t\cos\delta)dt$$

$$+ X(0) \left[\frac{\exp(-\omega_n t\cos\delta)\, \sin(\delta - t\omega_n\sin\delta)}{\sin\delta} \right] \qquad (8)$$

$$+ \frac{(2\xi\omega_n X(0) + X'(0))}{\omega_n\sin\delta} \left[\exp(-\omega_n t\cos\delta)\, \sin(\omega_n t\sin\delta) \right]$$
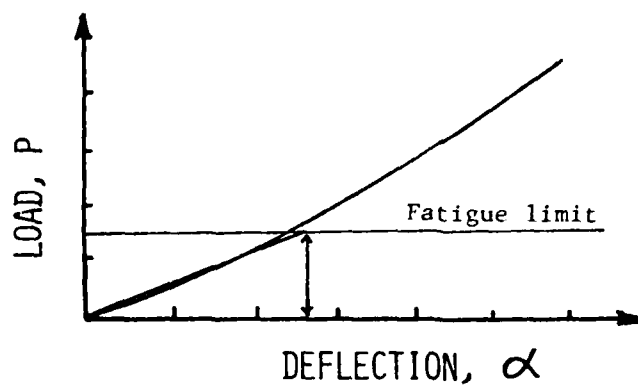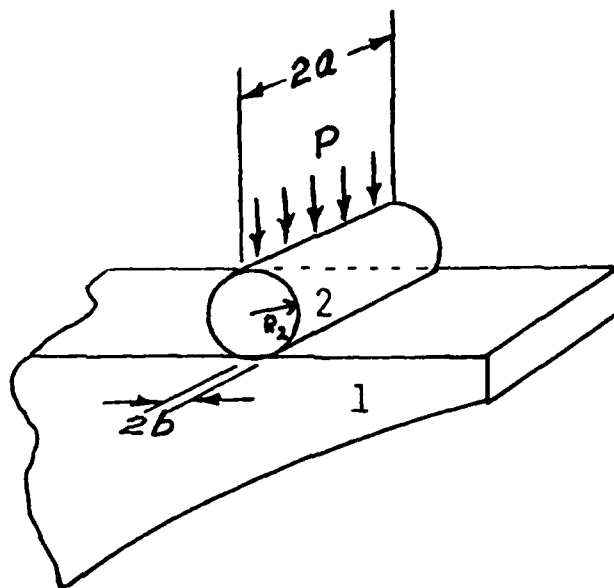
Fig. 3 Determination of surface compliance using linearlized
        Hertz contact theory

Model No. 2

The objective of employing model no. 1 is to show the effect of surface compliance as well as clearance on the dynamics of the driving element of the intermittent-motion mechanism. However, the model offers no information on the driven element. It is therefore not realistic. The study provides, nevertheless, valuable information on the effect of surface compliance which has shown to be significant. In model no. 2, we consider not only the dynamics of the driven element, i.e., M_1, but also its elasticity. This is a modification of the model in [10] where elasticity of element M_1 is not included.

Equation of Motion

During contact, the equations of motion of model no. 2 may be expressed as, referring to Fig. 2,

$$M_2 \ddot{X}_2 + C (\dot{X}_2 - \dot{X}_1) + K (X_2 - X_1) = P \tag{9}$$

$$M_1 \ddot{X}_1 + C (\dot{X}_1 - \dot{X}_2) + K (X_1 - X_2) = 0 \tag{10}$$

Introducint the relative displacement, X_c,

$$X_c = X_2 - X_1 \tag{11}$$

For $P(t)$ as an arbitrary function of time, we have, from Laplace transform, the solution is,

$$X_c(t) = \mathcal{L}^{-1} \frac{\overline{P}(S)}{(S^2 + 2\xi\omega_n S + \omega_n^2)M_2} + X_c(0) \left[\frac{\exp(-t\omega_n \cos\delta) \sin(\delta - t\omega_n \sin\delta)}{\sin\delta} \right]$$

$$+ \frac{2\xi\omega_n X_c(0) + X'(0)}{\omega_n \sin\delta} \left[\exp(-t\omega_n \cos\delta) \sin(t\omega_n \sin\delta) \right] \tag{12}$$

If $P(t)$ is a periodic forcing function, we have,

$$X_c(t) = A \exp(-\omega_n \delta t) \sin(\omega_n t + \Phi) + \frac{X\omega^2 \sin(\omega t + \Phi)}{\sqrt{(\omega_n^2 - \omega^2)^2 + (2\xi\omega_n \omega)^2}}$$

where X, ω and Φ are the amplitude, frequency and phase angle of the forcing function, respectively.

In the case of non-contact, $C = K_{eq} = 0$, a simple numerical integration scheme, for instance, the Runge-Kutta scheme can be used to yield solution.

The force-displacement relationship of the spring is shown in Fig. 4. During contact stages, the relationship is non-linear. This is because of elasticity and material compliance. The overall relationship, however, may be considered as piece-wise linear.
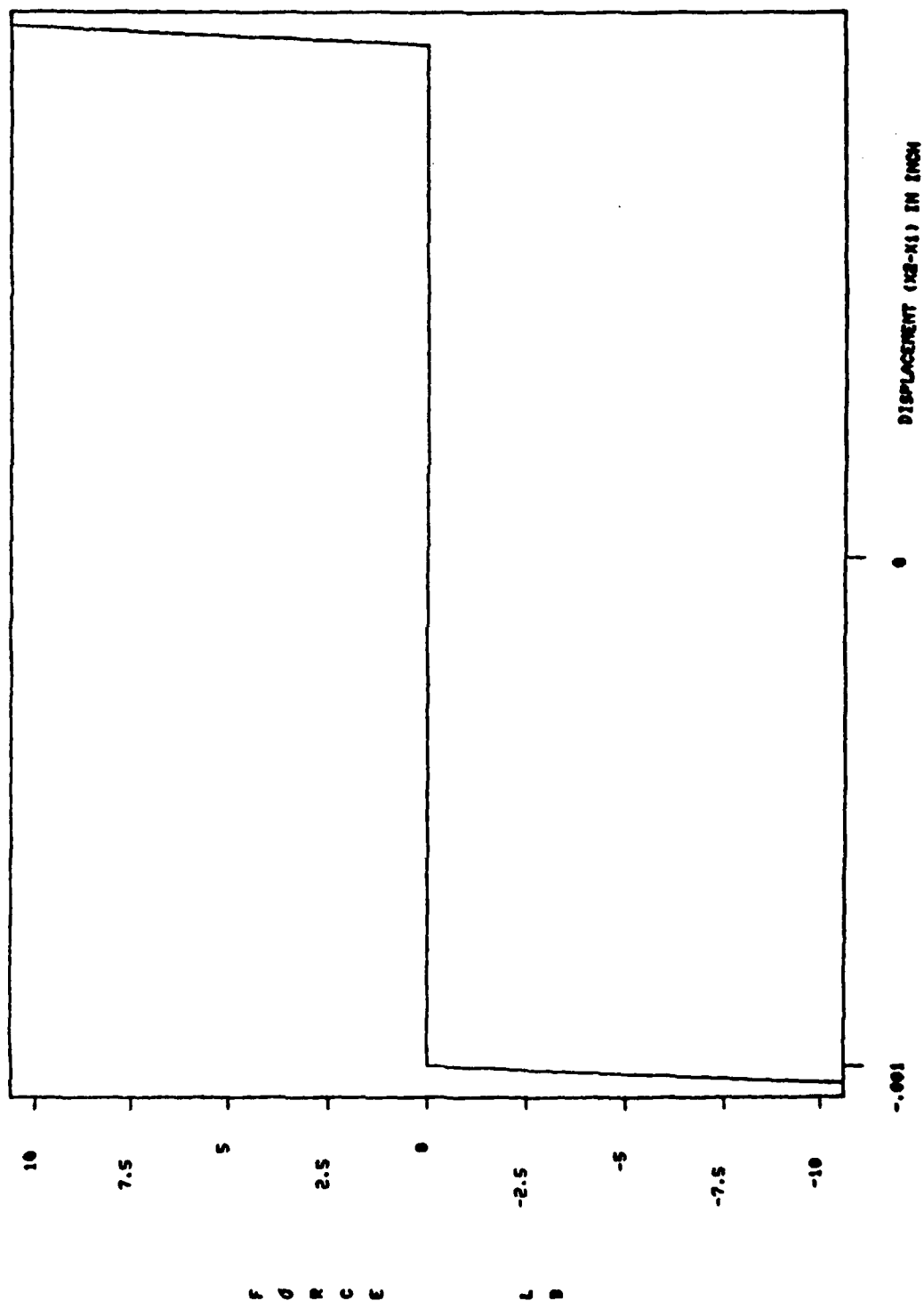
Fig. 4 The spring force and displacement relationship for model no. 2

Dynamic Load

In the design of high-speed Geneva mechanism, stress distribution on the Geneva wheel as well as the contact stress between pin and slot are of major concern. In order to evaluate these stresses, the load producing them must be known. But the determination of this load is not simple. Due to the inherent shock loading of the Geneva mechanism and other factors such as manufacturing error in pin slots and spacing, elastic deformations under load, imbalance, load and wheel inertias, the resulting action is a variable dynamic load, which is essentially a superposition of a waste load on a useful transmitted load. It is the major concern of this investigation to apply the models presented in the last section in order to predict this dynamic load.

Referring to Figs. 1 and 2, the dynamic load, P_d, is defined as,

$$P_d = K_{eq} \cdot X_c \qquad (14)$$

where K_{eq} and X_c are the equivalent spring stiffness and the spring deflection, respectively as defined previously. Eq. (12) gives the solution of X_c.

The spring deflection, X_c, as can be easily seen from eq. (12), depending on the Geneva load $P(S)$, and initial conditions, $X_c(0)$ and $X'_c(0)$. It is also an implicit function of many factors such as clearance, equivalent mass, spring stiffness and damping, etc.

A useful parameter, the dynamic load ratio is introduced and defined as follows:

$$P_r = \frac{P_d}{P} \qquad (15)$$

It is a dimensionless parameter used to measure the dynamic effect of the mechanism. Similar in function to the classical "design acceleration factor" [7] which is a function of the weight of the part and its natural frequency of vibration, the dynamic load ratio, however, is derived based on the "starting velocity" concept which is considered to be more accurate in the modelling of high-impact shock problems. The model is assumed to be accelerated up to some finite velocity in a negligible length of time and then maintains that velocity during the initial and most important phase of the shock motion. The parameter P_r is useful in the design of intermittent-motion mechanisms.

III. **DYNAMIC RESPONSE OF GENEVA MECHANISM.** The mathematical models presented in the previous section are applied to a particular type of intermittent-motion mechanism, the Geneva mechanism. There are several reasons to choose this mechanism for study. First, it is a popular indexing device which has been widely used in industry and military applications. Secondly, there are not many investigation of the dynamics of this mechanism on the record, except in a very few cases [13]. The mechanism has
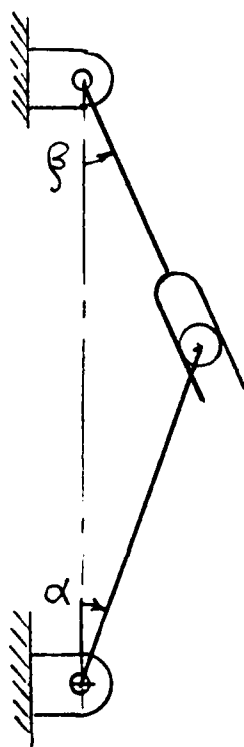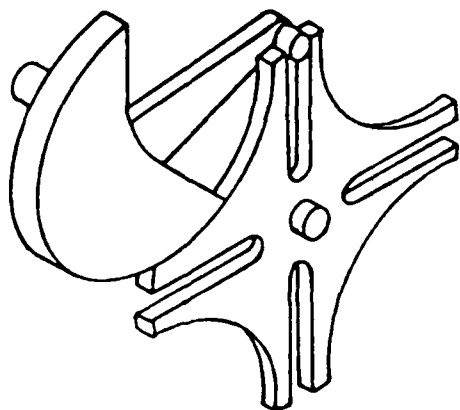
Fig. 5   The kinematics of
         Geneva mechanism
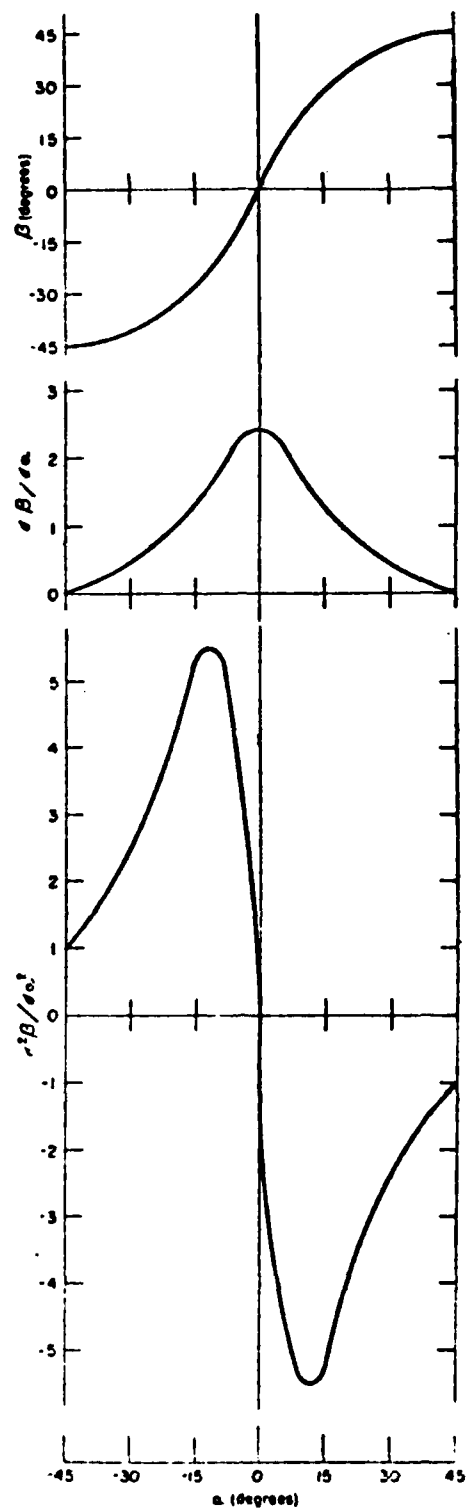
been operated at high speeds regardless of its inherent dynamic limitations and as a result, pin wear and wheel breakage have often occured. A comprehensive study of the subject is necessary in order to provide better understanding and design guidelines. In the following, a brief summary of the kinematic characteristics of the Geneva mechanism is given, then the results of applying the mathematical models are presented in graphical form, and finally a discussion is given.

The Geneva mechanism, although has its main advantage of simplicity, has poor dynamic characteristics. The output motion starts and ends with non-zero accelerations which correspond to infinite shock. Fig. 5 shows the motion graphs of a typical four-station Geneva. In this investigation, we are concerned here primarily with the determination of the dynamic load which is a essential information to be used for stress determination.

Pin Dynamics

Figs. 6 and 7 contain the time-displacement plots for the pin using model no. 1. Here, the assumptions are that the initial conditions are zero (i.e., with non-contact initial condition) and the Geneva wheel surface is assumed to be able to bounce in order to maintain the contact condition with the pin. Both of these assumptions are certainly unrealistic. Fig. 6 shows the effect of surface compliance. Notice that the force amplification is largest at the position slight off the mid-point of the Geneva travel which corresponds to the end of the pin working stroke, or the beginning of the return stroke. The large magnitude of displacement is due to the doubling of the clearance. Fig. 6 also shows the superposition of the vibratory effect due to material compliance on the static Geneva load curve. As the clearance reduces to zero, the vibration damps away and there is essentially no vibration at the later stage of the motion stroke (Fig. 7).

In practice, Geneva wheel moves, therefore, model no. 2 applies. Figs. 8 and 9 show the results of pin displacement and velocity, respectively using this model. The following assumptions are used: 1) surface of Geneva wheel can only be compressed and can not bounce; and 2) initial conditions are applied using the equaitons of motion of the contact case (with a pin velocity of 1.0 in/sec). Fig. 8 shows a striking phenomena that in the later half of the motion travel, there is considerably period of free-flight mode (i.e., non-contact) depending on the magnitude of the static Geneva load, $P(t)$. Force amplification factor obtained from model no. 2 is expected to be more accurate than the one obtained from the model no. 1. Pin velocity is shown in Fig. 9. There are several observations: 1) the graph characterizes by a successive sequence of free-flight and contact modes; 2) the pin in general follows the behavior of the applied load, $P(t)$. During the free-flight mode, the pin is acted by the load P alone, therefore, the pin velocity increases with an increasing slope until it reaches a position where the load reaches maximum.

Wheel Dynamics

The dynamics of Geneva wheel are shown in Fig. 10 and 11. Dynamic effect can be seen from these figures. It causes certain distortions of the kinematic profiles of wheel displacement and velocity (Fig. 5). During the non-contact period, the wheel separated from the pin, keeps at essentially constant velocity due to the inertia. In the contact region, acceleration remains almost constant while the velocity of the wheel changes abruptly. Since clearance has a dominant effect on the separation of pin and wheel, it effects therefore the dynamics of the Geneva wheel.

Geneva Dynamic Load

Fig. 12 shows the effect of pin initial velocity on the dynamic load ratio. There is a strong effect of initial condition on the first half stage of Geneva motion, while on the last half of motion, the effect is not apparent. The effect of surface compliance is just reverse. Fig. 13 shows it has a dominate effect only on the last half of the motion. Fig. 14 shows the effect of clearance on the dynamic load ratio, there is essentially no effect on the first half stage of motion, however, it has an important influence on the latter half. This is because the pin usually does not bounce during the early half of motion which is the working stroke.

Phase-plane plot

Fig. 15 contains the phase-plane plot of the motion of model no. 2. It is a result of a numerical calculation. The phase-plane analysis presents a convenient manner of displaying and interpreting the transient behavior of the nonlinear system. The following observations can be made:

(1) At the entering contact stage, in general, the pin does not exhibit bouncing at the surface. This can be seen from Fig. 15, or more clearly, from Fig. 16 which gives an amplified graph around the initial pin position, point A.

(2) The free-flight mode includes two types of motion characteristics:
   i) The initial bouncing stage. The pin leaves position A and impacts the left-hand side of surface. This motion is due to the kinematics of Geneva mechanism. The pin reaches the end of the slot and is making a return stroke.
   ii) The repeated bouncing stage. In this stage, the relative velocity, as can be seen from Fig. 15, varies with large amplitudes, from approximately, -60 to +54 in/sec. At the boundary of contact, i.e., $X=-r$, the slope of trajectory changes rapidly. This is due to the fact that all the kinetic energy at the moment has to be converted into strain energy of the material during impact. While on the bouncing stage, the process reverses, there is, however, very little change in slope.

(3) The relative velocity at the terminal position of the pin stroke, i.e. point D in Fig. 15, has finite value. This value would contribute toward the kinetic energy during the initial phase of the Geneva dwell motion, and hence causing vibration.

412

(4) The classical definition of the coefficient of restitution may be quantitatively evaluated using the phase-plane plot. For instance, the relative velocities at points B and C (Fig. 15) are 27.4 in/sec and 25.8 in/sec, respectively. Therefore, this gives a coefficient of restitution of 0.94.

IV. STRESS ANALYSIS-FINITE-ELEMENT APPROACH. In this section, our goal is to develop an automatic procedure for the determination of the Geneva wheel stress for a given configuration of the Geneva mechanism which is subjected to a known Geneva dynamic loading. First, we are concerned with the development of a mesh generation problem for the Geneva geometry in order to generate the superelements needed to define the Geneva element mesh. This sub-program is developed and is called SUPER. Secondly, a general mesh generation program [14] is used. The output of SUPER becomes the input to this program. Finally, data are prepared and they are the input to the finite-element program, NONSAP [15], which is a sturctural analysis program for static and dynamic responses of nonlinear systems.

A computational package for the analysis of Geneva stress is developed and it is called GSAP, the Geneva Stress Analysis Program. Fig. 17 shows a flow chart of the program. The finite-element mesh and finite-element nodal mesh of a four-station Geneva wheel, shown in Fig. 18, is shown in Figs. 19 and 20, respectively. The final output from GSAP is plotted in Fig. 21 which shows the stress distribution of the Geneva wheel.

The computer program, GSAP, can be used for the determination of Geneva stress for any number of station of Geneva mechanism. The user needs only to supply the design parameters of the Geneva mechanism and the program automatically generates the finite-element mesh and give the stress distribution. The program is very useful for the optimum design of high-speed Geneva mechanisms.

V. CONCLUSION. The dynamics and stress analysis of intermittent-motion mechanisms have been investigated. The following conclusions can be drawn:

(1) Dynamic models for intermittent-motion mechanisms are formulated which includes clearance and surface compliance. The models are the basis for study the dynamic response of these mechanisms.

(2) The dynamic response of a particular mechanism, the Geneva mechanism, is investigated.

(3) An automated finite-element computational procedure is developed for the determination of Geneva stress distribution.

REFERENCES

1. Bickford, J. H., _Mechanisms for Intermittent Motion_, Industrial Press, N. Y., 1972.

2. Lichtwitz, O., "Mechanisms for Intermittent Motion," Part 1, Machine Design, Dec. 1951, pp. 134-148.

3. Lee, T. W., and Shereshevsky, Y., "Kinematic Synthesis of Planar Two-Gear Drives with Prescribed Dwell Characteristics," ASME Paper 81-DET-2, to appear in J. Mechanical Design, Transc. ASME.

4. "Scanning the Field for Ideas," Machine Design, Dec. 8, 1966, p. 194; Ferguson Indexing Catalog No. 180, Ferguson Machine Company, St. Louis, Missouri.

5. Yang, A. T., and Hsia, L. M., "Multistage Geared Geneva Mechanism," J. Mechanical Design, Vol. 101, No. 1, Jan. 1979, pp. 41-46.

6. Crossley, F. R.E., Editor, _Proceedings of International Conference for Teachers of Mechanisms_, The Shoe String Press, Inc. 1961. pp. 110-111.

7. Langer, B. F., "Design to Withstand High-Impact Shock," Machine Design, August 1955, pp. 193-197.

8. Johnson, R. C., "Impact Forces in Mechanisms," Machine Design, June 12, 1958, pp. 138-146.

9. Kobrinskiy, A. E., and Babitsky, V. I., "Periodic Movements of a Two-Mass Vibration System in a Cavity," (in Russian), Trud. Mash. Mekh., Vol. 103, 1964, pp. 56-70.

10. Dobowsky, S. and Freudenstein, F., "Dynamic Analysis of Mechanical Systems with Clearances," Part I & II, J. Engg. Industry, Feb. 1971, pp. 305-316.

11. Dobowsky, S. and Gardner, T. N., "Dynamic Interactions of Link Elasticity and Clearance Connections in Planar Mechanical Systems," J. Engg. Industry, 1975, pp. 652-661.

12. Haines, R. S., "Survey: 2-Dimensional Motion and Impact at Revolute Joints," Mechanism and Machine Theory, Vol. 15, 1980, pp. 361-370.

13. Lee, T. W., "Optimization of High Speed Geneva Mechanisms," J. Mechanical Design, Vol. 103, No. 3, July 1981, pp. 621-630.

14. Durocher, L. L., and Gasper, A., "A Versatile Two-Dimensional Mesh Generator with Automatic Bandwidth Reduction," Computers & Structures, Vol. 10, 1979, pp. 561-575.

15. Bathe, Klaus-Jurgen, Wilson, E. L., and Iding, R. H., "NONSAP: A Structural Analysis Program for Static and Dynamic Response of Non-linear Systems," Report No. UCSESM 74-3, Division of Structural Engg. and Structural Mechanics, Dept. of Civil Engg., Univ. of Calif. Berkeley, Cc., Feb. 1974.
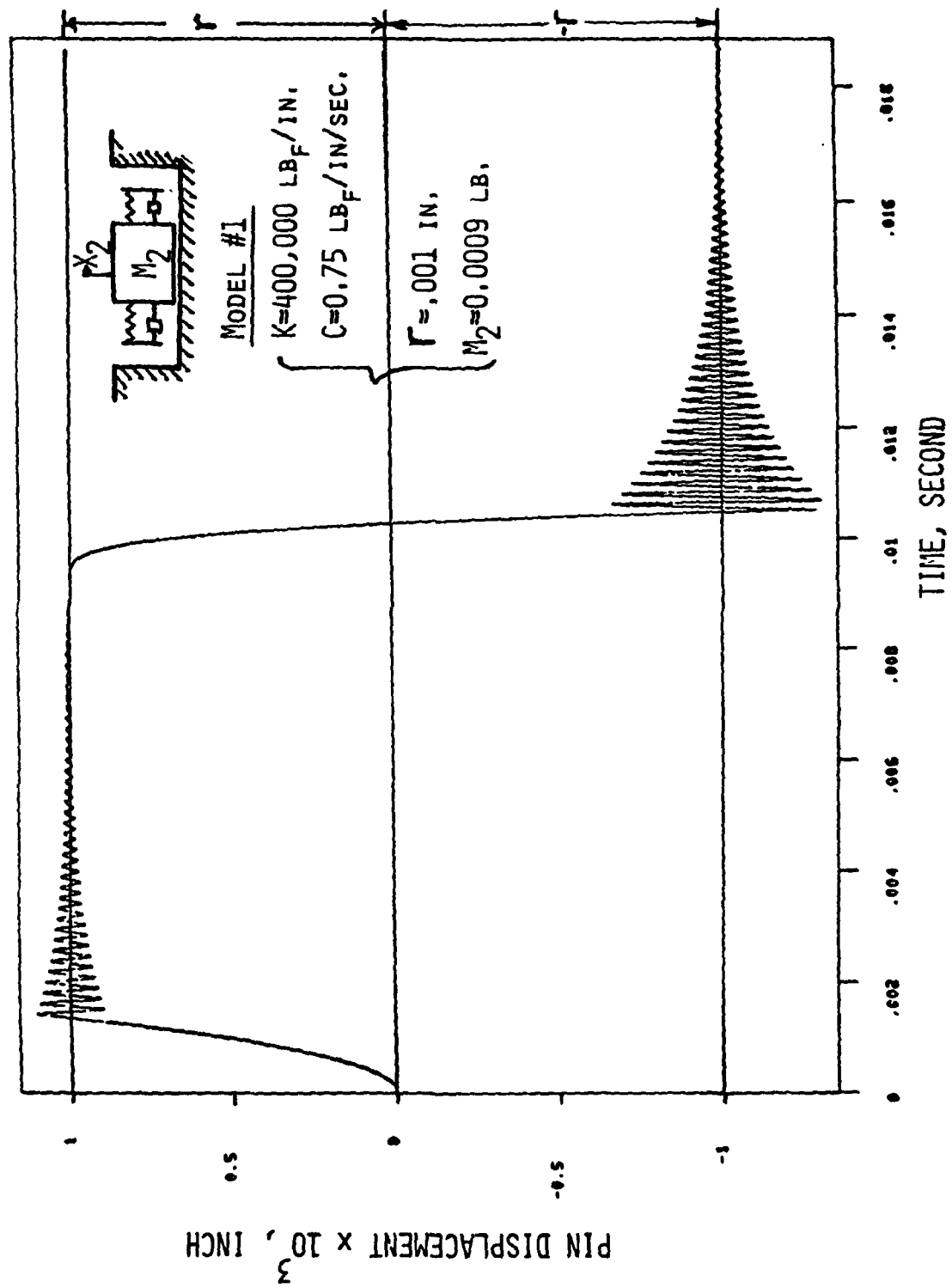
FIG. 6   THE DYNAMICS OF GENEVA PIN WITH CLEARANCE--PIN DISPLACEMENT

415
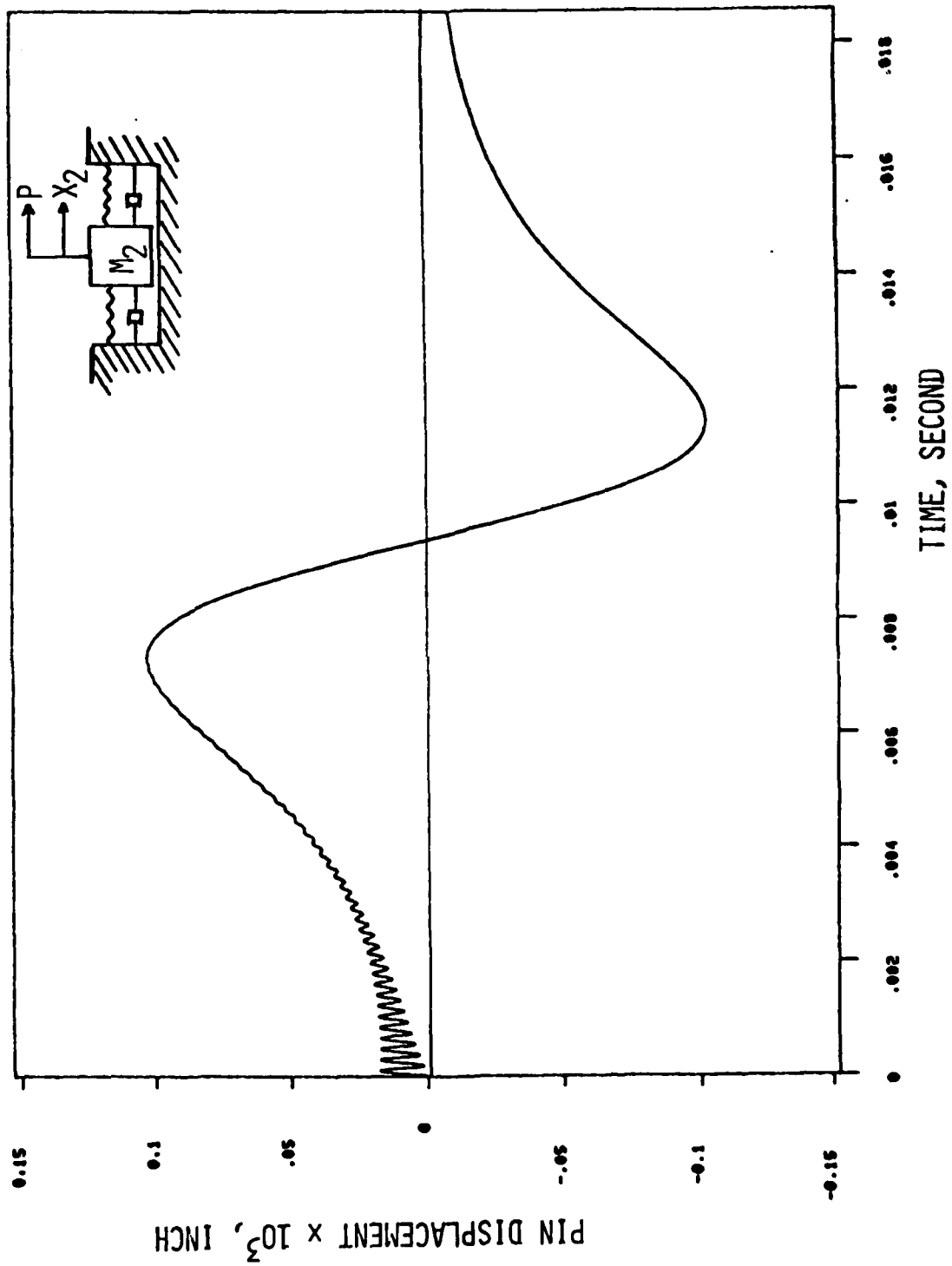
FIG. 7 THE DYNAMICS OF GENEVA PIN WITHOUT CLEARANCE--PIN DISPLACEMENT

416
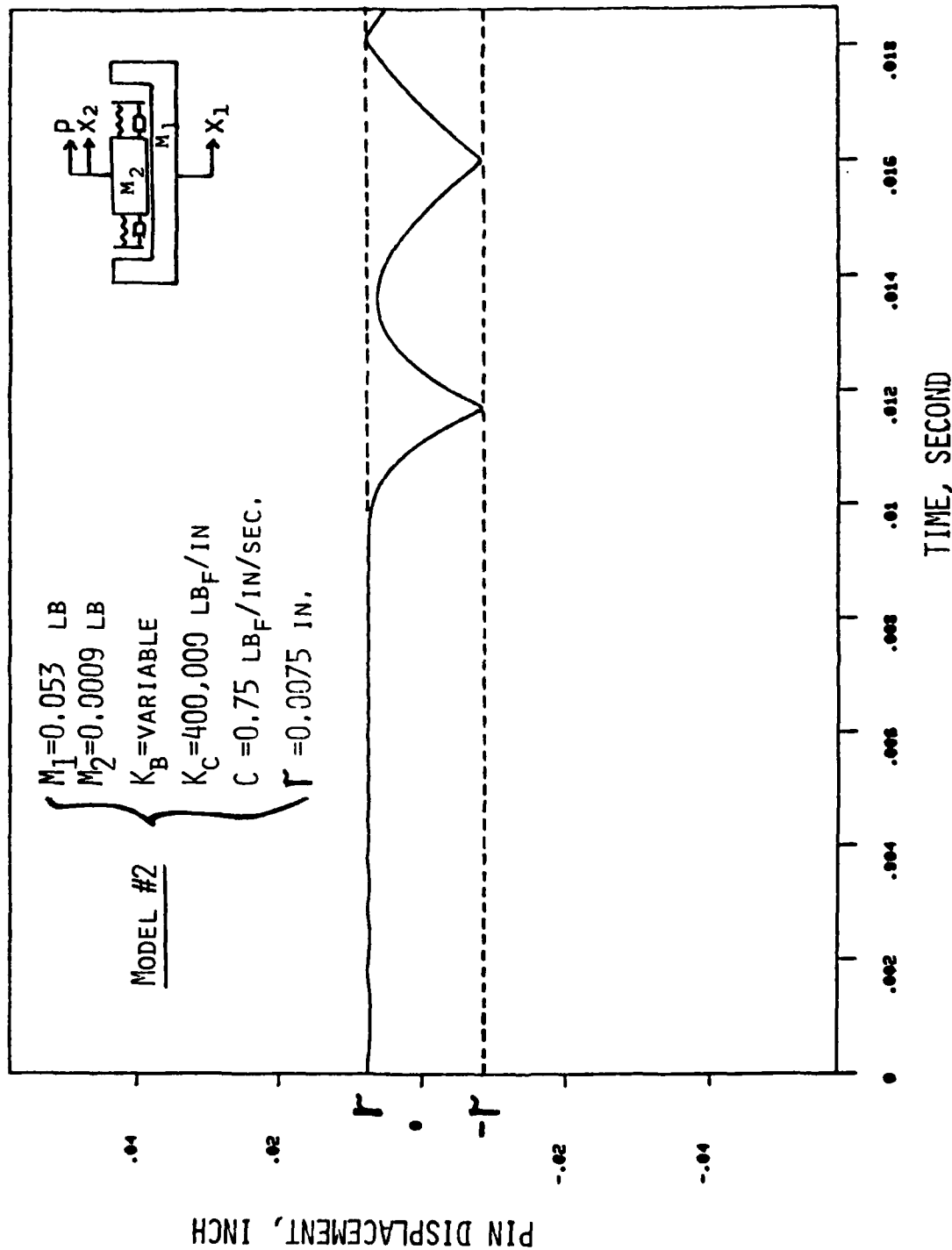
FIG. 8   THE DYNAMICS OF GENEVA WHEEL WITH CLEARANCE—PIN DISPLACEMENT

MODEL #2

$M_1 = 0.053$ LB
$M_2 = 0.0009$ LB
$K_B = $ VARIABLE
$K_C = 400,000$ LB_F/IN
$C = 0.75$ $LB_F/IN/SEC.$
$\Gamma = 0.0075$ IN.

PIN DISPLACEMENT, INCH

TIME, SECOND
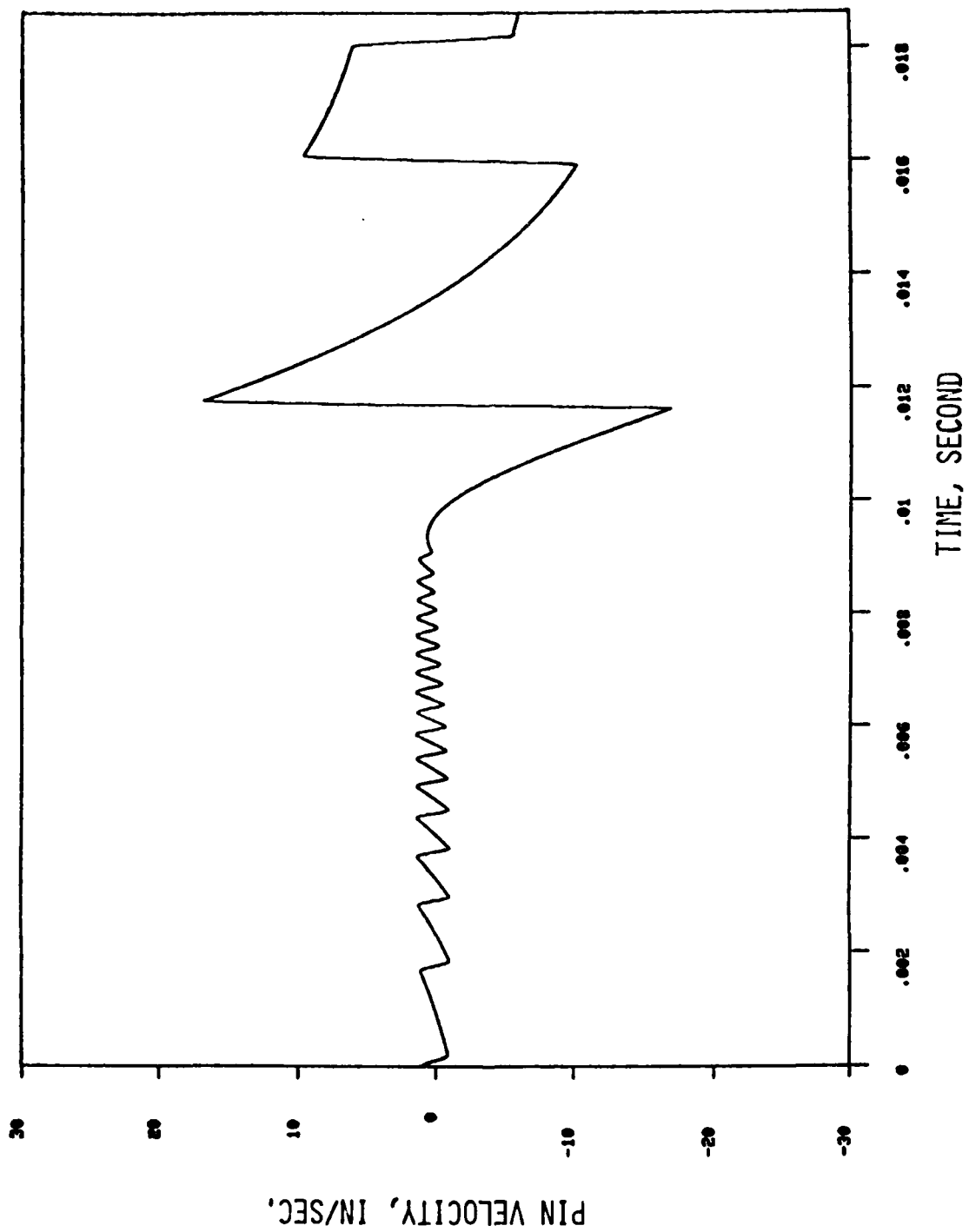
FIG. 9 THE DYNAMICS OF GENEVA PIN WITH CLEARANCE--PIN VELOCITY
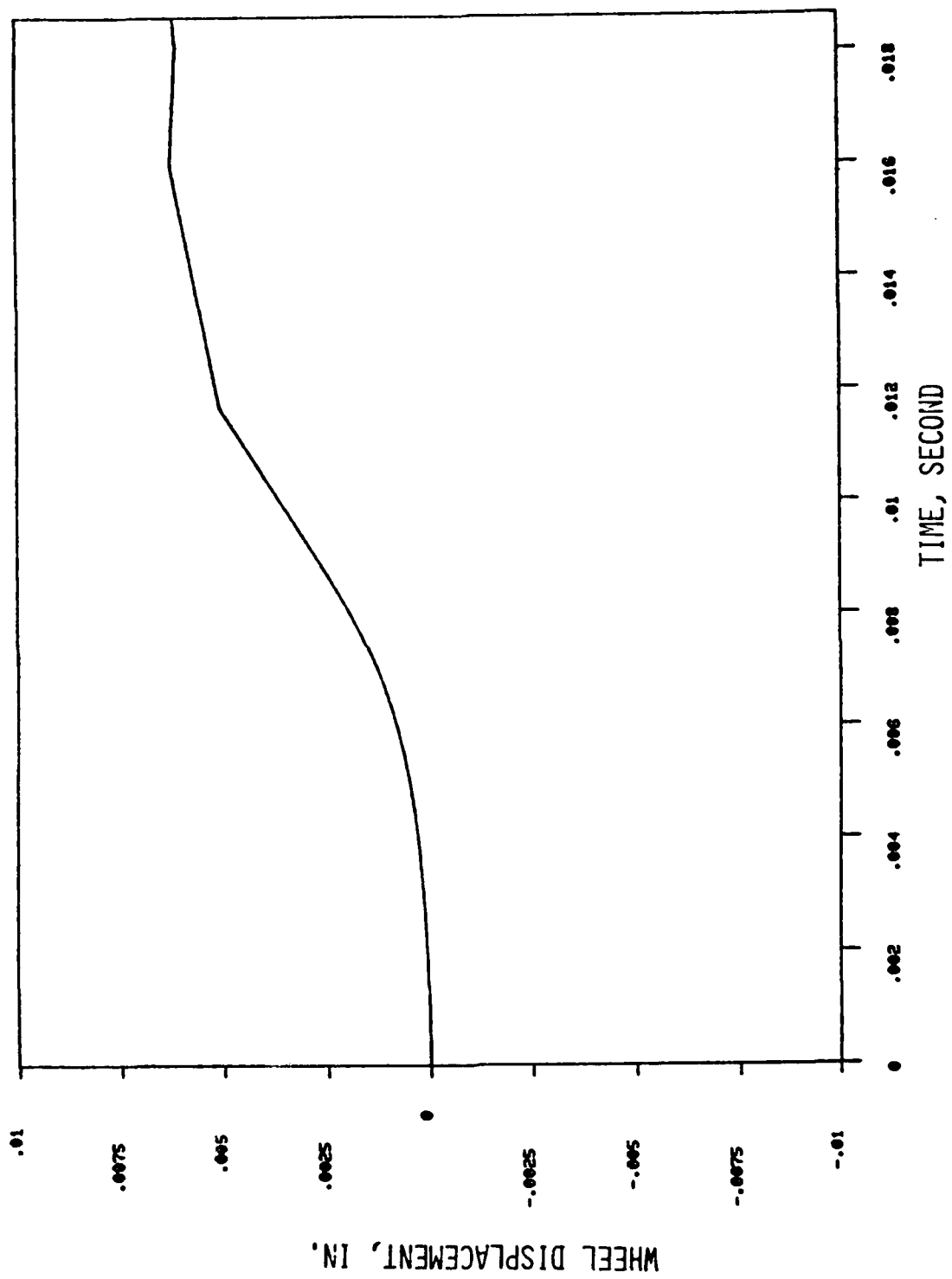
FIG. 10 THE DYNAMICS OF GENEVA MECHANISM--WHEEL DISPLACEMENT

419
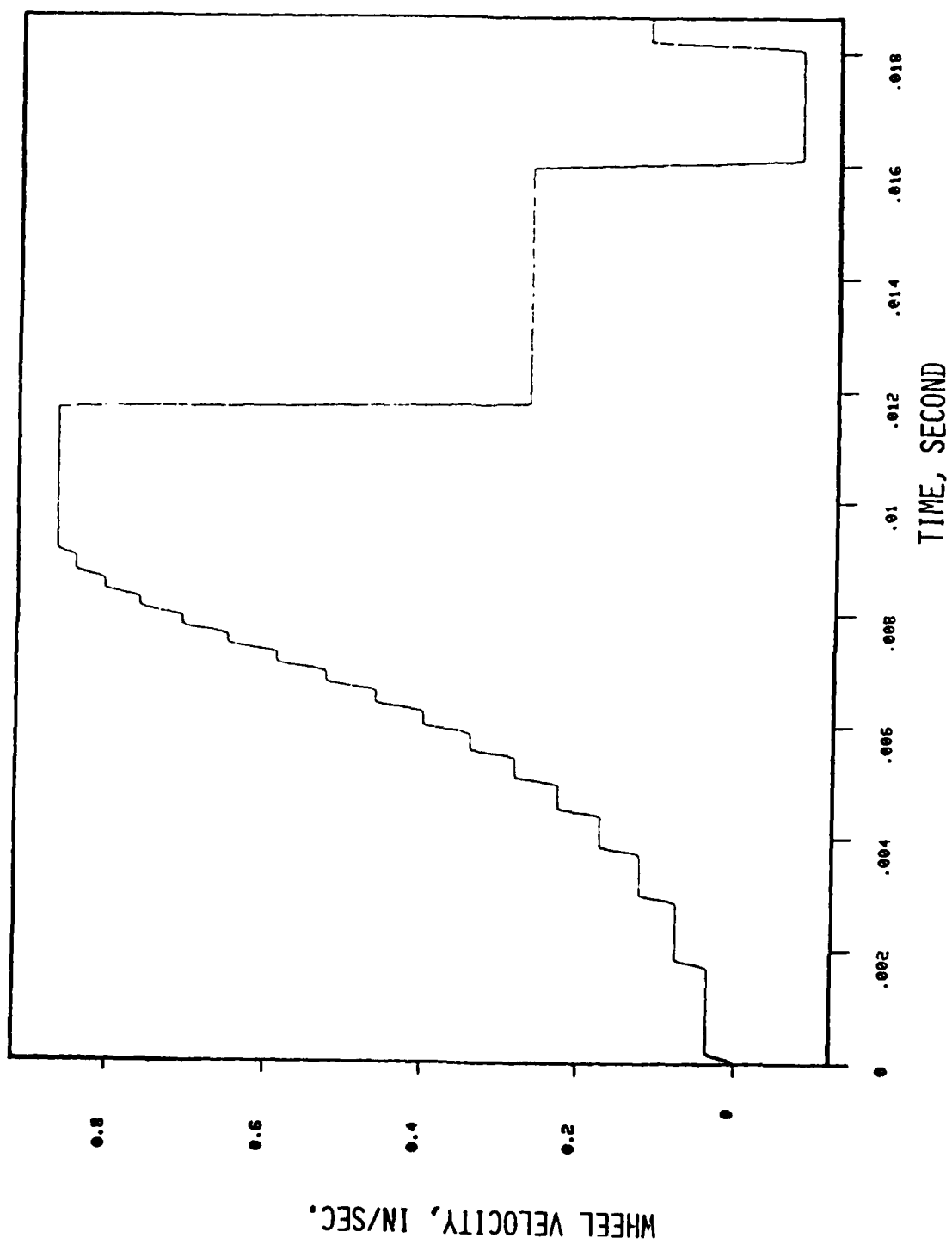
FIG. 11   THE DYNAMICS OF GENEVA MECHANISM WITH CLEARANCE--WHEEL ANGULAR VELOCITY
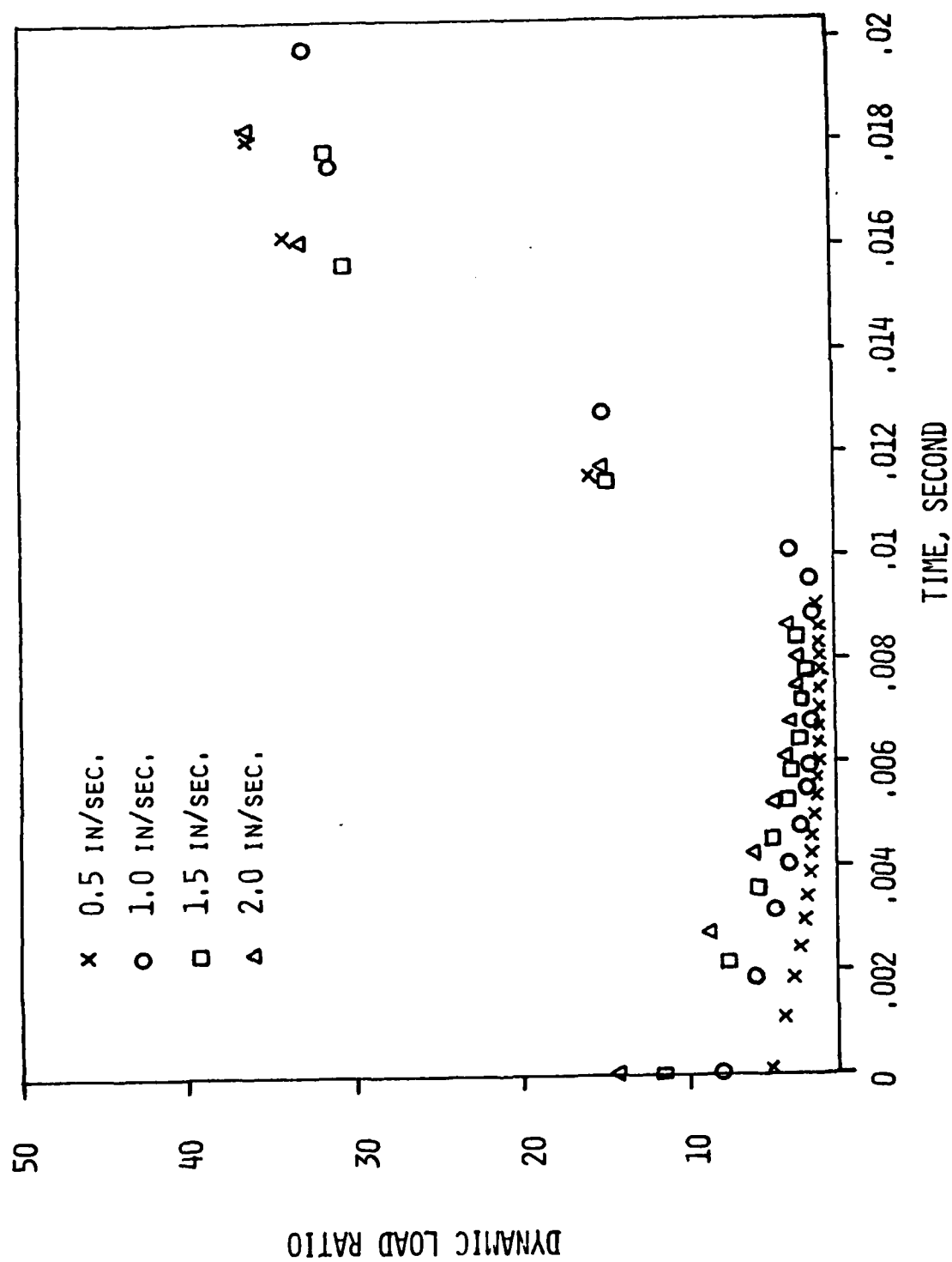
FIG. 12 THE EFFECT OF PIN VELOCITY ON THE DYNAMIC LOAD RATIO
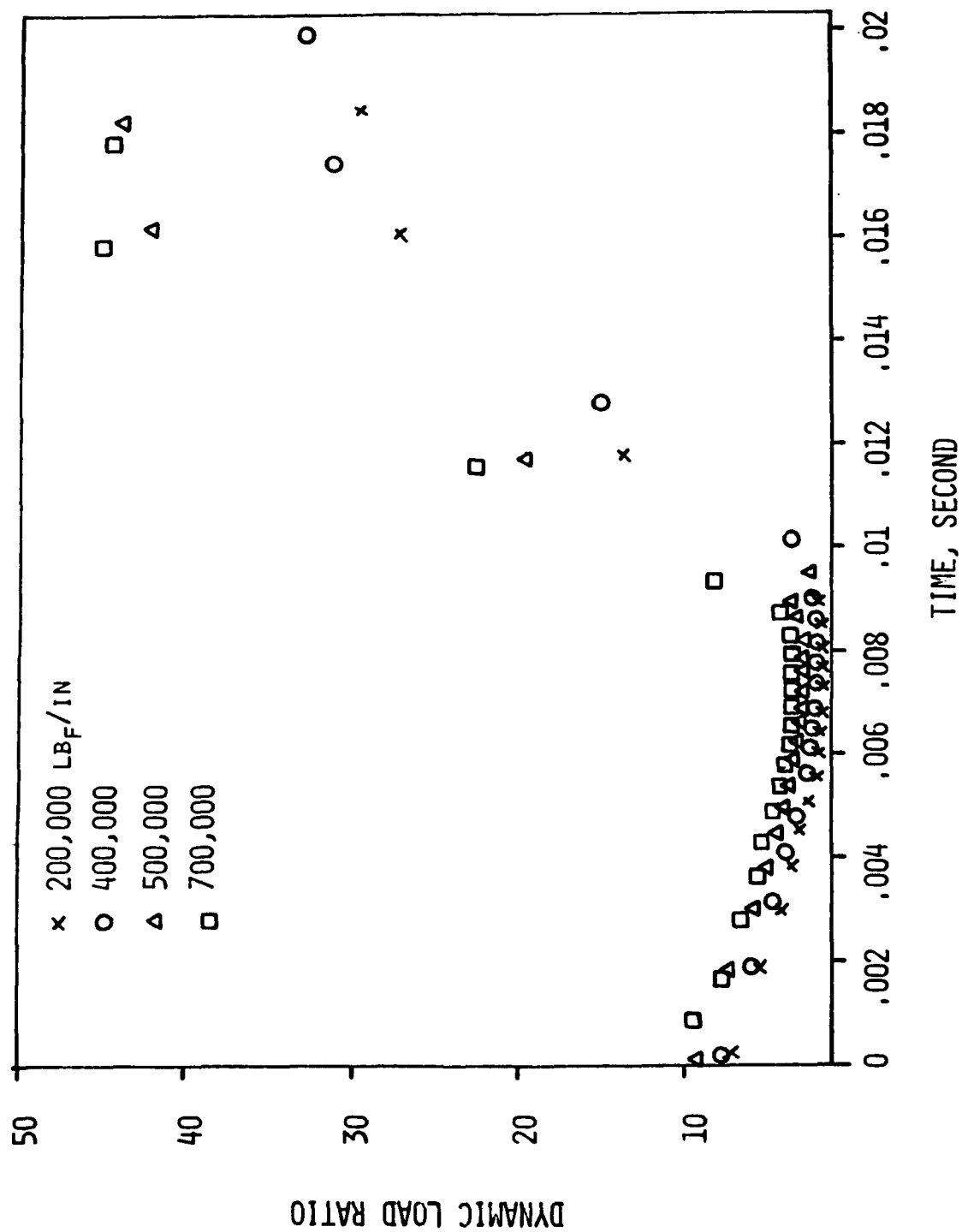
FIG. 13 THE EFFECT OF SURFACE COMPLIANCE ON THE DYNAMIC LOAD RATIO

422

FIG. 14 THE EFFECT OF CLEARANCE ON THE DYNAMIC LOAD RATIO

423

Wheel mass, $M_1 = 0.053$ lb.
Pin mass, $M_2 = 0.001$ lb.
Clearance, $\bar{r} = 0.075$ in.
Pin initial velocity, $\dot{X}_2(0) = 1.0$ in/sec
(enev.load, P, based on:
  $I_L = 0.001$ in^4.
RPM=800.

Contact mode ⟶

⟵ Free-flight mode ⟶

RELATIVE DISPLACEMENT, $(X_2 - X_1)$, in.

Contact mode

RELATIVE VELOCITY, $(\dot{X}_2 - \dot{X}_1)$, IN/SEC.
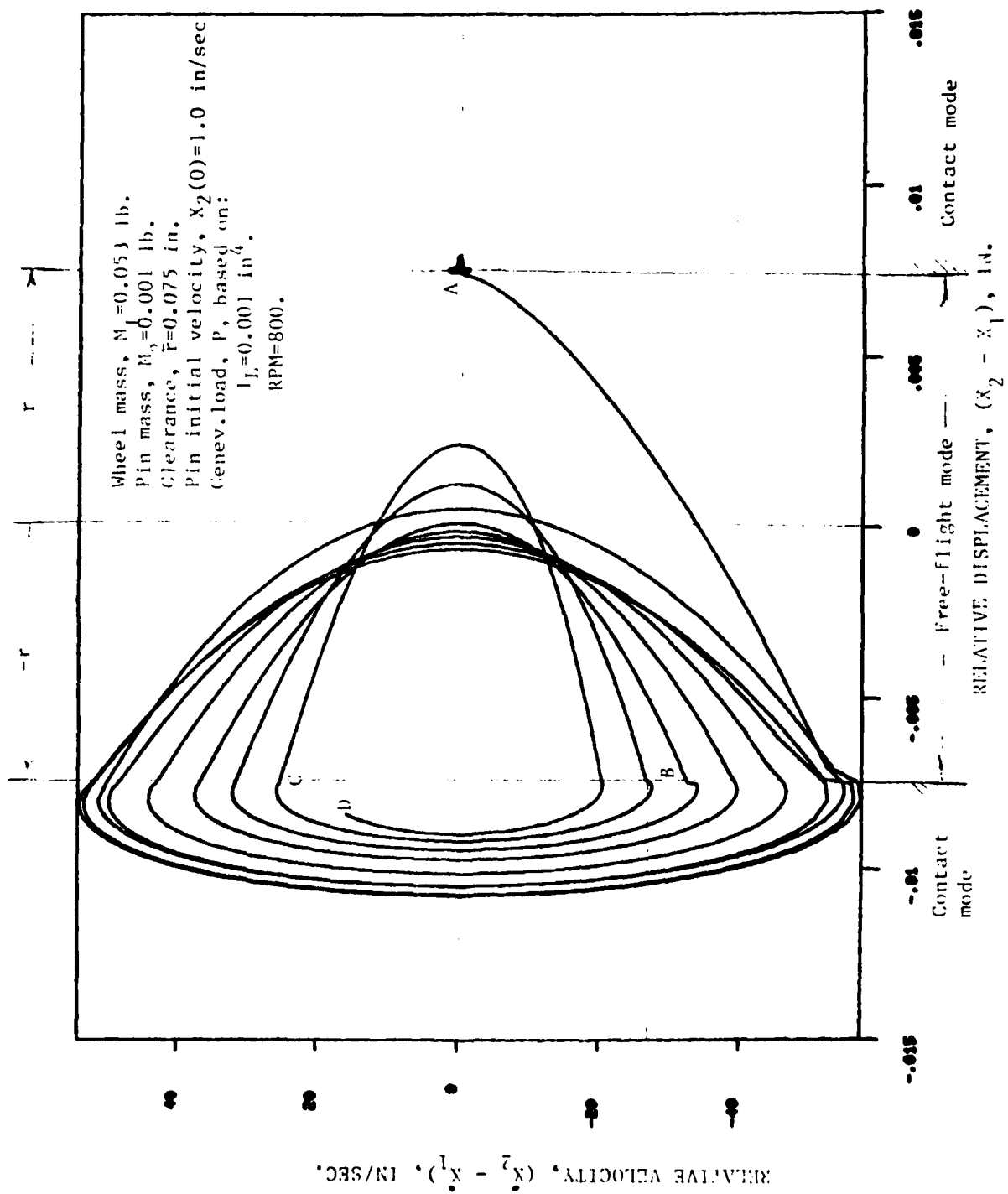
Fig. 15   Phase-plane plot of model no. 2

424

RELATIVE DISPLACEMENT, $(X_2 - X_1)$, IN.

RELATIVE VELOCITY, $(\dot{X}_2 - \dot{X}_1)$, IN/SEC.
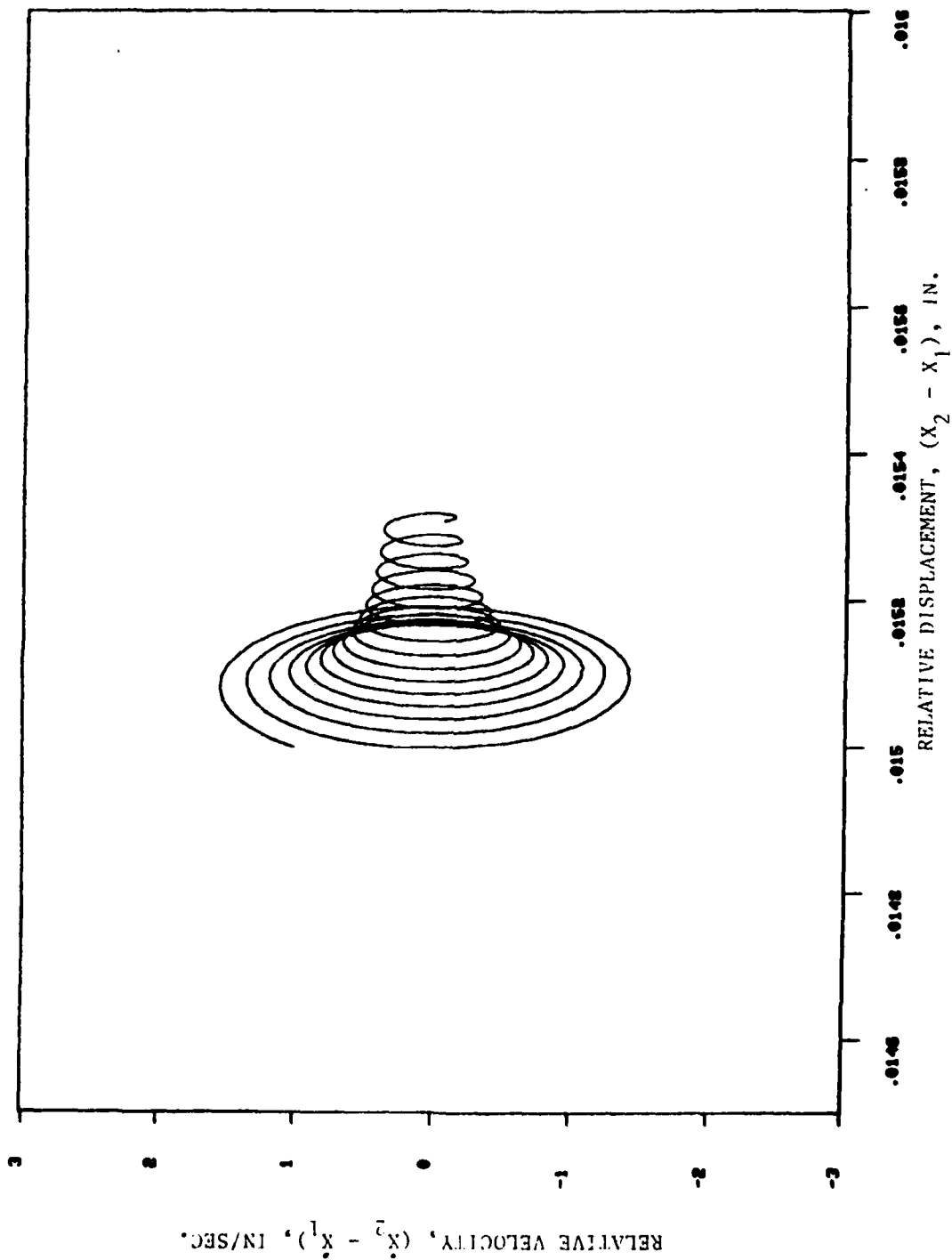
Fig. 16 An amplified graph around point A of Fig. 16

DP, DG, DC, DH, T, XN, RLOD, NOD, IDIRN, AMATL, ANU

```
                                          ┌──────────┐           ┌──────────┐
┌──────────┐           ┌──────────┐       │          │           │          │
│  SUPER   │───────────│   DATA   │───────│ REORDER  │
└──────────┘           └──────────┘       └──────────┘

                       ┌──────────┐       ┌──────────┐
                       │   MESH   │───────│  LINEAR  │
                       └──────────┘       └──────────┘

                       ┌──────────┐       ┌──────────┐
                       │ RENUMBER │───────│ OPTIMUM  │
                       └──────────┘       └──────────┘

                       ┌──────────┐
                       │  OUTPUT  │
                       └──────────┘

                       ┌──────────┐        STRESS
                       │  NONSAP  │──────▶ DEFLECTIONS
                       └──────────┘        RREQUENCY
```
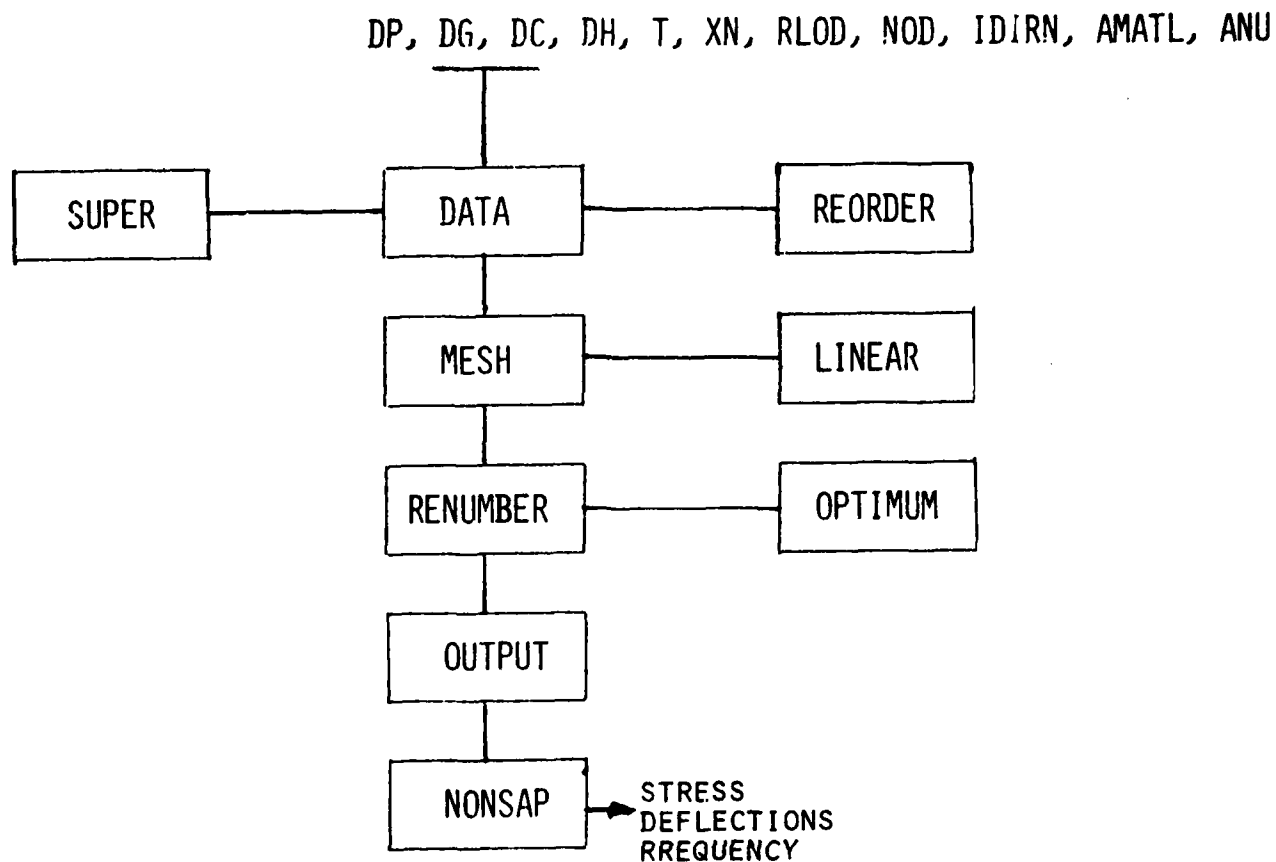
Input parameters

DP – Pin Diameter   RLOD – Applied Load
DG – Geneva Diameter   NOD   – Location of Applied Load
DC – Crank Diameter   IDIRN – Direction of Load
DH – Hub Diameter   AMATL – Material Modulus
T   – Tip Width   ANU   – Material Poisson Ratio
XN – Point Number

GENEVA STRESS ANALYSIS PROGRAM

Fig. 17A   Geneva stress analysis program-- flow chart

426

DATA   –   Reads all the data necessary to define the Geneva geometry.

SUPER   –   Generates the superelements needed to define the Geneva element mesh.

REORDER   –   Renumbers the superelements in such a way that as the nodes are generated for each superelement, no duplicate node numbers will be created.

MESH   –   Generates node numbers and nodal coordinates.

LINEAR   –   Generates the element connectivety array for a four noded quadrilateral.

RENUMBER   –   Determines how many nodes are directly connected to a given node and the node numbers of the nodes that are connected to a given node.

OPTIMUM   –   Renumbers the generated nodes to reduce nodal connectivety bandwidth.

OUTPUT   –   Outputs nodes, nodal coordinates. elements, and element connectivety array for input to NONSAP. Also, outputs load and material properties which are read by NONSAP.

NONSAP   –   A Structural Analysis Program for Static and Dynamic Responses of Nonlinear Systems.

GENEVA STRESS ANALYSIS PROGRAM - CONT'D.

Fig. 17B   Geneva stress analysis program-- subroutines
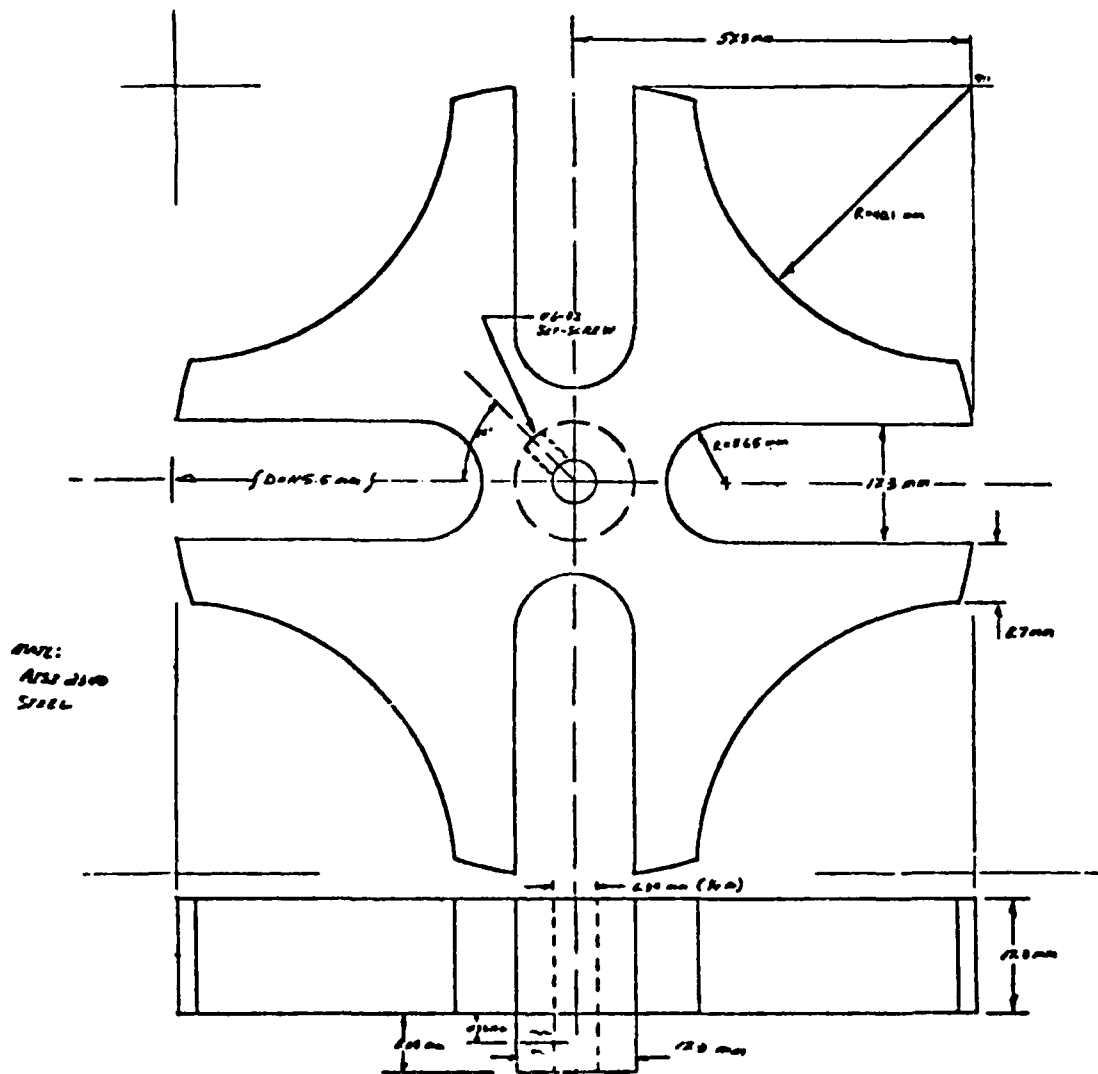
Fig. 18   A four-station Geneva mechanism

428
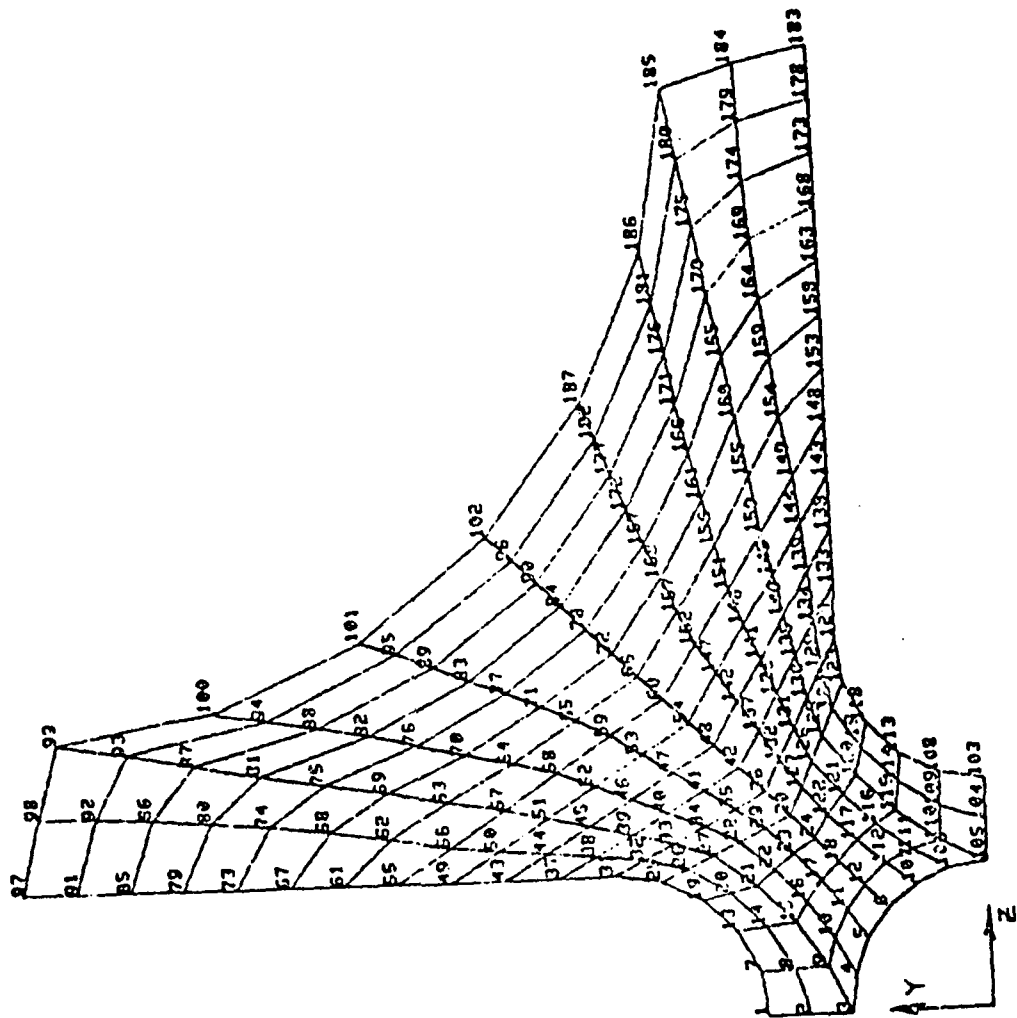
Fig. 19   A finite-element mesh

429
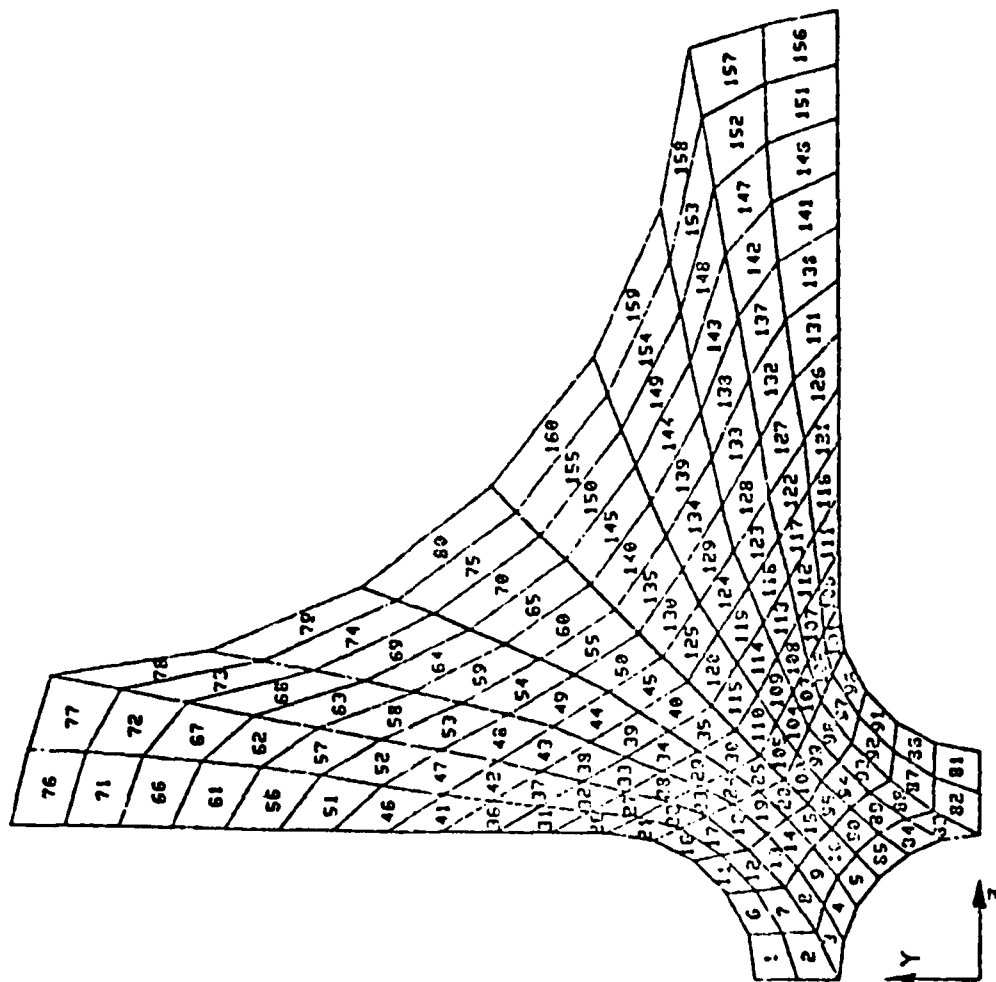
Fig. 20 A finite-element nodal mesh
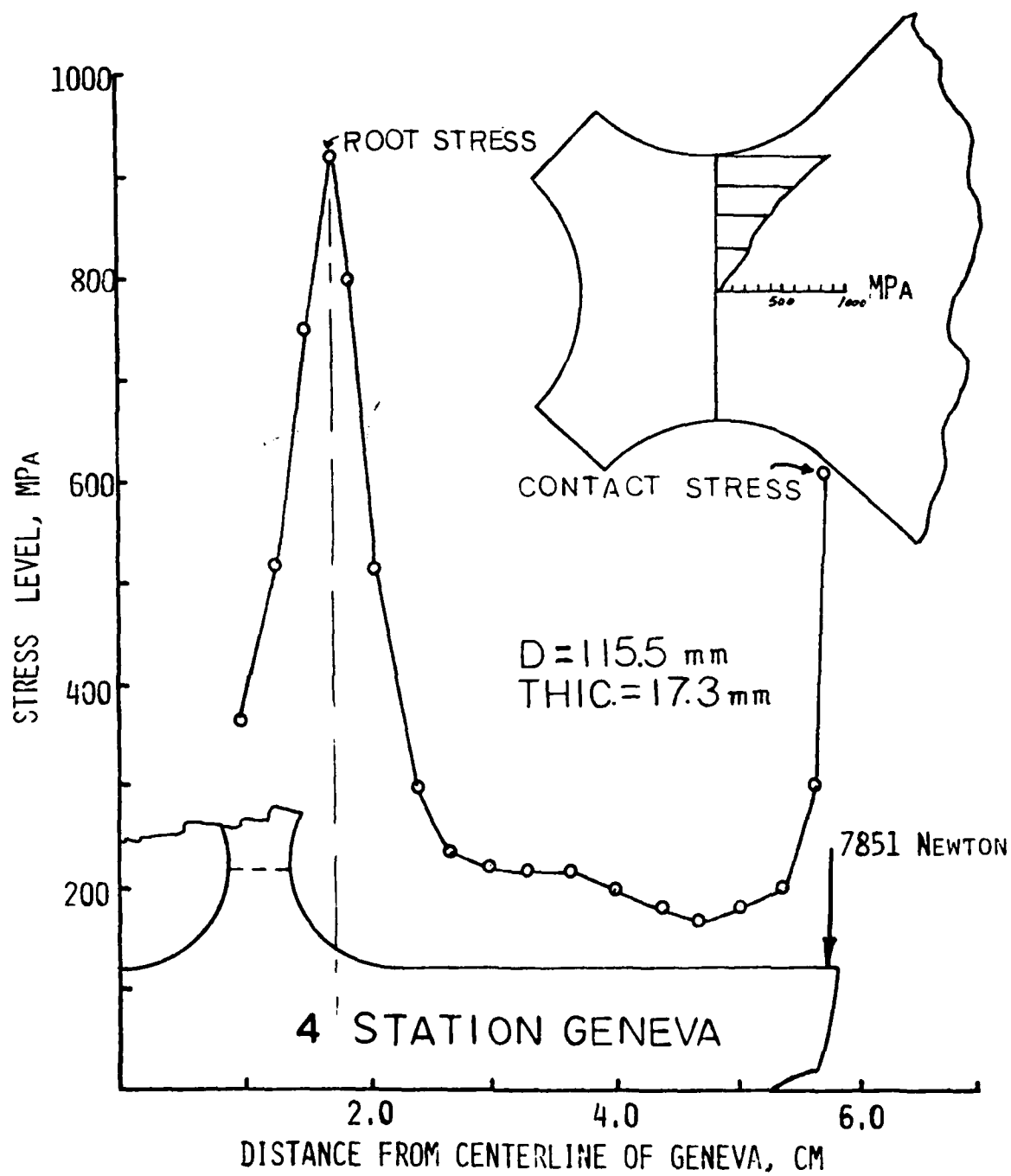
Fig. 21 Stress distribution for a four-station Geneva wheel

A NONLINEAR HYPERBOLIC VOLTERRA EQUATION
OCCURRING IN VISCOELASTICITY

John A. Nohel*
Mathematics Research Center
University of Wisconsin-Madison
Madison, WI   53706

ABSTRACT. A general model for the nonlinear motion of a one dimensional, finite, homogeneous, viscoelastic body is developed and analysed by an energy method. This note summarizes recent research of Dafermos and the author in which it is shown that under physically reasonable conditions the nonlinear boundary, initial value problem has a unique, smooth solution (global in time), provided the given data are sufficiently "small" and smooth; moreover, the solution and its derivatives of first and second order decay to zero as $t \to \infty$.

I. INTRODUCTION. In nonlinear systems of "hyperbolic" type, characteristic speeds are not constant so that weak waves are amplified and smooth solutions may blow up in finite time due to the formation of shock waves. It is interesting to consider situations where this destabilizing mechanism coexists (and thus competes) with dissipation.

In certain cases (e.g., viscosity of the rate type) dissipation is so powerful that waves cannot break and solutions remain globally smooth. A more interesting situation arises when the amplification and decay mechanisms have been predicted at the outset. Elementary dimensional considerations indicate that breaking of waves develops on a time scale inversely proportional to wave amplitude while dissipation proceeds at a roughly constant time scale. It should thus be expected that dissipation prevails and waves do not break when the initial data are "small". Results of this type were first obtained by T. Nishida for the quasilinear wave equation with first-order frictional damping for sufficiently smooth and small initial displacements and initial velocities.

A different and subtler dissipative mechanism is induced by memory effects of elastico-viscous materials. Dafermos and Nohel [3] have recently developed and analyzed such a one-dimensional nonlinear model for the homogeneous extension of an elastico-viscous rod whose ends are free of traction. Special cases of the present model, as well as other closely related problems were discussed by Dafermos [2] at the Twenty Fifth Conference of Army Mathematicians. The purpose of this note is to motivate the problem from physical considerations and to state the principal mathematical result. The reader is referred to [3] for the necessarily technical details of proofs and for references to earlier literature.

In the viscoelastic problem the dissipation mechanism is induced by memory effects of the viscoelastic materials (stress-strain relaxation function - the stress is a nonlinear functional rather than a function of the

strain). Using elementary energy methods, which are combined with frequency domain techniques for nonlinear Volterra equations, it is shown in [3] that under physically reasonable conditions on the stress-strain relaxation function, the known history of the displacement, the nonlinearities of the model, and on the assigned external body force, the boundary-history value problem (2.8), (2.9), (2.22) in the text which describes the model has a unique, smooth solution (global in time), provided the given data (history and external body force) are sufficiently smooth and "small". Moreover, the solution and its spacial and time derivatives of first and second order decay to zero as $t \to \infty$. Various modifications and generalizations of the model, including two and three dimensional problems, are also considered in [3]. The difficult and natural question of establishing the existence of shocks (breaking of waves) in finite time if the smooth data becomes sufficiently "large" which has not been solved up to this time in full generality, is under study. The existence of shocks in viscoelastic materials, but in a different physical and mathematical context, was demonstrated in [1] and confirmed by experiment.

2. THE MATHEMATICAL MODEL AND SUMMARY OF RESULTS.

A simple, one dimensional, nonlinear model for viscoelastic bodies, suggested by the research of Coleman and Gurtin [1], corresponds to the constitutive relation

$$\sigma(t,x) = \phi(e(t,x)) + \int_{-\infty}^{t} a'(t - \tau)\psi(e(\tau,x))d\tau , \qquad (2.1)$$

where σ is the stress, e the strain, a the relaxation function with $' = d/dt$, and ϕ, ψ assigned constitutive functions. The relaxation function is normalized so that $a(\infty) = 0$. When the reference configuration is in natural state, $\phi(0) = \psi(0) = 0$. Experience indicates that $\phi(e)$, $\psi(e)$, as well as the equilibrium stress

$$\chi(e) \overset{\text{def}}{=} \phi(e) - a(0)\psi(e) \qquad (2.2)$$

are increasing functions of e, at least near equilibrium ($|e|$ small). Moreover, the effect of viscosity is dissipative. To express mathematically the above physical requirements, we impose upon $a(t)$, $\phi(e)$, $\psi(e)$ and $\chi(e)$ the following assumptions:

$$a(t) \in W^{2,1}(0,\infty),$$

$$\qquad (2.3)$$

$$a(t) \text{ is strongly positive definite on } [0,\infty] ;$$

$$\phi(e) \in C^3(-\infty,\infty), \quad \phi(0) = 0, \quad \phi'(0) > 0 ; \qquad (2.4)$$

$$\psi(e) \in C^3(-\infty,\infty), \quad \psi(0) = 0, \quad \psi'(0) > 0 ; \qquad (2.5)$$

$$\chi'(0) = \phi'(0) - a(0)\psi'(0) > 0 . \qquad (2.6)$$

The notation $a \in W^{2,1}(0,\infty)$ means that a, a', a'' are integrable over $[0,\infty]$. Assumption (2.3), which requires that $a(t) - \alpha \exp(-t)$ be a positive definite kernel on $[0,\infty)$ for some $\alpha > 0$, expresses the dissipative character of viscosity. Smooth, integrable, nonincreasing, convex relaxation functions, e.g.,

$$a(t) = \sum_{k=1}^{k} \nu_k \exp(-\mu_k t), \quad \nu_k > 0, \quad \mu_k > 0 , \tag{2.7}$$

which are commnly employed in the applications of the theory of visco-
elasticity, satisfy (2.3).

We now consider a homogeneous, one dimensional body (string or bar) with
reference configuration $[0,1]$ of density $\rho = 1$ (for simplicity) and
constitutive relation (2.1), which is moving under the action of an assigned
body force $g(t,x)$, $-\infty < t < \infty$, $0 < x < 1$, with the ends of the rod free of
traction. We let $u(t,x)$ denote the displacement of particle x at time
t in which case the strain is $e(t,x) = u_x(t,x)$. Thus the equation of motion
$\rho u_{tt} = \sigma_x + \rho g$ here takes the form of the nonlinear (hyperbolic) Volterra
functional differential equation

$$u_{tt} = \phi(u_x)_x + \int_{-\infty}^{\infty} a'(t - \tau)\psi(u_x)_x d\tau + g \tag{2.8}$$

$$-\infty < t < \infty, \ 0 < x < 1 .$$

The physical problem of the motion of a viscoelastic body suggests that the
history of the motion of the body up to time $t = 0$ is assumed known, i.e.,

$$u(t,x) = v(t,x), \quad -\infty < t < 0, \quad 0 < x < 1 , \tag{2.9}$$

where $v(t,x)$ is a given sufficiently smooth function which satisfies
equation (2.8) together with appropriate boundary conditions, for $t \leqslant 0$. In
order to show that the motion of the viscoelastic bar remains smooth for all
$t > 0$, the mathematical task is to determine a smooth extension $u(t,x)$
of $v(t,x)$ on $(-\infty,\infty) \times [0,1]$ which satisfies (2.8) together with assigned
boundary conditions, for $-\infty < t < \infty$.

Upon setting

$$h = \int_{-\infty}^{0} a'(t - \tau)\psi(v_x)_x d\tau + g, \quad t \geqslant 0, \quad 0 \leqslant x \leqslant 1 , \tag{2.10}$$

$$u_0(x) = v(0,x), \quad u_1(x) = v_t(0,x), \quad 0 \leqslant x \leqslant 1 , \tag{2.11}$$

the history-value problem (2.8), (2.9) reduces to the initial-value problem

$$u_{tt} = \phi(u_x)_x + \int_{0}^{t} a'(t - \tau)\psi(u_x)_x d\tau + h , \tag{2.12}$$

$$0 \leqslant t < \infty, \quad 0 \leqslant x \leqslant 1 ,$$

435

$$u(0,x) = u_0(x), \quad u_t(0,x) = u_1(x), \quad 0 \leqslant x \leqslant 1 . \tag{2.13}$$

Conversely, (2.12), (2.13) can be reduced to (2.8), (2.9) by constructing a function $v(t,x)$ on $(-\infty,0] \times [0,1]$ which satisfies $v(0,x) = u_0(x)$, $v_t(0,x) = u_1(x)$,

$$\begin{cases} v_{tt}(0,x) = \phi(u_{0x})_x + h(0,x) , & 0 \leqslant x \leqslant 1 , \\[2mm] v_{ttt}(0,x) = \phi''(u_{0x})u_{0xx}u_{1x} + \phi'(u_{0x})u_{1xx} + \\[2mm] \qquad\qquad + a'(0)\psi(u_{0x})_x + h_t(0,x) , & 0 \leqslant x \leqslant 1 , \end{cases} \tag{2.14}$$

together with appropriate boundary conditions, for $t \leqslant 0$, and then defining $g(t,x)$ on $(-\infty,\infty) \times [0,1]$ by

$$g(t,x) = \begin{cases} v_{tt} - \phi(v_x)_x - \displaystyle\int_{-\infty}^{t} a'(t-\tau)\psi(v_x)_x d\tau , & t \leqslant 0, \quad 0 \leqslant x \leqslant 1 , \\[4mm] h - \displaystyle\int_{-\infty}^{0} a'(t-\tau)\psi(v_x)_x d\tau , & t \geqslant 0, \quad 0 \leqslant x \leqslant 1 . \end{cases} \tag{2.15}$$

The purpose of (2.14) is to ensure that $g(t,x)$, as defined by (2.15), has the *smoothness properties across* $t = 0$ *which are required in the existence theory.*

We now consider the problem consisting of the nonlinear equation (2.8) satisfying (2.9) and the case where the boundary of the body is free of traction. The latter leads to the boundary conditions

$$\sigma(t,0) = \sigma(t,1) = 0, \quad -\infty < t < \infty . \tag{2.16}$$

These and other types of boundary conditions are discussed in [3]. It is also shown in [3] that (2.16) is equivalent to the boundary condition $u_x(t,0) = u_x(t,1) = 0.$

The change of variable (superposition of a rigid motion)

$$u(t,x) = \bar{u}(t,x) + m_0 + m_1 t + \int_0^t \int_0^\tau \int_0^1 g(s,y)\,dy\,ds\,d\tau$$

shows that without loss of generality we may assume

$$\int_0^1 g(t,x)\,dx = 0, \quad -\infty < t < \infty , \tag{2.17}$$

$$\int_0^1 u(t,x)\,dx = 0, \quad -\infty < t < \infty . \tag{2.18}$$

Of the external body force g we require the following technical assumptions

$$\begin{cases} g(t,\cdot),g_t(t,\cdot),g_x(t,\cdot) & \text{in } C((-\infty,\infty); L^2(0,1)) \cap L^2((-\infty,\infty); L^2(0,1)) \\ g(t,x) = g_1(t,x) + g_2(t,x) \text{ with } g_{1tt}(t,\cdot),g_{2tx}(t,\cdot) \text{ in } L^2((-\infty,\infty(L^2(0,1)) \,. \end{cases}$$

(2.19)

The notation $g(t,\cdot) \in C((-\infty,\infty);L^2(0,1))$ means that the function $\int_0^1 g^2(t,x)\,dx$ is continuous on $(-\infty,\infty)$; $g(t,\cdot) \in L^2((-\infty,\infty);L^2(0,1))$ means that $\int_{-\infty}^\infty \int_0^1 g^2(t,x)\,dx\,dt < \infty$. As noted above, despite the presence of viscous dissipation, it is not to be expected that a global smooth solution of (2.8), (2.9), (2.16) will exist unless the amplitude of waves remains small. Consequently, one may only hope to obtain global existence results under the restriction that $g(t,x)$ be appropriately "small". We "measure" $g(t,x)$ by

$$G \stackrel{\text{def}}{=} \sup_{(-\infty,\infty)} \int_0^1 \{g^2 + g_t^2 + g_x^2\}(t,x)\,dx + \int_{-\infty}^\infty \int_0^1 \{g^2 + g_t^2 + g_x^2 + g_{1tt}^2 + g_{2tx}^2\}\,dx\,dt\,.$$

Our main result is

Theorem 2.1. Under assumptions (2.3)-(2.6), <u>there exists a constant</u> $\mu > 0$ <u>with the following property: For every</u> $g(t,x)$ <u>on</u> $(-\infty,\infty) \times [0,1]$ <u>which satisfies</u> (2.17) <u>and</u> (2.19) <u>with</u>

$$G \leqslant \mu^2 \,, \tag{2.20}$$

<u>and for any history</u> $v(t,x)$ <u>on</u> $(-\infty,0] \times [0,1]$, <u>with</u> $v(t,\cdot), v_t(t,\cdot),$ $v_x(t,\cdot), v_{tt}(t,\cdot), v_{tx}(t,\cdot), v_{xx}(t,\cdot), v_{ttt}(t,\cdot), v_{ttx}(t,\cdot), v_{txx}(t,\cdot),$ $v_{xxx}(t,\cdot)$ <u>in</u> $C((-\infty,0]; L^2(0,1)) \cap L^2((-\infty,0]; L^2(0,1))$, <u>which satisfies</u> <u>Equation</u> (2.8) <u>together with the boundary conditions</u> (2.16) <u>for</u> $t \leqslant 0$, <u>there</u> <u>exists a unique</u> $u(t,x)$ <u>on</u> $(-\infty,\infty) \times [0,1]$, <u>with</u> $u(t,\cdot), u_t(t,\cdot), u_x(t,\cdot)$ $u_{tt}(t,\cdot), u_{tx}(t,\cdot), u_{xx}(t,\cdot), u_{ttt}(t,\cdot), u_{ttx}(t,\cdot), u_{txx}(t,\cdot), u_{xxx}(t,\cdot)$ <u>in</u> $C((-\infty,\infty); L^2(0,1)) \cap L^2((-\infty,\infty); L^2(0,1))$, <u>which satisfies</u> (2.8), (2.9), (2.16), <u>as well as</u> (2.18). <u>Furthermore,</u>

$$u(t,\cdot), u_t(t,\cdot), u_x(t,\cdot), u_{tt}(t,\cdot),$$

$$u_{tx}(t,\cdot), u_{xx}(t,\cdot) \xrightarrow[{[0,1]}]{\text{unif.}} 0, \quad t \to \infty \,.$$

(2.21)

The general strategy used in the proof of Theorem 2.1 in [3] is as follows. First one establishes the existence of a unique smooth local solution u defined on a maximal interval $(-\infty,t_0) \times [0,1]$, with the property that when $T_0 < \infty$ a certain norm of the solution becomes infinite as $t \to T_0$; this is done by a fixed point argument (combined with a standard energy method for linear problems) on a suitably chosen abstract space of functions. Second, energy methods are combined with properties of strongly

437

positive kernels to show that due to the viscous dissipation of the integral term in (2.8), the aforementioned norm of remains uniformly bounded on the maximal interval, provided the data g and v are sufficiently smooth and small. By standard theory for nonlinear problems this means that $T_0 = +\infty$ and the smooth solution exists globally in t. This part of the analysis involves obtaining technically complicated a priori estimates of certain norms of the derivatives (in one space dimension, up to and including order 3) directly from the equation (2.8). It is here that it becomes convenient to use the equivalent form

$$u_{tt} = \chi(u_x)_x + \int_{-\infty}^{t} a(t - \tau)\psi(u_x)_{\tau x}\, d\tau + g ,$$

(2.22)

$$-\infty < t < \infty, \quad 0 \leqslant x \leqslant 1 ,$$

of equation (2.8) (equation (2.22) is obtained from (2.8) by integrating by parts with respect to τ and by using the definition of the equilibrium stress χ); it is therefore clear that assumption (2.6) plays a crucial role in the proof.

Another important role in the analysis is the present normalization of the kernel a with $a(\infty) = 0$ (see assumption (2.3)), which is different from that in the earlier literature (see [2] and [3] for further comments). The reader should note that a', not a, enters the constitutive relation (2.1), as well as the equation of motion (2.8). In the earlier literature in which only the special case $\psi \equiv \phi$ was studied, the normalization

$$a(t) = a_\infty + A(t) \qquad 0 \leqslant t < \infty ,$$

$a(0) = 1$, $a_\infty > 0$, $A \in W^{2,1}(0,\infty)$, A strongly positive was used. The normalization used here is crucial for generating the a priori estimates directly from equation (2.22) (equivalent to (2.8)). The reader should note that the present, normalization and (2.6) imply that if $\phi \equiv \psi$, $0 < a(0) < 1$. The physical appropriateness of the restriction $\phi \equiv \psi$, which was made in the earlier literature for technical reasons is by no means evident.

Some modifications of Theorem 2.1 for boundary conditions other than (2.16), as well as certain generalizations to finite viscoelastic bodies in 2 and 3 dimensions are discussed in [3].

REFERENCES.

1. B. D. Coleman and M. E. Gurtin, Waves in Materials with Memory II. On the growth and decay of one-dimensional acceleration waves, Archive for Rational Mech. and Anal. 19 (1965), 239-265.

2. C. M. Dafermos, Can dissipation prevent the breaking of waves, Trans. of the 26th Conference of Army Mathematicians, ARO Report 81-1, pp. 187-198.

3. C. M. Dafermos and J. A. Nohel, A nonlinear hyperbolic Volterra equation, Amer. J. Math. (to appear); available as Math. Research Center Tech. Summary Report #2095, June 1980.

THE DEVELOPMENT OF MASS DETONATION IN AMMUNITION STORES TREATED AS A STOCHASTIC PROCESS

Abdul R. Kiwan and Philip M. Howe
Ballistic Research Laboratory, USAARRADCOM
Aberdeen Proving Ground, MD 21005

ABSTRACT. The problem of mass detonation is of considerable interest from a prevention point of view. The process of propagation of the detonation from one ammunition round to another bears a strong analogy to several physical problems studied in percolation theory. For our study we replaced the ammunition rounds by abstract objects called sites and connected them by bonds along which the reaction can propagate with a fixed independent interaction probability p. This interaction probability, p, is a function of the physical conditions of the ammunition round, and the physical arrangements of the rounds relative to each other. The number of rounds, n, in a reaction cluster which consists of the detonated rounds and the connecting bonds is a function of the interaction probability p, the dimension of the ammunition lattice and the geometric arrangements of the rounds relative to each other. Concepts such as critical probability p_c, in percolation theory have analogues in our ammunition problem.

We constructed a multidimensional Monte Carlo model for our problem and used it to study a number of interesting aspects of the ammunition mass detonation problem. Our study dealt with the effects of dimensionality, of unequal interaction probabilities p, in different directions, as the case may be with some types of ammunition rounds, and included also the synergistic effects which arise from the simultaneous detonation of neighboring rounds.

I. INTRODUCTION. Fire and impact comprise the two principal sources of explosive incidents. As a result of fire or impact, one or more munitions within a storage area can detonate. Under certain commonly encountered munitions and munition configuration conditions, neighboring munitions can detonate "sympathetically," a chain reaction can establish, and we have what is called a mass detonation.

The conditions which control the development of a mass detonation are of considerable interest, and there is a special need to relate these conditions to characteristics of the individual munitions, and the nature of the storage array. Thus, if we change the probability that one round detonating can cause another round to detonate, through shielding or redesign of the munitions, how will changing that probability influence the expected explosion size? In particular, how small do we have to make the round-to-round interaction probability, p, in order to keep the expected explosion size below some (arbitrarily chosen) number of detonating munitions? Furthermore, how does the expected explosion size depend on the dimension of the storage lattice and the geometry of the arrangement? Other questions which arise are:

What are the values of p for which a finite, nonzero probability exists that an infinite number of rounds in an infinite stack will detonate?

Since large tests are expensive, only a few validation tests can be performed. It would be embarrassing to predict an explosion size and then obtain wildly different test results. Hence, what is the dispersion of the mean explosion size as a function of p?

In some physical situations, if two nearest neighbors detonate simultaneously, the probability of a third round, which has each of the above two rounds as nearest neighbors, detonating simultaneously is near unity. How does this affect explosion size?

The mathematical modeling of the evolution of an explosion in a stack of mass-detonable munitions falls within the realm of percolation theory[1,2,3] and has a very close similarity to stochastic models of phase transitions and propagation of epidemics[4,5]. The munitions are treated as lattice points and the development of the mass detonation is described in terms of lattice topology and interaction probabilities between lattice points, where the "interaction probability" is actually the probability that detonation of one munition can cause detonation of another neighbor.

II. MODEL DESCRIPTION. The problem of propagation of reaction from an ammunition round to other munitions in a munition store is seen to fit the model of an unoriented bond percolation problem with some differences. Thus, in this model the sites of a percolation lattice correspond to the ammunition rounds and the bonds represent the paths of interaction between rounds, with probability p being the probability of one round detonating causing a neighbor to detonate. In this model we assumed that a munition round can only be initiated by a nearest neighbor round. The number of nearest neighbors of a site depends on the dimension and topology of the lattice, or equivalently, in our ammunition problem, on the

[1] V. Shante and S. Kirkpatrick, "An Introduction to Percolation Theory," Advances in Physics, 20, 325 ff (1971).

[2] H. Stanley, R. Birgeneau, P. Reynolds, and J. Nicoll, "Thermally Driven Phase Transitions Near the Percolation Threshold in Two Dimensions," J. Phys. C.: Solid State Physics, 9, L553-560 (1976).

[3] J. Essam, "Graph Theory and Statistical Physics," Discrete Mathematics, 1, 83-112 (1971).

[4] D. Ludwig, "Final Size Distribution of Epidemics," Math. Biosciences, 23, 33-46 (1975).

[5] W. Goffman, and V. Newell, "Generalization of Epidemic Theory, an Application to the Transmision of Ideas," Nature, 204, 225-228 (1964)

dimension of the storage method and the arrangements of the rounds relative to each other. The number of bonds leaving a site is called the coordination number of the lattice and is denoted by c. The percolation probability, $P(p)$, for a lattice is defined in general as the probability that the fluid from a randomly selected atom (bond) source wets infinitely many other atoms (bonds). Thus mathematically

$$P(p) = \lim_{n \to \infty} P_n(p) \tag{1}$$

where $P_n(p)$ is the probability that a randomly selected atom source wets at least n other atoms. The critical probability p_c is defined as

$$p_c = \text{Supremum} \ [p/P(p) = 0] \tag{2}$$

hence, for $p > p_c$,

$$P(p) > 0, \tag{3}$$

i.e., there is a finite probability of getting an infinite cluster. The lattices encountered in the ammunition problem are considered finite although they may consist of a large number of rounds. This simplifies our computational process and we do not concern ourselves with the limiting process of equation (1). We point out here that the number of rounds in a munition reaction cluster is less than or equal to the corresponding cluster size of the analogous theoretical bond percolation problem. This difference arises because a munition round can only detonate once. Hence, munition reaction clusters do not have any closed loops as might be the case in the theoretical bond percolation problem. If N_m is the cluster size, $\{P_n(p)\}_m$ the probability of clusters of at least size n, $(P_c)_m$ is the critical probability for the munition problem, N_t, $(P_n(p))_t$, and $(p_c)_t$ are the corresponding quantities for the analogous theoretical bond percolation problem then

$$N_m \leq N_t \ . \tag{4}$$

This implies that

$$(P_n(p))_m \leq (P_n(p))_t \tag{5}$$

$$(P(p))_m \leq (P(p))_t \tag{6}$$

$$(p_c)_t \leq (p_c)_m \ . \tag{7}$$

The developed model is a computational one, based on Monte Carlo methods, and is capable of treating a bond, or a site percolation problem in one, two, or three dimensions. The computation is started

by setting up the computational lattice as specified by the input. A site of the lattice, representing a munition round, is selected at random. The selected round is considered to be detonated. If the input specified that more than one round is initially detonated then a program subroutine is called to select the remaining rounds of the initial reaction set (ISET) from the nearest neighbors of the randomly selected site. An array, (IND) in this computational model keeps record of the status of each round in the lattice. Thus, in a two dimensional bond problem, $IND(i, j, 1) = 1$, if the reaction propagated to the round at $(i, j, 1)$, $IND(i, j, 1) = 0$, otherwise. At the beginning of a typical cycle of calculations, the bonds emanating from all sites at the reaction front are examined to see which bonds propagate the reaction to their nearest neighbors and which bonds block the reaction. This determination is achieved by using a random number generator to generate a continuous random number, r, such that $0 > r > 1$, and r has a uniform probability density distribution $f_r(r_o)$. The sample space for r is partitioned into two events, (i) the event E_1, $(r \leq p)$, that the bond is unblocked and propagates the reaction to a neighboring round, (ii) the event, E_2, $(r > p)$, that the bond is blocked and does not propagate the reaction to a neighbor. Because of the assumption that a round can only be initiated by an immediate neighbor, the search process is limited to the first generation neighbors of the reaction front. The newly detonated rounds form the reaction front for the next cycle of calculations. The location of the new reaction front at the end of each cycle is saved in coordinate arrays. The calculation cycles are terminated when no new rounds are detonated. This will complete a trial and a new trial is initiated up to an input specified number of trials NTRIAL. At the end of each trial the total number of reacted rounds in the reaction cluster for the trial is saved in an array, $ND(j)$. At the end of the run, the mean reaction cluster size, and its standard deviation are computed and printed. A histogram of the reaction cluster size n, is printed together with values of the cumulative probabilities $P_n(p)$, and $Q_n(p)$ for a number of input specified values of n, where

$$Q_n(p) = 1 - P_n(p). \qquad (8)$$

Several values of the interaction probability can be computed in a single run. The developed code has a number of options that can be either selected on input or achieved with a change of a few cards. The code will print out the hierarchy of the reaction branching process through the ammunition lattice if input specified. It is also possible to treat the nonisotropic case of unequal interaction probabilities p_x, p_y, and p_z. Another option treats also the synergistic case of making the interaction probability $p = 1$, when two neighboring rounds detonate simultaneously.

III. MODEL APPLICATION.

The application of this model to various munition problems requires that we determine the number of trials (r) needed for a certain case, in order that the mean reaction cluster size, $\bar{n}$, lie within a small ϵ neighborhood of the expected value, $E(n)$. Let ℓ be the lattice size; p, the interaction probability. Let n_i be the cluster size on i^{th} trial.

$$1 \leq n_i \leq \ell. \quad (i = 1, 2, \ldots r) \qquad (9)$$

Let
$$p(n_i = j) = p(j), \qquad (10)$$

then
$$\sum_{j=1}^{\ell} p(j) = 1. \qquad (11)$$

Let n_i be drawn from a distribution whose mean is $E(n)$ and variance $\sigma^2(n)$. Let

$$\bar{n} = (\sum_{i=1}^{r} n_i)/r, \qquad (12)$$

and let $E(\bar{n})$, and $\sigma^2(\bar{n})$ be the expected value and variance of $\bar{n}$. It is well known that:

$$E(\bar{n}) = E(n), \qquad (13)$$

$$\sigma^2(\bar{n}) = \frac{\sigma^2(n)}{r}. \qquad (14)$$

We want to choose r sufficiently large so that,

$$\sigma(\bar{n}) = \sigma(n)/\sqrt{r} < \epsilon. \qquad (15)$$

Now $\sigma(n)$, and $\sigma(\bar{n})$ are not known, but

$$\sigma^2(n) \approx (\sum_{i=1}^{r} n_i^2 - r \cdot \bar{n}^2)/r, \qquad (16)$$

hence, we choose r sufficiently large so that (15) is satisfied. If we let

$$\epsilon = \lambda.\bar{n}, \qquad\qquad (17)$$

then (15) reduces to:

$$r > \sigma^2(n)/(\lambda.\bar{n})^2. \qquad\qquad (18)$$

For most cases $\sigma(n) \leq \bar{n}$, hence for $\lambda = 0.1$ and assuming equality to hold we find

$$r > 100. \qquad\qquad (19)$$

Computationally, we studied the convergence of the mean cluster size $\bar{n}$, as a function of the number of trials r in a 20 x 20 x 1 lattice for the cases p = 0.3, 0.4, 0.5, and 0.6 and found that r = 200 is sufficiently large for most cases of interest. Figure 1 shows the results of this study. The solid lines through the data points represent the means of these points.

Computational studies on a number of two and three dimensional lattices have shown that $d\bar{n}/dp$ attains a maximum for values of p close to the theoretical values of the critical probability p_c, for the corresponding infinite lattice. Hence, defining the critical probability for such a lattice to be the value of p for which the maximum is attained, we found that for 100 x 100 square lattice $p_c = 0.51$ and for 40 x 40 x 5 cubic lattice $p_c = 0.305$. The corresponding theoretical values for the infinite square and cubic bond percolation problems are 0.50 and 0.254.

The above model was used to study the variations of the mean cluster size $\bar{n}$, as a function of the interaction probability p, and the stacking method for three lattices L_1 = 100 x 80 x 1, L_2 = 40 x 40 x 5, and L_3 = 20 x 20 x 20. Figure 2 shows the results of the study and reveals the advantage of stacking ammunition in a two dimensional lattice over a three dimensional lattice. It is realized that the probability of hit is greater in the two dimensional case due to the larger exposed surface area. Figure 3 shows a comparison of the mean cluster size as a function of p, in a lattice for the isotropic case, the synergistic effects case, and the nonisotropic case where the interaction probability in one direction might be large as is the case with HEAT (High Explosive Anti-Tank) munitions. Figure 4 shows a comparison of three cases with decreasing interaction probability in one direction. Some HE munitions, e.g. the 155 mm projectile, have small interaction probability in a nose to nose configuration. The case $p_z = 0.01$ represents such a munition and is seen to be close to the two dimensional case if packed in a nose to nose configuration.
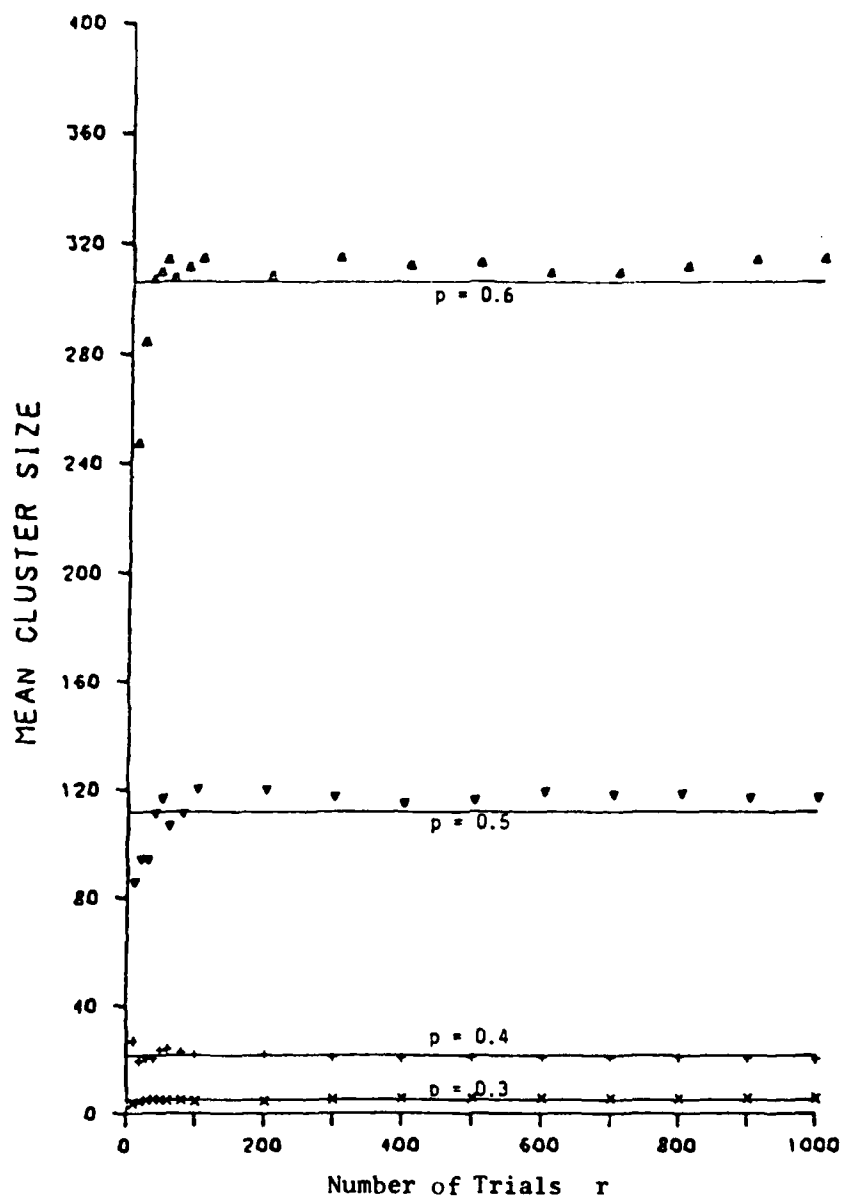
Figure 1 - Random Initiation of a 20 x 20 x 1 Lattice
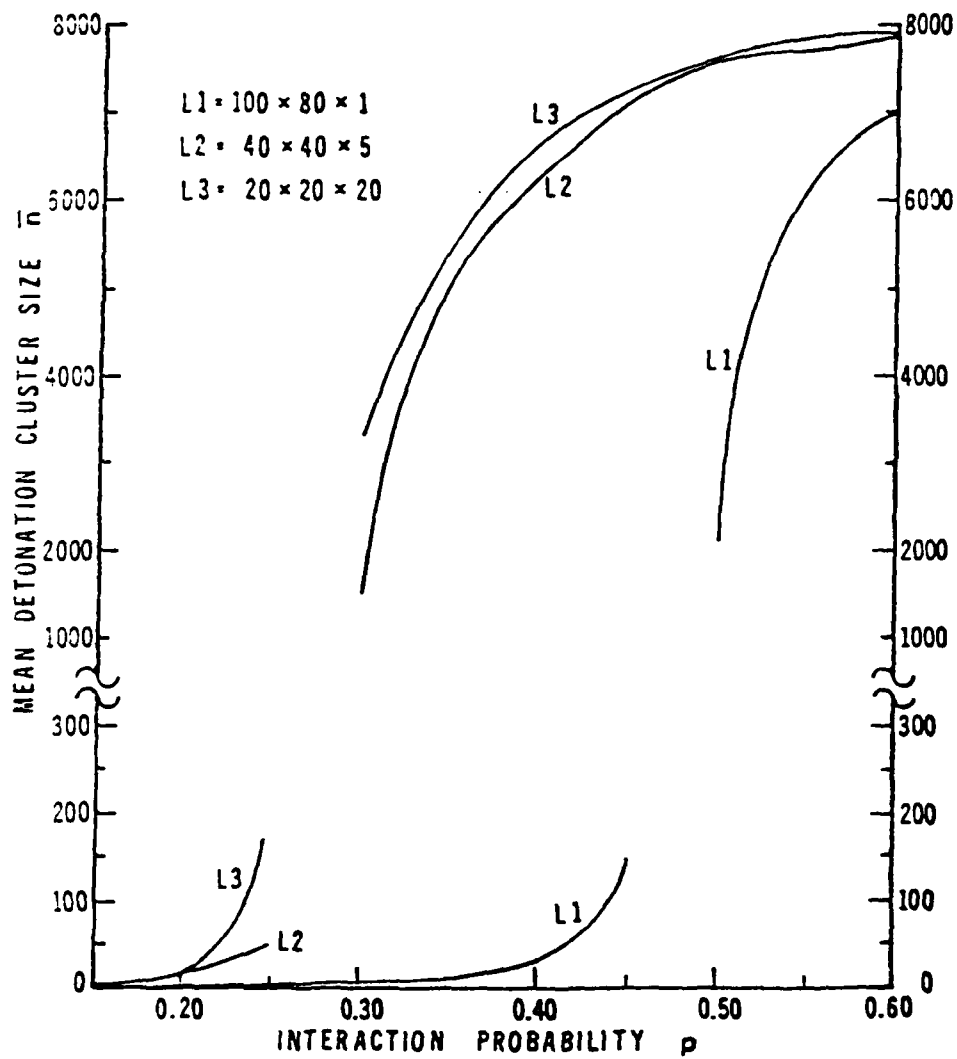
Figure 2 - Mean Cluster Size as a Function of Stacking Method
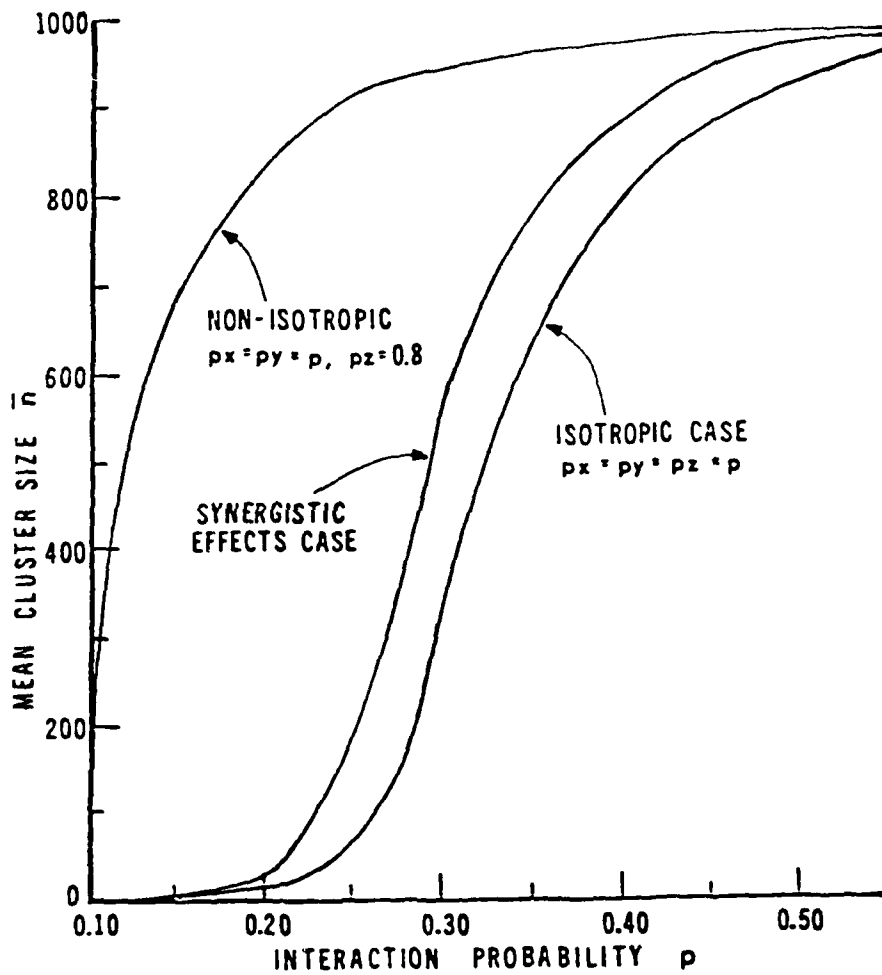
Figure 3 - Comparison of Mean Cluster Size in a 10x10x10 Stack Initiated at Center for Isotropic, Non-Isotropic and Synergistic Effects Cases
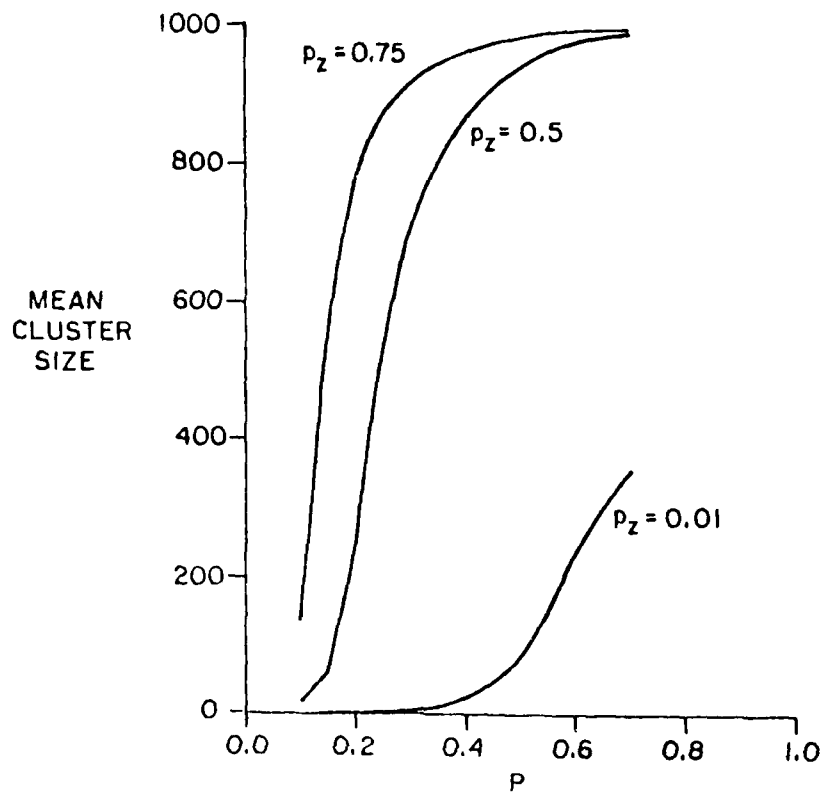
Figure 4 - Mean Cluster Size Variations With Interaction Probability p_z

IV. CONCLUSIONS.

The framework of percolation theory offers a means of studying the problem of propagation of the detonation in an ammunition store as a bond percolation problem.

The stochastic model constructed and used to study the survivability of an ammunition store shows that survivability depends on the inter-round interaction probability p, as well as on the stacking procedure of the ammunition.

For a given stacking method survivability dictates that the inter-action probability p, be less than a critical value p_c, for the lattice in question.

For given ammunition characteristics (p), and quantity, survivability dictates that they be preferably stacked in a manner as close to the two dimensional lattice as possible; rather than a three dimensional lattice.

448

TERRAIN MICROROUGHNESS AND THE DYNAMIC
RESPONSE OF VEHICLES

Richard A. Weiss
Mobility Systems Division
U. S. Army Engineer Waterways
Experiment Station, Vicksburg, MS 39180

ABSTRACT. The design of vehicles with particular operating character-
istics on rough terrain requires accurate descriptors of terrain roughness.
At present a one parameter description of surface roughness is available
that uses the standard deviation of a detrended elevation profile. In order
to introduce the frequency content of the terrain into the roughness de-
scription, a three parameter model of the surface roughness power spectrum
is developed whose parameters are determined from the values of the standard
deviation of displacement, slope and curvature obtained from a detrended
elevation profile. The three parameter model predicts five distinct types
of power spectra which can be used to classify terrain roughness including
the cases where periodic features are present. For some types of terrain
it is not necessary to use detrended data, and for these cases the power
spectra are developed using an undetrended formalism.

The three parameter roughness model can be used to predict the power
absorbed by the driver. The effects of vehicle geometry including wheel
size, wheel spacing and track length are introduced in a natural way through
the roughness model. Vehicle dynamics effects including the location of the
driver relative to the center of mass of the vehicle are introduced by trans-
mission functions. A comparison with experimental absorbed power data is
made.

PART I: INTRODUCTION. The dynamic response of a specified type of wheeled
vehicle operating on a terrain depends on the vehicle speed and the terrain
roughness. For satisfactory operation of both vehicle and driver, the dynamic
response of the vehicle must be predictable for a given type of terrain. To
achieve this prediction capability, the U. S. Army Engineer Waterways Experi-
ment Station (WES) was requested to develop improved methods of describing
terrain and use them to calculate the resulting vehicle and driver motion.

A description of terrain roughness is especially important for the de-
velopment of new vehicles because ride tests on various types of terrain are
required to evaluate new design concepts. An accurate surface roughness
description is required to separate the effects of a new vehicle design from
the effects introduced by the surface roughness properties of a test site.
Both the frequency content and the amplitude of an elevation profile will
influence the ride quality of a vehicle, and an effect observed during a
vehicle ride test may be due to a peculiarity of the terrain roughness rather
than a specific vehicle effect.

The development of new vehicle designs is helped by a thorough under-
standing of how changes in the geometry and dynamics of a vehicle will inter-
act with the terrain roughness to produce changes in the ride quality.

Especially important are the effects of geometry including wheel size, wheel spacing, driver location and track length, and the effects of dynamical parameters including spring constants, damping constants and the weight.[1] The effects of soil conditions are not treated although they may be important to the vehicle response.

Description of Terrain Roughness

A description of surface roughness begins with a measurement of an elevation profile, Figure 1a. Elevations are measured at small intervals (usually one foot or one half foot) over a distance of several hundred feet. Numerical differentiation gives the slope and curvature profiles. The measured elevations include gradual changes of elevation over a long distance. In some cases this nonstationary character of the measured elevation profile may have to be removed by a detrending procedure in order for the data to be processed. In other cases the measured elevation data can be used directly.

Roughness can be described as a stationary random process if the statistical properties of the profile height do not change with position along the profile. To remove nonstationary trends from the data a detrending procedure* is applied to the data which removes the very long wavelengths (the trend), see Figure 1b. The mathematical procedure for obtaining detrended data is given by[2]

$$F_d(x) = F(x) - \frac{1}{2\lambda} \int_0^\infty [F(x + a) + F(x - a)]e^{-a/\lambda} \, da \tag{1}$$

where $F_d(x)$ = detrended function

$\quad$ $F(x)$ = original function
$\quad\quad$ λ = filter constant (detrending constant)

Computer program RRFN has been developed to calculate the detrended data from the original input data.[1]

After removing the trend the question still remains as to the frequency constant of the terrain roughness. This is important because a dynamical system such as the spring support of a vehicle has a resonance frequency, and this resonance may be excited if the vehicle runs over a given terrain at a specified speed. Therefore it is of importance to know the wavelength content of the terrain roughness because this will determine the frequency content of the input displacement, velocity, and acceleration on the wheels of the moving vehicle. The wavelength content of a terrain displacement profile can be described by a power spectral density function.

The power spectral density (PSD) gives the spectral density of the variance of a random process.[2-4] Therefore,

$$\sigma^2 = V = \int_0^\infty \text{PSD} \, d\Omega \tag{2}$$

---

* "Detrend" means to remove the trend of the elevation variations.

where σ = RMS value of the random process = standard deviation for zero average value

V = variance

Ω = spatial frequency = reciprocal wavelength = number of cycles/meter

In this paper the RMS value and the standard deviation will be used interchangeably because the baseline can be chosen so that all average values are zero. The PSD gives a measure of the frequency content of the random process. For example, the surface displacement profile PSD is a measure of the wavelength content of this profile.

One Parameter Model

A descriptor commonly used in terrain roughness models is the standard deviation (RMS) of displacement obtained from a measured elevation profile. The one parameter roughness power spectrum can be calculated from the value of the RMS displacement. The one parameter power spectra of the surface displacement and slope can be written as[2,5]

$$P_d(\Omega) = \frac{C}{\Omega^2} \tag{3}$$

$$P_s(\Omega) = (2\pi)^2 \Omega^2 \left[\frac{\sin (\pi \Omega \Delta L)}{\pi \Omega \Delta L} \right]^2 P_d(\Omega) \tag{4}$$

where P_d = PSD of displacement profile

P_s = PSD of slope profile

C = roughness parameter

ΔL = interval of elevation of profile measurement

For the undetrended case the RMS displacement integral (2) does not converge with P_d given by equation (3), however the RMS slope integral (2) does converge with P_s given by equation (4). For the single parameter model a theoretical expression for the RMS value of the displacement can only be determined for detrended data, and the theoretical need for detrending is that it allows the elevation power spectrum integral to be evaluated. For this reason the value of the parameter C must be determined from detrended data. The spectral window function occurring in equation (4) introduces the interval of measurement of the elevation profile.

The power spectrum for a detrended elevation profile can be written as[2]

$$P_{d,DET}(\Omega, \lambda) = \frac{(2\pi\lambda)^4 \Omega^4}{[1 + (2\pi\lambda\Omega)^2]^2} P_d(\Omega) \tag{5}$$

$$= \phi^{-2} P_d(\Omega)$$

where the detrending function ϕ is defined by

$$\phi = 1 + (2\pi\lambda\Omega)^{-2} \tag{6}$$

451

Since the RMS integral of the slope power spectrum converges, Van Deusen uses the undetrended slope power spectrum given by equation (4) to calculate the RMS value of the slope. The integrals presented are[2]

$$\sigma_d^2 \text{ (Undetrended)} = \int_0^\infty P_d(\Omega)d\Omega \qquad \text{Diverges} \qquad (7)$$

$$\sigma_d^2 \text{ (Detrended,}\lambda) = \int_0^\infty P_{d,DET}(\Omega,\lambda)d\Omega = \frac{\pi^2\lambda C}{2} \qquad (8)$$

$$\sigma_s^2 \text{ (Undetrended)} = \int_0^\infty P_s(\Omega)d\Omega = \frac{2\pi^2 C}{\Delta L} \qquad (9)$$

where σ_d = standard deviation of terrain displacement

σ_s = standard deviation of terrain slope

A determination of the RMS displacement for detrended data (by computer program RRFN, for example) immediately determines the constant C, and there-fore the power spectrum for the undetrended data is calculated. Two basic theoretical concepts are introduced in the one parameter model: (a) the detrending function which allows the elevation RMS value to be calculated analytically, and (b) the slope spectral window function which introduces the measurement interval of the elevation profile. The value of σ_s can be used to calculate C directly from undetrended data using equation (9).

Three Parameter Model

A comparison of the one parameter monotonically decreasing power spectrum $P_d = C/\Omega^2$ with the power spectrum values obtained by calculating the Fourier transform of the autocorrection function of an elevation profile suggests that the one parameter representation is valid only for high spatial frequencies of the terrain roughness. Also, quasi-random terrain areas such as plowed or disked agricultural fields cannot be described by a one parameter model be-cause a pronounced peak occurs in the measured power spectrum at a frequency corresponding to the width of the plowed furrows.

A more complete description of surface roughness is needed, one that goes a step beyond a one parameter characterization that is based on a single RMS value of surface displacement. This paper introduces a three parameter rough-ness power spectrum model that can describe terrain areas having periodicities, and gives a better description of the roughness power spectrum in the long wavelength region.

The three power spectrum parameters are determined from the values of the standard deviations of the displacement, slope and curvature of a measured elevation profile (Figure 1a). The power spectrum determined by these param-eters is found to be of five distinct types of which the Van Deusen form $C\Omega^{-2}$ is one. The displacement power spectrum $P_d(\Omega)$ is found to be a complicated function of frequency that includes spectral windows of definite bandwidth.

The resulting frequency channels of power transmission and power suppression may be responsible for the anomalous dynamic response of some vehicles on a given terrain.

Actual terrain locations where military trucks and track vehicles are expected to operate can vary considerably in quality (frequency) as well as their RMS values of elevation. Terrain types such as trails, cultivated fields, virgin terrain, test courses, etc., are expected to be encountered by military off-road vehicles. An attempt is made to classify terrain roughness in terms of the five basic types of roughness power spectra by associating each terrain site with one of the five types of power spectra. The type of power spectrum associated with a terrain site will determine the nature of the dynamic response of a vehicle moving over that terrain. In this way the expected dynamic response of a vehicle can be related to a specific terrain site. A computer program TERR was developed to accomplish this work.[1]

Absorbed Power

Driver fatigue can be related to the power absorbed by a driver during the operation of a vehicle. Absorbed power is a physiological concept and by definition it is related to the acceleration power spectrum measured at the drivers seat.[6] Experience has shown that a driver can absorb no more than six watts of power and be physically able to drive a vehicle for an extended period of time.[7] It is of military interest to be able to predict the vehicle speed that corresponds to the six watt absorbed power level, and to determine the terrain roughness descriptors required to do this.

At present the six watt speed is estimated from the RMS value of surface displacement as determined from a detrended elevation profile.[8-13] This single parameter terrain roughness description is sometimes found to be inadequate because the frequency content of the ground surface elevation is not considered. The three parameter terrain roughness description was developed in part to improve the method of determining the six watt speed by including the effects of frequency content.

PART II: THEORETICAL ROUGHNESS MODELS

INTRODUCTORY REMARKS. Terrain areas can be natural or man-made or a com-
bination of both types. Natural terrain elevations appear to be random, but
some features such as windblown sand dunes have an apparent regularity. Man-
made areas such as roads, trails, plowed and disked fields, etc., can contain
apparent regularities although their elevation profiles are still character-
ized as random data. Plowed fields, for example, exhibit a quasi-sinusoidal
pattern and will have a power spectrum that peaks at a spatial frequency that
corresponds to the quasi-sinusoidal pattern. This case clearly cannot be
described by a one parameter power spectrum of the form $C\Omega^{-2}$ which is a
monotonically decreasing function of spatial frequency. This part of the
paper develops a three parameter power spectrum model that can be used to
describe random terrain roughness elevation which include regularities, man-
made or natural.

The power spectrum coefficients of the three parameter model are calcu-
lated from the RMS values of elevation, slope and curvature that are obtained
from a detrended elevation profile or from an undetrended elevation profile
when possible. The values of these three parameters can be used to classify
terrain roughness.

FORM OF THE THREE PARAMETER POWER SPECTRUM. This section suggests an
appropriate form for the three parameter roughness power spectrum. The choice
of the form of the three parameter power spectrum model is a natural extension
of the Van Deusen one parameter model $C\Omega^{-2}$. Figure 2a shows that the PSD of
the undetrended and detrended displacement profile is described by the form
$C\Omega^{-2}$ only in the region of large Ω (short wavelengths). For small Ω (long
wavelength) the PSD deviates from that predicted by $C\Omega^{-2}$. Additional param-
eters are required to describe the deviation from $C\Omega^{-2}$ in the region of small
Ω. Assuming that the short wavelength region is accurately described by the
form $C\Omega^{-2}$, the modification of the PSD must consist of terms $\Omega^{-\alpha}$ (with $\alpha > 2$)
that are added to the $C\Omega^{-2}$ term. In this way the modification of the PSD
becomes important only for small Ω and approaches the form $C\Omega^{-2}$ for large Ω.

The PSD for undetrended surface displacement can be written as a general-
ization of $C\Omega^{-2}$ in the form of a power series as follows

$$P_d = C\Omega^{-2} + D\Omega^{-3} + E\Omega^{-4} + \cdots \tag{10}$$

For practical calculation, the power series must be cut off at some finite
term. If two parameters are chosen to describe P_d in the form

$$P_d = C\Omega^{-2} + D\Omega^{-3} \tag{11}$$

then the measurement of both σ_d and σ_s is required to determine C and D. If
three parameters are chosen to describe P_d in the form

$$P_d = C\Omega^{-2} + D\Omega^{-3} + E\Omega^{-4} \tag{12}$$

then σ_d, σ_s and σ_c would be required to determine C, D, and E, where σ_c = standard deviation of curvature (second derivative of elevation with regard to space coordinate). In this paper the term curvature will be used to describe the second derivative.

Polynomial models beginning with the term $A\Omega^{1}$ such as

$$P_d = A\Omega^{-1} + C\Omega^{-2} + D\Omega^{-3} \tag{13}$$

are not valid for two reasons: (1) they do not approach the Van Deusen form $C\Omega^{-2}$ for large Ω, and (2) the integral $\int_0^\infty P_d\phi^{-2}d\Omega$ for detrended data has a logarithmic singularity and cannot be evaluated.

The short wavelength (high frequency) part of the power spectrum is described by the parameter C, while the long wavelength (low frequency) part of the power spectrum is described by the parameter E. The middle ranges of frequency are determined by the parameter D. The values of the power spectrum parameters C, D and E are determined by the type of terrain elevation profile that is measured, and these parameters can be used as descriptive numbers to classify terrain roughness.

CLASSIFICATION OF TERRAIN ROUGHNESS. This section shows how a terrain roughness classification can be developed in a natural way from the algebraic signs of the parameters C, D and E. Terrain roughness can be classified according to the shape of the power spectrum associated with the natural elevation profile. The shape of a theoretically predicted roughness power spectrum is determined by the values of the parameters C, D and E. These parameters will be determined from the values of σ_d, σ_s and σ_c associated with the elevation profile.

A priori, the values of the three parameters can be positive or negative yielding a total of $2 \times 2 \times 2 = 8$ possible types of power spectra. But the case $C < 0$, $D < 0$ and $E < 0$ must obviously be excluded because the power spectrum must be positive at least in some frequency range. This leaves seven possibilities. But of these seven cases two are redundant and only five physically distinct types of elevation power spectra are possible for the three parameter model. These are shown in Figure 2b. The basic forms of Type 2 and Type 3 remain unchanged for $D > 0$ or $D < 0$ so that either sign still represents only one spectral type, and this redundancy yields only five distinct spectral classes.

The one parameter power spectrum $C\Omega^{-2}$ is seen to be a special case of a Type 1 power spectrum with $C > 0$, $D = 0$ and $E = 0$. Type 1 power spectrum contains all frequencies with little power at the high frequencies. Type 2 has no power at high frequencies. Types 3 and 4 have pronounced peaks at definite

frequencies and can be used to describe a large scale rolling type of terrain. Type 4 with $D^2 < 4CE$ gives a power spectrum which is all negative and so this case must be excluded. Type 5B with $D^2 > 4CE$ describes the situation where a high frequency periodicity occurs within the terrain, such as in the case of plowed or disked fields. Type 5A with $D^2 < 4CE$ can be considered to be a special case of Type 1 where the power is positive for all frequencies.

Power spectra, by definition as the Fourier transform of an autocorrelation, are always positive. Therefore only the frequency ranges where $P_d(\Omega)$ is positive in Figure 2b are physically acceptable. The regions where $P_d(\Omega)$ become negative must be regarded as physically unacceptable for power transmission and $P_d(\Omega)$ is set equal to zero here. In this manner it is seen that the roughness power spectrum $P_d(\Omega)$ is not in general a simple function but rather may contain cutoff frequencies (Ω_0 and Ω_1) which produce "windows" (bright areas) and zero power areas (dark regions) of definite bandwidths. Therefore only in distinct frequency regions may power be transferred to a moving vehicle. The type of power spectrum exhibited by a given site is determined from measured values of σ_d, σ_s and σ_c from which the values of C, D and E are obtained.

The power spectra used are one-sided because they are defined only for positive frequencies. Sometimes two-sided power spectra are used which are defined for positive and negative frequencies. The two-sided power spectra can be obtained as mirror images of the one-sided power spectra. Power spectra must be symmetrical about the zero frequency axis because they are defined as Fourier transforms of autocorrelation functions which themselves are symmetrical. The power spectrum model given in (12) can be used for negative Ω by choosing $|\Omega|^3$, absolute value of Ω, in the regions of negative Ω.

The type of power spectrum obtained from an elevation profile will depend on the length of the measured profile. Therefore the classification of terrain areas will be scale dependent, and a comparison of two terrain areas should be made on the basis of equal elevation profile lengths. This paper does not investigate scale dependence.

The five possible types of roughness power spectra are associated with the choice of a three parameter power spectrum model. The choice of a greater number of parameters would produce more complicated power spectrum shapes. For example a four parameter model would exhibit two additional types of spectra giving a total of seven types. The three parameter choice made in this paper is justified by noting that Newton's law of motion relates the force acting on a vehicle to the acceleration input. Therefore as far as vehicle dynamics is concerned there are three stochastic kinematic quantities to be obtained: acceleration, velocity and displacement. This suggests a three parameter surface roughness model because the standard deviations of velocity σ_v and acceleration σ_a can be related to the standard deviations of the slope σ_s and curvature σ_c, respectively, of the terrain elevation profile (Part III). Therefore the calculation of the basic kinematic quantities associated with the vertical dynamic response of vehicles (σ_d, σ_v, σ_a) requires the three measured

roughness quantities σ_d, σ_s and σ_c from which three power spectrum parameters (C, D and E) can be determined.

THREE PARAMETER MODEL OF DETRENDED TERRAIN ROUGHNESS DATA. This section develops the formalism and mathematical details required to evaluate the power spectrum of a measured elevation profile from the RMS values of the elevation, slope and curvature obtained from the corresponding detrended elevation profile. This is done for each of the five types of power spectra described above.

For roughness power spectra of Types 1, 2 and 5 it is impossible to use values of σ_d, σ_s and σ_c obtained directly from undetrended data to calculate the power spectrum coefficients because the integral $\int_0^\infty P_d d\Omega$ diverges (at $\Omega = 0$) for the form of power spectrum given in equation (12). These three types of terrain roughness must be handled using detrended data and the values of σ_d, σ_s and σ_c for detrended data can be related to integrals of the form $\int_0^\infty P_d \phi^{-2} d\Omega$ which converges. For roughness spectra of Types 3 and 4 it is not necessary to use detrended data because the integrals defining σ_d, σ_s and σ_c are defined from a lower cutoff frequency Ω_0 and so the singularity at $\Omega = 0$ is avoided and undetrended data can be used. But the detrended formalism can be applied to spectra of Types 3 and 4, and this section evaluates the integrals that appear in the mathematical expressions for σ_d, σ_s and σ_c (for detrended data) for all five types of terrain roughness power spectra.

For the power spectrum given by equation (12), the values of P_d, P_s and P_c for undetrended data are

$$P_d = C\Omega^{-2} + D\Omega^{-3} + E\Omega^{-4} \tag{14}$$

$$P_s = (2\pi)^2 \Omega^2 (C\Omega^{-2} + D\Omega^{-3} + E\Omega^{-4}) \left[\frac{\sin(\pi\Omega\Delta L)}{\pi\Omega\Delta L} \right]^2 \tag{15}$$

$$P_c = (2\pi)^4 \Omega^4 (C\Omega^{-2} + D\Omega^{-3} + E\Omega^{-4}) \left[\frac{\sin(\pi\Omega\Delta L)}{\pi\Omega\Delta L} \right]^4 \tag{16}$$

The form for the slope and curvature PSD is developed in Reference 1.

The necessary integrals for the detrended scheme of the three parameter model will now be evaluated. This will be done for each of the five basic types of roughness power spectrum.

Type 1 Power Spectrum
The variance integrals of P_d and P_s cannot be performed directly on (14) and (15) because they are singular for $\Omega = 0$. In order to calculate C, D and E, the variance of the detrended displacement, slope and curvature profiles must be used. For the case of detrended data the displacement, slope and

curvature power spectral densities are $P_d\phi^{-2}$, $P_s\phi^{-2}$ and $P_c\phi^{-2}$ respectively where ϕ is defined by (7). From (14) - (16) the RMS values of the detrended terrain displacement, slope and curvature are

$$\sigma_d^2 = V_d = \int_0^\infty P_d\phi^{-2}d\Omega = Cf_1(\lambda) + Df_2(\lambda) + Ef_3(\lambda) \tag{17}$$

$$\sigma_s^2 = V_s = \int_0^\infty P_s\phi^{-2}d\Omega = Cg_1(\lambda) + Dg_2(\lambda) + Eg_3(\lambda) \tag{18}$$

$$\sigma_c^2 = V_c = \int_0^\infty P_c\phi^{-2}d\Omega = Ch_1(\lambda) + Dh_2(\lambda) + Eh_3(\lambda) \tag{19}$$

The values of σ_d^2, σ_s^2 and σ_c^2 are represented as a linear combination of integrals where the $f_i(\lambda)$, $g_i(\lambda)$ and $h_i(\lambda)$ are given, with $b = 2\pi\lambda$ and $a = \pi\Delta L$, as

$$f_1(\lambda) = \int_0^\infty \Omega^{-2}\phi^{-2}d\Omega = b^4 \int_0^\infty \frac{\Omega^2 d\Omega}{(1 + b^2\Omega^2)^2} \tag{20}$$

$$f_2(\lambda) = \int_0^\infty \Omega^{-3}\phi^{-2}d\Omega = b^4 \int_0^\infty \frac{\Omega d\Omega}{(1 + b^2\Omega^2)^2} \tag{21}$$

$$f_3(\lambda) = \int_0^\infty \Omega^{-4}\phi^{-2}d\Omega = b^4 \int_0^\infty \frac{d\Omega}{(1 + b^2\Omega^2)^2} \tag{22}$$

$$g_1(\lambda) = (2\pi)^2 \int_0^\infty \left(\frac{\sin a\Omega}{a\Omega}\right)^2 \phi^{-2}d\Omega = \frac{(2\pi)^2 b^4}{a^2} \int_0^\infty \frac{\Omega^2 \sin^2(a\Omega)d\Omega}{(1 + b^2\Omega^2)^2} \tag{23}$$

$$g_2(\lambda) = (2\pi)^2 \int_0^\infty \Omega^{-1} \left(\frac{\sin a\Omega}{a\Omega}\right)^2 \phi^{-2}d\Omega = \frac{(2\pi)^2 b^4}{a^2} \int_0^\infty \frac{\Omega \sin^2(a\Omega)d\Omega}{(1 + b^2\Omega^2)^2} \tag{24}$$

$$g_3(\lambda) = (2\pi)^2 \int_0^\infty \Omega^{-2} \left(\frac{\sin a\Omega}{a\Omega}\right)^2 \phi^{-2} d\Omega = \frac{(2\pi)^2 b^4}{a^2} \int_0^\infty \frac{\sin^2 (a\Omega) d\Omega}{(1 + b^2\Omega^2)^2} \qquad (25)$$

$$h_1(\lambda) = (2\pi)^4 \int_0^\infty \Omega^2 \left(\frac{\sin a\Omega}{a\Omega}\right)^4 \phi^{-2} d\Omega = \frac{(2\pi)^4 b^4}{a^4} \int_0^\infty \frac{\Omega^2 \sin^4 (a\Omega) d\Omega}{(1 + b^2\Omega^2)^2} \qquad (26)$$

$$h_2(\lambda) = (2\pi)^4 \int_0^\infty \Omega \left(\frac{\sin a\Omega}{a\Omega}\right)^4 \phi^{-2} d\Omega = \frac{(2\pi)^4 b^4}{a^4} \int_0^\infty \frac{\Omega \sin^4 (a\Omega) d\Omega}{(1 + b^2\Omega^2)^2} \qquad (27)$$

$$h_3(\lambda) = (2\pi)^4 \int_0^\infty \left(\frac{\sin a\Omega}{a\Omega}\right)^4 \phi^{-2} d\Omega = \frac{(2\pi)^4 b^4}{a^4} \int_0^\infty \frac{\sin^4 (a\Omega) d\Omega}{(1 + b^2\Omega^2)^2} \qquad (28)$$

Note the integrals g_1, g_2, h_1, h_2 and h_3 diverge where $a = 0$, so that σ_s and σ_c diverge for $\Delta L = 0$. Only for the case $\Delta L \neq 0$ are σ_d, σ_s and σ_c properly defined by infinite integrals when $\Omega \to \infty$. Also, the integrals representing σ_d and σ_s would diverge in the low frequency limit if the detrending factor ϕ^{-2} were not inserted into these integrals. In other words, whereas $\Delta L \neq 0$ avoids singularities at high frequencies, the detrending factor ϕ^2 avoids singularities at low frequencies.

The values of the integrals in (20) - (28) are evaluated in Reference 1 by complex integration using the contours shown in Figure 2c, and have the following values

$$f_1(\lambda) = \frac{\pi b}{4} \qquad (29)$$

$$f_2(\lambda) = \frac{b^2}{2} \qquad (30)$$

$$f_3(\lambda) = \frac{\pi b^3}{4} \qquad (31)$$

$$g_1(\lambda) = \frac{\pi^3 b}{a^2} \left[\frac{1}{2}\left(1 - e^{-2a/b} \right) + \frac{a}{b} e^{-2a/b} \right] \tag{32}$$

$$g_2(\lambda) = \frac{\pi^2 b}{a^2} \left[e^{2a/b} E_1 (2a/b) + e^{-2a/b} E*(2a/b) \right] \tag{33}$$

$$g_3(\lambda) = \frac{\pi^3 b^3}{a^2} \left[\frac{1}{2}\left(1 - e^{-2a/b} \right) - \frac{a}{b} e^{-2a/b} \right] \tag{34}$$

$$h_1(\lambda) = \frac{4\pi^5 b}{a^4} \left[\frac{3}{8} + \frac{e^{-4a/b}}{8} - \frac{e^{-2a/b}}{2} + \frac{a}{b} e^{-2a/b}\left(1 - \frac{1}{2} e^{-2a/b} \right) \right] \tag{35}$$

$$h_2(\lambda) = \frac{4\pi^4 b}{a^3} \left\{ e^{2a/b}E_1(2a/b) + e^{-2a/b}E*(2a/b) - \frac{1}{2}\left[e^{4a/b}E_1(4a/b) \right. \right.$$
$$\left. \left. + e^{-4a/b}E*(4a/b) \right] \right\} \tag{36}$$

$$h_3(\lambda) = \frac{4\pi^5 b^3}{a^4} \left[\frac{3}{8} - \frac{1}{2} e^{-2a/b}\left(1 - \frac{1}{4} e^{-2a/b} \right) - \frac{a}{b} e^{-2a/b}\left(1 - \frac{1}{2} e^{-2a/b} \right) \right] \tag{37}$$

where $E_1 (x)$ and $E*(x)$ are exponential integral functions which are tabulated in the literature. The exponential integrals are defined as follows

$$E_1(x) = -Ei(-x) = \int_x^\infty \frac{e^{-t}}{t} \, dt \tag{38}$$

$$E*(x) = Ei(x) = \int_{-\infty}^x \frac{e^t}{t} \, dt \tag{39}$$

For small values of x these functions have the following series expansions

$$E_1(x) = -\gamma - \log_e(x) + x - \frac{x^2}{2!2} + \frac{x^3}{3!3} - \frac{x^4}{4!4} + \frac{x^5}{5!5} - \cdots \qquad (40)$$

$$E^*(x) = \gamma + \log_e(x) + x + \frac{x^2}{2!2} + \frac{x^3}{3!3} + \frac{x^4}{4!4} + \frac{x^5}{5!5} + \cdots \qquad (41)$$

where γ = Euler constant = 0.5772157.

Type 2 Roughness Spectrum

Detrended data must be used for this case. The integrals defining V_d, V_s and V_c are (see Figure 2b)

$$\sigma_d^2 = \int_0^{\Omega_0} P_d \phi^{-2} d\Omega = C\Delta f_1(\lambda, \Omega_0) + D\Delta f_2(\lambda, \Omega_0) + E\Delta f_3(\lambda, \Omega_0) \qquad (42)$$

$$\sigma_s^2 = \int_0^{\Omega_0} P_s \phi^{-2} d\Omega = C\Delta g_1(\lambda, \Omega_0) + D\Delta g_2(\lambda, \Omega_0) + E\Delta g_3(\lambda, \Omega_0) \qquad (43)$$

$$\sigma_c^2 = \int_0^{\Omega_0} P_c \phi^{-2} d\Omega = C\Delta h_1(\lambda, \Omega_0) + D\Delta h_2(\lambda, \Omega_0) + E\Delta h_3(\lambda, \Omega_0) \qquad (44)$$

where the integrals $\Delta f_j(\lambda, \Omega_0)$, $\Delta g_j(\lambda, \Omega_0)$ and $\Delta h_j(\lambda, \Omega_0)$ are given by

$$\Delta f_1(\lambda, \Omega_0) = b^4 \int_0^{\Omega_0} \frac{\Omega^2 d\Omega}{(1 + b^2\Omega^2)^2} = \frac{b}{2}\left(\theta_0 - \sin\theta_0 \cos\theta_0\right) \sim \frac{b^4\Omega_0^3}{3} \qquad (45)$$

$$\Delta f_2(\lambda, \Omega_0) = b^4 \int_0^{\Omega_0} \frac{\Omega d\Omega}{(1 + b^2\Omega^2)^2} = \frac{b^2}{2}\sin^2\theta_0 \sim \frac{b^4\Omega_0^2}{2} \qquad (46)$$

$$\Delta f_3(\lambda,\Omega_0) = b^4 \int_0^{\Omega_0} \frac{d\Omega}{(1 + b^2\Omega^2)^2} = \frac{b^3}{2} \left(\theta_0 + \sin\theta_0 \cos\theta_0\right) \sim b^4\Omega_0 \qquad (47)$$

where

$$\theta_0 = \tan^{-1}(b\Omega_0) \qquad (48)$$

$$\Delta g_1(\lambda,\Omega_0) = \left(\frac{2\pi}{a}\right)^2 b^4 \int_0^{\Omega_0} \frac{\Omega^2 \sin^2(a\Omega) d\Omega}{(1 + b^2\Omega^2)^2} \qquad (49)$$

$$= \frac{1}{2}\left(\frac{2\pi}{a}\right)^2 b^4 \left[L_0(\Omega_0) - L_1^{(2a)}(\Omega_0) + L_2^{(2a)}(\Omega_0) - \cdots\right]$$

where

$$L_0(\Omega_0) = \Omega_0^3 \left(\frac{1}{3} - \frac{2}{5} b^2\Omega_0^2 + \frac{3}{7} b^4\Omega_0^4 - \frac{4}{9} b^6\Omega_0^6 + \frac{5}{11} b^8\Omega_0^8 - \cdots\right)$$

$$L_1^{(2a)}(\Omega_0) = \frac{\Omega_0^2 \sin(2a\Omega_0)}{2a} + \frac{2\Omega_0 \cos(2a\Omega_0)}{(2a)^2} - \frac{2 \sin(2a\Omega_0)}{(2a)^3}$$

$$L_2^{(2a)}(\Omega_0) = 2b^2 \left\{\left[4(2a)^2\Omega_0^2 - 24\right] \frac{\Omega_0 \cos(2a\Omega_0)}{(2a)^4}\right.$$

$$\left. + \left[(2a)^4\Omega_0^4 - 12(2a)^2\Omega_0^2 + 24\right] \frac{\sin(2a\Omega_0)}{(2a)^5}\right\}$$

$$\Delta g_2(\lambda,\Omega_0) = \left(\frac{2\pi}{a}\right)^2 b^4 \int_0^{\Omega_0} \frac{\Omega \sin^2(a\Omega) d\Omega}{(1 + b^2\Omega^2)^2} \qquad (50)$$

$$= \frac{1}{2}\left(\frac{2\pi}{a}\right)^2 b^4 \left[W_0(\Omega_0) - W_1^{(2a)}(\Omega_0) + W_2^{(2a)}(\Omega_0) - \cdots\right]$$

462

where

$$W_0(\Omega_0) = \frac{\Omega_0^2}{2} \left(1 - b^2\Omega_0^2 + b^4\Omega_0^4 - b^6\Omega_0^6 + b^8\Omega_0^8 - \cdots\right)$$

$$W_1^{(2a)}(\Omega_0) = \frac{\Omega_0 \sin(2a\Omega_0)}{2a} + \frac{\cos(2a\Omega_0)}{(2a)^2} - \frac{1}{(2a)^2}$$

$$W_2^{(2a)}(\Omega_0) = 2b^2\left\{\left[\frac{3\Omega_0^2}{(2a)^2} - \frac{6}{(2a)^4}\right]\cos(2a\Omega_0) + \frac{6}{(2a)^4} + \left[\frac{\Omega_0^2}{2a} - \frac{6}{(2a)^3}\right]\Omega_0 \sin(2a\Omega_0)\right\}$$

$$\Delta g_3(\lambda,\Omega_0) = \left(\frac{2\pi}{a}\right)^2 b^4 \int_0^{\Omega_0} \frac{\sin^2(a\Omega)d\Omega}{(1 + b^2\Omega^2)^2} \tag{51}$$

$$= \frac{1}{2}\left(\frac{2\pi}{a}\right)^2 b^4 \left[H_0(\Omega_0) - H_1^{(2a)}(\Omega_0) + H_2^{(2a)}(\Omega_0) - \cdots\right]$$

where

$$H_0(\Omega_0) = \Omega_0\left(1 - \frac{2}{3}b^2\Omega_0^2 + \frac{3}{5}b^4\Omega_0^4 - \frac{4}{7}b^6\Omega_0^6 + \frac{5}{9}b^8\Omega_0^8 - \cdots\right)$$

$$H_1^{(2a)}(\Omega_0) = \frac{\sin(2a\Omega_0)}{2a}$$

$$H_2^{(2a)}(\Omega_0) = 2b^2\left[\frac{\Omega_0^2 \sin(2a\Omega_0)}{2a} + \frac{2\Omega_0 \cos(2a\Omega_0)}{(2a)^2} - \frac{2\sin(2a\Omega_0)}{(2a)^3}\right]$$

$$\Delta h_1(\lambda, \Omega_0) = \left(\frac{2\pi}{a}\right)^4 b^4 \int\limits_0^{\Omega_0} \frac{\Omega^2 \sin^4 (a\Omega) d\Omega}{(1 + b^2\Omega^2)^2} \tag{52}$$

$$= \frac{1}{4} \left(\frac{2\pi}{a}\right)^4 b^4 \left\{ \frac{3}{2} L_0(\Omega_0) - 2 \left[L_1^{(2a)}(\Omega_0) - L_2^{(2a)}(\Omega_0) + \cdots \right] \right.$$

$$\left. + \frac{1}{2} \left[L_1^{(4a)}(\Omega_0) - L_2^{(4a)}(\Omega_0) + L_3^{(4a)}(\Omega_0) - \cdots \right] \right\}$$

where

$$L_1^{(4a)}(\Omega_0) = \frac{\Omega_0^2 \sin (4a\Omega_0)}{4a} + \frac{2\Omega_0 \cos (4a\Omega_0)}{(4a)^2} - \frac{2 \sin (4a\Omega_0)}{(4a)^3}$$

$$L_2^{(4a)}(\Omega_0) = 2b^2 \left\{ \left[4(4a)^2\Omega_0^2 - 24 \right] \frac{\Omega_0 \cos (4a\Omega_0)}{(4a)^4} \right.$$

$$\left. + \left[(4a)^4\Omega_0^4 - 12(4a)^2\Omega_0^2 + 24 \right] \frac{\sin (4a\Omega_0)}{(4a)^5} \right\}$$

$$\Delta h_2(\lambda, \Omega_0) = \left(\frac{2\pi}{a}\right)^4 b^4 \int\limits_0^{\Omega_0} \frac{\Omega \sin^4 (a\Omega) d\Omega}{(1 + b^2\Omega^2)^2} \tag{53}$$

$$= \frac{1}{4} \left(\frac{2\pi}{a}\right)^4 b^4 \left\{ \frac{3}{2} W_0(\Omega_0) - 2 \left[W_1^{(2a)}(\Omega_0) - W_2^{(2a)}(\Omega_0) + \cdots \right] \right.$$

$$\left. + \frac{1}{2} \left[W_1^{(4a)}(\Omega_0) - W_2^{(4a)}(\Omega_0) + \cdots \right] \right\}$$

where

$$W_1^{(4a)}(\Omega_0) = \frac{\Omega_0 \sin (4a\Omega_0)}{4a} + \frac{\cos (4a\Omega_0)}{(4a)^2} - \frac{1}{(4a)^2}$$

$$W_2^{(4a)}(\Omega_0) = 2b^2 \left\{ \left[\frac{3\Omega_0^2}{(4a)^2} - \frac{6}{(4a)^4} \right] \cos(4a\Omega_0) + \frac{6}{(4a)^4} + \left[\frac{\Omega_0^2}{4a} - \frac{6}{(4a)^3} \right] \Omega_0 \sin(4a\Omega_0) \right\}$$

$$\Delta h_3(\lambda,\Omega_0) = \left(\frac{2\pi}{a}\right)^4 b^4 \int_0^{\Omega_0} \frac{\sin^4(a\Omega)d\Omega}{(1 + b^2\Omega^2)^2} \tag{54}$$

$$= \frac{1}{4}\left(\frac{2\pi}{a}\right)^4 b^4 \left\{ \frac{3}{2} H_0(\Omega_0) - 2\left[H_1^{(2a)}(\Omega_0) - H_2^{(2a)}(\Omega_0) + \cdots \right] \right.$$
$$\left. + \frac{1}{2}\left[H_1^{(4a)}(\Omega_0) - H_2^{(4a)}(\Omega_0) + \cdots \right] \right\}$$

where

$$H_1^{(4a)}(\Omega_0) = \frac{\sin(4a\Omega_0)}{4a}$$

$$H_2^{(4a)}(\Omega_0) = 2b^2 \left[\frac{\Omega_0^2 \sin(4a\Omega_0)}{4a} + \frac{2\Omega_0 \cos(4a\Omega_0)}{(4a)^2} - \frac{2\sin(4a\Omega_0)}{(4a)^3} \right]$$

Type 3 Roughness Spectrum

Either the detrended or undetrended procedure can be used for this case. The integrals defining V_d, V_s and V_c for the detrended case are (see Figure 2b)

$$\sigma_d^2 = \int_{\Omega_0}^{\infty} P_d \phi^{-2} d\Omega = Cf_1(\lambda,\Omega_0) + Df_2(\lambda,\Omega_0) + Ef_3(\lambda,\Omega_0) \tag{55}$$

$$\sigma_s^2 = \int_{\Omega_0}^{\infty} P_s \phi^{-2} d\Omega = Cg_1(\lambda,\Omega_0) + Dg_2(\lambda,\Omega_0) + Eg_3(\lambda,\Omega_0) \tag{56}$$

$$\sigma_c^2 = \int_{\Omega_0}^{\infty} P_c \phi^{-2} d\Omega = Ch_1(\lambda,\Omega_0) + Dh_2(\lambda,\Omega_0) + Eh_3(\lambda,\Omega_0) \tag{57}$$

The integrals $f_j(\lambda, \Omega_0)$, $g_j(\lambda, \Omega_0)$ and $h_j(\lambda, \Omega_0)$ are given by

$$f_j(\lambda, \Omega_0) = b^4 \int_{\Omega_0}^{\infty} \frac{\Omega^{3-j} d\Omega}{(1 + b^2\Omega^2)^2} = f_j(\lambda) - \Delta f_j(\lambda, \Omega_0) \qquad (58)$$

$$g_j(\lambda, \Omega_0) = \left(\frac{2\pi}{a}\right)^2 b^4 \int_{\Omega_0}^{\infty} \frac{\Omega^{3-j} \sin^2 (a\Omega) d\Omega}{(1 + b^2\Omega^2)^2} = g_j(\lambda) - \Delta g_j(\lambda, \Omega_0) \qquad (59)$$

$$h_j(\lambda, \Omega_0) = \left(\frac{2\pi}{a}\right)^4 b^4 \int_{\Omega_0}^{\infty} \frac{\Omega^{3-j} \sin^4 (a\Omega) d\Omega}{(1 + b^2\Omega^2)^2} = h_j(\lambda) - \Delta h_j(\lambda, \Omega_0) \qquad (60)$$

Type 4 Power Spectrum

Either the detrended or undetrended scheme can be used for this case.
The integrals defining V_d, V_s and V_c for this case are (see Figure 2b)

$$\sigma_d^2 = \int_{\Omega_0}^{\Omega_1} P_d \phi^{-2} d\Omega = Cf_1(\lambda, \Omega_0, \Omega_1) + Df_2(\lambda, \Omega_0, \Omega_1) + Ef_3(\lambda, \Omega_0, \Omega_1) \qquad (61)$$

$$\sigma_s^2 = \int_{\Omega_0}^{\Omega_1} P_s \phi^{-2} d\Omega = Cg_1(\lambda, \Omega_0, \Omega_1) + Dg_2(\lambda, \Omega_0, \Omega_1) + Eg_3(\lambda, \Omega_0, \Omega_1) \qquad (62)$$

$$\sigma_c^2 = \int_{\Omega_0}^{\Omega_1} P_c \phi^{-2} d\Omega = Ch_1(\lambda,\Omega_0,\Omega_1) + Dh_2(\lambda,\Omega_0,\Omega_1) + Eh_3(\lambda,\Omega_0,\Omega_1) \qquad (63)$$

The integrals $f_j(\lambda,\Omega_0,\Omega_1)$, $g_j(\lambda,\Omega_0,\Omega_1)$ and $h_j(\lambda,\Omega_0,\Omega_1)$ are given by

$$f_j(\lambda,\Omega_0,\Omega_1) = b^4 \int_{\Omega_0}^{\Omega_1} \frac{\Omega^{3-j} d\Omega}{(1 + b^2\Omega^2)^2} = \Delta f_j(\lambda,\Omega_1) - \Delta f_j(\lambda,\Omega_0) \qquad (64)$$

$$g_j(\lambda,\Omega_0,\Omega_1) = \left(\frac{2\pi}{a}\right)^2 b^4 \int_{\Omega_0}^{\Omega_1} \frac{\Omega^{3-j} \sin^2 \frac{(a\Omega)}{2} d\Omega}{(1 + b^2\Omega^2)^2} = \Delta g_j(\lambda,\Omega_1) - \Delta g_j(\lambda,\Omega_0) \qquad (65)$$

$$h_j(\lambda,\Omega_0,\Omega_1) = \left(\frac{2\pi}{a}\right)^4 b^4 \int_{\Omega_0}^{\Omega_1} \frac{\Omega^{3-j} \sin^4 \frac{(a\Omega)}{2} d\Omega}{(1 + b^2\Omega^2)^2} = \Delta h_j(\lambda,\Omega_1) - \Delta h_j(\lambda,\Omega_0) \qquad (66)$$

Type 5B Power Spectrum

The detrended scheme must be used for this case. The integrals defining V_d, V_s and V_c are (see Figure 2b)

$$\sigma_d^2 = \int_0^{\Omega_0} P_d \phi^{-2} d\Omega + \int_{\Omega_1}^{\infty} P_d \phi^{-2} d\Omega \qquad (67)$$

$$= C\delta f_1(\lambda,\Omega_0,\Omega_1) + D\delta f_2(\lambda,\Omega_0,\Omega_1) + E\delta f_3(\lambda,\Omega_0,\Omega_1)$$

467

$$\sigma_s^2 = \int_0^{\Omega_0} P_s \phi^{-2} d\Omega + \int_{\Omega_1}^{\infty} P_s \phi^{-2} d\Omega \tag{68}$$

$$= C\delta g_1(\lambda,\Omega_0,\Omega_1) + D\delta g_2(\lambda,\Omega_0,\Omega_1) + E\delta g_3(\lambda,\Omega_0,\Omega_1)$$

$$\sigma_c^2 = \int_0^{\Omega_0} P_c \phi^{-2} d\Omega + \int_{\Omega_1}^{\infty} P_c \phi^{-2} d\Omega \tag{69}$$

$$= C\delta h_1(\lambda,\Omega_0,\Omega_1) + D\delta h_2(\lambda,\Omega_0,\Omega_1) + E\delta h_3(\lambda,\Omega_0,\Omega_1)$$

The integrals $\delta f_j(\lambda,\Omega_0,\Omega_1)$, $\delta g_j(\lambda,\Omega_0,\Omega_1)$ and $\delta h_j(\lambda,\Omega_0,\Omega_1)$ are given by

$$\delta f_j(\lambda,\Omega_0,\Omega_1) = \Delta f_j(\lambda,\Omega_0) + f_j(\lambda,\Omega_1) = f_j(\lambda) + \Delta f_j(\lambda,\Omega_0) - \Delta f_j(\lambda,\Omega_1) \tag{70}$$

$$\delta g_j(\lambda,\Omega_0,\Omega_1) = \Delta g_j(\lambda,\Omega_0) + g_j(\lambda,\Omega_1) = g_j(\lambda) + \Delta g_j(\lambda,\Omega_0) - \Delta g_j(\lambda,\Omega_1) \tag{71}$$

$$\delta h_j(\lambda,\Omega_0,\Omega_1) = \Delta h_j(\lambda,\Omega_0) + h_j(\lambda,\Omega_1) = h_j(\lambda) + \Delta h_j(\lambda,\Omega_0) - \Delta h_j(\lambda,\Omega_1) \tag{72}$$

Three Parameter Model of Undetrended
Terrain Roughness Data

This section considers the use of undetrended nonstationary elevation profiles to determine the surface roughness power spectrum. If the terrain roughness power spectrum has $E < 0$ as in cases Type 3 and Type 4 of Figure 2b there is a lower cutoff frequency Ω_0 for the power spectrum and the difficulties associated with for integrals for $\Omega \rightarrow 0$ do not arise. For this case undetrended roughness data can be used to determine the power spectrum coefficients C, D and E, and a detrending constant λ does not enter into the calculations. Types 1, 2 and 5 power spectra do not have a lower cutoff frequency and therefore must be obtained from detrended data.

Type 3 Power Spectrum

For a Type 3 roughness power spectrum that exhibits a lower frequency cutoff, the integrals expressing σ_d, σ_s and σ_c for undetrended data in terms of the power spectrum coefficients are (see Figure 2b)

$$\sigma_d^2 = \int_{\Omega_0}^{\infty} \left(C\Omega^{-2} + D\Omega^{-3} + E\Omega^{-4} \right) d\Omega = Cf_1(\Omega_0) + Df_2(\Omega_0) + Ef_3(\Omega_0) \tag{73}$$

$$\sigma_s^2 = \left(\frac{2\pi}{a} \right)^2 \int_{\Omega_0}^{\infty} \left(C\Omega^{-2} + D\Omega^{-3} + E\Omega^{-4} \right) \sin^2(a\Omega) d\Omega \tag{74}$$

$$= Cg_1(\Omega_0) + Dg_2(\Omega_0) + Eg_3(\Omega_0)$$

$$\sigma_c^2 = \left(\frac{2\pi}{a} \right)^4 \int_{\Omega_0}^{\infty} \left(C\Omega^{-2} + D\Omega^{-3} + E\Omega^{-4} \right) \sin^4(a\Omega) d\Omega \tag{75}$$

$$= Ch_1(\Omega_0) + Dh_2(\Omega_0) + Eh_3(\Omega_0)$$

where σ_d, σ_s and σ_c are obtained from undetrended data.

469

The integrals to be evaluated are

$$f_1(\Omega_0) = \int_{\Omega_0}^{\infty} \frac{d\Omega}{\Omega^2} \tag{76}$$

$$f_2(\Omega_0) = \int_{\Omega_0}^{\infty} \frac{d\Omega}{\Omega^3} \tag{77}$$

$$f_3(\Omega_0) = \int_{\Omega_0}^{\infty} \frac{d\Omega}{\Omega^4} \tag{78}$$

$$g_1(\Omega_0) = \left(\frac{2\pi}{a}\right)^2 \int_{\Omega_0}^{\infty} \frac{\sin^2(a\Omega)d\Omega}{\Omega^2} \tag{79}$$

$$g_2(\Omega_0) = \left(\frac{2\pi}{a}\right)^2 \int_{\Omega_0}^{\infty} \frac{\sin^2(a\Omega)d\Omega}{\Omega^3} \tag{80}$$

$$g_3(\Omega_0) = \left(\frac{2\pi}{a}\right)^2 \int_{\Omega_0}^{\infty} \frac{\sin^2(a\Omega)d\Omega}{\Omega^4} \tag{81}$$

$$h_1(\Omega_0) = \left(\frac{2\pi}{a}\right)^4 \int_{\Omega_0}^{\infty} \frac{\sin^4(a\Omega)d\Omega}{\Omega^2} \tag{82}$$

$$h_2(\Omega_0) = \left(\frac{2\pi}{a}\right)^4 \int\limits_{\Omega_0}^{\infty} \frac{\sin^4 (a\Omega)d\Omega}{\Omega^3} \tag{83}$$

$$h_3(\Omega_0) = \left(\frac{2\pi}{a}\right)^4 \int\limits_{\Omega_0}^{\infty} \frac{\sin^4 (a\Omega)d\Omega}{\Omega^4} \tag{84}$$

The integrals $f_1(\Omega_0)$, $f_2(\Omega_0)$, $f_3(\Omega_0)$, $g_2(\Omega_0)$, and $g_3(\Omega_0)$ diverge in the long wavelength limit $\Omega_0 \to 0$.

The evaluation of these integrals is done in Reference 1 and yields the following results

$$f_1(\Omega_0) = \Omega_0^{-1} \tag{85}$$

$$f_2(\Omega_0) = \frac{\Omega_0^{-2}}{2} \tag{86}$$

$$f_3(\Omega_0) = \frac{\Omega_0^{-3}}{3} \tag{87}$$

$$g_1(\Omega_0) = \frac{2\pi^2}{a^2} \left(\frac{1}{\Omega_0} - I_2^{(2a)}\right) \tag{88}$$

$$g_2(\Omega_0) = \frac{2\pi^2}{a^2} \left(\frac{1}{2\Omega_0^2} - I_3^{(2a)}\right) \tag{89}$$

$$g_3(\Omega_0) = \frac{2\pi^2}{a^2} \left(\frac{1}{3\Omega_0^3} - I_4^{(2a)}\right) \tag{90}$$

$$h_1(\Omega_0) = \left(\frac{2\pi}{a}\right)^4 \left(\frac{3}{8}\frac{1}{\Omega_0} - \frac{1}{2} I_2^{(2a)} + \frac{1}{8} I_2^{(4a)}\right) \tag{91}$$

$$h_2(\Omega_0) = \left(\frac{2\pi}{a}\right)^4 \left(\frac{3}{16} \frac{1}{\Omega_0^2} - \frac{1}{2} I_3^{(2a)} + \frac{1}{8} I_3^{(4a)}\right) \tag{92}$$

$$h_3(\Omega_0) = \left(\frac{2\pi}{a}\right)^4 \left(\frac{1}{8} \frac{1}{\Omega_0^3} - \frac{1}{2} I_4^{(2a)} + \frac{1}{8} I_4^{(4a)}\right) \tag{93}$$

where the I's are given by

$$I_2^{(2a)} = \frac{\cos (2a\Omega_0)}{\Omega_0} + 2a\,si(2a\Omega_0) \tag{94}$$

$$I_3^{(2a)} = \frac{\cos (2a\Omega_0)}{2\Omega_0^2} - \frac{a \sin (2a\Omega_0)}{\Omega_0} + 2a^2 Ci(2a\Omega_0) \tag{95}$$

$$I_4^{(2a)} = \frac{\cos (2a\Omega_0)}{3\Omega_0^3} - \frac{a \sin (2a\Omega_0)}{3\Omega_0^2} - \frac{2a^2 \cos (2a\Omega_0)}{3\Omega_0} - \frac{4}{3} a^3 si(2a\Omega_0) \tag{96}$$

$$I_2^{(4a)} = \frac{\cos (4a\Omega_0)}{\Omega_0} + 4a\,si(4a\Omega_0) \tag{97}$$

$$I_3^{(4a)} = \frac{\cos (4a\Omega_0)}{2\Omega_0^2} - \frac{2a \sin (4a\Omega_0)}{\Omega_0} + 8a^2 Ci(4a\Omega_0) \tag{98}$$

$$I_4^{(4a)} = \frac{\cos (4a\Omega_0)}{3\Omega^3{}_0} - \frac{2a \sin (4a\Omega_0)}{3\Omega_0^2} - \frac{8a^2 \cos (4a\Omega_0)}{3\Omega_0} - \frac{32}{3} a^3 si(4a\Omega_0) \tag{99}$$

and where sine integral and cosine integral functions are given by

472

$$si(t) = \int_{\infty}^{t} \frac{\sin x}{x} dx = -\frac{\pi}{2} + t - \frac{t^3}{3!3} + \frac{t^5}{5!5} - \frac{t^7}{7!7} + \cdots \qquad (100)$$

$$Ci(t) = \int_{\infty}^{t} \frac{\cos x}{x} dx = \gamma + \log_e t - \frac{t^2}{2!2} + \frac{t^4}{4!4} - \frac{t^6}{6!6} + \cdots \qquad (101)$$

where γ = Euler constant = 0.5772157. This completes the analytical evaluation of the integrals $f_j(\Omega_0)$, $g_j(\Omega_0)$ and $h_j(\Omega_0)$.

Type 4 Power Spectrum

A Type 4 roughness power spectrum exhibits a spectral window having lower and upper frequency cutoffs Ω_0 and Ω_1 respectively. The integrals defining σ_d, σ_s and σ_c are written as (see Figure 2b)

$$\sigma_d^2 = \int_{\Omega_0}^{\Omega_1} (C\Omega^{-2} + D\Omega^{-3} + E\Omega^{-4}) d\Omega = Cf_1(\Omega_0,\Omega_1) + Df_2(\Omega_0,\Omega_1) + Ef_3(\Omega_0,\Omega_1) \qquad (102)$$

$$\sigma_s^2 = \left(\frac{2\pi}{a}\right)^2 \int_{\Omega_0}^{\Omega_1} (C\Omega^{-2} + D\Omega^{-3} + E\Omega^{-4}) \sin^2 (a\Omega) d\Omega \qquad (103)$$
$$= Cg_1(\Omega_0,\Omega_1) + Dg_2(\Omega_0,\Omega_1) + Eg_3(\Omega_0,\Omega_1)$$

$$\sigma_c^2 = \left(\frac{2\pi}{a}\right)^4 \int_{\Omega_0}^{\Omega_1} (C\Omega^{-2} + D\Omega^{-3} + E\Omega^{-4}) \sin^4 (a\Omega) d\Omega \qquad (104)$$
$$= Ch_1(\Omega_0,\Omega_1) + Dh_2(\Omega_0,\Omega_1) + Eh_3(\Omega_0,\Omega_1)$$

where σ_d, σ_s and σ_c refer to undetrended data, and where the integrals $f_j(\Omega_0,\Omega_1)$, $g_j(\Omega_0,\Omega_1)$, and $h_j(\Omega_0,\Omega_1)$ must be evaluated analytically.

By writing the integrals in equations (102), (103) and (104) as $\int_{\Omega_0}^{\Omega_1} = \int_{\Omega_0}^{\infty} - \int_{\Omega_1}^{\infty}$, the following values of these integrals are obtained.

$$f_j(\Omega_0,\Omega_1) = f_j(\Omega_0) - f_j(\Omega_1) \qquad (105)$$

473

$$g_j(\Omega_0,\Omega_1) = g_j(\Omega_0) - g_j(\Omega_1) \tag{106}$$

$$h_j(\Omega_0,\Omega_1) = h_j(\Omega_0) - h_j(\Omega_1) \tag{107}$$

where the functions $f_j(\Omega)$, $g_j(\Omega)$, and $h_j(\Omega)$ are given by equations (85) through (93).

<div align="center">

Calculations of the Parameters
of the Roughness Power Spectrum

</div>

This section gives the procedure for explicitly calculating the power spectrum coefficients C, D and E, and also the cutoff frequencies Ω_0 and Ω_1 which occur in Type 1 - Type 5 power spectra. The values of the integrals $f_j(\lambda)$, $g_j(\lambda)$, $h_j(\lambda)$, and $\Delta f_j(\lambda,\Omega_0)$, $\Delta g_j(\lambda,\Omega_0)$, and $\Delta h_j(\lambda,\Omega_0)$ for the detrended case; $f_j(\Omega_0)$, $g_j(\Omega_0)$, and $h_j(\Omega_0)$ for the Type 3 undetrended case; and $f_j(\Omega_0,\Omega_1)$, $g_j(\Omega_0,\Omega_1)$, and $h_j(\Omega_0,\Omega_1)$ for the Type 4 undetrended case have now been evaluated. These integrals are used to calculate the coefficients C, D and E (and Ω_0 and Ω_1 where necessary) that describe the power spectrum of the actual terrain elevation profile.

The detrending proceudre can be applied whether or not there is a lower cutoff frequency Ω_0, and therefore this procedure can be applied to all of the five power spectrum types shown in Figure 2b. The detrending procedure must be applied to power spectra of Types 1, 2 and 5 because these cases have positive values of power spectrum in the limit $\Omega \to 0$. For Types 3 and 4 power spectra either the detrended or the undetrended formalism can be used. First the calculation of C, D and E for all five types of terrain roughness will be done using the detrended scheme, and then C, D and E will be calculated for spectral types 3 and 4 using the undetrended scheme.

Detrended Scheme

Type 1 (C > 0, D > 0, E > 0), Figure 2b.

The three simultaneous equations (17) - (19) yield

$$C = \frac{\begin{vmatrix} V_d & f_2(\lambda) & f_3(\lambda) \\ V_d & g_2(\lambda) & g_3(\lambda) \\ V_c^s & h_2(\lambda) & h_3(\lambda) \end{vmatrix}}{DET(\lambda)} \qquad D = \frac{\begin{vmatrix} f_1(\lambda) & V_d & f_3(\lambda) \\ g_1(\lambda) & V_d & g_3(\lambda) \\ h_1(\lambda) & V_c^s & h_3(\lambda) \end{vmatrix}}{DET(\lambda)} \tag{108}$$

$$E = \frac{\begin{vmatrix} f_1(\lambda) & f_2(\lambda) & V_d \\ g_1(\lambda) & g_2(\lambda) & V_s \\ h_1(\lambda) & h_2(\lambda) & V_c \end{vmatrix}}{DET(\lambda)} \qquad DET(\lambda) = \begin{vmatrix} f_1(\lambda) & f_2(\lambda) & f_3(\lambda) \\ g_1(\lambda) & g_2(\lambda) & g_3(\lambda) \\ h_1(\lambda) & h_2(\lambda) & h_3(\lambda) \end{vmatrix} \qquad (109)$$

which give C, D and E in terms of the measured variances V_d, V_s and V_c of detrended data.

Type 2 ($C < 0$, $D \lesseqgtr 0$, $E > 0$), Figure 2b.

The solution of the three simultaneous equations (17) - (19) give the power spectrum coefficients as

$$C = \frac{\begin{vmatrix} V_d & \Delta f_2(\lambda,\Omega_0) & \Delta f_3(\lambda,\Omega_0) \\ V_s & \Delta g_2(\lambda,\Omega_0) & \Delta g_3(\lambda,\Omega_0) \\ V_c & \Delta h_2(\lambda,\Omega_0) & \Delta h_3(\lambda,\Omega_0) \end{vmatrix}}{DET\Delta(\lambda,\Omega_0)} \qquad D = \frac{\begin{vmatrix} \Delta f_1(\lambda,\Omega_0) & V_d & \Delta f_3(\lambda,\Omega_0) \\ \Delta g_1(\lambda,\Omega_0) & V_s & \Delta g_3(\lambda,\Omega_0) \\ \Delta h_1(\lambda,\Omega_0) & V_c & \Delta h_3(\lambda,\Omega_0) \end{vmatrix}}{DET\Delta(\lambda,\Omega_0)} \qquad (110)$$

$$E = \frac{\begin{vmatrix} \Delta f_1(\lambda,\Omega_0) & \Delta f_2(\lambda,\Omega_0) & V_d \\ \Delta g_1(\lambda,\Omega_0) & \Delta g_2(\lambda,\Omega_0) & V_s \\ \Delta h_1(\lambda,\Omega_0) & \Delta h_2(\lambda,\Omega_0) & V_c \end{vmatrix}}{DET\Delta(\lambda,\Omega_0)} \qquad DET\Delta(\lambda,\Omega_0) = \begin{vmatrix} \Delta f_1(\lambda,\Omega_0) & \Delta f_2(\lambda,\Omega_0) & \Delta f_3(\lambda,\Omega_0) \\ \Delta g_1(\lambda,\Omega_0) & \Delta g_2(\lambda,\Omega_0) & \Delta g_3(\lambda,\Omega_0) \\ \Delta h_1(\lambda,\Omega_0) & \Delta h_2(\lambda,\Omega_0) & \Delta h_3(\lambda,\Omega_0) \end{vmatrix} \quad (111)$$

and the equation for Ω_0 as

$$\Omega_0 = \frac{-D - \sqrt{D^2 - 4CE}}{2C} \qquad (112)$$

These four equations determine C, D, E and Ω_0.

Type 3 ($C > 0$, $D \gtreqless 0$, $E < 0$), Figure 2b.

The solution of the three simultaneous equations (17) - (19) give the following expressions for the power spectrum coefficients

$$C = \frac{\begin{vmatrix} V_d & f_2(\lambda,\Omega_0) & f_3(\lambda,\Omega_0) \\ V_s^d & g_2(\lambda,\Omega_0) & g_3(\lambda,\Omega_0) \\ V_c^s & h_2(\lambda,\Omega_0) & h_3(\lambda,\Omega_0) \end{vmatrix}}{DET(\lambda,\Omega_0)} \qquad D = \frac{\begin{vmatrix} f_1(\lambda,\Omega_0) & V_d & f_3(\lambda,\Omega_0) \\ g_1(\lambda,\Omega_0) & V_s^d & g_3(\lambda,\Omega_0) \\ h_1(\lambda,\Omega_0) & V_c^s & h_3(\lambda,\Omega_0) \end{vmatrix}}{DET(\lambda,\Omega_0)} \qquad (113)$$

$$E = \frac{\begin{vmatrix} f_1(\lambda,\Omega_0) & f_2(\lambda,\Omega_0) & V_d \\ g_1(\lambda,\Omega_0) & g_2(\lambda,\Omega_0) & V_s^d \\ h_1(\lambda,\Omega_0) & h_2(\lambda,\Omega_0) & V_c^s \end{vmatrix}}{DET(\lambda,\Omega_0)} \qquad DET(\lambda,\Omega_0) = \begin{vmatrix} f_1(\lambda,\Omega_0) & f_2(\lambda,\Omega_0) & f_3(\lambda,\Omega_0) \\ g_1(\lambda,\Omega_0) & g_2(\lambda,\Omega_0) & g_3(\lambda,\Omega_0) \\ h_1(\lambda,\Omega_0) & h_2(\lambda,\Omega_0) & h_3(\lambda,\Omega_0) \end{vmatrix} \qquad (114)$$

and the following equation for Ω_0

$$\Omega_0 = \frac{-D + \sqrt{D^2 - 4CE}}{2C} \qquad (115)$$

These four equations determine the four unknowns C, D, E and Ω_0. The variances V_d, V_s and V_c refer to data detrended with the constant λ.

Type 4 (C < 0, D > 0, E < 0), Figure 2b.

The three simultaneous equations (17) - (19) yield

$$C = \frac{\begin{vmatrix} V_d & f_2(\lambda,\Omega_0,\Omega_1) & f_3(\lambda,\Omega_0,\Omega_1) \\ V_s^d & g_2(\lambda,\Omega_0,\Omega_1) & g_3(\lambda,\Omega_0,\Omega_1) \\ V_c^s & h_2(\lambda,\Omega_0,\Omega_1) & h_3(\lambda,\Omega_0,\Omega_1) \end{vmatrix}}{DET(\lambda,\Omega_0,\Omega_1)} \qquad D = \frac{\begin{vmatrix} f_1(\lambda,\Omega_0,\Omega_1) & V_d & f_3(\lambda,\Omega_0,\Omega_1) \\ g_1(\lambda,\Omega_0,\Omega_1) & V_s^d & g_3(\lambda,\Omega_0,\Omega_1) \\ h_1(\lambda,\Omega_0,\Omega_1) & V_c^s & h_3(\lambda,\Omega_0,\Omega_1) \end{vmatrix}}{DET(\lambda,\Omega_0,\Omega_1)} \qquad (116)$$

$$E = \frac{\begin{vmatrix} f_1(\lambda,\Omega_0,\Omega_1) & f_2(\lambda,\Omega_0,\Omega_1) & V_d \\ g_1(\lambda,\Omega_0,\Omega_1) & g_2(\lambda,\Omega_0,\Omega_1) & V_s^d \\ h_1(\lambda,\Omega_0,\Omega_1) & h_2(\lambda,\Omega_0,\Omega_1) & V_c^s \end{vmatrix}}{DET(\lambda,\Omega_0,\Omega_1)}$$

$$(117)$$

$$DET(\lambda,\Omega_0,\Omega_1) = \begin{vmatrix} f_1(\lambda,\Omega_0,\Omega_1) & f_2(\lambda,\Omega_0,\Omega_1) & f_3(\lambda,\Omega_0,\Omega_1) \\ g_1(\lambda,\Omega_0,\Omega_1) & g_2(\lambda,\Omega_0,\Omega_1) & g_3(\lambda,\Omega_0,\Omega_1) \\ h_1(\lambda,\Omega_0,\Omega_1) & h_2(\lambda,\Omega_0,\Omega_1) & h_3(\lambda,\Omega_0,\Omega_1) \end{vmatrix}$$

1.0

2.8 2.5

3.2 2.2

3.6

4.0 2.0

1.1

1.8

1.25 1.4 1.6

MICROCOPY RESOLUTION TEST CHART

NATIONAL BUREAU OF STANDARDS 1963 A

and the following equations for the bandwidth

$$\Omega_0 = \frac{-D + \sqrt{D^2 - 4CE}}{2C} \tag{118}$$

$$\Omega_1 = \frac{-D - \sqrt{D^2 - 4CE}}{2C} \tag{119}$$

These five equations determine the five unknown power spectrum parameters C, D, E, Ω_0 and Ω_1.

Type 5B (C > 0, D < 0, E > 0), Figure 2b.

The three simultaneous equations (17) - (19) yield

$$C = \frac{\begin{vmatrix} V_d & \delta f_2(\lambda,\Omega_0,\Omega_1) & \delta f_3(\lambda,\Omega_0,\Omega_1) \\ V^d & \delta g_2(\lambda,\Omega_0,\Omega_1) & \delta g_3(\lambda,\Omega_0,\Omega_1) \\ V_c^s & \delta h_2(\lambda,\Omega_0,\Omega_1) & \delta h_3(\lambda,\Omega_0,\Omega_1) \end{vmatrix}}{DET(\lambda,\Omega_0,\Omega_1)} \qquad D = \frac{\begin{vmatrix} \delta f_1(\lambda,\Omega_0,\Omega_1) & V_d & \delta f_3(\lambda,\Omega_0,\Omega_1) \\ \delta g_1(\lambda,\Omega_0,\Omega_1) & V^d & \delta g_3(\lambda,\Omega_0,\Omega_1) \\ \delta h_1(\lambda,\Omega_0,\Omega_1) & V_c^s & \delta h_3(\lambda,\Omega_0,\Omega_1) \end{vmatrix}}{DET(\lambda,\Omega_0,\Omega_1)} \tag{120}$$

$$E = \frac{\begin{vmatrix} \delta f_1(\lambda,\Omega_0,\Omega_1) & \delta f_2(\lambda,\Omega_0,\Omega_1) & V_d \\ \delta g_1(\lambda,\Omega_0,\Omega_1) & \delta g_2(\lambda,\Omega_0,\Omega_1) & V^d \\ \delta h_1(\lambda,\Omega_0,\Omega_1) & \delta h_2(\lambda,\Omega_0,\Omega_1) & V_c^s \end{vmatrix}}{DET(\lambda,\Omega_0,\Omega_1)} \tag{121}$$

$$DET(\lambda,\Omega_0,\Omega_1) = \begin{vmatrix} \delta f_1(\lambda,\Omega_0,\Omega_1) & \delta f_2(\lambda,\Omega_0,\Omega_1) & \delta f_3(\lambda,\Omega_0,\Omega_1) \\ \delta g_1(\lambda,\Omega_0,\Omega_1) & \delta g_2(\lambda,\Omega_0,\Omega_1) & \delta g_3(\lambda,\Omega_0,\Omega_1) \\ \delta h_1(\lambda,\Omega_0,\Omega_1) & \delta h_2(\lambda,\Omega_0,\Omega_1) & \delta h_3(\lambda,\Omega_0,\Omega_1) \end{vmatrix}$$

The equations for Ω_0 and Ω_1 are

$$\Omega_0 = \frac{-D - \sqrt{D^2 - 4CE}}{2C} \tag{122}$$

$$\Omega_1 = \frac{-D + \sqrt{D^2 - 4CE}}{2C} \tag{123}$$

These five equations determine C, D, E, Ω_0 and Ω_1.

For the detrended scheme the values of σ_d, σ_s and σ_c are obtained from data measured at intervals of ΔL and detrended with a factor λ. As such σ_d, σ_s and σ_c represent data that have been conditioned in order that the theoretical determination of C, D and E can be accomplished by equations (17) - (19). The expressions for ϕ^2 and $\sin(a\Omega)/a\Omega$ that occur in the right hand sides of equations (17) - (19) account for the detrending factor λ and the measurement interval ΔL, so that in principle the coefficients C, D and E are independent of the intervals of data measurement or the detrending technique, and reflect the actual roughness condition of the terrain. It is clear then that, as written in equation (14) through (16), P_d describes actual surface roughness, while P_s and P_c still contain a factor containing the arbitrarily selected value of ΔL. But ΔL can be set to zero at this point of the calculation to obtain the values of P_s and P_c for the actual terrain.

This concludes the calculation procedure of the power spectrum coefficients C, D and E from detrended elevation profile data.

Undetrended Scheme

Only Type 3 and Type 4 power spectra can be handled using undetrended data.

Type 3 ($C > 0$, $D \gtrless 0$, $E < 0$), Figure 2b.

For a Type 1 power spectrum the undetrended elevation profile can be used, and the power spectrum coefficients are determined by

$$C = \frac{\begin{vmatrix} V_d & f_2(\Omega_0) & f_3(\Omega_0) \\ V_s & g_2(\Omega_0) & g_3(\Omega_0) \\ V_c & h_2(\Omega_0) & h_3(\Omega_0) \end{vmatrix}}{DET(\Omega_0)} \qquad D = \frac{\begin{vmatrix} f_1(\Omega_0) & V_d & f_3(\Omega_0) \\ g_1(\Omega_0) & V_s & g_3(\Omega_0) \\ h_1(\Omega_0) & V_c & h_3(\Omega_0) \end{vmatrix}}{DET(\Omega_0)} \qquad (124)$$

$$E = \frac{\begin{vmatrix} f_1(\Omega_0) & f_2(\Omega_0) & V_d \\ g_1(\Omega_0) & g_2(\Omega_0) & V_s \\ h_1(\Omega_0) & h_2(\Omega_0) & V_c \end{vmatrix}}{DET(\Omega_0)} \qquad DET(\Omega_0) = \begin{vmatrix} f_1(\Omega_0) & f_2(\Omega_0) & f_3(\Omega_0) \\ g_1(\Omega_0) & g_2(\Omega_0) & g_3(\Omega_0) \\ h_1(\Omega_0) & h_2(\Omega_0) & h_3(\Omega_0) \end{vmatrix}$$

$$(125)$$

and the following equation for Ω_0

$$\Omega_0 = \frac{-D + \sqrt{D^2 - 4CE}}{2C} \qquad (126)$$

These four equations determine the four unknowns C, D, E and Ω_0 that describe a Type 3 power spectrum. The variances V_d, V_s and V_c refer to undetrended elevation profile data.

Type 4 $(C < 0, D > 0, E < 0)$, Figure 2b.

For an undetrended elevation profile with a Type 4 power spectrum of bandwidth $\Omega_1 - \Omega_0$, the power spectrum is calculated by

$$C = \frac{\begin{vmatrix} V_d & f_2(\Omega_0,\Omega_1) & f_3(\Omega_0,\Omega_1) \\ V_s^d & g_2(\Omega_0,\Omega_1) & g_3(\Omega_0,\Omega_1) \\ V_c^s & h_2(\Omega_0,\Omega_1) & h_3(\Omega_0,\Omega_1) \end{vmatrix}}{DET(\Omega_0,\Omega_1)} \qquad D = \frac{\begin{vmatrix} f_1(\Omega_0,\Omega_1) & V_d & f_3(\Omega_0,\Omega_1) \\ g_1(\Omega_0,\Omega_1) & V_s^d & g_3(\Omega_0,\Omega_1) \\ h_1(\Omega_0,\Omega_1) & V_c^s & h_3(\Omega_0,\Omega_1) \end{vmatrix}}{DET(\Omega_0,\Omega_1)} \qquad (127)$$

$$E = \frac{\begin{vmatrix} f_1(\Omega_0,\Omega_1) & f_2(\Omega_0,\Omega_1) & V_d \\ g_1(\Omega_0,\Omega_1) & g_2(\Omega_0,\Omega_1) & V_s^d \\ h_1(\Omega_0,\Omega_1) & h_2(\Omega_0,\Omega_1) & V_c^s \end{vmatrix}}{DET(\Omega_0,\Omega_1)}$$

$$(128)$$

$$DET(\Omega_0,\Omega_1) = \begin{vmatrix} f_1(\Omega_0,\Omega_1) & f_2(\Omega_0,\Omega_1) & f_3(\Omega_0,\Omega_1) \\ g_1(\Omega_0,\Omega_1) & g_2(\Omega_0,\Omega_1) & g_3(\Omega_0,\Omega_1) \\ h_1(\Omega_0,\Omega_1) & h_2(\Omega_0,\Omega_1) & h_3(\Omega_0,\Omega_1) \end{vmatrix}$$

and the following equations for the bandwidth

$$\Omega_0 = \frac{-D + \sqrt{D^2 - 4CE}}{2C} \qquad (129)$$

$$\Omega_1 = \frac{-D - \sqrt{D^2 - 4CE}}{2C} \qquad (130)$$

These five equations determine the five unknowns C, D, E, Ω_0 and Ω_1 that describe the Type 4 power spectrum. The variances V_d, V_s and V_c refer to an undetrended elevation profile.

<u>Dominant Frequencies of a</u>
<u>Terrain Elevation Profile</u>

Roughness power spectrum Types 3, 4 and 5 have a dominant wavelength for the undetrended elevation profile that can be calculated from equation (12) to be

$$\frac{1}{\lambda_D} = \Omega_D = \frac{-3D \pm \sqrt{9D^2 - 32CE}}{4C} \qquad (131)$$

479

For detrended elevation profile data all five spectral types will have a dominant frequency. An approximate expression that gives the dominant wavelength of detrended elevation data in terms of σ_d and σ_s is

$$\lambda_D = \frac{1}{\Omega_D} = 2\pi \frac{\sigma_d}{\sigma_s} \tag{132}$$

This expression is affected by the detrending process.

Numerical Analysis of Terrain
Elevation Data

A numerical study was done to determine the types of terrain roughness power spectra that are associated with actual terrain areas, and to determine their basic frequency content. Computer program RRFN (Reference 1) was developed to calculate values of σ_d, σ_s and σ_c from a measured elevation profile. The computer program RRFN performs the following specific functions:

a. It detrends the measured elevation profile for some choice of value of the detrending parameter.

b. It calculates the standard deviations of displacement, slope and curvature for the detrended and undetrended elevation profile.

Computer prgram TERR (Reference 1) was developed to calculate the roughness power spectra from the values of σ_d, σ_s and σ_c that are supplied by computer program RRFN. The computer program TERR contains all the integrals and mathematical functions that appear in Part II. Computer program TERR performs the following specific functions:

a. It calculates the power spectrum parameters C, D and E and cutoff frequencies Ω_0 and Ω_1 from detrended values of σ_d, σ_s and σ_c for spectral Types 1 through 5, and from undetrended values of σ_d, σ_s and σ_c for spectral Types 3 and 4.

b. It calculates the frequency dependence of all five types of terrain roughness power spectra.

The elevation profiles of 100 terrain sites were examined, and values of σ_d, σ_s and σ_c were calculated using computer program RRFN with a detrending constant $\lambda = 10$ ft. These values of σ_d, σ_s and σ_c were used as input for computer program TERR to calculate the values of the power spectrum coefficients C, D and E and the associated cutoff frequencies Ω_0 and Ω_1 that describe the spectral characteristics of the actual terrain. The results appear in Table 2. The values of C, D and E that appear in this table were calculated using the detrended data formalism.

480

The results in Table 2 show that the signs of the coefficients C, D and E can be positive or negative and the terrain sites can be separated into the five spectral classes described earlier and shown in Figure 2b. The frequency of occurrence is shown in Figure 2d which indicates that spectral Types 3, 4 and 5 are the most common spectral types.

Figures in Reference 1 show typical elevation profiles that correspond to the five types of roughness power spectra. These figures tend to support the conclusions that can be drawn from Figure 2b, namely: that Types 1 and 2 tend to contain mainly long wavelengths (20-60 ft) of relatively large amplitude, Types 3 and 4 tend to have a roughly sinusoidal pattern of medium sized amplitudes with medium sized wavelengths (5-10 ft), while Type 5 contains a high frequency component (wavelength less than 5 ft) of relatively small amplitude.

The frequency of occurrence of spectral types shown in Figure 2d probably depends on the type of terrain selected for this study in the sense that all of the areas selected were test sites used for the operation of vehicles. Other types of terrain, such as may be encountered in macroroughness studies like the elevations measured across a valley, may produce a somewhat different occurrence frequency diagram. The lengths of the elevation profiles used for this study were generally 300 ft. The selection of different profile lengths may also change the frequency occurrence diagram.

It was shown that spectral Types 3 and 4 exhibit a lower cutoff frequency Ω_0 and it is therefore possible to calculate the values of the power spectrum coefficients C, D and E using undetrended elevation profile data. Table 3 gives values of C, D and E calculated for Type 3 power spectra by both the detrended and the undetrended formalisms. The values of C, D and E predicted by both methods are essentially equal, as they should be since they refer to the natural terrain roughness and their values should be independent of the method of calculation.

The relationship of the values of σ_s and σ_c with the values of σ_d appears to be different for each of the five classes of terrain roughness. The relationship is shown in Figures 3a and 3b where it is seen that there is some tendency for the data to fall into distinct groups. Type 5 has the highest values of σ_s/σ_d and σ_c/σ_d due to the high frequency component associated with this spectral type. Types 1 and 2 have the lowest values of these ratios because they contain dominant low frequency components.

Figures 3c through 3e give the dependence of the values of σ_d, σ_s and σ_c on the choice of detrending parameter λ. The values of σ_d decrease rapidly with λ [1], while the values of σ_s and σ_c decrease more slowly. The relatively slow variation of σ_s and σ_c with λ [1] indicates that these two quantities are associated with the higher frequency components of the terrain profile, while σ_d is associated with the lower frequencies.

The values of the spectral coefficients C, D and E immediately give the roughness power spectra for the terrain displacement, slope and curvature as given by equations (14) - (16). The basic forms of $P_d(\Omega)$, $P_s(\Omega)$ and $P_c(\Omega)$ are shown in Figures 4a through 6e for spectral Types 1 through 5.

481

PART III: GEOMETRY AND KINEMATICS OF THE VEHICLE - GROUND CONTACT

Introductory Remarks

In the previous parts of this paper, terrain roughness was described in a manner independent of the geometrical characteristics of an operating vehicle. But the degree of roughness of a terrain area, as measured by the dynamic response of an operating vehicle, will depend on the geometry of the vehicle-ground contact areas. Therefore the terrain roughness description introduced earlier in this paper must be generalized to include the effects of the geometry of the ground contact area.

Two kinds of quantities can be distinguished in vehicle dynamics problems-- input and output variables. By input variables are meant all quantities measured or defined at the soil-vehicle contact points. Output quantities are all quantities measured or defined at points on the vehicle. A theoretical prediction of the output dynamical response of a vehicle requires an understanding of interaction of the geometry of the vehicle with the geometry of the ground surface because this interaction will produce a terrain roughness power spectrum that includes the effects of the terrain-vehicle contact geometry. This terrain-vehicle power spectrum serves as the input for calculations of the dynamical response of a vehicle. This part of the paper calculates the input power spectra for realistic vehicle-ground contact geometries.

Input Power Spectra for Single Point Contact with the Ground

This section derives the power spectra associated with the vertical velocity and acceleration of a point which is constrained to move along a specified elevation profile with a constant horizontal speed. This is done by first calculating the standard deviations of the vertical velocity and acceleration of the point in terms of the standard deviations of the slope and curvature.

The standard deviations of the vertical velocity and vertical acceleration of a point that follows the contours of the surface displacement profile are calculated as follows

$$\sigma_v^2 = \frac{1}{N} \sum_{j=1}^{N} \left(\frac{\Delta d_j}{\Delta t}\right)^2 = \frac{1}{N} u^2 \sum_{j=1}^{N} \left(\frac{\Delta d_j}{\Delta L}\right)^2 = u^2 \sigma_s^2 \tag{133}$$

$$\sigma_a^2 = \frac{1}{N} \sum_{j=1}^{N} \left(\frac{\Delta^2 d_j}{\Delta t^2}\right)^2 = \frac{1}{N} u^4 \sum_{j=1}^{N} \left(\frac{\Delta^2 d_j}{\Delta L^2}\right)^2 = u^4 \sigma_c^2 \tag{134}$$

where σ_v = standard deviation of vertical velocity of wheel-soil point of contact

σ_a = standard deviation of vertical acceleration of wheel-soil point of contact

v = vertical velocity of wheel-soil point of contact

a = vertical acceleration of wheel-soil point of contact

u = horizontal velocity of vehicle = $\dfrac{\Delta L}{\Delta t}$

Equations (133) and (134) are valid for both detrended and undetrended data. However, they are valid only for small values of slope, i.e. for the case when the curvature is essentially equal to the second derivative.

Therefore the RMS values of the slope and curvature immediately determine the RMS values of vertical velocity and vertical acceleration experienced by a point travelling over an elevation profile at a constant horizontal speed. This is done by

$$\sigma_v = u\sigma_s \tag{135}$$

$$\sigma_a = u^2\sigma_c \tag{136}$$

If the point travelling along the surface elevation has an associated mass, the standard deviation of the power delivered to this mass is approximately given by

$$\sigma_p = m\sigma_a\sigma_v = mu^3\sigma_s\sigma_c \tag{137}$$

where σ_p = standard deviation of power
m = mass of point

Although the values of σ_v and σ_a are of some interest, they cannot be used directly to calculate the corresponding RMS values of output velocity and acceleration. The calculation of these output quantities requires the input power spectra.

The power spectral density functions for input displacement, slope, curvature, vertical velocity, and vertical acceleration for a point contact will not be calculated. The PSD functions are expressed in terms of the spatial frequency Ω or the time frequency f that are related as follows

$$\Omega = \frac{f}{u} \tag{138}$$

where f = time frequency. The PSD functions are defined as follows

$$\sigma_d^2 = \int_0^\infty P_d(\Omega)\phi^2 d\Omega = \int_0^\infty P_d'(f)\phi^2 df \qquad (139)$$

$$\sigma_s^2 = \int_0^\infty P_s(\Omega)\phi^2 d\Omega = \int_0^\infty P_s'(f)\phi^2 df \qquad (140)$$

$$\sigma_c^2 = \int_0^\infty P_c(\Omega)\phi^2 d\Omega = \int_0^\infty P_c'(f)\phi^2 df \qquad (141)$$

$$\sigma_v^2 = \int_0^\infty P_v(\Omega)\phi^2 d\Omega = \int_0^\infty P_v'(f)\phi^2 df \qquad (142)$$

$$\sigma_a^2 = \int_0^\infty P_a(\Omega)\phi^2 d\Omega = \int_0^\infty P_a'(f)\phi^2 df \qquad (143)$$

where P_v = power spectrum of input velocity and P_a = power spectrum of input acceleration. Equations (138) through (143) can be used to determine the power spectra in terms of the time frequency.

From (133), (134) and (138) through (143) it follows that

$$P_v(\Omega) = u^2 P_s(\Omega) \qquad (144)$$

$$P_a(\Omega) = u^4 P_c(\Omega) \qquad (145)$$

Using (138) it is clear that

$$P_d'(f) = u^{-1} P_d(\Omega) \qquad (146)$$

$$P_s'(f) = u^{-1} P_s(\Omega) \qquad (147)$$

$$P_c'(f) = u^{-1} P_c(\Omega) \qquad (148)$$

484

$$P'_v(f) = u^{-1} P_v(\Omega) = uP_s(\Omega) = u^2 P'_s(f) \qquad (149)$$

$$P'_a(f) = u^{-1} P_a(\Omega) = u^3 P_c(\Omega) = u^4 P'_c(f) \qquad (150)$$

A summary of the one point power spectra is given as follows. Let

$$\psi(\Omega) = C\Omega^{-2} + D\Omega^{-3} + E\Omega^{-4} \qquad (151)$$

$$\psi\left(\frac{f}{u}\right) = C\left(\frac{u}{f}\right)^2 + D\left(\frac{u}{f}\right)^3 + E\left(\frac{u}{f}\right)^4 \qquad (152)$$

then

$$P_d(\Omega) = \psi(\Omega) \qquad (153)$$

$$P'_d(f) = u^{-1} \psi\left(\frac{f}{u}\right) = u^{-1} P_d(\Omega) \qquad (154)$$

$$P_s(\Omega) = (2\pi\Omega)^2 P_d(\Omega) \qquad (155)$$

$$P'_s(f) = \left(\frac{2\pi f}{u}\right)^2 P'_d(f) \qquad (156)$$

$$P_c(\Omega) = (2\pi\Omega)^4 P_d(\Omega) \qquad (157)$$

$$P'_c(f) = \left(\frac{2\pi f}{u}\right)^4 P'_d(f) \qquad (158)$$

$$P_v(\Omega) = (2\pi u\Omega)^2 P_d(\Omega) \qquad (159)$$

$$P'_v(f) = (2\pi f)^2 P'_d(f) \qquad (160)$$

$$P_a(\Omega) = (2\pi u\Omega)^4 P_d(\Omega) \qquad (161)$$

$$P'_a(f) = (2\pi f)^4 P'_d(f) \qquad (162)$$

Table 1 gives the units of the various power spectra.

Input Power Spectra for a Two Point Contact with the Ground

The power spectra for the case of two contact points with the ground can be obtained by using the spectral window functions given in equations (15) and (16). The various kinematic and terrain roughness power spectral are then given by[2,4]

$$P_d(\Omega) = \psi(\Omega) \tag{163}$$

$$P_d'(f) = u^{-1}\psi\left(\frac{f}{u}\right) = u^{-1} P_d(\Omega) \tag{164}$$

$$P_s(\Omega) = (2\pi\Omega)^2 \left[\frac{\sin(a\Omega)}{a\Omega}\right]^2 P_d(\Omega) \tag{165}$$

$$P_s'(f) = \left(\frac{2\pi f}{u}\right)^2 \left[\frac{\sin(af/u)}{af/u}\right]^2 P_d'(f) \tag{166}$$

$$P_c(\Omega) = (2\pi\Omega)^4 \left[\frac{\sin(a\Omega)}{a\Omega}\right]^4 P_d(\Omega) \tag{167}$$

$$P_c'(f) = \left(\frac{2\pi f}{u}\right)^4 \left[\frac{\sin(af/u)}{af/u}\right]^4 P_d'(f) \tag{168}$$

$$P_v(\Omega) = (2\pi u\Omega)^2 \left[\frac{\sin(a\Omega)}{a\Omega}\right]^2 P_d(\Omega) \tag{169}$$

$$P_v'(f) = (2\pi f)^2 \left[\frac{\sin(af/u)}{af/u}\right]^2 P_d'(f) \tag{170}$$

$$P_a(\Omega) = (2\pi u\Omega)^4 \left[\frac{\sin(a\Omega)}{a\Omega}\right]^4 P_d(\Omega) \tag{171}$$

$$P_a'(f) = (2\pi f)^4 \left[\frac{\sin(af/u)}{af/u}\right]^4 P_d'(f) \tag{172}$$

where $a = \pi L$ and L = distance between the two contact points. The one point power spectra given in equations (153) through (162) are regained by taking $a = 0$ in equations (163) through (172), i.e., the spectral window functions have a unit value for the case of one point of contact.

Spectral Window Functions for Vehicles

The calculations of the input power spectra for vehicles requires a knowledge of the spectral window functions for vehicles. The slope and curvature spectral window functions were introduced in the roughness power spectrum calculations to account for the finite interval of measurement of the ˟ˡevation profile. The same situation arises for a vehicle operating on a terrain site. When the absorbed power or vertical acceleration is measured at the driver's seat, the surface roughness is indirectly being measured. But now the sampling of the elevation profile is being done by the wheels of a truck or the track of a tank, and two physical situations must be considered. First, the sampling is done with finite contact lengths and second, there may be several unequal intervals of measurement as in the case of varius distances between the wheels on one side of a truck running over an elevation profile. Both of these physical situations must be described to calculate the spectral window functions for vehicles.

The spectral window functions can be obtained by averaging over all possible two-point intervals along the areas of contact with the ground. The two-point contact spectral window functions for the slope and curvature are given by equations (15) and (16). Single and multiple contact areas must be considered for the averaging process using equations (15) and (16).

Single Contact Area

For the case of a single contact area, such as produced by one wheel or by a tank track, the spectral window functions are calculated by integrating equations (15) and (16) over all two-point contact positions as shown in Figure 7a with the result that

$$asw^{(2)} = \frac{1}{T_L^2} \int_0^{T_L} \int_0^{T_L} \frac{\sin^2 [\pi\Omega(x - y)]}{[\pi\Omega(x - y)]^2} \, dx \, dy \qquad (173)$$

$$asw^{(4)} = \frac{1}{T_L^2} \int_0^{T_L} \int_0^{T_L} \frac{\sin^4 [\pi\Omega(x - y)]}{[\pi\Omega(x - y)]^4} \, dx \, dy \qquad (174)$$

where

$asw^{(2)}$ = slope spectral window function for single contact area

$asw^{(4)}$ = curvature spectral window function for single contact area

T_L = length of contact area in the direction of vehicle motion

These spectral window functions are evaluated in Reference 1 and have the following values for small values of ΩT_L

$$\text{asw}^{(2)}(T_L) = 1 + \alpha_2(\Omega T_L)^2 + \alpha_4(\Omega T_L)^4 + \alpha_6(\Omega T_L)^6 + \dots \qquad (175)$$

$$\text{asw}^{(4)}(T_L) = 1 + \beta_2(\Omega T_L)^2 + \beta_4(\Omega T_L)^4 + \beta_6(\Omega T_L)^6 + \dots \qquad (176)$$

where

$$\alpha_2 = -\frac{\pi^2}{18} \qquad (177)$$

$$\alpha_4 = +\frac{2\pi^4}{675} \qquad (178)$$

$$\alpha_6 = -\frac{\pi^6}{8820} \qquad (179)$$

$$\beta_2 = -\frac{\pi^2}{9} \qquad (180)$$

$$\beta_4 = +\frac{\pi^4}{75} \qquad (181)$$

$$\beta_6 = -\frac{17\pi^6}{13230} \qquad (182)$$

These expressions are valid for $\Omega < 1/T_L$, and are therefore low frequency approximations.

For large values of ΩT_L (high frequency) these spectral window functions have the following asymptotic values

$$\text{asw}^{(2)} \sim \frac{1}{\Omega T_L} \qquad (183)$$

$$\text{asw}^{(4)} \sim \frac{2}{3\Omega T_L} \qquad (184)$$

488

The spectral window functions for the case of a single contact area are shown in Figure 7b.

Multiple Contact Areas

The calculation of the spectral window functions for a multiple contact area geometry, such as is produced by the wheels of a truck, is accomplished by integrating equations (15) and (16) over all two-point contact positions as shown in Figure 7c, with the result that

$$
\text{ASW}^{(2)} = \frac{1}{(N + N!/2)T_L^2} \left\{ \sum_{i=1}^{N} \int_0^{T_L} \int_0^{T_L} \frac{\sin^2 [\pi\Omega(\xi_i - \eta_i)]}{[\pi\Omega(\xi_i - \eta_i)]^2} \, d\xi_i \, d\eta_i \right.
$$
$$
\left. + \sum_{\substack{i,j \\ i \neq j}}^{N} \int_{L_i}^{L_i + T_L} \int_{L_j}^{L_j + T_L} \frac{\sin^2 [\pi\Omega(\xi_i - \eta_j)]}{[\pi\Omega(\xi_i - \eta_j)]^2} \, d\xi_i \, d\eta_j \right\}
$$

(185)

$$
\text{ASW}^{(4)} = \frac{1}{(N + N!/2)T_L^2} \left\{ \sum_{i=1}^{N} \int_0^{T_L} \int_0^{T_L} \frac{\sin^4 [\pi\Omega(\xi_i - \eta_i)]}{[\pi\Omega(\xi_i - \eta_i)]^4} \, d\xi_i \, d\eta_i \right.
$$
$$
\left. + \sum_{\substack{i,j \\ i \neq j}}^{N} \int_{L_i}^{L_i + T_L} \int_{L_j}^{L_j + T_L} \frac{\sin^4 [\pi\Omega(\xi_i - \eta_j)]}{[\pi\Omega(\xi_i - \eta_j)]^4} \, d\xi_i \, d\eta_j \right\}
$$

(186)

where

$\text{ASW}^{(2)}$ = slope spectral window function for a truck

$\text{ASW}^{(4)}$ = curvature spectral window function for a truck

N = number of wheels on one side of a truck

L_i = position of wheel i

L_j = position of wheel j

ξ_i, η_j = integration variables

In equations (185) and (186) it is assumed that all wheels of the truck are the same size. The truck spectral window functions are normalized by the factor $(N + N!/2)T_L^2$ to give a unit value if the truck dimensions were shrunk to zero size to produce the case of a one point contact.

The truck spectral window functions defined by equations (185) and (186) are evaluated in Reference 1 for the three types of wheel geometries shown in

Figure 7d. For this evaluation it is assumed that the wheel-ground contact length is equal to the tire radius, $T_L = T_R$ where T_R = tire radius.

<u>a</u>. Four wheel truck

$$ASW^{(2)} = \frac{1}{3} \left\{ 2asw^{(2)}(T_R) + \left[\frac{\sin (\pi L_{12}\Omega)}{\pi L_{12}\Omega} \right]^2 \right\} \tag{187}$$

$$ASW^{(4)} = \frac{1}{3} \left\{ 2asw^{(4)}(T_R) + \left[\frac{\sin (\pi L_{12}\Omega)}{\pi L_{12}\Omega} \right]^4 \right\} \tag{188}$$

<u>b</u>. Six wheel truck

$$ASW^{(2)} = \frac{1}{6} \left\{ 3\, asw^{(2)}(T_R) + \left[\frac{\sin (\pi L_{12}\Omega)}{\pi L_{12}\Omega} \right]^2 + \left[\frac{\sin (\pi L_{13}\Omega)}{\pi L_{13}\Omega} \right]^2 \right.$$
$$\left. + \left[\frac{\sin (\pi L_{23}\Omega)}{\pi L_{23}\Omega} \right]^2 \right\} \tag{189}$$

$$ASW^{(4)} = \frac{1}{6} \left\{ 3\, asw^{(4)}(T_R) + \left[\frac{\sin (\pi L_{12}\Omega)}{\pi L_{12}\Omega} \right]^4 + \left[\frac{\sin (\pi L_{13}\Omega)}{\pi L_{13}\Omega} \right]^4 \right.$$
$$\left. + \left[\frac{\sin (\pi L_{23}\Omega)}{\pi L_{23}\Omega} \right]^4 \right\} \tag{190}$$

<u>c</u>. Eight wheel truck

$$ASW^{(2)} = \frac{1}{10} \left\{ 4\, asw^{(2)}(T_R) + \left[\frac{\sin (\pi L_{12}\Omega)}{\pi L_{12}\Omega} \right]^2 + \left[\frac{\sin (\pi L_{13}\Omega)}{\pi L_{13}\Omega} \right]^2 \right.$$
$$+ \left[\frac{\sin (\pi L_{14}\Omega)}{\pi L_{14}\Omega} \right]^2 + \left[\frac{\sin (\pi L_{23}\Omega)}{\pi L_{23}\Omega} \right]^2 + \left[\frac{\sin (\pi L_{24}\Omega)}{\pi L_{24}\Omega} \right]^2$$
$$\left. + \left[\frac{\sin (\pi L_{34}\Omega)}{\pi L_{34}\Omega} \right]^2 \right\} \tag{191}$$

$$ASW^{(4)} = \frac{1}{10} \left\{ 4 \; asw^{(4)}(T_R) + \left[\frac{\sin \; (\pi L_{12}\Omega)}{\pi L_{12}\Omega} \right]^4 + \left[\frac{\sin \; (\pi L_{13}\Omega)}{\pi L_{13}\Omega} \right]^4 \right.$$

$$+ \left[\frac{\sin \; (\pi L_{14}\Omega)}{\pi L_{14}\Omega} \right]^4 + \left[\frac{\sin \; (\pi L_{23}\Omega)}{\pi L_{23}\Omega} \right]^4 + \left[\frac{\sin \; (\pi L_{24}\Omega)}{\pi L_{24}\Omega} \right]^4$$

$$\left. + \left[\frac{\sin \; (\pi L_{34}\Omega)}{\pi L_{34}\Omega} \right]^4 \right\} \qquad (192)$$

where L_{ij} = distance between wheels i and j. Figure 7e shows typical averaged slope and curvature spectral window functions for a four wheel truck.

Equations (187) through (192) show that the truck spectral window functions introduce the relevant geometrical characteristics of the wheel-ground contact, including wheel spacing and tire radius. Equations (175) through (184) show that the relevant geometrical quantity for track-laying vehicles is the track length in contact with the ground. All these equations can be easily generalized to the case of half-track vehicles.

Contact Length Filter

A vehicle will not respond to the high frequency components of a terrain elevation profile because the finite contact length of a tire or a track with the ground tends to filter out these frequencies. For instance a track of length T_L will filter out all wavelengths shorter than $T_L/2$, while on a smaller scale a tire of radius T_R will filter out wavelengths shorter than $T_R/2$. The situation is shown in Figure 8a.

A low pass filtering action due to the finite contact length with the ground is physically plausible and necessary, but a rigorous theoretical derivation of the form of this filter has not been developed. In this report it is assumed that the filter is of the exponential type

$$e^{-F(\Omega, T_L)} \qquad (193)$$

where several forms of the filter function $F(\Omega, T_L)$ can be selected.

Two forms of the function $F(\Omega, T_L)$ were investigated in this report

$$F(\Omega, T_L) = \alpha \frac{\sigma_c}{\sigma_s} \Omega T_L = \alpha \frac{\sigma_c}{\sigma_s} \frac{T_L}{\lambda_w} \qquad (194)$$

$$F(\Omega, T_L) = \beta(\Omega T_L)^2 = \beta\left(\frac{T_L}{\lambda_w}\right)^2 \qquad (195)$$

where $\lambda_w = \Omega^{-1}$ = spatial wavelength. For the form appearing in equation (194) which is linear in T_L, it was found that a spatial frequency factor σ_c/σ_s had to be inserted to account for the dominant frequencies of the terrain. Only in this way was the parameter α found to have a constant value independent of terrain site and track length.

The values of α and β were determined empirically from experimental absorbed power data for trucks and track laying vehicles (see Part V) and are equal α = 118.8 in. (for detrended values of σ_s and σ_c), α = 123.2 in. for undetrended values of σ_s and σ_c) and β = 1.4. The form of the filter function given by equation (194) appears to describe the absorbed power data somewhat better than does the form in equation (195), so that all further calculations in this report were done using the filter function represented by equation (194). Figure 8b shows a typical exponential filter expressed in terms of ΩT_L.

The filter functions can also be written in terms of the time frequency using equation (138) as

$$F(f) = \alpha \frac{\sigma_c}{\sigma_s} \frac{fT_L}{u} = \alpha \frac{\sigma_c}{\sigma_s} f\tau \tag{196}$$

$$F(f) = \beta \left(\frac{fT_L}{u}\right)^2 = \beta (f\tau)^2 \tag{197}$$

where $\tau = T_L/u$ = time delay for transit of the vehicle-ground contact length. Figure 8c shows a typical exponential filter, given by equation (196), expressed in terms of the time frequency.

INPUT POWER SPECTRA FOR VEHICLES. Taking the spectral window functions and the low pass contact length filter in account and treating vehicles as rigid bodies gives the following expressions for the input roughness power spectra and the input kinematic power spectra for wheeled vehicles:

$$P_{di}(\Omega) = e^{-F} P_d(\Omega) \tag{198}$$

$$P_{si}(\Omega) = (2\pi\Omega)^2 e^{-F} ASW^{(2)} P_d(\Omega) \tag{199}$$

$$P_{ci}(\Omega) = (2\pi\Omega)^4 e^{-F} ASW^{(4)} P_d(\Omega) \tag{200}$$

$$P_{vi}(\Omega) = (2\pi u\Omega)^2 e^{-F} ASW^{(2)} P_d(\Omega) \tag{201}$$

492

$$P_{ai}(\Omega) = (2\pi u \Omega)^4 e^{-F} ASW^{(4)} P_d(\Omega) \qquad (202)$$

where P_{di}, P_{si}, P_{ci}, P_{vi} and P_{ai} = input vehicle power spectra for displacement, slope, curvature, vertical velocity and vertical acceleration respectively. These equations are valid for track vehicles with ASW[2] and ASW[4] replaced by asw[2] and asw[4] respectively.

Equations (198) through (202) show that the input kinematic power spectra for vehicles are related to the terrain roughness power spectrum that has been adjusted for vehicle geometry. The input kinematic power spectra would describe the motion of a vehicle if it were totally rigid. The actual vehicle response is calculated as a joint effect of these input kinematic power spectra and a transmission function which accounts for the impedance of the vehicle. The following Part IV develops the transmission function.

PART IV: DYNAMIC MODELS FOR MOVING VEHICLES

Introductory Remarks

It is of value to vehicle design engineers to be able to predict the ver-
tical dynamic displacement, velocity and acceleration at a point on a moving
vehicle and ultimately to predict the power absorbed by the driver. To do
this, the dynamic response of a vehicle to rough terrain must be known. The
dynamic response of a vehicle can be described by a transmission function.[14-16]

Because vehicles undergo pitching and rolling motions as well as vertical
motion (heave), the power absorbed by the driver will depend critically on his
location relative to the center of mass of the vehicle. It is important to be
able to separate and determine the contributions to the absorbed power due to
the surface roughness, the internal dynamics of the vehicle, and the location
of the driver. The driver location variable appears in the pitching motion
transmission function.

This paper uses simple linear viscoelastic spring models to describe the
dynamic response of a vehicle. It is known that linear viscoelastic models do
not adequately describe the dynamic properties of vehicles because the vehi-
cles contain nonlinear springs and dashpots, and Coulomb damping in addition
to viscoelastic damping. The linear viscoelastic models introduced here serve
as a simple expedient way to evaluate the roughness power spectrum method.

The transmission functions developed will be used in Part V to calculate
the power absorbed by the driver using a power spectrum method. The absorbed
power calculation requires the output acceleration power spectrum at the
drivers seat, and this can be calculated using a transmission function.

Vertical Motion Transmission Functions

Single Mass
Vertical Motion

The output power spectrum of a mechanical or structural system is related
to the input power spectrum through the transmission function for the system,
Figure 8d. The transmission function of a dynamical system is generally a
complex number whose imaginary part is a measure of the damping. For a linear
system the output power spectrum is given by

$$P_o'(f) = |T|^2 \, P_i'(f) \tag{203}$$

where $P_o'(f)$ = output power spectrum

  T = transmission function

494

$|T|$ = magnitude of transmission function

$P'_i(f)$ = input power spectrum

Mechanical transmission functions generally come in two forms, one relating output displacement to input force, and the other relating output displacement to input displacement.

If the input to a linear spring system is a force and the output is a displacement we have

$$P'_{do} = |T_{dF}|^2 P'_{Fi} \tag{204}$$

where P'_{do} = power spectrum of the output displacement

T_{dF} = transmission function relating input dynamic force to the output dynamic displacement

P'_{Fi} = power spectrum of the input force

The transmission function for this case is[4]

$$T_{dF} = \frac{1/k}{1 - (f/f_n)^2 + i2\xi f/f_n} = |T_{dF}| e^{-i\phi_{dF}} \tag{205}$$

$$|T_{dF}|^2 = \frac{k^2}{[1 - (f/f_n)^2]^2 + [2\xi f/f_n]^2} \tag{206}$$

$$\phi_{dF} = \tan^{-1} \left[\frac{2\xi f/f_n}{1 - (f/f_n)^2} \right] \tag{207}$$

where k = spring constant

$f_n = \sqrt{k/m}/2\pi$ = natural frequency

$\xi = C_D/(2\sqrt{km})$ = damping ratio

m = effective mass

C_D = damping constant

f = frequency

For application to vehicle dynamics a more useful transmission function is that which relates output displacement to input displacement. The output power spectrum of displacement is then given by

$$P'_{do}(f) = |T_{dd}|^2 P'_{di}(f) \tag{208}$$

where T_{dd} = transmission function relating the input dynamic displacement to the output dynamic displacement

P_{di} = power spectrum of input displacement

The transmission function for this case is given by[4]

$$T_{dd} = \frac{1 + i\sigma f}{1 - (f/f_n)^2 + i\sigma f} = |T_{dd}| e^{-i\phi_{dd}} \qquad (209)$$

$$|T_{dd}|^2 = \frac{1 + \sigma^2 f^2}{[1 - (f/f_n)^2]^2 + \sigma^2 f^2} \qquad (210)$$

$$\phi_{dd} = \tan^{-1} \left[\frac{\sigma f^3 / f_n^2}{1 - (f/f_n)^2 + \sigma^2 f^2} \right] \qquad (211)$$

where $\sigma = 2\xi/f_n$. It is easy to show that the velocity-velocity transmission function and the acceleration-acceleration transmission function satisfy the following conditions

$$|T_{dd}| = |T_{vv}| = |T_{aa}| \qquad (212)$$

where T_{vv} = transmission function relating input velocity to output velocity

T_{aa} = transmission function relating input acceleration to output acceleration

Therefore only the *displacement-displacement* transmission function needs to be considered for vehicle dynamics problems.

An important property of the transmission function is its value for zero frequency

$$T_{dd}(f = 0) = 1 \qquad (213)$$

This corresponds to a simple translation of whole dynamic system, so that the static output displacement equals the static input displacement. Note also that $|T_{dd}|^2 \to f^{-2}$ while $|T_{dF}|^2 \to f^{-4}$ in the high frequency limit. The transmission function for a vehicle running over rough terrain will depend on the vehicle speed because of the relation $f = u\Omega$. In particular, the value of $|T_{dd}|^2$ for the single degree of freedom model is obtained from equation (210) to be

$$\left|T_{dd}\right|^2 = \frac{1 + \sigma^2 u^2 \Omega^2}{\left(1 - u^2\Omega^2/f_n^2\right)^2 + \sigma^2 u^2 \Omega^2} \tag{214}$$

Note that for $u = 0$ the transmission function has the value of $\left|T_{dd}\right| = 1$.

Double Mass
Vertical Motion

Vehicles generally exhibit two resonance peaks – one associated with the vertical motion of the body ($\sim$1 Hz) and the other with the vertical motion of the wheel suspension system ($\sim$15 Hz). A displacement-displacement transmission function for a two-mass system is therefore required to accurately describe the dynamic response of a vehicle moving over rough terrain. The derivation of the two-mass transmission function is given in Reference 1, and is as follows (Figure 9a)

$$T_{dd} = \frac{A + iB}{E + iF} \tag{215}$$

$$\left|T_{dd}\right|^2 = \frac{(AE + BF)^2 + (BE - AF)^2}{\left(E^2 + F^2\right)^2} \tag{216}$$

where

$$A = 1 - \frac{\omega^2 C_B C_W}{k_B k_W} \tag{217}$$

$$B = \omega \left(\frac{C_B}{k_B} + \frac{C_W}{k_W}\right) \tag{218}$$

$$E = \left(1 - \frac{\omega^2 M_W}{k_W}\right)\left(1 - \frac{\omega^2 M_B}{k_B}\right) - \omega^2 \left(\frac{C_B C_W}{k_B k_W} + \frac{M_B}{k_W}\right) \tag{219}$$

$$F = \omega \left\{ \frac{C_W}{k_W} + \frac{C_B}{k_B} - \omega^2 \left[\frac{M_B(C_B + C_W)}{k_B k_W} + \frac{M_W C_B}{k_B k_W}\right]\right\} \tag{220}$$

where $\omega = 2\pi f$

C_B = damping constant for vehicle body

C_W = damping constant for wheel suspension system

M_B = mass of vehicle body = W_B/g

M_W = mass of wheels = W_W/g

497

k_B = spring constant of vehicle body

k_W = spring constant of wheel suspension system

It appears that track laying vehicles can be adequately described by a single mass transmission function, while wheeled vehicles generally require a double mass transmission function to describe their vertical motion. Typical vertical motion transmission functions for tanks and trucks are shown in Figure 9b. The dynamical parameters for several track laying vehicles are given in Table 4, and for several trucks in Tables 5 and 6.

Combined Pitching and Vertical Motion Transmission Function

Because a vehicle operating on rough terrain has a pitching motion, the values of the power absorbed by the driver are expected to depend on the geometrical location of the driver relative to the center mass. The pitching motion of a vehicle can be described by a transmission function. This section calculates the displacement-displacement transmission function for a combined pitching and vertical mode of motion. The model used for this calculation is shown in Figure 9c, and consists of a rigid rod representing the vehicle body that is supported by two damped springs at each end.

The equations of motion for this model are the following coupled linear differential equations[14]

$$m\ddot{x} + k_1 x_1 + C_1 \dot{x}_1 + k_2 x_2 + C_2 \dot{x}_2 = k_1 \eta_1 + C_1 \dot{\eta}_1 + k_2 \eta_2 + C_2 \dot{\eta}_2 \qquad (221)$$

$$J\ddot{\theta} - L_1[k_1 x_1 + C_1 \dot{x}_1] + L_2[k_2 x_2 + C_2 \dot{x}_2] = -L_1[k_1 \eta_1 + C_1 \dot{\eta}_1] + L_2[k_2 \eta_2 + C_2 \dot{\eta}_2] \qquad (222)$$

where

m = mass of vehicle

$\ddot{x}$ = vertical acceleration of center of mass

k_1 = equivalent spring constant of front support of vehicle

x_1 = vertical displacement of front support of vehicle

C_1 = equivalent damping of front support of vehicle

$\dot{x}_1$ = vertical velocity of front support of vehicle

k_2 = equivalent spring constant of rear support of vehicle

x_2 = vertical displacement of vehicle body directly above rear wheels

C_2 = equivalent damping constant of rear wheels and suspension

$\dot{x}_2$ = vertical velocity of truck body directly above rear wheels

η_1 = elevation of ground surface at front wheels

$\dot{\eta}_1$ = rate of change of η_1 due to passing vehicle

η_2 = elevation of ground surface at rear wheels

$\dot{\eta}_2$ = time rate of change of η_2 due to moving vehicle

J = moment of inertia about pitch axis through center of mass

L_1 = distance from front of vehicle to center of mass

L_2 = distance from rear of vehicle to center of mass

The solution of the coupled differential equations is given in Reference 1, and is given in the form of a transmission function. The displacement-displacement transmission function is given for a point in front of the center of mass and for a point behind the center of mass as follows

$$\left| T_F \right|^2 = \left(\xi_1^F \right)^2 + \left(\xi_2^F \right)^2 \tag{223}$$

$$\left| T_B \right|^2 = \left(\xi_1^B \right)^2 + \left(\xi_2^B \right)^2 \tag{224}$$

where

T_F = displacement-displacement transmission function for a point a distance z in front of the center of mass

T_B = displacement-displacement transmission function for a point a distance z behind the vehicle center of mass

z = distance from center of mass at which the motion is to be calculated

and where

$$\xi_1^F = R - zS \tag{225}$$

$$\xi_2^F = T - zU \tag{226}$$

$$\xi_1^B = R + zS \tag{227}$$

$$\xi_2^B = T + zU \tag{228}$$

$$R = (Z_1 W_1 + Z_2 W_2)/\left(W_1^2 + W_2^2\right) \tag{229}$$

$$S = (X_1 U_1 + X_2 U_2)/\left(U_1^2 + U_2^2\right) \tag{230}$$

$$T = (Z_2 W_1 - Z_1 W_2)/\left(W_1^2 + W_2^2\right) \tag{231}$$

$$U = (X_2 U_1 - U_2 X_1)/\left(U_1^2 + U_2^2\right) \tag{232}$$

$$Z_1 = \alpha_A(d - J\omega^2) - \omega\alpha_B g - b\beta_A + \omega h \beta_B \tag{233}$$

$$Z_2 = \alpha_B(d - J\omega^2) + \omega\alpha_A g - b\beta_B - \omega h \beta_A \tag{234}$$

$$W_1 = (k - m\omega^2)(d - J\omega^2) - \omega^2 Cg - b^2 + \omega^2 h^2 \tag{235}$$

$$W_2 = \omega C(d - J\omega^2) + \omega g(k - m\omega^2) - 2\omega bh \tag{236}$$

$$X_1 = \beta_A W_1 - \beta_B W_2 - bZ_1 + \omega h Z_2 \tag{237}$$

$$X_2 = \beta_B W_1 + \beta_A W_2 - bZ_2 - \omega h Z_1 \tag{238}$$

$$U_1 = W_1(d - J\omega^2) - \omega g W_2 \tag{239}$$

$$U_2 = \omega g W_1 + W_2(d - J\omega^2) \tag{240}$$

$$\alpha_A = k_1 + k_2 \cos(\omega L/u) + \omega C_2 \sin(\omega L/u) \tag{241}$$

$$\alpha_B = \omega C_1 - k_2 \sin(\omega L/u) + \omega C_2 \cos(\omega L/u) \tag{242}$$

$$\beta_A = L_2[k_2 \cos{(\omega L/u)} + \omega C_2 \sin{(\omega L/u)}] - L_1 k_1 \tag{243}$$

$$\beta_B = L_2[\omega C_2 \cos{(\omega L/u)} - k_2 \sin{(\omega L/u)}] - \omega C_1 L_1 \tag{244}$$

$$L = L_1 + L_2 \tag{245}$$

$$b = k_2 L_2 - k_1 L_1 \tag{246}$$

$$d = k_1 L_1^2 + k_2 L_2^2 \tag{247}$$

$$h = C_2 L_2 - C_1 L_1 \tag{248}$$

$$g = C_1 L_1^2 + C_2 L_2^2 \tag{249}$$

$$C = C_1 + C_2 \tag{250}$$

$$k = k_1 + k_2 \tag{251}$$

The derived transmission function can be used to calculate the motion of a vehicle at any position along the length of the vehicle relative to the center of mass. In this way a prediction of the dependence of the power absorbed by a driver on his location relative to the center of mass can be made. Figure 9d shows a typical transmission function for the combined vertical and pitching modes of motion.

PART V: ABSORBED POWER AND VEHICLE RESPONSE

Introductory Remarks

Quantities often measured for a vehicle moving over rough terrain are the power absorbed by the driver and the vertical acceleration at the drivers seat. The power absorbed by the driver is the energy dissipated as heat. It represents the energy lost due to vibration damping in the human body. Absorbed power is a physiological concept that has been developed as a measure of driver fatigue on prolonged exposure to vehicle induced vibrations.[7] It has been found empirically that the maximum power that a driver can absorb and still function reasonably is six watts. Therefore it is of importance to be able to estimate the vehicle speed at which six watts of power is being dissipated by the driver. The six watt speed clearly depends on internal vehicle characteristics, the location of the driver relative to the center of mass of the vehicle, and the surface roughness.

Two methods are used to obtain the six watt speed. The first is a formal power spectrum method of calculating the power absorbed by the driver which includes a consideration of vehicle dynamics. The second is a regression analysis of the six watt speed measured for vehicles operating different types of terrain. The power spectrum method introduces the terrain roughness and vehicle geometry through the power spectra described in Parts II and III, and the vehicle dynamics through the transmission functions introduced in Part IV. The regression analysis uses directly the detrended values of σ_d, σ_s and σ_c to describe the terrain roughness, the track length or tire radius to describe the vehicle geometry, and the dimensionless Froude numbers to describe the dynamical characteristics of vehicles.

Output Power Spectra and Vehicle Response

It will be shown subsequently that the calculation of the absorbed power and total power of the driver requires the output acceleration and velocity power spectra. The power spectra of the vertical motion of a point on a vehicle can be obtained from equation (208) and equations (198) through (202) to be

$$P_{do}(\Omega) = \left| T_{dd} \right|^2 e^{-F} P_d(\Omega) \tag{252}$$

$$P_{vo}(\Omega) = (2\pi u \Omega)^2 \left| T_{dd} \right|^2 e^{-F} ASW^{(2)} P_d(\Omega) \tag{253}$$

$$P_{ao}(\Omega) = (2\pi u \Omega)^4 \left| T_{dd} \right|^2 e^{-F} ASW^{(4)} P_d(\Omega) \tag{254}$$

The vehicle speed enters directly in equations (253) and (254), but the dependence on the vehicle speed is also indirectly introduced through the

transmission function, as for instance in equation (214). The corresponding power spectra expressed in terms of the time frequency are obtained using equation (154) to be

$$P'_{do}(f) = \left|T_{dd}\right|^2 e^{-F} P'_d(f) \tag{255}$$

$$P'_{vo}(f) = (2\pi f)^2 \left|T_{dd}\right|^2 e^{-F} ASW^{(2)} P'_d(f) \tag{256}$$

$$P'_{ao}(f) = (2\pi f)^4 \left|T_{dd}\right|^2 e^{-F} ASW^{(4)} P'_d(f) \tag{257}$$

The standard deviations of the vertical displacement, velocity, acceleration and absorbed power at a point on the vehicle can be calculated from integrals of the output power spectra, given by equations (252) - (254), over the frequency ranges of the five basic types of roughness power spectra. Equations (252) - (254) show that P_{do} and P_{vo} diverge for $f = 0$ (or $\Omega = 0$). This is identically the same problem that was encountered in the roughness models of Parts I and II where it was shown that $P_d(\Omega)$ diverge for $\Omega = 0$. Therefore the same difficulties that appear in the roughness models of spectral types 1, 2 and 5 appear in the vehicle response problem. Equations (254) and (257) show that $P_{ao}(\Omega)$ and $P'_{ao}(f)$ are not divergent for $\Omega = 0$, corresponding to the situation that $P_c(\Omega)$ is not divergent for $\Omega = 0$ as described in Part II.

The divergent integrals resulting from the calculation of the RMS values of the output vertical displacement and velocity can be evaluated in inserting a filter function similar to that defined in equation (6). Thus the following integration factor can be used

$$\phi^{-2} = \frac{(2\pi\gamma^1\Omega)^4}{\left[1 + (2\pi\gamma^1\Omega)^2\right]^2} \tag{258}$$

where γ^1 = filter constant. This integration factor is not necessary for the calculation of absorbed power because this calculation involves only the acceleration power spectrum.

The standard deviations of the vehicle displacement, velocity and acceleration are given by

$$\sigma_{do}^2 = \int_0^\infty P_{do}(\Omega)\phi^{-2}d\Omega = \int_0^\infty P'_{do}(f)\phi^{-2}df \tag{259}$$

$$\sigma_{vo}^2 = \int_0^\infty P_{vo}(\Omega)\phi^{-2} d\Omega = \int_0^\infty P'_{vo}(f)\phi^{-2}df \tag{260}$$

$$\sigma_{ao}^2 = \int_0^\infty P_{ao}(\Omega)d\Omega = \int_0^\infty P'_{ao}(f)\ df \tag{261}$$

The integrals in equation (259) through (261) are evaluated only in the regions for which the power spectra are positive.

<div align="center">

**Absorbed Power and Six Watt Speed Calculated
by Power Spectrum Method**

</div>

The absorbed power is related to the vertical acceleration of the driver (at the drivers seat) and is defined in terms of the vertical acceleration power spectrum as follows[6]

$$A_p = \int_0^\infty H_a^2(f)P'_{ao}(f)df = \int_0^\infty A'_p(f,u)df \tag{262}$$

where
$\qquad A_p$ = absorbed power (watts)

$\qquad H_a(f)$ = human factor function $\left[\sqrt{watts}/(ft/sec^2)\right]$

$\qquad P'_{ao}(f)$ = output vertical acceleration power spectrum at the location of the drivers seat

$\qquad A'_p(f,u)$ = absorbed power spectral function

The human factor function $H_a(f)$ is empirically determined and has the form of a band pass filter.[6] This function appears in Figure 9e.

The frequency dependence of the absorbed power is given by equations (254), (257) and (262) as

$$A_p(\Omega,u) = (2\pi u\Omega)^4 \left|T_{dd}\right|^2 e^{-F} H_a^2 ASW^{(4)} P_d(\Omega) \tag{263}$$

$$A'_p(f,u) = (2\pi f)^4 \left|T_{dd}\right|^2 e^{-F} H_a^2 ASW^{(4)} P'_d(f) \tag{264}$$

where $A_p(\Omega,u) = uA'_p(f,u)$. Equations (262) and (264) show that five basic quantities enter into the absorbed power calculation, and these depend on the vehicle dynamics, vehicle geometry, driver location and terrain roughness:

$\qquad$ <u>a</u>. transmission function

$\qquad$ <u>b</u>. low pass filter associated with the ground contact length

$\qquad$ <u>c</u>. human factor function

<div align="center">504</div>

<u>d</u>. curvature spectral window function for vehicle

<u>e</u>. power spectrum of terrain elevation

The roughness power spectrum is given by the three parameter model, and refers to actual terrain described by the parameters C, D and E of Part II.

Because the functions T_{dd} and H_a that appear in equations (263) and (264) are intrinsically functions of the time frequency f, while the functions e^{-F} and $ASW^{(4)}$ are intrinsically functions of the spatial frequency Ω, it follows from $f = u\Omega$ that the absorbed power given by equation (262) always depends on the vehicle speed. The six watt vehicle speed is obtained from the absorbed power equation (262) by taking $A_p = 6$ watts.

It should be pointed out that the absorbed power dissipated by the driver is not the same as the total power associated with the kinetic and potential energies of the motion of the driver. The RMS value of the total power delivered to the driver is given by

$$\sigma_{po} = \frac{W_D}{g} \sqrt{\int_0^\infty P_{vo}(\Omega) P_{ao}(\Omega) d\Omega} \tag{265}$$

where

σ_{po} = RMS value of total power of driver

W_D = weight of driver

A comparison of the experimental values of absorbed power with values predicted by the numerical integration of equations (262) and (264) are shown in Figures 10a through 11c for a series of track laying vehicles. Figure 11d gives a comparison between predicted and measured values of the six watt speed for track laying vehicles. A similar procedure for trucks appears in Figures 12a through 12d.

Linear Regression Prediction of the Six Watt Speed

The six watt speed is the vehicle speed at which the driver is absorbing six watts of power; it is a measure of ride quality. A high value for the six watt speed means a smooth ride, and a low value means a rough ride. The value of the six watt speed depends on both terrain and vehicle characteristics.

For the purpose of the design and testing of vehicles, it is important to have a simple expression for the six watt speed giving its dependence on terrain roughness parameters and on vehicle parameters. In this way the results of vehicle tests conducted at different terrain areas with different types of vehicles can be compared, and an evaluation of design changes can be made. The vehicle parameters describe the geometry and internal dynamics, while the

terrain parameters describe the displacement, slope and curvature of an elevation profile.

Values of the six watt speed for several vehicles have been measured for a number of terrain sites where elevation profiles have been determined. The regression analysis given here represents the six watt speed as simple powers of the terrain roughness parameters and the vehicle parameters. This analysis is valid only if the six watt speed is a monotonically increasing or decreasing function of the chosen parameters. It was found that the vehicle dynamics parameters k, m and C could not be successfully brought into the regression analysis, and therefore only terrain roughness and vehicle geometry were considered.

A regression analysis incorporating k, m and C could not be accomplished because the dependence of the six watt speed of these parameters could not be represented by a simple power law. The dependence on the vehicle weight, for example, was found to be either direct or inverse depending on the choice of the resonance frequency or the damping ratio as a basic vehicle dynamics parameter; both choices gave essentially the same quality of fit to the measured six watt speeds. This suggests that the dependence of the six watt speed on the vehicle weight is more complicated than a simple power law. In fact, the six watt speed is expected to initially increase with the vehicle weight producing a smoother ride, and then decrease with additional weight giving a rougher ride due to hitting the bump stops.

It is possible to find a direct correlation between the six watt speed, the three terrain roughness descriptors σ_d, σ_s and σ_c for detrended data, and the vehicles parameters. Both wheeled vehicles and track laying vehicles were considered for this study.

Track Laying Vehicles

Seven mathematical forms were chosen for the regression analysis of the six watt speed for track laying vehicles. They are as follows:

$$u_6 = A\sigma_d^{\alpha} \tag{266}$$

$$u_6 = A\sigma_s^{\beta} \tag{267}$$

$$u_6 = A\sigma_c^{\gamma} \tag{268}$$

$$u_6 = A\sigma_d^{\alpha} T_L^{\delta} \tag{269}$$

$$u_6 = A\sigma_d^{\alpha} J_L^{\eta} \tag{270}$$

$$u_6 = A\sigma_d^\alpha \, T_L^\delta \, J_L^\eta \tag{271}$$

$$u_6 = A\sigma_d^\alpha \, \sigma_s^\beta \, \sigma_c^\gamma \, T_L^\delta \, J_L^\eta \tag{272}$$

where

u_6 = six watt speed of vehicle

$\sigma_d, \sigma_s, \sigma_c$ = RMS values of displacement, slope and curvature, respectively, of a detrended elevation provile (λ = 10 ft)

T_L = track length

J_L = jounce length

The coefficients in equations (266) through (272) were obtained by fitting these equations to measured six watt speeds. Eight track laying vehicles were used in this analysis, LEO 2AV, M60 A1, ATR, SM1, AISV, HIMAG-5, MICV and the M113. The six watt speed was measured for these vehicles for a total of twenty-four terrain sites. The dimensions of the quantities shown in equations (266) through (272) are chosen to be as follows: $[u_6]$ = mph, $[\sigma_d]$ = in, $[\sigma_s]$ = 1, $[\sigma_c]$ = in.$^{-1}$, $[T_L]$ = in. and $[J_L]$ = in.

This data combined with a library regression computer program gave the following results for the six watt speed and the coefficient of fit (cf):

$$u_6 = \frac{23.55}{\sigma_d^{0.50}} \tag{266a}$$

$$cf = 0.29$$

$$u_6 = \frac{9.62}{\sigma_s^{0.190}} \tag{267a}$$

$$cf = 0.02$$

$$u_6 = \frac{47.2}{\sigma_c^{0.211}} \tag{268a}$$

$$cf = 0.04$$

$$u_6 = \frac{0.393 \, T_L^{0.874}}{\sigma_d^{0.875}} \tag{269a}$$

$$cf = 0.70$$

$$u_6 = \frac{3.33 \ J_L^{0.98}}{\sigma_d^{0.85}}$$ (270a)

$$cf = 0.82$$

$$u_6 = \frac{1.324 \ T_L^{0.289} \ J_L^{0.761}}{\sigma_d^{0.897}}$$ (271a)

$$cf = 0.84$$

$$u_6 = \frac{0.944 \ \sigma_s^{0.708} \ T_L^{0.412} \ J_L^{0.672}}{\sigma_d^{1.20} \ \sigma_c^{0.407}}$$ (272a)

$$cf = 0.86$$

Equations (266a) through (268a) show that the detrended displacement σ_d is the relevant terrain roughness parameter for track laying vehicles, while σ_s and σ_c play secondary roles. Equations (269a) through (271a) show that the jounce length J_L is the primary vehicle parameter for track laying vehicles while the track length T_L plays a secondary role. The best fit to the measured six watt speed data is given by equation (272a) with all parameters included, but the fit is not much better than given by equation (270a) with only the two parameters σ_d and J_L. A comparison between the experimental six watt speed and those predicted by equation (272a) is shown in Figure 13a.

When the vehicle dynamics parameters k, m and C are eventually brought into the expression for u_6, they should be entered as nondimensional parameters in the form of the damping ratio and the Froude numbers.[17]

Wheeled Vehicles

Seven mathematical forms were chosen for the analysis of the six watt speed for wheeled vehicles. They are expressed in terms of the tire radius (T_R) and wheel base length (L_{WB}) as follows:

$$u_6 = A\sigma_d^{\alpha}$$ (273)

$$u_6 = A\sigma_c^{\gamma}$$ (274)

$$u_6 = A\sigma_s^{\beta}$$ (275)

$$u_6 = A\sigma_s^{\alpha} \ L_{WB}^{\delta}$$ (276)

$$u_6 = A\sigma_s \, T_R^\varepsilon \tag{277}$$

$$u_6 = A\sigma_s^\alpha \, L_{WB}^\delta \, T_R^\varepsilon \tag{278}$$

$$u_6 = A\sigma_d^\alpha \, \sigma_s^\beta \, \sigma_c^\gamma \, L_{WB}^\delta \, T_R^\varepsilon \tag{279}$$

The coefficients in equations (273) through (279) were obtained by fitting these equations to measured six watt speeds for trucks. Five trucks were used in this analysis: PAC-CAR, TARADCOM-HMTT, 10 ton (8x8) - Cargo truck A; DRAGON WAGON, 10 ton (8x8) - Cargo truck B; GERMAN MAN, 10 ton (8x8) - Cargo truck C; M656, 5 ton (8x8); M520E1 GOER, 8 ton (4x4); and the Czeckoslovakian TATRA 813.

A library regression routine (MULFIT) was used to analyze the six watt speed data for these five trucks, and gave the following results for the six watt speed and the coefficient of fit (cf):

$$u_6 = \frac{14.87}{\sigma_d^{0.544}} \tag{273a}$$

$$cf = 0.38$$

$$u_6 = \frac{0.0411}{\sigma_c^{1.12}} \tag{274a}$$

$$cf = 0.51$$

$$u_6 = \frac{0.789}{\sigma_s^{0.996}} \tag{275a}$$

$$cf = 0.62$$

$$u_6 = \frac{1285}{\sigma_s^{0.996} \, L_{WB}^{1.415}} \tag{276a}$$

$$cf = 0.76$$

$$u_6 = \frac{217.9}{\sigma_s^{0.966} \, T_R^{1.742}} \tag{277a}$$

$$cf = 0.80$$

$$u_6 = \frac{317.7}{\sigma_s^{0.996} \, L_{WB}^{0.166} \, T_R^{1.59}} \tag{278a}$$

$$cf = 0.80$$

$$u_6 = \frac{1099 \; \sigma_d^{0.475} \; \sigma_c^{0.942}}{\sigma_s^{2.22} \; L_{WB}^{0.166} \; T_R^{1.59}} \tag{279a}$$

$$cf = 0.82$$

Equations (273a) through (275a) show that the detrended slope σ_s is the significant terrain roughness parameter for wheeled vehicles, while σ_c and σ_d play subordinate roles. The best fit to the measured six watt speeds of wheeled vehicles is given by equation (279a) with all variables included, but this fit is not much better than shown in equation (277a) with only two parameters σ_s and T_R. A comparison between the experimental values of the six watt speed and those predicted by equation (279a) is given in Figure 13b. The relatively poor agreement shown in Figure 13b suggests that an alternative vehicle parameter, such as the jounce length, is required to obtain a better correlation between measured and predicted six watt speeds for wheeled vehicles.

Dimensional Analysis

Dimensional analysis uses relationships between nondimensional quantities which remain valid irrespective of the scale of the physical system.[17] The procedure is to calculate a set of relevant dimensionless parameters for a physical system. For this study the physical system is a vibrating vehicle moving over rough terrain.

The Froude numbers for a physical system are given by[17]

$$\xi = \frac{MV^2}{FL} \tag{280}$$

where ξ = Froude number, M = characteristic mass, V = characteristic speed, F = characteristic forces operating in the system, and L = characteristic length.

The Froude numbers associated with a linear harmonic oscillator are

$$\xi_1 = \frac{MV^2}{KL^2} \sim \frac{V^2}{f_R^2 L^2} = \left(\frac{V}{f_R L}\right)^2 \tag{281}$$

$$\xi_2 = \frac{MV^2}{CVL} = \frac{MV}{CL} \tag{282}$$

where f_R = resonance frequency of vehicle, K = spring constant of vehicle, and C = damping constant of vehicle. Because the resonance frequency of a vehicle is a directly measurable quantity, equation (281) is used as the appropriate Froude number and therefore the appropriate dimensionless parameter for representing the six-watt speed for vehicles is

$$\xi_{u_6} = \frac{u_6}{f_R T_L} \tag{283}$$

For wheeled vehicles the characteristic lengths would be the tire radius and wheelbase length. The other dimensionless parameter for a vibrating system is the damping ratio

$$\xi_D = \frac{C}{2\sqrt{KM}} \tag{284}$$

A third parameter that was examined is the ratio of jounce length to ground contact length

$$\xi_L = J_L/T_L \tag{285}$$

For a vibration problem it is the vehicle mass $M = W/g$ that enters (281) through (284) not the vehicle weight. Dimensionless parameters such as $W/(KL)$ and $W/(CV)$ are inappropriate for a vibration problem. The correct dimensionless parameters equivalent to (283) are $MV/(CL)$ and $CV/(KL)$. This can be seen from the extreme case of zero gravity where $g = 0$ and $W = 0$ but $M =$ some fixed value; in this case vibrations can still occur. On the other hand for a statics problem, such as deformation of a solid (vehicle) under the action of gravity, it is the weight and not the mass that enters the appropriate dimensionless parameters.

Terrain roughness has been described by the three parameters σ_d, σ_s and σ_c. Within this description the terrain roughness dimensionless parameters are

$$\xi_s = \sigma_s \tag{286}$$

$$\xi_{cd} = \sigma_c \sigma_d \tag{287}$$

A combination of these parameters that was examined is

$$\xi_R = \frac{\sigma_s}{\sigma_c \sigma_d} \tag{288}$$

A number of dimensionless relationships were developed with corresponding coefficients of fit from data for eight track laying vehicles, and are as follows

$$\xi_{u_6} = 0.011 \, \xi_R^{1.28} \tag{289}$$

$$cf = 0.60$$

511

$$\xi_{u_6} = \frac{0.012 \; \xi_R^{1.21}}{\xi_D^{0.246}} \qquad\qquad (290)$$

$$cf = 0.70$$

$$\xi_{u_6} = \frac{0.027 \; \xi_s^{2.06}}{\xi_D^{0.23} \; \xi_{cd}^{1.57}} \qquad\qquad (291)$$

$$cf = 0.74$$

$$\xi_{u_6} = \frac{0.025 \; \xi_s^{2.06}}{\xi_D^{0.23} \; \xi_{cd}^{1.57} \; \xi_L^{0.02}} \qquad\qquad (292)$$

$$cf = 0.74$$

Equation (292) shows an insignificant dependence on the ratio of jounce length to track length. A comparison of measured values of $u_6/(f_R T_L)$ with those values is shown predicted by equation (291) is shown in Figure 13c.

PART VI: CONCLUSIONS

CONCLUSIONS. This paper generalizes the method of characterizing the ground surface displacement profile by a one parameter power spectrum of the form $C\Omega^{-2}$. A three parameter model of the power spectrum of the terrain displacement profile data is introduced in such a manner that the additional parameters will more accurately describe the contribution of the long wavelengths to the surface roughness, and will describe the cases where periodicities are present in the terrain such as in the case of plowed fields.

The three roughness power spectrum parameters are used to calculate the power spectra and standard deviation values of the vertical displacement, velocity, acceleration and power absorbed by the driver for a vehicle operating on rough terrain. A comparison of theoretical and experimental results was made.

The theoretical and experimental studies of terrain roughness and dynamic vehicle response yields the following conclusions:

a. A three parameter power spectrum model can be used to classify terrain roughness into five basic types which adequately describe natural and manmade terrain features including periodicities (Parts I and II).

b. The three parameters of the roughness power spectrum can be determined from the standard deviations of the displacement, slope and curvature of a detrended elevation profile, but in some cases undetrended data can be used (Part II).

c. The power absorbed by the driver of a vehicle depends on: (1) the human factor function relating absorbed power to the acceleration power spectrum, (2) the vehicle transmission function that describes the internal dynamics of a vehicle, (3) the low pass ground contact length filter that describes the filtering effect of a track or wheel, (4) the vehicle spectral window functions that introduce the geometry of the vehicle-ground contact, and (5) the three parameter roughness power spectrum that introduces surface roughness (Parts III, IV and V).

d. The six watt speed for track laying vehicles can be related by a regression analysis to the vehicle geometry and the three roughness descriptors σ_d, σ_s and σ_c for detrended data. The significant terrain roughness parameter for track laying vehicles is σ_d, while for wheeled vehicles it is σ_s (Part V).

LITERATURE CITED

1. Weiss, R., "Characterization of Terrain Roughness, Volume I, Microroughness Description and Its Application to the Dynamic Response of Vehicles," Draft Report, Sep 1980, U. S. Army Engineer Waterways Experiment Station, CE, Vicksburg, MS.

2. Van Deusen, R. D., "A Statistical Technique for the Dynamic Analysis of Vehicles Traversing Rough Yielding and Non-yielding Surfaces," Contract Report No. NASW-1287, May 1966, Advanced Projects Organization, Chrysler Corp, Detroit, MI.

3. Blackman, R. B. and Tukey, J. W., The Measurement of Power Spectra, Dover Publications, New York, 1958.

4. Bendat, J. S. and Piersol, A. G., Random Data: Analysis and Measurement Procedures, Wiley-Interscience, New York, 1971.

5. Bekker, M. G., Introduction to Terrain-Vehicle Systems, University of Michigan Press, Ann Arbor, 1969.

6. Lins, William F., "Human Vibration Response Measurement," Technical Report No. 11551, June 1972, U. S. Army Tank Automotive Command, Warren, MI.

7. Pradko, F., Lee, R. and Kaluza, V., "Theory of Human Vibration Response," presented at the Winter Annual Meeting and Energy Systems Exposition of the American Society of Mechanical Engineers, New York, NY, 27 Nov-1 Dec 1966.

8. Schreiner, B. G., "Ride and Shock Test Results for the Leopard 2 AV Tank," Miscellaneous Paper M-77-3, Mar 1977, U. S. Army Engineer Waterways Experiment Station, CE, Vicksburg, MS.

9. _____, "Ride and Shock Test Results for the M60A1, XM-1 Chrysler, and XM-1 General Motors Tanks."

10. Schreiner, B. G. and Randolph, D. D., "Ride and Shock Test Results and Mobility Assessment of Czechoslovakia Tatra 813, U. S. M520E1 GOER, and U. S. M656 Cargo Trucks," Technical Report GL-79-9, July 1979, U. S. Army Engineer Waterways Experiment Station, CE, Vicksburg, MS.

11. _____, "Ride and Shock Test Results and Mobility Assessment of German M.A.N., U. S. M520E1 GOER, and U. S. M656 Cargo Trucks," Technical Report GL-79-17, Sept 1979, U. S. Army Engineer Waterways Experiment Station, CE, Vicksburg, MS.

12. _____, "Ride and Shock Test Results and Mobility Assessment of Selected 10-Ton Cargo Trucks," Technical Report GL-79-5, May 1979, U. S. Army Engineer Waterways Experiment Station, CE, Vicksburg, MS.

13. Robinson, J. H. Randolph, D. D. and Schreiner, B. G., "Ride and Shock Test Results and Mobility Assessment of Selected 1/4- to 1-1/4-Ton Vehicles," Technical Report GL-79-3, Mar 1979, U. S. Army Engineer Waterways Experiment Station, CE, Vicksburg, MS.

14. Jacobsen, L. S. and Ayre, R. S., Engineering Vibrations, McGraw-Hill Book Co., New York, 1958.

15. Snowdon, J. C., Vibration and Shock in Damped Mechanical Systems, John Wiley, New York, 1968.

16. Crafton, P. A., Shock and Vibration in Linear Systems, Harper & Brothers, New York, 1961.

17. Duncan, W. J., Physical Similarity and Dimensional Analysis, Edward Arnold and Co., London, 1953.

Table 1

Units of the Power Spectra

C	in.
D	dimensionless
E	in.$^{-1}$
$P_d(\Omega)$	in.^{3}
$P_d'(f)$	in.^{2} sec
$P_v(\Omega)$	in.^{3} sec^{-2}
$P_v'(f)$	in.^{2} sec^{-1}
$P_a(\Omega)$	in.^{3} sec^{-4}
$P_a'(f)$	in.^{2} sec^{-3}
$P_s(\Omega)$	in.
$P_s'(f)$	sec^{-1}
$P_c(\Omega)$	in.$^{-1}$
$P_c'(f)$	in.$^{-2}$ sec

Table 2

Calculated Values of the Roughness Power Spectrum Coefficients

PROFILE ID	LOCATION	DETRENDED (λ=10 ft)			$C, 10^{-3} \ln$	$D, 10^{-5}$	$E, 10^{-8} \ln^{-1}$	$\Omega_0, 10^{-3} \ln^{-1}$	$\Omega_1, 10^{-3} \ln^{-1}$	SPECTRUM TYPE
		$\sigma_d, \ln$	σ_s	$\sigma_c, \ln^{-1}$						
AISV1	Huntsville, Alabama	1.32	.049	.0053	0.8952	1.069	-0.5426	0.4876	-	3
AISV2		0.57	.038	.0043	0.6596	0.4937	-0.4364	0.7987	-	3
AISV3		0.72	.031	.0033	0.3188	0.5067	-0.3299	0.6264	-	3
AISV4AT		0.57	.032	.0042	0.8920	-0.3634	0.2464	0.8396	4.611	5
FTKCTA1	Ft Knox, Kentucky	2.03	.048	.0046	0.4125	1.592	-0.1924	0.1205	-	3
FTKCTA2		5.53	.088	.0058	-1.469	8.889	1.837	60.73	-	2
FTKSTV1		4.84	.106	.0069	-3.027	15.91	-5.945	0.3763	52.19	4
FTKSTV4		1.70	.083	.0061	-1.541	10.07	-7.370	0.7405	64.58	4
FTKSTV9		3.26	.078	.0063	-0.4240	6.742	-2.461	0.3654	158.6	4
SR1LT82	Ft Knox, Kentucky	0.59	.031	.0035	0.4388	0.3193	-0.2434	0.6957	-	3
SR1RT82		0.54	.026	.0027	0.1871	0.4236	-0.3040	0.6962	-	3
SR2LT83		0.78	.030	.0035	0.4937	0.1405	-0.0248	0.1666	-	3
SR2RT83		1.06	.037	.0038	0.3689	0.8359	-0.4369	0.5112	-	3
SR4LT83		3.38	.075	.0051	-1.325	7.671	-2.850	0.3740	57.53	4
SR4RT83		3.33	.074	.0047	-1.591	7.972	-3.157	0.3992	49.70	4
SR5LT83		2.63	.065	.0059	0.3615	3.623	-1.068	0.2939	-	3
SR5RT83		2.27	.047	.0033	-0.4325	2.818	-0.7725	0.2753	64.87	4
HOOD1DM	Ft Hood, Texas	0.51	.026	.0029	0.2900	0.2546	-0.1887	0.6874	-	3
HOOD2DM		1.39	.104	.0139	10.00	-4.701	2.783	0.6948	4.00	5
HOOD3DM		1.91	.078	.0082	1.874	3.422	-2.135	0.6040	-	3
HOOD1T(T1M)		1.56	.078	.0092	3.445	0.8938	-0.6377	0.5827	-	3
HOOD2TX		0.94	.046	.0055	1.275	0.1801	-0.1139	0.4735	-	3
HOOD3T(3TM)		0.57	.026	.0030	0.3472	0.1545	-0.0950	0.5477	-	3
HOOD4T(T4M)		1.23	.039	.0042	0.5681	0.6459	-0.1959	0.2956	-	3
SR1HETM		0.42	.023	.0023	0.1060	0.4027	-0.3063	0.7459	-	3

Table 2 (Continued)

PROFILE ID	LOCATION	DETRENDED (λ=10 ft) σ_{d},in	σ_{s}	σ_{c},in^{-1}	C,10^{-3}in	D,10^{-5}	E,10^{-8}in^{-1}	Ω_{0},10^{-3}in^{-1}	Ω_{1},10^{-3}in^{-1}	SPECTRUM TYPE
T21	Hi Mag	0.73	.038	.0038	0.291	1.092	-0.815	0.732	-	3
T24	Courses,	1.07	.048	.0047	0.387	1.850	-1.290	0.687	-	3
T22	Ft Knox,	1.89	.129	.0147	7.874	5.247	-4.755	0.808	-	3
T13	(Right Track)	3.41	.084	.0061	-1.337	9.279	-4.145	0.450	68.93	4
T14	"	5.15	.104	.0053	-4.413	17.53	-6.144	0.354	39.36	4
T38C	"	0.79	.038	.0040	0.440	0.839	-0.600	0.691	-	3
T36	"	1.02	.039	.0039	0.325	1.086	-0.665	0.602	-	3
T30	"	1.98	.071	.0052	-1.078	7.151	-4.684	0.662	65.70	4
T32	"	3.68	.088	.0059	-1.999	11.01	-4.922	0.451	54.64	4
T33	"	2.36	.052	.0038	-0.454	3.377	-1.117	0.332	74.05	4
E1	"	0.79	.033	.0031	0.109	0.992	-0.671	0.672	-	3
E3	"	0.97	.036	.0035	0.213	1.028	-0.626	0.601	-	3
E5	"	1.62	.048	.0039	-0.196	2.715	-1.478	0.547	137.7	4
E7	"	3.50	.078	.0047	-1.998	9.246	-3.817	0.417	45.85	4
E9	"	2.31	.050	.0039	-0.240	2.810	-0.745	0.266	116.8	4
APG38	APG,MD	2.65	.113	.0088	-2.00	17.120	-12.020	0.707	84.60	4
APG40	"	1.04	.045	.0051	0.96	0.596	-0.350	0.541	-	3
APG41	"	0.47	.027	.0034	0.51	-0.035	0.0046	0.175	0.512	5
APG42	"	1.18	.092	.0112	5.38	0.496	-0.950	0.946	-	3
APG43	"	0.30	.018	.0024	0.30	-0.167	0.113	0.795	4.68	5
APG44	"	3.93	.082	.0057	-1.42	8.830	-2.6300	0.299	61.70	4
APG29	"	2.15	.096	.0111	4.74	1.999	-1.152	0.514	-	3
APG31	"	3.18	.076	.0059	-0.71	6.978	-2.764	0.398	98.44	4
APG32	"	1.95	.0490	.0045	0.27	1.963	-0.571	0.290	-	3
APG34	"	1.55	.080	.0103	5.31	-1.949	1.422	1.005	2.661	5
APG36	"	3.71	.075	.0064	0.24	4.822	-0.023	0.0047	-	3
APG37	"	0.83	.032	.0038	0.64	0.018	0.075	-	-	1

Table 3

Comparison of Detrended and Undetrended Methods for a Type 3 Roughness Spectrum

PROFILE ID	DETRENDED SCHEME						UNDETRENDED SCHEME					
	σ_d in	σ_s	σ_c in^{-1}	C 10^{-3}in	D 10^{-5}	E 10^{-8}in^{-1}	σ_d in	σ_s	σ_c in^{-1}	C 10^{-3}in	D 10^{-5}	E 10^{-8}in^{-1}
APG48LI	1.39	0.045	0.0049	0.80	0.79	-0.23	23.57	0.053	0.0055	1.21	0.351	-0.011
APG52RI	0.96	0.033	0.0034	0.30	0.65	-0.33	1.91	0.038	0.0036	0.31	0.81	-0.53
APG52LI	1.03	0.039	0.0042	0.55	0.71	-0.38	3.58	0.045	0.0045	0.68	0.63	-0.20
APG53RI	1.42	0.053	0.0049	0.22	2.62	-1.66	3.79	0.060	0.0052	0.43	2.32	-1.24
APG53LI	1.25	0.053	0.0048	0.12	2.84	-1.85	3.13	0.059	0.0052	0.40	2.43	-1.62
APG56RI	2.25	0.046	0.0040	0.108	1.82	-0.05	8.54	0.058	0.0042	0.125	1.97	-0.42
APG56LI	1.83	0.039	0.0034	0.072	1.34	-0.15	3.74	0.048	0.0035	-0.06	1.86	-0.87

Table 4

Dynamical Parameters of Track Vehicles

Vehicle Type	Weight lb	Spring Constant lb/in.	Damping Constant lb sec/in.	Track Length in.
M113A1	24,200	6,060	3110	105
MICV	43,000	8,400	720	150
AISV	2,940	300	80	50.25
HIMAG-5	79,910	10,000	400	168
LEO 2AV	111,000	15,750	8000	188.3
M60 A1	106,000	20,000	8000	171

Table 5

Dynamical Parameters for Trucks

Vehicle Type	Body			Wheel Assembly		
	Weight lb	Spring lb/in.	Damping lb sec/in.	Weight lb	Spring Constant lb/in.	Damping Constant lb sec/in.
PAC-CAR TARADCOM-HMTT 10 ton (8x8)	46,179	4718	830	5131	75,490	830
DRAGON WAGON 10 ton (8x8)	44,136	4509	822	4904	72,150	822
GERMAN MAN 10 ton (8x8)	47,610	4864	887	5290	77,829	887
M656 5 ton (8x8)	23,040	2354	250	2560	37,664	250
M520E1-GOER 8 ton (4x4)	41,400	2500	1000	--	--	--

Table 6

Geometrical Properties of Trucks

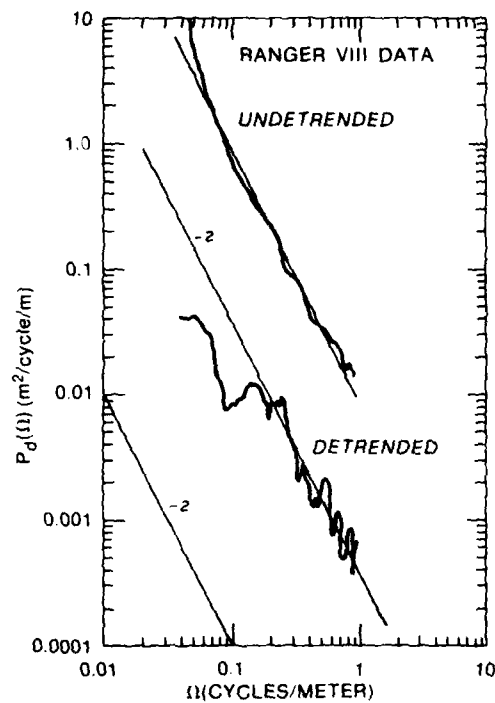| Vehicle Type	Tire Radius in.	L_{12} in.	L_{13} in.	L_{14} in.	L_{23} in.	L_{24} in.	L_{34} in.
PAC-CAR TARADCOM-HMTT 10 ton (8x8)	26	58	190	248	132	190	58
DRAGON WAGON 10 ton (8x8)	26	58	202	260	144	202	58
GERMAN MAN 10 ton (8x8)	23.75	65.5	209.5	275	144	209.5	65.5
M656 5 ton (8x8)	22	56.25	147.75	204	91.5	147.75	56.25
M520E1-GOER 8 ton (4x4)	34.5	235	--	--	--	--	--
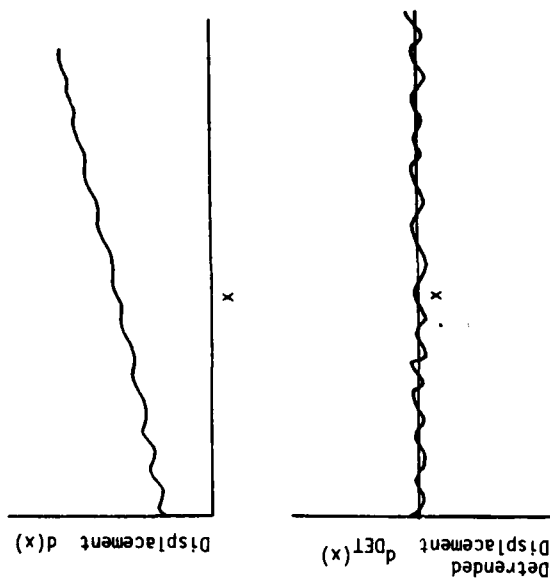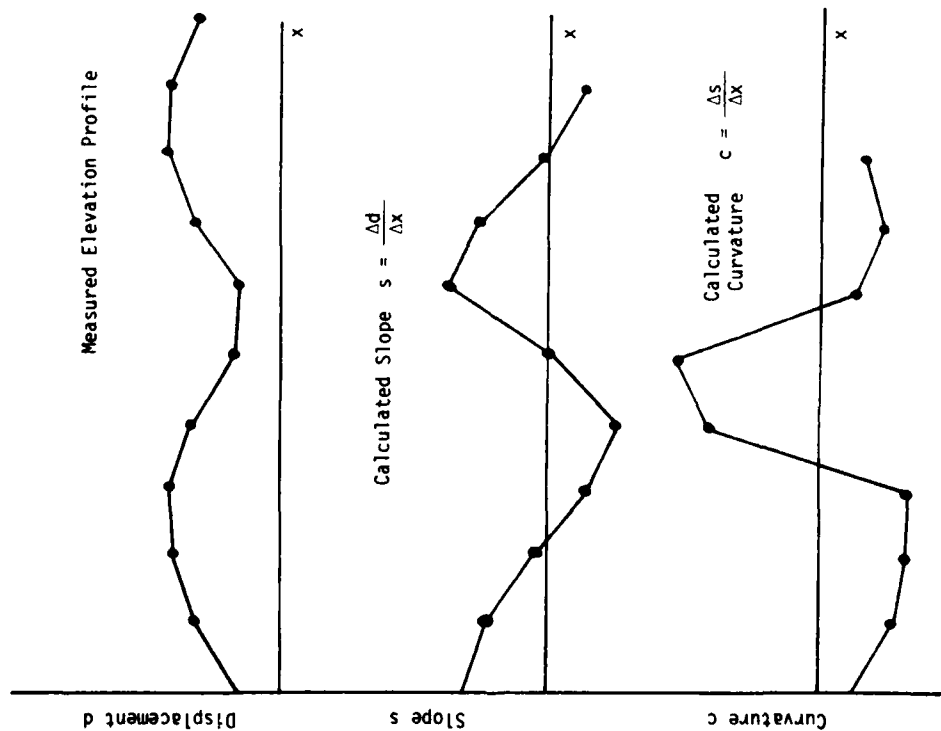
Figure 1

$$d_{DET}(x,\lambda) = d(x) - \frac{1}{2\lambda} \int_0^\infty [d(x+a) + d(x-a)]e^{-a/\lambda}\, da$$

λ = detrending constant

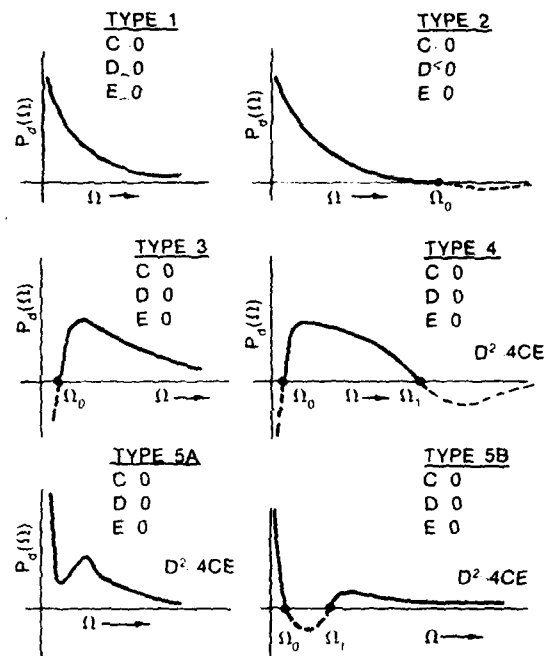COMPUTER PROGRAM RRFN DETRENDS $\left\{\begin{array}{l}\text{DISPLACEMENT}\\ \text{SLOPE}\\ \text{CURVATURE}\end{array}\right.$

a

b
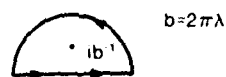
c
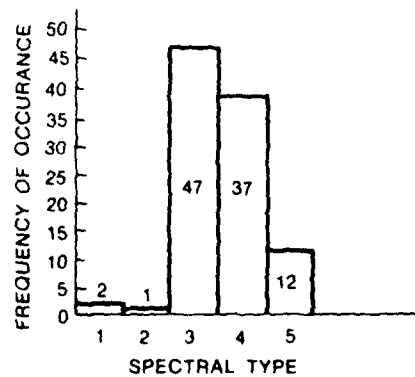
d

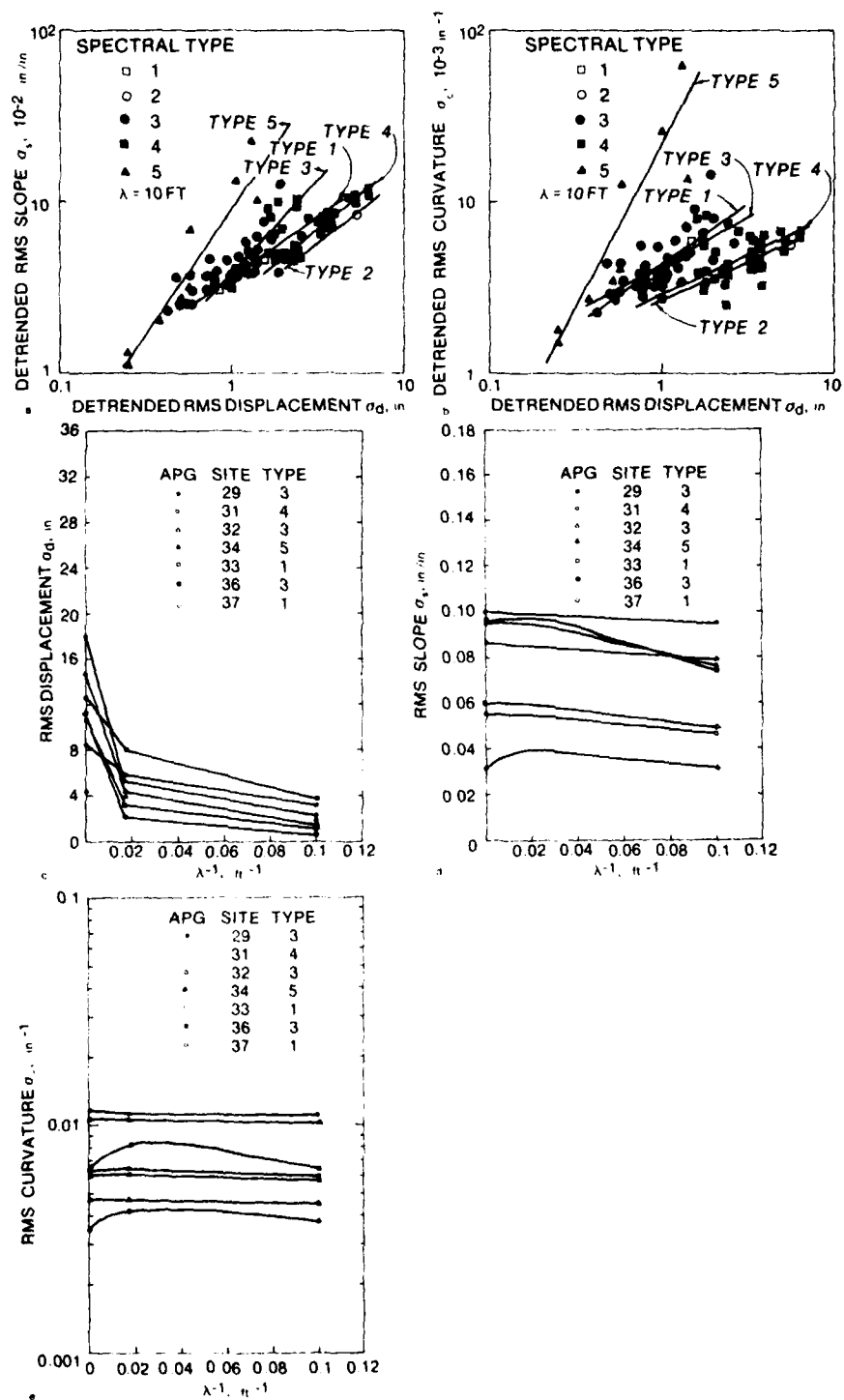Figure 2

Figure 3

Figure 4
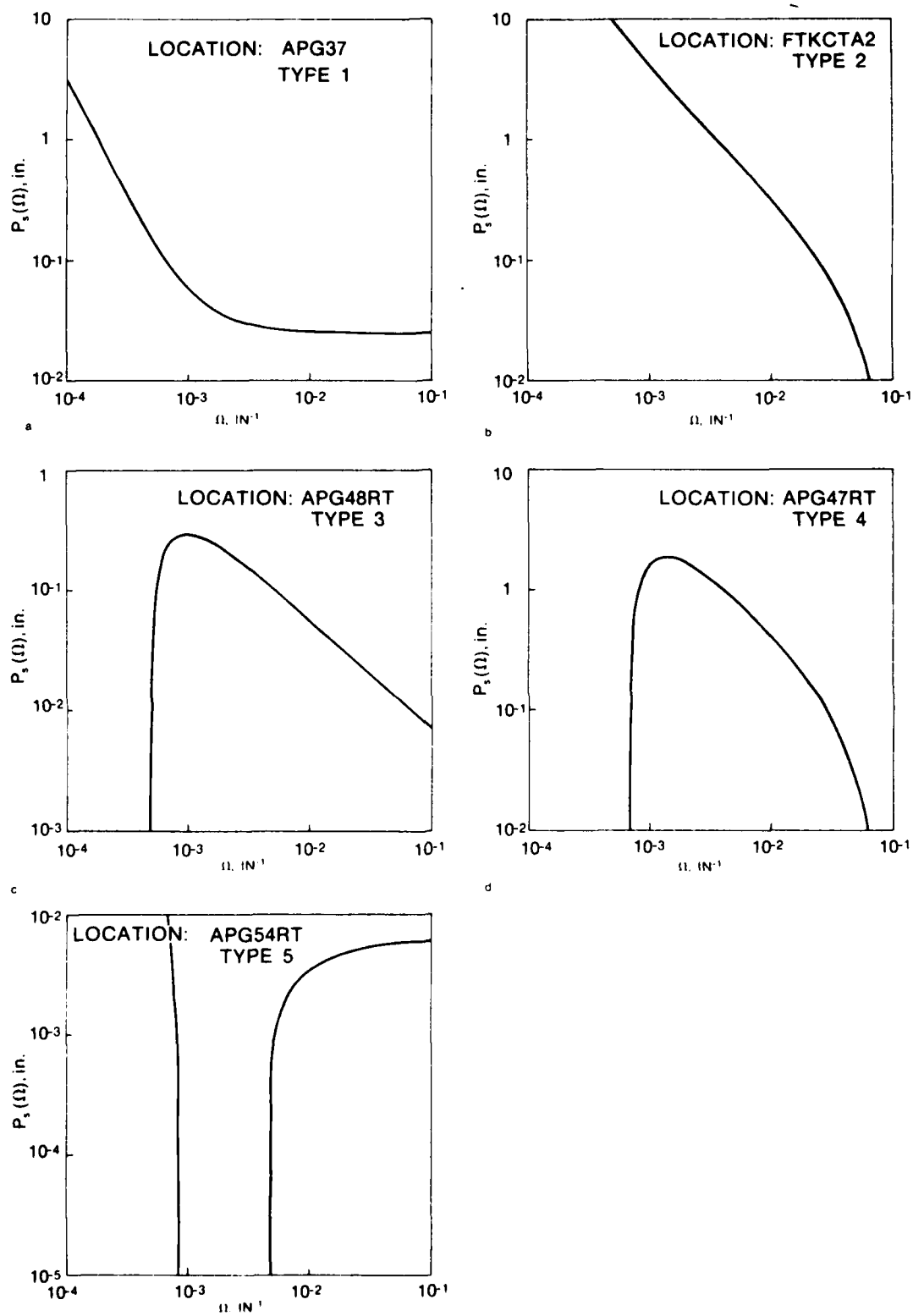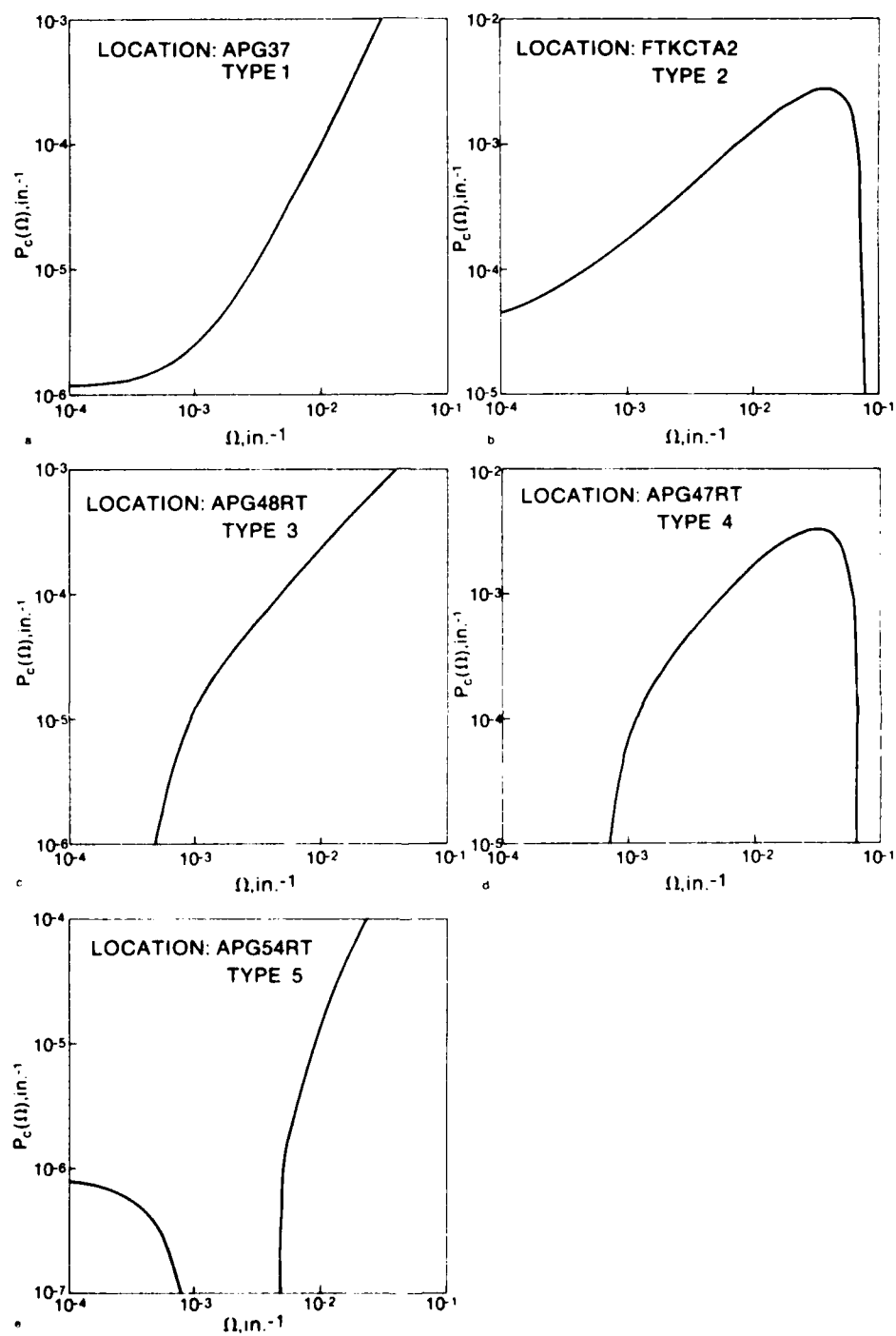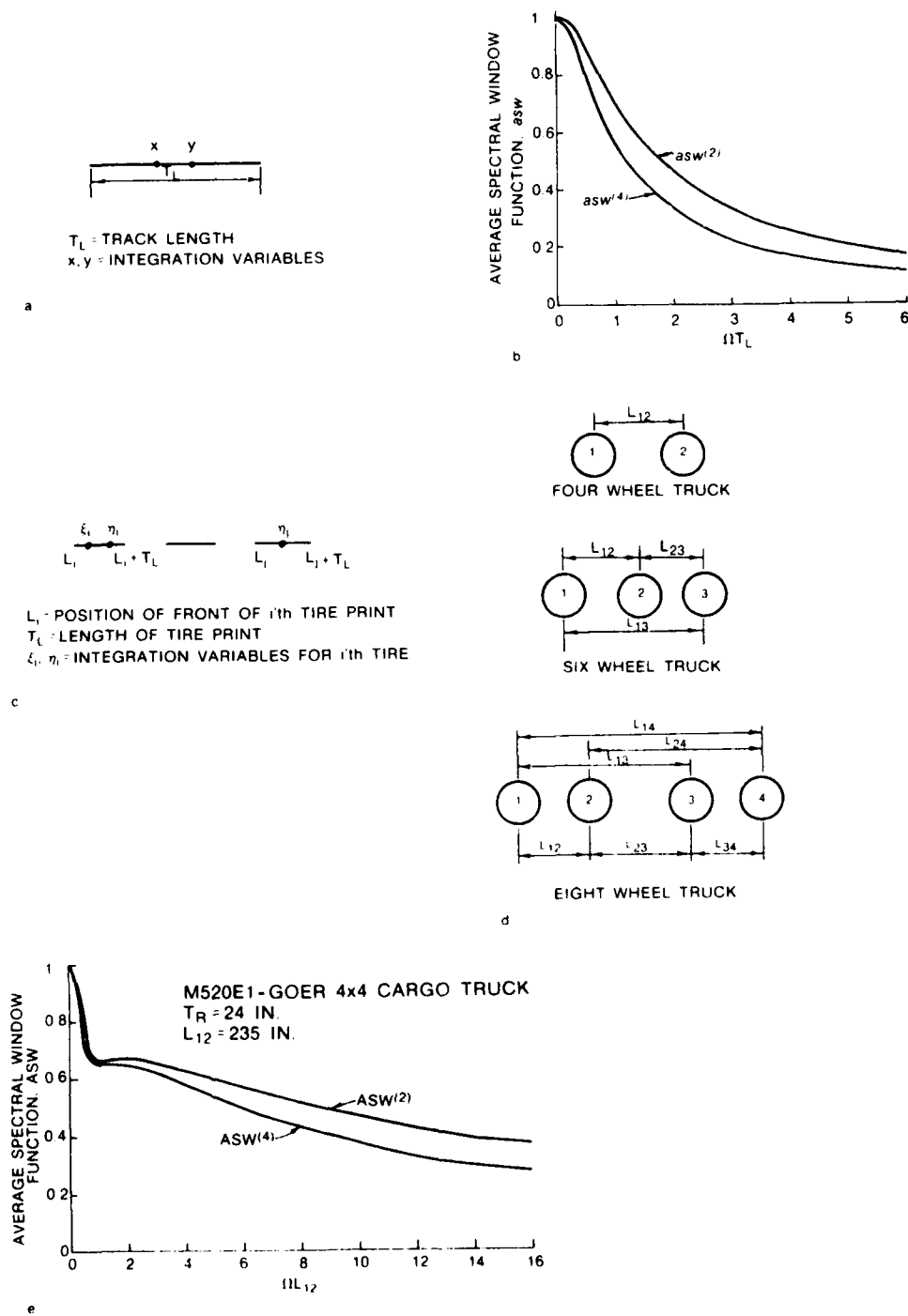
525

Figure 5

Figure 6

T_L = TRACK LENGTH
x, y = INTEGRATION VARIABLES

a

AVERAGE SPECTRAL WINDOW FUNCTION, asw

$asw^{(2)}$
$asw^{(4)}$

ΩT_L

b

L_{12}

FOUR WHEEL TRUCK

L_i = POSITION OF FRONT OF i'th TIRE PRINT
T_L = LENGTH OF TIRE PRINT
ξ_i, η_i = INTEGRATION VARIABLES FOR i'th TIRE

c

L_{12} L_{23}
L_{13}

SIX WHEEL TRUCK

L_{14}
L_{24}
L_{13}
L_{12} L_{23} L_{34}

EIGHT WHEEL TRUCK

d

AVERAGE SPECTRAL WINDOW FUNCTION, ASW

M520E1-GOER 4x4 CARGO TRUCK
T_R = 24 IN.
L_{12} = 235 IN.

$ASW^{(2)}$
$ASW^{(4)}$

ΩL_{12}

e

Figure 7

528
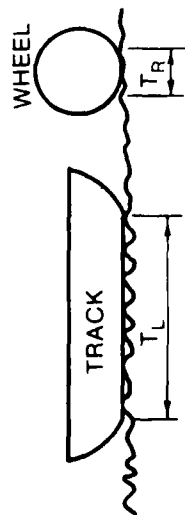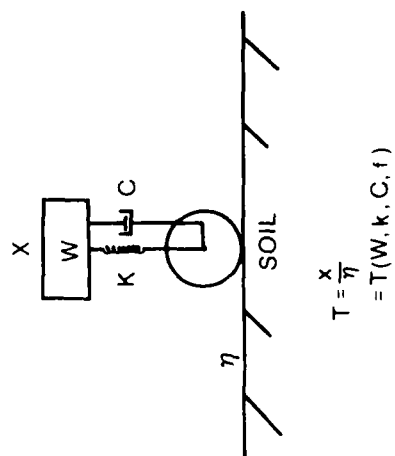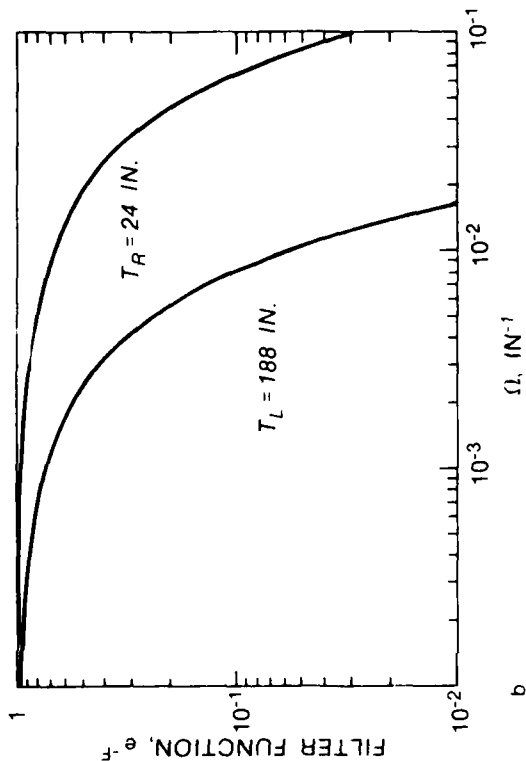
Figure 8

TRANSMISSION FUNCTION FOR VERTICAL MOTION
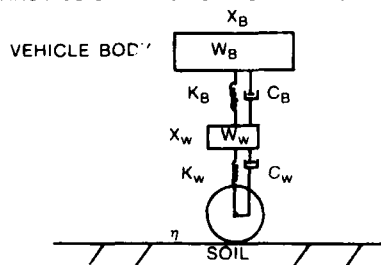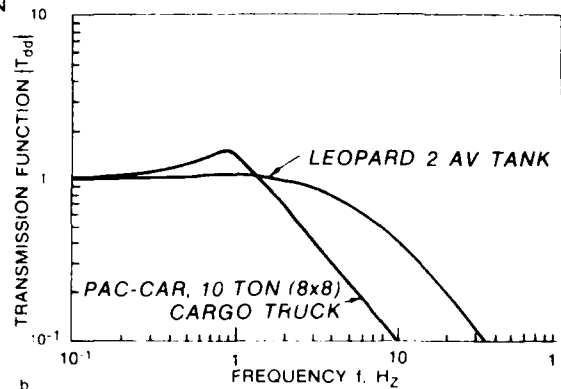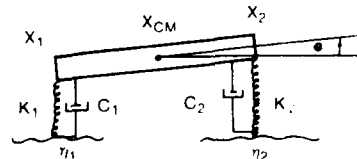
Figure 9

530
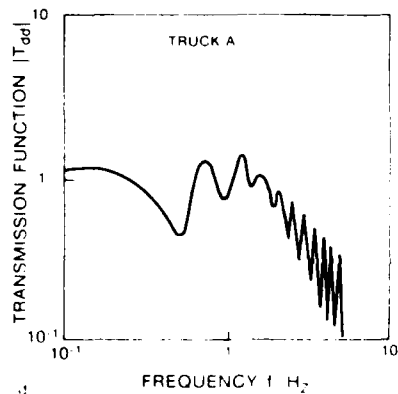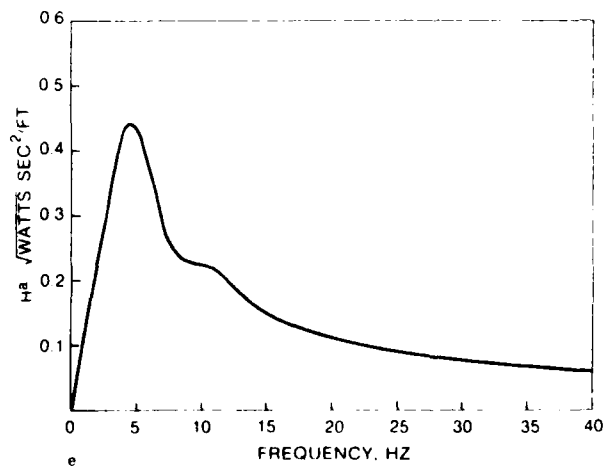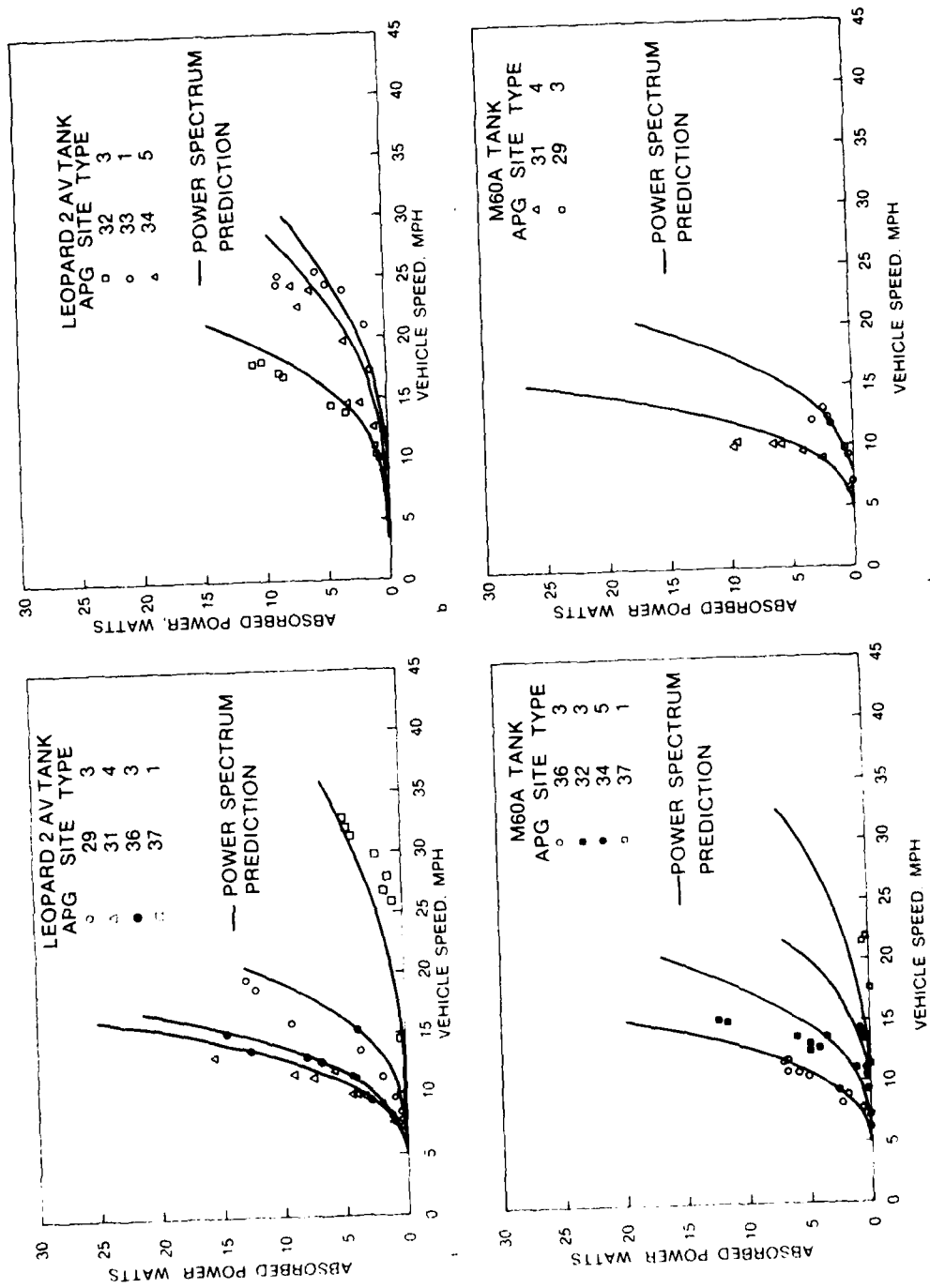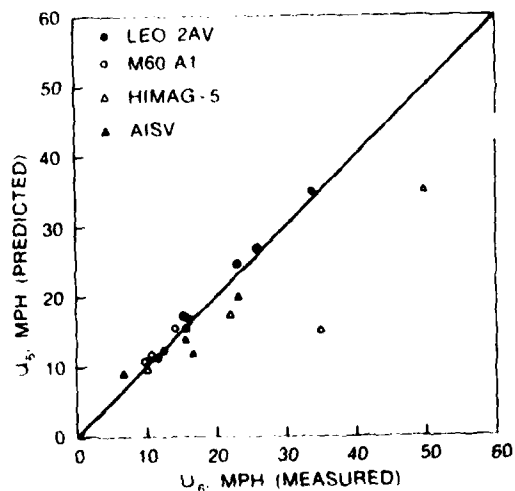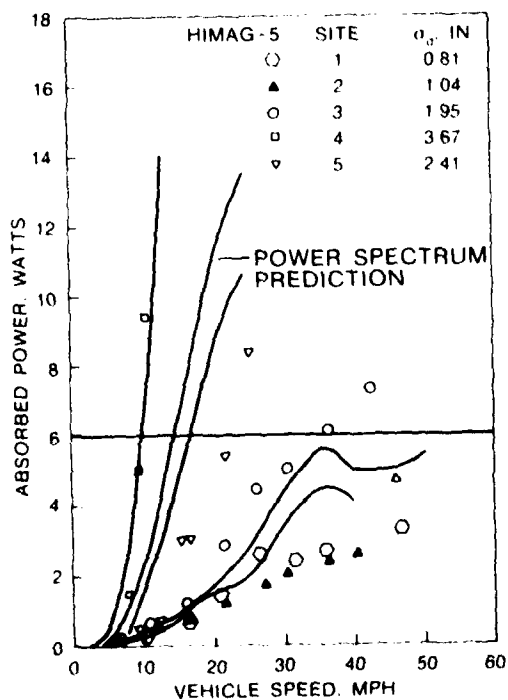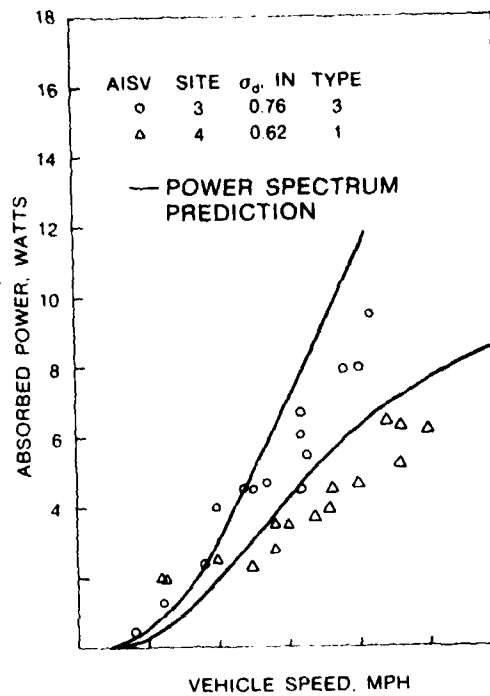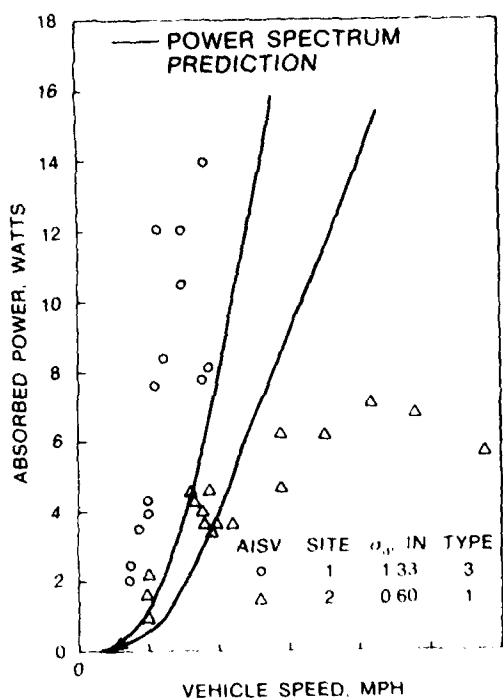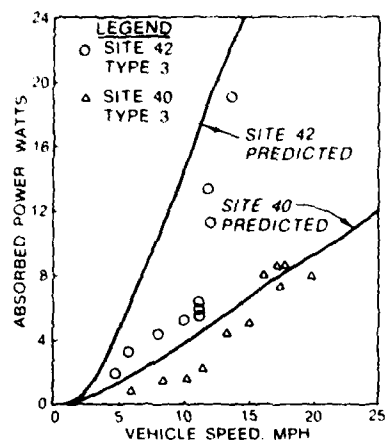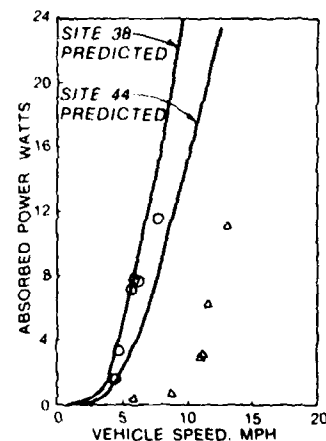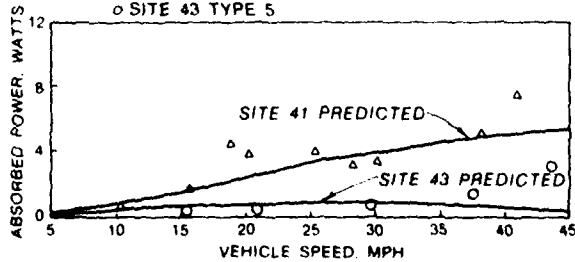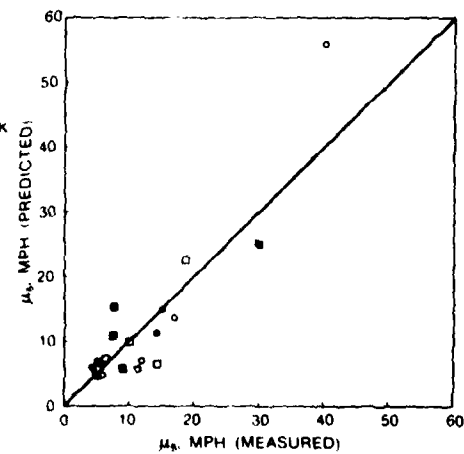
Figure 10

Figure 11

Figure 12

Figure 13

534
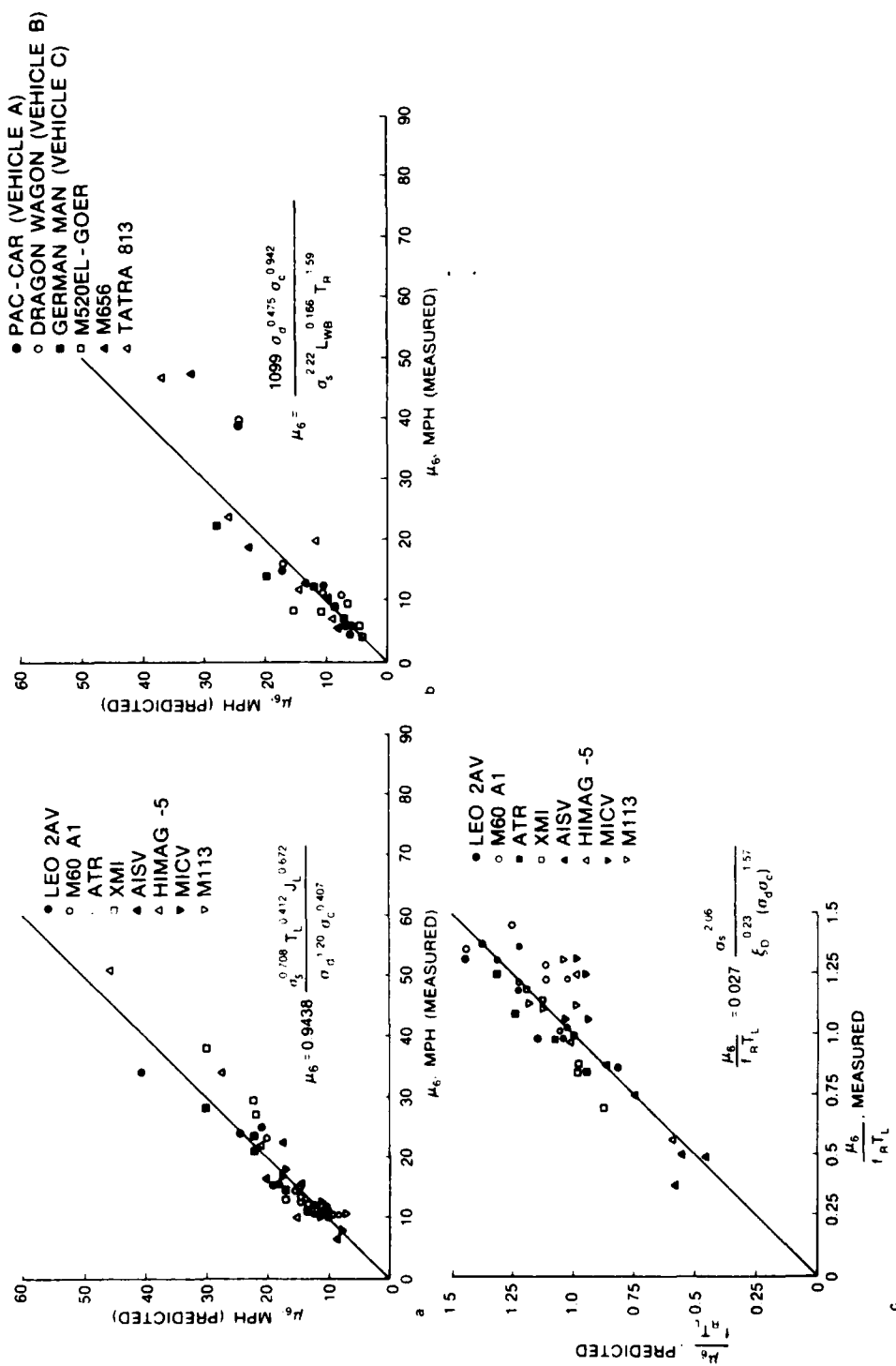
AN ASYMPTOTIC THEORY OF DEFLAGRATIONS AND DETONATIONS

A. K. Kapila
Department of Mathematical Sciences
Rensselaer Polytechnic Institute
Troy, New York   12181

ABSTRACT.   Combustion waves propagating through a reactive gas are studied in the plane, one-dimensional geometry.   An asymptotic theory is developed which yields the steady structures of the waves in a simple, analytical form.   The theory, based on the limits of small heat release and large activation energy, covers all possible deflagrations and detonations except those strong detonations that are far removed from the Chapman-Jouguet point.

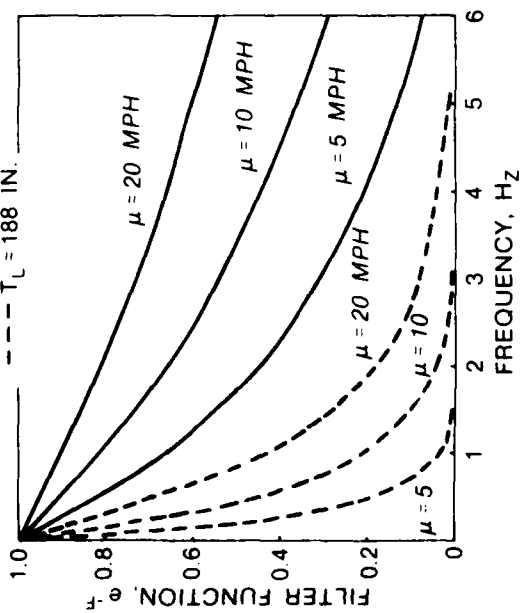I.   INTRODUCTION   A satisfactory mathematical treatment of the deflagration-to-detonation transition (DDT) is not yet available, not even for the planar, one-dimensional situation. In order to study the transient process, it would be particularly convenient if the steady wave structures were available in a simple, analytical form, amenable to further analysis.   The object of this paper is to construct such a steady description of the plane waves by means of an asymptotic analysis of the governing equations.

The subject of steady, plane combustion waves is an old one [1].   Previous work most relevant to the present study is that of Bush and Fendell, who employed large activation-energy asymptotics to compute the structure of slow deflagrations [2] and Chapman-Jouguet detonations [3].   In contrast, we present wave structures for arbitrary Mach numbers.   Since our aim is to obtain analytical results, potentially useful for the DDT analysis, we employ the additional approximation of low exothermicity. It restricts the study to low-amplitude or weakly nonlinear waves, but produces explicit analytical solutions for all possible deflagrations and detonations, except strong detonations far from the CJ point.

II.   EQUATIONS OF MOTION.   In a reference frame attached to the wave, the equations of reactive gas dynamics, for plane one-dimensional flow, are

$$\bar{v}' - \bar{v} - \frac{\bar{p}}{\gamma M_o^2} = 0 \quad , \tag{1a}$$

$$\bar{T}'' - \bar{T}' + \frac{\gamma - 1}{\gamma}(1 + \bar{v})\bar{p}' + (\gamma - 1)M_o^2 \bar{v}'^2 + \alpha w = 0 \quad , \tag{1b}$$

$$\bar{p} + \bar{v} - \bar{T} + \bar{p}\,\bar{v} = 0 \quad , \tag{1c}$$

$$\frac{1}{Le} Y'' - Y' - w = 0 \ , \tag{1d}$$

$$w = \frac{D}{M_o^2} \frac{\overline{Y}}{1 + \overline{v}} \exp\left[- \frac{E}{1 + \overline{T}}\right] \ , \tag{1e}$$

$$\overline{p} + \overline{v} + \overline{\rho} \ \overline{v} = 0 \ . \tag{1f}$$

This dimensionless system has been obtained by choosing, as characteristic quantities, the diffusion length, the wave speed, and the upstream (cold-boundary) values of pressure, temperature and density. The dimensional pressure $\tilde{p}$ is given by $\tilde{p} = \tilde{p}_o(1 + \overline{p})$, where $\tilde{p}_o$ is the upstream pressure, so that $\overline{p}$ measures the dimensionless deviation from upstream pressure. Similar remarks apply to $\overline{\rho}$, the density deviation, and $\overline{T}$, the temperature deviation. The gas velocity is given by $\overline{v}$, while Y is the reactant mass fraction. The dimensionless parameters appearing in the equations are M_o, the mach number of the wave; Le, the Lewis number; α, the heat of reaction; D, the Damkohler number and E, the activation energy. Prime denotes differentiation with respect to the spatial coordinate ζ. Equation (1f) will henceforth be eliminated from explicit consideration since it merely defines $\overline{\rho}$. The remaining equations are to be solved for $\overline{p}$, $\overline{T}$, $\overline{v}$ and Y under the boundary conditions

$$\overline{p} = \overline{T} = \overline{v} = 0, \ Y = 1 \ \text{at} \ \zeta = -\infty \tag{2a}$$

$$d\phi/d\zeta = 0 \ \text{for} \ \phi = \overline{p}, \ \overline{T}, \ \overline{v} \ \text{and} \ Y, \ \text{at} \ \zeta = \infty \ . \tag{2b}$$

The mach number M_o is also to be determined. The cold-boundary difficulty is dealt with by invoking the notion of a flame holder, which may be assumed to supply the gas at a prescribed temperature $\overline{T}_i$ (>0) at the location $\zeta = 0$. However, we prefer to retain the doubly infinite domain $-\infty < \zeta < \infty$, but introduce the mathematical essentials of a flame holder by specifying that

$$w \equiv 0 \ \text{for} \ \zeta < 0 \ , \ \overline{T}(0) = \overline{T}_i > 0 \ , \tag{3}$$

and that $\overline{p}$, $\overline{T}$, $\overline{v}$, Y and their first derivatives are continuous at $\zeta = 0$.

One might have expected the cold-boundary difficulty to have been obviated in the face of the limit $E \to \infty$. However, that happens only when the limit $E \to \infty$ serves to limit the reaction to a thin zone. Such is not the case here, as we shall see.

III. HUGONIOT RELATIONS. Evaluation of eqns. 1(a-e) at $\zeta = \infty$ yields the Hugoniot relations which specify the final state of the system for a given M_o [1]. The final state corresponds to a deflagration or a detonation. Provided that M_o satisfies

$$(1 - M_o^2) \geq 2\alpha(\gamma + 1)M_o^2 ,$$ (4)

each M_o corresponds to two final states, given by

$$\overline{v}_\infty = \frac{\overline{p}_\infty}{\gamma M_o^2} = \frac{1-M_o^2}{(\gamma+1)M_o^2} \left[1 \pm \left\{ 1 - \frac{2\alpha(\gamma+1)M_o^2}{(1-M_o^2)^2} \right\}^{\frac{1}{2}} \right] .$$ (5)

Here the + (−) sign corresponds to strong (weak) waves.[*] In (4), equality corresponds to the CJ (Chapman-Jouguet) points. At these points,

$$M_{o_\pm} \simeq \left| 1 + \frac{\alpha(\gamma+1)}{2} \right|^{\frac{1}{2}} \pm \left| \frac{\alpha(\gamma+1)}{2} \right|^{\frac{1}{2}} ,$$ (6)

where the upper (lower) sign corresponds to the upper (lower) CJ point. For deflagrations, (4) implies $0 < M_o \leq M_{o_-}$ while for detonations, $1 < M_{o_+} \leq M_o$.

IV. THE LIMITS $E \to \infty$, $\alpha \to 0$. We characterize the largeness of activation energy by setting

$$E = 1/\varepsilon , \quad \varepsilon \to 0,$$ (7)

and consider a distinguished limit in which

$$\alpha = \varepsilon g , \quad g = O(1).$$ (8)

---

[*]The terms weak and strong refer to the strength of the wave relative to its strength at the corresponding CJ point. Both weak and strong waves can have low amplitudes.

For $M_O^2 - 1 = O(1)$, (8) reduces (5), for the weak waves, to

$$\bar{v}_\infty = - \frac{\bar{P}_\infty}{\gamma M_O^2} \sim \epsilon \frac{g}{1-M_O^2} , \qquad (9)$$

implying that the wave strength, measured by, say $\bar{p}_\infty$ (pressure jump across the wave) is $O(\epsilon)$. For strong waves, (5) reduces to

$$\bar{v}_\infty = - \frac{\bar{P}_\infty}{\gamma M_O^2} \sim \frac{2(1-M_O^2)}{(\gamma+1)M_O^2} - \epsilon \frac{g}{1-M_O^2} , \qquad (10)$$

i.e. the wave strength is $O(1)$. At the CJ points, (6) becomes

$$M_{O_\pm} \sim 1 \pm [\tfrac{1}{2} \epsilon g (\gamma + 1)]^{\frac{1}{2}} \qquad (11)$$

whence (5) assumes the form

$$\bar{v}_\infty = - \frac{\bar{P}_\infty}{\gamma M_O^2} \sim \left(\frac{2\epsilon g}{\gamma+1}\right)^{\frac{1}{2}} , \qquad (12)$$

showing that the CJ wave strength is $O(\epsilon)^{\frac{1}{2}}$.

The above reduction implies that the only waves not accessible to a small amplitude theory are those strong deflagrations and strong detonations that are far away from the CJ points. However, strong deflagrations are disallowed by structure considerations [1]. Therefore, the near-CJ waves and all weak waves are within the realm of the weakly nonlinear theory although different analyses are required to describe them since the wave strengths are $O(\epsilon)$ in one case and $O(\sqrt{\epsilon})$ in the other.

For the sake of brevity, calculations are presented only for deflagrations away from the CJ point, and even then, most of the details are omitted. For additional details and computations for other waves, the reader is referred to [4].

V. DEFLAGRATIONS AWAY FROM THE CJ POINT: $1 - M_O^2 = O(1)$

Since the weak waves have $O(1)$ strengths, it is convenient to introduce new variables as follows:

$$\bar{p} = \epsilon p, \quad \bar{v} = \epsilon v, \quad \bar{T} = \epsilon T \qquad (13)$$

538

while Y remains unchanged. We also let

$$\overline{T}_i = \epsilon \, T_i \; . \tag{14}$$

We shall find that the wave structure consists of three main zones: an induction zone R_I in which T undergoes an o(1) change, an explosion zone R_E in which T changes by an O(1) amount, and a completion zone R_C in which T again undergoes an o(1) change to approach its final, downstream value. We shall also find that in most of the wave, the dominant balance is convective-reactive. We now discuss each zone, in turn.

Induction Zone R_I

This zone is found to consist of two parts. In the first, $\zeta = O(1)$. Eqn. (1e) shows that the reaction term w is exponentially small, since D/M_o^2 is O(1). Therefore, we employ the expansions

$$T = \delta T_1 + \ldots, \quad p = \delta p_1 + \ldots, \quad v + \delta v_1 + \ldots, \quad Y = 1 + \delta Y_1 + \ldots \tag{15}$$

where

$$\delta = e^{-1/\epsilon^2} \; . \tag{16}$$

We also take the ignition temperature to be

$$T_i = \delta \, T_{1i} \; . \tag{17}$$

When the above expansions are substituted into (1a-e) and the boundary conditions (2a) applied, we obtain the solution

$$p_1 = \begin{cases} 0, \; \zeta < 0 \; , \\[2ex] \dfrac{gD}{\beta^2 M_o^2} \, (1 - e^{-\beta\zeta} - \beta\zeta), \; \zeta > 0 \; , \end{cases} \tag{18}$$

$$T_1 = \begin{cases} D_1^- \, e^{\zeta}, \; \zeta < 0 \; , \\[2ex] C_1^+ + \dfrac{DT_{1\infty}}{M_o^2} \, \zeta - \dfrac{\gamma-1}{\gamma} \; \dfrac{gD}{\beta^2(1+\beta)M_o^2} \, e^{-\beta\zeta}, \; \zeta > 0 \; , \end{cases} \tag{19}$$

539

$$v_1 = T_1 - P_1 \,, \tag{20}$$

$$Y_1 = \begin{cases} - \dfrac{D}{LeM_o^2} \, e^{Le\,\zeta} \,, & \zeta < 0 \,, \\[2ex] - \dfrac{D}{LeM_o^2} \, (1+Le\,\zeta) \,, & \zeta > 0 \,, \end{cases} \tag{21}$$

where

$$\beta = \frac{1-M_o^2}{\gamma M_o^2} > 0 \,, \quad C_1^+ = \frac{D}{M_o^2} \left(T_{1\infty} + \frac{\gamma-1}{\gamma} \, \frac{g}{\beta^2} \right) \,, \tag{22}$$

$$D_1^- = \frac{D}{M_o^2} \left\{ T_{1\infty} + \frac{\gamma-1}{\gamma} \, \frac{g}{\beta(1+\beta)} \right\} \,, \quad T_{1\infty} = \frac{1-\gamma M_o^2}{1-M_o^2} \, g \,.$$

In obtaining the above solution we have disallowed exponential growth as $\zeta \to +\infty$, anticipating such behavior to be unmatchable with the regions beyond. The wave speed M_o is determined by applying the flame holder condition $T_1(0) = T_{1i}$ to (19). The result is

$$M_o^2 = \frac{-1 + \{1 + \dfrac{4gD}{T_{1i}}(\gamma-1)\}^{\frac{1}{2}}}{2(\gamma-1)} \,. \tag{23}$$

This result is a crucial one; it shows that M_o is determined uniquely in terms of the parameters g and D, and in particular, T_{1i}.

The linear growth in the formulas (18), (19) and (21) indicates a breakdown of the above expansion when ζ becomes exponentially large. In order to proceed further, we let

$$\zeta = (\varepsilon/\delta) \, x \tag{24}$$

and recognize that for $x = O(1)$, the diffusive terms in the set (1a-e) become exponentially small when compared with the convective terms. The dominant balance is convective-reactive and the appropriate expansions are

$$T = \epsilon T_1 + \ldots, \quad p = \epsilon p_1 + \ldots, \quad v = \epsilon v_1 + \ldots, \quad Y = 1 + \epsilon Y_1 + \ldots . \quad (25)$$

These expansions, when substituted into (1a-e) and subjected to matching with the solution (18-21), lead to the solution

$$-T_1 = \frac{\beta T_{1\infty}}{g} \, p_1 = T_{1\infty} \, Y_1 = \ln (1-\lambda x), \quad v_1 = T_1 - p_1 \; , \quad (26)$$

where

$$\lambda = \frac{D}{M_o^2} \, T_{1\infty} \; . \quad (27)$$

From (22) we recall that $T_{1\infty}$, and therefore λ, is positive if $0 < M_o^2 < 1/\gamma$ and negative if $1/\gamma < M_o^2 < 1$. Therefore, the above solution becomes singular at $x = 1/\lambda$ for $\lambda > 0$ and at $x = \infty$ for $\lambda < 0$. This singularity is reminiscent of thermal runaway in ignition problems, and is therefore dealt with in much the same way as the explosion analysis employed there [5,6].

Explosion Zone R_E

The new spatial coordinate σ appropriate for this zone is defined by the nonlinear scaling

$$\sigma = -\epsilon \ln (1-\lambda x), \quad \sigma \overset{>}{_<} 0 \text{ for } \lambda \overset{>}{_<} 0, \quad (28)$$

and we seek the expansions

$$T = T_o + \epsilon T_1 + \ldots, \quad p = p_o + \epsilon p_1 + \ldots, \quad v = v_o + \epsilon v_1 + \ldots, \quad Y = Y_o + \epsilon Y_1 + \ldots .$$
$$(29)$$

Substitution into (1a-e) followed by matching with region R_I yields the solution

$$T_o = \sigma, \quad p_o = -\frac{g\sigma}{\beta T_{1\infty}}, \quad v_o = T_o - p_o, \quad Y_o = 1 - \frac{\sigma}{T_{1\infty}} \; . \quad (30)$$

Also, we get

$$T_1 = \sigma^2 - \ln \left(1 - \frac{\sigma}{T_{1\infty}}\right) \tag{31}$$

with similar expressions for p_1, v_1 and Y_1. As $\sigma \to T_{1\infty}$, eqns. (30) show that

$$T_o \to T_{1\infty}, \quad p \to p_{1\infty} \equiv -\frac{g\gamma M_o^2}{1-M_o^2}, \quad v_o \to v_{1\infty} \equiv \frac{g}{1-M_o^2}, \quad Y_1 \to 0 \ ,$$

i.e. the leading terms in the expansions (29) approach the downstream values specified by the Hugoniot conditions. However, (31) shows that T_1 (and similarly, p_1, v_1 and Y_1) is logarithmically singular at $\sigma = T_{1\infty}$. This singularity is smoothed out in the completion zone, discussed below.

Completion Zone R_c

The cases $T_{1\infty} > 0$ and $T_{1\infty} < 0$ need to be treated separately; we shall only consider the former. We employ the transformation

$$\sigma = T_{1\infty} - \epsilon \ln (-\eta/\epsilon)$$

and observe that the new variable $\eta \to -\infty$ as $\epsilon \to 0$, $\sigma < T_{1\infty}$ fixed. Also, we seek the expansions

$$T = T_{1\infty} + \epsilon T_2 + \ldots, \quad p = p_{1\infty} + \epsilon p_2 + \ldots, \quad v = v_{1\infty} + \epsilon v_2 + \ldots, \quad Y = \epsilon Y_2 + \ldots \ .$$

The by-now-familiar procedure yields

$$T_2 = T_{2\infty} + \tau \ ,$$

$$p_2 = \frac{\gamma M_o^2}{\gamma M_o^2 - 1} \left(T_{2\infty} + p_{1\infty} v_{1\infty} + \tau\right) \ ,$$

$$v_2 = \frac{-1}{\gamma M_o^2 - 1} \left(T_{2\infty} + p_{1\infty} v_{1\infty} + \tau\right) \ ,$$

$$Y_2 = -\frac{1}{T_{1\infty}} \tau \ ,$$

where τ is given inplicitly by

$$\int_{-1}^{\tau} \frac{e^{-x}}{x} \, dx = -\frac{1}{T_{1\infty}} e^{-T_{1\infty}^2 + T_{2\infty}} (\eta - \eta_0) \, ,$$

η_0 being an integration constant. It can be shown that as $\eta \to \infty$. $\tau \to 0$ exponentially, so that T_2, p_2, v_2 and Y_2 approach their downstream values.

This completes the analysis of deflagrations away from the lower CJ point. The corresponding profiles for T, p, v and Y are displayed in Fig. 1 (for $M_0^2 < 1/\gamma$) and Fig. 2 (for $M_0^2 > 1/\gamma$) on the (exponentially large) x-scale. The profiles are all monotonic in Fig. 1, and the net temperature change across the wave is positive. The deflagrations displayed in Fig. 2 exhibit a net temperature drop across the wave. The temperature now decreases monotonically, except in the first part of the induction region where it has an exponentially small maximum.

VI. OTHER WAVES. Weak detonations, weak and strong detonations near the upper CJ point, and deflagrations near the lower CJ point can all be analyzed in an analogous manner. We only present the corresponding profiles here, referring the reader to [4] for details. Away from the CJ point, the profiles of a weak detonation are shown in Fig. 3. Our analysis also yields an explicit formula for the weak-deflagration wave speed. Near-CJ weak detonations resemble Fig. 3, except that the wave strength is now $O(\sqrt{\epsilon})$. Similarly, near-CJ deflagrations resemble Fig. 2. Fig. 4 shows the temperature profile of a near-CJ strong detonation. We observe the familiar ZND structure, consisting of an adiabatic shock followed by a fast deflagration.

VII. FINAL REMARKS. A final remark regarding the structure of deflagrations needs to be made. Our analysis is based on the assumption that $M_0 = O(1)$. Then, the deflagrations are not isobaric, and their structure is essentially convective-reactive, as obtained here. By contrast, the reactive-diffusive structure, obtained for example in [2], rests on the assumption the $M_0 \ll 1$, i.e. the waves are essentially isobaric. In our terminology, the wave-speed formula computed in [2] reduces to

$$M_0^2 = \frac{2\epsilon^2 Le}{g^2} D \exp\left[-\frac{E}{1+\epsilon g}\right]. \tag{32}$$

By contrast, our formula (23), in the limit $M_o \to 0$, takes the form

$$M_o^2 = \frac{\varepsilon g}{T_i - 1} D \exp(-E)$$

where T_i is now the actual, dimensionless temperature of the flame holder (rather than an ε perturbation of the upstream temperature). In order to compare the above two results, it is necessary to interpret T_i as the O(1) flame temperature. We then observe that M_o decreases as T_i increases, as it should, and that with $T_i - 1$ taken to be O(1), both (32) and (33) yield the same leading-order result

$$\ln \frac{M_o^2}{D} \sim - E .$$

REFERENCES

1. F. A. Williams, Combustion Theory, Addison Wesley (1965).

2. W. B. Bush and F. E. Fendell, Asymptotic analysis of laminar flame propagation for general Lewis numbers, Comb. Sci. Tech. 1 (1970), pp. 421-428.

3. W. B. Bush and F. E. Fendell, Asymptotic analysis of the structure of a steady planar detonation, Comb. Sci. Tech. 2 (1971), pp. 271-285.

4. A. Kapila, B. J. Matkowsky and A. vanHarten, An asymptotic theory of deflagrations and detonations (1981), to appear.

5. A. Liñán and F. A. Williams, Theory of ignition of a reactive solid by constant energy flux, Comb. Sci. Tech. 3 (1971), pp. 91-98.

6. A. K. Kapila, Dynamics of ignition, SIAM J. Appl. Math. 39 (1980), pp. 21-36.
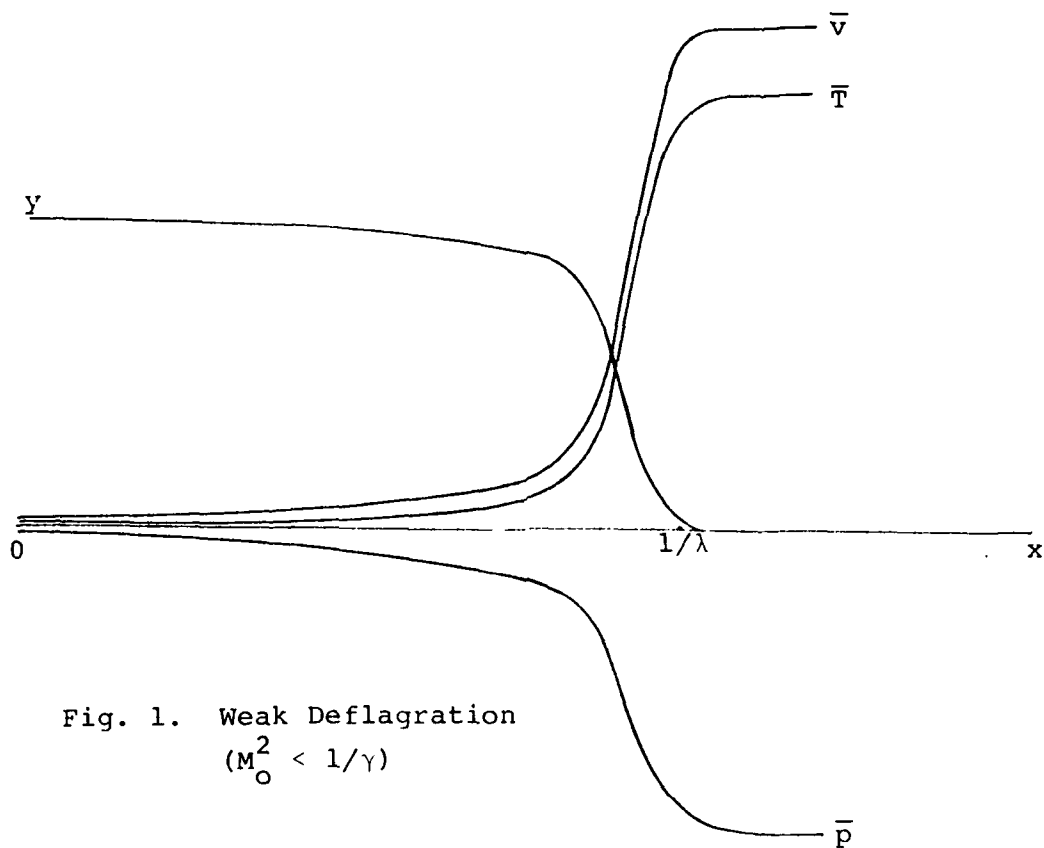
Fig. 1. Weak Deflagration
$(M_o^2 < 1/\gamma)$
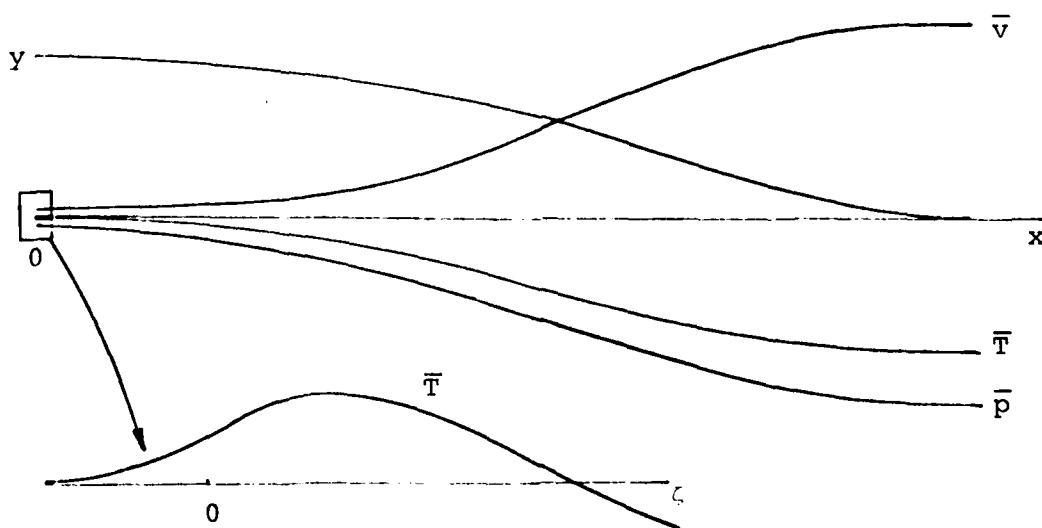
Fig. 2. Weak deflagration
$(M_o^2 > 1/\gamma)$
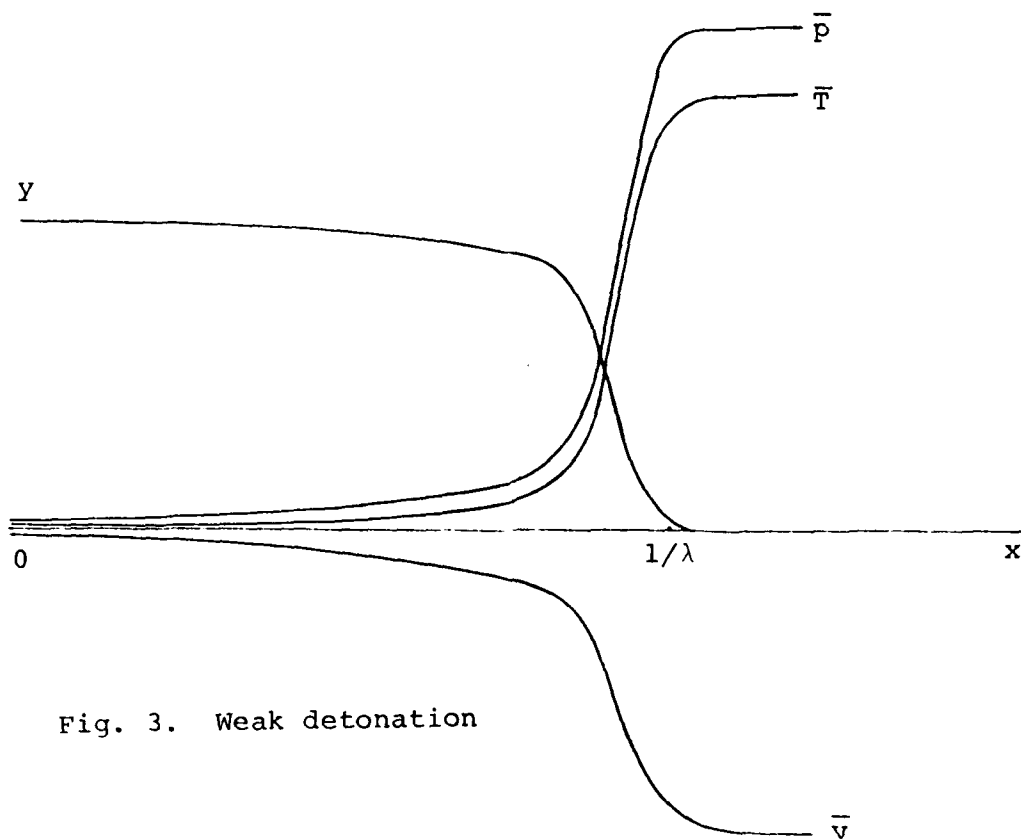
Fig. 3. Weak detonation
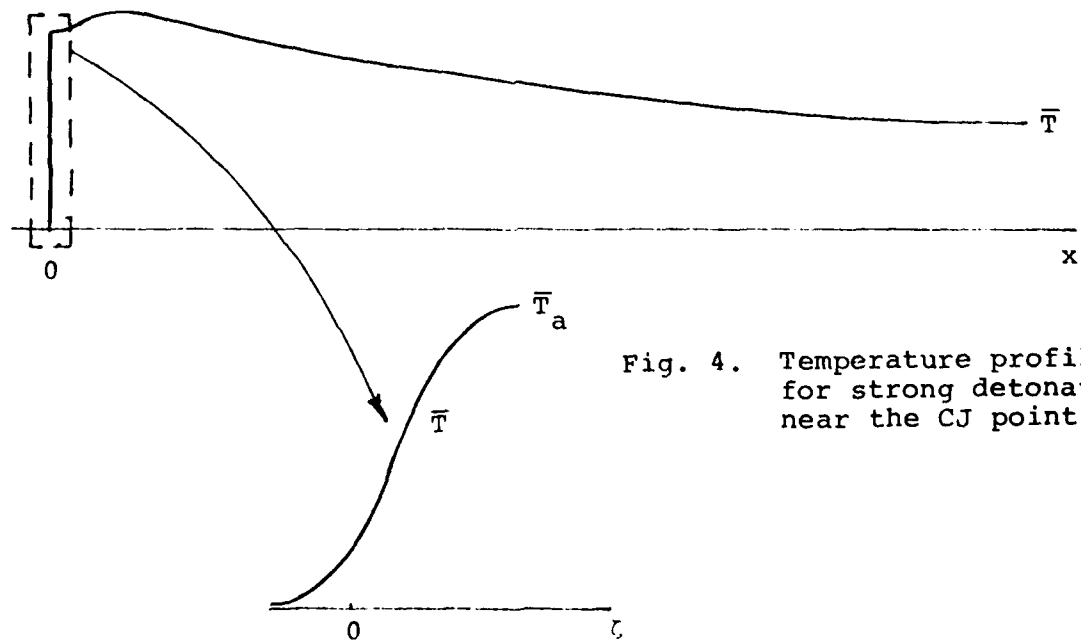
Fig. 4. Temperature profile for strong detonation near the CJ point

COMPARISON TECHNIQUES FOR SOME COMBUSTION MODELS

Jagdish Chandra
U. S. Army Research Office
Research Triangle Park, NC 27709

and

Paul Wm. Davis
Worcester Polytechnic Institute
Worcester, MA 01609

In this paper we present a brief survey of applications of the theory of differential inequalities to several problems arising in combustion theory. A main tool employed is a comparison theorem for systems of nonlinear parabolic differential equations [2]. Another analytical approach which is exploited in a significant way is a constructive procedure for solution of nonlinear initial boundary value problems associated with such systems of partial differential equations. In this "system doubling" technique [5], the solution to the non-linear problem is constructed by a monotone iterative scheme. The iterates in this scheme are obtained by solving a linear system of partial differential equations twice the size of the original problem. The initial iterates are upper and lower solutions (in some appropriate sense) of the original problem and are shown to be bounds themselves on the solutions constructed by the mono-tone iterations.

Both approaches are intuitively appealing because the mathematical arguments have convincing physical parallels. Consider, for example, the consumption of a reactant at dimensionless concentration and temperature $c(x,t)$ and $\theta(x,t)$ respectively:

$$(1) \qquad c_t = k \Lambda c - c^m f(\theta)$$

$$(2) \qquad \sigma \theta_t = \Lambda \theta + \delta c^m f(\theta)$$

$$(3) \qquad \theta(x,t) = o \quad , \quad c_\nu(x,t) = o \quad , \quad x \in \partial\Omega$$

$$(4) \qquad \theta(x,o) = o \quad , \quad c(x,o) = 1 \quad , \quad x \in \Omega.$$

Here k is the material diffusion (inverse Lewis number), $m>o$ the order of the reaction, σ the characteristic thermal diffusion time (Damköhler number), δ the chemical heat release rate (Frank-Kamenetskii parameter), ϵ inverse activation energy, and the Arrhenius kinetics $f(\theta) = \exp(\frac{\theta}{1+\epsilon\theta})$. Λ is the Laplacian opera-tor on the region Ω, containing the reactant and the subscript ν denotes dif-ferentiation normal to the boundary $\partial\Omega$ of Ω.

Consuming reactant at the zero temperature rate should yield upper bounds on both reactant concentration and temperature (because excess reactant is available). Indeed, it is shown in [3] that any solution $(\bar{c},\bar{\theta})$ of

$$(5) \qquad \bar{c}_t \geq k\Delta\bar{c} - \bar{c}^m$$

$$(6) \qquad \sigma\bar{\theta}_t \geq k\Delta\bar{\theta} + \delta\bar{c}^m f(\bar{\theta})$$

$$(7) \qquad \bar{\theta}(x,t) \geq o \quad , \quad \bar{c}_\nu(x,t) \geq o \quad , \quad x \in \partial\Omega$$

$$(8) \qquad \bar{\theta}(x,o) \geq o \quad , \quad \bar{c}(x,o) \geq 1 \quad , \quad x \in \Omega$$

is an upper bound on the exact solution (c,θ) of (1)-(4). For example, we obtain rigorously from one such solution of (5)-(8) that

$$\theta(x,t) \leq (\delta/o)e^{1/\varepsilon}$$

(Finite activation energy guarantees finite maximum temperature.)

Further application of the comparison ideas of [2] also show relationships among important parameters in the complete model (1)-(4), the Semenov approximation (no spatial dependence; k=o in (1), $\Delta\theta$ replaced by $-\theta(t)$ in (2) and (3) eliminated), and the Frank-Kamenetskii approximation (stationary approximation given by $o = \Delta\theta + \delta f(\theta)$, $\theta(x) = o$ on $\partial\Omega$ and neglect the consumption of the reactant). The temperatures and (reasonably defined) critical values of the heat release parameter δ are ordered from smallest to largest as: Frank-Kameneskii approximation at infinite activation energy ($\varepsilon=o$, the classical F-K value δ_{crit}), Frank-Kameneskii approximation at finite activation energy,

the complete model (1)-(4). In particular cases, these relations have been observed previously in numerical and asymptotic calculations. The infinite activation energy induction times of both the complete model (1)-(4) and the Semenov approximation are bounded below by the adiabatic induction time σ/δ.

One may also obtain decay rates and global, nonlinear stability estimates [4]. To illustrate the results obtained in [4] , consider, for the sake of simplicity, m=1. We then have

$$o \leq c(x,t) \leq e^{-t}$$

$$o \leq \theta(x,t) \leq \phi(x)e^{-\beta t/\sigma},$$

where $o < \beta < \min(\sigma,\mu_1)$, μ_1 is the smallest eigenvalue of the Laplacian on Ω subject to the temperature boundary condition, and ϕ solves

$$\Delta\phi + \beta\phi = -\delta f(\infty)$$

subject to the temperature boundary condition as well. These bounds illustrate the interaction between thermal diffusion and reactant vessel geometry through the ratio β/σ as well as the global asymptotic stability of the burned state c=o, $\theta=o$ without unnecessary restrictions on parameters like δ [1]. Other

bounds in [4] show the role of the order of reaction, for example, reactant is consumed in finite time when $0<m<1$.

Finally, some work in progress indicates that the "system doubling" technique introduced in [5] may be coupled with multi-scale asymptotic methods to provide rigorous analyses of certain oscillatory flame phenomena. For example, an isothermal, autocatalytic scheme with a long history [6,7,9],

$$\text{external diffusion} \longrightarrow A$$
$$A + X \xrightarrow{k_1} B + 2X$$
$$X + Y \xrightarrow{k_2} B + 2Y$$
$$A + Y \xrightarrow{k_3} B$$
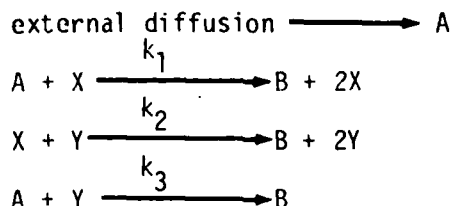
exhibits oscillations in the intermediates X and Y. Here A is the initial reactant, B is the final product and k_i, $i=1,2,3$ are the reaction rate constants. One choice of scales yields the model

$$(9) \qquad a'(t) = -\epsilon (x+y)a + \epsilon n(1-a)$$

$$(10) \qquad x'(t) = k(a-y)x$$

$$(11) \qquad y'(t) = k^{-1}(x-a)y, \qquad ' = \frac{d}{dt}$$

where $\epsilon = \sqrt{k_1 k_2}\,/k_2 << 1$, $k = (k_1/k_3)^{1/2}=O(1)$ and the diffusion parameter $n=O(1)$.

An asymptotic analysis of equations (9)-(11) shows a,x,y decaying to steady-state values determined by n at $O(1)$ and oscillations in x, y at $O(\epsilon)$. The frequency of these oscillations increases as a decreases to its $O(1)$ steady-state value; the x and y oscillations are 90° out of phase (with y leading) with mean values and amplitudes determined by k and the value of a to $O(\epsilon)$. Oscillation in a appear at $O(\epsilon^2)$; their phase and amplitude relative to those of x and y are determined solely by k.

Preliminary calculations suggest that the equations defining the terms in the asymptotic expansions for a, x, and y which are obtained from the usual solvability conditions of the multi-scale formalisms, can be recast as a "doubled system" to provide the necessary bounds that rigorously confirm the asymptotic character of the formal series. What is more interesting is that these ideas appear to be equally well suited for treatng a class of physically more significant thermokinetic models associated with hydrocarbon autoignition [8]. These results will be presented elsewhere.

REFERENCES

(1) Amman, H., Existence and Stability of Solutions for Semilinear Parabolic Systems and Applications to Some Diffusion-Reaction Equations, Proc. Roy. Soc. (Edin.), 81A, 35-47, (1978).

(2) Chandra, J. and Davis, P., Comparison Theorems for Systems of Reaction-Diffusion Equations, Applied Nonlinear Analysis, V. Lakshmikantham (Ed.), Academic Press, N. Y., 79-27, (1979).

(3) _____, Rigorous Bounds and Relations Among Spatial and Temporal Approximations in the Theory of Combustion, Comb. Sci. Tech., 23, 153-162, (1980).

(4) _____, Stability of the Burned State in a Combustion Model (submitted for publication).

(5) Chandra, J., Dressel, F., and Norman, P., A Monotone Method for a System of Nonlinear Parabolic Differential Equations, Proc. Roy. Soc. (Edin) 87A, 209-217, (1981).

(6) Frank-Kamenetskii, D. Zh. Fiz.Khim., 14 30-35, (1940).

(7) Gray, B. and Aarons, L., Small Parasitic Parameters and Chemical Oscillations, Chemical Oscillations, Faraday Soc., 129-136 (1974).

(8) Halstead, M., Kirsch, L., Prothero, A., and Quinn, C., A Mathematical Model for Hydrocarbon Autoignition at High Pressures, Proc. Roy. Soc. Lond, A, 346, 515-538 (1975).

(9) Lotka, A., Undamped Oscillations Derived from the Law of Mass Action, J. Amer. Chem. Soc., 42, 1595-1599 (1920).

A GENERALIZED BURGERS EQUATION FOR PLANE WAVES
IN A COMBUSTIBLE ATMOSPHERE

J. F. Clarke

Aerodynamics, Cranfield Institute of Technology
Bedford, MK43 OAL, England

ABSTRACT.   When small amplitude plane waves propogate through an ambient combustible atmosphere that is undergoing a spatially homogeneous adiabatic thermal-explosive event their first-order behaviour is shown to be governed for early times by a Burgers equation with some additional terms. These terms specifically describe effects due to atmospheric heating and, most significantly, to perturbation of the Arrhenius chemical reaction rate factor. This latter influence is responsible for amplification of the wave system. Some approximate analytical solutions are found for two cases: (i) it is shown how this phenomenon interacts with both classical acoustic damping due to diffusion and modulations due to progressive ambient heating in acoustic-amplitude signals: (ii) for larger amplitude signals the fitting of discontinuous frozen shock waves by a modulated equal areas rule allows for the assessment of non-linear wave behaviour in the presence of chemical amplification.

Finally it is shown that when chemical amplification rates become large the wave system becomes dispersive in character, is still amplified, and almost certainly propagates signals in both spatial directions. The general situation described in the paper is relevant to studies of deflagration-to-detonation-wave transition.

1.   INTRODUCTION.   Burgers equation was originally constructed to display in the most direct possible way the balance between non-linear convection and diffusion in plane wave systems in certain types of atmosphere. Subsequently Lighthill (1956) showed that its utility as a model equation is strongly reinforced by the fact of its proving to be a proper first approximation in a scheme of rational approximations for problems of plane wave evolution.

The transition from deflagration to detonation in combustible mixtures must involve strong coupling between gas dynamics and exothermic chemical processes and it is therefore interesting to enquire if there is not some equation that, in the spirit of the original Burgers equation, incorporates all of the simplest elements of the crucial physical processes in such a way as to reveal the essence of their interactions in some well set, first-order fashion.

It will be assumed that the ambient atmosphere is spatially uniform and undergoing a single n-th order irreversible combustion reaction with Arrhenius activation-energy kinetics. This atmopsphere's flow velocity is uniformly equal to zero and its density is therefore fixed at the constant value ρ_i In view of the ambient chemical activity and the usually large values of activation energy the atmosphere will be undergoing a self-heating process that will be initially slow but which will, after an induction time interval t_i, run away into a rapid explosive event that raises the initial ambient pressure, p_{oi} asymptotically close to a final value p_{om} in a very brief interval of time. The mass fraction of the ambient reactant material will diminish from its initial value of q_{oi}. the value of $q_o(t)$ when $t = o$, towards zero; i.e. the reactant is ultimately all consumed.

The adiabatic thermal-explosive event that has just been described is now presumed to be spatially perturbed by the movement of a piston, beginning at time $t = 0$ from its initial position at $x = 0$. There will be a value $a_{fo}(t)$ of the sound speed in the ambient atmosphere that changes with time as the ambient-explosive events proceed. The subscript f denotes the important fact that it is the *frozen* sound speed (e.g. Clarke & McChesney, 1976) that is required here. The disturbances produced by movement of the piston will not only create velocities $u = u(x,t)$ in the gas itself but will also perturb a_{fo} so that its local value becomes $a_f = a_f(x,t)$. The characteristic curves in the x,t plane for a set of "diffusion-free" and hence first-order conservation equations are well known to be given by

$$\frac{\partial x}{\partial t} = u \pm a_f \quad .$$

In particular, those undiffused wavelets that propagate in the direction of x-positive will be labelled with the parameter β, whose precise definition can await subsequent developments. For the present it is sufficient to note that

$$\left(\frac{\partial x}{\partial t}\right)_\beta = u + a_f \quad . \qquad \qquad 1.$$

It is advantageous to non-dimensionalise the system of conservation and other equations, using ρ_i, $\rho_i a_{foi}^2$, a_{foi} and q_{oi} as measures of densities, pressures, velocities and mass-fractions, respectively; t_i is the natural scale for the time and $a_{fo} \cdot t_i$ performs the same service for distance. If the activation energy parameter ϵ is defined so that

$$\epsilon = P_{oi}/\rho_i E_A \quad . \qquad \qquad 2.$$

where E_A is the Arrhenius activation energy, the induction time t_i can be written in the form

$$t_i = \epsilon \left(e^{1/\epsilon}\right)\left\{nWpq_{oi}^{n-1}\left[(p_{om}/p_{oi}) - 1\right]\right\} \quad . \qquad \qquad 3.$$

where W is the molecular weight of the reactant and p is the pre-exponential factor (with dimensions of reciprocal time).

For various reasons it is slightly more convenient to use γt_i, where γ is the ratio of the *frozen* specific heats of the gas mixture, rather than t_i itself (note that γ is assumed constant) in the non-dimensionalisations described above. All of the diffusive, that is to say, viscous, heat-conduction and mass-diffusion, terms in the set of dimensionless conservation equations now appear with $1/Re$ as a multiplier, where Re is a Reynolds number, defined by

$$Re = \gamma t_i a_{foi}^2 \rho_i / \frac{4}{3} \eta_i \quad . \qquad \qquad 4.$$

552

where η_i is the initial ambient value of the dynamic viscosity coefficient. The group of terms $\frac{4}{3}\eta_i / \gamma \rho_i a_{foi}^2$ that appears in (4) is roughly of the order of the mean molecular collision interval. It is a fair estimate for simple reactions to say that this time is comparable with p^{-1}, the reciprocal of the pre-exponential factor, whence a guide to the size of Re is provided by the relation

$$Re \approx t_i p = \epsilon(e^{1/\epsilon}) / \left\{ W[(p_{om}/p_{oi}) - 1] \right\} \quad .$$

5.

The last result in (5) follows from (3) and the decision to examine only the first-order reaction case, $n = 1$. Table 1 gives some typical values of the quantities Re and t_i for three ϵ values; the numbers in parentheses give the appropriate power of 10

Table 1

$1/\epsilon$	25	30	35
Re	2.4(7)	3.0(9)	3.8(11)
t_i, sec	2.4(-2)	3.0(0)	3.8(2)

by which to multiply the number that precedes them.

The piston speed is given in the form

$$\bar{u}_p = \sigma D'(T/\sigma) \quad .$$

6.

so that the boundary condition is

$$\bar{u}(\sigma^2 D(T/\sigma), T) = \sigma D'(T/\sigma) \quad ,$$

7.

where D is the piston displacement function and D' is its derivative, the piston speed function. T is the dimensionless time, $\bar{u}$ is the dimensionless gas velocity ($\bar{u} = \bar{u}(\bar{x}, T)$ in general) and σ is an amplitude and "frequency" parameter. It will subsequently be supposed that

$$\sigma \ll 1 \quad .$$

8.

It is useful to define a dimensionless wavelet-like coordinate ξ as follows:

$$\sigma \xi = T - \bar{x} \quad .$$

9.

Equations (1) & (9) translate into

$$\sigma \left(\frac{\partial \xi}{\partial T} \right)_\beta = 1 - \bar{u} - \bar{a}_{fo} - \bar{a}_r = -\sigma \beta_T \xi_\beta \quad ;$$

10.

553

where $\tilde{a}_1$ is the dimensionless perturbation to the dimensionless ambient frozen sound speed. Note that

$$\beta_\xi \equiv \left(\frac{\partial \beta}{\partial \xi}\right)_T \quad , \quad \beta_T \equiv \left(\frac{\partial \beta}{\partial T}\right)_\xi \quad .$$

The derivative ξ_β can usefully be chosen to be of order unity, at least in the neighbourhood of the piston face. Indeed, integration of (10) followed by the decision to make

$$\beta = T/\sigma \quad \text{when} \quad \bar{x} = \sigma^2 \, D(T/\sigma) \tag{11a.}$$

gives

$$\sigma(\xi - \beta + \sigma D(\beta)) = \int_{\sigma\beta}^{1} [1 - u' - \tilde{a}_{fo}(\tilde{T}) - \tilde{a}'_f] \, \partial\tilde{T} \quad , \tag{11b.}$$

where $\bar{u}'$, $\tilde{a}'_f$ are functions of β and $\tilde{T}$ and the integration is taken at fixed β. Then

$$\xi_\beta = \tilde{a}_{fo}(\sigma\beta) + \tilde{a}_f(\beta,\sigma\beta) - \frac{1}{\sigma} \int_{\sigma\beta}^{1} [\tilde{a}'_{f\beta} + \bar{u}'_\beta] \, \partial\tilde{T} \quad . \tag{12.}$$

On the piston face the integral vanishes; it will be presumed that β-derivatives of $\tilde{a}_f$ and $\bar{u}$ are well behaved and $O(\sigma)$; then ξ_β is indeed of order unity there, because $\tilde{a}_{fo}$ is of this order and the perturbation $\tilde{a}_f$ is small in view of (8). Note that ξ_β *may* vanish locally when the integral in (12) is positive and $O(\sigma)$.

2.   **PERTURBATION EQUATIONS.**   If all of the appropriate dimensionless conservation equations, *including* proper account of the diffusive effects, are *transformed into versions* which have β & T as the independent variables one can now propose the asymptotic developments

$$\bar{\psi} \sim \sigma \psi^{(1)}(\beta,T) \quad , \quad \psi = u, p, \rho, a_1 \tag{13.}$$

$$\bar{q} \sim \sigma^2 q^{(1)}(\beta,T) \tag{14.}$$

in the limit as $\sigma \to o$ with β,T fixed. Note that $\bar{q}$ is the dimensionless perturbation to the ambient dimensionless reactant mass fraction $\bar{q}_0$. The system of equations contains other parameters than σ, of course, notably ϵ and Re, as well as local dependent variable factors such as ξ_β and $\bar{p}_{0T}$. The complete problem is quite complicated; fuller details, as well as discussion of several items outside the scope of the present paper, have been given by Clarke (1981). For the present it is adequate to observe that, on the general supposition that ξ_β and $\epsilon^{-1} \bar{p}_{0T}$ do not behave in an extreme way (the meaning of "extreme" will shortly become clear) the proposed limit leads to the following equations for $p^{(1)}$, $\rho^{(1)}$, $q^{(1)}$ and $u^{(1)}$, *provided* that

$$\sigma/\epsilon = o(1) : \tag{15.}$$

554

$$p^{(1)} = \bar{a}_{fo}^2 \, \rho^{(1)} = \bar{a}_{fo} \, u^{(1)} \quad ; \tag{16a,b.}$$

$$q_\beta^{(1)} = -\ [(\gamma - 1)\xi_\beta / \bar{Q}\bar{a}_{fo}^4] \frac{1}{\epsilon} P_{oT} \ u^{(1)} \quad . \tag{17a.}$$

where
$$\gamma\bar{Q} = [(p_{oni}/p_{oi}) - 1] \quad ; \tag{17b.}$$

$$u_T^{(1)} = \left\{ A(T) - \frac{1}{2} \bar{a}_{fo}^{-1} \bar{a}_{foT} \right\} u^{(1)} + (\delta_o/2\sigma^2 \, \mathrm{Re}\,\xi_\beta)(u_\beta^{(1)}/\xi_\beta)_\beta \quad . \tag{18.}$$

where
$$\delta_o = \bar{\eta}_o + \frac{(\gamma-1)}{\mathrm{Pr}} \bar{\lambda}_o \quad . \tag{19.}$$

and $\bar{\eta}_o$, $\bar{\lambda}_o$ are the dimensionless dynamic viscosity and thermal conductivity in the ambient atmosphere: Pr is the Prandtl number,

$$\mathrm{Pr} = \frac{4}{3} \eta_i \, C_{pf} / \lambda_i \tag{20.}$$

and C_{pf} is the frozen specific heat at constant pressure (assumed constant here). Also

$$A(T) \equiv \frac{1}{2} \left[(\gamma-1)\bar{a}_{fo}^{-4} + \epsilon\bar{a}_{fo}^{-2} \right] \frac{1}{\epsilon} P_{oT} > 0 \quad . \tag{21.}$$

Note that in the ambient atmosphere

$$\frac{1}{\epsilon} P_{oT} = \exp\{\frac{1}{\epsilon}(1 - \frac{1}{\gamma \bar{p}_o})\} \bar{q}_o^n \quad . \tag{22.}$$

Thus $A(T)$ at least *begins* from the value unity at time $T = o$, since it is necessary to have

$$\gamma\bar{p}_o(o) = 1 \quad ; \quad \bar{q}_o(o) = 1 \quad . \tag{23.}$$

Observing that δ_o is the classical diffusivity of sound it is also important to note the role of the scale factor ξ_β in the last, diffusive, term in (18). Since, as remarked at the end of the Introduction, ξ_β can become small as time progresses it is clear that the diffusive effects *may* become large for *any* values of the product $\sigma^2 \mathrm{Re}$. The vanishing, or near-vanishing, of ξ_β is a purely local effect that is associated with the existence of shock waves and it will be convenient to deal with this behaviour in a particular approximate way, as will be outlined below in Section 4.

Meanwhile, it is evident that when σ^2 is small enough to make $\sigma^2 \mathrm{Re}$ of order unity, the diffusive terms must be retained in (18) under all circumstances. In terms of the coordinate Ξ, defined by

$$\sigma\Xi = \sigma\xi + \int_o^T \bar{a}_{fo}(\widetilde{T})d\widetilde{T} - T = \int_o^T \bar{a}_{fo}(\widetilde{T})d\widetilde{T} - x \quad , \tag{24.}$$

and signifying by its value the location of any purely acoustic (zero-amplitude) wavelet in the time-dependent ambient atmosphere, (18) can be written in the form

$$u_T^{(1)} - \frac{1}{2}(\gamma+1)u^{(1)}u_\Xi^{(1)} = \left\{ A(T) - \frac{1}{2}(\ln \bar{a}_{fo})_T \right\} u^{(1)} + \Delta(T)u_{\Xi\Xi}^{(1)} \quad , \qquad 25.$$

where

$$\Delta(T) \equiv \frac{1}{2}\, \delta_o \big/ \sigma^2 Re \quad . \qquad 26.$$

and $u_T^{(1)}$ in (25) signifies the derivative taken at fixed Ξ, as opposed to fixed β in (18).

Equation (25) is the augmented version of Burgers equation that we have been seeking, albeit under the strict observance of the ordering in (15). When the ambient atmosphere is chemically inert the coefficient of $u^{(1)}$ vanishes and $\Delta(T)$ becomes a constant; the result is the original Burgers equation. The existence of chemical activity in the atmosphere introduces the term in $u^{(1)}$ which, via its dependence on $A(T)$, displays the direct significance of perturbation of the (Arrhenius) chemical rate, as well the effect of atmospheric heating through the term $-\frac{1}{2}(\ln \bar{a}_{fo})_T$.

Unlike the original Burgers equation, (25) does not seem to have a linearising, Cole-Hopf type of transformation. Some approximate analytical solutions will be sought in the sections to follow that provide reasonably compact illustrations of the physical processes that the equation describes. The case $\epsilon = O(\sigma)$ has been examined by both Blythe (1978) and Clarke (1978, 1979, 1981) but will not be dealt with here.

3.   ACOUSTIC WAVES.   With the assumption that the amplitude of the input from the piston is small by an amount *additional* to the $O(\sigma)$ scale required by (6) it is possible to linearise (25). For example, if one makes

$$D'(T/\sigma) = M \exp(iwT/\sigma) \qquad 27.$$

where M is a constant such that

$$M \ll 1 \quad , \qquad 28.$$

equation (25) can be approximated by

$$\dot{u}_T^{(1)} + \bar{a}_{fo}(T)\dot{u}_{\bar{x}}^{(1)} = A(T)\dot{u}^{(1)} + \sigma^2 \Delta(T)\dot{u}_{xx}^{(1)} \; ; \; u^{(1)} = \bar{a}_{fo}^{1/2} u^{(1)} \quad . \qquad 29.$$

That is to say the non-linear term in (25) is formally banished by replacing the original $\sigma \to o$ limit by $\sigma \to o$ *and* $M \to o$ together. Note that (29) is now written in terms of differentiations at fixed $\bar{x}$ and fixed T, which are not individually $O(1)$ operations. It is not hard to see that they are in fact $O(\sigma^{-1})$ operations whence, recognising this and defining a pair of 'fast' variables T_f, x_f via

$$\sigma T_f = 1 \quad , \quad \sigma x_f = \bar{x} \qquad \qquad 30.$$

equation (29) becomes

$$\left\{ \dot{u}^{(1)}_{T_f} + \bar{a}_{fo}(T)\dot{u}^{(1)}_{x_f} \right\} = \sigma \left\{ A(T)\dot{u}^{(1)} + \Delta \dot{u}^{(1)}_{x_f x_f} \right\} \quad . \qquad 31.$$

where the terms in $\{\ \}$ brackets are now $O(1)$ in the limits $\sigma \to o$, $M \to o$. It is now sensible to propose a solution of (31) in the form

$$\dot{u}^{(1)} \sim \exp\left\{ \frac{i}{\sigma} \Theta(\bar{x},T) \right\} \sum_{n=o}^{} \sigma^n A_n(\bar{x},T) \qquad 32.$$

that will be valid away from the wavehead at $\bar{x} = 1$. The amplitude and phase functions, A_n and Θ, depend upon the 'slow' variables $\bar{x}$, T and allow for the *initially slow* changes due to self-heating that take place in the adiabatic thermal-explosive atmosphere. Substitution of (32) into (29) shows that A_o and A_1 must satisfy the equations

$$\sigma^o : i\left\{ \Theta_T + \bar{a}_{fo}(T)\Theta_{\bar{x}} \right\} A_o = 0 \quad : \qquad 33.$$

$$\sigma^1 : i\left\{ \Theta_T + \bar{a}_{fo}(T)\Theta_{\bar{x}} \right\} A_1 + A_{oT} + \bar{a}_{fo}(1)A_{o\bar{x}}$$

$$= \left\{ A(T) - \Theta^2_{\bar{x}} \Delta(T) \right\} A_o \quad . \qquad 34.$$

It follows after a few manipulations that a good approximation for $u^{(1)}$ suitably far behind the wavehead (e.g. $\bar{x} \leqslant 1 - O(\sigma)$) is

$$u^{(1)} \sim M\left[\bar{a}_{fo}(\phi) \big/ \bar{a}_{fo}(T) \right]^{1/2} \exp\left\{ iw\phi/\sigma \right\} \quad .$$

$$. \exp\left\{ \int_\phi^T A(\widetilde{T})d\widetilde{T} - \left[w\big/\bar{a}_{fo}(\phi) \right]^2 \int_\phi^1 \Delta(\widetilde{T})d\widetilde{T} \right\} \quad , \qquad 35.$$

where ϕ is defined by

$$\bar{x} = \int_\phi^T \bar{a}_{fo}(\widetilde{1})d\widetilde{1} \quad . \qquad 36.$$

Furthermore the phase Θ must be given by $w\phi$ whence the local wavenumber k and local frequency $\widetilde{w}$ are given by

$$-\Theta_{\bar{x}} = w\big/\bar{a}_{fo}(\phi) \qquad \equiv k \quad , \qquad 37.$$

$$\Theta_T \sim w \ddot{a}_{fo}(T)/\ddot{a}_{fo}(\phi) \sim \tilde{w} \quad , \qquad\qquad 38.$$

respectively.

For the given harmonic, constant amplitude, input from the piston at $\bar{x} = 0$ the consequent situation is now clear. The self-heating of the ambient explosive atmosphere makes $\ddot{a}_{fo}(T) \geqslant \ddot{a}_{fo}(\phi)$, since $\phi \leqslant T$, and there is a small amplitude reduction of $u^{(1)}$ as a result (see the [ ] bracket term in (35); note from (16a,b) that $p^{(1)}$ has a related term $[\ddot{a}_{fo}(\phi)\ddot{a}_{fo}(T)]^{1/2}$ and $\rho^{(1)}$ a term $[\ddot{a}_{fo}(\phi)/\ddot{a}_{fo}^3(T)]^{1/2}$). The lines of constant phase on an $\bar{x} - T$ diagram follow paths dictated by the time-varying ambient sound speed $\ddot{a}_{fo}(T)$, since $(\partial \bar{x}/\partial T)_\phi$ has this value (see (36)). The diffusive effects lead to the classical type of amplitude reduction, that goes like $\exp(-k^2 \dot{x})$ where k^2 is defined in (37) and $\dot{x}$ is a weighted average distance, as can be seen from the last term in (35) together with (36). Finally there is the chemically-induced term, involving the function $A(T)$ (see (35) and (21)), which leads to an *amplification* of the input disturbance. It can be shown that this term may easily overwhelm the diffusive damping *and* the atmospheric heating effect, so that the whole disturbance grows with distance from the input piston at least for sufficiently small local wavenumbers or, more crudely, values of w. The local wavenumber k decreases from one wavelet to another (see (37)) but remains fixed on a given wavelet, while the local frequency $\tilde{w}$ also changes with time (see (38)). These results should be compared with those found by Toong and his co-workers. The most recent of their papers is by Abouseiff & Toong (1981) and contains references to numerous earlier works; briefly, the amplification effect is broadly confirmed, partly through a rather different theory that postulates k = constant at the outset and looks for growth or decay of wave amplitude with time and partly, and most importantly, by a series of ingenious experiments in a reacting mixture of hydrogen and chlorine that is very like the theoretical model considered here.

4. **NONLINEAR SMALL DISTURBANCES.** When σ^2 is large enough to make $\sigma^2 Re \to \infty$ in the limit as $\sigma \to 0$ the diffusive terms in (18) become negligible away from regions where ξ_β is small. The latter condition only occurs in association with the appearance of shock waves and one can allow for the latter in a satisfactory approximate way by fitting an appropriate frozen (i.e. fixed $\bar{q}$) Rankine-Hugoniot shock wave into the field, as will be described below. The solution of (18) minus its diffusive terms is

$$u^{(1)} = g(\beta) f(T) \quad , \qquad\qquad 39.$$

where

$$g(\beta) = D'(\beta)/f(\sigma\beta) \quad , \qquad\qquad 40.$$

$$f(T) \equiv \ddot{a}_{fo}^{-1/2}(T)\exp\left\{ \int_0^T A(\tilde{T})d\tilde{T} \right\} \quad . \qquad\qquad 41.$$

the solution (39) – (41) satisfies condition (6), since β is equal to $1/\sigma$ on the piston path. It then also follows from (9) & (11b) that

$$x \quad B(\beta) + \int_0^1 \ddot{a}_{fo}(s)\,ds + \tfrac{1}{2}\sigma(\gamma + 1)g(\beta)\int_0^1 f(s)\,ds \qquad\qquad 42.$$

where

$$B(\beta) \equiv \int_0^{\sigma\beta} \ddot{a}_{fo}(s)\,ds + \tfrac{1}{2}\sigma(\gamma + 1)g(\beta)\int_0^{\sigma\beta} f(s)\,ds - \sigma^2 \, l X(\beta) \quad . \qquad\qquad 43.$$

and these last two formulae give the proper first estimate of the fixed $-\beta$ wavelet shape on the $\bar{x}, \tau$ plane.

Any fixed $-\bar{q}$ shock discontinuities that may be required to make the field described by (39) (43) single-valued in $\bar{x}, \tau$ space will be weak and therefore will bisect the angle between any pair of fixed β wavelets that meet on the shock path $\dot{x} = \bar{x}_s(T)$. If $\beta_{1,2}$ are the relevant values of β ahead of, and downstream of, the shock respectively the bisection condition can be written as

$$(\dot{\bar{x}}_s - \bar{x}_1)_{\beta = \beta_1} + (\dot{\bar{x}}_s - \bar{x}_\tau)_{\beta = \beta_2} = 0 \quad , \qquad\qquad 44.$$

where $\dot{\bar{x}}_s$ is the time derivative of $\bar{x}_s$ and $\bar{x}_\tau$ is found from (42) with β fixed (at either β_1 or β_2 of course). Substitution of (42) into (44) leads to a relationship between $\beta_1(T)$ and $\beta_2(T)$ that can be integrated to give

$$[B(\beta_2) \quad B(\beta_1)] \, [g(\beta_2) + g(\beta_1)]$$

$$= 2 \int_{\beta_1}^{\beta_2} g(s) B'(s)\,ds \quad , \qquad\qquad 45.$$

which is an "equal areas" rule (e.g. Whitham, 1974 Section 2·8) modulated to take account of the fact that the piston launches disturbances into an atmosphere whose character is changing steadily with time. It is proper to neglect the last two, $O(\sigma^2)$, terms on the right hand side of (43) in general. When the atmosphere is inert, $\bar{a}_{fo} = 1$, $A = 0$ and $f = 1$; then $B(\beta) = \sigma\beta$, $g(\beta) = D'(\beta)$ and (45) reduces to the classical equal areas rule. The same is approximately true if the piston launches, say, a single *short* pulse of disturbance into the explosive atmosphere; e.g.

$$D'(\beta) = M \sin w \beta \quad ; \quad 0 \leqslant \beta - \pi/w \quad ; \qquad\qquad 46.$$

$$= 0 \quad ; \quad \beta < 0 \, , \, \pi/w < \beta \, .$$

where M and w are both $O(1)$ quantities now. The shock strength in terms of the value of $u^{(1)}$ downstream of the wave, namely $u_2^{(1)}$, can be shown to be given by

$$u_2^{(1)} = u^{(1)}(\beta_2(T), T)$$

$$= M f(T) \left\{ 1 - 2(\tfrac{1}{2}(\gamma + 1) M w \int_0^T f(s)\,ds)^{-1}]^2 \right\}^{1/2} \quad . \qquad\qquad 47.$$

(Remember that $u^{(1)}(\beta_1(1), 1) = 0$ by virtue of (46).) Since $f(1)$ exceeds unity for $T > 0$ in the explosive atmosphere the shock forms at the leading edge of the pulse slightly earlier than the classical inert atmosphere formation time of (see (47))

$$T_{sh} = 2/(\gamma + 1)Mw \quad .$$

48.

If the pulse duration in real time is very short compared with $\sigma M \pi_1$, then a shock *will* form before the ambient explosive event takes place.

The existence of the term $f(T)$ in the numerator in (47) is significant and points directly to the strong amplification of the shock that can arise from perturbation of the ambient reaction rate. The direct sensitivity of $f(T)$ to activation energy is evident through (21), (22) and (41): the larger the value of E_A the smaller is the value of ϵ and the larger is the value of $A(T)$ in general. Other illustrations of the present and related results have been given by the writer (Clarke, 1978, 1979; also 1981 for more details of the present analysis).

The results of this and the previous Section make it clear that small disturbances of acoustic or greater amplitudes will, in a general way, be at least sustained by their influence on the ambient reaction rate and, more probably than not, will actually grow significantly in amplitude, at least during the early stages of ambient exothermic activity. For times closer to ambient thermal runaway than those implicit in the decision to treat $A(T)$, or equivalently, $\bar{p}_{oT}/\epsilon$ as $O(1)$ in the $\sigma \to o$ limit (see Section 2, prior to (15)) the analysis must be modified, as shown in the next Section.

5.   THE BREAKDOWN OF UNIDIRECTIONAL PROPAGATION.   Still under the general requirement that σ/ϵ is $o(1)$ it is evident (from (39) - (41), for example, for the larger amplitude waves) that $(\partial u^{(1)}/\partial 1)_\beta$ will cease to be $O(1)$ when $A(T)$ moves out of this order class. Breakdown of the asymptotic scheme for the estimation of $u^{(1)}$ occurs only through this fact, since it can easily be shown that $(\partial u^{(1)}/\partial \beta)1$ will not behave in the same way.

Details of the necessary revisions of the theory are rather lengthy, and will not be fully described here. Suffice it to say that one must now use

$$u \sim \sigma u_e^{(1)}(\tau, \beta) \quad .$$

49.

together with

$$\bar{p} \sim \sigma p_e^{(1)} \; ; \; \bar{\rho} \sim \sigma \rho_e^{(1)} \; ; \; \bar{q} \sim \sigma q_e^{(1)}$$

50a, b, c

(all functions with a subscript $-e$ are functions of τ and β), where τ is a new time variable, namely

$$\sigma \tau = T - T_h \quad ,$$

51.

and T_b is a fixed time defined in the following way. Writing

$$\bar{B} \equiv 1 - 1/\gamma\bar{p}_o \qquad 52.$$

the factor $A(T)$ can be expressed in the form (see (21) and (22) and drop the term proportional to $\epsilon\bar{a}_{fo}^{-2}$)

$$A(T) = \tfrac{1}{2}(\gamma - 1)(1 - \bar{B})^2 \bar{q}_o^n \exp\{\bar{B}/\epsilon\} \quad . \qquad 53.$$

Then, with

$$\bar{B} = -\epsilon \ln\sigma + \epsilon B^{(1)} = b + \epsilon B^{(1)} \quad , \qquad 54.$$

$A(T)$ is $O(1/\sigma)$ because b is roughly in the range 0.3 to 0.4 for typical ϵ and σ values; $B^{(1)}$ is hypothesised to be $O(1)$ as $\sigma \to o$. The time T_b is now given by the relation

$$\bar{B}(T_b) \equiv 1 - 1/\gamma\bar{p}_o(T_b) = b \quad . \qquad 55.$$

with $\dot{x}$ defined by

$$T - \bar{x} = \sigma\xi = T_b + \sigma(\tau - x) \qquad 56.$$

and φ defined so that

$$\rho_c^{(1)} = \varphi_{\dot{x}}, \quad u_c^{(1)} = \varphi_T \qquad 57a, b$$

it can be shown that the potential satisfies the equation

$$(\varphi_{TT} - \bar{a}_{fo}^2 \varphi_{\dot{x}\dot{x}})_T = \Omega(\varphi_{TT} - \tfrac{1}{\gamma}\bar{a}_{fo}^2 \varphi_{xx}) \quad . \qquad 58.$$

where

$$\Omega = \bar{q}_{ob}^n (1 - b)^2 (1 - b\tau)^{-1} \quad . \qquad 59.$$

$$b = [\gamma/(\gamma\bar{Q})^n](1 - b)^2 \{(1 - \bar{B}_m)^{-1} - (1 - b)^{-1}\}^n \quad . \qquad 60.$$

and $\bar{B}_m$ is the value of $\bar{B}$ when $\bar{p}_o$ is equal to $\bar{p}_{om}$. The particular form of Ω arises from the fact that if $\bar{B}$ has the form (54) then $\epsilon \to o$ as $\sigma \to o$ is essential if b is to be $O(1)$, evaluation of $B^{(1)}$ under these circumstances shows that it is equal to $-\ln(1 - b\tau)$ and the particular form of Ω in (59) is a consequence. There is an

implication that solutions of (58) may break down as $\tau \to b^{-1}$, if for no other reason than the fact $\dot{B}$ and hence $\bar{p}_0$ will not be properly described in such circumstances.

The matching conditions for $\bar{u}$ require

$$u_c^{(1)}(\tau \to \infty, \beta) \to u^{(1)}(T_b, \beta) = g(\beta)f(T_b) \quad . \qquad\qquad 61.$$

where the last result follows from (39). As $\tau \to -\infty$, $\Omega \to 0$, and (58) reverts to the wave equation for propagation at the fixed frozen isentropic sound speed $\bar{a}_{fb} \equiv \bar{a}_{fo}(T_b)$. Thus the 'early' stages of motion in the τ time scale are simply an acoustic-like continuation of the wave system at time T_b; since τ like intervals of time are relatively brief, non-linear correction is relegated to second-order significance within them. As τ increases, Ω becomes positive and the right-hand side of (58) begins to assume significance. Evidently (58) is describing a simple hierarchical wave system (Whitham, 1974, ch. 11). The motion is dispersive, with wave speeds between the frozen isentropic value $\bar{a}_{fb}$ and the frozen isothermal value $\bar{a}_{fb}/\sqrt{\gamma}$. Because the relaxation frequency Ω in (58) & (59) is positive, the wave system is *unstable* and the waves will be amplified. From the source-like character of the right-hand side of (58) and the need to obey conditions like (61) for all β (or, equivalently, x) at some 'fixed' $\tau(\to -\infty)$ it is highly probable that waves of *both* families, propagating along $\dot{x} > 0$ *and* $\dot{x} < 0$, are generated. It is very significant that perturbations in $\bar{q}$ have been promoted in the present τ time intervals to first order size (see (50c)) from the second order size that they had originally (see (14)).

Thus (58) is describing the way in which first-order chemical activity is participating in the wave-propagation processes, and chemical heat release cannot prefer to generate waves of one particular class, it must produce waves of both classes.

REFERENCES

Ahousieff, C. E. & Toong, T. Y. (1981). "Nonlinear wave-kinetic interactions in irreversibly reacting media." J. Fluid Mech., *103*, 1.

Blythe, P. A. (1978). "Wave propagation and ignition in a combustible mixture." 17th Symposium (International) on Combustion. The Combustion Institute, Pittsburgh, PA, USA.

Clarke, J. F. (1978). "Small amplitude disturbances in an exploding atmosphere." J. Fluid Mech., *89*, 343.

Clarke, J. F. (1979). "On the evolution of compression pulses in an exploding atmosphere, initial behaviour." J. Fluid Mech., *94*, 195.

Clarke, J. F. (1981). "Plane waves in reacting gases. Part II waves in explosive atmospheres." Lecture notes, Lehrgehen für Mechanik, RWTH, Aachen, West Germany, CoA Memo 8016, Cranfield Institute of Technology.

Clarke, J. F. & McChesney, M. (1976). "Dynamics of Real Gases." Butterworths, London.

Lighthill, M. J. (1956). "Viscosity effects in sound waves of finite amplitude." in "Surveys in Mechanics." G. K. Batchelor & R. M. Davies, editors. Cambridge University Press.

Whitham, G. B. (1974) "Linear and nonlinear waves." John Wiley, New York.

DEFLAGRATION TO DETONATION TRANSITION[*]

G.S.S. Ludford and D.S. Stewart[**]
Department of Theoretical and Applied Mechanics
Cornell University, Ithaca, N.Y. 14853

ABSTRACT. Transition from plane steady deflagration to plane steady detonation is examined in one particular case, related to the ignition of a combustible mixture at the closed end of a tube. Two conjectures are made: a deflagration of strength $O(\beta)$, where β is the heat release, requires a disturbance $O(\beta^{\frac{1}{2}})$ to make it evolve into a detonation; and the outcome of a shock overtaking a deflagration is an overall steady detonation with oscillatory structure. Some doubt is cast on the first conjecture.

I. INTRODUCTION.

In spite of the long history of deflagrations and detonations, the transition of the former into the latter (DDT) still lacks a theory. Progress has foundered on such questions as the adequacy of a laminar description, which have only complicated the issues. In dealing with detonation structure per se, Oppenheim & Rosciszewski [5] dismissed these questions by asserting that "only a thorough understanding of the so-called "laminar" wave structure can provide proper basis for the assessment of the effects of turbulence and other time dependent and multidimensional phenomena that may accompany the detonation process".

The first steps in the case of DDT are simple descriptions of steady plane deflagrations and detonations, the emphasis being on simple. Detonations have now been treated by Lu & Ludford [4] and deflagrations by Stewart & Ludford [9]. (The deflagrations concerned are "fast", not just those obtained by the so-called combustion approximation [9] where the Mach number is vanishingly small). Here we move on to the transition question and immediately find that the subject is too general to treat in its entirety. The object of this paper is to isolate the mathematical problem involved in one particular plane transition.

II. HUGONIOT DIAGRAM FOR $\beta \ll 1$.

The most promising line of attack assumes that the heat release is small: for steady deflagrations and detonations the formulas are then particularly simple [6], involving no more than exponential functions. One is immediately led to a conjecture about transitions in general, suggested by a simple property of the Hugoniot diagram (Fig. 1) to be derived next.

The density ρ, velocity u and pressure p on the two sides of a deflagration or detonation (treated as a discontinuity) must satisfy

---

$$\rho_1(U - u_1) = \rho_2(U - u_2), \quad \rho_1(U - u_1)^2 + p_1 = \rho_2(U - u_2)^2 + p_2, \quad (1)$$

$$(U - u_1)^2/2 + \gamma p_1/(\gamma - 1)\rho_1 + \beta = (U - u_2)^2/2 + \gamma p_2/(\gamma - 1)\rho_2 \quad (2)$$

Here U is the velocity of the discontinuity and $|\beta|$ is the heat released by the reaction there; if the mass flux is from side 1 to side 2, as we shall assume, then β is positive. When the velocities are eliminated from these three equations, a relation between ρ_1, p_1, p_2, ρ_2 is obtained, namely

$$\frac{\gamma}{\gamma-1}\left(\frac{p_1}{\rho_1} - \frac{p_2}{\rho_2}\right) - \frac{1}{2}\left(\frac{1}{\rho_1} + \frac{1}{\rho_2}\right)(p_1 - p_2) + \beta = 0. \quad (3)$$

For given state 1, the locus of the state 2 in the $1/\rho$, p-plane is a hyperbola, known as the Hugoniot diagram.
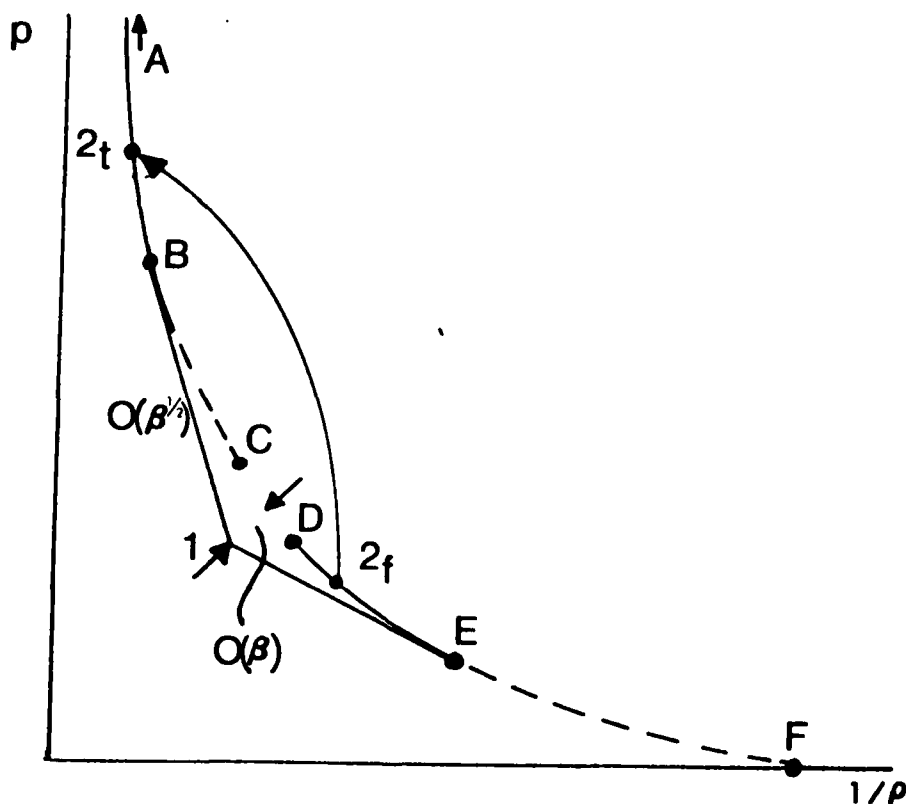

Figure 1. Hugoniot diagram for $\beta \ll 1$

Not all of the hyperbola is physically acceptable. Those parts on which density or pressure is negative must be excluded, as must that part to the right of the vertical and above the horizontal through the point 1 (since velocities are imaginary). The discontinuities corresponding to the remaining parts AC and DF are detonations and deflagrations, respectively. The point B divides the detonations into strong (above) and weak (below), while E divides the deflagrations in the same way (right and left). Analysis of the reaction zone within the discontinuity shows that strong deflagrations do not exist and that weak detonations, unlike strong ones, only exist for special reaction rates; accordingly BC and EF are drawn dashed to indicate their exclusion from the subsequent discussion.

We are left then with the strong detonations, together with the so-called Chapman-Jouget (C-J) detonation corresponding to the point B, and the weak deflagrations, together with the so-called C-J deflagration corresponding to the point E. At both the upper and lower C-J points (B and E) the velocity of the discontinuity relative to the burnt gas is equal to the speed of sound there. As A is approached, the velocity of the discontinuity becomes infinite while at D it is zero. For $\beta \ll 1$, the hyperbola comes to a distance $O(\beta)$ from the point 1; hence, both the upper and lower C-J points are $O(\beta^{\frac{1}{2}})$ away, the simple property of the Hugoniot diagram mentioned earlier.

If the initial deflagration is steady, corresponding to the point 2_f, and the final detonation is also steady, corresponding to 2_t, then the transition involves a change $O(\beta^{\frac{1}{2}})$. It is, therefore, natural to conjecture that, to effect the transition from a steady deflagration to a steady detonation, at least a threshold disturbance $O(\beta^{\frac{1}{2}})$ must be applied. This conjecture, which Matkowsky claims to have made first, will be examined later; here we merely note that it explains why no detonation was produced in the quasi-steady theory of Stewart & Ludford [10].

III. SHOCK-INDUCED TRANSITION. The object is to focus current discussion of transitions by considering a specific problem in which a deflagration evolves into a detonation under the action of an external disturbance. The problem is derived from a standard example of DDT which, in its original mathematical form, has the transition process suppressed. We refer to the ignition of a reaction mixture in a tube closed at one end. When ignition is supposed to occur at the end wall itself, a C-J wave propagates away, immediately followed by a centered rarefaction wave (Courant & Friedrichs [3]). The transition is eliminated by this mathematical idealization.

To obtain a transition problem without introducing complications associated with a more realistic description of the ignition process, the mixture is supposed to be ignited with the end opened, so that a steady deflagration wave propagates down the tube. The end is subsequently closed or, more generally, moved with constant velocity. The (uniform) backward motion of the burnt gas behind the deflagration is incompatible with the motion of the end wall; the resultant shock wave overtakes the deflagration wave and produces transition (Fig. 2).
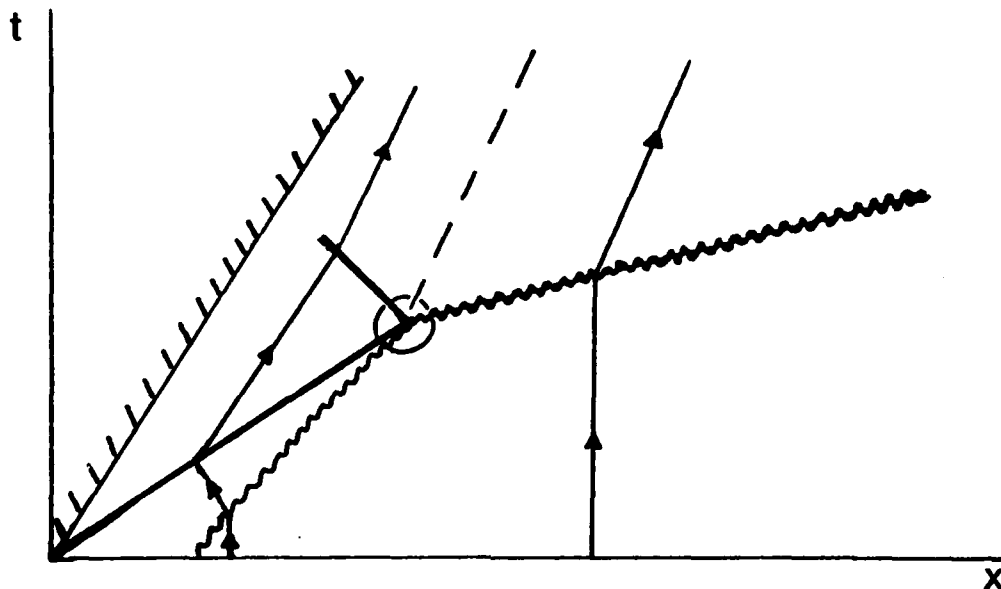
Figure 2.   Outcome of a sufficiently strong shock ⚊⚊
            overtaking a deflagration ∿∿∿. The
            lines ∿∿∿ and ⚊⚊ represent a detonation
            and contact discontinuity, respectively.

Figure 2 applies if the wall velocity is sufficiently large; from the
collision emerges a detonation wave together with a contact discontinuity and
a back shock. More precisely, we assert that such a collection of disconti-
nuities forms a consistent description: the detonation wave satisfies the
equations (1,2), with $p_2 > p_1$, the back shock satisfies the same conditions
with $\beta = 0$, and the contact discontinuity has velocity and pressure continuous
across it. The consistency of the description does not mean it is correct, how-
ever: the transition question, i.e., whether the collision results in the con-
figuration shown, remains.

The transition problem associated with such a collision can now be posed
(cf. Fig. 3a): given initial conditions corresponding to a shock wave approach-
ing a steady deflagration wave, determine the ultimate conditions. The appro-
priate distance and time scales for analyzing the problem are not, of course,
those used in Figure 2 but the much smaller ones based on thermal diffusivity
(blowing up the region ringed in that figure). Before making a second conjecture,
about these ultimate conditions, we shall examine the configuration in Figure 2
more carefully, with a view to shedding more light on the first conjecture.
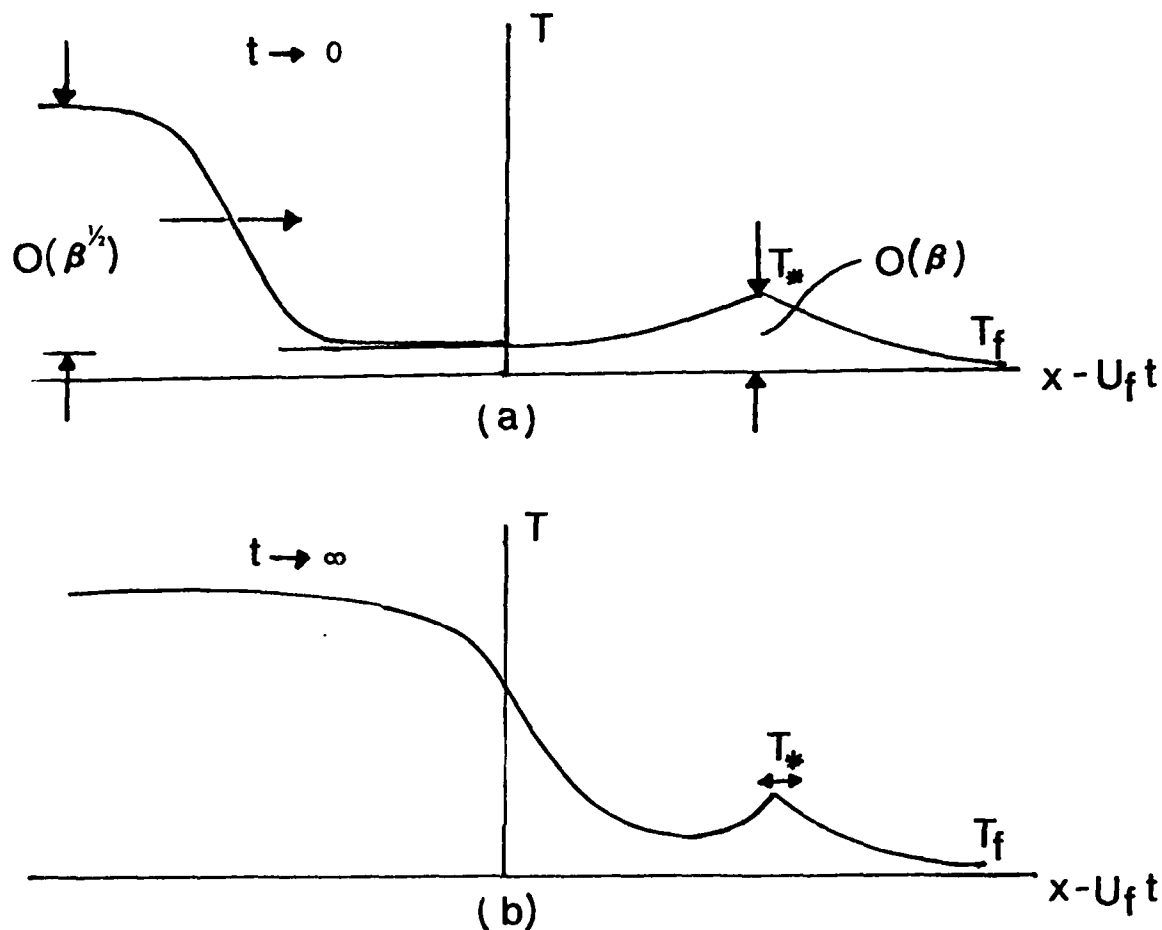
Figure 3. Collision process for $\beta \ll 1$: (a) initially
shock overtakes deflagration; (b) ultimate
oscillatory structure of detonation (conjectured)

Numerical calculations were made for $\beta = .5$; the results are believed
to be typical. Instead of prescribing the reaction properties of the mixture
and calculating the Mach number M of the deflagration discontinuity, M was
taken to be .2 (which is less than the Chapman-Jouget value for the β as-
sumed). The main result is shown in Figure 4, where the dashed curve (corre-
sponding to weak detonations) is to be discarded. The configuration of Figure
2 then leads only to the curve QR, so that there is a minimum wall velocity,
corresponding to a C-J detonation, for its validity. Also shown in Figure 4 is
the curve for $\beta \to 0$, obtained analytically.
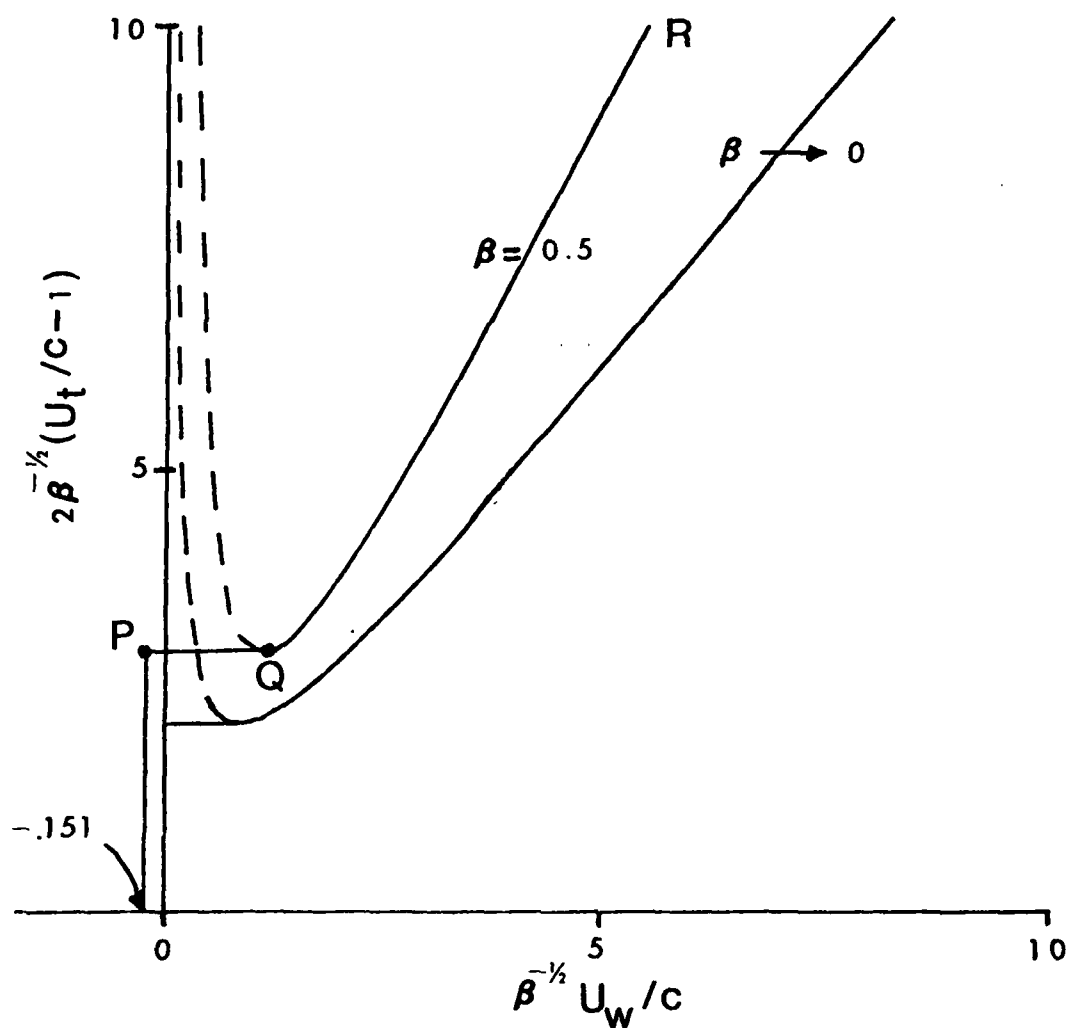
Figure 4. Detonation velocity U_t as a function of wall velocity U_w for deflagration velocity $U_f = .2c$ and $\beta = .5$, c being the speed of sound in the fresh mixture. The lines —— and --- correspond to strong (or C-J) and weak detonations, respectively. The curve QR is obtained for the configuration of Figure 2, and the horizontal line PQ for that of Figure 5.

For wall velocities smaller than the minimum, the (discarded) weak detonations produce lower pressures than the limiting C-J detonation, which suggests inserting a centered rarefaction wave immediately behind this detonation. The resulting modification is shown in Figure 5. Numerical calculations confirm the configuration, producing the horizontal extension PQ in Figure 4. At P the wall velocity is equal to that of the burnt gas behind the deflagration, i.e., the wall is being withdrawn just fast enough for no shock wave to be produced.
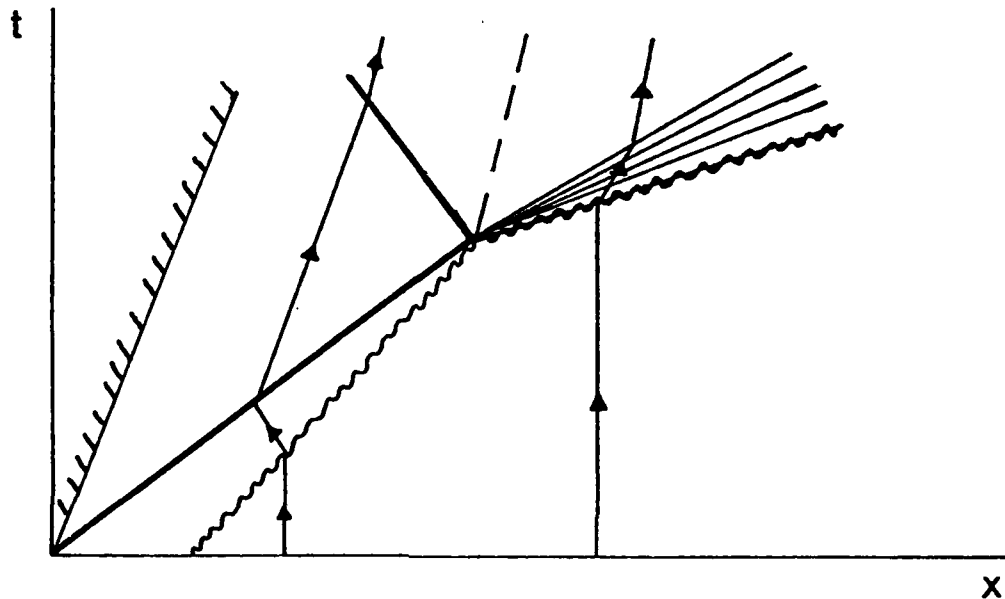
Figure 5. Modification of Figure 2 for weaker shock strengths. The detonation is now C-J with a centered rarefaction lying immediately behind.

This limiting case is important: unless contradicted by the solution of the transition problem, it shows that an arbitrarily small disturbance will induce a deflagration to change into a detonation. (The fact that the system of discontinuities after the collision in Figure 5 can solve the same initial-value problem as a single deflagration has been noted by Cherny [2], but without reference to DDT. For $\beta << 1$, when the withdrawn velocity is zero, the conclusion amounts to a counterexample of the first conjecture (Sec. II): a vanishingly small disturbance, on the scale $\beta^{1/2}$, produces transition. In fact, counterexamples are also obtained for certain positive wall velocities, because the distance between B and D in Figure 1, on the basis of the conjecture, is a definite multiple of $\beta^{1/2}$.

569

IV. CONDITIONS FOR STEADY DEFLAGRATIONS AND DETONATIONS. A discussion of the collision process is clearly needed; for vanishingly small disturbance the question reduces to the stability of deflagration waves. Before coming to the second conjecture, about the ultimate conditions in the transition problem, we shall show that the configurations cannot be exactly as implied by Figures 2 and 5: the detonation wave that emerges from the collision is not necessarily steady.

The argument depends on the theory of steady plane deflagrations and detonations presented in [9] and [4]. The theory involves an ignition temperature T_* which, as a property of the fresh mixture ahead of both the deflagration and detonation waves, applies to the reaction (at flame sheets) inside both. Stewart and Ludford [9] show that a structure exists for a steady plane deflagration only if the ignition temperature lies in a certain interval, say

$$\check{T}_*(\beta) \leq T_* < \hat{T}_*(\beta); \tag{4}$$

the corresponding restriction for detonations, say

$$\check{T}_*(\beta,M) \leq T_* \leq \hat{T}_*(\beta,M), \tag{5}$$

was obtained by Lu & Ludford [4]. Here $M(T_*)$ is the Mach number of the detonation in Figure 2 or 5 when the deflagration corresponds to T_*. Except for $\hat{T}_*$, which is the adiabatic flame temperature of the mixture, the limits of these inequalities must, in general, be obtained numerically. The limit $\check{T}_*$ corresponds to the C-J deflagration, while $\hat{T}_*$ and $\check{T}_*$ correspond, respectively to the DNZ detonation and a weak detonation/shock combination.

The question is whether the T_* selected in the interval (4) leads to values of $\hat{T}_*$ and $\check{T}_*$ lying above and below it; if not, the mixture cannot support the steady detonation. (We ensure that T_* lies in the interval (4) by merely choosing a deflagration velocity less than the C-J value for the β concerned). The implication would be that the detonation could not be steady. The answer for general β will be available soon; here we note that it it not so when β is small enough, because the value

$$\check{T}_* = [1 + 0(\beta^{1/2})]T_f \tag{6}$$

found by Stewart, Kapila & Ludford [6] lies above

$$\hat{T}_* = (1 + \beta/\gamma)T_f . \tag{7}$$

Here the function $0(\beta^{1/2})$ is positive and T_f is the temperature of the fresh mixture.

V. THE SECOND CONJECTURE. Consider $\beta \ll 1$. Since a steady detonation cannot emerge from the collision, we are left with the question of what does emerge. The question can only be settled by considering the transition problem itself; and there is one way in which Figures 2 and 5 would still be correct. The essential requirement is that conditions far upstream and downstream in the ultimate structure (Fig. 3b) should be fixed. Such a requirement would be met by a structure that was steady on the $\beta^{\frac{1}{2}}$-scale but had an unsteady perturbation $O(\beta)$ that died out at infinity in both directions.

Such a structure is sketched in Figure 3b. Since an ignition temperature $O(\beta^{\frac{1}{2}})$ above T_f is required for a steady detonation, the flame sheet is unable to assume a steady final position. On the other hand, reaction takes place as soon as the temperature reaches the flame temperature in Figure 3a, which is $O(\beta)$ above T_f. The conjecture is that ultimately the flame sheet oscillates at the front of a shock-like disturbance, forming an overall steady detonation with a pulsating structure.

This conjecture highlights the need for a study of the transition problem. For general β, numerical methods will undoubtedly be needed; but, for $\beta \ll 1$, experience [9], [6], [10] suggests that analysis will prevail, and the conjecture indicates how.

REFERENCES

[1] J. Buckmaster & G.S.S. Ludford. Theory of Laminar Flames, Cambridge: University Press (to appear).

[2] G.G. Cherny. Lectures on the Theory of Exothermic Flows Behind Shock Waves (International Centre for Mechanical Sciences, Udine, Courses and Lecture No. 36), p. 43. New York: Springer, 1973.

[3] R. Courant & K.O. Friedrichs. Supersonic Flow and Shock Waves, p. 223. New York: Interscience, 1948. (Reprinted by Springer, 1976).

[4] G.C. Lu & G.S.S. Ludford. Asymptotic analysis of plane steady detonations. SIAM J. Appl. Math. (to appear).

[5] A.K. Oppenheim & J. Rosciszewski. Determination of the detonation wave structure. Ninth Symposium (International) on Combustion, pp. 424-441. New York: Academic Press, 1963.

[6] D.S. Stewart, A.K. Kapila & G.S.S. Ludford. Deflagrations and detonations for small heat release. J. Fluid Mech. (to appear).

[7] D.S. Stewart & G.S.S. Ludford. Fast deflagration waves, Technical Report No. 116, ARO Grant No. DAAG-29-79-G-0121, Dept. of Theoretical & Applied Mechanics, Cornell University, July 1980.

[8]   D.S. Stewart & G.S.S. Ludford. Deflagration and detonation for small heat release, Technical Report No. 121, ARO Grant No. DAAG-29-79-G-0121, Dept. of Theoretical & Applied Mechanics, Cornell University, August 1980.

[9]   D.S. Stewart & G.S.S. Ludford. Fast deflagration waves. J. Fluid Mech. (to appear). Summary: A theory of deflagrations and its application. Proceedings of the First Specialists Meeting of the Combustion Institute, pp. 155-161 (Bordeaux, 1981).

[10] D.S. Stewart & G.S.S. Ludford. The equation governing the propagation of fast deflagration waves for small heat release. Transactions of the 27th Conference of Army Mathematicians, pp. 185-199, ARO Report 82-1, 1982.

1.0

1.1

1.25   1.4   1.6

2.8   2.5
3.2   2.2
3.6
4.0   2.0

1.8
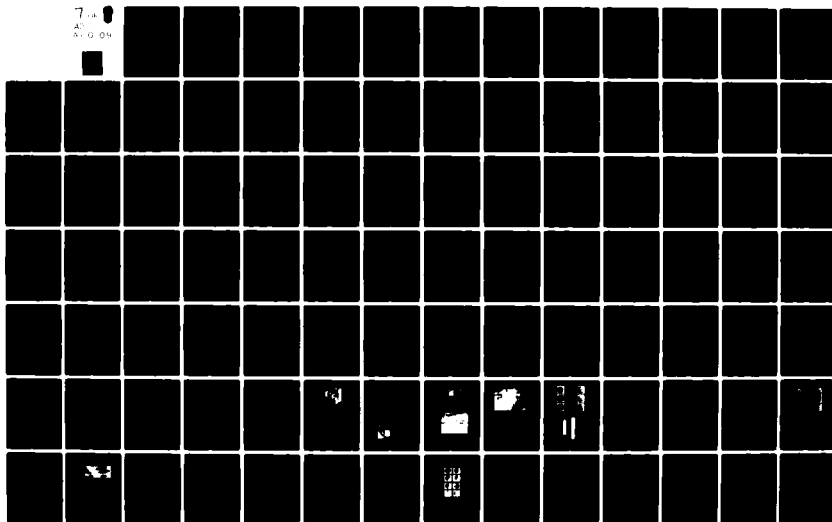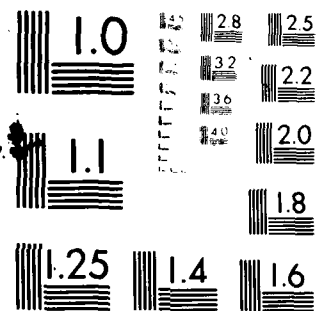
MICROCOPY RESOLUTION TEST CHART
NATIONAL BUREAU OF STANDARDS 1963 A

NUMERICAL SIMULATION OF THE GAS DYNAMIC CYCLE
OF COMPLEX, LARGE-SCALE SHOCK TUBES

Andrew Mark
Terminal Ballistics Division
Ballistic Research Laboratory
U.S. Army Armament Research and Development Command
Aberdeen Proving Ground, Maryland 21005

ABSTRACT. The quasi-one-dimensional Euler equations are applied to a geometrically complicated shock tube and integrated by an implicit numerical technique. The driver section consists of many contractions so that rarefaction waves generated there catch up to the main shock and mitigate it progressively to the point where it has the appearance of an exponentially decaying wave of the type generated by a free air blast. The computational capability is tested to an extreme because of the severe area contractions and high initial diaphragm pressures. The shock capturing numerical technique used for these cases employs coordinate stretching and clustering for sharp shock definition. Operation of a rarefaction wave eliminator is computationally exercised and is shown to well define a blast-type waveform if its closure rate is selected judiciously.

I. INTRODUCTION. The ban on open-air nuclear testing forces the blast community to seek alternate means of generating pressure signatures capable of simulating the blast from tactical and strategic nuclear weapons. The pressures generated by these simulations can then be applied to model or real targets to assess their vulnerability. There are commonly two methods for experimentally simulating pressures from nuclear devices: first, detonation of large quantities of high explosives; or, second, creating the appropriate waveform in specialized shock tubes. Although both methods are currently employed, the former is becoming prohibitively expensive and large-scale blast simulators appear as increasingly attractive alternatives. These simulators (shock tubes) are physically large enough to accomodate full sized tanks, helicopters, tactical aircraft, etc. A number of moderate size such devices exist in the U.S. and abroad with the largest and newest in Gramat, France. This device is schematically illustrated in Fig. 1. Several prominent features are evident in this Figure. The first is the driver section consisting of seven large pressure vessels which discharge through conical nozzles into the driven section. The driver lengths for this blast simulator are about 44 m and the driven section is 105 m. Items to be tested are placed from 60 to 75 m into the driven tube. The cross section diameter is nominally 12 m. The third distinguishing feature is the rarefaction wave eliminator (RWE) which consists basically of a louvered wall at the end of the driven section. The RWE is shown removed from the driven section in Fig. 1. Its purpose is to regulate the outflow as a function of time so that signals generated at the end of the tube do not propagate upstream into the subsonic flow following shock exit. It allows the simulation of very long duration blast waves and provides a substantial cost savings in construction since, with a RWE, the same waveforms are obtained in tubes a fraction of the length.

The U.S. Army and other government agencies are looking into developing a simulator designed primarily for tactical nuclear blast simulation. An additional feature in its design concept will be to incorporate a thermal irradiation capability of the magnitudes associated with tactical nuclear devices. One then has the capability for studying blast/thermal synergism in a controlled environment. The focus of this work, however, is to make preliminary computational designs and predict the performance of the gas dynamic operating cycle of this complex shock tube by: (a) requiring the computations to simulate 3-D above ground bursts by shaping the waveform; (b) simulating a long driven section (or long duration pulse) by incorporating an active rarefaction wave eliminator; and (c) obtaining long flowing times by requiring severe area contractions and high diaphragm pressures.

The computational technique employed in this study is that due to Beam and Warming[2,5,6]. The one-dimensional application in this work is a stepping stone for extensions to 2- and 3-dimensional blast problems.

II. THEORETICAL CONSIDERATIONS. Application of the implicit finite-difference scheme described by Warming and Beam[2] is most elegant in multi-dimensions where one can take advantage of all its attributes. Yet even in the quasi-one-dimensional application most of the essential qualities are retained. The governing equations, for our problem, written in weak conservation form, retain that generality when transformed to a uniformly spaced computational space. Central spatial differencing casts the difference equation into a block tridiagonal structure which is solved for the increments in the dependent variables at each successive time step without iteration.

A. Governing Equations. The differential Euler equations which describe one-dimensional flow with variable area may be written in the following form:

$$\frac{\partial}{\partial t}(\bar{q}A) + \frac{\partial}{\partial x}(\bar{E}A) + \bar{H} = 0,\tag{1}$$

where the vectors $\bar{q}$, $\bar{E}$, and $\bar{H}$ are:

$$\bar{q} = \begin{bmatrix} \rho \\ \rho u \\ e \end{bmatrix}, \quad \bar{E} = \begin{bmatrix} \rho u \\ (\rho u^2 + p) \\ u(e + p) \end{bmatrix}, \quad \text{and} \quad \bar{H} = \begin{bmatrix} 0 \\ -p\frac{\partial A}{\partial x} \\ 0 \end{bmatrix}.\tag{2}$$

This set of three scalar equations represent the conservation of mass, momentum, and energy, per unit volume, with the usual notation of ρ as density, u as velocity, e as total energy, and p as pressure. A represents the cross-sectional area of interest which may vary with coordinates x and/or t, where x is a linear dimension and t is time. As written, the equations are in weak conservation form because of the vector $\bar{H}$. If $A \neq f(x)$, the $\bar{H}$ vanishes and the equations revert to their strong

conservation form. Either form is shown by Peyret and Viviand[3] to locate (capture) shocks accurately in the grid.

The physical, independent variables (x,t) are transformed into a uniformly spaced computational grid by a general transformation of the form

$$\xi = f(x,t)$$

$$\tau = t \tag{3}$$

The resulting transformed version of equation (1) is then

$$\frac{\partial \overline{Q}}{\partial \tau} + \frac{\partial \overline{E}}{\partial \xi} + \overline{h} = 0 \tag{4}$$

where it is noted that the weak conservation form is retained. In equation (4) we define

$$\overline{Q} = \overline{q}\tilde{A} = \begin{bmatrix} \rho\tilde{A} \\ \rho u\tilde{A} \\ e\tilde{A} \end{bmatrix}, \quad \overline{E} = \overline{q}\tilde{A}\xi_t + \tilde{E}\tilde{A}\xi_x = \begin{bmatrix} \rho\tilde{A}\xi_t + \rho u\tilde{A}\xi_x \\ u\tilde{A}\xi_t + (\rho u^2 + p)\tilde{A}\xi_x \\ e\tilde{A}\xi_t + u(e + p)\tilde{A}\xi_x \end{bmatrix},$$

$$\overline{h} = \begin{bmatrix} 0 \\ -p\frac{\partial A}{\partial \xi} \\ 0 \end{bmatrix}, \tag{5}$$

where subscripts x and t mean differentiation and $\tilde{A} = A/\xi_x$. The system of equations (4), together with the ideal gas equation of state

$$p = (\gamma - 1) (e - \tfrac{1}{2}\rho u^2), \tag{6}$$

where γ is the ratio of specific heats, constitutes the governing set of one-dimensional Euler equations with arbitrary geometry. These equations will be numerically applied to a variable area shock tube problem with the implicit delta formulation of Warming and Beam[2].

B. Implicit Numerical Scheme. Euler implicit time differencing and central spacial differences are employed for the derivative terms in equation (4) while the source term, $\overline{h}$, is evaluated explicitly. Equation (4) then becomes

$$\overline{Q}_j^{n+1} - \overline{Q}_j^n + \frac{\Delta\tau}{2\Delta\xi} (\overline{E}_{j+1}^{n+1} - \overline{E}_{j-1}^{n+1}) + \Delta\tau\overline{h} = 0$$

$$+ O(\Delta\tau, \Delta\xi^2) \tag{7}$$

where the subscript "j" refers to a spacial grid point and superscript "n" to a time step. The terms containing the vector $\overline{E}$ are nonlinear functions of

the conserved flow variables $\bar{Q}$ and the system of equations (7) can be solved by an iterative scheme. However, as suggested by Lomax[4], when these terms are locally linearized the equation set (7) can be solved directly (non-iteratively) with only one inversion. This can be shown to be equivalent to one iterative step[5], and retains the formal accuracy of equation (7). Performing local linearization and defining the increment in the variable $\bar{Q}$ by

$$\Delta\bar{Q}_j = \bar{Q}_j^{n+1} - \bar{Q}_j^n \tag{8}$$

one obtains the "delta" form of the algorithm in matrix notation as

$$\left[\bar{\bar{I}} + \Delta\tau\delta_\xi(\bar{\bar{A}})\right]_j^n \cdot (\Delta\bar{Q})_j = -\Delta\tau\delta_\xi(\bar{E})_j^n - \Delta\tau(\bar{h})_j^n \tag{9}$$

where the double bar indicates a k x k matrix and δ_ξ implies central spacial differencing. The above notation is favored by Beam and Warming[2,5,6] and clearly points to the solution in terms of the flow variable increment $\Delta\bar{Q}$. The solution of the dependent variables at the next time step, therefore, is

$$\bar{Q}_j^{n+1} = \bar{Q}_j^n + \Delta\bar{Q}_j^n \tag{10}$$

In equation (9) $\bar{I}$ is the identity matrix and A is the Jacobian of the convective terms with respect to the flow variables, $\partial\bar{E}/\partial\bar{Q}$. The notation in equation (9) requires the dot product to be carried out prior to the spacial differencing. Although the "delta" formulation leads to numerical efficiency and analytical simplicity, it should be pointed out that Briley and McDonald[9] were first to extensively apply the local linearization concept and implement the algorithm in its "non-delta" form. Finally, the actual implementation of equation (9) finds the left-hand term in brackets to be a tridiagonal system which allows for easy application of a solution algorithm.

C. Dissipation. To control phase errors associated with the highest frequencies, a fourth order dissipation term is explicitly added to equation (9). This is of the form

$$\left.\frac{\partial^4 Q}{\partial\xi^4}\right|_j \quad \frac{Q_{j+2} - 4Q_{j+1} + 6Q_j - 4Q_{j-2}}{(\Delta\xi)^4} = \Delta\nabla\Delta\nabla Q_j \tag{11}$$

where Δ and ∇ represent forward and backward difference operators respectively. The final form of the computational algorithm which has been programmed is

$$\left[\bar{\bar{I}} + \Delta\tau\delta_\xi(\bar{\bar{A}})\right]_j^n \cdot (\Delta\bar{Q})_j = -\Delta\tau\delta_\xi(\bar{F})_j - \Delta\tau(\bar{h})_j^n + \Delta\nabla\Delta\nabla\bar{Q}_j^n \tag{12}$$

Since the order of this term is higher than the order of the truncation error, formal accuracy is maintained. At boundary mesh points the dissipation is of second order.

D. Grids. For most situations computed in this paper the algorithm of equation (12) remained stable and a uniform grid spacing was adequate. Under conditions of a large initial pressure ratio and severe area constrictions, portions of the flow would experience density undershoots. This was usually resolved by clustering about a point with a hyperbolic relationship of the form

$$\xi = \alpha \sinh^{-1} \beta(x-x_o) \tag{13}$$

or

$$\xi = \alpha \tanh \beta(x-x_o) \; . \tag{14}$$

In these equations x_o is the point about which one clusters and β parametrically adjusts the density of grid points about x_o. The coefficient α stretches the ordinate such that $\Delta\xi \equiv 1$.

E. Initial and Boundary Conditions. The variables in the governing equation were nondimensionalized by the following (where ^ signifies a nondimensional variable)

$$\hat{\tau} = \tau a_1/L$$

$$\hat{\xi} = \xi/L$$

$$\hat{\rho} = \rho/\rho_4$$

$$\hat{u} = u/a_1 \tag{15}$$

$$\hat{p} = p/\rho_4 a_1^2$$

$$\hat{e} = e/\rho_4 a_1^2$$

The subscripts 1 and 4 refer to the initial atmospheric and driver conditions, L is the length of the shock tube, and a is the sound speed. To initialize the computation

$$\hat{\rho}_4 = 1, \; \hat{p}_4 = \frac{T_{41}}{\gamma} \; , \; \hat{e}_4 = \frac{T_{41}}{(\gamma)(\gamma-1)} \; , \; \hat{\rho}_1 = \frac{T_{41}}{P_{41}} \; , \; \hat{p}_1 = \frac{T_{41}}{\gamma P_{41}} \; ,$$

$$\hat{e}_1 = \frac{1}{(\gamma)(\gamma-1)P_{41}} \tag{16}$$

577

where T_{41} and P_{41} are the initial temperature and pressure ratio across the diaphragm. Under the severe conditions mentioned in the previous section it was sometimes necessary to spread the diaphragm over several grid points so as to "soften" the starting process. After several time steps this initial diffusion would not be evident when compared to a control case without the distribution.

The reflective boundary at the left-hand side was computed by means of image points, such that

$$\rho_1 = \rho_3$$

$$u_1 = -u_3$$

$$(17)$$

$$e_1 = e_3$$

$$u_2 = 0$$

and the outflow boundary was computed from backward differences at the exit plane formulated such that it did not violate domain of dependence. The variable specified here was the absolute static pressure. Inflow was not considered.

III. RESULTS.

A. General Considerations. This section shows how the computational results obtained with the algorithm of equation (9) can be combined to model geometrically complicated blast simulators in a quasi-one-dimensional sense. The schematics depicted on the left hand side of Figure 2 represent various ways in which the waveform in a particular shock tube may be shaped to eventually achieve a desired result. In every case the dotted line represents the location of the diaphragm. The dots in the tube schematics are meant to correspond roughly to the test station and represent the location of the respective static overpressure waveform in the right hand side of the Figure. The term overpressure is the excess pressure over atmospheric (ambient) and is preferred by the blast community to absolute pressure. This term will be used consistently throughout and is to be construed as such wherever "p" appears. The waveforms are time varying functions and are obtained by continually sampling the flow at the location of the dot.

Part (a) of Figure 2 represents a conventional shock tube. At the test station, the pressure rises instantaneously to a plateau value and remains there until it is destroyed by a rarefaction wave. In this particular case the rarefaction wave is the result of the shock exiting the tube and initiating a left traveling rarefaction wave. Had the sampling station been farther to the left, the left traveling rarefaction wave generated by the starting process (bursting of the diaphragm) would have reflected from the closed end and caused the decay. In either case the result is essentially the same. Of course, this basic configuration does not approach the desired result

depicted in 2(f) of the same Figure. This waveform is meant to represent the ideal, classical exponentially decaying wave that results from a surface burst and it is this waveform that we try to generate with our mathematical shock tube. The shock tube that generates this type of waveform is therefore called a "blast simulator".

Figures 2(b) and 2(c) are alternate ways of achieving similar results. The essential feature of the waveform is that the plateau no longer exists but rather a decay is present. In 2(b) the driver contains a number of baffles (area constrictions) and in 2(c) the driver is in the shape of a cone. The left traveling rarefaction wave in 2(b) caused by the bursting of the diaphragm encounters a baffle, partially reflects from it and travels to the right; partially passes through until it, encounters the next baffle and reflects to the right; etc. This process could theoretically be continued with a large number of baffles. The right traveling rarefaction waves that reflect from the baffles catch the main shock and progressively weaken it. This weakening is depicted by the overall decay in the first half of the pressure waveform. The detail in the decay (undulations) depends on the number of baffles, their relative placement and the size of opening. The driver in Figure 2(c) can be thought of as the limiting case of a large number of baffles that progressively decrease in hole diameter as we move to the left from the diaphragm. The result is that the undulations depicted in 2(b) disappear to produce a smoothly varying exponential-like decay.

Figure 2(d) depicts a shock tube with a contraction at the diaphragm and a divergent nozzle. There are two prominent features associated with the pressure history for this configuration. First, a decaying pressure spike is evident. This is caused by the expansion process of the divergent section and the fact that the nozzle is operated in the choked mode. Second, the mass flow into the divergence and the driven section is restricted by the throat area and although when the process is started the flow initially reacts as if the situation were that of 2(a) it quickly adjusts to a mass flux dictated by the throat. Realizing it can't keep up the mass flux demanded in 2(a) the pressure plateau accomodates the lesser mass flux. These features permit control of the initial wave decay rate and, because of low driver mass emission, prolong the blowing times required for long duration waveforms. Eventually, the waveforms in Figures 2(b), (c), and (d) suffer the consequence of the rarefaction the same as in Figure 2(a). This brings us to our last important feature in the design of blast simulators; namely: the rarefaction wave eliminator (RWE).

Figure 2(e) shows the RWE at the end of a simple shock tube. Its purpose, as the name implies, is to negate the detrimental effects caused by the rarefaction wave from the open end. Besides having no business in a waveform that tries to mimic a blast wave, it poses several other problems. It produces a flow acceleration and subjects items to be tested to unrealistically high dynamic loads. This is especially troublesome when an item is to be tested near the limit of its survivability. The rarefaction wave can potentially destroy the test item. The RWE is computationally modeled as a contraction or baffle placed at the end of the tube. The effects for a straight tube are shown in the right hand side of 2(e). The dotted line in

the pressure trace represents the result without a RWE (i.e., the condition depicted in 2(a)). The extension of the plateau comes about when the shock wave exits the end of the tube; partially reflects as a shock from the closed portion of the RWE; partially generates a rarefaction wave from the open portion of a strength so as to cancel the shock. The resulting extended plateau is then only destroyed by the diaphragm generated rarefaction wave and its reflection from the closed end.

The general features described in Figure 2 can be combined and parametrized such that the operational gas dynamic cycle of the resultant shock tube would, in waveform, approach that of Figure 2(f). The remainder of this paper will show how this is accomplished by using the French facility described in Reference 1 as an example.

B. A Blast Simulator Model. The Gramat Facility in France[1] consists of a driven tube with a nominal diameter of 12 m. In order to accommodate some aircraft a 20 m diameter facility would be required for the U.S. In planning for the driver design for such a facility we are faced with engineering a pressure vessel 20 m in diameter by roughly 50 m long if we adopt the model of Figure 2(b). This is, of course, impractical and the French have resorted to a technique devised jointly by them and the Germans[7]. The technique involves using a number of "small" diameter rechargeable pressure vessels with the nozzle end directed into the driven tube (as seen schematically in Figure 1). This allows one to build driver pressure vessels that are of manageable size and facilitates installation of diaphragms. If one adds the divergent cone feature of 2(d) one evolves a schematic of the Gramat Facility as shown in Figure 3. Although only four tubes are shown, Gramat actually has seven[1]. The decaying wave in this facility is produced by using variable length driver tubes. The effect of this is to approach the configuration of Figure 2(c). The diaphragms for all the drivers are at the throat and when they burst simultaneously, generate left-traveling rarefaction waves which reflect from their respective closed ends at different times and therefore alter the main shock progressively.

The quasi-one-dimensional computational model is shown in Figure 4. In the driver, the cross-sectional areas at any given location are simply lumped into a single area and the stair-stepped driver results. One can now better see that this approach to driver design is in the spirit of a conical driver (Figure 2(c)). The RWE, which in reality is a series of louvers, is modeled computationally as a single lumped opening.

C. Waveforms Without RWE. For the purpose of conciseness, let us designate the configuration of Figure 1 as "standard". Let us also designate a sampling station for the pressure-time history at 67.5 m into the driven section (from the left). If we normalize by the total length this corresponds to a test position of x = .75. A waveform produced at this location for an initial pressure ratio across the diaphragm of 24.4 atmospheres is shown in Figure 5. This initial pressure ratio is used for all subsequent computations. It represents a moderate pressure in the test section appropriate for testing trucks, electronic shelters, etc. For armored vehicles, such as tanks and personnel carriers, pressures four or five times as great are

in order. On the other end of the scale, light-skinned vehicles such as air-
craft seldom get exposed to more than 10-15 kPa (several psi). The waveform
in this Figure (Figure 5) exhibits all the features talked about earlier; a
sharp rise ① across the shock, the divergence expansion ② , the decay due
to the various length drivers ③ , and the sudden relief by the rarefaction
wave ④ . It is often debated how best to approach the elimination of the
rarefaction wave. There are two schools of thought. One proposes the use of
a RWE while the other simply advocates extending the driven section. Ulti-
mately, costs will dictate. So that one can make a comparison, three graphs
are presented in Figure 6 for the same initial conditions and sampled at the
same location (x = 67.5 m from the left end) of the driven section. The
graphs represent pressure-time histories for driven sections that are 25,
50, and 100% longer than the standard. In the computations, the number of
mesh points was increased proportionately so as to maintain the same grid
spacing. It is therefore evident that even doubling the driven end still
produces a rarefaction wave of significance. The situation becomes worse
for higher initial pressure ratios. The rarefaction wave arrives sooner and
becomes stronger. It therefore appears as though if we want to do without
the complication of a RWE, we have to build a driven section about three
times as long as the standard. This does not seem practical both from a
cost constraint and from its shear physical length. Therefore we turn our
attention to modeling the operation of the RWE. Let us preface that topic
by stating that the French standard configuration (i.e., 105 m long driver,
≈ 12 m diameter) is nearly as short as it can be. It takes about 5 diameters
for the flow to settle into a one dimensional state and about that much dis-
tance to prevent the contact surface from reaching the test section. Then we
have about a 15 m test section and the final 30 meters or so serves to allow
test items to slide without damaging the RWE.

D. Waveforms With RWE. An account of how the French RWE is intended
to operate is given in Reference 1. Physically it consists of banks of
louvers which pivot about an axis much like a venetian blind. The open area
could theoretically be varied according to a feedback system since we know
we must maintain a closure rate to generate compression waves of a magni-
tude to negate the rarefaction waves traveling up the tube. This is thought
to be unnecessarily complicated[1] and a simple pre-programmed A = f(t) varia-
tion is used to control the louvers. In particular Reference 1 advocates a
linear time variation. We shall qualitatively compare the results from a
computation and a record from the Gramat facility. Such a record is depicted
in Figure 7[8]. Its comparison computation is given in Figure 8. The dotted
line in Figure 8 represents the operation of the RWE. It is set to an ini-
tial value (.34) and remains motionless for a preset delay, until the shock
wave reaches the end of the tube. Then it begins to close linearly as
shown, dwells for a short time at some minimum opening, and subsequently it
is allowed to open. The resultant pressure-time history is shown with the
solid line. The initial setting for the open area of the RWE is that recom-
mended in Reference 1. Actually, if one were to set it to match the shock
strength when it reaches the exit, it would be ≈ .48. The value of .34 is a
compromise based on the "average" pressure-time history. No matter what one
does, however, the rarefaction wave at about .4 s will always be present.
This wave comes from the decay of the initial peak due to the divergence.
Its duration is only about .020 s and any closure slower than this will

produce an effect like that in the figure. The difference will be that for an initial opening larger than .34 the hump (reflected wave) at ≈ .38 s will be smaller and for a smaller initial opening it will be larger. It is interesting to note that almost all the corresponding features exist in the computation the way they do in the experimental record. In addition the computation shows rarefaction waves at about .6, .85, 1.05, etc. These come from the diaphragm bursting and the rarefaction wave reflecting from the stepped driver configuration. In the experimental record, this effect is washed out. The effects of these rarefactions are also seen in the computations without the RWE, especially in the 100% version (see Figure 6). There it is also evident that the first of these waves arrive at the test station coincidentally with the arrival of the stronger rarefaction from the open end (t ≈ .4 s).

Fianlly, the idea of the more rapid closure of the RWE to negate the rarefaction wave at t ≈ .4 s can be tested very simply by performing the computation with a bi-linear closure function. The resulting pressure-time history is given by the solid line in Figure 9. The area closure function is shown with the dotted line. One can see the favorable effect and overall smooth approach toward the abscissa.

E. Waveform With Thermal Radiation Source (TRS). Thus far, we have discussed the blast-only modeling aspects of large-scale shock tubes. In order for these shock tubes to be more realistic in simulating nuclear bursts, a thermal source should also be considered. This is true both for the physical and computational shock tube models.

The thermal pulse from a nuclear device precedes the air blast. For distances of interest for tactical equipment from ground zero, the time between the thermal and blast pulses is of the order of 1 second. Adding the capability of thermally irradiating a target and then applying a blast loading is a step closer to a real simulation. This can be done physically by incorporating a thermal radiation source in front of the target. The drawback in the physical shock tube is that the hot thermal products will still be in the target area when the shock arrives. As the shock passes through the hot gases its wave characteristics are altered. This section points to the fact that, in attempting to reproduce both the thermal and blast characteristics of a nuclear device in a physical shock tube (large thermal/blast simulator), we need to concern ourselves with the thermal radiation products confined within the tube.

One can obtain a qualitative insight into this thermal-blast interaction process by computationally modeling the Gramat facility, including a region of remnant thermal radiation products. Such a model is depicted in Figure 10 where the shaded area represents the distribution of hot products and point "A" is the measuring station in the test section. The solid line in Figure 11 represents the predicted static overpressure (as in Figure 9) for the blast-only test, while the dashed line represents a combined thermal/blast test. The hot products were modeled with air, having a sound speed 1.73 times tha ambient value. The shock wave which arrives at the measuring station is attenuated by about 25% in amplitude and arrives somewhat sooner

since it traveled for some distance through higher sound speed air. The
perturbation on the thermal/blast wave at t ≈ .35 s occurs because the rare-
faction wave eliminator is now "detuned" for this type of wave. All these
anomalies point to the fact that a venting mechanism needs to be incorporated
into the design of a large thermal/blast simulator if realistic combined
testing is to be expected.

IV. CONCLUSIONS. Based on this computational study it is certainly
feasible to parameterize a number of different important functions of a
Large Blast Simulator. In general it is not advisable to build a long tube
as opposed to one with a RWE. The quality of the wave one obtains computa-
tionally depends to a large degree on the proper functioning of the RWE. The
waveform resulting from the bi-linear operation of the RWE appears very ade-
quate for most experimental purposes. It may be possible to shorten or
lengthen the waveform by adjusting the closure rate in the latter stages of
the closing cycle. For combined thermal/blast testing, the hot thermal radi-
ation products need to be eliminated prior to the arrival of the blast wave
so that realistic simulation of nuclear bursts are realized.

VI. REFERENCES.

1. Crosnier, J. R., and Monzac, J. B. G., "Large Diameter High Performance
   Blast Simulators," Proceedings of the Fifth International Symposium on
   Military Application of Blast Simulation, Stockholm, Sweden, May 23-26,
   1977.

2. Warming, R. F., and Beam, R. M., "On the Construction and Application of
   Implicit Factored Schemes for Conservation Laws," SIAM-AMS Proceedings,
   Symposium on Computational Fluid Dynamics, New York, NY, April 1977.

3. Peyret, R., and Viviand, H., "Computations of Viscous Compressible Flow
   Based on the Navier-Stokes Equations,: AGARD-AG-212, 1975.

4. Lomax, H., "Stable Implicit and Explicit Numerical Methods for Integra-
   ting Quasi-Linear Differential Equations with Parasitic-Stiff and
   Parasitic-Saddle Eigenvalues," NASA TN D-4703, 1968.

5. Beam, R. M., and Warming, R. F., "An Implicit Factored Scheme for the
   Compressible Navier-Stokes Equations II: The Numerical ODE Connection,"
   Paper No. 79-1446, AIAA 4th Computational Fluid Dynamics Conference,
   Williamsburg, VA, July 23-24, 1979.

6. Beam, R. M., and Warming, R. F., "An Implicit Factored Scheme for the
   Compressible Navier-Stokes Equations," AIAA Journal, Vol. 16, No. 4,
   April 1978, pp. 393-402.

7. Amann, H., "Theoretical and Experimental Investigations for the Driving-
   Mechanism of a Large-Diameter Shock Tube," 4th International Symposium
   on Military Applications of Blast Simulations, Southend-on-Sea, England,
   9th to 12th September 1974.

8. Private Communication from Dr. Fritz Oertel, Ballistic Research Labora-
   tory, November 1980.

9. Briley, W. R., and McDonald, H., "Solution of the Three-Dimensional
   Compressible Navier-Stokes Equations by an Implicit Technique,"
   Proceedings of the 4th International Conference on Numerical Methods in
   Fluid Dynamics, Lecture notes in Physics, Vol. 35, Springer-Verlag,
   Berlin, 1975.
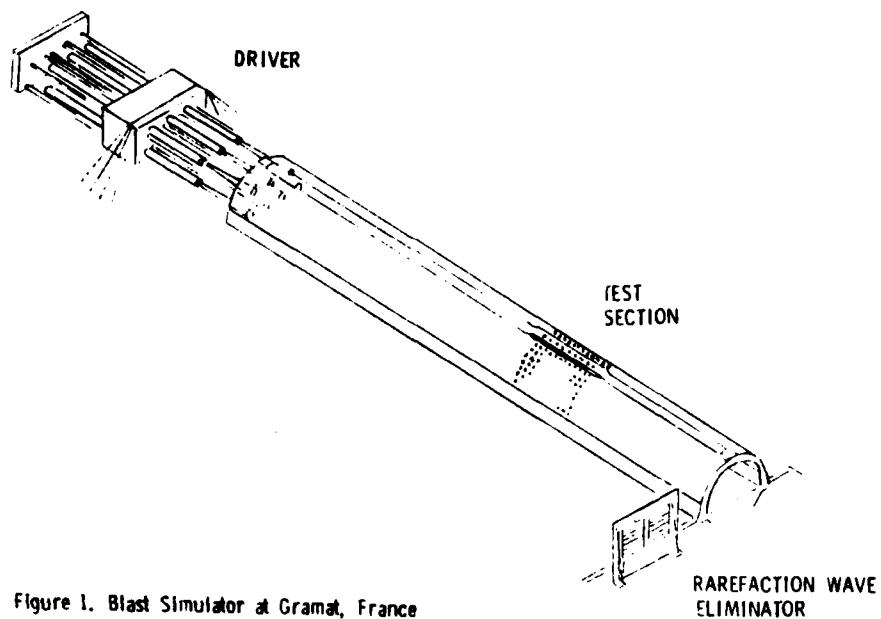
Figure 1. Blast Simulator at Gramat, France
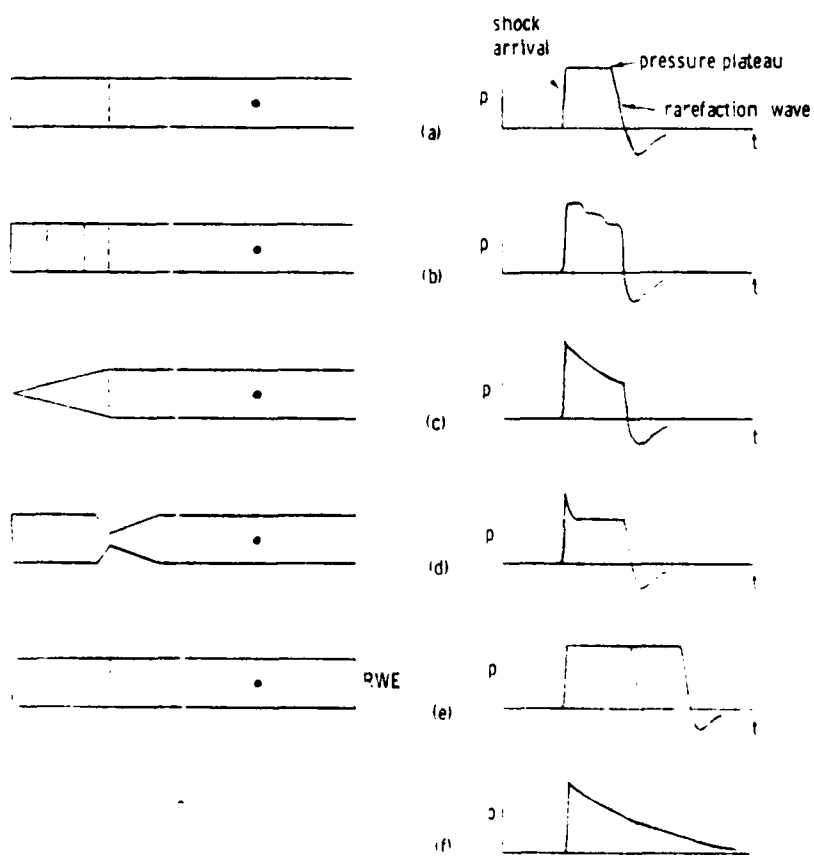
Figure 2. Shock Tube Configurations and Waveforms

585
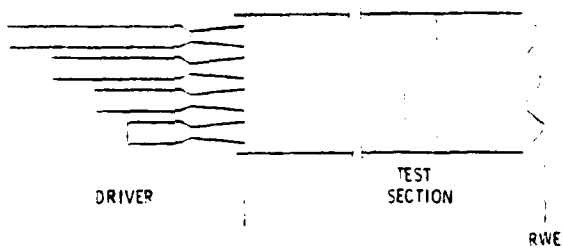
Figure 3. The Gramat Facility Model
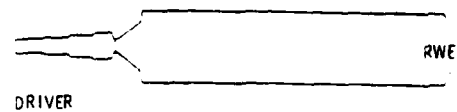
Figure 4. Computational Model
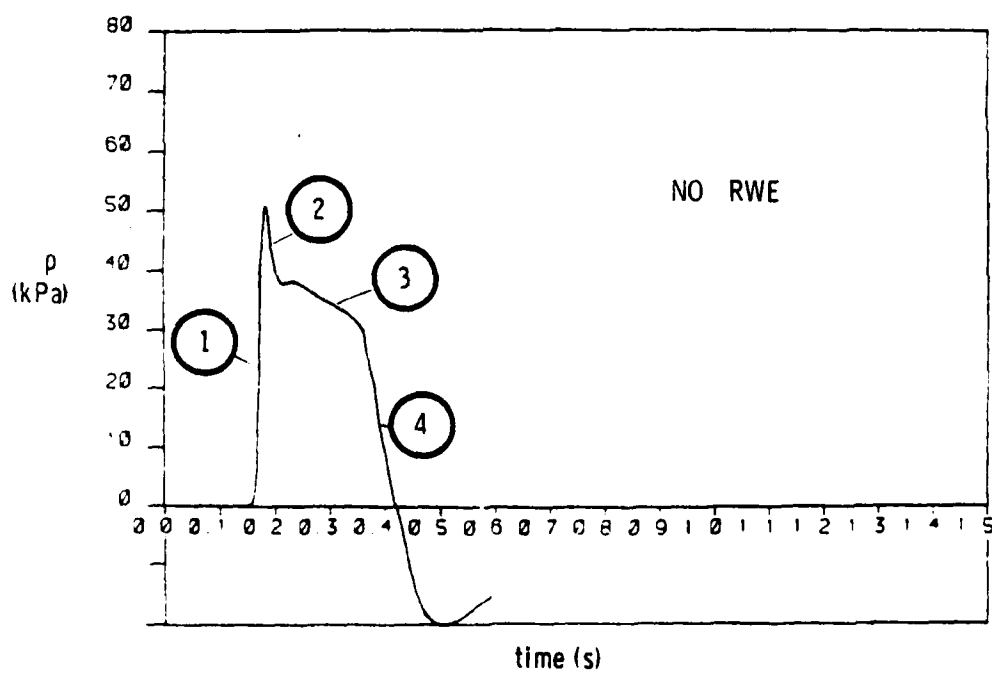
Figure 5. Overpressure at x = .75 for P_{41} = 24.4 (std French)
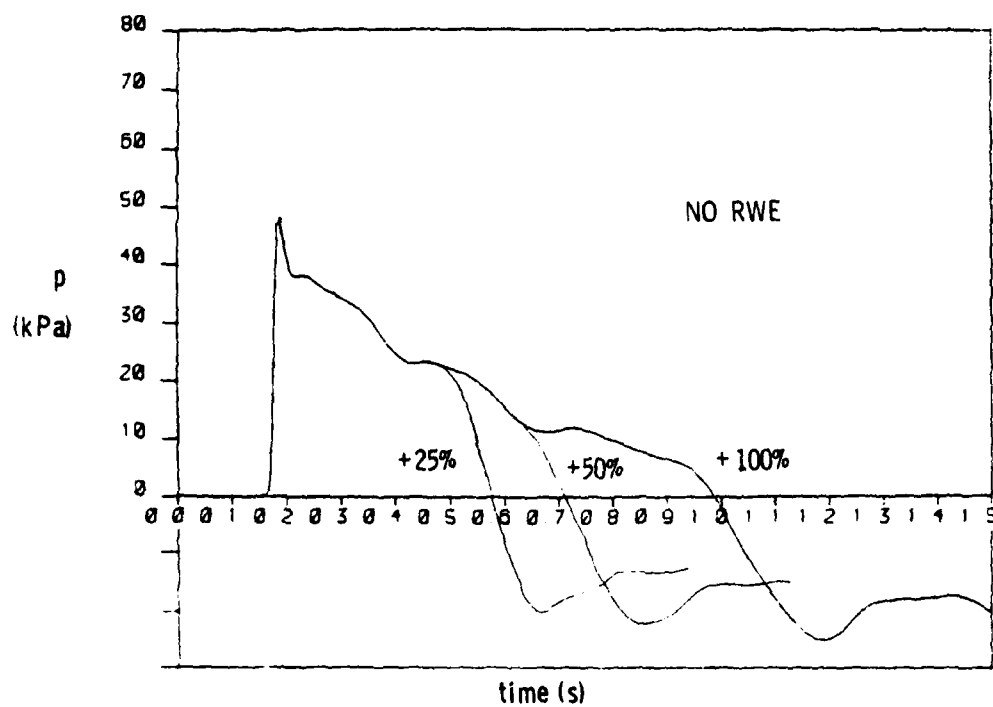
Figure 6. Overpressures at x=67.5m (from left end of driver) for Three Driven Lengths
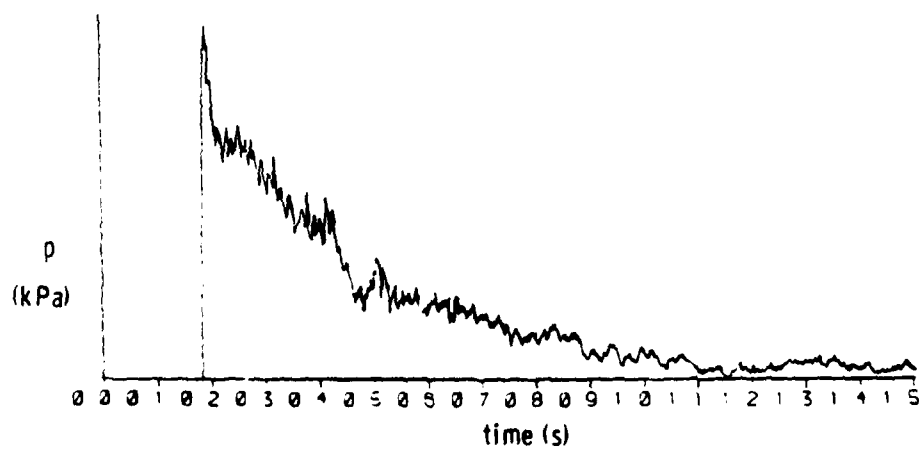
Figure 7. Typical Overpressure-Time Record from the Gramat Blast Simulator
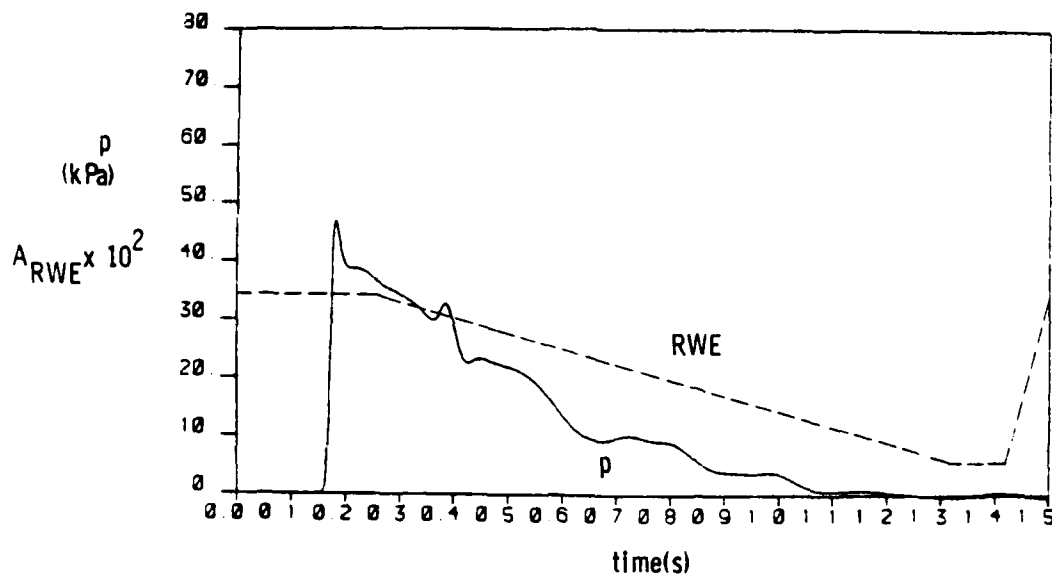
Figure 8. Computed Overpressure-Time History with Linear RWE Closure
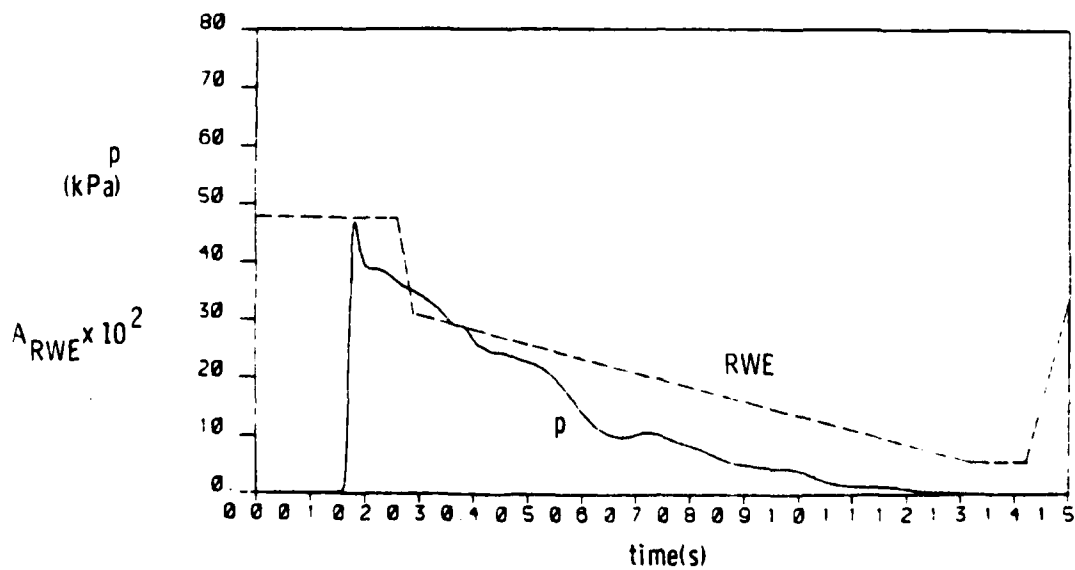
Figure 9. Computed Overpressure-Time History with Bi-Linear RWE Closure
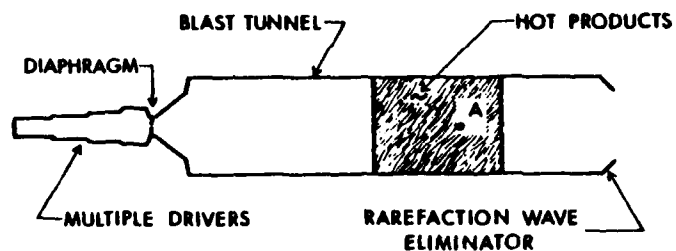
Figure 10. Schematic of One-Dimensional Model of
Large Blast Simulator at Centre d'Etudes
de Gramat, France.
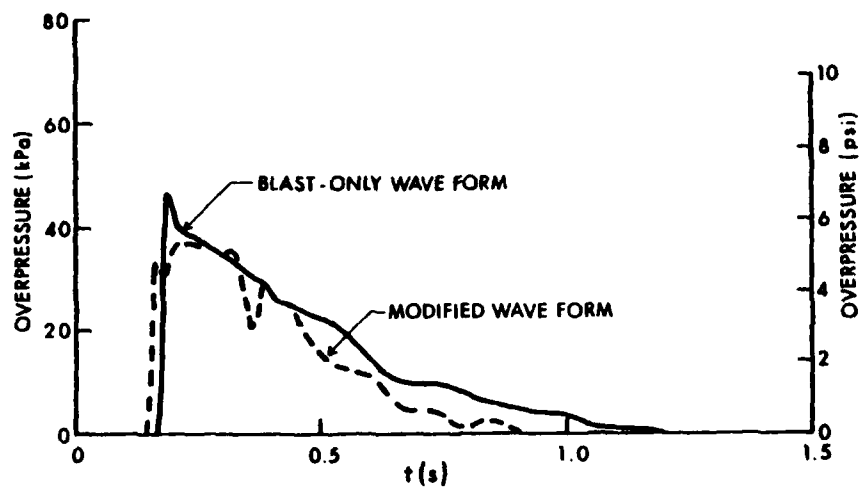
Figure 11. Predicted Static Pressure Modification
in Large Blast Simulator Without
Venting of TRS Products.

589

AN ADAPTIVE FINITE ELEMENT METHOD FOR
INITIAL-BOUNDARY VALUE PROBLEMS

Stephen F. Davis
Computational Interior Ballistics Branch
Interior Ballistics Division
Ballistic Research Laboratory, USA ARRADCOM
Aberdeen Proving Ground, Maryland 21005

ABSTRACT. A finite element method is developed to solve initial-boundary value problems for vector systems of partial differential equations in one space dimension and time. The method automatically adapts the computational mesh as the solution progresses in time and is, thus, able to follow and resolve relatively sharp transitions, such as mild boundary layers, shock layers, or wave fronts. This permits an accurate solution to be calculated with fewer mesh points than would be necessary with a uniform mesh.

The overall method contains two parts, a solution algorithm and a mesh selection algorithm. The solution algorithm is a finite element-Galerkin method on trapezoidal space-time elements, using either piecewise linear or cubic polynomial approximations and the mesh selection algorithm builds upon similar work for variable knot spline interpolation.

A computer code implementing these algorithms has been written and applied to a number of problems. These computations confirm that the theoretical error estimates are attained and demonstrate the utility of variable mesh methods for partial differential equations.

1. INTRODUCTION. In this paper we construct an adaptive grid finite element procedure to find numerical solutions to M-dimensional vector systems of partial differential equations of the form.

$$\underset{\sim}{u}_t + \underset{\sim}{f}(x, t, \underset{\sim}{u}, \underset{\sim}{u}_x) - [D(x, t, \underset{\sim}{u})\underset{\sim}{u}_x]_x = 0 ,$$

$$o < x < a, \ t > o$$

(1)

Subject to the initial and linear separated boundary conditions

$$\underset{\sim}{u}(x, o) = \underset{\sim}{u}^o(x), \ o < x < a$$

(2)

$$A_{11}(t) \ \underset{\sim}{u}(o, t) + A_{12}(t) \ \underset{\sim}{u}_x(o, t) = \underset{\sim}{b}_1(t) ,$$

(3)

$$A_{21}(t) \ \underset{\sim}{u}(a, t) + A_{22}(t) \ u_x(a, t) = \underset{\sim}{b}_2(t), \ t > o .$$

There are k_1 boundary conditions at $x = o$ and k_2 boundary conditions at $x = a$. We are primarily concerned with solving diffusion problems where D is positive definite and $k_1 + k_2 = 2M$; however, we will not restrict ourselves to this case, but instead we assume that conditions are specified so that problem (1)-(3) has an isolated solution.

Our goal is to construct a general purpose computer code which will solve (1)-(3) when the solution $\underset{\sim}{u}(x,t)$ contains sharp transitions such as boundary layers, shock layers, or wave fronts. In order to resolve such nonuniformities with a minimum number of mesh points, it is desirable to concentrate the mesh within the transition layers. Since these transition layers can move, it is necessary for the mesh to adapt itself to the evolving solution. Our approach involves (i) the accurate discretization of (1)-(3) on a nonuniform mesh and (ii) the determination of the proper mesh point locations.

The problem (1)-(3) is discretized using a finite element-Galerkin method on trapezoidal space-time elements. This approach is similar to that of Jamet and Bonnerot [3, 14] and it was chosen because it is generally easier to generate high order approximations to partial differential equations on a nonuniform mesh with finite element methods than with finite difference methods. The accuracy and order of convergence of these methods are analyzed in Davis [6] and are demonstrated experimentally in Section 4 of this paper.

Adaptive mesh selection strategies typically involve some recomputation of the solution. That is, an initial solution is computed on a coarse mesh and this is used to determine whether to accept the result, redo the calculation using more mesh points in some portion of the domain, redo the calculation using a more accurate method, or redo the calculation using some combination of more mesh points and a more accurate method. Algorithms of this type have been successfully applied in many areas of numerical computation but the expense involved in recomputing the solution of partial differential equations at possibly every time step eliminated these methods from consideration in this case.

Instead, we developed an algorithm which initially places a fixed number of mesh points in optimal locations and then attempts to move them so that their locations remain optimal. This type of algorithm has been used by Lawson [17], deBoor [7, 8], and Jupp [15] for variable knot spline interpolation. Their work motivated our mesh selection algorithms.

A different approach to this problem was proposed by Miller and Miller [18] and later extended by Galinas, et al. [10]. They approximated the solution of a parabolic partial differential equation by piecewise linear polynomials where both the polynomial coefficients and the mesh on which they were defined were unknown functions of time. These functions were determined by minimizing the residuals in a least squares sense. They found that the mesh points tended to coalesce in certain situations. To avoid this, they added a number of spring and damping terms to their discrete equations.

An advantage of the above approach is that it readily extends to higher dimensional problems. However, it couples the mesh selection method to the solution method and we do not believe that this is necessary or desirable. This coupling can dramatically increase the size of the discrete system without a corresponding increase in order of accuracy. Furthermore, the entire solution procedure fails if an acceptable mesh cannot be calculated. Under the same circumstances, our method continues to compute a solution on a suboptimal mesh. To date, detailed comparisons of the two methods have not been carried out but we hope to do this in a future paper.

In Section 2 of this paper, we sketch the derivation of a finite element-Galerkin approximation to (1)-(3) using trapezoidal space-time elements. In Section 3, we describe a practical and efficient mesh selection procedure that approximately minimizes the L_2 error of the computed solution. Readers desiring a more detailed derivation are referred to Ref. [5]. In Section 4, we apply the method to a number of problems and discuss the computed results. Finally, in Section 5, we present an overall discussion of this effort and some possible future efforts.

2. FINITE ELEMENT SOLUTION PROCEDURE. Problem (1)-(3) is discretized using a finite element-Galerkin on the strip S_n defined as follows:

$$S_n := \left\{ (x, t) \,\middle|\, 0 \le x \le a, \; t_n \le t \le t_{n+1} \right\} . \tag{4}$$

We choose a set of k linearly independent "test" or "weight" functions $v_i(x,t) \; \varepsilon \; C^\circ(S_n)$, $i = 1,2,\ldots,k$ and a set of k linearly independent "trial" functions $\phi_i(x,t) \; \varepsilon \; C^\circ(S_n)$, $i = 1,2,\ldots,k$. The solution $u(x,t)$ to problem (1)-(3) is approximated by $U(x,t)$ defined by

$$U(x, t) = \sum_{i=1}^{k} C_i(t) \, \phi_i(x, t) . \tag{5}$$

The coefficients $C_i(t)$ are chosen so that $U(x,t)$ satisfies

$$\mathcal{E}(\underset{\sim}{\mathit{U}}, v_i) := \int_{t_n}^{t_{n+1}} \int_0^a \left\{ - \underset{\sim}{\mathit{U}}\, v_{i_t} + \underset{\sim}{f}(x,\, t,\, \underset{\sim}{\mathit{U}},\, \underset{\sim}{\mathit{U}}_x)\, v_i \right.$$

$$\left. + D(x,\, t,\, \underset{\sim}{\mathit{U}})\, \underset{\sim}{\mathit{U}}_x\, v_{i,x} \right\} dxdt + \int_0^a \underset{\sim}{\mathit{U}}\, v_i dx \, \Bigg|_{t=t_n}^{t_{n+1}} \tag{6}$$

$$- \int_{t_n}^{t_{n+1}} D(x,\, t,\, \underset{\sim}{\mathit{U}})\, \underset{\sim}{\mathit{U}}_x\, v_i\, dt \, \Bigg|_{x=0}^{a} = 0 \quad,$$

$$i = 1,2,\ldots,k$$
$$n = 0,1,2,\ldots$$

$$P\underset{\sim}{\mathit{U}}(x,\, 0) = P\, \underset{\sim}{\mathit{u}}^{\,0}(x) \tag{7}$$

$$A_{11}(t_{n+1})\, \underset{\sim}{\mathit{U}}\,(0,\, t_{n+1}) + A_{12}(t_{n+1})\, \underset{\sim}{\mathit{U}}_x(0,\, t_{n+1}) = \underset{\sim}{b}_1(t_{n+1})$$

$$\tag{8}$$

$$A_{21}(t_{n+1})\, \underset{\sim}{\mathit{U}}(a,\, t_{n+1}) + A_{22}(t_{n+1})\, \underset{\sim}{\mathit{U}}_x(a,\, t_{n+1}) = \underset{\sim}{b}_2(t_{n+1})$$

where P is an interpolation operator. With appropriate modifications at the boundaries, Equations (6) and (8) define an MK dimensional nonlinear algebraic system for determining the Galerkin coordinates $C_i(t_{n+1})$, $i = 1,\ldots,k$ in terms of $\underset{\sim}{C}_i(t_n)$, $i = 1,2,\ldots,k$. Since $\underset{\sim}{C}_i(0)$, $i = 1,\ldots,k$ are determined by the initial conditions (7), Equations (5) and (8) define a marching algorithm for determining $\underset{\sim}{\mathit{U}}(x,t)$ in successive strips S_n, $n = 0,1,\ldots$.

It is apparent that both the accuracy of the computed solution and the ease with which it can be computed are strongly dependent on the choice of functions $\phi_i(x,t)$, $i = 1,\ldots,k$, and $v_i(x,t)$, $i = 1,\ldots,k$. How these functions are chosen is an active area of research. For this study, we choose

$$v_i(x,\, t) = \phi_i(x,\, t),\, i = 1,2,\ldots k \tag{9}$$

and define the functions $\phi_i(x,t)$, $i = 1,2,\ldots k$, by the following prescription.

We introduce a mesh $\{0 = x_1^n < x_2^n < \ldots < x_N^n = a\}$ at $t = t_n$ and a different mesh $\{0 = x_1^{n+1} < x_2^{n+1} < \ldots < x_N^{n+1} = a\}$ at $t = t_{n+1}$. If the corresponding points x_i^n and x_i^{n+1} are connected by a straight line denoted by $x_i(t)$, the strip S_n is divided into a set of $N-1$ trapezoids. We let T_i^n denote the trapezoid with vertices (x_i^n, t_n), (x_{i+1}^n, t_n), (x_{i+1}^{n+1}, t_{n+1}), and (x_i^{n+1}, t_{n+1}) (cf. Figure 1).

The functions $\phi_i(x,t)$ are choosen to have small support. In particular, we construct ϕ_i in such a way that ϕ_i is nonzero only on $T_{i-1}^n \cup T_i^n$. To do this we map each trapezoid T_i^n into the rectangle

$$R = \left\{ (\xi, \tau) \mid -1 \le \xi \le 1, \ 0 \le \tau \le 1 \right\} \tag{10}$$

and choose the $\phi_i(x,t)$ to be a function only of ξ on T_j^n, $j = i-1, i$. Currently, we allow $\phi_i(x,t)$ to be either a piecewise linear or a piecewise Hermite cubic polynomial in ξ on T_j^n.

This construction permits us to write $F(U,v)$ as the sum of contributions from each trapezoid. Thus,

$$F(U,v) = \sum_{i=1}^{N-1} \iint_{T_i^n} \left\{ -U v_t + f(x, t, U, v_x)v + D(x, t, U)U_x v_x \right\} dxdt$$

$$\tag{11}$$

$$= \sum_{i=1}^{N-1} \left[\int_{x_i(t)}^{x_{i+1}(t)} U v \, dt \right]_{t=t_n}^{t_{n+1}} - \left[\int_{t_n}^{t_{n+1}} D U_x v \, dt \right]_{x=0}^{a} = 0$$

The integrals in Equation (11) are transformed into integrals over R and evaluated numerically. We use the Trapezoidal rule to evaluate the τ in integrals and a three-point Guass-Legendre rule (cf. Abramowitz and Stegun [1], Chap. 25) to evaluate the ξ integrals. The resulting system of nonlinear algebraic equations is solved by the Newton-Raphson method.

3. ADAPTIVE MESH SELECTION STRATEGY. In Section 2, we developed a finite element method which computes solutions to systems of partial differential equations on nonuniform trapezoidal grids. In this section, we construct an algorithm which selects a grid at $t=t_{n+1}$ so that the L_2 norm of the error at t_{n+1} is approximately minimized. This algorithm is based on the variable knot spline interpolation work of deBoor [7, 8], Lawson [17], and Jupp [15].

It is well known (cf. [21, 22]) that errors in finite element-Galerkin methods for problems like (1)-(3) satisfy estimates of the form

$$||u - U||_{L_2} \le C ||u - PU||_{L_2} \tag{12}$$

where PU interpolates u in the trial space. Thus, the error in the computed solution to the partial differential equation can be bounded by an interpolation error. The following result (cf. eg., Pereyra and Sewell [20]) indicates how this interpolation error can be minimized for piecewise polynomial interpolants.

Lemma   Let $\Pi_N : = \{o = x_1 < x_2 < \ldots < x_N = a\}$ be a partition of $[o,a]$ into $N-1$ subintervals and let $u(x) \in C^{\ell+1}[o,a]$. The piecewise polynomial of degree ℓ on (x_i, x_{i+1}), $i = 1,2,\ldots,N-1$, that interpolates u on Π_N, has minimal L_2 error when the knots x_i, $i = 1,2,\ldots,N-1$ are chosen so that

$$h_i^{\ell+1} \; |u^{(\ell+1)}(\xi_i)| \; = E, \quad i = 1,2,\ldots,N-1 , \tag{13}$$

where $u^{(\ell)}$ is the ℓth derivative of u with respect to x, $\xi_i \in (x_i, x_{i+1})$, E is a constant and $h_i = x_{i+1} - x_i$.

This Lemma states that the interpolation error is minimized by selecting the partition in such a way that the quantity $h_i^{\ell+1}|u^{(\ell+1)}(\xi_i)|$ is equidistributed. Since the constant E is not known a priori, we follow Lawson [17] and Jupp [15] and *rewrite* Equation (13) in the form

$$p_i : = h_{i+1}/h_i = \left\{ |u^{(\ell+1)}(\xi_i)/u^{(\ell+1)}(\xi_{i+1})| \right\}^{1/(\ell+1)} , \tag{14}$$

$$i = 1,2,\ldots,N-2$$

This gives us N-2 equations for the N-1 unknown h_i's. The remaining equation is obtained by noting that

$$h_1 + h_2 + \ldots + h_{N-1} = x_N - x_1 \tag{15}$$

This can be expressed in terms of the p_i's by defining

$$Z : = 1 + p_1 + (p_1 p_2) + (p_1 p_2 p_3) + \ldots + (p_1 p_2 p_3 \cdots p_{N-2}) \tag{16}$$

and observing that

$$Z = (h_1 + h_2 + h_3 + \ldots + h_{N-1})/h_1$$

$$\tag{17}$$

$$= (x_n - x_1)/h_1$$

To obtain a new mesh, we choose $\xi_i = x_{i+1}$. Numerical experiments have shown that other choices of ξ_i do not much change the final grid point locations.

We compute $U^{(\ell+1)}(\xi_i)$ at $t=t_n$ by finite differences and assume that $U^{(\ell+1)}(\xi)$ is linear between data points. In addition, to prevent p_i from becoming infinite or indeterminate, we impose a lower bound on $|U^{(\ell+1)}(\xi)|$. If $|U^{(\ell+1)}(\xi)| \le \tau$ for some small, empirically chosen number τ, then $|U^{(\ell+1)}(\xi)| = \tau$.

The grid point locations are determined by successive approximation with relaxation as follows:

1. Set $\nu = 0$, $\Omega = 1$, $x_i^{(o)} = x_i^n$, $i = 1,2,\ldots,N$.

2. Calculate

$$p_i^{(\nu+1)} = \left[|U^{(\ell+1)}(x_{i+1}^{(\nu)})| / |U^{(\ell+1)}(x_{i+2}^{(\nu)})| \right]^{1/(\ell+1)} ,$$

$$i = 1,2,\ldots,N-2 ,$$

$$\hat{z}^{(\nu)} = 1 + p_1^{(\nu)} + (p_1^{(\nu)} p_2^{(\nu)}) + \ldots + (p_1^{(\nu)} p_2^{(\nu)} \ldots p_{N-2}^{(\nu)}) ,$$

$$h^{(\nu)} = (x_N^{(\nu-1)} - x_1^{(\nu-1)})/\hat{z}^{(\nu)}$$

and set

$$x_1^{(\nu)} = x_1^{(\nu-1)} , \quad x_N^{(\nu)} = x_N^{(\nu-1)}$$

3. If $\nu > 1$ and

$$|\hat{z}^{(\nu)} - z^{(\nu-1)}| \ge |z^{(\nu-1)} - z^{(\nu-2)}| , \quad \text{compute a new } \Omega$$

4. For $i = 1,2,\ldots,N-2$, calculate

$$\hat{x}_{i+1}^{(\nu)} = \hat{x}_i^{(\nu)} + h_i^{(\nu)}$$

$$h_{i+1}^{(\nu)} = h_i^{(\nu)} p_i^{(\nu)}$$

$$x_{i+1}^{(\nu)} = \Omega \hat{x}_{i+1}^{(\nu)} + (1-\Omega) x_{i+1}^{(\nu-1)}$$

5. Calculate

$$z^{(\nu)} = (x_N^{(\nu)} - x_1^{(\nu)})/(x_2^{(\nu)} - x_1^{(\nu)})$$

6. If $|z^{(\nu)} - z^{(\nu-1)}| < \varepsilon$, the error tolerance,

Then stop.

else set

$\nu = \nu + 1$ and go to 2.

The choice of relaxation factor is discussed in Isaacson and Keller [13, Chapter 3].

The algorithm just described computes an optimal grid at a time level t_n where the solution U^n is known. To obtain an estimate of the optimal grid at time level t_{n+1} prior to computing the solution there, it is necessary to extrapolate the optimal grids from previous time levels. It was somewhat surprizing to us that numerical experiments seemed to favor zero order extrapolation; i.e., the optimal grid computed at time level t_n is used at time level t_{n+1}. Multi-level extrapolation consistently overestimated the distance that a mesh point should move in one time step and then overcorrected this error in the next time step. In some cases, this caused the mesh to oscillate wildly when, in fact, the solution changed very little. On the other hand, the optimal mesh, determined at the previous time level, tended to follow the solution even when it contained rapidly moving fronts.

Under some circumstances, our mesh selection strategy could create severely distorted trapezoidal elements. This would cause an unacceptable degradation in the accuracy of the finite element method (cf. eg. [2], [4]). To prevent this, we modified the mesh selection scheme in such a way that element distortion is limited. Details can be found in Ref. [5].

4. COMPUTED RESULTS. In this section, we examine the performance of the previously described method on three test problems. These problems were chosen to exercise various facets of the method and illustrate how the method might be expected to perform on more difficult problems.

Example 1

We solve a simple linear heat equation

$$u_t = u_{xx} + f(x) , \quad 0 < x < 1, \ t > 0 \tag{18}$$

with initial conditions, boundary conditions, and source f chosen so that the exact solution is

$$u(x, t) = \tanh(r_1(x-1) + r_2 t) . \tag{19}$$

The solution (19) is a wave that travels in the negative x direction when r_1 and r_2 are positive. The values r_1 and r_2 determine the steepness of the wave and its speed of propagation. We created this problem to study how effectively the adaptive grid algorithm concentrates grid points in transition regions, follows moving fronts, and reduces errors below those of fixed grid methods.

Figure 2 shows the mesh computed by our adaptive mesh algorithm when applied to this problem with $r_1 = r_2 = 5$, uniform time step of $\Delta t = .01$, 10 elements per time step and linear approximations. Note that the grid points are concentrated in the region of maximum curvature and that they move to the left with the wave. As the wave front passes out of the domain, $|u_{xx}|$ becomes small compared to τ and the grid points move toward a uniform distribution. It is clear that the grid adapts to the solution and follows its progress as expected.

For all of the calculations presented here, the parameter τ was chosen as an approximation to the truncation error in $u^{(\ell+1)}$. Numerical experiments showed that this was small enough to permit the grid to concentrate where it should, but not so small that the grid oscillated wildly in an attempt to adapt itself to small randomly distributed errors. In general, it seems that τ should be chosen as small as possible but not so small that the grid oscillates when the solution is smooth.

Figure 3 shows the local error vs. x at t = 1.0, when our scheme is applied to this problem with $r_1 = r_2 = 100$, uniform time steps of $\Delta t = .01$, 20 elements per time step and linear approximations. Note that the mesh selection scheme concentrates points within the wave front and, thus, computes the wave accurately. Computations using a fixed, uniform grid experience large errors at the wave front. Note also that the mesh selection scheme attempts to distribute the local error evenly over the domain and, thus, as indicated in Section 3, approximately minimize the error in L_2.

Table 1 presents comparisons at t = 1.0 of computations with $r_1 = r_2 = 100$, using cubic approximations on uniform and variably spaced grids. Note that the variable grid computations are consistently more accurate than the uniform grid computations.

Example 2 (Burgers' Equation)

$$u_t = - u u_x + \varepsilon u_{xx} , \quad 0 < x < 1, \quad t > 0$$

$$u(x, o) = \sin \pi x, \quad u(o, t) = u(1, t) = 0$$

$$\tag{20}$$

and

$$\varepsilon = 5 \times 10^{-3} .$$

It is well known that the solution to this problem is a wave that steepens and moves to the right until a shock layer forms at x = 1. After a time of $O(1/\epsilon)$ the wave dissipates and the solution decays to zero. Figures 4 and 5 show the results of computations on this problem using linear approximations on a uniform mesh and a variable mesh with a constant time step $\Delta t = 0.1$ and 10 elements per time step. The results in Figure 4 are typical of finite difference or finite element calculations for this problem. Spurious oscillations develop in the computed solution unless the mesh width is of the same order as the width of the shock layer, $O(\sqrt{\epsilon})$ in this example. The variable mesh results in Figure 5 largely surpress these oscillations by automatically concentrating the mesh in the shock region as the wave steepens.

When this example is solved using cubic approximations on a uniform mesh we find that the solution U_i^n is computed accurately at the nodes but there are large errors in the slope of the solution U_{xi}^n when the mesh is not suitably fine in the shock region. This effect is exhibited in Figure 6 where the solution at t = 0.6 is shown for a calculation performed with $\Delta t = 0.1$ and N = 10. The cubic Hermite trial functions were used to calculate the solution between mesh points.

Once again these problems are corrected when the mesh adapts with the solution. Figure 7 shows the results of a similar computation using cubic approximations on a variable mesh. Both the function values and slope values are computed accurately at the nodes.

Example 3

$$b_t = \left[\mu(s)b_x\right]_x - \left[b\chi(s)s_x\right]_x$$

$$s_t = -k(s)b \tag{21}$$

$$o < x < 5, \ t > o \ .$$

This two component nonlinear system was studied by Keller and Odell [16] as a model for the chemotactic motion of bacteria. The quantity $b(x,t)$ denotes bacterial density and s(x,t) denotes the concentration of critical substrate (bacterial food). If the functions μ, χ, and k satisfy conditions derived by Keller and Odell [16], Equations (21) have traveling wave solutions. These solutions have been computed by Odell and Keller [19] and are interpreted as traveling bands of bacteria. For our study we chose k(s) = 1, $\mu(s) = \mu_o$, and $\chi(s) = \delta_o/s$ where μ_o and δ_o are constants. The initial conditions are shown in Figure 8a and the boundary conditions are

$$b(o, \ t) = b(5, \ t) = 0, \ S(o, \ t) = 1$$

We solved this problem for $\delta_o/\mu_o = 2$ using cubic approximations, uniform time steps of $\Delta t = .005$ and 50 elements per time step. The computed solutions at t = 0, 0.1, 0.5, and 1.0 are shown in Figures 8a, b, c, and d, respectively.

This example was chosen to show that, with appropriate modification, our adaptive grid algorithm may be applied to vector systems of equations. Details of these modifications can be found in Ref. [5].

5. DISCUSSION AND CONCLUSIONS. The computations presented in the last section show that it is possible to construct an accurate and stable adaptive finite element method for nonlinear systems of partial differential equations and that such techniques offer advantages over fixed grid methods. In particular, we have shown that the error estimates obtained by Davis [6] are actually realized in practice and that the adaptive mesh algorithm correctly concentrates the mesh in a sharp transition and is able to follow moving fronts. Examples 2 and 3 of Section 4 indicate that this method is also useful for nonlinear equations and vector systems of equations.

In the present study, we used piecewise polynomial functions for both the trial and test spaces. However, recent work of Flaherty and Mathon [9], Heinrich, et al. [11], and Hemker [12] indicates that exponential and "upwinded" polynomial functions may give superior test spaces for singularly perturbed problems. We plan to incorporate these functions into our methods.

All of our calculations were performed with a constant time step. Examples 2 and 3 of Section 4 indicate that it would be most desirable to be able to vary the time step during the calculation. Our code presently allows for this, but as yet, we have not implemented an algorithm to adaptively alter the time step. We plan to add this feature to our code shortly.

Other areas for future study include free boundary problems and higher dimensional problems. The present work has shown that it is possible to construct a proactical adaptive finite element method. Future work must refine this method and test it on a greater variety of problems.

REFERENCES

1. M. Abromowitz and I.A. Stegun, Handbook of Mathematical Functions, Dover, New York, 1965.

2. I. Babuska and A.K. Aziz, "On the Angle Condition in the Finite Element Method," SIAM J. Numer. Anal., Vol. 13 (1976), pp. 214-226.

3. R. Bonnerot and P. Jamet, "Numerical Computation of the Free Boundary for the Two Dimensional Stefan Problem by Space-Time Finite Elements," J. Comp. Phys., Vol. 25 (1977), pp. 161-181.

4. P.G. Ciarlet and P.A. Raviart, "Interpolation Theory Over Curved Elements with Applications to Finite Element Methods," Computer Methods in Applied Mechanics and Engineering, Vol. 1 (1972), pp. 217-249.

5. S.F. Davis and J.E. Flaherty, "An Adaptive Finite Element Method for Initial-Boundary Value Problems for Partial Differential Equations," SIAM J. Sci. & Stat. Comp., to appear.

6. S.F. Davis, "An Adaptive Grid Finite Element Method for Initial-Boundary Value Problems," Ph.D. Dissertation, Rensselaer Polytechnic Institute, Troy, New York, 1980.

7. C. DeBoor, "Good Approximation by Splines with Variable Knots II," Conference on the Numerical Solutions of Differential Equations, Lecture Notes in Math., Vol. 363, Springer Verlag, New York, 1978.

8. C. DeBoor, "A Practical Guide to Splines," Applied Mathematical Sciences, Vol. 27, Springer Verlag, New York, 1978.

9. J.E. Flaherty and W. Mathon, "Collocation with Polynomial and Tension Splines for Singularly Perturbed Boundary Value Problems," SIAM J. Sci. & Stat. Comp., Vol. 1 (1980), pp. 260-289.

10. R.J. Galinas, S.K. Doss, and K. Miller, "The Moving Finite Element Method: Application to General Partial Differential Equations with Multiple Large Gradients," J. Comp. Phys., Vol. 40 (1981), pp. 202-249.

11. J.C. Heinrich, P.S. Huyakorn, O.C. Zienkiewicz, and A.R. Mitchell, "An Upwind Finite Element Scheme for Two-Dimensional Convective Transport Equations," Int. J. Numer. Meths. Engr., Vol. 11 (1977), pp. 131-143.

12. P.W. Hemker, "A Numerical Study of Stiff Two-Point Boundary Problems," Ph.D. Dissertation, Mathematisch Centrum, Amsterdam, 1977.

13. E. Isaacson and H.B. Keller, Analysis of Numerical Methods, J. Wiley and Sons, New York, 1966.

14. P. Jamet and R. Bonnerot, "Numerical Solution of the Eulerian Equations of Compressible Flow by a Finite Element Method Which Follows the Free Boundary and Interfaces," J. Comp. Phys., Vol. 18 (1975), pp. 21-45.

15. D.L. Jupp, "Approximations to Data by Splines with Free Knots," SIAM J. Numer. Anal., Vol. 15 (1978), pp. 328-343.

16. E.F. Keller and G.M. Odell, "Necessary and Sufficient Conditions for Chemotactic Bands," Math. Biosci., Vol. 27 (1975), pp. 309-317.

17. C.L. Lawson, "Segmented Rational Minmax Approximations, Characteristic Properties and Computational Methods," J.P.L. Technical Report, pp. 32-57, 1963.

18. K. Miller and R. Miller, "Moving Finite Elements," to be published.

19. G.M. Odell and E.F. Keller, "Traveling Bands of Chemotactic Bacteria Revisited," J. Theor. Biol., Vol. 56 (1976), pp. 243-247.

20. V. Pereyra and E.G. Sewell, "Mesh Selection for Discrete Solution of Boundary Problems in Ordinary Differential Equations," Numer. Math., Vol. 23 (1975), pp. 261-268.

21. G. Strang and G.J. Fix, An Analysis of the Finite Element Method, Prentice Hall, Englewood Cliffs, New Jersey, 1973.

22. M.F. Wheeler, "A. Priori, L_2 Error Estimates for Galerkin Approximations to Parabolic Partial Differential Equations," SIAM J. Numer. Anal., Vol. 10 (1973), pp. 723-759.

TABLE 1

Results of Computations at $t = 1$ for Example 1 with $r_1 = r_2 = 100$ using Cubic
Approximations on Uniform and Variably Spaced Grids.

N	Δt	Uniform Spacing		Variable Spacing	
		$\|\|e\|\|_{L_2}$	$\|\|e\|\|_\infty$	$\|\|e\|\|_{L_2}$	$\|\|e\|\|_\infty$
10	0.01	0.607 E-1	0.801 E-1	0.130 E-1	0.232 E-1
14	0.005	0.319 E-1	0.257 E-1	0.332 E-2	0.602 E-2
20	0.01	0.214 E-1	0.394 E-1	0.167 E-1	0.951 E-1
	0.005	0.185 E-1	0.309 E-1	0.483 E-2	0.950 E-2
	0.0025	0.138 E-1	0.405 E-2	0.353 E-3	0.170 E-2
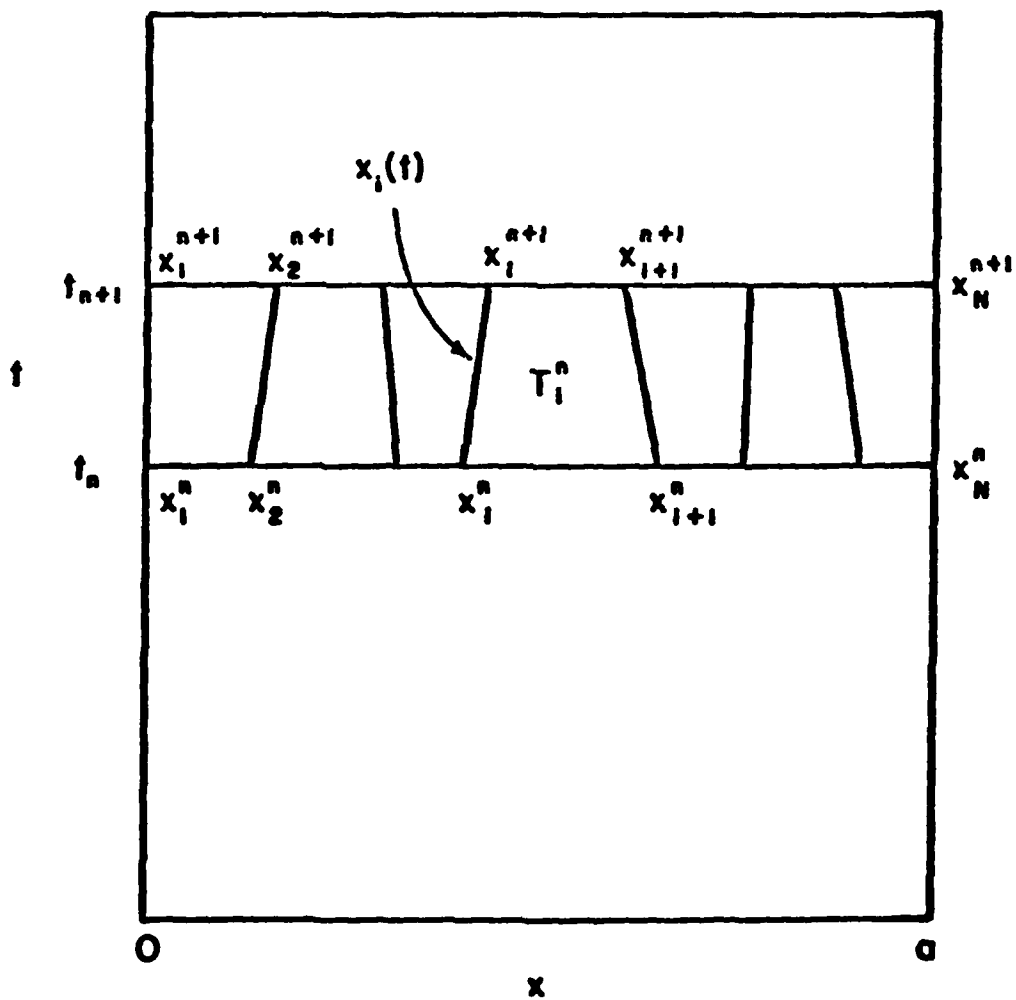
Figure 1: Space-time discretization for the time step $t_n \leq t \leq t_{n+1}$.
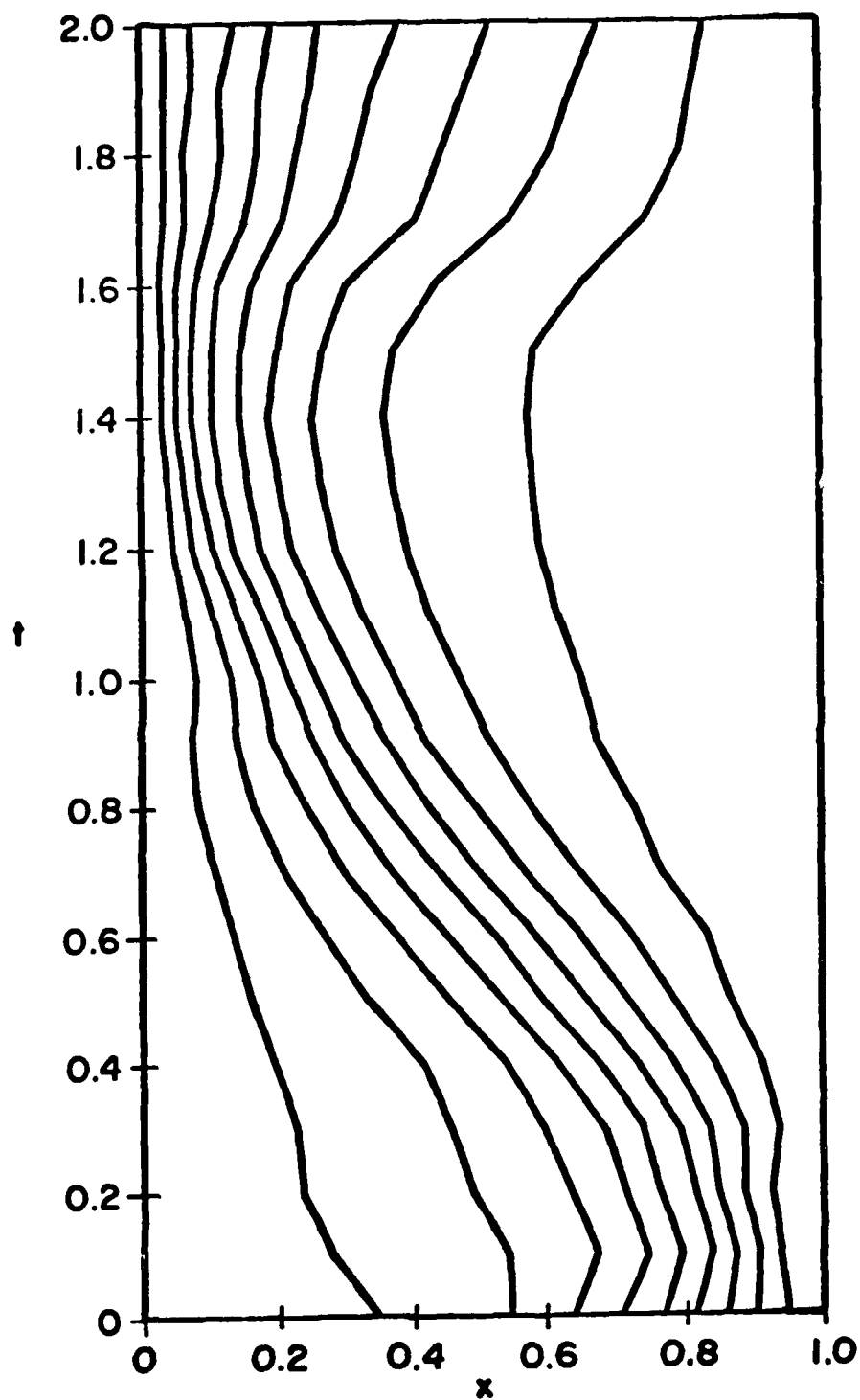
Figure 2: Mesh selected for Example 1 with $r_1 = r_2 = 5$, uniform time steps of $\Delta t = 0.1$, $N = 10$, and linear approximations.
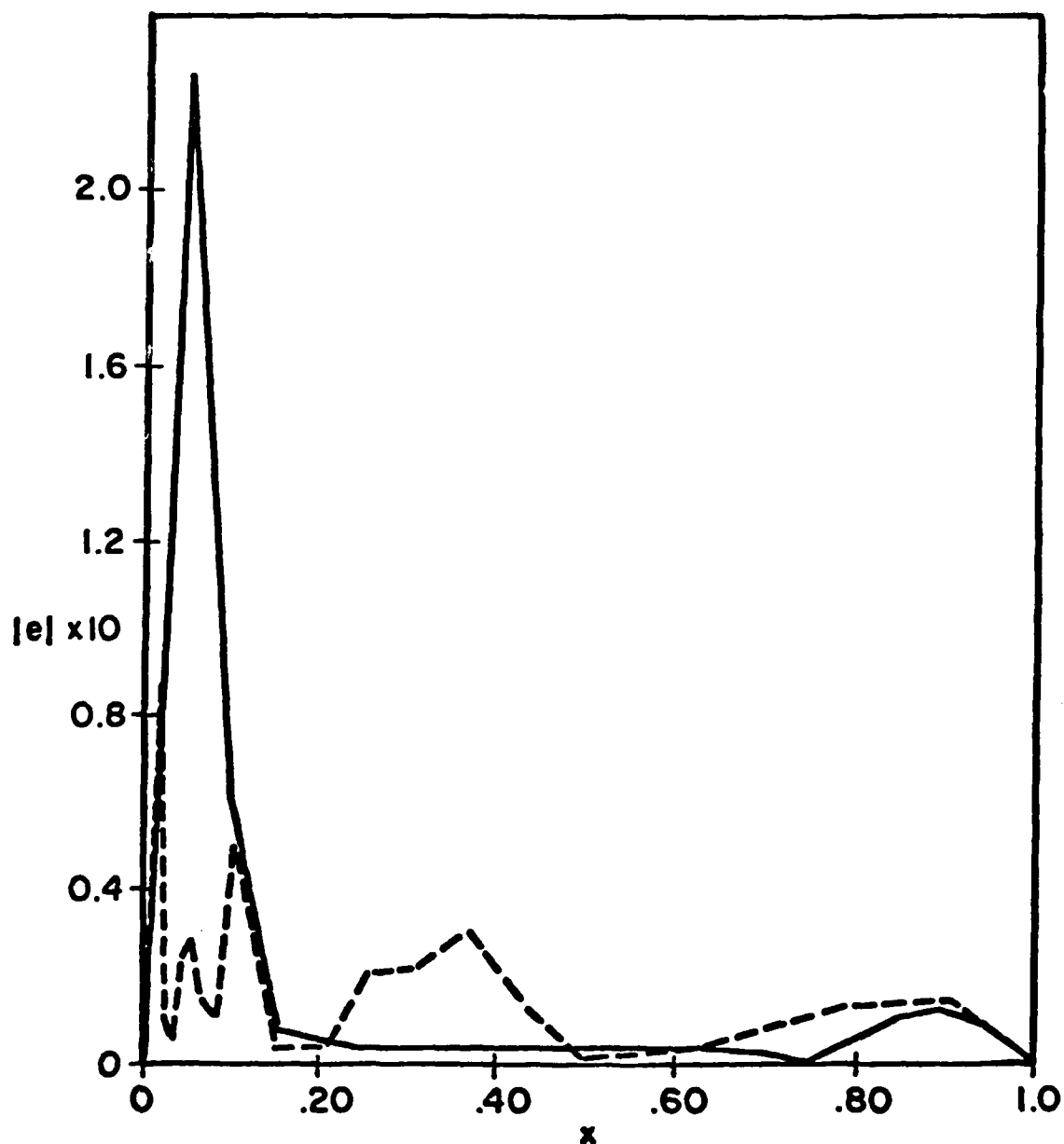
Figure 3: Local error at t = 1.0 for Example 1 with $r_1 = r_2 = 100$, uniform time steps of $\Delta t = 0.01$, N = 20, and linear approximations. The solid curve was computed on a fixed uinform mesh, the broken curve on a variable mesh.
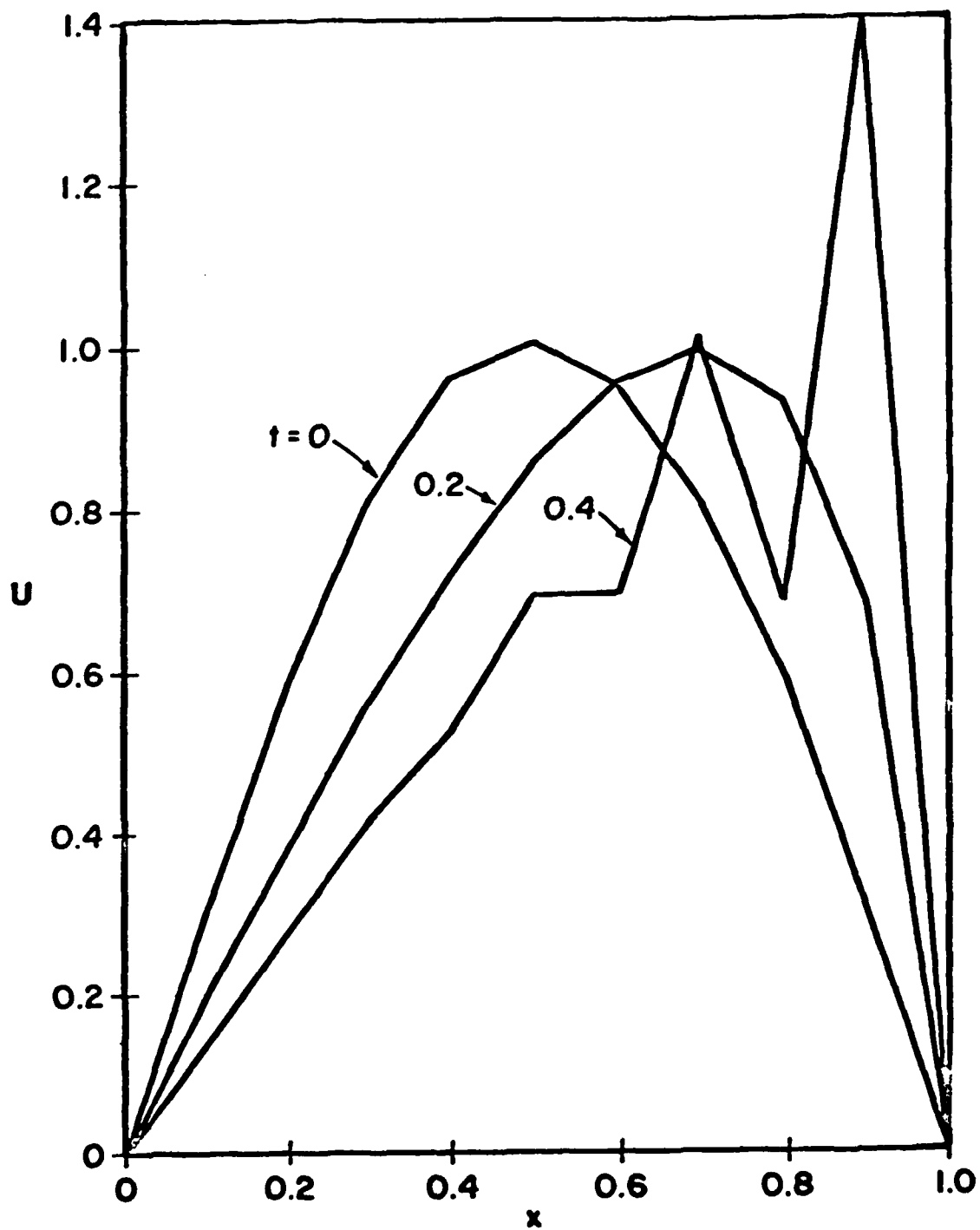
Figure 4: Solution of Example 2 for various values of t using linear approximations on a uniform mesh with $\Delta t = 0.1$ and $N = 10$.

608

Figure 5: Solution of Example 2 for various values of t using linear approximations, uniform time steps of $\Delta t = 0.1$, and a variable mesh with $N = 10$ elements per time step.

Figure 6: Solution of Example 2 at t = 0.6 using cubic approximations on a uniform mesh with Δt = 0.01 and N = 10.

Figure 7: Solution of Example 2 for various values of t using cubic approximations uniform time steps of $\Delta t = 0.01$, and a variable mesh with N = 10 elements per time step.

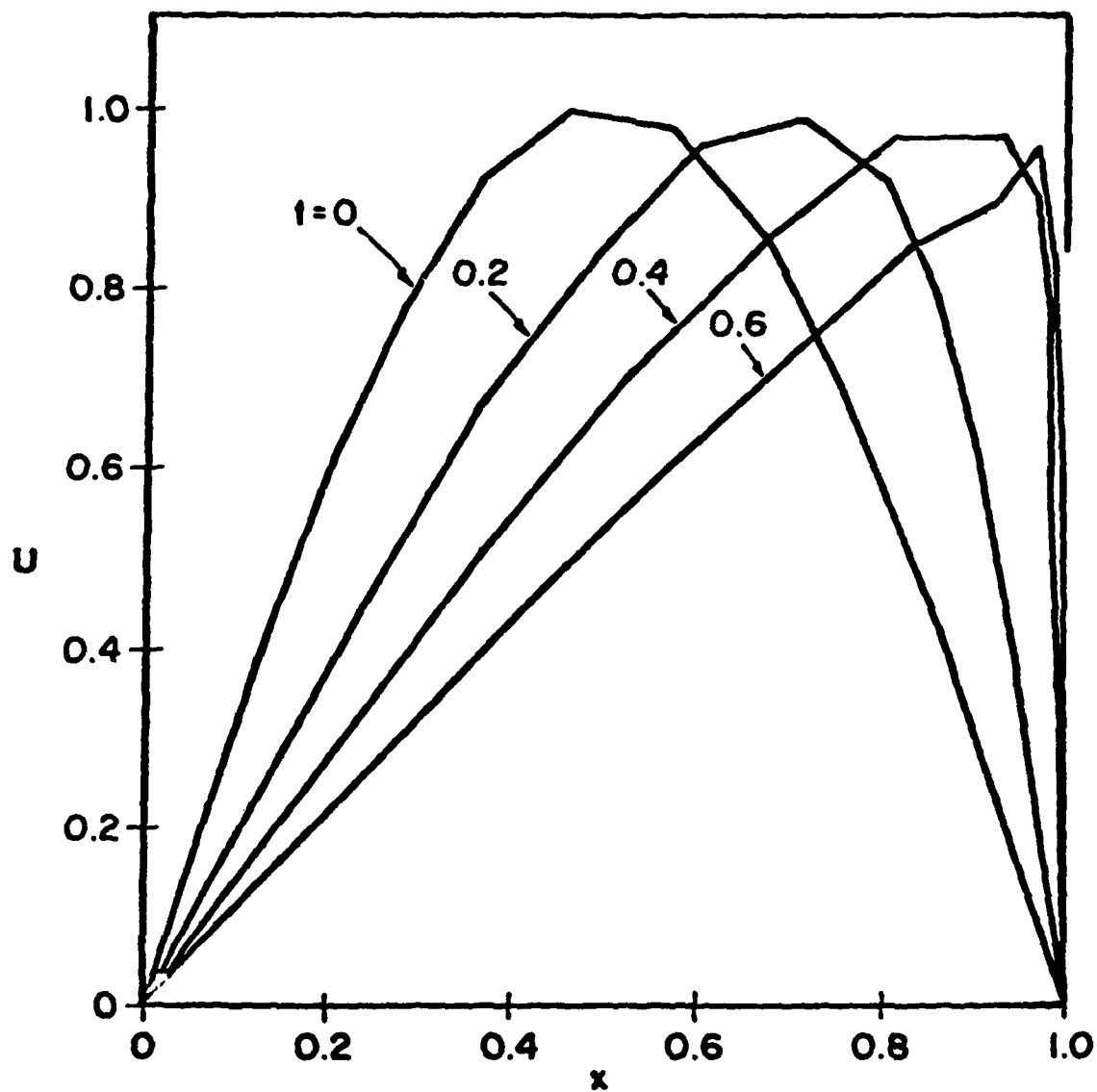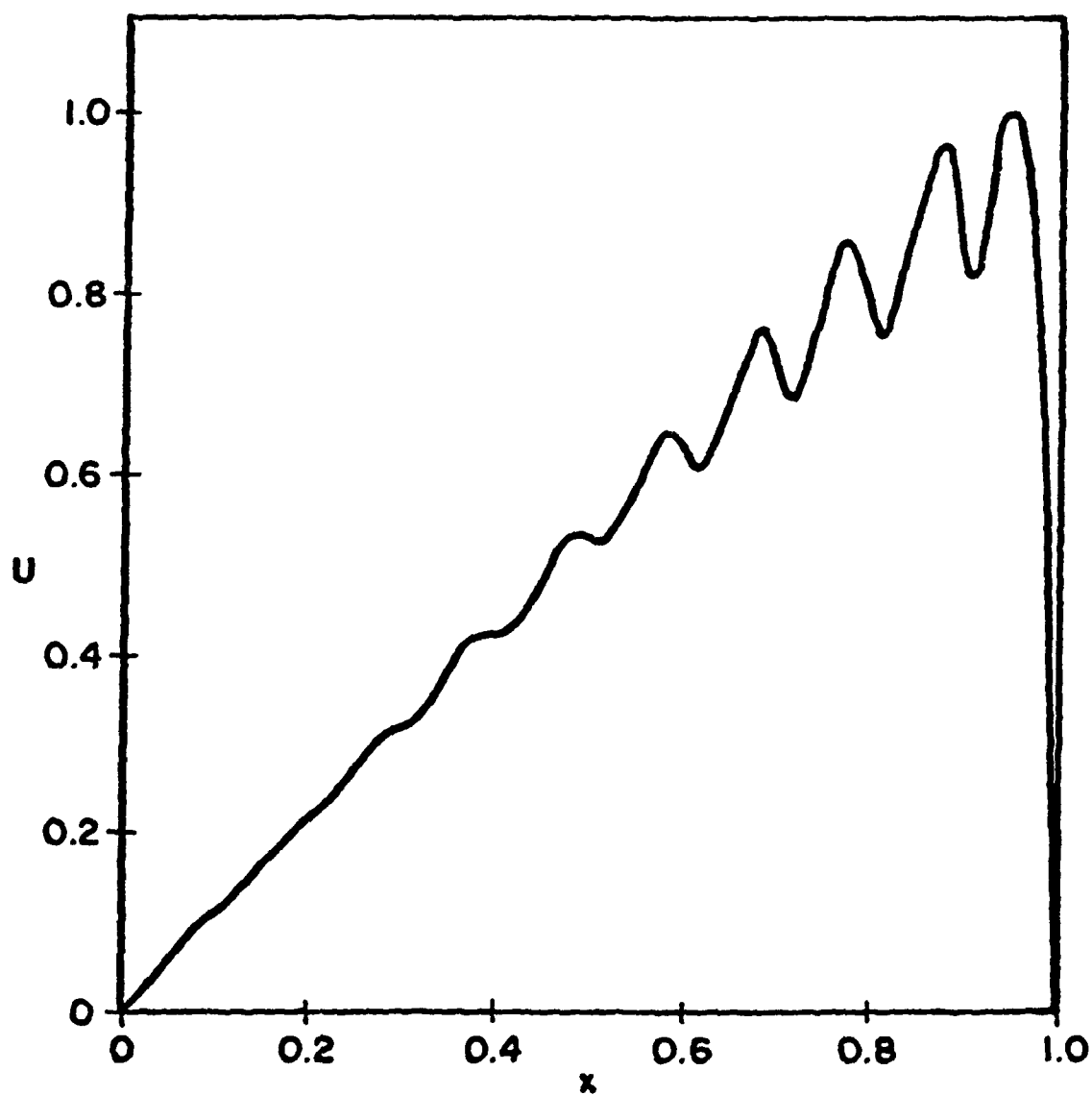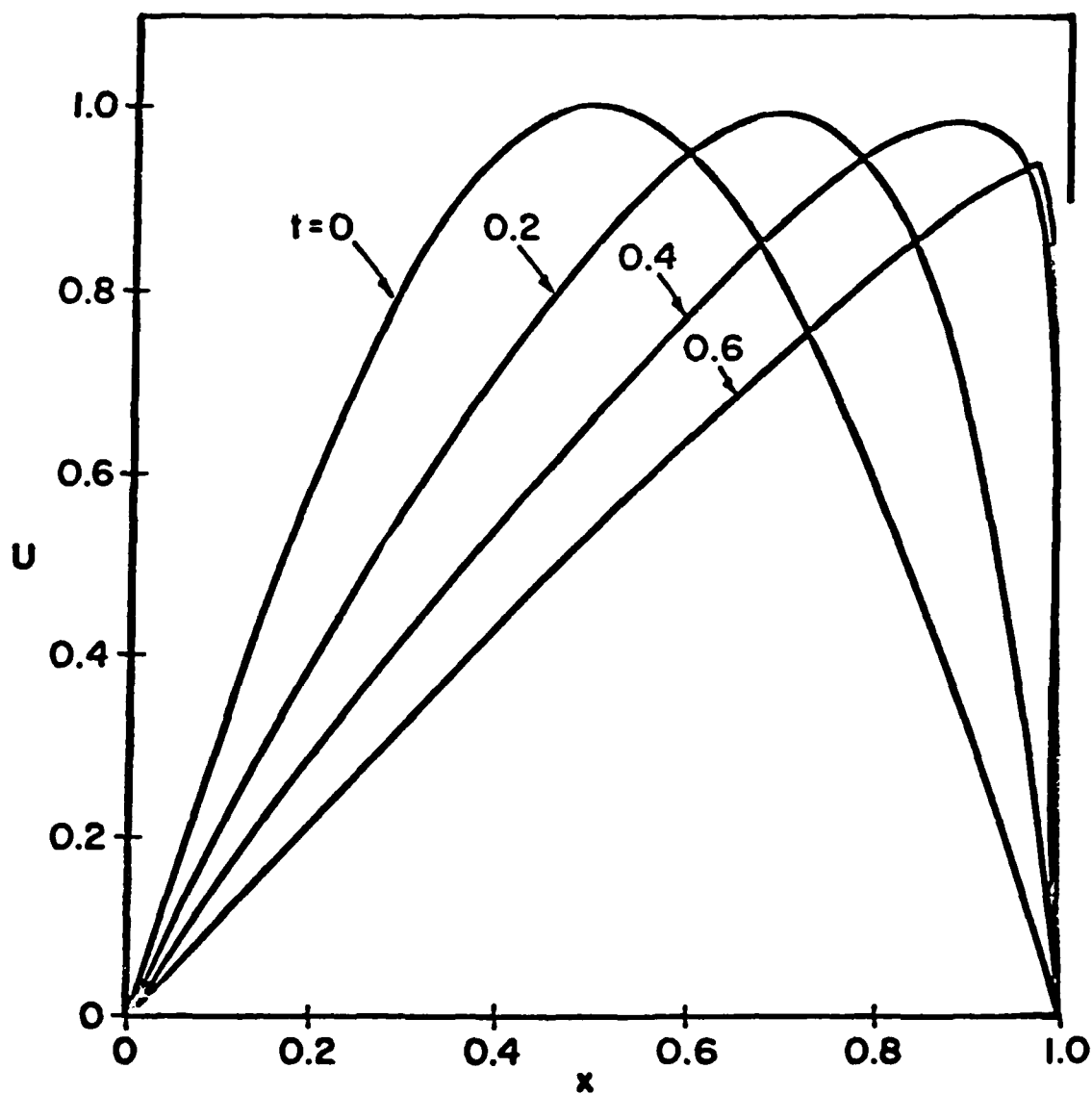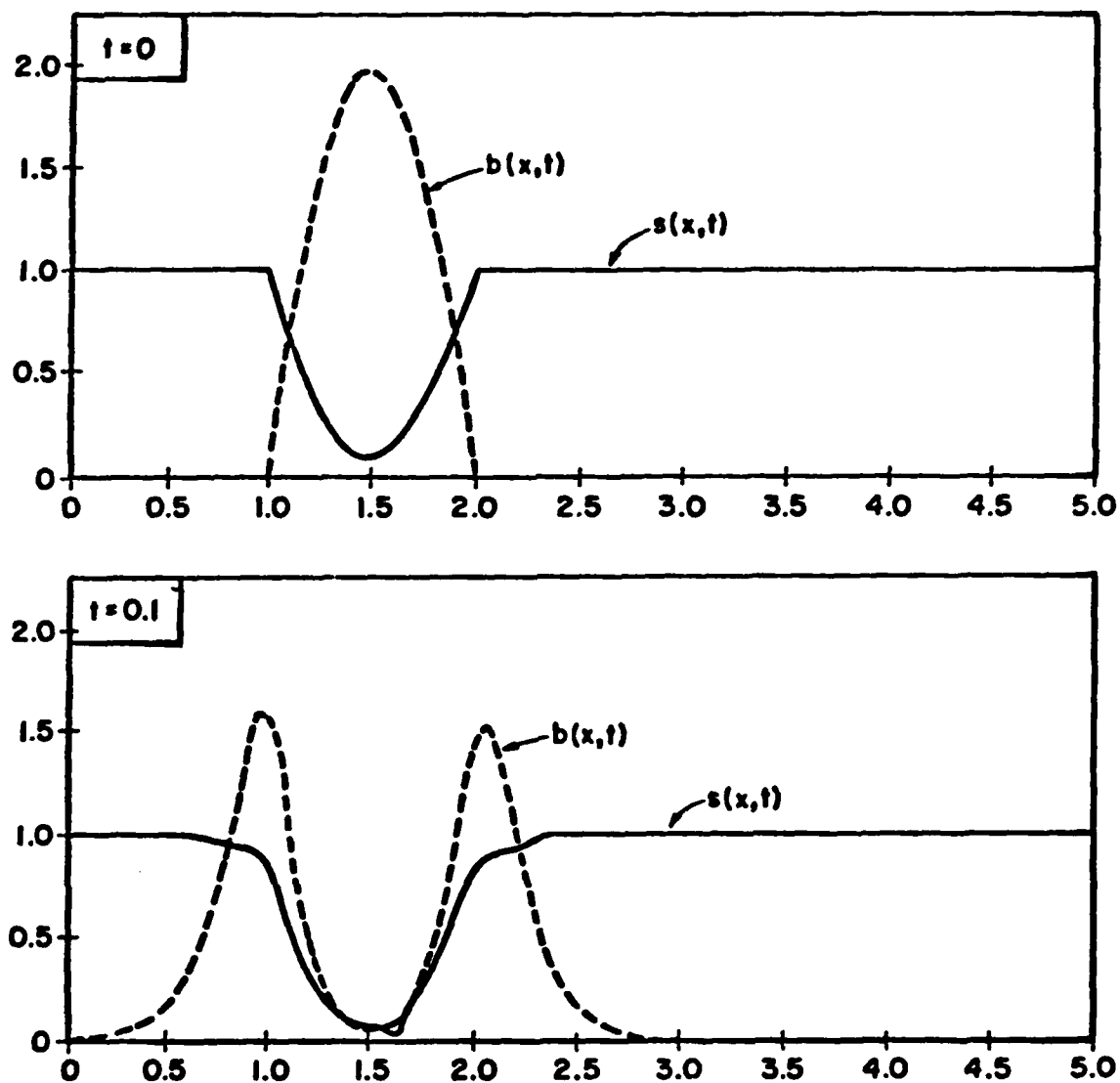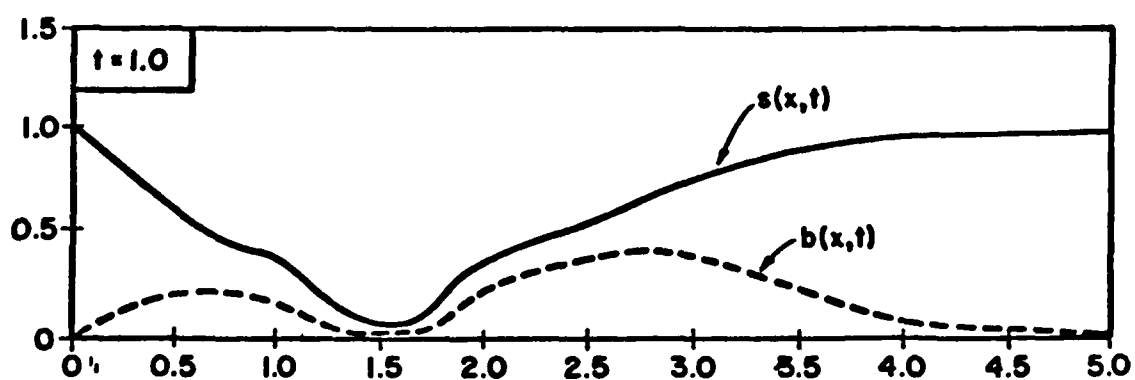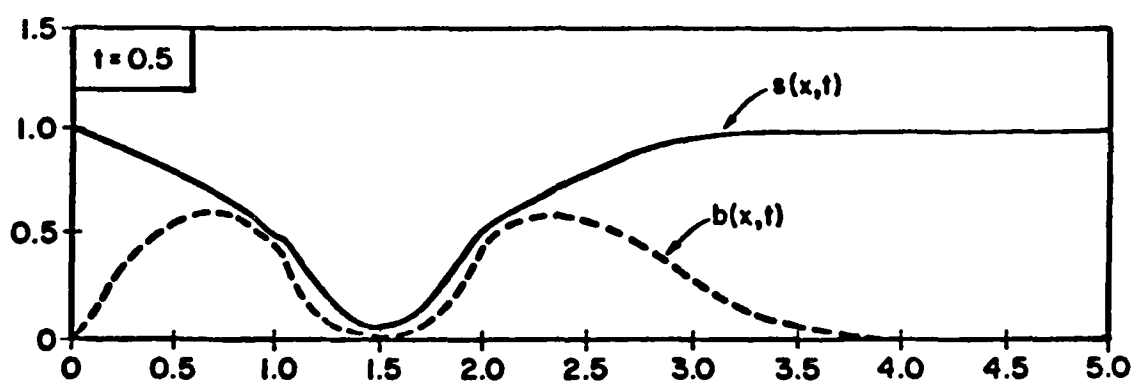Figure 8: Computational results for Example 3 with $\delta_o/\mu_o = 2.0$ using uniform time steps of $\Delta t = 0.005$, $N = 50$, and cubic approximations at $t = 0$, 0.1, 0.5, and 1.0.

MODELING OF GASEOUS AND
HETEROGENEOUS DETONATION PHENOMENA*

Martin Sichel
Department of Aerospace Engineering
The University of Michigan
Ann Arbor, MI 48109

ABSTRACT.   Detonation phenomena in which the structure of the reaction zone affects the behavior of the detonation are considered.   Various theories for predicting the energy needed for the high explosive or direct initiation of detonations in gaseous media and in sprays are described.   The determination of the critical initiation energy appears to be associated with a singularity of the governing equations.   The structure of spray detonations is described for liquid fuel sprays with both a high and low vapor pressure. Single fluid, two fluid, and explosion theories which have been used for modeling spray detonations are outlined.   It is shown that the droplet breakup process and the ignition of the microspray which is formed during drop disintegration are the central phenomena governing the behavior of spray detonations.   Attempts at modeling these basic processes are discussed. It is remarkable that complex combustion processes often lead back to the very basic problem of ignition.

I. INTRODUCTION.   A number of interesting mathematical problems arise in modeling the phenomena which are involved in the initiation and propagation of gaseous and two-phase detonations.   The objective of this paper is to point out and isolate some of these problems.   Modeling of combustion phenomena is generally successful only if done in close concert with experimental measurements.   Therefore, the physical phenomena of interest will first be described, at least qualitatively using experimental data where it is available; then, various attempts at analytical modeling and some of the mathematical problems that arise as a result will be presented.

Deflagrations and detonations are the main types of reaction fronts encountered in nature.   On the surface it appears that the mathematics of such reaction fronts is thoroughly understood, and certainly there is an extensive discussion of the conditions governing their propagation in the well known monograph by Courant and Friedrichs [1] .   A key result is that the propagation of subsonic deflagrations is governed by the actual structure of the reaction front, and the structure of such laminar flames or deflagrations has been the subject of intense analytical and numerical research during the past decade.   Detonations can be treated as supersonic

---

exothermic discontinuities and the velocity of a steadily propagating detonation is structure independent. Self-supporting detonations generally propagate at the Chapman Jouguet (C-J) velocity determined by the condition that the fluid velocity is sonic with respect to the detonation front at the end of the reaction zone. Computation of the propagation velocity and the pressure, density and temperature ratios across such C-J waves requires a tedious calculation of the chemical equilibrium at the end of the reaction zone; however, in the all gaseous case standard computer codes are available for computing these C-J conditions [2], [3].

Even in the standard case of steadily propagating detonations, the situation is no longer straighforward when the fuel and oxidizer exist as different phases. Then changes of phase within the detonation front must be taken into account in establishing the C-J conditions [4]. The many possibilities with regard to phase are indicated in Table I below.

	Single Phase			Two Phase	
Fuel	gas	solid	liquid	solid (dust)	liquid (droplets)
Oxidizer	gas	solid	liquid	gas	gas

Table I: Phase Classification of detonations.

Only gaseous and two phase detonations will be considered here. The literature dealing with solid and liquid explosives, especially with regard to military applications, is extensive and this area represents a separate field in itself.

Consideration of unsteady flame and detonation propagation opens a completely new mathematical problem area. Starting with the basic work of Sedov [5], and exemplified by more recent studies [6], [7], a series of self similar solutions dealing with unsteady propagation of deflagrations, detonations and shock waves have been explored. The generation of blast waves and detonations by deflagration waves [8], [9] is perhaps of special interest since it demonstrates the coupling between the two types of combustion fronts.

The processes described above can be modeled without considering the detailed structure of the detonation front. There are, however, a number of important detonation phenomena which cannot be understood without considering the detailed structure of the detonation front, and these are the focus of the present paper. Spin detonations and the diameter dependence of the propagation velocity in tubes are among the earliest known structure

dependent detonation properties. Some of the earliest observations of spin detonations are discussed by Lewis and von Elbe [10] ; a more recent example is provided by the observation of CH_4-air detonations by Wolański et al [11] . Figures 1 and 2 from Ref. [11] show a spark Schliern photo and schematic sketch of such a wave. The effect of tube diameter is closely related to the well-known diameter effect in the case of unconfined solid explosives and is discussed extensively in the milestone paper of Wood and Kirkwood [12] . The influence of tube diameter upon gaseous detonations velocity depends on the interaction between the wall boundary layer and the structure as shown in the pioneering analysis of Fay [13] which has provided the basic model for most subsequent analyses of this problem. Detonability limits as well as the quenching diameter of detonations propagating through tubes also are intimately related to the structure as indicated by the kinetic analysis of Belles [14] and the detailed study of wall effects by Tsuge [15] .

Detonations can be induced or initiated in a combustible material by a deflagration as already mentioned above or by the sudden release of a finite amount of energy as by a high explosive. This latter mode of initiation is sometimes called direct initiation and is intimately coupled to the behavior of the reaction zone. This interdependence was recognized by Zel'dovitch et al [16] in formulating a qualitative criterion for estimating the minimum high explosive charge needed to induce a detonation in a combustible medium. These authors stated that the direct initiation of spherical detonations requires that when the pressure behind the initiating blast has decayed to the C-J value, the shock radius must be at least of the order of the reaction zone thickness of the mixture.

The reaction zones of steadily propagating detonations are not necessarily one dimensional but frequently are made up of a series of cells generated by transverse waves. This phenomenon is also intimately related to the structure of the wave as discussed by Strehlow [17] and by Fickett and Davis [18] . Under some conditions detonations may propagate in an oscillatory fashion as in the case of a blunt body propagating through a combustible mixture. This behavior is illustrated by the striking herringbone pattern behind a blunt projectile moving through a hydrogen-air mixture shown in Figure 3 which is taken from [19] . This oscillatory behavior is also intimately related to the structure of the reaction front.

It is in the interaction of the structure and propagation that some of the most interesting problems in detonation theory arise. In gaseous detonations it is necessary to consider the interaction between the kinetics of the combustion reaction and the fluid dynamics of propagation. In two phase detonations, there is the added complication of the droplet or particle

combustion mechanisms. Before proceeding to a more detailed consideration of these problems, it appears appropriate to briefly discuss some of the models which have been proposed for the structure of a detonation front.

The simplest model for the structure is that of Zel'dovitch, von Neumann, and Doering [18] in which the detonation is treated as a shock discontinuity followed by a reaction zone in which the heat of combustion is released. The reaction zone is terminated by the C-J plane where the velocity relative to the detonation becomes sonic. Either an exact or approximate kinetic scheme for the combustion reaction is needed to determine the extent and structure of this reaction zone. A qualitative sketch of the variation of reaction zone pressure and temperature compiled using this model is shown in Figure 4(a). The complexity and uncertainity of the kinetics of most combustion reactions has led to the use of approximate reaction zone models in many cases. Two of the most common which are discussed in detail by Korobeinikov et al [20] are the two front and the combined induction-reaction zone models. In the two front model an induction zone of length ℓ_I in which there are no measurable chemical changes, is followed by a discontinuous reaction front in which all the heat release takes place as shown in Figure 4(b). In the combined induction-reaction zone model, an induction zone of length ℓ_I is followed by a reaction zone of length ℓ_R where the combustion heat release occurs as shown in Figure 4(c).

The models described above are steady and one dimensional; however, the unstable waves (Fig. 3) and the waves with cellular structure [17] are anything but steady and one dimensional. Nevertheless, the local structure of the wave generally is treated using models like those discussed above and in the case of overdriven detonations, the steady structure appears to provide a reasonable description. Thus, Figure 5 taken from [21] shows the structure of an overdriven detonation induced is an H_2-O_2 mixture by a sphere traveling at a velocity above the C-J value.

The structure of detonations propagating through clouds of fuel droplets suspended in a gaseous oxidizer is governed by the mechanism of droplet breakup as well as by the kinetics of the fuel-oxidizer reactions [22],[23]. The resultant structure differs drastically from that of a pure gaseous detonation, and depends upon the average droplet diameter, the droplet size distribution, the vapor pressure of the liquid fuel and a host of other parameters. If the droplets are very small or have a high enough vapor pressure, the behavior of such spray detonations may also revert to that of a purely gaseous detonation. An illustration of the complexities involved is provided by the Schlieren photograph of a detonation propagating through a row of 2600μ droplets of diethylcyclohexane shown

in Figure 6(a). Figure 6(b) is a schematic sketch explaining some of the phenomena shown in Figure 6(a). Right after passage of the leading shock, the droplet is subject to the supersonic flow induced by this shock wave so that a bow shock immediately forms upstream of the droplet. As a result of this induced flow, the droplet begins to broaden and a micromist which is stripped from the forward surface of the droplet is entrained in the droplet wake. This behavior is particularly well illustrated in Figure 7 which shows a nonburning 2700μ drop 14μ sec after the passage of a Mach 3.5 shock. In the case of burning droplets, the wake explodes after sufficient time has elapsed as shown in Figure 6(a).

A number of dust air and dust oxygen mixtures have also been found to be highly detonable [24], [25], and, in fact, grain dust has been found to be a highly explosive material. A laser photograph of an oats-oxygen and oats-air detonation is shown in Figure 8. The phenomena which govern the structure of dust detonations are quite different from those involved in spray detonations. The particles are again accelerated by the supersonic flow induced by the leading shock, but now do not shatter. The ignition or induction mechanism now depends mainly upon the convective heating of the particle, the heterogeneous reactions which can occur both on the surface and within the porous interior of the particle, and upon the reaction of the volatiles which are evolved as the particle temperature increases. Radiation which is generally ignored in gaseous and spray detonations, appears to play an important role in dust detonations. The difference between the droplet or dust and gas velocities can also have a significant effect upon the structure of two phase detonation and in some cases, appears to result in unstable behavior [26].

Some of the many phenomena touched by the discussion above will now be described in greater detail starting with the problem of the direct initiation of gaseous detonations. This will be followed by a discussion of the propagation of detonations through sprays.

II. THE DIRECT INITIATION OF GASEOUS DETONATIONS.
The sudden release of energy in a gaseous combustible fuel oxidizer mixture causes a decaying blast wave to propagate into the mixture. The high temperature behind this wave results in a combustion front at some induction distance ℓ_I behind the leading shock. Depending on the amount of energy which is released, the induction length ℓ_I continually increases until the blast wave has completely decayed, or the length ℓ_I reaches some limiting value as transition from a blast wave to a detonation occurs. This process is referred to as "direct initiation" and the key problem is to establish the minimum or critical energy release E_c for which such

initiation will occur. Both a decaying wave and one in which transition to a detonation occurs are shown in Figure 9 taken from the review by Lee [27]. It appears clear that the magnitude of E_c will depend upon the interaction between the decaying blast wave and the growth of the induction length ℓ_I.

The modeling problem of direct initiation is to develop a theory of the a priori calculation of the critical energy E_c. The Zel'dovitch criterion [16], which has already been described, provides a qualitative means of estimating E_c. Bach et al [28] dealt with this problem by still treating the combustion front as a discontinuity; however, with a reduced heat release Q_e which is only a fraction $F(\eta, z)$ of the total heat release Q per unit mass of fuel-oxidizer mixture. Here $\eta = M_s^{-2}$ with M_s the wave Mach number and $z = R_s/R_o$ where R_s is the wave radius and R_o is the explosion radius. $F(\eta, z)$ is an empirical function based on physical considerations of the induction process. Approximate analytical solutions due to Sakurai [29] are used to describe the flow between the blast center and the decaying shock front where conditions are determined using the Rankine-Hugoniot conditions and the modified heat release Q_e.

Overall energy conservation as described by Eq. 1 below, is used to determine the shock motion

$$E_o = \int_0^{R_s} \left[p/(\gamma-1) \right] + \frac{1}{2}(\rho u^2) \quad k_j \quad dr$$

$$- \int_0^{R_s} \left[\frac{P_o}{(\gamma-1)} \right] k_j \quad dr - \int_0^{R_s - \ell_I} \rho\, Q \quad k_j\, dr \qquad (1)$$

Here E_o = the energy instantaneously deposited at the center of the blast wave; $j = 0, 1, 2$ and $k_j = 1, 2\pi, 4\pi$ for planar, cylindrical and spherical symmetry; p, ρ, and u are pressure, density, and particle velocity respectively, and the subscript zero refers to the undistrubed conditions ahead of the wave front. The problem is then reduced to the solution of the following two ordinary differential equations

$$\frac{d\eta}{dz} = \frac{2\eta\theta}{z} \; ; \quad \frac{d\tau}{dz} = \eta^{1/2} \qquad (2)$$

where $\tau = C_o t/R_o$ and C_o is the speed of sound in the unburned explosive. The relation between the acceleration parameter θ, which is defined as $R_s \dot{R}_s / \dot{R}_s^2$, and the other variables in Eq. (2) is determined by the energy conservation equation (1).

The resultant system of nonlinear equations, which also depends upon the empirical function $F(\eta, z)$, can only be integrated numerically after some further simplifying assumptions are introduced. The computed wave trajectory is found to depend upon the parameter $\delta = \Delta/R_0$ where Δ is the experimentally observed induction distance for plane C-J detonations. Mach number profiles calculated for $M_{CJ} = 8$, which is an average value for stoichiometric and equimolar acetylene oxygen mixtures, and an auto ignition shock strength of $M_c = 2.8$ were computed by Bach et al [28] for various values of δ, and are shown in Figure 10. Smaller values of δ correspond to higher initiation energies.

When δ exceeds a certain critical value δ_c (0.091 in the present case), which implies that $E_0 < E_{oc}$, the initial blast wave decays to an acoustic wave. When $\delta < \delta_c$ (or $E_0 > E_{oc}$) the blast wave first decays and then re-accelerates to a self-sustaining C-J detonation. Especially when δ is only slightly less than δ_c, there may be an extensive region where the propagation Mach number is substantially below the Chapman-Jouguet value M_{CJ}. Near the critical condition $\delta \simeq \delta_c$ the solution appears to be inherently unstable and tends to become oscillatory. The re-establishment of a detonation in these cases appears to involve the formation of an unsteady or transverse wave structure as shown in Figure 9(c). The behavior shown in Figure 10 appears to agree with experimental observations.

Since the explosion length R_0 is given by

$$R_0^{\,j+1} = E_0/\rho_0 C_0^{\,2} k_j \tag{3}$$

the critical initiation energy E_{oc} follows from the definition of δ and is given by

$$E_{oc} = k_j \rho_0 C_0^{\,2} (\Delta/\delta_c)^{j+1} \tag{4}$$

The behavior described above can, in a sense, be tied to the chosen behavior of the heat release function $F(\eta, z)$ which is designed to cut off all combustion heat release when $M_s < M_c$. Thus $F(\eta, z) = 0$ for $z > \delta$, $\eta \geq \eta_c$. But the behavior described above also suggests that the critical value of the initiation energy E_{oc} or δ_c is associated with a mathematical singularity in the equations describing the direct initiation phenomenon. The numerical studies of direct initiation by Chernyi [30]

and by Boni and Wilson [31],[32] provide further evidence for the existence of such a singularity. Chernyi [30] used the combined induction-reaction zone model for the reaction zone and then carried out numerical calculations for two different values of the initiation energy. The trajectories of the leading shock, i.e., r_s and of the flame front r_f are shown in Figures 11(a) and (b) for values of E_o below and above E_{oc}.

The drastic separation of the deflagration from the shock front in Figure 11(a) is especially significant. At the higher energy the deflagration and shock remain coupled together although the deflagration is observed to oscillate with respect to the leading shock at large values of the dimensionless time as shown in magnified form in the second part of Figure 11(b). Boni and Wilson [31] used a finite difference code to study the direct initiation of spherical detonations in methane-air mixtures. Their computations started with the detonation of a spherical tetryl charge. They did not use the simplified reaction zone structure described above, but used a grossly simplified kinetic scheme to represent the CH_4-air reaction. Figure 12 shows the trajectories of the flame front behind the leading shock for several different tetryl charge sizes, and once again a drastic transition from a coupled to an uncoupled reaction front is evident. It is almost as if the solution trajectories encounter a saddle-point like singularity when the E_o lies below the critical value.

A very simple analysis which starts from the energy equation (1) can be used to demonstrate the connections between E_{oc} and a singularity in the governing equations [33]. Neglecting the energy of the undisturbed medium and using the dimensionless variables

$$\psi = \rho/\rho_o, \quad \phi = u/\dot{R}_s, \quad f = p/\rho_o \dot{R}_s^2, \quad \xi = r/R_s,$$

this equation can be reduced to the following expression for the Mach number of propagation M_s:

$$M_s^2 = \frac{1}{I} \left\{ \frac{E_o}{\rho_o C_o^2 k_j R_s^{j+1}} + \frac{Q}{C_o^2} \int_0^{[1-(\ell_I/R_s)]} \psi \, \xi^j d\xi \right\} \tag{5}$$

where I is the integral

$$I = \int_0^1 \left(\frac{\psi \phi^2}{2} + \frac{f}{\gamma-1} \right) \xi^j \, d\xi \tag{6}$$

The detailed behavior of the dimensionless density ψ, velocity ϕ, and pressure f between the leading shock and the blast center $r = \xi = 0$ is required before the integrals in (5) and (6) can be evaluated. In addition

the variation of ℓ_I with the wave Mach number must also be known. At this point the following rather drastic assumptions will be adopted:

(a) $I = \text{const} = Q/(j+1) M_{CJ}^2 C_o^2$

(b) $\ell_I/R_s \ll 1$

(c) The density ρ in the induction zone is constant and equal to the value at the shock.

While these assumptions should not affect the qualitative behavior of Eq. (5), they will, of course, affect the quantitative accuracy of any initiation parameters derived from Eq. (5). The choice of I in (a) ensures that $M_s \rightarrow M_{CJ}$ as $\ell_I/R_s \rightarrow 0$.

Equation (5) can now be reduced to the following rather simple expression for the propagation Mach number M_s:

$$M_s^2 = M_{CJ}^2 \left[1 + \left(\frac{R_s^*}{R_s} \right)^{j+1} - (j+1) \frac{\rho_s}{\rho_o} \frac{\ell_I}{R_s} \right] \tag{7}$$

R_s^* is what is called the critical radius and is that value of R_s where the combustion and blast energies are equal so that

$$R_s^* = \left[(j+1) E_o/k_j \rho Q \right]^{1/(j+1)} \tag{8}$$

The second term on the right of (7) represents the effect of the initiating blast while the third term measures the influence of the induction length ℓ_I. Equation (7) reproduces, at least qualitatively, the behavior shown in Figure 10, that is, M_s drops to a minimum below M_{CJ} and then gradually accelerates back to M_{CJ} when initiation does occur.

The possibility of singular behavior becomes evident when the derivative dM_s/dR_s is evaluated from (7). The crucial step is taking the variation of the induction length ℓ_I with Mach number M_s into account. The result is:

$$\frac{dM_s}{dR_s} = \left[\frac{\rho_s}{\rho_o} \frac{\ell_I}{R_s^2} - \frac{R_s^{*j+1}}{R_s^{j+2}} \right] \Bigg/ \left[\frac{2M_s}{(j+1)M_{CJ}^2} + \frac{\rho_s}{\rho_o} \frac{\ell_I}{R_s} \frac{d(\ell n \ell_I)}{dM_s} \right]$$

$$= N/D \tag{9}$$

The numerator $N < 0$ for very small values of R_s but changes sign and becomes positive when

$$R_s = \frac{\rho_0}{\rho_s} \left(\frac{R_s^*}{\ell_I} \right)^{1/j} R_s^* \tag{10}$$

Thus, M_s passes through a minimum at this value of R_s as do the trajectories shown in Figure 10. All this presupposes that the denominator $D > 0$ in Eq. (10). However, while $[2M_s / (j+1) M_{CJ}^2] > 0$ always, the derivative $d(\ell n \ell_I)/ dM_s < 0$ so that the denominator D may also vanish. In fact, when the critical radius R_s^* decreases to a value R_{sc}^*, N and D vanish simultaneously so that the minimum point of the trajectory is replaced by a singularity. For $R_s^* < R_{sc}^*$ the slope $dM_s / dR_s \to -\infty$ as $R_s \to R_s^*$. This suggests that the value E_{oc} associated with R_{sc}^* corresponds to the critical initiation energy E_{oc}.

The condition $D = N = 0$ is sufficient to determine both M_{sc} the Mach number at the critical point and the associated value of R_{sc}^* and hence E_{oc}. The condition $D = 0$ leads to the following equation for M_{sc}:

$$2M_{sc} + \frac{j+1}{j} (M_{CJ}^2 - M_{sc}^2) \left[\frac{d(\ell n \ell_I)}{dM_s} \right]_{M_s = M_{sc}} = 0 \tag{11}$$

and Eq. (11) demonstrates the intimate relation between the singularity and the behavior of the induction zone ℓ_I. A qualitative sketch of the Mach number trajectories for $E_o > E_{oc}$ and $E_o < E_{oc}$ is shown in Figure 13. The detailed computation of E_{oc} for a simplified relation between ℓ_I and M_s is described in Ref. [33].

The fact that usually $\ell_I / R_s << 1$ and that most induction reactions have a very high activation energy suggests the possibility of applying asymptotic methods [34]. Nicholls et al [35], and Oza [36] developed an analysis of the direct initiation problem on this basis which provides some interesting insights into the physics and mathematics of this process. A two front mode of the reaction zone is used. There are two length scales: the radius R_s forms a global or outer scale while induction length ℓ_I represents an inner scale. For the outer or global problem the detonation front is treated as a discontinuity; however, the jump from

the conditions in the undistrubed fuel oxidizer mixture to the conditions behind the front depend upon the structure of the reaction zone. The treatment of the global or hydrodynamic problem then is quite similar to that of Bach et al [28] except for replacement of the empirical heat release function $F(\eta, z)$ by a detailed analysis of the induction region.

Arrhenius kinetics for a single second order irreversible reaction is used in the induction zone. Thus with

$$a A + b B \to c C \tag{12}$$

(A-fuel, B-oxidizer, C-combustion products), the species conservation equation becomes

$$\bar{\rho} \, \frac{\partial Y_A}{\partial \bar{t}} + \bar{u} \, \frac{\partial Y_A}{\partial \bar{r}} = - \mathcal{B} \, \bar{\rho} \, Y_A{}^a Y_B{}^b \, e^{-\bar{T}_a / \bar{T}} \tag{13}$$

where Y_A and Y_B are the mass fractions of A and B, and barred quantities and the pre-exponential factor $\mathcal{B}$ are dimensional. $\bar{T}_a$ is the activation temperature $\bar{E}_a / \mathcal{R}$, and $\bar{E}_a$ and $\mathcal{R}$ are the activation energy and universal gas constant. A system with high activation energy so that $\beta = \bar{T}_s / \bar{T}_a \ll 1$, is considered, where $\bar{T}_s$ is the temperature of the gas immediately behind the shock. On the basis of the second order reaction it now is possible to also define the chemical time

$$\bar{t}_c = [\mathcal{B} \, Y_{Ao}{}^{a-1} \, Y_{Bo}{}^{b}]^{-1} \tag{14}$$

and an associated chemical length

$$\bar{\ell}_c \simeq t_c \, a_o \, M_s \, e^{\bar{T}_a / \bar{T}_s} \tag{15}$$

The following dimensionless stretched variables are now introduced with shock fixed coordinates:

$$\rho = \bar{\rho}/\bar{\rho}_o \qquad h = \bar{h}/\bar{C}_{po} \bar{T}_o \qquad Y_i = Y_{il}/Y_{io}$$

$$p = \bar{p}/\bar{p}_o \qquad w = (\dot{\bar{R}}_s - \bar{u})/\dot{\bar{R}}_s \qquad \tau = \bar{t}/\bar{\tau}_B$$

$$T = \bar{T}/\bar{T}_o \qquad \eta = (\bar{R}_s - \bar{r})/\bar{\ell}_c \qquad \bar{\tau}_B = R_s/\dot{R}_s \tag{16}$$

When these variables are substituted into the equations for one dimensional unsteady flow without transport effects or body forces, the small parameters (ℓ_c / R_s) and β appear. This suggests the use of a double expansion of the form

$$f = f_s + \beta f_1 + (\bar{\ell}_c / \bar{R}_s) \, f^{(1)} + \ldots \tag{17}$$

for the parameters of the flow.

The first term in the expansion (17) represents the effect of the high activation energy upon the induction process while the second term of $O(\bar{l}_c / \bar{R}_s)$ reflects the influence of the wave curvature. The question of how these effects interact will depend upon the relative magnitudes of β and $\bar{l}_c / \bar{R}_s$. Nicholls et al[35] assumed that $\bar{l}_c / \bar{R}_s \ll \beta$ which appears to be in accord with physical reality. Then to order β the conservation equations are steady, and the mass momentum and energy equations reduce to the following simple set of algebraic equations:

$$\rho_1 w_s + w_1 \rho_s = 0$$
$$\rho w_s^2 + 2 w_1 w_s \rho_s + p_1 / (\gamma_o M_s^2) = 0$$
$$T_1 + [(\gamma_o - 1)/2] M_s^2 2 w_1 w_s - Q \tilde{Y}_{A1} = 0 \tag{18}$$

with $Q = \bar{Q} / \bar{C}_{po} \bar{T}_o$.

The species equation becomes

$$w_s [d Y_{A1} / d \eta)] = e^{T_1 / T_s} \tag{19}$$

This system of equations is readily solved for the temperature coefficient T_1 with the result

$$T_1 = -T_s \ln[1 - (\eta / w_s A_1)] \tag{20}$$

where

$$A_1 = (T_s / Q)[(\gamma+1)(M_s^2 - 1)] \Big/ [(\gamma+1)(M_s^2 - 1) - 2(\gamma-1)(1 + \frac{\gamma-1}{2} M_s^2)]$$

The solution for T_1 diverges as $\eta \rightarrow w_s A_1$ and this value of η, denoted as η_I is chosen as the dimensionless induction distance so that

$$\bar{l}_I = \bar{l}_c w_s A_1 \tag{21}$$

It is interesting that this definition of induction distance is similar to that introduced by Hermance [37] in his study of adiabatic ignition.

Combining this treatment of the induction zone with the solution for the hydrodynamic flow between the detonation front and blast center makes it possible to compute Mach Number-radius trajectories for different values of the initiation energy. A set of such trajectories computed for a

stoichiometric acetylene oxygen mixture is shown in Fig. 14 taken from Ref. 36. The parameter t_γ is the ratio of a characteristic chemical time to a characteristic explosion time and varies inversely with the energy of the initiating blast wave. The singular nature of the transition from initiation of a detonation to a decaying wave with decreasing initiator energy is once again evident.

The asymptotic analysis described here indicates that the direct initiation of a detonation bears a very close relation to the classical problem of the adiabatic ignition of a fuel-oxidizer mixture. It is no surprise that with $(l_c / \bar{R}_s) \ll \beta \ll 1$, the flow behind the shock reduces to a quasi steady one in which induction occurs as the fluid moves downstream of the leading shock. The novel feature is now that the starting conditions T_s, ρ_s etc. depend upon the variation of l_I at preceding times which in turn depends on the size of the exploding charge. These features depend upon the solution of the outer problem. The asymptotic analysis described here is unfortunately incomplete. Thus, to treat the end of the induction zone would require a detailed analysis similar to that of Kassoy [38], which takes the consumption of the fuel into account.

Several approaches to modeling the direct initiation of gaseous detonations have been described, and all indicate that E_{oc} is governed by the relationship between the growth of an induction length l_I and the decay of the initiating blast wave. The critical energy E_{oc} appears to be associated with a singularity in the governing equations but the precise character of this singularity remains to be determined. The asymptotic analysis described above, depends upon the condition $\bar{l}_I/\bar{R}_s \ll \beta \ll 1$. The analysis raises the interesting question of how to deal with the cases when $\bar{l}_I/\bar{R}_s \sim O(\beta)$ or $\beta \ll l_I/\bar{R}_s \ll 1$. In the former case, the changes within the reaction zone due to wave curvature will be important. The role of higher order terms like those of order $\beta(\bar{l}_I/\bar{R}_s)$ remains to be established. When the initiating energy E_o only slightly exceeds E_{oc} oscillatory behavior not unlike that discussed in the Introduction is observed. Various aspects of detonation stability have been discussed by Fickett and Davis [18] and the numerical computation of an oscillating detonation front by Fickett and Wood [39] is especially noteworthy. However, the precise relation of this oscillatory behavior to direct initiation remains to be determined. Invariably, the initiation of detonations, especially with E_o close to E_{oc}, is associated with the formation of transverse waves. This is evident from Figure 9. While the relationship between transverse cell formation and initiation is discussed by Bach et al [28], its precise relation to the initiation

process remains to be determined. Consideration of the direct initiation of gaseous detonations has thus raised a number of subsidiary problems, many of which are mathematical in nature. A consideration of spray detonations introduces a whole new set of questions and these are discussed in Section III below.

III. DETONATIONS THROUGH SPRAYS.

As already mentioned in the introduction, the initiation and propagation of detonations through sprays introduces an entirely new set of physical phenomena because the ignition of the fuel depends crucially upon the droplet shattering process. Certain key features of the structure and propagations of spray detonations have been established [40] ,[41] . The breakup of the fuel usually dominates the detonations structure so that the reaction zone is much longer than in the gaseous case; however, the kinetics of the reaction between the vaporized fuel and the oxidizer can also play a very important role [42] ,[43] . In addition, the volatility of the fuel may have major effects on the character of the structure.

Detonations in non-volatile droplet clouds of diethylcyclohexane were studied by Dabora et al [44] while Bar Or et al [45] made detailed studies of mono-dispersed clouds of decane in a sectored shock tube designed to simulate cylindrical detonations. Certain key features of non-volatile detonations have been established by these studies. After passage of the leading shock the droplets are in a region of supersonic flow so that a bow shock forms ahead of the droplet. The droplets are accelerated and deformed by this convected flow while a microspray, formed by boundary layer stripping is usually entrapped in the wake. Because of Taylor Instability the droplet may then shatter into a group of much smaller droplets [46] . After a certain ignition time , t_{ig} , the combustible mixture sometimes explodes so that a weak blast wave propagates toward the leading shock and into the region downstream of the detonation. The remaining fuel is then consumed smoothly until droplet burning is complete at time t_{cc} . Whether or not the wake explosions, which are such a distinct characteristic of some spray detonations, occur seems to depend on the properties of the fuel and oxidizer and the size of the fuel droplets [43] .

Many features of this process are illustrated in Figures 6 and 7, which have already been discussed. A typical Schlieren streak record of a detonating mono disperse spray of 400μ decane droplets in oxygen recorded by Bar Or et al [45] is shown in Figure 15, and a sketch explaining the main features of this record is shown in Figure 16. The wake generated blast waves are an especially notable feature. The wave shown in Figure 15 was initiated by an explosive charge placed at the vertex of the sectored shock tube mentioned above and the streak records were photographed through

628

windows about halfway along the 140cm radius sectored shock tube.
During the direct initiation of detonations in non-volatile sprays the velocity
of the wave drops below the C-J value and then slowly appears to reacceler-
ate to the C-J value. This behavior is evident from Figure 17 which shows
Mach number trajectories for 400μ decane droplets in oxygen for different
values of the energy E_o of the high explosive initiator. The similarity of
these curves to the trajectories shown in Figure 10 for the direct initiation
of gaseous detonations should be noted. The fact that the wave velocity is
appreciably below the C-J value seems to characterize most non-volatile
spray detonations.

The situation will be quite different for a volatile spray. A typical
Schlieren streak record of a detonating spray of 400μ heptane droplets in
oxygen is shown in Figure 18. Now a detonation front propagating at the
C-J velocity corresponding to the equilibrium vapor pressure is observed.
The droplets break up and explode as before but apparently have no
influence upon the propagation of the main detonation front. In a related
experiment, Pierce and Nicholls [47] found that in systems consisting of
non-volatile diethyl cyclohexane droplets in an atmosphere of hydrogen
and oxygen, the detonation velocity was unaffected by the combustion of the
droplets behind the reaction zone of the H_2-O_2 detonation.

Modeling of the direct initiation and propagation of spray detonations
is possible at several different levels of complexity. Perhaps the simplest
approach is to use Eq. (7), discussed in Section II above, to describe the
wave trajectory of a detonations initiated by a high explosive charge. Then
the questions which arises immediately is how to define the induction length
l_I for a spray detonation. A relatively simple model of droplet combustion
based on empirical results for droplet breakup can be used for this purpose.

A single droplet which has crossed a shock wave at time t = 0 is
shown in Figure 19. During interval t the droplet will move a distance x
while the shock moves a distance $u_s t$. The distance S between the
shock and the particle will then be $S = u_s t - x$. The particle breakup will
be complete after a certain interval t_s when $x = x_s$ and $S = l_B$ the
breakup distance. Measurements show that at breakup [48], [49] a
dimensionless time

$$T_s = (t_s u_2 / D_o)(\rho_2 / \rho_l)^{1/2} \tag{23}$$

always has the same constant value while the distance x_s can be determined
from

$$X_s = \frac{x_s}{D_o} = A T_s^2 \tag{24}$$

where D_o is the initial particle diameter, and A is an empirical constant. Fishburn [46] has pointed out that the dimensionless time T_s defined in Eq. (23) also characterizes the time required for the droplet to deform after shock passage and can be derived by balancing the gas dynamic pressure on the liquid droplet against the liquid inertia in the radial direction. From Eqs. (22)-(24) it now follows that

$$\ell_B = [(1 - \frac{\rho_o}{\rho_2})^{-1} (\frac{\rho_o}{\rho_2})^{1/2} (\frac{\rho_e}{\rho_o})^{1/2} T_s - A T_s^2] D_o = F D_o \tag{25}$$

where the relation $(U_s / U_2) = [1 - (\rho_o / \rho_2)]^{-1}$ between shock velocity and density has been used. For hydrocarbon detonations (ρ_o / ρ_2) is almost independent of M_s; thus, ℓ_B will be proportional to the initial droplet diameter D_o for a given fuel and a fixed ambient density. Waldman et al [48] have suggested values of 3.5 and 0.8 for T_s and A while Ranger and Nicholls [49] suggest values of 5.0 and 1.1 respectively and these values are certainly comparable.

In the two front model of gaseous detonation structure ℓ_I is usually taken as the induction length of the reactions behind the shock. An equivalent definition of induction length can be developed for spray detonations by recognizing that the main effect of ℓ_I is a deficit in the combustion energy release behind the leading shock [45]. (This concept is also used by Bach et al [28] to define the heat release function $F(\eta, z)$). On the basis of the discussion above a typical heat release pattern from an individual fuel droplet might be like that shown in Figure 20(a). Here m_o is the initial droplet mass and q is the combustion heat release per unit mass of fuel so that $m_o q$ is the combustion energy of each droplet. Figure 20(a) illustrates a typical case where the microspray of mass Δm_μ which starts to form right after shock passage, ignites explosively at a distance ℓ_{ig} behind the shock. After that burning is continuous and equal to the droplet breakup rate until breakup and burning are complete at a distance ℓ_B behind the shock. The area above the curve in Figure 20(a) is now the energy deficit due the finite duration of droplet breakup and combustion. A two phase induction length ℓ_I will now be defined as the induction length of an equivalent two front wave which has the same energy deficit but with all the combustion energy released at distance ℓ_I behind the

shock as shown in Figure 20(b). From this definition, it follows directly that

$$\frac{\ell_I}{\ell_B} = \frac{\ell_{ig}}{\ell_B} + \int_{\ell_{ig}/\ell_B}^{1} \frac{m}{m_o} d\left(\frac{x}{\ell_B}\right) \tag{26}$$

where x is the distance from the shock.

Experiments have shown [50] that during the shock induced breakup of water drops:

$$\frac{m}{m_o} = \frac{1}{2}\left[1 + \cos \pi \left(\frac{t}{t_B}\right)\right] \tag{27}$$

where t_B is the droplet breakup time. Assuming that $(t/t_B) \cong (x/\ell_B)$ it then follows from Eq. (26) that

$$\frac{\ell_I}{\ell_B} = \frac{1}{2}\left[1 + \frac{\ell_{ig}}{\ell_B} - \frac{\sin \pi(\ell_{ig}/\ell_B)}{\pi}\right] \tag{28}$$

If $\ell_{ig} = \ell_B$ so that combustion occurs only after complete breakup, it follows from Eq. (26) that $\ell_I = \ell_B$ as is to be expected.

Although this model may appear overly simplified, it accounts for the most important features of droplet shattering and burning. The shattering process is introduced through the empirical expression (25) for ℓ_B and breakup rate (27). The kinetics of the wake explosions enters through the ignition length ℓ_{ig}. This model also highlights some of the additional difficulties involved in analyzing spray detonations. Only a mono-disperse spray is considered. The effect of micromist burning on the breakup process is ignored although this may be important [44]. The effect of the blast waves from the exploding droplets treated by Dabora [51] and Pierce [52] is not considered.

Wave trajectories computed using M_s from Eq. (7) with ℓ_I computed using Eq. (28) are compared to experimentally measured trajectories in Figure 21 taken from [45]. The induction and breakup lengths were, in this case, taken from corresponding streak photos of the detonation, and the corresponding ℓ_I was taken constant at 4cm. Agreement is quite good at large values of R_s consistent with the asymptotic character of the theory used to derive Eq. (7).

631

When D_o, the droplet diameter, is below a certain size, the behavior of the spray detonation reverts to that of a gaseous detonation as indicated by the experiments of Lu et al [43] who used a nebulizer to produce a very fine spray. The ultra simple theory discussed above can provide an estimate of the droplet diameter $D_o = D_{oc}$ where this transition in behavior occurs. As already indicated by Eq. (25), the breakup distance ℓ_B varies almost linearly with the droplet diameter D_o so that for sufficiently small droplets the distance behind the lead shock where breakup is essentially complete will be much smaller than the chemical induction length ℓ_c. In this limit, when $(\ell_B/\ell_c) \ll 1$, the droplet breakup will be so rapid that it has a negligible effect on the induction process. On the other hand, with $\ell_B/\ell_c \gg 1$, the droplet breakup will be the determining factor. These considerations suggest that the droplet diameter D_o for which $\ell_c = \ell_B$ be chosen as the critical or transition value D_{oc}. If τ_s is the chemical induction time of the fuel of interest and $\ell_c/R_s \ll 1$ it follows that

$$\ell_c \stackrel{\sim}{=} U_s (\rho_o/\rho_2) \tau_s \tag{29}$$

so that

$$D_{oc} = \ell_c/F$$

with F defined by Eq. (25). For stoichiometric methane, propane and decane air mixtures respectively, this criterion leads to $D_{oc} = 36, 11,$ and 4.6μ respectively [53].

The simple theory described above completely ignores the details of the two phase flow in the reaction zone which will depend upon the interaction between the gas flow and the accelerating and deforming droplets. Borisov et al [54] have developed what are essentially single fluid equations to deal with this problem and these have been used by Gubin and Sichel [55] to compute the structure and velocity of a steadily propagating spray detonation. The equations of continuity, momentum, and energy in the reaction zone are as follows:

$$\sigma_\mu u + \rho u + \tau W = \rho_o u_o + \sigma_o W_o \tag{30}$$

$$\sigma_\mu u^2 + \rho u^2 + \sigma W^2 + p = \rho_o u_o^2 + \sigma_o W_o^2 + p_o \tag{31}$$

$$\sigma_\mu u(CT_\ell + Q_o + \frac{u^2}{2}) + \rho u (\frac{u^2}{2} + h) + \sigma W(CT_\ell + Q_o + \frac{W^2}{2})$$

$$= \rho_o u_o (\frac{u_o^2}{2} + h_o) + \sigma_o W_o (CT_{\ell o} + Q_o + \frac{W_o^2}{2}) \tag{32}$$

Here W is the droplet velocity, σ_μ is the concentration of the micro-mist which has been stripped from the droplet and σ is the droplet mass per unit mixture volume. The subscript zero denotes the start of the reaction zone and Q_o is the heat of reaction of the fuel.

A number of subsidiary relations had to be introduced before this system of equations could be solved. The empirial relation of Ranger and Nicholls [49] was used for the variation of W with time and Eq. (27) was used for the droplet mass. Finally, a modified version of the two front reaction zone model was used to determine the propagation velocity. Thus, it was assumed that only that micromist generated by droplet stripping during ignition time t_I contributed to the propagation velocity. At $t = t_I$ the combustion of this micromist is assumed to occur in a very narrow front. The calculation of t_I was based on the empirical expression

$$t_i = 10^{-10} p^{-1} \exp(-E/R\ T) \tag{33}$$

due to Mullins [56]. In order to take the variation of temperature T into account, the total reaction time was subdivided into a number of time steps Δt_j and an ignition time t_{ig} was calculated for each step using Eq. (33). The ignition time delay was then determined from the condition

$$\sum \frac{\Delta t_j}{t_{ij}} = 1 \tag{34}$$

The precise basis for this procedure is not entirely clear although Eq. (34) has also been used by other investigators studying reactive systems.

Profiles of dimensionless pressure, $\overline{P}$, temperature $\overline{T}$, particle mass $\overline{m}$ and particle velocity $\overline{W}$ are shown in Figure 22. The increase in pressure and temperature is particularly significant and is typical of two phase systems. The increase arises because in shock fixed coordinates, the particles are moving with a higher velocity than the gas immediately behind the shock. As the particles decelerate, they cause an increase in the gas temperature and pressure. The variation of detonation velocity with droplet size is shown in Figure 23 for a kerosene-oxygen mixture. For large droplets (> 100μ) the detonation velocity is appreciably less than the ideal C-J value, and the results appear in good agreement with measurements. For $D_o < 20\mu$ the behavior becomes indistinguishable from that of a gaseous detonation, a result which supports the development of the transition diameter D_{oc} presented above.

Spray detonations are observed to propagate at velocities appreciably below the C-J value. There is, however, considerable disagreement about the cause of this behavior. Two explanations for sub C-J velocities have been presented so far; one associated with the initiation process and the influence of the large induction zone, a second related to incomplete combustion of the fuel droplets. Since most of the data used by Gubin and Sichel [55] came from experiments in which the detonation was initiated by a hydrogen oxygen detonation tube, the observed velocity deficits could well be associated with the initiation process. A third explanation based on losses to the walls of the detonation tube can also be justified in some cases [57].

Another basic approach often used in two phase flow problems is to treat the spray and the surrounding gas as two separate fluids which interact with each other through source terms in the conservation equations of each fluid. This approach was applied by Eidelmann and Burcat [58] and by Mitrofanov et al [59] who investigated the direct initiation of cylindrical [59], and spherical [58] spray detonations. For spherical symmetry the equations of mass, momentum and energy conservation of the gaseous phase used by Eidelman and Burcat [58] are:

$$\frac{\partial \rho_1}{\partial t} + \frac{1}{r^2} \frac{\partial(r^2 V_1 \rho_1)}{\partial r} = \delta\rho_2 \tag{35}$$

$$\frac{\partial(\rho_1 V_1)}{\partial t} + \frac{1}{r^2} \frac{\partial}{\partial r}(r^2 \rho_1 V_1^2) + \frac{\partial p}{\partial r} = -\rho_2 M + \delta\rho_2 (V_2 - V_1) \tag{36}$$

$$\frac{\partial}{\partial t}[\frac{p}{\gamma-1} + \frac{1}{2}\rho_1 V_1^2] + \frac{1}{r^2} \frac{\partial}{\partial r}[r^2 \left\{ \frac{p}{\gamma-1} + \frac{1}{2}\rho_1 V_1^2 \right\} V_1]$$
$$+ \frac{1}{r^2} \frac{\partial}{\partial r}(r^2 p V_1) = -\rho_2 V_1 M - \delta\rho_2 \frac{(V_1^2 - V_2^2)}{2} + \rho_2 \delta Q \tag{37}$$

where the subscript 1 here denotes the gas phase. The left hand sides of Eqs. (35)-(37) are quite standard. It is the source terms which are the distinguishing feature of the two fluid approach and also are the major cause of uncertainty in the validity of the final results. The interpretation of these terms is as follows:

$\delta\rho_2 \equiv$ rate of mass addition due to droplet evaporation

$\rho_2 M \equiv$ momentum loss due to particle drag

$\delta\rho_2 (V_2 - V_1) \equiv$ momentum change due to evaporation from droplets moving at a velocity different from the gas velocity

$\rho_2 V_1 M \equiv$ work due to particle drag

$$\delta \rho_2 \frac{(V_1^2 - V_2^2)}{2} \equiv \text{change in kinetic energy because of difference between particle and gas velocity}$$

$$\rho_2 \delta Q \equiv \text{combustion energy release}$$

The detailed formulation of these terms is described in references [58] and [59]. It is assumed that the fuel vapor burns at the instant of evaporation so that these models fail to account for the influence of chemical kinetics. The source terms, of course, also appear in the equation for the liquid phase which are as follows:

$$\frac{\partial \rho_2}{\partial t} + \frac{1}{r^2} \frac{\partial}{\partial r} (r^2 \rho_2 V_2) = -\delta \rho_2 \tag{38}$$

$$\frac{\partial (\rho_2 V_2)}{\partial t} + \frac{1}{r^2} \frac{\partial}{\partial r} (r^2 \rho_2 V_2^2) = \rho_2 M - \delta \rho_2 V_2$$

The internal energy of the fuel droplets is neglected so that the energy equation is replaced by the droplet conservation equation:

$$\frac{\partial N}{\partial t} + \frac{1}{r^2} \frac{\partial}{\partial r} (r^2 N V_2) = 0 \tag{39}$$

Here, the subscript 2 refers to the droplets and N is the droplet number density. If ρ_ℓ is the density of the liquid $\rho_2 = (\pi/6) D^3 \rho_\ell N$ where D is the instantaneous droplet diameter.

Eidelman and Burcat [58] solved this set of two fluid equations numerically for a stochiometric mixture of 100μ heptane droplets in oxygen. The resultant variation of the shock front velocity with radius is shown in Figure 24 for different values of the initiation energy E_o.

These curves again demonstrate the decay to sub C-J velocities followed by re-acceleration to the C-J value. Because of the absence of any kinetics in the formulation the complete decay or quenching and the singular behavior associated with the critical energy E_{oc} does not appear to arise in these two fluid numerical studies. Mitrofanov [59] obtained similar results; however, he did in some cases incorporate a chemical kinetic ignition delay time into his calculations. Then he did find that initiation failed when E_o is below a certain critical value.

The wake explosions described above are not considered in either the single fluid or two fluid models. Nevertheless, Eidelman and Burcat [58] did observe the appearance of secondary shock waves within the reaction zone. One of these shocks is shown in Figure 25 taken from

Ref. [26], which shows reaction zone profiles for a detonation in a mixture of 300μ decane droplets and oxygen. The precise origin of these secondary waves is not clear, although it does appear certain that the waves represent a physical phenomenon rather than a numerical instability. The waves appear to arise in very thick reaction zones and may be associated with the region of near sonic flow toward the end of the reaction zone. Because of the dominant role of secondary explosions is so many observed heterogeneous detonations a number of models based entirely on this explosion phenomenon have been developed. Perhaps one of the earliest of these "Shock models" is due to Cherepanov [60] who computed the propagation velocity assuming that combustion occurs through a series of periodic explosions at the C-J plane. Since half the energy is carried downstream beyond the C-J plane by this mechanism, U_s / U_{so}, the ratio of the propagation velocity U_s to the premixed detonation velocity U_{so} has the value of $1/\sqrt{2} = 0.71$. This result is not too far from a number of experimental observations.

A far more detailed shock theory for the propagation of spray detonations was developed by Pierce [52]. The mono-disperse spray is assumed to be arranged in a succession of sheets. The droplet wakes in each sheet explode after an induction time t_I has elapsed from the instant of passage through the leading shock. The resultant blast waves coalesce to form two plane blast waves, one moving downstream and one moving upstream toward the leading shock. The interaction of the upstream moving wave with the leading shock causes this shock to accelerate. The continual blast wave-shock interactions result in wave oscillations similar to those also observed experimentally by Pierce [61]. A schematic sketch depicting the behavior of the droplets behind the wave is shown in Figure 26, and the blast wave coalescence process is shown in Figure 27. After ignition the remainder of the droplets are assumed to burn at a constant rate. In some ways this model is thus similar to the simplified model used above to develop an equivalent induction length. The major features of this analytical model are shown in the x-t diagram in Figure 28 which is centered on the explosion center at a distance x_I (ignition length) behind the cloud. Numerical methods and various approximations were used to obtain solutions based upon this complex model as described in detail by Pierce [52]. A typical pressure distribution within a detonations computed on this basis is shown in Figure 29. When this pressure variation is translated into a pressure transducer response the resultant traces are very similar to those observed experimentally.

A much simpler "shock theory" was developed by Dabora [51] in order to estimate the critical initiation energy E_{oc}. The critical energy E_{oc} is determined by requiring the accelerating effect of the blast wave from the exploding droplet wake to balance the decay of the initiating blast wave at the critical radius R_s*. It is assumed that the combustion energy of the complete droplet is fed into the blast wave. As in the simplified theory, a key parameter which arises in Dabora's theory is $t_I/t_B \doteq \ell_I/\ell_B$, i.e., the ratio of the ignition time to the droplet breakup time.

A consideration of the models described above leads to the conclusion that there are really two fundamental processes which govern the initiation and propagation of detonations through sprays. These are:

1. The mechanism of droplet breakup

2. The chemical reactions and micromist evaporation which determine the delay between the onset of droplet shattering and either the wake explosion or the start smooth combustion.

Each of these problems represents a subject in itself. It is especially interesting that, as in the direct initiation of gaseous detonations described above, the ignition delay problem plays a central role in spray detonations as well. All of the spray detonation models described above depend crucially upon the inputs derived from analytical models or empirical descriptions of these two processes.

A detailed analysis of the droplet breakup process which is applicable to spray detonations has been developed by Fishburn [46]. The parameter which governs the mode of droplet breakup is the dimensionless group $W_e R_e^{-1/2}$ where W_e is the Weber number defined by

$$W_e = \frac{\rho_g U_g^2 D_o}{\sigma} \tag{40}$$

where ρ_g and U_g are the gas density and velocity relative to the drop and σ is the surface tension of the fluid. R_e is, of course, the Reynolds number $U_g D_o / \nu_g$. For spray detonations $W_e R_e^{-1/2} \gg 1$ and then boundary layer stripping becomes an important part of the breakup process.

Experiments [46] ,[48] ,[49] ,[62] indicate that breakup starts with the deformation of the droplet and the formulation of interacting liquid and gaseous boundary layers on the liquid surface. Because of this boundary layer a micromist starts to be stripped away from the outer edge of the deformed droplet. At some stage the droplet becomes unstable and breaks up into smaller droplets which again are atomized by boundary layer stripping. Most of this sequence is illustrated in Figure 30 taken from Ref. [49] , which shows the breakup of 750μ water droplets behind a shock of the relatively low Mach number, $M_s = 2.0$.

Fishburn's work [46] illustrates the many physical phenomena which must be modeled in order to analyze this complex breakup process. The first step is to determine the droplet deformation rate. A number of studies of this problem have been carried out in connection with rain drop deformation for instance. The potential flow analysis of Burgers [46] is used to describe the initial stages of deformation. The further progress of deformation is then determined using an approximate analysis of Reinecke and Waldman [63] . The key result is that the maximum deformation occurs when the dimensionless time

$$T = (t\, U_2 / D_o)(\rho_2 / \rho_\ell)^{1/2} \tag{41}$$

is approximately 1.0. As already noted, a fixed value of $T = T_s$ also characterizes the total droplet breakup time. A very simple argument can be used to develop this important result. Right after shock passage the total aerodynamic force on a particle of diameter D_o will be of the order $\frac{1}{2}\rho_2 U_2^2 \pi\,(D_o^2/4)$. This force results in droplet deformation which involves the acceleration of liquid in a direction transverse to the velocity u_2 of the gas. If it is assumed that during deformation time t_d, the droplet mass is moved a transverse distance D_o , then equating the aerodynamic force to the transverse acceleration yields the relation:

$$\frac{1}{2}\rho_2 U_2^2 \pi\,\left(\frac{D_o^2}{4}\right) = \rho_\ell\,\frac{\pi D_o^3}{6}\,\frac{D_o}{t_d^2} \tag{42}$$

from which it immediately follows that

$$T_d = \frac{t_d U_2}{D_o}\,\left(\frac{\rho_2}{\rho_\ell}\right)^{1/2} = 1.16 \tag{43}$$

This result is remarkably close to that determined analytically by Fishburn.

Boundary layer stripping occurs near the periphery of the deformed droplet. Ranger and Nicholls [49] estimated the stripping rate by using an integral analysis of the coupled laminar air-liquid boundary layer on the droplet surface. A more detailed analysis using the Blasius series was made by Fishburn [46]. The significant result is that stripping cannot account for the observed droplet breakup rates.

To explain this difficulty, Fishburn [46] noted that the windward surface flow will be unstable to small disturbances due to the acceleration of the droplet. Taylor [64] investigated this type of instability and provided the starting point of Fishburn's analysis. Because of this instability waves on the windward surface are amplified and ultimately cause the droplet to breakup into a series of smaller droplets. Estimates of this highly nonlinear process are carried out by Fishburn [46]. The smaller droplets once again are broken up by boundary layer stripping. On the basis of this model, Fishburn obtained results in excellent agreement with the empirical breakup rate expression of Reineke and Waldman [50] (Eq. (27)) which has already been introduced in connection with the approximate spray detonation analysis.

The droplet wake ignition problem is an extended form of the classical problem of thermal ignition first considered by Semenov [65] and Frank-Kamenetskii [66]. In the basic problem a semi-infinite slab of reactive material with constant and equal boundary temperatures is considered. Essentially this is a heat conduction problem with a heat source driven by a reaction governed by Arrhenius Kinetics. It is found that steady solutions fail to exist when a parameter δ_s which depends on the conditions of the problem exceeds a certain minimum value. Many extensions of the original problem have been considered and both asymptotic and numerical techniques have been used to obtain improved solutions [67]. In terms of a normalized temperature variable θ and a displacement variable ϵ the basic problem is governed by the differential equation

$$\frac{d^2\theta}{d\epsilon^2} + \frac{N}{\epsilon} \frac{d\theta}{d\epsilon} = -e^{-1/\theta} \tag{44}$$

with

$$\frac{d\theta}{d\epsilon}(0) = 0 , \qquad \theta(L) = \theta_s$$

and with $N = 0, 1, 2$ for plane, cylindrical, and spherical geometry. The major difficulty in all thermal ignition problems arises from the nonlinear Arrhenius term on the right side of Eq. (44).

Actually, of course, ignition is an unsteady phenomenon so that a complete treatment requires consideration of an equation of the form

$$\frac{\partial \theta}{\partial \tau} = (\frac{\partial^2 \theta}{\partial \epsilon^2} + \frac{N}{\epsilon} \frac{\partial \theta}{\partial \epsilon}) + e^{-1/\theta} \tag{45}$$

where τ is a suitably defined normalized time variable. A discussion of problems of this type has been presented by Merzhanov and Averson [68]. In all of these problems the density is taken to be constant. Compressibility introduces further complications since the reactive heat release may generate shocks and acoustic waves. Some of these problems have been considered by Kassoy [69].

The droplet wake ignition problem is even more complex. A schematic view of the wake of an accelerating deforming fuel droplet is shown in Fig. 31. In the classical problem the concentration of fuel is fixed at the beginning. Now the amount of fuel vapor will depend on the rate at which the micromist is generated and evaporates into the wake. If only the vapor in the wake region is considered, there is not only a chemically driven heat source but also a mass source governed by droplet stripping and micromist evaporation. The size of the wake region and the boundary conditions at the edge of the wake now will depend on the droplet deformation and trajectory. Attempts at solving the wake ignition problem have been made by Pierce [52] and by Pierce et al [23]. The numerous approximations and empirical parameters which had to be used made it difficult to identify the main governing parameters. There is thus a need for the formulation and study of relatively simple model problems which, however, include the main physical phenomena.

IV. DISCUSSION. The present review has been limited to a discussion of the direct initiation and propagation of gaseous and heterogeneous detonations. Consideration of some of the experimental results shows that the physical phenomena involved can be quite complex. Modeling of these phenomena, in which the reaction zone of the detonation plays a key role, can lead to problems of considerable mathematical interest.

The direct initiation of gaseous detonations can be tied to the classical problem of the adiabatic ignition of a fuel oxidizer mixture. The novel feature is that the initial conditions for each element of the combustible mixture as it crosses the leading shock wave depends on the variation of the induction length ℓ_I at preceding times.

Two basic processes are found to govern the behavior of spray detonations: the mechanism of droplet breakup, and the ignition of the droplet wake. This ignition problem is an extended version of the classical Semenov, Frank-Kamenetskii problem of thermal ignition of a reactive medium.

ACKNOWLEDGEMENT

REFERENCES

1. Courant, R., and Friedrichs, K.O., <u>Supersonic Flow and Shock Waves</u>, Interscience, (1948).

2. Gordon, S. and McBride B., "Computer Program for Calculation of Complex Chemical Equilibrium Compositions, Rocket Performance, Incident and Reflected Shocks and Chapman-Jouguet Detonations," NASA SP-273, (1971).

3. M. Cowperthwaite and W.H. Zwisler, "Tiger Computer Program Documentation," Lawrence Livermore Laboratory, Stanford Research Institute, January 1973.

4. Nicholls, J.A., Dabora, E.K., and Ragland, K.W., "A Study of Two Phase Detonation as It Relates to Rocket Motor Combustion Instability," NASA Contractor Report CR-272, The University of Michigan, August 1965.

5. Sedov, L.I., <u>Similarity and Dimensional Methods in Mechanics</u>, 4th Edition, Academic Press, New York, (1959).

6. Oppenheim, A.K., Kuhl, A.L., Ludstrom, E.A., and Kamel, M.M., "A parametric study of self-similar blast waves," <u>J. Fluid Mech.</u>, <u>52</u>,

7. Barenblatt, G.I., Guirguis, R.H., Kamel, M.M., Kuhl, A.L., Oppenheim, A.K., Zel'dovich, Ya.B., "Self-similar explosion waves of variable energy at the front," <u>J. Fluid Mech.</u>, <u>99</u>, 841 (1980).

8. Kuhl, A.L., Kamel, M.M., and Oppenheim, A.K., "Pressure Waves Generated by Steady Flames," <u>Fourteenth Symposium (International) on Combustion</u>, The Combustion Institute, Pittsburgh, 1201, (1973).

9. Strehlow, R.A., "The Blast Wave from Deflagrative Explosions, An Acoustic Approach," paper presented at 13th Loss Prevention Symposium, AIChE., Philadelphia, PA, June 1980.

10. Lewis, B. and vonElbe, Guenther, <u>Combustion Flames and Explosions of Gases</u>, Academic Press, (1961).

11. Wolański, P., Kauffman, C. W., Sichel, M., and Nicholls, J. A., "Detonation of Methane Air Mixtures," presented at Eighteenth Symposium (International) on Combustion, Waterloo, Ontario, August 1980.

12. Wood, W. W., and Kirkwood, J. G., "Diameter effect in condensed explosives. The relation between velocity and radius of curvature of the detonation wave," J. Chem. Phys., 22, 1920 (1954).

13. Fay, J. A., "Two Dimensional Gaseous Detonations: Velocity Deficit," Phys. Fluids, 2, 283, (1959).

14. Belles, F. E., Seventh Symposium (International) on Combustion, Butterworths, 745, (1959).

15. Tsugé, S., Combust. Sci. and Tech., 3, (1971).

16. Zel'dovich, Y. B., Kogarko, S. M., and Simonov, N. N., "An experimental investigation of spherical detonation of gases," Sov. Phys. Tech. Phys., 1, 1698 (1956).

17. Strehlow, R. A., "The nature of transverse waves in detonations," Astronaut. Acta, 14, 539, (1969).

18. Fickett, W., and Davis, W. C., Detonation, Univ. of California Press, (1979).

19. Lehr, H. F., "Experiments on Shock-Induced Combustion," Astronautica Acta, 17, 589, (1972).

20. Korobeinikov, V. P., Levin, V. A., Markov, V. V., and Chernyi, G. G., "Propagation of Blast Waves in a Combustible Gas," Astronautica Acta, 17, 529, (1972).

21. Ruegg, F. W., and Dorsey, W. W., "A missile technique for the study of detonation waves," J. Res. Nat. Bur. Stand., 66C, 51, (1962).

22. Ragland, K. W., Dabora, E. K. and Nicholls, J. A., The Physics of Fluids, 11, (1968).

23. Pierce, T. H., Kauffman, C. W., and Nicholls, J. A., "Mechanism of ignition in shock wave interactions with reactive droplets," AIAA Paper 75-163, (1975).

24. Kauffman, C. W., Ural, E., VanDyk, R., and Nicholls, J. A., "The Explosive Combustion of Coal Dust," Eastern States Section Technical Meeting, Combustion Institute, Miami, Florida, November 1978.

25. Kauffman, C. W., Wolanski, P., Ural, E., Nicholls, J. A., and VanDyk, R., "Shock Wave Initiated Combustion of Grain Dust," Symposium on Grain Dust, USDA, Manhattan, KS, October 1979.

26. Eidelman, S. and Sichel, M., "The Transitional Structure of Detonation Waves in Multi-Phase Reactive Media," to be published in Comb. Sci. and Tech.

27. Lee, J. H., Ann. Rev. Phys. Chem., 28, 75, (1977).

28. Bach, G. G., Krystautas R., and Lee, J. H., "Initiation criteria for diverging gaseous detonations," Thirteenth Symposium (International) on Combustion, The Combustion Institute, Pittsburgh, PA, 1097, (1971).

29. Sakurai, A., Exploding Wires, (W. G. Chance and H. K. Moore, eds.), Plenum Press, 264, (1959).

30. Chernyi, G. G., "On problems involving gas flows associated with gasdynamic discontinuities," Acta Astronautica, 2, 839, (1975).

31. Boni, A. A., and Wilson, W. C., "A Study of Explosion Hazards in Unconfined Vapor Clouds," (to be published).

32. Boni, A. A., and Wilson, C. W., "A Study of Detonation in Methane Air Clouds," Sixth International Colloquium on Gas Dynamics of Explosions and Reactive Systems, Stockholm, (1977).

33. Sichel, M., "Determination of the Critical Energy and of Sub-critical Propagation in the Direct Initiation of Detonations," presented at meeting of the Eastern States Section of the Combustion Institute, Miami Beach, FL, December 1978.

34. Liñan, A., (Private communication), (1974).

35. Nicholls, J. A., Sichel, M., Oza, R. D., and Vandermolen, R., "Detonability of Unconfined Natural Gas-Air Clouds," Seventeenth Symposium (International) on Combustion, Edwards Bros., 1223, (1979).

36. Oza, R. D. , "Theoretical Determination of Minimum Energy Required for the Direct Initiation of Detonations," PhD thesis, The University of Michigan, Ann Arbor, MI, (1979).

37. Hermance, C. E. , "Ignition Analysis of Adiabatic, Homogeneous Systems Including Reactant Consumption," AIAA J. , 11, 1728, (1973).

38. Kassoy, D. R. , "Perturbation Methods for Mathematical Models of Explosion Phenomena," Q. Jl. Mech. Appl. Math, XXVIII, Pt. 1 (1975).

39. Fickett, W. and Wood, W. W. , "Flow calculations for pulsating one dimensional detonations," Phys. Fluids, 9, 903, (1966).

40. Dabora, E. K. , and Weinberger, L. P. , "Present Status of Detonations in Two Phase Systems," Acta Astronautica, 1, 361, (1974).

41. Borisov, A. A. , and Gel'fand, B. E. , "Review of Papers on Detonation in Two Phase Systems," Arch. Thermodynamiki i Spalaia, 7, (2), 273 (1976).

42. Lu, P. L. , and Slagg, N. , "Chemical aspects in shock ignition of fuel drops," Acta Astronautica, 1, 1219, (1974).

43. Lu, P. L. , Slagg, N. and Fishburn, B. D. , "Relation of Chemical and Physical Processes in Two Phase Detonations," paper presented at Sixth International Colloquium on Gas Dynamics of Explosions and Reactive Systems, Stockholm, Sweden, August (1977).

44. Dabora, E. K. , Ragland, K. W. , Nicholls, J. A. , "Drop Size Effect in Spray Detonations," Twelfth Symposium (International) on Combustion, The Combustion Institute, Pittsburgh, PA, (1969).

45. Bar Or, R. , Sichel, M. , and Nicholls, J. A. , "The Propagation of Cylindrical Detonations in Monodisperse Sprays," Eighteenth Symposium (International) on Combustion, Waterloo, Canada, August (1980). Also see
Bar Or, R. ,"Experimental Study of Cylindrical, Two Phase Detonations in Monodisperse Sprays," PhD thesis, The University of Michigan, (1979).

46.   Fishburn, B. D., "Boundary layer stripping of liquid drops
        fragmented by Taylor instability," Acta Astronautica, 1, 1267,
        (1974).

47.   Pierce, T. H., and Nicholls, J. A., "Time Variation in the
        Reaction Zone Structure of Two Phase Spray Detonations,"
        Fourteenth Symposium (International) on Combustion, The
        Combustion Institute, Pittsburgh, PA , (1973).

48.   Waldman, G. D., and Reinecke, W. G., and Glenn, D. C.,
        "Raindrop Breakup in the Shock Layer of a High-Speed Vehicle,"
        AIAA J., 10, 1200, (1972).

49.   Ranger, A. A., and Nicholls, J. A., "Aerodynamic Shattering of
        Liquid Drops," AIAA J., 7, 285, (1969).

50.   Reinecke, W. G., and Waldman, G. D., "A General Correlation
        of Flow Induced Drop Acceleration, Deformation, and Shattering,"
        Fifth International Conference on Erosion by Liquid and Solid
        Impact, ELSIV, Newham College, Cambridge, England (1979).

51.   Dabora, E. K., "A Model for Spray Detonation," Acta Astronautica,
        6, 269, (1979).

52.   Pierce, T. H., "Experimental and Theoretical Study of the
        Structure of Two-Phase Detonations in Sprays," PhD thesis, The
        University of Michigan, Ann Arbor, MI , (1972).

53.   Sichel, M., and Chen, Y. C., "The Role of Droplet Breakup in the
        Induction Zone of Two Phase Detonations," paper presented at
        the Meeting of the Eastern States Section of the Combustion
        Institute, Atlanta, GA , November (1979).

54.   Borisov, A. A., Gel'fand, B. E., Gubin, S. A., Kogarko, S. M.,
        and Podgrebenko, A. L., "The Reaction Zone of Two-Phase
        Detonations," Astronautica Acta , 15, 411, (1970).

55.   Gubin, S. A., and Sichel, M., "Calculation of the Detonation
        Velocity of a Mixture of Liquid Fuel Droplets and a Gaseous
        Oxidizer," Comb. Sci. and Tech. 17, 109, (1977).

56.   Mullins, S. B., Fuel, 32, 327, (1953).

57. Ragland, K. W., "The Propagation and Structure of Two Phase Detonations," PhD thesis, The University of Michigan, Ann Arbor, MI , (1967).

58. Eidelman, S., and Burcat, A., "The Evolution of a Detonation Wave in a Cloud of Fuel Droplets: Part I, Influence of the Igniting Explosion," AIAA J., 9, 1103, (1980).

59. Mitrofanov, V. V., Pinaev, A. V., and Zhdan, S. A., "Calculations of detonation waves in gas-droplet systems," Acta Astronautica, 6 , 281, (1979).

60. Cherepanov, G. P., "The Theory of Detonations in Heterogeneous Systems," Translated from PMTF No. 4, Moscow, April (1965).

61. Pierce, T. H., and Nicholls, J. A., "Time Variation in the Reaction Zone Structure of Two-Phase Spray Detonations," Fourteenth Symposium (International) on Combustion, The Combustion Institute, Pittsburgh, PA , 1277, (1973).

62. Ranger, A. A., "The Aerodynamic Shattering of Liquid Drops," PhD thesis, The University of Michigan, Ann Arbor, MI (1968).

63. Reinecke, W. G., and Waldman, G. D., "An investigation of water drop disintegration in the region behind strong shock waves," Third International Conference on Rain Erosion and Related Phenomena, Hampshire, England (1970).

64. Taylor, G. I., "The instability of liquid surfaces when accelerated in a direction perpendicular to their planes," Proc. Roy. Soc., A201, 192, (1950).

65. Semenov, N. M., Z. Phys. 48, 571, (1928).

66. Frank-Kamenetskii, D. A., Diffusion and Heat Transfer in Chemical Kinetics, 2nd ed., Plenum Press, New York, (1969).

67. Gill, W., Donaldson, A. B., and Shouman, A. R., "The Frank-Kamenetskii Problem Revisited. Part I. Boundary Conditions of First Kind," Comb. and Flame, 36, 217, (1979).

68. Merzhanov, A. G., and Averson, A. E., "The Present State of the Thermal Ignition Theory: An Invited Review," Comb. and Flame, 16, 89, (1971).

69. Kassoy, D. R., "Gas Dynamics Aspects of Thermal Explosions," paper presented at 27th Conference of Army Mathematicians, West Point, N. Y., June 10-12, 1981.

FIGURE 4. LASER SCHLIEREN PHOTOGRAPHS OF DETONATIONS
WITH DIFFERENT MIXTURE COMPOSITIONS

A - 8% CH₄ - LEAN LIMIT
B - 9.5% CH₄ - STOICHIOMETRIC MIXTURE
C - 11% CH₄ - CONCENTRATION FOR MAX VELOCITY
D - 14% CH₄ - CLOSE TO THE RICH LIMIT
E - 15.5% CH₄ - DECAYING WAVE (ABOVE RICH LIMIT)

Fig. 1 Spark Schlieren photograph of spinning
detonations in methane-air mixtures. [From Ref. 11]

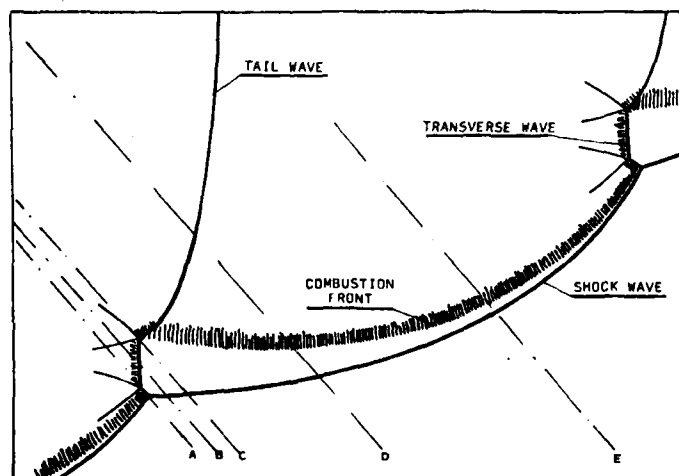Fig. 2 Schematic sketch of the structure of a spin
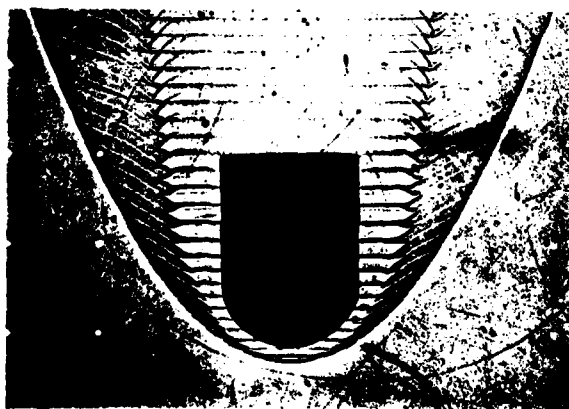detonation unrolled onto a plane. [From Ref. 11]

Fig. 4 Reaction zone models.

(a) ZEL'DOVITCH VON NEUMANN DOERING

(b) TWO FRONT

(c) COMBINED INDUCTION — REACTION ZONE

Fig. 3 An oscillatory detonation induced by a blunt body moving into a stoichiometric H_2-air mixture at the C-J detonation velocity. [From Ref. 19]
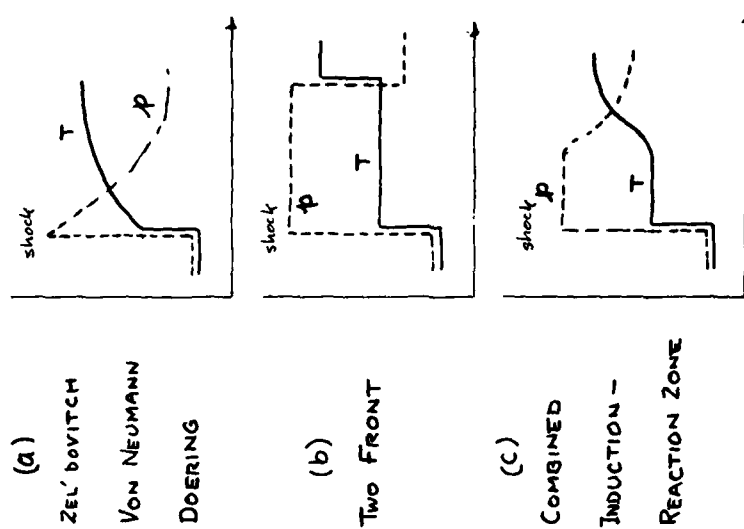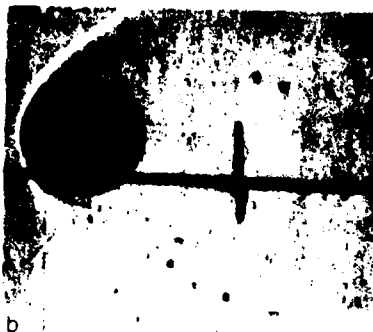
Fig. 5 Overdriven detonation induced by a
sphere moving into an H_2-O_2 mixture at a speed
above the C-J detonation velocity. [From Ref. 21].

Fig. 6(a) Schlieren photograph of a detonation propagating
through a row of 2600 μ droplets of
diethylcyclohexane in O_2. [Photo by E. K. Dabora]

Fig. 7 Schlieren photograph of a non-burning 2700 µ drop in a shock induced flow field. [From Ref. 49]

DROPLET BREAKUP AND COMBUSTION

$We = Weber\ No = \dfrac{\rho_2 u_2^2 D_0}{\sigma_\ell} \sim O(10^3) \sim \dfrac{dynamic\ force}{surface\ tension}$
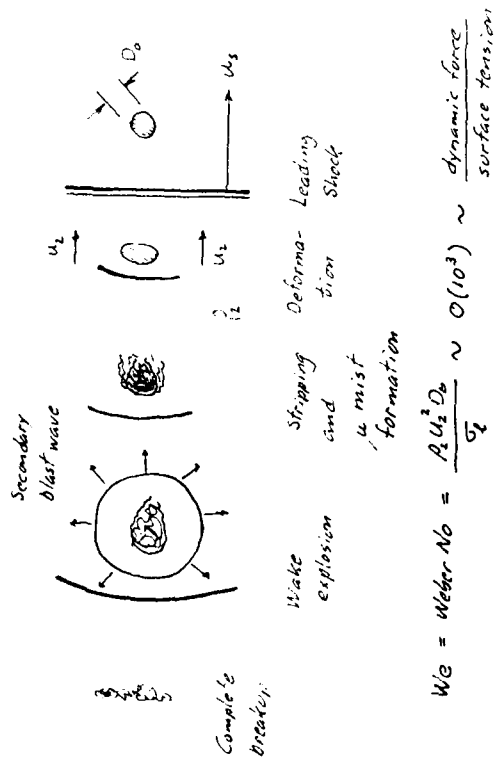
Fig. 6(b)   Schematic sketch to explain Fig. 6(a).

651

32.3μS

80μS

16μS

a. SUBCRITICAL: 80 Torr 2C₂H₂+5O₂; Igniter: LASER SPARK

23.0μS

12.5μS

6.0μS
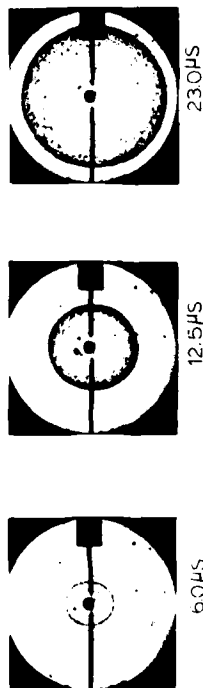
b. SUPERCRITICAL: 120 Torr H₂+Cl₂; Igniter: ELECTRICAL SPARK

20.3μS

14.4μS

6.5μS

c. CRITICAL: 100 Torr 2C₂H₂+5O₂; Igniter: LASER SPARK

Fig. 9 Spark Schlieren photographs of spherical detonations illustrating direct initiation using a laser spark. [From Ref. 27]

a. Oats/oxygen – V = 1567 m/s, c = 250 ± 20 g·m⁻³

b. Oats/air – V = 1540 m/s, c = 250 ± 20 g·m⁻³

Fig. 8 Laser-Schlieren photographs of detonations in oats dust-air and oxygen mixtures. [From Ref. 24]

Fig. 11(a) Variation of shock and flame radii r_s and r_f when $E_o < E_{oc}$. [From Ref. 30]

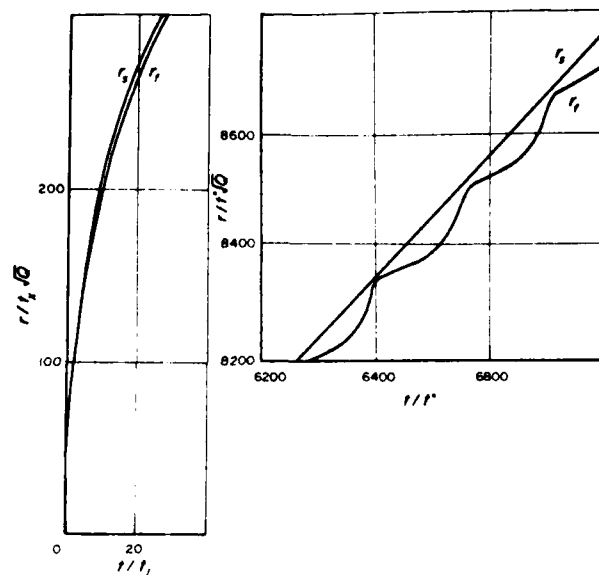Fig. 10 $M_s - R_s$ trajectories computed for different values of the parameter δ. [From Ref. 28]

Fig. 11(b) Variation of shock and flame radii
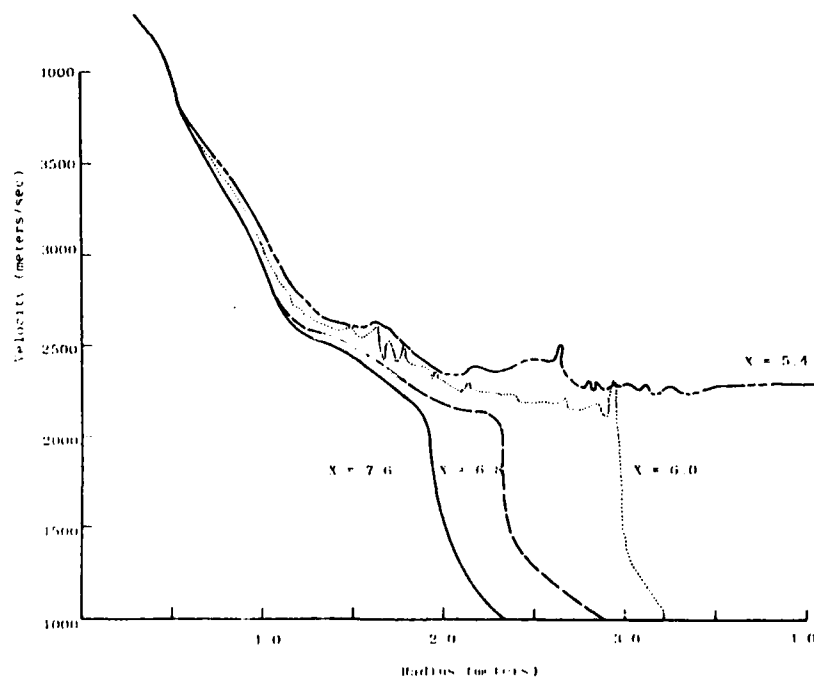r_s and r_f when $E_o > E_{oc}$. [From Ref. 30]

Fig. 12 Flame front trajectories computed by
Boni and Wilson. [From Ref. 31]

654
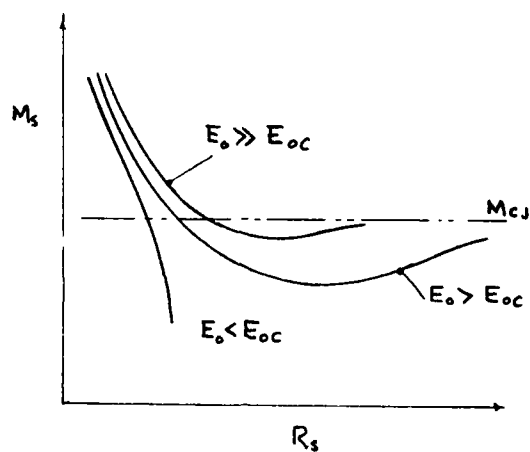
Fig. 13   Variation of M_S with R_s for $E_o > E_{oc}$
and $E_o < E_{oc}$. [From Ref. 33]
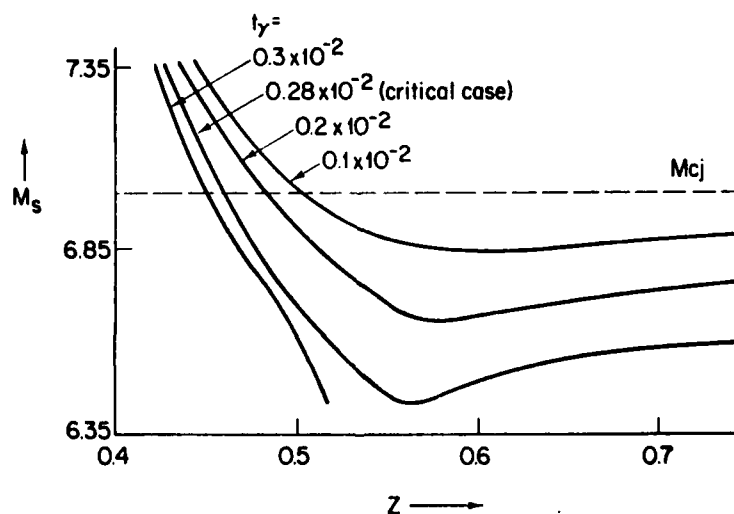
Fig. 14   Variation of M_S with R_s computed using the
asymptotic theory for $E_o > E_{oc}$ and $E_o < E_{oc}$. [From Ref. 36]
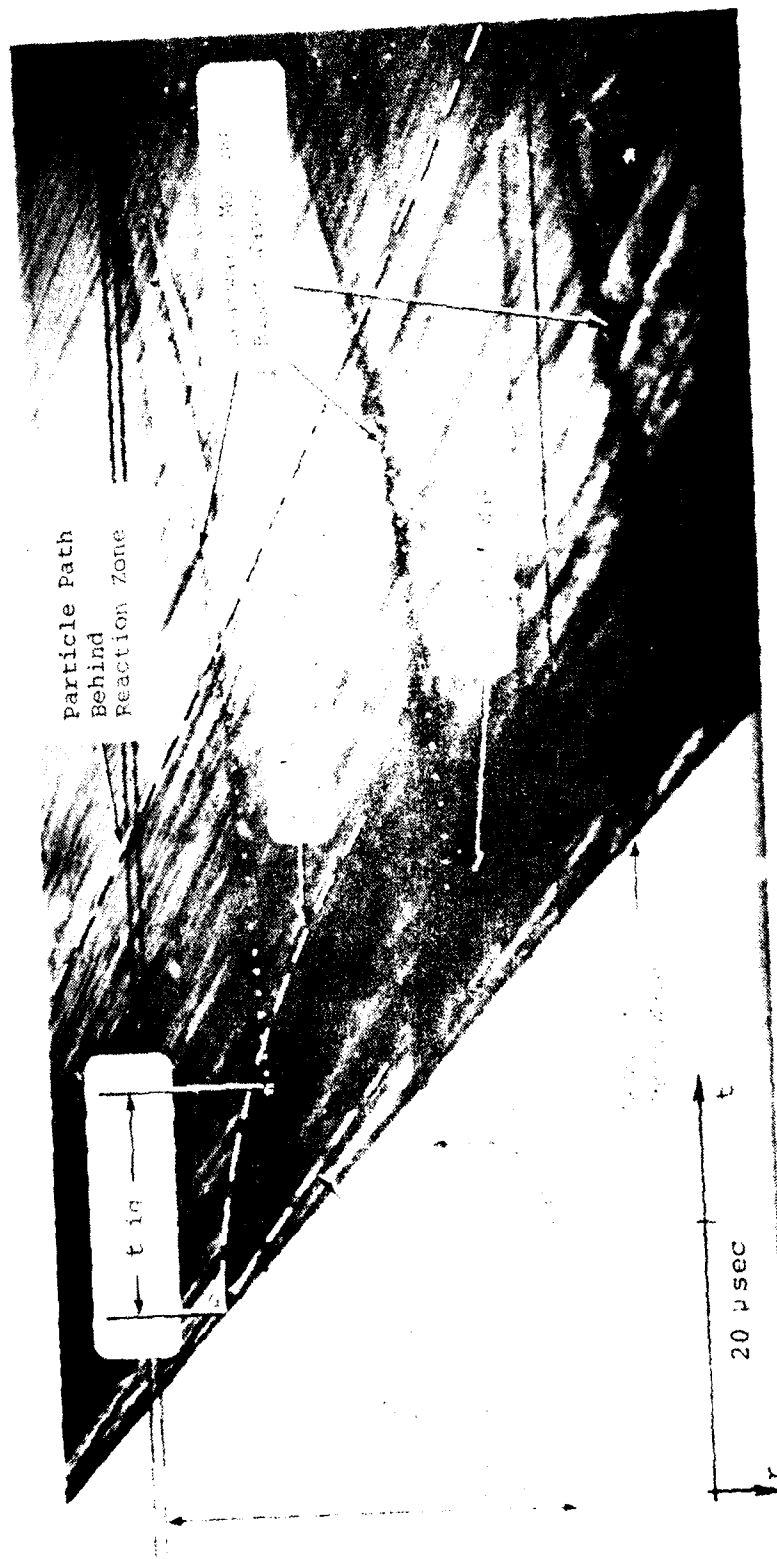
Fig. 15 Streak-Schlieren record of a detonating 400 μ droplet decane-oxygen spray. [From Ref. 45]
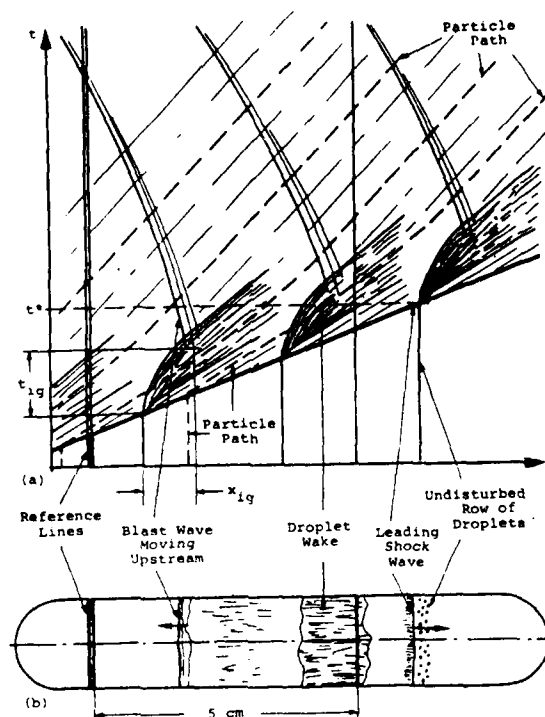
Fig. 16   Explanatory sketch for Fig. 15. [From Ref. 45]
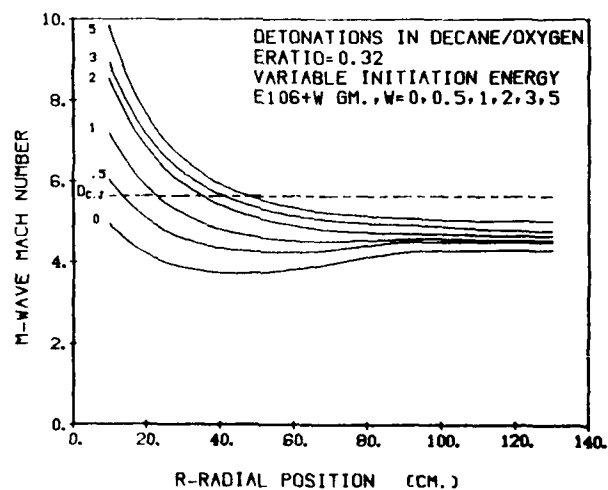
Fig. 17   Measured M_s - R_s trajectories for 400 μ decane

drops in O_2 for different values of E_o . [From Ref. 45]

657
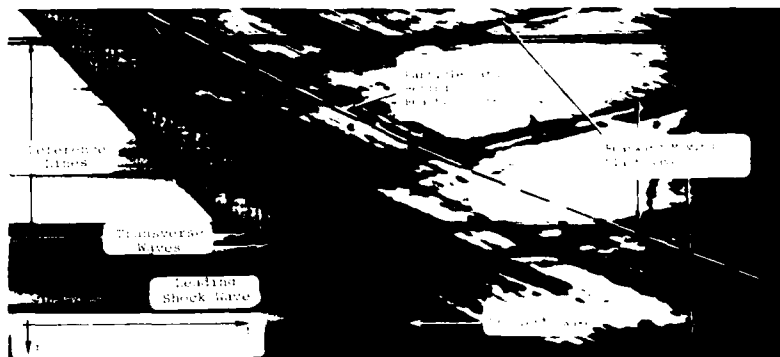
Fig. 18 Streak-Schlieren record of a detonating 400 μ
droplet heptane-oxygen spray. [From Ref. 45]
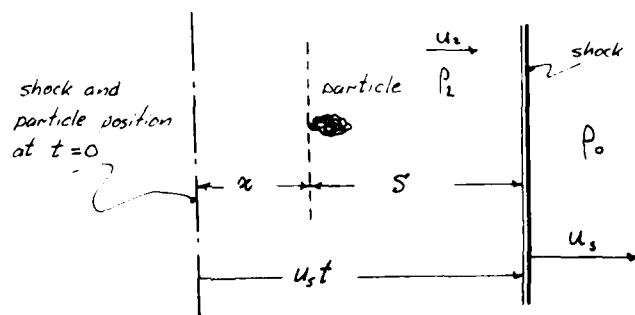
Fig. 19 Droplet break-up distance. [From Ref. 53]

Spray Detonation:

Droplet heat release pattern
(mono-disperse)

Equivalent two front
detonation
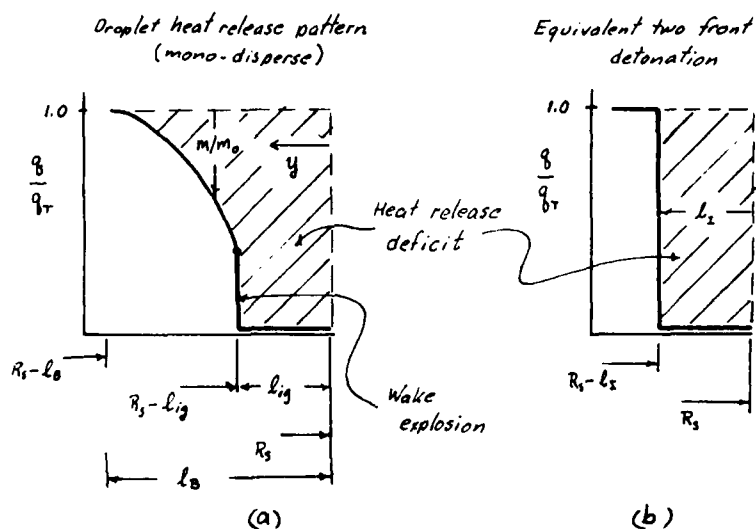
Fig. 20 (a) Droplet heat release pattern.
        (b) Equivalent two front wave.
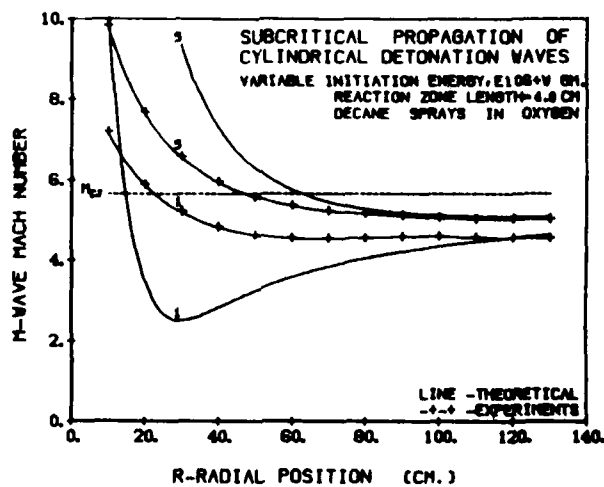
Fig. 21   Comparison of theoretical and experimental
          wave trajectories. [From Ref. 53]

659
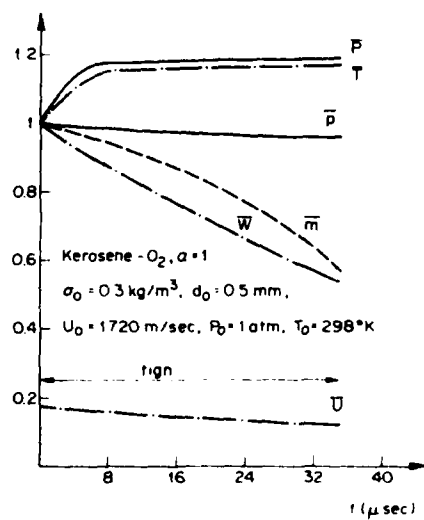
Fig. 22   Variation of flow parameters in the reaction
zone of a two-phase detonation. [From Ref. 55]
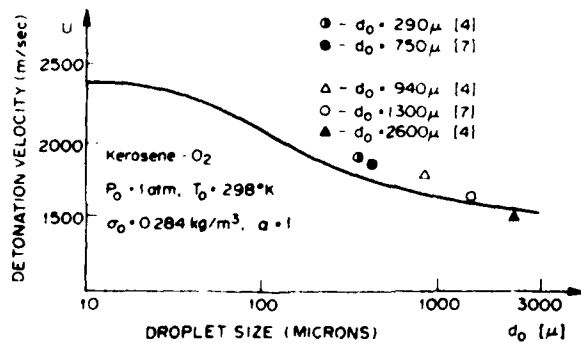
Fig. 23   Computed and measured variation of detonation
velocity with droplet size for kerosene sprays in O_2 .
[From Ref. 55]

MACH NO, M

Figure 8. The Structure of the Detonation Wave with a Secondary Shock Near the Leading Shock Front at a Radius of 0.9 m for Case 4 in Table I. (s - secondary wave)

Fig. 25 Secondary shock wave (second peak behind main shock) in the reaction zone of a two-phase detonation. [From Ref. 26]

Fig. 24 Computed variation of detonation velocity with radius for different initiation energies. [From Ref. 58]
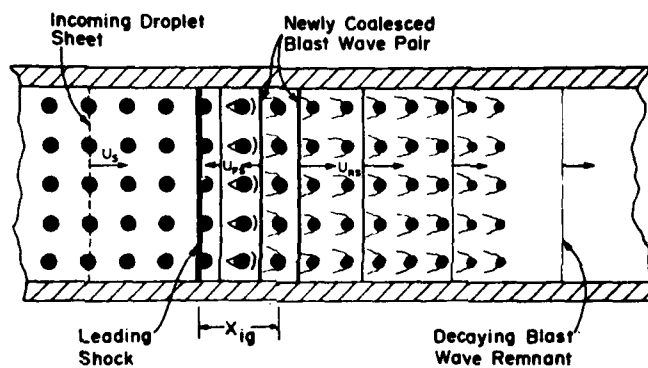
Fig. 26 Exploding fuel droplets behind
the leading shock of a spray detonation.
[From Ref. 52]
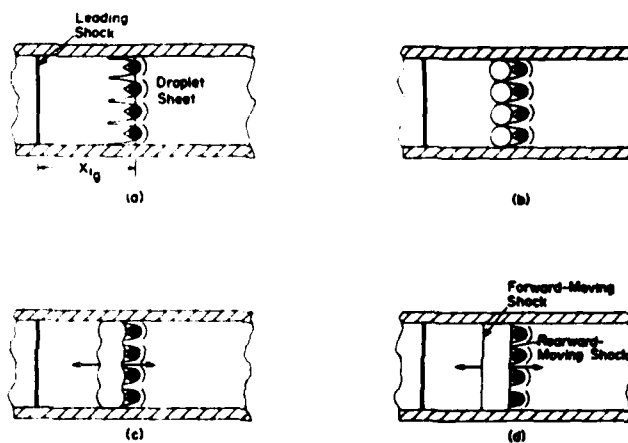
Fig. 27 Coalescence of shock waves from fuel droplets.
[From Ref. 52]
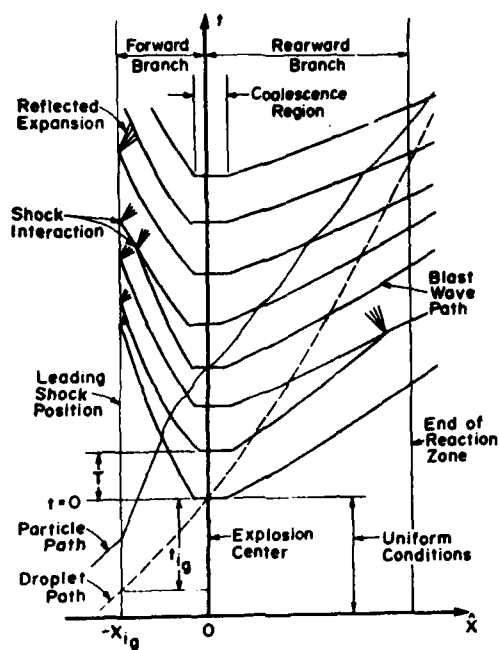
Fig. 28 x-t diagram of exploding droplets
behind a spray detonation. [From Ref. 52]
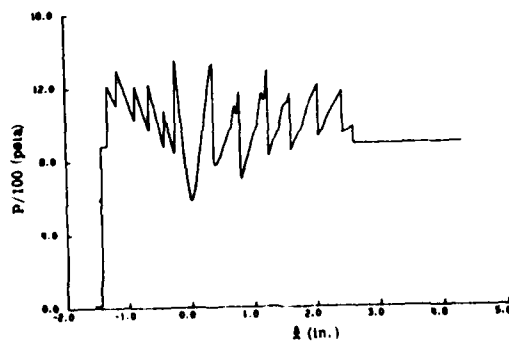
Fig. 29 Typical computed pressure distribution
behind a spray detonation. [From Ref. 52]
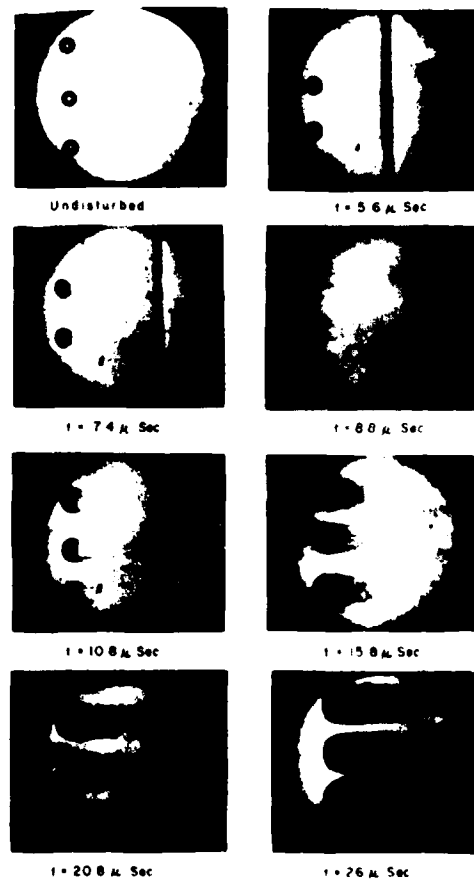
Fig. 30　Breakup of 750 μ water droplets
behind a shock wave.　[From Ref. 49]
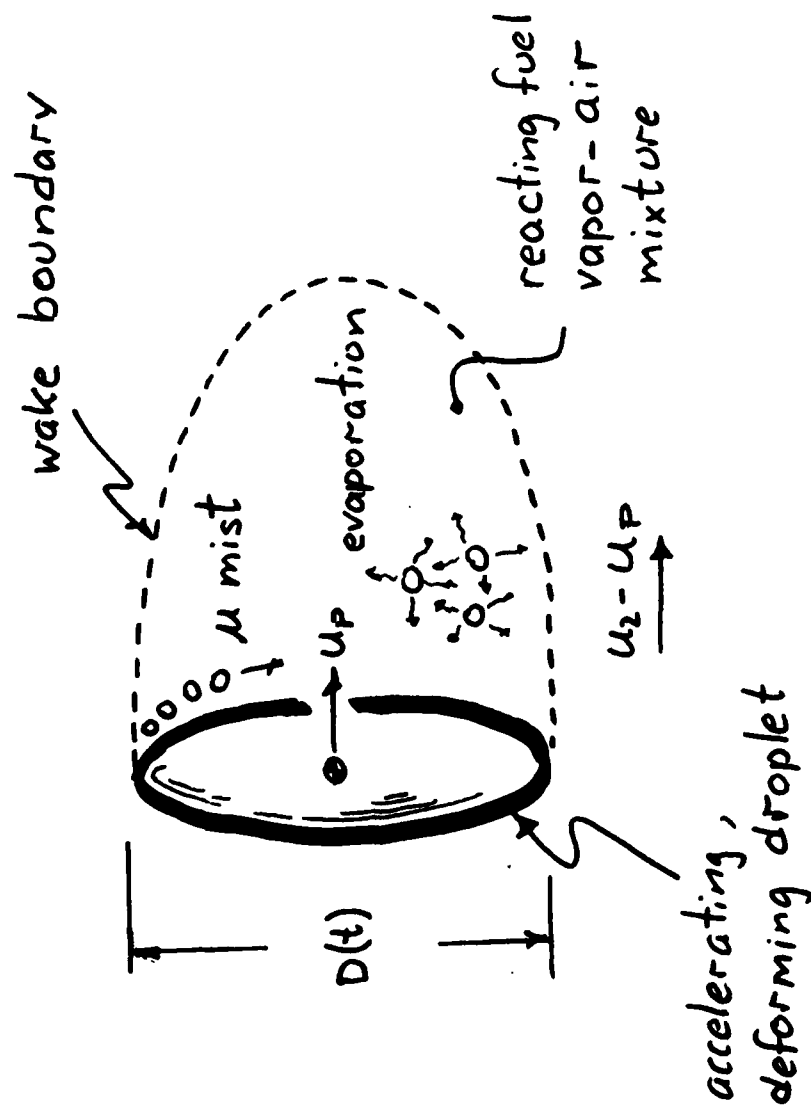
Fig. 31   Schematic diagram of fuel droplet wake.

TRANSLATION, INTERACTION AND SCATTERING OF EULER EQUATION V-STATES VIA CONTOUR DYNAMICS

Edward A. Overman, II and Norman J. Zabusky
Institute for Computational Mathematics and Applications
Department of Mathematics and Statistics
University of Pittsburgh
Pittsburgh, PA 15261

Abstract. To understand the transport of energy and mass by localized states of realistic unbounded fluid systems, we have undertaken a simulation study of the Euler equations in two spatial dimensions. For our localized states, we use the translating V-states discovered by Deem and Zabusky. These piecewise-constant dipolar regions of vorticity are stationary states in an appropriate frame of reference. We use an improved contour dynamical algorithm, again based on the Green's function of the Poisson equation, to advance the location of the boundaries of the regions of vorticity. The scattering geometry has zero "impact parameter" (coaxial V-states) and we perform head-on and head-tail interactions. We readily observe the excitation of internal degrees of freedom, by observing contour parameters including curvature and perimeter variation. For "weak" interactions we observe phase shifts and the near recurrence to initial states. For "strong" interactions we observe phase shifts, "breaking" (filament formation) and, for head-tail interactions, merger of like-signed vorticity regions. We are attempting to elucidate this rich panorama of phenomena with point vortex models.

I. INTRODUCTION. It is now well-known that solitary (nonlinear-dispersive) waves can transport energy over long distances and deposit them in small inhomogeneous spatial regions. Some of these systems can be described by nondissipative temporal plus one-space dimensional equations whose solitary waves are solitons. These systems are "integrable" and the solitons can interact with each other and preserve themselves through an interaction. If small amounts of dissipation are added to some of these systems they become nonintegrable or "near-integrable" and the soliton becomes a slowly decaying solitary entity. However, in many cases the essential features of the solitons are preserved through interaction. Some aspects of this subject are discussed in a review paper by one of the authors [1].

We now ask: Can one find localized stationary entities in two space dimensions that can transport energy (and mass) and deposit it locally? Furthermore, how robust are these entities when interacting? Nuclear physicists have begun to study these nonlinear dynamical problems [2,3] with finite-difference simulations of particle-like entities characterized by "confinement potentials." McWilliams and Zabusky [4] have examined "modon" interactions by finite-difference simulations. These modons are stationary solutions of the geostrophic β-plane equations [5] that have continuous distributions of vorticity in localized regions. In the present paper we will apply a recently improved contour dynamical algorithm [6] to study the interaction of translating V-states of the two-dimensional

Euler equations, the generic equations of nondissipative fluid dynamics. This is an unbounded-domain Green's function approach and we are not constrained by an underlying lattice. We will study parameter regions where the interactions lead to: the formation of new stationary states; the near-recurrence of initial states; or the strong deformation and breaking of initial states.

The translating V-states, discovered by Deem and Zabusky [7], are localized dipolar regions of piecewise-constant vorticity. They are stationary states of the two-dimensional Euler equations in a frame of reference translating with velocity U. They can be thought of as a simple piecewise-constant "desingularization" of two oppositely-signed point vortices. From Kelvin's theorem, one is only concerned with the motion of their boundaries. Figure 1 [8] shows the contours bounding a sequence of typical states. We use No. 8 (between No. 7 and No. 9) in all the studies presented below.

In Section II we discuss an improved contour dynamical algorithm and a key diagnostic, the contour curvature. In Section III we discuss the results obtained from various simulations. In Section IV we indicate possible directions for future research.
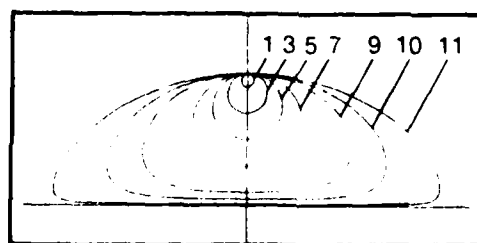
Fig. 1.   Translating V-states of the 2D Euler equations. The lower-half plane contours are symmetric.

II. EULER EQUATIONS, ROTATING V-STATES, CONTOUR DYNAMICAL ALGORITHM AND DIAGNOSTICS.

The Euler equations in two space dimensions can be written in vorticity-stream function form as

$$\omega_t + u\omega_x + v\omega_y = 0, \quad \Delta\psi \equiv \psi_{xx} + \psi_{yy} = -\omega, \tag{1a,b}$$

where

$$u = \psi_y, \quad v = -\psi_x. \tag{1c}$$

If the vorticity is composed of a set of piecewise-constant finite-area-vortex regions (or FAVR's), that is, each member of the set is a characteristic function χ_i of magnitude ω_i and boundary Γ_i, or $\omega(x,y,t) = \sum_i \omega_i \chi_i(x,y,t)$, then

$$\psi(x,y) = -(2\pi)^{-1} \sum_i \iint_{\mathbb{R}^2} \omega_i \chi_i \ G(x-\xi, \ y-\eta)d\xi d\eta, \tag{2}$$

where we use the two-dimensional Green's function

$$G = (1/2)\log\left[(x-\xi)^2 + (y-\eta)^2\right] = (1/2)\log r^2 \tag{3}$$

for flow in an unbounded domain. Eq. (1a) says that every point of the fluid including the boundary is convected with the flow. The evolution equation for boundary points is the area-preserving mapping

$$(x_t, y_t) \equiv (u(x,y,t), v(x,y,t)) = (2\pi)^{-1} \sum_i \omega_i \int_{\partial D_i} \log r(d\xi, d\eta), \tag{4}$$

where $(x,y) \in \partial D_i$ and $(\xi,\eta) \in \partial D_i$. We have used Green's theorem to replace the area integral over the domain of χ_i by the line integral over its boundary, ∂D_i, thus reducing the dimension by one.

It is well known that two point (singular) vortices of opposite circulation $\pm \Gamma$ and separation $2\bar{x}$ translate parallel to one another with speed

$$U^* = |\Gamma|/4\pi\bar{x}. \tag{5}$$

To find a symmetric uniformly translating doubly-connected region of finite-area and piecewise-constant vorticity, we apply the boundary condition

$$\underset{\sim}{n} \cdot \underset{\sim}{v}_{particle} = \underset{\sim}{n} \cdot \underset{\sim}{v}_{boundary}, \tag{6}$$

or

$$\partial_s \psi + U(dy/ds) = 0, \tag{7}$$

and integrate once to obtain

$$\psi(x,y) + Uy = c_i, \quad (x,y) \in \Gamma_i, \tag{8}$$

where $i = 1,2$ corresponds to the contours, and ψ is obtained from (2) as a line integral over both contours. Since the location of the boundary is unknown, Eq. (7) is a nonlinear integral equation. It has been solved by Pierrehumbert and Landau and Zabusky [8]. Results from the latter that we called "V-states" are illustrated in Fig. 1. We used state No. 8 (between Nos. 7 and 9) which had the following properties:

$$x_2 = 0.2; \qquad \bar{x} = 0.5873; \qquad \alpha = 1.346$$

$$A = 0.68135; \qquad P = 3.0976;$$

$$U = 0.088193; \qquad U/U^* = 0.95526;$$

where

x_2 = vertical distance from the x-axis to the closest contour point;

1.0 = vertical distance from the x-axis to the furthest contour point;

α = maximum horizontal "diameter"/$(1-x_2)$;

A = area within one contour;

P = perimeter of the contour;

$\bar{x}$ = distance from the x-axis to the center-of-area;

U = translation velocity (the bifurcation parameter);

U/U^* = normalized translation velocity ratio with U^* given in (5).

The contour dynamics algorithm is obtained by discretizing Eq. (4), [6] i.e.,

$$(\dot{x}_m, \dot{y}_m) = \sum_i \sum_{n=1}^{N_i} \Delta u_{m,n} (\cos \theta_n, \sin \theta_n) \tag{9}$$

where the i-sum is over all the contours. We assume that nodes n and $n+1$ are connected by a straight line segment of length h_n at an angle θ_n (from node n to $n+1$). Carrying out the integration in Eq. (4) exactly we obtain

$$\Delta u_{m,n} = \frac{h_n}{2\pi} [(1+A_n) \ln r_{m,n+1} - A_n \ln r_{m,n} - 1 + B_n \arctan (2B_n/C_n) + \pi |B_n| H(-C_n)],$$

$$\tag{10}$$

where $r_{m,n}$ is the straight line distance between nodes m and n,

$$A_n = \frac{(x_n - x_m)(x_{n+1} - x_n) + (y_n - y_m)(y_{n+1} - y_n)}{h_n^2}, \tag{11a}$$

$$B_n = \frac{(x_n - x_m)(y_{n+1} - y_n) - (y_n - y_m)(x_{n+1} - x_n)}{h_n^2}, \tag{11b}$$

$$C_n = \frac{r_{m,n}^2 + r_{m,n+1}^2}{h_n^2} - 1, \tag{11c}$$

and H is the Heaviside step function, i.e.,

AD-A110 109   ARMY RESEARCH OFFICE RESEARCH TRIANGLE PARK NC   F/6 12/1
                TRANSACTIONS OF THE TWENTY-SEVENTH CONFERENCE OF ARMY MATHEMATI--ETC(U)
                JAN 82
UNCLASSIFIED   ARO-82-1   NL

END
DATE
FILMED
3 82
DTIC

MICROCOPY RESOLUTION TEST CHART

NATIONAL BUREAU OF STANDARDS
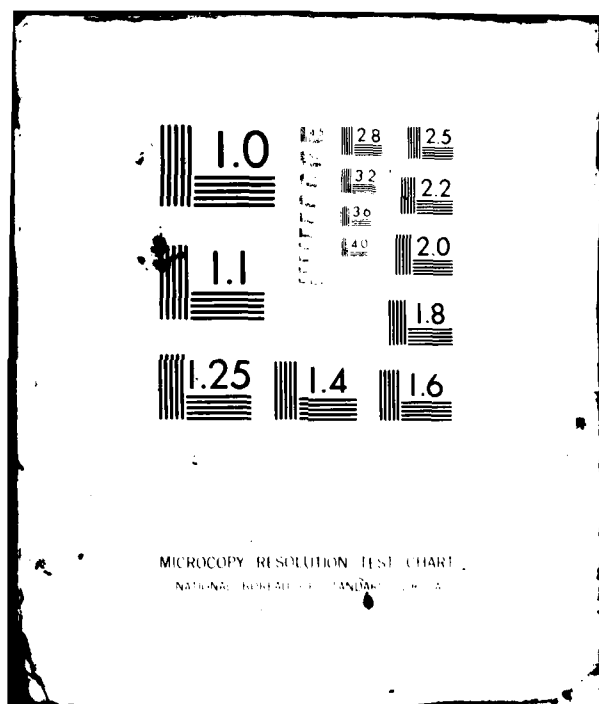
$$H(z) = \begin{cases} 1 & \text{if } z > 0 \\ \\ 0 & \text{if } z < 0 \text{ .} \end{cases}$$

If $n = m$, Eq. (10) simplifies to

$$\Delta u_{m,m} = \frac{1}{2\pi} [\ln r_{m,m+1} - 1], \tag{12a}$$

since $A_m = B_m = 0$, while if $n = m - 1$

$$\Delta u_{m,m-1} = \frac{1}{2\pi} [\ln r_{m,m-1} - 1], \tag{12b}$$

since $A_{m-1} = -1$ and $B_{m-1} = 0$.

Eq. (10) differs from the previously given value (Ref. 6, Eq. 18) in the last term. This term appears only when $C_n < 0$ or, equivalently, if the angle between the lines from node m to node n and from node m to node $n+1$ is $\geq \pi/2$. This may occur if a contour breaks and forms filaments whose sides approach or if two different contours approach close to one another in a merger, because the node-insertion-and-removal algorithm maintains $h_n \geq h_{min}$, an apriori prescribed value. The velocities in (9) are used to move the contour node (x_n, y_n) with an Euler-predictor and a trapezoidal-corrector algorithm.

The time step Δt is determined by the maximum change in area (or angular momentum) to be allowed per unit time. (Since we are solving a Lagrangian system of equations, we do not have a Courant condition to determine the time step.) In all the runs shown here the relative area change per step is $\Delta A/A = 0.84375 \times 10^{-6}$ and Δt is readjusted every 20 time steps. We find that $.015 \leq \Delta t \leq .02$ for all the runs.

In the improved node insertion-and-removal algorithm we insert and remove nodes using both local [9] and global adaptive methods. Locally, we attempt to set the internodal distance h_k to

$$\ell_k = c_1 |\kappa_k|, \tag{13}$$

which is inversely proportional to the local curvature but we require it to satisfy two constraints

$$h_{max}^{(g)} \geq h_k \geq h_{min}, \tag{14a}$$

and

$$(1-r)h_{k-1} \le h_k \le (1+r)h_{k-1}. \tag{14b}$$

In all the runs $c_1 = 0.1$ (which places $\sim 20\pi$ nodes on a circle of unit radius), $h_{min} = 0.01$ and $r = 0.3$. Globally, we choose $h_{max}^{(g)}$ to take into account the possibility that one part of a contour may approach another part or that two contours may approach each other. This is done by setting

$$h_{max}^{(g)} = \max [\min\{h_{max}, c_2 \, d_{min}\}, h_{min}] \tag{15}$$

where d_{min}, obtained by a search algorithm, is the minimum distance from node k to a point on a neighboring contour or a "nonadjacent" point on the same contour. Usually, $h_{max}^{(g)}$ will be the minimum of h_{max}, the maximum allowed distance between nodes, or $c_2 \, d_{min}$ (in all our runs $h_{max} = 0.20$ and $c_2 = 0.50$).

As diagnostics we monitor the perimeter, P, area, A, (a quantity conserved in the continuum representation) and contour curvature, $\kappa(s) = x_s y_{ss} - x_{ss} y_x$. The vertical scale has a geometric variation $(1^2, 2^2, 3^2, 4^2, 5^2)$ and the curves are "clipped" at $+ 5^2$. The curvature is computed numerically by differentiating a periodic cubic spline that is fit to the nodes (as described in Ref. 9, Appendix C). If contours "sharpen" and "break", as observed below, this differentiation can give rise to small-scale oscillations because the cubic spline has difficulty fitting such distributions. These oscillations do not affect our velocities since the curvature is not used explicitly in (10).

III. DYNAMICAL EVOLUTION OF PAIRS OF TRANSLATING V-STATES. In this first study of translating V-state interactions, we simplify the parameter space by choosing zero "impact-parameter" (or coaxial) collisions. The resulting symmetry allows us to reduce the computational load by a factor of 4. We use state No. 8 throughout and obtain different areas by rescaling all distances linearly. It is obvious that one can always find parameter regions where the interactions can be characterized as "near-integrable." That is, if we replace the V-state by oppositely-signed point vortices, then we can integrate the system exactly, as Love [10] did for overtaking (head-tail) interactions. Table 1 gives parameters for the cases discussed below.

We will observe that the head-on or "approaching" interactions tend to be "weaker" than the head-tail or "overtaking" interactions. That is,

in the former case the final states although perturbed, seem to have a smaller tendency to break. In particular, Fig. 2 (Case 1) is a composite which shows two approaching V-states with $\Gamma_1/\Gamma_2 = -1.0$ and unlike area reform into an outgoing asymmetric apparently stationary configuration. It is travelling in a north-easterly direction with a velocity intermediate between those of the incoming V-states, and is undoubtedly an asymmetric translating V-state. At $t = 0$ they are maximally separated ($\bar{x}_{c0} = 4.0$) and the highest state shown is at $t = 60$. The time increment between states is $\Delta t = 12$. The unconnected circles indicate the discretization used. The number of nodes on contours (1,2) increased from (64,66) at $t = 0$ to (77,115) at $t = 60$, respectively. (The large number on the nearly circular small V-state (No. 2) arises because of its larger curvature.) Note the lower half plane contains a symmetrical result. The "x" marks the centroids of the figures. The numbers on the contours label the same node and give one a feeling for the rotation. This case is repeated in panel a of Fig. 3.

Case 2, given in panel b of Fig. 3 is the result of increasing the circulation ratio $|\Gamma_1/\Gamma_2|$ by 2.0. Hence, the approaching V-states undergo a complicated interaction where No. 1 passes below No. 2. Fig. (4a) shows the trajectories on the (x,y) plane and Fig. (4b) shows an (x,t) "phase-shift" diagram. There is no apparent velocity change.

Case 3, given in Fig. 3c is the result of decreasing the circulation $|\Gamma_1/\Gamma_2|$ to 2/3 compared to Case 1. During the interaction, No. 1 passes above No. 2 and No. 1 is left in an excited (distorted) state as it translates to the right. A careful perusal shows the perimeter to be oscillating in time.

Fig. 5 shows two head-on cases where the area of the vortex regions are the same but the circulation ratio $|\Gamma_1/\Gamma_2|$ is now 1/4 (panel a) and 1/6 (panel b) compared to Case 1. This causes No. 1 to loop above No. 2, consistent with Case 3, but now No. 1 shows a tendency to break. Had we continued to decrease the circulation ratio, it is reasonable that a piece of No. 1 would have been elongated around No. 2, before it escaped to the right.

Fig. 6 (a,b,c,d) shows four head-tail cases (6,7,8,9), where the area ratio is 4:1 and the circulation ratios (Γ_1/Γ_2) are (1/16, 1/8, 3/16, 3/8). As one increases the circulation ratio toward unity, the "wrap-around" tendency becomes stronger. Finally, capture is observed in panel d.

Fig. 7 (a,b,c) shows three head-tail cases (10,11,12), where the area ratio is 1:1 and the circulation ratios (Γ_1/Γ_2) are (1.0, 2.0, 3.0). Aside from the difference in areas, cases 9, 10 and 11 (Figs. 6d, 7a and 7b, respectively) bear a resemblance. Thus, in the range $3/8 \leq \Gamma_1/\Gamma_2 \leq 8/3$ one expects merging to occur for head-tail inter-

actions. As the circulation ratio increases beyond 2.0, there is less
of a tendency toward capture, but both contours have high-curvature
regions. Note Figs. 8b and 8c show the initial and final curvatures
of case 12. The circumferences have increased from (2.985,2.985) at
t = 0 to (6.033,4.113) at t = 20 and the number of nodes has in-
creased from (64,64) to (252,157), respectively.

IV. DISCUSSION. Certain qualitative features of our contour
dynamical results are consistent with the coaxial modon scattering
finite-difference results of McWilliams and Zabusky [4], for example,
phase shifts and trajectories. The modons are continuous dipolar dis-
tributions of vorticity that satisfy the quasigeostrophic β-plane
equations and weak radiation effects are operative during the close
encounters. Thus, not only can velocity changes be found, but it is
possible for the monopolar components of an incoming modon to separate
permanently. However, the precise character of the excitations and the
"breaking" (or "enstrophy" cascade) is more clearly seen with contour
dynamical methods. To understand the details behind this panorama of
new information will require more analytical and computational studies.
For distant interactions, where contours are weakly perturbed it is
possible that we may obtain insight by replacing the V-states by several
point vortices. However, for close interactions of realistic vorticity
distributions, we will require V-states containing several nested contours.

Table 1: Parameters for Coaxial Translating V-State Interactions

$(\omega_1 = 1.0, \ \Gamma_1 = 1.0, \ V_{10} = +0.088, \ A_1 = 0.6846, \ P_1 = 2.985;$
$A_2 = A_1, \ P_2 = P_1 \ \text{or} \ A_2 = 0.1711, \ P_2 = 1.493)$

Case	ω_2	Γ_2	Γ_1/Γ_2	A_1/A_2	$\bar{y}_{10}/\bar{y}_{20}$	$\bar{x}_{c0}^{*}$	V_{20}	V_{10}/V_{20}	Run
1	-4.0	-0.6846	-1.0	4	2	4	-0.176	-1/2	XS 2S02
2	-2.0	-0.3422	-2.0	4	2	8	-0.88	-1.	XS 2S03
3	-6.0	-1.0266	-2/3	4	2	4	-0.264	-1/3	XS 2S04
4	-4.0	-2.7384	-1/4	1	1	4	-0.352	-1/4	XS 2S07
5	-6.0	-4.1076	-1/6	1	1	4	-0.528	-1/6	XS 2S08
6	0.25	0.042775	1/16	4	2	4	0.011	8.0	XS 2009
7	0.5	0.08555	1/8	4	2	4	0.022	4.0	XS 2008
8	0.75	0.25665	3/16	4	2	4	0.033	8/3	XS 2003
9	1.5	0.12833	3/8	4	2	4	0.066	4/3	XS 2007
10	1.0	0.6846	1.0	1	1	-3	0.088	1.0	XS 2004
11	2.0	1.3692	2.0	1	1	-4	0.176	1/2	XS 2001
12	3.0	2.0538	3.0	1	1	-4	0.264	1/3	XS 2006

*) $\bar{x}_{c0} = \bar{x}_{20} - \bar{x}_{10}$

676

REFERENCES

1. N. J. ZABUSKY, Computational synergetics and mathematical innovation.
   J. Comp. Phys. <u>43</u> (1981). To be published.

2. V. G. MAKHANKOV, Computer experiments in soliton theory. Comput.
   Phys. Commun. <u>21</u> (1980), 1-49.

3. YU. A. SIMONOV and J. A. TJON, Inelastic effects in classical field-
   theoretical models with confinement. Ann. of Phys. <u>129</u> (1980),
   110-130.

4. J. C. MCWILLIAMS and N. J. ZABUSKY, Interactions of isolated vortices,
   I. Modons colliding with modons. Geophys. Astrophys. Fld. Dyn. (1981).
   To be published.

5. G. R. FLIERL, V. D. LARICHEV, J. C. MCWILLIAMS, and G. M. REZNICK,
   The dynamics of baroclinic and barotropic solitary eddies. Dyn.
   Atmospheres and Oceans <u>5</u> (1980), 1-41.

6. N. J. ZABUSKY, M. H. HUGHES, and K. V. ROBERTS, Contour dynamics for
   the Euler equations in two-dimensions. J. Comput. Phys. <u>30</u> (1979),
   96-106.

7. G. S. DEEM and N. J. ZABUSKY, Stationary V-states: Interactions,
   recurrence and breaking. Phys. Rev. Lett. <u>40</u> (1978), 859.

8. M. LANDAU and N. J. ZABUSKY, Stationary solutions of the Euler
   equations in two dimensions. Singly- and doubly-connected V-states.
   Submitted for publication. Also see R. T. PIERREHUMBERT, A family
   of steady translating vortex pairs with distributed vorticity.
   J. Fluid Mech. <u>99</u> (1980), 129-144.

9. N. J. ZABUSKY and E. A. OVERMAN, II, Regularization of contour
   dynamical algorithms. J. Comput. Phys. To be published.

10. A. E. H. LOVE, On the motion of paired vortices with a common axis.
    Proc. Lond. Math. Soc. <u>XXV</u> (1894), 185- .
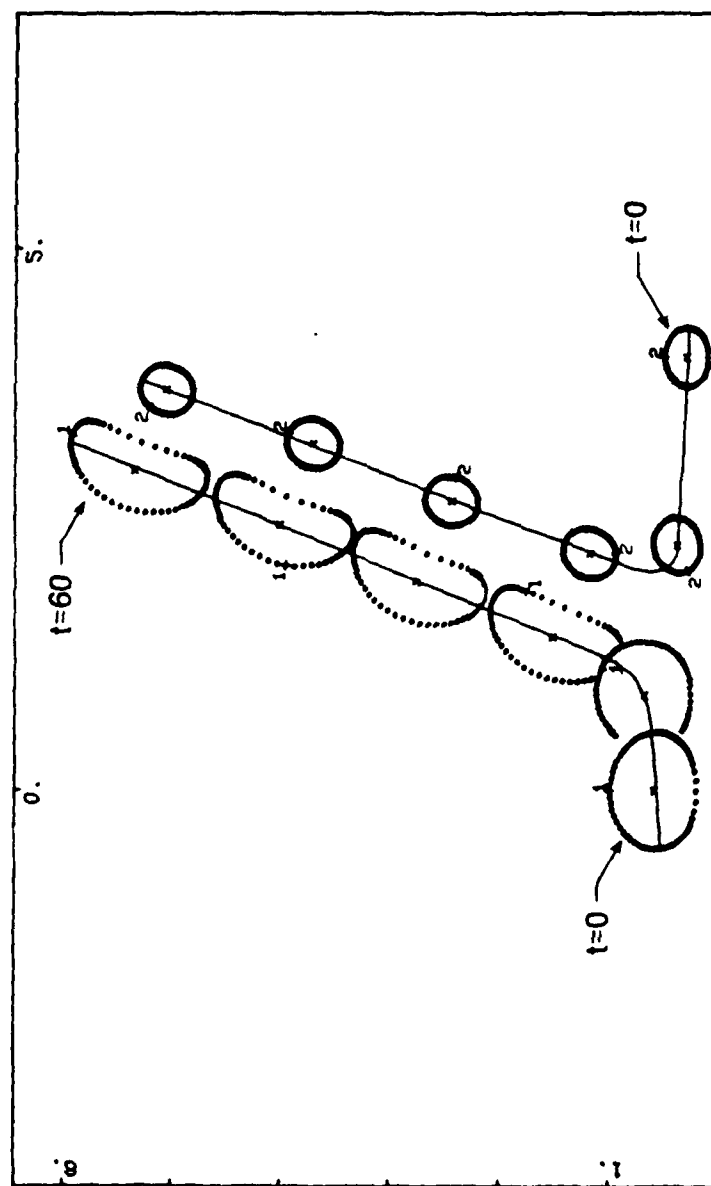
Fig. 2

Head-or interaction $\Gamma_1/\Gamma_2 = -1.0$, case 1.
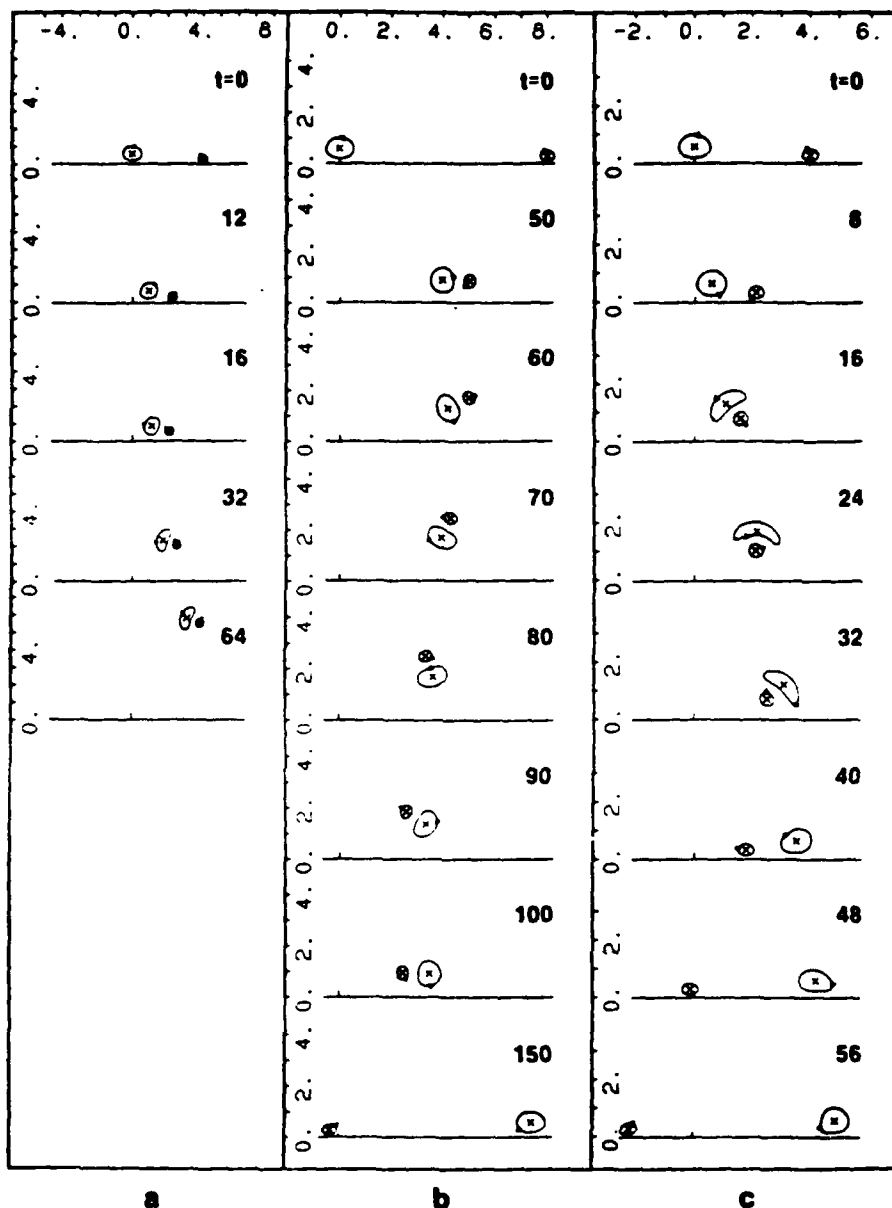
Fig. 3

Head-on interactions:

(a) Case 1, $\Gamma_1/\Gamma_2 = -1.0$;

(b) Case 2, $\Gamma_1/\Gamma_2 = -2.0$; and

(c) Case 3, $\Gamma_1/\Gamma_2 = -2/3$.

679

TIME BETWEEN DOTS = 10.0
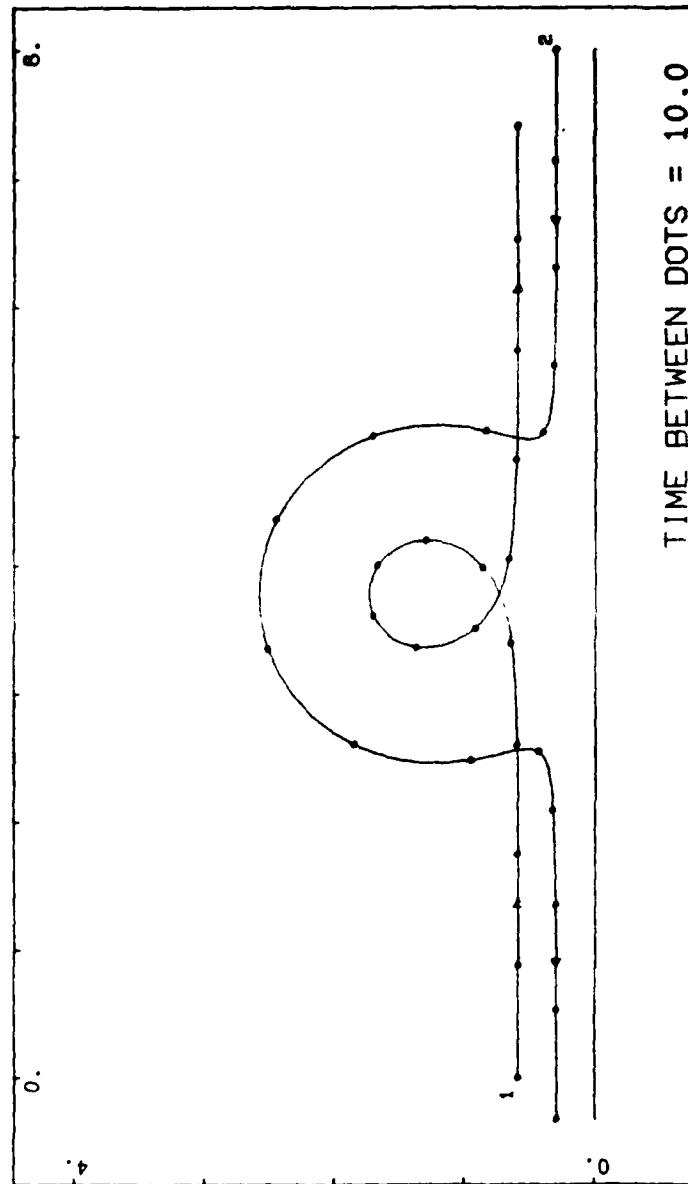
F_{IG} 4a

(a) Case 2. (x,y) trajectory diagram.

TIME BETWEEN DOTS = 10.0
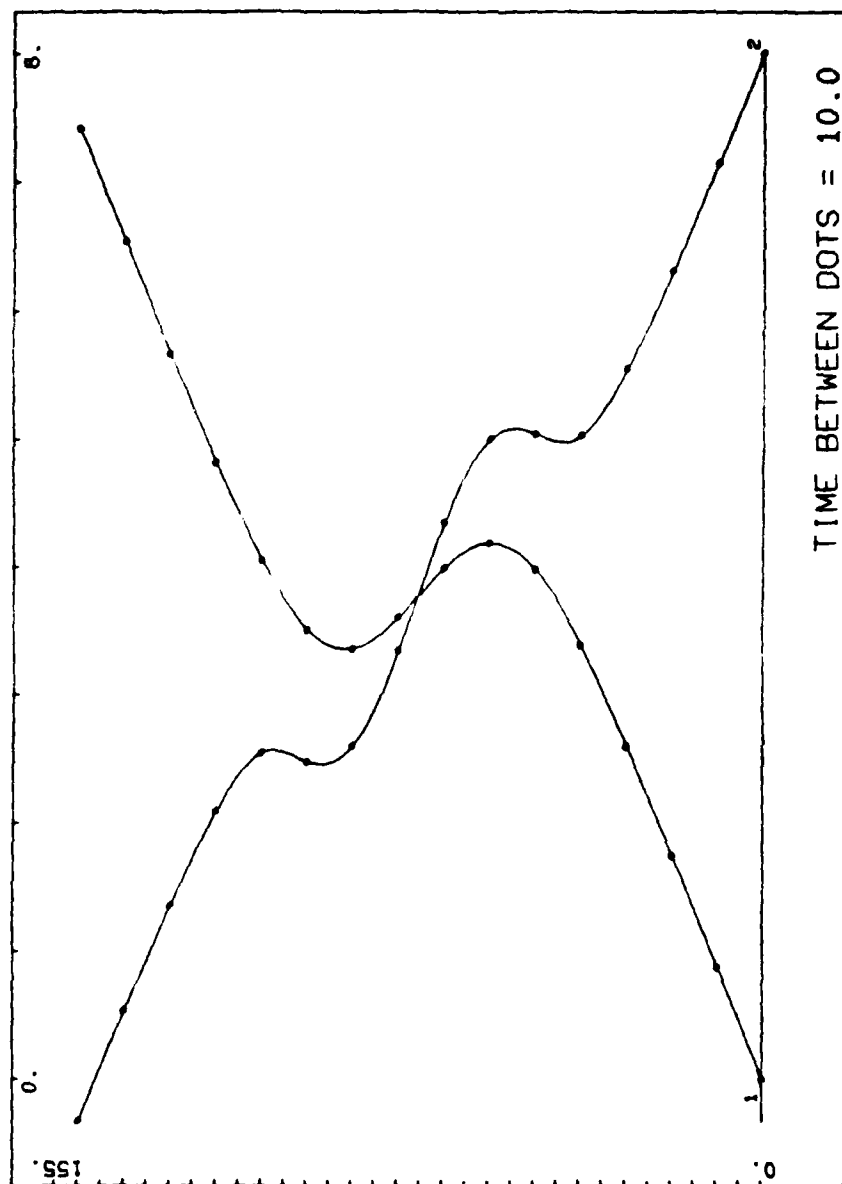
Fig. 4b

(b) Case 2. (x,t) phase-shift diagram.
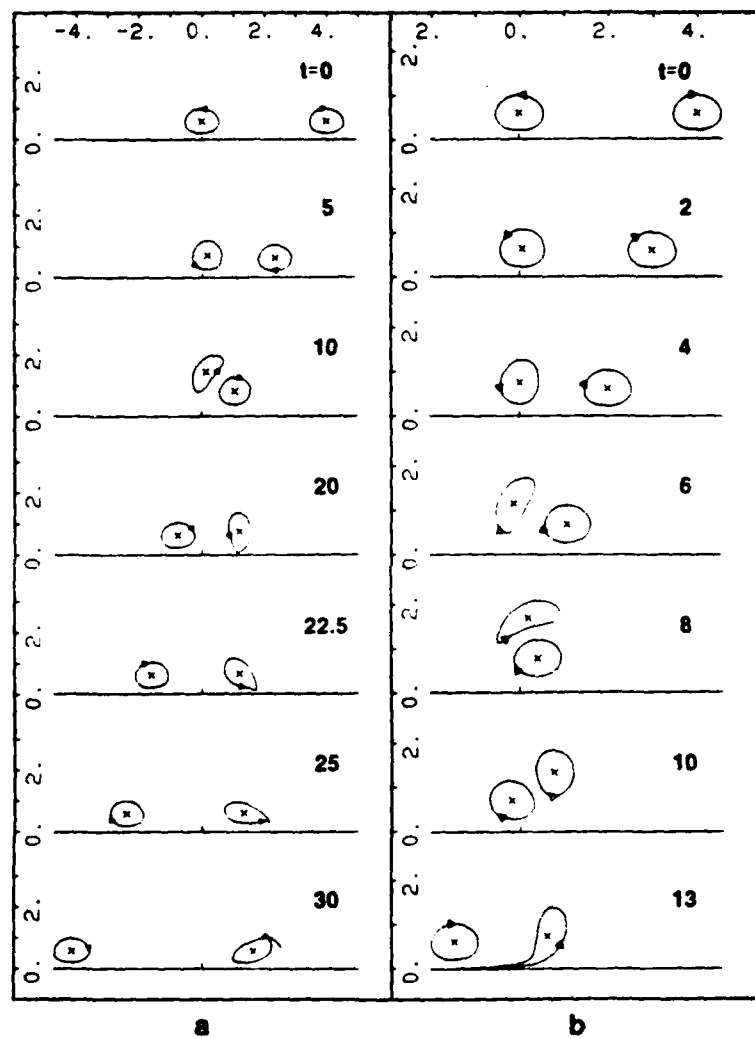
Fig. 5

Head-on interactions:

(a) Case 4, $\Gamma_1/\Gamma_2 = -1/4$; and

(b) Case 5, $\Gamma_1/\Gamma_2 = -1/6$.
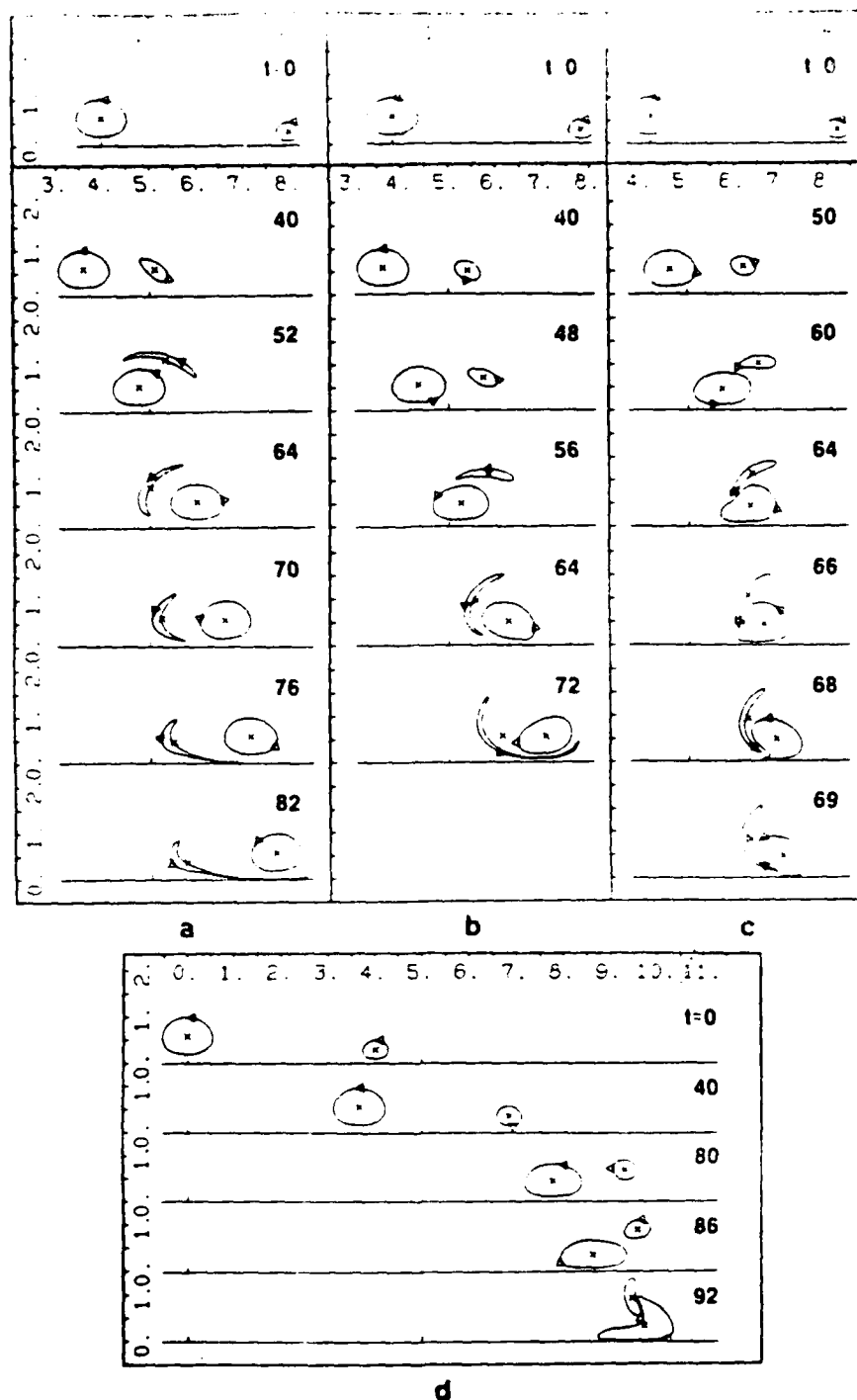
FIG. 6

Head-tail interactions:

(a) Case 6, $\Gamma_1/\Gamma_2 = 1/16$;

(b) Case 7, $\Gamma_1/\Gamma_2 = 1/8$;

(c) Case 8, $\Gamma_1/\Gamma_2 = 3/16$; and

(d) Case 9, $\Gamma_1/\Gamma_2 = 3/8$.

683

Head-tail interactions:

(a) Case 10, $\Gamma_1/\Gamma_2 = 1.0$;

(b) Case 11, $\Gamma_1/\Gamma_2 = 2.0$; and

(c) Case 12, $\Gamma_1/\Gamma_2 = 3.0$.

Notice that the scales of panel a differ from those of panels b and c.

FIG. 7

684

TIME = 20.0

t=20

t=0

c

a

b
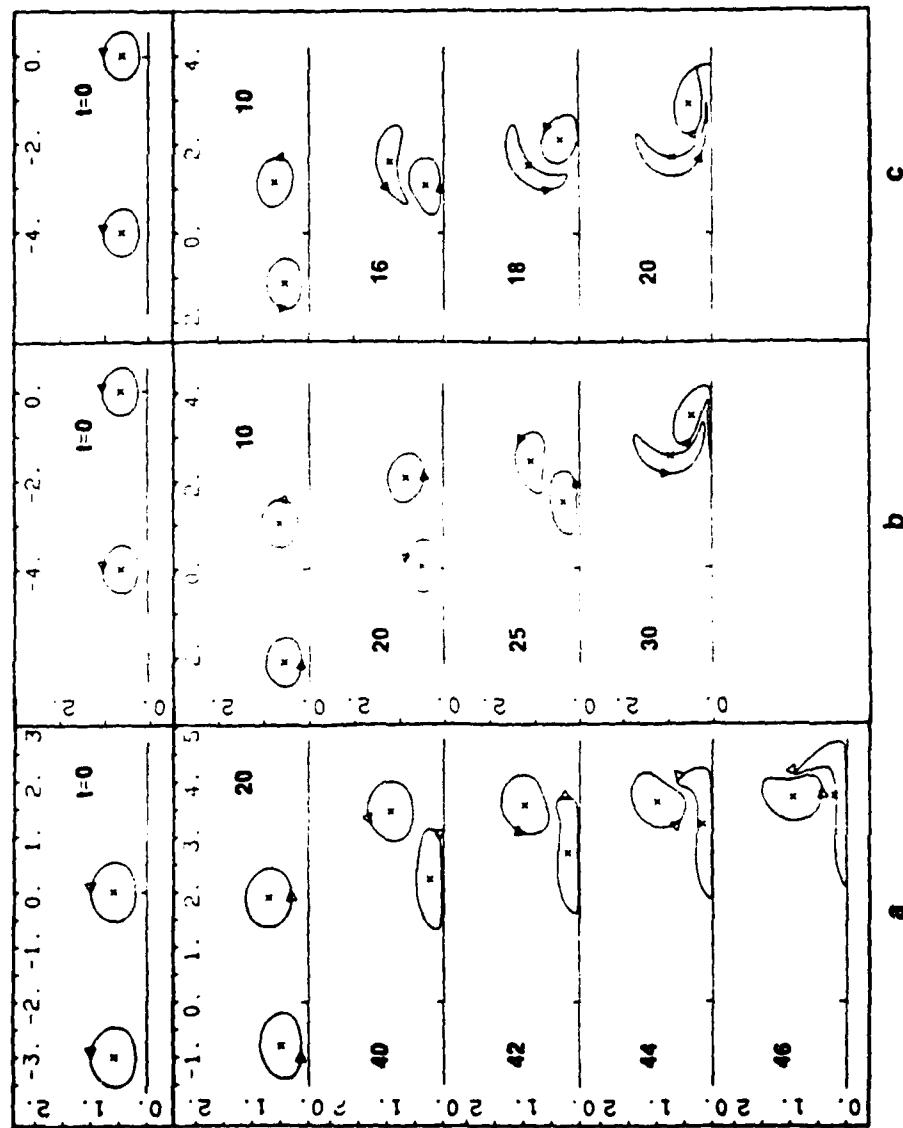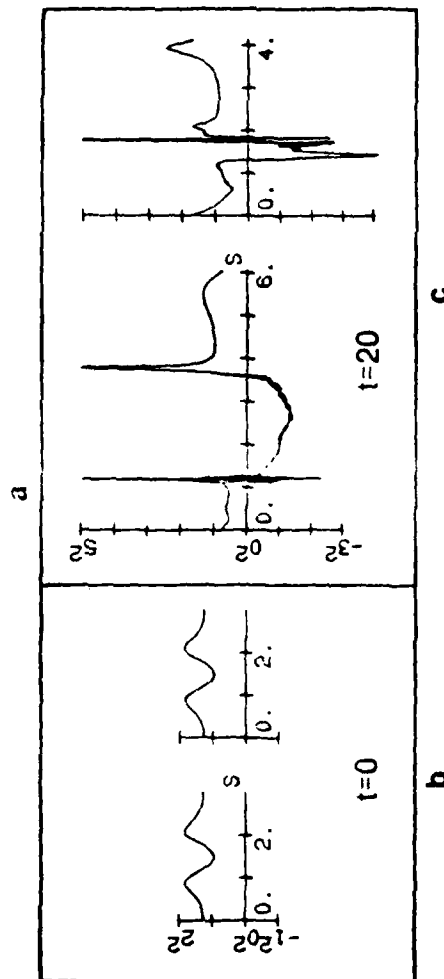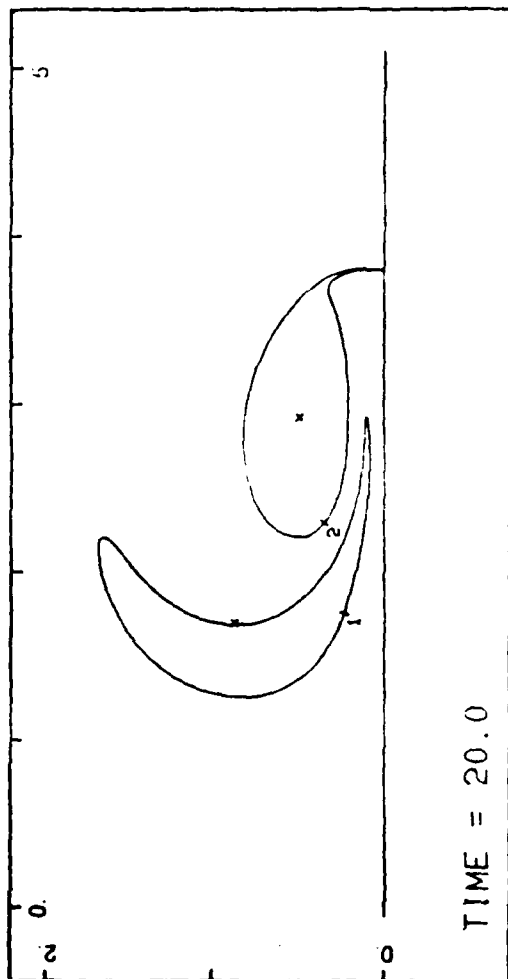
FIG. 8

(a) Upper-half plane v-states, case 12, t=20.

(b) Initial curvatures for case 12.

(c) Final curvatures for case 12.

GASDYNAMIC ASPECTS OF THERMAL EXPLOSIONS

J. Bebernes[*] and D. R. Kassoy[+]
University of Colorado
Boulder, Colorado 80309

Abstract. A mathematical model is developed for the induction period of a thermal explosion in a confined reacting, compressible gas mixture. A high activation energy asymptotic analysis is used as the method of solution development. Very early in the process, on the acoustic time scale of the vessel, an acoustic field is generated by spatially variable thermal expansion in the gas. The familiar induction period process is shown to develop on the conduction time scale of the vessel. Unlike previous theories for rigid materials the describing equations include effects of compressibility and deformation. The former effect is shown to cause a gaseous system to have a thermal runaway sooner than an equivalent rigid system. The effect of deformation is observed in the form of a rapidly expanding hot spot. Typical numerical solutions are presented along with theoretical considerations of the integrodifferential equation which describes the energy balance. A final-value analysis descibes the thermal runaway singularity. The nonuniformity in the asymptotic expansions is shown to imply that a sequence of dramatic gas dynamic events will follow the induction period process.

[*]Department of Mathematics

[+]Mechanical Engineering Department

1. Introduction

The mathematical theory of thermal explosions has been developed for both spatially homogeneous and spatially distributed systems. Asymptotic methods based on a high activation energy approximation were used first to develop solutions for the homogeneous problem (Kassoy [1976]). More recently there have been several studies of the high activation energy thermal explosion in a confined rigid combustible material (Kapila [1980]), Kassoy and Poland [1980, 1981], Bebernes and Kassoy [1981]. During an induction period, with a duration measured by the conduction time scale of the vessel, heat released by chemical reaction is redistributed by thermal conduction. As the temperature in the container increases the reaction rate grows dramatically. Eventually the characteristic time for heat release becomes significantly smaller than the conduction time in a well defined hot spot embedded in the system. Thereafter the heat released is used almost entirely to increase the hot spot temperature, further accelerating the reaction rate, because the time-scale is too short to permit heat to be conducted away. During this rapid explosion period the hot spot evolves into a fireball of great intensity. Meanwhile beyond the boundary of the fireball, the system is nearly invarient because the energy balance is controlled by the much slower conduction process. The rapid fireball reaction process slows down only when the fuel in the fireball is almost entirely consumed. Eventually the fireball heats the cooler, nearly unreacted material around it by conductive transfer. Under the appropriate circumstances a deflagration then propagates toward the container wall.

The rigid combustible thermal explosion model is limited in applicability relative to physical reality. In particular a consistent model includes neither mass diffusion nor material deformation. The latter is particularly important during the evolution of the fireball. A real material will expand in proportion

688

to the local increase in temperature. As a result stress waves will propagate

into the surrounding medium. In some cases the waves will destroy the physical

integrity of the confined explosive.

In an attempt to overcome the limitations of the rigid model we describe

here a model for the thermal explosion occurring in a confined compressible,

perfect, reactive gas mixture. The problem is described by the complete equation

of motion for a compressible, ideal, reactive gas mixture. All transport proper-

ties are included. Simplifications are confined to the details of the chemical

reaction and material properties.

The inclusion of material compressibility in the model means that one must

consider physical processes on the acoustic time scale as well as those occurring

on the conduction and reaction time scales. In particular, material expansion

associated with localized heating causes mechanical disturbances in the gas.

These are propagated as acoustic waves at the local speed of sound. Under appro-

priate circumstances the initially linear acoustic processes can become nonlinear

leading to the formation of shock waves. The interaction of the shock with re-

active gas introduces an entirely new set of combustion processes into the confined

thermal reaction system.

In the present paper we summarize some of the significant developments in

our work on gaseous thermal explosions, citing where appropriate, more detailed

descriptions of the phenomena and mathematics of interest. The complete mathemat-

ical model is given along with the assumptions that have been invoked. We then

describe the essential characteristics of processes on the early, short acoustic

time scale, and the mathematical analysis of the induction period process. The

nonuniformities in the asymptotic expansions are examined in order to rationalize

the next step in the solution development process. We then explain how the

expanding hot spot generates a benign acoustic field when the characteristic reaction time and the acoustic time are comparable. The possibility of shock wave formation is considered from the physical viewpoint. A discussion of consequences follows.

2. Modelling Assumptions and Describing Equations

The reactive mixture of ideal gases has been modelled with a single molecular weight and a single constant diffusion coefficient. In addition the thermal conductivity, viscosity and specific heat are assumed to be constants. The chemical reaction is defined by a single-step irreversible mechanism with Arrhenius-type kinetic parameters. The initial reactant mixture is assumed to be stoichiometric, at rest and a temperature T_o' and a fuel mass fraction Y_{Fo} throughout (Primes denote dimensional quantities). The gas is bounded by two infinite parallel plates which are rigid, impermeable, and separated by a distance of $2\ell'$. The gas temperature at the plates is assumed to be maintained at T_o'.

The non-dimensional describing equations for this problem are

$$\rho_t + u\rho_x = -\rho \, u_x \tag{1a}$$

$$\rho[u_t + u \, u_x] = -\frac{P_x}{\gamma} + \frac{4}{3} M \, P_r \, u_{xx} \tag{1b}$$

$$\rho[T_t + u \, T_x] = \varepsilon \, M\gamma \, \delta\rho^n Y^n \, \exp\left((T-1)/\varepsilon T\right)$$
$$+ M \gamma \, T_{xx} - (\gamma-1) \, P \, u_x$$
$$+ \frac{4}{3} M \gamma \, (\gamma-1) \, P_r \, (u_x)^2 \tag{1c}$$

$$\rho[Y_t + uY_x] = -\varepsilon M \gamma \delta \rho^n Y^n \Gamma \exp((T-1/T) + \frac{M}{Le}(\rho Y_x)_x \qquad (1d)$$

$$\rho = \rho T \qquad (1e)$$

$$\rho = T = Y = 1 \; , \quad u = 0 \; , \quad t = 0 \; , \quad 0 \le x \le 1 \qquad (1f)$$

$$\rho_x = T_x = Y_x = u = 0 \quad , \quad x = 0 \qquad (1g)$$

$$Y_x = u = 0 \quad , \quad T = 1 \; , \quad x = 1 \qquad (1h)$$

The conditions in (1g) imply symmetry along the center line of the slot.
The energy equation (1c) has been written in internal energy form because
the process occurs at constant volume. The variables and parameters are
defined by

$$\rho = \frac{\rho'}{\rho_o'} \qquad t = \frac{t'}{\ell'/c_o'} \qquad u = \frac{u'}{c_o'} \qquad x = \frac{x'}{\ell'}$$

$$\gamma = \frac{\overline{C}_{po}}{\overline{C}_{vo}} \qquad p = \frac{P'}{P_o'} \qquad M = \frac{\kappa_o'}{\ell' c_o'} \qquad Pr = \frac{\mu_o'\overline{C}_{po}'}{k_o'}$$

$$T = \frac{T'}{T_o'} \qquad \varepsilon = \frac{R'T_o'}{E'} \qquad \delta = B'\left(\frac{\rho_o' Y_{Fo}'}{W'}\right)^{n-1} \frac{\rho_o' Y_{Fo}'\overline{h}_o'\ell'^2}{k_o'T_o'} \frac{\exp(-1/\varepsilon)}{\varepsilon}$$

$$Y = \frac{Y_F'}{Y_{Fo}'} \qquad Le = \frac{k_o'}{\rho_o'\overline{C}_{po}'D_o'} \qquad \Gamma = \frac{\overline{C}_{vo}'T_o'}{Y_{Fo}'h_o'}$$

$$\kappa_o' = \frac{k_o'}{\rho_o'\overline{C}_{po}'} \qquad c_o' = \sqrt{\gamma R'T_o'}$$

where the subscript o denotes a value at time t = 0. The five dependent

variables ρ, u, p, T, and Y represent density, velocity, pressure, temperature, and fuel mass fraction respectively. The independent variable x is the spatial coordinate. In the definition of t, c_o' is the speed of sound in the gas initially. The specific heats at constant pressure and constant volume are denoted by $\overline{C}_{p\,o}'$ and $\overline{C}_{v\,o}'$ respectively. The parameter M is the ratio of the acoustic to conduction times in the vessel, where κ_o' represents the initial thermal diffusivity. In the Prandtl number, Pr, and the Lewis number, Le, μ_o', k_o', and D_o' are the dynamic viscosity, thermal conductivity, and diffusion coefficient respectively. In the non-dimensional activation energy, ϵ, and the Frank-Kamenetskii parameter, δ, R', E', h_o', and W' are the universal gas constant, activation energy, heat of reaction, and molecular weight respectively. The term B' is the pre-exponential factor of the Arrhenius-type rate law. The exponent n is the overall reaction order; the sum of the individual reaction orders for fuel and oxidizer.

The parameter Γ is a measure of the thermal energy in the system relative to the maximum heat generated by the chemical reaction.

A typical laboratory experiment might start with the reactive gas at $P_o' = 5\text{kPa}$ and $T_o' = 575^\circ\text{K}$. The reactions of interest have activation energies E' of 40 kcal/mole or higher. Under these conditions with the plates separated by a distance of 10 cm., it is found that γ, Pr, δ, Le, and Γ are $O(1)$ quantities while $\epsilon \le 0.03$ and $M = O(10^{-4})$. The two parameters M and ϵ are considered independent since ϵ reflects the chemistry of the system and M does not. The solution to the system (1) is sought when ϵ and $M \ll 1$ for specified $O(1)$- values of γ, Pr, δ, Le, and Γ.

3. Acoustic-Time Solution

Poland [1979] and Poland and Kassoy [1981] have described the solution of the acoustic time-scale when $t = O(1)$. In the core of the vessel, $-1 < x < 1$, one finds a spatially homogeneous increase in T and p of $O(\epsilon M)$, relative to the initial values, caused by the chemical heat release in the system. In order to accommodate the wall condition on T in (1h) a conductive wall boundary layer of thickness $O(M^{\frac{1}{2}})$ must exist adjacent to the boundary. Relative to the warm core the gas in the boundary layer contracts as it cools to the wall value. As a result the outer edge of the boundary layer behaves like a piston being withdrawn from a gas filled region. This disturbance of $O(\epsilon M^{3/2})$ causes an acoustic wave system to be propagated into the core. As an example the core pressure solution has the form

$$p \sim 1 + \epsilon M \delta \gamma t - \epsilon M^{3/2} \gamma \bar{K} \left[\frac{2}{3} t^{3/2} + 2^{\frac{1}{2}} \sum_{m=1}^{\infty} (-1)^m P(\zeta_m) \frac{\cos m\Pi x}{m^{3/2}} \right] + O(\epsilon M^2)$$

(2)

$$P(\zeta_m) = C_2(\zeta_m) \sin \zeta_m - S_2(\zeta_m) \cos \zeta_m , \quad \zeta_m = m\Pi t, \bar{K} = 2\gamma\delta/\Pi^{\frac{1}{2}}$$

where $C_2(\zeta_m)$ and $S_2(\zeta_m)$ represent Fresnel integrals (Abramowitz and Stegun [1964]). The first part of the $O(\epsilon M^{3/2})$ term represents an accumulated pressure relief due to the continuous generation of expansion waves by the contracting boundary layer. The second term which is bounded for all t represents the momentary acoustic field. When $t = O(1/M)$, which means that $\tau = \gamma M t = O(1)$, we observe a nonuniformity in the asymptotic expansion for p. This difficulty occurs because the conduction boundary layer grows to an $O(1)$- thickness when the conduction time scale ($\tau = O(1)$) is reached. If (2) is written in terms of the limit $\epsilon \to 0$, t fixed, then we obtain the matching form of the pressure variables which is employed as an initial condition for the conduction-time solution;

$$p \sim 1 + \varepsilon \left[\delta\tau - (2/3)\bar{\gamma}^{-\frac{1}{2}} \gamma\bar{K}\tau^{3/2} + 0(\tau^2) \right] + 0(\varepsilon M^{3/2}) \tag{3}$$

The last term is explicitly dependent on both t and τ. Similar results can be obtained for each of the variables. These terms are used to define the asymptotic expansions and scaling required in the subsequent induction period analysis. Details are given in Poland and Kassoy [1981].

4. The Induction Period Solutions

The asymptotic expansions for the induction period take the form

$$\xi \sim 1 + \varepsilon \left[\xi_1(\tau,x) + M^{3/2} \xi_A(\tau,t,x) + \dots \right] + 0(\varepsilon^2) \tag{4}$$

where $\xi = \rho, T, p$ or Y , $\tau = \gamma M t$ and

$$u = \varepsilon M \left[\gamma u_1(\tau,x) + M^{\frac{1}{2}} u_A(\tau,t,x) + \dots \right] + 0(\varepsilon^2 M) \tag{5}$$

The ξ_1, u_1 terms represent variables that change on the long conductive time scale τ , while the ξ_A, u_A variables change on the much shorter acoustic time scale t as well. In fact the latter variables represent the further evolution of the acoustic disturbances during the induction period. The presence of two explicit time scales implies that a multiple time scale analysis will be required.

If (4) and (5) are substituted into (1) then the describing equations for the conduction controlled solution can be found in the form

$$\rho_{1_\tau} + u_{1_x} = 0 \quad , \quad P_1 = p_1(\tau) \quad , \quad P_1 = \rho_1 + T_1 \tag{6a,b,c}$$

$$T_{1_\tau} = \delta e^{T_1} + T_{1_{xx}} - (\gamma-1) u_{1_x} \tag{7}$$

$$Y_{1_\tau} = -\delta e^{T_1} + \frac{1}{\gamma Le} Y_{1_{xx}} \tag{8}$$

$$\xi_1 = u_1 = 0 \qquad 0 \le x \le 1 , \quad \tau = 0 \tag{9}$$

$$\xi_{1_x} = u_1 = 0 \qquad x = 0 , \quad \tau > 0 \tag{10}$$

$$u_1 = T_1 = Y_{1_x} = 0 \qquad x = 1 , \quad \tau > 0 \tag{11}$$

If (6) is used in (7) then we obtain

$$\gamma T_{1_\tau} = \delta e^{T_1} + T_{1_{xx}} + (\gamma-1) \frac{dp_1}{dt} \tag{12}$$

Furthermore if mass conservation is invoked then the integral of (6c) across the slot can be reduced to

$$p_1 (\tau) = \int_0^1 T_1(\tau,x) dx \tag{13}$$

Eqs. (12) and (13) can be combined to produce an integro-differential equation for T_1. The integral form of the last term in (12) describes heating of the gas in the slot due to spatially homogeneous compression. If the transformation $\hat{\sigma} = \tau/\gamma$ is employed, then we obtain the standard form

$$T_{1_{\hat{\sigma}}} = \delta e^{T_1} + T_{1_{xx}} + \left(\frac{\gamma-1}{\gamma}\right) \int_0^1 T_{1_{\hat{\sigma}}} dx \tag{14}$$

Once a solution of (14) and (9)-(11) is obtained the remaining variables can be obtained from (6a,c) and (8). Numerical solutions obtained by the method of lines for the case $\delta = 2$, $\Gamma = 0.4$, Le = 1, are shown in Figs. (1-3) for T_1, Y_1 and u_1. In particular we note that each of the variables is growing rapidly as the escape or runaway time $\tau_\epsilon \approx 0.7463^+$ is approached. A formal analysis of the properties of (14) is given in section 5.

A final-value analysis of (6a,b), (8), (13) and (14) has been developed to describe the detailed nature of the thermal runaway process. As in the case of the thermal explosion in a rigid combustible (Kassoy and Poland [1980]) the study is concerned with a conduction controlled region, $0 < x \le 1$, and a hot spot region, $x = n\sigma^{\frac{1}{2}}$ where $n = 0(1)$ in the limit $\sigma = (\tau_e - \tau) \to 0$. For example, in the former we find that ρ_1, T_1, p_1, and Y_1 approach a well-defined value obtained from the numerical solution as $\sigma \to 0$. However, $u_1 \sim (1-x)\sigma^{-\frac{1}{2}}$. This implies that as $\sigma \to 0$ u itself becomes larger than $0(\epsilon M)$. In the hot-spot events are more singular. The temperature and the velocity are described by

$$T \sim 1 + \epsilon \left(\ln \frac{1}{\delta\sigma} + g_o(n) + 0(\sigma^{\frac{1}{2}}) \right) + \ldots \tag{15}$$

$$u \sim \epsilon M\gamma \left[U_1(n)\sigma^{-\frac{1}{2}} + 0(1) \right] + \ldots \tag{16}$$

where $g_o(n)$ and $U_1(n)$ are well-defined functions. The expanison in (15) is nonuniform where $\epsilon^2 n \sigma = 0(1)$, which represents the usual thermal runaway singularity (Kassoy and Poland [1981]). In addition one may observe from (16) that at the hot spot edge, where $U_1 (n \to \infty)$ is finite, there is significant growth in the local Mach number as $\sigma \to 0$ due to the accelerating temperature rise and associated gas expansion. The acoustic disturbance field represented

by ξ_A, u_A in (4) and (5) can be reduced to the classical linear wave equation for u_A, with homogeneous boundary conditions. The initial condition, derived from the appropriate form of (5) is

$$u_A(\tau \to 0, t \gg 1, x) = (\bar{K}/\Pi) \sum_{m=1}^{\infty} \frac{(-1)^m \sin m\Pi x}{m^{3/2}} \cos [\zeta_m - \frac{\Pi}{4}] \qquad (17)$$

Eq. (17), which represents the form of the disturbance generated during the acoustic time period, is also the exact solution. There is no further evolution of the acoustic field because the waves propagate basically in the uniform, invarient background field represented by the initial state of the system.

5. A Qualitative Analysis of the Induction Model

If we begin with the nondimensional model analagous to (1) for a reactive ideal gas in an arbitrary open bounded container $\Omega \subset \mathbb{R}^n$ without making any symmetry assumptions as in §2 for the special slot container geometry, carry out the same asymptotic analysis as described in §§3 and 4, then we obtain, analagous to (14), the following induction period model for the thermal explosion process of a reactive gas confined to Ω:

$$\Theta_t - \Delta \Theta = \delta e^{\Theta} + \frac{\gamma-1}{\gamma} \frac{1}{\text{vol } \Omega} \int_{\Omega} \Theta_t(y,t) \, dy \qquad (18)$$

$$\Theta(x,0) = \Theta_0(x) \quad , \qquad x \in \Omega$$

$$\Theta(x,t) = 0 \quad , \qquad x \in \partial\Omega \quad t > 0 \qquad (19)$$

where $\Theta(x,t) (= T_1$ in (14)) is the temperature perturbation, $\Theta_0(x)$ is the initial temperature perturbation, γ is the gas constant, and δ is the

697

Frank-Kamenetskii parameter.

We would like to address the following questions. 1) Can we describe the time-history of $\Theta(x,t)$? 2) What happens as δ, γ vary? 3) Can we distinguish between explosive and nonexplosive events? 4) How does a gaseous fuel compare with a solid fuel in identical bounded containers?

The implicit integro-partial differential equation (18) can be put in more tractable form by integrating it over Ω and then observing that

$$\frac{1}{\gamma} \int_{\Omega} \Theta_t \; dy = \int_{\Omega} [\Delta \dot{\Theta} + \delta \, e^{\Theta}] \; dy \tag{20}$$

From this, we have that (18) – (19) is the same problem as (21) – (19) which in turn is equivalent to (22) – (19) where (21) and (22) are given by

$$\Theta_t - \Delta \Theta = \delta \, e^{\Theta} + \frac{\gamma-1}{\text{vol } \Omega} \int_{\Omega} [\Delta \Theta + \delta \, e^{\Theta}] \; dy \tag{21}$$

and

$$\Theta_t - \left[\Delta \Theta + \frac{\gamma-1}{\text{vol } \Omega} \int_{\partial \Omega} \frac{\partial \Theta}{\partial \nu} \; d\sigma \right] = \delta e^{\Theta} + \frac{\gamma-1}{\text{vol } \Omega} \; \delta \int_{\Omega} e^{\Theta} \; dy \tag{22}$$

where ν is the exterior unit normal to $\partial \Omega$ and $d\sigma$ is the element of surface area on $\partial \Omega$. The equivalence of (21) and (22) follows from the divergence theorem.

Using these equivalent formulations of the induction model (Bebernes-Bressan [1982]), the following results can be proven.

1) For any $\delta > 0$, $\gamma \geq 1$, and $\Theta_0 \epsilon L^2 (\Omega)$, $\sup \Theta_0(x) < \infty$, problem (18)-(19)

has a unique solution $\Theta(x,t)$ on $x(0,t)$, on $\Omega x[0,\sigma)$, $\sigma > 0$, where either

a) $\sigma = + \infty$ or b) $\sigma < \infty$ and $\lim_{t \to \sigma_-} \sup_{x \epsilon \overline{\Omega}} \Theta(\lambda, t) = \infty$.

If Ω is a ball B of radius 1 in R^m and $\Theta_0(x) \equiv 0$, the following is

also true.

2) For $\delta > 0$, $\gamma \geq 1$, the solution $\Theta(x,t)$ of (18)-(19) is nonnegative,

radially symmetric, and nondecreasing on $[0,\sigma)$. Thus, one need not assume

a fortiori that the temperature perturbation has a symmetric spatial profile.

Formally when $\gamma = 1$, problem (18)-(19) reduces the classical ignition

model for a solid fuel

$$\chi_t - \Delta \chi = \delta e^\chi \tag{23}$$

with

$$\chi(x,0) = \chi_0(x) \equiv 0 \quad , \qquad x \epsilon \Omega \quad ,$$

$$\chi(x,t) = 0 \qquad , \qquad x \epsilon \partial\Omega \quad , \qquad t > 0 \tag{24}$$

The associated steady state problem is:

$$-\Delta\Psi = \delta e^\Psi \tag{25}$$

$$\Psi(x) = 0 \quad , \qquad \partial\Omega \tag{26}$$

It is known (Bebernes-Kassoy [1981]) that: a) for any $\delta > 0$,

(23)-(24) has a unique nonnegative nondecreasing solution $\chi(x,t)$ on

$\overline{\Omega} x [0,t^*)$, $t^* > 0$, where either $t^* = + \infty$ or $t^* < \infty$ and $\lim_{t \to t^*} \sup_{x \epsilon \overline{\Omega}} \chi(x,t) = + \infty$;

b) there is a critical value $\delta_{FK} > 0$ such that for $\delta \leq \delta_{FK}$ the solution

$\chi(x,t)$ of (23)-(24) exists on $\Omega \times [0,\infty)$ so $t^* = +\infty$ and $\chi(x,t) \leq \Psi(x)$ where $\Psi(x)$ is the minimal solution of (25)-(26);   c) there is a $\delta^* > \delta_{FK}$ such that for $\delta > \delta^*$, $t^* < +\infty$ and the solution $\chi(x,t)$ of (23)-(24) blows up in finite time. In addition δ^* is precisely known and good error bounds on t^* are known.

3) For $\delta>0$, $\gamma \geq 1$, the solution $\Theta(x,t)$ of (18)-(19) satisfies

$$\chi(x,t) \leq \Theta(x,t) \leq \phi(x,t)$$

for all $x \in B$, $t \geq 0$ on their common interval of existence where X is the solution of (23)-(24) and $\phi(x,t)$ is the solution of (27)-(24) where

$$\phi_t - \Delta \phi = \delta e^\phi + \frac{\gamma - 1}{vol \ \Omega} \ \delta \int_\Omega e^\phi \ dy \tag{27}$$

From this result we can conclude that the temperature for an ideal gas is always greater than that for a solid fuel in identical bounded containers and hence a gas explodes sooner than a solid fuel. Physically, this can be explained by the additional generation of heat due to the compression of the gas.

6. Further Developments

The final value analysis of the hot spot development in section 4 showed that as the explosion time t_e is approached $(\sigma \to 0)$ the hot spot temperature perturbation increases like $\ln \sigma$ and the speed like $\sigma^{-\frac{1}{2}}$. Given the definition of σ we can write

$$\frac{(t_e - t)}{t_A} = \frac{\sigma}{M} \tag{28}$$

where t_e' is the dimensional explosion time and $t_A' = \ell'/C_o'$ is the acoustic time in the vessel. When $\sigma >> 0$ (M), the hot spot development occurs on a time scale long compared to t_A'. However, when $\sigma = 0$ (M), the hot spot time scale and t_A' are commensurate. This means in effect that the reaction time is now as short as t_A'. In this case $T \sim 1 + O(\varepsilon \ell n M)$ and $u = O(M^{\frac{1}{2}})$ as may be observed from (15) and (16). The edge of the hot spot now acts as a localized piston which drives an acoustic disturbance into the adjacent conduction-controlled zone. The time scale of the process, $O(t_A')$ is long enough to permit the waves to traverse the container many times. In this sense the expanding spot generates a noise field in the container. The basic pressure field is essentially spatially uniform because the acoustic waves facilitate pressure relief. During this period the hot spot temperature is $O(\varepsilon \ell n M)$ different from the initial state.

Eventually the accelerating reaction in the hot spot causes the reaction time to be shorter than the acoustic time. This occurs when $\varepsilon \ell n(1/\sigma) \equiv \tilde{s} = O(1)$ which implies that the temperature is now fundamentally different from the initial value. Given the definition of σ one can write

$$\frac{(t_e' - t')}{t_A'} = \frac{e^{-\tilde{s}/\varepsilon}}{M} << 1 \tag{29}$$

for $\tilde{s}$ fixed $\varepsilon \to 0$. The local Mach number in the hot spot $u = O(\varepsilon M e^{\tilde{s}/\varepsilon})$. One may observe that this latter value can be a significant fraction of one for appropriate values of ε and M. It can be shown that this vigorous expansion rate can lead to the generation of a nonlinear acoustic signal

which "breaks", thus forming a shock at a distance from the center of the hot spot which is small relative to the container size. The analysis of this process is similar to Cole's [1968] study of the shock wave generated by an accelerating piston. Of fundamental interest is the shock wave strength as a function of the physico-chemical parameters of the reacting system. The details of this dependence remain to be carried out.

It is useful to speculate on the possibility that shock generation by the developing hot spot can lead to direct initiation of a detonation. If the shock is sufficiently strong the induced temperature rise will initiate a rigorous chemical reaction just behind the wave. Should the local reaction time be commensurate with the local transit time of the shock, then the reaction zone will move with the shock. And so a detonation is initiated!

Bibliography

Abramowitz, M. and Stegum, I.A., (1964), Handbook of Mathematical Functions, National Bureau of Standards, Washington, D.C.

Bebernes, J. and Bressan, A.,(1982),"Thermal behavior for a confined reactive gas," J. Differential Equations, to appear.

Bebernes, J. and Kassoy, D.,(1981),"A mathematical analysis of blowup for thermal reactions -- the spatially nonhomogeneous case," SIAM J. Appl. Math. 40 (1981), 476-484.

Cole, J. D. (1968), Perturbation Methods in Applied Mathematics, Blaisdell.

Kapila, A. (1980), "Reactive-diffusive system with Arrhenius kinetics: dynamics of ignition", SIAM Appl. Math 39, pp. 21-36.

Kassoy, D. R. (1976) "Extremely Rapid Transient Phenomena in Combustion, Ignition and Explosion" SIAM-AMS Proceedings 10, pp. 61-72.

Kassoy, D. R., and Poland, J.,(1980), "The thermal explosion confined by a constant temperature boundary: I - The induction period solution," SIAM Appl. Math. 39, pp. 412-430.

Kassoy, D. R., and Poland, J.,(1981), "The thermal explosion confined by a constant temperature boundary: II - The extremely rapid transient," SIAM Appl. Math. 41, pp. 231-246.

Poland, J., and Kassoy, D. R., (1981), "The thermal explosion in a confined reactive gas: The induction period solution," submitted to Comb. and Flame.
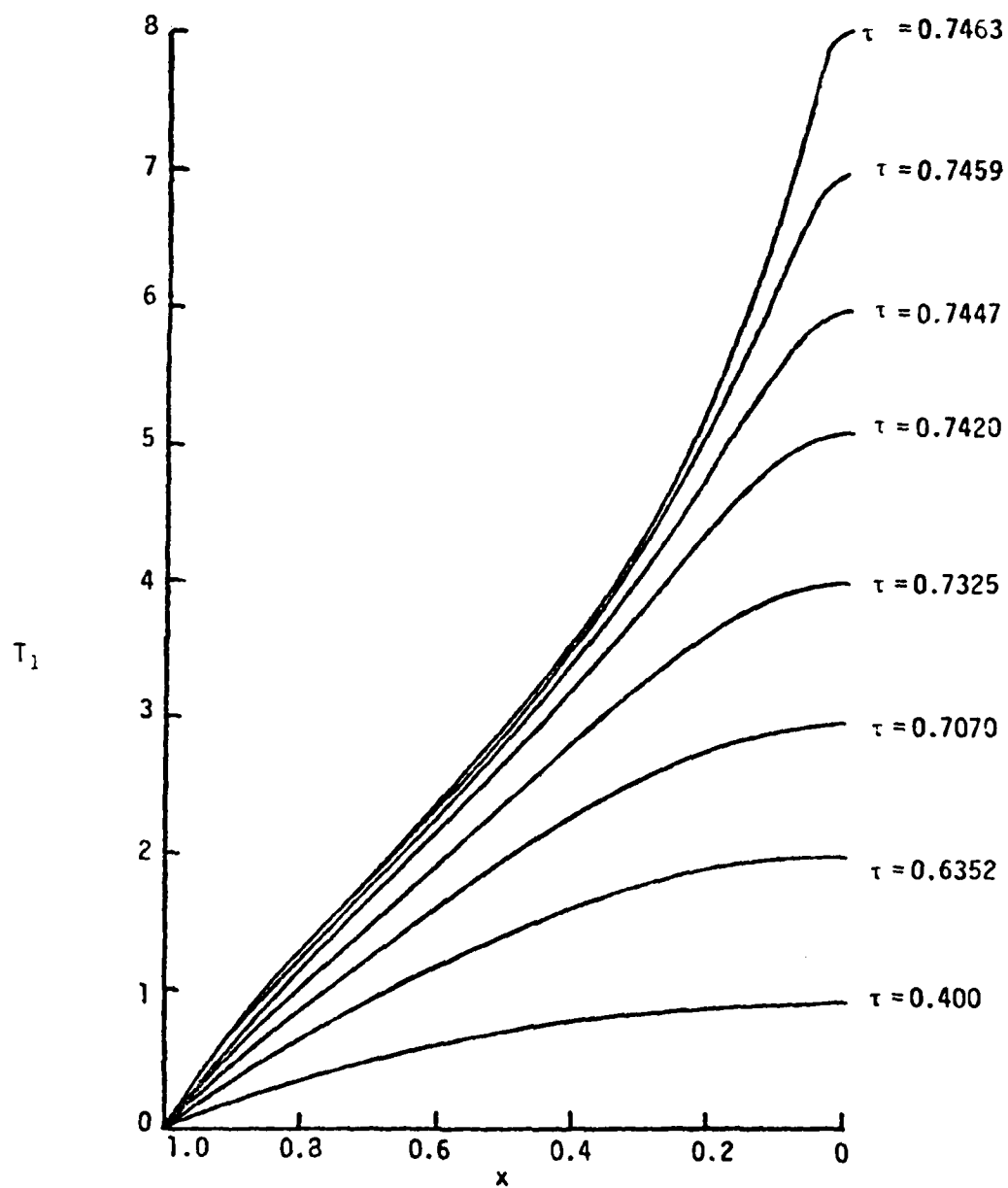
Fig. 1. The variation of the spatial distribution of T_1 with τ
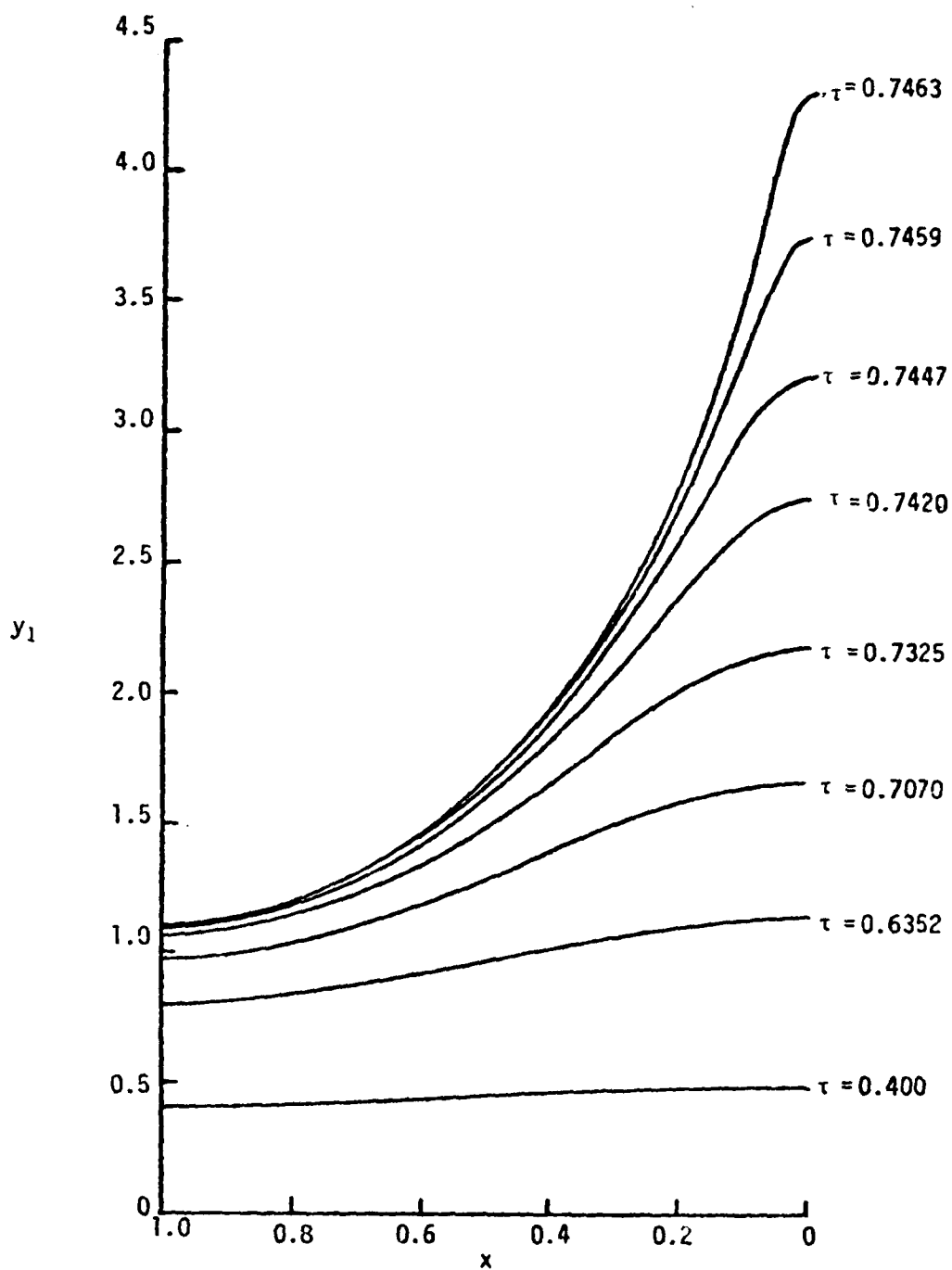
Fig. 2. The variation of the spatial distribution of Y_1 with τ
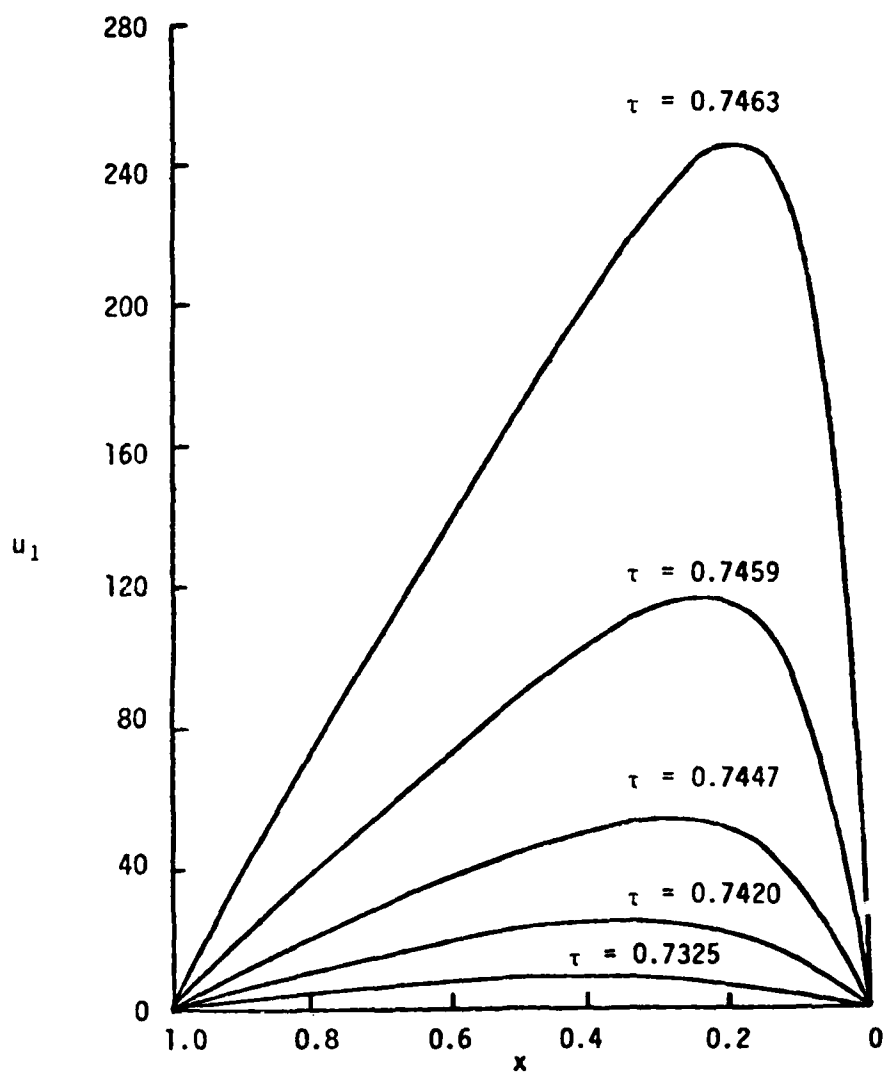
Fig. 3. The variation of the spatial distribution of u_1 with τ

TRANSITION FROM TRAVELING TO STATIONARY LOADS IN A HOLLOW CYLINDER

Alexander S. Elder
U.S. Army Armament Research and Development Command
Ballistic Research Laboratory
Aberdeen Proving Ground, MD 21005

ABSTRACT. In this paper we formulate the equations for elastic strains for internal loads moving with constant velocity in a hollow cylinder. The Green-Lame´ potentials given by Hermmann and his associates are modified for moving loads according to ideas set forth by Ian Sneddon, using sin s(z-ct) and cos s(z-ct) as separation factors in the wave equations. The remaining separation factors involve sin(nθ), cos(nθ), and combinations of Bessel functions. In these expressions, s is a parameter, z the distance from the origin along the z axis, c the velocity of travel, and t the time. Six linearly independent solutions are obtained which are sufficient to satisfy three boundary conditions at each of the two cylindrical surfaces. Response to a step function is formulated in terms of Fourier integrals, using the Cauchy discontinuous factor.

At zero velocity, which corresponds to static loading, the six linearly independent solutions reduce to four. The displacements for static loading and the corresponding biharmonic potentials are obtained by a limiting process, thus recovering the six independent solutions required for an infinite hollow cylinder. In the limit, the wave functions tend to harmonic functions as the velocity of travel tends to zero, the four solutions described above are derived from these potentials. Biharmonic potentials of the form

$$\chi = r \, \frac{\partial \phi}{\partial r} \, , \qquad \hat{\Omega} = r \, \frac{\partial \hat{\psi}}{\partial r} \, ,$$

where ϕ and $\hat{\psi}$ are harmonic potentials, give rise to the same displacement as obtained above by a limiting process. This analysis shows that the transition from moving to stationary loads is continuous and that no abrupt changes in calculated values should occur.

---

1. INTRODUCTION

In this paper we derive formulas for calculating the response of a hollow cylinder to internal loads moving with uniform velocity. This analysis is based on the historic Green-Lame theory of wave motion[1] and recent work on free vibrations of a hollow cylinder[2]. Only steady state conditions are considered; transients which may arise at the beginning of motion are ignored. Formulas for moving sinusoidal loads are discussed in detail. The response to a moving step function can be obtained by using Cauchy's discontinuous factor.

The transition from traveling to stationary loads is obtained by a limiting process. The biharmonic functions required for the stationary load arise from the confluence of the displacements due to the vector and scalar wave functions at zero velocity. This solution is also derived independently from appropriate elastic potentials. This analysis shows that the calculated displacements for moving loads approach the calculated values for stationary loads as the velocity of travel approaches zero. Physically, this requirement is obvious. Hence computations for low velocities will serve as a critical test of the analysis and computations.

The results are required to interpret strain measurements obtained with an instrumented gun tube in which arrays of strain gages and pressure gages were mounted in close proximity along the length of the tube. Tube strains based on the measured pressures were calculated according to thick walled cylinder theory[3], using appropriate mechanical properties for the gun steel. At low velocities the measured and calculated strains agreed reasonably well, but at high projectile velocities the calculated strain distribution profiles were significantly different from the measured strain histories.

This effect is well known in the theory of moving loads[4]. Prof. Ian Sneddon of Glasgow University, a pioneer in the field, suggested this problem to the author during a recent visit.

---

[1] Gurtin, M.E., Elasticity, Encylcopedia of Physics, Volume VI a/2, Mechanics II, Springer Verlag, New York, 1972. See pages 212-214.

[2] Armenakas, A.E., Hermmann, G., and Gazis, D.C. Free Vibrations of Circular Cylindrical Shells, Pergamman Press, New York, 1969.

[3] Elder, A.S. and Zimmerman, K.L., Stresses in a Gun Tube produced by Internal Pressure and Shear, BRL Memorandum Report No. 2495, June 1975. AD #A012765.

[4] Fryba, L., Vibrations of Solids and Structures under Moving Loads, Noordhoff International Publishing, Gronigen The Netherlands, 1972. See Chapter 17 and Reference 203.

The analysis is given in considerable detail to facilitate verification of formulas required for programming. Formulation is limited to subsonic velocities which occur in practice; analysis of the moving load problem for supersonic velocities is quite difficult and will not be considered at the present time.

II. FORMULAS FOR WAVE MOTION IN CYLINDRICAL COORDINATES

In the absense of body forces the equation of motion may be written in the form

$$(\lambda+2\mu)\nabla\nabla\cdot\hat{u} - \mu\,\nabla\times(\nabla\times\hat{u}) = \rho\,\frac{\partial^2 u}{\partial t^2} \tag{1}$$

where λ and μ are the Lamé constants. The speed of the dilatational wave is

$$c_1^2 = (\lambda+2\mu)/\rho \tag{2}$$

and the velocity of the shear wave is

$$c_2^2 = \mu/\rho \quad, \tag{3}$$

where ρ is the density of the elastic material. The equation of motion becomes

$$c_1^2\,\nabla\nabla\cdot\hat{u} - c_2^2\,\nabla\times(\nabla\times\hat{u}) = \frac{\partial^2\hat{u}}{\partial t^2} \tag{4}$$

The Green-Lamé solution is

$$\hat{u} = \nabla\phi + \nabla\times\hat{\psi} \tag{5}$$

in which the potentials ϕ and $\hat{\psi}$ satisfy the equations

$$c_1^2\,\nabla^2\phi = \frac{\partial^2\phi}{\partial t^2} \tag{6}$$

and

$$C_2^2 \; \nabla^2 \hat{\psi} \;=\; \frac{\partial^2 \hat{\psi}}{\partial t^2} \tag{7}$$

In cylindrical coordinates we have

$$\nabla^2 \phi \;=\; \frac{\partial^2 \phi}{\partial r^2} \;+\; \frac{1}{r} \; \frac{\partial \phi}{\partial r} \;+\; \frac{1}{r^2} \; \frac{\partial^2 \phi}{\partial \theta^2} \;+\; \frac{\partial^2 \phi}{\partial z^2} \tag{8}$$

The vector potential is given in terms of three components

$$\hat{\psi} \;=\; \hat{e}_r \, \psi_r \;+\; \hat{e}_\theta \psi_\theta \;+\; \hat{e}_z \, \psi_z \quad , \tag{9}$$

where $\hat{e}_r$, $\hat{e}_\theta$, and $\hat{e}_z$ are unit vectors in cylindrical coordinates[5].

$$\begin{aligned}
\nabla^2 \hat{\psi} \;=\; & \hat{e}_r \;\; \nabla^2 \psi_r \;-\; \left(\frac{\psi_r}{r^2} \;-\; \frac{2}{r^2} \; \frac{\partial}{\partial \theta} \, \psi_\theta \right) \\[2mm]
& +\; \hat{e}_\theta \;\; \nabla^2 \psi_\theta \;-\; \left(\frac{\psi_\theta}{r^2} \;+\; \frac{2}{r^2} \; \frac{\partial}{\partial \theta} \, \psi_r \right) \\[2mm]
& +\; \hat{e}_z \;\; \nabla^2 \psi_z
\end{aligned} \tag{10}$$

The following scalar partial differential equations are finally obtained:

$$c_1^2 \;\; \nabla^2 \, \phi \;=\; \frac{\partial^2 \phi}{\partial t^2} \tag{11}$$

$$c_2^2 \; \left(\nabla^2 \, \psi_r \;-\; \frac{\psi_r}{r^2} \;+\; \frac{2}{r^2} \; \frac{\partial}{\partial \theta} \, \psi_\theta \right) = \frac{\partial^2}{\partial t^2} \, \psi_r \tag{12}$$

$$c_2^2 \; \left(\nabla^2 \, \psi_\theta \;-\; \frac{\psi_\theta}{r^2} \;-\; \frac{2}{r^2} \; \frac{\partial}{\partial \theta} \, \psi_r \right) = \frac{\partial^2}{\partial t^2} \, \psi_\theta \tag{13}$$

---

[5] Chou, P.C. and Pagano, N.J., *Elasticity: Tensor, Dyadic, and Engineering Approaches*, D. Van Nostrand Company, Inc. Princeton, 1967, pages 245-265.

$$c_2^{-2} \, \nabla^2 \psi_z = \frac{\partial^2}{\partial t^2} \psi_z \tag{14}$$

Four components of the displacement vector are obtained from solutions of these equations. Since only three components are required, we can specify one additional condition. We choose a relation between ψ_r and ψ_θ which will facilitate separation of variables, following the ideas outlined in Reference 2.

III. SEPARATION OF VARIABLES FOR SINUSOIDAL LOADS MOVING WITH CONSTANT VELOCITY

The scalar potential can be obtained directly by separation of variables. For brevity let

$$H_1 = \cos(n\theta)\sin[s(z - ct)] \tag{15}$$

$$H_2 = \cos(n\theta)\cos[s(z - ct)] \tag{16}$$

$$H_3 = \sin(n\theta)\sin[s(z - ct)] \tag{17}$$

$$H_4 = \sin(n\theta)\cos[s(z - ct)] \tag{18}$$

and

$$\phi_i = H_i \, f(r), \quad i = 1,2,3,4. \tag{19}$$

In these equations n is an integer since the stresses must be periodic in a complete cylinder. The constant c is the velocity of travel. We assume

$$0 < \epsilon < c < c_2 - \epsilon \, , \tag{20}$$

where

$$0 < \epsilon << 1 \, . \tag{21}$$

Let

$$\alpha_1^2 = c^2/c_1^2 \tag{22}$$

$$\beta_1^2 = 1 - \alpha_1^2 \tag{23}$$

Then

$$f'' + \frac{1}{r} f' - \left(\frac{n^2}{r^2} + \beta_1^2 s^2\right) f = 0 \tag{24}$$

and

$$f = A_1 I_n(\beta_1 sr) + A_2 K_n(\beta_1 sr) \tag{25}$$

The axial component of the vector potential can be treated in a similar manner. We let

$$\psi_z = H_i g_z(r), \quad i = 1,2,3,4 \tag{26}$$

$$\alpha_2^2 = c_2^2/c^2 \tag{27}$$

$$\beta_2^2 = 1 - \alpha_2^2 \tag{28}$$

then

$$g_z = A_3 I_n(\beta_2 sr) + A_4 K_n(\beta_2 sr) \tag{29}$$

The radial and tangential components of the vector potential are coupled. The following four combinations lead to separable solutions:

$$\psi_r = H_1 g_r, \qquad \psi_\theta = -H_3 g_\theta \tag{30}$$

$$\psi_r = H_2 g_r, \qquad \psi_\theta = -H_4 g_\theta \tag{31}$$

$$\psi_r = H_3 g_r, \qquad \psi_\theta = H_1 g_\theta \tag{32}$$

$$\psi_r = H_4 g_r, \qquad \psi_\theta = H_2 g_\theta \tag{33}$$

The combination given in Eq. (32) is discussed in Reference 2; the remaining combinations are introduced to satisfy a variety of boundary conditions on the inner radius. We note that

$$\frac{\partial}{\partial \theta} \, H_1 = - n H_3 \tag{34}$$

$$\frac{\partial}{\partial \theta} \, H_2 = - n H_4 \tag{35}$$

$$\frac{\partial}{\partial \theta} \, H_3 = n H_1 \tag{36}$$

$$\frac{\partial}{\partial \theta} \, H_4 = n H_2 \tag{37}$$

On referring to Eqs. (12) and (13) we find

$$r^2 g_r'' + r g_r' - (n^2 + 1 + \beta_2^2 s^2 r^2) g_r + 2 n g_\theta = 0 \tag{38}$$

$$r^2 g_\theta'' + r g' - (n^2 + 1 + \beta_2^2 s^2 r^2) g_r - 2 n g_\theta = 0 \tag{39}$$

If we let

$$g_\theta = - g_r \tag{40}$$

we find

$$r^2 g_r'' + r g_r' - [(n + 1)^2 + \beta_2^2 s^2 r^2] g_r = 0 \tag{41}$$

713

and

$$g_r = A_5 I_{n+1}(\beta_2 sr) + A_2 K_{n+1}(\beta_2 sr) \qquad (42)$$

If on the other hand we let

$$g_\theta = g_r \quad , \qquad (43)$$

then

$$r^2 g_r'' + r g_r' - [(n - 1)^2 + \beta_2^2 s^2 r^2] g_r = 0 \qquad (44)$$

and

$$g_r = A_7 I_{n-1}(\beta_2 sr) + A_8 K_{n-1}(\beta_2 sr) \qquad (45)$$

In this paper the radial and tangential components are based on Eqs. (40), (41) and (42).

As mentioned previously, a complete solution to a specified boundary value problem may be obtained if one of the components of the vector potential is set equal to zero. Hence, although unique solutions for the displacements are expected, the choice of potentials leading to a solution is not unique.

Pao and Mow[6] use vector potentials $\hat{L}$, $\hat{M}$, and $\hat{N}$, which are derived from scalar functions α, ψ, and χ in their analysis of diffraction wave in an elastic solid. The relation between this solution and the solution of Hermann and Gazis may be obtained by equating formulas for the displacements.

IV. COMPONENTS OF THE VECTOR DISPLACEMENT

Each component of the vector displacement consists of one term from the scalar potential and two terms from the vector displacement, according to Eq. (5). These terms must have the same trignometric factor. In addition, the signs of g_r and g_θ are chosen so these functions involve Bessel functions of order $n+1$ when $g_\theta = -g_r$. The sign of g_z is chosen so the divergence can be written in the form

$$\nabla \cdot \hat{\psi} = H_i h(r), \quad i = 1,2,3,4 \qquad (46)$$

[6] Pao, Y and Mow, C, *Diffraction of Elastic Waves and Dynamic Stress Concentrations*, Crane Russak, Publishers, 1971. See pages 218 ff.

where

$$h(r) = \frac{1}{r} \frac{\partial}{\partial r} (r\psi_r) - \frac{n}{r} g_\theta + sg_z \qquad (47)$$

We consider four cases, as shown in the table below.

TABLE 1. TRIGNOMETRIC FACTORS FOR SCALAR AND VECTOR POTENTIALS

	Function	$f(r)$	$g_r(r)$	$g_\theta(r)$	$g_z(r)$	$h(r)$
Case	I	H_1	H_4	H_2	H_3	H_4
	I-I	H_2	H_3	H_1	$-H_4$	H_3
	III	H_3	H_2	$-H_4$	H_1	H_2
	IV	H_4	H_1	$-H_3$	$-H_2$	H_1

The displacement components for each case are obtained from the potentials.

Case I

$$ru = [rf' + srg_\theta + ng_z] H_1 \qquad (48)$$

$$rv = [-nf - srg_r - rg_z'] H_3 \qquad (49)$$

$$rw = [srf + \frac{\partial}{\partial r} rg_\theta - ng_z] H_2 \qquad (50)$$

Case II

$$ru = [rf' + srg_\theta - ng_z] H_2 \qquad (51)$$

$$rv = [nf + srg_r + rg_z'] H_4 \qquad (52)$$

$$rw = [- srf + \frac{\partial}{\partial r} rg_\theta - ng_r] H_1 \qquad (53)$$

Case III

$$ru = [rf' + srg_\theta - ng_z] H_3 \qquad (54)$$

$$rv = [nf - srg_r - rg'_z] H_1 \qquad (55)$$

$$rw = [srf - \frac{\partial}{\partial r} rg_\theta + ng_r] H_4 \qquad (56)$$

Case IV

$$ru = [rf' + srg_\theta + ng_z] H_4 \qquad (57)$$

$$rv = [nf + srg_r + rg'_z] H_2 \qquad (58)$$

$$rw = [-srf + \frac{\partial}{\partial r} rg_\theta + ng_r] H_3 \qquad (59)$$

Next, we express the displacements and divergence for Case I in terms of Bessel functions of order n and n+1. The following identities are used to eliminate derivatives:

$$XI_n'(X) = nI_n(X) + XI_{n+1}(X) \qquad (60)$$

$$XK_n'(X) = nK_n(X) - XK_{n+1}(X) \qquad (61)$$

$$XI'_{n+1}(X) = -(n + 1)I_{n+1}(X) + XI_n(X) \qquad (62)$$

$$XK'_{n+1}(X) = -(n + 1)K_{n+1}(X) - XK_n(X) \qquad (63)$$

On carrying out details of the analysis we find

716

$$ru = \left\{ A_1[nI_n(\beta_1 sr) + \beta_1 srI_{n+1}(b_1 sr)] \right.$$

$$+ A_2[nK_n(\beta_1 sr) - \beta_1 srK_{n+1}(\beta_1 sr)]$$

$$+ A_3 nI_n(\beta_2 sr) + A_4 nK_n(\beta_2 sr)$$

$$\left. - A_5 srI_{n+1}(\beta_2 sr) - A_6 \beta_2 srK_{n+1}(\beta_2 sr) \right\} \cos(n\theta)\sin[s(z - ct)] \quad (64)$$

$$rv = \left\{ - A_1 nI_n(\beta_1 sr) - A_2 nK_n(\beta_1 sr) \right.$$

$$+ A_3[- nI_n(\beta_2 sr) + \beta_2 srI_{n+1}(\beta_2 sr)]$$

$$+ A_4[- nK_n(\beta_2 sr) + \beta_2 srK_{n+1}(\beta_2 sr)]$$

$$\left. - A_5 srI_{n+1}(\beta_2 sr) - A_6 srK_{n+1}(\beta_2 sr) \right\} \sin(n\theta)\sin[s(z - ct)], \quad (65)$$

$$rw = \left\{ A_1 srI_n(\beta_1 sr) + A_2 srK_n(\beta_1 sr) \right.$$

$$\left. - A_5 srI_n(\beta_2 sr) + A_6 \beta_2 srK_n(\beta_2 sr) \right\} \cos(n\theta)\cos[s(z - ct)] \quad (66)$$

The divergence of the vector potential is

$$\nabla \cdot \hat{\psi} = [(A_3 + A_5\beta_2)sI_n(\beta_2 sr) + (A_4 - A_5\beta_2)sK_n(\beta_2 sr)]\sin(n\theta)\cos[s(z - ct)] \quad (67)$$

Formulas for the displacement and divergence corresponding to Cases II, III, and IV can be written down by inspection.

The divergence of the vector potential enters into calculations of the rotation vector. The analysis prior to Part IX of this report follows reference 2 in using a vector potential with non-solenoidal divergence, as this approach considerably simplifies the analysis. In Part IX a solenoidal vector potential, for which the divergence is zero, is derived by separation of variables. Formulas the vector displacement and its deriatives remain unchanged, but a simpler formula for the rotation vector is obtained. The usual approach by means of the Newtonian potential is not appropriate since the hollow cylinder is a multiply connected region.

V. STRAINS, ROTATION VECTOR, AND STRESSES

The strains are obtained from the displacements by means of the formulas

$$\epsilon_r = \frac{\partial u}{\partial r} \tag{68}$$

$$\epsilon_\theta = \frac{u}{r} + \frac{\partial v}{r\partial \theta} \tag{69}$$

$$\epsilon_z = \frac{\partial w}{\partial z} \tag{70}$$

$$\gamma_{r\theta} = \frac{\partial u}{r\partial \theta} + \frac{\partial v}{\partial r} - \frac{v}{r} \tag{71}$$

$$\gamma_{rz} = \frac{\partial u}{\partial z} + \frac{\partial w}{\partial r} \tag{72}$$

$$\gamma_{z\theta} = \frac{\partial v}{\partial z} + \frac{\partial w}{r\partial \theta} \tag{73}$$

We calculate the strains in terms of Bessel functions for Case I. The remaining three cases can be treated in a similar manner. Let

$$r^2 \epsilon_r = H_1 \sum_1^6 A_i R_{1,i} \tag{74}$$

$$r^2 \epsilon_\theta = H_1 \sum_1^6 A_i R_{2,i} \tag{75}$$

$$r^2 \epsilon_z = H_1 \sum_1^6 A_i R_{3,i} \tag{76}$$

$$r^2 \gamma_{r\theta} = H_3 \sum_1^6 A_i R_{4,i} \tag{77}$$

$$r^2 \gamma_{rz} = H_2 \sum_1^6 A_i R_{5,i} \tag{78}$$

$$r^2 \gamma_{\theta z} = H_4 \sum_1^6 A_i R_{6,i} \tag{79}$$

The $R_{i,j}$ functions depend on the radius, and can be expressed in terms of Bessel functions of orders n and n+1.

$$R_{1,1} = [\beta_1^2 s^2 r^2 + (n^2-n)] I_n(\beta_1 sr) - \beta_1 sr I_{n+1}(\beta_1 sr) \tag{80}$$

$$R_{1,2} = [\beta_1^2 s^2 r^2 + (n^2-n)] K_n(\beta_1 sr) + \beta_1 sr K_{n+1}(\beta_1 sr) \tag{81}$$

$$R_{1,3} = (n^2-n) I_n(\beta_2 sr) + \beta_2 sr I_{n+1}(\beta_2 sr) \tag{82}$$

$$R_{1,4} = (n^2-n) K_n(\beta_2 sr) - \beta_2 sr K_{n+1}(\beta_2 sr) \tag{83}$$

$$R_{1,5} = -\beta_2 s^2 r^2 I_n(\beta_2 sr) + (n+1) sr I_{n+1}(\beta_2 sr) \tag{84}$$

$$R_{1,6} = \beta_2 s^2 r^2 K_n(\beta_2 sr) + (n+1) sr K_{n+1}(\beta_2 sr) \tag{85}$$

$$R_{2,1} = -(n^2-n) I_n(\beta_1 sr) + \beta_1 sr I_{n+1}(\beta_1 sr) \tag{86}$$

$$R_{2,2} = -(n^2-n) K_n(\beta_1 sr) - \beta_1 sr K_{n+1}(\beta_1 sr) \tag{87}$$

$$R_{2,3} = -(n^2-n) I_n(\beta_2 sr) - \beta_2 nsr I_{n+1}(\beta_2 sr) \tag{88}$$

$$R_{2,4} = -(n^2-n) K_n(\beta_2 sr) + \beta_2 nsr K_{n+1}(\beta_2 sr) \tag{89}$$

$$R_{2,5} = -(n+1) sr I_{n+1}(\beta_2 sr) \tag{90}$$

$$R_{2,6} = -(n+1) sr K_{n+1}(\beta_2 sr) \tag{91}$$

$$R_{3,1} = -s^2 r^2 I_n(\beta_1 sr) \tag{92}$$

$$R_{3,2} = -s^2 r^2 K_n(\beta_1 sr) \tag{93}$$

$$R_{3,3} = 0 \tag{94}$$

$$R_{3,4} = 0 \tag{95}$$

$$R_{3,5} = \beta_2 s^2 r^2 I_n(\beta_2 sr) \tag{96}$$

$$R_{3,6} = -\beta_2 s^2 r^2 K_n(\beta_1 nsr) \tag{97}$$

$$R_{4,1} = -2(n^2 - n)I_n(\beta_1 sr) - \beta_1 nsrI_{n+1}(\beta_1 sr) \tag{98}$$

$$R_{4,2} = -2(n^2 - n)K_n(\beta_1 sr) + \beta_1 nsrK_{n+1}(\beta_1 sr) \tag{99}$$

$$R_{4,3} = -[2(n^2 - n) + \beta_2 s^2 r^2]I_n(\beta_2 sr) + 2\beta_2 srI_{n+1}(\beta_2 sr) \tag{100}$$

$$R_{4,4} = -[2(n^2 - n) + \beta_2 s^2 r^2]K_n(\beta_2 sr) - 2\beta_2 srI_{n+1}(\beta_2 sr) \tag{101}$$

$$R_{4,5} = -\beta_2 s^2 r^2 I_n(\beta_2 sr) + 2(n + 1)srI_{n+1}(\beta_2 sr) \tag{102}$$

$$R_{4,6} = \beta_2 s^2 r^2 K_n(\beta_2 sr) + 2(n + 1)srK_{n+1}(\beta_2 sr) \tag{103}$$

$$R_{5,1} = snrI_n(\beta_1 sr) + \beta_1 s^2 r^2 I_{n+1}(\beta_1 sr) \tag{104}$$

$$R_{5,2} = snrK_n(\beta_1 sr) - \beta_1 s^2 r^2 K_{n+1}(\beta_1 sr) \tag{105}$$

$$R_{5,3} = nsrI_n(\beta_2 sr) \tag{106}$$

$$R_{5,4} = nsrK_n(\beta_2 sr) \tag{107}$$

$$R_{5,5} = -\beta_2 nsrI_n(\beta_2 sr) + (\beta_2^2 + 1)s^2 r^2 I_{n+1}(\beta_2 sr) \tag{108}$$

$$R_{5,6} = \beta_2 nsrK_n(\beta_2 sr) + (\beta_2^2 + 1)s^2 r^2 K_{n+1}(\beta_2 sr) \tag{109}$$

$$R_{6,1} = -2nsrI_n(\beta_1 sr) \tag{110}$$

$$R_{6,2} = -2nsrK_n(\beta_1 sr) \tag{111}$$

$$R_{6,3} = -nsrI_n(\beta_2 sr) - \beta_2 s^2 r^2 I_{n+1}(\beta_1 sr) \tag{112}$$

$$R_{6,4} = -nsrI_n(\beta_2 sr) + \beta_2 s^2 r^2 K_{n+1}(\beta_2 sr) \tag{113}$$

$$R_{6,5} = \beta_2 nsrI_n(\beta_2 sr) - s^2 r^2 I_{n+1}(\beta_2 sr) \tag{114}$$

$$R_{6,6} = -\beta_2 nsrK_n(\beta_2 sr) - s^2 r^2 K_{n+1}(\beta_2 sr) \tag{115}$$

The dilatation e is the sum of the principle strains.

$$e = \varepsilon_r + \varepsilon_\theta + \varepsilon_z \tag{116}$$

We write

$$r^2 e = \sum_1^2 R_{7,i} \tag{117}$$

where

$$R_{7,1} = -\alpha_1^2 s^2 r^2 I_n(\beta_1 sr) \tag{118}$$

$$R_{7,2} = -\alpha_1 s^2 r^2 K_n(\beta_1 sr) \tag{119}$$

We note that

$$\alpha_1 \to 0 \text{ as } c \to 0$$

Hence

$$e \to 0 \text{ as } c \to 0$$

In general, therefore, the solution in terms of wave functions does not yield a valid solution in the limit as the velocity of travel approaches zero. Pure torsion is an exception, as shear strains only are involved, and the dilatation is zero under both static and dynamic loading conditions.

The rotations are given by the formulas

$$2\omega_z = \frac{1}{r} \frac{\partial u}{\partial \theta} - \frac{\partial v}{\partial r} \tag{120}$$

$$2\omega_\theta = \frac{\partial u}{\partial z} - \frac{\partial w}{\partial r} \tag{121}$$

$$2\omega_z = \frac{1}{r} \frac{\partial rv}{\partial r} - \frac{1}{r} \frac{\partial u}{\partial \theta} \tag{122}$$

We set

$$2r^2\omega_z = H_3 \sum_8^{10} A_i R_{8,i} \tag{123}$$

$$2r^2\omega_\theta = H_2 \sum_8^{10} A_i R_{9,i} \tag{124}$$

$$2r^2\omega_r = H_4 \sum_8^{10} A_i R_{10,i} \tag{125}$$

for Case I.

$$R_{8,3} = nsrI_n(\beta_2 sr) + \beta_2 s^2 r^2 I_{n+1}(\beta_2 sr) \tag{126}$$

$$R_{8,4} = nsrK_n(\beta_2 sr) - \beta_2 s^2 r^2 K_{n+1}(\beta_2 sr) \tag{127}$$

$$R_{8,5} = \beta_2 nsrI_n(\beta_2 sr) + s^2 r^2 I_{n+1}(\beta_2 sr) \tag{128}$$

$$R_{8,6} = -\beta_2 nsrK_n(\beta_2 sr) + s^2 r^2 K_{n+1}(\beta_2 sr) \tag{129}$$

$$R_{9,3} = nsrI_n(\beta_2 sr) \tag{130}$$

$$R_{9,4} = nsrK_n(\beta_2 sr) \tag{131}$$

$$R_{9,5} = \beta_2 nsr I_n(\beta_2 sr) - \alpha_2 s^2 I_{n+1}(\beta_2 sr) \tag{132}$$

$$R_{9,6} = - \beta_2 nsr K_n(\beta_2 sr) - \alpha_2 s^2 K_{n+1}(\beta_2 sr) \tag{133}$$

$$R_{10,3} = - \beta_2 s^2 r^2 I_n(\beta_2 sr) \tag{134}$$

$$R_{10,4} = - \beta_2 s^2 r^2 K_n(\beta_2 sr) \tag{135}$$

$$R_{10,5} = \beta_2 s^2 r^2 I_n(\beta_2 sr) \tag{136}$$

$$R_{10,6} = - \beta_2 s^2 r^2 K_n(\beta_2 sr) \tag{137}$$

The stresses are derived from the strains by means of generalized Hookes' law.

$$\sigma_r = \lambda e + 2\mu\varepsilon_r \tag{138}$$

$$\sigma_\theta = \lambda e + 2\mu\varepsilon_\theta \tag{139}$$

$$\sigma_z = \lambda e + 2\mu\varepsilon_z \tag{140}$$

$$\tau_{r\theta} = \mu\gamma_{r\theta} \tag{141}$$

$$\tau_{rz} = \mu\gamma_{rz} \tag{142}$$

$$\gamma_{\theta z} = \mu\gamma_{\theta z} \tag{143}$$

For case I we write

$$r^2 \sigma_r = H_1 \sum_1^6 A_i S_{1,i} \tag{144}$$

$$r^2 \sigma_\theta = H_1 \sum_1^6 A_i S_{2,i} \qquad (145)$$

$$r^2 \sigma_z = H_1 \sum_1^6 A_i S_{3,i} \qquad (146)$$

$$r^2 \tau_{r\theta} = H_3 \sum_1^6 A_i S_{4,i} \qquad (147)$$

$$r^2 \tau_{rz} = H_2 \sum_1^6 A_i S_{5,i} \qquad (148)$$

$$r^2 \tau_{rz} = H_4 \sum_1^6 A_i S_{6,i} \qquad (149)$$

Then

$$S_{j,i} = \lambda R_{7,1} + 2\mu R_{j,i}, \quad j = 1,2,3; \quad i = 1,3,5 \qquad (150a)$$

$$S_{j,i} = \lambda R_{7,2} + 2\mu R_{j,i} \quad j = 1,2,3; \quad i = 2,4,6 \qquad (150b)$$

$$S_{j,i} = \mu R_{j,i} \quad j = 4,5,6; \quad i = 1,2,3,4,5,6 \qquad (151)$$

Stresses and strains for Cases II, III, and IV can be obtained in a similar manner. The $R_{i,j}$ functions must be calculated for each case to determine the correct algebraic signs in Eqs. (80) - (115) and Eqs. (118) - (119). A similar remark applies to the formulas for the rotations.

VI.   RESPONSE TO AN INTERNAL TRAVELING PRESSURE PULSE

First we consider a sinusoidal pressure pulse traveling with velocity c. The boundary conditions are

$$\sigma_r = \sigma_0 \cos(n\theta) \sin\left[s(z - ct)\right], \quad r = a \qquad (152)$$

$$\tau_{r\theta} = 0, \quad r = a \qquad (153)$$

$$\tau_{rz} = 0, \quad r = a \qquad (154)$$

$$\tau_r = 0, \quad r = b \tag{155}$$

$$\tau_{r\epsilon} = 0, \quad r = b \tag{156}$$

$$\tau_{rz} = 0, \quad r = b \tag{157}$$

These boundary conditions lead to a set of six linear equations for the A_i coefficients.

$$\sum_{1}^{6} A_i S_{1,i}(a) = a^2 \sigma_o \tag{158}$$

$$\sum_{1}^{6} A_i S_{4,i}(a) = 0 \tag{159}$$

$$\sum_{1}^{6} A_i S_{5,i}(a) = 0 \tag{160}$$

$$\sum_{1}^{6} A_i S_{1,i}(b) = 0 \tag{161}$$

$$\sum_{1}^{6} A_i S_{4,i}(b) = 0 \tag{162}$$

$$\sum_{1}^{6} A_i S_{5,i}(b) = 0 \tag{163}$$

These equations can be solved for the A_i provided c is greater than zero and less than the velocity of the shear wave, according to Eq. (20). It is convenient to write the final results in terms of determinants, using Cramer's rule and then combining the separate terms. Let D(s) be the determinant for Eqs. (158) - (163):

$$D(s) = \begin{vmatrix} S_{1,1}(a) & S_{1,2}(a) & S_{1,3}(a) & S_{1,4}(a) & S_{1,5}(a) & S_{1,6}(a) \\ S_{4,1}(a) & S_{4,2}(a) & S_{4,3}(a) & S_{4,4}(a) & S_{4,5}(a) & S_{4,6}(a) \\ S_{5,1}(a) & S_{5,2}(a) & S_{5,3}(a) & S_{5,4}(a) & S_{5,5}(a) & S_{5,6}(a) \\ S_{1,1}(b) & S_{1,2}(b) & S_{1,3}(b) & S_{1,4}(b) & S_{1,5}(b) & S_{1,6}(b) \\ S_{4,1}(b) & S_{4,2}(b) & S_{4,3}(b) & S_{4,4}(b) & S_{4,5}(b) & S_{4,6}(b) \\ S_{5,1}(b) & S_{5,2}(b) & S_{5,3}(b) & S_{5,4}(b) & S_{5,5}(b) & S_{5,6}(b) \end{vmatrix} \quad (164)$$

The remaining determinants use the appropriate $R_{j,i}$ or $S_{j,i}$ for the first row; the remaining five rows are identical with the corresponding rows of $D(s)$. We have for instance

$$S_r = \begin{vmatrix} S_{1,1}(r) & S_{1,2}(r) & S_{1,3}(r) & S_{1,4}(r) & S_{1,5}(r) & S_{1,6}(r) \\ \cdots & \cdots & \cdots & \cdots & \cdots & \cdots \end{vmatrix} \quad (165)$$

$$S_{r\theta} = \begin{vmatrix} S_{4,1}(r) & S_{4,2}(r) & S_{4,3}(r) & S_{4,4}(r) & S_{4,5}(r) & S_{4,6}(r) \\ \cdots & \cdots & \cdots & \cdots & \cdots & \cdots \end{vmatrix} \quad (166)$$

$$S_{rz} = \begin{vmatrix} R_{1,1}(r) & R_{1,2}(r) & R_{1,3}(r) & R_{1,4}(r) & R_{1,5}(r) & R_{1,6}(r) \\ \cdots & \cdots & \cdots & \cdots & \cdots & \cdots \end{vmatrix} \quad (167)$$

Determinates for the remaining stresses and strains can be written down by inspection. The stresses for Case I are given by

$$r^2 \sigma_r = H_1 S_r / D(s) \quad (168)$$

$$r^2 \sigma_\theta = H_1 S_\theta / D(s) \quad (169)$$

$$r^2 \sigma_z = H_1 S_z / D(s) \quad (170)$$

$$r^2 \tau_{r\theta} = H_3 S_{r\theta} / D(s) \quad (171)$$

726

$$r^2 \tau_{rz} = H_2 S_{rz}/D(s) \tag{172}$$

$$r^2 \tau_{\theta z} = H_4 S_{\theta z}/D(s) \tag{173}$$

Formulas for the strains are obtained in a similar manner.

$$r^2 \varepsilon_r = H_1 R_r/D(s) \tag{174}$$

$$r^2 \varepsilon_\theta = H_1 R_\theta/D(s) \tag{175}$$

$$r^2 \varepsilon_z = H_1 R_z/D(s) \tag{176}$$

$$r^2 \gamma_{r\theta} = H_3 R_{r\theta}/D(s) \tag{177}$$

$$r^2 \gamma_{rz} = H_2 R_{rz}/D(s) \tag{178}$$

$$r^2 \gamma_{\theta z} = H_4 R_{\theta z}/D(s) \tag{179}$$

We can also solve problems specified by the boundary conditions

$$\sigma_r = 0, \quad r = a \tag{180}$$

$$\tau_{r\theta} = \tau_o \cos(n\theta) \sin[s(z - ct)], \, r = a \tag{181}$$

$$\tau_{rz} = 0, \quad r = a \tag{182}$$

and

$$\sigma_r = 0, \quad r = a \tag{183}$$

$$\tau_{r\theta} = 0, \quad r = a \tag{184}$$

$$\tau_{rz} = \tau_o \cos(n\theta) \sin[s(z - ct)] \tag{185}$$

It is assumed the outside surface is stress-free according to Eqs. (155)-(157). The R_{ij} and S_{ij} functions must be derived for each case.

Formulas for the response to a traveling step function of pressure are obtained by writing the stresses and strains in terms of Fourier integrals. In place of Eq. (152) we write

$$\sigma_r = \sigma_o \cos(n\theta)\left\{ \frac{1}{2} + \frac{1}{\pi} \int_0^\infty \frac{\sin[s(z - ct)]}{sD(s)} ds \right\}, \quad r = a, \quad (186)$$

Then

$$\sigma_r = \sigma_o \cos(n\theta), \quad z < ct \quad (187)$$

$$\sigma_r = \frac{1}{2} \sigma_o \cos(n\theta), \quad z = ct \quad (188)$$

$$\sigma_r = 0, \quad z > ct \quad (189)$$

The term

$$\sigma_r = \frac{1}{2} \sigma_o \cos(n\theta), \quad r = a \quad (190)$$

leads to elementary solutions obtained by evaluating the corresponding Fourier integral at the origin. The number of terms depends in part on the multiplicity of the zero at the origin of the complex s plane[*].

$$r\sigma_r = \frac{1}{\pi}\sigma_o \cos(n\theta) \int_0^\infty \frac{\sin[s(a - ct)]}{sD(s)} ds \quad (191)$$

leads to Fourier integrals involving functions occurring on the right hand side of Eqs. (175) - (184). We have

$$\sigma_r = \frac{1}{\pi} \cos(n\theta) \int_0^\infty \frac{\sin[s(x - ct)]}{sD(s)} S_r ds \quad (192)$$

[*]Appendix A. These elementary solutions can be expressed in terms of zonal harmonics.

$$\sigma_\theta = \frac{1}{\pi} \cos(n\theta) \int_0^\infty \frac{\sin[s(z-ct)]}{sD(s)} S_\theta \, ds \tag{193}$$

$$\sigma_z = \frac{1}{\pi} \cos(n\theta) \int_0^\infty \frac{\sin[s(z-ct)]}{sD(s)} S_z \, ds \tag{194}$$

$$\tau_{r\theta} = \frac{1}{\pi} \sin(n\theta) \int_0^\infty \frac{\sin[s(z-ct)]}{sD(s)} S_{r\theta} \, ds \tag{195}$$

$$\tau_{rz} = \frac{1}{\pi} \cos(n\theta) \int_0^\infty \frac{\sin[s(z-ct)]}{sD(s)} S_{rz} \, ds \tag{196}$$

$$\tau_{\theta z} = \frac{1}{\pi} \sin(n\theta) \int_0^\infty \frac{\cos[s(z-ct)]}{sD(s)} S_{\theta z} \, ds \tag{197}$$

The corresponding formulas for the stráins are

$$\varepsilon_r = \frac{1}{\pi} \cos(n\theta) \int_0^\infty \frac{\sin[s(z-ct)]}{sD(s)} R_r \, ds \tag{198}$$

$$\varepsilon_\theta = \frac{1}{\pi} \cos(n\theta) \int_0^\infty \frac{\sin[s(z-ct)]}{sD(s)} R_\theta \, ds \tag{199}$$

$$\varepsilon_z = \frac{1}{\pi} \cos(n\theta) \int_0^\infty \frac{\sin[s(z-ct)]}{sD(s)} R_z \, ds \tag{200}$$

$$\gamma_{r\theta} = \frac{1}{\pi} \sin(n\theta) \int_0^\infty \frac{\sin[s(z-ct)]}{sD(s)} R_{r\theta} \, ds \tag{201}$$

729

$$\tau_{rz} = \frac{2}{\pi} \cos(n\theta) \int_0^\infty \frac{\sin[s(z - ct)]}{sD(s)} R_{rz} \, ds \qquad (202)$$

$$\tau_{\theta z} = \frac{2}{\pi} \sin(n\theta) \int_0^\infty \frac{\cos[s(z - ct)]}{sD(s)} R_{\theta z} \, ds \qquad (203)$$

The total value of the stresses and strains is obtained by adding solutions to the problem defined by Eq. (174).

Solutions to problems involving other boundary conditions may be obtained in a similar manner. In certain cases the Fourier integrals will be divergent. In these cases the limits of integration should be taken between $-\infty$ and $+\infty$, and the Cauchy principal value calculated. The factor $2/\pi$ must be replaced by $1/\pi$.

VII. HARMONIC AND BIHARMONIC FUNCTIONS AS LIMITS OF WAVE FUNCTIONS

As the velocity of travel approaches zero, the wave functions tend to harmonic functions in the limit, as shown below. However, in general, a static problem requires biharmonic functions as well as harmonic functions for a complete solution*. A second limiting process involving an indeterminate quotient is required to extract the biharmonic functions from the wave functions.

We recall the basic equations of Part II.

$$\hat{u} = \nabla\phi + \nabla \times \hat{\psi} \qquad (5)$$

$$c_1^2 \nabla^2 \phi = \frac{\partial^2 \phi}{\partial t^2} \qquad (6)$$

$$c_2^2 \nabla^2 \hat{\psi} = \frac{\partial^2 \hat{\psi}}{\partial t^2} \qquad (7)$$

We find from Eqs. (19), (29), (30), (31), (32), and (23) that

---

*Problems involving pure shear, such as torsion of an axisymmetric solid, are exceptions. A scalar biharmonic function is required in problems involving a change in volume, since dilatation derived from a scalar harmonic function is zero.

730

$$\frac{\partial \psi}{\partial t^2} = - c^2 S^2 \phi \tag{204}$$

$$\frac{\partial^2 \hat{\psi}}{\partial z^2} = - c^2 S^2 \hat{\psi} \tag{205}$$

On letting $c \rightarrow 0$ we find

$$\nabla^2 \phi = 0 \tag{206}$$

$$\nabla^2 \hat{\psi} = 0 \tag{207}$$

where

$$\phi = [A_1 I_n(sr) + A_2 K_n(sr)]\cos(n\theta)\sin(sz) \tag{208}$$

$$\hat{\psi} = e_r[A_5 I_{n+1}(sr) + A_6 K_{n+1}(sr)]\cos(n\theta)\cos(sz) \tag{209}$$

$$- e_\theta[A_5 I_{n+1}(sr) + A_6 K_{n+1}(sr)]\cos(n\theta) \sin(sz)$$

$$+ \hat{e}_z[A_3 I_n(sr) + A_4 K_n(sr)]\sin(n\theta)\sin(sz)$$

The corresponding displacements are found by setting $c = 0$, $\beta_1 = 1$, $\beta_2 = 1$ in Eqs. (64) - (66). We can eliminate two of the A_i coefficients in the result by writing

$$A_7 = A_1 + A_3 \tag{210}$$

$$A_8 = A_2 + A_6 \tag{211}$$

$$A_9 = A_3 - A_5 \tag{212}$$

$$A_{10} = A_4 - A_6 \tag{213}$$

Then

$$ru = [A_7 n I_n(sr) + A_8 n k_n(sr) + A_9 sr I_{n+1}(sr) - A_{10} sr K_{n+1}(sr)]\cos(n\theta)\cos z \tag{214}$$

$$rv = [-A_7 n I_n(sr) - A_8 n K_n(sr) - A_9 sr I_{n+1}(sr) + A_{10} sr K_{n+1}(sr)]\sin(n\theta)\sin z \tag{215}$$

$$rw = [(A_7 - A_9)sr I_n(sr) - (A_8 + A_{10})sr K_n(sr)]\cos(n\theta)\cos z \tag{216}$$

We note that the six independent solutions for the displacements for the wave equation reduce to four when the velocity of travel becomes zero. Moreover, the displacements vanish if

$$A_i = 0, \quad i = 7,8,9,10. \tag{217}$$

To obtain additional solutions, let

$$A_i = 1/\beta_1 - \beta_2) \quad, \quad i = 1,2 \tag{218}$$

in Eqs. (217), (218), and (219). We define the functions

$$F_1 = [n I_n(\beta_1 sr) - n I_n(\beta_2 sr)]/(\beta_1 - \beta_2) \tag{219}$$

$$F_2 = [n K_n(\beta_1 sr) - n K_n(\beta_2 sr)]/(\beta_1 - \beta_2) \tag{220}$$

$$F_3 = [\beta_1 sr I_{n+1}(sr) - sr I_{n+1}(sr)(\beta_2 - sr)]/(\beta_1 - \beta_2) \tag{221}$$

$$F_4 = [\beta_1 sr K_{n+1}(\beta_1 sr) - sr K_{n+1}(\beta_2 sr)]/(\beta_1 - \beta_2) \tag{222}$$

$$F_5 = [\beta_2 sr I_{n+1}(\beta_2 sr) - sr I_{n+1}(\beta_2 sr)]/(\beta_1 - \beta_2) \tag{223}$$

$$F_6 = [\beta_2 sr K_{n+1}(\beta_2 sr) - sr K_{n+1}(\beta_2 sr)]/(\beta_1 - \beta_2) \tag{224}$$

$$F_7 = [sr I_n(\beta_1 sr) - \beta_2 sr I_n(\beta_2 sr)]/(\beta_1 - \beta_2) \tag{225}$$

$$F_8 = [sr K_n(\beta_1 sr) - \beta_2 sr K_n(\beta_2 sr)]/(\beta_1 - \beta_2) \tag{226}$$

On referring to Eqs. (64), (65), and (66) we find

$$ru = [\beta_1(F_1 + F_3) + \beta_2(F_2 - F_4)]\cos(n\theta)\sin[s(z - ct)] \tag{227}$$

$$rv = [-\beta_1(F_1 + F_3) + \beta_2(F_2 + F_6)]\sin(n\theta)\sin[s(z - ct)] \tag{228}$$

$$rw = [\beta_1 F_1 - \beta_2 F_8]\cos(n\theta)\cos[s(z - ct)] \tag{229}$$

Each of the F_i functions has the indeterminate form 0/0 when $c = 0$, $\beta_1 = 1$, $\beta_2 = 1$; this is obviously true also for the displacements. The limits of these indeterminate forms can be found by the ordinary rules of calculus. When the velocity c is small we have

$$1 - \beta_1 \sim \frac{1}{2}\alpha_1^2 \quad, \quad 1 - \beta_2 \sim \frac{1}{2}\alpha_2^2 \quad. \tag{230}$$

and

$$\lim_{c \to 0} \frac{1 - \beta_1}{1 - \beta_2} = \frac{\mu}{\lambda + 2\mu} \tag{231}$$

on referring to Eqs. (2), (3), (22), (23), (27), and (28). The limits of the F_i functions can be found by using two terms of Taylor's series:

$$I_n(\beta_1 sr) = I_n(sr) + (\beta_1 - 1)sr I_n'(sr) + \delta(\beta_1 - 1)^2 \tag{232}$$

$$K_n(\beta_1 sr) \sim K_n(sr) + (\beta_1 - 1)srK_n'(sr) + 6(\beta_1 - 1)^2 \qquad (233)$$

$$I_{n+1}(\beta_1 sr) = I_{n+1}(sr) + (\beta_1 - 1)srI_n'(sr) + 6(\beta_1 - 1)^2 \qquad (234)$$

$$K_{n+1}(\beta_1 sr) = K_{n+1}(sr) + (\beta_1 - 1)srK_n'(sr) + 6(\beta_1 - 1)^2 \qquad (235)$$

Additional formulas are obtained by substituting β_2 for β_1.

As c approaches zero we find

$$\lim F_1 = nsrI_n'(sr) \qquad (236)$$

$$\lim F_2 = nsrK_n'(sr) \qquad (237)$$

$$\lim F_3 = -\frac{\mu}{\lambda + \mu} srI_{n+1}(sr) + srI_{n+1}'(sr) \qquad (238)$$

$$\lim F_4 = -\frac{\mu}{\lambda + \mu} srK_{n+1}(sr) + srK_{n+1}'(sr) \qquad (239)$$

$$\lim F_5 = -\frac{\lambda + 2\mu}{\lambda + \mu} srI_n I_{n+1}(sr) \qquad (240)$$

$$\lim F_6 = -\frac{\lambda + 2\mu}{\lambda + \mu} srK_{n+1}(sr) \qquad (241)$$

$$\lim F_7 = \frac{\lambda + 2\mu}{\lambda + \mu} srI_n(sr) + srI_n'(sr) \qquad (242)$$

$$\lim F_8 = \frac{\lambda + 2\mu}{\lambda + \mu} srK_n(sr) + srK_n'(sr) \qquad (243)$$

The derivatives may be eliminated by means of Eqs. (60) - (63). The displacements corresponding to these limits are

$$ru = \lim_{c \to 0} [\beta_1(F_1 + F_3) + \beta_2(F_2 - F_4)]\cos(n\theta)\sin[s(z - ct)] \qquad (244)$$

$$rv = \lim_{c \to 0} [- \beta_1(F_1 + F_3) + \beta_2(F_2 + F_6)]\sin(n\theta)\sin[s(z - ct)] \qquad (245)$$

$$rw = \lim_{c \to 0} [\beta_1 F_7 - \beta_2 F_8]\cos(n\theta)\cos[s(z - ct)] \qquad (246)$$

The total displacements due to static loading are obtained by adding these displacements to the displacements obtained from the harmonic potentials, Eqs. (217) - (219). We now have a total of six linearly independent solutions for the displacements. The strains can be derived from the displacements and the stresses follow immediately from Eqs. (156) and (151). Thus six independent stress formulas are obtained for meeting six boundary conditions of the type given by Eqs. (152) - (157) with c=0.

VIII. BIHARMONIC SCALAR AND VECTOR POTENTIALS FOR STATIONARY LOADS

It is possible to derive the displacements given by Eqs. (250) - (252) from vector and scalar potentials according to Eq. (5). Harmonic scalar and vector potentials are given by Eqs. (211) and (212). We now derive the additional biharmonic potentials required for Eqs. (250) - (252).

For the scalar potential, assume

$$\chi = r \frac{\partial \phi}{\partial r} \qquad (247)$$

Then

$$\frac{\partial \chi}{\partial r} = r \frac{\partial^2 \phi}{\partial r^2} + \frac{\partial \phi}{\partial r} \qquad (247a)$$

or

$$\frac{\partial \chi}{\partial r} = - \frac{1}{r} \frac{\partial^2 \phi}{\partial \theta^2} - r \frac{\partial^2 \phi}{\partial z^2} \qquad (247b)$$

since ϕ is a scalar harmonic function it follows, after some routine analysis, that'

Love, A.E.H., A treatise on the Mathematical Theory of Elasticity, Dover Publications, New York, 1944. See pages (274) - (277), especially Eqs. (86) and (87).

735

$$\nabla^2 \chi = - 2 \frac{\partial^2 \phi}{\partial z^2} \tag{248}$$

and

$$\nabla^4 \chi = 0 \tag{249}$$

Other scalar biharmonic functions are given by the Eqs. (8), (9), and (10)

$$\chi = r^2 \phi \tag{250}$$

$$\chi = (r \sin\theta)\phi \tag{251}$$

$$\chi = (r \cos\theta)\phi \tag{252}$$

$$\chi = z\phi \tag{253}$$

However, the biharmonic functions given by Eqs. (250) - (251) seem to be most closely related to scalar potentials for wave motion, as they can also be derived from a scalar wave function by a limiting process. We have for instance

$$\beta_1 = \sqrt{1 - c^2/c_1^2} \tag{254}$$

$$\phi_1 = \frac{1}{2} [A_1 I_n(\beta_1 sr) + A_2 K_n(\beta_1 sr)][\sin s(z + ct) + \sin[s(z-ct)] \tag{255a}$$

or

$$\times \cos(n\theta)$$

[8]Fung, G.C., Foundations of Solid Mechanics, Prentice Hall, Inc., Englewood Cliffs, NJ., Page 208.

[9]Neuber, H. Theory of Notch Stresses: Principles for Exact Stress Calculation. David Taylor Model Basin, Washington, D.C. Translation 74, Novermber 1945. See pages (25) and (128).

[10]Elder, A.S., Traveling and Stationary Loads on the Half Space, BRL Report, to be published. See section titled "Biharmonic Functions as Limits of Wave Functions."

$$\phi_1 = \frac{1}{2} \left[A_1 I_n(\beta_1 sr) + A_2 K_n(\beta_1 sr) \right] \sin(sz)\cos(sct)\cos(n\theta) \tag{255b}$$

This scalar potential represents two equal loads traveling with the same speed in opposite directions.

$$\frac{\partial \phi_1}{\partial s} = \frac{1}{2} \left[A_1 \beta_1 r I_n'(\beta_1 sr) + A_2 \beta_1 r K_n'(\beta_1 sr) \right] \left[\sin[s(z+ct)] + \sin[s(z-ct)]\cos(n\theta) \right.$$

$$\tag{256}$$

$$+ \frac{1}{2} \left[A_1 I_n(\beta_1 sr) + A_2 K_n(\beta_1 sr) \right]$$

$$\times \left[(z+ct)\cos s(z+ct) + (z-ct)\cos[(z+ct)]\cos(n\theta) \right.$$

$$\frac{\partial \phi_1}{\partial s} = \left[A_1 (\beta_1 r I_n'(\beta_1 sr) + A_2 \beta_1 r K_n'(\beta_1 sr) \right] \sin(sz)\cos(sct)\cos(n\theta)$$

$$+ \left[A_1 I_n(\beta_1 sr) + A_2 K_n(\beta_1 sr) \right] \left[z\cos(sz) \right] \cos(sct)\cos(n\theta) \tag{256a}$$

$$+ \left[A_1 I_n(\beta_1 sr) + A_2 K_n(\beta_1 sr) \right] \left[ct\sin(sz) \right] \sin(sct)\cos(n\theta)$$

On allowing c to approach zero, we find

$$\frac{\partial \phi_1}{\partial s} = \left[A_1 r I_n'(sr) + A_2 r K_n'(sr) \right] \sin(sz)(n\theta)$$

$$+ \left[A_1 z I_n(sr) + A_2 z K_n(sr) \right] \sin(sz)\cos(n\theta)$$

we also have

$$\chi = r \frac{\partial}{\partial r} \left[A_1 I_n(sr) + A_2 K_n(sr) \right] \sin(sz)\cos(n\theta) \tag{257a}$$

or

$$\chi = \left[A_1 sr I_n'(sr) + A_2 sr K_n'(sr) \right] \sin(sz)\cos(n\theta) \tag{257b}$$

which yields two terms in Eq. (256b) except for a factor s. The remaining two terms of (256b) corresponds to Eq. (253).

The biharmonic vector potential can be derived in a similar manner. We assume

737

$$\hat{\omega} = r \frac{\partial \hat{\psi}}{\partial r} \tag{258}$$

where

$$\hat{\omega} = \hat{e}_r \, \omega_r + \hat{e}_\theta \omega_\theta + \hat{e}_z \, \omega_z \tag{259}$$

Then

$$\omega_r = r \frac{\partial}{\partial r} \, \psi_r \tag{260}$$

$$\omega_\theta = r \frac{\partial}{\partial r} \, \psi_\theta \tag{261}$$

$$\omega_z = r \frac{\partial}{\partial r} \, \psi_z \tag{262}$$

We find as before

$$\frac{\partial}{\partial r} \, \omega_r = r \, \frac{\partial^2}{\partial r^2} \, \psi_r + \frac{\partial}{\partial r} \psi_r \tag{263}$$

with similar equations for ω_θ and ω_z. The second derivations are eliminated by using the three equations which result when the derivatives with respect to time are set equal to zero in Eqs. (11), (12), and (13). On referring to Eq. (8) we find

$$\frac{\partial}{\partial r} \, \omega_r = \frac{1}{r} \, \psi_r + \frac{2}{r} \, \frac{\partial}{\partial r} \, \psi_\theta - \frac{1}{r} \, \frac{\partial^2}{\partial \theta^2} \, \psi_r - r \, \frac{\partial^2}{\partial z^2} \, \psi_r \tag{264}$$

$$\frac{\partial}{\partial r} \, \omega_\theta = \frac{1}{r} \, \psi_\theta - \frac{2}{r} \, \frac{\partial}{\partial \theta} \, \psi_r - \frac{1}{r} \, \frac{\partial^2}{\partial \theta^2} \, \psi_\theta - r \, \frac{\partial^2}{\partial z^2} \, \psi_\theta \tag{265}$$

and

$$\frac{\partial}{\partial r} \, \omega_z = - \frac{1}{r} \, \frac{\partial^2}{\partial \theta^2} \, \psi_z - r \, \frac{\partial^2}{\partial z^2} \, \psi_z \tag{266}$$

We finally obtain

$$\nabla^2 \omega_r - \frac{1}{r^2} \omega_r + \frac{2}{r^2} \frac{\partial}{\partial \theta} \omega_\theta = -2 \frac{\partial^2}{\partial z^2} \psi_r \qquad (267)$$

$$\nabla^2 \omega_\theta - \frac{1}{r^2} \omega_\theta - \frac{2}{r^2} \frac{\partial}{\partial \theta} \omega_r = -2 \frac{\partial^2}{\partial z^2} \psi_\theta \qquad (268)$$

and

$$\nabla^2 \omega_z = -2 \frac{\partial^2}{\partial z^2} \psi_z \qquad (269)$$

Consequently -

$$\nabla^2 \hat{\omega} = -2 \frac{\partial^2 \hat{\psi}}{\partial z^2} \qquad (270)$$

and

$$\nabla^4 \hat{\omega} = 0 \qquad (271)$$

The biharmonic scalar and vector potentials are not independent, but are coupled through Naviers equation.

$$(\lambda + 2\mu)\nabla\phi + \mu\nabla\times\hat{\omega} = 0 \qquad (272)$$

or

$$\frac{\partial^2}{\partial z^2} [(\lambda + 2\mu)\nabla\phi + \mu\nabla\times\hat{\psi}] = 0 \qquad (273)$$

This equation is satisfied if

$$(\lambda + 2\mu) \nabla\phi + \mu\nabla\times\hat{\psi} = 0 \qquad (274)$$

or, in scalar form,

$$(\lambda + 2\mu) \frac{\partial \phi}{\partial r} + \mu \left(r \frac{\partial}{\partial \theta} \psi_z - \frac{\partial}{\partial z} \psi_\theta \right) = 0 \tag{275}$$

$$(\lambda + 2\mu) r \frac{\partial \phi}{\partial \theta} + \mu \left(\frac{\partial}{\partial z} \psi_r - \frac{\partial}{\partial r} \psi_z \right) = 0 \tag{276}$$

$$(\lambda + 2\mu) \frac{\partial \phi}{\partial z} + \mu \left(\frac{1}{r} \frac{\partial r}{\partial r} \psi_\theta - \frac{1}{r} \frac{\partial}{\partial \theta} \psi_r \right) = 0 \tag{277}$$

We use Case I as an example.

$$\phi = [A_1 I_n(sr) + A_2 K_n(sr)] \cos(n\theta) \sin(sz) \tag{278}$$

$$\psi_r = [A_5 I_{n+1}(sr) + A_6 K_{n+1}(sr)] \sin(n\theta) \cos(sz) \tag{279}$$

$$\psi_\theta = - [A_5 I_{n+1}(sr) + A_6 K_{n+1}(sr)] \cos(n\theta) \cos(sz) \tag{280}$$

$$\psi_z = [A_3 I_n(sr) + A_4 K_n(sr)] \sin(n\theta) \sin(sz) \tag{281}$$

Relations among the A_i components are obtained by substituting these scalar components into Eqs. (11) - (14) and carrying out the indicated analysis.

We finally obtain

$$\chi = \frac{1}{\lambda + 2\mu} [\beta_{11} sr I_n'(sr) + \beta_{12}(sr) K_n'(sr)] \cos(n\theta) \sin(sz) \tag{282}$$

$$\psi_r = \frac{1}{\mu} [\beta_{11} sr I_n'(sr) - \beta_{12} sr K_{n+1}'(sr)] \sin(n\theta) \cos(sz) \tag{283}$$

$$\psi_\theta = \frac{1}{\mu} [\beta_{11} sr I_{n+1}'(sr) + \beta_{12} sr K_{n+1}'(sr)] \cos(n\theta) \cos(sz) \tag{284}$$

$$\psi_z = \frac{1}{\mu} [-\beta_{11} sr I_n'(sr) + \beta_{12} sr K_n'(sr)] \sin(n\theta) \sin(sz) \tag{285}$$

where β_{11} and β_{12} are related linearly to the A_i coefficients. The derivatives may be eliminated by using standard formulas, so that the final result can be expressed in terms of trigonometric factors and Bessel functions of order n and n+1.

Thus we have a complete solution for static loading in terms of scalar and vector potentials. By contrast, Love's strain function uses a single biharmonic scalar potential based on the Galerkin vector. The discplacements in our analysis are given in terms of first partial derivatives of the potential functions, consistent with the Green-Lame formulation of wave motion, whereas Love's strain function expresses displacements as second derivatives of a scalar potential. The present analysis illustrates a logical connection between static and dynamic problems for the elastic deformation of a hollow cylinder.

IX. HELMHOLTZ THEORY

Helmholtz's theorem concerning resolution of a vector consists of two parts:

$$\hat{u} = \nabla\phi + \nabla\times\hat{\chi} \tag{286}$$

$$\nabla \cdot \hat{\chi} = 0 \tag{287}$$

The vector potential ψ of Eq. (5), as derived in the previous analysis, is generally not solenoid, as required by Eq. (287). A solenoidal vector is obtained by a gauge transformation, as outlined by McQuistan (11). In the course of McQuistan's analysis a Newtonian potential is used to solve Poisson's partial differential equation, and the proof is restricted to simply connected regions. Unfortunately a hollow cylinder is multiply connected and this proof does not apply. We solve Poisson's equation by separation of variables. We have three cases to consider:

1) $\hat{\psi}$ is a harmonic vector potential

2) $\hat{\psi}$ is a biharmonic vector potential

3) $\hat{\psi}$ is a vector wavefunction.

In each case we assume

$$\hat{\chi} = \hat{\psi} + \nabla\eta \tag{288}$$

where η is a scalar. Then

---

[11] McQuistan, Richmond B, *Scalar and Vector Fields, A Physical Intepretation*, John Wiley and Sons, Inc. New York, 1965. See pages 256-264.

$$\nabla \cdot \hat{\chi} = \nabla \cdot \hat{\psi} + \nabla \cdot \nabla \eta \qquad (289)$$

which, in view of Eq. (287), reduces to

$$\nabla^2 \eta = - \nabla \cdot \hat{\psi} \qquad (290)$$

Since the vector potential $\hat{\psi}$ has been calculated previously, Eq. (290) is Poisson's equation for the scalar η. In each case we have

$$\nabla \cdot \hat{\psi} = \frac{1}{r} \frac{\partial}{\partial r} (r\psi_r) + \frac{1}{r} \frac{\partial}{\partial \theta} \psi_\theta + \frac{\partial}{\partial z} \psi_z \qquad (291)$$

where

$$\hat{\psi} = \hat{e}_r \psi_r + \hat{e}_\theta \psi_\theta + \hat{e}_z \psi_z \qquad (292)$$

and $\hat{e}_r$, $\hat{e}_\theta$, and $\hat{e}_z$ are the unit vectors in cylindrical coordinates. For Case 1 we have

$$\psi_r = [A_5 I_{n+1}(sr) + A_6 K_{n+1}(sr)] \sin(n\theta)\cos(sz) \qquad (293)$$

$$\psi_\theta = - [A_5 I_{n+1}(sr) + A_6 K_{n+1}(sr)]\cos(n\theta)\cos(sz) \qquad (294)$$

$$\psi_z = [A_3 I_n(sr) + A_4 K_n(sr)]\sin(n\theta)\sin(sz) \qquad (295)$$

After some routine analysis we find

$$\nabla \cdot \hat{\psi} = [(A_3 + A_5)s I_n(sr) + (A_4 - A_6)s K_n(sr)]\sin(n\theta)\cos(sz) \qquad (296)$$

We use the semi-inverse method to solve Eq. (290), as a lucky guess may save considerable analysis. Assume

$$\eta = C [(A_3 + A_5) I_n'(sr) + (A_4 - A_6)K_n'(sr)]\sin(n\theta)\cos(sz) \qquad (297)$$

where C is an unknown constant.

Then

$$\nabla^2 n = 2 \, C \, s^2 [(A_3 + A_5) I_n(sr) + (A_4 - A_6) K_n(sr)] \sin(n\theta) \cos(sz) \quad (298)$$

On referring to Eqs. (290) and (291) we see that

$$C = -1/2s \quad (299)$$

and consequently

$$n = -\frac{1}{2s} [(A_3 + A_5) I_n'(sr) + (A_4 - A_6) K_n'(sr)] \sin(n\theta) \cos(sz) \quad (300)$$

The biharmonic vector, Case 2, may be treated in a similar manner. We have

$$\psi_r = [\beta_1 sr I_{n+1}'(sr) - \beta_2 sr K_{n+1}'(sr)] \sin(n\theta) \cos(sz) \quad (301)$$

$$\psi_\theta = - [\beta_1 sr I_{n+1}'(sr) - \beta_2 sr K_{n+1}'(sr)] \cos(n\theta) \cos(sz) \quad (302)$$

$$\psi_z = [- \beta_1 sr_n'(sr) + \beta_2 sr K_n'(sr)] \sin(n\theta) \sin(sz) \quad (303)$$

We find

$$\nabla \cdot \vec{\psi} = [\beta_1 s I_n(sr) + \beta_2 s K_n(sr)] \sin(n\theta) \cos(sz) \quad (304)$$

Hence

$$\nabla^2 n = - [\beta_1 s I_n(sr) + \beta_2 s K_n(sr)] \sin(n\theta) \cos(sz) \quad (305)$$

On preceeding as in the previous case, we find

$$n = -\frac{1}{2} [\beta_1 r I_n'(sr) + \beta_2 r K_n'(sr)] \sin(n\theta) \cos(sz) \quad (306)$$

This result is well known. If the right hand side of Poisson's equation is a harmonic function, biharmonic functions can be used to solve Poisson's Equation. For instance, if

$$\nabla^2 \eta = \phi, \tag{307}$$

and

$$\eta = -\frac{1}{2} r \frac{\partial \phi}{\partial r} \tag{308}$$

then

$$\nabla^2 \eta = \frac{\partial^2 \phi}{\partial z^2} \tag{309}$$

and we can readily prove that η is biharmonic.

For the wave function, Case 3, we have

$$\psi_r = [A_5 I_{n+1}(\beta_2 sr) + A_6 K_{n+1}(\beta_2 sr)]\sin(n\theta \cdot \cos[s(z - ct)] \tag{310}$$

$$\psi_\theta = -[A_5 I_{n+1}(\beta_2 sr) + A_6 K_n(\beta_2 sr)]\cos(n\theta)\cos[s(z - ct)] \tag{311}$$

$$\psi_z = [A_3 I_n(\beta_2 sr) + A_4 K_n(\beta_2 sr)]\sin(n\theta)\sin[s(z - ct)] \tag{312}$$

where ψ_r, ψ_θ, and ψ_z are components of the vector potential. We have shown that

$$\nabla \cdot \hat{\psi} = [(A_3 + \beta_2 A_5)s I_n(\beta_2 sr) + (A_4 - \beta_2 A_6)s K_n(\beta_2 sr)]\sin(n\theta)\cos[s(z - ct)] \tag{67}$$

Assume

$$\eta = C[(A_3 + \beta_2 A_5)s I_n(\beta_2 sr) + (A_4 - \beta_2 A_6)s K_n(\beta_2 sr)]\sin(n\theta)\cos[s(z - ct)] \tag{313}$$

where the constant C is unknown. Then

$$\nabla^2 \eta = -C\{(\beta_2 2 - 1)s^2 (A_3 + \beta_2 A_5)s I_n(\beta_2 sr) + (A_4 - \beta_2 A_6)K_n(\beta_2 sr)\}$$
$$\times \sin(n\theta)\cos[s(z - ct)] \tag{314}$$

But

$$\alpha_2^2 = 1 - \beta_2^2 \quad \text{so that}$$

$$C = -1/s^2\alpha_2^2 \tag{315}$$

and

$$\eta = -\frac{1}{s\alpha_2^2}\ [(A_3 + \beta_2 A_5)I_n(\beta_2 sr) + (A_4 - \beta_2 A_6)K_n(\beta_2 sr)]\sin(n\theta)\cos s(z-ct) \tag{316}$$

This result is not valid for $\alpha_2 = 0$, corresponding to zero velocity of travel.

Next we recompute the vector displacement by substituting $\hat{\chi}$ from Eq. (288) into Eq. (286). We find

$$u = \nabla\phi + \nabla\times\hat{\psi}+\nabla\times\nabla\eta \tag{317}$$

The third term on the right hand side of this equation is zero, so we recover Eq. (5) in the formula for the vector displacement.

$$\hat{u} = \nabla\phi + \nabla\times\hat{\psi} \tag{5}$$

Formulas for the stresses and strain, which involve partial derivatives of $\hat{u}$, remain unchanged.

The vector potential is given by

$$\hat{\omega} = \frac{1}{2}\ \nabla\times\hat{u} \tag{318}$$

or

$$\hat{\omega} = \frac{1}{2}\ \nabla\ \times \nabla\phi + \frac{1}{2}\ \nabla \times \nabla \times \hat{\psi} \tag{319}$$

But

$$\nabla \times \nabla\phi = 0 \tag{320}$$

and

$$\nabla \times \nabla \times \hat{\psi} = \nabla (\nabla \cdot \hat{\psi}) - \nabla^2 \hat{\psi} \tag{321}$$

Hence

$$\hat{\omega} = -\frac{1}{2} \nabla^2 \hat{\psi} \tag{322}$$

An analogous formula is found for the dilatation

$$e = \nabla \cdot \hat{u} \tag{323}$$

$$e = \nabla \cdot \nabla \phi + \nabla \cdot \nabla \times \hat{\psi} \tag{324}$$

But

$$\nabla \cdot \nabla \times \hat{\psi} = 0 \tag{325}$$

So that

$$e = \nabla^2 \phi \tag{326}$$

The results obtained by using $\hat{\chi}$ in place of $\hat{\psi}$ conform to all the requirements of Helmholtz theory provided the z axis is excluded from the region under consideration. The scalar potential η is determined so that Eq. (287) is satisfied and $\hat{\chi}$ is solenoidal. The potential $\hat{\chi}$ is a single valued function of θ since $\sin(n\theta)$ and $\cos(n\theta)$ are periodic.

The modified Bessel functions of the second kind, which occur in the analysis, have a logarithmic branch point at the origin of the complex s plane. However, this logarithm is eliminated from the integrands of the Fourier integrals, and the singularity at the origin is a pole. The integrands become single valued functions of the complex variable s, thus simplfying the application of residue theory. The proof requires additional analysis, and is given in Appendix A for dynamic problems.

IX. DISCUSSION AND CONCLUSIONS

In this paper we have formulated the equations governing elastic strains in a hollow cylinder due to stationary loads and loads moving with constant subsonic velocity. In addition, scalar and vector potentials are derived for stationary loads, showing the connection between static loading and the Green-

Lame formulation of wave motion. Six linearly independent solutions are obtained for the moving solutions, corresponding to the six boundary conditions on the cylindrical surfaces. However, when the velocity of travel is set equal to zero, two solutions are lost by confluence of the solutions and only four linearly independent solutions remain. Two additional solutions are obtained by a limiting method, so a total of six linearly independent solutions is available. Biharmonic scalar and vector potentials are also derived from which these two additional solutions can be calculated.

The distribution of characteristic roots is not yet determined. We speculate the roots in the first quadrant of the complex s plane lie between the imaginary axis* and a smooth curve passing through the complex eigenvalues for static loading. To verify this, the characteristic roots for a traveling load on a solid rod will be calculated first, as the calculations should be relatively simple, before investigating the eigenvalues for a hollow cylinder.

The planned programming will follow the general pattern developed for static loading-of a hollow cylinder, but simplified and streamlined to expedite the calculations. Each type of loading will be considered separately. Axisymmetric loading will be considered first as an extention of our thick walled cylinder analysis.

The analysis in Parts I - VIII is based on the work of Herrmann and his associates, in which the vector potential ψ is not required to be solenoidal. In order to conform to the classical Helmholtz theory, a new vector solenoidal potential χ is derived. The previously derived formulas for the displacements, strains, and stresses are not changed. The formula for the vector rotation is simplified, and becomes the vector counterpart of the scalar formula for the dilatation.

---

*Free vibrations of a hollow cylinder lead to real values of ω, the circular frequency, and real eigenvalues when the eigenvalues are expressed in Bessel functions of the first kind, provided ω is not too large. Pure imaginary eigenvalues arise when modified Bessel functions are used.

REFERENCES

1. Gurtin, M.E., Elasticity, Enc. of Phys., Volume VI a/2, Mechanics II, Springer Verlag, New York, 1972. See pages 212-214.

2. Armenakas, A.E. Herrmman, G., and Gazis, D.C. Free Vibrations of Circular Cylindrical Shells, Pergamman Press, New York, 1969.

3. Elder, A.S. and Zimmerman, K.L., Stresses in a gun Tube produced by Internal Pressure and Shear, BRL Memorandum Report No. 2495, June 1975. AD #A012765.

4. Taylor, L., Vibrations of Solids and Structures ᵘ ᵘer Moving Loads, Noordhoff International Publishing, Gronigen The Netherlands, 1972. See Chapter 17 and Reference 203.

5. Chou, P.C. and Pagano, N.J., Elasticity: Tensor, Dyadic, and Engineering Approaches, D. Van Nostrand Company, Inc. Princeton, 1967, pages 245-265.

6. Pao, Y and Mow, C., Diffraction of Elastic Waves and Dynamic Stress Concentrations, Crane Russak, Publishers, 1971. See pages 218 ff.

7. Love, A.E.H., A Treatise on the Mathematical Theory of Elasticity, Dover Publications, New York, 1944. See pages (274) - (277), especially Eqs. (66(and (67).

8. Fung, G.C., Foundations of Solid Mechanics, Prentice Hall, Inc., Englewood Cliffs, NJ., Page 208.

9. Neuber, H. Theory of Notch Stresses: Principles for Exact Stress Calculation. David Taylor Model Basin, Washington, D.C. Translation 74, November 1945. See pages (25) and (128).

10. Elder, A.S., Traveling and Stationary Loads on the Half Space, BRL Report, to be published. See section titled "Biharmonic Functions as Limits of Wave Functions."

11. McQuistan, Richmond B, Scalar and Vector Fields, A Physical Intepretation, John Wiley and Sons, Inc. New York, 1965. See pages 256-264.

12. Timoshenko, S. and Goodier, J.N., Theory of Elasticity Second Edition, McGraw Hill Book Company, Inc., page 385.

A1 Hobson, E.W., The Theory of Spherical and Ellipsoidal Harmonics, University Press, Cambridge, 1931. See Chapter IV.

A2 Dougall, John, An Analytical Theory of the Equilibrium of an Isotropic Elastic Rod of Circular Cross Section, Transactions of the Royal Society of Edinburg, Vol XLIX, Part IV, (No. 17), pages 895-978). (1913).

A3 Abramowitz, M, and Stegun, S.A., Editors. Handbook of Mathematical Functions, with Formulas, Graphs, and Mathematical Tables. U.S. Department of Commerce, Applied Mathematic Series No. 55, 1964. See Eq. (9.6.11), page 375.

REFERENCES (continued)

A4 Elder, A.S. and Zimmerman, K.L., "Stresses in a Gun Tube Produced by Internal Pressure and Shear". BRL Memorandum Report No. 2495, June 1975.

APPENDIX A

QUASI-STATIC SOLUTIONS OF THE WAVE EQUATION

APPENDIX A

QUASI-STATIC SOLUTIONS OF THE WAVE EQUATION

Stresses given in Part V of this report have the generic form

$$\sigma = G(\theta, r, z) + F(\theta, r, z) \tag{A1}$$

where $G(\theta, r, z)$ is the limiting form of the stress at a great distance from the discontinuity in loading and $F(\theta, r, z)$ is a Fourier integral giving the local effects of this discontinuity. Both solutions can be obtained from scalar and vector wave functions. However, $G(\theta, r, z)$ is of a simpler type, and can be obtained from a scalar harmonic function in the independent variables θ, r, $(z-ct)/\beta_1$ and a vector harmonic function in the variables θ, r, $(z-ct)/\beta_2$. These solutions can be expanded in power series in the variable $(z-ct)$; logarithmic solutions may also occur. Exponentially decaying terms do not occur, so the stresses given by $G(\theta, r, z)$ persist at considerable distances.

The scalar wave function is a solution of

$$c_1^2 \nabla^2 \phi = \frac{\partial^2 \phi}{\partial t^2} \tag{A2}$$

where c_1 is the dilatational wave speed. If $\phi[\theta, r, (z-ct)/\beta_1]$ is a scalar wave function, then $\phi[\theta, r, z/\beta_1]$ is a scalar harmonic function. We have in expanded form

$$c_1^2 \left[\frac{\partial^2 \phi}{\partial r^2} + \frac{1}{r} \frac{\partial \phi}{\partial r} + \frac{1}{r^2} \frac{\partial^2 \phi}{\partial \theta^2} + \frac{\partial^2 \phi}{\partial z^2} \right] = \frac{\partial^2 \phi}{\partial t^2} \tag{A2b}$$

We note that

$$\frac{\partial^2 \phi}{\partial t^2} = c^2 \frac{\partial^2 \phi}{\partial z^2} \tag{A3}$$

so that

$$c_1^2 \left[\frac{\partial^2 \phi}{\partial r^2} + \frac{1}{r} \frac{\partial \phi}{\partial r} + \frac{1}{r^2} \frac{\partial^2 \phi}{\partial \theta^2} \right] + [c_1^2 - c^2] \frac{\partial^2 \phi}{\partial z^2} = 0 \tag{A4}$$

But

$\beta_1^2 = (c_1^2 - c^2)/c_1^2$. We define

$$\zeta_1 = z/\beta_1 \qquad\qquad (A5)$$

Then

$$\frac{\partial^2 \phi}{\partial r^2} + \frac{1}{r}\frac{\partial \phi}{\partial r} + \frac{1}{r^2}\frac{\partial^2 \phi}{\partial \theta^2} + \frac{\partial \phi}{\partial \zeta_1^2} = 0 \qquad\qquad (A6)$$

Analysis of the vector potential yields similar results. If $\hat{\psi}[\theta, r, (z-ct)/\beta_2]$ is a solution of the vector wave equation

$$c_2^2 \nabla^2 \hat{\psi} = \frac{\partial^2 \psi}{\partial t^2} \qquad\qquad (A7)$$

then $\hat{\psi}[\theta, r, z/\beta_2]$ is a solution of the vector harmonic equation

$$\nabla^2 \hat{\psi} = 0 \qquad\qquad (A8)$$

where c_2 is the velocity of the shear wave and $\beta_2^2 = (c_2^2 - c^2)/c_2^2$.

We assume that

$$0 < c < c_2 \qquad\qquad (A9)$$

in the preceeding analysis.

The finite series for $G(\theta, r, z-ct)$ can be derived from harmonic scalar potentials in the variables θ, r, z/β_1 and the vector harmonic potentials in the variables in the θ, r, z/β_2. It is sufficient to consider scalar and vector harmonic functions in the variables θ, r, z, as the required potentials in terms of θ, r, $z-ct$) can be obtained by appropriate changes in the independent variable z.

We consider the scalar form of Laplaces equation in detail. We have

752

$$\frac{\partial^2 \phi}{\partial r^2} + \frac{1}{r} \frac{\partial \phi}{\partial r} + \frac{1}{r^2} \frac{\partial^2 \phi}{\partial \theta^2} + \frac{\partial^2 \phi}{\partial z^2} = 0 \qquad \text{(A10)}$$

We assume

$$\phi = F \sin n\theta \qquad \text{(A11)}$$

then

$$\frac{\partial^2 F}{\partial r^2} + \frac{1}{r} \frac{\partial F}{\partial r} - \frac{n^2 F}{r^2} + \frac{\partial^2 F}{\partial z^2} = 0 \qquad \text{(A12)}$$

The function

$$F_o = (A_o + A_1 \log r)(1 + \beta_1 z) \qquad \text{(A13)}$$

is an obvious solution when $n = 0$. For $r > 0$ we have solutions of the type

$$F = (A_o r^{-n} + A_1 r^n)(1 + \beta_1 z) \qquad \text{(A14)}$$

The general separable solutions involve Bessel and trignometric functions. We require non separable solutions in ascending powers of z. Both positive and negative powers of r are required in order to satisfy boundary conditions at the inner and outer cylindrical surfaces. The required harmonic function can be obtained by expressing spherical harmonic in terms of cylindrical coordinates and rearranging terms in ascending powers of z, references (A1) and (A2).

These potentials can be obtained in an elementrary manner by assuming

---

A1Hobson, E.W., *The Theory of Spherical and Ellipsoidal Harmonics, University Press, Cambridge, 1931. See Chapter IV.*

A2Timoshenko, S. and Goodier, J.N., *Theory of Elasticity, McGraw Hill Book Company, 1951. The fourth order harmonic* ϕ_u *given on page 348 occurs in the torsion problem. Details will be described in a forthcoming BRL Report.*

$$F_k = G_o + z^2 G_2 + z^4 G_4 + \ldots \tag{A14a}$$

or

$$F_{k+1} = z G_1 + z^3 G_3 + z^5 G_5 \ldots \tag{A14b}$$

where

$$G_i = A r^k + B r^{-k}, \quad i = 0, 1 \tag{A15}$$

The remaining G_i functions, which are also functions of r alone, can be obtained recursively from the formula

$$\frac{\partial^2 G_i}{\partial r^2} + \frac{1}{r} \frac{\partial G_i}{\partial r} - \frac{n^2}{r^2} G_i = (i+2)(i+1) G_{i+2} \tag{A16}$$

which is obtained by substituting the preceding expressions for F_k into Eq. (A10), carrying out the indicated operations, and equating the successive powers of z to zero.

As an example, set

$$n = 0, \quad k = 4, \quad A = 3, \quad B = 3 \tag{A17}$$

We find

$$F_k = 3r^4 - 24r^2 z^2 + 8z^4 + 3r^{-4} - 24r^{-6} z^2 + 8r^{-8} z^4 \tag{A18}$$

The potential given by the first line can be used in the analysis of torsional loads and differs only by a constant from the potential ϕ_4 given in reference 12, page 348.

Next we consider the contribution of the Fourier integral to the total solution. We have either

$$F_s(\theta, r, z) = \sin n\theta \int_{-\infty}^{\infty} \frac{N_\sigma(r,s)}{D(s)} \frac{\sin[s(z-ct)]}{s} \, ds \tag{A19a}$$

754

or

$$F_c(\theta, r, z) = \cos n\theta \int_{-\infty}^{\infty} \frac{N_\sigma(r,s)}{D(s)} \frac{\sin s \; s(z-ct)}{s} \, ds \tag{A19b}$$

for stresses which are odd in z. The cosine replaces the sine under the integral sign if the stress is even in z. For values of z which are not too small we calculate F_s or F_c by the theory of residues, which is validated in cases of interest by Jordan's lemma. If z>ct we use a contour in the upper half plane, indented at the origin of the complex s plane. If z<ct we use the corresponding contour in the lower half plane. The complex variable theory follows suggestions in a landmark paper by Dougall (A2). Dougall uses an entirely different set of potentials to calculate the displacements and strains, however, his remarks on the nature and distribution of the characteristic roots are still valid.

It is obvious the characteristic functions for the solid rod do not have a branch point at the origin of the complex s plane, since only ordinary or modified Bessel functions of the first kind, are involved. These functions are analytic in the entire complex plane with the exception of essential singularities of exponential type at infinity. A detailed analysis is required for the hollow cylinder, since functions of the first and second kind are both required in order to satisfy boundary conditions at the inner and outer cylindrical surfaces. Bessel functions of the second kind have a logarithmic singularity at the origin, plus a finite Laurent series in the case of functions of integral orders greater than zero. We must show the characteristic functions do not have a branch point at the origin; multiple poles will in general occur due to the reciprocal powers in the Laurent series.

To this end, we write D(s) in extended form. We have from Eq. (164)

$$D(s) = \begin{vmatrix} S_{1,1}(a) & S_{1,2}(a) & S_{1,3}(a) & S_{1,4}(a) & S_{1,5}(a) & S_{1,6}(a) \\ S_{4,1}(a) & S_{4,2}(a) & S_{4,3}(a) & S_{4,4}(a) & S_{4,5}(a) & S_{4,6}(a) \\ S_{5,1}(a) & S_{5,2}(a) & S_{5,3}(a) & S_{5,4}(a) & S_{5,5}(a) & S_{5,6}(a) \\ S_{1,1}(b) & S_{1,2}(b) & S_{1,3}(b) & S_{1,4}(b) & S_{1,5}(b) & S_{1,6}(b) \\ S_{4,1}(b) & S_{4,2}(b) & S_{4,3}(b) & S_{4,4}(b) & S_{4,5}(b) & S_{4,6}(b) \\ S_{5,1}(b) & S_{5,2}(b) & S_{5,3}(b) & S_{5,4}(b) & S_{5,5}(b) & S_{5,6}(b) \end{vmatrix} \tag{164}$$

[A2] Dougall, John, An Analytical Theory of the Equilibrium of an Isotropic Elastic Rod of Circular Cross Section, Transactions of the Royal Society of Edinburg, Vol XLIX, Part IV, (No. 17), pages 895-978. (1913).

755

To eliminate the apparant branch point from the determinant D(s) we manipulate
the columns in pairs. The entries in D(s) are given in detail in Figures A1 and
A2. The entries in A1 are analytic functions of s. The enteries in A2 contain
a logarithmic singularity at the origin, which we eliminate algebraically. For
convenience assume that n is even. Then (A3)

$$K_n(sr) = \ln(s)I_n(sr) + \ln(r)I_n(sr) + L_n(sr) + P_n(sr) \qquad (A19)$$

where $L_n(sr)$ is a Laurent series having a pole of order n at the origin in the
complex s plane and $P_n(sr)$ is a power series in ascending powers of (sr), with
zero and positive powers only. Similarly

$$K_{n+1}(sr) = -\ln(s)I_n(sr) - \ln(r)I_n(sr) - L_{n+1}(sr) - P_{n+1}(sr) \qquad (A20)$$

Now multiply columns 1, 3, and 5 by $\ln(s)$ and subtract the results from columns
2, 4, and 6 respectively. We find the logarithm of s is eliminated. If n is
an odd integer we add instead of subtracting. In either case, we find D(s) is
an analytic function of s except for poles. A multiple pole generally occurs
at the origin.

It is believed the characterisitic roots are simple except at the origin.
Asymptotic methods may be used for characteristic roots of large modulus.
The smallest non zero root can be examined by expanding D(s) in a Laurent
series. Extensive calculations have shown the characteristic equations arising
from axisymmetric loading are simple for a large range of wall ratios (A4).
Moreover, a double zero leads to functions of the type R(r)×
[s(z-ct) sin s(z-ct) + cos s(z-ct)], which do **not** satisfy the wave equations.
Classical methods of determining the multiplicity of characteristic roots are
forbiddingly difficult when applied to the determinant D(s); hence detailed
analylis will be reserved for specific types of loading under consideration.

[A3] *Abramowitz, M, and Stegun, C.A., Editors. Handbook of Mathematical Functions,
with Formulas, Graphs, and Mathematical Tables. U.S. Department of Commerce,
Applied Mathematic Series No. 55, 1964. See Eq. (9.6.11), page 375.*

[A4] *Elder, A.S. and Zimmerman, K.L., "Stresses in a Gun Tube Produced by Internal
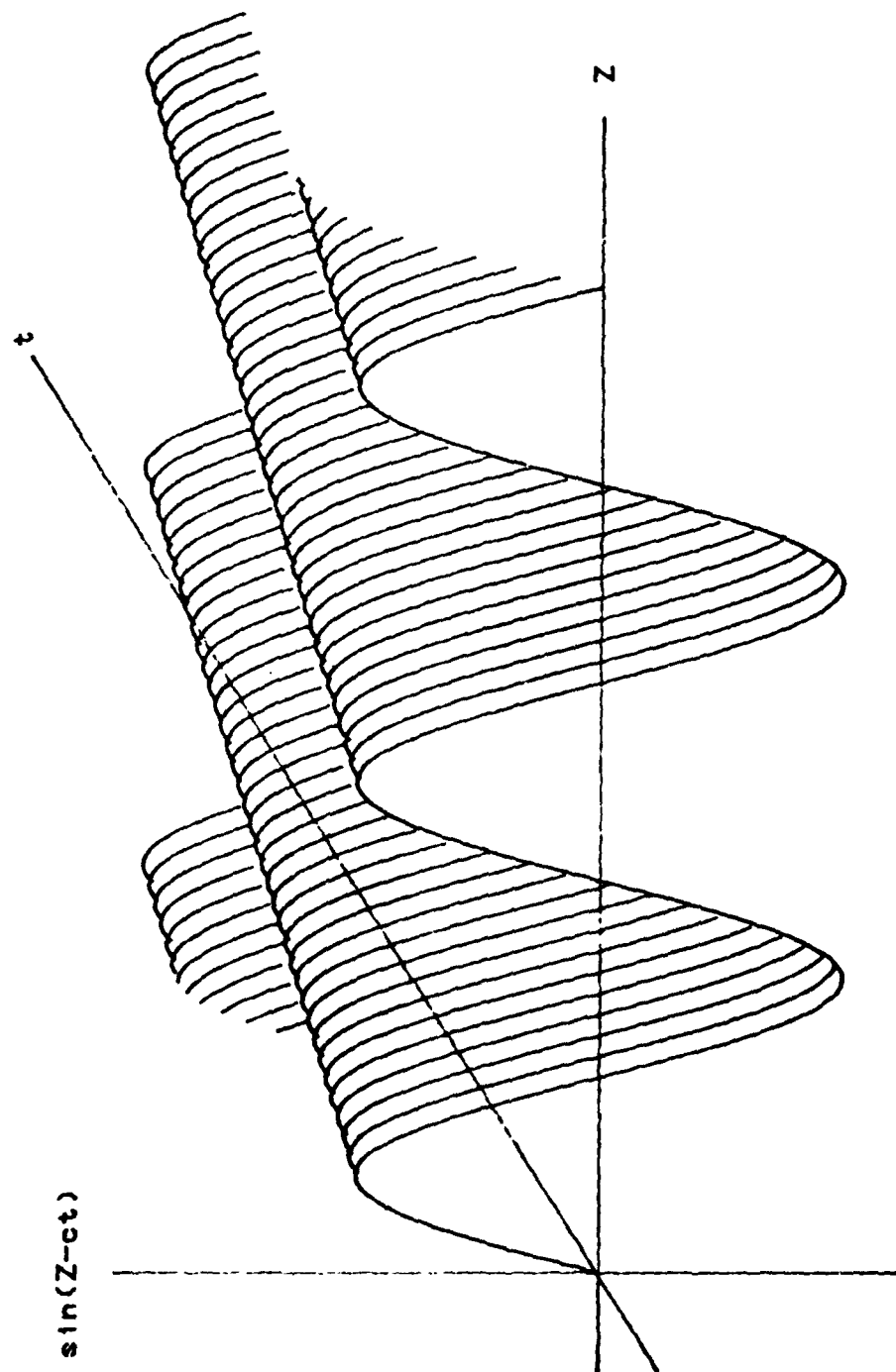Pressure and Shear". BRL Memorandum Report No. 2495, June 1975.*

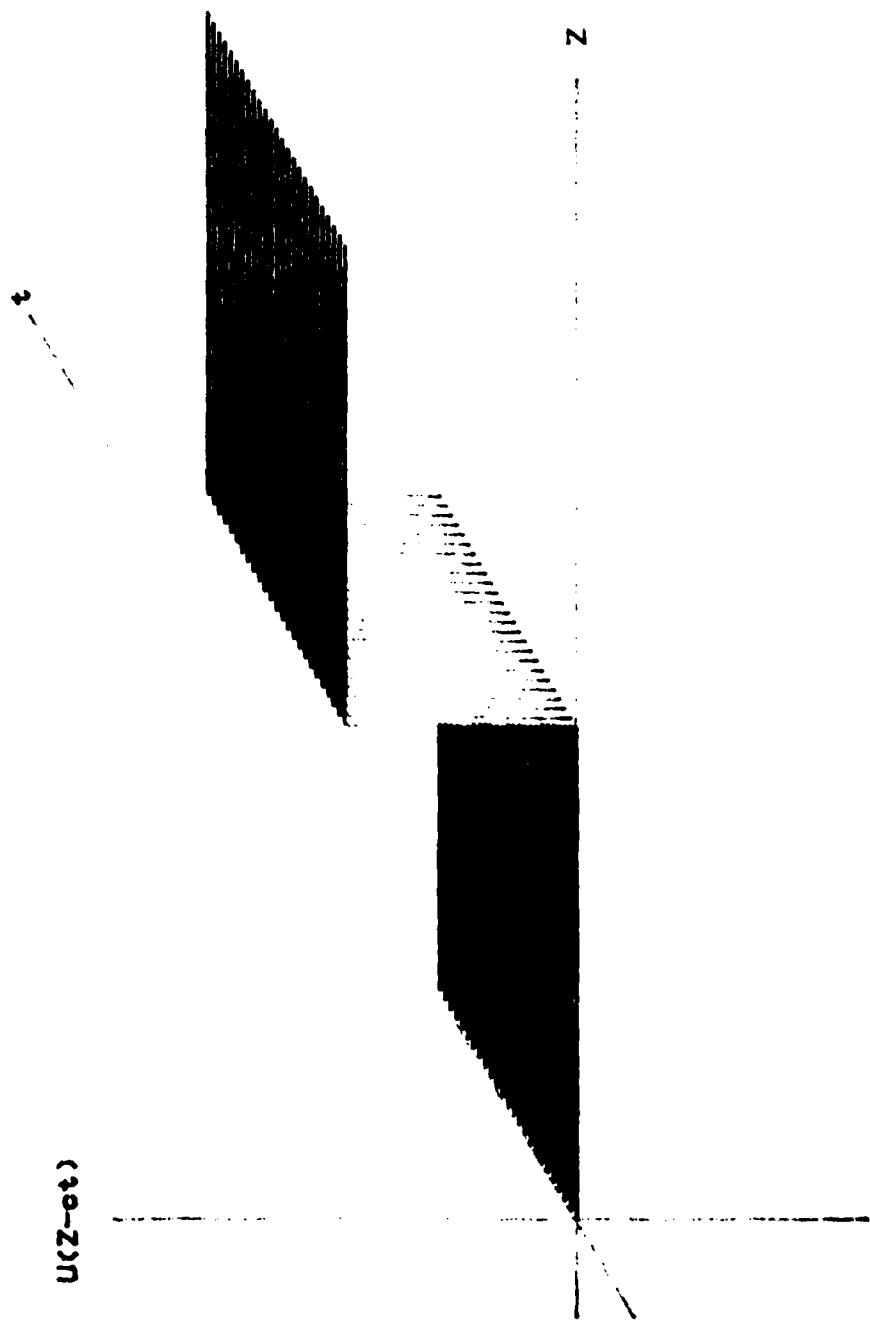Figure A1.   Sinusoidal Pressure Pulse in a Hollow Cylinder

757

Figure A2. Stepped Pressure Pulse in a Hollow Cylinder

758

REGISTRATION LIST

27th Conference of Army Mathematicians*

1. Chairman

   Dr. Jagdish Chandra, US Army Research Office,
   Research Triangle Park, North Carolina
   Autovon 935-3331

2. Host

   COL Jack m. Pollin, Department of Mathematics
   United States Military Academy, West Point, New York

3. COL David H. Cameron, Department of Mathematics,
   United States Military Academy, West Point, New York

4. Professor Roger Alexander, Department of Mathematical Sciences,
   Rensselaer Polytechnic Institute, Troy, New York
   9741110 - 518 270-6384

5. Dr. Jerry Bebernes
   University of Colorado (Dept of Math)
   Boulder, Colorado 80309
   303 492 7563

6. Prof J.L. Bona,
   Mathematics Research Center,
   University of Wisconsin-Madison
   610 Walnut Street
   Madison, Wisconsin
   600 263 2677

7. Prof. J. Buckmaster
   University of Illinois at Champaign-Urbana
   Champaign, Illinois
   217 333 1803

8. Dr. P.C.T. Chen
   Benet Weapons Laboratory, Watervliet Arsenal
   Watervliet, New York
   974 4287

*This registration list was compiled by Captain Gordon S. Dietrick.

759

9. Dr. Yu Chen
    Rutgers University
    P.O. Box 909
    Piscataway, NJ 08854
    201-932-4450

10. Dr. Shih C. Chu
    US Army Armament Research and Development Command
    Dover, New Jersey
    880 4168/2690

11. Prof John F. Clarke
    Cranfield Institute of Technology
    England

12. Professor Paul Clavin
    Universite de Provence
    France

13. Dr. Julian L. Davis
    U.S. Army Arament Research and Development Command
    Dover, New Jersey
    880 4168/2553

14. Prof Paul W. Davis
    Worcester Polytechnic Institute, MA
    617 753 1411

15. Dr. Stephen Davis
    Ballistic Research Laboratory
    Aberdeen Proving Ground, Maryland

16. Prof. Richard C. DiPrima
    Rensselaer Polytechnic Institute
    Troy, New York 12181
    518 270 6414

17. Dr. Donald Drew
    Army Research Office
    P.O. Box 12110
    Research Triangle Park, NC 27709

18. Prof Joseph E. Flaherty
    Department of Mathmatical Sciences
    Rensselaer Polytechnic Institute
    Troy, New York
    518 266 5907

19. Dr. Barry Fishburn
    US Army Armament Research and Development Command
    Dover, New Jersey

20. Prof. Bernard A. Fleishman
    Rensselaer Polytechnic Institute
    Troy, New York
    518-270-6347

21. Dr. Gerald S. Garfinkel
    U.S. Army White Sands Missle Range
    White Sands, New Mexico

Also
    Ft. Lee, VA
    687 2419

22. Dr. Robert Genter
    U.S. Army Armament Research and Development Command
    Dover, New Jersey

23. Dr. T.N.E. Greville
    Mathematics Research Center
    University of Wisconsin-Madison
    Madison, Wisconsin
    608 263 2657

24. Dr. Aaron Gupta
    Ballistic Research Laboratory
    Aberdeen Proving Ground, Maryland
    283 5574

25. Dr. Frank E. Grubbs
    Aberdeen Proving Ground, Maryland
    283 2682

26. Dr. J.M. Heimerl
    Ballistic Research Laboratory
    Aberdeen Proving Ground, Maryland
    301 278 4322

27. Dr. George W. Hoppe
    National Guard Bureau Comptroller Div.
    Pentagon, Room 2E 413
    Washington, D.C. 20310
    227 4409

28. Dr. M.A. Hussain
    Benet Weapons Laboratory
    Watervliet Arsenal
    Watervlier, New York

29. Prof Ashwani Kapila
    Rensselaer Polytechnic Institute
    Troy, New York
    518 270 6414

30. Prof. David R. Kassoy
    U of Colorado
    Mechanical Engineering Dept
    Boulder, CO 80309
    303 492 7694/7151

31. Dr. John H. Keefer
    Ballistic Research Laboratory
    Aberdeen Proving Ground, Maryland
    283-3685

32. Dr. A.R. Kiwan
    Ballistic Research Laboratory
    Aberdeen Proving Ground, Maryland
    283 3200/5534

33. Dr. Douglas E. Kooker
    Ballistic Research Laboratory
    Aberdeen Proving Ground, Maryland
    283-3200

34. Dr. Robert Launer
    US Army Research Office
    Research Triangle Park, NC 27709
    935 3331

35. Prof. Ting W. Lee
    Department of Mechanical and Aerospace Engineering
    Rutger, the State University
    New Brunswick, New Jersey
    201 932 3680

36. Prof. S.S. Lin
    Mathematics Research Center
    University of Wisconsin-Madison
    Madison, Wisconsin
    608 263 4659

37 - 38. Prof. G.S.S. Ludford and D.S. Stewart
    Cornell University
    Ithaca, New York
    607 256 5062

39. Dr. Stephen Margolis

40. Dr. Andrew Mark
    Ballistic Research Laboratory
    Aberdeen Proving Ground, Maryland   (283 5574)

41. Moshe Matalon
    Northwestern University
    Evanston, Illinois
    312 492 5585

42. Professor Bernard J. Matkowsky
    Northwestern University
    Evanston, Illinois
    312 492 5396

43. Prof John A. Nohel
    Mathematics Research Center
    Univeristy of Wisconsin-Madison
    Madison, Wisconsin
    608 263 4659

44. Dr. A.P. Parker
    Army Materials and Mechanics Research Center
    Watertown, Massachusetts
    955 3259

45. Prof. Aubrey B. Poore
    Colorado State University
    FT. Collins, CO 80523
    303 491-6326

46. Prof. W.G. Pritchard
    Mathematics Research Center
    University of Wisconsin-Madison
    Madison, Wisconsin
    608 263 2664

47. Dr. S.L. Pu
    Benet Weapons Laboratory
    Watervliet Arsenal
    Watervliet, New York
    518 226 5907

48. Prof. L.B. Rall
    Mathematics Research Center
    University of Wisconsin-Madison
    Madison, Wisconsin
    608 263 2664

49. Dr. Ronald L. Racicot
    Benet Weapons Lab
    Watervliet, New York 12189
    974 5606

50. Dr. Rodolfo R. Rosales
    MIT
    Cambridge, Mass 02139
    617 253 2784

51. Dr. Edward W. Ross
    U.S. Army Natick Research and Development Command
    Natick, Massachusetts
    955 2750

52. Dr. E.M. Schmidt
    Ballistic Research Laboratory
    Aberdeen Proving Ground, Maryland
    301 278 3786

53. Dr. James Schmitt
    Ballistic Research Laboratory
    Aberdeen Proving Ground, Maryland
    283 3313

54. Prof. I.J. Schoenberg
    Mathematics Research Center
    University of Wisconsin-Madison
    Madison, Wisconsin
    608 233 0742

55. Prof Ridgway Scott
    U of Michigan + MCR
    Madison, Wis. 53706.
    263 2663

56. Dr. Raymond Sedney
    Ballistic Research Laboratory
    Aberdeen Proving Ground, Maryland
    283 3816

57. Dr. C.N. Shen*
    Benet Weapons Laboratory
    Watervliet Arsenal
    Watervliet, New York
    518 266 5606

58. Dr. Norman Slagg
    US Army Armament Research and Development Command
    Dover, New Jersey
    880 6150

59. Dr. C.N. Shen*
    Benet Weapons Laboratory
    Watervliet Arsenal
    Watervliet, New York

60. Prof. Martin Sichel
    U of Michgan
    Ann Arbor, Mich 48109
    313 764 3388

61. Dr. T.E. Simkins
    Benet Weapons Laboratory
    Watervliet Arsenal
    Watervliet, New York
    974 5745

62. Dr. Robert E. Singleton
    ARO
    Research Triangle Park, NC 27709
    935 3331

63. Dr. Mitchell Smooke

---

*Listed twice.

64. Prof Ram Srivastav
    State University of New York-Stony Brook
    Stony Brook, New York

65. Dr. James Thompson
    U.S. Army Tank-Automotive Research and Development Command
    Warren, Michigan
    786 5780

66. Dr. Dennis M. Tracey
    Army Materials and Mechanics Research Center
    Watertown, Masschusetts
    955 3260/3492

67. Dr. Trybol
    Arberdeen Proving Ground, Maryland 21005

68. Dr. A. VanHarten
    Northwestern Univeristy
    492 3741

69. Dr. John D. Vasilakis*
    Benet Weapons Laboratory
    Watervliet Arsenal
    Watervliet, New York
    974 5811

70. Dr. Richard A. Weiss
    U.S. Army Waterways Experiment Station
    Vicksburgh, Mississippi

71. Prof. F.A. Williams
    Princeton University
    609 452 5271

72. Dr. Julian J. Wu
    Benet Weapons Laboratory
    Watervliet Arsenal
    Watervliet, New York
    974 5019

73. Dr. R. Yalamanchili
    U.S. Army Armament Research and Development Command
    Dover, New Jersey
    880 5677/2539

74. Prof. John Vasilakis*

75. Professor Norman Zabusky
    University of Pittsburgh
    Pittsburgh, Pennsylvania
    421 624-1464

---

*Listed twice.

REPORT DOCUMENTATION PAGE		READ INSTRUCTIONS BEFORE COMPLETING FORM
1. REPORT NUMBER ARO Report 82-1	2. GOVT ACCESSION NO. AD-A110109	3. RECIPIENT'S CATALOG NUMBER
4. TITLE (and Subtitle) TRANSACTIONS OF THE TWENTY-SEVENTH CONFERENCE OF ARMY MATHEMATICIANS		5. TYPE OF REPORT & PERIOD COVERED
		6. PERFORMING ORG. REPORT NUMBER
7. AUTHOR(s)		8. CONTRACT OR GRANT NUMBER(s)
9. PERFORMING ORGANIZATION NAME AND ADDRESS		10. PROGRAM ELEMENT, PROJECT, TASK AREA & WORK UNIT NUMBERS
11. CONTROLLING OFFICE NAME AND ADDRESS Army Mathematics Steering Committee on Behalf of the Chief of Research, Development and Acquisition		12. REPORT DATE January 1982
		13. NUMBER OF PAGES 766
14. MONITORING AGENCY NAME & ADDRESS(if different from Controlling Office) U. S. Army Research Office P. O. Box 12211 Research Triangle Park, NC 27709		15. SECURITY CLASS. (of this report) UNCLASSIFIED
		15a. DECLASSIFICATION/DOWNGRADING SCHEDULE

16. DISTRIBUTION STATEMENT (of this Report)

Approved for public release; distribution unlimited. The findings in this report are not to be construed as official Department of the Army position unless so designated by other authorized documents.

17. DISTRIBUTION STATEMENT (of the abstract entered in Block 20, if different from Report)

18. SUPPLEMENTARY NOTES

This is a technical report resulting from the Twenty-Seventh Conference of Army Mathematicians. It contains most of the papers in the agenda of this meeting. These treat various Army applied mathematical problems.

19. KEY WORDS (Continue on reverse side if necessary and identify by block number)

activation-energy asymptotics	difference schemes
combustion systems	beam vibrations
crack problems	finite element methods
weight functions	impact stress
elastic-plastic deformations	intermittent motion
flame propagation	Volterra equations
gun exhaust flows	stochastic processes
mach stem formation	deflagration and detonations
singular integral equations	comparison techniques
interpolation formulas	elastic strain problems
variational methods	Burgers equation
interval analysis	detonation phenomena
terrain microroughness	Euler equation
explosive blast loading	thermo explosions

DD FORM 1473 1 JAN 73   EDITION OF 1 NOV 65 IS OBSOLETE

DAT FILM